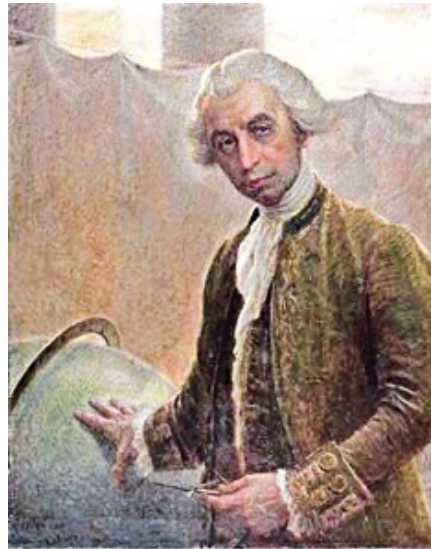




ОТЕН 2022 ОЛЕН 5055



RUDJER BOSKOVIC
(1711 - 1787)

PROCEEDINGS

TOPICS

AERODYNAMICS AND FLIGHT DYNAMICS
AIRCRAFT

WEAPON SYSTEMS AND COMBAT VEHICLES

AMMUNITION AND ENERGETIC MATERIALS

INTEGRATED SENSOR SYSTEMS AND ROBOTIC SYSTEMS

TELECOMMUNICATION AND INFORMATION SYSTEMS

MATERIALS AND TECHNOLOGIES

QUALITY, STANDARDIZATION, METROLOGY, MAINTENANCE AND EXPLOITATION



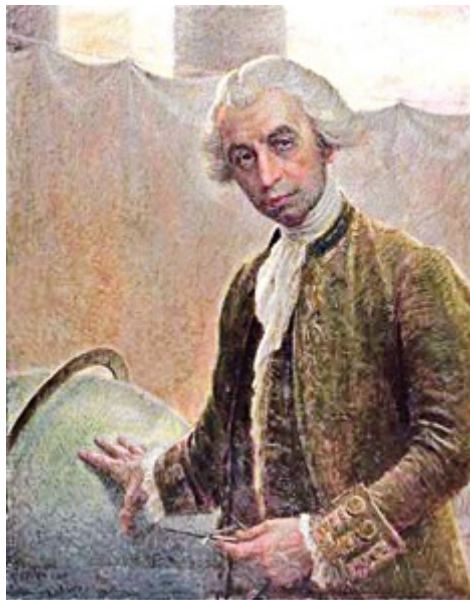
Belgrade, 13-14 October 2022
MILITARY TECHNICAL INSTITUTE
Belgrade, Serbia



10th INTERNATIONAL SCIENTIFIC CONFERENCE
ON DEFENSIVE TECHNOLOGIES

OTEH 2022

Belgrade, 13-14, October 2022



Rudjer Boskovic

(1711 – 1787)

He has left an indelible imprint in mathematics, astronomy, physics, optics, geodesy, architecture, archeology, pedagogy, philosophy, literature and diplomacy.

Publisher

The Military Technical Institute
Ratka Resanovića 1, 11030 Belgrade

Publisher's Representative

Col **Bojan Pavković**, PhD (Eng)

Editors

Col **Miodrag Lisov**, PhD (Eng)

Ljubica Radović, PhD (Eng)

Technical Editing

Liljana Kojićin

Printed by

The Military Technical Institute
Ratka Resanovića 1, 11030 Belgrade

CIP - Каталогизacija у публикацији
Народна библиотека Србије, Београд

NAUČNO-stručni skup iz oblasti odbrambenih
tehnologija (10 ; 2022 ; Beograd)
Proceedings [Elektronski izvor] / 10th
International Scientific Conference on
Defensive Technologies, OTEH 2020, Belgrade,
13-14 October 2022 ; [organized by] Military
Technical Institute, Belgrade ; [editors Miodrag
Lisov, Ljubica Radović]. - Belgrade : Military
Technical Institute, 2022 (Beograd : Military
Technical Institute) – 1 elektronski optički diske
(CD-ROM) ; 12 cm

Sistemska zahtevi: Nisu navedeni. - Nasl. sa
naslovne strane dokumenta. -
Bibliografija uz svaki rad.

ISBN 978-86-81123-85-0

1. Vojnotehnički institut (Beograd)
a) Војна техника - Зборници
b) Технички материјали – Зборници
c) Телекомуникациони системи - Зборници

10th INTERNATIONAL SCIENTIFIC CONFERENCE

ОТЕН 2022

ON DEFENSIVE TECHNOLOGIES



SUPPORTED BY

MINISTRY OF DEFENCE

www.mod.gov.rs

MINISTRY OF EDUCATION, SCIENCE
AND TECHNOLOGICAL DEVELOPMENT

www.mp.gov.rs



Organized by

MILITARY TECHNICAL INSTITUTE

1 Ratka Resanovića St., Belgrade 11000, SERBIA

www.vti.mod.gov.rs

ORGANIZING COMMITTEE

Nenad Miloradović, PhD Eng, Assisstant Minister for Material Resources, Serbia,
President of the Organizing Committee

col **Slavko Rakić**, PhD Eng, Head of Department for Defense Technologies, Serbia

col **Bojan Pavković**, PhD Eng, Director of the Military Technical Institute, Belgrade, Serbia

lt col gen **Goran Radovanović**, PhD Eng, Rector of the University of Defense, Serbia

brig gen **Milan Popović**, Department for Planning and Development GS SAF, Serbia

col **Slaven Vujić**, PhD Eng, Department for Strategic Planning, Serbia

col **Srdan Blagojević**, PhD Eng, Head of the Military Academy, Belgrade, Serbia

col **Miroslav Vukosavljević**, PhD, Head of the Military Medical Academy, Belgrade, Serbia

col **Nenko Brkljač**, PhD Eng, Director of the Technical Test Center, Belgrade, Serbia

Prof. **Jovanka Šaranović**, PhD, Strategic Research Institute MoD RS, Belgrade, Serbia

Marina Soković, PhD Eng, Assisstant Minister for Science, Ministry of Education Science and Technological Development, Serbia

Saša Lazović, PhD Eng, Assisstant Minister for Technological Development, Trasfer of Technology and Innovation System, Ministry of Education Science and Technological Development, Serbia

col **Dejan Đorđević**, PhD, Director of Military Geographical Institute, Belgrade, Serbia

Vladan Đokić, PhD, Rector of the University of Belgrade, Serbia,

Vladimir Popović, PhD Eng, Dean of the Faculty of Mechanical Engineering, Belgrade, Serbia

Dejan Gvozdić, PhD Eng, Dean of the Faculty of Electrical Engineering, Belgrade, Serbia

Petar Uskoković, PhD Eng, Dean of the Faculty of Technology and Metallurgy, Serbia

Srdan Kolaković, PhD Eng, Dean of the Faculty of Technical Sciences, Novi Sad, Serbia

Aleksandar Milašinović, PhD Eng, Dean of the Faculty of Mechanical Engineering, University of Banja Luka, Republic of Srpska

Danijela Milošević, PhD Eng, Dean of the Faculty of Technical Sciences, Čačak, University of Kragujevac, Serbia

Jugoslav Petković, Director of JUGOIMPORT - SDPR, Belgrade, Serbia

Jovanka Andrić, Director of "Krušik", Valjevo, Serbia

Zoran Stefanović, Director of "Sloboda", Čačak, serbia

Dobrosav Andrić, Director of "Prvi Partizan", Užice, Serbia

Stanoje Biočanin, Director of "Prva Iskra-namenska", Barič, Serbia

Mladen Petković, Director of "Zastava oružje", Kragujevac, Serbia

Saša Batočanin, Director of "Prva Petoletka - Namenska", **Trstenik**, Serbia

Vladimir Cizelj, Vlatacom Institute, Serbia

Dragan Kovačević, Director of IRITEL, Serbia

SECRETARIAT

Elida Vasiljević, MSc, secretary

Svetlana Ilić, MSc, assistant secretary

Jelena Pavlović, MSC

Nebojša Grebović, PhD

Liljana Kojičin

SCIENTIFIC COMMITTEE

Miodrag Lisov, PhD, Military Technical Institute, Serbia, President

Ljubica Radović, PhD, Military Technical Institute, Serbia

Col. **Ivan Pokrajac**, PhD, Military Technical Institute, Serbia

Zijah Burzić, PhD, Military Technical Institute, Serbia

Gretchihin Leonid Ivanovich, PhD, State College of Aviation, Minsk, Belarus

Taek Lyul Song, PhD, Hanyang University, South Korea

Evgeny Sudov, PhD, R&D Applied Logistic Centre, Moscow, Russia

Steven Berber, PhD, Auckland University, New Zealand

Srećko Stopić, PhD, RWTH Aachen University, Germany

Constantin Rotaru, PhD, Henri Coanda Air Force Academy, Brasov, Romania

Zbyšek Korecki, PhD, University of Defence, Brno, Czech Republic

Radi Ganev, PhD, University of structural engineering and architecture “Lyuben Karavelov”, Sofia, Bulgaria

Prof. **Tomaž Vuherer**, PhD Eng, Faculty of Mechanical Engineering, Maribor, Slovenia

Gorazd Kosec, PhD Eng, SIJ ACRONI, Jesenice, Slovenia

col **Ivan Vulić**, PhD, Eng, University of Defence, Beograd, Serbia

col **Boban Pavlović**, PhD, Eng, Military Academy, Beograd, Serbia

col **Dragan Trifković**, PhD, Eng, Military Academy, Beograd, Serbia

col **Damir Jerković**, PhD, Eng, Military Technical Institute, Beograd, Serbia

col **Aleksandar Kari**, PhD, Eng, Military Technical Institute, Beograd, Serbia

Biljana Marković, PhD, Eng, Faculty of Mechanical Engineering, Sarajevo, Bosnia and Herzegovina

Milan Tica PhD, Eng, Faculty of Mechanical Engineering, University of Banja Luka, Republic of Srpska (B&H)

Prof. **Fadil Islamović**, PhD, Eng, Rector University of Bihać, Bosnia and Herzegovina

Strain Posavljak, PhD, Eng, Faculty of Mechanical Engineering, Banja Luka, Republic Srpska

Jasmina Stevanović, PhD, Eng, Director of the Institute of Chemistry Technology and Metallurgy, Belgrade, Serbia

Branko Livada, PhD, Eng, Vlatacom Institute, Belgrade, Serbia

Milorad Obradović, PhD Eng, Vlatacom Institute, Belgrade, Serbia

Marija Samardžić, PhD Eng, Military Technical Institute, Serbia

Miloš Pavić, PhD Eng, Military Technical Institute, Serbia

col **Slobodan Simić**, PhD Eng, Military Academy, Belgrade, Serbia

col **Zlate Veličković**, PhD Eng, Military Academy, Belgrade, Serbia

Silva Dobrić, PhD, Military Medical Academy, Belgrade, Serbia

Srećko Manasijević, PhD Eng, Lola Institute, Belgrade, Serbia

Stevica Graovac, PhD Eng, Mihajlo Pupin Institute, Belgrade, Serbia

Nikola Zogović, PhD Eng, Mihajlo Pupin Institute, Belgrade, Serbia

Slobodan Savić, PhD Eng, Faculty of Engineering Sciences, Kragujevac, Serbia

Dragan Šešlija, PhD Eng, Faculty of Technical Sciences, Novi Sad, Serbia

Predrag Elek, PhD Eng, Faculty of Mechanical Engineering, Belgrade, Serbia

Aleksandar Simonović, PhD Eng, Faculty of Mechanical Engineering, Belgrade, Serbia

Jelena Svorcan, PhD Eng, Faculty of Mechanical Engineering, Belgrade, Serbia

Vencislav Grabulov, PhD Eng, IMS Institute, Belgrade, Serbia

Ivan Kostić, PhD Eng, Faculty of Mechanical Engineering, Belgrade, Serbia

col **Saša Bakrač**, PhD Eng, Military Geographical Institute, Belgrade, Serbia

col **Ljubiša Tomić**, PhD Eng, Technical Test Center, Belgrade, Serbia

col **Mihajlo Ranisavljević**, PhD Eng, Military Technical Institute, Serbia

lt col **Saša Brzić**, PhD Eng, Military Technical Institute, Serbia

Tihomir Kovačević, PhD Eng, Military Technical Institute, Serbia

Danica Bajić, PhD Eng, Military Technical Institute, Serbia

Biljana Ilić, PhD Eng, Military Technical Institute, Serbia

Bojana Fidanovski, PhD Eng, Military Technical Institute, Serbia

PREFACE

Military Technical Institute, the first and the largest military scientific-research institution in the Republic of Serbia with over 70 years long tradition, has been traditionally organizing the OTEH scientific conference, devoted to defense technologies. The Conference is supported by the Ministry of Defense and it takes place every second year.

Its aim is to gather scientists and engineers, researchers and designers, manufactures and university professors in order to exchange ideas and to develop new relationships.

The 10th International Scientific Conference OTEH 2022 is scheduled as follows: lecture on the occasion of “Rudjer Boskovic”, given by Prof. Slobodan Ninkovic, PhD, and two plenary lectures: “Artificial Intelligence in Function of Developing Innovation Products“, given by Prof. Miljan Vucetic, PhD Eng, and “High Performance Multi-functional Panels for Extreme Loading Events“ given by prof. Constança Rigueiro, PhD , as well as working sessions according to the Conference topics.

The papers which will be presented at the Conference have been classified into the following topics:

- Aerodynamics and Flight Dynamics
- Aircraft
- Weapon Systems and Combat Vehicles
- Ammunition and Energetic Materials
- Integrated Sensor Systems and Robotic Systems
- Telecommunication and Information Systems
- Materials and Technologies
- Quality, Standardization, Metrology, Maintenance and Exploitation.

The Proceedings contain 103 reviewed papers which have been submitted by the authors from 13 different countries. I would also like to emphasize that we have 14 papers with authors from abroad. The quality of papers accepted for publication achieved very high standard. I expect stimulated discussion on many topics that will be presented online, during two days of the Conference.

On behalf of the organizer I would like to thank all the authors and participants from abroad, as well as from Serbia, for their contribution and efforts which made this Conference possible and successful.

I would also like to thank the Ministry of Education, Science and Technological Development of the Republic of Serbia for its financial support.

Finally, dear guests and participants of the Conference, I would like to wish you a pleasant and successful work during the Conference. I am looking forward to see you again at the tenth Conference in Belgrade. All the best and stay healthy.

Belgrade, October, 2022

Col. Miodrag Lisov PhD Eng
President of the Scientific Committee
OTEH 2022



10th INTERNATIONAL SCIENTIFIC CONFERENCE
ON DEFENSIVE TECHNOLOGIES
OTEH 2022

Belgrade, Serbia, 13 – 14 October 2022



Plenary lectures

Constana Rigueiro



HIGH PERFORMANCE MULTI-FUNCTION PANELS FOR EXTREME LOADING EVENTS

DAMJAN CEKEREVAC

ISISE, University of Coimbra, Coimbra, damjan.cekerevac@uc.pt

CONSTANÇA RIGUEIRO

ISISE, Institute Polytechnic of Castelo Branco, Castelo Branco, constanca@ipcbr.pt

JOSÉ CAMPOS

LEDAP/ADAI, University of Coimbra, Coimbra, andrade.campos@dem.uc.pt

EDUARDO PEREIRA

ISISE, University of Minho, Guimarães, eduardo.pereira@civil.uminho.pt

ALDINA SANTIAGO

ISISE, University of Coimbra, Coimbra, aldina@dec.uc.pt

Abstract: *Global climate change has led to extreme events (high tides, storm surges and floods) resulting in severe consequences for coastal areas and communities. In addition, the increasing terrorist attacks on unprotected targets has resulted in efforts to develop infrastructure that acts as protective barriers. Resistant wall protection to blast requires a precise blast information. This paper aims to present the research already carried out by the authors related to metallic panels when subject to blast action.*

Keywords: *Blast, Impact, Sandwich pannels, Energy dissipation, Numerical modeling.*

1. INTRODUCTION

Sandwich panel solutions have been used for a wide range of applications, namely façade and roofing systems, temporary protection of public spaces or multi-purpose interior walls. These portable systems provide adaptability to the spaces; they are designed for safety and resistance to permanent, transient and accidental actions such as fire.

This article presents a framework of the research already done related to these metallic structural systems and their applicability. Since they have enormous potential to be multifunctional, able to protect critical infrastructures (as already been used by oil and gas sector) and mitigate the extreme climatic effects. The research under development pretends to propose a design of new kind of lightweight multi-layer sandwich structure with improved mechanical properties and high blast resistance.

2. LITERATURE REVIEW

Half of the world's population lives by the sea and three quarters of all large cities are located near large stretches of water. Coastal zones are a privileged place, where the population is concentrated and consequently activities such as commerce, industry and tourism are developed. Portugal is an example of this, with the intensive occupation of a large part of its coastal strip. According to the United Nations, between 1901 and 2010, the rise in

the average sea level occurred at an accelerated rate, the fastest in the last 2,800 years. This rise, associated with global warming and greenhouse gas emissions, leads to various effects: coastal erosion, flooding, contamination of fresh-water reserves, among others [1]. These changes lead to the exceptional occurrence of extreme meteorological phenomena such as storms and waves and have serious consequences for coastal areas and communities. To face the challenges of climate change effects it is necessary to provide sustainable solutions to protect coastal communities and infrastructures.

Regarding the solutions developed for coastal protection (onshore and foreshore) there is a great diversity; however these solutions do not present a wide consensus among experts about their efficiency, long-term durability, costs and influence on Habitat [3]. The development and implementation of coastal protection solutions should not only meet safety and sustainability criteria (minimum environmental impacts) in the marine environment, but also maximize adaptability for other uses, such as supporting human activities and promoting biological colonization (Figure 1).

In the area of infrastructure protection, several types of structures and protection devices are presented in [5] (Figure 2). According to [4], collisions of vessels with bridges are a frequent type of accidental action that can result in severe damage to the structure and lead to loss of life, as well as environmental pollution due to induced leaks. Thus, accidental loads resulting from vessel

collisions represent an important scenario to be considered when assessing the safety of these devices. The most common devices in protection systems are made of steel due to their behavior when subjected to impact forces. However, they are vulnerable to corrosion and fire [6]. Moreover, some of these protection systems can cause serious damage to vessels and can be expensive for bridges located in poor geological areas [5]. In addition, in order to avoid compromising the integrity of vessels, the design of these protection systems must have a compromise between strength and ductility, as required by the Norwegian standards in this field [7].



Figure 1. Protective systems in the marine environment



Figure 2. Examples of infrastructure protection systems in a maritime environment

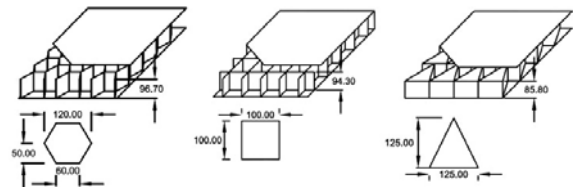
Due to the possibility of terrorist attacks on civil structures, the consideration of blast from fuel explosions, sonic booms or shock waves [8] cannot be neglected in this analysis of extreme actions. The tendency is to reinforce and or protect structures that have not previously been conceived to deal with this type of threat. Blast mitigation strategies traditionally used in industrial plants can provide additional safety. One such solution is the blast wall, which can be used for façade systems or for the protection of assembly areas and evacuation routes of metro and train stations or airports, for example.

Possessing the favourable combination of strength and toughness, traditional solutions widely used by both the civilian and military sectors were typically monolithic and based on high-strength steel, aluminium [9,10] and ceramic materials [11,12]. These systems provide adequate protection for heavy armoured vehicles, aircraft and helicopters, but when low weight, mobility and

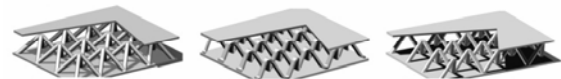
adaptability are the key design parameters, their use becomes limited. In order to meet these requirements, lightweight and flexible solutions are important, with preference given to mixed steel solutions (considering composite materials).

The development of (lightweight) protection elements has been the subject of research in the last two decades, namely structural steel sandwich panels to mitigate the effect of accidental actions. The investigation of stainless steel sandwich panels subjected to extreme loads can be found in [13, 14, 15,16].

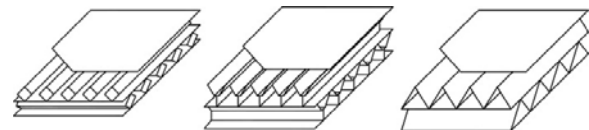
Sandwich panels allow energy to be dissipated through plastic deformation of the core and sheets/plates, making them more efficient than a single sheet [17]. Corrugated plates, honeycomb cores (Fig. 3a)), or with latticed or folders elements (Fig. 3b)), perform well, even for underwater blasts [18]. In [14, 15], the behaviour of these systems is analysed and it is demonstrated that they allow high levels of energy to be dissipated. In [19], the authors studied the effectiveness of orthotropic (Fig. 3c) and honeycomb typologies and the core sandwich panels with orthotropic elements showed great potential when subjected to blast loads. These systems with auxetic material in their core also show good energy absorption capacities and 3D printing can be used to manufacture them easily, where the sheet is printed over the core, avoiding the separation/ detachment [14].



a) Honeycomb core typologies: hexagonal, square and triangular [19].



b) Types with latticed or folded elements in its core [14]



c) Orthotropic types: diamond, Y-shaped and triangular [19].

Figure 3. Examples of different types of sandwich panels systems

In this compilation of the research already done, it is concluded that it is necessary to perform tests to complete and support the knowledge of these structural systems, particularly regarding the optimal configuration under impact or instantaneous loads and the fluid-structure interaction [15]. Complementarily, the explosion behaviour is revealed to have a huge potential, which can be improved through the introduction of alternative composite materials, such as fibre-reinforced polymers

and the consideration of dissipative connections of these to the primary structure, [20,21,22].

3. DISCUSSION AND DIRECTION OF THE RESEARCH

3.1. Efficiency of blast walls for protection of soft targets

This item deals with the research focused on the assessment of the blast response of protection walls. The studies developed by the authors in [20,21,22] represent an effort to improve the knowledge on the behavior of blast protection of soft targets by the use of structural blast mitigation solutions already used in oil and gas industrial facilities and in earthquake design.

Here a parametric study is performed through numerical modeling. Two common types of pannels (bulkhead and corrugated) with both fixed and pinned boundary conditions are subjected to directly defined pressure loads. Their responses are compared in order to evaluate the effects on the primary steelwork. Reaction forces, displacements and energy dissipation is calculated. Possible benefits deriving from typological and geometrical modifications of the local element are also presented.

Numerical modelling

The behavior of the thin two-way elements that are prone to large deformations was analyzed with the software Abaqus. The explicit dynamic solution method was applied due to its computational efficiency. Shell elements S4R with 10 mm of size was chosen. The adopted mesh was according DNV recommendations [23]. The structural steel S355 was adopted. The dynamic non-linear behavior of the material, the strain rate effect, strain hardening and the damage evolution were taken from [21]. In this study the interaction between the load and the element was not considered. The load was defined by specifying the pressure variation, according to DNV [23] and API [24] recommended practices, Figure 4.

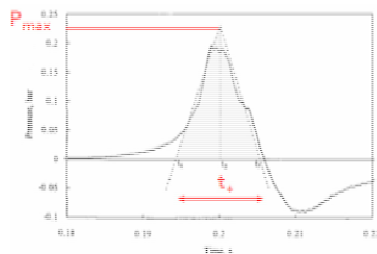


Figure 4. The pressure variation resulting from an explosion, [22]

Results and discussion

The study here developed was conducted in order to identify the most favorable plate type regarding the blast response. The Figure 5 identifies the element sections, which the parameters were analyzed. The displacements

in the central node, the factored reaction forces for fixed and pinned plates are given in the Figure 6 and Figure 7, respectively. As the reaction forces are computed in the nodes, the magnitude of these forces depends on the size of the mesh element. For this reason, the value of the reaction force must be factored by the ration of the element size and the length of the support.

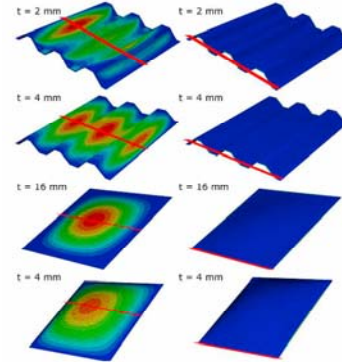


Figure 5. Sections in which the results were analyzed: Displacements (left) and reactions (right) [21]

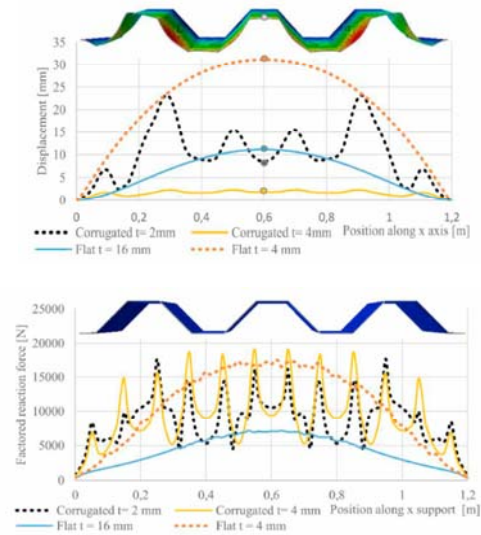


Figure 6. Displacements and factored reaction forces in fixed plates. [21]

The results from the FEM analysis demonstrate it is more economical to use corrugated plates instead of bulkheads if the deflection of the element is the relevant design criterion. In this case, it appears to be more reasonable to allow some flexibility in the edges since the overall response of the plate would be more favourable due to the much higher energy dissipation. On the other hand, even though much heavier, the thick bulkhead seems to perform better if the magnitude of the reaction forces is the primary design criterion. Using this approach, it is possible to trace the plastic deformation of elements in time, distribution of stresses and to measure the energy dissipation for different solutions. This results demonstrate the importance of geometry and boundary conditions, even for the safe design of supporting structure. This research also emphasised the importance of having a precise blast load in order to obtain a more adequate blast resistant wall protection design.

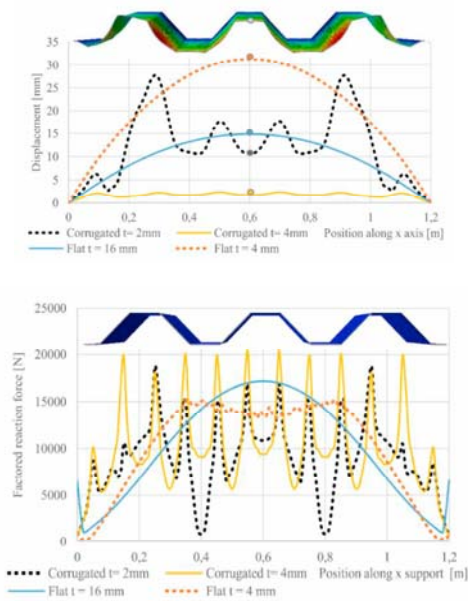


Figure 7. Displacements and factored reaction forces in pinned plates.

3.2. Explosive blasting resistance metal foil using Autodyn simulation

Confined underwater blast wave generators (WBG), consisting of an explosive charge inside of a water tank, generate a wide range of the produced blast impulses and surface area distribution, avoiding the generation of high velocity fragments and reducing atmospheric sound wave, leading to a more precise blast wall design. Air and underwater explosions (UNDEX) are important for design of not only the warships and submarines, but also for offshore platforms and infrastructures for fuel transportation, such as pipelines [25].

The study already developed [18], presents the 2D simulations of WBG, using Ansys Autodyn ©, projecting water against a thin stainless steel plate as a function of water tank size and for different values of stand-off distances. The phenomenological transmission of the shock, through the multi-material domain, is presented and discussed.

The basics of the shock physics necessary for understanding of detonation front formation and propagation as well as the fundamental equations of expansion of detonation products can be found in the literature [26-28]. More information about the material modelling and dynamic simulations in Autodyn are available in [29] and [30]. The following chapters provide basic assumptions for material modelling and dynamic simulations applied in the current study.

Numerical modelling

For the material characterization, in general, is necessary the equation of state, material strength model and material failure model. For the inert materials such as metals and liquids, the equation of state is commonly given by the form of Mie-Gruneisen equation of state combined with experimental shock velocity-particle velocity relation

[31]. In the case of products of explosive materials used in this study, Autodyn offers Jones-Wilkins-Lee (JWL) Equation of State (EOS) [30]. Concerning the strength model, the Piecewise JC model available in Autodyn was used [32]. The failure mode of materials defined in this study was erosion criteria.

Before the implementation of the experimental case study a mesh sensitivity (the mesh element size of 0,1 mm was the most promising), computational demand, critical length of explosive, particularities of different discretization methods and overall performance of the model with emphasis on distribution of pressure and velocities through defined domain was done.

Particular cases: results and discussion

This group of simulations is performed to study transmission of the shock through multi-material domain, assess the use of WBG for experimental study of thin plates and to help de-sign appropriate experimental samples.

The models for the assessment of the thin plate's kinetic energy and impulse in y direction (Figure 8) was created with Eulerian solver as explained in [18]. Particular simulation cases have their dimensions varied, where "wg" stands for water gap (representing the height of water above pbx: 7,5, 15 and 30 mm), "sd" represents the stand-off distance (3,75, 7,5 and 15 mm) and "ag" represents the air behind the stainless steel plate. Here is presented three models MP1(wg=7,5 mm; sd=0 mm), MP2 (wg=7,5 mm; sd=3,75 mm), and MP3 (wg=7,5 mm; sd=7,5 mm).

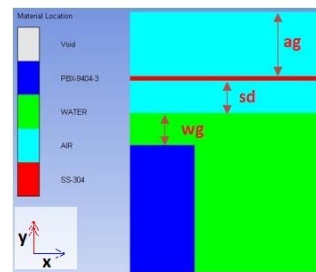


Figure 8. Layout of the particular cases models

The curves of the Figure 9 show that the kinetic energy of the stainless steel thin plate can be controlled by the water gap and stand-off distance. For the constant water gap, the kinetic energy reduces with increase of the stand-off distance. The overlap and the comparison of the thin stainless steel plates position for these three cases (MP1, MP2 and MP3) is shown in the Figure 10. These show that for the constant water gap, the increase of stand-off distance leads to lower movements of the plate.

The expansion of detonation products and the pressure transmission through water and air was observed for models with Lagrangian solver. An example of pressure transmission through these different material zones and expansion of detonation products is shown in the Figure 11 for model MP11(wg=7,5 mm; sd=7,5 mm).

The left image (a) shows the pressure at the end of the PBX 9304-3 material zone, whereas the central (b) and

the right (c) image show the pressures at the end of water (wg) and air (sd) zone.

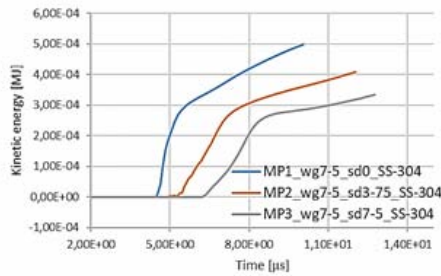


Figure 9. Kinetic energy for models with water gap of 7,5 mm

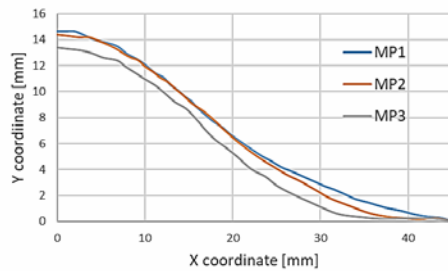


Figure 10. Comparison of the stainless steel position for the case of MP1, MP2 and MP3

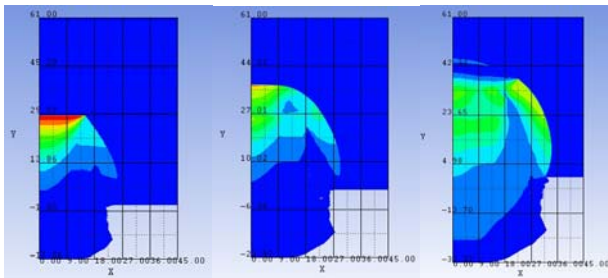


Figure 11. Pressure transmission and expansion of detonation products for the model MP11 (wg=7,5 mm; sd=7,5 mm)

The main conclusions of the work are: 1. WBG can be used effectively for small scale blast test of plates. The kinetic energy of the element can be controlled by the size of the water tank and the stand-off distance; 2. The increase of the water tank size and of the stand-off distance will in both cases lead to a reduction of the kinetic energy and of the impulse in the thin plate; 3. The increase of the stand-off distance will slightly delay the response of the plate and affect the size of the impacted area.

4. FINAL REMARKS AND FUTURE RESEARCH

Due to the research already developed it can be conclude that the design of new kind of lightweight multi-layer sandwich structure with improved mechanical properties and high blast resistance requires an accurate blast information. This demands the validation of model and constants by the correlation, with experimental results, of water blast and stainless steel plate deformation, showing

the role of the resistant blast wave wall. The research under development will take the following steps:

1. Definition of JWL parameters (EOS) for emulsion explosive in Autodyn based on theoretical calculations performed by THOR Code;
2. Propose new coefficients in existing empirical equations of Sadovsky and Zamyshlyayev for blast properties of emulsion explosive;
3. Validate the numerical model concerning propagation of the blast wave through the non-reacted emulsion and water domain with experimental results already existent.
4. With the numerical procedure validated for emulsion and water domain the attention will be focused on the experimental response of the plated elements, which include the following configurations: a. Single steel plate; b. Double steel plate; c. Steel sandwich panels with aramid honeycomb core; d. Steel sandwich panels with aluminum foam; e. Sandwich panels with aramid sheets and fabric honeycomb core;

Acknowledgement

This work was supported by the Portuguese Ministry of Science, Technology and Higher Education (Ministério da Ciência, Tecnologia e Ensino Superior) under the individual contract [Grant SFRH/BD/146533/2019]

References

- [1] IPCC Special Report on the Ocean and Cryosphere (SROCC), Published 05 Nov 2019 <https://www.ipcc.ch/srocc/download-report/>
- [2] United Nations. Sustainable Development Goals (SDGs) - United Nations. 2015. <https://sdgs.un.org/goals>.
- [3] Schoonees, T., Gijón Mancheño, A., Scheres, B. et al.. Hard Structures for Coastal Protection, Towards Greener Designs. Estuaries and Coasts 42, 1709–1729. 2019. <https://doi.org/10.1007/s12237-019-00551-z>
- [4] Titus Manohar, C.R. Suribabu, G. Murali, M.P. Salaimanimagudam. A novel steel-PAFRC composite fender for bridge pier protection under low velocity vessel impacts, structures, volume 26, 765-777, 2020. <https://doi.org/10.1016/j.istruc.2020.05.005>
- [5] Wei Fana, Wei Guo, Yang Sun, Baisheng Chen, Xudong Shao. Experimental and numerical investigations of a novel steel-UHPFRC composite fender for bridge protection in vessel collisions, Ocean Engineering, volume 165, 1-21. 2018. <https://doi.org/10.1016/j.oceaneng.2018.07.028>.
- [6] AASHTO. Guide specification and commentary for vessel collision design of highway bridges, 2nd ed., 2009. Washington, DC.
- [7] Constança Rigueiro, João Ribeiro, Aldina Santiago. Numerical assessment of the behaviour of a fixed offshore platform subjected to ship collision, X International Conference on Structural Dynamics, EURO DYN 2017, September 2017, Roma, Italy. Journal Procedia Engineering, No. 199, pp. 2494-2499. <https://doi.org/10.1016/j.proeng.2017.09.415>

- [8] D. Balkan i Z. Mecitoğlu. Nonlinear dynamic behavior of viscoelastic sandwich composite plates under non-uniform blast load: Theory and experiment, *International Journal of Impact Engineering*, t. 72, pp. 85-104. 2014.
- [9] M. Grujicic, B. Pandurangan i B. d'Entremont. The role of adhesive in the ballistic/structural performance of ceramic/polymer-matrix composite hybrid armor, *Materials & Design*, t. 41, pp. 380-393. 2012.
- [10] J. Godzimirski, J. Janiszewski, M. Rośkowicz i Z. Surma. 2015. Ballistic resistance tests of multi-layer protective panels, *Eksplotacja i Niezawodność - Maintenance and Reliability*, t. 17, br. 3, pp. 416-421, 2015.
- [11] S. Signetti, F. Bosia, S. Ryu i N. M. Pugno. A combined experimental/numerical study on the scaling of impact strength and toughness in composite laminates for ballistic applications, *Composites Part B: Engineering*, V. 195, p. 108090. 2020. <https://doi.org/10.1016/j.compositesb.2020.108090>
- [12] Y. Gao, W. Zhang, P. Xu, X. Cai i Z. Fan. Influence of epoxy adhesive layer on impact performance of TiB2-B4C composites armor backed by aluminum plate, *International Journal of Impact Engineering*, t. 122, pp. 60-72. 2018.
- [13] Damjan Čekerevac, Constança Rigueiro, Eduardo Pereira. Characterization of accidental scenarios for offshore structures, *Special Issue: Proceedings of Eurosteel 2017, Volume1, Is-sue2-3*, 4341-4350. 2017. <https://doi.org/10.1002/cepa.493>
- [14] Tarlochan, F.. Sandwich Structures for Energy Absorption Applications: A Review. *Materials*, 14, 4731. 2021. <https://doi.org/10.3390/ma14164731>
- [15] Z. Xue and J. W. Hutchinson. A comparative study of impulse-resistant metal sandwich plates, *International Journal of Impact Engineering*, vol. 30, Issue 10, 1283-1305. 2004. <https://doi.org/10.1016/j.ijimpeng.2003.08.007>
- [16] J. W. Hutchinson and Z. Xue. Metal sandwich plates optimized for pressure impulses, *International Journal of Mechanical Sciences*, vol. 47. 2005. <https://doi.org/10.1016/j.ijmecsci.2004.10.012>
- [17] V. Rubino, V. S. Deshpande and N. A. Fleck. The dynamic response of end-clamped sandwich beams with a Y-frame or corrugated core, *International Journal of Impact Engineering*, vol. 35, 829-844. 2008. <https://doi.org/10.1016/j.ijimpeng.2007.10.006>
- [18] Damjan Čekerevac, Constança Rigueiro, Eduardo Pereira and José Campos. Explosive blasting resistant metal foil using autodyn simulation, XII Congresso de Construção Metálica e Mista, Coimbra, Portugal, 2019.
- [19] R. Alberdi, J. Przywara and K. Khandelwal. Performance evaluation of sandwich panel systems for blast mitigation, *Engineering Structures*, vol. 56. 2013. <https://doi.org/10.1016/j.engstruct.2013.08.021>
- [20] Damjan Čekerevac, Constança Rigueiro, Eduardo Pereira. Measures for Soft Target Protection Inspired in Other Blast Vulnerable Structures, In: Hofreiter L., Berezutskyi V., Figuli L., Zva-ková Z. (eds) *Soft Target Protection*. NATO Science for Peace and Security Series C: Environmental Security. Springer, Dordrecht. 2020. https://doi.org/10.1007/978-94-024-1755-5_6
- [21] Damjan Čekerevac, Constança Rigueiro, Eduardo Pereira. Efficiency of blast walls for primary steelwork protection of soft targets, *Transportation Research Procedia*, Vol. 40, 16-23. 2019. <https://doi.org/10.1016/j.trpro.2019.07.004>
- [22] Damjan Čekerevac, Constança Rigueiro, Eduardo Pereira. Performance of Structural Blast Mitigation Measure for Oil and Gas Industrial Facilities, *Key Engineering Materials* 812, 92-99, 2019. <https://doi.org/10.4028/www.scientific.net/KEM.812.92>
- [23] DNV, 2010. DNV-RP-C204: Design against accidental loads, s.l.: Det Norske Veritas.
- [24] API, 2006. Recommended Practice for the Design of Offshore Facilities Against Fire and Blast Loading, s.l.: American Petroleum Institute.
- [25] Z. Wang, X. Liang, A. S. Fallah, G. Liu, L. A. Louca and L. Wang, "A novel efficient method to evaluate the dynamic response of laminated plates subjected to underwater shock," *Journal of Sound and Vibration*, vol. 332, no. 21, pp. 5618-5634, 2013.
- [26] D. B. Hayes, "Introduction to Stress Wave Phenomena," Sandia Laboratories, Albuquerque, 1976.
- [27] Z.-Y. Liu, "Overdriven detonation phenomenon and its applications to ultra-high pressure generation," Kumamoto University, Kumamoto, Japan, 2001.
- [28] H. Hamashima, Y. Kato, Y. Nadamitsu and S. Itoh, "Determination of JWL parameters from underwater explosion test for ideal and non-ideal explosives," *Science and Technology of Energetic Materials*, vol. 64, no. 6, pp. 248-253, 2003.
- [29] ANSYS, *Autodyn User's Manual*, Canonsburg: ANSYS, Inc., 2013.
- [30] J. Ambrósio, R. Ferreira, R. Mendes, J. Campos, P. M. S. Santos, B. P. M. Duarte, N. Oliveira, J. Pereira and P. B. Lourenco, "Prediction and Experimental Results of Confined Underwater Blasting Generators," in 44th International Conference of the Fraunhofer ICT, Germany, 2013.
- [31] P. Harris and L. Avrami, "Technical report No. 4423: Some Physics of the Gruneisen Parameter," Picatinny Arsenal, Dover, New Jersey, 1972.
- [32] E. L. Lee, H. C. Hornig and J. W. Kury, "Adiabatic expansion of high explosive detonation products," Lawrence Radiation Laboratory University of California, Livermore, 1968.
- [33] G. Johnson and W. Cook, "A Constitutive Model and Data for Metals Subjected to Large Strains, High Strain Rates, and High Temperatures," in *Proceedings 7th International Symposium on Ballistics*, Hague, 1983.

CONTENTS

PLENARY LECTURES

ARTIFICIAL INTELLIGENCE IN FUNCTION OF DEVELOPING INNOVATION PRODUCTS, Miljan Vucetic, PhD, Vlatcom Institute of High Technologies/Singidunum University, Belgrade, Serbia

- XII **HIGH PERFORMANCE MULTI-FUNCTIONAL PANELS FOR EXTREME LOADING EVENTS**, Constança Rigueiro, PhD, Polytechnic Institute of Castelo Branco, Institute for Sustainability and Innovation in Structural Engineering, castelo Branco, Portugal

1. SECTION : AERODYNAMICS AND FLIGHT DYNAMICS - AFD

- 2 **MEASUREMENT OF HOVER PERFORMANCES FOR MINI UNMANNED AIRCRAFT VEHICLE**, Marija Samardžić, Lazar Petrović, Uros Ivković, Snežana Zurovac
- 8 **PREDICTION OF QUASI-STEADY FLUTTER VELOCITIES OF TAPERED COMPOSITE PLATES AT LOW MACH NUMBERS: ANALYSIS AND EXPERIMENT**, Mirko Dinulović, Aleksa Maljević, Branimir Krstić
- 13 **ON THE USE OF HIGH PITCH SWEEP RATES IN TIME-LIMITED SUPERSONIC WIND TUNNEL TESTS**, Dijana Damljanović, Đorđe Vuković, Biljana Ilić, Goran Ocokoljić, Stefan Krstić
- 19 **NUMERICAL ANALYSIS OF A PROPELLER IN GROUND EFFECT**, Jelena Svorcan, Aleksandar Kovačević, Toni Ivanov, Aleksandar Simonović
- 25 **NUMERICAL INVESTIGATION OF WING STRAKES AERODYNAMIC INFLUENCE USING MODIFIED SDM MODELS**, Jelena Šobot, Ivan Kostić, Olivera Kostić, Marija Samardžić
- 30 **VORTEX INDUCED DOWNWASH EFFECT ON STATIC STABILITY OF SUBSONIC AIR TO SURFACE MISSILE**, Ivan Marić, Anja Gavrilović, Ilija Nenadić, Goran Ocokoljić

2. SECTION : AIRCRAFT - A

- 37 **BUILDING OF PROBABILISTIC-STATISTICAL MODEL OF ENGINE FAILURES**, Olga Filippenko, Dana Belskaya, Volha Poletayeva
- 41 **STRENGTH CALCULATION OF LATERALZ LOADED TWO DIMENSIONAL PLANE STRUCTURAL ELEMENT**, Bogdan Bogdanović, Tonko Mihovilović
- 46 **LANDING GEAR BRAKES TESTING**, Teodor Babić, Marina Ostojić, Tamara Nikolić, Nikola Bogavac
- 50 **POWERPLANT COOLING FLIGHT TESTS**, Marina Ostojić, Tamara Nikolić, Nikola Bogavac
- 55 **TOTAL FATIGUE LIFE ESTIMATION OF AIRCRAFT STRUCTURAL COMPONENTS USING STRAIN ENERGY DENSITY METHOD**, Stevan Maksimović, Katarina Maksimović, Ivana Vasović Maksimović, Mirjana Đurić, Mirko Maksimović
- 61 **TESTING OF AAD FOR RESERVE PARACHUTE CANOPIES**, Stevan Jovičić, Jelena Šobot, Ljubiša Tomić, Ivo Obradović
- 66 **OPTIMIYING THE CROSS-SECTION OF ELASTIC BEAM OF THE BEARINGLESS ROTOR OF AN ULTRALIGHT HELICOPTER**, Dalibor Petrović, Ivan Mudri, Vladimir Stanković

3. SECTION : WEAPON SYSTEMS AND COMBAT VEHICLES - WSCV

- 72 **EFFICIENCY ANALYSIS OF A FRAGMENTATION WARHEAD AGAINST SOFT TARGETS**, Omar Awad al Ameri, Edge Halcon, Predrag Elek
- 80 **SIMULATION MODEL OF TERRITORY CELL DEFENCE against HELICOPTER AS A HYBRID THREAT**, Radomir Janković, Momčilo Milinović
- 86 **PLANETARY GEAR PAIR DESIGN USING METAHEURISTIC ALGORITHMS**, Miloš Sedak, Maja Rosić
- 92 **APPLICATION OF DRONES WITH ARTIFICIAL INTELLIGENCE FOR MILITARY PURPOSES**, Aleksandar Petrovski, Marko Radovanović, Aner Behlić
- 101 **THE PROCEDURE FOR TESTING THE FUNCIONAL CHARACTERISTICS OF TANK GEARBOXES DEVELOPED ON THE BASIS OF T-72 TANKS**, Žarko Svilar, Obren Stojić, Željko Bulatović, Stojko Biočanin
- 107 **THE DESIGN OF TECHNICAL SOLUTION FOR THE FUEL LEVEL TRACKING IN MODERNIZED BVP M-80AB2**, Obren Stojić, Goran Jerkin
- 114 **FUZE VAF-M17 MICROCONTROLLER SOFTWARE**, Marko Živković, Dragan Domazet, Nikola Latinović
- 121 **FUZE VAF-M17 ELECTRONIC BLOCK TEST SOFTWARE**, Nemanja Deura, Dragan Domazet, Prof.Dr Srećko Nijemčević
- 128 **LOAD OF REMOTE CONTROLLED BATTLE STATION UPPER CARRIAGE WITH INTEGRATED AUTOMATIC GRENADE LAUNCHER**, Milan Ivković, Vladimir Milovanović, Bogdan Nedić, Stefan Djurić

4. SECTION : AMMUNITION AND ENERGETIC MATERIALS - AEM

- 134 **CLASSICAL AND INSTRUMENTAL METHODS FOR DETERMINATION OF RESIDUAL SOLVENT IN NITROCELLULOSE GUNPOWDER**, Magdalena Rakić, Mirjana Dimić, Bojana Fidanovski
- 138 **COMPARATIVE ANALYSIS FOR DETERMINATION OF STABILIZER CONTENT IN GUNPOWDER AND DOUBLE BASE PROPELLANT BY HPLC METHOD**, Mirjana Krstović, Magdalena Rakić, Ljiljana Jelisavac, Mirjana Dimić, Jelena Mojsilović, Bojana Fidanovski
- 144 **EXPERIMENTAL INVESTIGATION ON THE PERFORATION OF HIGH-HARDNESS STEEL PLATE BY AN API PROJECTILE**, Predrag Elek, Radovan Đurović, Nebojša Hristov, Damir Jerković, Aleksa Aničić
- 150 **DESIGN OF SUITABLE PYROTECHNIC DELAY COMPOSITION WITH WIDELY USED COMPONENTS**, Jelena Mojsilović, Jelena Petković-Cvetković, Dragica Kosrić, Jovica Nešić, Jela Ilić, Mirjana Krstović
- 155 **NUMERICAL ANALYSIS OF THE INHOMOGENEOUS OBSTACLE INFLUENCE ON THE PRECURSOR SHAPED CHARGE WARHEAD PERFORMANCE**, Miloš Marković, Predrag Elek, Dejan Jevtić, Radovan Đurović, Ivana Todić
- 161 **NUMERICAL ANALYSIS OF THE TUNGSTEN CARBIDE-COBALT CORED BULLET PENETRATING THE HIGN-HARDNESS STEEL PLATE**, Radovan Đurović, Predrag Elek, Miloš Marković, Dejan Jevtić, Mihailo Erčević
- 169 **INFLUENCE OF DIFFERENTLY CURED POLYMERIC BINDERS ON RHEOLOGY PROPERTIES OF PLASTIC EXPLOSIVES**, Danica Bajić, Ivan Dimitrijević, Slavica Terzić
- 176 **SYNTHESIS-THE CORE COMPONENT OF ENERGETIC MATERIALS RESEARCH**, Jasmin T. Lechner, Thomas M.Klapotke

- 181 **DETONATOR TESTING SOFTWARE**, Vladimir Drinčević, Dragan Domazet, Nikola Latinović
- 186 **INVESTIGATION ON THE DISTRIBUTION OF COMPONENTS IN RECYCLE DOUBLE BASED PROPELLANTS**, Iskra Piroeva, Stela Atanasova-Vladimirova, Feyzim Hodzhaoglu, Radi Ganev

5. SECTION : INTEGRATED SENSOR SYSTEMS AND ROBOTIC SYSTEMS - ISSRS

- 190 **SLIDING MODE CONTROLLER DESIGN FOR DC MOTOR DRIVEN ELECTROMECHANICAL FIN ACTUATOR**, Zlatko Petronijević, Pavle Adamović, Nebojša Jovičić, Aleksandar Stefanović, Miloš Pavić
- 195 **LEAD COMPENSATOR DESIGN FOR DC MOTOR DRIVEN ELECTROMECHANICAL FIN ACTUATOR**, Pavle Adamović, Zlatko Petronijević, Nebojša Jovičić, Aleksandar Stefanović, Miloš Pavić
- 201 **UAV ENGINE SPEED CONTROLLER FOR HOVER PERFORMANCE MEASUREMENT**, Lazar Petrović, Marija Samardžić, Uroš Ivković, Snežana Zurovac
- 205 **OPTIMIZATION OF THE ALGORITHM FOR ESTIMATING TIME OF ARRIVAL OF THE ACOUSTIC WAVE FRONT BY CHOOSING THE SIGNAL FILTERING METHOD**, Miodrag Vračar, Stevo Vračar
- 210 **CONTROL SYSTEM DESIGN AND INTEGRATION OF A BLOWDOWN WIND TUNNEL MODEL SUPPORT PITCH MECHANISM**, Biljana Ilić, Mirko Milosavljević, Stefan Krstić, Goran Ocokoljić, Dijana Damljanović
- 217 **MILITARY PROVING GROUND ELECTRO-OPTICAL SURVEILLANCE SYSTEM DESIGN**, Saša Vujić, Miloš Radisavljević, Branko Livada, Branko Tomić, Dragana Perić, Dragan Domazet
- 223 **APPLICATION OF INFRARED THERMOGRAPHY IN MONITORING OF PETROL ENGINE WITH AIR COOLING**, Ljubiša Tomić, Gordana Majstorović, Nenad Munić, Aleksandar Kovačević, Darko Vasiljević
- 227 **PERFORMANCE COMAPRISON OF METALLIC REFLECTOR AND PRINTED PLANAR ANTENNAS FOR MOBILE INFANTRY RADARS**, Boro Reljić, Zoran Golubičić, Igor Dotlić, Svetislav Marić, Marijan Herceg
- 232 **SIMPLE RADAR SYSTEM FOR DRONE SURVEILLANCE AND ACQUISITION**, Zoran Golubičić, Slobodan Simić, Svetislav Marić, Bojan Zrnić, Bogdan Pavković
- 237 **DESIGN, FABRICATION AND PERFORMANCE EVALUATION OF PASSIVE CORNER REFLECTOR FOR GROUND SURVEILLANCE RADAR TESTING**, Aleksa Zejak, Radule Zejak, Slobodan Simić, Boro Reljić, Igor Dotlić
- 242 **SIDE LOOKING DRONE RADAR FOR BURIED VEHICLES IN THE FORESTALL ENVIRONMENT**, Slobodan Simić, Zoran Golubičić, Aleksa Zejak, Boro Reljić, Eugen Šimara
- 246 **DEVELOPMENT OF THE DEVICE BASED ON THE DSPIC30F6014A MICROCONTROLLER FOR MEASUREMENT OF AXLE POSITION ANGLE**, Vladimir Lapčević
- 253 **ACTIVE DISTURBANCE REJECTION CONTROL OF UNMANNED TRACKED VEHICLE**, Goran Banjac, Momir Stanković, Stojadin Manojlović
- 260 **SOFTWARE FOR VIDEO STREAMS SYNCHRONIZATION IN LONG RANGE SURVEILLANCE SYSTEMS**, Aleksandar Simić, Tamara Parojčić, Miroslav Perić, Dragan Domazet

- 268 **DESIGN OF CONTROL SOFTWARE FOR EXTREME PERFORMANCE GYRO-STABILIZED PAN TILT POSITIONER FOR ELECTRO-OPTICAL SYSTEMS**, Miloš Radisavljević, Miloš Stanković, Đorđe Vulović, Dragan Domazet
- 275 **AUTONOMOUS ROBOT EXPLORATION IN GAZEBO SIMULATOR**, Novak Zagradjanin, Nikola Knežević, Kosta Jovanović, Bojana Pavković
- 281 **DESIGNING THE CONTROLLED GENERATOR OF A HOMOGENOUS MAGNETIC FIELD**, Radosav Surla, Nebojša Mitrović, Pavel Crnomarković
- 286 **A NEW INFRARED RADIATION DETECTION SYSTEM AS AN INSPIRATION FOR THE POTENTIAL CONSTRUCTION OF A RADIOMETRIC DETECTOR**, Marina Simić-Pavlović, Ljubiša Tomić, Branko Kolarić, Darko Vasiljević

6. SECTION : TELECOMMUNICATION AND INFORMATION SYSTEMS - TIS

- 290 **NOVEL APPROACH TO RECONFIGURATION POWER LOSS REDUCTION PROBLEM BY SIMULATED ANNEALING TECHNIQUE**, Branko Stojanović, Tomislav Rajić, Aleksandar Kovačević
- 296 **BIRD AND DRONES SPECTROGRAMS AND HOW TO DIFFER THEM**, Jovan Radivojević, Dejan Stanojević, Aleksandar Lebl
- 303 **SOFTWARE ALGORITHM FOR DRONE PRESENCE DECISION ON THE BASE OF RADAR SPECTROGRAMS**, Dejan Stanojević, Jovan Radivojević, Aleksandar Lebl
- 310 **ANALYSIS AND DESIGN OF HIGH GAIN FLAT PATCH ANTENNA**, Saša Gundelj, Aleksandar Stefanović, Saša Antonović, Igor Goršić
- 314 **DRONE CLASSIFICATION BASED ON RADIO FREQUENCY: TECHNIQUES, DATASETS, AND CHALLENGES**, Boban Sazdić-Jotić, Boban Bondžulić, Ivan Pokrajac, Jovan Bajčetić, Mohammed Mokhtari
- 321 **TDOA BASED APPROACH FOR ACCURATE TARGET LOCALIZATION BASED ON HYBRID GENETIC ALGORITHM**, Maja Rosić, Miloš Sedak, Mirjana Simić, Predrag Pejović
- 328 **GNS3 SIMULATION OF IS-IS PROTOCOL IN NETWORK COMPOSED OF JUNIPER ROPUTER**, Pavel Crnomarković, Radoslav Surla
- 333 **SIGNAL CENSTELLATION DISTORTION AND ITS IMPACT ON CUMULANT-BASED AMC PERFORMANCE**, Vladimir D. Orlić, Rade R. Božović
- 340 **DESIGNING THE PORTABLE BIOMETRIC STATION FOR MILITARY APPLICATION**, Dejan Čiprovski, Boško Božilović, Saša Božinović, Dragan Domazet
- 346 **INTERCEPT PROBABILITY ANALYSIS OF WIRELESS SENSOR NETWORKS WITH OPTIMAL SENSOR SCHEDULING**, Aleksandra S. Panajotović, Dejan N. Milić, Ivica B. Marjanović, Jelana A. Anastasov, Nikola M. Sekulović, Daniela M. Milović
- 351 **EVALUATION OF LORA WIRELESS TECHNOLOGY FOR MILITARY APPLICATIONS**, Uroš Pešović, Slađana Đurašević, Mihailo Knežević
- 356 **FLIGHT PLAN PREPARATION FOR POINT CLOUD DATA COLLECTION UTILIZING THE LASER SCANNER ALS80HP**, Dejan Đorđević, Ivan Potić, Zlatan Milonjić, Miloš Basarić, Saša Bakrač

7. SECTION : MATERIALS AND TECHNOLOGIES - MT

- 362 **SOLVING MILITARI-TECHNICAL PROBLEMS USING INVENTOLOGY**, Dušan Rajić
- 368 **CHARACTERIZATION AND HEAT TREATMENT OF ARMOUR STEEL OF NEW GENERATION**, Borut Kosec, Blaž Karpe, Aleš Nagode, Zijah Burzić, Igor Radosavjević, Gorazd Kosec

- 372 **DIMETHOATE AND OMETHOATE HYDROLYSIS IN AQUEOUS SOLUTIONS AND THE ASSESSMENT OF THEIR NEUROTOXIC EFFECTS**, Dragana D. Vasić Anićijević, Vladan J. Anićijević, Tamara Lazarević-Pašti
- 376 **WASTE-DERIVED CARBON MATERIAL FOR MALATHION ADSORPTION**, Vladan J. Anićijević, Katarina Kokanov, Tamara Tasić, Vedran Milanković, Tamara Lazarević-Pašti
- 380 **THE DESIGN AND SYNTHESIS OF THE THREE NOVEL DUAL REVERSIBLE INHIBITORS OF ACETYLCHOLINESTERASE BASED ON THE TACRINE AND AROYLACRYLIC ACID PHENYLAMIDE SUBSTRUCTURES**, Tamara Vujatović-Velimirov, Milan R. Nikolić, Maja Vitorović-Todorović
- 387 **HIGHLY EFFECTIVE NANOFIBERS WITH CATALYTIC CWA DEGRADATION ACTIVITY FOR CHEMICAL PROTECTION – CURRENT STATE-OF-THE ART**, Maja Vitorović-Todorović, Sonja Đ Bauk, Tamara Vujatović-Velimirov
- 392 **ASSESSMENT OF THE EFFECTIVENESS OF PERSONAL PROTECTION AGAINST THE EFFECTS OF RADIOLOGICAL CONTAMINANTS**, Sreten Ilić, Nataša Pajić, Željko Senić, Tatjana Golubović
- 398 **INFLUENCES OF ELECTROLYTE TYPE AND AGITATION REGIMES ON STRUCTURAL MECHANICAL PERFORMANCE OF ELECTROLYTICALLY DEPOSITED COPPER COATINGS ON DIFFERENT CATHODES**, Ivana Mladenović, Nebojša Nikolić, Jelena Lamovec, Dragan Tanasković, Miloš Vorkapić, Vesna Radojević, Dana Vasiljević-Radović
- 405 **FIRE-RESISTANT COMPOSITES BASED ON ACRYLIC-FUNCTIONALIZED LIGNIN AND POLYESTER RESIN OBTAINED FROM WASTE POLY(ETHYLENE TEREPHTHALATE)**, Nataša Knežević, Aleksandar Jovanović, Jovana Bošnjaković, Milena Milošević, Milica Rančić, Aleksandar Marinković, Jelena Gržetić
- 412 **SILVER COATED TEXTILES AS ELECTROCHEMICAL PSEUDOCAPACITIVE MATERIALS**, Stevan Stupar, Mihael Bučko, Dušan Mijin, Denis Dinić, Tanić Milan, Marina Knežević, Jelena Karanović
- 418 **INHIBITION OF ACID CORROSION OF MILD STEEL BY AQUEOUS EXTRACT OF OLIVE LEAVES**, Souad Touazi, Adjouati Bachir Abderaouf, Ziane Aymene, Nadia Zaidi, Mihael Bučko, Laid Makhoulfi
- 423 **AIR AND PRECIPITATION TESTING AS PART OF ENVIRONMENTAL RADIATION MONITORING IN THE VICINITY OF NUCLEAR FACILITIES**, Jovana Knežević, Nataša Lazarević, Sofija Forkapić, Kristina Bikit Šreder, Vesna Radumilo, Dalibor Arbutina
- 429 **DETERMINATION OF GAMMA PHOTON ATTENUATION COEFFICIENT OF LIGHTWEIGHT BUILDING AND INSULATION MATERIALS USED FOR OVERBUILDING IN SERBIA**, Milan Tanić, Denis Dinić, Stevan Stupar, Mirjana Čujić, Marko Anđelović
- 434 **MANUFACTURING OF FIBER –REINFORCED POLYMER COMPOSITE THERMAL INSULATION BY VACUUM TECHNIQUE**, Marica Bogosavljević, Jelena Grčetić, Slavko Mijatov, Saša Brzić, Tihovim Kovačević
- 439 **DEVELOPMENT OF POLYMER COMPOSITE LINER AS INSULATION MATERIAL: RHEOLOGICAL, MECHANICAL AND THERMAL PROPERTIES**, Slavko Mijatov, Saša Brzić, Tihomir Kovačević, Marica Bogosavljević, Jelena Gržetić, Mladen Timotijević
- 447 **DIGITAL THREAD FOR ADDITIVE MANUFACTURING**, Slobodan Malbašić, Srdjan Živković, Veljko Petrović, Aleksa Grubić

- 452 **IMPACT OF THE DIFFERENT ACTIVE FILLING HEIGHT OF THE FILTER ON THE SORPTIVE CHARACTERISTICS OF FILTERING**, Marina Ilić, Tatjana Marković, Biljana Mihajlović, Vukica Grković, Sonja Bauk
- 460 **INFLUENCE OF PRODUCTION PARAMETERS ON THE QUALITY OF SEMIFINISHED RIFLED PISTOL BARRELS**, Maja Mladenović, Nada Ilić, Jovana Mandić, Igor Radisavljević, Slobodan Ilić
- 465 **MECHANICAL CHARACTERISTICS OF ALUMINIUM SANDWICH PANELS WITH ALUMINIUM HONEYCOMB CORE**, Jelena Marinković, Igor Radisavljević, Srdja Perković
- 473 **PREPARATION AND CHARACTERIZATION OF HORSE SERUM BUTYRYLCHOLINESTERASE IMMOBILIZED ON PAPER-BASED CELLULOSE MATRIX**, Sonja Bauk, Maja Vitorović-Todorović, Marina Ilić, Tamara Vujatović, Tatjana Marković
- 479 **INFLUENCE OF DIFFERENTLY CURED POLYMERIC BINDERS ON RHEOLOGY PROPERTIES OF PLASTIC EXPLOSIVES**, Danica Bajić, Ivan Dimitrijević, Slavica Terzić
- 486 **USING SELF-ADHESIVE CONDUCTIVE TEXTILE AND COPPER TAPE ON TEXTILE**, Dušan Nešić, Dragan Tanasković, Miloš Vorkapić
- 491 **POLYESTER KNITWEAR IMPREGNATED WITH PVB/IF-WS₂ SYSTEM AS POTENTIAL CAMOUFLAGE MATERIAL**, Aleksandra Samolov, Danica Bajić, Katarina Mišković, Radoslav Sirovatka, Milan M. Stanojević, Dragan Knežević
- 495 **DEVELOPMENT AND PRODUCTION OF ULTRA-HIGH-STRENGTH STRUCTURAL STEEL S1100QL**, Jan Foder, Andrej Skumavc
- 501 **FRACTURE ANALYSIS OF VEHICLE-MOUNTED TELESCOPING COMMUNICATIONS MAST**, Nada Ilić, Ljubica Radović, Maja Mladenović, Jovana Mandić, Vesna Pejović
- 506 **APPLICATION OF IT TECHNOLOGY IN WASTEWATER TREATMENT**, Miljan Miletić, Marina Ilić, Tatjana Marković
- 514 **CHARACTERIZATION OF HETEROGENEOUS SENSING LAYERS IN GRAPHENE-BASED GAS SENSORS**, Stevan Andrić, Ivana Jokić, Miloš Frantlović, Katarina Radulović, Marko Spasenović
- 519 **POLYCHLOROPRENE BASED RUBBER COMPOSITIONS FOR GASKET PRODUCTION**, Marija Kluz, Jela Galović, Aleksandar Milojković, Ljiljana Jelisavac, Tanja Milošević
- 524 **THE INFLUENCE OF CHEMICAL COMPOSITION ON MECHANICAL PROPERTIES OF FLOW FORMED STEEL TUBES**, Igor Radovanović, Snežana Blagojević, Ljubica Radović, Dragomir Glišić
- 528 **EXPERIMENTAL INVESTIGATIONS OF THE INFLUENCE OF TEMPERATURE AND EXPLOITATION TIME ON THE FATIGUE CHARACTERISTICS OF X20 STEEL**, Dženana Gačo, Fadil Islamović, Srđa Perković, Miodrag Lisov, Radica Prokić-Cvetković
- 534 **THE INFLUENCE OF THE HEAT INPUT ON THE IMPACT ENERGY OF THERMALLY SIMULATED HSLA STEEL WELDMENTS**, Mersida Manjgo, Tomaž Vuherer, Srđa Perković, Miodrag Lisov, Zijah Burzić
- 541 **MIG WELDING PROCESS ON THE MECHANICAL PROPERTIES OF BUTT WELDED JOINTS OF DISSIMILAR ALUMINUM ALLOYS 2024-T351 /6082-T6**, Dragan Milčić, Tomaž Vuherer, Ljubica Radović, Miodrag Milčić, Maja Mladenović, Andreja Radovanović, Nenad Radović

- 548 **ANFIS FOR PREDICTING REMOVAL EFFICIENCY OF METHYLENE BLUE ONTO CORDIA MIXA-A**, Ahmed Khaleel Igrahim, Amir Alsammarrai, Salwa Hadi Ahmed
- 557 **ANFIS PREDICTION IN PLASMA ARC CUTTING**, Madina Isametova, Miloš Mlovančević, Dalibor Petković
- 567 **ANFIS PREDICTION IN PLASMA ARC CUTTING**, Madina Isametova, Miloš Mlovančević, Dalibor Petković

8. SECTION: QUALITY, STANDARDIZATION, METROLOGY, MAINTENANCE AND EXPLOITATION - QSMME

- 575 **SECURITY SYSTEM DESIGN USING A SOFTWARE SOLUTION**, Predrag Ranitović, Sanja Lončar
- 585 **RISK MANAGEMENT AT PUBLIC COMPANY „NUCLEAR FACILITIES OF SERBIA”**, Bojan Radoš, Nataša Lazarević, Jovana Knežević, Dalibor Arbutina
- 591 **DATA-DRIVEN RELIABILITY OF ELECTRONIC EQUIPMENT**, Slavko Pokorni
- 595 **IMPLEMENTATION OF Y-FACTOR METHOD FOR NOISE FIGURE MEASUREMENT USING EMI MEASURING RECEIVER**, Nenad Munić, Aleksandar M. Kovačević, Nenko Brkljač, Ljubiša Tomić, Miroslav Jovanović
- 600 **CONTROLLING INTERNAL AUDITING AT THE MINISTRY OF DEFENCE**, Igor Đorić, Mihajlo Ranisavljević, Marko Milojević
- 610 **PROPOSAL OF SOLUTION FOR HYDRAULIC CONTROL OF OUTBOARD ENGINE ON "RIB-720 CANDO"**, Dragan Trifković, Darko Stričić, Enis Dauti, Predrag Dobratić, Serif Bajrami, Jelena Paunović



10th INTERNATIONAL SCIENTIFIC CONFERENCE
ON DEFENSIVE TECHNOLOGIES
OTEH 2022

Belgrade, Serbia, 13 – 14 October 2022



SECTION I

Aerodynamics and flight dynamics - AFD

CHAIRMAN
Marija Samardzic, PhD

MEASUREMENT OF HOVER PERFORMANCES FOR MINI UNMANNED AIRCRAFT VEHICLE

MARIJA SAMARDŽIĆ

Military Technical Institute, Belgrade, marija.samardzic.vti@gmail.com

LAZAR PETROVIĆ

Military Technical Institute, Belgrade, lazar.petrovic.node@gmail.com

UROŠ IVKOVIĆ

Military Technical Institute, Belgrade, uske80@gmail.com

SNEŽANA ZUROVAC

Military Technical Institute, Belgrade, zurovac@medianis.net

Abstract: This paper presents measurement of hover performances for quadcopter unmanned aircraft vehicle (UAV). The tests took place in the Experimental Aerodynamic Laboratory at Military Technical Institute, Belgrade. Mini unmanned aircraft vehicle DJI Phantom was chosen as a UAV test model. The main objective of the presented test was to measure forces and moments generated on the UAV model as a function of the rotors RPM. The UAV model was run through a range of defined rotors RPM numbers in hover mode. The rotors speed control were conducted to match the target RPM. The forces and moments were measured using internal six-component wind tunnel balance. To match expected values of the forces and moments, calibration of the six-component balance was done for two load ranges. The UAV model was modified from its typical consumer configuration to facilitate connection to the internal balance. Measurement of hover performances was performed on the calibration rig in the T-38 wind tunnel calibration laboratory.

Keywords: unmanned aircraft vehicle, hover performances, aerodynamic load, wind tunnel balance.

1. INTRODUCTION

Mini unmanned aircraft vehicles are being used more and more every day. The areas of application can be various: from the use of recreational aviation enthusiasts to professional field recording for various purposes. The UAV of certain configurations, with the most advanced construction and performance, are also used for military purposes. One of the first indicators of the potential capabilities of an UAV is its payload. In addition to the appropriate flight characteristics, one of the most important parameters for evaluating the capability of an UAV is the weight of additional payload that the aircraft can carry. In the process of designing new or testing already existing UAV, the possibility of experimental determination of aerodynamic forces and moments as a function of the air speed, vehicle attitude and rotor speed is of great importance [1-4]. The most often, the first stage of such experiments is determination of the forces and moments on the UAV in the hover mode. This paper presents the measurements of the hover performance of a mini UAV in the calibration laboratory of the T-38 wind tunnel. The presented results are the first part of extensive testing, the continuation of which is planned in the small subsonic wind tunnel T-32. The main goal of the presented tests is to measure the normal force (thrust), in the hovering mode and verify the selection of the internal

wind tunnel balance. This balance should enable the measurement of all six aerodynamic force components in the UAV model wind tunnel testing.

2. MINI UNMANNED AIRCRAFT VEHICLE MODEL

DJI Phantom aircraft is chosen for hover and wind tunnel testing, Figure 1. This is commercially available multicopter whose primary mission is photographic surveillance. The unmanned aircraft vehicle was modified from their original configuration to facilitate testing on the calibration rig and in the T-32 wind tunnel. The most significant changes were made in the internal electronics.



Figure 1. DJI Phantom aircraft

The basic quadcopter UAV physical characteristics are shown in Table 1 [5].

Table 1. The DJI Phantom physical characteristics

Parameters	Range
Operating temperature	from -10° to 50°C
Power consumption	3.12 W
Take-off weight	< 1200 g
Max ascent/descent speed	6 m/s
Max flight velocity	10 m/s
Diagonal distance (motor center to motor center)	350mm
Weight	670 g
Weight (with battery)	800 g

3. INTERNAL WIND TUNNEL BALANCE FOR THE MEASUREMENTS OF THE AERODYNAMIC LOAD

In the Experimental Aerodynamic Laboratory at the Military Technical Institute, measurements of the aerodynamic load on the mini UAV models have not been performed so far. Selection of the suitable internal wind tunnel balance for measurements of the aerodynamic load is a very important step in conducting the experiment preparation. The dimensions and geometry of the wind tunnel balance should be such that it can be placed in a rather narrow space inside the model. The wind tunnel balance should also enable the measurement of the aerodynamic components with the required accuracy, taking into account that some components will have very small values.

The expected values of the aerodynamic load on the DJI Phantom model are determined based on the available published experimental results. The results of the tests on the six different UAV models are presented in the reference [6]. Table 2 shows the nominal flight weight for the tested six models.

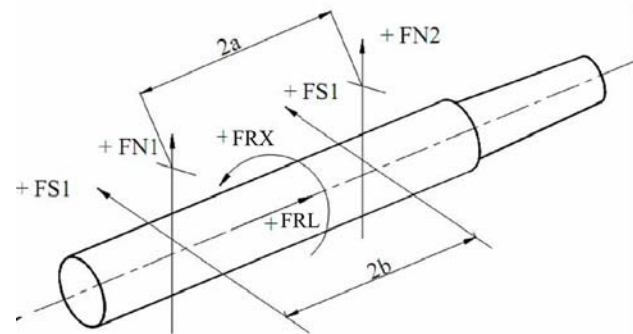
Table 2. Model nominal flight weight [6]

Model	Nominal Flight Weight (including cameral payload) [N]
3DR SOLO	14.678
DJI Phantom 3	12.453
3DR Iris+	12.453
Drone America x8	56.923
Straight Up Imaging Endurance	26.682

One and the same six-axis load cell was used for all five aircraft shown in Table 2. Measuring range of the six-axis load cell is: 222 N in x- and y- direction (axial and side force), 444 N in z-direction (normal force) and maximum moments of 17 Nm (rolling moment, yawing moment and pitching moment). A load cell with a smaller measuring range was originally planned for testing lighter aircrafts.

Due to appearance of large vibrations during the first wind tunnel tests on lighter model, the same six-axis load cell was used in the tests of all models [6].

Take-off weight for the model DJI Phantom is less than 11.8 N [5]. Based on this data, as well as on the measured data for models shown in Table 2, for testing of the DJI Phantom model 0.75 inch ABLE internal balance was selected. The six basic components of the balance consist of two normal force elements ($FN1$ and $FN2$) for determination of normal force (Z) and pitching moment (M), two side force ($FS1$ and $FS2$) for determination of side force (Y) and yawing moment (N), dual force element (FRX) for determination of axial force (X) and dual moment element (FRL) for determination of rolling moment (L), Figure 2.



$$a = 0.0381 \text{ m}, b = 0.03175 \text{ m}$$

Figure 2. Basic component of the 0.75 inch ABLE internal balance

The calibration of the six-component balance was performed for two load ranges: nominal operating load range and reduced load range, Table 3. The calibration was performed on the calibration rig in the T-38 wind tunnel calibration laboratory, Figure 3. The balance calibration was consisted of the manual application of dead weights. This process was used for both positive and negative loadings at various stations along the calibration body. Summary of achieved accuracy of the calibration, as obtained in a checkout after the calculation of the calibration matrix, for both load ranges, is given in Table 4.

Table 3. The six-component balance load range

Nominal operating load range					
X	Y	Z	L	M	N
[N]	[N]	[N]	[Nm]	[Nm]	[Nm]
111	356	668	6.8	25	11
Reduced load range					
X	Y	Z	L	M	N
[N]	[N]	[N]	[Nm]	[Nm]	[Nm]
34	84	170	2.1	6.5	2.7



Figure 3. The six-component balance on the T-38 calibration rig

Table 4. Summary of achieved accuracy of the balance calibration

Nominal operating load range						
Component	X	Y	Z	L	M	N
Err. [N, Nm]	0.312	1.033	-0.527	0.028	0.037	0.039
P. Err. [%]	0.281	0.290	-0.079	0.411	0.146	0.0352
Std.d. [%]	0.083	0.057	0.020	0.081	0.030	0.068
Reduced load range						
Component	X	Y	Z	L	M	N
Err. [N, Nm]	-0.116	-0.161	0.144	-0.017	0.026	0.014
P. Err. [%]	-0.341	-0.192	0.084	-0.798	0.398	0.518
Std.d. [%]	0.117	0.045	0.023	0.153	0.068	0.112

In Table 4 are:

Err. – maximum difference between applied and measured load,

P.Err. – maximum difference between applied and measured load calculated in relation to the component full scale,

Std.d – standard deviation of the errors calculated in relation to the component full scale.

In the measurements of hover performances of the DJI Phantom calibration matrix for the balance reduced load ranges was used.

4. MODEL MOUNTING ON THE CALIBRATION RIG

Measurements of the UAV test model aerodynamic characteristics were conducted with the model mounted on the calibration rig in the T-38 wind tunnel calibration laboratory, Figure 4. The camera gimbal mounting hole was used to support the model and serve as attachment points to the internal six-component balance.



Figure 4. DJI Phantom model in the T-38 wind tunnel calibration laboratory

The model is mounted on the internal six-component balance via suitable adapter. The six-component balance is connected via a cone to the sting, which is placed on the calibration rig, Figure 5. The same six-component balance and sting will be used for the testing of the DJI Phantom in the small subsonic wind tunnel T-32.

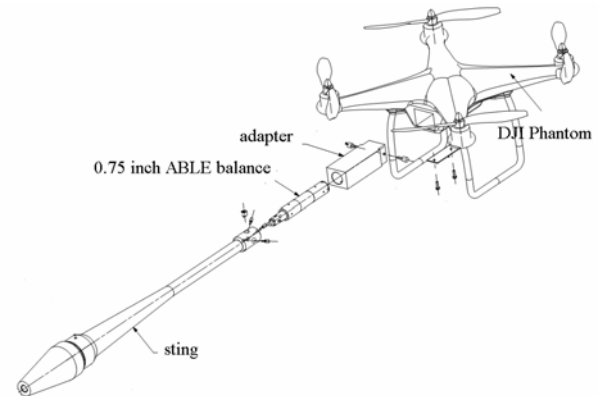


Figure 5. DJI Phantom model mounting

The DJI Phantom model mounted on the calibration rig is shown in Figure 6.



Figure 6. DJI Phantom model on the calibration rig

5. UAV SPEED CONTROL

The control of the number of revolutions of each drone engine is controlled by a central controller that receives data from sensors (GPS, electronic compass, altimeter, camera...), remote control and the current state of the engine and battery, and on the basis of that data determines whether the number of engine revolutions should be increased or decreased.

Testing the characteristics of the drone implies a constant number of revolutions of the engine during the measurement. The number of revolutions of the engine is the result of the state of all sensors, so it is not possible to achieve a constant number of revolutions of the engine using the remote control. Simulating the data of all the sensors that affect the engine's behavior would be a more demanding task than creating a computer-controlled controller individually for each engine.

In presented hover tests the required engine speeds as well as its characteristics are set using a computer. Speed measurement is performed optically or by sampling the voltage on one phase of the motor. The ESC management protocol used is the 50 Hz PWM Standard. The communication protocol between the PC and the interface is RS485. The microcontroller used was PIC12F1572. The control program was written in the C programming language and a compiler from the microcontroller manufacturer was used.

6. EXPERIMENTAL RESULTS

In hover test rotor RPM were varied in two ways. In the first part of the hover tests, the rotor speed was changed uniformly for all of the rotors on the model in order to quantify the effects of RPM on the model forces and moments, especially on the normal and axial forces. In the second part of the hover tests differential rotor speed was tested to measure moments on the vehicle. The moment centre is in the rotor plane at the point equidistant from all four rotors, Figure 7. The numbering of the rotors is shown in Figure 8.

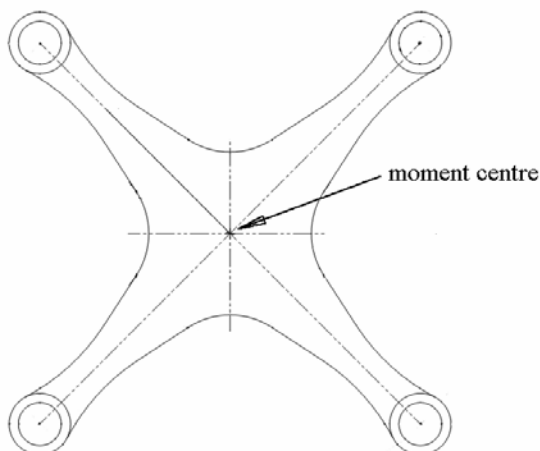


Figure 7. Moment centre

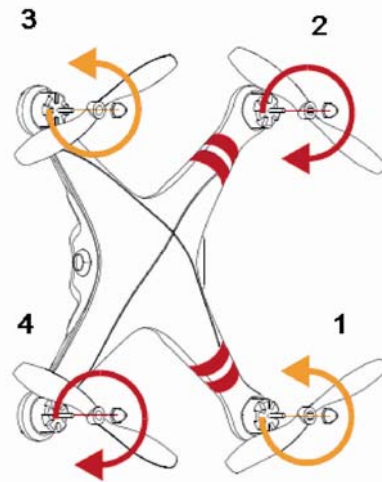


Figure 8. Rotor numbering [5]

The test matrix is presented in Table 5 and Table 6.

Table 5. Test matrix - uniform RPM

Uniform RPM				
Run number	RPM1	RPM2	RPM3	RPM4
1	4200	4200	4200	4200
2	4500	4500	4500	4500
3	4800	4800	4800	4800
4	5000	5000	5000	5000
5	5300	5300	5300	5300
6	5500	5500	5500	5500
7	6000	6000	6000	6000
8	6500	6500	6500	6500

Table 6. Test matrix - differential RPM

Differential RPM				
Run number	RPM1	RPM2	RPM3	RPM4
9	5300	0	0	0
10	0	5300	0	0
11	0	0	5300	0
12	0	0	0	5300
13	4200	4200	6400	6400
14	6400	6400	4200	4200
15	4200	6400	6400	4200
16	6400	4200	4200	6400

Measured forces and moments are reported in the axis system shown in Figure 9. The positive direction of the x-axis is from the moment centre toward the sting.

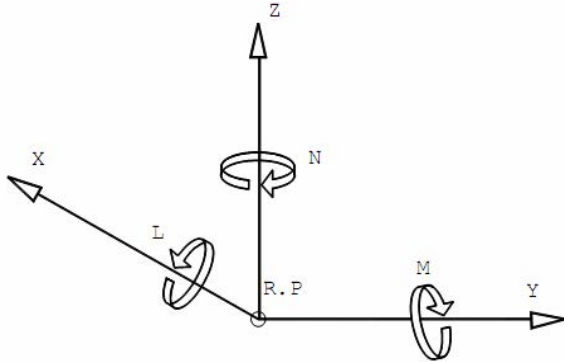


Figure 9. Directions of the forces and moments

Measured values of the normal force for the uniform rotor RPM is given in Table 7.

Table 7. Aerodynamic forces – uniform RPM

Uniform RPM	
Run number	Normal forces elements Normal force
1	RPM1=RPM2=RPM3=RPM4=4200 FNI=4.4037N FN2=1.0777N Z=5.4814N
	RPM1=RPM2=RPM3=RPM4=4500 FNI=5.1341N FN2=1.3115N Z= 6.4456N
2	RPM1=RPM2=RPM3=RPM4=4800 FNI=5.8540N FN2=1.4252N Z=7.2792N
	RPM1=RPM2=RPM3=RPM4=5000 FNI=6.3746N FN2=1.6476N Z=8.0222N
3	RPM1=RPM2=RPM3=RPM4=5300 FNI=7.3449N FN2=1.3314N Z=8.6763N
	RPM1=RPM2=RPM3=RPM4=5500 FNI=8.0358N FN2=1.7496N Z= 9.7854N
4	RPM1=RPM2=RPM3=RPM4=6000 FNI= 9.6877N FN2=2.1670N Z=11.8547N
	RPM1=RPM2=RPM3=RPM4=6500 FNI=11.5832N FN2=2.5297N Z= 14.1129N

Figure 10. shows the measured values of the normal force as a function of the rotors speed (rotor speed was changed uniformly for all of the rotors).

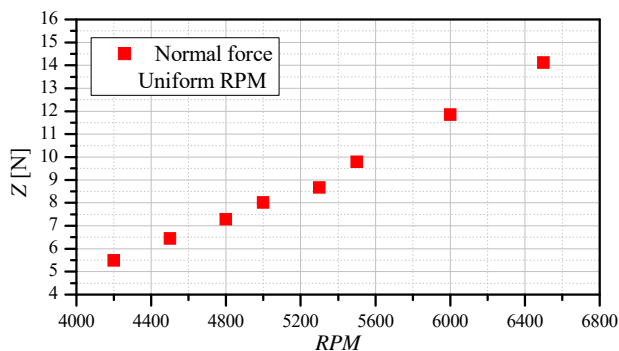


Figure 10. Normal force as a function of the RPM

Components of the aerodynamic load measured in the

tests with differential rotors speed is shown in Table 8.

Table 8. Aerodynamic forces – differential RPM

Differential RPM						
Run number	X [N]	Y [N]	Z [N]	L [Nm]	M [Nm]	N [Nm]
9	RPM1=5300 RPM2=RPM3=RPM4=0					
	-0.09665	0.10291	2.34133	0.28509	-0.2994	0.06101
10	RPM2=5300 RPM1=RPM3=RPM4=0					
	-0.09023	-0.1867	2.4092	-0.2997	-0.3059	-0.06715
11	RPM3=5300 RPM1=RPM2=RPM4=0					
	0.02020	-0.1456	2.3722	-0.2994	0.2976	0.05209
12	RPM4=5300 RPM1=RPM2=RPM3=0					
	0.0053	0.1279	2.3535	0.2928	0.3063	-0.05255
13	RPM1=RPM2=4200 RPM3=RPM4=6400					
	-0.12564	-0.0004	9.48768	0.00349	0.44021	0.00734
14	RPM1=RPM2=6400 RPM3=RPM4=4200					
	-0.25343	-0.1156	9.79388	0.02840	-0.5469	-0.00777
15	RPM1=RPM4=4200 RPM2=RPM3=6400					
	-0.28165	-0.2162	9.66346	-0.4791	-0.0412	-0.01285
16	RPM1=RPM4=6400 RPM2=RPM3=4200					
	-0.12025	0.00155	9.80596	0.54010	-0.0292	0.00586

7. CONCLUSIONS

The main goal of the presented tests was to examine the possibility testing of mini unmanned aircraft vehicle in the Experimental Aerodynamic Laboratory at Military Technical Institute. This paper described the test setup of the mini UAV model in hover mode. The test generated data show that the defined test setup enables quality measurements of hover performance for mini UAV. The same test setup will be used to continue testing the mini UAV, which is planned in a small subsonic wind tunnel T-32.

ACKNOWLEDGEMENTS

This work was supported by the Ministry of Education, Science and Technological Development of the Republic of Serbia (Contract No. 451-03-68/2022-14/200325).

References

- [1] THEYS,B., DIMITRADIS,G., ANDRIANNE,T., HENDRICK,P., De SCHUTTER,J.: *Wind Tunnel Testing of a VTOL MAV Propeller in Titled Operating Mode*, 2014 International Conference on Unmanned Aircraft Systems (ICAUS), 2014, pp.1064-1072.
- [2] BARIS,E., BRITCHER,C.P., ALTAMIRANO,G.: *WIND Tunnel Testing of Static and Dynamic Aerodynamic Characteristics of a Quadcopter*, AIAA AVIATION 2019 Forum, June 17-21, 2019, Dallas, Texas, pp.1-12, AIAA 2019-2973
- [3] SIMMA,M., MJOEN,H., BOSTROM,T.: *Measuring Wind Speed Using the Internal Stabilization System of Quadrotor Drone*, Drones, 23 (4), (2020), pp.1-10.

- [4] BAZIN,J.M., FIELDS,T.D., SMITH,A.J.: *Feasibility of In-Flight Quadrotor Individual Motor Thrust Measurements*, AIAA Atmospheric Flight Mechanics Conference, January 4-8, 2016, San Diego, California, USA, pp. 1-12, AIAA 2016-1760
- [5] PHANTOM Advance Manual, V1.4, DJI Innovations, 2013.03.22 Revision
- [6] RUSSELL,C., WILLINK,G., THEODORE,C., JUNG,J., GLASNER,B.: *Wind Tunnel and Hover Performance Tests Results for Multicopter UAS Vehicle*, NASA/TM-2018-219758, Ames Research Center, 2018.



PREDICTION OF QUASI-STEADY FLUTTER VELOCITIES OF TAPERED COMPOSITE PLATES AT LOW MACH NUMBERS: ANALYSIS AND EXPERIMENT

MIRKO DINULOVIC

University of Belgrade, Faculty of Mechanical Engineering, mdinulovic@mas.bg.ac.rs

ALEKSA MALJEVIC

University of Belgrade, Faculty of Mechanical Engineering, aleksa.maljevic1999@gmail.com

BRANIMIR KRSTIC

University of Defense, Military Academy, Belgrade, branimir.krstic@va.mod.gov.rs

Abstract: In the present work, based on existing quasi-steady aerodynamics theories, equations of motion for tapered composite plates are derived for a subsonic flow field. The required tapered plate frequencies of oscillation in bending and torsion are computed using the Rayleigh-Ritz principle. The material model for orthotropic materials is adopted for composites based on Ackerman and Tsai and Hanh theories for QI composite lay-ups., and initial composite material elastic coefficients are obtained based on composite micromechanics theories. The combination of these sets of equations rendered the possibility to solve the equations of motion for the lifting surface characteristic section in the closed-form and give an estimate of stability loss, and flutter velocity for tapered composite plates in the subsonic flow field.

Using the proposed approach, calculated flutter velocities are experimentally verified by performing the tests in a subsonic wind tunnel in the flow field from 5 m/s to 30 m/s. Furthermore, the results are compared to numerical results obtained using commercial software NASTRAN/Flight Loads. Good agreement between the proposed model, numerical results, and experiment is obtained, and based on this analysis it can be concluded that the proposed model can be used with acceptable accuracy for flutter velocity estimation for tapered composite plates in a low Mach number flow fields.

Keywords: flutter, quasi-isotropic laminates, stability loss.

1. INTRODUCTION

The flexibility of modern aircraft structures requires the analysis of the interaction between elastic, inertial, and aerodynamic forces even in the early design stages. Aeroelastic instability, known as flutter is a dynamic instability characterized by sustained structural oscillations. It directly arises from the interaction between the inertial, elastic, and aerodynamic forces acting on the lifting surfaces and potentially may lead to complete structural failure. The flutter instability (coupled-mode flutter) arises when two eigenmodes of fluid-structure interaction coincide, leading to high-amplitude structure oscillations, hence, dynamic instability. High amplitudes induce large strains, followed by high stresses in the structure, which may lead to failure.

With the objective to determine flight conditions (flight speed, primarily), close to 80% of flutter analyses in the industry is based on a numerical approach, relying on well-established K, P, and P-k algorithms (CFA). This approach leads to very good results, confirmed by experiments and flight tests, however, it requires tedious modeling and very often relatively expensive software modules not readily available.

In the present work quasi-steady flutter theory, expressed through the NACA flutter boundary equation [1], is used to estimate the flutter velocities of tapered composite fins exposed to low Mach number axial flow. The original theory is adapted for the orthotropic materials in the form of quasi-isotropic composite laminates and is based on the Ackerman, Tsai, and Hanh theory [2], since nowadays, composites are being extensively used in airframe design.

Results obtained, for the flutter boundary velocity for the quasi-isotropic material structures (very often used nowadays in airframe construction) are compared to numerical (CFA) results and experimental results from subsonic wind tunnel testing at low Mach and small Reynolds numbers (Re).

2. NACA FLUTTER MODEL

National advisory committee for aeronautics in technical note No 4197 has defined the flutter boundary velocity, for the preliminary design of lifting surfaces on missiles in the following form. (eq.1):

$$\left(\frac{V_f}{a}\right)^2 = \frac{G_e}{\frac{39.3 \cdot A^3}{\left(\frac{t}{c}\right)^3 \cdot (A+2)} \left(\frac{\lambda+1}{2}\right) \cdot \left(\frac{p}{p_0}\right)} \quad (1)$$

In the previous equation (eq. 1) V_f represents flutter boundary speed, a is the speed of sound, G_e is the shear modulus of elasticity, t is the lifting surface average thickness, p/p_0 is the ratio of the fluid pressure to standard pressure and A and λ are aspect and taper ratio respectively.

Based on Akkerman, Tsai, and Hanh's quasi-isotropic (QI) theory [2], the previous relation (eq.1) is modified for the composite materials, that are manufactured in the laminate form with QI stack-up. This stack-up is of particular interest, especially in the initial phases of the design, and is often used with composite materials during design phases that include the initial sizing of the laminates [3-4]. Any stack-up that satisfies the following relation (eq. 2) is considered to be quasi-isotropic [3]:

$$\left[0^\circ / \frac{180^\circ}{m} \dots (m-1) \frac{180^\circ}{m}\right]_{ns} \quad (2)$$

In equation 2, m represents the number of different orientations in the laminate ($m \geq 3$) and is the number of repetition sequences. This lamination type excludes unfavorable coupling effects and composite (in-plane) stiffness is independent of composite orientation, which may be the main reason why this type of stack-up is often used as the starting point in the early stages of the design [4].

The objective is to express the elastic coefficient G_e (shear modulus) given in equation 1 in terms of principal lamina properties (Young's moduli E_1 and E_2 , in-plane lamina shear modulus G_{12} , and major Poisson's ratio ν_{12}) and further by means of equivalent laminate properties based on above-mentioned theory [2].

Using the laws of composite lamina micromechanics, composite lamina elastic coefficient required (principal lamina props.), and based on constituent (fiber and matrix) properties, moduli can be obtained from the following system of equations (eq. 3) [3, 5]:

$$\begin{aligned} E_1 &= V_F \cdot E_f + V_m \cdot E_m, \\ \nu_{12} &= V_F \cdot \nu_f + V_m \cdot \nu_m, \\ E_2 &= \frac{E_m}{1 - \sqrt{V_F} \left(1 - \frac{E_m}{E_2^f}\right)}, \\ G_{12} &= \frac{G_m}{1 - \sqrt{V_F} \left(1 - \frac{G_m}{G_{12}^f}\right)} \end{aligned} \quad (3)$$

Composite constituent properties (E_f , E_m , and G_m) are usually obtained from material OEM, data found in the literature [5], or by experiment. Phases volume fractions (V_F and V_m) are determined by the composite design and

are usually within the 55 – 65 [%] range for V_f , for fly-worthy aerospace structural components.

Based on these data the effective in-plane shear modulus required by the NACA flutter boundary equation (eq.1), in terms of principal lamina elastic coefficients, for QI stack-up can be expressed in the following form [2].

$$G_{xy} = \frac{1}{2} \cdot G_{12} + \frac{1}{8} \frac{E_1 \cdot (E_1 + E_2 - 2\nu_{12}E_2)}{E_1 - 2\nu_{12}^2E_2} \quad (4)$$

Substituting equations 3 – 4 in the initial flutter equation (eq.1), for QI laminates reads:

$$V_f = a \cdot \left[\frac{(A+2)}{78.6 \cdot A^3} \cdot \left(\frac{t}{\frac{2}{S} \cdot \int_0^{b/2} c(y) \cdot dy} \right)^3 \cdot \frac{\left(G_{12} + \frac{1}{4} \frac{E_1 \cdot (E_1 + E_2 - 2\nu_{12}E_2)}{E_1 - 2\nu_{12}^2E_2} \right)}{\left(\frac{c_t / c_r + 1}{2} \right) \cdot \left(\frac{p}{p_0} \right)} \right]^{1/2} \quad (5)$$

In equation 5 fin chord (denoted with c in equation 5) is taken as the mean aerodynamic chord, for tapered plates, and is calculated using the known relation, given here for completeness.

$$C_{mac} = \frac{2}{S} \cdot \int_0^{b/2} c(y) \cdot dy \quad (6)$$

In the previous equation (eq.6), S is fin planform area, b is fin's total span, and $c(y)$ chord length at y span coordinate

3. NUMERICAL ANALYSIS

Using Commercial software MSC Nastran/Flight Loads, flutter speed, for the e-glass composite fin, of QI stack up $[0^\circ/45^\circ/-45^\circ/90^\circ]_s$, thickness 0.65 [mm] is calculated. Geometric dimensions of the fin analyzed are as follows: Root chord, $C_r=180$ [mm], tip chord $C_t=90$ and span $b/2 = 262$ [mm]. The numerical model is presented in the following figure (Figure 1):

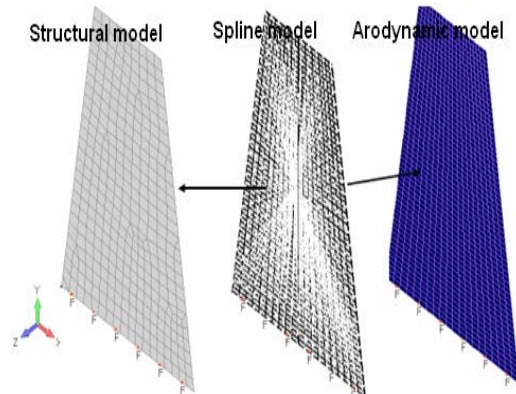


Figure 1. Flutter numerical model

The complete fin flutter model consists of a structural model and the aerodynamic model. The structural model consists of 172 laminate finite type finite elements (Classic Lamination Theory), that discretize the complete missile fin domain. The aerodynamic model computes the aerodynamic forces, based on the vortex panel method. To ensure the transfer of aerodynamic loading onto fin structure both models are mutually interconnected with beam-type splines. This kind of flutter model, enables analysts to obtain the flutter velocities, hence the fin dynamic stability loss. The algorithm used for this coupled flutter numerical model was a very well-known P-k algorithm [6].

For the geometry given, composite material characteristics, and subsonic flow conditions, the result obtained is that flutter occurs at 18.5 m/s.

Using the same geometry and material characteristics, using the analytic NACA model, described in previous sections (eq.6 at flight altitude corresponding to $p/p_0 = 1$ [-]), obtained value for the flutter speed is 16.7 m/s.

Fin mode shapes in bending and twisting (bending frequency $f_1 = 7.98$ [Hz], twisting frequency $f_2 = 28.68$ [Hz]) are presented in Figure 2. These frequencies are of great importance for the problem analyzed (composite fin bending-torsion flutter). The algorithm for modal extraction used in this example was the complex Lanczos algorithm since it was found that this algorithm for problems of similar size does not miss any modes, it is fairly fast and does not require fine mesh, which can be of importance when several case scenarios have to be analyzed. This was concluded based on the sensitivity analysis performed and results obtained from the experimental modal analysis.

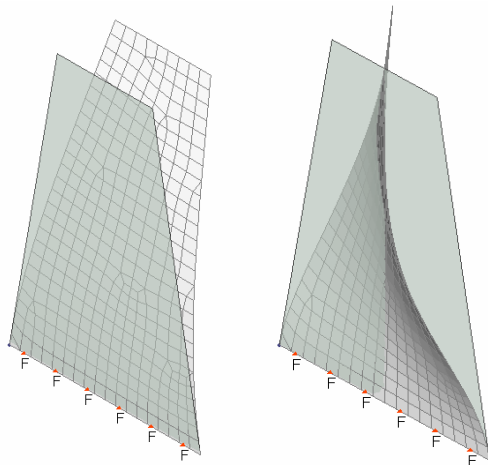


Figure 2. Mode shapes in bending and twisting

Frequency values obtained by Lanczo's method are compared to results obtained by the Rayleigh-Ritz method for natural frequencies calculations for cantilevered beams. The natural frequency of the cantilever beam is:

$$\omega_n = \frac{\lambda_n}{b^2} \sqrt{\frac{D}{\rho \cdot t}} \quad (7)$$

In equation 7 ρ is material density and D is plate flexural

rigidity computed from the following relation:

$$D = \frac{E_{eq} \cdot t^3}{12(1 - \nu_{eq}^2)} \quad (8)$$

Using the same theory as for the shear modulus of QI laminates [2], Young's modulus of elasticity for quasi-isotropic laminates is obtained using the following equation:

$$E_{eq} = 2 \cdot (1 + \nu_{xy}) \cdot G_{xy} \quad (9)$$

Poisson ratio (ν_{xy}) in this analysis for e-glass laminates is set to 0.3. Coefficients λ_n in equation 7 are the function of boundary condition, material type, and analyzed plate taper ratio. Coefficients λ_n for isotropic materials as a function of taper ratio (tip chord/root chord) are given in the following table (Table 1):

Table 1. Coefficients λ_n for isotropic materials (frequency parameters Ritz Method) [7]

C_{tip} / C_{root}	Mode 1 λ	Mode 2 λ
2	3.51	5.37
1	3.49	8.55
0.5	3.47	14.90

Ritz coefficients presented in table 1 are further modified for quasi-isotropic materials and plate aspect ratio. For the first three modes of vibrations of cantilevered, tapered thin plates λ_n coefficients are presented in the following figure (Figure 3.)

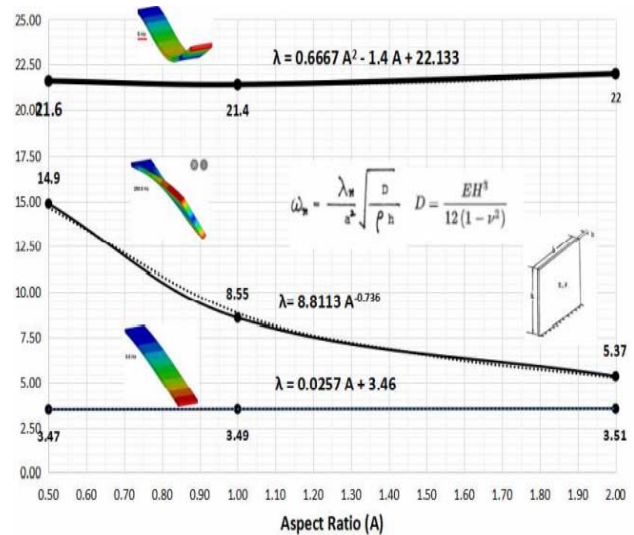


Figure 3. Mode shapes coefficients

4. WIND TUNNEL EXPERIMENT

To ensure and verify the validity of the proposed methodology, for the aeroelastic stability of the QI tapered e-glass plates, tests in a subsonic wind tunnel are performed at relatively low Mach number flows (up to 30 m/s). A specially designed support structure is used to support the test samples (e-glass tapered fins) and is

placed in the test section of the tunnel. Test samples are presented in figure 4. and the complete test setup (wind tunnel working section) in figure 5. The wind tunnel used for this experiment is a subsonic wind tunnel at the University of Belgrade, faculty of mechanical engineering.

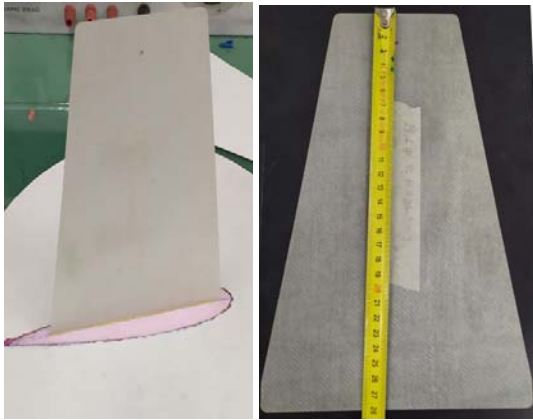


Figure 4 E-glass tapered plate for wind tunnel flutter test



Figure 5 Wind tunnel flutter test setup

The support structure with a clamped sample at the root chord, positioned in the test section of the wind tunnel, is presented in figure 4. In order to monitor the magnitude of the amplitudes during an oscillation cycle, accelerometers connected to the DAQ system were mounted on the test plate at the location of the root chord. The PCE PFM2 micro manometer with pitot tube is used to determine airflow velocity. The system can increase or decrease air-flow velocities in the wind tunnel by 0.5 m/s increments, with acceptable air-flow stabilization times.

Table 2. Samples Geometric and material data

Charact.	
Root chord	180 [mm]
Tip chord	90 [mm]
Span	262 [mm]
thickness	0.65 [mm]
QI	$[0^{\circ}/45^{\circ}/-45^{\circ}/90^{\circ}]_s$
E_1	41 000 [MPa] / ref [5]
E_2	10 400 [MPa] / ref [5]
G_{12}	4300 [MPa] / ref [5]
G_E	7962.59 [MPa] / equation 4

The experimental results for flutter velocities versus calculated values based on equation 5 and the numerical model (section 3) for the fin geometry (Table 1) are presented in table 2. Experimental velocity data is obtained based on 5 fin samples, with 10 runs in the wind tunnel. The flow velocity was gradually increased until the flutter was observed. The flow speed was then reduced to 10 m/s and ramped close to the flow speed where the flutter occurred in the previous run. The loss of stability of the test sample is presented in figure 5.

Table 3. Flutter velocity comparative results

Model	Flutter velocity [m/s]
NACA	16.7
Experiment	19.6 – 21.5 / (5 test samples / 10 runs)
Numerical P-K	18.2



Figure 6 wind tunnel flutter test

5. CONCLUSION

In the present work, the NACA boundary flutter equation was adopted for tapered composite thin plates, based on Akkerman, Tsai, and Hanh’s quasi-isotropic (QI) theory. Flutter velocities for the e-glass tapered fin are calculated and results obtained compared with numerical analysis (CFA) based on the P-k algorithm and experimentally obtained results in the wind tunnel at subsonic flow speeds in the range of 10 – 30 m/s. Based on the results obtained and the analysis performed the following can be concluded:

1. Modified NACA boundary equation tends to underestimate flutter speeds by 15 -25 % when compared to experimentally obtained data
2. Bearing in mind that flutter is a very complex phenomenon, this approach is advisable especially in the early stages of the design

- (preliminary sizing) since it leads to conservative, hence safe designs.
3. CFA approach based on the P-k algorithm renders results very close to experimentally obtained velocities, however, it requires tedious modeling and very often expensive software modules as well as extensive CPU resources and long computing time.

References

- [1] MARTIN, D.: *Summary of flutter experiences as a guide to the preliminary design of lifting surfaces on missiles*, NACA TN 4197, 1958.
- [2] AKKERMAN, R.: *On the properties of quasi-isotropic laminates*, Composites: Part B, 33 (2002) 133-40.
- [3] Tsai, S., and Hahn, T.: *Introduction to Composite Materials*, Lancaster: Technomic, 1980.
- [4] MASSARD, T.: *Computer sizing of composite laminates for strength*, Journal of Reinforced Plastics and Composites, 3(4), (1984)
- [5] DANIEL I. and ISHAI O.: *Engineering Mechanics of Composite Materials*, 2nd ed., Oxford press, 2006
- [6] WEIXING YUAN, XIAOYANG Z., and POIREL D.: *Flutter Analysis Solution Stabilization for the PK-Method*, AIAA Aviation 2021 Forum.
- [7] YOUNG, D.: *Continuous Systems*, Handbook of Engineering Mechanics, McGraw-Hill, 1962.



ON THE USE OF HIGH PITCH SWEEP RATES IN TIME-LIMITED SUPERSONIC WIND TUNNEL TESTS

DIJANA DAMLJANOVIĆ

Military Technical Institute, Belgrade, didamlj@gmail.com

ĐORĐE VUKOVIĆ

Military Technical Institute, Belgrade, vdjole@sbb.rs

BILJANA ILIĆ

Military Technical Institute, Belgrade, biljana.ilic@icloud.com

GORAN OCOKOLJIĆ

Military Technical Institute, Belgrade, ocokoljic.goran@gmail.com

STEFAN KRSTIĆ

Military Technical Institute, Belgrade, stefankrstic18@gmail.com

Abstract: *In high Reynolds number blowdown facilities with limited run time, such as the VTI's T-38 wind tunnel in Belgrade, tests at high stagnation pressure level often can not last long enough for execution of a sweep in the desired angle-of-attack range. Recently, during supersonic wind tunnel testing of a hypervelocity standard model it was investigated how angle-of-attack sweep range could be extended by increasing the pitch sweep rate up to 12° per second and whether the high sweep rates affected the test data. The optimum pitch sweep rate was investigated and established in the early stage of the VTI's T-38 facility exploitation period and a majority of reference wind tunnel data was obtained with the pitch rate of about 2° per second. The wind tunnel balance responses in the performed Mach 2 tests at all pitch rates of 2, 3, 4, 8 and 12° per second was excellent. The total axial force, normal force and the pitching moment were practically identical at all pitch rates. Unfortunately, the base pressure data showed a very high dependency on pitch rates because of the lag in pressure piping and, consequently, the forebody axial force, calculated on the basis of base pressure measurement, showed certain discrepancies. This should be important to all who deal with 'base drag corrected' supersonic data. Some recommendations and experience gained during tests are given.*

Keywords: *wind tunnel, supersonics, pitch sweep rate, base pressure, forces and moments.*

1. INTRODUCTION

In the situation of reduced time available for wind tunnel tests and constrained energy consumption, it is imperative that all wind tunnel systems and experimental setup be optimally set to achieve the parameters best matched with customer requirements. Today, when saving energy means saving time, as well as investments and environment, optimization of both facility operation and testing is a must for the wind tunnel community. First, accurate and complete wind tunnel calibrations have to be established, maintained, and placed under process control to avoid a risk of substantial investments in obtaining inaccurate wind tunnel data. Second, the optimization of the experimental setup has to be done by selecting the proper model scale, stagnation pressures, appropriate measuring equipment and model supports, as well as optimum sweep rates. All of these elements are emphasized in supersonic wind tunnel tests. The constraints related to model size, load range of available instrumentation versus transient and steady aerodynamic loads, and available run times, are often decisive in the selection of the conditions for a high-speed wind tunnel test [1].

Considering the above-mentioned trends, there is a surprising lack of research investigating the possibilities to reduce wind tunnel run times, thus also reducing the energy consumption, by increasing model sweep rates. The tests performed at subsonic Mach numbers from 0.3 to 0.75 in the NAE Canada trisonic wind tunnel demonstrated that pitch rates of up to 15°/s did not affect the force, moment and pressure data [2]. Apart from this research, there have not been found other published works on this subject. In the VTI T-38 wind tunnel, the possibilities to reduce run times by increasing pitch sweep rates have recently been investigated during supersonic testing of a hypervelocity standard model. The primary goal was to observe the possible effect of high pitch rates on the wind tunnel measurement data. The results and conclusions are summarized in this article.

2. EXPERIMENTAL FACILITY

The designed supersonic operating envelope of the VTI T-38 wind tunnel (Fig.1) in Belgrade, Serbia is limited by the minimum pressures needed to start and maintain a supersonic flow and by the structural safety limits [1].

Mach number is limited to an interval from 0.2 to 4 by the structural safety limits, and the mechanical design of both the choke flaps and flexible nozzle.

Stagnation pressure in the test section can be maintained between 1.1 bar and 15 bar, depending on the Mach number and regulated to 0.1% of nominal value. Run times range from 6 s to 60 s, depending on the Mach number and stagnation pressure. Models are usually supported in the test section by a tail sting mounted on a pitch-and-roll mechanism by which the desired aerodynamic angles can be achieved. The mechanism supports both step-by-step and continuous (pitch-sweep) movement of the model during measurements.



Figure 1. Pressurized air storage tanks of the VTI T-38 wind tunnel

In high Reynolds number blowdown facilities with limited run time, such as the VTI T-38 wind tunnel [3], tests at high stagnation pressure level often cannot last long enough for execution of a sweep in the desired angle-of-attack range. The optimum pitch sweep rate was established in the early stage of the facility exploitation period and a majority of reference wind tunnel data were obtained based on the pitch rate of 2°/s.

3. TEST MODEL

Test data on the HB hypervelocity standard models have been used to establish reference data for the correlation of the VTI T-38 experimental results with those from other aerodynamic facilities [4]. The compared data comprise the normal force curve slope and zero-lift total axial-force coefficient results at Mach numbers from 1.5 to 4.

Recently, during supersonic wind tunnel testing of the 100 mm dia. HB-2 standard model it was investigated how much sweep range during a run can be extended by applying high pitch rates. In addition, the effect of high pitch rates on the wind tunnel test data was studied.

HB standard model is an axisymmetric cone-cylinder with 25° nose cone half-angle [5][6]. The HB-2 configuration has a 10° tail flare, added to make the model less sensitive to viscous effects. The reference length for the definition of model geometry is the diameter D of the cylindrical part of model forebody. Model length is defined as 4.9D and moments' reduction centre is at 1.95D from the nose.

The 100 mm dia. HB-2 model (Fig.2), designed and produced in the VTI's workshop for the T-38 wind tunnel, is intended for measurement of forces and moments, and has been designed so that it can be tested on at least three different force balances, using suitable mounting adaptors for the model. The design enables simple assembly and disassembly of the model, which makes it suitable for use as a quick-check standard that could be easily installed in the wind tunnel instead of some currently tested model.

In the tests presented in this paper, the aerodynamic forces and moments acting on the model were measured by the VTI-produced 44 mm internal six-component strain gauge balance, labelled as VTI KV44. With the nominal axial force range of 2200 N, the balance has been designed specifically for supersonic wind tunnel tests. It has been calibrated to the accuracy better than 0.2% F.S. (based on 95% measurement certainty) for all components except for the axial force, for which the accuracy of 0.38% F.S. was achieved.



Figure 2. The 100 mm dia. HB-2 standard model in the VTI T-38 wind tunnel

Base pressure was measured on the model in the centre of the base area, at the entrance to the sting cavity at the rear side of the model. Base pressure coefficient (C_{pb}) and base axial force coefficient (C_{Ab}) are calculated as:

$$C_{pb} = \frac{p_b - p_{st}}{q}, \quad (1)$$

$$C_{Ab} = -C_{pb} \frac{S_b}{S_{ref}}, \quad (2)$$

where p_b is base pressure, p_{st} is freestream static pressure, q is dynamic pressure, while the reference area (S) and base area (S_b) are calculated as follows:

$$S = \pi(D)^2 / 4, \quad (3)$$

$$S_b = \pi(1.6D)^2 / 4. \quad (4)$$

Forebody axial force coefficient (C_{Af}) is calculated by subtracting the base axial force coefficient from the total

axial force coefficient (C_A) obtained from the balance measurement:

$$C_{Af} = C_A - C_{Ab}. \quad (5)$$

4. RESULTS AND DISCUSSION

4.1. Uncertainty of measurements

In order to discuss wind tunnel data, it is necessary to determine uncertainty of measurements, outside of which any possible pitch rate effects can be detected [7].

The overall uncertainty of a measurement in wind tunnel tests is roughly proportional to a multiple of random error (estimated by standard deviation σ), which is latter often used to express the degree of the accuracy of measurements [8]. Based on the known accuracies of individual sensors in wind tunnel tests, it is possible to estimate the standard deviations of various quantities which are computed from several independently measured quantities. This estimation is done by varying the data for each directly measured quantity for a small amount (equal to the accuracy of the sensor used), performing the complete calculation of the aerodynamic coefficients, and by noting the changes in the calculated output values.

Table 1 presents estimates of maximum expected errors in determining the aerodynamic coefficients from the main six-component balances, expressed for each quantity as two standard deviations (2σ) with approximately 95% confidence level. Estimates are presented for Mach 2, and for the model attitude defined by $+10^\circ$ angle of attack and 0° rolling angle, including the sting deflection. It is assumed that the dimensions of the model are exact. The test results obtained using the VTI KV44 six-component balance are compared with the results from reference runs performed using the ABLE Mk18 six-component balance.

Table 1. Measurement uncertainties of relevant aerodynamic coefficients for Mach 2 tests

HB-2 100 mm standard model		
Measurement uncertainties	Wind tunnel balance	
	ABLE Mk18	VTI KV44
$2\sigma C_A$	± 0.0036	± 0.017
$2\sigma C_N$	± 0.022	± 0.0067
$2\sigma C_m$	± 0.017	± 0.0089
$2\sigma C_{Ab}$	± 0.00087	± 0.00087

By performing two runs with identical flow conditions, a level of repeatability can be obtained and together with measurement uncertainties, the scatter of data can be established. For reference, the main balance and pressure data from two identical runs, performed one after the other, are shown in the figures in the following sections.

4.2. Averaging the wind tunnel test data

Model support mechanism in the VTI T-38 wind tunnel enables control of model position in pitch and roll planes. Position of the model support in these two planes is

measured by high-accuracy encoders. The mechanism's pitching angle is calculated for each sample from the encoder output using the third-order polynomial function that was determined in the previous calibration.

Since the model was moving continuously in pitching angle range from -5° to $+19^\circ$ during the measurement, it was necessary to select certain model positions for which the data were to be reduced. For this purpose, a list of 25 pitching angles at approximately 1° intervals was prepared for each run. During data reduction process, the data were segmented in such a manner that for each model position only the data lying in the interval of approximately $\pm 0.25^\circ$ from the selected pitching angles were averaged, thus giving the 25 "steps" for which the results are listed in the tables and graphs.

Generally, the averaging interval at each model position is a little narrower, as the software automatically adjust it so as to obtain an average of a whole number of periods of the model/sting oscillation at natural frequency.

The average values of measured angles are calculated for each data segment (desired model position) using the n samples lying in the averaging interval:

$$pit = \frac{1}{n} \sum_{i=1}^n pit_i \quad (6)$$

The average values of the pressures, temperature, Mach number, Reynolds number and main balance data in the run are calculated using the equivalent relations.

In these HB-2 model tests it was necessary to sample the data at a rate high enough to allow the averaging of sufficient samples over the desired range of angle-of-attack. Not the same numbers of raw data samples were averaged for all runs, but raw samples were averaged from within the same range of angle-of-attack for all runs at all pitch rates, see Table 2.

Table 2. High pitch sweep rate tests parameters

HB-2 100 mm standard model testing Mach 2, Stagnation pressure 2.5 bar Pitch sweep range -5° to $+19^\circ$			
Pitch rate, $^\circ/s$	Channel sampling rate, 1/s	Data acquisition time, s	Number of samples in the averaging interval
2	250	12	62
2	250	12	62
3	250	8	41
4	250	6	31
8	500	3	31
12	500	2	20

4.3. Measurement of the base pressure

The accurate measurement of the base pressure in the supersonic wind tunnel tests is complicated by the lag in the measured values, caused by the combination of the low pressure levels and the relatively long pneumatic piping. In the VTI T-38 wind tunnel, the piping from the sensing port to the transducer is about seven meters long, and the time needed for establishing the pressure in the

pneumatic installation is not negligible. This time lag particularly complicates the measurement of the base pressure in the pitch sweep tests. In order to realize measurement as accurately as possible, limited pitch rates are used, allowing for the base pressure establishment in the piping. On the other side, low pitch rates extend the required run time, thus directly increasing energy consumption. Decreasing run time is an obvious course of action that is needed in order to achieve energy savings.

The effect of higher pitch rates on the base pressure measurement is analyzed in the VTI T-38 wind tunnel, the goal of the study being to determine the maximum pitch rate that will not have an adverse effect on the measurement accuracy with the existing base pressure pneumatic piping. As anticipated, wind tunnel tests of the HB-2 model at Mach 2 showed a significant effect of the pitch rates on the base pressure measurement. Significant discrepancies in the base pressure data are present for pitch rates above 3°/s, and they become more prominent for higher pitch rates, as is shown in Tables 3 and 4, as well as in Fig. 3.

Table 3. High pitch rate tests: Base pressure

HB-2 100 mm standard model testing, Mach 2 Stagnation pressure 2.5 bar, Pitch angle +19°			
Pitch rate,°/s	P_b , bar	ΔP_b , mbar	ΔP_b , %FS
2	0.08845	0.00	0.000
2 (repeat run)	0.08874	0.29	0.016
3	0.09083	2.38	0.136
4	0.09452	6.07	0.347
8	0.10338	14.93	0.853
12	0.10796	19.51	1.115
$2\sigma P_b = 0.038\%FS$, $2\sigma P_b = \pm 0.665$ mbar			

Table 4. High pitch rate tests: Base pressure coefficient

HB-2 100 mm standard model testing, Mach 2 Stagnation pressure 2.5 bar, Pitch angle +19°		
Pitch rate,°/s	C_{pb}	ΔC_{pb}
2	-0.25880	0.00
2 (repeat run)	-0.25798	0.00082
3	-0.25767	0.00113
4	-0.25377	0.00503
8	-0.24291	0.01589
12	-0.24068	0.01812
$2\sigma C_{pb} = \pm 0.00087$		

Based on the results, it is clear that pitch rates higher than 3°/s in the wind tunnel tests requiring the base pressure measurement would not be possible without improving the base pressure response, i.e., without modifications of the transducer placement, its type or the corresponding pneumatic piping. Thus, for the supersonic tests in the VTI T-38 wind tunnel in the future, the recommended course of action is to move the base pressure transducer to a more suitable place. It has to be close enough to the model, mounted on a stable support and isolated from the wind tunnel vibrations. In the past, some trials were performed with the base pressure transducer placed in a service cavity in the vertical strut of the model support system, reducing the piping length by about 4 m. A significant reduction in lag was observed, but thermal

stabilization of the transducer, as well as accessibility of pressure tubing for venting against moisture condensation remained issues to be solved in the future.

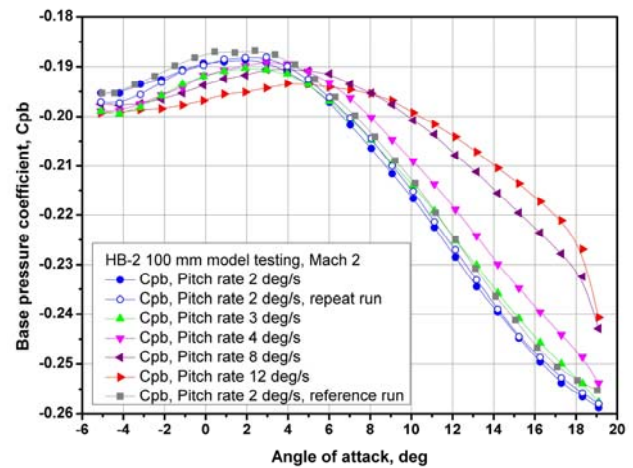


Figure 3. Base pressure coefficient for different pitch rates in the HB-2 model Mach 2 tests

On a case to case basis, depending on the model size and design, it would be possible for a transducer to be placed inside the model. The transducer diaphragm then must be aligned with the pitch plane to eliminate the effects of gravitational and other accelerative forces [2].

In addition, when selecting the transducer type for the base pressure measurement, it should be careful to choose the one with relatively low internal volume and fast response. Some high accuracy digital transducers have the response time from 0.10 s to 0.25 s. It is not satisfactory for measurement of the base pressure, which tends to change fast during model movement.

4.4. Measurement of the forces and moments

Contrary to the base pressure measurement, the VTI KV44 balance response in the high pitch rate tests of the 100 mm dia. HB-2 model was excellent. The coefficients of the axial force, the normal force, and the pitching moment are given in Fig.4-Fig.6, respectively.

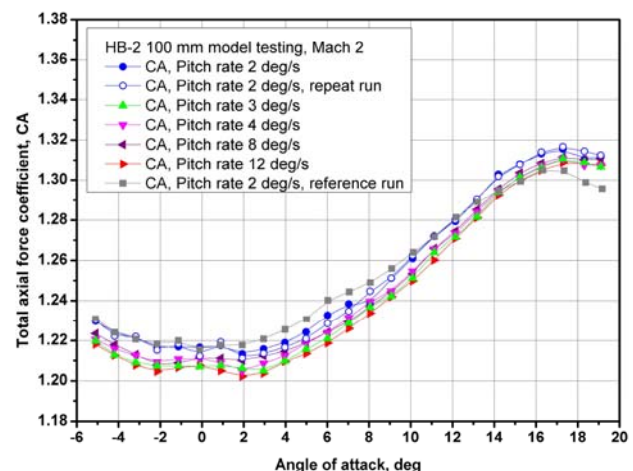


Figure 4. Total axial force coefficient for different pitch rates in the HB-2 model Mach 2 tests

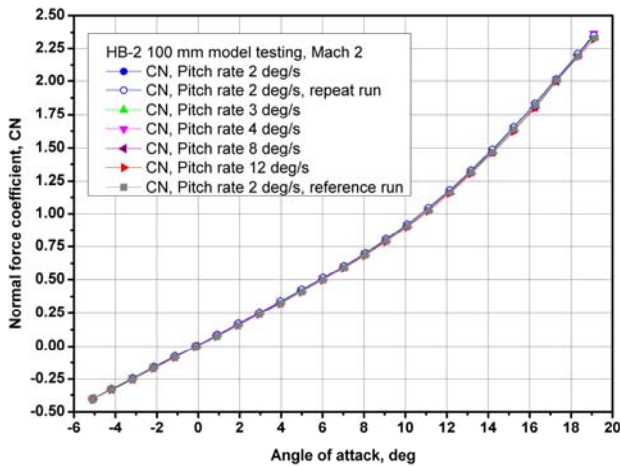


Figure 5. Normal force coefficient for different pitch rates in the HB-2 model Mach 2 tests

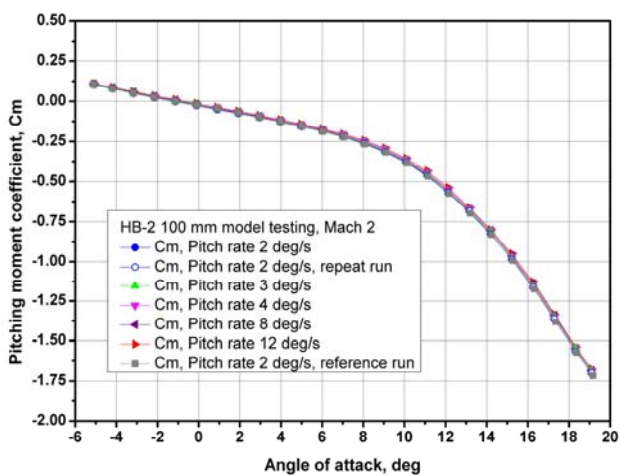


Figure 6. Pitching moment coefficient for different pitch rates in the HB-2 model Mach 2 tests

Force and moment data were in good agreement with data from the reference run performed using the ABLE Mk18 balance, and well within measurement uncertainties. The forebody axial force, however, depends on the base pressure, as in (5), and it is shown in Fig. 7. It is clear that pneumatic lag in the base pressure measurement for pitch rates higher than 3°/s introduces the error in the base axial force results (Fig.8).

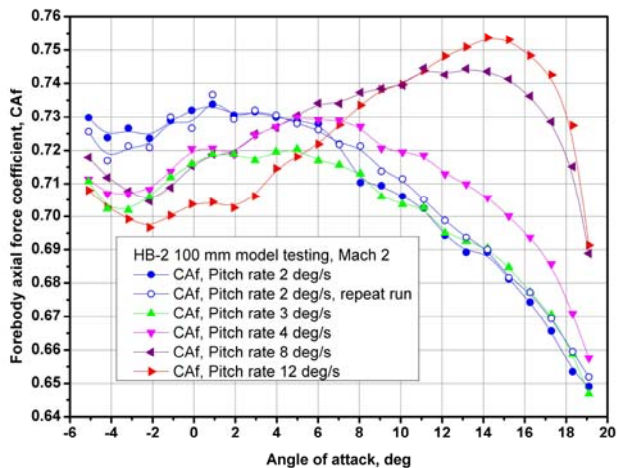


Figure 7. Forebody axial force coefficient for different pitch rates in the HB-2 model Mach 2 tests

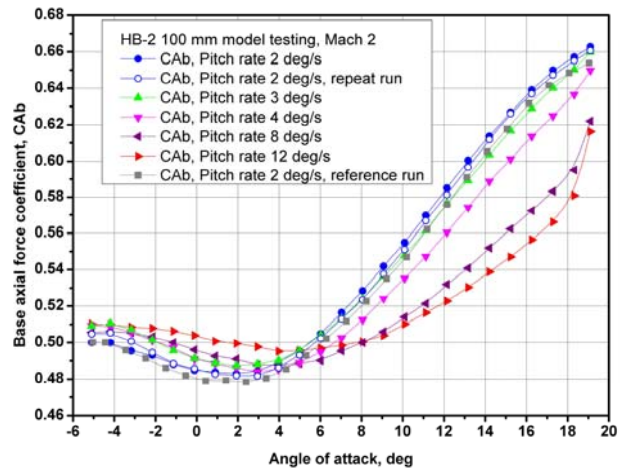


Figure 8. Base axial force coefficient for different pitch rates in the HB-2 model Mach 2 tests

The differences in the wind tunnel data between repeated runs at 2°/s sweep rate are small and well within the measurement uncertainties.

It is evident that differences in the base pressure and all related quantities between runs at the different sweep rates increase with the angles of attack, because of the higher rate of change of the base pressure and pneumatic lag in the installation.

5. CONCLUSION

The tests performed in the VTI T-38 wind tunnel with the goal to observe the possible effect of high pitch rates on the wind tunnel measurement data were useful and resulted in the following recommendations, aimed to improve the facility testing practice in the future:

- For the currently employed base pressure measurement system, the pitch rates higher than 3°/s have an adverse effect on measurement accuracy of the base pressure and, consequently, the forebody drag. The discrepancies in the forebody axial force observed for high pitch rates are of interest to those who deal with 'base drag corrected' supersonic wind tunnel data.
- The base pressure measurement system should be modified in the manner to improve the pneumatic lag. It is expected that it could be accomplished by mounting the transducer closer to the model and by minimizing the volume of the required piping. The issue with thermal stabilization of the transducers has to be solved.
- The measurement of the forces and moments do not show any dependency on the pitch rates up to 12°/s at Mach 2. The correlations of the force and moments data using the Able and VTI balances are in a very good agreement and within the measurement uncertainties.
- The run time limitation in the VTI T-38 high supersonic range can be overcome by using pitch rates of 3°/s for the currently employed base pressure measurement system.
- The tests were performed using the no-wing-cylinder-tail-flared model and it is recommended to continue research using models of different aerodynamic forms.

Winged forms would be of particular interest.

ACKNOWLEDGEMENTS

This work was supported by the Ministry of Defence and the Ministry of Education, Science and Technological Development of the Republic of Serbia (Contract No.451-03-68/2022-14/200325).

References

- [1] DAMLJANOVIĆ, D., VUKOVIĆ, Đ.: *Selection Criteria of Optimal Conditions for Supersonic Tests in a Blowdown Wind Tunnel*, Scientific Technical Review, 66(1) (2016) 29-39.
- [2] ATRAGHJI, E., DIGNEY, J.R.: *High Pitch Rates for Use in Short Duration Wind Tunnels*, in AGARD Wind Tunnel Design and Testing Tech. Mar. 1976.
- [3] MEDVED, B., ELFSTROM, G.M.: *The Yugoslav 1.5 m trisonic blowdown wind tunnel*, in: A Collection of Technical Papers of the 14th AIAA Aerodynamic Testing Conference, AIAA, Reston, VA, 1986, AIAA-86-0746-CP.
- [4] DAMLJANOVIĆ, D., RAŠUO, B., VUKOVIĆ, Dj., MANDIĆ, S., ISAKOVIĆ, J.: *Hypervelocity ballistic reference models as experimental supersonic test cases*, Aerospace Science and Technology 52 (2016) 189–197
- [5] GRAY, J.D.: *Summary report on aerodynamic characteristics of standard models HB-1 and HB-2*, AEDC-TDR-64-137, Arnold Engineering Development Center, 1964.
- [6] GRAY, J.D., LINDSAY, E.E.: *Force tests of standard hypervelocity ballistic models HB-1 and HB-2 at Mach 1.5 to 10*, AEDC-TDR-63-137, Arnold Engineering Development Center, 1963.
- [7] HEMSCH, M., GRUBB J., KRIEGER W., CLER D.: *Langley wind tunnel data quality assurance – check standard results (invited)*, in: Proceedings of the 21st AIAA Advanced Measurement Technology and Ground Testing Conference, AIAA, Reston, VA, 2000, 1–22.
- [8] DAMLJANOVIĆ, D., ISAKOVIĆ, J., RAŠUO, B.: *T-38 Wind tunnel data quality assurance based on testing of a standard model*, Journal of Aircraft, 50 (4) (2013) 1141–1149, AIAA, Inc.
- [9] VUKOVIC, Dj., DAMLJANOVIC, D.: *Evaluation of a force balance with semiconductor strain gages in wind tunnel tests of the HB-2 standard model*, Proc IMechE Part G: Journal of Aerospace Engineering, 229(12) (2015) 2272–2281.
- [10] CÉRESUÉLA, R.: *Mesurés d'efforts et de pressions sur la maquette balistique étalon H.B.2 ($2 \leq \text{Mach} \leq 16.5$)*, Note technique 13/1879 A, ONERA, 1964.
- [11] CÉRESUÉLA, R.: *Maquettes étalons HB.1 et HB.2 caractéristiques aérodynamiques mesurées dans le souffleries de l'O.N.E.R.A. de Mach 2 à Mach 16.5*, Note technique N123, ONERA, 1968.



NUMERICAL ANALYSIS OF A PROPELLER IN GROUND EFFECT

JELENA SVORCAN

University of Belgrade, Faculty of Mechanical Engineering, Belgrade, jsvorcan@mas.bg.ac.rs

ALEKSANDAR KOVAČEVIĆ

University of Belgrade, Faculty of Mechanical Engineering, Belgrade, akovacevic@mas.bg.ac.rs

TONI IVANOV

University of Belgrade, Faculty of Mechanical Engineering, Belgrade, tivanov@mas.bg.ac.rs

ALEKSANDAR SIMONOVIĆ

University of Belgrade, Faculty of Mechanical Engineering, Belgrade, asimonovic@mas.bg.ac.rs

Abstract: Detailed studies of propeller flows are regaining both interest and significance worldwide, as the number of their different design and applications (particularly for futuristic urban air vehicles) continues to grow. An additional distinctive characteristic of small-scale unmanned air vehicles (UAV) propellers is that they are meant to operate in a wide range of (previously considered atypical) operating conditions, including backward flight, flight in the vicinity of obstacles, hard/ground surfaces, etc. These specific requirements raise the issue of the effects of ground proximity on their aerodynamic performance. This paper computationally investigates flows around a small-scale, custom-made propeller in ground effect. Different ground distances are considered and novel thrust and power relations (dependencies) on them are proposed. In order to obtain sufficiently reliable and accurate results and capture the most significant flow features, Reynolds-averaged Navier-Stokes (RANS) equations are solved by finite volume method. In addition, interesting flow visualizations are presented. Although the obtained thrust trend correlates well with the conventionally used semi-empirical formula, more realistic estimations are obtained for small ground distances. Furthermore, the positive effects of ground vicinity on rotor aerodynamic performances are once again confirmed and quantified.

Keywords: propeller, turbulence, RANS, IGE.

1. INTRODUCTION

Numerous diverse aerial platforms, equipped with rotors that generate sufficient amounts of thrust, are designed, investigated, manufactured, and flown worldwide [1-3]. Their low cost, flexible operability and maneuverability enable a wide range of different applications, including scientific measurements, infrastructure inspection, deliveries, surveillance, crop/spray dispersion in agriculture, etc. These tasks often demand that the aircraft comes quite close to the referent surface, which may significantly affect its aerodynamic performance since the shed vortices interact with the rigid boundaries.

This flow phenomenon, when the streamtube of induced velocities formed by the rotor rotation dilates (expands) and adjusts to the surface downstream instead of narrowing, is entitled “ground effect” (IGE). It has been known and successfully modelled (firstly by simple potential flow theory and now by more complex computational models) for decades [4-6]. A rather simple expression can be used to estimate the increase of thrust T_{IGE} relative to the thrust of an isolated rotor T_{OGE} with respect to the relative distance from the ground z/R (where z is the absolute distance) at constant torque/power of an arbitrary rotor of radius R [4]:

$$\frac{T_{IGE}}{T_{OGE}} = \frac{1}{1 - \left(\frac{R}{4z}\right)^2} \quad (1)$$

It may be observed that Eq. 1 doesn't take into account any specific geometric features of the inspected rotor. Nowadays, with the increased availability and constant advancement of CFD techniques, it is possible to estimate more accurately (up-to several percent) the aerodynamic performances of a particular rotor/propeller in ground effect, including small-scale geometries operating at relatively low Reynolds numbers (Re). Here, low-to-medium Re imply several tens to several hundreds of thousands where transitional flow and laminar separation bubbles (LSBs) may be present. Since these regimes include various flow phenomena, it is best to perform detailed analyses of a particular geometry whenever possible.

Here, a small-scale fixed-pitch propeller/rotor designed for a small quadcopter in hover and in ground effect is numerically investigated. The blade geometry was defined through an optimization study whose details can be found in [7]. Previously mentioned simple semi-empirical relation (based purely on the distance from the ground and rotor size) is complemented by a detailed CFD study. The

employed numerical approach (previously tried on an isolated rotor) has been validated through grid convergence study and comparison to available experimental data performed at the University of Belgrade, Faculty of Mechanical Engineering [7]. The propeller, connected to an electric motor, and powered by a battery pack, was mounted on a sliding stand. Thrust was measured by a load cell, whereas power was implicitly estimated from the measured voltage and current.

Few additional explanations should be provided here, before continuing with the details of the current research. The observed differences in measured and computed thrust were not greater than 15% and were much less for the torque. From numerous numerical studies, differing in complexity and starting assumptions, the authors came to the following conclusions. The differences in the two sets of results are the consequence of several factors. Employing the RANS approach, that completely models and simplifies turbulent motion, contributes up-to 5%. Similarly, medium mesh resolution (comprising several million cells, where geometry is generally well represented, but without extra fine refinement of the leading edge and cells in the wall vicinity) results in approximately 4% error. The greatest contributor to the wrong estimate of thrust seems to come from neglecting the actual experimental set-up, and all the additional objects positioned close to the rotor that may affect its wake, even slightly. That is, “dirty” experimental set-up may contribute around 7-10%. Similarly, if numerical results were to be compared to the wind tunnel data, the effects of its walls should be taken into account, for greater accuracy and reliability of numerical estimation.

So, even though some deficiencies of RANS analyses of this flow phenomena are well-known (and can even be quantified), this is still the most usually employed numerical approach, mostly because of a satisfactory balance between the accuracy of results and computational cost and speed. Also, its credibility (veracity) can be augmented by putting in additional effort into the phases of geometric design, mesh generation and appropriate numerical set-up. With ground effect, we are mostly interested in the increase of thrust at the same power (or decrease of power for the same thrust) in comparison to the performance of an isolated rotor. Therefore, the obtained relative changes (ratios) can be accepted as sufficiently reliable and a good starting point for the estimation of small-scale propeller performances in ground vicinity.

2. METHODOLOGY

Particularities of the employed numerical approach are given below.

2.1. Rotor geometry and computational domains

The diameter of the investigated propeller, illustrated in Fig. 1, is $D = 73.2$ cm. Reynolds number based on the chord located at $\frac{3}{4}$ blade span and at nominal rotational frequency of 3289 rpm is 300,000 (where numerous flow phenomena such as LSB may be expected).

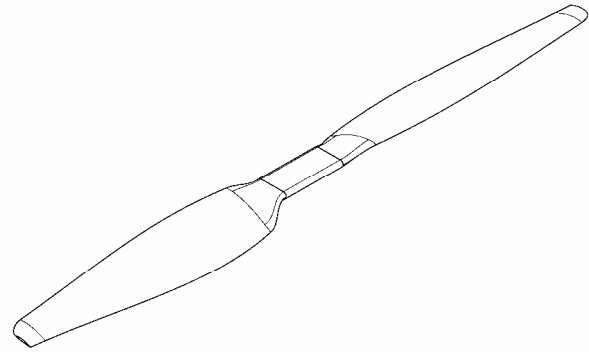


Figure 1. Propeller geometry

Propeller is surrounded by the smaller “rotating” part of the domain, while both parts are located within a much bigger “stationary” zone. In order to appropriately simulate “ground effect”, several different outer computational domains had to be modeled, corresponding to the ground distance $z = [0.15$ m, 0.20 m, 0.25 m, 0.30 m, 0.35 m, 0.40 m, 0.50 m], respectively. These values were chosen to adequately capture changes in thrust. All the outer zones are cylinders of the same outer radius 3.5 m, extending -2 m in upstream, and z to 8 m (for isolated rotor) in downstream direction. In order to achieve some kind of similarity, the inner, “rotating” part of the domain was the same for all models, which means it has to fit into the shortest domain. This cylinder extends from -0.2 m to 0.1 m in streamwise, and 0.6 m in radial direction, respectively.

2.2. Computational grids

Likewise, while the “rotor” grid remained the same, different “stator” meshes had to be generated for each considered ground distance z . Overall, all generated grids are sufficiently fine, unstructured hybrid meshes (defined after grid convergence studies). Some details are provided in Figs. 2 and 3.

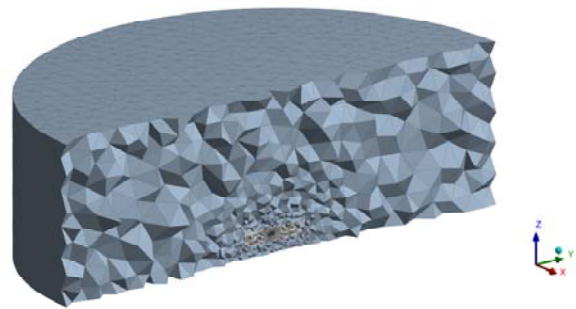


Figure 2. Cross-section of a generated grid

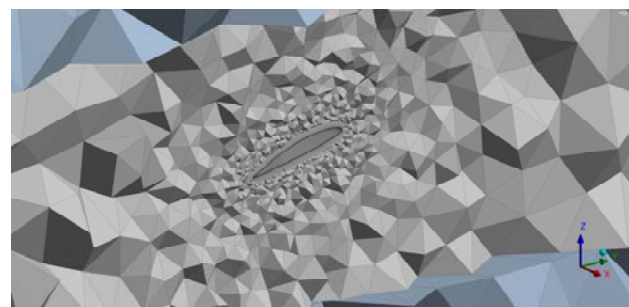


Figure 3. Detail around the blade

Meshes are additionally refined in close proximity to the propeller that is also encompassed by 25 layers of thin prismatic cells to better capture sudden (quite distinct) changes of flow quantities within the boundary layer. Small differences in the number of cells originate from differences in geometry, but all meshes number from 5.3 to 5.4 million cells (control volumes).

2.3. Numerical set-up

The governing RANS equations for 3D, incompressible flows, closed by the $k-\omega$ SST turbulence model, were solved in ANSYS Fluent by the finite volume method. Propeller rotation was accounted for by the quasi-steady multiple reference frames (MRF) approach, where additional terms are simply added to the equations in the “rotating” part of the domain. Even though this is the simplest approach, it gives sufficiently accurate results for statistically steady, nearly axisymmetric flows. Angular velocities close to nominal were assigned to the inner, quasi-rotating zone.

Since hovering condition in ground effect is the main focus of this study, zero values of gauge pressure along the inlet and slip velocity condition along the outlet surface, respectively, are assumed. Blade walls are rotational and no slip. Air is considered incompressible, and a pressure-based solver is used together with the SIMPLEC pressure-velocity coupling scheme. All spatial discretizations are of the 2nd order. The computations are performed until achieving the convergence of aerodynamic forces and moments (thrust and torque).

3. RESULTS AND DISCUSSION

Computed and approximated increases in thrust, while keeping constant angular velocity and nearly constant torque (and power), are illustrated in Fig. 4.

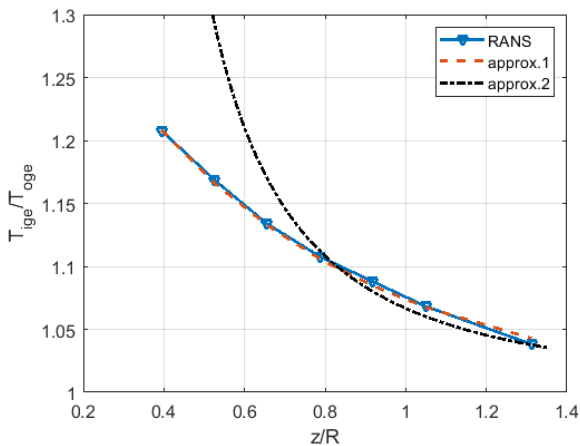


Figure 4. $T_{IGE}/T_{OGE} = f(z/R)$

Approximation 2 is represented by Eq. 1, whereas approximation 1 is derived for this particular propeller geometry, and can be written in the following form:

$$\frac{T_{IGE}}{T_{OGE}} = 1 + 0.41e^{-1.72\frac{z}{R}} \quad (2)$$

Although other functions could have been used also, this form was chosen for its asymptotic behavior, i.e. for infinite z , the ratio T_{IGE}/T_{OGE} goes to 1. The approximation proposed here is less steep than the usually employed general semi-empirical relation and gives more realistic estimates for small ground distances ($z/R < 0.8$). At higher ground distances, the two approximations seem sufficiently similar. For more clarity, the values illustrated in Fig. 4 are also listed in Table 1.

Table 1. Computed relative changes in thrust for different ground distances

z (m)	z/R	T_{RANS}/T_{OGE}	$T_{approx1}/T_{OGE}$	$T_{approx2}/T_{OGE}$
0.15	0.3937	1.2079	1.2083	1.6757
0.20	0.5249	1.1688	1.1662	1.2933
0.25	0.6562	1.1338	1.1326	1.1698
0.30	0.7874	1.1077	1.1058	1.1121
0.35	0.9186	1.0879	1.0844	1.0800
0.40	1.0499	1.0682	1.0674	1.0601
0.50	1.3123	1.0382	1.0429	1.0377

Similarly, it is possible to make an approximation of the power decrease while keeping constant thrust, which is illustrated in Fig. 5. The obtained numerical results indicate that, in ground proximity, the same levels of thrust can be achieved for nearly 30% less power, which can lead to significant savings and prolonged flight endurance.

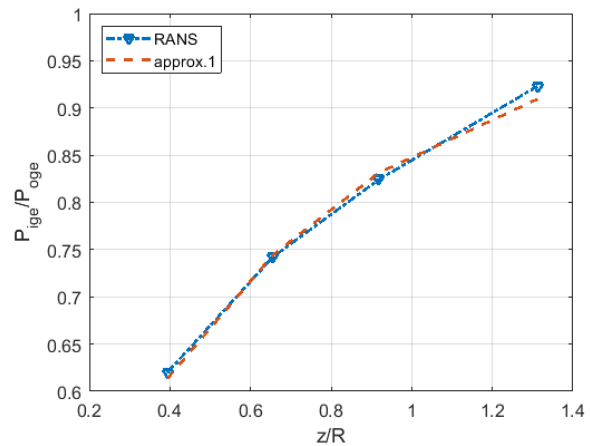


Figure 5. $P_{IGE}/P_{OGE} = f(z/R)$

The novel approximation proposed here, and sketched in Fig. 4, can be written as:

$$\frac{P_{IGE}}{P_{OGE}} = 1 - 0.72e^{-1.58\frac{z}{R}} \quad (3)$$

Since power required for hover comprises two parts, induced and profile, that account for the air acceleration through the rotor and blade drag, respectively, it is necessary to define a separate approximate expression (Eq. 3), instead of simply using the one for the thrust (Eq. 2) at the power $3/2$. Furthermore, the requirement of

asymptotic character of the fitting curve is again satisfied. In both cases, the R -square (R^2) of the proposed fits was above 0.995.

Ground effect can qualitatively be represented by different flow visualizations. Figure 6 illustrates three different computed fields of induced velocities in mid-plane, for $z = 0.2$ m, $z = 0.5$ m and infinite z (isolated rotor). In all cases, the greatest contributions of the outer blade segments are clearly visible, as well as the nearly non-existing induced velocities around the blade roots. When the outlet boundary is close to the rotor, the streamtube adjusts and slides along it. The wakes shed from the two blades remain distinct and expand outwards. On the other hand, for the isolated rotor, the two wakes merge and the total structure contracts as the flow continues to accelerate downstream.

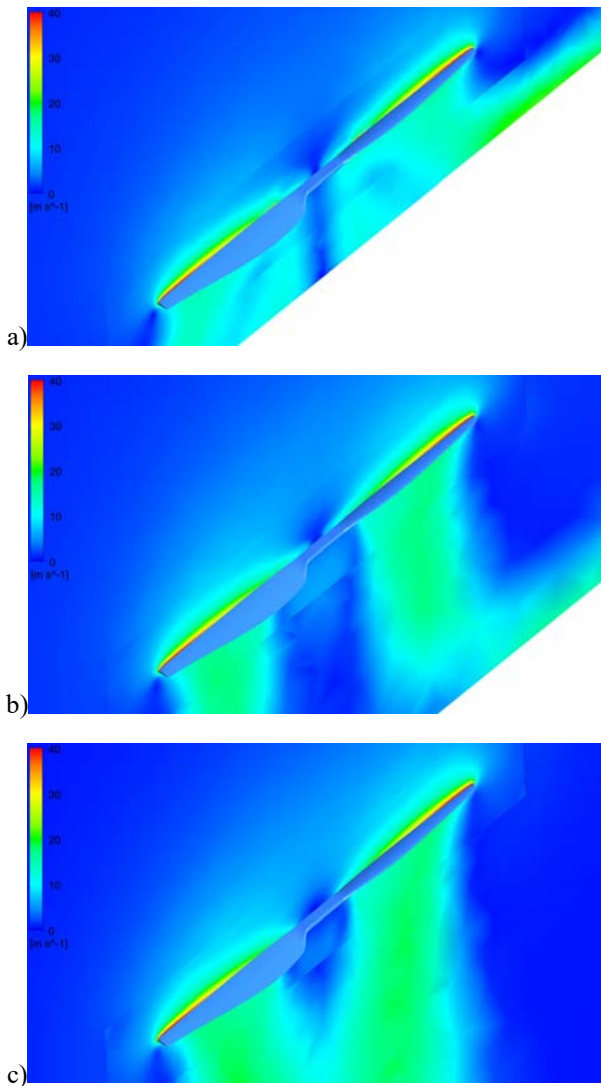


Figure 6. Induced velocities at: a) $z = 0.2$ m, b) $z = 0.5$ m, and c) infinite z

It is also possible to compare pressure distributions along the propeller blades for different ground distances, as illustrated in Fig. 7. Zones of lower pressure along the upper blade surfaces near the tips seem less affected by the ground vicinity in comparison to the blade root segments, where differences in pressure contours are more visible. The benefits of ground effect are apparently

caused by prolonged zones of negative gauge pressure that stretches towards the blade root and leading edge.

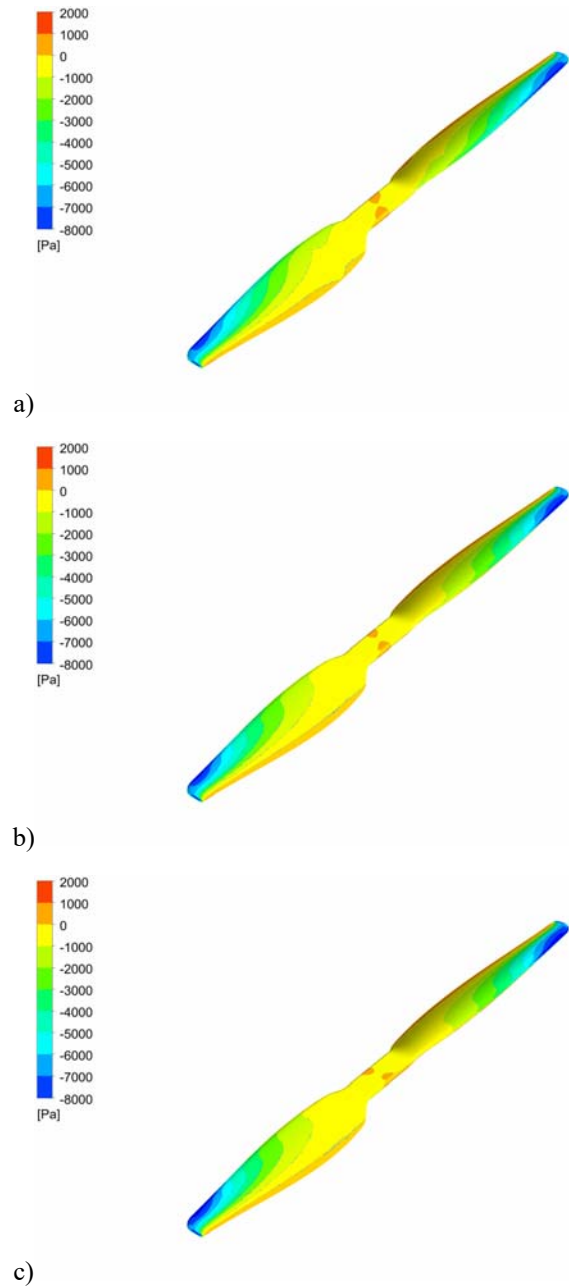


Figure 7. Gauge pressure along the propeller at: a) $z = 0.2$ m, b) $z = 0.5$ m, and c) infinite z

These statements can be further validated by inspecting the vortices shed from the blades at different ground distances (Fig. 7). Again, tip vortices appear similar in all cases. Primary vortical structures are slightly better differentiated in the case of an isolated rotor and seem to disperse somewhat more quickly if ground surface is relatively close to the rotor. On the other hand, root vortices seem more pronounced as the rotor approaches the ground. At lower distances from the ground z , there seem to be more mixing and instabilities around the central part of the propeller that result in more accelerated air flow. It should be kept in mind, however, that these visualizations directly depend on the way the turbulent motion is resolved.

Most of the general findings presented here match the well-known theoretical models that are usually used for the analysis of rotor performance as well as the numerical results presented in [5].

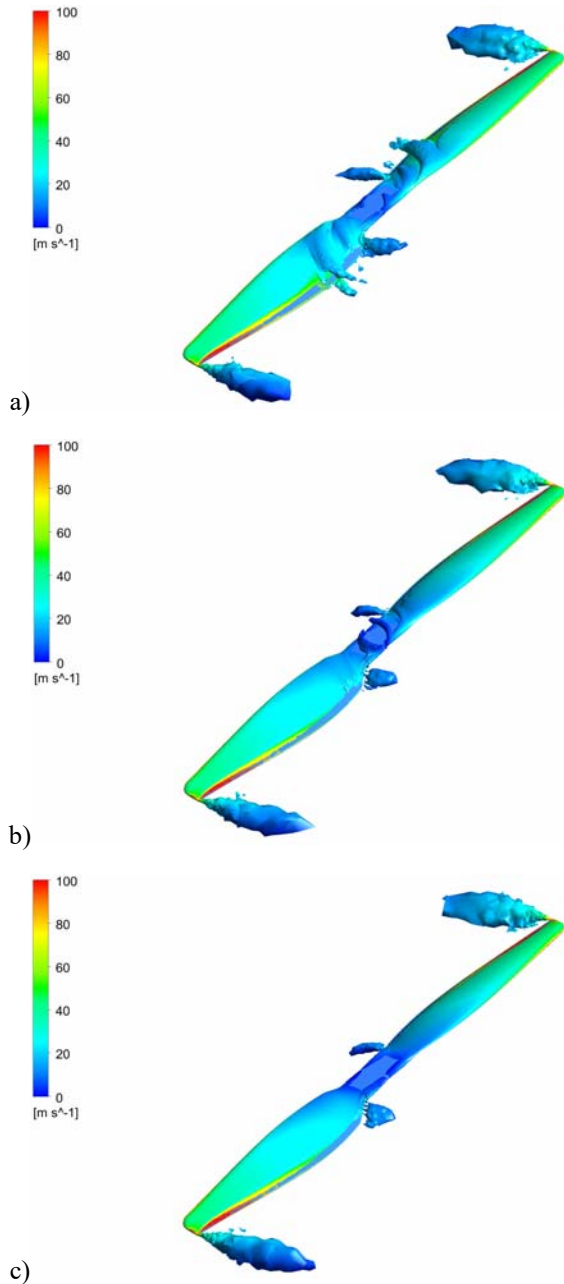


Figure 8. Vortical structures at: a) $z = 0.2$ m, b) $z = 0.5$ m, and c) infinite z

Final quantification of different flow behavior along the blade with respect to ground distance z is provided in Fig. 9 by pressure coefficient distributions.

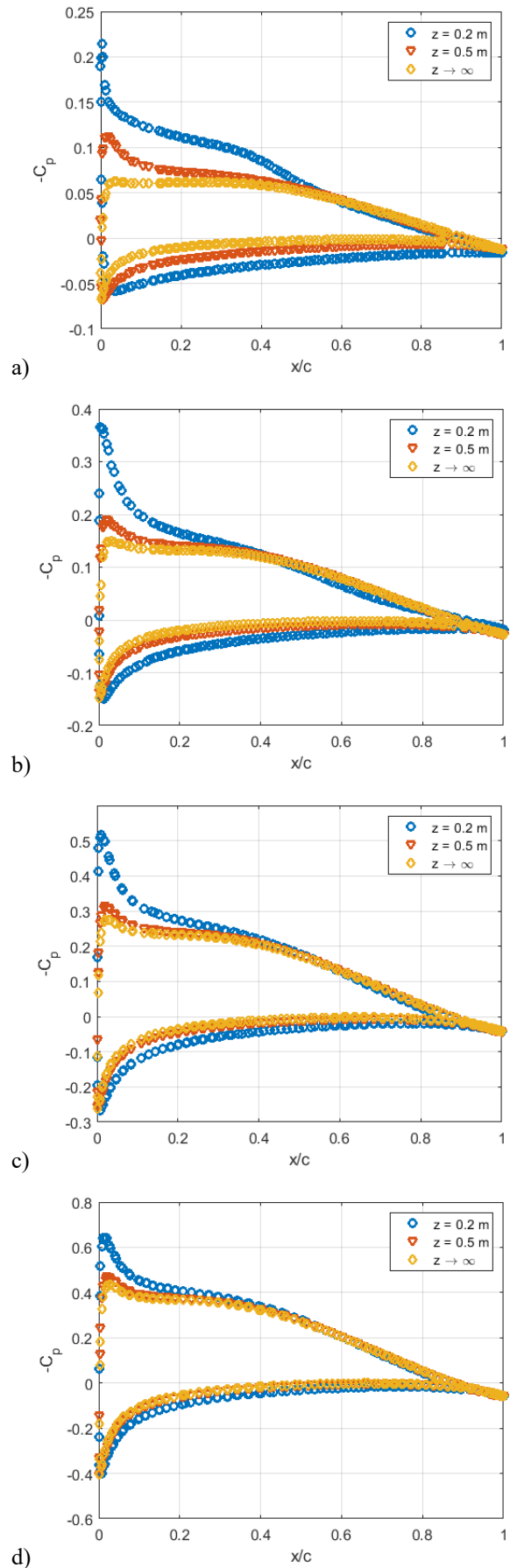


Figure 9. Pressure coefficient distributions in cross-sections located at: a) $y = 0.10$ m, b) $y = 0.15$ m, c) $y = 0.20$ m, and d) $y = 0.25$ m

Pressure coefficient distributions in cross-sections located at 26%, 39%, 52% and 65% blade span clearly indicate that the flows mostly differ in the vicinity of the leading edge, on both the upper and lower blade surfaces.

4. CONCLUSIONS

A fixed-pitch small-scale hovering propeller of a quadcopter (or any delivery UAV) in ground effect was numerically investigated by solving RANS equations for incompressible fluid. Increase of thrust at constant power (and vice versa) with respect to the relative distance from the ground was determined and mathematically formulated. Furthermore, interesting flow visualizations are presented.

Some more particular contributions and findings of this research study are as follows:

- Atypically small distances from the ground were considered,
- Small-scale propeller geometry operating at low Re was analyzed whereas most previous studies were focused on helicopter rotors,
- Novel approximations of changes of thrust and power in ground vicinity are proposed,
- More realistic estimations are obtained for lower ground distances,
- Some important and distinctive flow features are captured, illustrated and discussed.

Although the presented novel relations are derived for a particular propeller geometry, they are also applicable to other “similar” small-scale propellers (of comparable shape, size, and operating conditions). However, the actual sensitivity study of the coefficients appearing in Eqs. 2 and 3 might be the topic of a future study.

ACKNOWLEDGEMENT

This research work is supported by the Ministry of Education, Science, and Technological Development of Republic of Serbia through contract no. 451-03-68/2022-14/200105.

References

- [1] DELORME, Y., STANLY, R., FRANKEL, S.H., GREENBLATT, D.: *Application of Actuator Line Model for Large Eddy Simulation of Rotor Noise Control*, Aerospace Science and Technology, 108 (2021) 106405.
- [2] HERNICZEK, M.K., JEE, D., SANDERS, B., FESZTY, R.: *Rotor blade optimization and flight testing of a small UAV rotorcraft*, Journal of Unmanned Vehicle Systems, 7(4) (2019) 325-344.
- [3] ZHAO, Q., SHENG, C.: Predictions of HVAB rotor in hover using hybrid RANS/LES methods-II, AIAA SciTech Forum 2022, AIAA 2022-1550.
- [4] LEISHMAN, J.G.: *Principles of Helicopter Aerodynamics*, Cambridge University Press, New York, 2006.
- [5] GAROFANO-SOLDADO, A., SANCHEZ-CUEVAS, P.J., HEREDIA, G., OLLERO, A.: Numerical-experimental evaluation and modelling of aerodynamic ground effect for small-scale tilted propellers at low Reynolds numbers, Aerospace Science and Technology, 126 (2022) 107625.
- [6] COOMBES, M., NEWTON, S., KNOWLES, J., GARMORY, A.: *The influence of rotor downwash on spray distribution under a quadrotor unmanned aerial system*, Computers and Electronics in Agriculture, 196 (2022) 106807.
- [7] KOVAČEVIĆ, A., SVORCAN, J., HASAN, M.S., IVANOV, T., JOVANOVIĆ, M.: *Optimal propeller blade design, computation, manufacturing and experimental testing*, Aircraft Engineering and Aerospace Technology, 93(8) (2021) 1323-1332.



VORTEX INDUCED DOWNWASH EFFECT ON STATIC STABILITY OF SUBSONIC AIR TO SURFACE MISSILE

IVAN MARIĆ

Military Technical Institute, Belgrade, ivanmaric094@gmail.com

ANJA GAVRILOVIĆ

Military Technical Institute, Belgrade, agavrilovic213@gmail.com

ILIJA NENADIĆ

Military Technical Institute, Belgrade, ilijanenadic98@gmail.com

GORAN OCOKOLJIĆ

Military Technical Institute, Belgrade, ocokoljic.goran@gmail.com

Abstract: This paper is an aerodynamical analysis of differences that occur between semi-empirical determination of static stability of subsonic air to surface missile and wind-tunnel data when substantial downwash effect due to vortices on wing surfaces is present. The existence of vortex downwash is confirmed and displayed by numerical CFD computation, and methods of circumventing its effects are reviewed.

Keywords: aerodynamics, semi-empirical, vortex, downwash, CFD.

1. INTRODUCTION

To successfully achieve flight, missiles must be dynamically stable. This can be done in two ways – either by spin stabilisation or by ensuring the static stability of the missile.

The long-term trend in missile design, however, is toward increasing performance and maneuverability. This has most commonly resulted in moderate to high incidence angle flight, in which the most practical solution for stability is a statically stable missile with a desired static margin.

In order to achieve desired maneuverability, the missile must also have the required normal force, which is a function of the incidence angle, and the required control force to reach such desired incidence angle. The total normal force can be increased by increasing the size of, or adding new wing surfaces, keeping static stability of the missile in mind.

Each wing surface creates a downwash effect, thus changing the flow conditions on the wing surface behind it. In severe conditions, vortex induced downwash can completely change the desired performance of the wing surface, and result in destabilisation of the missile.

2. MISSILE DESCRIPTION

Coordinate system for aerodynamic coefficients further discussed is shown in Figure 1.

To achieve desired maneuverability requirements for air to surface missile, a canard controlled configuration was selected, and the missile is shown in Figure 2.

Since the deflection of the control surfaces in that case coincides with the desired change in pitch or yaw, the total normal force of the missile should increase with the maneuver. The downside to this design is that the angle of incidence and the angle of control deflection also coincide, which could lead to the stalling effect on the control surface on moderate angles of incidence [1].

To circumvent this, the size of canards was increased accordingly, giving higher control forces for lower deflection angles.

Since the wing position and size were predetermined, and could not change, a third wing section was added to the missile, to increase desired normal force and achieve an adequate static margin.

The body shape, diameter and length were also predetermined, with the reference point being chosen to coincide with the starting missile center of mass.

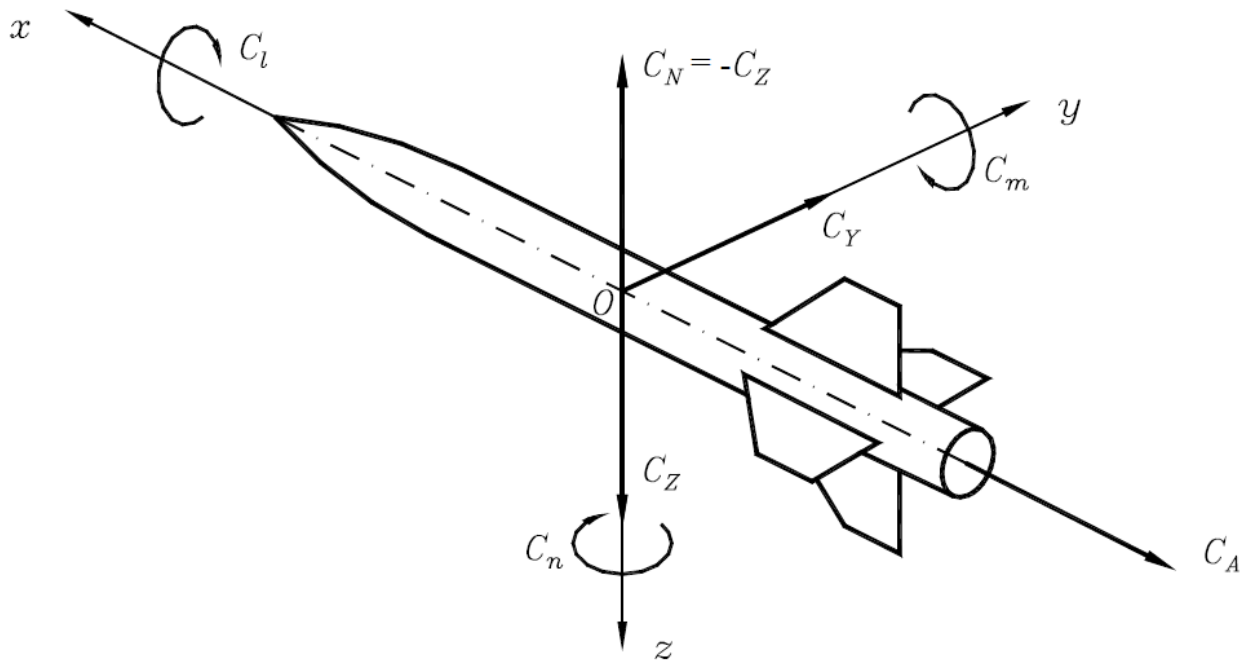


Figure 1. Body coordinate system, where point O is center of mass

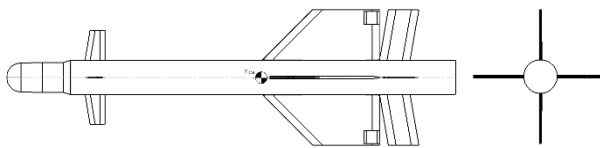


Figure 2. Configuration of subsonic air to surface missile

3. AERODYNAMIC ANALYSIS

3.1. Semi-empirical method

Using semi-empirical aerodynamics [2], preliminary aerodynamic analysis of subsonic air to surface missile was computed. Of note here is the pitching moment coefficient C_m , and namely its derivative C_m^α , which is crucial for static stability.

The missile will be statically stable if the following condition is met:

$$C_m^\alpha < 0 \tag{1}$$

In other words, the slope of $C_m(\alpha)$ must be negative for relatively small values of α , with α being the angle of attack.

The function $C_m^\alpha(M)$ for the missile is presented in Figure 3, where M is the Mach number.

It is evident from Figure 3, that (1) is satisfied, and C_m^α changes little with the Mach number until $M = 0.9$.

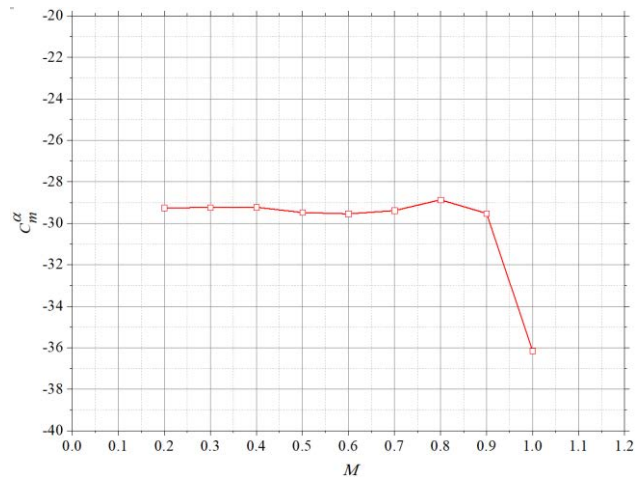


Figure 3. $C_m^\alpha(M)$ as a result of semi-empirical analysis of subsonic air to surface missile, for α in radians

3.2. Wind Tunnel tests and data

After semi-empirical analysis, a model of the subsonic air to surface missile was tested in T-35 Wind tunnel of the Military Technical Institute in Belgrade tunnel on $M = 0.4$, and data revealed that the condition (1) was not met, as is seen in Figure 5.

Since the tests of control effectiveness, shown also in Figure 5, indicate the existence of stalling effect at only $\alpha \approx 9^\circ$, restoring of stability cannot be done by altering canard size, without significant loss of control effectiveness.

Deflection angles are defined in Figure 4.

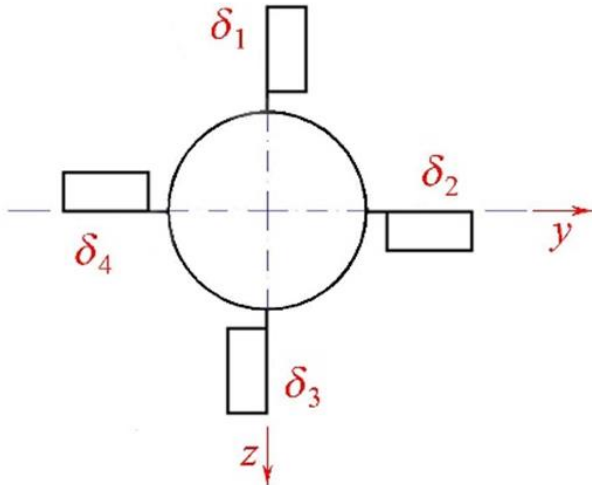


Figure 4. Positive signs of deflection angles

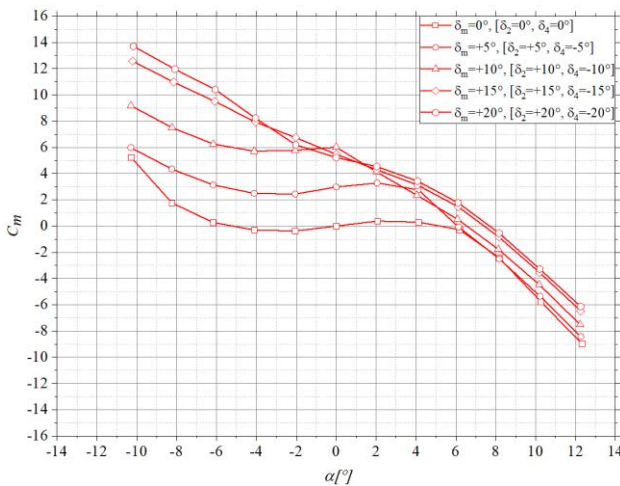


Figure 5. Pitching moment coefficient $C_m(\alpha)$ for different control deflections

In order to determine the cause of instability, and to make the missile stable, several more wind tunnel tests in T-35 wind tunnel were performed [3].

First, two tests in which the third wing section was moved 100mm and 200mm further back, in order to move the center of pressure behind the reference point of the missile, making it stable. Further, if the loss of stability is due to appearance of vortex induced downwash between second and third wing sections, moving the third section back should remove it from the vortex and increase its aerodynamic characteristics.

The final test was to determine if the downwash from canards was impacting the other wing sections, and decreasing stability [4]. This was done by rotating the canards 45° relative to the second and third wing sections.

The results of these wind tunnel tests are presented in Figure 6.

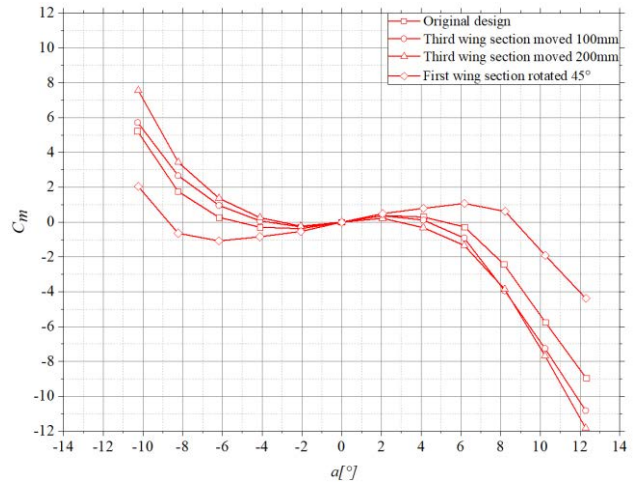


Figure 6. Pitching moment coefficient $C_m(\alpha)$ for different control deflections

As can be seen, rotating the canards 45°, yields the worst results for stability, making it more unstable.

Moving the third wing section does increase the stability of the subsonic air to surface missile, but at an unexpectedly ineffective rate, noticeable only at $\alpha > 2^\circ$.

Because the missile launcher solution makes it impossible to rotate just the second or just the third wing section 45° in order for the vortex induced downwash to avoid the section behind, there will always be interference due to the vortex between the second and third wing sections.

Since the ratio of thicknesses of the second and third wing section is greater than double ($t_{II}/t_{III} = 2.66$), this is the suspected cause of substantial vortex induced downwash interference.

If this ratio $t_{II}/t_{III} = 2.66$ is used as the vortex induced downwash correction coefficient in semi-empirical computation, as is presented in Table 1, a satisfactory value of C_m^α is achieved for the original configuration.

A more accurate correction coefficient for configurations in which the third wing section was moved is obtained if relative distance of second and third wing sections is taken into account. The following semi-empirical formula is sufficiently accurate up to $l = 500mm$.

$$k = \bar{t} - l(0.25 + 5l^2) \tag{2}$$

Here the ratio of thicknesses is denoted with \bar{t} , and l is the distance between trailing and leading edges in meters. The results are listed in Table 1.

Table 1. C_m^α values for semi-empirical and wind tunnel tests

Configuration	C_m^α	C_m^α 100mm	C_m^α 200mm
Semi-empirical	-29.23	-35.11	-41.99
T-35 Wind tunnel	10.46	8.97	6.29
k = 2.66	10.51	9.76	9.01
Equation (2)	10.51	8.95	6.30

3.3. Numerical analysis

Existence of vortex induced downwash and interference of second and third wing sections was proven by CFD numeric computation in Fluent [5]. Computations were done for the original configuration, as well as the configuration in which the third wing section was translated 100m to the rear of the missile.

In Figure 7, results from CFD simulations show that the turbulent flow from the trailing edge of the second wing section, completely engulfs the third wing section in turbulent flow, thus diminishing its aerodynamic characteristics substantially.

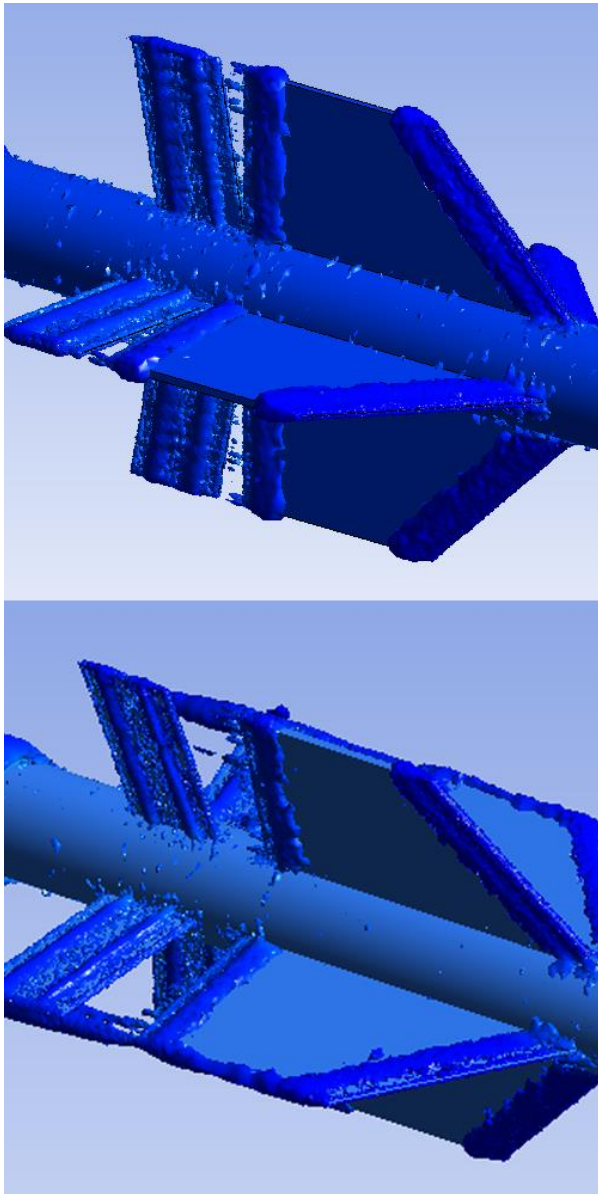


Figure 7. CFD vortex induced downwash interference and turbulent flow on the third wing section

Stability characteristics were calculated for $\alpha = 2^\circ$, and the corresponding pitching moment coefficient C_m is shown in Figure 8, along with wind tunnel data obtained in T-35 wind tunnel. Stability derivative C_m^α for these numerically obtained moments is presented and compared with tunnel data in Table 2.

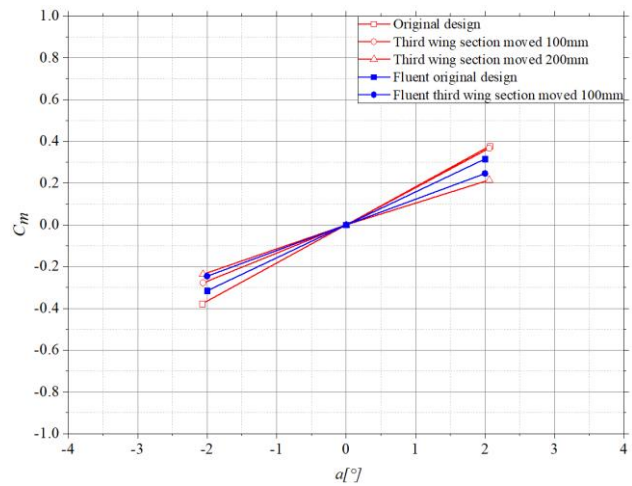


Figure 8. $C_m(\alpha)$ obtained numerically and in T-35 wind tunnel around $\alpha = 0^\circ$

Table 2. C_m^α values for CFD analysis and wind tunnel tests

Configuration	C_m^α	C_m^α 100mm
CFD	9.05	7.05
T-35 Wind tunnel	10.46	8.97

The numerical simulation, as is evident, provides highly satisfactory results that closely align with wind tunnel data, as well as visual confirmation of aerodynamic phenomena that occur during vortex induced downwash interference.

4. CONCLUSION

Since there is no way to change the size and position of the second wing section, nor rotate the second or the third wing section 45° relative to one another, there will always exist a loss of stability due to vortex downwash interference between the two sections. The missile is subsonic, so disturbances in the flow are spread faster than flight speed.

The canard position is also predetermined, and their size cannot decrease to increase stability due to loss of control effectiveness.

Using equation (2), third wing section will need to move 550mm from the second section trailing edged, which is well outside the missile body.

The solution would be to move the control surfaces behind the second wing section, in order to avoid stalling effect, since the angle of incidence and control deflection are opposite. This would result in loss of normal force during control, but the first wing section would be fixed, and could be changed to compensate both stability loss (predicted accurately using equation (2), and confirmed in Fluent) and to reach desired static margin and maneuverability of air to surface missile.

For subsonic missiles, it is necessary to accurately predict and account for vortex effects during preliminary design, which can be done using equation (2) for stability prediction and Fluent for further pre-tunnel corrections.

References

- [1] Jack N. Nielsen: *Missile Aerodynamics*, NIELSEN ENGINEERING & RESEARCH, INC, Mountain View, California, 1988.
- [2] А. А. Лебедев, Л. С. Чернобровкин: *Динамика полета беспилотных летательных аппаратов*, Машиностроение, Москва, 1973.
- [3] J. B. Barlow, W. H. Rae, Jr, A. Pope: *Low Speed Wind Tunnel Testing*, John Wiley & Sons, New York, 1999.
- [4] S. Janković: *Aerodinamika projektila*, Mašinski fakultet Univerziteta u Beogradu, Beograd, 1979.
- [5] ANSYS, Inc. Ansys Fluent Theory Guide (2015). <http://www.pmt.usp.br/academic/martoran/notasmodelosgrad/ANSYS%20Fluent%20Theory%20Guide%202015.pdf>

NUMERICAL INVESTIGATION OF WING STRAKES AERODYNAMIC INFLUENCE USING MODIFIED SDM MODELS

JELENA ŠOBOT

Technical Test Centre, Vojvode Stepe 445 Belgrade, jsobot@outlook.com

IVAN KOSTIĆ

University of Belgrade, Faculty of Mechanical Engineering, Aeronautical Dept., Kraljice Marije 16 Belgrade, ikostic@mas.bg.ac.rs

OLIVERA KOSTIĆ

University of Belgrade, Faculty of Mechanical Engineering, Aeronautical Dept., Kraljice Marije 16 Belgrade, okostic@mas.bg.ac.rs

MARIJA SAMARDŽIĆ

Military Technical Institute, Ratka Resanovića 1 Belgrade, marija.samardzic@vti.vs.rs

Abstract: Many contemporary jet fighters and combat airplanes are equipped with wing strakes, or leading edge root extensions. Their role is to improve maneuvering characteristics and delay stall of swept low aspect ratio wings. Positioned in front of the airplane's center of gravity, they also generate destabilizing contribution to the longitudinal static stability. Aim of this paper was to perform CFD analyses of several characteristic strake shapes, and investigate their global aerodynamic influence on the lift, moment and drag coefficients and the longitudinal static stability derivative. The adopted calculation algorithm was first implemented on the Standard Dynamic Model (SDM), and the results for two subsonic Mach numbers were verified using experimental data obtained during one of the T-38 wind tunnel calibration tests at the Military Institute in Belgrade. After that, several SDM modifications were made, all generally denoted as the Modified Dynamic Models. The first two have provided a lift where the SDM's original double wedge strakes were removed, and the horizontal tail was modified to obtain inherently stable configuration at all angles of attack. Three assigned strake forms - elliptic, ogive and triangular of the same exposed area were added to it, with intention to generate longitudinally unstable configurations. The elliptic form gave the largest increase in lift coefficient, the best lift to drag ratios at high angles of attack, and the most favorable influence on the longitudinal static stability. Presented analyses will be a starting point for future investigations of more complex, multi segment strake shapes.

Keywords: Wing strakes, aerodynamic analysis, modified SDM models, CFD calculations, ANSYS Fluent.

1. INTRODUCTION

One of very common features on many modern jet fighter aircraft with swept, low aspect ratio and delta wings are the strakes. They were first implemented on the Northrop F-5A „Freedom Fighter“ [1, 2] in 1959, which were proportionally small in size. The advantages of their implementation were recognized both in operational use and through numerous wind tunnel investigations, such as presented in [3]. As a consequence, the 1972's F-5E version was equipped with larger strakes (Fig. 1). Also known as the leading edge root extensions (LERX), strakes were progressively growing in size with time, both on the „western“ and the „eastern“ jet fighter planes [4]. Finally, on some designs their length has practically become equal, or exceeded the wing's root chord (Fig. 2).

The primary role of strakes is to act as vortex generators and improve maneuvering characteristics at moderate, and delay stall at high angles of attack, by energizing airflow on the upper wing surface [5, 6]. Although these vortices

contribute to the local drag increase, energized boundary layer delays flow separation on the upper wing surfaces, and the overall effect may even be the total drag decrease.



Figure 1. Double wedge strakes on Northrop F-5E (picture @ I. Kostić)

Since strakes are positioned in front of the airplane's center of gravity (CG), in the sense of the longitudinal static stability they are destabilizers, and the amount of

this influence depends on their shape, aerodynamic area and distance from the CG.

One of the most comprehensive studies is presented in [7], where vortex breakdown characteristics of 43 strakes were analyzed. They were inspired by the development of the F-16 and F/A-18 lightweight fighters. Many other reports such as [8] and [9], were based on, or derived from these two jet fighters, years after they were put to the operational use.



Figure 2. Strakes on F/A-18C (picture @ I. Kostić)

Purpose of this work is numerical CFD investigation of aerodynamic influence of several wing strake geometries, assuming symmetrical flow conditions. Although some strake analyses in literature have been performed on isolated wing-strake configurations [10], authors of this paper have decided to use the Standard Dynamic Model (SDM, Fig. 3) as starting 3D geometry, which includes the fuselage with canopy, air intake and ventral fins, and the tail surfaces. Although the SDM was originally aimed for wind tunnel calibrations, numerous CFD analyses were performed using this model for their verification purposes, such as [11, 12, 13, etc.].



Figure 3. SDM model and pitch/yaw apparatus for wind tunnel calibrations in VTI (photo @ VTI)

In this work, the first obtained CFD results for the original SDM have been evaluated using experimental results from the Military Technical Institute in Belgrade.

After that, the SDM model was modified in two steps to obtain longitudinally statically stable configuration. Finally, it was equipped with the new elliptic, ogive and triangular strakes, and their influence on the lift, drag, moment coefficients and the longitudinal static stability characteristics has been calculated. All altered geometries were generally denoted as MDM-s (Modified Dynamic Models).

2. CALCULATION MODEL

CFD calculations presented in this article have been done using the commercial ANSYS Fluent software. For symmetrical flow conditions a half model control volumes were applied. In order to eliminate the influence of the SDM's large end-fuselage diameter on drag results for the new strakes, a "sting" of the same diameter has been added behind all SDM/MDM geometries. By that the base drag has been eliminated, while the contribution of the sting to all coefficients was excluded.

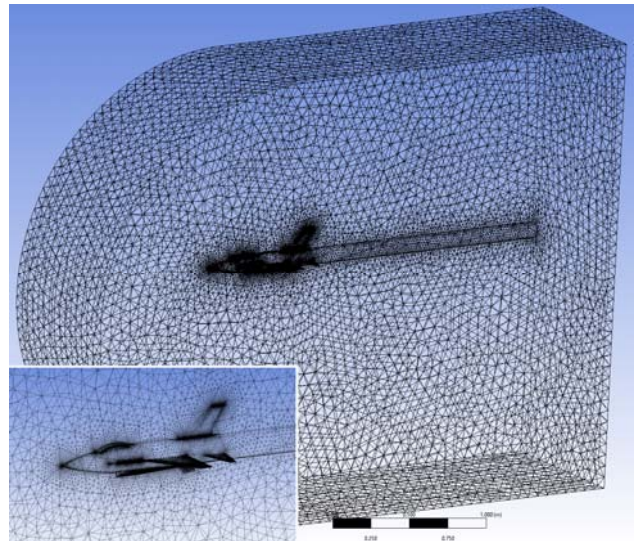


Figure 4. Half-model mesh with 1.1 million elements

Analyses were performed on unstructured meshes with about 1.100.000 elements (Fig. 4), using RANS equations with $k-\omega$ SST turbulence model. Applied calculation algorithm is the same as in [14, 15], where more details about it can be found.

3. COMPARISONS WITH EXPERIMENT

The initial CFD results were compared with the wind tunnel test results, obtained for the SDM calibration model at the Military Technical Institute (VTI, serb. Vojnotehnički institut) in Žarkovo – Belgrade [16]. Computational and experimental results for test Mach numbers $M = 0.3$ and $M = 0.61$, for the lift coefficient C_L and the moment coefficient C_m , and the derived longitudinal static stability derivative dC_m/dC_L are presented in Fig's 5 ÷ 8. The drag coefficient C_d values were not provided in VTI report. Computations at this stage were performed twice, first without, and then with the inflation layer implemented in the CFD analyses.

Considering the C_m , obtained agreements are good (Fig's

5 and 6), while for the C_l agreements are fair at small and medium angles of attack. At higher angles of attack, experiments show a slight increase in lift curve slopes for both Mach numbers, while the CFD's slopes remain practically constant. On these graphs, differences in results obtained without and with the inflation layer are hardly recognizable.

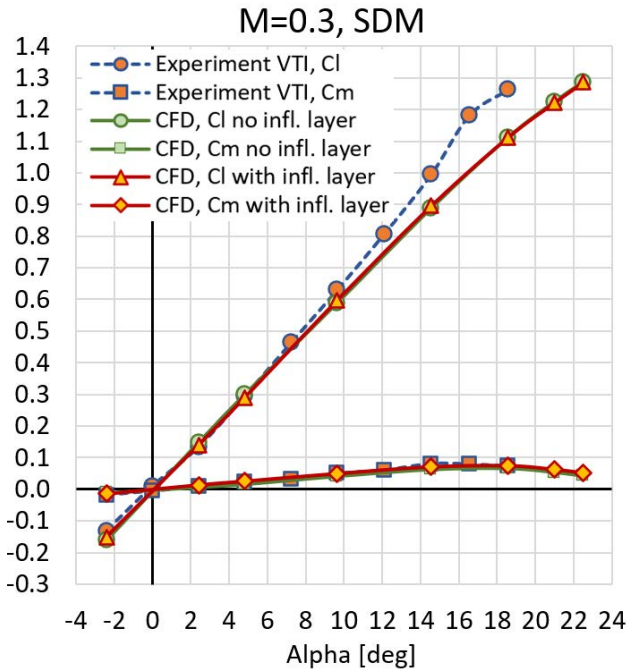


Figure 5. Lift and moment coefficients for $M=0.3$

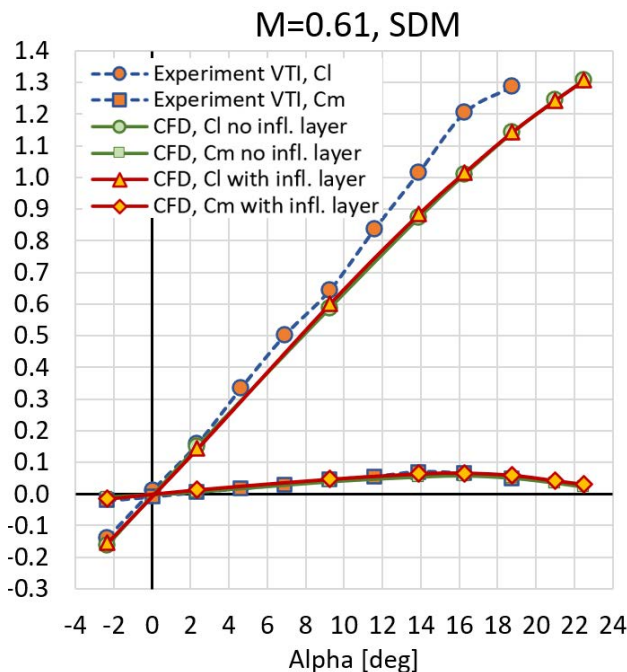


Figure 6. Lift and moment coefficients for $M=0.61$

Diagrams for the dC_m/dC_l derivatives at both Mach numbers (Fig's 7 and 8) show noticeable scatter in experimental results at low and medium angles of attack. Such as the numerical calculations, experimental methods are also prone to certain inherent and inevitable faults. In this case, small measurement and averaging errors (hardly

noticeable at experimental C_l and C_m curves in Fig's 5 and 6), increase in magnitude when converted to derivatives. In this case, the CFD results have provided quite good "averaging" of the experimental scatters. Both CFD and experiment also show that the original SDM configuration is longitudinally statically unstable at small and medium angles, while at high angles of attack it becomes stable.

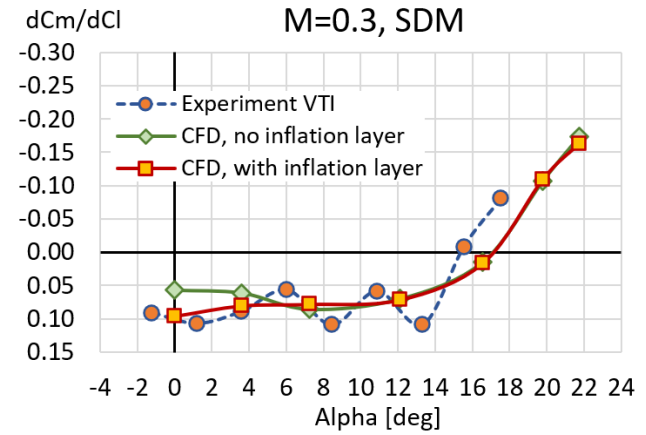


Figure 7. Longitudinal static stability for $M=0.3$

Figures 7. and 8. also indicate that calculations without and with the inflation layer coincide well, except at small angles of attack. In this domain results obtained with the inflation layer are much closer to the experiment, and this option was applied in all oncoming calculations.

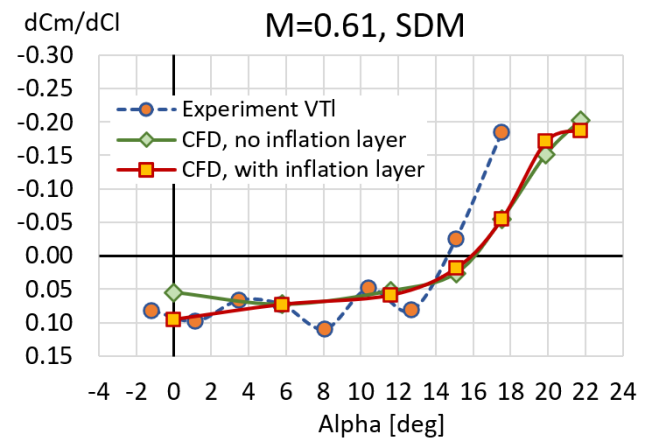


Figure 8. Longitudinal static stability for $M=0.61$

Presented analyses show that here adopted CFD model can be used for the preliminary comparative numerical investigations of the different strake shapes and their influence on longitudinal aerodynamic characteristics.

4. INITIAL SDM MODIFICATIONS

Since the SDM model (Fig. 9 (a)) originally has medium size double wedge strakes, the next step was to exclude them from the aerodynamic configuration, and provide space for the implementation of new strake shapes. In that sense, the first SDM modification was generated, denoted as MDM-NS (Modified Dynamic Model – No Strakes), shown in Fig. 9 (b). All aerodynamic analyses for this version, as well as for all other configurations presented

in this article, were performed only for the Mach number $M = 0.61$.

Figure 10. shows that the maximum lift coefficient of the MDM-NS is smaller than of the SDM, while the moment coefficient first increases up to $\text{Alpha} = 7^\circ$ and then it continues to progressively decrease.

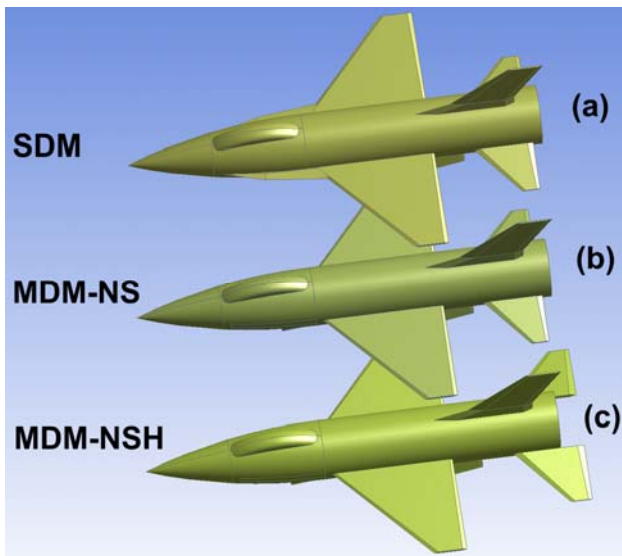


Figure 9. Two initial MDM modifications derived from the original SDM, with strakes removed.

While original SDM is longitudinally unstable up to the calculated $\text{Alpha} = 16^\circ$, the MDM-NS is also unstable, but in a narrower domain, to about $\text{Alpha} = 9^\circ$ (Fig. 11).

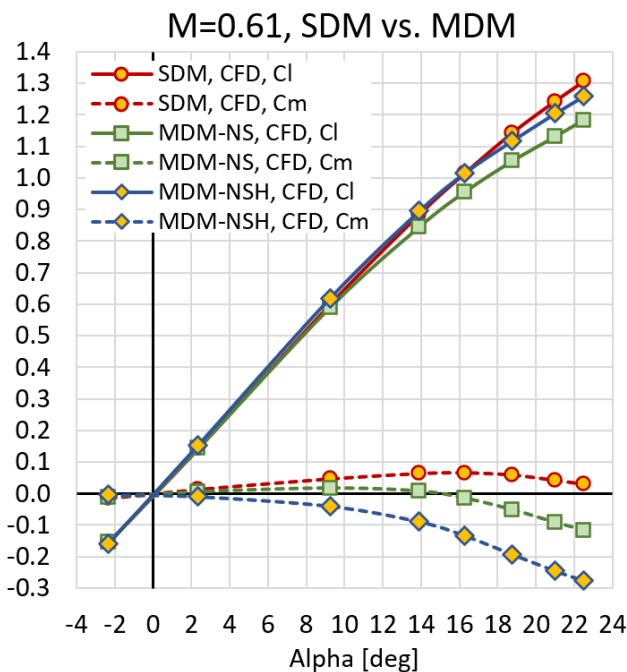


Figure 10. Lift and moment coefficients obtained by CFD

With aim to determine the effective influence of new strakes on the longitudinal static stability, a decision was adopted to modify the MDM-NS and make it longitudinally statically stable in the entire range of angles of attack (still without strakes). After scaling the original horizontal tail by factor 1.2 in chordwise and

spanwise directions taking the root leading edge as origin, and then translating it back by 40 mm, the new version has been obtained, denoted as MDM-NSH (Modified Dynamic Model – No Strakes with Horizontal tail modified), Fig. 9 (c)

Figure 10 shows that its entire moment curve has negative slope, while its dC_m/dC_l derivative (Fig. 11) is also entirely in the negative domain, indicating the posted inherent stability requirement has been satisfied for all angles of attack.

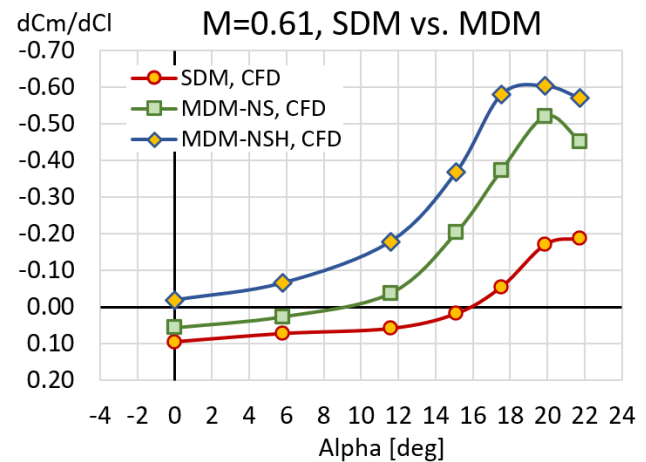


Figure 11. Calculated longitudinal static stabilities

5. RESULTS AND DISCUSSION FOR NEW STRAKE GEOMETRIES

Using the MDM-NSH as a new starting loft, three different strake types were added. The MDM-ST1 was obtained by adding quarter-elliptic strakes, the MDM-ST2 was modeled by adding ogive strakes, while MDM-ST3 was generated by adding triangular, single wedge strakes (Fig's 12 (d), (e) and (f) respectively).

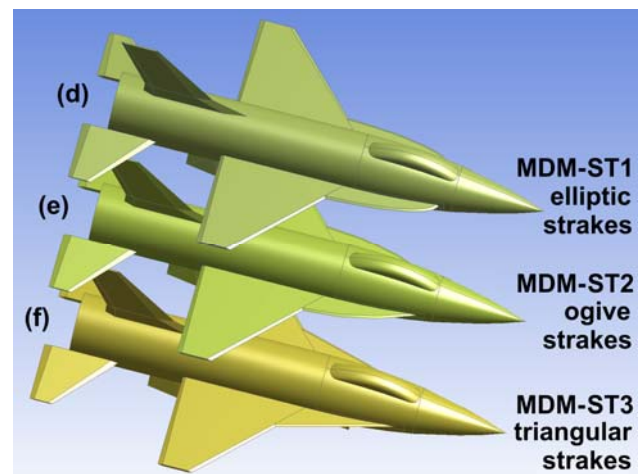


Figure 12. New strake-added modifications, developed from the statically stable MDM-NSH.

They all have the same theoretical planform area of 77 cm^2 , while their true area is a bit smaller, i.e. it is the theoretical area reduced by the domains covered by parts of fuselage and wing leading edge, which are practically the same for all three types. This way they have the same

area exposed to the air flow, and their comparative investigations can provide useful conclusions considering their aerodynamic efficiency and influence. In this work, analyses were limited only to the strake influence on global lift, drag and moment coefficients, while future work should also include detailed insights in local pressure distributions, vortex pattern influences, etc.

Figure 13 indicates that the elliptic ST1 provides the largest increase in lift coefficient ΔC_l with respect to the calculated value for NSH at $\text{Alpha} = 22.5^\circ$ (17.3%), while ΔC_l contributions of ST2 (16.2%) and ST3 (12.8%) versions are smaller.

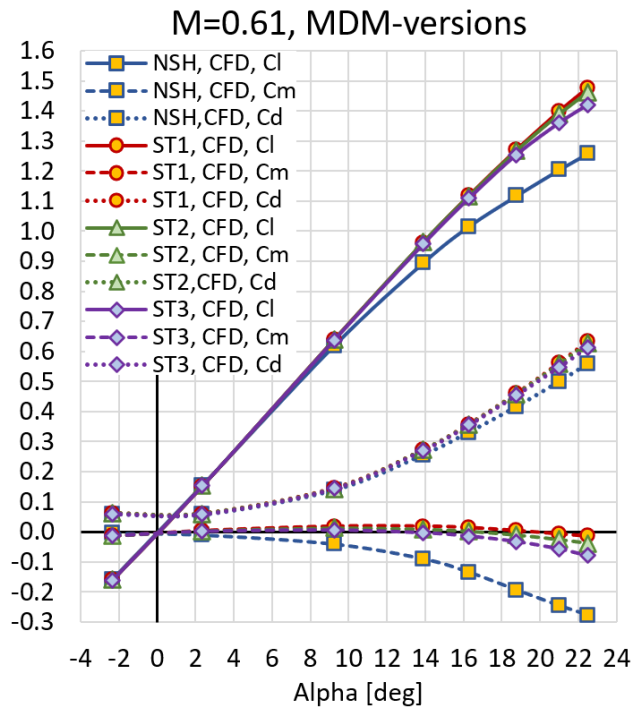


Figure 13. Lift, drag and moment coefficients

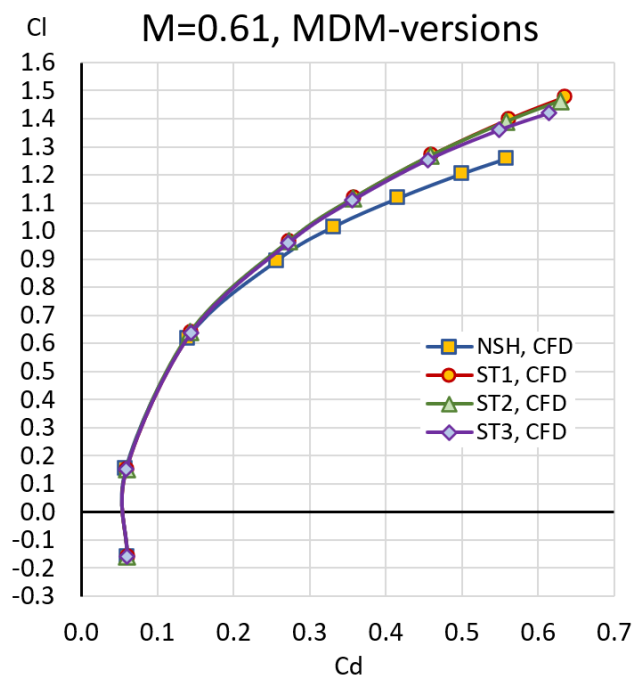


Figure 14. Calculated drag polars

The same generally applies for the drag coefficients at $\text{Alpha} = 22.5^\circ$, where ST1 generates proportionally the largest ΔC_d increase (13.7%) with respect to the NSH, while values for ST2 (12.7%) and ST3 (10%) are also smaller. On the other hand, if drag polars are analyzed (Fig. 14) instead of the C_d -Alpha diagrams, the situation is quite different. In the upper half of the C_l domain, the elliptic ST1 version produces the smallest drag coefficient for the same lift coefficient generated (although differences between the three new strakes are hardly visible). So in this C_l domain, all three strake types generate noticeably smaller C_d for the same C_l values, than the NSH version. In fact, the MDM configurations with strakes, due to the enlarged exposed wing area but also owing to their shape, contribute more to the lift coefficient increase than to the increase in drag coefficient at high angles of attack, compared to the C_l - C_d ratios obtained by NSH version. Thus all three strake types, ST1, ST2 and ST3 have increased the configuration's C_d vs. C_l aerodynamic efficiency at angles of attack in the range $\text{Alpha} = 10^\circ \div 22.5^\circ$, which is one of the primary roles of the strake implementation. In that sense, the elliptic form has certain advantage over the ogive and triangular versions.

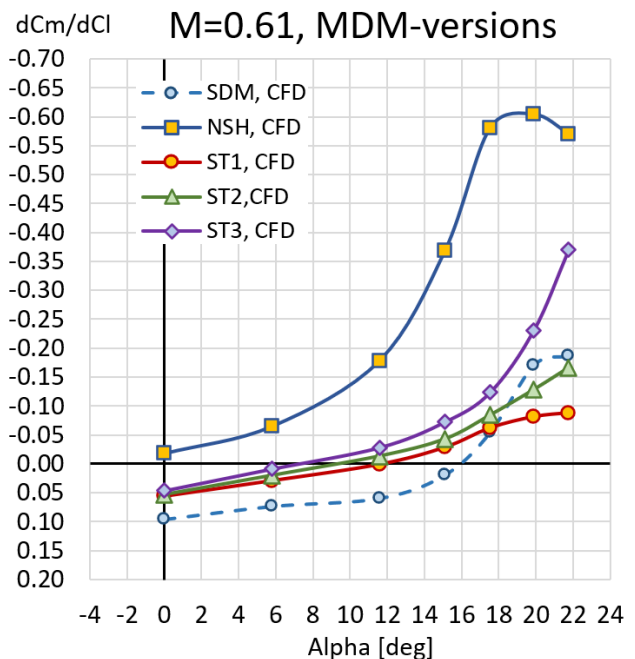


Figure 15. Longitudinal static stability of the SDM, compared to four MDM versions.

Adjusting their shape, size and position, wing strakes on contemporary jet fighters can be used to fine-tune the amount of the desired longitudinal static instability and thus provide enhanced longitudinal maneuverability (but with mandatory use of fly-by-wire controls). Equipped with ST1, ST2 and ST3 modifications, the inherently stable NSH version was converted to unstable at smaller and medium angles of attack. The largest destabilizing influence was achieved by ST1, up to $\text{Alpha} = 12^\circ$, while ST2 and ST3 provided instability up to $\text{Alpha} = 9^\circ$ and 7.5° respectively (Fig. 15). So the elliptic strake form proved to be the most efficient „destabilizer“, with the same exposed area.

Another very important aspect is the trend of change of the derivative dC_m/dC_l with the angle of attack. From Fig. 15 it is obvious that the original SDM, as well as the MDM versions NSH and ST3 show sudden divergence of the longitudinal static stability after a certain angle of attack, from instability (or small stability) at small, to extremely large stability values at high angles of attack. In operational design work, this trend would be very unfavorable.

In that sense, the ST1 version is also the best, with almost linear increasing trend with small gradient. This version would enable, with reasonably small additional length and/or area enlargements, to shift almost the entire dC_m/dC_l curve in the domain of positive values, and generate unstable configuration in a wide angle of attack domain, with acceptable instability levels for operational use. With ST2, ST3 and the original SDM that would be a very difficult task, since their instabilities at small angles of attack could be unacceptably large.

6. CONCLUSION

This paper presents preliminary investigations of the aerodynamic influence of several characteristic wing strake configurations, implemented to the 3D geometry loft derived from the Standard Dynamic Model. Computational analyses, performed in this work using the commercial ANSYS Fluent software, were evaluated by comparisons with experimental results obtained during the T-38 wind tunnel SDM calibration tests at the Military Technical Institute in Belgrade. The initial modification of the longitudinally statically unstable original SDM model was obtained by removing its double wedge strakes. This gave the first MDM-NS version, which was still longitudinally unstable. In the next step, the horizontal tail was enlarged and shifted backwards, by which the MDM-NSH model was generated. It was longitudinally stable in the entire domain of analyzed angles of attack. This modification was used as the test bed for three wing strake types. The first MDM-ST1 was added with elliptic, the second MDM-ST2 with ogive, and the third MDM-ST3 with triangular strakes. All evaluations were based on the strake influence on global lift, drag and moment coefficients. The ST1 version generated the largest increase in lift coefficient C_l at higher angles at attack, but the same applied for the drag coefficient C_d . On the other hand, since the relative increase in C_l was greater than in C_d compared to the NSH, the elliptic ST1 strakes provided best improvements in C_d vs. C_l aerodynamic effectiveness. When used as longitudinal destabilizing surfaces for modern fly-by-wire combat plane applications, the ST1 version also gave results which appear to be the most suitable. These investigations will provide a starting point for future analyses of more complex strakes, including multi-segment configurations.

References

- [1] <https://www.northropgrumman.com/what-we-do/air/f5-tiger/> accessed on June 5th 2022.
- [2] https://en.wikipedia.org/wiki/Northrop_F-5 accessed on June 5th 2022.
- [3] WENTZ, W.H. JR., KOHLMAN, D.L.: Wind Tunnel Investigations of Vortex Breakdown on Slender Sharp-Edged Wings, NASA CR-98737, 1968.
- [4] https://en.wikipedia.org/wiki/Leading-edge_extension#Leading-edge_root_extension accessed on June 5th 2022.
- [5] BERTIN, J.J., CUMMINGS, R.M.: Aerodynamics for Engineers, Pearson, Prentice-Hall, NJ, 2008.
- [6] RAYMER, D.P.: Aircraft Design: a Conceptual Approach, AIAA Education Series, 2012.
- [7] FRINK, N.T., LAMAR, J.E.: Water-Tunnel and Analytical Investigation of the Effect of Strake Design Variables on Strake Vortex Breakdown Characteristics, NASA TP 1676, Langley Research Center, Hampton, Virginia, 1980.
- [8] SMITH, C.W., RALSTON, J.N., MANN, H.W.: Aerodynamic Characteristics of Forebody and Nose Strakes Based on F-16 Wind Tunnel Test Experience, NASA CR 3053, Langley Research Center, 1979.
- [9] ERICSON, G.E.: Wind Tunnel Investigation of Vortex Flows on F/A-18 Configuration at Subsonic Through Transonic Speeds, NASA TP 3111, 1991.
- [10] YUTUK, K.: Adjoint-based Aerodynamic Shape Optimization of a Strake-Delta Wing Configuration, M.Sc. Thesis, Middle East Technical University, Department of Aerospace Engineering, 2021.
- [11] TATAR, M., MASDARI, M.: Investigation of pitch damping derivatives for the Standard Dynamic Model at high angles of attack using neural network, Aerospace Science and Technology, 92 (2019) 685-695.
- [12] SCHMIDT, S., NEWMAN, D.: Estimation of Dynamic Stability Derivatives of a Generic Aircraft, 17th Australasian Fluid Mechanics Conference, Auckland, New Zealand, 2010.
- [13] GHOREYSHI, M., JIRASEK, A., CUMMINGS, R.M.: Reduced order unsteady aerodynamic modeling for stability and control analysis using computational fluid dynamics, Progress in Aerospace Sciences, 71 (2014) 167-217.
- [14] ŠOBOT, J., KOSTIĆ, I., KOSTIĆ, O.: Comparative aerodynamic analysis of F-16C jet fighter at subsonic and supersonic speeds using panel and viscous CFD methods, The 9th International Scientific Conference on Defensive Technologies, OTEH 2020, 23-28, Belgrade, 2020.
- [15] ŠOBOT, J., KOSTIĆ, I., KOSTIĆ, O.: CFD evaluation of transonic flow analysis around jet trainer aircraft, The 7th International Congress of Serbian Society of Mechanics, F1c 1-7, Sremski Karlovci, 2019.
- [16] JANJIKOPANJI, G.: Experimental determination of stability derivatives for SDM model in the T-38 wind tunnel, V3-2707-025, Internal Report in Serbian, VTI, Belgrade, 1993.



10th INTERNATIONAL SCIENTIFIC CONFERENCE
ON DEFENSIVE TECHNOLOGIES
OTEH 2022

Belgrade, Serbia, 13 – 14 October 2022



SECTION II

Aircraft - A

CHAIRMAN
Prof. Jelena Svorcan, PhD



BUILDING OF PROBABILISTIC- STATISTICAL MODEL OF ENGINE FAILURES

OLGA FILIPPENKO

Belarusian State Academy of Aviation, Minsk, VSME-11@yandex.ru

DANA BELSKAYA

Belarusian State Academy of Aviation, Minsk, belskaya_dana@mail.ru

VOLHA POLETAYEVA

Belarusian State Academy of Aviation, Minsk, volhapaletayeva@gmail.com

Abstract: *the article is devoted to the construction of probabilistic-statistical models for the reliability of engines of various aircraft. The probabilistic-statistical model is based on the Weibull distribution. The constructed model of reliability allows to estimate the reliability, operating time, gamma- percentile resource. The model includes an adequacy test based on the χ^2 distribution. Models are universal and can be used for military and civil aircraft.*

Keywords: *probabilistic-statistical model of operation, aircraft, Weibull distribution, reliability function, gamma-percentile resource, operating time .*

1. INTRODUCTION

The engine is the basic element of the working element of any aviation system.

In addition, the engine is an expensive piece of equipment whose failures must be minimized. The quality of engine performance has an impact on flight safety, and improving safety a priority for both civil and military aviation.

Purpose of the work: building of failure model for the CF34-10E and CFM56-3B1 engines, analyzing the obtained data statistics, identifying the causes of failures.

Work tasks:

- building and implementation of probabilistic-statistical model;
- causes of failures identification and analysis;
- calculation and evaluation of certain reliability characteristics of engines.

The relevance of the topic is due to the provision of safety by preventing the occurrence of failures and reducing their intensity.

The scientific novelty of the topic lies in establishing links between the use of natural science methods of probabilistic-statistical modeling for solving and implementing reliability problems in the operation of aircraft engines [1-3].

The results obtained with the help of the model can be used as recommendations when carrying out maintenance work when servicing equipment on BOEING 737-300 aircraft with CFM56-3B1 engines and EMBRAER 175/195 with CF34-10E engines in addition to the existing analytical systems.

2. MATERIALS AND METHODS

Aircraft engines can be divided into three broad groups:

- piston;
- jet engines;
- missile.

Let us discuss jet engines in detail. According to the creation of jet thrust, jet engines are divided into direct and indirect reaction engines. Direct-acting engines include turbojet, bypass turbojet, turbojet with afterburner, bypass turbojet with afterburner. Indirect reaction engines are turboprop, turboshaft, turbopropfan [4].

The work deals with CF34-10E and CFM56-3B1 engines.

The article compares the engines of the Boeing 737-300 and EMBRAER 175/195 aircraft. Airplanes fly with the help of bypass turbojet engines with a high bypass ratio, so we will analyze this type of aircraft engines in more detail.

Bypass turbojet engines are based on the principle of attaching an additional mass of air to the turbojet engine passing through the outer circuit of the engine, which makes it possible to obtain engines with a higher flight efficiency compared to conventional turbojet engines.

After passing through the inlet, the air enters the low-pressure compressor, called the fan. After the fan, the air is divided into two streams. Part of the air enters the outer circuit and, bypassing the combustion chamber, forms a jet stream in the nozzle. The other part of the air passes through an internal circuit that is completely identical to the turbojet, with the difference that the last stages of the turbine in the turbojet are the fan drive.

One of the most important parameters of a bypass turbojet

engine is the bypass ratio (m), that is, the ratio of air flow through the external circuit to the air flow through the internal circuit.

A turbojet engine with a high bypass ratio ($m > 2$) is a turbofan engine. Here, the low-pressure compressor is converted into a fan, which differs from the compressor in a smaller number of steps and a larger diameter, and the hot jet practically does not mix with the cold one.

All bypass turbojet engines can be divided into two groups: bypass turbojet engines with mixing flows behind the turbine and turbofan engines without mixing flows.

In a mixed-flow bypass turbojet engine, air flows from the external and internal circuits enter a single mixing chamber. In the mixing chamber, these flows are mixed and leave the engine through a single nozzle with a single temperature. The bypass turbojet engines with mixing flows behind the turbine are more efficient, however, the presence of a mixing chamber leads to an increase in the dimensions and weight of the engine.

Advantages of turbofan engines:

- the ability to save fuel without losing power, which is so important for jet engines;
- in addition, these motors are less noisy;
- another advantage is the presence of a simplified reverse thrust system. When braking the aircraft, the thrust of the external circuit is used.

The disadvantages of turbofan engines include:

- a large mass;
- size.

Any additional components of the engine design are an additional weight, which is very important for aviation, and an additional contour of considerable size is a rather significant increase in the mass of the engine. Large dimensions lead to an increase in the value of air drag during flight.

Stages of building a model are the following:

1. Determination of elements with minimum operating time and causes of failures;
2. Building a statistical model;
3. Calculation of reliability characteristics from the model and their comparison with the obtained data;
4. Model estimation.

3. RESULTS AND DISCUSSION

Further in the article, engine models CF34-10E and CFM56-3B1 are built and the main reliability characteristics are calculated.

Following the steps of building the model, the results for the CF34-10E engine were obtained:

Table 1 shows the most frequently failed elements, the reasons for their failures and how to eliminate them.

Table 1. Most common engine failures of CF34-10E

Element	Problem	Action
FAN BLADES	ENG #2 fan blades damage	the fan blade #6 of the rh engine has been replaced

T25 SENSOR	Negative test result	T25 sensor is removed from engine#2
T12 SENSOR	ENG#2 short time dispatch EICAS MSG	the T12 sensor ENG#2 has been replaced
T2.5 TEMP SENSOR	CMC active message: ND T25 CH A-B INPUTS DISAGREEE	ENGINE #2 T2.5 temp sensor is replaced

Next, a statistical model is built, which is based on the Weibull distribution [4].

MTBF for Weibull distribution:

$$\lambda[t] = b \frac{t^{b-1}}{a^b} \tag{1}$$

$$T_0 = \frac{M[t]}{\Gamma\left(1 + \frac{1}{b}\right)} = M[t] \tag{2}$$

In accordance with the model, the operating time was 7333 hours. The time interval in which failures occur with a given sample is from 4991 hours to 8446 hours.

Based on the model, the results of operating time for CF34-10E were obtained from the Pareto diagram:

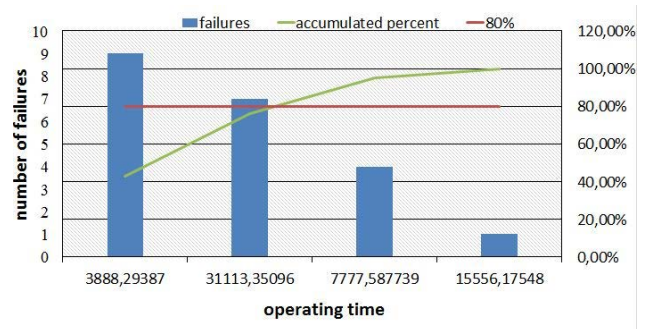


Figure 1. Pareto Diagram for CF34-10E

From Figure 4, the Pareto diagram of the number of failures from the total operating time intervals is obtained. Failure rates above 80% are acceptable and understandable. At the initial stage, the installed equipment is run-in, then stable operation of the engines is observed.

The values of the lifetime bias parameter b and intensity λ were calculated using the maximum likelihood method (MLE)

$$b = \left(\sum_{i=1}^n \frac{t_i^\alpha}{n} \right)^{\frac{1}{\alpha}} \tag{3}$$

and method of moments

$$b = \frac{\bar{x}}{\Gamma\left(1 + \frac{1}{\alpha}\right)} \tag{4}$$

The maximum likelihood method (MLE)– a method for

estimating the parameters of an assumed probability distribution given some observed data. It is implemented through the maximization of the likelihood function so that, according to the assumed statistical model, the observed data is the most probable.

The method of moments consists in equating the theoretical methods of distribution with the corresponding empirical moments obtained from the sample.

Since the model is calculated according to Weibull, we estimate the lifetime bias parameter b . The value b obtained is close to the operating time. The result is presented in Table 2.

Table 2. Calculation of the distribution parameter b and λ for the Weibull distribution for engine CF34-10E

	maximum likelihood method	method of moments
$\lambda \cdot 10^6, h^{-1}$	132	135
b, h	7551	7423

At the same time, the calculation error in method of moments with the maximum likelihood method for parameter b was 1,7%. The error in calculating the intensity in the two considered methods was 1,72%.

The article also calculates the gamma- percentile resource with the Weibull distribution law in accordance with the equations (Table 3):

$$T_\gamma = \frac{T_{ep}}{K_b} \left(\ln \frac{1}{\gamma} \right)^{\frac{1}{b}} \tag{5}$$

$$T_\gamma = H_k^W (1 - \gamma) \alpha + b \tag{6},$$

where H_k^W - quantile Weibull distribution.

The calculation results of the gamma-percentile resource are shown in Table 3

Table 3. Calculation gamma- percentile resource on eq.(5) and (6) for CF34-10E

	Eq. (5) with coefficient of variation	Eq. (6) with quantile
$T_{p\gamma}, h$	7615	7423

At the same time, the calculation the gamma- percentile resource error in eq. (5) with the eq. (6) was 2,5%.

The data obtained are due to a rather short service life, as well as a small failure statistic.

The estimate of the critical value for χ^2 was 7.815, from the experimental data 2.41. This result indicates the adequacy of the model.

For comparison let us analyze the CFM56-3B1 engine.

Table 4. Most common engine failures of CFM56-3B1.

Element	Problem	Action
START SWITCH	Engine 1 start switch does not return to "off" position during start.	The start switch of the first engine has been replaced.

FAN BLADES	The fan blades of the left engine No. 5 and No. 6 show signs of unbanding. Wear more than 0.1 mm.	Two pairs of fan blades (5-24 and 6-25) have been replaced.
THE FAN BLADES	Birdstrikes	Fan blades No. 16, 17, 18 have been replaced.

The operating time for CFM56-3B1 was 6582 hours.

The results of operating time for CFM56-3B1 were obtained from the Pareto diagram:

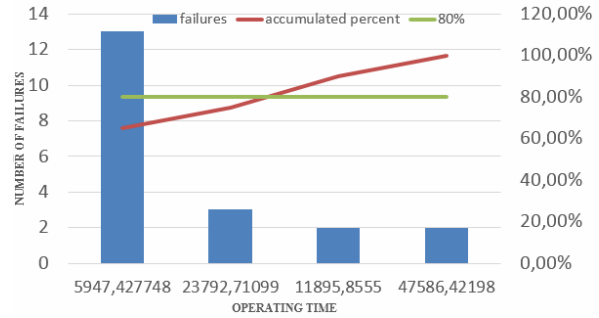


Figure 2. Pareto Diagram for CFM56-3B1

Pareto diagrams will reveal the intervals of elements when maintenance is necessary.

The values of the lifetime bias parameter b and intensity λ were calculated using the maximum likelihood method and method of moments and presented in table 5.

Table 5. Calculation of the distribution parameter b and λ for the Weibull distribution for engine CFM56-3B1

	maximum likelihood method	method of moments
$\lambda \cdot 10^4, h^{-1}$	75	70
b, h	7333	7284

At the same time, the calculation error in method of moments with the maximum likelihood method was 0,6%. Their values were comparable with the calculated operating time. The estimate of the intensity error was 7%.

The result is presented in Table 6.

Table 6. Calculation gamma- percentile resource on eq.(5) and (6) for CFM56-3B1

	Eq. (5) with coefficient of variation	Eq. (6) with quantile
$T_{p\gamma}, h$	6379	6582

At the same time, the calculation the gamma- percentile resource error in eq. (5) with the eq. (6) was 3,1%.

The data obtained are due to a rather short service life, as well as a small failure statistic.

The estimate of the critical value for χ^2 was 7.815, from the experimental data 6,244. This result indicates the adequacy of the model. Thus, based on the constructed engine models, we can conclude on their reliability. The evaluation results are shown in the table 7.

Table 7. The evaluation results.

Parameters	CFM56-3B1	CF34-10E
Operating times	+	-
Pareto diagram	-	+
Indicates the adequacy of the model	-	+
Gamma- percentile resource	-	+
Result	1/4	3/4

The table 7 shows comparisons of some of the reliability characteristics of engines.

Let's come to the main conclusions when comparing the reliability characteristics of engines:

- 1) it follows from the calculations that the engine CFM56-3B1 has a longer operating time;
- 2) the interval of reliable operation from the Pareto diagram is higher for the engine CF34-10E;
- 3) it can be seen from the χ^2 criterion that the engine CF34-10E model is more adequate;
- 4) the engine CF34-10E has a higher gamma -percentile resource then the CFM56-3B1.

As can be seen from the indicated table, the reliability of the engine CF34-10E is higher.

4. CONCLUSION

The statistics of engine failures of the above aircraft is best described by a model built on the basis of the Weibull distribution. For more successful forecasting, it is necessary to consider a larger fleet of aircraft. This will improve the accuracy of the obtained characteristics and correct the forecast.

The paper considers two types of engines used in civil aircraft- CFM56-3B1 and CF34-10E. The characteristics are calculated within the framework of the model based on the Weibull distribution. Based on the method of moments and the maximum likelihood method, the Weibull distribution parameters were estimated for both engines. The values obtained by the methods for each engine have a high degree of agreement. The error of the obtained results does not exceed 10%.

In the work, the operating time, gamma- percentage resource are calculated, the adequacy of the model is assessed.

The paper compares the obtained parameters for two types of engines. From the comparison it follows that the engine CF34-10E has a higher reliability.

However, the assessment obtained during comparison cannot be considered final, since only a few characteristics were calculated. With a larger number of calculated parameters, a different set of parameters and other initial statistics, the result may be different. The calculation model used, based on the Weibull distribution, can be considered simplified. However, with more statistics of the received data, this model can be extended, which will have a significant impact on its capabilities. As can be seen from the data matching, the model for which the calculations were made allows a good estimate of the

parameters indicated in the article.

Model advantages:

- the model is universal;
- model is simple to use;
- model is easy to match.

The constructed model is of practical importance, because:

- it provides an assessment of the characteristics of failures of engine elements and analysis of the obtained parameters;
- it allows you to calculate and evaluate the running time of engines, to carry out a number of preventive measures to eliminate failures;
- it allows you to adjust the performance of restoration, repair and other types of maintenance work;
- for military aircraft, the construction of such models seems necessary, because it allows you to make adjustments to routine and repair work.

The model gives some recommendations for technical operation. The using of condition-based maintenance with parameter control, rather than operating hours, is most beneficial in terms of minimizing maintenance costs.

The model used in the calculation of various reliability parameters is universal, because it can be applied to various types of aircraft. It should be noted that when making additions, it is possible to make reliability assessments not only of engines, but of other aircraft systems.

This model can be useful for assessing the reliability of military aircraft, as it allows you to make operational decisions on repair and operation.

References

- [1] FILIPPENKO, O.S., BELSKAYA D.E.: *Construction of aircraft anti-icing system failure models Boeing 737-300/500*, V-th international scientific and practical conference Aviation: history, modernity, development prospects, BSAA, Minsk, 2021, p.623.
- [2] KIRILENKO A.I., FILIPPENKO V.S., BELSKAYA D.E.: *Construction of models of failures of anti-icing and radio engineering systems of an aircraft Boeing 737-300/500*// Aviation Bulletin, №3, 2020., Minsk, 2020., p.36-40.
- [3] BELSKAYA, D.E., FILIPPENKO, O.S.: *Building a model of aircraft engine failures in the discipline "Probabilistic-statistical models of aircraft operation"*, international scientific and practical conference VARB, Military education and science in the context of digital transformation of knowledge, Minsk, 2020., p.288.
- [4] COX, D.R., SNELL, E.J.: *Applied statistics: principles and examples*, Chapman and Hall, London, New York, 1981.



STRENGTH CALCULATION OF LATERALLY LOADED TWO DIMENSIONAL PLANE STRUCTURAL ELEMENT

BOGDAN S. BOGDANOVIĆ
SERBIA, bogdanovic00@gmail.com

TONKO A. MIHOVILOVIĆ
UTVA AI, SERBIA, tonkojetonko@gmail.com

Abstract: Laterally loaded plane structural elements have very wide use in aircraft structures. Dimensions of these elements should be defined very carefully, because of demands for smaller mass and reliable exploitation. These, plane elements behave like plates, membranes and most often like mixture of them. It means that corresponded strength calculation is very complex. For practical use it was very useful to make strength calculation much simpler. It could be done by introducing some assumptions, which do not change the essence of element behavior. In this paper some simplified procedure, based on assumptions like these, for plane element strength calculation is shown. Also a numerical example is given.

Keywords: plane structural element, membrane, plate, strength calculation.

1. INTRODUCTION

Two dimensional plane structural elements are most frequently used as locally loaded parts of secondary structures. Term lateral load means that load acts in direction normal to the element's plane. Usually, elements are walls of:

- passenger cabin under pressure,
- Some fluid compartment, gasoline, or oil tanks.

Main role of elements of such type is to transfer different types of lateral load, concentrated or uniformly distributed, to the primary structure elements. Elements could be reinforced, or rarely without reinforcements; it does depend on:

- Element size,
- Element load, or
- Both.

2. BEHAVIOR OF LATERALLY LOADED PLANE ELEMENT

Term "element behavior" describes the way how element:

- accepts lateral load, and
- transfers it to the surrounding (primary) structure.

All this is defined by corresponding stresses and deformation of element. There are two different ways of behavior for considered element type under lateral load such as:

- Plate, and/or
- Membrane

It should remark that both ways of behavior are more or

less always present. Dominance of one or other way depends on:

- Element flexural rigidity, and
- Load intensity.

Usually, elements of greater flexural rigidity behaves more like plate, smaller flexural rigidity elements have membrane like behavior. On the other side lower load intensity produces plate, and higher load intensity membrane behavior. Generally, best criterion for elements behavior estimation is the relative magnitude of transverse (lateral) deflection under load compared with total element thickness. Transverse deflection of plates is approximately one or two tenths of thickness, for membrane it is about ten times elements thickness, or even more.

2.1. Element behaves like plate

Some basic characteristics of elements plate behavior are:

- Loads are resisted by bending and shear of elements cross sections,
- Lateral deflections and slopes are relatively small, so that $\frac{\delta^2 w}{\delta x^2}$ and $\frac{\delta^2 w}{\delta y^2}$ are good approximation to the curvature
- Elements supports on the surrounding primary structure are loaded mostly (only) in vertical plane (normal to the element)

Relations, connecting bending, and twisting moments, with internal shear forces and lateral loads are:

$$Q_x = \frac{\partial M_x}{\partial x} + \frac{\partial M_{yx}}{\partial y} \quad (1)$$

$$Q_y = \frac{\partial M_y}{\partial y} + \frac{\partial M_{yx}}{\partial x} \quad (2)$$

$$q = \frac{\partial Q_y}{\partial X} + \frac{\partial Q_x}{\partial x} \quad (3)$$

Here are:

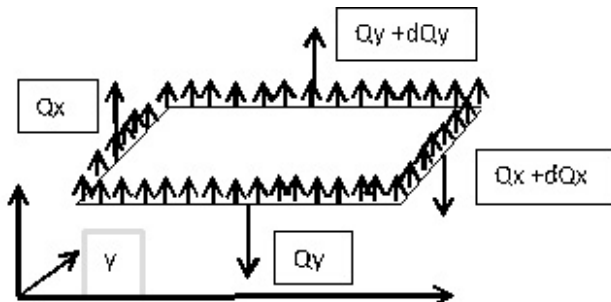


Figure 1. Load and internal shear forces on plate element

Equations (1), (2).. (3) are derived under assumption that:

- No stress acts in the middle surface of element, and
- It means that deformed surface is developable.

Basic relation between lateral loads (q), deflection (w) and element rigidity (D) is given:

$$\frac{\delta^4 w}{\delta x^4} + 2 \frac{\delta^4 w}{\delta x^2 \delta y^2} + \frac{\delta^4 w}{\delta y^4} = \frac{q}{D} \quad (4)$$

Usually, most important results for practical use are:

- maximum stress and deformations values

These values should be obtained by performing analytic computation, but also using lot of tables and expressions [1]:

$$W_{\max} = W_{MAX} = \infty \frac{qa^4}{Et^3} \quad (5)$$

$$S_{MAX} = \beta \frac{qa^2}{t^2} \quad (6)$$

Marks in (5), (6) are:

W_{MAX} [m] - maximum deflection,

S_{MAX} [bar] – maximum stress values

α, β [] – deflection, stress coefficient

a [m], t [m] – plate short side, thickness

E [bar] – plate material modulus of elasticity

$\partial M_x, \partial M_y, \partial M_{xy}$, [Nm] – bending, twisting moments

Q_x, Q_y , [N] – internal shear forces,

Coefficient values α, β are given in corresponding

q [N/m²] – lateral load tables in literature [1].

2.2. Element behaves like membrane

Membrane length (a):

Some basic characteristics of elements membrane behavior are:

- Loads are resisted by tension and stretching of middle surface,
- Lateral deflections and slopes are relatively great,
- Elements supports on the surrounding primary structure are loaded in both vertical and horizontal planes

$$\delta = \int_0^a dl - a \quad (9)$$

After using equation (8) and integration it is obtained:

$$\delta = \frac{q^2 a^2}{24 s^2 t^2} \quad (10)$$

On the other side is:

One dimensional problem retains the general problem feature. It will be treated first because of simplicity Relation connecting tension stress (force) with deformation and load, is:

$$\frac{d^2 w}{dx^2} = -\frac{q}{st} \quad (7)$$

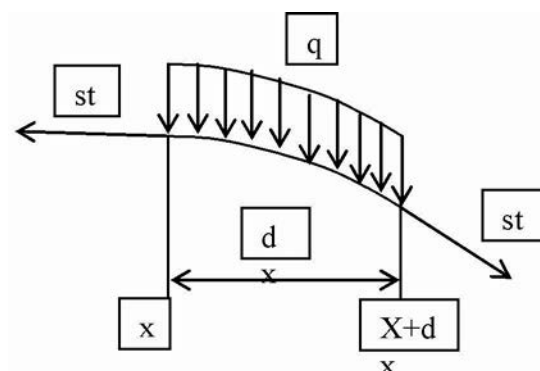


Figure 2. Load and internal tension forces on one dimensional membrane element

Equation (7) is differential equation of a parabola and its solution is:

$$w = \frac{qx}{2st}(a-x) \quad (8)$$

In equation (8) there are two unknowns:

s – stress and

w - deformation

Firstly, stress value (s) will be determined by computing the membrane stretch as a difference between curved arc length (dl) and original

$$\delta = \frac{s \cdot a}{E} \quad (11)$$

Combining (10) and (11) the final expression for stress is:

$$s = 0.347 \left[E \left(\frac{q \cdot a}{t} \right)^2 \right]^{\frac{1}{3}} \quad (12)$$

Expression (12) shows the nonlinearity of problem because stress varies as fractional exponent of load.

Solution for complete two dimensional problem is performed. Obtained expressions for maximum stress and deformation have similar shape as these for one dimensional membrane and for plate:

$$W_{MAX} = n_1 a \left(\frac{q \cdot a}{E \cdot t} \right)^{\frac{1}{3}} \quad (13)$$

$$S_{MAX} = n_2 \left(E \frac{q \cdot a}{t} \right)^{\frac{1}{2}} \quad (14)$$

It is worth to note that maximum stress value occurs at the middle of the long panel side.

Marks in (13), (14) are:

w_{MAX} [m] - maximum deflection,

s_{MAX} [bar] – maximum stress values

n_1, n_2 , [] – deflection, stress coefficient

a [m], t [m] – membrane long side, thickness

Coefficient values n_1, n_2 are given in corresponding tables in literature [1].

2.3. Element behaves like plate membrane combination

In most often cases laterally loaded two dimensional element behaves like some plate – membrane combination. It means that one part of lateral load is reacted by plate, and the other one by membrane action. A relatively good approximation for maximum values deformation calculation could be obtained simply by adding together parts of load carried through plate and membrane actions:

$$q = q_{PLATE} + q_{MEM} \quad (15)$$

Values q_{PLATE} , q_{MEM} could be obtained by solving equations (5) and (13) for corresponding loads part:

$$q_{PLATE} = \frac{w_{MAX} \cdot E \cdot t^3}{a \cdot a^4} \quad (16)$$

$$q_{MEM} = \frac{w_{MAX}^3 \cdot E \cdot t}{n_1^3 a^4} \quad (17)$$

Putting (16) and (17) in (15) and rearranging it is obtained:

$$q = \frac{1}{a} \frac{E \cdot t^3}{a^4} \cdot W_{MAX} + \frac{1}{n_1^3} \frac{E \cdot t}{a^4} \cdot W_{MAX}^3 \quad (18)$$

In (18) there is not any interaction between plate and membrane behavior, and since the system is NONLINEAR obtained result will be approximative

Table 1. Plate coefficient

b/a	α	β
1.0	0.0443	0.2874
1.2	0.0616	0.3756
1.4	0.0770	0.4518
1.6	0.0906	0.5172
1.8	0.1017	0.5688
2.0	0.1106	0.6102
3.0	0.1336	0.7134
All edges are simply supported		

Table 2. Membrane coefficient

a/b	1.0	1.5	2.0	2.5
n_1	0.318	0.228	0.16	0.125
n_2	0.356	0.37	0.336	0.304

3. PLATE AND MEMBRANE DEFORMATION AND STRESS CALCULATION

There are several steps for plate and membrane deformation and stress calculation:

- Maximum values for deflection W_{MAX} will be obtained by solving cubic equation (18) using corresponding procedure
- Values for q_{PLATE} and q_{MEM} will be obtained using W_{MAX} and expressions (16) and (17)
- Corresponding stress values for plate s_{PLATE} and membrane s_{MEM} , will be calculated using q_{PLATE} and q_{MEM} and expression (6) and (14)

4. NUMERICAL EXAMPLE

As a numerical example maximum deformation, maximum plate, membrane and total stresses for a uniformly laterally loaded plane two dimensional simply supported element will be calculated. Load data are shown in Table 3:

Table 3. Load data

Load		
$F_{total 1}$	A	q_1
[daN]	[cm ²]	[daN/cm ²]
216	296.36	0.728843

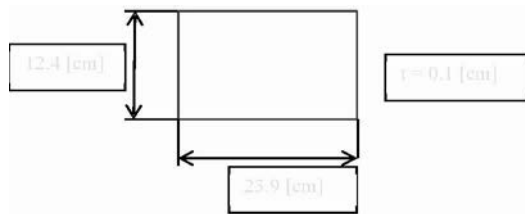


Figure 3. Two dimensional plane element

Calculation is made of several steps:

1. Definition of plate deflection and stress coefficients,
2. Definition of membrane deflection and stress coefficients,
3. Cubic equation solution – w_{MAX} calculation
4. Calculation of load part reacted by element like a plate
5. Calculation of load part reacted by element like a membrane
6. Calculation of plate bending stresses
7. Calculation of membrane tension stress

Step 1

Plate deflection and stress coefficients are obtained by interpolation using data from Table 1; obtained results are shown in Tables 4 and 5

Table 4. Plate deflection coefficient α

a	b	b/a	b/a_1	b/a_2	$\Delta b/a_1$
[cm]	[cm]	[]	[]	[]	[]
12.4	23.9	1.9274	1.8	2	0.2
$\alpha(1.8)$	$\alpha(2)$	$\Delta\alpha_1$	$\Delta b/a_2$	$\Delta\alpha_2$	α
[]	[]	[]	[]	[]	[]
0.1017	0.1106	0.0089	0.1274	0.0057	0.1074

Table 5. Plate stress coefficient β

a	b	b/a	b/a_1	b/a_2	$\Delta b/a_1$
[cm]	[cm]	[]	[]	[]	[]
12.4	23.9	1.9274	1.8	2	0.2
$\beta(1.8)$	$\beta(2)$	$\Delta\beta_1$	$\Delta b/a_2$	$\Delta\beta_2$	β
[]	[]	[]	[]	[]	[]
0.5688	0.6102	0.0414	0.1274	0.0264	0.5952

Step 2

Membrane deflection and stress coefficients are obtained by interpolation using data from Table 2; obtained results are shown in Tables 6 and 7.

Table 6. Membrane deflection coefficient n_1

a	b	a/b	a/b_1	a/b_2	$\Delta a/b_1$
[cm]	[cm]	[]	[]	[]	[]
12.4	23.9	1.9274	1.5	2	0.5
$n_1(1.5)$	$n_1(2)$	Δn_{11}	$\Delta a/b_2$	Δn_2	n_1
[]	[]	[]	[]	[]	[]
0.228	0.16	-0.068	0.4274	-0.0581	0.1699

Table 7. Membrane stress coefficient n_1

a	b	a/b	a/b_1	a/b_2	$\Delta a/b_1$
[cm]	[cm]	[]	[]	[]	[]
12.4	23.9	1.9274	1.5	2	0.5
$n_2(1.5)$	$n_2(2)$	Δn_{21}	$\Delta a/b_2$	Δn_2	n_2

[]	[]	[]	[]	[]	[]
0.37	0.336	-0.034	0.4274	-0.0291	0.3410

Step 3

Equation (18) could be rearranged. It is incomplete (or reduced) cubic equation; without second degree member:

$$\frac{1}{n_1^3} \frac{E \cdot t}{a^4} \cdot W_{MAX}^3 + \frac{1}{a^4} \frac{E \cdot t}{a^4} \cdot W_{MAX} - q = 0 \quad (19.1)$$

or

$$K_{31}w^3 + K_{11}w + q_1 = 0 \quad (19.2)$$

Starting values for coefficients K_{11} and K_{31} are calculated using data from tables 4 and 6, obtained results are shown in Table 8.

Table 8. Cubic equation coefficient – starting values

E	t	t^3	α
[bar]	[cm]	[cm ³]	[]
735000	0.1	0.001	0.10737
b	b^4	$A=Et^3$	$B=ab^4$
[cm]	[cm ⁴]	[daNcm]	[cm ⁴]
23.9	326280.9	735	35032.83
$K_{11}=A/B$	a	a^4	n_1
[]	[cm]	[cm ⁴]	[]
0.02098	23.9	326280.9	0.169871
n_1^3	$C=Et$	$D=n_1^3a^4$	$K_{31}=C/D$
[]	[]	[cm ⁴]	[]
0.004902	73500	1599.371	45.95558

Using values from Table 7 and 3, equation (19.2) is now:

$$45.95558w^3 + 0.02098w - 0.728843 = 0 \quad (20)$$

Before solving, cubic equation (20) should be rearranged to:

$$K_{32}w^3 + K_{12}w + q_2 = 0 \quad (21)$$

Values for coefficients K_{32} , K_{12} and q_2 are given in Table 9.

Table 9. Cubic equation coefficient – calculation values

K_{32}	K_{12}	q_2
1	0.000457	- 0.01586

Cubic equation - shape for solution is:

$$w^3 + 0.000457w - 0.01586 = 0 \quad (22)$$

First step in solution of eq. (22) is to calculate its discriminant; calculation and obtained results are shown in Table 10.

Table 10. Cubic equation - discriminant

K_{12}	q_2	q_2^2	$q_2^2/4$
0.000457	-0.01586	0.000252	6.29E-05
K_{12}^3	$K_{12}^3/27$	D	
9.52E-11	3.52E-12	6.29E-05	

Obtained value for discriminant is:

$$D = 6.29E - 05 > 0$$

In case like this Cardano's formula for cubic equation roots solution will be applied. Such type of cubic equation has one real root value x_1 , and the other two are conjugate complex.

$$x_1 = \sqrt[3]{-\frac{q_2}{2} + \sqrt{\frac{q_2^2}{4} + \frac{K_{12}^3}{27}}} + \sqrt[3]{-\frac{q_2}{2} - \sqrt{\frac{q_2^2}{4} + \frac{K_{12}^3}{27}}} \quad (23)$$

Complete real root calculation and obtained results are given in Table 11.

Table 11. Real root calculation and obtained value

q_2	K_{12}	$q_{2/2}$	$A=(q_{2/2})^2$
-0.01586	0.000457	-0.00793	6.29E-05
$K_{12/3}$	$B=(K_{12/3})^3$	$(A+B)$	
0.000152	3.52E-12	6.29E-05	
$C=(A+B)^{1/2}$	$E=-(q_{2/2})+C$	$F=-(q_{2/2})-C$	$G=E^{1/3}$
0.00793	0.01586	-2.2E-10	0.25125
$H=F^{1/3}$	$x_1=G+H$	w [cm]	
-0.00061	0.25064	0.25064	

Load distribution; calculation and results, corresponding stress values for plate and membrane are shown in Tables 12, 13, 14, 15.

Table 12. Part of load accepted by membrane action

w	w^3	E	t	n_1	n_1^3
[cm]	[cm ³]	[bar]	[cm]	[]	[]
0.2506	0.0157	735000	0.1	0.17	0.0049
a	a^4	$A=w^3Et$	$B=n_1^3a^4$	q_{mem}	
[cm]	[cm ⁴]	[daNcm ²]	[cm ⁴]	[bar]	
23.9	326281	1157.28	1599.4	0.724	

Table 13. Part of load accepted by plate action

w	E	t	t^3	α
[cm]	[bar]	[cm]	[cm]	[]
0.2506	735000	0.1	0.001	0.1073
a	a^4	$A=wEt^3$	$B=aa^4$	q_{plate}
[cm]	[cm ⁴]	[daNcm ²]	[cm]	[bar]
23.9	326281	184.220	35033.	0.0053

Table 14. Membrane stress in element - tension

q_{mem}	a	t	$A=qa$	$B=A/t$	$C=B^2$
[bar]	[cm]	[cm]	[daN/cm]	[bar]	[bar ²]
0.7236	23.9	0.1	17.2937	172.97	29907
E	$D=EC$	$F=D^{1/3}$	n_2	$\sigma_{tens.}$	
[bar]	[bar ³]	[bar]	[]	[bar]	
735000	2.2E+10	2801.3	0.34094	955.1	

q_{plate}	a	a^2	t	t^2
[bar]	[cm]	[cm ²]	[cm]	[cm ²]
0.005259	12.4	153.76	0.1	0.01
β	$A=a^2q$	$B=A/t^2$	$\sigma_{comp.}$	$\sigma_{tens.}$
[]	[daN]	[bar]	[bar]	[bar]
0.595176	0.808548	80.85482	48.12283	-48.1228

Table 15. Plate stress in element – tension/compression

$\sigma_{mem. tens.}$	$\sigma_{plate tens.}$	$\sigma_{plate comp.}$	$\sigma_{tot. 1}$	$\sigma_{tot. 2}$
[bar]	[bar]	[bar]	[bar]	[bar]
955.050	48.123	-48.123	1003.17	906.93

Table 16. Total stresses in element

$\sigma_{mem. tens.}$	$\sigma_{plate tens.}$	$\sigma_{plate comp.}$	$\sigma_{tot. 1}$	$\sigma_{tot. 2}$
[bar]	[bar]	[bar]	[bar]	[bar]
955.050	48.123	-48.123	1003.17	906.93

5. CONCLUSION

The simplified procedure for stresses and strain values definition in a laterally loaded two dimensional structural elements is shown. Numerical example is presented. Procedure should be the basis for detailed calculation of much complicated load cases, particularly on the elements of the secondary aircraft structures, which must include the stiffness of surrounding structural elements.

References

- [1] Bruhn, E.F.: Analysis and Design of Flight Vehicle Structures Tri – State Offset Company Cincinnati Ohio 45202
- [2] Rašković, D.: Tablice iz otpornosti materijala, Naučna knjiga Beograd 1963
- [3] Levy, S.: Bending of Rectangular Plates With Large Deflections NACA TR 737, 1942
- [4] Levy, S.: Square Plates With Clamped Edges Under Normal Pressure Producing Large Deflections, NACA TR 740, 1942
- [5] Timoshenko, S.: Theory of Plates and Shells McGraw – Hill N.Y. 1940



LANDING GEAR BRAKES TESTING

TEODOR BABIĆ

Utva Aviation Industry, Pančevo, teodorbabic@gmail.com

MARINA OSTOJIĆ

Utva Aviation Industry, Pančevo, majce74@yahoo.com

TAMARA NIKOLIĆ

Utva Aviation Industry, Pančevo, tn.aircraft@yahoo.com

NIKOLA BOGAVAC

Utva Aviation Industry, Pančevo, bogavacnikola55@gmail.com

Abstract: Utva Aviation Industry is in the process of certifying airplane Sova according to CS-23 regulations. Using different means of compliance, we are showing that our airplane is designed and manufactured to comply with all requirements.

Along with numerous flight tests, we performed a flight test to show compliance of landing gear brakes with specific requirements. During the landing, we proved that brakes are able to prevent the wheels from rolling on a paved runway under specified conditions. Also, the pressure specified by the brake manufacturer was not exceeded while landing in previously determined landing distance.

Keywords: Brakes, flight testing, landing distance, pressure.

1. INTRODUCTION

UTVA Aviation Industry is finalizing the certification process of prototype Sova in normal and utility category.

Analysis and flight tests were performed in order to show compliance with CS 23 requirements.

In this paperwork, compliance and tests for CS 23 Subpart D (Design and Construction) will be demonstrated.

2. CERTIFICATION

CS 23.735 Brakes requirements:

- a) The landing brake kinetic energy capacity rating of each main wheel brake assembly must not be less than the kinetic energy absorption requirements determined from the following formula:

$$KE = \frac{1}{2}MV^2/N$$

KE = kinetic energy per wheel (J)

M = mass at design landing weight (kg)

V = aeroplane speed (m/s)

N = number of main wheels with brakes

- b) Brakes must be able to prevent the wheels from rolling on a paved runway with take-off power in the critical engine, but need not prevent movement of the aeroplane with wheels locked.

- c) During the landing distance determination required by CS 23.75, the pressure in the wheel braking system must not exceed the pressure specified by the brake manufacturer.

3. ANALYSIS

- a) The kinetic energy the brake should absorb when slowing the plane to a stop is given by the formula

$$KE = \frac{1}{2}MV^2/N$$

In chapter 5 of the document "Analysis of increase in the maximum landing mass of the main leg and nose leg of the UTVA 75A aircraft" the value of kinetic energy was determined to be 198.15 kJ.

In paragraph 23.735(a)(2) is defined that kinetic energy can be calculated with the formula:

$$KE = \frac{mV_{s0}^2}{2N} = \frac{1200 \cdot 25,7^2}{2 \cdot 2} = 198,15 \text{ kJ}$$

$m = 1200 \text{ kg}$ take off max mass

$V_{s0} = 50 \text{ kts} = 25,7 \text{ m/s}$ lift loss speed

$N = 2$ number of wheels with brakes

b) When taking off from Vršac Airport (flight No. 122), the minimum take-off and landing length was determined by holding the brakes at maximum power, in order to achieve the shortest take-off length. The diagram shows that the aircraft was idling at full power and maximum rpm and then went into the take-off phase

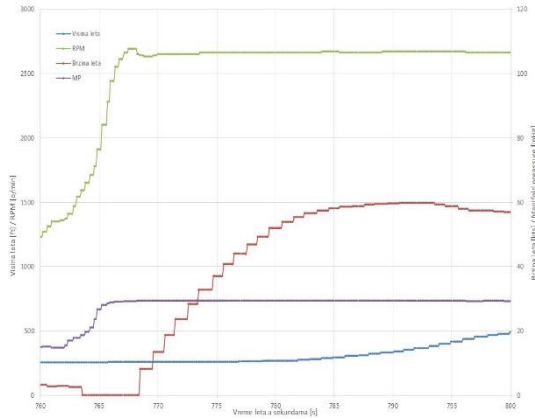


Figure 1. Flight parameters during flight No.122

From the condition that all absorbed kinetic energy is converted into thermal energy, i.e. $KE=Q$ and by knowing the formula for thermal energy :

$$Q = m_d c_p \Delta T$$

we may evaluate mass of braking disc:

$$m_d = \frac{Q}{c_p \Delta T} = \frac{198,15}{0,49 \cdot 773,15} = 0,52 \text{ kg}$$

Braking cylinder is made of steel, like hollow cylinder, with outer diameter $d_s = 190 \text{ mm}$ and internal diameter $d_u = 133 \text{ mm}$. Knowing density of steel is $\rho = 7850 \text{ kg/m}^3$, braking disc thickness can be evaluated as :

$$h = \frac{4m_d}{\rho \pi (d_s^2 - d_u^2)} = \frac{4 \cdot 0,52}{7850 \cdot \pi (0,19^2 - 0,13^2)} = 4,58 \cdot 10^{-3} \text{ m} = 4,58 \text{ mm}$$

Previous value corresponds to condition when wheels do not roll, at maximum gas and pressed brakes. Disc thickness on "SOVA" aircraft is 5mm, so braking disc complies to requirements.

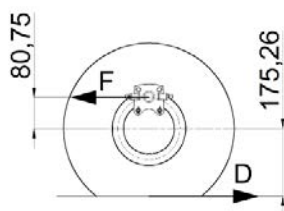


Figure 2. Brake dimensioning

Reduction of disc thickness of 2mm is expected as a result of exploitation for 400 braking cycles. Taking into account the need for a reserve, a value of 7 mm is adopted for the thickness of the brake disc.

c) According to the test plan, on 04/23/2020. three flights were performed, during which the landing was made on the concrete runway in Vršac. The aim of this test was to measure the pressure in the brake system during braking on a track length of 245.77 m previously determined in paragraph CS 23.75. The pressure in the brakes measured during braking must not exceed 30 bar.

The brake temperature measured after braking should be around 500 °C.

Before starting the test, it was necessary to perform the following activities:

- on the right landing gear wheel, instead of standard connector, place an adapter, so that the thread for the pressure gauge 1/2 NPT is positioned in the plane's flight direction
- position the manometer into the adapter in the plane's flight direction (figure 2)
- take transparent tape and wrap it around the landing gear wheel in several circles so that the hose, tube, adapter and pressure gauge are fixed
- place the camera on the landing gear right wheel so that the lens is directed towards the pressure gauge and secure it with transparent tape.



Figure 3a. Pressure gauge installation

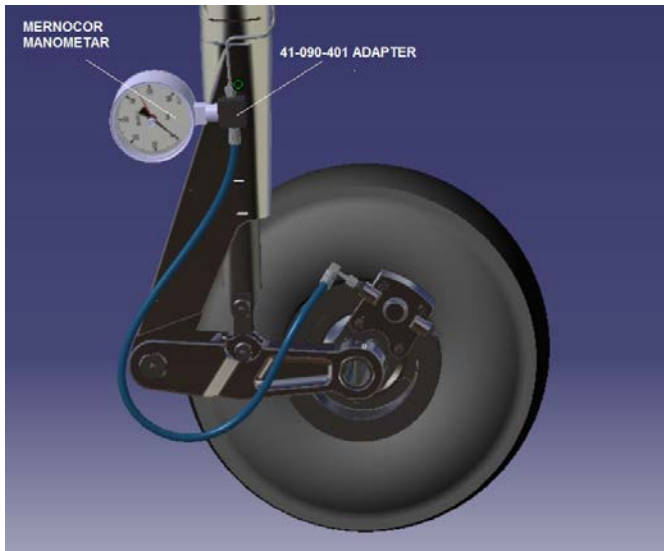


Figure 3b. Pressure gauge installation

The instruments for testing the brake system of the Sova aircraft consists of the following devices:

- MVP-50P
- GT-50
- G500
- pressure gauge MERNOKOR E1805771161
- laser thermometer DT8011H
- camera.

Test procedure:

- Front centering, with maximum mass, i.e. 1200 kg.
- Pour the fuel into both tanks up to the filler cap, i.e. a total of 150 l
- Maximum oil quantity (8 Qts).
- 115 kg of ballast on the co-pilot seat (point 1) and a total of 9 kg on the passenger seats (points 2 and 3), the center of mass is then at 27.3% MGC.
- In order to check the correctness of the pressure gauge, it is necessary to carry out a test on the ground of the airport "Utva" Pančevo by taxiing on the runway at 70% of rotation speed and perform sudden braking
- After the ground test, reset the pressure gauge and fly to "Vršac" airport.
- When landing on the concrete runway of the "Vršac" airport, brake suddenly so that the landing distance is as short as possible. This test should be performed as part of the runway length test during landing.
- As soon as possible, take the DT8011H laser thermometer, point it towards the brake disc, measure the temperature, record it and take a picture with a camera
- Write down the measured value and take a picture with the camera.

Test results:

During braking, before wheel slippage, pressure values of 29 ÷ 32 bar were measured in the brake system (figures 1 – 3).



p=32 bar



p = 30 bar



p=29 bar

Figure 4. Measured pressure values during braking

The operating pressure in the brake system installation is 40 bar. The system was designed and tested for a pressure 2.5 times higher than operating pressure, which is 100 bar. It was demonstrated that all joints can withstand the pressure values obtained by braking on a concrete runway during landing.

3. CONCLUSION

Different means of compliance are used during the aircraft certification process. Consultations with test pilot, writing test plans, pre-flight and post-flight checks, the testing itself and finally analyzing the obtained data make the flight testing very interesting and demanding.

Utva engineers are very proud and thankful for having such a good test pilot and flight test team which made it

easy to successfully perform all necessary flight tests in order to certify "Sova" aircraft.

References

- [1] Certification Specifications for Normal, Utility, Aerobatic and Commuter Category Aeroplanes CS 23, Amendment 3, Book 1
- [2] Certification Specifications for Normal, Utility, Aerobatic and Commuter Category Aeroplanes CS 23, Amendment 3, Book 2
- [3] EASA Part 21
- [4] Zlatko Rendulić, *Mehanika leta*
- [5] Prof. dr Vladimir Milošević, *Ispitivanje aviona u letu*
- [6] Aleksandar Petrović, „Analiza povećanja maksimalne mase sletanja glavne noge i nosne noge aviona UTVA 75A“



POWERPLANT COOLING FLIGHT TESTS

MARINA OSTOJIĆ

Utva Aviation Industry, Pančevo, majce74@yahoo.com

TAMARA NIKOLIĆ

Utva Aviation Industry, Pančevo, tn.aircraft@yahoo.com

NIKOLA BOGAVAC

Utva Aviation Industry, Pančevo, bogavacnikola55@gmail.com

Abstract: Flight testing is necessary in the process of showing compliance of the airplane with specific design requirements. Utva Aviation Industry performed numerous flight tests of Sova airplane in order to prove its safety. Along with airplane design, structure, performance and equipment, it was necessary to show compliance of the powerplant.

In this paper there is the analysis of the flight tests of the powerplant cooling in the most critical climbing case with maximum ambient atmospheric temperature for which approval is requested. Flight test report results are presented with defined minimum speed for these conditions proving our four-seater meets all requirements in its category.

Keywords: Flight testing, powerplant cooling, critical conditions, minimum speed, test analysis.

1. INTRODUCTION

Certifying an aircraft is a long and demanding process. It was a challenge for Utva engineers and flying test team to define the means of compliance with CS 23 paragraphs [1, 2], write flight test plans and perform flight testing [3, 4] in order to comply with the requirements.

In this paper, compliance for several paragraphs of CS 23 E (Powerplant) will be demonstrated.

2. CERTIFICATION

Requirements:

The CS 23.1041 “Colling-General” prescribes that the powerplant and auxiliary power unit cooling provisions must maintain the temperatures of powerplant components and engine fluids and auxiliary power unit components and fluids within the limits established for those components and fluids under the most adverse ground and flight operations to the maximum altitude and maximum ambient atmospheric temperature conditions for which approval is requested, and after normal engine and auxiliary power unit shutdown.

The CS 23.1043 “Cooling-Test” prescribes that if the tests of compliance with paragraph CS 23.1041 are conducted under ambient atmospheric temperature conditions, deviating from the maximum for which approval is requested, (minimal temperature for the certification is 38°C/100°F), the following correction must be applied to the recorded powerplant temperatures:

$$\text{Corrected temperature} = \text{true temperature} + 1.0 [100 - 0,0036 (Hp) - \text{true OAT}] \quad (1)$$

where:

- Pressure height - H_p [ft]
- Outside air temperature – OAT [°F]

Temperatures of engine fluids and powerplant components for which temperature limits are established, must be corrected by adding to them the difference between the maximum ambient atmospheric temperature for the relevant altitude for which approval has been requested (38°C/100°F) and the temperature of the ambient air at the time of the first occurrence of the maximum fluid or component temperature recorded during the cooling test.

The CS 23.1047 “Cooling test procedure for reciprocating engine-powered aeroplane” prescribes that the compliance with CS 23.1041 must be shown for the climb stage of flight. The aircraft must be flown in the configurations, at the speeds and following the procedures recommended in the aircraft flight manual, corresponding to the applicable performance requirements, which are critical relative to cooling.

Tests:

Aircraft Sova has Lycoming engine IO-390-A3A6 installed. In order to have specific CS paragraphs fully satisfied, the temperatures of all powerplant components and fluids that are recorded/measured during tests must be within the permitted limits.

Table 1. Temperature limits requirements

Component temp. [°F]	Max allowed
Oil temperature [°F]	235
CHT [°F]	475
EGT [°F]	1700
Battery temperature [°F]	110

In order to show compliance of the aircraft with the requirements of the mentioned paragraphs of the CS 23 regulation, the aircraft was tested in the following way: Data recording in flight was done using MVP-50P device, APIBOX, GT-50. Observed and processed data after this test were:

- Pressure height - Hp [ft]
- Indicated airspeed - IAS [kts]
- Outside air temperature – OAT [°C]
- Oil temperature [°F]
- Cylinder head temperature – CHT [°F]
- Exhaust gas temperature – EGT[°F]
- Propeller speed [RPM]
- Testing time - t [s]
- Engine vacuum pressure – [inHg]
- Battery temperature [°F] (using GT-50 device)

Procedures for showing compliance with paragraphs CS 23.1041, CS 23.1043, CS 23.1047 were made on the basis of recommendations from the Flight Test Guide (FTG) for the certification of CS-23, section 5 Cooling, paragraphs 246 and 248.

- Perform the flight in an atmosphere without visible moisture during the flight.
- The configuration of the aircraft is with front centering (22%) and a maximum mass of 1200 kg.
- Pour fuel into both tanks up to the filler cap, i.e. total of 150 liters.
- The amount of oil must be critical, i.e. minimum for flight (4 Qts).
- Establish level flight at 1500 feet and maintain altitude at 75% maximum engine power (2450 RPM) until temperatures of all power unit components and fluids stabilize. (The temperature is stabilized when the change is less than 2°F per minute).
- After temperatures have stabilized, increase power to maximum and perform a climb maneuver corresponding to airspeed of 70 kts.
- Continue climbing to a maximum altitude of 10.500 ft.
- Monitor the parameters on the MVP-50P and the GT-50 device which is set to measure the temperature in the battery area.
- Record the temperature from the GT-50 device in intervals of one minute, due to impossibility of automatic recording.
- If at a speed of 70 kts, all parameters of the power unit are within the permitted limits, repeat the test with a speed of 65 kts on the route.
- If, at a speed of 65 kts, all powerplant parameters are within the permitted limits, repeat the test at speed of 60 kts on the route.

Analysis:

Record data from APIBOX and MVP-50P devices. If temperature is lower (minimum 38°C), the obtained values should be corrected using Eq. (1).

Make diagrams from the flight, as well as temperature diagrams of powerplant components. Analyze the temperatures and notice if the temperatures of the powerplant components are exceeded.

For the purpose of testing the powerplant cooling, the following devices were used: MVP-50P (for reading the temperature of the cylinder head, exhaust gases, engine RPM and oil temperature in the engine); APIBOX (for reading the external air temperature, pressure altitude and aircraft speed), while the temperature in the battery compartment was read from the GT-50 device.

The testing was performed in 2 (two) flights, flight No. 62 and flight No. 205.

Flight No. 62 was conducted on October 2, 2020 in weather conditions where the ambient temperature at sea level was less than 38°C, so the obtained values were corrected using the Eq. (1) There was no presence of moisture during the flight. The flight took place in the Pančevo airport area, under the ambient conditions given in the Table 2.

Table 2. Ambient conditions during flight No. 62

Time	Wind speed [kts]	Wind direction	Temperature [°C]	Pressure [mbar]
13:50	5.6	140	28.5	994.5
13:57	1.7	130	30.8	
Take off				
14:00	2.1	270	30.8	
14:05	6.0	200	30.3	
14:10	2.7	265	30.2	
14:15	2.7	260	30.1	
14:20	4.0	220	30.1	
14:25	2.6	220	29.5	
14:30	2.0	158	30.9	
14:35	2.2	130	31.1	
14:39	4.2	192	31.2	994.3
Landing				

After the engine was started and warmed up to operating temperatures, takeoff and climb were conducted at maximum engine power and speed of 70 kts. The climb was performed at least 6 minutes after fluid and component temperature peaks were obtained or up to a maximum altitude of 10.500 ft with RICH configuration and max RPM.

Data collection was done with APIBOX device, MVP-50P, and reading from the GT-50 device. The pilot used radio communication to inform about the battery temperature by reading the GT-50 device, and based on that data, the diagram in Figure 4 was created.

Table 3. Cooling results with 70 [kts] on path

	MVP t. [°F]	Max corrected t. [°F]	Max allowed t. [°F]
Oil temperature [°F] 4940 ft Hp / 68°F OAT	206	220	235
CHT [°F] 1693 ft Hp / 86°F OAT	425	433	475
EGT [°F] 252 ft Hp / 91°F OAT	1354	1362	1700
Battery temperature [°F] 1718 ft Hp / 83°F OAT	93	104	110

Since the air temperature on the day of the test was lower than required 38°C, then the Eq. (1) was used for the MAXIMUM ACHIEVED CORRECTED temperature values-

The flight parameters during this flight are given in diagrams on the Figure 1.

The diagrams on Figures 2 to 4 show the graphical values of temperatures of fluids and components at a speed of 70 kts on path for which the temperature limits are given in Table 3.

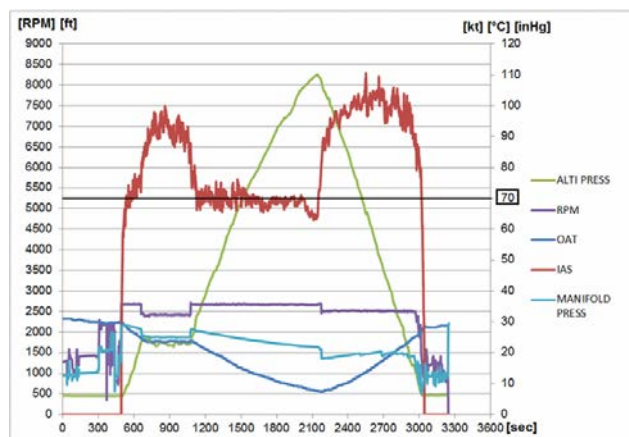


Figure 1. Flight parameters at 70 [kts]

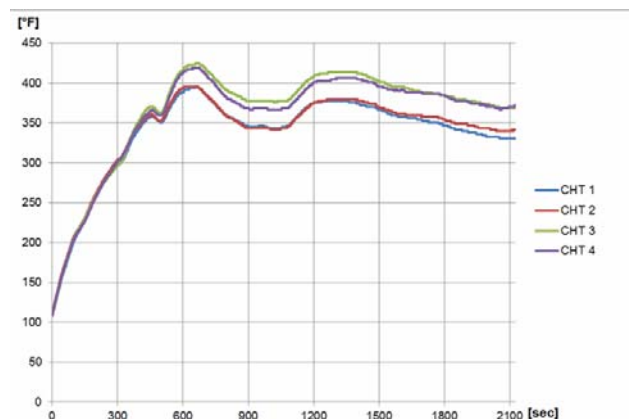


Figure 2. CHT at 70 [kts]

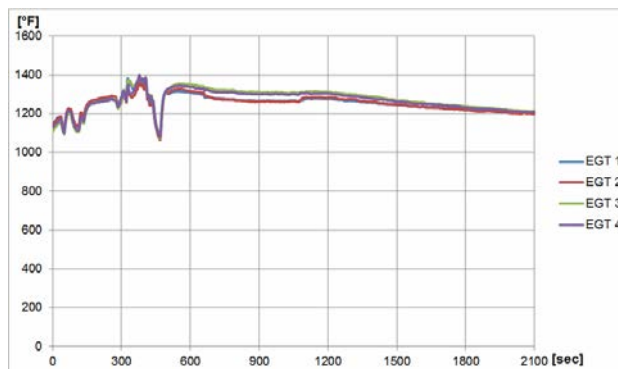


Figure 3. EGT at 70 [kts]

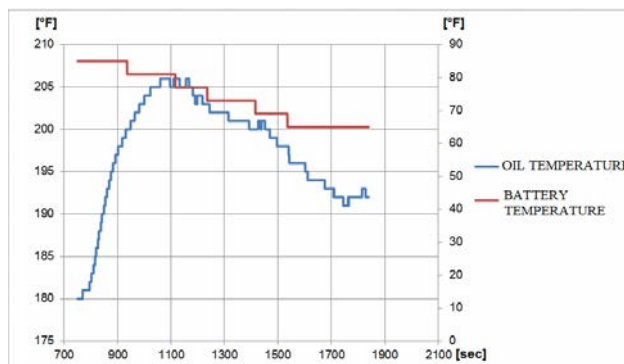


Figure 4. Oil and battery temperature at 70 [kts]

Figures 1-4 show that during the flight No. 62 at 70 kts, all requested parameters were within the limitations.

Considering that during the cooling test of the power unit, the maximum permissible temperature values were not reached at a speed of 70 kts on the path, the test was performed at a speed of 65 kts on the path in flight No. 205.

Flight 205 was performed on August 23, 2021 in weather conditions where the ambient temperature at sea level was 38°C, so there was no need to make a temperature correction. There was no presence of moisture during the flight.

The flight took place in the Pančevo airport area, under the ambient conditions given in the Table 4.

Table 4. Ambient conditions during flight No. 205

Time	Wind speed (kts)	Wind direction	Temperature (°C)	Pressure (mbar)
14:50	4.0	110	39.0	1001.2
14:57 Take off	2.2	120	38.4	
15:00	3.1	120	38.1	
15:05	3.9	100	38.8	
15:10	4.1	110	39.0	
15:15	4.0	120	39.1	
15:20	3.7	140	39.5	
15:25	5.1	130	39.9	
15:30	3.8	120	40.8	
15:35	4.6	130	41.0	
15:39 Landing	5.2	140	41.4	1001.1

After the engine was started and warmed up to operating temperatures, takeoff and climb were conducted at maximum engine power and speed on the path of 65 and 60 kts. The climb was made at least 6 minutes after fluid and component temperature peaks were obtained or up to a maximum altitude of 10.500 ft.

Table 5. Cooling results with 65 [kts] on path

	MVP t. [°F]	Max allowed t. [°F]
Oil temperature [°F] 3900 ft Hp / 74°F OAT	230	235
CHT [°F] 3000 ft Hp / 68°F OAT	435	475
EGT [°F] 637 ft Hp / 94°F OAT	1341	1700
Battery temperature [°F] 3300 ft Hp / 81°F OAT	99	110

Since the air temperature on the day of the test was 38°C at sea level, then the Eq. (1) was not used.

The flight parameters during this flight are given in diagrams on the Figure 5.

The diagrams on Figures 6 to 8 show the graphical values of temperatures of fluids and components at a speed of 65 kts on the path for which the temperature limits are given in Table 5.

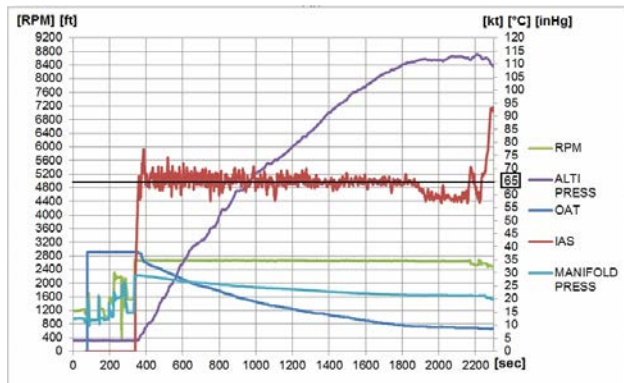


Figure 5. Flight parameters at 65 [kts]

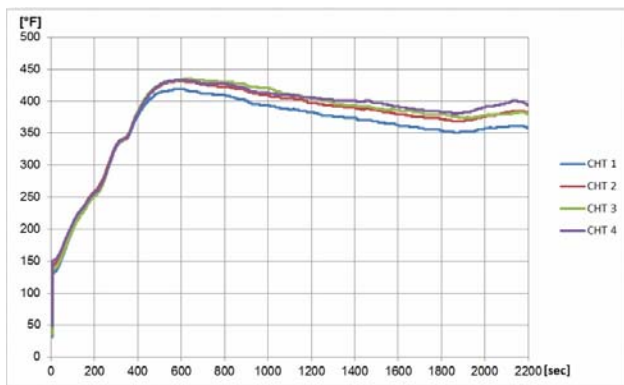


Figure 6. CHT at 65 [kts]

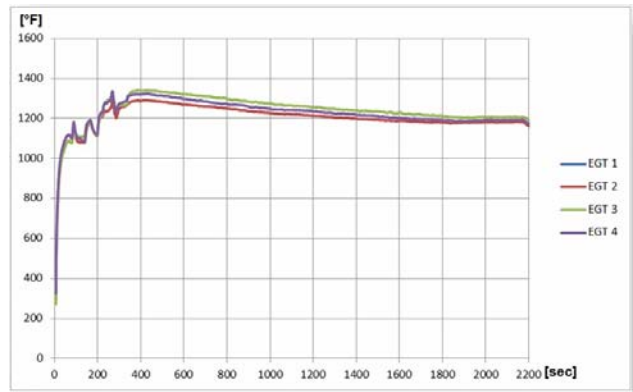


Figure 7. EGT at 65 [kts]

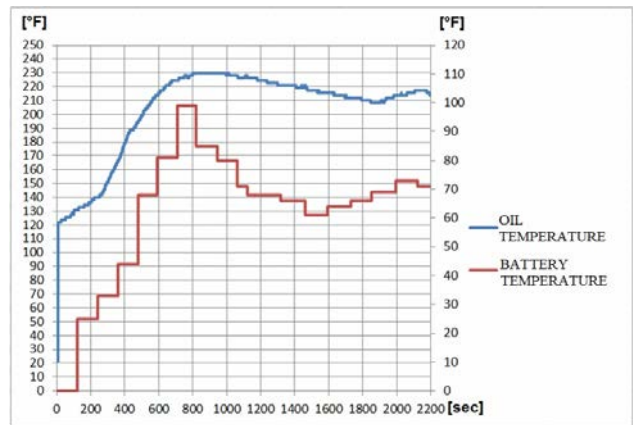


Figure 8. Oil and battery temperature at 65 [kts]

Figures 5-8 show that during the flight No. 205 at 65 kts, all requested parameters were within the limitations.

Considering that during the cooling test of the power unit, the maximum permissible temperature values were not reached at a speed of 65 kts on the path, the test was started at a speed of 60 kts on the path in the same flight.

Table 6. Cooling results with 60 [kts] on path

	MVP t. [°F]	Max allowed t. [°F]
Oil temperature [°F] 3600 ft Hp / 75°F OAT	230	235
CHT [°F] 3250 ft Hp / 78°F OAT	445	475
EGT [°F] 3450 ft Hp / 79°F OAT	1364	1700
Battery temperature [°F] 3528 ft Hp / 79°F OAT	105	110

Since the air temperature on the day of the test was 38°C at sea level, then the Eq. (1) was not used.

The flight parameters during this flight are given in diagrams on the Figure 9.

The diagrams on Figures 10 to 12 show graphical values of temperatures of fluids and components at a speed of 60 kts on a path for which temperature limits are given in Table 6.

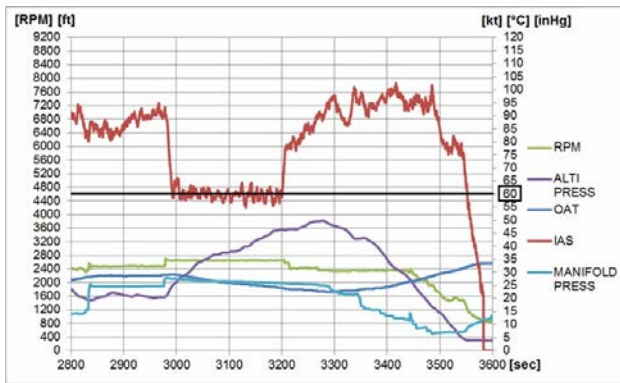


Figure 9. Flight parameters result at 60 [kts]

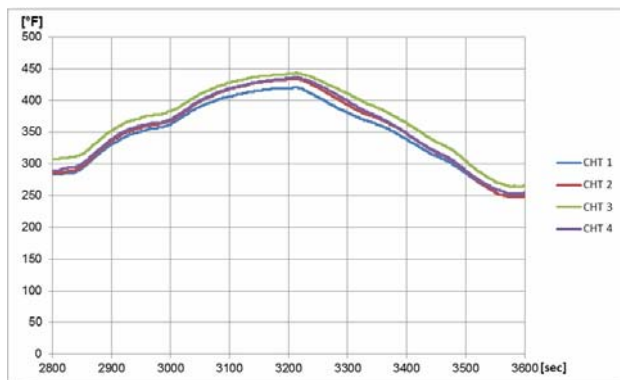


Figure 10. CHT at 60 [kts]

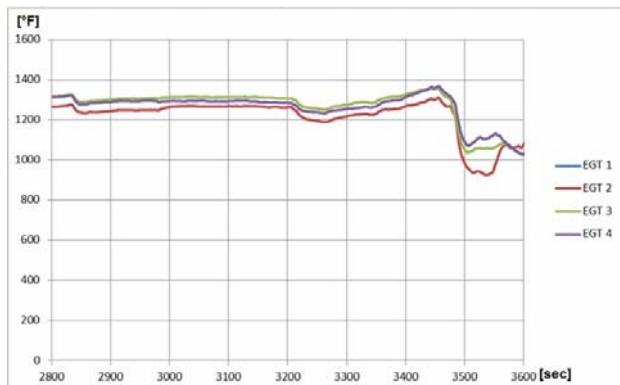


Figure 11. CHT at 60 [kts]

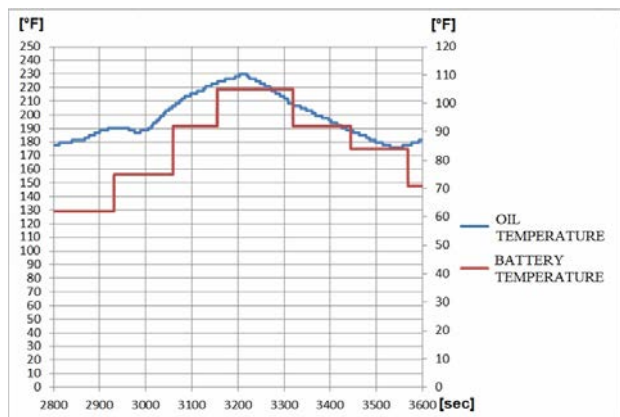


Figure 12. Oil and battery temperature at 60 [kts]

Figures 9-12 show that during the flight No. 205 at 60 kts, all requested parameters were within the limitations.

The “Lycoming Operational & Installation Manual” states that during takeoff, climb and maximum cruise speed the mixture control should be "RICH", so we did not "lean" the mixture as required in AMC 23.1047 (a)(8) (iii).

Since the engine manufacturer stated that the maximum power is the same as the maximum continuous power, then the climb was made at maximum power continuously for more than 6 minutes, not as specified in AMC 23.1047 (a)(8)(ii) & (iii).

The power unit cooling test was performed with a critical amount of oil of 4 Qts, at maximum power and with a speed on the path of 70, 65 and 60 kts.

Testing of power unit cooling with a speed of 70 and 65 kts on path met the certification requirements because the maximum values of the component and fluid temperatures were not exceeded.

Power unit cooling test at 60 kts on path was aborted at 3250 ft because No. 3 cylinder head temperature reached the maximum recommended temperature of 435°F prescribed by Lycoming for extended engine life and tended to further growth.

The recommended minimum speed on the path in the climbing phase with a minimum amount of oil in the engine and an ambient temperature of 38°C is 65 kts.

3. CONCLUSION

Utva Aviation Industry is approved by Civil Aviation Directorate as a Design and Production organization.

Designing, producing and testing the aircraft at one place made the certification process of Sova easier.

R&D team considered this certification process as a chance to prove that Serbian industry is still competing in civil aviation with the world-known companies.

During these flight tests, compliance with paragraphs CS 23.1041, CS 23.1043 and CS 23.1047 was shown. Speed of 65 kts was defined as recommended minimum climbing speed with specified CS 23 requirements.

References

- [1] Certification Specifications for Normal, Utility, Aerobatic and Commuter Category Aeroplanes CS 23, Amendment 3 Book 1
- [2] Certification Specifications for Normal, Utility, Aerobatic and Commuter Category Aeroplanes CS 23, Amendment 3 Book 2
- [3] RENDULIĆ, Z.: Mehanika leta
- [4] MILOŠEVIĆ, V.: Ispitivanje aviona u letu



TOTAL FATIGUE LIFE ESTIMATION OF AIRCRAFT STRUCTURAL COMPONENTS USING STRAIN ENERGY DENSITY METHOD

STEVAN MAKSIMOVIĆ

Military Technical Institute, Belgrade, s.maksimovic@mts.rs

KATARINA MAKSIMOVIĆ

City of Belgrade – City Government, Belgrade, kmaksimovic@mts.rs

IVANA VASOVIĆ MAKSIMOVIĆ

Lola Institute, Kneza Višeslava 70, Belgrade, ivanavvasovic@gmail.com

MIRJANA ĐURIĆ

Military Technical Institute, Belgrade, minadjuric12@gmail.com

MIRKO MAKSIMOVIĆ

Belgrade Waterworks and Sewerage, Kneza Miloša 27, Belgrade, maksimovic.mirko@gmail.com

Abstract: This paper is aimed at developing a suitable computation method for estimating the fatigue life of structural elements exposed to the load spectrum. The total fatigue life can be divided into two parts, until the appearance of the initial damage and the other part represents the remaining life, i.e. until the effective fracture. The conventional approach to estimating the total life requires that low-cycle fatigue characteristics of the material be used until the initial damage occurs, and dynamic characteristics of the material for the remaining life. In order to obtain a more efficient method, the Strain Energy Density (SED) method was used in this paper. The essence of this approach is to use the same low - cycle fatigue characteristics of the material to estimate the life expectancy and the remaining life. This work is focused to developing efficient computation method and software for total fatigue life of metal aircraft structural components. To obtain efficient computation method, here the same fatigue low cyclic material properties for crack initiation and crack growth are used together with finite element method (FEM) for stress analyzes. To validate quality computation methods and in-house software for fatigue life estimations computation results are compared with experiments. The results show that the predicted results agree well with the test data.

Key words: Aircraft structures, Fatigue, Crack initiation, Crack growth, Total fatigue life, FEM

1. INTRODUCTION

In the work related to fatigue behavior of real aircraft structural components under service loading, one of the fundamental issues is the evaluation and formulation of adequate relations which should describe fatigue life. Fatigue as a very complex process can be considered and analyzed as: 1) crack initiation phase and 2) crack propagation phase. In this paper we developed computational model for total fatigue life estimation of aircraft structural components.

Aircraft structural components and structural components of the other mechanical systems are components with geometrical discontinuities and the same are known as components with notches or notched structural components. As a rule, cracks appear at critical points which lie in the bases of notches. Because of that notches have important role in process of fatigue life investigation. Total fatigue life (TFL) of a particular aircraft structural component is sum of crack initiation and crack growth life (CIL and CGL), and mainly depends of number, form, size, position and arrangement

of its notches. CIL computation of aircraft structural components understands knowing: aircraft flight cycles, cyclic events in flight cycles, cyclic properties of material used or nominated for workmanship, stress-strain response at critical point or point of expected crack initiation and damages provoked by all cyclic events.

Stress-strain response at critical point (local stress-strain response) for all cyclic events and method of identification and counting of those events, have special importance. Local stress-strain response may be determined by strain gage measurement, by the finite element method (FEM) and by the methods that relate local stresses (σ_{loc}) and strains (ϵ_{loc}) to nominal values. Identification and counting of cyclic events in aircraft flight cycles may be carried out using rain flow counting method, range pair method [1] and alike good method of reservoir [2]. Method of exact damages and CIL computation has not been developed so far. All known is based on numerous hypotheses (rules). Because of simplicity, Palmgreen-Miner's rule of linear damage accumulation is mostly in use [1-5]. For TFL computation, several investigators [6,7] have combined the two approaches by combining the computed results

for crack initiation and crack growth. The aim of this paper is to compute (to predict) TFL (TFL = CIL + CGL) of notched structural components using the same input parameters (cyclic properties) for CIL and CGL computation.

Methodologies of CIL and CGL computation of notched structural components based on criterions of low cycle fatigue (LCF) [1,8] and strain energy density (SED) [9] are described in this paper. The results obtained by computation and experimentally obtained results are compared.

2. CRACK INITIATION LIFE OF STRUCTURAL ELEMENTS

To estimate the age until the appearance of initial damage of structural elements subjected to cyclic loads and where material plasticization occurs in critical zones, it is necessary to use the material's cyclic behavior curves. For this purpose, the SWT relation was used. The Smith-Watson-Topper (SWT) relation for describing the low-cycle fatigue curve has the form:

$$P_{SWT} = \sqrt{\sigma_{\max} \frac{\Delta \varepsilon}{2} E} = \sqrt{(\sigma'_f)^2 (N_f)^{2b} + E \sigma'_f \varepsilon'_f (N_f)^{b+c}} \quad (2)$$

where the influence of mean stresses is included via the dependence

$$\sigma_{\max} = \sigma_m + \frac{\Delta \sigma}{2} \quad (2.2)$$

The notation P_{SWT} in (2.1) refers to the Smith-Watson-Topper parameter. The relation SWT (2.1) defines that there is no fatigue damage in situations where the value of the maximum stress, σ_{\max} , is zero or has a negative value, which is not entirely true.

3. CRACK GROWTH MODEL BASED ON STRAIN ENERGY DENSITY METHOD

In this work fatigue crack growth method based on energy concept is considered and then it is necessary to determine the energy absorbed till failure. This energy can be calculated by using cyclic stress-strain curve. Function between stress and strain, as recommended by Ramberg-Osgood provides good description of elastic-plastic behavior of material, and may be expressed as:

$$\Delta \varepsilon = \frac{\Delta \sigma}{E} + 2 \left(\frac{\Delta \sigma}{2k'} \right)^{\frac{1}{n'}} \quad (3.1)$$

where E is the modulus of elasticity, $\Delta \varepsilon/2$ is strain amplitude and $\Delta \sigma/2$ is stress amplitude. Equation (3.1) enables the calculation of the stress-strain distribution by knowing low cyclic fatigue properties. As a result the energy absorbed till failure become [8,9]:

$$W_c = \frac{4}{1+n'} \sigma'_f \varepsilon'_f \quad (3.2)$$

where σ'_f is cyclic yield strength and ε'_f - fatigue ductility coefficient. Given the fact that strain energy density method is considered, the energy absorbed till failure must be determined after the energy concept is based on the following fact: The energy absorbed per unit growth of crack is equal to the plastic energy dissipated within the process zone per cycle. This energy concept is expressed by:

$$W_c \delta a = \omega_p, \quad (3.3)$$

where W_c is energy absorbed till failure, ω_p - the plastic energy and a - the crack length. In equation (3.3) it is necessary just to determine the plastic energy dissipated in the process zone ω_p . By integration of equation for the cyclic plastic strain energy density in the units of Joule per cycle per unit volume [8,9] from zero to the length of the process zone ahead of crack tip d^* it is possible to determine the plastic energy dissipated in the process zone ω_p . After integration relation of the plastic energy dissipated in the process zone becomes:

$$\omega_p = \left(\frac{1-n'}{1+n'} \right) \frac{\Delta K_I^2 \psi}{E I_{n'}} \quad (3.4)$$

where ΔK_I is the range of stress intensity factor, ψ - constant depending on the strain hardening exponent n' , $I_{n'}$ - the non-dimensional parameter depending on n' . Fatigue crack growth rate can be obtained by substituting Eq. (3.2) and Eq. (3.4) in Eq. (3.3):

$$\frac{da}{dN} = \frac{(1-n')\psi}{4E I_{n'} \sigma'_f \varepsilon'_f} (\Delta K_I - \Delta K_{th})^2, \quad (3.5)$$

where ΔK_{th} is the range of threshold stress intensity factor and is function of stress ratio i.e.

$$\Delta K_{th} = \Delta K_{th0}(1-R)^\gamma, \quad (3.6)$$

ΔK_{th0} is the range of threshold stress intensity factor for the stress ratio $R = 0$ and γ is coefficient (usually, $\gamma = 0.71$). Finally number of cycles till failure can be determined by integration of relation for fatigue crack growth rate:

$$N = B \int_{a_0}^{a_c} \frac{da}{(\Delta K_I - \Delta K_{th})^2}, \quad B = \frac{4E I_{n'} \sigma'_f \varepsilon'_f}{(1-n')\psi} \quad (3.7)$$

and

$$\Delta K_I = Y S \sqrt{\pi a}, \quad (3.8)$$

Equation (3.7) enables us to determine crack growth life of different structural components. Very important fact is that equation (3.7) is easy for application since low cyclic

material properties (n' , σ'_f , ε_f) available in literature are used as parameters. The only important point is stress intensity factor which, depending on the geometry complexity and the type of loading, could be determined by using analytical and/or numerical approaches.

From fatigue crack growth relations (3.5) and (3.6) it can be seen that they require only mechanical and low-cyclic fatigue properties E , σ'_f , ε_f and n' , which presents great advantage by application of this method.

4. NUMERICAL VALIDATION

The validity of the considered computation total fatigue life estimation method can only be assessed through a comparison with experimental data which is the focus of this section. In addition, stress intensity factors were obtained by using analytical and numerical approaches. In the case where numerical simulation was used for stress intensity factor for crack growth life estimation the evaluated polynomial expressions were used for corrective function which include geometry of structural element.

4.1. Structural analysis of aircraft wing-fuselage joint

Computation estimates of the total life were made here, which include calculations until the appearance of initial damage, as well as an estimate of the residual life after the appearance of the initial crack, i.e. during the crack propagation. For this purpose, a part of the wing structure at the wing/fuselage junction was considered. In order to verify the computation procedure for the estimation of the life, representative parts of the wing were made in the form of "complex" test specimen, which represent a real part of the structure of the wing of the aircraft. Computation estimates of life, as well as tests, were performed with the same ("real") load spectrum. In the following discussions, only the essential part of the

research results will be presented, both in the domain of computation estimates and the results of fatigue tests. Fig. 1 shows part of aircraft wing-fuselage joint.



Figure 1. Part of aircraft wing-fuselage joint

The analysis of the stress state was performed using FEM [10]. For this purpose, due to the systematicity of the research, a linear analysis of FEM as well as an elastic-plastic analysis of FEM were applied. Elastic-plastic analysis was performed using FEM for the cyclic characteristics of the behavior of duraluminium, Table 2

Figure 2 shows the load spectrum of part of the wing-fuselage connection (one block corresponds to 50 hours of aircraft flight). Table 1 shows the load spectrum as well as the corresponding stresses for each load level in the spectrum. To determine the stress state for certain load levels, the elastic-plastic analysis of FEM was used. The material of the wing joint, that is, the part of the wing that is the subject of analysis, is made of duraluminium alloy 2024-T351, whose cyclic behavior curve of the material is shown in Table 2.

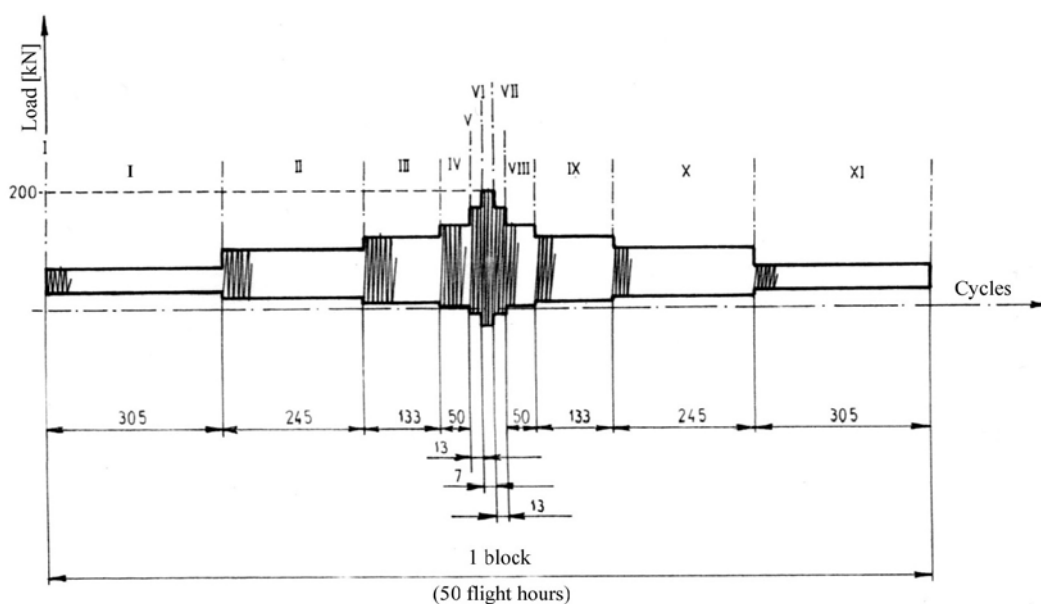


Figure 2. Load spectrum in the wing-fuselage connection (per one screw in the wing-fuselage connection)

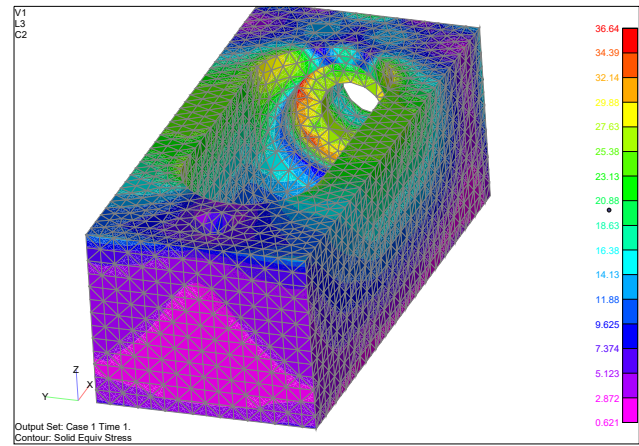
Table 1. Load spectrum and corresponding stresses in the critical position in the wing/fuselage connection section

Load level	n_i	F_{\min} [kN]	F_{\max} [kN]	σ_{\min} [MPa]	σ_{\max} [MPa]
I	305	13.3	33.3	58.8	147.2
II	245	9.30	46.6	41.0	205.5
III	133	6.0	60.0	28.0	279.8
IV	50	3.0	73.3	13.3	313.8
V	13	-4.6	86.6	20.3	336.5
VI	7	-14.0	100.0	61.9	366.4
VII	13	-4.6	86.6	20.3	336.5
VIII	50	3.0	73.3	13.3	313.8
IX	133	6.0	60.0	28.0	279.8
X	245	9.3	46.6	41.0	205.5
XI	305	13.3	33.3	58.8	147.2

Figure 3 shows the finite element model of the wing part at the point of connection of the wing to the fuselage of the aircraft. When it comes to structural elements with complex geometric shapes and loads, it is necessary to first determine the potentially critical zone in which the occurrence of damage under the effect of cyclic loads is first expected. For this purpose, the finite element method (FEM) was used in this case. When it comes to estimating the age until the appearance of initial damage, a precise calculation of stress states is required, especially in the critical zone of the structure. Two methods can be used to determine the elastic-plastic stress state: a) Using the linear analysis of FEM, cyclic material behavior curves and Neuber curves whose intersection determines the elastic-plastic stress state; b) Using elastic-plastic FEM analysis for all load levels within the spectrum, Fig. 3. The elastic-plastic analysis of the FEM was used for the computation assessment of the life until the appearance of initial damage, and the computation results are given in table 1. Neuber's approach based on the use of linear FEM analysis is used here only as a control computation.

Table 2. Low-Cyclic material properties of duraluminium 2024 T351

Property	Value
Modulus of elasticity, E [MPa]	70430.0
Cyclic strength coefficient, K' [MPa]	794
Cyclic strain hardening exponent, n'	0.0919
Fatigue strength coefficient, σ'_f [MPa]	740.0
Fatigue strength exponent, b	-0.0701
Fatigue ductility coefficient, ϵ'_f	0.334
Fatigue ductility exponent, c	-1.2

**Figure 3.** Elastic-plastic FEM analysis in the part of the wing structure for the maximum load in the spectrum (Level VI in the spectrum)

Initial fatigue life estimation

For a given load block, Fig. 2, as well as the stress states determined for each load level, the number of blocks until the appearance of initial damage can be determined. SWT (Swish-Watson-Topper) relation, given by equation (2.1), was used to estimate the fatigue life until the appearance of initial damage, expressed through the number of blocks N_{bl} . The last relation takes into account the effects of medium stresses on the estimate of remaining life, and experience has shown that it is the most accurate for life estimates with the influence of medium stresses. Finally, to estimate the lifetime until the appearance of initial damage, the elastic-plastic analysis of FEM was used to determine the stress states in conjunction with the SWT (Swish-Watson-Topper) relation. Using this approach, the number of blocks until the appearance of initial damage, $N_{bl,i}$, was determined. The computation initial fatigue life until the appearance of initial damage, expressed through the number of blocks, using previous relations, is given in Table 3.

Table 3. Estimated initial fatigue life to failure of the wing-fuselage connection according to (SWT) and Morrow

Podaci o opterećenju				Podaci o materijalu				Broj blokova SWT	
2024 T351 Naziv: 2024 T351				Naziv Materijala: 2024 T351				480.1830472088	
Smin1	58.800	Smax1	147.200	n1	305	Kprim:	794	Broj blokova Morrow	505.5855210519
Smin2	41.000	Smax2	205.500	n2	245	E:	70430	n prim:	0.0919
Smin3	28.000	Smax3	279.800	n3	133	Epsilonf:	0.334	b:	-0.0701
Smin4	13.300	Smax4	313.800	n4	50	Sigmaf:	740	c:	-1.2
Smin5	20.300	Smax5	336.500	n5	13	Kt:	1.49	Broj nivoa	11
Smin6	61.900	Smax6	366.400	n6	7				
Smin7	20.300	Smax7	336.500	n7	13				
Smin8	13.300	Smax8	313.800	n8	50				
Smin9	28.000	Smax9	279.800	n9	133				
Smin10	41.000	Smax10	205.500	n10	245				
Smin11	58.800	Smax11	147.200	n11	305				
Smin12	0.000	Smax12	0.000	n12	0				
Smin13	0.000	Smax13	0.000	n13	0				
Smin14	0.000	Smax14	0.000	n14	0				
Smin15	0.000	Smax15	0.000	n15	0				
Smin16	0.000	Smax16	0.000	n16	0				
Smin17	0.000	Smax17	0.000	n17	0				
Smin18	0.000	Smax18	0.000	n18	0				
Smin19	0.000	Smax19	0.000	n19	0				
Smin20	0.000	Smax20	0.000	n20	0				
Smin21	0.000	Smax21	0.000	n21	0				

	Maksim	Minima	sig1	sig2	eps1	eps2	E1	BrojCiklusa	DeltaN/Nf	Izabrani test
	147.2	58.8	219.2995	87.582719	0.0031145	0.00124	0.00209	5522804.3	18107.555	Morrow
	205.5	41	305.1526	60.047720	0.0043629	0.00088	0.00291	3501810.8	14293.105	Morrow
	279.8	28	398.5146	23.342555	0.0062108	0.00088	0.00398	971327.44	7303.2139	Morrow
	313.8	13.3	428.6573	-19.01452	0.0073078	0.00094	0.00449	125191.51	2503.8303	Morrow
	336.5	20.3	445.1848	-25.82688	0.0081647	0.00147	0.00486	53123.145	4086.3957	Morrow
	366.4	61.9	464.2674	10.641242	0.0095030	0.00306	0.00542	42304.004	6043.4292	Morrow
	336.5	20.3	445.1848	-25.82688	0.0081647	0.00147	0.00486	53123.145	4086.3957	Morrow
	313.8	13.3	428.6573	-19.01452	0.0073078	0.00094	0.00449	125191.51	2503.8303	Morrow
	279.8	28	398.5146	23.342555	0.0062108	0.00088	0.00398	971327.44	7303.2139	Morrow
	205.5	41	305.1526	60.047720	0.0043629	0.00088	0.00291	3501810.8	14293.105	Morrow
	147.2	58.8	219.2995	87.582719	0.0031145	0.00124	0.00209	5522804.3	18107.555	Morrow
	147.2	58.8	219.2995	87.582719	0.0031145	0.00124	0.00209	3413680.8	11192.396	SWT
	205.5	41	305.1526	60.047720	0.0043629	0.00088	0.00291	2376607.9	9700.4406	SWT
	279.8	28	398.5146	23.342555	0.0062108	0.00088	0.00398	688602.92	5177.4655	SWT
	313.8	13.3	428.6573	-19.01452	0.0073078	0.00094	0.00449	123980.54	2479.6108	SWT
	336.5	20.3	445.1848	-25.82688	0.0081647	0.00147	0.00486	65790.842	5060.8340	SWT
	366.4	61.9	464.2674	10.641242	0.0095030	0.00306	0.00542	63862.278	9123.1825	SWT
	336.5	20.3	445.1848	-25.82688	0.0081647	0.00147	0.00486	65790.842	5060.8340	SWT
	313.8	13.3	428.6573	-19.01452	0.0073078	0.00094	0.00449	123980.54	2479.6108	SWT
	279.8	28	398.5146	23.342555	0.0062108	0.00088	0.00398	688602.92	5177.4655	SWT
	205.5	41	305.1526	60.047720	0.0043629	0.00088	0.00291	2376607.9	9700.4406	SWT
	147.2	58.8	219.2995	87.582719	0.0031145	0.00124	0.00209	3413680.8	11192.396	SWT

$N_{bl, i=480}$ (SWT) (Computation estimate of the life until the appearance of the initial damage)

$N_{bl, i=505}$ (Morrow) (Computation estimate of the life until the appearance of the initial damage)

4.3 Residual fatigue life estimation

In addition to the estimation of the age until the appearance of the initial damage, the results of which are for the part of the wing, loaded with the load spectrum Fig. 2, determined in the previous point and shown in Table 1, it is necessary to make a computation estimate of the residual fatigue life, that is, during the crack growth. To estimate the residual life, it is necessary to assume initial damage in the form of surface cracking. Based on the maximum stress value, determined by elastic-plastic analysis of FEM, the critical position is defined, Fig. 3. This is where the initial damage is defined in the form of an initial surface crack. The calculation estimate of the remaining life is based on the knowledge of the stress intensity factor in an analytical form. Since it is a complex construction, there are no known analytical expressions for SIF. For this purpose, the finite element method was used to determine the analytical expression for SIF. 3-D singular finite elements around the assumed surface crack line were used to determine the SIF. The complete procedure for defining analytical expressions for SIF was performed using FEM.

As mentioned before, in order to establish an analytical expression for SIF, FEM was again used, assuming several depths of surface cracks. For this purpose, singular finite elements around the tip of the crack were

used. Figure 4 shows the stress state for one "depth" of crack.

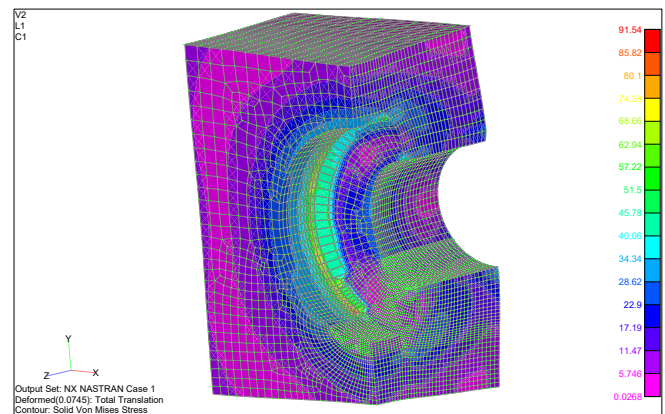


Figure 4. Distribution of the stress state for a crack depth of 3.5 mm

For the analysis of crack propagation, i.e. for the estimation of the residual fatigue life, the strain energy density (SED) method was used, using the relation (3.5). The estimate of the remaining life, during the crack propagation, expressed through the number of blocks is: $N_{bl,p}=52$ (Computation estimate of the residual, i.e. during the crack propagation). So, the SED method was used to estimate the residual life, described in detail in section 3 of this paper, on the one hand, while establishing analytical expressions for SIF using FEM, on the other hand.

5. CONCLUSION

This paper deals with research in the domain of estimating the total fatigue life of aircraft structures under the effect of cyclic loads. The goal is certainly to provide an efficient calculation method. For this purpose, the strain energy density method (SED) was developed for crack propagation analysis. Unlike the conventional method, which uses the dynamic characteristics of the material for calculation, this method uses the low-cycle fatigue characteristics of the material, which are also used in the estimation of the life until the appearance of initial damage. This, in turn, reduces the additional experimental tests required for the experimental determination of the dynamic characteristics of the material. Since the finite element method (FEM) is used in the work for the analysis of the stress state, it enables complex structures such as aircraft structures, which makes this approach not only efficient but also general. In order to differ from the conventional approach where low-cycle material properties are used to estimate the fatigue life until the occurrence of initial damage and dynamic properties to estimate the residual life, here low-cycle fatigue properties of the material are used in both cases. The total fatigue life of the part of the wing-fuselage connection of the aircraft (shown in Fig. 1) until the effective failure of 807 load blocks was experimentally determined. The computation estimate determined the total fatigue life to effective failure of 557 blocks. The obtained difference between computation results and experiment is 18.6%.

ACKNOWLEDGEMENT

This research has been supported by the research grants No. 451-03-68/2022-14/200066, of the Serbian Ministry of Education, Science and Technological Development.

References

- [1] BANNANTINE, J.A., COMER, J., HANDROCK, J.: *Fundamentals of Material Fatigue Analysis*, Prentice-Hall, Englewood Cliffs, New Jersey, 1990.
- [2] KOSTAES, D.: *Fatigue Behaviour and Analysis*, Talat Lecture 2401, Technische Universität München, EAA – European Aluminium Association, 1994.
- [3] PALMGREN, A.: *Die Lebensdauer von Kugellagern*, Verfahrenstechnik, Berlin, 68 (1924) 339-341.
- [4] MINER, M.A.: *Cumulative Damage in Fatigue*, Journal of Applied Mechanics, 67 (1945) A159-A164.
- [5] FATEMI, A., L. YANG, L.: *Cumulative Fatigue Damage and Life Prediction Theories: A Survey of the State of the Art for Homogeneous Materials*, International Journal of Fatigue, 20 (1) (1998) 9-34.
- [6] MAKSIMOVIĆ, S.: *Fatigue Life Analysis of Aircraft Structural Components*, Scientific Technical Review, Vol. LV, No.1, 2005.
- [7] BOLJANOVIĆ, S., MAKSIMOVIĆ, S.: *Fatigue crack growth modeling of attachment lugs*, International Journal of Fatigue, 58(1) (2014) 66-74.
- [8] MAKSIMOVIĆ, K., POSAVLJAK, S., MAKSIMOVIĆ, M., VASOVIĆ MAKSIMOVIĆ, I., and BALAC, M.: *Total Fatigue Life Estimation of Aircraft Structural Components Under General Load Spectra*; The Editor(s) (if applicable) and The Author(s), under exclusive license to Springer Nature Switzerland AG 2021. N. Mitrovic et al. (Eds.): CNNTech 2020, LNNS 153, pp. 394–412, 2021. Print ISBN 978-3-030-58361-3; Online ISBN 978-3-030-58362-0; https://doi.org/10.1007/978-3-030-58362-0_23
- [9] MAKSIMOVIĆ M., VASOVIĆ MAKSIMOVIĆ, I., MAKSIMOVIĆ, K., TRIŠOVIĆ, N., MAKSIMOVIĆ, S.: *Residual Life Estimation of Cracked Aircraft Structural Components*; FME Transactions; 46 (1) (2018) 124-128; doi:10.5937/fmet1801124M; Faculty of Mechanical Engineering, Belgrade
- [10] MSC/NASTRAN finite element software code: *Theoretical Manuals*.



TESTING OF AAD FOR RESERVE PARACHUTE CANOPIES

STEVAN JOVIČIĆ

Technical Test Center, Belgrade, stevanjovicic@gmail.com

JELENA ŠOBOT

Technical Test Center, Belgrade, jsobot@outlook.com

LJUBIŠA TOMIĆ

Technical Test Center, Belgrade, ljubisa.tomic@gmail.com

IVO OBRADOVIĆ

Technical Test Center, Belgrade, boki.deki@mts.rs

Abstract: The purpose of the AAD (Automatic Activation Device) is to initiate the opening of the reserve container to save the skydiver. The AAD functions by severing the reserve container closing-loop thereby releasing the flaps of the reserve container. Operating principle of AAD is an electronic automatic activation device, operating on the principle of pressure reading. The primary means for detecting the altitude and fall rate is a pressure sensor. The altitude is calculated based on the difference between two atmospheric pressures. The AAD is an electronic device and as such may not always work properly even when installed and used properly. Testing of these devices functionality and its manual quality was a mandatory task before such an important part of a parachute assembly become part of the equipment of the Serbian airborne forces.

Keywords: AAD, parachute, reserve, testing.

1. INTRODUCTION

Intention of an AAD producers is to provide users with maximum comfort and safety when using the automatic activation device. All efforts are directed to the cutter reliability when cutting the reserve parachute closing loop when its activation criteria are met. Although the device will work properly, it does not guarantee the functionality of the other parts of the parachute kit. The device itself does not exclude the possibility of severe injury or even death. The device is only one of the ways to increase the likelihood of resolving a critical situation the user may find himself in when skydiving.

The basis for safe jumps are quality training, appropriate health condition, mental abilities, quality equipment for performing jumps from authorized manufacturers and familiarization with the procedures of dealing with an emergency.

Only when these conditions are met, the automatic activation device may help to increase the likelihood of resolving an emergency, if such occurs. The AAD is an electronic device and as such may not always work properly even when installed and used properly.

Testing of these devices functionality and its manual quality was a mandatory task before such an important part of a parachute assembly become part of the equipment of the Serbian airborne forces.

2. OPERATING PRINCIPLE

The AAD is an electronic automatic activation device, operating on the principle of pressure reading. The primary means for detecting the altitude and fall rate is a pressure sensor. The altitude is calculated based on the difference between two atmospheric pressures. The pressure at current altitude and pressure on landing location "GROUND ZERO". The pressure on the landing location is measured and set after switching on the device during calibration.

This pressure is automatically adjusted by a change in barometric pressure during the day without the need for user intervention. The information collected is evaluated by means of a microprocessor and ingenious software and it is converted to real fall rate and altitude. The device is activated only in the case the preset criteria are met; the criteria differ depending on the set profiles.

The AAD device is capable of meeting the preset criteria of fall rate in combination with altitude above the landing location, cut the reserve parachute closing loop by means of the cutter and thus initiate the deployment sequence.

3. CONSTRUCTION

The AAD is designed to best meet the requirements for durability and correct operation in all situations. It works with minimum power consumption, which allows it to maintain sufficient capacity of the energy source for its

entire service life without having to replace the battery. It is built inside a minimum-size cover and thus gives the skydiver the possibility to open the reserve parachute without using the manual handle.

The consists of a processing unit with the battery, processor, electronic circuits and a pressure sensor, figure 1. The processing unit is connected to the control unit by means of a cable; the control unit contains a multifunction display and control button, Figure 2. The cutter connected in the processing unit body via a connector as a removable part of the device, Figure 3. The cutter is made of stainless steel and cuts the reserve parachute closing loop, if necessary, the principle of work is given on the Figure4. Before a complete installation, user must read the Manual provided by the container manufacturer carefully, Figure 5.



Figure 1. Processing unit with battery



Figure 2. Control unit with display



Figure 3. Cutter

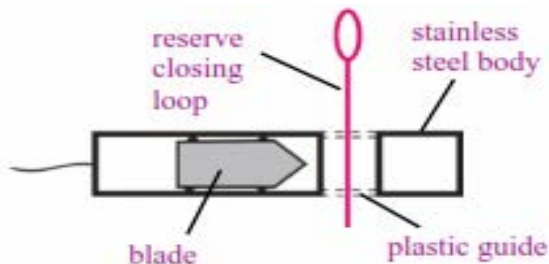


Figure 4. Cutter, principle of work



Figure 5. AAD on position in a container

Technical data of the AAD:

- Length, width, height of the processing unit (85 x 43 x 32 mm)
- Length, width, height of the control unit (65 x 18 x 6.5 mm)
- Length, diameter of the release unit (43 x 8.0 mm)
- Cable length of the control unit (1200 mm)
- Cable length of the release unit (500 mm)
- Volume (150 cm³)
- Weight (210 grams)
- Storing temperature (+ 71° to - 50° centigrade)
- Storing pressure 200 to 1075 hPa
- Working temperature (+ 63° to - 32° centigrade)
- Maximum allowable humidity up to 99,9 % rel. humidity
- Waterproof up to 15 minutes down to a depth of 15 feet (up to 24 hours down to a depth of 5 feet)
- Altitude adjustment range according 200 to 1075 hPa
- Operating range above sea level - 1600 feet to + 65500 feet
- Functioning period 14 hours
- Power supply lifetime warranty
- Maintenance 4 and 8 years from date of manufacture
- Total lifetime 12.5 years from date of manufacture

3. FLYING MODE

The AAD may be switched on in several modes. The mode is selected when the device is switched on and remains active until it is switched off again - the selection is not permanent.

The various modes are used to distinguish the type of jump and they determine the device behavior. First, basic mode is used most often - when the skydiver performs the jump at an airport (dropzone) and the aircraft take-off point and the landing location are thus the same - they are at the same elevation.

Second mode must be always used when the take-off and landing locations are at different elevations. This type of mode allows user to enter the elevation difference between the aircraft take-off point and the landing location during the switch on sequence.

If the device is switched on in first or basic mode, the current profile is shown on the display. If the device is switched on in the second or offset mode, the display shows “offset”, the first letter of the profile, the entered elevation difference between the aircraft take-off point and the landing location, and the units icon [1].

When the button is depressed, the full description of the current profile is displayed.

List of modes:

- First or basic mode is used when the skydiver takes-off and lands at the same place, Figure6.

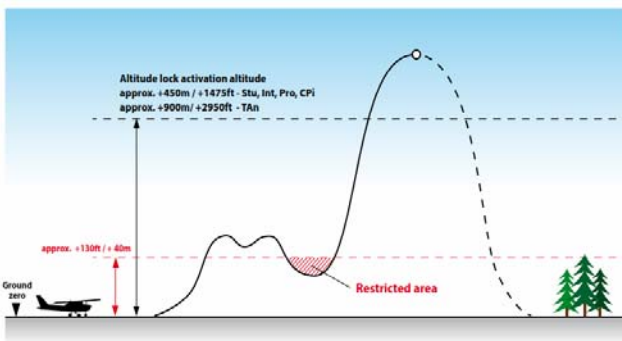


Figure 6. First or basic mode. Flight profile

- Second or offset mode

It is designed for situations when the landing location is higher (elevation) than the elevation at which the device was switched on, Figure7.

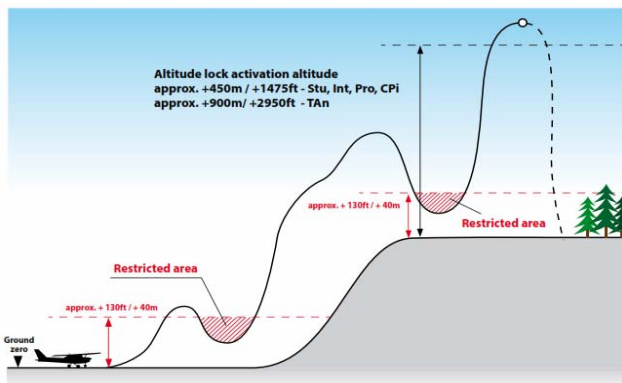


Figure 7. Second or offset mode. Flight profile

- Third mode is designed for situations when the landing location is lower (elevation) than the elevation at which the device was switched on, Figure8.

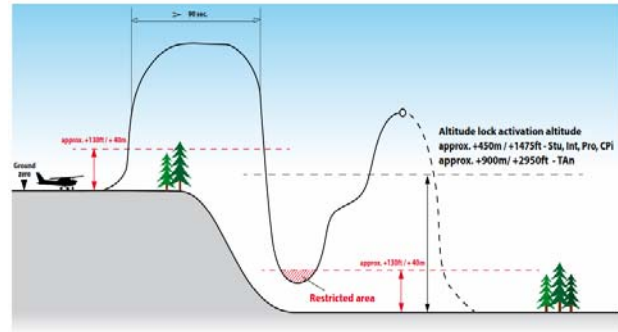


Figure 8. Third mode, Flight profile

- Interesting and important thing is that the AAD requires the plane to immediately climb above Ground Zero for a correct detection of start-up and remain above this altitude until the skydivers jump off. In the next phase of the flight it is necessary to exceed the Altitude lock according to the preset device profile (approx. 450 m / 1 475 ft - approx. 900 m / 2 950 ft - TAn) to unlock the device. [2], [3], [4]

4. TESTING

According to the current regulations in Serbian army the verification test was carried out with the aim of:

- To evaluate:
 - Functionality of the device in laboratory conditions, considering the purpose,
 - modernity and perspective of applied technical and technological solutions
 - whether the product meets the manufacturer's declared characteristics,
 - ease of handling and maintenance.
- To give a conclusion on the usability of the product, considering its capabilities and declared characteristics by the manufacturer.

4.1. Laboratory testing

As a part of laboratory tests, the following was realized:

- Checking the correctness of work and
- Testing of functional characteristics.

According to the operating instructions, the control part of the device is correct if it successfully implements the self-checking. During the specified procedure, data on the control unit should be displayed the serial number and the date of production, the current atmospheric pressure value and the date of the following service inspection (depending on the operating mode). During this check, it is necessary that the cable with the cutter is also connected.

The testing of functional characteristics was performed in order to check the declared characteristics of the device in controlled conditions, through the simulation of the pressure change and its gradient in vacuum chamber. Tests were performed in vacuum chamber at VZ „Moma Stanojlović”, Figure10.

In the chosen operational mode, a declared feature is to activate cutter on specified height (457 m), when vertical speed exceed 35 m/s, and the height of the dropping was H=1740 m.

After analyzation of the obtained results, recorded with the camera to:

- The AAD did activate the cutter when vertical speed was $w = 40,7$ m/s, based on the activation signal, performed its function, and cut the steel wire which was set to the proper position, Figure9.

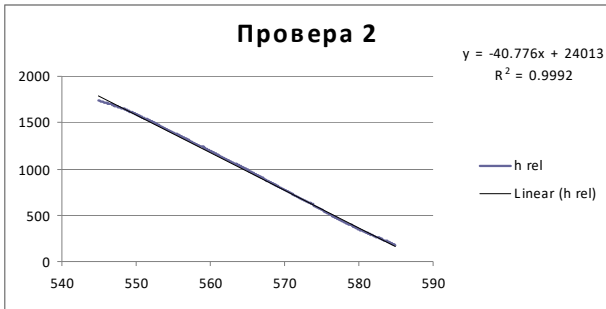


Figure 9. Flight profile of „free fall”



Figure 10. Vacuum chamber and activated cutter

4.2 Real condition testing

After testing the AAD in laboratory conditions, next step was a functional test of the complete parachute in real conditions, by dropping parachute dummies and realisation of parachute jumps done by experienced paratroopers.

According to the test plan and program, the functional correctness of the parachute was checked after exposure of complete parachute to extreme environmental temperature values (-40°C to +93.3°C) for 16 hours.

Functionality was confirmed in 6 drops of the parachute dummies at maximum declared load under the canopies of the main and reserve parachutes.

One of the points of testing the parachute was to check the functionality of the reserve parachute in case when parachute was activated by AAD.

Table 1. Test data for test kit number 1 and test kit number 2.

Test date	25.01.2022.	11.03.2022.
Parachute kit	1	2
Main parachute Type	10	20
Reserve parachute Type	11	22

Automatic activation device	111	222
Selected automate mode	1035	1035
Automate work area height	=(30-405) m	=(30-405) m
Automate work velocity	w>35 m/s	w>35 m/s
Declared „arming” height	765 m	765 m
Place of start position	a. Batajnica	a. Kovin
Elevation of start position	86 m	78 m
Temperature (°C)	-8 °C	-4 °C
Pressure (mbar)	1025 mbar	1022 mbar
Wind (m/s)	no wind	wind 4 m/s
Place of dropping	a. Kovin	a. Kovin
Aircraft	Mi-17	Mi-17
Max.height in flight	870 m (QFE)	900 m (QFE)
Height of dropping	600 m (QFE)	600 m (QFE)
Free fall time	11,1 s	11,4 s

On that occasion it was noticed that there is a software problem which one was not observed during the laboratory functionality check of the AAD device. As a result of the existence of problems in the software, an additional dropping of the parachute dummy was realized, Figure 11 and Figure 12. But result was the same, nothing was activated and the dummies were fall all the way to the ground. Measuring equipment were totally destroyed, Figure13.



Figure 11. First fail dropp with dummy

The test was terminated, the manufacturer was informed about noticed problem, which turned out to be caused by a software flaw in the definition of the flight profile in a chosen operational mod of AAD.



Figure 12. Second fail dropp with dummy

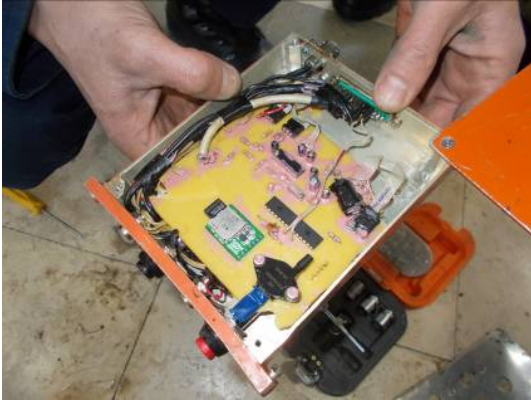


Figure 13. Destruction of measurement equipment

Since the AAD is a device whose functionality directly affects the saving of the user's life a software error is not acceptable. Due to the complexity of the software it is not possible to determine whether it is the only one established, so the AAD was rejected by the Serbian army.

A software error is very difficult to detect, especially with such devices like AAD, where an accidentally selected flight profile during deploying led to the deactivation of the device. In our case AAD based on the collected data, concluded that the jump was canceled and blocked the operation of cutter.

Very similar tests are carried out in other by numerous institutions dealing with quality assessment of technical products, like Vojenski tehnicki ustav s.p, odštepny zavod VTULaPVBO Praha, Czech republic or AirTEC GmbH Bad Vunenberg, Germany, the PIA AAD Design and testing report format when the manufacturer releases the following test report about his own product. According to test program the full examination volume includes tests according to the stated standards [5]:

- MIL-STD-810E Environmental Test Methods
- MIL-STD-45662A Calibration System Requirements
- RTCA/DO-160C Environmental Conditions and Test Procedures
- MIL-STD 331B Procedure C1 for Temp. and Humidity test

- RTCA/DO-178B Software considerations in Airborne Systems and Equipment Certifications
- MIL-STD-461D Requirements of the control of electromagnetic interference, emissions and susceptibility
- MIL-STD-331B Appendix F electrostatic discharge.

5. CONCLUSION

The AAD is an electronic automatic activation device, operating on the principle of pressure reading. All efforts are directed to the cutter reliability when cutting the reserve parachute closing loop when its activation criteria are met. Although the device will work properly, it does not guarantee the functionality of the other parts of the parachute kit.

Similar tests are carried out in other worldwide institutions dealing with quality assessment of technical products. What they have in common is the use of similar or even the same standards and the evaluation of the fulfillment of the requirements specified in those standards.

Submitting the results of internal tests or tests by third parties leads to a more reliable assessment of the quality of the technical products.

Serious manufacturers of technical products are thus encouraged to test their products in recognized institutions dealing with the quality assessment of technical products.

References

- [1] USER MANUAL m² multi AAD, Jevicko, Czech Republik, 2020.
- [2] *Cypres Test report TS120 cv3b*, March, 2004.
- [3] *www.militarycypres.cc Military CYPRES 2 Users guide* AirTec GmbH & KG Bad Vunnenberg, Germany, 2020.
- [4] *www.augustobartelle.com.*, Easing Minds, Saving Lives: Why we AAD
- [5] *www.sskinc.com*. Philosophy of reliability

OPTIMIZING THE CROSS-SECTION OF ELASTIC BEAM OF THE BEARINGLESS ROTOR OF AN ULTRALIGHT HELICOPTER

DALIBOR PETROVIĆ

University of Defence – Military Academy, Belgrade, daliborpetrovic140@gmail.com

IVAN MUDRI

Serbian Air Force, Belgrade, ivan.mudri2015@gmail.com

VLADIMIR STANKOVIĆ

Serbian Air Force, Kraljevo, vladastankovic1995@gmail.com

Abstract: The main element of bearingless rotor of a helicopter is elastic beam, which replaces all three hinges (flapping hinge, lead-lag hinge, and feathering hinge), and it has to be well designed in order to provide necessary movements of the rotor blade, without exceeding the permitted stresses in the material. The goal of this study is to find optimal size of cross-section of the head of the bearingless rotor of an unmanned helicopter in respect to feathering function. The study considers the influence of the size of the cross-section to feathering properties, by analyzing the results obtained by finite elements method. The optimal size of cross-section is found by approximating feathering function with corresponding polynomial with divided differences and using the least squared error and the mean squared error to find the size of cross-section that leads to minimal error. The optimal values for the cross-section obtained by using the the least squared error the mean squared error were compared and it was concluded that both approaches can be applied for optimizing the size of the cross-section.

Keywords: Bearingless rotor, Elastic beam, Finite element, Finite differences, Mean squared error

1. INTRODUCTION

Constant strive of helicopter manufacturers to simplify main rotor construction, has been obtained by implementing compliant elements - elastic beams in the construction [1]. Elastic beam has, in its shape, size, and composition material, replaced three hinges (pitch, flap, and lead-lag hinge), which were used earlier as blades' connection to the main rotor hub. In attempts to achieve the best possible rotor characteristics, similar to, or even exceeding those of hinged rotor systems, there are different types of beams proposed in the practice, differing in cross sections and lengths [2]. In order to get improved pitch, flap and lead-lag properties, adequate design of the elastic beam is crucial, as it is practically the only part of the bearingless system that affects control characteristics. Due to highly connected dynamic and structural demands, put in front of the elastic beam, regarding geometrical properties as length, cross-sectional area, different spacing between multiple beams in root and end segment, etc. it is necessary to use mathematical optimisation methods to obtain suitable geometrical values that provide required dynamical properties. Although all of the required parameters are in direct connection, it is difficult to simultaneously observe and analyze all of them, having in mind that each of these parameters is very complex by itself. For all above mentioned reasons, this analysis will aim effects of cross-sectional area on the blade pitch change characteristics (elastic beam torsion).

2. TECHNICAL ISSUE

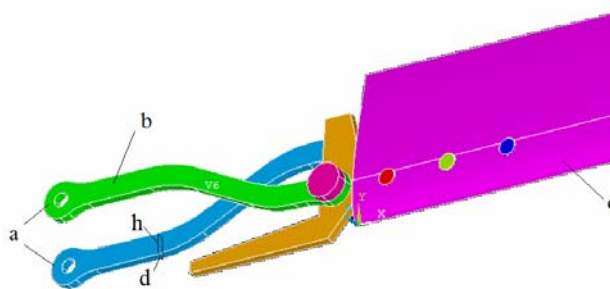


Figure 1. Elastic element and rotor blade: a) elastic element, b) elastic beams, c) rotor blade, d) beam cross-sectional height, h) beam cross-sectional width

The main technical issue in bearingless rotor systems is achieving required freedom of movement by deforming of the elastic element (Figure 1), connecting the rotor blade with the hub. Elastic element consists of two elastic beams, placed one above the other at a certain distance. Beams have composite structure, made of laminated steel bonded by rubber. The steel ensures necessary strength and toughness, while the rubber provides non-linear deformation characteristics. In difference to the present examples of the main rotor elastic elements, consisted mostly of single elastic beam per element, with different cross-section forms like „+“ or „I“ beams or other open or closed shapes, analysed beam will have rectangular cross section shape. Selection of the rectangular cross-section

provides great load-bearing capabilities combined with simplified design and manufacture process, intending to lower the overall cost. To obtain required movement properties, pitch and flap [3] characteristics in particular, it is necessary to define the cross-sectional area of the elastic beam [4].

3. OPTIMISATION DEMANDS AND INITIAL INPUT DATA

The primary goal in determining optimal dimension of the elastic beam of the helicopter rotor is to achieve the necessary movement dynamics without exceeding the permitted stresses in the material. The realization of this goal was carried out by optimization [5] of the cross-sectional area of the elastic element, and therefore, of the elastic beam. When determining the optimal size of the cross-section of the elastic beam, the height of the element (d) was varied, while the width (h) was fixed.

Bearing in mind that relatively thin beams may allow for significant or even excessive deflections, namely torsion and bending, and thus lead to increased vibrations level on rotor blades and hub (which would further demand installation of a dampening mechanism) minimal beam thickness in this analysis will be $d=7\text{mm}$.

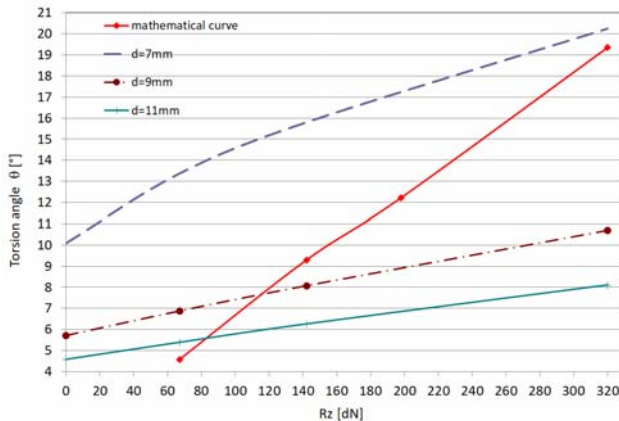


Figure 2. Rotor blade pitch angle value change (torsion angle value) in correlation with lifting force

The initial input data were obtained by finite element analysis [6,7]. That method simulated behavior of elastic beams, $l=240\text{mm}$ in length, and of thickness $d=7\text{mm}/9\text{mm}/11\text{mm}$. Analysis included following conditions:

Root end of elastic beams were fixed (simulating connection to rotor hub), so as to achieve zero movement at their contact surfaces; Centrifugal force, with magnitude of $F_c=3000\text{daN}$, loading the elastic element, acts at blade's center of mass, while aerodynamical force acts at the blade's center of thrust, located at $0,75R$ (measured from the axis of rotation). Analysis included blade pitch angle changes at different aerodynamic lift values: $R_z=67\text{daN}$, $R_z=142\text{daN}$ and $R_z=320\text{daN}$, representing thrust at blade's angular position of 0_0 in autorotation and forward level flight at 120km/h and 180km/h , respectively. Acquired blade's pitch angle values are drawn on Figure 2.

4. INTERPOLATION OF FUNCTIONS WITH MULTIPLE VARIABLES

The blade pitch angle (torsion angle) change function, denoted as θ , is considered as a function of two variables: beam cross-section thickness d and magnitude of aerodynamic force R_z , i.e., $\theta(d, R_z)$. The approximation of the function $\theta(d, R_z)$ has been made by using interpolating polynomial of two variables with divided differences [8] based on given values $\theta(d_i, R_{z_j})$, $i=0, \dots, n$, $j=0, \dots, n$. The following section will briefly present the interpolation of a function of two variables by using a polynomial with divided differences.

Interpolation is a type of approximation of a function, in which it is required that the values of approximant coincide with the values of function in the given set of points. If the approximant is polynomial, it is named as interpolation polynomial. The construction of interpolation polynomial of two variables is performed as the extension of interpolation of function of one variable. In this study, we will construct interpolation polynomial of two variables with divided differences of the function $\theta(d, R_z)$.

Let us assume that the function $\theta(d, R_z)$ is given by its values in $(n+1)^2$ points $\theta_{ij} = \theta(d_i, R_{z_j})$, $i = 0, \dots, n$, $j = 0, \dots, n$, which are presented in the table 1:

Table 1. The torsion angle change in relation to aerodynamical force and the elastic beam thickness

θ_{ij}	R_{z_0}	R_{z_1}	...	R_{z_n}
d_0	$\theta(d_0, R_{z_0})$	$\theta(d_0, R_{z_1})$...	$\theta(d_0, R_{z_n})$
d_1	$\theta(d_1, R_{z_0})$	$\theta(d_1, R_{z_1})$...	$\theta(d_1, R_{z_n})$
...
d_n	$\theta(d_n, R_{z_0})$	$\theta(d_n, R_{z_1})$...	$\theta(d_n, R_{z_n})$

The divided differences for function $\theta(d, R_z)$ are defined in iterative manner [9]. More precisely, divided differences of order $i+j$ (order i regarding the first variable d , and order j regarding the second variable R_z) are defined via two divided differences of order $(i-1)+j$ or via two divided differences of order $i+(j-1)$.

The divided difference of order $0+0$ are defined as the value of the function in the given point:

$$\theta[d_0; R_{z_0}] = \theta(d_0, R_{z_0}) \quad (1)$$

The divided difference of order $1+0$ is defined via two divided differences of order $0+0$:

$$\theta[d_0, d_1; R_{z_0}] = \frac{\theta[d_1; R_{z_0}] - \theta[d_0; R_{z_0}]}{d_1 - d_0} \quad (2)$$

Similarly, the divided difference of order $0+1$ is defined as:

$$\theta[d_0; R_{z_0}, R_{z_1}] = \frac{\theta[d_0; R_{z_1}] - \theta[d_0; R_{z_0}]}{R_{z_1} - R_{z_0}} \quad (3)$$

The divided difference of order 1+1 is calculated as:

$$\begin{aligned} \theta[d_0, d_1; Rz_0, Rz_1] &= \\ &= \frac{\theta[d_1; Rz_0, Rz_1] - \theta[d_0; Rz_0, Rz_1]}{d_1 - d_0} = \\ &= \frac{\theta[d_0, d_1; Rz_1] - \theta[d_0, d_1; Rz_0]}{Rz_1 - Rz_0} \end{aligned} \quad (4)$$

Note that divided difference is symmetric operator. As it can be seen from (4), divided difference of order 1+1 can be calculated by using either two divided differences of order 1+0 or two divided differences of order 0+1, as it is shown in (2) and (3), respectively.

The divided difference of order 2+0 is defined as the difference of two divided differences of order 1+0:

$$\theta[d_0, d_1, d_2; Rz_0] = \frac{\theta[d_1, d_2; Rz_0] - \theta[d_0, d_1; Rz_0]}{d_2 - d_0} \quad (5)$$

Each of the two divided differences of order 1+0 is calculated by using two divided differences of order 0+0, as it is shown in (2).

Similarly, the divided difference of order 0+2 is calculated as:

$$\theta[d_0; Rz_0, Rz_1, Rz_2] = \frac{\theta[d_0; Rz_1, Rz_2] - \theta[d_0; Rz_0, Rz_1]}{Rz_2 - Rz_0} \quad (6)$$

Each of the two divided differences of order 0+1 is calculated by using two divided differences of order 0+0, as it was shown in (3).

:

:

In general, the divided difference of order $i+j$ is defined as:

$$\begin{aligned} \theta[d_0, d_1, \dots, d_i; Rz_0, Rz_1, \dots, Rz_j] &= \\ &= \frac{\theta[d_1, \dots, d_i; Rz_0, \dots, Rz_j] - \theta[d_0, \dots, d_{i-1}; Rz_0, \dots, Rz_j]}{d_i - d_0} = \\ &= \frac{\theta[d_0, \dots, d_i; Rz_1, \dots, Rz_j] - \theta[d_0, \dots, d_i; Rz_0, \dots, Rz_{j-1}]}{Rz_j - Rz_0} \end{aligned} \quad (7)$$

The symmetric property of divided differences can be also be observed from (7). More precisely, divided differences of order $i+j$ are defined via two divided differences of order $(i-1)+j$ or via two divided differences of order $i+(j-1)$. The divided difference of order $(i-1)+j$ is calculated via two divided differences of order $(i-2)+j$ or two divided differences of order $(i-1)+(j-1)$, etc.

If we have the values $\theta(d_i, Rz_j)$, $i, j = 0, 1, \dots, n$, $0 \leq i+j \leq n$, then we can calculate all divided differences of order $i+j$, where $i, j = 0, 1, \dots, n$ and $0 \leq i+j \leq n$. From the definition of the divided differences, it is obvious that each divided difference can be represented via the values of function in the given set of points.

Let us introduce the notation $a_{ij} = \theta[d_0, \dots, d_i; Rz_0, \dots, Rz_j]$ for divided difference of order $i+j$. Then the polynomial with divided differences [6] that approximates function $\theta(d, Rz)$ is as follows:

$$\begin{aligned} P_\theta(d, Rz) &= \\ &= \sum_{k=0}^n \sum_{i+j=k} a_{ij} (d-d_0) \dots (d-d_{i-1}) \cdot (Rz-Rz_0) \dots (Rz-Rz_{j-1}) \end{aligned} \quad (8)$$

$$P_\theta(d, Rz) = \sum_{k=0}^n \sum_{i+j=k} \theta[d_0, \dots, d_i; Rz_0, \dots, Rz_j] \cdot (d-d_0) \dots (d-d_{i-1}) \cdot (Rz-Rz_0) \dots (Rz-Rz_{j-1}) \quad (9)$$

In this particular case, we have $n=2$ and the data given in table 2:

Table 2. Pitch angle value in relation to aerodynamic force and elastic beam thickness

θ_{ij}		Rz_0	Rz_1	Rz_2
		67dN	142dN	320dN
d_0	7mm	13.37	15.8	20.25
d_1	9mm	6.88	8.07	10.7
d_2	11mm	5.39	6.26	8.11

Using the values given in table 2, we can construct polynomial with divided differences $P_\theta(d, Rz)$ that approximates the function $\theta(d, Rz)$. This polynomial of two variables is constructed using (8) and (9), having the following form:

$$\begin{aligned} P_\theta(d, Rz) &= 3.37 - 3.245 \cdot (d-7) + 0.0324 \cdot (Rz-67) + \\ &+ 0.0083 \cdot (d-7) \cdot (Rz-67) - \\ &- 2.92 \cdot 0.0000 \cdot (Rz-67) \cdot (Rz-142) + \\ &+ 0.626 \cdot (d-7) \cdot (d-9) \end{aligned} \quad (10)$$

As the mathematical form of the curve $\theta(Rz)$ is known (it is derived theoretically), the error function can be defined as the sum of the squared deviations [10,11] of the polynomial $P_\theta(d, Rz)$ to $\theta(d, Rz)$ for Rz_0, \dots, Rz_n (in our case $n=2$). The error function defined in this way allows us to determine the optimal value of d in function of pitch angle change. The error function will be a function of the variable d . More precisely, it is obtained as:

$$G(d) = \sum_{i=0}^n (\theta(d_i, Rz_i) - \theta(Rz_i))^2 \quad (11)$$

$$\begin{aligned} G(d) &= (P_\theta(d, Rz_0) - \theta(Rz_0))^2 + \\ &+ (P_\theta(d, Rz_1) - \theta(Rz_1))^2 + (P_\theta(d, Rz_2) - \theta(Rz_2))^2 \end{aligned} \quad (12)$$

As the mathematical form of the curve $\theta(Rz)$ is known, we can easily obtain the values in the required points. More precisely, we have

$$\begin{aligned} \theta(Rz_0) &= \theta(67) = 4.57, \theta(Rz_1) = \theta(142) = 9.29, \\ \theta(Rz_2) &= \theta(320) = 19.35, \end{aligned}$$

as the values for the curve $\theta(Rz)$. It also applies:

$$\begin{aligned} \theta(d, Rz_0) &= \\ &= (0.626 \cdot d - 4.382) \cdot (d - 9) - 3.245 \cdot d + 36.085 \end{aligned} \quad (13)$$

$$\begin{aligned} P_\theta(d, Rz_1) &= \\ &= (0.626 \cdot d - 4.382) \cdot (d - 9) - 2.623 \cdot d + 34.158 \end{aligned} \quad (14)$$

$$\begin{aligned} P_\theta(d, Rz_2) &= \\ &= (0.626 \cdot d - 4.382) \cdot (d - 9) - 1.145 \cdot d + 29.58 \end{aligned} \quad (15)$$

After performing mathematical calculus, we obtain:

$$\begin{aligned} G(d) &= ((0.626 - 4.382) \cdot (d - 9) - 3.245d + 31.515)^2 \\ &+ ((0.626 - 4.382) \cdot (d - 9) - 2.62d + 24.87)^2 \\ &+ ((0.626 - 4.382) \cdot (d - 9) - 1.145d + 10.233)^2 \end{aligned} \quad (16)$$

Our goal is to find the value for d for which the minimum of the function error $G(d)$ is achieved, i.e., the optimal pitch angle for which the deviation from the pitch angle function is the smallest. Since it is a quadratic non-negative function, $G(d)$ has a unique global minimum, which is obtained as the zero of the first derivative, as a solution to the nonlinear equation $G'(d)=0$.

$$\begin{aligned} G'(d) &= (2.5 \cdot d - 22.32)((0.626 \cdot d - 4.38) \cdot (d - 9) - \\ &- 1.15 \cdot d + 10.23) + 2 \cdot (1.252 \cdot d - 13.26) \cdot \\ &\cdot ((0.626 \cdot d - 4.38) \cdot (d - 9) - 3.25 \cdot d + 31.52) + \\ &+ 2 \cdot (1.252 \cdot d - 12.64)((0.626 \cdot d - 4.38) \cdot (d - 9) - \\ &- 2.62 \cdot d + 24.87) \end{aligned} \quad (17)$$

The next step is to solve the nonlinear equation $G'(d)=0$. By applying some of the numerical methods for finding zeros of a nonlinear function (for example Newton's method [10,11]), we obtain that the optimal value is approximately $d_{opt} = 9.97\text{mm}$.

Let us now use different approach to find the optimal value for d . More precisely, we define the error in the mean square sense over the observed interval for Rz :

$$G_1(d) = \int_{Rz_0}^{Rz_n} [P_\theta(d, Rz) - \theta(Rz)]^2 dRz \quad (18)$$

Here, $P_\theta(d, Rz)$ is a polynomial with divided differences (10) that approximates the step change function obtained from Table 1. Note the use of mathematical curve $\theta(Rz)$ leads to integral that is difficult to calculate. For this reason, in (18) we will use an approximant of $\theta(Rz)$, i.e., $P_2(Rz)$ that is interpolation polynomial of the second degree that approximates the mathematical curve $\theta(Rz)$. The polynomial $P_2(Rz)$ is constructed from the known values of the mathematical curve $\theta(Rz)$ in the points $Rz_0 = 67$, $Rz_1 = 142$, and $Rz_2 = 320$:

$$\theta(67) = 4.57, \theta(142) = 9.29, \theta(320) = 19.35$$

In particular, the constructed interpolation polynomial $P_2(Rz)$ is:

$$P_2(Rz) = -0,000026 \cdot Rz^2 + 0,068234Rz + 0,112177 \quad (19)$$

The error function to be minimized is defined as the deviation error $P_\theta(d, Rz)$ from $P_2(Rz)$ in the mean square sense on the interval $[Rz_0, Rz_2]$:

$$G_1(d) = \int_{Rz_0}^{Rz_n} [P_\theta(d, Rz) - P_2(Rz)]^2 dRz \quad (20)$$

$$\begin{aligned} G_1(d) &= \\ &= \int_{67}^{320} \left[\begin{aligned} &(3,37 - 3,245 \cdot (d - 7) \\ &+ 0,0324 \cdot (Rz(67)) \\ &+ 0,0083 \cdot (d - 7) \cdot (Rz(67)) \\ &- 2,92 \cdot 0,00001 \cdot (Rz(67)) \cdot (Rz(142)) \\ &+ 0,626 \cdot (d - 7) \cdot (d - 9) \\ &- (-0,000026 \cdot Rz^2 + 0,068234 \cdot Rz \\ &+ 0,112177) \end{aligned} \right]^2 dRz \end{aligned} \quad (21)$$

As $G_1(d)$ is a non-negative quadratic function, it has a unique global minimum which is obtained as the zero of its first derivative $G_1'(d)$.

$$\begin{aligned} G_1'(d) &= 396.58 \cdot d^3 + 11603.77 \cdot d^2 - \\ &- 106435 \cdot d + 302614.7 \end{aligned} \quad (22)$$

By solving the equation $G_1'(d) = 0$ by using Newton's method, we obtain the value $d_{opt} = 9.69$.

5. CONCLUSION

This study shows possibility of elastic beam cross-section optimisation in relation to pitch angle change function, by applying combination of interpolated functions of two variables with divided differences, approximating function with corresponding polynomial with divided differences and using the least squared error and the mean squared error. Input data was obtained by analysis of the behavior of the elastic beam with thickness $d=7\text{mm}$, 9mm and 11mm , using the finite elements method. While the thickness varied for this analysis, the width of the beam was kept unchanged. The goal of this study is to determine the optimal size of the cross-sectional area of the bearingless main rotor hub to satisfy required dynamical characteristics of the rotor. The pitch angle change function was approximated by polynomial with divided differences. When the magnitude of the deviation from designated curve was calculated by least squared error method, resulting optimal value was 9.97mm , but when mean squared error method was applied, the resulting optimal value was 9.69mm . As resulting optimal values in both cases are close, that leads to conclusion that both of these methods can be used in determining of the optimal thickness of the elastic beam cross-section.

References

- [1] LNDERJIT, C.: Design and analysis trends of helicopter rotor systems, Sathana, June 1994, 19(3), 427-466.
- [2] MANOJ, K.D., SUNG, N.J., TAE, J.K.: Evolutionary Shape Optimization of Flexbeam Sections of a Bearingless Helicopter Rotor. Composites Research, 27(6) (2014) 207-212.

- [3] JYOTI,R.M., RANJAN,G.: Modeling Helicopter Rotor Blade Flapping Motion Considering Nonlinear Aerodynamics, CMES, 27(1) (2008) 25-36.
- [4] MANOJ,K.D., KYU,B.L., SUNG,N.J., TAE,J.K.: Particle Swarm Assisted Genetic Algorithm for the Optimal Design of Flexbeam Sections. International Journal of Aeronautical & Space Sciences,14(4) (2013) 341–349.
- [5] HAMILTON,B.K., PETERS,J.R.: Multi-objective/loading optimization for rotating composite flexbeams. NASA. Langley Research Center, Recent Advances in Multidisciplinary Analysis and Optimization, Part 1, (1989).
- [6] TAE,Y.C., HAN,Y.R., HAE,C.S., SANG,J.S., Young,J.K., Deog,K.K.: Structural Analysis of a Bearingless Rotor using an Improved Flexible Multibody Model. Journal of Aircraft, 50(2) (2013) 539-550.
- [7] STTEYN,J.: Design, Manufacture And Test Of A Bearingless Rotor Hub For The 24% Scale Model Of The Rooivalk Attack Helicopter, Thesis presented in partial fulfillment of the requirements for the degree of Masters of Engineering at the University of Stellenbosch, 2000.
- [8] KUNKLE,T.: Multivariate differences, polynomials, and splines. J. Approx. Theory, 84 (1996) 290–314.
- [9] NEAMTU,M.: Multivariate divided difference. I. Basic properties. SIAM J. Numer.Anal. (29) (1992) 1435–1445.
- [10] RADUNOVIĆ,D.: Numeričke metode, Akademska misao, Beograd, 2004.
- [11] BURDEN,R.L., FAIRES,J.D.: Numerical Analysis. Brooks/ Cole: USA, (2001) 104–163.



10th INTERNATIONAL SCIENTIFIC CONFERENCE
ON DEFENSIVE TECHNOLOGIES
OTEH 2022

Belgrade, Serbia, 13 – 14 October 2022



SECTION III

Weapon systems and combat vehicles - WSCV

CHAIRMAN
Prof. Predrag Elek, PhD



EFFICIENCY ANALYSIS OF A FRAGMENTATION WARHEAD AGAINST SOFT TARGETS

OMAR AWAD AL AMERI

HALCON/EDGE, Abu Dhabi, UAE

University of Belgrade – Faculty of Mechanical Engineering, Belgrade, alameriomar.ac@gmail.com

PREDRAG ELEK

University of Belgrade – Faculty of Mechanical Engineering, Belgrade, pelek@mas.bg.ac.rs

Abstract: The efficiency of the weapon system has been usually studied by altering the guidance and control or aerodynamics of the missile. This research investigated methods of enhancing the efficiency of the weapon system against soft targets based on the fragmentation warhead design. Different warhead geometric configurations, initiation points, as well as premade fragment material and shapes have been studied to enhance overall weapon efficiency against soft target. The study considered the static fragment distribution and velocity as the base for the analysis. A new vulnerability code has been developed based on the mean area of effectiveness to prove the study using both simulations and field tests. There were significant improvements on the weapon efficiency by altering the warhead parameters. The simulated results showed good correspondence with the test results. The newly developed vulnerability code can be considered as an additional system engineering analysis tool for the calculations of weapon efficiency.

Keywords: Fragmentation warhead; Efficiency; Vulnerability; Soft Targets.

1. INTRODUCTION

Nowadays there are different warhead due to the variation of targets that the weapon is built to attack. The usual targets that weapon designers look for are personnel, light armored vehicles, tanks, bunkers, aircrafts, fortifications, magazines, radars, missiles, ships, etc. Based on the selected target, the warhead can be with preformed fragments, controlled fragmentation, natural fragmentation, shaped charge, EFP, penetrator, incendiary, blast, thermobaric or a multipurpose warhead with combined effect [1-3].

Personnel are one of the main targets that a weapon designer is looking for. Personnel are either unprotected or behind protecting shield.

There are different software that are used to analyze fragmentation warhead. The premade fragmentation warhead was investigated using the finite element method as well as an analytical method. The software used are ANSYS Autodyn and Matlab.

The purpose of the paper is to study the efficiency of a weapon based on fragmentation warhead design parameters. ANSYS Autodyn and a developed vulnerability code were used to study the efficiency of a weapon based on its integrated warhead and fuze and selected target. The aim of this paper is to develop a tool that a warhead designer can use to analyze different interception scenarios between the weapon and the soft targets. The results of the fragment and velocity distribution are inputted into the developed code for mean area of effectiveness determination, which allows the

warhead designer to design the warhead based on the weapon impact angle, weapon impact velocity, and target.

2. ALGORITHM

The mean area of effectiveness defines that for a density of a target in an element of area it will be incapacitated once the warhead is detonated. It is calculated using input derived from either finite element software Autodyn or arena test. For the analysis on this paper, Autodyn was used, as well as the test data from one of the warhead configurations used in the simulations. The algorithm that is used to derive the mean are of effectiveness values is shown in Figure 1.

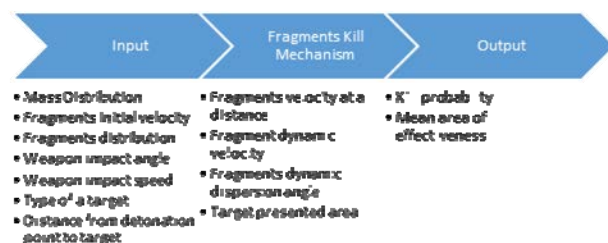


Figure 1. Mean area of effectiveness calculation algorithm.

As shown in Figure 1, to get the mean area of effectiveness, fragments mass distribution, fragments initial velocity, fragments distribution in each polar zone, weapon impact angle and speed, type of target and distance from detonation point to target must be inputted. These inputs will lead to calculations of fragments velocity at a distance, fragments dynamic velocity,

fragments dynamic dispersion angle as well as the target presented area. These calculations lead to the calculations of the kill probability and the mean area of effectiveness. The vulnerability software was verified by continuous testing at Halcon. The weapon target interaction is shown in Figure 2.

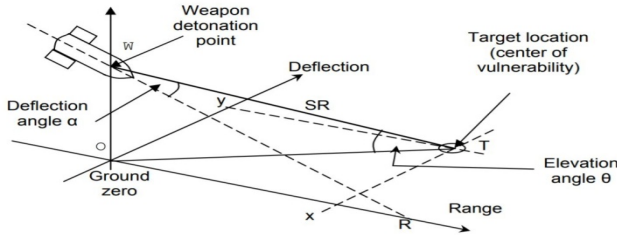


Figure 2. Weapon and target interaction geometry [4].

Equation 1 shows the mean area of effectiveness for a target that is uniformly distributed over the ground plane. Double integration is used to obtain the mean area of effectiveness.

$$\frac{E_c}{\sigma} = \int_{-\infty}^{\infty} \int_{-\infty}^{\infty} P_K(x, y) dx dy \quad (1)$$

where,

E_c - Expected number of casualties.

σ - Density of the targets.

$P_K(x, y)$ - Probability that the target will be killed.

$\frac{E_c}{\sigma}$ - Mean area of effectiveness [m²].

The mean area of effectiveness is a weighted area that is determined for each element of area that has a probability to be killed. Figure 3 shows the geometry of weapon and target interaction for mean area of effectiveness calculations in equation 1.

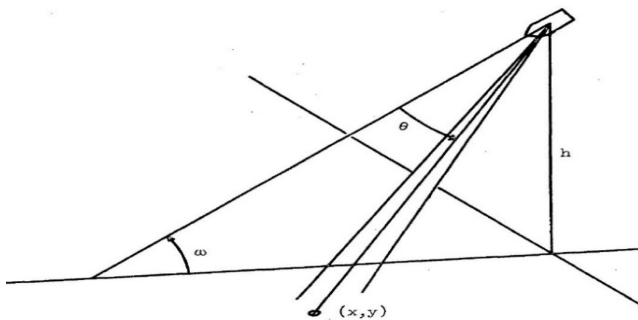


Figure 3. Geometry used for mean area of effectiveness calculations [5].

In Figure 3 it is assumed that the warhead is getting closer to the ground with impact angle ω and impact velocity V_h . The height of warhead burst from the ground is h . From mentioned geometry, the probability that the target will be killed by the accelerated fragments shall be calculated. The fragments are ejected from the projectile at an angle ϕ from the projectile main axis. In order to have a complete analysis on the probability that the target will be killed, fragments mass, fragments distribution, fragments initial velocity, fragments velocity at a distance

from point of detonation, impact angle, impact velocity, and target presented area and probability of hit must be calculated.

Kokinakis and Sperrazza [6] developed a model to calculate the probability of kill or incapacitation of the target if the target is hit by a projectile or fragment. Different scenarios were considered in which personnel is protected or unprotected. According to the model, the probability of target kill/incapacitation is defined by:

$$P_{hk} = 1 - e^{-a \left(m \cdot V_r^{\frac{3}{2}} - b \right)^n} \quad (2)$$

where,

m - Fragment mass (g)

V_r - Fragment velocity at a distance r (m/s)

a, b, n - Sperrazza criteria parameters found in [6].

The values of a, b and n are related to the tactical role and post wounding time defined in [6].

Once that the conditional kill probability is calculated using presented method the probability of kill can be calculated as in equation 3. Poisson distribution is used for kill probability calculation [5]. The sum is for the weight fraction multiplied by the probability of kill.

$$P_k = 1 - e^{-\frac{\eta \cdot A_t}{R^2} \sum_{i=1}^n q_i P_{hki}} \quad (3)$$

where,

P_k - Probability of kill.

η - The ratio between total number of fragments in the polar zone (N) per the polar zone number that the fragments are at (Ω), $\eta = \frac{N}{\Omega}$.

R - Fragment traveling distance (m)

q - The fraction of the fragments in the spray or specified polar zone.

A_t - Target presented area (m²)

In order to calculate the mean area of effectiveness the double integral shown in equation 1 shall be transformed to polar coordinates as in equation 4.

$$MAE = \int_{r_0}^{r_i} \int_{\phi_0}^{\phi_i} r P_k(r, \phi) dr d\phi \quad (4)$$

where,

r - Distance from the burst point to a point on the ground.

ϕ - Angle in the ground plane measured from the projection of the projectile trajectory to the line connecting the origin to the point in the ground plane.

3. NUMERICAL SIMULATION ANALYSIS

Ansys Autodyn was used for numerical simulation using hydrocode models [7]. Explicit Coupled Euler-Lagrange approach was used in the analysis. Warheads with premade fragments were analyzed in variant with a simple

cylindrical warhead, as well as warheads with explosive shaped inside it. The purpose of the analysis is to compare the fragment distribution difference and the mean area of effectiveness between varieties of warheads. The Euler domain was used for the explosive, liner, casing and the bulkheads, since the part deform within a fixed space. The Lagrangian domain was used for the fragments, which allows the mesh to move with the deformed parts. A flow out boundary condition was used to allow flow of the explosive without reflection at the end of the Euler space. Euler 3D multi material part was used in order to apply part fill for the parts that were in Lagrange domain and transformed them to the Eulerian domain. The Euler 3D material was air and the Lagrangian material transformed to Euler were explosive, epoxy, case and bulkheads. A plane symmetry boundary condition in the y-axis was used to allow for half symmetry analysis. A geometric strain erosion model was used with a value of 1.5.

The models used for the efficiency study were a cylindrical, cylindrical with liner, non-uniform barrel, barrel and half barrel shape warheads. The cylindrical and half barrel warheads were analyzed with varying the

initiation point. The materials and dimensions used for the analysis are the same for all warheads and the mass varied. The warhead caliber used was 100 mm and the length was 190 mm. The case thickness used was 2 mm. The fragment shape was sphere for all warheads with diameter of 5 mm. The material used for the fragment was high carbon steel, while the case, liner and the bulkheads material were Acrylic Styrene Acrylonitrile (ASA) using additive manufacturing. In the simulation polycarbonate was used instead of ASA due to availability of material data. The explosive material used was composition B and the material that was used to hold the fragments was epoxy resin. The medium surrounding the warhead was air. The element size on the fragment was 1 mm while the Euler element size was 0.25 mm. The mesh type for the fragment was multizone, while for the Euler part it was box. The simulations were run using 8 CPU, which gave the final results faster than using either lower or higher number of CPU. The simulation has been stopped once the air leaked from the other side of initiation and the fragment velocity started to converge. Figures 4 to 7 show the models used for the simulation.

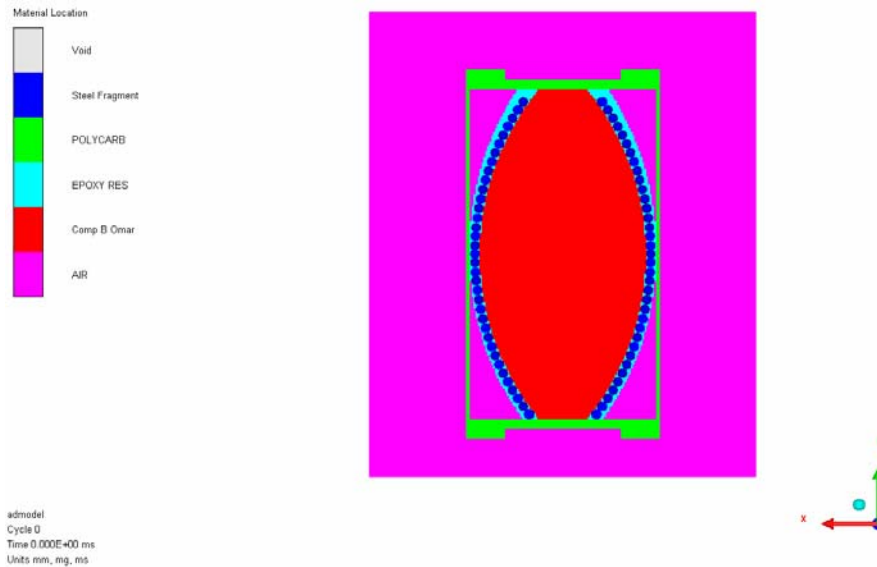


Figure 4. The Barrel Shape Used in the Simulation.

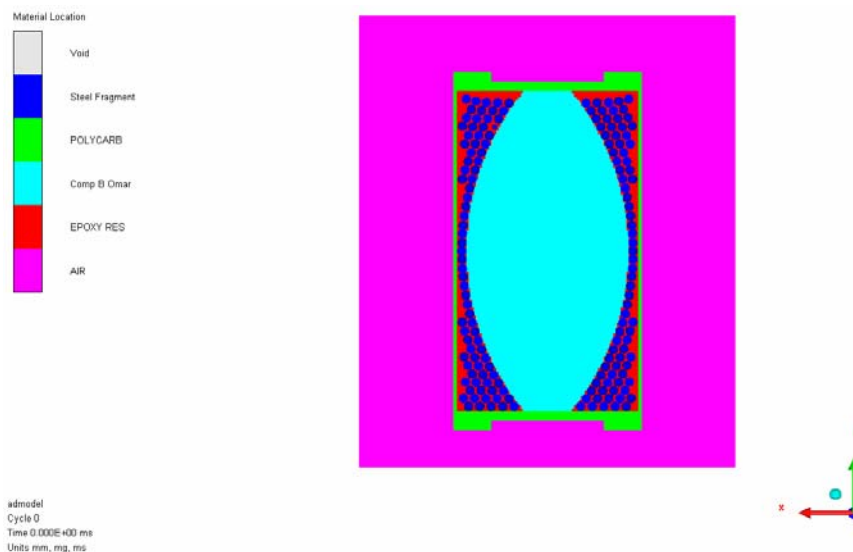


Figure 5. Non Uniform Barrel Shape Used in the Simulation.

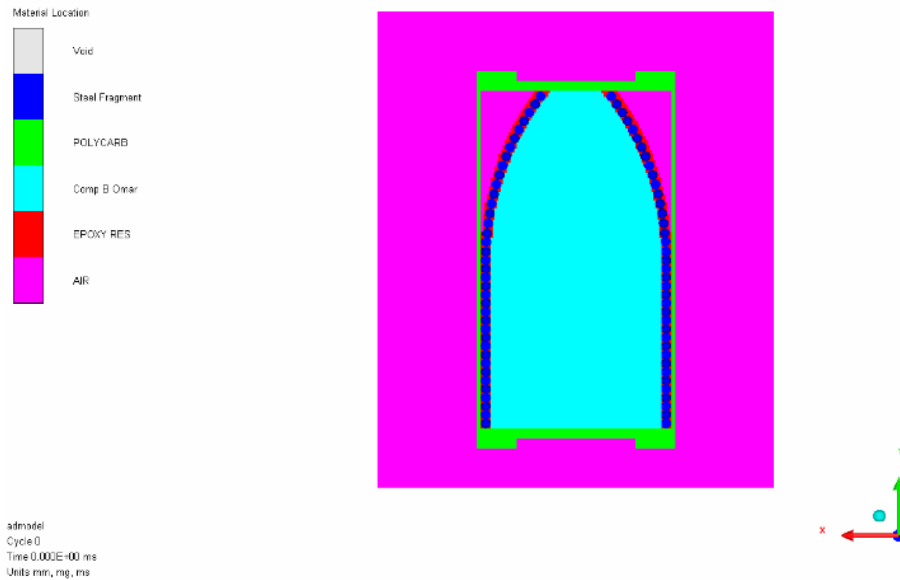


Figure 6. Half Barrel Shape Used in the Simulation.

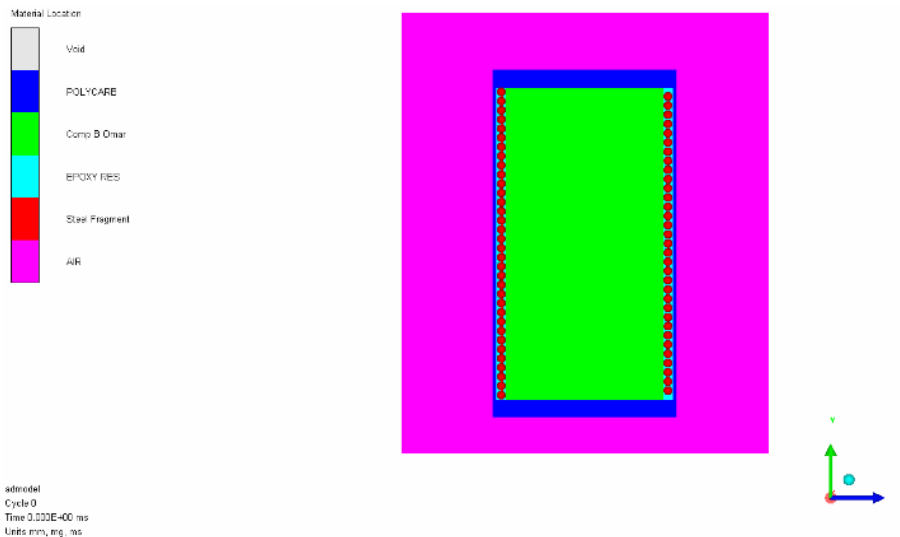


Figure 7. Cylindrical Shape Used in the Simulation.

The results of fragment number and velocity distribution are shown in Figures 8 and 9 below.

The static fragment distribution illustrated in Figure 8 shows that the non-uniform barrel shape warhead has the widest fragment distribution amongst all warheads and the cylindrical warhead has the least fragment distribution. Also, the barrel shape warhead showed wide fragment distribution but with smaller number of fragments compared to the non-uniform barrel shape warhead. Moreover, the cylindrical warheads with center and two point initiation from front and rear have almost the same distribution and better than the cylindrical warhead with one point initiation, as well as the two side initiation from the rear cylindrical warhead. The half barrel shape warhead with both small side initiation and big side initiation showed almost the same distribution. The half barrel shape warhead initiated from the small side showed slightly higher number of fragments to the rear than the one initiated from the big side. Also, more

fragments to the front side in the half barrel warhead initiated from the big side than that of the half barrel warhead initiated from the small side. Finally, the non-uniform barrel warhead showed high fluctuations and various peaks between the polar zones, which are very interesting phenomena that will be studied in the future.

The fragment velocity distribution illustrated in Figure 9 shows that the highest velocity distribution is for the non-uniform barrel shape warhead followed by the barrel shape warhead. The half barrel with big side initiation shows higher velocity distribution up to 80 degrees polar zone and then the half barrel with small side initiation shows higher velocities than those of the big side initiation. The highest velocity is achieved by the cylinder shape warhead with two point initiation from the front and rear of the warhead. The rest of the cylindrical warheads showed almost same velocity distribution except for the center point initiation which showed higher velocities toward the rear.

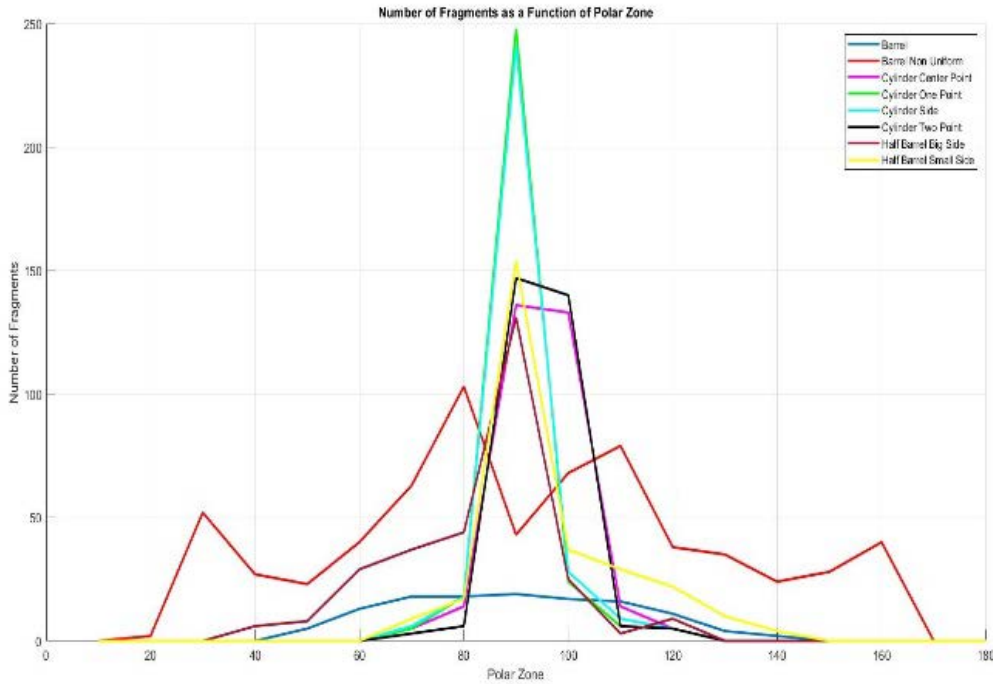


Figure 8. Comparison of Number of Fragments as a Function of Polar Zone for all Warheads.

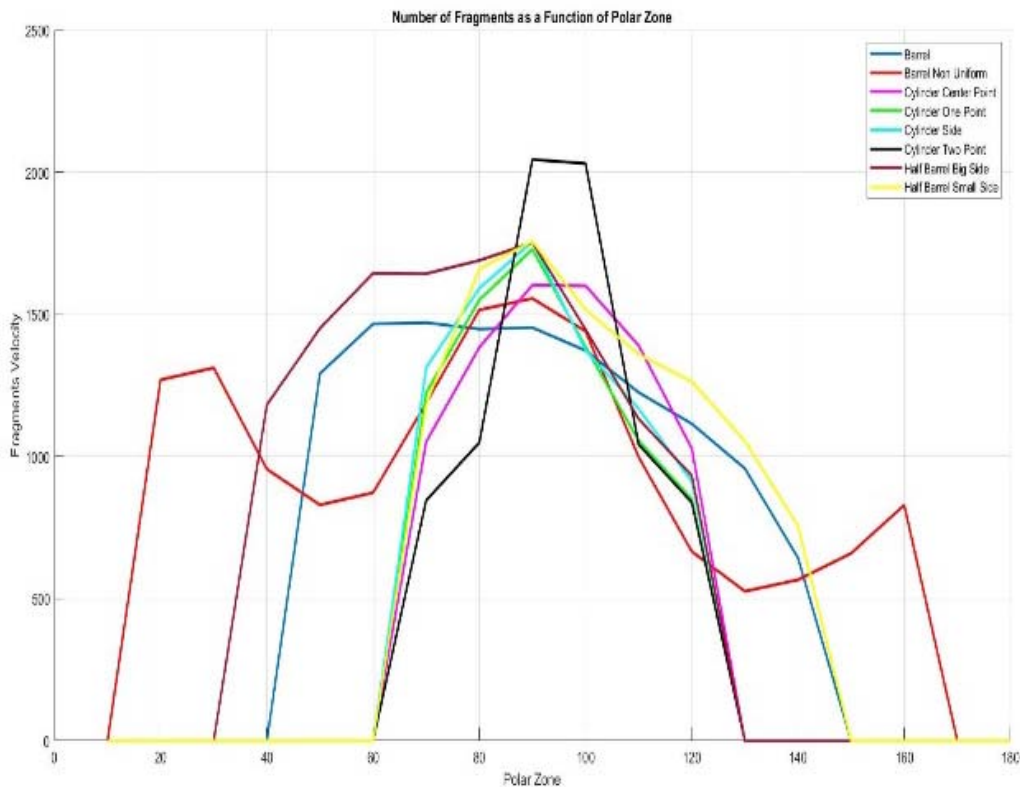


Figure 9. Comparison of Fragments Velocity Distribution as a Function of Polar Zone for All Warheads.

The mean area of effectiveness is calculated to illustrate the efficiency of the warhead when intercepting with the target. Figure 10 shows the visualization of the mean area of effectiveness using different colors where kill

probability is calculated for non-uniform barrel shape warhead with 70° impact angle, 200 m/s impact velocity and 2 m height of burst. The kill probability is illustrated as PK in the Figure .

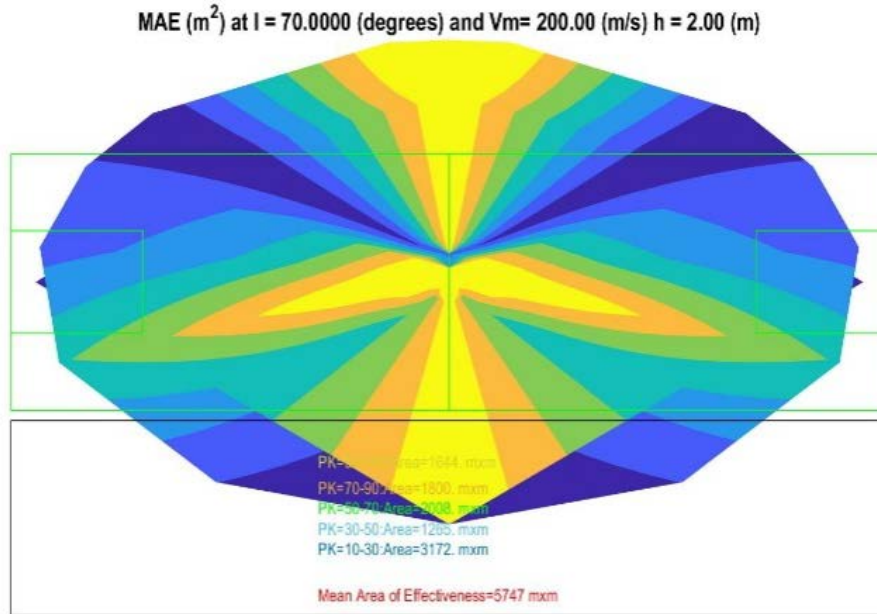


Figure 10. Mean Area of Effectiveness for 70 Degrees Impact Angle, 200 m/s Impact Velocity and 2 m Height of Burst.

Table 1 shows the mean area of effectiveness as well as the area for 90-100% kill probability for all warheads analyzed. The impact speed was the same for all scenarios with a value of 200 m/s. The impact angle and height of burst were varied. The abbreviations IA, HOB and PK represent the impact angle, height of burst and kill probability respectively.

Table 1: Total Mean area of effectiveness and 90-100% PK Mean Area of Effectiveness for All Warheads Simulated.

Warhead Type	Scenario		MAE (m ²)	
	IA (°)	HOB (m)	(90-100%) PK	Total
Non-Uniform Barrel	45	0	1635	5774
		2	2119	5347
	60	0	1540	6133
		2	1944	5164
	80	0	1404	5234
		2	1392	4785
Barrel	45	0	135	1265
		2	359	1914
	60	0	634	2672
		2	1521	5590
	80	0	1379	4963
		2	1343	4559
Cylinder One Point	45	0	544	2381
		2	731	2404
	60	0	248	2071
		2	726	2383
	80	0	628	2455
		2	1951	5260
Cylinder Two Points	45	0	558	2372
		2	727	2383
	60	0	333	2161
		2	744	2386

Cylinder Side	80	0	652	3071
		2	1497	5306
	45	0	544	2380
		2	731	2406
	60	0	247	2077
		2	726	2383
80	0	641	2559	
	2	1951	5260	
Cylinder Center	45	0	299	2121
		2	750	2412
	60	0	158	1694
		2	737	2413
	80	0	648	2431
		2	1728	5014
Half Barrel Big Side	45	0	778	3949
		2	744	2486
	60	0	669	3601
		2	1222	4029
	80	0	574	2143
		2	1698	4864
Half Barrel Small Side	45	0	384	2334
		2	750	2514
	60	0	205	1939
		2	1510	5014
	80	0	1407	5146
		2	2015	5403

The non-uniform barrel shape warhead showed the highest values of the total and 90-100% PK mean area of effectiveness at 45° and 60° impact angle amongst all warheads. The values of the mean area of effectiveness were increasing as the height of burst increase for all warheads when the impact angle was 80° except for the barrel and non-uniform barrel shape warhead. For the cylindrical shape warheads it has been shown that their optimum scenario is when the weapon has impact angle of 80° with 2 m height of burst.

4. COMPARISON BETWEEN TEST RESULTS AND SIMULATION

The analyzed warheads are under testing and one of the models was tested successfully. Figure 11 shows setup for horizontal arena and Figure 12 shows the setup for vertical arena test.



Figure 11. Horizontal Arena Test Setup.

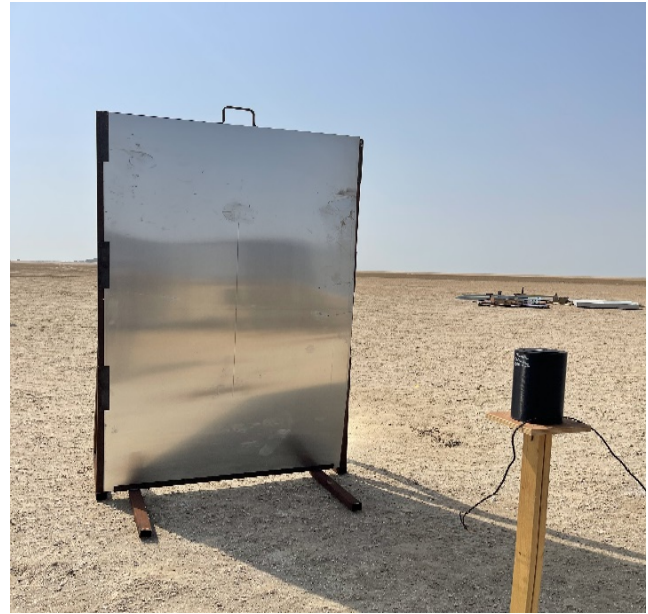


Figure 12. Vertical Arena Test Setup.

The non-uniform barrel warhead shape was analyzed and the comparison between the test data and the simulation results are shown in Figure 13.

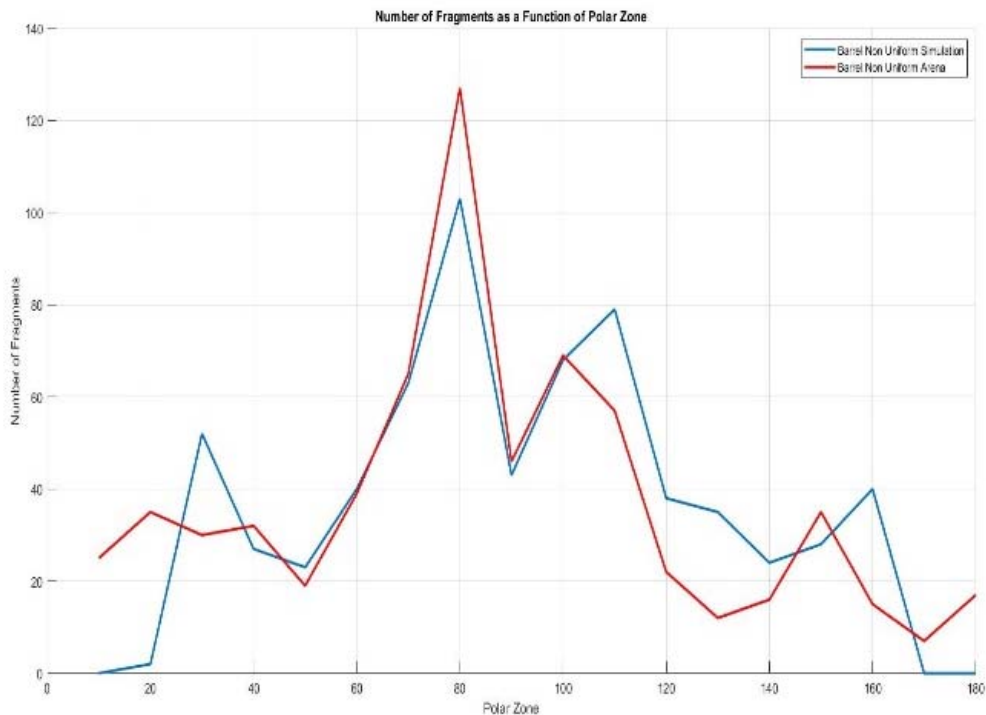


Figure 13. Number of fragments as a function of polar zone: comparison between the results of test and simulation for non-uniform barrel shape warhead.

The fragment spatial distribution results for the non-uniform barrel shape warhead from the simulation and the arena test showed excellent correspondence. The pattern is almost the same except for the lower polar zones and higher polar zones. The lower polar zones from the simulation shows a value of zero while the arena test result shows small number of fragments present.

5. CONCLUSION

The paper considers improvement of numerical and analytical modeling techniques for evaluation of fragmentation warhead efficiency. The developed numerical models within Autodyn and code in MATLAB showed the usefulness and potential to assist designer to predict the warhead and soft target interaction.

Various scenarios in terms of warhead design configurations and initiation variants were considered and for each scenario the values for Mean area of effectiveness have been determined. Detailed analysis of the obtained results provides certain guidelines for choosing the optimal configuration of the warhead and its initiation. Specifically, a wider fragment distribution for the non-uniform barrel shape warhead showed significant improvement in weapon target interaction especially at lower impact angles.

Good agreement between the simulation results and the arena test result for the non-uniform barrel shape warhead was demonstrated.

The code will be enhanced in future work to include more targets as well as different interaction geometries.

References

- [1] Lloyd R.M. (2001). *Physics of direct hit and near miss warhead technology*. Progress in Astronautics and Aeronautics, AIAA, Vol. 194.
- [2] Zukas, J.A. (2004). *Introduction to hydrocodes*. Elsevier Science, Amsterdam.
- [3] Carlucci, D.E., Jacobson, S.S. (2008): *Ballistics: Theory and design of guns and ammunition*, CRC Press.
- [4] Driels, M. R. (2013). *Weaponizing conventional weapon system effectiveness*. Reston, VA: AIAA, American Inst. of Aeronautics and Astronautics.
- [5] Meyers, K. A. (1963). *Lethal Area Description* (Tech.). Maryland: Aberdeen Proving Ground.
- [6] Kokinakis, W., Sperrazza, J. (1965). *Criteria for Incapacitating Soldiers with Fragments and Flechettes*. Aberdeen Proving Ground, MD.
- [7] DeSalvo, G.J., Swanson, J.A. (1985). *ANSYS Engineering Analysis System User's Manual*. Texas, USA., New York, 1989.



SIMULATION MODEL OF TERRITORY CELL DEFENCE AGAINST HELICOPTER AS A HYBRID THREAT

RADOMIR JANKOVIĆ

Union University School of Computing, Belgrade, rjankovic@raf.rs

MOMČILO MILINOVIĆ

Faculty of Mechanical Engineering, Belgrade, mmilinovic@mas.bg.ac.rs

Abstract: A discrete events simulation model of a system consisting of several self-propelled air-defence missile-gun systems which apply swarming tactics defending three-dimensional territory cell against helicopter as a hybrid threat is presented in this paper. The system consists of three-dimensional territory cell as a combat space, helicopter as a hybrid threat, several self-propelled missile-gun defending systems, and the command-information system which enables control of such a defence. Territory cell is a space defined by surface coordinates and maximal height of defenders' combat actions against targets in the air. Helicopter is defined as a hybrid threat, breaking through three-dimensional territory cell towards its target, in order to execute unconventional combat actions against its target. Its success is defined by its arrival at predefined distance of its target. One or several self-propelled missile-gun defending systems apply swarming tactics to arrive in positions suitable for their missile and artillery weapons' fire actions counter helicopter. Defenders' command information system enables operation in four different modes: stand-alone, within a battery, within a command post, and with a command post and early warning radar. The imperfections of such a system are also considered and represented by probability of occasional lacks of position information of hybrid threat and other moving parts of the simulated system. The necessary definitions have been given, as well as starting assumptions, the simulated system description, the simulation model basics and the simulator algorithm.

Keywords: modelling; hybrid warfare; territory cell defence; helicopter; self-propelled missile-gun system.

1. INTRODUCTION

We are living in dangerous times, burdened by various conflicts, ranging from local and regional ones, up to general inter-civilization wars, in which even those countries and their armed forces that tend to stay neutral, are subjects of huge pressures, different forms of hybrid warfare in particular.

Hybrid warfare can be defined as “conflict involving a combination of conventional military forces and irregulars (guerrillas, insurgents, and terrorists), which could include both state and non-state actors, aimed at achieving a common political purpose” [1].

As conflicts in the future will have elements of both conventional and irregular activities, a hybrid strategy will be required to combat the hybrid threat [2].

In this paper, two opponent arms are considered as being used by participants in hybrid warfare:

- Armed attack helicopter, as a hybrid threat (HHT), which is a suitable platform [3] for unconventional warfare actions (missile attacks, and/or diversion team transport);
- Self-propelled missile-gun systems (SPMGS), which defend helicopter's target (TARGET), situated in the middle of 3-dimensional territory cell (TC) around it.

For small countries, and their armed forces, tending to be neutral, it is worth researching possible issues of such hybrid conflicts, because they are likely to occur even outside a conventional war, officially declared between states. Having in mind recent procurements of general-purpose armed attack helicopters and state of the art in neighbour states' armed forces, it isn't impossible that hybrid threats of that kind could occur in foreseeable future. In addition, there is not much published practical experience of SPMGS use in such hybrid conflicts.

In order to get more knowledge and develop suitable tactical procedures for using such weapons in hybrid warfare, a research is proposed using technique of discrete events simulation. This technique proved itself worthy in authors' earlier research, when several simulators have been developed, mainly in the area of artillery and mechanized units at the battalion level swarming tactics ([4], [5], [6], [7]) application in defence counter passive and active threats ([8], [9], [10]). In ([11], [12]), artillery and missile were units introduced in the research, i.e. self-propelled missile systems, which defend a 2-dimensional ground territory cell (TC) counter an active threat, using swarming tactics combined with a synchronized multi-missile attack.

The goal of this paper is to present the approach to simulation modelling of 3-dimensional territory cell defence against a helicopter as a hybrid threat.

In Section 2, the system to be simulated has been presented, by description of its components: 3-dimensional territory cell, helicopter as hybrid threat, self-propelled missile-gun systems as defenders, and command-information system.

In Section 3, simulation model algorithm has been presented, as well as the simulated system performance measure, and possibilities of the simulator realization.

It is expected that such simulators, once realized, could be useful cost effective tools for preliminary research of new tactical procedures, needed for application in such future hybrid conflicts.

2. SIMULATED SYSTEM

The simulated system consists of: 3-dimensional territory cell (TC), helicopter as a hybrid threat (HHT), self-propelled-missile-gun systems (SPMGS) as TC defenders, and command-information system (CIS).

2.1. Territory cell

Territory cell (TC), actually the battlefield, is a rectangle 3-dimensional space, with relative origin of coordinates in one of its base's corners, and characterized by maximal values of its coordinates (X_{max} , Y_{max} , $Z_{max} = A_{Mmax}$), where A_{Mmax} is the maximal altitude at what the defender's self-propelled missile-gun system (SPMGS) can launch missiles at a helicopter as a hybrid threat (HHT) in the air.

Within TC, a HHT's **target** (TARGET) is situated on the ground, presented by its coordinates T ($X_T = X_{max}/2$, $Y_T = Y_{max}/2$, Z_T).

2.2. Helicopter as a hybrid threat

In the beginning of the simulation, **helicopter as a hybrid threat** (HHT) is on random position, at any of the TC vertical sides; after that it directs itself towards its TARGET, according to its prescribed motion law and with its maximal possible velocity, V_{HHTmax} .

HHT can attack its TARGET by guided missiles, with maximum effective range $R_{MHHTmax}$, and is capable to transport diversion team of N_{dt} persons.

HHT mission is assumed to be successful, provided it manages to approach its TARGET at defined minimal distance $D_{HHT-TARGETmin}$, according to its mission type: missile attack to TARGET, or transport of a diversion team.

2.3. Self-propelled missile-gun systems

Self-propelled ground-to-air missile-gun systems (SPMGS) are randomly deployed in the beginning of the simulation, across the whole defended CT ground area.

SPMGS mission is to destroy HHT before it reaches defined minimal distance to TARGET, $D_{HHT-TARGETmin}$.

SPMGS is capable to launch missile on the move, in salvos consisting of 2 missiles launched simultaneously. The hit probability of HHT by one such salvo is:

$$p_s = 1 - (1 - p_m)^2 \quad (1)$$

Where:

p_m : probability of HHT hit by 1 missile

SPMGS can launch the second salvo of 2 missiles after delay time of t_{2s} . If SPMGS fails to hit HHT in both first and second salvo, it abandons attempt to destroy HHT by means of missiles.

SPMGS is also capable to attack HHT by means of its automatic guns, with a hit probability of p_g . That is applied in cases when SPMGS is in such position that it can't hit HHT by missiles, due to its distance and/or height, or failure of both first and second missiles salvos.

SPMGSs apply an offensive-defensive tactics against HHT, in the following two phases:

- **Swarming**, during which they direct themselves towards HHT, in order to approach it at their missiles' or guns' possible attack zone (PAZ);
- **Attack** HHT with their missiles or guns, according to fulfilment of conditions required for each type of combat action.

PAZ for SPMGS missiles is defined by:

- Missile maximum/minimum range (R_{Mmax} , R_{Mmin});
- Missile maximum/minimum altitude (A_{Mmax} , A_{Mmin});
- Maximum/minimum elevation angle (α_{Emax} , α_{Emin}).

PAZ for SPMGS guns is defined by:

- Gun maximum/minimum range (R_{Gmax} , R_{Gmin});
- Gun maximum/minimum altitude (A_{Gmax} , A_{Gmin});

SPMGS can move by its maximum velocity $V_{SPMGSmax}$, and within its maximum mobility range $R_{SPMGSmax}$.

SPMGS can operate in one of the following modes:

- Stand-alone (SA);
- Within a battery (WB);
- Within a command post (WCP);
- With command post and external radar (WCPR).

One single SPMGS can operate in SA or WCPR mode. At least two SPMGSs can operate in WB, WCP or WCPR.

2.4. Command information system

Command-information system (CIS) provides to all SPMGS information of HHT current position, as well as the positions of every other SPMGS and other parts of the system of interest.

CIS is implemented on every SPMGS (sensors, computers and communication facilities) in all modes of operation, and supplies information in its basic intervals Δt . In addition, in WCPR mode, it can obtain information from external radar, in intervals Δt_{ext} .

In the earlier realised simulators in this research, CIS has been modelled as a perfect one, i.e. in every of its basic time interval Δt it provided information on current positions of every moving part of the simulated system, the threat in the first place.

In [13], the notion of **CIS imperfection** has been introduced, presented by lack of expected information in some of its basic intervals Δt . The approach to CIS imperfection modelling is that its measure is the probability of CIS information absence (p_{CIS}) in any interval Δt . In the simulator, p_{CIS} is the input parameter, which has its chosen value during simulation experiment. The consequence of CIS imperfection is the uncertainty of active HHT real position, which affects the activity of SPMGSs, directing to HHT based on the unreliable information.

In previously realized simulators, both the threat and the TC defenders were situated and moving on the TC ground surface, so the concept of 2-dimensional CIS parallax has been introduced [13], defined as the difference between the threat real current position and its fake position, estimated from unreliable imperfect CIS information.

Having in mind that a helicopter as HHT is capable of flying in the whole TC altitude range (from TC ground surface to A_{Mmax}), it is necessary to introduce the new concept of **3-dimensional CIS parallax** (depicted in **Figure 1**), and to use both 2-D and 3-D CIS parallax, according to HHT current position in simulation.

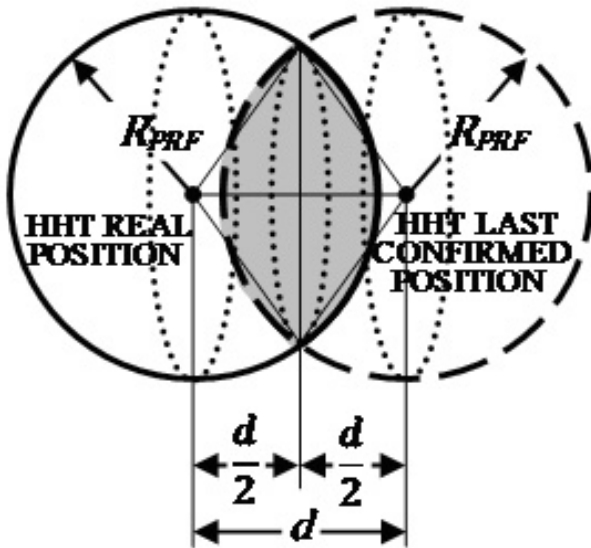


Figure 1. CIS 3-dimensional parallax

In cases of information absences in one or more interval Δt , SPMGSs are heading themselves towards the last confirmed HHT position, so the criteria for possible actions against HHT are accordingly updated and it is estimated whether the conditions for missiles launching or automatic gunfire are met.

In the simulation, as well as in the real world system, **CIS parallax** can appear (**Figure 1**), defined as the difference between real current HHT position and its fake position, which is estimated from unreliable imperfect CIS information. The CIS parallax measure is distance d between real and the last confirmed AT position:

$$d = \sqrt{(x_{\text{HHT}} - x_{\text{cHHT}})^2 + (y_{\text{HHT}} - y_{\text{cHHT}})^2 + (z_{\text{HHT}} - z_{\text{cHHT}})^2} \quad (2)$$

Where:

$(x_{\text{HHT}}, y_{\text{HHT}}, z_{\text{HHT}})$: HT real coordinates

$(x_{\text{cHHT}}, y_{\text{cHHT}}, z_{\text{cHHT}})$: HHT last confirmed coordinates

Imperfect CIS 3-D parallax could have two different effects to SPMGS CT defence mission:

- Within current simulation pass, it could happen that until HHT arrives to its TARGET, due to uncertain estimation of HHT position by imperfect CIS, the criteria for possible missile salvo launch (CMSL) and possible gunfire action (CGFA) were not fulfilled, so in that pass there will be no otherwise possible missile or gunfire attack at HHT;
- Due to imperfect CIS 3-D parallax, the false fulfilment of possible CMSL or CGFA criteria could happen, which results by launching of missile or gunfire attack at HHT that could be unsuccessful.

Both of these phenomena influence the success of the combined tactics of swarming and missile or gunfire attack, which results in increased number of failures in simulation. The first phenomenon happens during the whole simulation: as well as in the real world system, SPMGSs head towards HHT based on its current position $(x_{\text{HHT}}, y_{\text{HHT}}, z_{\text{HHT}})$, which is provided by CIS in every interval Δt . In cases this information fails in some of those intervals, SPMGSs are directed to the last confirmed HHT position $(x_{\text{cHHT}}, y_{\text{cHHT}}, z_{\text{cHHT}})$ and they will continue to do it that until the new information about HHT real position comes from CIS. As for HHT, it constantly moves towards its TARGET, no matter what SPMGSs do in the meantime.

The consequence is that in some simulation passes in the experiment it could happen that the launching or gunfire criterion is not fulfilled until the HHT mission completes, regardless the fact that it would happen if CIS was perfect and was timely providing the reliable HHT position information in every time interval Δt .

On the other hand, if at the moment of the launching or gunfire criteria fulfilment such decision is made based on uncertain HHT position due to CIS parallax, it could happen that the real proximity missile fuse zone, or possible gunfire zone around HHT are missed, due to imperfect CIS information.

The probability p_{MSL} that the decision of launching missile salvo by SPMGS is the right one, in the simulator is calculated as:

$$p_{\text{MSL}} = \frac{V_{\text{ZMSL}}}{\frac{4}{3} R_{\text{PRF}}^3 \pi} \quad (3)$$

Where:

V_{ZMSL} : intersection volume of the real proximity missile fuse zone sphere, and the one got based on the fake HHT position (2 identical spherical caps of the height $h = R_{\text{PRF}} - d/2$);

R_{PRF} : missile proximity fuse action radius.

In **Figure 1** CIS 3-D parallax general case is presented, when both the real V_{ZMSL} and that one calculated based on the fake HHT position, due to CIS imperfection, are in air

over TC. Depending on the real to fake HHT positions distance d , the probability p_{MSL} can be determined as:

For $d = 0$, $p_{MSL} = 1$
 For $d \geq 2 R_{PRF}$, $p_{MSL} = 0$
 For $0 < d < 2 R_{PRF}$, p_{MSL} is calculated as:

$$p_{MSL} = \frac{\left(R_{PRF} - \frac{d}{2}\right)^2 \left(2R_{PRF} + \frac{d}{2}\right)}{2R_{PRF}^2} \quad (4)$$

3. SIMULATION MODEL

The simulator algorithm is depicted in **Figure 2**.

INITIALIZATION of simulator comprises the experiment parameters entering, such as:

- Number of completed simulation passes in the experiment (SAMPLE);
- Territory cell characteristics;
- Number and characteristics of SPMGS;
- HHT characteristics;
- HHT to its TARGET motion law or itinerary;
- Criterion for missile salvo launch decision (CMSL);
- Criterion for gun fire action (CGFA);
- Counters starting values: SUCCESS=0, FAILURE=0

END OF EXPERIMENT condition is met when the count-down counter of completed number of simulation

reached 0 (SAMPLE=0). If the condition is met, the simulation stops and the report of results of interest is generated. If it is not, the simulation continues.

INITIAL DEPLOYMENT comprises: starting positions of HHT and SPMGSs. At the beginning of the simulation passes, HHT in one of the TC vertical edges, and SPMGSs randomly situated on TC ground surface.

It is examined if the TC defence operates in WCPR mode. If it is in WCPR mode, it is examined whether HHT is detected by external radar. If HHT is detected, its position is passed to all SPMGSs. If it is not, it is examined whether HHT is detected by any SPMGS radar.

If HHT is detected neither by external radar, nor by any of SPGMS radars, the simulation clock is advanced by one of the command-information system's basic interval Δt . Then, it is examined whether the simulation clock value is still less than the time instant when HHT reaches its TARGET ($t < T_m$).

If $t < T_m$, HHT advances to its new position on its way to TARGET, and SPMGSs move towards HHT's last known position, depending on if they detected by means of the information provided by the external radar, or by some of their own radars. If they still have no such information, they don't move, until they get it, one way or the other.

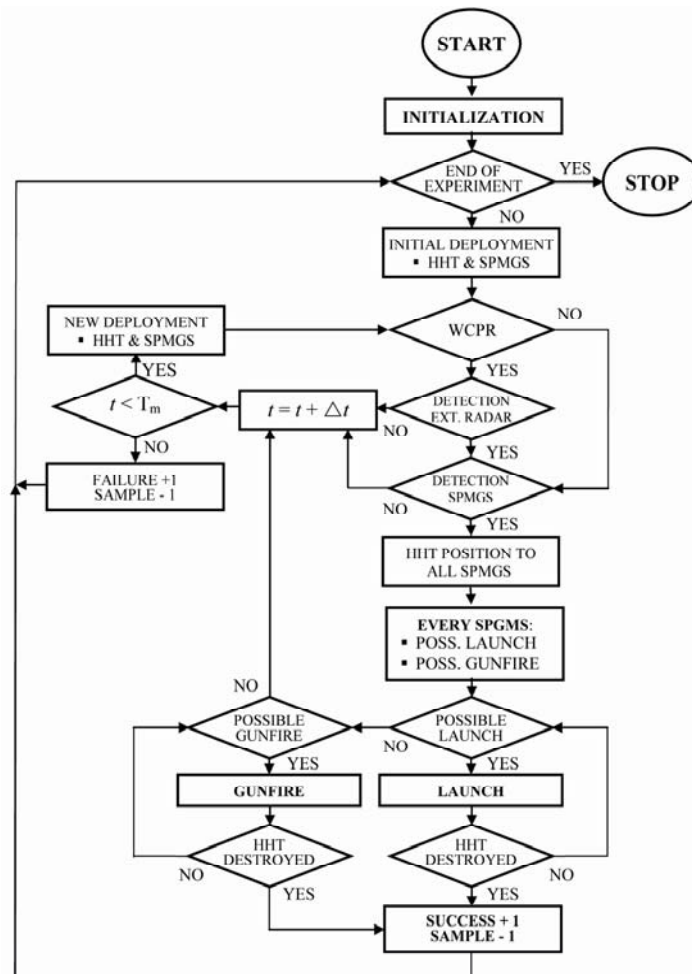


Figure 2. Simulation algorithm

After HHT and SPMGSs finished taking their NEW DEPLOYMENT, it is examined whether TC defence is in WCPR mode, and the simulation continues, as described.

If $t \geq T_m$, in actual simulation pass HHT is not destroyed before it completed its mission, the FAILURE counter is increased by 1 (FAILURE+1), the experiment termination counter is decreased by 1 (SAMPLE-1), and it is examined whether the experiment is over. If is over (SAMPLE=0), the simulation stops, otherwise it continues, as described. If HHT has been detected, and/or its position has been transferred to SPMGS, for every SPGMS it is examined whether there are some of them who can launch missiles at HHT. If there is any possible

LAUNCH, it is executed, and it is examined if HHT is destroyed. The SPMGS LAUNCH scenario is depicted in **Figure 3**. The SPMGS missile launch is possible if HHT is in missile possible attack zone (PAZ, Section 2.3), and in time instant $t = T_2$, the inequality (5) is true:

$$D_{\text{HHT-TARGET}}(t = T_2) \geq D_{\text{HHT-TARGETmin}} \quad (5)$$

Where:

$D_{\text{HHT-TARGETmin}}$: minimal HHT distance to its TARGET, that qualify HHT mission accomplished.

SPMGS reaction time t_r (**Figure 3**) is the time interval from HHT acquisition to firing of the first missile.

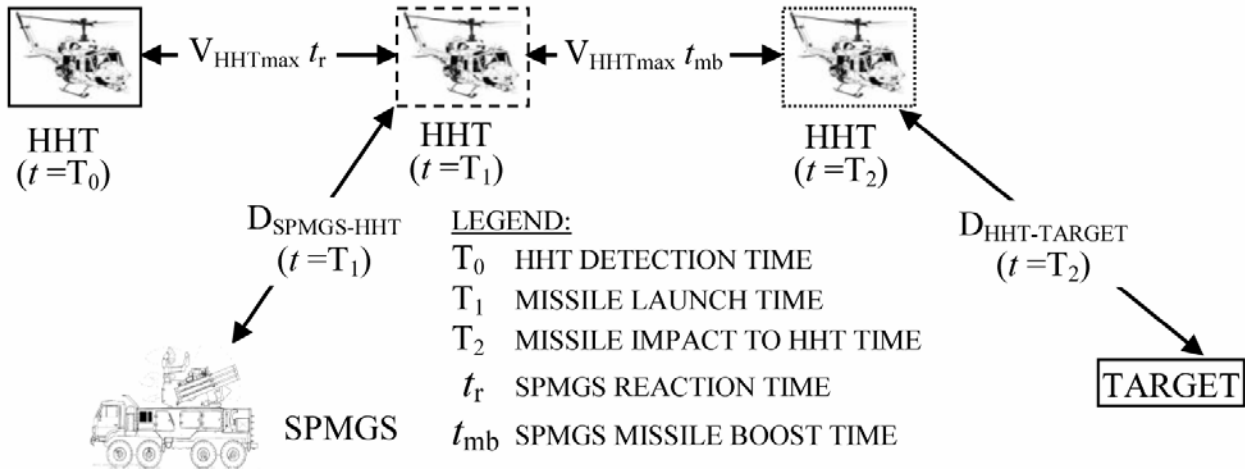


Figure 3. SPMGS LAUNCH scenario

If there is no more possible LAUNCH, for every SPMGS it is examined whether there are some of them who can open gunfire at HHT. The SPMGS GUNFIRE is possible if HHT is in gunfire possible attack zone (PAZ, Section 2.3). If there is any possible GUNFIRE, it is executed, and it is examined if HHT is destroyed.

If HHT is destroyed either by missiles, or by gunfire, the SUCCESS counter is increased by 1 (SUCCESS+1), the experiment termination counter is decreased by 1 (SAMPLE-1), and it is examined whether the experiment is over (SAMPLE=0). If it is over, the simulation stops, otherwise it continues.

If HHT is destroyed neither by missiles, nor by gunfire, the simulation clock is advanced by one of the command-information system's basic interval Δt , and the simulation continues, as described.

Primary performance measure in the simulation is the probability of success of territory cell defence, defined as:

$$P_{\text{SUCCESS}} = \frac{\text{SUCCESS}}{\text{SUCCESS} + \text{FAILURE}} \quad (6)$$

Where:

SUCCESS: counter of simulation passes, ended by successful TC defence – HHT destruction

FAILURE: counter of simulation passes, ended by unsuccessful TC defence – HHT survival

GPSS World simulation language (Minuteman Software, [14]) has been chosen for the simulator algorithm

implementation, due to its suitability for discrete events system simulation and easy availability of the tool on the Internet.

4. CONCLUSION

Hybrid attacks are challenging pressures to which small and neutral countries are especially exposed, even out of conventional wars, officially declared between states.

Hybrid conflicts have elements of both conventional and irregular activities, so hybrid strategy will be required to combat against hybrid threat.

On tactical level, it is worth studying and devising new tactical procedures for using known conventional arms in the hybrid warfare environment.

The approach to discrete events simulation modelling of 3-dimensional territory cell defence by self-propelled missile-gun systems against a helicopter as a hybrid threat has been proposed in this paper.

A new simulation algorithm of a self-propelled missile-gun systems group, using swarming tactics and combined missile and automatic guns attack against helicopter has been developed and presented, as well as defined such system's performance measure, and possibility of the simulator realization.

Such a defence depends on a real-time information of the hybrid threat exact position, provided by the command-information system. Having in mind that a helicopter is a

threat from the air, the new concept of 3-dimensional command information system parallax has been introduced, as the difference between helicopter's real position and its fake position, estimated from unreliable imperfect command-information system.

The authors believe that such simulators could be useful cost-effective tools for preliminary research of new tactical procedures, needed for application in future hybrid conflicts.

References

- [1] MURRAY, W., MANSOOR, P. *Hybrid Warfare: Fighting Complex Opponents from the Ancient World to the Present*, Cambridge University Press, New York, 2012.
- [2] GRIMSRUD, K. *Moving into the Future: Allied Mobility in a Modern Hybrid Warfare Operational Environment*, School of Advanced Military Studies, US Army Command and General Staff College Fort Leavenworth, KS, 2018.
- [3] De DURAND, E., MICHEL, B., TENENBAUM, E. La guerre des hélicoptères. L'avenir de l'aéromobilité et de l'aérocomba , Focus stratégique, no. 32 bis, June 2012.
- [4] ARQUILLA, J., RONFELFT, D. *Swarming and the Future of Conflict*, Rand Corporation, 1999.
- [5] EDWARDS, S.J.A. *Swarming and the future of warfare*, Rand Corporation, 2005.
- [6] HENKIN, Y. On Swarming: Success and Failure in Multidirectional Warfare, from Normandy to the Second Lebanon War, *Defence Studies*, 14, 3, 310–332, 2014.
- [7] RATIU, A. Swarming – Doctrinary – Operational – Concept – Possible Solution to the Challenges of the Current Military Confrontations, *Scientific Bulletin*, 21(2), (2016) 128–134.
- [8] JANKOVIC,R., MILINOVIC,M., JEREMIC,O., NIKOLIC,N. On Application of Discrete Event Simulation in Armoured and Mechanized Units Research, *Proceedings of the 1st International Symposium & 10th Balcan Conference on Operational Research*, Thessaloniki, Greece, Vol.2, 28-35, 2011.
- [9] JANKOVIC,R. Computer Simulation of an Armoured Battalion Swarming, *Defence Science Journal*, 61(1), (2011), 36–43.
- [10] JANKOVIC, R. Data Structures and Control Mechanisms for Multi-target Swarming Simulators, *Electronic Letters*, 48(16), (2012), 997-998.
- [11] JANKOVIC, R., MILINOVIC, M. An Approach to Simulation of the Swarming and Synchronized Missile Attack Against an Active Threat, *Proceedings of the 8th International Conference on Defensive Technologies (OTEH 2018)*, Belgrade, Serbia, 101-105, 2018.
- [12] JANKOVIC, R., MILINOVIC, M. Simulator of Swarming and Synchronized Missile Impact Counter an Active Threat, *Proceedings of the XLVI International Symposium on Operational Research (SYM-OP-IS)*, 2019.
- [13] JANKOVIC, R., MILINOVIC, M. Modelling of Command Information System Imperfection in Military Swarming Systems Simulators, *Proceedings of the 9th International Conference on Defensive Technologies (OTEH 2020)*, Belgrade, Serbia, 145-150, 2018.
- [14] Minuteman Software, GPSS World. <http://www.minutemansoftware.com/simulation.htm>



PLANETARY GEAR PAIR DESIGN USING METAHEURISTIC ALGORITHMS

MILOŠ SEDAK

Faculty of Mechanical Engineering, University of Belgrade, Belgrade, msedak@mas.bg.ac.rs

MAJA ROSIĆ

Faculty of Mechanical Engineering, University of Belgrade, Belgrade, mrosic@mas.bg.ac.rs

Abstract: This paper considers the problem of formulating the non-linear optimization model for determining the optimal parameters of planetary gearbox, which is solved using a metaheuristic optimization algorithm. To determine the optimal parameters of the planetary gearbox it is necessary to formulate complex objective functions and minimize them, which is often a conflicting problem. To solve this complex optimization problem, in this paper we propose to employ metaheuristic algorithms, which characterize pseudo-randomness and the ability to find the global optimal solution to the multimodal optimization problems. The proposed metaheuristic method is based on the Genetic Algorithm (GA) which is hybridized with the local-search Nelder-Mead method. For the considered optimization problem, the appropriate software is implemented in the MATLAB software package, to verify the results. Inside the considered optimization module, we have defined the appropriate objective functions and constraints which determine the construction of the planetary gearbox. The optimal parameters of the planetary gearbox obtained using the proposed metaheuristic algorithm are compared with the results obtained using several well-known algorithms in the literature. The simulation results of the proposed optimization method indicate a significant improvement in planetary gearbox performance compared to the parameters obtained with well-known algorithms.

Keywords: Optimization, Planetary gear trains, Gear efficiency.

1. INTRODUCTION

Planetary gearboxes find widespread use in a variety of mechanical systems, including industrial drives, rotorcraft, automobiles, wind turbines, and other similar applications [1,2]. In these types of mechanical systems, planetary gearboxes can offer more compact dimensions and higher power densities with less noise and higher torque-to-weight ratios, in particular when compared to standard parallel axis gear trains. However, the design of such gearboxes necessarily involves several planetary branches, which also affects efficiency [1]. This is because the total efficiency of planetary gear sets is determined by the various gear mesh areas in planetary gear sets. The primary objective is to increase the service life of the components while simultaneously decreasing the weight and power loss associated with the design of the gearbox.

Nowadays, it is necessary to accurately forecast power losses during the design stage of the gearbox. This enables the designer to make appropriate design adjustments prior to the gear box being manufactured and put through its tests. There are a great number of articles that concentrate on gear efficiency and power loss, both of which are connected to concerns about the efficiency of parallel axis gear systems [3, 4]. The bulk of research focuses on mechanical power loss. Few papers have been written on the power losses of planetary systems, and the majority of those that have concentrated on the power losses that occur in planetary gear sets, which are often the result of experiments. In most cases, such models

investigate efficiency via the analysis of gear train kinematics. More specifically, they use speed and torque equations to evaluate the effectiveness of planetary gearboxes [3]. These studies do not take into account the power loss that occurs as a result of lubricant interactions when non-uniform gear normal loads are being applied. However, these studies fail to simultaneously consider the minimization of mass and the maximization of gearbox efficiency.

Many engineering optimization problems have recently been approached using natural-world-inspired metaheuristic algorithms, such as the Genetic Algorithm (GA) [5], particle swarm optimization (PSO), differential evolution (DE), ant colony optimization (ACO), firefly algorithm (FA), grey wolf optimization (GWO) [6], and others. Weight minimization, power loss reduction, and other gearbox optimization problems are only a few of the many for which the GA has been actively used as a promising optimization strategy from the group of EAs [5].

The use of evolutionary algorithms (EAs) to address optimization issues in the multiobjective optimization (MOO) of gearbox parameters has proven fruitful [6, 7]. Although evolutionary algorithms (EAs) were first developed for use in tackling unconstrained single objective optimization problems, researchers have recently found ways to include constraint management approaches into these algorithms and adjust the algorithms to be capable to tackle multiobjective problems. Limits on the choice of number of objectives,

variables, different kinds of constraints, conflict between different kinds of constraints, and a close link between the constraints and the objective function all contribute to the difficulty of constrained multiobjective optimization problems [8].

There have been several EAs developed for multiobjective optimization, and as a result, in recent years there have been numerous publications in academic journals that discuss multiobjective optimization of gearboxes. The majority of the papers [6, 7] depend on the well-known non-dominant genetic algorithm (NSGA) and other enhanced forms of this algorithm to tackle the multiobjective optimization issues in the field of gearbox design. However, a number of works have recently been published in the literature that address MOO issues utilizing hybrid versions of well-known EAs [6].

As a consequence of this, the multiobjective planetary gearbox optimization problem that is being discussed in this study is tackled with the help of a hybrid strategy that is presented in this paper. The GA algorithm's capacity for global search is combined with the NM algorithm's superior ability to perform local search, resulting in the hybrid algorithm's capabilities. The outcomes of the computational simulation provide further evidence that the strategy that was suggested is preferable.

This paper is organized as follows. Firstly, in Section 2 the considered optimization problem is formulated and the appropriate penalty method for dealing with constraints is introduced. Next, in Section 3 the procedure of the GA and NM methods of the hybrid algorithm are outlined. In Section 4 the corresponding simulation results are presented. Finally, the conclusions are drawn in Section 5.

2. OPTIMIZATION PROBLEM FORMULATION

Many researchers have been drawn to the problem of minimum mass design and boosting the efficiency of planetary gearboxes, due mostly to the necessity for low mass design in aerospace engineering. In this study, we will look at how to optimize the mass and efficiency of a single stage planetary gearbox, as shown in Fig. 1.

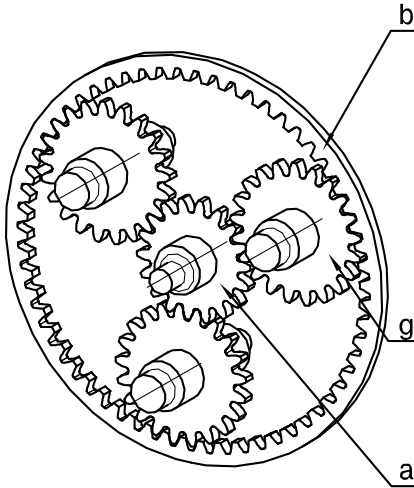


Figure 1. Illustration of a single-stage planetary gearbox considered in the optimization model

Here, (a) represents the sun gear, (b) represents the ring gear, and (g) represents the planet gear. Because weight and efficiency are mutually incompatible objectives, the described optimization problem transforms into a multiobjective optimization problem, denoted as

$$\min_{\mathbf{x} \in \mathcal{D}} [W(\mathbf{x}), \eta_{aH}^b(\mathbf{x})], \quad (1)$$

subject to the n equality and m inequality constrains

$$\begin{aligned} g_i(\mathbf{x}) &\leq 0, \quad i = 1, \dots, m \\ h_j(\mathbf{x}) &= 0, \quad j = 1, \dots, n. \end{aligned} \quad (2)$$

The first objective is the mass of the single stage planetary gearbox, which under the assumption of the homogenous material can be defined as

$$W(\mathbf{x}) = \rho \sum_{i=1}^n V_i, \quad (3)$$

where ρ is the density and V_i is the volume of the i th structural element. Therefore, the mass of the considered planetary gearbox is given as follows:

$$W(\mathbf{x}) = \rho \frac{\pi}{4} b \left[d_{(a)}^2 + n_w (d_{a(b)}^2 - D^2) + (d_{(g)}^2 - d_s^2) \right] \quad (4)$$

where $d_{(a)}$ is the pitch circle of the sun gear, $d_{a(b)}$ is tip diameter of the ring gear, d_s is outside bearing diameter, $d_{(g)}$ is the pitch circle of the planet gear, $n_w = 3$ is the number of planet gears, D denotes outside diameter of a ring gear and b is the width of a gearbox.

The second objective of the considered optimization problem deals with the efficiency of the planetary gearbox and can be described according to the expression

$$\eta_{aH}^b = \frac{1 - \eta_{ag}^H \eta_{gb}^H u_{ab}^H}{1 - u_{ab}^H}, \quad (5)$$

where η_{ag}^H and η_{gb}^H denote relative efficiency of the sun-planet gears and relative efficiency of planet-ring gears, respectively. These efficiencies can be determined according to the numerical procedure given in [1]. Furthermore, u_{ab}^H denotes the relative gear ratio.

The corresponding constraints of the considered optimization problem, take into considerations the strength of the gear, through the factor of safety, and achievable size constraints. Functional constraints in the form of inequality are given as

$$g(\mathbf{x}) = \frac{[\sigma_F]}{\sigma_F} - S_F > 0 \quad (6)$$

where σ_F is the working bending stress, $[\sigma_F]$ is the allowable bending stress and S_F is bending stress factor of safety. Moreover, to prevent any interference of teeth during the meshing process, the assembly requirement

that must be met would be that the central sun gear and planet gears must always mesh simultaneously. Regarding this, the equality requirement is described as

$$h_i = \frac{z_a z_b}{n_w D(z_g, z_b)} - i = 0 \quad (7)$$

Finally, taking into consideration the given optimization problem in Eq. (1) and corresponding constraints in Eqs. (6) and (7) the nonempty feasible domain is defined as follows

$$\mathcal{D} = \{ \mathbf{x} \in R^n \mid g(\mathbf{x}) \leq 0 \wedge h(\mathbf{x}) = 0 \} \quad (8)$$

2.1. Penalty method for multiobjective optimization

Because the proposed evolutionary algorithm is incapable of dealing directly with constrained situations, a method for dealing with the constraints must be devised. This work considers the penalty approach to be a popular and straightforward constraint-handling strategy that effectively approximates the constrained optimization problem with the unconstrained optimization problem using the penalty function [8]. For each objective $f_i, \forall i = 1, 2$ a pseudo-objective function F_i is defined in the following form

$$F_i(\mathbf{x}) = f_i(\mathbf{x}) + \sum_{j=1}^m P_j(\mathbf{x}), \quad (9)$$

where $P_j(\mathbf{x})$ is the penalty function corresponding to the j th constraint. The penalty function is used to remove any solution that violates the constraint. As a result, the limited optimization problem may be transformed into an unconstrained minimization problem that has the following form

$$\min_{\mathbf{x} \in R^n} [F_1(\mathbf{x}), F_2(\mathbf{x})]. \quad (10)$$

The penalty function can be defined as

$$P_i(\mathbf{x}) = \begin{cases} 0, & \mathbf{x} \in \mathcal{D} \\ s_i(\mathbf{x})R_i & \mathbf{x} \notin \mathcal{D}, \\ & i = 1, \dots, m \end{cases} \quad (11)$$

where R_i is the penalty factor that measures the importance of the i th penalty function and $s_i(\mathbf{x})$ is a continuous function that considers the equality and inequality constraints, defined as

$$s_i(\mathbf{x}) = g_i^2(\mathbf{x}), \quad i = 1, \dots, m. \quad (12)$$

According to the formulation of the penalty function in Eq. (11), the penalty method directly analyses every viable option based on their objective function values, while the penalty function is applied to the infeasible alternatives, lowering their fitness value. A significant drawback of the penalty technique is the insufficient

selection of the punishment factor, which has a significant impact on the efficiency of the search process. The severity of the penalty is determined mostly by the degree of infraction and varies appropriately.

3. GENETIC ALGORITHM

As a member of the class of metaheuristic optimization algorithms, the genetic algorithm may be used to find optimum solutions to multimodal optimization problems at the global level. GA processes are inspired by natural genetics and natural selection mechanisms [5].

The process of utilizing GA to identify the global optimum solution begins with the generation of a population of initial solutions. There are two types of GA in the literature: binary GA and real-valued GA. Each solution in the Binary GA is represented by a chromosome, which is a fixed-length vector of binary variables. Binary vectors are used to encode each potential solution. The number of optimization parameters used and the desired encoding accuracy define the length of this vector. The GA consists of three evolutionary operators, selection, crossover, and mutation, which are applied to the population of solutions in each generation with the goal of guiding the population towards the global optimum.

During the selection phase, the GA uses the associated objective function value of each individual to choose chromosomes from the population that have favorable mating qualities. In this method, the chromosomes that lack the qualities required to solve the optimization problem are removed from the population. The selection method employs chromosome fitness values to decide which individuals are selected for mating and removes chromosomes that lack critical features for the effective solution of the optimization issue. The chromosomes are chosen using a roulette wheel, with individuals with lower objective function values, which is advantageous for minimization problems, being more likely to be chosen. The i th individual's selection probability is calculated as

$$P_i = \frac{F_i}{\sum_{j=1}^{N_p} F_j}, \quad i \in \{1, \dots, N_p\}, \quad (13)$$

where F_i is denoting an objective function value of the chromosome. The cumulative probability C_i of the i -th individual is determined according to the following expression

$$C_i = \sum_{j=1}^{N_p} F_j. \quad (14)$$

After assigning a cumulative probability to each individual in the population, they are subjected to a selection method in which a suitable individual is chosen based on a random number r that must meet the following equation

$$C_{i-1} < r \leq C_i, \quad i \in \{1, 2, \dots, N_p\}, \quad (15)$$

where r denotes the random number generated between 0 and 1.

One of the most essential aspects of GA is the crossover operator, which integrates and utilizes the available information stored in chromosomes to impact the search direction throughout the optimization process. The crossover operator combines the information of two previously picked individuals in the selection process to produce offspring that share both individuals' important advantages. Such offspring may have the abilities required to solve the optimization issue successfully. As seen in Fig. 2, two-point crossover is carried out by picking two random crossing spots along the chromosomal length, indicated as c_1 and c_2 . As a consequence, the encoded binary values encompassed by these points may be exchanged between individuals.

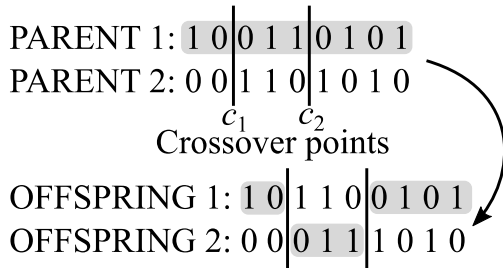


Figure 2. The illustration of two-point crossover operator

Mutation is a GA operator that adds previously unknown solutions into the GA population. To avoid damaging valuable information, just a tiny fraction of the population gets altered. Mutation occurs when random binary changes occur on a chromosome. To reflect the unpredictability of the alterations, each digit of the gene being mutated is changed to either 0 or 1. The mutation rate must be low, since if it is high, a good chromosome may accidentally mutate into a poor one.

The selection, crossover, and mutation operators are repeated, and the population evolves through consecutive iterations toward the global optimal solution of the considered optimization problem until the termination condition is fulfilled. Although most evolutionary algorithms employ the maximum number of iterations as a termination criterion, the relative error of the average objective function value of the population between two successive iterations is also used. As a result, the algorithm may be stopped by comparing the objective function value of population in successive iterations when it falls below a specific threshold, which is stated in the following

$$\left| \frac{f_{avg}^{(k)} - f_{avg}^{(k-1)}}{f_{avg}^{(k)}} \right| \leq \varepsilon, \quad (16)$$

where ε is a small positive real number, in which

$$f_{avg}^{(k)} = \frac{1}{N_p} \sum_{i=1}^{N_p} f_i, \quad (17)$$

represents the average objective function value of the

entire population in k th iteration.

4. NELDER-MEAD METHOD

The Nelder-Mead is a direct local search method that doesn't require the knowledge of the first derivative of the objective function, which is widely applied in solving different convex optimization problem n s [9]. The process of NM method is based on transforming $n+1$ points during the iterations at the vertices of a simplex, for dimensional optimization problem. The main operations on a simplex, which consists of three points $S := \{\mathbf{x}_1, \mathbf{x}_2, \mathbf{x}_3\}$, applied in order to transform simplex and converge to optimal solution and produce new points are displayed on Fig. 3, and include: reflection \mathbf{x}_r , expansion \mathbf{x}_e , contraction \mathbf{x}_c and shrinkage.

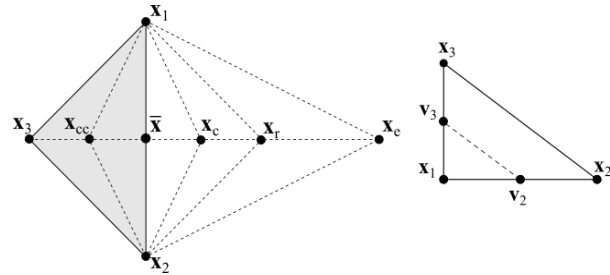


Figure 3. The illustration of four main transformations performed on simplex in Nelder-Mead method for two-dimensional optimization problem

The initial untransformed simplex is bounded by vertices ordered by the objective function value, e.g. \mathbf{x}_1 , \mathbf{x}_2 and \mathbf{x}_3 , where the last point denotes the worst point. To transform the initial simplex and provide a new point through applying the abovementioned operations firstly we determine a centroid point $\bar{\mathbf{x}}$ which halves the line segment between points \mathbf{x}_1 and \mathbf{x}_2 . During each iteration one of the transformations is applied and a new point is generated which replaces the point \mathbf{x}_3 in the current simplex. In this way the points on the simplex are improved until it converges towards the optimum point.

Therefore, to apply the NM method the following operations are performed.

Initialization. Firstly, to start with the optimization process, the initial simplex is generated around the provided initial solution by adding to this point the scaled value of unit vector in each direction, e.g.

$$\mathbf{x}_{i+1} := \mathbf{x}_1 + \lambda \mathbf{e}_i, \quad i = 1, \dots, n, \quad (18)$$

where $\lambda \in R$ is represents the unit vector scale factor, usually set as $\lambda = 1$, and \mathbf{e}_i denotes the unit vector of the i th axis. To form the initial simplex, the generated point are sorted in ascending order based on the objective function value, such that the following is true

$$f(\mathbf{x}_1) \leq f(\mathbf{x}_2) \leq \dots \leq f(\mathbf{x}_{n+1}). \quad (19)$$

Simplex generation. To transform the initial simplex the four transformations are applied. Firstly, we determine the

centroid \bar{x} is the centroid of the n best vertices which can be calculated as

$$\bar{x} := \frac{1}{n} \sum_{i=1}^n x_i. \quad (20)$$

Reflection. Then, the reflection point is the first one that is created, by reflecting the worst point x_{n+1} around the axis which contains the points x_n and x_{n-1} , as follows

$$x_r := \bar{x} + \alpha(\bar{x} - x_{n+1}), \quad (21)$$

The newly generated point lies on the line that contains points x_{n+1} and \bar{x} . In order to check if the point x_r is kept in the simplex the expression $f(x_r) < f(x_1)$ must be satisfied. Then, we try to further explore the solution space with expansion. Otherwise, is $f(x_1) \leq f(x_r) < f(x_n)$, the worst point is replaced with generated point x_r and no additional transformations are performed.

Expansion. This operation is performed in order to further extend the search area if the reflection vertex points to the right direction. The expansion point is generated along the line which contains the points \bar{x} and x_r according to the expression:

$$x_e = \bar{x} + \beta(x_r - \bar{x}). \quad (22)$$

If $f(x_e) < f(x_r)$, the new expansion point is pointing to the optimal solution and vertex x_{n+1} is replaced by x_e and iteration terminated. Otherwise, replace x_{n+1} with x_r and terminate iteration.

Contraction. After the reflection point is generated, and expansion is not the desired direction in the movement of the simplex, the contraction is applied. Depending on whether contraction point lies inside or outside of the current simplex we recognize two types of contraction which can be performed, outside and inside contraction. Outside contraction is performed when $f(x_n) \leq f(x_r) < f(x_{n+1})$, and the point x_c is determined as follows:

$$x_c := \bar{x} + \gamma(x_r - \bar{x}). \quad (23)$$

On the other hand, if $f(x_n) \leq f(x_r) < f(x_{n+1})$, inside contraction is performed to generate a point x_{cc} as follows

$$x_{cc} := \bar{x} - \gamma(\bar{x} - x_{n+1}). \quad (24)$$

If $f(x_{cc}) < f(x_{n+1})$, replace x_{n+1} by x_{cc} and terminate the iteration; otherwise, perform shrinkage.

Shrinkage. The last transformation which is applied on the simplex is aimed to reduce the size of a simplex as it converges towards the global optimal solution. In this regard, shrinkage is performed on all vertices except x_1 , according to the expression

$$v_i := x_1 + \delta(x_i - x_1). \quad (25)$$

In Eqs. (21) – (25) the following real valued parameters are provided α , β , γ and δ which control each respecting operation. For 2D optimization problem these parameters can be set as $\alpha = 1$, $\beta = 2$, $\gamma = 0.5$, and $\delta = 0.5$ [6].

The iterative process of applying the above transformations is repeated until the points of the simplex become close to the optimal solution, i.e.

$$\frac{1}{n+1} \sum_{i=1}^{n+1} \|x_i^{(k)} - x_i^{(k+1)}\|^2 \leq \varepsilon, \quad (26)$$

where $x_i^{(k)}$ and $x_i^{(k+1)}$ are the vertices in iteration k and $k+1$, respectively and ε is an arbitrarily small positive number.

5. SIMULATION RESULTS

The numerical simulation results are shown in this chapter to validate the improvements in the optimum design solution utilizing the proposed GA-NM technique.

The optimization procedure that takes into considerations the minimization of gearbox mass and maximization of efficiency is applied to an example planetary gear set. The planetary gear set in this example is made up of a floating sun gear and three evenly spaced planetary gears, with the internal gear permanently attached to the housing. Table 1 shows the essential design characteristics of the planetary gearbox under consideration.

Table 1. Parameters of the planetary gear set used in this paper

Parameters	Symbol	Value
Input Power [kW]	P_a	200
Input speed [rpm]	n_a	2750
Pressure angle [degree]	α_n	20
Gear material	18CrNi8	
Gear surface Roughness [μm]	R_a	0.8
Factor of safety against bending	$S_{F\min}$	1.2
Factor of safety against pitting	$S_{H\min}$	1.25
Number of planet gears	n_{pg}	3

Due to conflicting objectives, the solution to the MOO problem is a Pareto set. To compare a single solution to the reference values, the ideal solution must be identified. Ideal solutions are best for each unique objective, independent of other objective functions. Because the ideal solution doesn't exist in the Pareto set, it's estimated from the Pareto frontier's objective values. Compromise solutions to the MOO issue are found as the Pareto curve cosssets to the ideal solution, where Euclidian distance is used to measure proximity.

Furthermore, in aircraft applications, the minimizing of the planetary gearbox's volume, and hence its mass, is

critical. The mentioned MOO issue has been carried out in this respect, with the objectives being the volume of the gears in the gearbox and the power loss of the planetary gear set. The obtained Pareto curves for this scenario are shown in Figure 4.

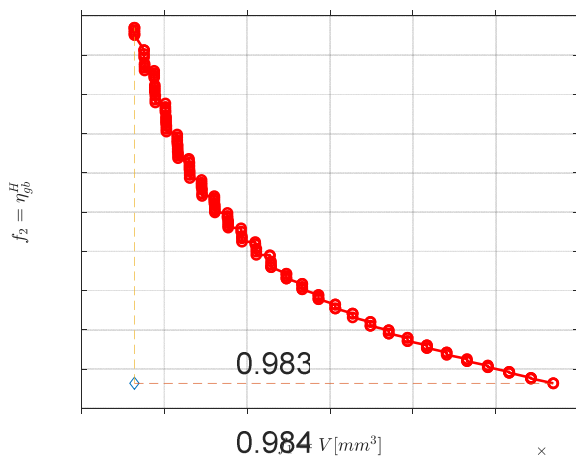


Figure 4. 2D illustration of the Pareto frontier for planetary gearbox volume and efficiency

From the results depicted in Fig. 4 it can be observed that the considered objective functions are conflicting. Analyzing the obtained Pareto set, starting from the left to right and moving along the Pareto set it can be observed that with the increase in the value of gearbox volume, leads to simultaneous decrease in the value of the planetary gearbox efficiency, and vice versa. Therefore, the ideal solution is determined as $[5.175 \times 10^{10} \quad 0.9924]$ while the compromise solution is $[5.314 \times 10^{10} \quad 0.9892]$. Compared to the industrial gearbox reference [10] it leads to the 10% reduction in gearbox weight and improvement of 0,25% in efficiency. The observations made on the numerical simulations show that the proposed gear optimization procedure based on hybrid GA-NM algorithm can achieve better design solutions, compared to the traditional algorithms, however with the cost of higher number of iterations.

6. CONCLUSION

This paper considers the topic of developing a non-linear optimization model for determining the optimal parameters of a planetary gearbox, which is solved using a metaheuristic optimization technique. To identify appropriate planetary gearbox parameters, complex multimodal objective functions are minimized, which are conflicting problems. In the paper, a hybrid metaheuristic algorithm is proposed to address this challenging optimization problem. The proposed metaheuristic method combines the GA with local-search Nelder-Mead. In the considered multiobjective optimization problem, the appropriate objectives are developed, such as weight minimization of the gearbox and maximization of gearbox efficiency. The ideal planetary gearbox settings obtained using the proposed metaheuristic method are compared

with results from well-known algorithms. The proposed optimization method improves planetary gearbox performance compared to well-known algorithms. In the future, work can be done on making more objective functions and putting them into more complicated multi-objective models to add to the optimization problem and make the solution more accurate.

AKNOWLEDGMENT

The research of M. Sedak was supported by the Serbian Ministry of Education and Science under Grant No. TR35006. The research of M. Rosić was supported by the Serbian Ministry of Education and Science under Grant TR35029.

References

- [1] Nutakor, C., Kłodowski, A., Sopenan, J., Mikkola, A. and Pedrero, J.I., 2017. Planetary gear sets power loss modeling: Application to wind turbines. *Tribology International*, 105, pp.42-54.
- [2] Arnaudov, K. and Karaivanov, D.P., 2019. *Planetary gear trains*. CRC Press.
- [3] LancasA Kahraman, DR Hilty, and A Singh. An experimental investigation of spin power losses of a planetary gear set. *Mechanism and Machine Theory*, 86:48–61, 2015.
- [4] C Nutakor, A Klodowski, A Mikkola, and J Sopenan. Simulation model of power losses for sun and planet gear pair used in a wind turbine gearbox. In *The 14th IFToMM World Congress, Taipei, Taiwan*, pages 25–30, 2015.
- [5] Mendi, F., Başkal, T., Boran, K. and Boran, F.E., 2010. Optimization of module, shaft diameter and rolling bearing for spur gear through genetic algorithm. *Expert Systems with Applications*, 37(12), pp.8058-8064.
- [6] Maputi, E.S. and Arora, R., 2020. Multi-objective optimization of a 2-stage spur gearbox using NSGA-II and decision-making methods. *Journal of the Brazilian Society of Mechanical Sciences and Engineering*, 42(9), pp.1-22.
- [7] Miler, D., Žeželj, D., Lončar, A. and Vučković, K., 2018. Multi-objective spur gear pair optimization focused on volume and efficiency. *Mechanism and Machine Theory*, 125, pp.185-195.
- [8] Datta, R. and Deb, K. eds., 2014. *Evolutionary constrained optimization*. Springer.
- [9] Gao, F., Lixing H., "Implementing the Nelder-Mead simplex algorithm with adaptive parameters", *Computational Optimization and Applications*, 51 (2012) 259-277.
- [10] Standard, A.G.M.A., 2006. Design manual for enclosed epicyclic gear drives. *Alexandria, VA: American Gear Manufacturers Association*, pp.1-104.



APPLICATION OF DRONES WITH ARTIFICIAL INTELLIGENCE FOR MILITARY PURPOSES

ALEKSANDAR PETROVSKI

University “Goce Delchev” - Shtip, Military academy “General Mihailo Apostolski”, Skopje,
aleksopetrovski@gmail.com

MARKO RADOVANOVIC

University of defence, Military academy, Belgrade, markoradovanovicgdb@yahoo.com

ANER BEHLIC

University “Goce Delchev” - Shtip, Military academy “General Mihailo Apostolski”, Skopje,
kadet.behlic.aner@gmail.com

Abstract: *One does not have to look far to see how Artificial Intelligence (AI) – the ability of machines to perform tasks that typically require human intelligence – is transforming the international security environment in which all involved security forces operates. Due to its cross-cutting nature, AI will pose a broad set of international security challenges, affecting both traditional military capabilities and the realm of hybrid threats, and will likewise provide new opportunities to respond to them. AI will have an impact on all of core tasks of every collective defense, crisis management, and cooperative security systems. With new opportunities, risks, and threats to prosperity and security at stake, the promise and peril associated with this foundational technology are too vast for any single actor to manage alone. As a result, cooperation is inherently needed to equally mitigate international security risks, as well as to capitalize on the technology’s potential to transform enterprise functions, mission support, and operations.*

The aim of the paper is to present drones that learn on their own, i.e., that possess artificial intelligence, and which can be used for military purposes. The paper presents the possibility of autonomous use of drones with artificial intelligence in combat and non - combat operations of the army. Drones supported by GIS, C5IRS (command, control, computers, communications, cyber-defense (C5), intelligence, surveillance, and reconnaissance (ISR) and AI will give significantly advantage on the ground, because they can operate alone and will learn in line with the ground situation. With the fusion of human, information, and physical elements increasingly determining decisive advantage in the battlespace, interoperability becomes even more essential.

Keywords: Drone, UAV, Artificial Intelligence, GIS, C5IRS, Security, YOLOv5.

1. INTRODUCTION

Modern combat operations require the use of the most sophisticated combat means in order to efficiently perform the assigned tasks. The use of unmanned aerial vehicles is an indispensable segment of modern combat operations. Due to its versatile use and different capabilities, it provides a wide range of capabilities to units equipped with this type of combat equipment. By applying unmanned aerial vehicles integrated into the C5IRS system, it is possible to have a real-time image from the battlefield, which gives the decision maker the possibility of timely and efficient command of forces in the operation. Modern types of unmanned aerial vehicles are used in modern combat operations, from commercial to armed unmanned aerial vehicles. Both foreign and domestic authors have dealt with this topic. Milić et al. analyze the possibility of using drones in operations in urban environments.[1] Radovanovic et al. (2020) shows the possibility of using civilian drones in the protection and monitoring of the land security zone. [2] Adamski analyzes the effectiveness of UCAVs used in modern armed conflicts. [4] Jović analyzes the combat use of

drones in a counter-terrorist operation. [5] Petrovski and Radovanović analyze the use of drones in cooperation with the C5IRS system for the needs of the army.[6] Ilić and Tomašević analyze the impact of the Nagorno-Krabah conflict on the perception of combat drones.[7] Radovanovic et al. analyzes the possibility of implementing drones in mortar units in order to increase the efficiency of fire support units by applying a fire management system in cooperation with the C4IRS system.[8] Bares performs interoperability modeling for the C4IRS system in a collective security system.[9] Petrovski et al. analyzes the application of GIS in cooperation with the C5IRS system in geography for the needs of the military.[10] Radovanovic et al. analyzes the selection of UAVs for the needs of military and police tactical units using the fuzzy AHP - VIKOR model of multicriteria decision making.[11] Žnidaršič et al. shows several types of drones and anti-drone means for implementation in the units of the Serbian Army.[12] Petrovski and Toshevski present the application of GIS in geo-reconnaissance and C5IRS for military purposes. [13]

2. DEFINITION AND CLASSIFICATION OF UNMANNED AIRCRAFT

So far, there is no generally accepted definition of unmanned aerial vehicles as well as their classification, so the European Association of Unmanned Vehicles Systems - EUROUVS has defined the classification of unmanned aerial vehicles in relation to purpose flight altitude, flight duration, speed, Maximum takeoff weight - MTOW, aircraft dimensions, signal range, etc. [14]

According to the model of control and management of unmanned aerial vehicles, they are divided into autonomous systems, self-control systems, radar or radio beam control systems, telecommand control systems and combined systems (autonomous, non-autonomous). In relation to flight altitude, take-off weight and maximum range, drones are divided into four categories. [14][15]

- Category 1 (weight up to 1 kg, flight altitude up to 50 m, AGL - Above Ground Level, range up to 150 m);
- Category 2 (mass greater than 1 kg to 5 kg, flight altitude up to 150 m AGL, range up to 500 m);
- Category 3 (mass greater than 5 kg to 20 kg, flight altitude up to 300 m AGL, range up to 2500 m);
- Category 4 (mass greater than 20 kg, flight altitude greater than 300 m AGL, range greater than 2500 m)

Petrovski and Radovanović defined the terms drone and UAV and their classification (figure 1). [6] The term UAV has a broad meaning, it means with a motor that is remotely controlled by the operator or it is a means that has a certain level of autonomy (control is done using communication software, and often uses artificial intelligence and different types of sensors), which they can be used once or repeatedly and can carry deadly or non-lethal cargo, transmit data in real time, using as a WiFi station and ect. It is a synthesis of the means and devices necessary to manage it. They differ in purpose, construction characteristics (shape, dimensions, weight, payload, maximum flight altitude, maximum range, flight time, speed, etc.) of the environment in which they are used, the energy source with which they are driven. Depending on the purpose, they can be used in different environments such as land, water, air and space, and a wide range of possibilities has created a condition for application in defense and security (for the needs of the army and police - original purpose). agriculture, construction, traffic, trade, communication, science, medicine, research, architecture, video and photography, geology, forestry, mining, oceanography, environmental management, sports, mapping, etc. The term drone is more general than the term unmanned aerial vehicle, because all unmanned aerial vehicles can be called drones, while a drone does not necessarily have to be an unmanned aerial vehicle. [6]

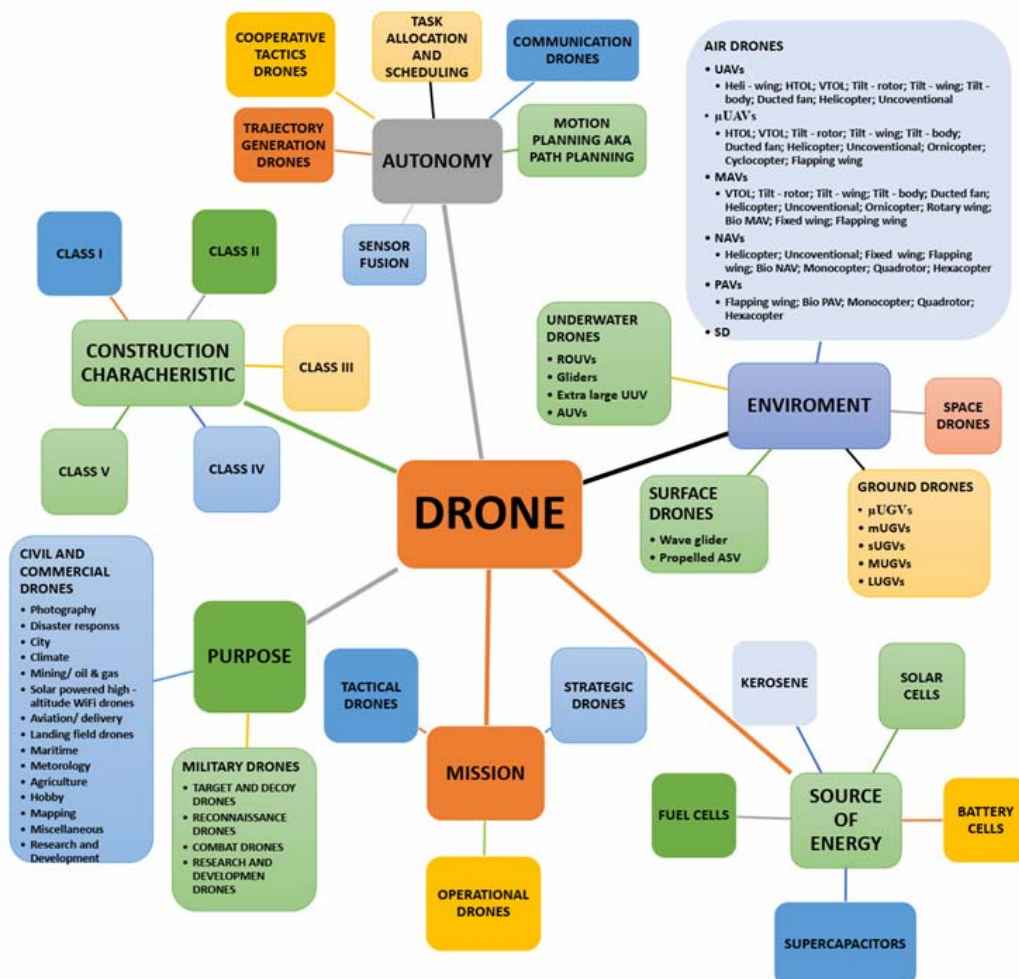


Figure 1: Classification of drones

Based on the classification of unmanned aerial vehicles, it is concluded that the characteristics of unmanned aerial vehicles usually depend on their purpose. It is necessary to analyze the tactical and technical characteristics of unmanned aerial vehicles in order to consider their possibility of use in modern combat operations.

Military use of unmanned aerial vehicles can be classified into three groups: naval, land and air use, while for civilian purposes it can be used in various areas of human activity, such as in geodesy (photogrammetry), agriculture, industrial production, civil protection, disaster management, critical infrastructure surveillance, environmental protection, police surveillance, protection and rescue of people, intelligence and security services, journalism, commercial activities and leisure.

3. APPLICATION OF DRONES WITH ARTIFICIAL INTELLIGENCE FOR MILITARY PURPOSES

Drones have improved military capabilities around the world in many ways. It will also continue to change military warfare through the following: The Use of Military Drones: The Impact on Land Forces and Legal Implications Command and Control –Drones can relay crucial information on enemy movements, locations, and positions of strategic targets. This information allows commanders to be more efficient and make better decisions when in the field.

Drone technology itself is a relatively new area of military technology, but military engineers took to combining drones with artificial intelligence rather quickly to create a product that in some cases might be comparable to the performance of human reconnaissance teams. Shield.AI, AeroVironment, and Lockheed Martin all showcase how military defense contractors are combining current computer vision technology and image recognition with drones to solve military problems without the need of endangering human life. Shield AI's drone can purportedly navigate unknown lands without the need for GPS tracking. Such a UAV could give military troops the capability to collect data that could allow them to move faster and check if they are being pursued during tactical reconnaissance, tracking, combat assessment, and cartographic missions. Drones could allow operators to make decisions without being concerned that they might be ambushed from the rear, for example.

Implementing artificial intelligence for drones is a combination of mechanical devices, navigational instruments, and machine vision. The AI behind the drone

needs to be trained using a supervised learning process. I think that this will be much harder to achieve than you can imagine as combat drone technology is in my opinion capable of being the most lethal and effective tools ever created for intermediate & close combat scenarios.

The Army's office for countering small drones sees artificial intelligence and machine learning as key technologies for defeating enemy systems, service officials said Oct. 15. And drone swarms could be used for simultaneous, multi-directional attacks in ways that could overwhelm human defenders. The aerospace and defence industry initially made drones for counterinsurgency and defence, which have proven helpful in these environments. Today, many Military Warfare industries develop drone technology integrated into more military programs worldwide. They provide many benefits and advantages that make them extremely useful for different roles. Military drones have come to revolutionize warfare. They are roving on land, streaking through the skies, and diving under the seas. Since their creation, more than fifty years ago, drones have constantly evolved to the present, becoming one of the main artificial intelligences (AI) weapons, integrated into military forces throughout the world. As a result, more military forces are looking to use drones to increase their combat and surveillance capacity.

Military advantages are in autonomous weapons systems act as a force multiplier. That is, fewer warfighters are needed for a given mission, and the efficacy of each warfighter is greater. Next, advocates credit autonomous weapons systems with expanding the battlefield, allowing combat to reach into areas that were previously inaccessible. Finally, autonomous weapons systems can reduce casualties by removing human warfighters from dangerous missions.

4. YOLOV5 METHOD FOR ENHANCED MILITARY DRONE SURVEILLANCE WITH AI SOFTWARE CAPABILITIES

This article covers real-world model incorporate in either drones or the AI software behind them: In this article, we'll look at several military drones and UAVs with AI capabilities. There are a variety of use cases for AI when it comes to drone technology. The military seems to commonly apply AI for allowing its drones to fly on their own, which requires machine vision.

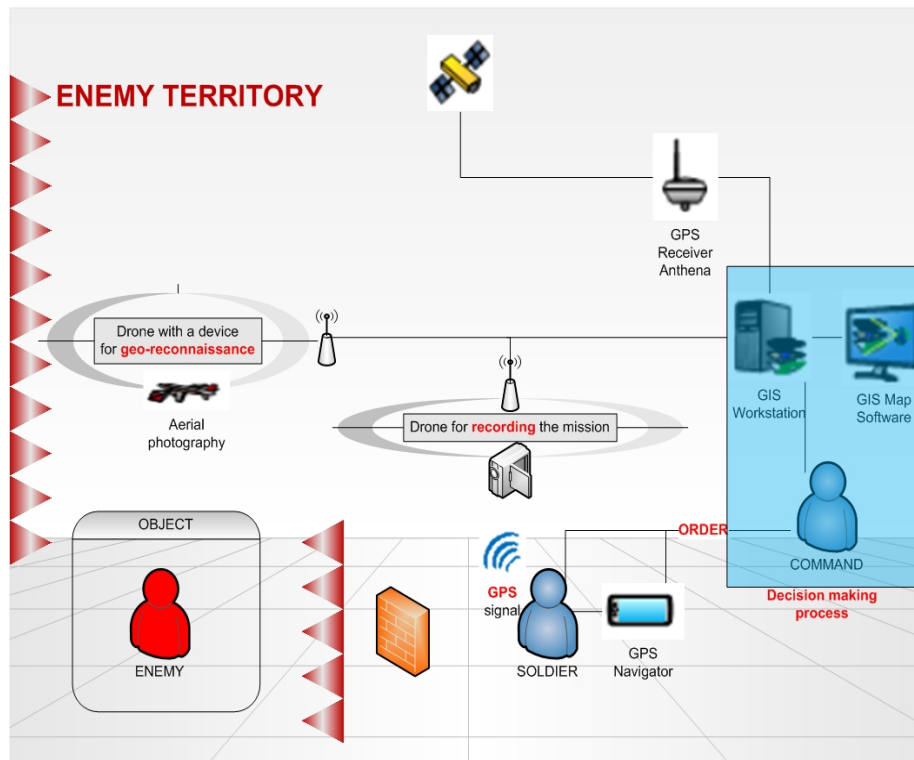


Figure 2: Model of Geo-reconnaissance and commanding (GRC) information system in UAV supported with C4IRS systems and AI (Petrovski A. and Mihajlo T. defined this model - figure 2)

4.1. YOLOv5 Method for enhanced military drone surveillance

The proposed framework aims to detect objects of critical military importance based on the images received from the video stream of military surveillance drones. The actions will be taken depending on the obtained result. Figure 3 summarizes the suggested methodology of this paper.

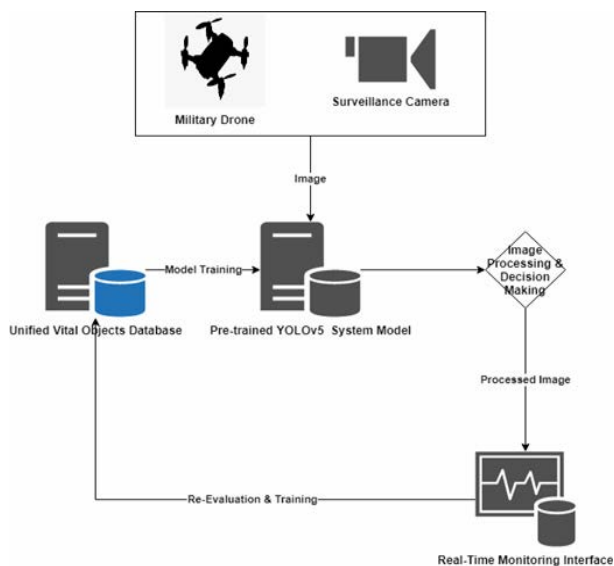


Figure 3: Overview of the Methodology

Firstly, a unified Vital Objects Database is created by using verified images of objects that are critical for military surveillance such as weapons, bunkers, military buildings, vehicles, tanks, and artillery pieces, collected

from various internet and local sources. Furthermore, upon that dataset a YOLOv5 model is trained and evaluated. A Surveillance Camera is set up on a military surveillance drone, which is connected to the System Model. The camera forwards real-time video through the system model which processes the data in real time. Moreover, the processed image is projected on the Real-Time Monitoring Interface which shows the result of image processing, including alarms for detection of vital military objects. False positives and vital military objects which weren't detected by the system but self-identified by the human operator, are captured and further forwarded to the unified Vital Objects Database, where they are re-evaluated and used for further training of the system.

This paper proposes a real-time vital Military Objects detection system based on Convolution Neural Network using the YOLOv5 (You Only Look Once) framework. The main contributions of this approach include:

- 1) The proposed system can be implemented easily on already existing surveillance drones
- 2) It detects vital military objects with high accuracy from large distances.
- 3) The software used for development is free and open source.
- 4) A unified large dataset for vital military objects including weapons, vehicles, tanks, buildings, bunkers and artillery pieces, with various scenarios and conditions.
- 5) It aids military commanders and personnel in decision making, tracking, and identification of vital military objects.

4.2. YOLOv5 Approach for Vital Military Objects Detection

YOLO is based on Convolution Neural Network (CNN) and represents a very fast end-to-end object detection algorithm. [16] Continuous improvements have made it achieve top performances on two official object detection datasets: Pascal VOC (visual object classes) [17] and Microsoft COCO (common objects in context). [18]

The network architecture of YOLOv5 is shown in Figure 4. There are three reasons why YOLOv5 is chosen as the main method for training the system model. Firstly, YOLOv5 incorporated cross stage partial network (CSPNet) [18] [19] into Darknet, creating CSPDarknet as its backbone. CSPNet solves the problems of repeated gradient information in large-scale backbones, and integrates the gradient changes into the feature map, thereby decreasing the parameters and FLOPS (floating-point operations per second) of model, which not only ensures the inference speed and accuracy, but also reduces the model size. In

military surveillance task, detection speed and accuracy are imperative, and compact model size also determines its inference efficiency on resource-poor edge devices. Secondly, the YOLOv5 applied path aggregation network (PANet) [19] as its neck to boost information flow. PANet adopts a new feature pyramid network (FPN) structure with enhanced bottom-up path, which improves the propagation of low-level features. At the same time, adaptive feature pooling, which links feature grid and all feature levels, is used to make useful information in each feature level propagate directly to following subnetwork. PANet improves the utilization of accurate localization signals in lower layers, which can obviously enhance the location accuracy of the object. Thirdly, the head of YOLOv5, namely the YOLO layer, generates 3 different sizes (18×18 , 36×36 , 72×72) of feature maps to achieve multi-scale prediction [20], enabling the model to handle small, medium, and big objects.

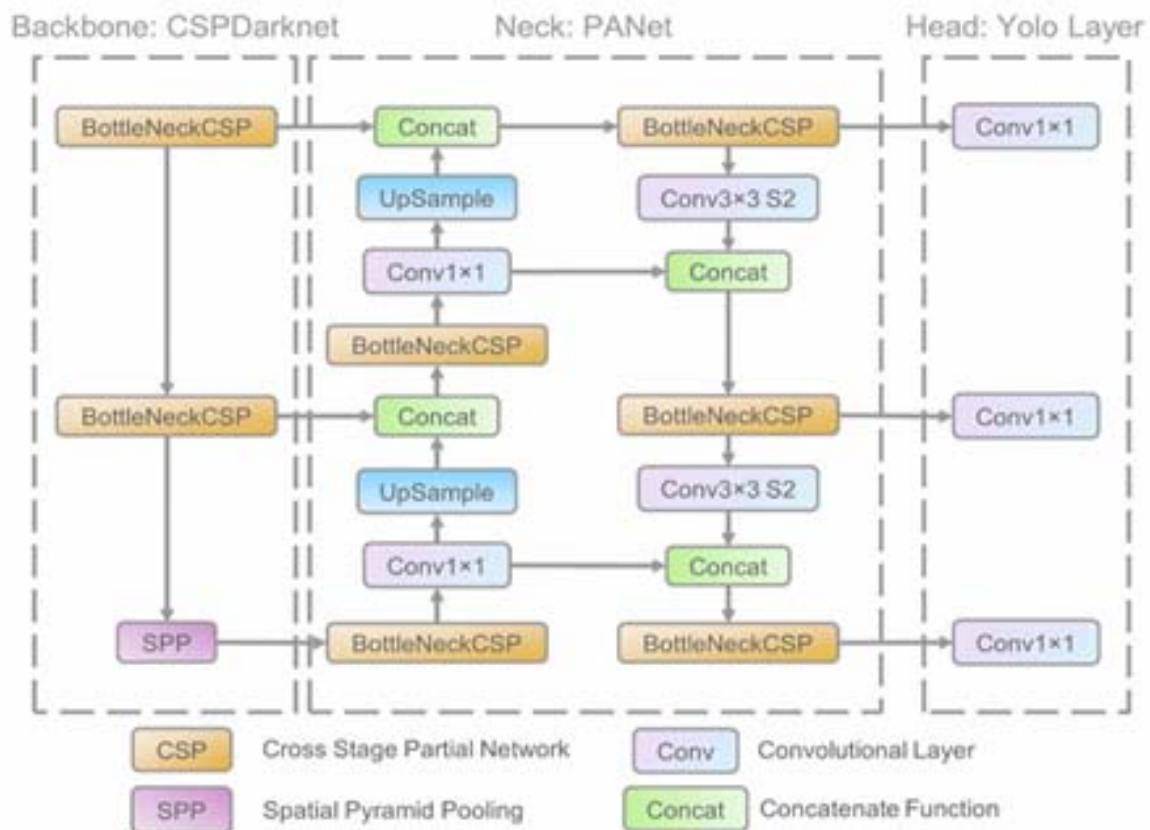


Figure 4: The network architecture of YOLOv5. It consists of three parts: (1) Backbone: CSPDarknet, (2) Neck: PANet, and (3) Head: YOLO Layer. The data are first input to CSPDarknet for feature extraction, and then fed to PANet for feature fusion. Finally, YOLO Layer outputs detection results (class, score, location, size) [22]

In the YOLO method, the input images are only seen once through the neural network, and it predicts the detected object in the image. It works by dividing the input image into different grids based on predefined grid size and then predicts the probability of the desired object in each grid. It predicts all the classes and the object bounding that are in the image in one run of the Algorithm.[23]

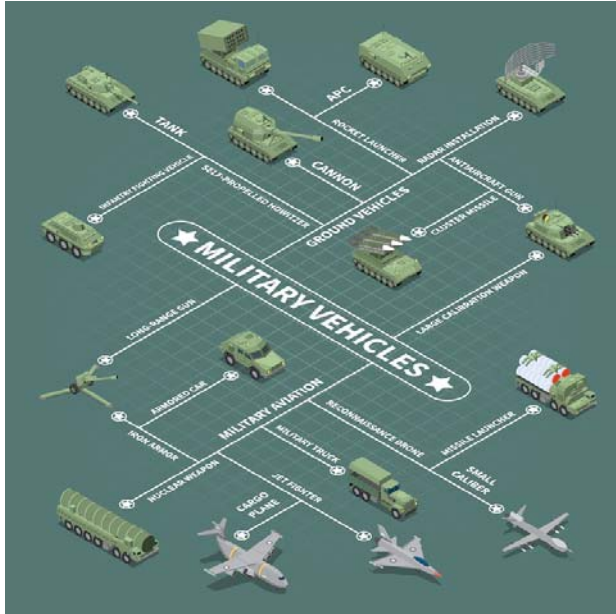


Figure 5: Overview of military vehicles that can be recognize with drone pre-input images in data bases.

The proposed YOLOv5 based (pre-trained) solution is extremely lightweight and fast to recognize the critical objects of military importance. Good accuracy and the fps are two important things to consider when working on real-time surveillance and data gathering.

4.3. Model Training Process & Dataset

To train, validate and evaluate the model a customized dataset was built. The finalized dataset contains around 10000 images of military trucks, tanks, that were collected from publicly available datasets, Google images, and local sources as presented in Table 1.

Table 1. Distribution of images in the dataset

Dataset type	Size & Type	Source
Military Trucks, Tanks, APC	6772 images	Military Vehicles – Mendeley Data[23]
Military Tanks	1078 images	Military Tanks – Kaggle[23]
Military Artillery, Tanks, MRL Systems, Trucks	1000 images	Moving and Stationary Target Acquisition and Recognition (MSTAR) Dataset[23]
Stationary Military Equipment, Artillery, Command posts & fire stations	2000 images & 20 videos	Local Sources

The images cover a verity of scenarios Military Targets in various scenarios and terrain including day and night

time, forests, desert, and urban, as seen in Figure 6. However, even then the dataset is severally limited, therefore, we included several videos with different Military Targets in different conditions such as size, shape and color. In order to successfully adopt and train the dataset in YOLOv5 the dataset itself was assigned labels and the annotating bounding boxes. The value of the annotating box coordinate in each image is then normalized between 0-1. This process was carried out using Roboflow [23], which makes it possible to annotate and make data labels in the desired format. Furthermore, the dataset is carefully split into 3 different categories for training, validation and testing. Additionally, by carefully assigning the images to each category, we avoided a biased model by using data with a similar number of images for each class which forms a balanced dataset.

First and foremost, in the model training process we fine-tune the YOLOv5m model which is already pre-trained on the COCO data set. Furthermore, Transfer learning was used to train on the unified dataset. Moreover, various augmentation processes such as HSV, color spacing, mosaic, image scaling were applied. The hyperparameters that are fine-tuned are used here, such as SGD optimizer, 0.01 learning rate, 0.0005 weight decay and then finally 600 epochs on batch size 32.

The model was built using Google Collaboratory resources to process the dataset.



Figure 6: Training Process on the Unified Dataset, annotating Military Targets by class (Tanks, APC's, Artillery, MRL Systems)

5. RESULTS AND DISCUSSION

To evaluate the performance of the proposed system, the trained model was tested in different environments including forests, mountains, open fields, etc. The results are performed with a confidence threshold of 0.4. Initially, when performed on the handpicked test data

from the unified dataset, we achieved on average 0.922 $\text{map}@0.5$. Furthermore, From the displayed confusion matrix in Figure 7 it can be seen that the models can label maximum of the data quite correctly Also from Figure 9 it can be seen that the model can confirm whether there is a Military Target on the image quite correctly.

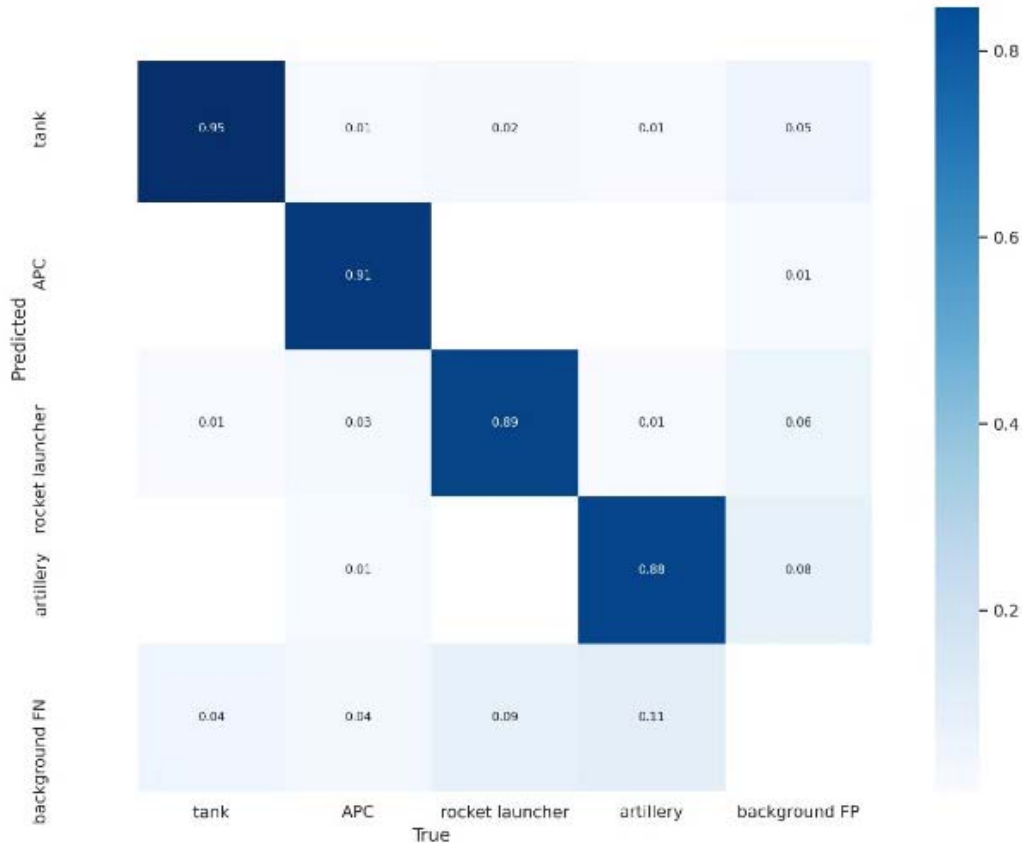


Figure 7: Confusion Matrix of the model

This obtained value and prediction results shown on performance graphs in Figure 8 prove that there is a pretty good potential to use the YOLOv5 algorithm to detect Military Targets in real-time during drone surveillance.

The confidence value of the Military Targets the model recognizes is quite high also. Moreover, we can see the performance of the suggested model applied to validation data through performance graphs in Figure 8.

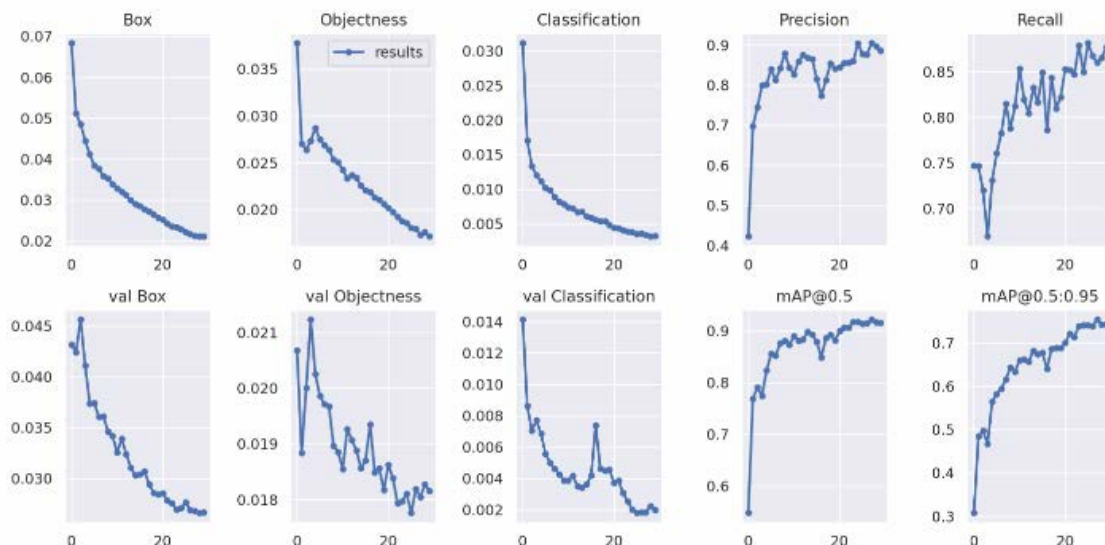


Figure 8: Result Graphs obtained from model training and validation

The model is lightweight and fast enough to deploy. It can be incorporated with in-built capturing tools, in this case, Surveillance Cameras mounted on drones, and predict recognition in almost real time with minimum delays.



Figure 9a: Examples of predicted output's



Figure 9b: Examples of predicted output's

6. CONCLUSION

The use of unmanned aerial vehicles equipped with AI and modern technical devices (high resolution cameras, infrared and thermal cameras, microphones, various types of sensors, guided and non-guided missiles and other accessories) integrated into the C5IRS system significantly increases the efficiency of units engaged in combat operations. The use of this sophisticated technology enables timely and accurate information about the event in real time, as well as the destruction of the target without risk to humanity, while transmitting the situation to the battlefield command center. Unmanned aerial vehicles can still be used to deliver medical supplies and other necessary combat and non-combat equipment to units in the area of operation.

The use of unmanned aerial vehicles in combat operations, regardless of limitations, increases the efficiency and effectiveness of the units engaged in the operation, and also increases the protection and reduces the risk to the engaged personnel. Based on the tactical and technical characteristics of unmanned aerial vehicles, it is possible to realize various tasks.

Today's environment also requires the collective capabilities and efforts of multiple organizations. Unfortunately, traditional C4ISR systems weren't built with interoperability in mind—in the past, they were designed to meet mission-specific requirements and to solve a particular set of problems facing an organization.

However, it is difficult to say that the proposed model does not have any shortcomings. The model may cause errors and consider, non-military vehicle, and other military like objects, as real targets. These issues mainly increase as the distance of the target increases, which the camera then captures in an unclear image, which confuses the model. However, longer training times, more concrete and larger datasets would highly likely yield a good result in this process and eliminate most of the false positives.

Further research should be focused on the integration of the modern C6ISR system (combat command) to the combat systems of the army and the advantages that the mentioned system provides to units during the execution of a modern combat operation in a different environment.

ACKNOWLEDGEMENTS

This scientific work in same parts was written as a result of unifying the results of research in two scientific research projects funded by the Ministry of Defense of the Republic of Serbia, under numbers VA-DH/1/21-23 „Uticaj savremenog okruženja na izvođenje borbenih dejstava u urbanim sredinama” (*Influence of contemporary environment on the conduct of combat activities in urban spaces*), i VA-DH/1/22-24 „Model upravljanja razvojem sposobnosti sistema odbrane” (*Management model for defense system capability development*).

References

- [1] MILIĆ, A., RANĐELOVIĆ, A., RADOVANOVIĆ, M.: *Use of drones in operations in the urban environment*, 5th International Scientific conference Safety and crisis management – Theory and practise Safety for the future – SecMan 2019, Belgrade: Regional Association for Security, (2019) 124-130.
- [2] RADOVANOVIĆ, M., MILIĆ, A., RANĐELOVIĆ, A.: *Mogućnost upotrebe dronova u zaštiti Kopnene zone bezbednosti*, 15. Međunarodna konferencija rizik i bezbednosni inženjering, Visoka tehnička škola strukovnih studija u Novom Sadu i Fakultet tehničkih nauka, Novi Sad, (2020) 303 - 311.
- [3] ADAMSKI, M.: *Effectiveness analysis of UCAV used in modern military conflicts*, Aviation, 24 (2) (2020).
- [4] JOVIĆ, Ž.: *Combat engagement of drones in USA counterterrorist operations*, Bezbednost, 58(3) (2016) 171-190.
- [5] PETROVSKI, A., RADOVANOVIĆ, M.: *Application of detection reconnaissance technologies use by drones in collaboration with C4IRS for military interested*, Contemporary Macedonian Defence, 21 (40) (2021) 117-126.
- [6] ILIĆ, D., TOMAŠEVIĆ, V.: *The impact of the Nagorno-Karabakh conflict in 2020 on the perception of combat drones*, Serbian Journal of Engineering Management, 6(1) (2021) 9-21.
- [7] RADOVANOVIĆ, M., SAMOPJAN, M., PETROVSKI, A.: *Possibility of Implementation of Drons in Mortar Units in Order to Increase the Efficiency of Fire Support Units*, 24. Međunarodna

- DQM konferencija Upravljanje kvalitetom i pouzdanošću ICDQM -2021, Prijedor, (2021) 307–315.
- [9] BARES, M.: *Interoperability Modeling of the C4ISR Systems*, RTO SCI Symposium on “System Concepts for Integrated Air Defense of Multinational Mobile Crisis Reaction Forces”, held in Valencia, Spain, published in RTO MP-063. (2001) 16-1 – 16-16.
- [10] PETROVSKI, A., TANESKI, N., BOGATINOV, D.: *Geography in Geospatial Intelligence - C4ISR and Cyber Security*, 5th International Scientific conference Safety and crisis management – Theory and practise Safety for the future – SecMan 2019, Belgrade: Regional Association for Security, (2019) 64-72.
- [11] RADOVANOVIĆ, M., PETROVSKI, A., ŽINDRAŠIĆ, V., RANĐELOVIĆ, A.: *Application of the fuzzy AHP -VIKOR hybrid model in the selection of an unmanned aircraft for the needs of tactical units of the armed forces*, Scientific Technical Review, 71(2) (2021) 26-35.
- [12] ŽNIDARŠIĆ, V., RADOVANOVIĆ, M., STEVANOVIĆ, D.: *Modeling the organisational implementation of a drone and counter-drone operator into the Serbian Armed Forces rifle section*, Vojno delo, 72 (3) (2020) 84 -109.
- [13] PETROVSKI, A., TOSHEVSKI, M.: *Gis in Army: Application of GIS in Geo-Reconnaissance And C4IS in Army Purposes*, 2nd International Scientific Conference GEOBALCANICA, Skopje, (2016) 153-160
- [14] AGBEYANGI, A., ODIETE, J., OLORUNLOMERUE, A.: *Review on UAVs used for Aerial Surveillance*, Journal of Multidisciplinary Engineering Science and Technology, 3 (10) (2016) 5713-5719.
- [15] ARJOMANDI, A., AGOSTINO, S., MAMMONE, M.: *Classification of Unmanned Aerial Vehicle*, Report for Mechanical Engineering class, University of Adelaide, Australia, 2006.
- [16] REDMON, J., DIVVALA, S., GIRSHICK, R., FARHADI, A.: *You only look once: Unified, real-time object detection*, in Proceedings of the IEEE conference on computer vision and pattern recognition, (2016) 779-788
- [17] EVERINGHAM, M., ESLAMI, S.A., VAN GOOL, L., WILLIAMS, C.K., WINN, J., ZISSERMAN, A.: *The pascal visual object classes challenge: A retrospective*. International Journal of Computer Vision, 111 (1) (2015) 98–136.
- [18] LIN, T.Y., MAIRE, M., BELONGIE, S., HAYS, J., PERONA, P., RAMANAN, D., DOLLÁR, P., ZITNICK, C.L.: *Microsoft coco: Common objects in context*, In Proceedings of the 13th European Conference on Computer Cision (ECCV 2014), Zurich, Switzerland, (2014) 740–755.
- [19] WANG, C.Y., MARK LIAO, H.Y., WU, Y.H., CHEN, P.Y., HSIEH, J.W., YEH, I.H.: *CSPNet: A new backbone that can enhance learning capability of cnn*, In Proceedings of the IEEE Conference on Computer Vision and Pattern Recognition (CVPR 2020), Washington, DC, USA, (2020) 390–391.
- [20] WANG, K., LIEW, J.H., ZOU, Y., ZHOU, D., FENG, J.: *Panet: Few-shot image semantic segmentation with prototype alignment*, In Proceedings of the IEEE International Conference on Computer Vision (ICCV 2019), Seoul, Korea, (2019) 9197–9206.
- [21] REDMON, J., FARHADI, A.: *Yolov3: An incremental improvement*, arXiv 2018, arXiv:1804.0276
- [22] XU, R., LIN, H., LU, K., CAO, L., LIU, Y.: *A Forest Fire Detection System Based on Ensemble Learning*, Forests, 12 (2) (2021) 217: 1-17.
- [23] REDMON, J., FARHADI, A.: *Yolo9000: better, faster, stronger*, in Proceedings of the IEEE conference on computer vision and pattern recognition, (2017) 7263–7271.
- [24] <https://data.mendeley.com/datasets/njdjkbxdpn/1>
- [25] <https://www.kaggle.com/datasets/antorecepjana/military-tanks-dataset-images>
- [26] <https://www.sdms.afri.af.mil/index.php?collection=master>
- [27] www.roboflow.com



THE PROCEDURE FOR TESTING THE FUNCTIONAL CHARACTERISTICS OF TANK GEARBOXES DEVELOPED ON THE BASIS OF T-72 TANKS

ŽARKO SVILAR

Military Technical Institute, Belgrade, svilarzarko@hotmail.com

OBREN STOJIC

Military Technical Institute, Belgrade, obren88@gmail.com

ŽELJKO BULATOVIĆ

Military Technical Institute, Belgrade, zetonbulat@gmail.com

STOJKO BIOČANIN

Academy of Applied Technical Studies, Belgrade, stojkobiocanin@gmail.com

Abstract: For the purposes of installing new or overhauled tank gearboxes in domestic tanks developed on the basis of the Soviet T-72 tank, it is necessary to inspect their functionality and quality. The inspection is performed at the request of the customer from the Ministry of Defense of the Republic of Serbia, prior to the installation of the gearbox inside the vehicle. This procedure was developed parallel to the development of domestic M-84 and M-84A tanks; it is still relevant and is constantly improved on. The conditions have been defined, a test bench has been assembled and the procedure for functional testing of gearboxes has been standardized in order to verify the compliance with the requirements set in the appropriate Quality Insurance Regulation (Serb. PKP).

Keywords: tank, T-72, M-84, M-84A, Vihor, testing, gearboxes.

1. INTRODUCTION

With the purchase of a license in the 1980s (construction and technical documentation) for a T-72 tank produced in the former USSR, the former Yugoslavia, and later the Republic of Serbia as its legal successor, created a field for the development of quality scientific analysis [1] and theoretical studies related to tank issues [2], and as a scientific support in the education of professional staff and for mass production of tanks for the needs of the armed forces of our country at that time (M-84 and M-84A tanks).

Among the significant technical achievements in this field is the formation of a test bench and the development of a procedure for testing the functional characteristics of gearboxes used in testing new (purchased on the market) or overhauled gearboxes for our T-72, M-84 and M-84A tanks, and for the needs of the Ministry of Defense. Gearboxes (left and right) are tested with the side gears and associated pumps, according to the predefined requirements [3-5]. The purpose of testing new, as well as overhauled gearboxes, is to check their functional characteristics. The introduction of this procedure enabled further development tests, so the significant success in this area was achieved on complex projects of the Vihor tank prototype, development of an electro-hydraulic system for semi-automatic and automatic gear transmissions, Integral power pack "IPG 1200", etc.

Although the foundations of this procedure were laid more than thirty years ago, it is constantly being improved by introducing modern measuring equipment, automatization of the certain testing phases and results recording, etc. These tests are performed in the Laboratory for Vehicle Subsystems of VTI in Kumodraž with a frequency of 4 - 5 gearboxes per year.

2. TESTING PROCEDURE

2.1. General requirements

Gearboxes with side gears and associated pumps (left and right) for T-72, M-84, M-84A and VIHOR tanks can be tested on the test bench. All these gearboxes are identical in external dimensions, with the gearboxes for the VIHOR tank having five transmission gears, while the others have seven transmission gears. With this in mind, it is necessary to install a suitable hydraulic distributor on the test bench, considering the number of gears in the gearbox.

According to [3], when testing the gearbox on the test bench, it is necessary to provide:

- Oil pressure on the hydraulic distributor regulator
- $p=11\pm 0.5$ bar at II, III, IV, V, VI and VII transmission gear (for Vihor at II, III, IV and V gear)
- $p=17\pm 0.5$ bar at I gear and the reverse gear (RG).

d) Temperature of the oil at the gearbox outlet $100 \pm 10^\circ\text{C}$, at the rotational speed of $2060 \pm 50 \text{ min}^{-1}$ at the inlet of the gearbox,

e) Flow of oil for the lubrication of the gearbox of 30 to 42 l/min, while it is allowed to reduce the flow in VI and VII gears (for Vihor in IV and V gears) to 29 l/min,

f) Total oil flow in the hydro system of $70 \pm 10 \text{ l/min}$,

g) Pressure of the lubricant oil is $2^{+0.5} \text{ bar}$. It is allowed to increase the pressure up to 3 bar in VI and VII gears (for Vihor in IV and V gears), while at the same

time the flow of the lubricating oil must be 30 to 42 l/min.

Gearbox testing is performed with the TSZp-8 oil or some other oil applicable for these gearboxes. The technological test mode starts when the oil temperature at the transmission outlet reaches 40°C . The control test mode starts after the end of the technological mode.

Tables 1 and 2 provide the test modes and the maximum permitted power applied to drive the unloaded gearbox in relevant gears, as well as the rotation speed of the gearbox output shaft for M-84 (T-72), M-84A and Vihor tanks [3].

Table 1. Testing modalities for M-84 (T-72) and M-84A tank gearboxes

Mode	Gear transmission	Input shaft rotation speed [rpm]	Operating time in each gear [min]	Maximum power applied to drive the transmission [kW]		Side gear output shaft rotation speed [rpm]	
				Right	Left	Tank M-84 (T-72)	Tank M-84A
1	2	3	4	5	6	7	8
Technological	N-1-2-3-4-5-6-7-RG	1300 ± 50	3	Do not control	Do not control	Do not control	Do not control
Control	N	2060 ± 50	3	15	20	-	-
	1		3	15	20	46 ± 5	50 ± 5
	2		3	15	20	86 ± 9	94 ± 9
	3		3	15	20	108 ± 11	118 ± 11
	4		3	15	20	136 ± 14	148 ± 14
	5		3	16	22	186 ± 19	203 ± 19
	6		3	18	24	258 ± 26	281 ± 26
	7		3	18	24	378 ± 38	412 ± 38
	RG		3	18	24	26 ± 3	29 ± 3

Table 2. Testing modalities for Vihor prototype tank

Mode	Gear transmission	Input shaft rotation speed [rpm]	Operating time in each gear [min]	Maximum power applied to drive the transmission [kW]		Side gear output shaft rotation speed [rpm]
				Right	Left	Tank Vihor
1	2	3	4	5	6	7
Technological	N-1-2-3-4-5-RG	1300 ± 50	3	Do not control	Do not control	Do not control
Control	N	2060 ± 50	3	15	20	-
	1		3	15	20	65 ± 6
	2		3	15	20	101 ± 10
	3		3	15	20	168 ± 17
	4		3	18	24	272 ± 27
	5		3	18	24	412 ± 41
			RG		3	18

The oil leakage in the transmission friction assemblies in each gear must not exceed 2 l/min, provided that per one friction assembly it must not exceed 1 l/min.

Certain transmission stages are achieved by engaging friction assemblies (couplings) in the following order:

- Neutral friction assembly F4
- I friction assemblies F3 i F4
- II friction assemblies F4 i F6
- III friction assemblies F3 i F6
- IV friction assemblies F1 i F4

- V friction assemblies F1 i F3
- VI friction assemblies F2 i F4
- VII friction assemblies F2 i F3
- Reverse gear friction assemblies F3 i F5

2.2. Test bench

The test bench is designed to enable the development and complex functional testing of gearboxes with side gears and associated pumps of the T 72, M 84, M 84A and

VIHOR tanks. Figures 1 and 2 show the test benches for testing the left and right gearboxes. The left gearbox (Figure 1) is tested with its own thrust pump, while the right (Figure 2) is tested with an auxiliary thrust pump. This auxiliary pump provides the required oil flow and pressure to control and lubricate the gearbox. Direction of rotation of the transmission input shaft, viewed from the side of the drive, when testing the left gearbox is clockwise, and when testing the right gearbox, the direction is opposite.

Test benches consist of the following components:

- propulsion groups,
- housings with adapters,
- gearshift steering mechanism,

- hydraulic installations with auxiliary pump,
- oil cooling system and
- control and measuring devices.

2.2.1. Propulsion group

The propulsion group consists of a 75 kW electric motor (1), manufactured by SEVER, with a variable flow hydraulic pump F1V.107.Ma.g - REXROTH HYDROMATIK (2) and a variable flow hydraulic motor AGV.80.Ma - REXROTH HYDROMATIK (3). These hydraulic components make it possible to achieve the desired number of rotations at the gearbox inlet.

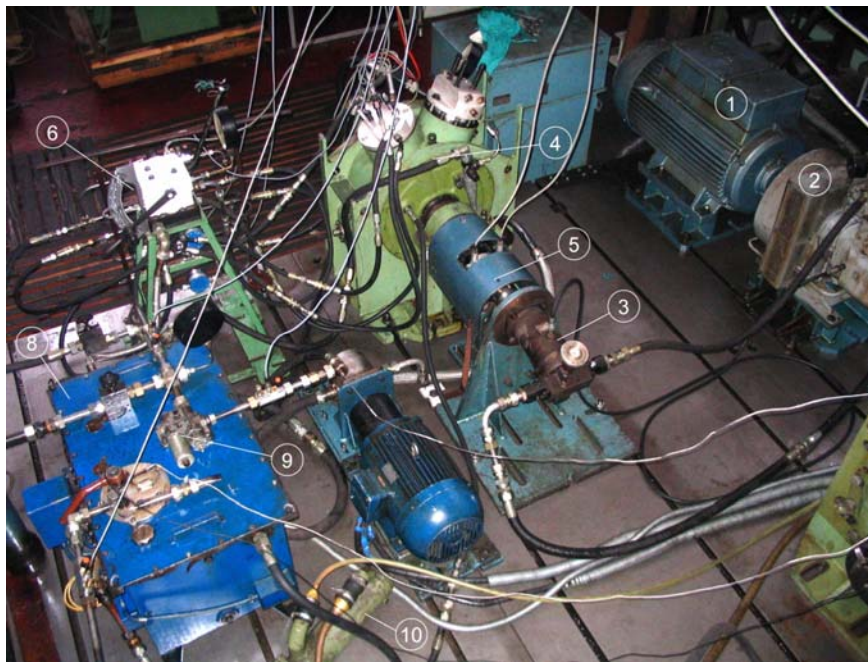


Figure 1. A test bench for the left gearbox inspection

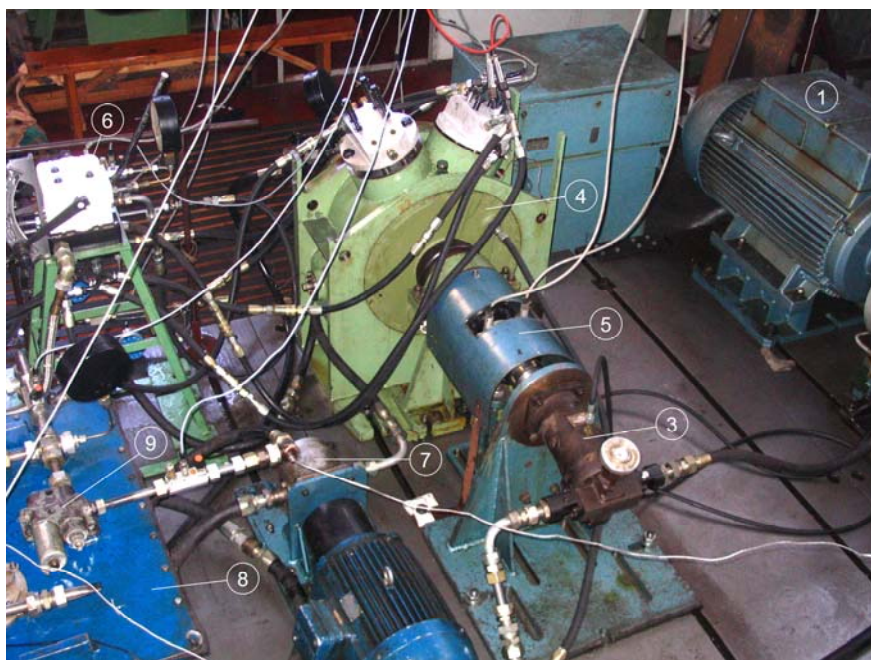


Figure 2. A test bench for the right gearbox inspection

2.2.2. Housing with adapters

Housing solution with adapters (4), enables the conducting of tests of the left and right gearbox. The adapters are used to drain the oil, which comes from the hydraulic distributor, into the appropriate friction assemblies of the gearbox, depending on the engaged transmission gear. The connection of the gearbox with the hydraulic motor is realized through the gear wheel couplings and a torsion dynamometer (5).

2.2.3. Mechanism for the gear shift control

The gearshift is controlled manually, from the command desk (6), via the lever system. The right hydraulic distributor, utilized from the serial production, is located on the command section.

2.2.4. Hydraulic installation with the auxiliary pump

The hydraulic installation consists of an auxiliary gear pump (7) with a capacity of 160 l/min, a reservoir (8) with a volume of app.120 l with a valve device (9) and a piping system. The auxiliary pump provides pressure in the steering system only when testing the right gearbox (Figure 2).

2.2.5. Oil cooling system

The heated oil from the gearbox housing, which is pumped by its own gear pump, is cooled via the cooler (10) by circulating the flowing water from the water supply network back to the reservoir.

2.2.6. Control and measuring devices

Control and measuring devices are used for control and registration of parameters, when testing gearboxes, defined in [3]. During testing on the test bench, the following parameters are measured and recorded (Figures 3 and 4):

- torque and rotational speed on the input shaft of the gearbox (M_u , n_u),
- pressures in the friction assemblies of the gearbox (p_1 , p_2 , p_3 , p_4 , p_5 and p_6),
- oil pressure in the control system (p_u)
- oil pressure in the gearbox lubrication system (p_p)
- total oil flow in the hydraulic system (Q_u),
- gearbox lubrication oil flow (Q_p)
- oil flows (leakages) in the friction assemblies of the gearbox (Q_1 , Q_2 , Q_3 , Q_4 , Q_5 i Q_6),
- oil temperature at gearbox inlet (t).

In addition to the above, the parameters that could not be shown on the hydraulic diagrams are also measured (Figures 3 and 4):

- side gear output shaft rotational speed (n_i),
- oil temperature at gearbox outlet (t_i).

To measure the input parameters on the gearbox, on the test bench, a torsionmeter from the company HBM, T30FN range 2000Nm, 3000 min^{-1} is used. The HBM MA1

sensor-inductive encoder and DV2556 preamplifier are used to generate the output speed signal. As a torque amplifier, the MD3555 amplifier is used, and for the rotational speed the N3556, as well as the digital indicator DA3418.

The pressures in the friction assemblies are measured by the pressure transmitters with measuring tapes from HBM Company P4AK and KWS 3082 amplifiers, as well as the digital indicator DA3418. The remaining pressures in the system are measured using the manometers with an elastic measuring element from HAENNI Company. To measure the flow, except for leakages, HDT RE2 turbine flow meters are used, along with the Q300 indicating instruments. For measuring the leakages, HDT, GFM-5 volumetric flow sensors with a range of up to 5 l/min are used, together with SEG1060 indicating instruments. Type J sensors and a Fluke 2190A thermometer are used to measure temperatures.

2.3. Hydraulic scheme of the test bench

Figures 3 and 4 show the hydraulic diagrams of the test bench when testing the left and right gearboxes. The labels on the figures are: EM - electric propulsion motor; HP - hydraulic pump; HM hydraulic motor; M - tested gearbox; RM - hydraulic distributor (distribution mechanism); VU - valve device; R - oil reservoir; PP - auxiliary oil pump and F1, F2, F3, F4, F5 and F6 - friction assemblies in the gearbox.

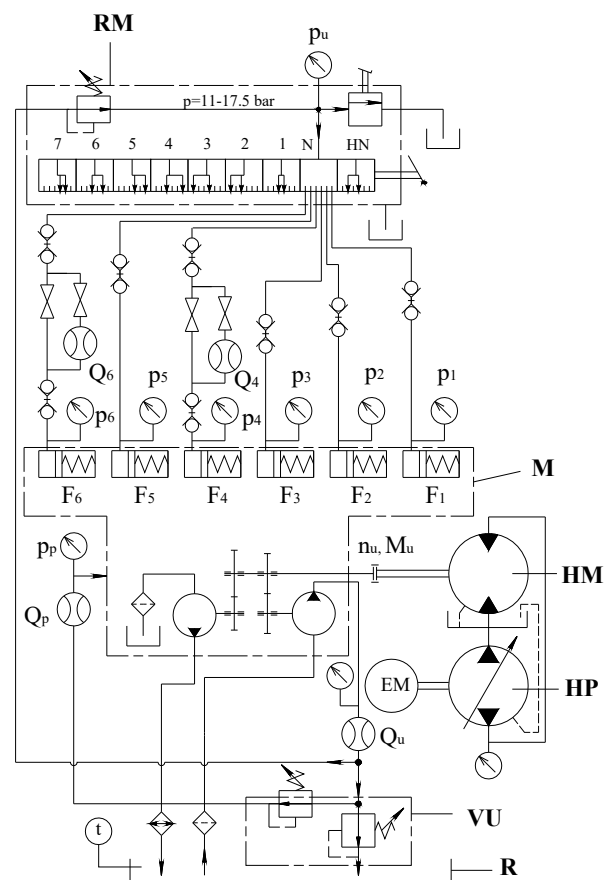


Figure 3. Hydraulic scheme of the test bench for the left gearbox inspection

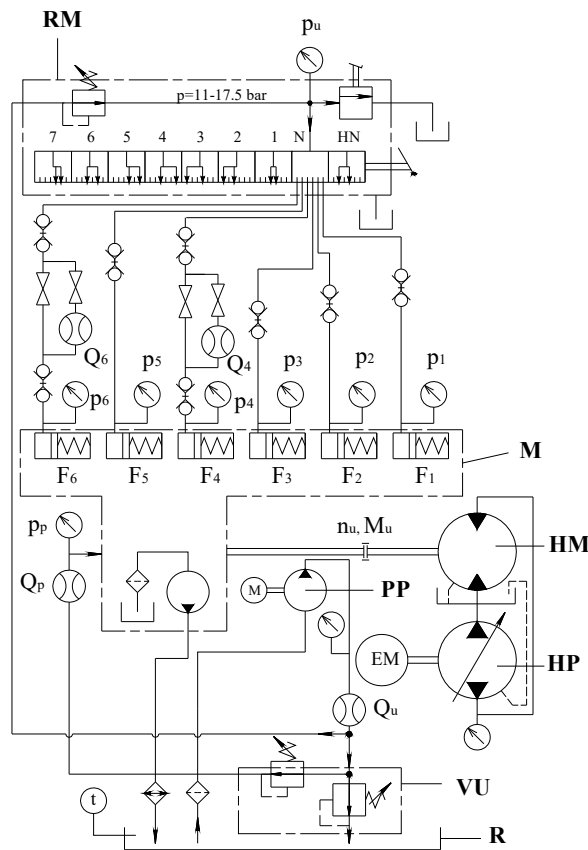


Figure 4. Hydraulic scheme of the test bench for the right gearbox inspection

2.4. Measurement of oil leakage in friction assemblies

When measuring oil leakage (losses) in the friction assemblies, it is necessary to install appropriate flow meters in the appropriate hydraulic lines, which connect the hydraulic distributor and the adapter on the gearbox housing. Since two friction assemblies are included in each transmission, two flow meters are installed for each gear. Figures 3 and 4 show the example of the measurement of the leakage in the II transmission (couplings F4 and F6 are included). The meter with pipelines and taps is given in Figure 5, and its hydraulic scheme is provided in Figure 6. As shown, the flow meters are placed in the parallel line with the main line.



Figure 5. Section of the installation with the flow meter

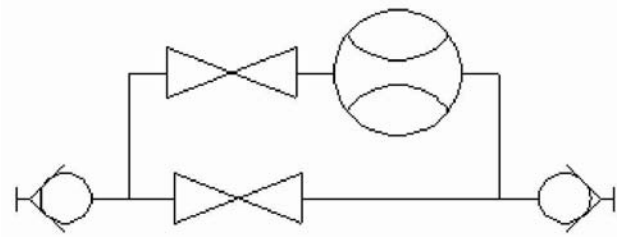


Figure 6. Hydraulic scheme of the installation with the flow meter

The assembly of the section of the installation containing the flow meter (when measuring leakages in individual gears) is done with the help of automatic couplings. Before switching on the gear, it is necessary to open the tap in the main line and close the tap in the auxiliary line (it is located in front of the flow meter). When the gear is engaged and when the measured values reach constant values (rotation speed and torque), it is necessary to open the tap in front of the flow meter, and close it in the main line. In this way, the oil flow, *i.e.* the oil leakage in the friction coupling, is directed to the auxiliary line where the flow meter is located. This procedure is repeated for each gear.

3. TESTING RESULTS

When testing the gearbox, it is necessary to provide the conditions described in the section 2.1, in relation to Tables 1 and 2. In each transmission, the parameters are measured and registered on the basis of which a conclusion can be made if the gearbox is operational. Based on the measured input rotation speed and torque, the power utilized to drive the unloaded gearbox is calculated according to the following formula:

$$P = M \cdot \omega = M \cdot n \cdot \frac{\pi}{30000} \quad (1)$$

where:

P - Power [kW]

M - Torque [Nm]

n - rotational speed [rpm]

The measurement results are continuously recorded, while the maximum values of the power for the operation of the unloaded gearbox are obtained by calculation. By comparing the measured leaks and the calculated power values for the transmission drive with the permitted values, the quality of the transmission is determined.

4. CONCLUSION

The paper describes the original procedure of verification tests of the functional characteristics of gearboxes for tanks developed on the basis of the T-72 tank. By comparing the measured leaks and the calculated values of the power for the transmission drive in relation to the permitted values, the quality of the transmission is determined, and a decision is made whether it can be installed in the vehicle or not. The procedure can be

applied to the new and reconditioned gearboxes. Although the foundations of this procedure were laid 30 years ago, it is still relevant and is constantly being improved. The test bench, where the tests are performed, is located in the VTI's Laboratory for Vehicle Subsystems in Kumodraž, and the frequency of tests is app. 4 - 5 gearboxes per year.

The validation of the applied method is supported by the fact that during the decades-long examination of tank gearboxes according to the described procedure, the external clients have never filed any complaint.

References

- [1] Milorad Dragojević: Combat vehicles, UDK 623.438.3, Belgrade, 1990.
- [2] Slavko Muždeka: Bases of combat vehicles, ISBN 978-86-335-0369-3, Belgrade, 2012.
- [3] PKP 1153 – Tank basic 125 mm M-84 and M-84A, Gearboxes with pumps and side gears, 1990.
- [4] Tank M-84, Description, handling, basic and technical maintenance (Book I), UDK 623.438.3.004, 1988.
- [5] Tank M-84, Workshop maintenance and overhaul (Book I), UDK 623.438.3.004, 1988.

THE DESIGN OF TECHNICAL SOLUTION FOR THE FUEL LEVEL TRACKING IN MODERNIZED BVP M-80AB2

OBREN STOJIĆ

Military Technical Institute, Belgrade obren88@gmail.com

GORAN JERKIN

Military Technical Institute, Belgrade goranjer@yahoo.com

Abstract: Within the modernization of the infantry fighting vehicle (Serb. BVP), a new concept of the modernized vehicle has been adopted, which included a displacement of fuel tanks. The fuel tanks are moved from the fighting compartment to the over-tracks panels in the rear part of the vehicle, one on the left and one on the right side. According to this, it was necessary to study the problem both theoretically and practically, and to provide a new functional solution for tracking the fuel level in the tanks. This included the selection of the sensors for detecting the fuel level in the tanks, the indicator placed on the driver's control board used to indicate the current fuel level in each of the tanks, the designing of electrical scheme to connect the sensors and the indicator, the designing and making of appropriate electrical installation. All this had to be installed on the vehicle and the functionality of the new solution in whole had to be checked.

Key words: BVP, modernization, fuel system, sensor, indicator, electrical scheme.

1. INTRODUCTION

The BVP M-80A infantry fighting vehicle represents the most important and widespread modification of the BVP M-80 vehicle. This vehicle served as the basis for the development of other vehicle variants for different purposes.

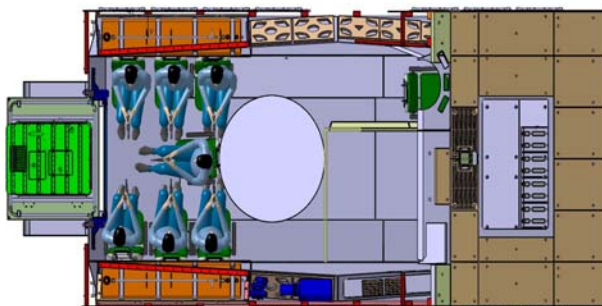


Figure 1. Conceptual solution of the PT modernized base of the BVP vehicle

The centre of modernization on BVP M-80A is on modernization of the basis of the vehicle which consists of the change of the concept of the vehicle's basis, the goal of it being the increase of commodity for the crew and the useful space. The goal of modifying (cutting) the lateral diagonal panels of the infantry vehicle and moving the fuel reservoir out of the vehicle (on the continuous track panels), was to increase the space for the crew and equipment and the increase of the security of the crew against explosions of the fuel and fires. For the new construction of the fuel reservoir (Figure 2), it was necessary to choose appropriate sensors for detecting the

fuel level in the reservoir, the indicator on the control panel of the driver and serves for pointing the current fuel level in each of the reservoirs, project electrical scheme for connecting the giver and the indicator and make appropriate electrical installation.

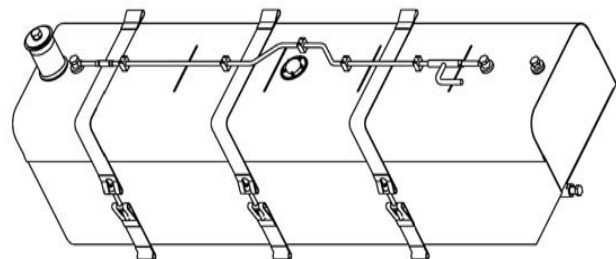


Figure 2. New construction of the fuel tank

Solving the problems described demanded studying the basic principles of the functioning of the sensors and indicators, their availability at the market, so as some of the existing solutions, about which we will discuss in this study.

2. ANALYSIS OF THE EXISTING METHODS OF THE SOLUTIONS FOR TRACKING THE FUEL LEVEL IN THE FUEL RESERVOIRS

Measuring the level of liquid in some of the reservoirs gives the insight to the liquid volume, and when the density is familiar the liquid volume, we have at disposition in the reservoir too. Beside visual and mechanical methods, which, historically looking, are the oldest, the most important in the contemporary techniques are electrical methods for measuring the levels.

The methods of measuring can be divided into continual and discrete. With continual methods we can continuously track the current level, while discrete measuring gives the signal when the liquid level increases or decreases, in comparison to the set point.

2.1. Traditional methods of continual measuring of the liquid level

In Figure 3 there are some of the methods for continuous level measuring shown. The device in Figure 3a uses the float which tracks the changes of the level and, affecting the converter for measuring translatory position gives the electrical signal proportional to the liquid level.

In Figure 3b there is the device which functions at the similar principle. In this case the float hangs on the rope over the reel. In that way, the moving of the rope converts into the angular position which is measured by the adequate converter, most frequently by helicoidal potentiometer. By this method the highest precision of the liquid level measuring is achieved.

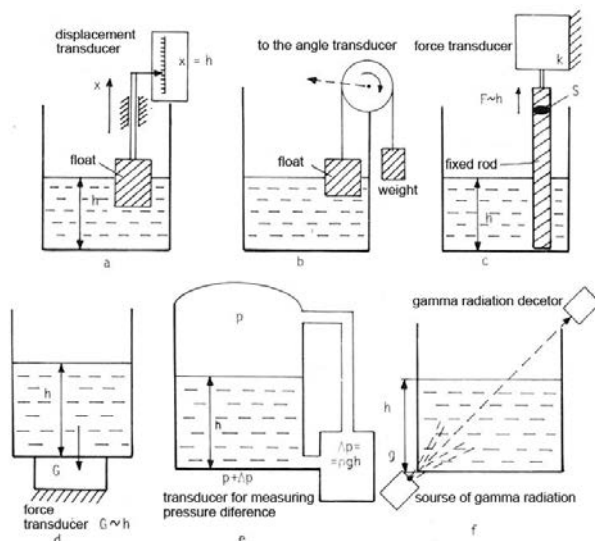


Figure 3. Shows some of the methods for continuous level measurement

In the Figure 3c the rod of constant intersection is fixed onto the converter for force measuring. When the reservoir is empty the weight of the rod affects the converter. The end of the rod is then just above the bottom. When the liquid is poured into the bowl, the rod starts raising because of the thrust force. The thrust force is in linear proportion to the liquid level.

Direct measuring of the liquid level, no matter the geometry of the reservoir, can be conducted by electrical scale which measures the weight of the reservoir continuously.

In the devices of this type, the measuring tracks or magnetostrictive converters for force measuring are used, Figure 3d.

In the Figure 3e the method of measuring the level according to differentiating the pressure at the bottom and on the top of the bowl, is shown. The difference of pressure is in linear dependence of the level. In this case it is

necessary to know the density of the liquid. The principle of continuous determination of the liquid level according to absorption of radiation, is shown in Figure 3f.

The device consists of the source of the radiation and detector of radiation set so the rays can go through the liquid layer which is in proportion to the level. The output signal of the radiation detector, for adequate liquid, is calibrated directly in the units of the level.

2.2. Capacity converters for continuous measuring of the liquid level

Capacity converters have the shape of the plate or coaxial cylinder with constant longitudinal capacity, Figure 4 [2]. The space between the electrodes is set so that the liquid can easily fulfil the interspace to the level equal to the liquid level. The good feature of the capacity converters is that they don't have the moving parts so that they are not prone to wearing out. Besides that, the prices of these converters are relatively low, and the accompanying circuits are mostly of the simple construction.

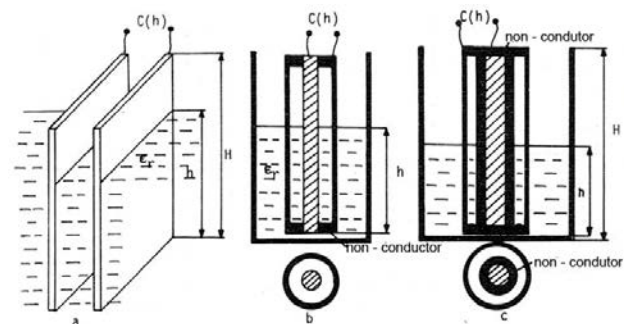


Figure 4. Capacitive transducers for continuous level measurement

The plate and coaxial converters are used for measuring the liquid levels which, in electrical view, conduct as good dielectrics. For example, those are different oils, gasoline, petroleum, all liquid carbon dioxides. Frequently, only one electrode is used at the plate converters for measuring the level of dielectrical liquids, and it is set in parallel to the metal wall which plays the part of the other electrode. Coaxial converter is used for measuring with liquids which act as conductors. Those are piped water, water from rivers and seas, and different acids. In order to disable the galvanized contact between the electrodes, the inner electrode is covered with the layer of the isolator of constant thickness. In the part of the converter which is sunk into the liquid, only isolator of the inner electrode serves as the dielectric. The converter above the liquid level has the shape of cylindrical capacitor, with the double layer of dielectric, one of which is the air. The common feature of all capacity converters for continuous measuring the liquid levels is that their capacity is near linear to the function of the level [2].

2.3. The bridges for measuring the levels by capacitive converters

In Figure 5, there are typical alternate measuring bridges for measuring the levels by capacitive converters. The

power supply of the bridges is conducted from the sinus generator while the instrument for measuring effective values at the voltage is used as the indicator. The first bridge is of symmetrical type. The balance of the bridge is achieved by variable capacitor C1 in the zero or some other referenced position.

The output signal of the bridge represents nonlinear function of capacitance, so the scale of the voltmeter is nonlinearly calibrated by the level.

The second bridge also has symmetrical construction, whereby the secondaries of symmetrical transformer play the part of two branches. The bridge is characterized by some advantages because of the small impact of parasite capacitance of the converters C1 and C2. The variable capacitor Cd is used for balancing the bridge.

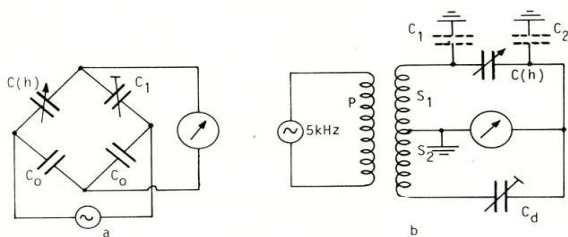


Figure 5. Alternating bridges for level measurement with capacitive transducers

2.4. The method of discrete measuring of the liquid level

The devices for discrete measuring of the liquid levels give the discrete signal when at one moment the level surpasses some certain critical value, Figure 6. The signal is used for automatically protection of overflowing the reservoir, or as the alarm in case when the liquid level drops below the lowest value allowed.

In case of conductive liquids, the pair of electrodes which act as an open switch in the air, and as a closed switch in the liquid, is used as the most simplified conductor, Figure 6a.

For dielectric liquids the small aerial capacitor, whose capacitance increases dramatically at the moment of sinking, is used, Figure 6b.

In Figure 6c there is the device with self-heated resistors vertically set at equal mutual space. Converters are included in relay devices on whose ends there are the lightbulbs. When the resistor is in the air, the output signal is equal to the zero and the adequate lightbulb does not light up. The converters sunk in the liquid give the signal so that the adequate lightbulbs light up. Thus, the indicator with the lightbulb gives the quasi-continuous Figure from which the current level can be seen.

Optoelectronic conductors for discrete measuring of transparent and non-transparent liquids are shown in the Figures 6d and 6e. The sensor for transparent liquids consists of the prism, light bulb and photo electronic detector.

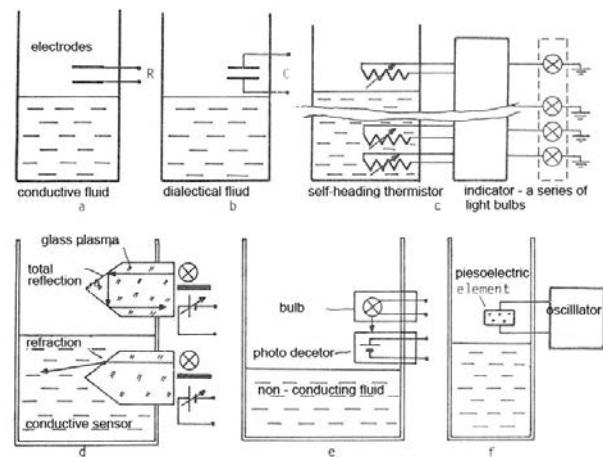


Figure 6. Discrete methods of liquid level measurement

For non-transparent liquids it is enough to set the lightbulb and the photodetector one opposite the other. At the moment when the non-transparent liquid fills the space between the lightbulb and the detector, the change of the output signal occurs.

In Figure 6f there is the discrete method of measuring where piezoelectric and magnetolectric vibrator switched as the oscillatory element of some oscillator, are used as the converter. When the converter is in the air the damping has the low values, the oscillators can keep up. When the liquids come into contact with the converter, mechanical losses increase which cause the end of oscillations of the oscillator. The disappearance of the output voltage from the oscillator represents the signal when a set level is surpassed. The advantage of this method is that it doesn't depend on electrical or optical characteristics of the fluids.

2.5. The description of the fuel level measuring on the existing BVP M-80A

The reservoirs for fuel are located in the middle of the back part of the fighting vehicle. They are made from aluminium sheet and set on the front and back carrier of the reservoir, and covered by the felt sealants. Showing the fuel level in the reservoirs is conducted from the indicator of the fuel level to the control panel of the driver, by including the switch of the fuel level indicator for left and right reservoir.

BVP M-80A has got electrical fuel level giver type 403, and the electrical fuel level indicator is used as an indicator, type 404, which were produced by Teleoptik from Zemun [1].

The electrical fuel level is of the potentiometer type. The position of the scroller on the potentiometer is determined by the position of the float in the reservoir. Otherwise, when the reservoirs are smaller, when the precision is not obligatory (e.g., cars), the indicators with float fastened by the lever which rotates around the immobile support, are used. The other end of the lever moves the scroller of the round potentiometer, thus getting the electrical signal proportional to the level.

The electrical fuel level indicator servers for pointing the fuel level together with the giver (Figure 7). It is made with the electrical scale inbuilt in a metal protective box with the inner lightning of the dial. It works on the principle of electromagnetic coupling, crossed coil and rotating magnet. Including the indicator in the circuit, the hand takes the position which matches the fuel level in the reservoir.



Figure 7. Type 404 fuel gauge

When the fuel level in the reservoir decreases to the value between $1/6$ and $1/9$ of the reservoir volume, the signal contact switches off, and the lightbulb signalling the fuel level switches on (the red light turns on). This is enough to make a warning to the driver that the reservoir should be refilled. Electric fuel level indicator is built in the control panel at the angle of 15° to 90° . That is the angle which the flat line of the dial makes the horizontal flat line. It is protected from the water breaking into it on the front side. Rated voltage is 24V in one way. The giver and the indicator are connected by the cable electric installation, according to the scheme connection in Figure 8 [1].

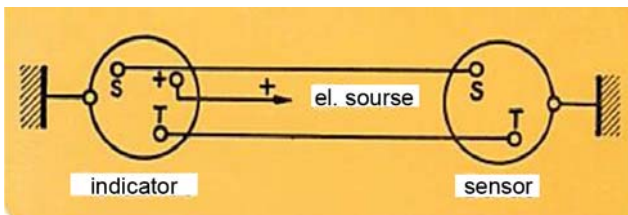


Figure 8. Schematic of the connection of the transmitter 403 and the pointer 404

2.6 The description of the measuring of the fuel level in the reservoirs on the prototype and modernized BVP M-80AB1

The HYDAC system for showing the liquid level is applied on the prototype I of modernized BVP M-80AB1. HNT 1200 is chosen as the giver (Figure 9). It is the magnetostrictive sensor with extremely precise measuring of the liquid level. The available lengths of the sensor are from 250 to 700 mm. In this case, the sensor HNT1226-B-0410-000 with the output signal from 0 to 10V, the length 410 mm, is chosen, and it is due to the construction of the reservoir on the modernized IFV. The output signal enables the connecting with every measuring and control devices from HYDAC ELEKTRONIC. HYDAC offers the givers HNT1200 in the main box made of noncorrosive steel, resistant to the pressures, for implantation in the reservoir. Two fuel level givers were needed for the implantation, one on every reservoir



Figure 9. HYDAC HNT 1200 magnetostrictive transmitter

The principle of the measuring for this giver is based on measuring the time of the signal passing (ultrasound range) through the medium (Figure 10). The ultrasound time passing is proportional to the distance and it is measured electronically [4].

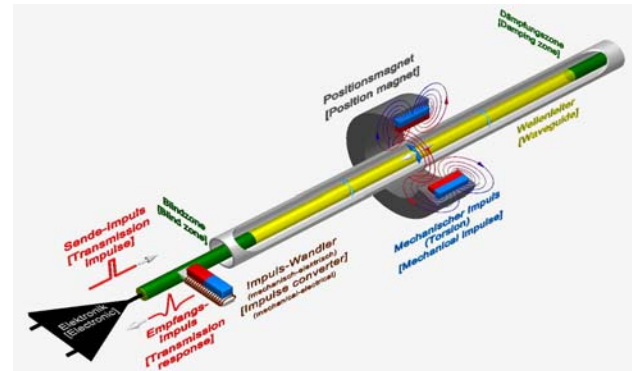


Figure 10. Principle of operation of a magnetostrictive sensor

Ferromagnetic wire (magnetostrictive measuring element, waveguide) is set in the protective pipe and the impulse of the current passes through it. The current impulse makes radial magnetic field around the wire. The contactless magnetic system which generates vertical magnetic field relative to the wire, is used as the position sensor (the permanent magnet). When the two magnets meet at the measuring point, the torsional impulse starts off radially from the wire and vertically from the floating magnet, this torsional impulse moves as the structural one in both directions of the wire.

Ultrasound signal is recorded by the converter in the head of the sensors and is converted in the output electric signal. The time difference between the starting impulse and returning torsional impulse is corrected to the output signal by the measuring electronics, which is proportional to the moving and makes it available as analogue or digital signal, which is pointed on the pointing device. These givers are precise, they can be used for oil level measuring, but are very expensive, 300 euros [4].

As the indicator for these sensors HYDAC offered digital unit HDA 5500. HDA 5500 are microprocessor, controlled units for display and supervision, designed for installation in the laboratories. There are different versions available with three analogue inputs maximum, analogue output and up to four relay outputs. Analogue input signals are displayed in accordance to the settings the user chooses. In our case we used HDA5500-0-1-DC-000 device, which has one analogue input.

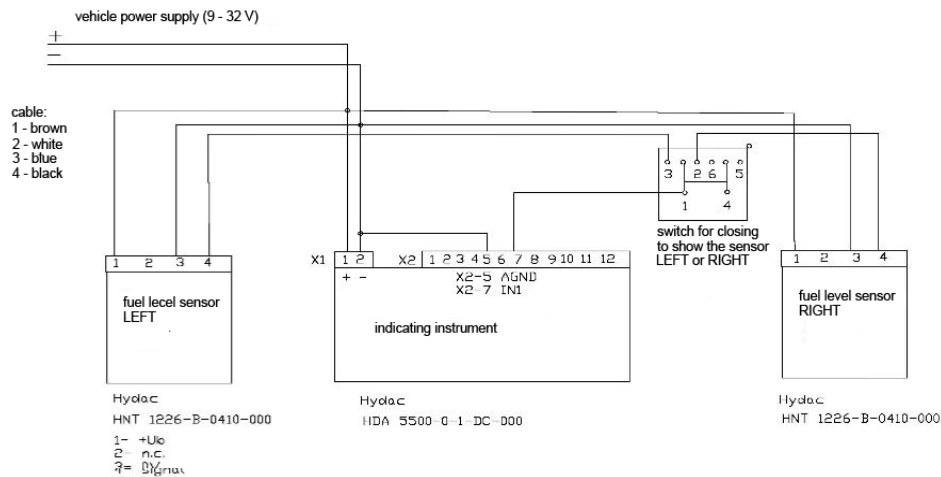


Figure 11. - Electrical connection diagram of the fuel level measurement system in BVP M-80AB1

With the help of the switch the display of the fuel level is enabled in the left or right reservoir depending on the position the switch is in. All those devices are interconnected by cable installation according to the given electric scheme of connecting (Figure 11). A new place for installation had to be chosen because of its construction and the lack of the space on the existing control panel, and the previous device was round and a lot smaller. The switch for choosing the left or right sensor had to be moved too. In Figure 11 there is a new place for installation shown, and the device with the switch too.

The sensor chosen was not satisfactory because of the temperature characteristics (work on 0° -50° C), so as due to low mechanical characteristics caused by vibrations appearing on the spot of installation on the vehicle. Namely, designed for the work in the laboratory conditions, so it cannot be used for the installation, and for that reason it was necessary to choose a new indicator for BVP M-80AB2. Due to the price of the sensor used it was necessary to consider a new fuel level giver. A new electronic installation had to be set because of the change of the indicator and the giver, and the place of the installation.

3. THE DEVELOPMENT OF THE SYSTEM FOR FUEL LEVEL MEASURING ON THE PROTOTYPE AND MODERNIZED VEHICLE BVP M-80AB2

For the prototype II, a new modernized vehicle BVP M-80AB2, and due to the working conditions and price, it was necessary to choose new fuel level givers, so as a new indicator. Namely, the previously chosen system installed on the prototype I, was not satisfactory considering all the conditions set.

While choosing the indicator the place for installation, the construction of the reservoir and its dimensions all had to be considered. In comparison to the giver chosen, an adequate indicator had to be chosen, considering the chosen giver, whereby the place for installation on the control panel of the driver had to be considered also.

3.1. Choosing the fuel level sensors

The device VDO Ø54 mm Fuel tubular sender 400 mm was chosen considering the conditions set for the fuel level sensor. The label of the type: VDO 224-011-000-400G (Figure 12). This is the tubular sensor of the fuel level with the resistance (empty-full) 74.9-2.5 Ω, length 400 mm diameter of the tube 54 mm, voltage 24 V. Temperatures for functioning -25° to 65° C [3].



Figure 12. Place of installation of indicator with switch

The principle of functioning of the tubular devices is somewhat different in comparison to potentiometer devices. The fuel goes through the technological hole which is located at the bottom of the device, to the protective nozzle. The float is on the surface of the fuel. As the result of the element position change, there is a change of the resistance with increasing or decreasing the fuel level.

When the fuel reservoir is full, the float is on the top of the protective nozzle. With decreasing of the fuel, the float drops, which causes the increase of the resistance in the area of the wire.

The fuel level giver is chosen according to the dimensions of the reservoir. As the depth of the reservoir is 400 mm,

there will be a certain amount of the fuel which the giver will not be able to show, but regardless to that, it is necessary to refill the reservoir as soon as the scale on the indicator comes ear zero.

VDO is well-known producer of the givers and indicators. It is used in automobile industry and shipbuilding. The price is 100euros, which is more acceptable in comparison to HYDAC.

3.2. The choosing of the fuel level indicator in the reservoirs according to the giver chosen

The device VDO Cockpit International Fuel level 90-0.5 Ω , 52 mm, 24 V (Figure 13) was chosen as the fuel level indicator. The label of the type: VDO 301-040-002G. Temperatures for functioning -30° to 85° C. Operating voltage 21.5-30V dc [3].

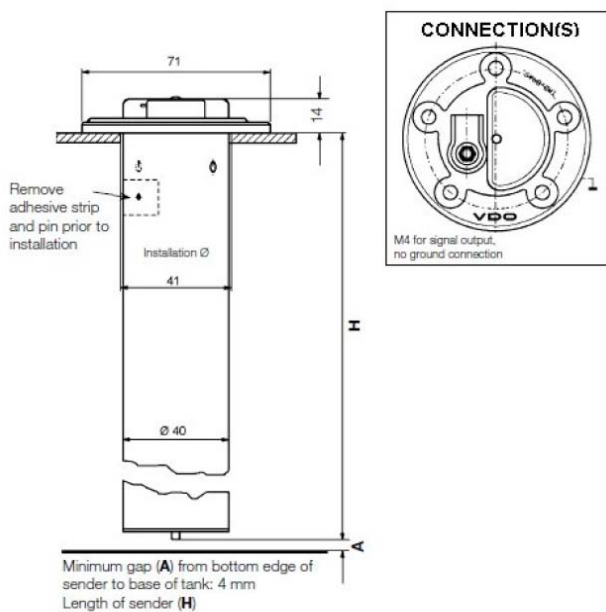


Figure 13. VDO fuel level sender

3.3. Choosing the place for installation of the fuel level giver

The characteristics of the indicator which VDO offers for installation on the existing control panel are: diameter 52mm, operating voltage 24V, signals empty-full: 90-0.5 Ω . Due to these characteristics the installation is possible on the existing control panel (Figure 14), i.e., on the place the giver and the indicator were installed first on BVP M-80A, Figure 15.



Figure 14. Place of installation of indicators and switches

The chosen indicator satisfies the demanded conditions in the view of operating on the temperature and vibrations which appear on the vehicle. And due to its construction and the mode of connecting- it is more acceptable than HYDAC's device which is installed on BVP M-80AB1. Namely, now it's possible to install the indicator and the switch on the same place on the control panel as in BVP M-80A.



Figure 15. VDO fuel level indicator

3.4. Electrical schemes and installation for connecting the giver and the indicator

These are the demands which are defined with modernization of infantry fighting vehicle:

When installing new devices in modernized BVP M-80AB1/AB2 there must not be degradation in the supplying of the power for consumers and recharging of the batteries, in comparison to BVP M-80A.

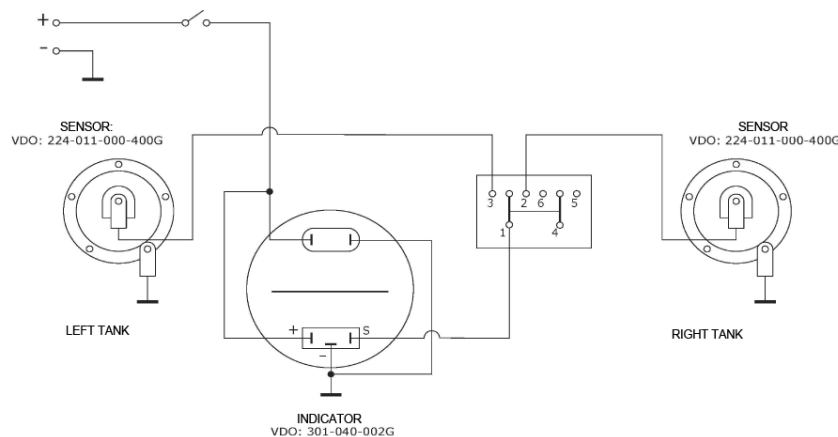


Figure 16. Connection diagram

Electrical installation needs to be rated voltage 24V and there needs to be the switch of the mass. Electrical installation, electrical devices and systems, and measuring and control devices of BVP M-80AB1/AB2 should be produced class K2 according to SORS 5706. Other demands for electrical equipment which is not modernized should be in accordance with PKP electric equipment of BVP M-80A. In modernized BVP M-80AB2 the existing electrical installation and electrical equipment will be kept with reparation and instalment of extra installation considering the needs of voltage of the new components installed of the modernized set (TKI equipment).

All devices in new system should be connected by cable electrical installation according to the scheme of connecting. In Figure 16, the scheme of connecting and electrical installation for newly installed system for fuel level display is presented.

4. CONCLUSION

For modernized BVP M-80AB2 it was necessary to design technical solution of the fuel level tracking system in the reservoir. First, the available methods and existing givers used for this kind of measuring were analysed. Then, the previous solutions of these systems of continuous track fighting vehicles were analysed. The analysed systems included BVP M-80A and prototype I

BVP M-80AB1. In the next phase, the sensor adapted to the demands and conditions of the vehicle was chosen. The sensor chosen was the one which can be installed on provided places on the reservoirs, meets the demands and the price is lower than in previous solution. The sensor selection made it possible for the indicator to be chosen in the system which accomplished full functionality and satisfies temperature and mechanical demands, and fits in the old place on the control panel. The problem of placing the indicators, which occurred in previous solution, was avoided by this. In the end, electrical scheme for connecting the system elements was defined. Thus, the system allowing the fuel level tracking in the reservoirs of BVP M-80AB2 was completed. At the moment, the check of the vehicles operating is being conducted on the field.

5. References

- [1] Infantry fighting vehicle BVP M-80A Description, manual and technical maintenance (UDK 623.438.15.004)
- [2] dr Dragan Stanković, Physical technical measurements – Measurement of non-electrical values by electrical means.
- [3] VDO – Vehicle Electronics Catalogue, 2016.
- [4] Hydac International - Electronic Product Catalogue, 2018.

FUZE VAF-M17 MICROCONTROLLER SOFTWARE

MARKO ŽIVKOVIĆ

Metropolitan University, Vlatacom Institute, Belgrade, marko.zivkovic@vlatacom.com

DRAGAN DOMAZET

Metropolitan University, Belgrade, dragan.domazet@metropolitan.ac.rs

NIKOLA LATINOVIĆ

Vlatacom Institute, Belgrade, nikola.latinovic@vlatacom.com

Abstract: This paper provides detailed description of the microcontroller software workflow for the fuze vAF-M17 alongside with detailed hardware and software architecture. Fuze vAF-M17 together with arming initiator vFI-M17 is intended for use with the aerial bombs MK-82, MK-84, BLU-109 and has the same functional characteristics as fuze FMU-139. The heart and brain of the fuze vAF-M17 that manages its whole operation, is the 8-bit microcontroller. Hardware and software are designed in a way so that the main emphasis is on the handling safety to prevent any unwanted effects. For that purpose, the design of the hardware took into account the differential pressure-measuring unit which is installed inside the arming initiator and which gives the information about the velocity of the aviation bomb. The electronics has the knowledge that the first safety condition is fulfilled and that the aviation bomb has reached a clear distance from the aircraft and the pilot to perform the needed functionality of the fuze (activating the explosive filling inside the bomb through detonation). Another important sensor for proper functioning is the accelerometer, which has a possibility of impact detection that can be preset by an operator with a desired “g” value.

Keywords: fuze, microcontroller, software, military, vlatacom.

1. INTRODUCTION

Fuze vAF-M17 together with initiator vFI-M17 is intended for use with the bombs MK-82, MK-84, BLU-109, and has the same functional characteristics as fuze FMU-139. Bomb fuze vAF-M17 is designed to initiate an explosion at fuze device. It is powered from the Lithium battery 10.8V. Its arming time and its function delay time are selected before flight by means of two rotary switches with 16 positions. The electric fuze remains safe until it is energized from its own lithium battery. Because of the safety interlocks, electrical charging can occur only after the bomb is released from the aircraft. At this time, the fuze receives electric power required for selection of the desired arming and delay times.

Fuze functions after the bomb is released from the aircraft in ACTIVE mode, and if special environmental sensor, located in the initiator detects air stream, which means that the bomb is released from the aircraft and is moving away from the aircraft reaching a safe distance. If the air stream doesn't exist arming will not happen and explosion will not occur.

When arming conditions are fulfilled the fuze becomes armed, and is free to operate on impact and the bomb explosive charge can be detonated.

Detonation delay time starts when shock sensor detects that the bomb hit the target.



Figure 1. Fuze vAF-M17

2. ELECTRONIC BLOCK OF THE FUZE

Electronics circuit of the fuze provides:

- Checking if all necessary conditions for arming are satisfied.
- Electrical pulse for activation of the Arming capsule (EID)
- Detection of the bomb impact on target.
- Electrical pulse for activation of the Detonator capsule (ED) after detonation delay time is finished.
- Test basic characteristics of the fuze and its functionality

Block diagram of the electronic block of the fuze is shown in Figure 3.

The heart of the fuze vAF-M17 electronic block is the microcontroller (PIC18F45J50), 8 bit with 10 bit AD converter, 32k program memory, 3776 bytes SRAM memory, 22 IO ports, SPI, I2C, USB, USART etc.

There are two rotary switches located on vAFRSW PCB which are accessible from front side of the fuze, Figure 2. Arming rotary switch serves for arming time setting. Delay rotary switch serves as detonation delay time setting. Each rotary switch has 16 positions. One with 12 arming times and the other with 13 detonation delay times. When one or both rotary switches are in the position 'x' arming process and detonation delay processes are blocked, fuze is passive and can't activate the bomb explosives. The microcontroller reads rotary switches positions immediately after battery is connected to the microcontroller.

There are two modes of operation:

- Functional mode of operation
- Operation Test mode

Power supply of the electronic block is three lithium batteries (3x3.6V) with a shelf life of 15 years. Battery (BAT+) is connected to the initiator via CONF 4-pin connector. When launch sensor is active, when the bomb is released from the aircraft in ACTIVE mode, this battery voltage comes as MP1 signal via CONF connector to electronic circuits. MP1 (VC) voltage comes to EID FIRING CIRCUIT (AFC), ED FIRING CIRCUIT (DFC) and VOLTAGE REGULATOR VR3. Voltage VC charges firing capacitors CA and AFC and CD in DFC circuits which serves for activation EID and ED capsules.

Capacitance of these capacitors is (440 μ F) each. Charging starts when the microcontroller enables this process immediately when the bomb is released in ACTIVE. Capacitors are charged for approximately one second. Charged energy in these capacitors are much greater than needed for proper activation of the capsule and can be given by:

$$E = \frac{1}{2} * (C * V^2) \approx 22 \text{ mJoul}$$

Energy stored in capacitor (CA) discharges through the EID capsule, when all conditions for that are satisfied.

Energy stored in capacitor (CD) discharges through the ED capsule, when all conditions for that are satisfied.

Power supply from battery via MP1 switch connects to a voltage regulator VR3 which provides power supply VDD=3V DC for microcontroller, accelerator sensor, and other parts.

When the fuze is connected with a computer, in the Operation Test mode, energy capacitors are not charged. In this case only microcontroller, accelerometer sensor and circuits for capsules continuity testing works. Power supply, 5VC, from the computer, comes via TEST connector and diodes D3 to input of the voltage regulator VR3. By this way always same power supply is obtained, VDD=3V.

The continuity (bridge wire) of the arming and detonator capsules can be checked in the Operational TEST mode of operation using two electronic circuits EID Capsule TEST and ED Capsule TEST. This test is done by passing a current about 2.1mA (much less than MNFC, 100mA), and monitor the capsule continuity. If continuity exists, then the microcontroller generates a TRUE signal which means that the connection between EBAF and bridge wire is ok and that bridge wire inside the capsules is ok.

DATA, MP2I, from environmental sensor, ENV5, located in the initiator, comes from collector of transistor Q1 and via sprial cable, CONF connector and MP1/MP2 ESD protection circuit to input of the microcontroller, input MP2. If this data is TRUE (HIGH level) microcontroller concludes that the bomb moves away from the aircraft and arming process can be continued.

The fuze utilizes a semiconductor accelerometer, g sensing device (ADXL377), for the detection of the bomb impact on the target.

The (ADXL377) device is a small, thin and low power complete 3-axis accelerometer with conditioned analog signal voltage outputs. The (ADXL377) measures acceleration resulting from motion, shock, or vibration with a full-scale range of ± 200 g.

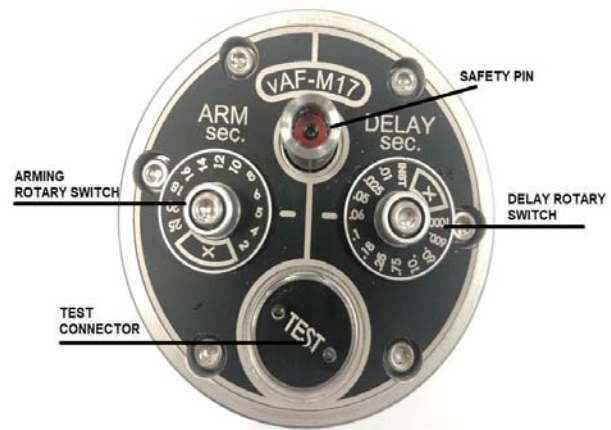


Figure 2. Arming and detonation delay time setting rotary switches

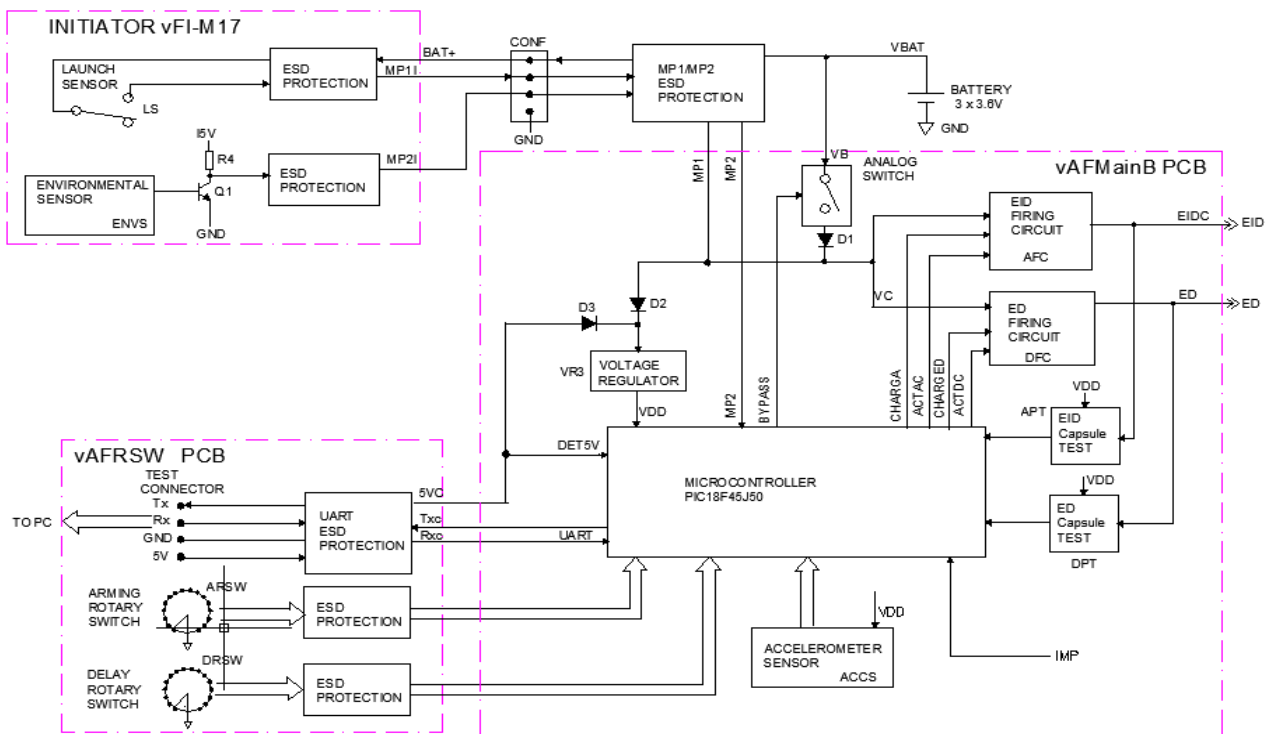


Figure 3. Electronic block diagram of the fuze

3. MICROCONTROLLER PIC18F45J50

The heart and brain of the fuze vAF-M17 that manages its whole operation, is the microcontroller, Figure 4. The microcontroller used in the fuze design vAF-M17 is PIC18F45J50 with 44-Pin, Low-Power, High-Performance USB microcontrollers.

Main features:

- Power supply is 2.15V to 3.6V.
- External or Tunable Internal Oscillator (31 kHz to 8 MHz, or up to 48 MHz with PLL)
- Two 8/bit Timers and Three 16 bit Timers
- Allows independent I/O mapping of many peripherals
- 10-Bit, up to 13-Channel Analog-to-Digital (A/D) Converter module:
- High/Low-Voltage Detect module
- Two Enhanced USART modules:
- Supports RS-485, RS-232 and LIN/J2602

- Auto-Wake-up on Start bit
- Four Programmable External Interrupts
- Two Master Synchronous Serial Port (MSSP) modules Supporting Three-Wire SPI (all four modes) and I2C™ Master and Slave modes
- Single-Supply In-Circuit Serial Programming™ (ICSP™) via two pins
- In-Circuit Debug (ICD) w/Three Breakpoints via 2 Pins
- Operating Voltage Range of 2.0V to 3.6V
- On-Chip 2.5V Regulator
- Flash Program Memory of 10,000 Erase/Write Cycles Minimum and 20-Year Data Retention
- Sleep mode: CPU off, Peripherals off, SRAM on,
- Fast Wake-up, Currents Down to 105 nA, Typical
- Auto-Baud Detect

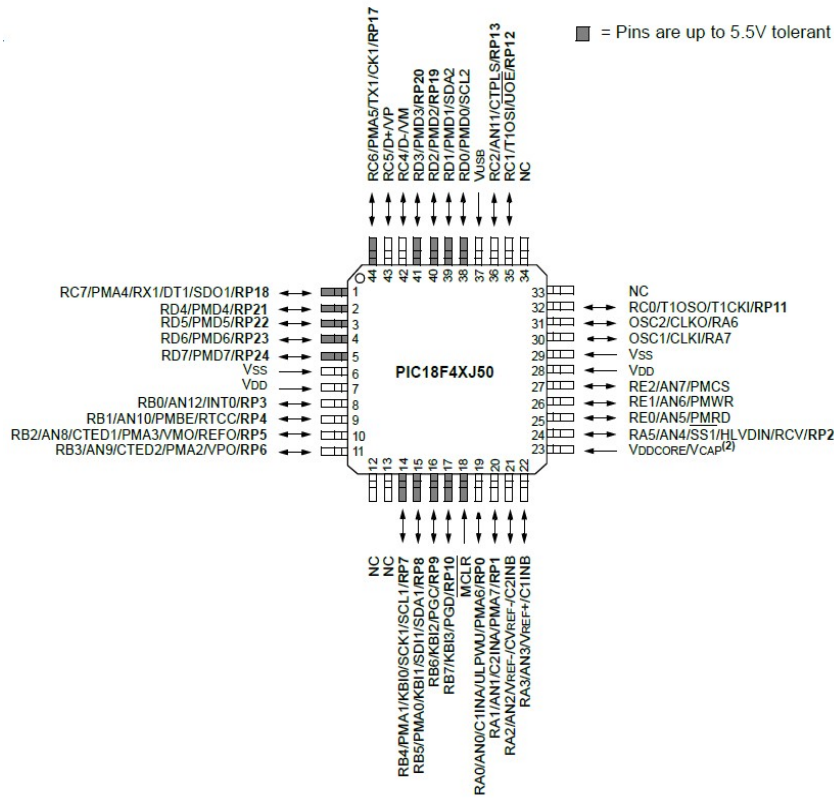


Figure 4. Microcontroller PIC18F45J50 pin out

4. MICROCONTROLLER SOFTWARE

Basic microcontroller state diagram is shown on Figure 5.

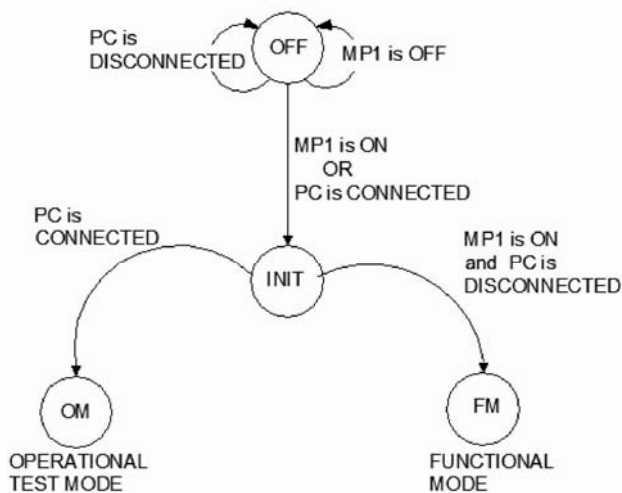


Figure 5. Basic microcontroller state diagram

When MP1 switch, located in the initiator, is open, (the initiator is in safe position inside the bomb) and when a computer is not connected with the electronic block, microcontroller does not work because there is no power supply. If MP1 switch is ON or if a computer is connected the microcontroller goes in the INIT state, initialization state.

If a computer is disconnected and MP1 switch is ON, the

microcontroller performs regular operation routine and this is the fuze Functional mode of operation.

If a computer is connected, the microcontroller goes to Operation TEST mode of operation. This will happen if before that signal MP1 is False (Switch MP1 in the initiator is open).

4.1. Functional mode of the fuze operation

Microcontroller performs Functional mode of operation when a computer is not connected with the electronics and when the MP1 switch is closed. Microcontroller state diagram in functional mode of operation is shown on Figure 6.

First step is reading position of the rotary switches and creating command for start charging process of the capacitors for activation EID and ED capsules.

After that the microcontroller goes in Arming process and starts the timer (TIMER0). After that the microcontroller waits 0.9 of Arming time, defined by position of the rotary switch. When this time has expired, microcontroller goes to state MP2 CHECKING. Microcontroller remains in this state until it detects the MP2 signal that it is TRUE. If the microcontroller detects MP2 signal that it is TRUE after the arming time has expired the microcontroller goes in the state of NO ARMING and remains there forever.

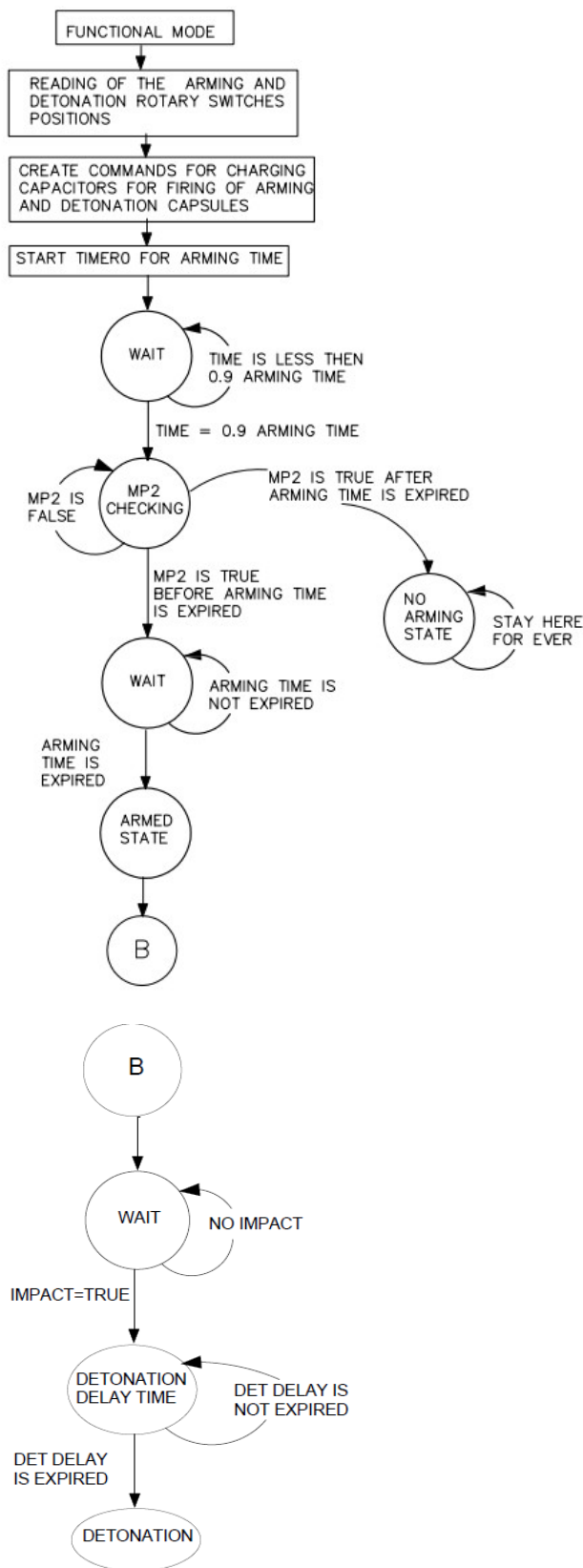


Figure 6. Microcontroller operational mode state diagram

If the microcontroller detects MP2 signal that it is TRUE before the arming time has expired, it goes in the WAIT state. When arming time has expired the microcontroller goes in the ARMED state. Fuze is armed and EID capsule should be activated.

After completion of the ARMED state, detonation process begins. First step of the detonation process is to check if the impact occurred. The microcontroller remains in this state until it detects the impact signal greater than preset value of the 'g' threshold. When the microcontroller detects that impact is greater than preset 'g' threshold, it start the timer (TIMER0) for detonation delay time. When detonation delay time expires ED capsule should be activated and should lead to explosion.

4.1.1. Software flow diagram for functional mode of operation

Software flow diagram for functional mode of fuze operation is shown on Figure 7.

As soon as microcontroller gets power supply it starts initialization. Most important task is to disable the firing circuits for EID and ED capsule. After initialization phase, the microcontroller reads positions of arming and detonator rotary switches and arming time begins (2 seconds is minimal arming time).

Microcontroller monitors signal MP2, which is high (TRUE) when the pressure of the air stream is greater than 0.4 Psi, coming from the comparator inside the initiator. A true data means: 3 consecutive readings of HIGH level of the signal MP2 from the comparator output. Interval between reading is 100 μ sec.

Microcontroller begins to monitor signal MP2 after 0.9 of arming time. If this signal is TRUE before the arming time has expired arming process can be continued. When preset arming time is finished, flag <arming> is TRUE, microcontroller generates command ACTAC, sends it to the EID firing circuit. EID capsule should be activated.

If MP2 signal becomes TRUE after the arming time has expired, arming process will stop, no arming state and microcontroller remains in this state forever.

If signal MP2 is FALSE arming process can not be finished and microcontroller remains in this state forever, further functions of the fuze are blocked. Thus the fuze cant and will not activate the bomb filling.

Following, the microcontroller starts to monitor data from accelerometer sensor. When data from any axis (X, Y or Z) are greater than preset 'g' threshold, and if the fuze is armed, then the microcontroller starts detonation process, that is the detonation delay time.

If rotary switch for detonation delay is set at position INST, the microcontroller immediately after detecting that data from the accelerometer sensor have exceeded the preset threshold and after checking that the fuze is armed, it activates the ED firing circuit and ED capsule. When detonation delay time is finished the microcontroller activates the ED capsule, via ED firing circuit, which further activates the KL-34 and TD capsule as well as the booster of the fuze.

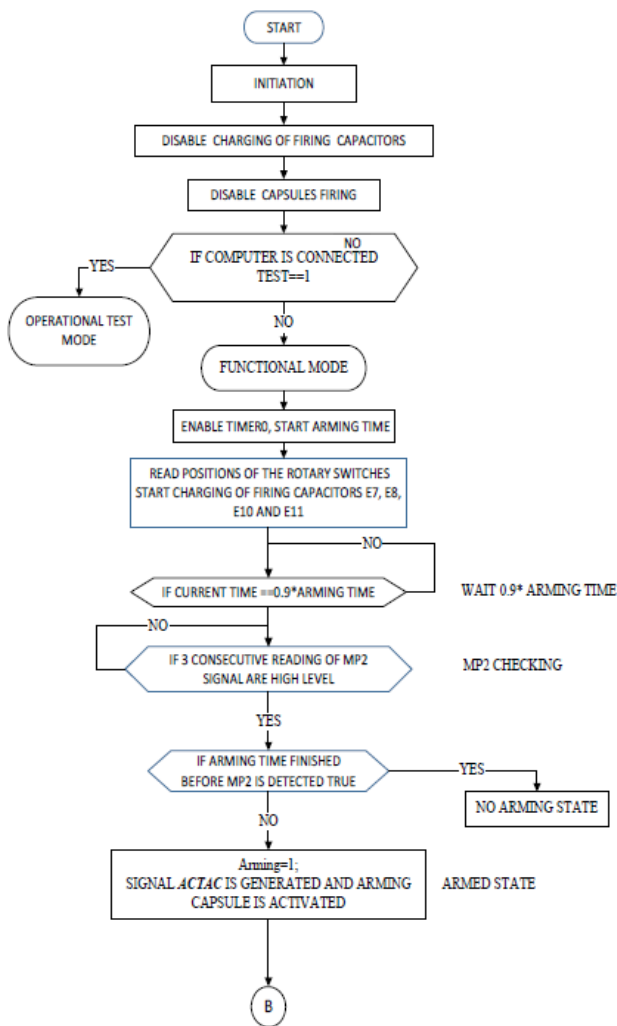


Figure 7. Workflow of the microcontroller Functional mode of operation

4.2. Operational TEST mode

Microcontroller performs Operational TEST mode of operation when a computer is connected with electronics.

During this TEST mode of operation the following parameters can be checked:

Arming rotary switch functionality

- Delay rotary switch functionality
- SAT time
- Continuity of the EID capsule
- Continuity of the ED capsule
- Battery voltage
- Voltage at accelerator sensor outputs for X, Y and Z
- Written value for 'g' threshold
- Firmware version written in the microcontroller
- Write new value for 'g' threshold

In order to perform operational test it is necessary to connect the fuze with a computer using the interface and appropriate cable. Connecting the fuze and a computer can be performed using serial interface USB UART. The interface module is a separate part which is using a module CP2102 USB UART IC. In order to use this interface on a computer driver CP210x-Windows-Driver

(Silicon Labs Company) must be installed.

Microcontroller state diagram in TEST mode of operation is shown on Figure 8.

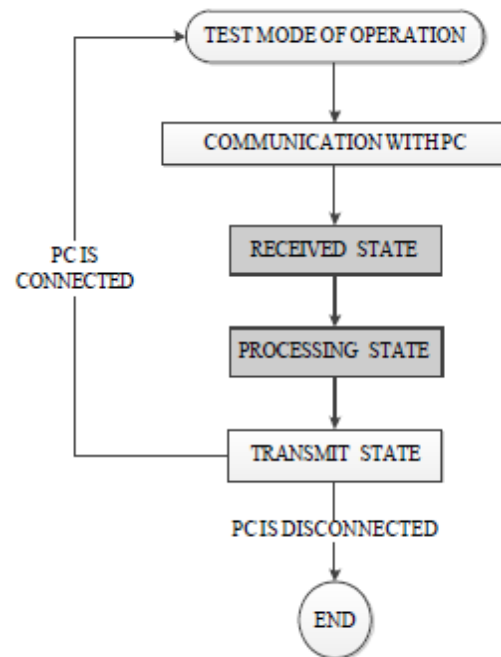


Figure 8. State diagram in TEST mode of operation

TEST mode of operation is possible only if the computer with appropriate software (vAF-M17 fuze test) is connected with the EBAF.

The computer is set as master and the fuze (or EBAF) is slave. The communication performs using 1200 bps. The computer sends request "[R]" to EBAF.

EBAF, upon receiving the request "[R]", goes in PROCESSING STATE (subroutine proc_received) and sends following data to the PC: [B*****[C*[E*[A*[D*[G***[S*****[Y*****[X*****[Z* ***[V**]

Microcontroller goes in this routine when a computer is connected with the EBAF. As soon as the microcontroller gets power supply it starts initialization. Most important task is to disable charging of the energetic capacitors and primer drivers.

5. CONCLUSION

Safety and arming are primary roles performed by a fuze to preclude initiation of the munitions before the desired position or time. Safety and arming device prevent fuze arming until an acceptable set of conditions has been achieved and subsequently allows arming and functioning.

In order to preclude unintended fuze arming, the fuze safety system shall not initiate the arming sequence but only as a consequence of an intentional launch. Also the fuze design shall prohibit premature fuze arming or functioning if any or all electrical safety or energy control features fail in any given state or credible mode. These

modes include both random and induced failures which occur prior to, during or after application of electrical power to the fuze. All of these procedures and sequences are controlled and supervised by the brain, which is the microcontroller inside the fuze itself.

Thus taking into account all the safety and arming requirements, Vlatacom Institute developed the entire microcontroller software workflow for the purposes of project P126.

References

- [1] H.P. Culling, "Statistical Methods Appropriate for Evaluation of Fuze Explosive-Train Safety and Reliability," *NAVORD Report 2101*.
- [2] [A.N. Dorofeyev, V.A. Kuznetsov, R.S. Sarkisyan, "Aviation Ammunition (Selected Chapters)", *Aviatsionnyye Boyepripasy*, 1960, 1-58; 136-510.
- [3] "Aircraft Bombs, Fuzes and Associated Components", *NAVWEPS OP 2216 (Volume 1)*
- [4] "Bombs and Bomb Components", *Departments of the Army, The Navy, and The Air Force, April 1966*
- [5] Gary A. Evans, "Systems Engineering Investigation of Navy Electrical Bomb Fuzing", *Naval Air Warfare Center, Patuxent River, Maryland*



FUZE VAF-M17 ELECTRONIC BLOCK TEST SOFTWARE

NEMANJA DEURA

Metropolitan University, Vlatacom Institute, Belgrade, nemanja.deura@vlatacom.com

DRAGAN DOMAZET

Metropolitan University, Belgrade, dragan.domazet@metropolitan.ac.rs

SREĆKO NIJEMČEVIĆ

Metropolitan University, Vlatacom Institute, Belgrade, srecko@vlatacom.com

Abstract: Detailed explanation of the test procedure for the aviation fuze vAF-M17 is described. The fuze vAF-M17 main purpose is to be implemented inside aviation bombs such as MK-82, MK-84 and BLU-109 penetrator bomb. Complete block schematic of hardware and software architecture of the system is covered in this paper, which is designed to simulate real-time conditions of an aviation bomb drop from an aircraft from the viewpoint of electronics. Required parameters that are measured during testing are amplitude and length of the arming, that is detonating impulse, which is used for activating certain electro-explosive devices for aligning the explosive train (arming position). System, which is described in this paper, is capable to simulate initiator vFI-M17 function essential for providing environmental conditions for activating the fuze. More than 10 various test scenarios are implemented which are going to be described further in the paper.

Keywords: fuze, simulation, software, military, vlatacom.

1. INTRODUCTION

The fuze is a device that detonates a munition's explosive material under specified conditions. In addition, a fuze will have safety and arming mechanisms that protect users from premature or accidental detonation. The fuze may contain only the electronic or mechanical elements necessary to signal or actuate the detonator, but some fuzes contain a small amount of primary explosive to initiate the detonation. Fuzes for large explosive charges may include an explosive booster. [1] [2]

The fuze is essentially a binary state mechanism. In the context of weapon system hardware, a fuze and warhead are unique in that they are expected to remain functionally quiescent until a bona fide target is encountered, and then to function as intended in a fraction of a millisecond. Guidance systems may recover from transient malfunctions; target-tracking radars may experience numerous false alarms without significantly compromising their utility; and missile airframes may flex and recover, but the fuze-warhead process is singular and irreversible. [2]

The warhead usually contains a powerful but relatively insensitive high explosive that can only be initiated by the heat and energy from a primary explosive. The primary explosive is a component of the fuze subsystem and is normally loaded in the detonator. If the detonator is designed properly, it can only be activated by a unique fire signal received from the target-sensing device. A detonator can be designed to activate when it receives either electrical energy (high voltage) or mechanical energy (shock or stab) from the target sensor. [2]

The fuze vAF-M17 and the initiator vFI-M17 that have

been developed are a sub-system designed for use with standard general purpose aircraft bombs such as the MK-81, MK-82, MK-83 and MK-84 as well as penetration aircraft bomb BLU-109.

Each individual component of the vAF-M17 fuze and the vFI-M17 initiator is subjected to functional tests before being installed on the final product, after which the complete product is subjected to certain tests. These tests can be factory (FAT) or site (SAT) tests whose test requirements are obtained based on MIL standards. This paper will describe a small segment of these tests, with an emphasis on the software that was developed for the purpose of testing the main electronic board of the vAF-M17 fuze.

Functional testing of the fuze vAF-M17 main board is performed using equipment shown at Figure 1.

Testing equipment:

1. vAFMainB PCB completely assembled (Electronic block of the fuze, EBAF)
2. Referent PCB board vAFRSW,
3. Computer with 2 USB ports,
4. Application software vAFM17 Fuze Test software
5. National instrument Data Acquisition Module (DAQ) USB6361, NI DAQ
6. Interface vAF USB-UART
7. Driver for vAF USB-UART interface: (Silicon Labs CP210x USB-UART Bridge)
8. Power supply, adjustable from 5V to 15V
9. Interface box vAFM17-EBAF-NI-INT with appropriate cables.

The following can be tested using this equipment and software:

- Functionality of Arming delay rotary switch
- Functionality of Detonation delay rotary switch
- Battery voltage at load with the current greater than 5mA
- MP1 switch functionality
- MP2 switch functionality
- Arming capsule activation sequence (all scenarios are performed to check the operation of the microcontroller)
- Accuracy of arming time
- Firing pulse from the output of the arming capsule driver- waveform, amplitude and width
- Detonation capsule activation sequence
- Firing pulse from the output of the detonation capsule driver - waveform, amplitude and width
- Accuracy of Detonation delay time

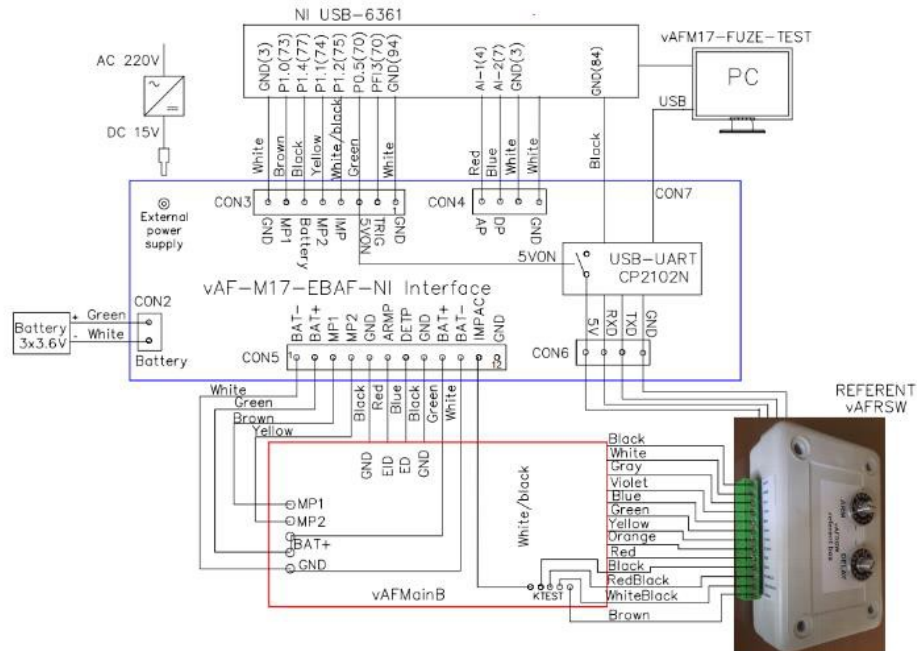


Figure 1. Fuze vAF-M17 main board testing equipment diagram

2. SOFTWARE DESCRIPTION

The purpose of the developed software is to test the operation of the electronics of the fuze vAF-M17 in factory before assembling of the fuze.

The fuze microcontroller (uC) has two modes of operation (Functional or normal mode of operation and Test mode of operation mode). If the uC is powered up by USB connection it goes to test mode of operation – otherwise, if it is powered up by MP1 signal, it goes to normal functional mode.

In Normal operation mode, the following can be tested:

- Launch sensor (MP1 switch) functionality
- Environmental sensor, MP2 signal, functionality
- Arming capsule activation sequence (all scenarios are performed to check the operation of the microcontroller)
- Accuracy of Arming time
- Arming pulse characteristics: waveform, amplitude and width
- Detonation capsule activation sequence
- Detonation impulse characteristics: waveform, amplitude and width.
- Detonation delay time accuracy.

Table 1. List of signals and NI DAQ ports

No.	Signal	Analog /Digital	Input/ Output	NI DAQ Port	Description
1	MP1	Digital	Output	P1.0	Simulates switch MP1 inside the initiator
2	MP2	Digital	Output	P1.1	Simulates signal From pressure Sensor located inside the initiator
3	Impact	Digital	Output	P1.2	Simulates impact the bomb; After this signal detonation delay time begin.
4	Battery	Digital	Output	P1.4	Disconnects power supply from the EBAF; Reset EBAF
5	AP	Analog	Input	AI-1	Puls generated by arming capsula driver
6	DP	Analog	Input	AI-2	Puls generated by detonation capsula driver (ED)

Test results can be saved into Microsoft access DB, and report of testing generated after performing the test.

3. SOFTWARE OPERATION

Figure 2 shows the main screen of the software

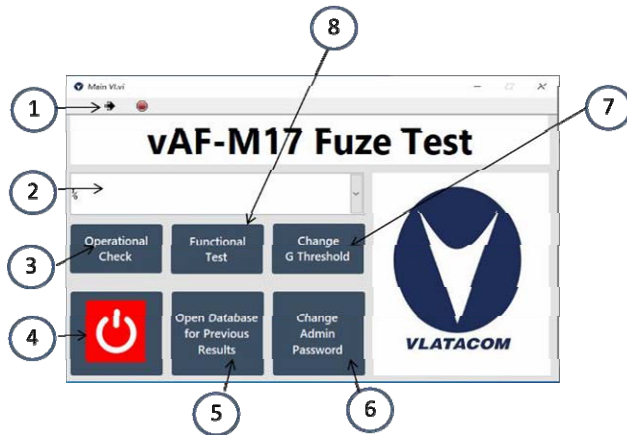


Figure 2. Software main screen

Table 2. List of control and indicators of the main screen

No.	Control/indicator
1)	Toolbar (Run, stop or pause running). When the user launch the software the application will run automatically
2)	VISA Resource name of the USB-UART interface. The user must select this from the dropdown list before starting any test.
3)	Operational Check: activate uC in test mode of operation. (USB should be connected) and get uC response of several parameters (as listed in software requirements in test mode of operation)
4)	Stop running the application.
5)	Open Database for Previous Results: possibility to see, and/or print previous UUT Results.
6)	Change Administrator password, (the only privilege of the administrator, is that he can change "g threshold" value)
7)	Change 'g' threshold
8)	Functional Test: activate uC in normal, fuze functional mode of operation to test EBAF regular functionality.

3.1. Operational check

When user clicks on "Operational Check" button on the main screen, DAQ device activates (vAF-M17 NI-USB-UART adapter) to connect USB to the uC via USB-UART adapter. Then SW keep sending a query command to the uC "[R]" and receive response string (see table 5-2), parse this string, and display different parameters on the operational check screen.

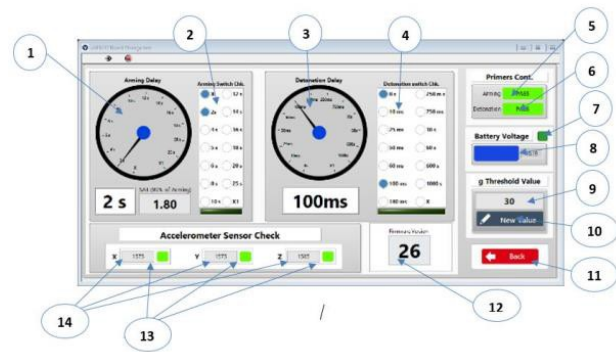


Figure 3. Operational Check Screen

Table 3. List of control and indicators of the operational check screen

No.	Control/indicator
1)	Arming Rotary Switch indicator
2)	Arming Switch position check
3)	Detonation delay Rotary Switch indicator
4)	Detonation Delay Switch position check
5)	Arming primer continuity indicator
6)	Detonation primer continuity indicator
7)	Battery voltage check indicator
8)	Battery voltage measurement indicator
9)	'g' threshold value indicator
10)	Open window to allow administrator user to change the 'g' threshold
11)	Close the screen, go back to the main menu
12)	Firmware version indicator
13)	Accelerometer sensor check indicators (X, Y, and Z)
14)	Accelerometer's voltage indicator (X, Y, and Z) read by uC

3.2. Functional test

Upon clicking of "Functional Test" button on the main screen, DAQ Device activates the vAF-M17 NI-USB-UART adapter to power up the uC in test mode and get the current position of the rotary switches, then wait for any user interaction.

Arming and Detonation pulses are monitored continuously independent on any other functionality of the software. The user will be informed and pulses will be displayed whenever any impulse is fired.

The user can perform test on the fuze board manually (MP1, MP2, and impact signals are generated manually via controls on the screen) or automatically (MP1, MP2, and impact signals are generated automatically by the software).

Switching to automatic mode will disable the control of these three signals.

3.2.1. Controls, and indicators

Figure 4 shows the Functional Test screen, and a description of every control or indicator is described below.

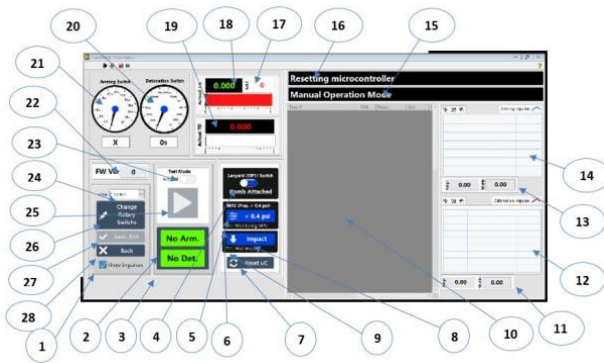


Figure 4. Functional Test screen

Table 4. List of control and indicators of the functional check screen

No.	Control/indicator
1)	Show Impulses Check box – to show/hide Impulses waveform windows
2)	Arming State indicator
3)	Detonation State indicator
4)	Lanyard (MP1) Switch simulation control (only Active in manual mode)
5)	MP2 (Press > 0.4 psi) simulation Control (only Active in manual mode)
6)	Monitoring MP2 indicator (only Active in manual mode) to indicate that uC is in the state of monitoring MP2.
7)	Reset uC Control (only Active in manual mode)
8)	Impact Simulation control (only Active in manual mode)
9)	Wait Impact indicator (only Active in manual mode) to indicate that uC is in the state of waiting impact after Arming has occurred.
10)	Test results (only Active in automatic mode) show test results of UUT in auto mode.
11)	Detonation Impulse Characteristics indicator (Amplitude, pulse width)
12)	Detonation Impulse indicator This indicator, as well as Characteristics indicator are updated every time Detonation impulse is generated
13)	Arming Impulse Characteristics indicator (Amplitude, pulse width).
14)	Arming Impulse indicator This indicator, as well as Characteristics indicator are updated every time Arming impulse is generated
15)	Program State indicator
16)	uC State indicator
17)	SAT time indicator (set according to the position of Arming time rotary switch)
18)	Arming time counter indicator (the range of this indicator is set according to the position of Arming time rotary switch)
19)	Detonation delay time counter indicator (the range of this indicator is set according to the position of Detonation delay rotary switch)
20)	Detonation Delay switch indicator
21)	Arming time switch indicator
22)	uC Firmware version indicator
23)	Test mode switch control

24)	uC VISA control
25)	Start/Stop automatic test (Active only in auto mode)
26)	Change Rotary switch, open screen to allow user change Arming, and Detonation delay rotary switches (Active only in manual mode)
27)	Save, exit – save result (shown in the result window) and exit this screen to the main screen (Active only after finishing automatic test)
28)	Back – Exit operational test screen, without saving results, and go back to the main screen

3.2.2. Performing functional test manually

If the user switches to manual mode, the software enables (MP1, MP2, and impact signals). The user can start to apply these signals to the uC, to simulate the functionality of the initiator's MP1, and MP2 signals, and accelerometer sensor's impact signal, to check the response of the uC upon different conditions.

Upon clicking on the MP1 switch on the test screen, DAQ device will send MP1 signal to the uC and the battery will connect to the fuze board. At this moment, the Arming counter start to count the Arming time and "Monitoring MP2" indicator goes to high during the SAT time.

The user can click on (MP2, and/or Impact) at any time during Arming time counting, which immediately applies the corresponding signal to the uC.

The Software continuously monitors both Arming, and Detonation impulses, to be detected and displayed to the user whenever any of them is generated.

Upon detecting Arming pulse (Figure 5), Software will deactivate MP1 immediately, to check the functionality of BYPASS signal.

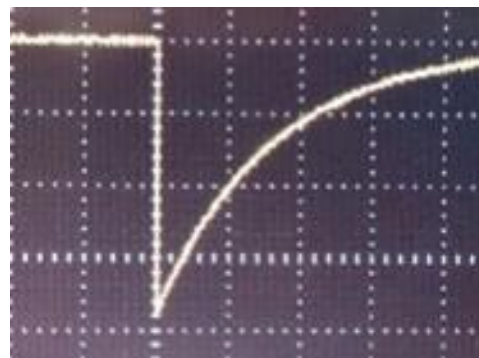


Figure 5. Arming or Detonation pulse waveform

Upon Clicking on "MP1" software disables "MP1", "Test Mode", and "Change Rotary Switches" buttons. Because uC, at this moment is powered and running in functional mode, and cannot go to test mode unless the user resets the uC, clicking on "Reset uC" button.

Upon clicking on "Reset uC" button, DAQ device will disconnect the battery from uC, disable MP1, MP2, and Impact signals. The software will prevent the user to interact with it for 10 seconds (time for Arming, and Detonation capacitor to completely discharge). After this

time, “MP1”, “Change Rotary Switches”, and “Test Mode” buttons will be enabled again.

Upon Detecting Arming pulse, or Detonation pulse, the following sequence will be executed:

- Interface box will generate a digital signal after a delay time introduced by the interface box (Approximately 10 ms)
- This digital signal will trigger DAQ device to start acquiring data from “Primers Impulses” task.

Note: This triggering signal is generated from the interface box if Arming impulse, or Detonation impulse is generated

- DAQ device start acquiring analog data from “Primers Impulses” task (two channels), and return acquired data from both channels to the software. Table 5 shows the detailed acquiring information of the “Primers Impulses” task
- Software will filter the acquired data and return only samples with values less than -1 V (to detect which impulse is generated), and update the waveform graph of the generated impulse.
- Software will analyze the acquired data to calculate the generated impulse characteristics (Amplitude, and Pulse width) and display this information on the related indicator, as well as Actual Arming time.
- After detecting Arming pulse, “Wait Impact” indicator will be active waiting for the user to simulate impact by clicking on “Impact” button.
- When user click on “Impact” button, DAQ device generates a pulse that goes to the Impact pin in the UUT to simulate Impact
- At this moment, Detonation timer will start counting.
- Upon detecting Detonation pulse from UUT, the Detonation timer will stop, actual Detonation time will appear at Detonation counter, Detonation pulse will be displayed at graph and pulse characteristics will be displayed at the related indicators.
- The user has to click on “Reset uC” button to be able to start the above mentioned process again

- The user can change Arming, and Detonation time rotary switches position by clicking on “Change Rotary switches” button to enable communication with UUT to acquire the new position, and update the test screen indicators.
- Acquiring Actual Arming, or Detonation delay times is acquired by DAQ device, as described in the following sub section.

Table 5. Acquiring information of "Primers Impulses" DAQmx task

Sampling Rate	500 kS/s
Sample time (Pulse width resolution)	2 us
Total No. of Samples	100 kS
Total acquiring time	200 ms
Pre trigger Samples	70 kS
Pre trigger acquiring time	140 ms
Post trigger Samples	30 kS
Post trigger acquiring time	60 ms

3.2.3. Performing functional test automatically

The purpose of automatic test is to:

- Checks UUT condition after manufacturing.
- Checks all possible situations that may occur in reality, to ensure that UUT response to different situations safely, and operably.
- Save results for the above two checks to MS Access database
- Enable user to retrieve old data, and print test report for any UUT test event

When the user clicks on “Start Automatic test”, the following sequence will be executed:

- DAQ device activates vAF-M17 NI-USB-UART adapter to enable communication with UUT and operational check window (Figure 6) appears to test the following:
 - Proper battery voltage indication.
 - Arming, and Detonation capsules continuity.
 - Arming, and Detonation switches operations.

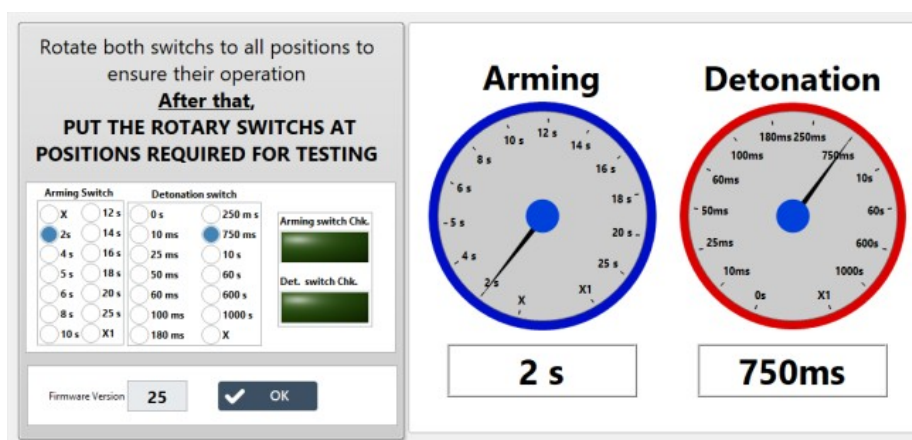


Figure 6. UUT operational check during automatic functional test

- Software reports the result of the above step, as well as ‘g’ threshold value, Firmware version, and Arming, and detonation switches positions.
- Apply ten different scenarios to UUT, to test operation of the UUT under different conditions

Table 6 displays all test scenarios description, and table 7 displays the combination of (MP1, MP2, and Impact) signals during every test.

Note: Tests number 8, 9, and 10 require change in the rotary switches positions, screen shown in Figure 7 will appear, to ask user to change the positions of Arming, and/or Detonation rotary switches according to step number.

During test execution, result window is updated according to each step result (Figure 8), the user also can show/hide the impulses indicators by checking/unchecking “Show impulses” Check box Show impulses

After executing all test steps, the “Save and exit” button Save, Exit will be activated to enable user to enter test information, to be saved in the database. (Figure 9), pressing “OK” button in this screen will save a record into DB, and return to the main screen.

Table 6. Automatic test scenarios

Test No.	Condition	Description
1	Dropping with lanyard attached	Apply Pressure, and Impact while not pulling the lanyard. and wait for 1.3 of (TA+TD) to ensure that there is no Arming or Detonation
2	Safe Separation	Pull lanyard, apply pressure (MP2) before “SAT Time”, then Unset (MP2) for the remaining Arming time, wait for 1.3 of (TA+TD) time to ensure no Arming or Detonation
3	Normal Arming Condition	Apply normal Arming condition, (Arming impulse is expected with proper impulse characteristics to activate Arming primer) without applying impact, wait for 1.3 of TD to ensure no Detonation.
4	Drop in storage	Set Impact and wait for Arming, and Detonation for 1.3 of (TA+TD) to ensure no Arming or Detonation
5	Impact Before Arming test	Apply Arming condition, and Set Impact signal until 0.8 of TA, then unset it, Arming impulse should be generated, wait for 1.3 of TD, to ensure no Detonation.
6	Arming with no impact (Soft Landing)	Apply Arming condition, with no Impact signal, Arming impulse should be generated, wait for 1.3 of TD, to ensure no Detonation.
7	Normal Detonation Condition	Apply normal Arming and Detonation conditions, (Arming, and Detonation impulses are expected with proper impulse characteristics to activate both primers)
8	‘X’ Position for Arming Rotary switch	Apply normal Arming and Detonation process with Arming switch set to ‘X’ position, wait for 1.3 of (TA+TD) to ensure no Arming or Detonation

9	‘X’ Position for Detonation Rotary switch	Apply normal Arming and Detonation conditions with Detonation delay switch set to ‘X’ position, wait for 1.3 of (TA+TD) to ensure no Arming or Detonation
10	‘Inst’ Position for Detonation Rotary switch	Apply normal Arming and Detonation conditions, with Detonation delay switch set to ‘Inst’ position (Arming, and Detonation impulses are expected)

Table 7. (MP1, MP2, and Impact) signals during automatic test steps

No	Initial state			Change			Result		
	MP1	MP2	IMP	At time	MP1	MP2	Imp	Arm	Det.
1	F	T	T	NO Change				NO	NO
2	T	T	T	0.8 * (TA)		F		NO	NO
3	T	T	F	NO Change				YES	NO
4	T	F	T	NO Change				NO	NO
5	T	T	T	0.8 * (TA)			F	YES	NO
6	T	F	F	0.8 * (TA)		T		YES	NO
7	T	T	T	NO Change				YES	YES
8	T	T	T	NO Change				NO	NO
9	T	T	T	NO Change				NO	NO
10	T	T	T	NO Change				YES	YES

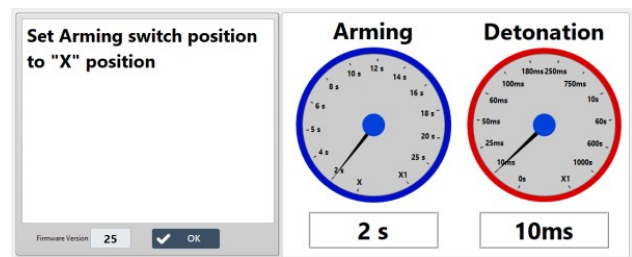
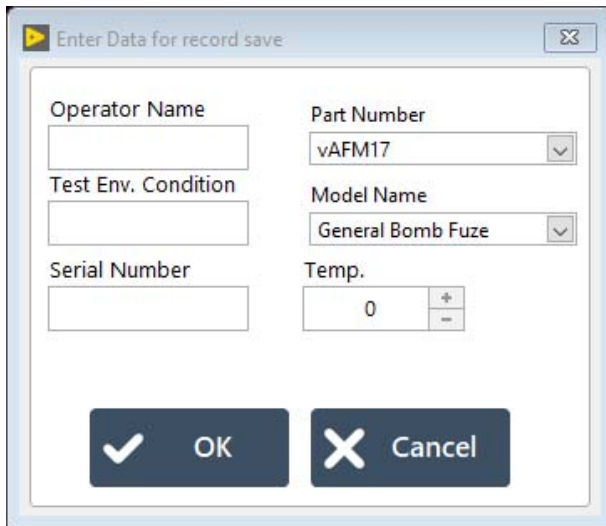


Figure 7. Change Rotary switches in step 8

Running						
Performing Test No. 3 (Normal Arming Conditions)						
Test #	Chk.	Nom.	Act.	L Limit	U Limit	Result
Battery Voltage	-	10.00	10.14	9.00	11.00	PASS
Arming RS Check	-	-	-	-	-	PASS
Detonation RS Check	-	-	-	-	-	PASS
Arming P cont.	-	-	-	-	-	PASS
Detonation P cont.	-	-	-	-	-	PASS
Arming Switch	-	2.00	-	-	-	-
Detonation Switch	-	0.01	-	-	-	-
G Threshold	-	30	-	-	-	-
FW Ver	-	25	-	-	-	-
X Axis	-	1500	1572	1450	1750	PASS
Y Axis	-	1500	1572	1450	1750	PASS
Z Axis	-	1500	1582	1450	1750	PASS
Test 1						
Arming impulse	NO	-	NO	-	-	PASS
Detonation impulse	NO	-	NO	-	-	PASS
Test 2						
Arming impulse	NO	-	NO	-	-	PASS
Detonation impulse	NO	-	NO	-	-	PASS

Figure 8. Test result window



The screenshot shows a dialog box titled "Enter Data for record save". It contains the following fields and controls:

- Operator Name: Text input field.
- Test Env. Condition: Text input field.
- Serial Number: Text input field.
- Part Number: Dropdown menu with "vAFM17" selected.
- Model Name: Dropdown menu with "General Bomb Fuze" selected.
- Temp.: Numerical input field with "0" and increment (+) and decrement (-) buttons.
- OK button: A dark blue button with a white checkmark and the text "OK".
- Cancel button: A dark blue button with a white 'X' and the text "Cancel".

Figure 9. Save test information screen

4. CONCLUSION

Based on the test results, it can be concluded that the software performs its function. With this software it is

possible to test and simulate real operating conditions of the main board of the vAF-M17 fuze and thus confirm its functionality. The test software as well as the hardware ensures better reliability of the fuze, as each individual main board of the vAF-M17 fuze is tested before assembly into the final product. This software and hardware were developed for the needs of the P126 project of the Vlatacom Institute, in order to ensure adequate testing of the manufactured products.

References

- [1] Young, C. G. "Notes on Fuze Design". Journal of the United States Artillery.
- [2] "Chapter 14 Fuzing". Fundamentals of Naval Weapons Systems. Weapons and Systems Engineering Department, United States Naval Academy – via Federation of American Scientists.
- [3] Fuze vAF-M17 Technical Description
- [4] Brad A. Myers, Graphical user interface programming
- [5] M. Jaiswal, Software Architecture and Software Design, 2019 - ISSN:2395-0056



LOAD OF REMOTE CONTROLLED BATTLE STATION UPPER CARRIAGE WITH INTEGRATED AUTOMATIC GRENADE LAUNCHER

MILAN IVKOVIĆ

Faculty of Engineering University of Kragujevac, Kragujevac, milan.ivkovic@kg.ac.rs

VLADIMIR MILOVANOVIĆ

Faculty of Engineering University of Kragujevac, Kragujevac, vladicka@kg.ac.rs

BOGDAN NEDIĆ

Faculty of Engineering University of Kragujevac, Kragujevac, nedic@kg.ac.rs

STEFAN DJURIĆ

Faculty of Engineering University of Kragujevac, Kragujevac, sdjuricrs@gmail.com

Abstract: The paper presents a numerical analysis, using the finite element method, for the case of static and dynamic loading of the upper carriage of the remote-controlled combat station, due to the recoil force generated by the operation of the integrated automatic grenade launcher 30mm M93. The paper describes the problem of integrating the BGA 30mm M93 automatic grenade launcher onto the combat platform, and based on the dimensions of the automatic launcher, modeling of the automatic launcher stand with cradle was carried out. As a result of the weapon dynamics equations and internal ballistics calculations, the pressure force of the gunpowder gases and the recoil force of the automatic grenade launcher were calculated. The paper also presents the results of the dynamic analysis of the finite element model of the upper gun carriage loaded with the obtained impulse recoil force for different elevation angles of the weapon.

Keywords: Remote weapon station, finite element analysis, recoil force, carriage construction

1. INTRODUCTION

The development of new weapons follows its adequate way of integration into the combat platform in order to achieve the greatest possible tactical mobility, and the possibility of occupying the best possible position in relation to the target.

Modern tendencies and strategies of warfare exclude conventional methods and strategies of warfare. The actions of the armies in the war zones were reduced to the minimum necessary weapons resources and the number of engaged military personnel. One of the increasingly present models of battlefield modernization is reflected in the frequent use of remote combat stations and more advanced equipment for observing and detecting targets. Modern constructions of remotely controlled combat stations consist of weapons with a combat kit, stabilizing weapons cradle, fire control systems, opto-electronic observation and aiming systems coupled with the gun barrel.

Today's current military operations show the need for fire protection of lightly armored vehicles during hostilities and during the logistical delivery of equipment on the battlefield. For the above reasons, in order to improve the combat capabilities of light and medium combat vehicles in the world, as well as in our country, a program for the development of light remotely controlled combat stations (RWS) was launched.

One of the main prerequisites for the integration and successful use of this type of combat systems is the achieved precision and accuracy of shooting with as little dispersion of hits on the given line of fire as possible, which is largely influenced by the design of the combat platform.

This paper deals with the development and analysis of a remote controlled weapon station model with the integrated of the domestic automatic grenade launcher BGA 30 mm M93.

2. CONSTRUCTION OF COMBAT PLATFORM UPPER CARRIAGE

This paper analyzes the integration of the automatic grenade launcher BGA 30 mm M93 on a light combat platform, and the final appearance of such a system depends on the dimensions of the weapon, the method of installation, the type of movement, the degree of armor protection and other characteristics that are conditioned by the tactical and technical requirements that the system should satisfy.

Combat platforms are light constructions and usually consist of upper carriages of different shapes with a pivot and a cradle in which mainly machine guns, automatic cannons and automatic grenade launchers are fixed [1]. During the firing action, the loads and moments caused by the recoil force of the weapon, as well as the weight of the oscillating mass, are transferred from the

weapon cradle to the upper carriage from the integrated weapon system. The forces transmitted to the gun carriage are significantly less than the pressure force of the powder gases generated in the barrel of the weapon during shooting. In the case of direct integration of the weapon, without spring shock absorbers, the forces acting on the carriage assembly can be neutralized by the forces of the deformation work of the elastic base, which is sufficiently resistant and rigid to meet the structural requirements.

The demands placed on the construction of the carriage of the combat station are the satisfaction of the conditions of stability of the system against overturning, resistance to all loads in a static and dynamic sense caused by alternating shock loads when firing weapons and reduction of forced oscillations that can affect the accuracy of shooting and scattering of hits.

Based on the known structural parameters of the automatic grenade launcher BGA 30 mm M93, table 1, the goal is to calculate the forces and loads acting on the entire assembly of the automatic launcher, which are transferred to the structure of the upper carriage of the platform by the cradle.

Table 1. Construction parameters of automatic grenade launcher BGA 30 mm M93 [1]

Weapon data	BGA 30mm M93
Mass of empty weapons	35kg
Mass of grenade	0,360kg
Mass of bolt	4,3kg
Barrel length	300mm
Weapon length	825mm
Effective range	1700m
The initial projectile velocity at the mouth of the barrel	185m/s
Maximum pressure of powder gases in the barrel	150MPa

Based on the geometric dependence of the positions of the arms cradle supports, the center of gravity of the weapon, the axis of the barrel channel (the place where the force of the gunpowder gases acts) and the position of the pivot, a schematic representation of the forces given in Figure 1 was created. For these conditions, the equations of stability and loading of the upper carriage are derived.

During the firing action, the gun carriage is loaded with a recoil force, R , at an elevation angle, α , by the weight of the system, G , and at the place where the pivot, reactions of connections F_a and F_b occur. From the conditions of the balance of forces in the system, we obtain the reactions on analytical way, which we will be confirmed with numerical analysis.

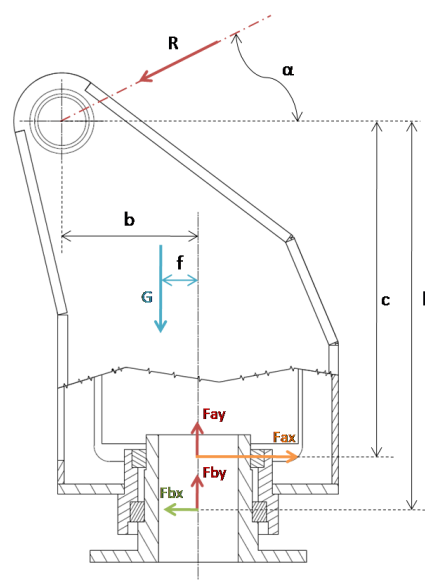


Figure 1. Schematic representation of the forces acting on the upper carriage during firing

3. INTEGRATED WEAPON

The BGA 30 mm M93 works on the blowback principle, it belongs to the group of automatic weapons that use bolt recoil for operation. With such systems, the barrel is immobile, and the bolt is not locked to the barrel or the box during firing, so the system with the so-called by free recoil bolt [2].

The ammunition of automatic grenade launchers in the internal ballistic sense uses the principle of a high and low pressure chamber [3].

The force that causes the tension of the carriage actually represents the recoil force of the entire weapon and is equal to the braking force of the bolt, R . During firing, powder gases are created behind the projectile and a certain amount of energy is spent partly on projectile motion and partly on the recoil of weapon parts. The pressure force of the created powder gases propels the projectile and acts on the walls of the barrel and the bottom of the shell, and thus on the face of the bolt, tending to move it backwards. This force $P_{kn}[N]$ is calculated through the pressure p [bar] acting behind the projectile, obtained as a result of internal ballistic calculations [4].

In the automatic grenade launcher 30 mm M93, during firing, the bolt movement is opposed by the friction force on the contact surfaces of the moving parts (about 5%), the resistance force of the return springs (about 15%) and the hydraulic resistance force (about 80%) which together constitute the resistance force R [1]:

$$R = F_{tr} + 2F_{op} + F_{hk} - m_t g \sin \alpha \quad (1)$$

The last part in equation (4.2.4) refers to the weight component of the recoil mass, which, when the barrel of the weapon is elevated by an angle α , reduces the effect of the recoil resistance force.

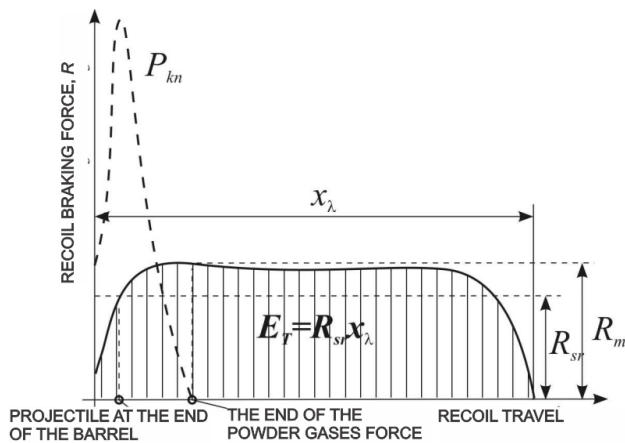


Figure 2. Diagram of recoil braking force []

Bolt braking mechanisms have the role of transforming a short-term, but large impulse of recoil force IT into a long-term impulse of resistance force IR, which is significantly smaller. Figure 2 shows a graphical representation of the transformation diagram of the braking force.

In the OCTAVE program, a software solution was created that calculates the forces of resistance to the movement of the shutter in the course of time and the distance traveled and provides graphical representations of all the calculated functions. [5,6]

The total resistance force, whose graph and values are given in Figure 3, includes previously defined components - friction force, spring resistance force and hydraulic brake resistance force. The largest share, and therefore the influence on the law of change of force R, has the resistance force of the hydraulic brake.

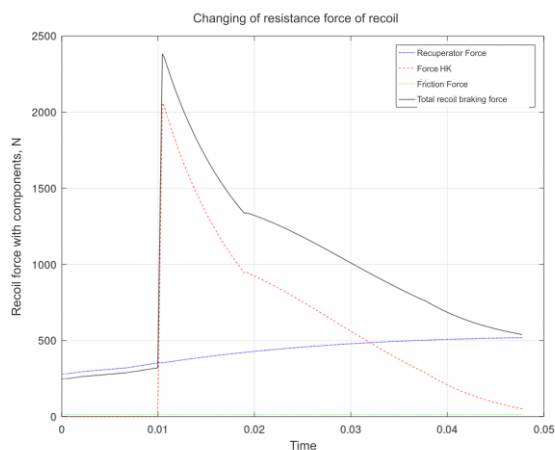


Figure 3. Components of the recoil resistance force and the total recoil resistance force [6]

A calculated resultant recoil resistance force R is transmitted to the platform, creating forced oscillations of the system. When the force becomes equal to zero, the system continues to move, which has the character of damped self-oscillations, until it stops completely in the equilibrium position. [7,8]

4. BATTLE STATION UPPER CARRIAGE MODEL AND NUMERICAL LOAD ANALYSIS

The CAD model of the battle station integration platform for operational purposes was created in the CATIA V5 R21 software package [22]. The model represents a simplified version of the combat platform designed according to industry requirements. For the sake of simpler small-scale production, it is planned to manufacture the assembly of the upper carriage using the technology of welding sheets and plates of different thicknesses. Based on the CAD model, the positions of the barrel axis, the appearance of the upper carriage, as well as the masses of the cradle and the upper carriage were obtained.

The finite element model was created with by the of the mid-surfaces model based on the existing geometry in the FEMAP software package.

In order to satisfy the basic principles of the finite element method based on continuum mechanics, with the use of available tools in the software, the existing model was simplified, and the weld zones were approximated by transitional zones and continuous joints at the welding points of the central part and sides of the carriage, Figure 4 [9]. At the same time, care was taken to ensure that the dimensions of the models remain unchanged.

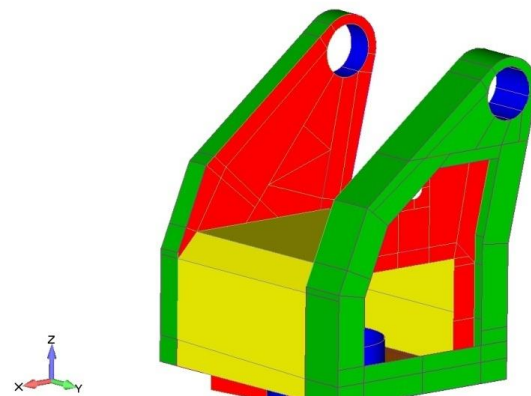


Figure 4. Display of the model of the middle surfaces of the structure of the upper carriage in the software package FEMAP.

The creation of a finite element mesh is the most important item of structural analysis, because the geometric and material properties of the structure are transferred through it. For the elements of the supporting structure of the upper carriage, 2D finite elements generated on the midsurface geometry were chosen and given the properties of shell elements (plates) that represent the thin-walled construction created by bending and welding the corresponding plates and sheets [10,11]. The layout of the generated finite element mesh is shown in Figure 5.

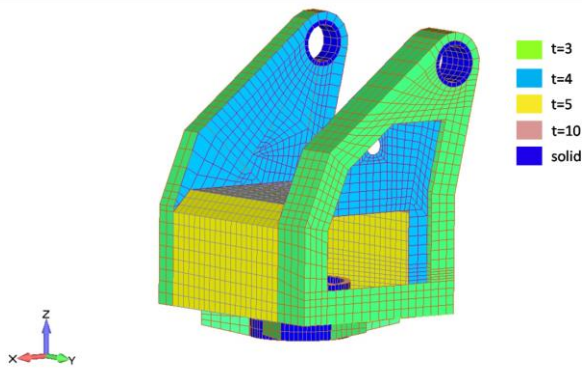


Figure 5. MKE upper carriage construction model

In order to check the model and match the analytical model with the numerical one, an analysis was performed for the case of static loading, where the model was loaded with the maximum recoil force of the weapon, which is 240 dN. In the case of dynamic analysis, a load of variable force as a function of time, $f(t)$, is given, which is obtained as a result of the weapon's dynamics.

As part of the dynamic analysis of the loading of the upper carriage by impulse recoil force for different elevation angles, 400 output sets of solutions were obtained for each analysis. The total simulated time represents an interval of 0.2s during which the gun carriage is loaded with an impulse recoil force and during which the maximum stresses appear as a response of the construction before the system calms down. Eight analyzes were performed for a range of elevation angles from -10° to 60° with an arithmetic difference of 10° .

The most important quantities that were analyzed within the work are displacements and stresses that occur in the critical zones of the structure for different elevation angles, that is, the directions of dynamic load actions.

5. RESULTS OF THE ANALYSIS

For the set analysis parameters and the generated finite element model, results were obtained for the effective (Von-Mises) stress fields of the upper carriage model under the action of dynamic load at different elevation angles α . Based on the load analysis of the upper carriage for different elevation angles, the changes in the values of the maximum stresses and deformations in the zones of the most loaded elements of the structure were monitored and were shown graphically depending on the time of the dynamic load (weapon firing) and the elevation angle.

The effective stress field chosen for the critical case of loading the upper carriage, elevation angle ($\alpha = 20^\circ$), is shown in Figure 6, where the maximum value of the stress, when the load is applied, is 116.5 MPa, while the place of the maximum stress is shown in the figure 7.

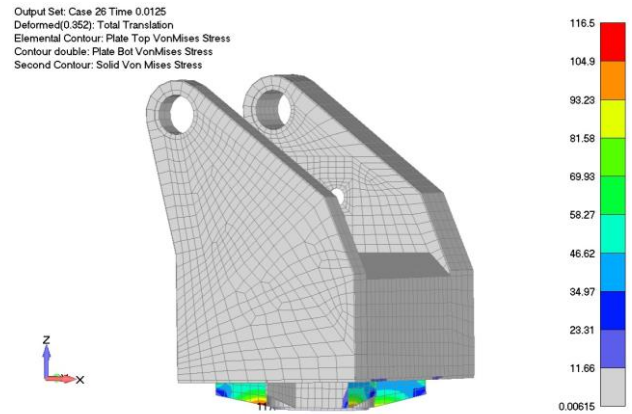


Figure 6. The effective (Von-Mises) stress field of the upper carriage for the elevation angle ($\alpha = 20^\circ$), moment 0.0125s

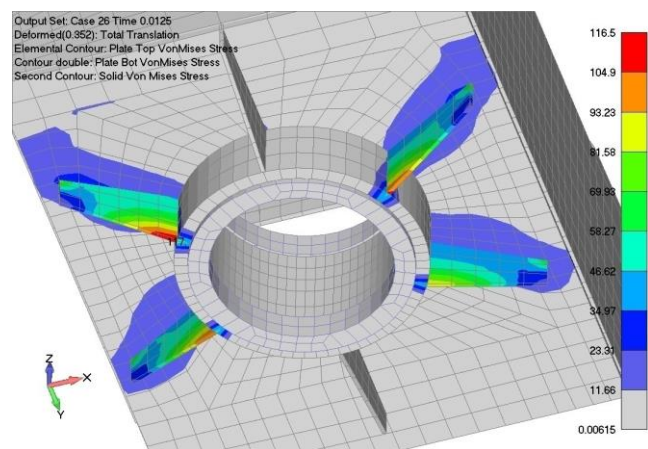


Figure 7. Place of maximum (Von-Mises) stress of upper carriage for elevation angle ($\alpha = 20^\circ$), moment 0.0125s

The field of total displacements of the upper carriage model under the action of dynamic load at the elevation angle ($\alpha = 20^\circ$) is shown in Figure 8. From the displayed image and the palette for displacement values, it can be seen that the total displacement that occurs during the action of the recoil force is 0.352mm

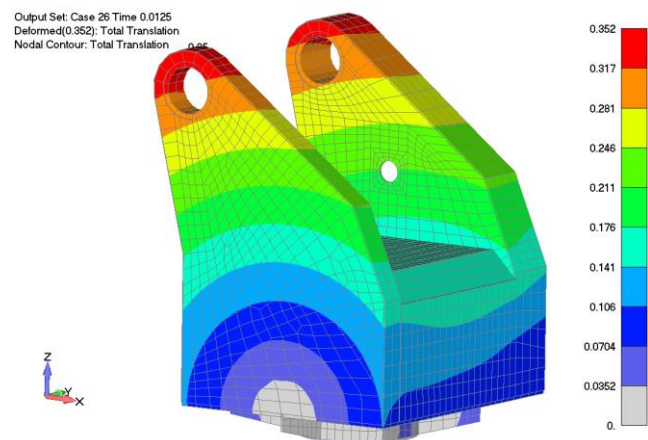


Figure 8. Display of the field of total displacements for an elevation angle of 20° , time instant of 0.0125s

Figure 9 shows a graphic representation of the increase in the stress of the construction, in the zone of

the most loaded element, depending on the time interval of the dynamic load for different elevation angles. From the picture, you can see the trend of increasing load for elevation angles from -10° to 60° and the time of settling down of the forced oscillations of the entire platform caused by the dynamic effect of the recoil force of the automatic grenade launcher. It is also possible to observe the moment of action of the maximum stresses and displacement of the construction, an interval of 0.0125s.

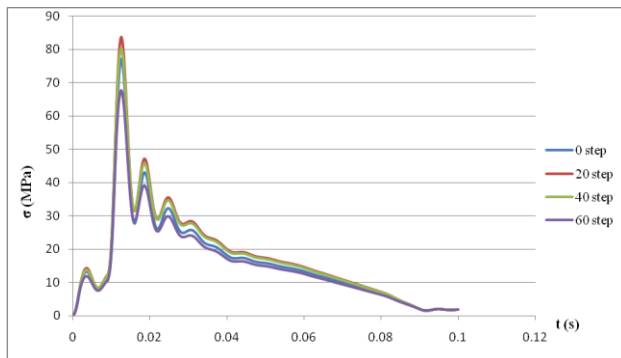


Figure 9. Graphic representation of the effective stress for the rib element of the structure depending on the time interval for different elevation angles.

6. CONCLUSION

In the framework of the paper, the results of the analysis of the loading of the upper carriage during a simulated single fire from an integrated weapon were given, and the values of the effective stresses and total displacements for the loaded configurations were presented. Based on the numerical analysis of the dynamic loading of the upper carriage by the force of recoil, the most loaded parts of the upper carriage were observed.

Through this work, experience was gained for further improvement and optimization of the combat station system. The recoil force can be further reduced by placing the automatic grenade launcher on a stand with spring shock absorbers, which would further reduce weapon oscillations and increase accuracy.

The practicality of this method is its predictive capabilities, where based on the numerical analysis, using the finite element method, the dynamic loading of the structure of the upper carriage of the remotely controlled combat station and the processing of the results of the analysis for the case of burst fire, the possibility of predicting the maximum number of firings from the integrated weapon due to which there will be no stress increase above the critical value for the given construction material. Applying these methods would reduce the resources necessary for the development of a new system and reduce the number of tested models in order to confirm the validity of the construction.

REFERENCES

- [1] Aleksandar Kari: Daljinski upravljive borbene stanice, Materijal za predavanja iz predmeta integracija naoružanja na mobilne platforme, 2017
- [2] Uputstvo za korišćenje i održavanje – 30 mm bacač granata automatski, Zastava oružje.
- [3] Jaramaz S., Micković D. Primena principa komore visokog/niskog pritiska na optimizaciju pogona municije za automatski bacač granata, Mašinski fakultet, Beograd, 2001.
- [4] M. Petrović, Mehanika automatskog oružja, Vojnoizdavački zavod, Beograd, 2009.
- [5] Ljubiša Tančić: Unutrašnje balističko projektovanje, Beograd 2014. god.
- [6] Nina Živanović, Aleksandar Kari: BEHAVIOUR SIMULATION OF LIGHT MOBILE PLATFORM UNDER THE INFLUENCE OF INTEGRATED WEAPON'S RECOIL FORCE, OTEH, Beograd 2018. god.
- [7] Zoran Ristić: Konstrukcija automatskog naoružanja, skripta Bg. – Kg. 2014. god.
- [8] M. Kalezić, Projektovanje artiljerijskih sistema, Knjiga JEDAN, Beograd, 2010.
- [9] Kojić M., Slavković R., Živković M., Grujović N.: Metod konačnih elemenata I, Mašinski fakultet, Kragujevac, 1998. - pristupljeno 16.9.2021. godine
- [10] M. Živković: Nelinearna analiza konstrukcija, Mašinski fakultet, Kragujevac, 2006.
- [11] Живковић М., Вуловић С.: *NONLINEAR STATIC AND DYNAMIC STRUCTURAL ANALYSIS*, Крагујевац, 2013.



10th INTERNATIONAL SCIENTIFIC CONFERENCE
ON DEFENSIVE TECHNOLOGIES
OTEH 2022

Belgrade, Serbia, 13 – 14 October 2022



SECTION IV

Ammunition and energetic materials - AEM

CHAIRMAN
assoc. prof. Jovica Bogdanov, PhD



CLASSICAL AND INSTRUMENTAL METHODS FOR DETERMINATION OF RESIDUAL SOLVENT IN NITROCELLULOSE GUNPOWDER

MAGDALENA RAKIĆ

Military Technical Institute, Belgrade, magdalenaracic@gmail.com

MIRJANA KRSTOVIĆ

Military Technical Institute, Belgrade, mbkrstovic@gmail.com

MIRJANA DIMIĆ

Military Technical Institute, Belgrade, mirjanadimicjevtic@gmail.com

BOJANA FIDANOVSKI

Military Technical Institute, Belgrade, b.fidanovski@gmail.com

Abstract: The production of nitrocellulose gunpowder includes as indispensable two solvents: ethanol and diethyl ether. Both solvents, in very high concentration, are present during the production. One of the last steps, in standard procedure, is removing the solvents from the system. This operation enables keeping and protecting ballistic performances and stability of gunpowder. However, some of the solvents remains in the gunpowder and the amount of residual solvents must be monitored. Previous technique included only classical method for determination of residual solvents. As a result, the total quantities of residual solvents were obtained. The aim of the presented paper is to develop a new approach to individual residual solvents determination, separately, by instrumental method – gas chromatography method.

Key words: nitrocellulose gunpowder, moisture content, residual solvents, classical method, instrumental - gas chromatography method.

1. INTRODUCTION

Chemical stability of the ammunition which commonly contain nitrocellulose gunpowder is one of the most concerned property of such composition [1]. During the production of nitrocellulose gunpowder, a large quantity of organic solvents (ethanol – EtOH and diethyl ether – Et₂O) are used [2]. High concentration of both solvents (added into system as a mixture - 2:1 of diethyl ether and ethanol, respectively) must be present in process for better gunpowder mass shaping [3, 4]. Furthermore, concentration of 25 % of ethanol in gunpowder has effect on lower friction and impact sensitivity of pure nitrocellulose which providing safe handling in gunpowder production [5].

However, it is well known that, ethanol and diethyl ether are extremely flammable liquids of sweet-smell and high volatility [6]. Therefore, during the manufacturing process of nitrocellulose gunpowder, solvents vapor comes in contact with air making a gas mixture. That gas mixture is highly explosive and could cause a detonation effect with nitrocellulose gunpowder, which indicates the safety and compliance with the production procedure must be at an extremely high level [5].

Near last phases of gunpowder production, the gunpowder mixture has approximately 15-20 % of solvents [4]. This huge percentage of solvents directly affects gunpowder ballistic stability control. Namely, precise and acceptable

calculation of solvent percentages should be done before the manufacturing process starts. In the classical approach, maximum solvent concentration should be among the 0.7 to 1.3 %, which would neutralize the potential unwanted gelatinization process and enable safe ammunition storage [7]. So, the crucial step during production, is removing solvents from the gunpowder mixture. Two different operations, which are defined by the gunpowder manufacturing procedure, are involved during the residual solvent elimination process [8]. In practice, the safety of gunpowder is evaluated during the quality-control process i.e. by experimental measurements. As a result, only acceptable safety can guarantee their application.

In addition to measure residual solvents, determination of moisture content is also very important examination from the aspect of preserving ballistic performance. Namely, if the moisture content decreases over time, there will be an increase in the initial gunpowder combustion rate, and also an increase in the maximum pressure of the gunpowder gases. On the other hand, if moisture content increases over time, the gunpowder ignition will be difficult, initial speed will be in decrease and eventually the range of the projectile will be reduced.

This paper presents a new approach of investigations of classical chemical and instrumental method, especially, instrumental method – chromatography. Although, the classical chemical method is mainly and only involved in experimental measurement of residual solvents, the

growing tendency in the world, is to employ modern instrumental methods for monitoring the content of residual solvents.

2. MATERIALS AND METHODS

Two different types of nitrocellulose gunpowder (NC-16 and NC-161), sampled from the different lots (label as *a*, *b*, *c* for NC-16 and *p*, *q*, *r* for NC-161) were examined. All samples were examined according to the classical gravimetric method and instrumental GC (Gas Chromatography) method.

2.1. Classical method - gravimetric method

Samples preparation

Dimension of samples for classical method were performed by further technique. All nitrocellulose gunpowder grains with dimension of 2.0 mm or less were used as they were, i.e. in their original shape. Larger samples were milled into smaller pieces.

Experimental procedure for measurement of the moisture content in nitrocellulose gunpowder

Firstly, clean and dry measurement vessel with lid was measured. Samples with the mass of 5.000 g whose dimensional preparation has been completed, were placed in it. After drying (two hours at the temperature of 80 °C) and cooling the samples, experimental measurement of moisture content was calculated, according to the following equation (1):

$$\text{moisture content} = \frac{a}{m} * 100\% \quad (1)$$

a – difference in sample mass before and after drying, g and

m – mass of the examined sample of nitrocellulose gunpowder, g.

Experimental procedure for measurement of the volatility substances in nitrocellulose gunpowder

Firstly, clean and dry measurement vessel with lid was measured. Samples with the mass of 10.000 g whose dimensional preparation has been completed, were placed in it. After drying (five hours at the temperature of 100 °C) and cooling the samples, volatile substances content was determined according to the following equation (2):

$$\text{volatility substances} = \frac{a}{m} * 100\% \quad (2)$$

After determination of volatile substances content, the value of residual solvents can be calculated according to the equation (3):

$$\text{residual solvents} = VS - MC \quad (3)$$

VS – calculated result of volatility substances, equation (2), mas.% and

MC – calculated result of moisture content, equation (1),

mas.%.

2.2. Instrumental method – Chromatography

Samples preparation

For instrumental method dimensional preparation of nitrocellulose sample, i.e. chopping or grinding, is not allowed. So, all nitrocellulose gunpowder was used as it is.

Experimental procedure for measurement of the residual solvents in nitrocellulose gunpowder

First step in identification of residual solvents from the examined samples was distillation process. Therefore, it was necessary to prepare heating bath, the distillation flask, Liebig condenser and Erlenmeyer flask, and connect the distillation apparatus. Nitrocellulose gunpowder samples with the mass of 5.000 g with approximately 80 cm³ of 15 % of solution of sodium hydroxide were placed into distillation flask. The distilled water was poured into Erlenmeyer flask. The heating was performed in heating bath and the distillation process can started. After two hours of heating or until volume of 100 cm³ of distillate was separated, distillation process should be in progress.

Second step was the identification process by gas chromatography method. Namely, this instrumental method is based on recognition of compounds using the same pure compounds which are in the examined samples. This step depends on comparison of the chromatography peak from the standard and chromatography peak from the samples. The calculation of each compound concentration, follows next equations (4) and (5):

$$\%EtOH = \frac{P_{EtOH}}{m_{uz} * P_{us}} * \frac{P_{us} * m_{EtOH}}{P_{EtOH}} \quad (4)$$

$$\%Et_2O = \frac{P_{Et_2O}}{m_{uz} * P_{us}} * \frac{P_{us} * m_{Et_2O}}{P_{Et_2O}} \quad (5)$$

The gas chromatograph equipped with thermostat for column heating, manual injector and "TCD" detector was used.

Chromatographic conditions: detector (TCD, heated at 220 °C and with reference flow of 20 mL min⁻¹), column HP-PLOT Q, oven (heating on 110 °C) and the hydrogen gas as mobile phase. The GC system has the total flow rate of 39 mL min⁻¹ and the pressure of 2.45 psi. The volume of the injection sample solution was 1 μL [9, 10].

Calibration: The calibration was done with ethanol and diethyl ether solution. The concentration of the calibration solution corresponded to the mass of the test samples and, at the same time, it should satisfy the range of concentrations in the examined samples [9, 10].

3. RESULTS AND DISCUSSION

In order to preserve and protect ballistic performance in the nitrocellulose gunpowder for both types of examined

samples, humidity was tested by gravimetric method. According to the equations (1), (2) and (3), results were obtained and shown in the Table 1 and 2. Besides, results of residual solvents collected using the classical method were also shown in the same Tables. For every examined lot, the values of three measurements are given as mean values obtained from three measurements.

Table 1. Results of the mass concentration of moisture content and residual solvent for NC-16 by gravimetric method

Nitrocellulose gunpowder samples	Classical method - gravimetric method	
	moisture content	residual solvents
NC-16, <i>a</i>	1.00	0.49
NC-16, <i>a</i>	0.99	0.56
NC-16, <i>a</i>	1.01	0.59
NC-16, <i>b</i>	0.82	0.68
NC-16, <i>b</i>	0.75	0.53
NC-16, <i>b</i>	0.94	0.52
NC-16, <i>c</i>	0.84	0.53
NC-16, <i>c</i>	0.76	0.48
NC-16, <i>c</i>	0.88	0.51

Table 2. Results of the mass concentration of moisture content and residual solvent for NC-161 by gravimetric method

Nitrocellulose gunpowder samples	Classical method - gravimetric method	
	moisture content	residual solvents
NC-161, <i>p</i>	0.93	0.63
NC-161, <i>p</i>	0.86	0.53
NC-161, <i>p</i>	0.80	0.59
NC-161, <i>q</i>	1.03	0.46
NC-161, <i>q</i>	0.87	0.39
NC-161, <i>q</i>	1.03	0.55
NC-161, <i>r</i>	0.82	0.43
NC-161, <i>r</i>	0.75	0.58
NC-161, <i>r</i>	0.67	0.54

A precisely defined range for amount of moisture minimizes the potential risk of initiation of unwanted gelatinization process. Nitrocellulose gunpowder NC-16, sampled from the different lots label with *a*, *b*, *c* shown in Table 1, gave satisfactory concentration of moisture content. The results of moisture content for NC-161, sampled from the lots label: *p*, *q*, *r* (Table 2.); were slight lower than results of NC-16 samples, but they are also in the range. Considering that the moisture content test was very sensitive, due to the large influence of humidity from the atmosphere. Minor deviations within the 3 measurements in both samples for all examined lots were expected. Although, NC-16 and NC-161 nitrocellulose gunpowder have approximately similar composition, the possibly explanation for difference between the results could lie in residual solvents.

On the other hand, obtained values for residual solvents, by gravimetric method, were in the range for both tested

samples, Table 1 and 2. Acceptable agreement between 3 measurements in every lots indicated good homogeneity of the samples.

Since two different types of solvents remained in the nitrocellulose gunpowder, in addition to the standard gravimetric method, an instrumental method was employed for monitoring the content of residual solvents. Namely, the base of our research was checking the residual solvent using chromatography. The gas chromatography was chosen as an instrument method which could identify and give the precise value of each solvents separately. In order to recognize and identify each solvent in NC samples the special preparation of the calibration solution, as well as described distillation process, should be done.

The average values of the residual solvents, which were calculated using equations (4) and (5), were shown in Table 3 and 4. The average value presented the value of three measurements, as mean values obtained from three measurements.

Table 3. Results of average value of concentration of each residual solvents separately, ethanol (EtOH) and diethyl ether (Et₂O), from NC-16 by instrumental method

Nitrocellulose gunpowder samples	Instrumental method – gas chromatography	
	EtOH	Et ₂ O
NC-16, <i>a</i>	0.49	1.40
NC-16, <i>b</i>	1.08	1.61
NC-16, <i>c</i>	0.93	2.19

Observing independently the results of each solvent, in all three lots, disagreement between measurements appeared probably due to differences in batch production. Particularly, batch production involves small batches which are always checked by quality control. If the results are inconsistent, it can be fixed without big losses compared to the mass production [11]. In this case lot with label *a*, needs to be changed or modified depending on requirements and needs of examined nitrocellulose gunpowder, or should be use in less percentages in final mixture of end product.

On the other hand, comparing the results from NC-16 sample, Table 1, the values of the residual solvents obtained by gravimetric method were much lower than the total amount of average value of residual solvents obtained by GC method, Table 3.

According to the results it is obvious that gravimetric method gives an information only for residual ethanol. Namely, procedures for measurement the residual solvents required drying on the temperature of 100 °C, by classical method. Knowing the fact that boiling temperature of ethanol is 78.4 °C [6, 12] and for diethyl ether is 346.0 °C [6, 12], obviously, more ethanol was released than diethyl ether, by first method. Besides, GC method used oven and detector, TCD which was heated at 220 °C, so the diethyl ether, as a second solvent can be relisted, identified and calculated with minimal error.

The instrumental method was also used for obtaining the results for NC-161, for all three lots, Table 4.

Table 4. Results of average value of each residual solvent separately, ethanol (EtOH) and diethyl ether (Et₂O) from NC-161 by instrumental method

Nitrocellulose gunpowder samples	Instrumental method – gas chromatography	
	EtOH	Et ₂ O
NC-161, <i>p</i>	1.02	1.32
NC-161, <i>q</i>	1.11	1.25
NC-161, <i>r</i>	1.08	1.35

The results of residual solvents for NC-161 sample, by obtained by GC method, shown better mutual agreement than the results for NC-16 presented in Table 3. That implicated more appropriated batch production, i.e. easier joining of lots for final product placement.

Although the sums of these values are, again, higher than the results obtained by classical method, the same conclusion can be made. Despite the preparation process – distillation, allowed collecting of all released gasses which evaporated in a closed system, the chromatography method enables better agreement between the results from the aspects of collecting and giving much more precise individual values for each residual solvent, than the classical method.

4. CONCLUSION

Two different type of methods, classical and instrumental method, were in used for determination the residual solvents from the nitrocellulose gunpowder NC-16 and NC-161 (analyzing the tree different lots for each NC samples, separately).

The moisture contents were determined using the classical method as a standard method for measured the water contend in the laboratory. The obtained results of moisture content in gunpowder were based on classical – gravimetric method which leads to the qualitative monitoring of released humidity by heating gunpowder on the precise temperature and time. The collected results for both NC samples for all lots are in the range, which minimized the potential risk of the degelatinization process and satisfied the conditions of safety. This information is important from the aspect of safety and application of gunpowder in ammunition.

The residual solvents were, firstly, analyzed by classical method. The obtained results presented the difference between moisture content and volatile substance. Although this approach satisfied the standard of quality-control for manufacturing the nitrocellulose gunpowder, it does not provide the precise value for each solvent.

On the other hand, inclusion of an instrumental method – gas chromatography method, in determination the exact concentration of individual solvent can be of great importance. Preparation process for instrumental method was consisted of distillation process, which enabled the collection of all released gasses that evaporated in a closed system. The GC method was depending on recognition of compounds using the same pure compounds which are in the examined samples. After

comparison of the chromatography peak for the standard and chromatography peak from the samples, calculation of concentration of the ethanol and diethyl ether gave their precise results. This separated concentration of ethanol and diethyl ether can be of great influence for the removing process during manufacturing and can facilitate calculations for the batch production. Our results are encouraging and should be validated by a larger sample size.

ACKNOWLEDGEMENT

This work was supported by the Ministry of Education, Science and Technological Development of the Republic of Serbia, Contract No. 451-03-68/2022-14/200325

References

- [1] Gang Lia, Chaoyang Zhan, Review of the molecular and crystal correlations on sensitivities of energetic materials, *Journal of Hazardous Materials*, 398, (122910), (2020), , 1-15
- [2] RAKIĆ M.: Classical methods of chemical stability - comparison of analyses for gunpowder, *Scientific technical review*, , *Vol.71, (1), (2021), 25-29*
- [3] Zhanhong.You, Chapter -Gunpowder, Thirty great investigation of China, (2020), 647-662
- [4] Bob Ashford, A new interpretation of the historical data on the gunpowder industry in devon and cornwall, *Baltimor, J. Trevithick soc.* 43, (2016), 65-73
- [5] E.P.Boltrukevich, G.S. Ratanov, Experimental determination of the mean particle size of the condensed phase in the combustion products of gunpowder, *Combustion explosion and shock waves*, 15, (2), (1979), 284-286
- [6] VOLLHARDT K.P.C, SCHORE N.E.: *Organska hemija, struktura i funkcija*, IV izdanje, Data status, Beograd, (2004).
- [7] Petar Maksimovic, Tehnologija eksplozivnih materija, Beograd, (1972).
- [8] Gawera Habyesali, Design of a production line for nitrocellulose-based gunpowder, thesis, Makerere University, (2018).
- [9] Jelisavac Lj., Hemijska stabilnost i vek upotrebe baruta I raketnih goriva (Chemical stability and lifetime of the propellants), *KumNTI, Vojnotehnički institut, Belgrade, Vol. LXIII, No.2, (2009).*
- [10] Geoffery A. Dorsey, Detection of volatile components in solids and thin films by gas chromatography of evolved gases, *Anal. Chem.* 41, (2), (1969), 350-352
- [11] Marek Wirkus, Alicja Kukulika, Issues of Measuring the Course of Batch Production Processes, *Procedia engineering*, 182, (2017), 387-395
- [12] Robert Neilson Boyd and Robert Thornton Morrison, *Organic Chemistry*, Prentice Hall; 6th edition, (1992).



COMPARATIVE ANALYSIS FOR DETERMINATION OF STABILIZER CONTENT IN GUNPOWDER AND DOUBLE BASE PROPELLANT BY HPLC METHOD

MIRJANA KRSTOVIĆ

Military Technical Institute, Belgrade, mbkrstovic@gmail.com

MAGDALENA RAKIĆ

Military Technical Institute, Belgrade, magdalenarakic@gmail.com

LJILJANA JELISAVAC

Military Technical Institute, Belgrade, jelisavach@yahoo.com

MIRJANA DIMIĆ

Military Technical Institute, Belgrade, mirjanadimicjevtic@gmail.com

JELENA MOJSILOVIĆ

Military Technical Institute, Belgrade, mojsilovic.jeca@gmail.com

BOJANA FIDANOVSKI

Military Technical Institute, Belgrade, b.fidanovski@gmail.com

Abstract: Gunpowders and double-based propellants contain nitrocellulose (NC) as their main energetic component. This type of i.e. NC ammunition has slow decomposition period during the time and even under ambient conditions can cause self-ignition. This reaction is spontaneous and cannot be stopped, but can be retarded using small amount of organic compound. Usually those organic compounds are: diphenylamine (DPA) or urea derivatives (e.g. ethyl or methyl centralite), which are known as stabilizers. One of the most important requirements for keeping gunpowder and double base propellant in the area of good chemical stable state for the long storage period is presence of stabilizer in satisfactory concentration in the ammunition. Content of stabilizer can be determined by high performance liquid chromatography method. Sample preparation for determination of the stabilizer content depends on type of gunpowder or double base propellant tested, according to standard procedures method for chemical stability examination by HPLC. Future more, sample preparation includes a very long time for the extraction (around 48 hours) without any external influence, and finally, large amount of solvent – dichloromethane. This paper presents the comparative analysis of different samples preparation in two different solvents (dichloromethane and acetonitrile) by the same method. Using acetonitrile as solvent for extraction results can be provided for less than 12 hours, with the same precision.

Keywords: double-base propellant, gunpowder, stabilizer, nitrocellulose, high performance liquid chromatography.

1. INTRODUCTION

Single-based gunpowders have nitrocellulose (NC) as energetic component, while double-based propellants have two energetic constituents – NC and nitroglycerin (NG). Both of these type of ammunition are based on nitrate ester polymer, which has negative characteristic – slow thermal decomposition during the time. This chemical process has huge influence and, in the same time changing mechanical, chemical [1] and ballistic [2] properties of energetic materials. This progression, known as chemical aging of ammunition, is happening even under ambient conditions. Free radicals: NO^\bullet and NO_2 are products of NC decomposition responsible for autocatalytic exothermic degradation which effect temperature decreasing and, in extreme situation, can cause self-ignition. This reaction is spontaneous and

cannot be stopped, but can be slow down using small amount of organic compounds which are added to increase the stability of NC. Their role is to be main acceptor of free radical nitrogen oxides and acids formed from them [3]. These organic compounds, named stabilizers, are added in ammunition formulations up to 5 wt. %, enough to provide optimal chemical characteristics for longer time. This is the reason why monitoring the stabilizer represents one of the most important methods for chemical stability evaluation.

On the other hand, standard procedures for determination of the chemical stability of NC gunpowder and propellants are based on monitoring and periodical measurement of the content of stabilizer in naturally aged samples. This type of monitoring can only give an information about current chemical stability, without any prediction of total lifetime for ammunition.

Gunpowders and double-based propellants are usually stabilized by diphenylamine (DPA) or urea derivatives (e.g. ethyl or methyl centralite). DPA is usually used in single-based and spherical gunpowder, because it is experimentally proven that DPA accelerates denitration of NG, so DPA is not good choice for double-based gunpowder and propellants. To solve this problem, DPA derivatives (2-NDPA) as primary stabilizer, or urea derivatives are in use in double base gunpowder and in propellants.

During the aging, DPA transits into its derivatives (Fig1.), and, what is more importance, most of them also have stabilizing effect. [4] Despite, the fact that DPA has more than 30 derivatives isolated until now and only a few of them are interesting from the aspect of chemical stability for ammunition – N-NODPA, 2-NDPA and 4-NDPA. Reason for that lies in the fact that the higher DPA derivatives has been consumed at the moment when ballistic shelf life is reached [4].

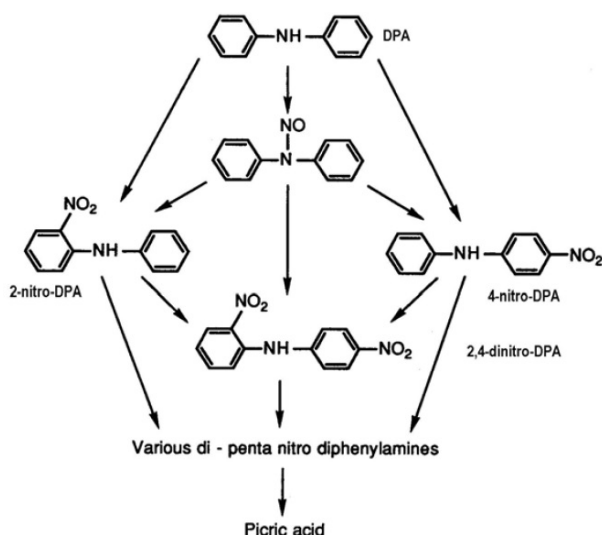


Figure 1. Schematic reaction routes for degradation of DPA in an aging propellant [5]

Ethyl (Fig.2) and methyl (Fig.3) centralite are also common stabilizers in double base propellants and gunpowders formulations.

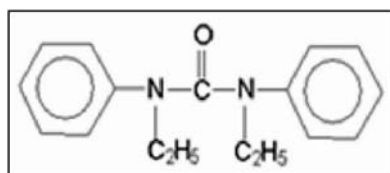


Figure 2. Ethyl centralite

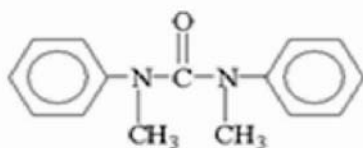


Figure 3. Methyl centralite

During the long time, a whole range of measures and procedures for the control of chemical stability of

gunpowder and propellants were developed all around the world. Some of them are classical methods and some are instrumental. The main focus of instrumental methods are in different kinds of chromatography – high performance liquid chromatography (HPLC), gas chromatography (GC), thin-layer chromatography or UV-Vis spectrophotometry.

HPLC or GC methods are widely used because they can provide results in short time with satisfactory precision. GC method works on high temperature, so it is not appropriated for double base propellant and gunpowder samples with diphenylamine (DPA) stabilizers. Namely, increase in temperature has a direct effect on derivation: N-NO DPA, 2-NDPA and 4-NDPA, which became instable and undergo partly or completely into the DPA [6]. To prevent hazards and get realistic information about existence of stabilizer, it is better to use some other chromatography methods to analyze sample based on DPA stabilizer.

HPLC method prevents this problem completely and represent optimal method for determination not only thermal sensitive DPA derivatives, but also thermally sensitive NG, second energetic compound in double-based energetic materials.

For gunpowder and propellant samples which are stabilized with urea derivatives, preparation is not limited by temperature, as it is in the case with DPA samples. It allows samples preparation with saponification method, a grain gunpowder or propellant is treated by NaOH with heating. In short time, approximately 2 hours, sample dissolved completely. In next step, in separation funnel, extraction is performed in dichloromethane. The solution prepared in this way, can be detected on GC.

However, HPLC method was chosen as method which allows quantitative detection not only for thermally sensitive DPA and its derivatives, but also for: urea derivatives, NG and other organic compounds (plasticizers and explosives). Results shown in this paper present comparative analysis of samples preparation in dichloromethane and acetonitrile for different type of ammunition which were subject of periodic control and technical inspection in Military technical institute for the most common stabilizers in Serbian Military ammunition – diphenylamine (DPA) or urea derivatives (e.g. ethyl or methyl centralite).

The aim of this paper was to present some possible modifications for sample preparation which gave an opportunity to resolve samples preparation problems regarding the handling of large amount of solvent and a long time of extraction.

2. EXPERIMENTAL PART

Materials and samples preparation

Ten different gunpowders and double based propellants were examined. All of them were subjected to natural aging, due to the fact that they were subject of periodic control and technical inspection.

Preparation of samples

Gunpowder or double based propellants were milled in small pieces, sifted through sieves with aperture of 2mm before the extraction process. After milling, each of the samples were measured with mass of 1.000 g and placed into the flask.

Extraction in dichloromethane

Examined sample was placed into the flask, 50 cm³ of dichloromethane was added and flask was left in dark place at room temperature for 48 hours. After that time, 5 cm³ of solution was transmitted to a 10 cm³ flask, dichloromethane was removed at low temperature (approximately 40°C) and 10 cm³ of acetonitrile was added. To provide adequate result, it was necessary to filtrate the sample through 0.5 µm PTFE filter before use.

Extraction in acetonitrile

Examined sample was placed into the flask, 50 cm³ of acetonitrile was added. Extraction included 4 hours using magnetic stirrer and then 4 hours using the ultrasound. Finally, the examined solution, was obtained by separation from the precipitate using a centrifuge. After all this steps, 5 cm³ of volume was transmitted to a 10 cm³ flask, and 5 cm³ of acetonitrile was added. To provide adequate result, it is necessary to filtrate the sample through 0.5 µm PTFE filter before use.

HPLC method

HPLC is an instrumental method for separation, identification and quantification of organic compounds. This technique relies on injecting a pressurized liquid solvent through column filled with a solid adsorbent material (stationary phase). Due to the fact that each component interacts slightly different with stationary phase, different component has different retention time, which provided separation of component in examined sample [7].



Figure 4. High Performance Liquid Chromatograph

For quantitative detection of stabilizer content in prepared samples High Performance Liquid Chromatograph "Waters 1525 EF Binary HPLC Pump" with a thermostat for column heating, the manual injector "Rheodine Model 7125", and the photodiode array detector "Waters 2998

PDA" were used, Fig.4.

Detection, identification and quantification for each of the organic compounds requires calibration which is prepared in adequate solvent (acetonitrile) in optimal concentration. Calibration curve has to cover the range of concentration of the examined samples, taking into account the mass of the samples, as well. To provide best result, each stabilizer has its own curve, made by 5 solvents with different concentration and satisfying precision. Stabilizer calibration solutions are prepared in the concentration range of 0.5 to 3%. All calculations were performed in relation to the sample weight of 1g.

It is mandatory to analyze calibration and sample under same chromatographic conditions. For the analysis of those samples and calibration standards, the following elements of equipment were used: detector PDA (220 nm), column C18 (length 150 mm, ID 4.6 mm and particle size 3µm), column temperature (not above 35°C ± 0.5°C and the mobile phase, acetonitrile: water (67:33 v/v), and the flow rate of 1.2 mL min⁻¹. The volume of the injection sample solution was 10 µL [8].

According to the device working instructions, chromatogram was took of the calibration sample solutions, and then automatic data processing was performed. The results were given in %mass, with an accuracy of two decimal places.

3. RESULTS AND DISCUSSION

The results of determination stabilizer content for samples based on DPA are shown in Table 1. There were four samples of single-based gunpowder stabilized by DPA and one double-based rocket propellant (DBRP) stabilized with 2-NDPA.

Table 1. Result of mass concentration of samples stabilized with DPA and/or it derivatives

No	Samples of gunpowder and propellant	Stabilizer	Extraction		
			Dichloromethane solvent	Acetonitrile solvent	
1.	NC-01	DPA and derivatives DPA	DPA	0.79	0.79
			N-NO DPA	0.31	0.32
			2-N DPA	0.02	0.02
			4-N DPA	0.05	0.06
2.	NC-16	DPA and derivatives DPA	DPA	1.21	1.21
			N-NO DPA	0.12	0.13
			2-N DPA	0.03	0.03
			4-N DPA	0.02	0.01
3.	NC-42	DPA and derivatives DPA	DPA	1.05	1.04
			N-NO DPA	0.08	0.08
			2-N DPA	0.01	0.02
			4-N DPA	0.01	0.01
4.	NCD-06	DPA and derivatives DPA	DPA	1.13	1.13
			N-NO DPA	0.21	0.20
			2-N DPA	0.05	0.06
			4-N DPA	0.03	0.04
5.	DBRP 1	2-NDPA	1.80	1.80	

Results are given in mass%, in two decimals. According to standard procedures for older single based gunpowder content of effective stabilizer represent sum of content DPA, NNO-DPA and 4-NDPA. On the other hand, according to NATO standard [9], effective stabilizer is calculated as sum of DPA and 0.85% NNO-DPA.

According to obtained results, both sample preparations give the same results, with a minor error on the second decimal place.

Due to the fact that effective stabilizer represents sum of DPA and its derivatives, it was crucial to ensure good separation of all peaks of interest.

Proper peak separation for sample of NCD-06, stabilized by DPA is shown in Figure 5, for preparation in dichloromethane. Except DPA and its derivatives, one more peak was detected. It was DNT explosive, which is added to gunpowder formulation for ballistic modification.

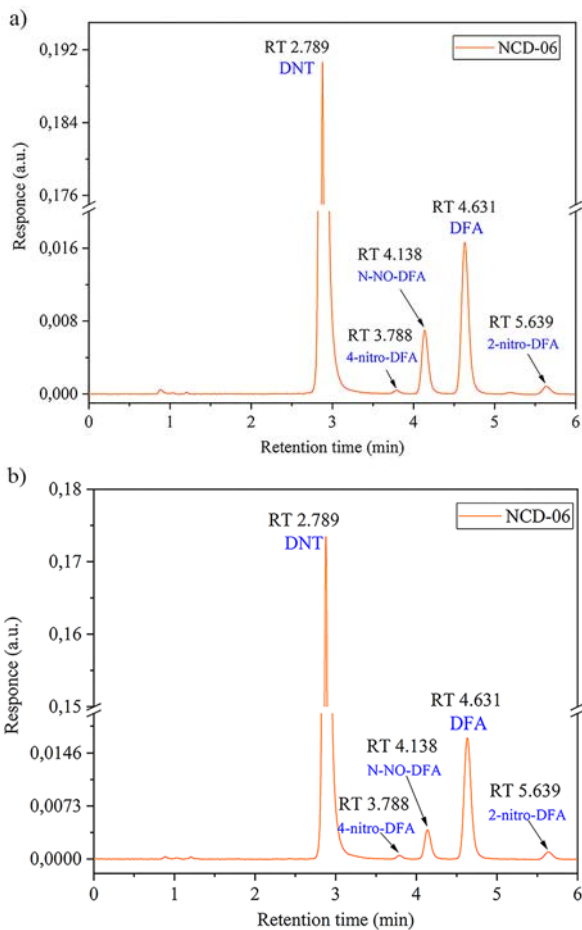


Figure 5. Chromatograms of single-based gunpowder NCD-06, a) extraction in acetonitrile, b) extraction in dichloromethane

The results of stabilizer content determination for five double-based propellant samples, based on urea derivatives (e.g. ethyl or methyl centralite) are shown in Table 2. Results are given in mass%, in two decimals.

Table 2. Result of mass concentration of samples stabilized with urea derivatives

No	Samples of gunpowder and propellant	Stabilizer	Extraction	
			Dichloromethane solvent	Acetonitrile solvent
1.	DBRP 2	C I	1.55	1.55
2.	DBRP 3	C I	2.47	2.46
3.	DBRP 4	C II	2.83	2.84
4.	DBRP 5	C II	1.34	1.34
5.	DBRP 6	C II	1.83	1.84

Double-based propellant stabilized by urea derivatives also had a good matching result for samples preparation in different solvents. In this case, separated peak was detected very easy, because this type of stabilizer is insensitive to high temperature and quite stable, without decomposition into its derivatives, for a long time.

Another separated peak of great importance, ethyl centralite (CI), was registered, Fig.6, in sample DBRP 3 prepared in acetonitrile. Beside CI, two more peaks were identified on this chromatogram. The first peak was for NG, expected for double based propellants, and the other one presented the peak from plasticizer, i.e. diethyl phthalate.

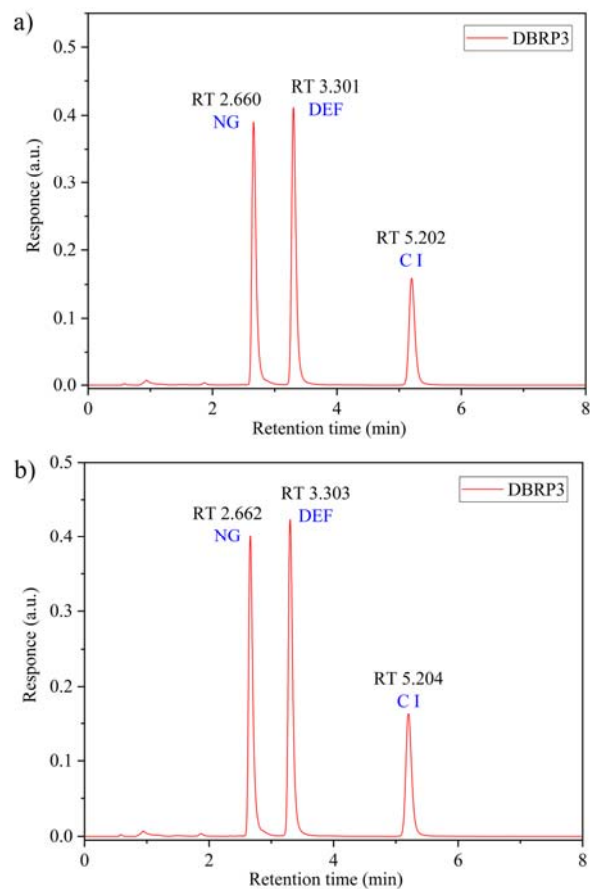


Figure 6. Chromatograms of double-based propellant DBRP 3, a) extraction in acetonitrile, b) extraction in dichloromethane

According to the results obtained by HPLC method, both sample preparation methods provide information about presence of DNT or TNT explosives and enable mass% calculation for those organic compound in samples. On the other hand, only samples prepared in acetonitrile provide realistic information about RDX or HMX presence. As it shown in Figure 7b, sample DBRP 5 prepared in dichloromethane had HMX in very low concentration, according to sample prepared in acetonitrile (Figure 7a).

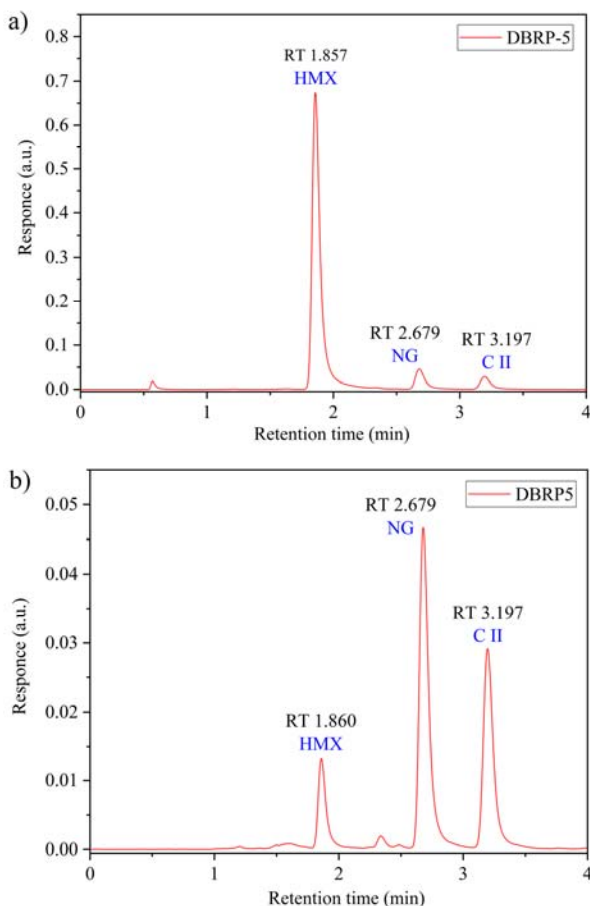


Figure 7. Chromatograms of double-based propellant DBRP 5, a) extraction in acetonitrile, b) extraction in dichloromethane

Reason for that is the fact that those types of explosives (HMX, RDX) are not completely soluble in dichloromethane and require assisted extraction by magnetic stirrer and the ultrasound.

4. CONCLUSION

Comparative analysis was performed of determination of stabilizer content in 10 types of gunpowder and double base propellant by HPLC method, in two different solvents, dichloromethane and acetonitrile, with different approach in samples preparation. The comparative analysis of the samples found that approximately the same values were obtained for preparations in different solvents. For each sample three injects were performed and the result represent the mean value. The obtained results confirmed reproducibility in related to the

preparation method.

Both samples preparations have advantages and disadvantages, but both give satisfactory results.

Samples prepared in dichloromethane requires 48 hours extraction, but without any active laboratory equipment or personnel participation. It is quite convenient for preparation of large number of samples. After the extraction process, dichloromethane should be removed from the samples, which required solvent evaporation on 40C. This process might have influence on thermal sensitive DPA derivatives if temperature is not strictly controlled.

On the one hand, using acetonitrile as solvent saves time and gives results for less than 12 hours, but demands active preparation and equipment (magnetic stirrer, ultra sound and centrifuge), so it is not suitable for preparation a large number of samples. However, this solution had one huge benefit – it provides separation not only for stabilizer and NG, but also for explosives such as RDX and HMX which cannot be found using the dichloromethane solution. It means that sample preparation in acetonitrile provides more information – stabilizer content, NG and explosives if the examined sample contain them. The uniform method for detection of the organic compound from only one sample preparation can be create according to the obtained results. Moreover, all of those information can be provided for less than a day, which represent the standard to which most countries strive.

ACKNOWLEDGEMENT

The authors thank to the Ministry of Education, Science and Technological Development of the Republic of Serbia for the support of the research through the Contract No. 451-03-68/2022-14/200325.

References

- [1] TRACHE D., KHIMECHE, K.: Study on the influence of ageing on chemical and mechanical properties of N,N'-dimethyl-N,N'-diphenylcarbamide stabilized propellants, *J. Therm. Anal. Calorim*, 2013. vol.111, no.1, pp.305–312.
- [2] K. P N and S. B T N, Mechanical and Ballistic Property Variations of a Solid Propellant during Accelerated Ageing, *Int. J. Des. Manuf. Technol.*, vol. 1, no. 1, pp. 71–73, 2007.
- [3] LINDBLOM, T.: Reactions in the System Nitro-cellulose/Diphenylamine with Special Reference to the Formation of a Stabilizing Product Bonded to Nitro-cellulose, *Comprehensive Summaries of Uppsala Dissertations from the Faculty of Science and Technology*, pp. 1-2, 2004.
- [4] Curtis N.J., Rogasch P.E., Determination of derivatives of diphenylamine in australian gun propellants, *Propellants, Explos., Pyrotech.* 12, pp.158-163, 1987.
- [5] W.A. SCHROEDER, E.W. MALMBERG, L.L. FONG, K.N. TRUEBLOOD, J.O. LANDERL AND

- E. HOERGER, Chromatographic Investigation of Smokeless Powder, *Ind. Eng. Chem. Anal.*, 41 2818 (1949).
- [6] THOMAS, J.L., LINCOLN, D., MCCORD, B.R.: Separation and Detection of Smokeless Powder Additives by Ultra Performance Liquid Chromatography with Tandem Mass Spectrometry (UPLC/MS/MS), *J. Forensic Sci.*, 2013., vol.58, no.3, pp.609–615.
- [7] RAKIĆ M, KRSTOVIĆ M, MIJATOV S, DIMIĆ M, FIDANOVSKI B.: Comparative analysis of volumetric and instrumental method for determination of nitroglycerin content in gunpowder *Sci. Tech. Rev.*, 2021, Vol.71, No.2, pp.41-45
- [8] JELISAVAC, L., BOBIĆ, N., STOJILJKOVIĆ, S., DIMIĆ, M., BRZIĆ, S., TERZIĆ, S.: Analysis of the Aging Process of Double-Base Propellants Without an Organic Stabilizer, *Sci. Tech. Rev.*, 2014., vol.64, no.3, pp.3–9.
- [9] AOP-48 Ed.2: Explosives, nitrocellulose based propellants – stability test procedures and requirements using stabilizer depletion, Brussels: North Atlantic Treaty Organization, Military Agency for Standardization, 2008.



EXPERIMENTAL INVESTIGATION ON THE PERFORATION OF HIGH-HARDNESS STEEL PLATE BY AN API PROJECTILE

PREDRAG ELEK

University of Belgrade, Faculty of Mechanical Engineering, Belgrade, pelek@mas.bg.ac.rs

RADOVAN ĐUROVIĆ

University of Belgrade, Faculty of Mechanical Engineering, Belgrade, rdjurovic@mas.bg.ac.rs

NEBOJŠA HRISTOV

University of Defence, Military Academy, Belgrade, nebojsa.hristov@va.mod.gov.rs

DAMIR JERKOVIĆ

University of Defence, Military Academy, Belgrade, damir.jerkovic@va.mod.gov.rs

ALEKSA ANIČIĆ

Agency for Testing, Stamping and Marking of Weapons, Devices and Ammunition, Kragujevac, tehnika@aiz.rs

Abstract: *In the present study, penetration of a 6 mm thick ARMOX 500T high-hardness steel plate by a 7.62x39 mm armor-piercing incendiary bullet with a hard steel core was experimentally investigated. Projectile's impact velocity has been varied in order to determine its influence on the interaction between the penetrator and the target during the penetration process. The initial velocity was measured by the optical measurement system while the residual velocity was measured using the contact screens. Analytical model for the impact velocity calculation was experimentally verified. Based on the obtained ballistic test results, ballistic limit velocity of the target plate was determined and the residual versus impact velocity curve was formed. Furthermore, categorization of the performed firings was conducted in accordance with the observed penetration process outcomes. Finally, target material failure mechanism and its change due to the increase in the projectile's impact velocity was investigated.*

Keywords: *terminal ballistics, experimental investigation, penetration mechanics, armor-piercing, high-hardness armor*

1. INTRODUCTION

Small-arms armor-piercing incendiary (API) ammunition is designed for both the perforation of light-armored targets and the ignition of the inflammable materials. Most commonly, it comprises a hard core made from tungsten alloy or alloyed steel which serves as a kinetic-energy penetrator and the incendiary mixture which ignites the combustible materials located behind the armor [1]. As the high-hardness armor (HHA) steels are extensively used as lightweight armor [2], evaluation of their ballistic resistance against the API bullets is highly important.

Although the prediction of the penetration process outcome may be obtained with the use of empirical equations or analytical models, their usage is often limited and may lead to the results which greatly differ from the experimental data [3]. Due to the complexity of the observed processes and the number of influential parameters, work in the field of penetration mechanics is considered to be experimental in its nature [4]. In the present study, the experimental research was conducted with the aim to determine the influence of the projectile's impact velocity on the ballistic performance of both the ARMOX 500T HHA steel and the 7.62x39 mm API

projectile. Projectile's impact velocity influence was observed as it is one of the major influential factors in the penetration of metallic materials, together with the material properties of the target and the penetrator and the impact geometry conditions [5]. In order to determine the sole influence of the impact velocity on the penetration process outcome, all the other parameters were kept constant, including the angle of incidence which was kept normal as that condition represents the worst-case scenario [6] from the point of target vulnerability.

A description of the experimental set-up, instrumentation and methods is given, together with the description of the projectile and the target properties. Analytical model for the calculation of the projectile's velocity drop was verified experimentally and utilized for the determination of the impact velocity. Evaluation of the errors which may occur during the tests was conducted. Residual versus impact velocity curve based on the modified Recht-Ipson empirical model was formed and the values of parameters were determined. Distinct penetration outcomes were identified and the representative photographs were given. Change in the failure mode of the target material with the change in the impact velocity was observed and analyzed.

2. EXPERIMENT

2.1. Target and projectile properties

The present study is based on an experimental investigation of the ARMOX 500T ballistic behavior when subjected to impact by a 7.62x39 mm armor-piercing incendiary projectile at the normal incidence angle and under the various impact velocities.

ARMOX 500T high hardness steel was chosen as a target material as it is extensively used for the combined protection from the penetration and blast effects. For the purpose of the present investigation, it was procured in the form of a 6 mm thick square-shaped plate with the edge size of 500 mm. The plates were quenched and tempered and their mechanical properties were determined by the manufacturer prior to the delivery (Table 1).

Table 1. Mechanical properties of the target material as per the manufacturers Inspection Certificate

Target type	ARMOX 500T plate
Thickness	Nominal: 6 mm
	Measured: 6.34 – 6.38 mm
Density	8 g/cm ³
Hardness	530 HBW
Yield strength $R_{p0.2}$	1468 MPa
Ultimate Tensile Strength R_m	1687 MPa
Elongation	A ₅ : 11%
	A ₅₀ : 13%

Schematic drawing and the configuration of the 7.62x39 mm M 82 API bullet used in the ballistic tests may be seen in Fig. 1. The projectile comprises a hard steel core encased in the copper jacket with the lead-antimony filler between. The length of the core is 20.4 mm and its diameter is 6 mm.

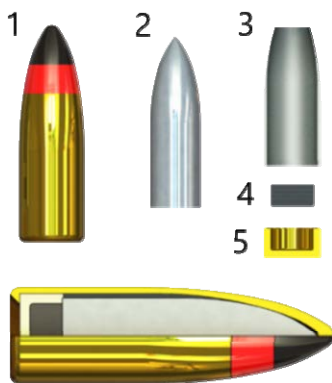


Figure 1. 7.62x39 mm API M 82 projectile: 1 – Jacket, 2 – Steel core, 3 – Lead-Antimony filler, 4 – Incendiary mixture, 5 – Tombac cup

The thermite incendiary mixture is inserted in a tombac cup and placed in the rear end of the projectile. Ignition of the incendiary mixture occurs upon the projectile's contact with the obstacle due to the influence of the inertial and frictional forces [1]. The mass of the projectile is 7.55 g, while the mass of the hard steel core is 3.6 g. The hardness of the steel core was measured and found to be 61 HRC.

2.2. Experimental set-up

Schematic representation of the experimental set-up may be seen in Fig. 2. The research was carried out by firing the 7.62x39 mm API projectiles through the ballistic test barrel into the 6 mm thick ARMOX 500T steel plate targets which were mounted in the rigid frame and placed at the distance of 25 m from the muzzle. The impact surface of the target was kept perpendicular to the projectile's trajectory throughout the experiment. A fixed boundary between the plate and the frame was achieved by the use of the clamps on the plate's corners. As stated in [6], for the high-velocity ballistic impacts in which the distance between the single shot and the plate's boundary is greater than several projectile diameters, the boundary conditions can be assumed to be of minor importance. For that reason, the distances between the adjacent shots and between the shots and the boundaries was kept equal or greater than ten projectile diameters.

The initial velocities of the projectiles have been varied in a broad range in order to determine the influence which the impact velocity has on the projectile's residual velocity and the penetration process. This was achieved by the change in the propellant charge mass. Seven velocity groups were formed starting at the 430 m/s and up to the 740 m/s with no less than five firings in each group. For the purpose of the initial velocity measurement, the infrared optical velocity measuring system was used. It comprised a chronograph and two identical IR light-barriers which were placed at the distances of 1.5 and 3.5 meters from the muzzle thus providing the V2.5. When the change in the light intensity caused by the occurrence of the projectile between the emitters and the detectors of the first barrier becomes large enough to be detected, the counter will be activated and it will be stopped only when the second barrier detects the passage of the projectile. Based upon the measured time of flight and the known value of the distance between the barriers, the initial velocity can be determined.

Ballistic properties of several intermediate cartridges including those of the 7.62x39 mm steel-cored AP projectile were investigated and the set of equations describing the projectile motion were defined [7]. Based on those equations and the measured initial velocity, the impact velocity at the distance of 25 meters can be calculated. However, additional tests were made with the aim to determine the spread in the values of impact velocities and the difference between the calculated and the measured values. Those tests were conducted without the target and with the pairs of contact screens placed both in front and behind of the holding frame. A contact screen (Fig. 3) consists of two 0.1 mm thick aluminium

foils separated by a 5 mm thick cardboard layer that acted as insulator and prevented the flow of the electrical current between the foils thus keeping the circuit open. In the case of screen being penetrated by a projectile or sufficiently large fragment which can provide electrical contact between the foils, the circuit would become

closed thus triggering the time counter. The front pair of contact screens (marked with 4 in Fig. 2) was used for the measurement of the impact velocity, while the rear pair (marked with 6) was used for the measurement of the velocity drop caused by the front pair of screens.

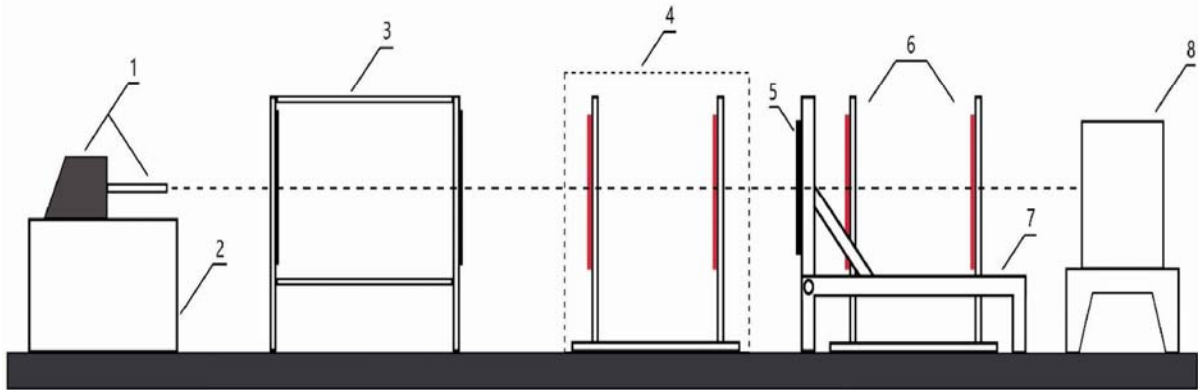


Figure 2. Scheme of the experimental set-up: 1 – Ballistic breech and test barrel, 2 – Universal stand, 3 – IR velocity measuring system, 4 – Contact screens for the impact velocity measurement, 5 – Target plate, 6 – Contact screens for the residual velocity measurement, 7 – Supporting frame, 8 – Catching box

Upon ending the impact velocity measurement tests, the front pair of contact screens was removed together with its supporting frame in order to evade the inducement of yaw angle and the velocity drop prior to the projectile's impact. On the other hand, the rear pair of contact screens wasn't removed and was kept operating throughout the experiment with the purpose of measuring the projectile's residual velocity. Advantage of the contact screen based velocity measuring system is that it is insensitive to the flash and light effects of the burning incendiary mixture. Those effect can cause the deterioration of the functionality when some of the other velocity measuring systems are employed, e.g. the high-speed cameras [8]. Furthermore, it is relatively inexpensive and makes it possible to trace the trajectory of the projectile after the perforation. Comparison of the residual velocities obtained by the contact screens and the acceleration data integration has shown that the measurement error when using the contact screens is minor [9].

A catching box filled with sand was used for the soft recovery of the penetrators and the target plate fragments. Mass and geometric properties of the collected specimens were measured in order to obtain the insight into the failure mechanisms. Furthermore, the properties of the openings in the target plate formed during the perforation process were measured and analyzed with the same goal.

The obtained experimental results and their analysis can be found in the following sections.

3. RESULTS

The impact velocity measurement was conducted and the results which may be seen in the Fig. 4 were acquired. In addition, the analytical model for the calculation of the projectile's velocity change during the flight was developed and the curves were formed for the $V_{2.5}$ velocities corresponding to those measured during the tests. The value of the drag coefficient used in the model was equal to 0.343, as defined in [7] for the 7.62x39 mm AP projectile. Even though the drag coefficient changes its value with the change of the Mach number, the comparison between the measured and calculated data shows that the difference is not greater than 0.6% in any of the firings and thus, the assumption was made that the constant value of the drag coefficient may be used.

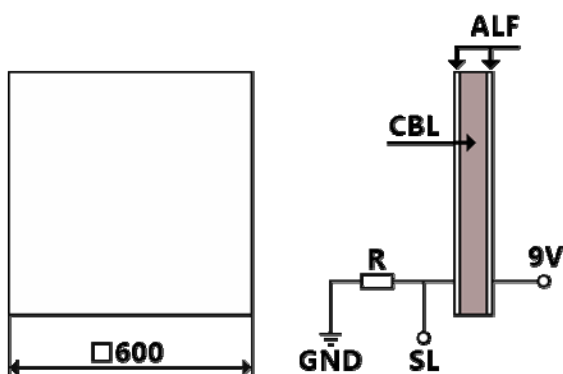


Figure 3. Scheme of a contact screen: ALF – Aluminum foil, CBL – Cardboard layer, SL – Signal line

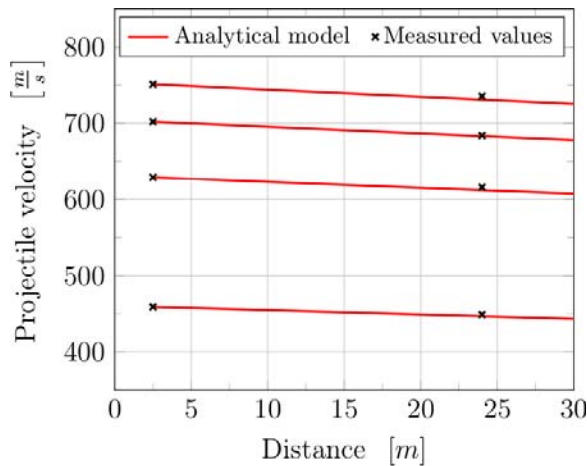


Figure 4. Projectile's velocity decrease – comparison between the analytical model and the measured values

The velocities obtained by the rear pair of contact screens have shown that the velocity drop caused by the passage of the projectile through the two pairs of contact screens was equal to 3.2% at most. During the residual velocity measurement tests, the front pair of contact screens was removed thus reducing the number of screens which the projectile has to penetrate and consequently, the induced velocity drop was also reduced to the value which is considered as acceptable.

Upon the verification of the developed analytical model, calculation of the impact velocity became possible.

3.1. Residual velocities

Seven test groups were formed with no less than five firings in each of them, with the only difference between the groups being in the values of their nominal $V_{2.5}$ velocities. The lowest velocity group had the nominal value of 430 m/s as the risk of projectile getting stuck in the barrel could arise if the lower velocities were selected. On the other hand, the highest value of initial velocity was 740 m/s as this is the standard ordnance velocity for the selected bullet type. Intermediate groups were placed at the 470, 520, 560, 600 and 680 m/s. Change in the initial velocity value has been achieved through the change in the propellant mass and even though this was done with great care, slight variation in the measured values of velocities are observed. However, this poses no threat to the objectives of the conducted research.

Results obtained during the tests may be seen in Fig. 5 where the measured residual velocities are plotted against the impact velocities. Close-up views of the target's impact and rear surfaces and two of multiple recovered penetrator fragments are also displayed. Based on the in situ analysis of the target plate and the contact screens, the firings were divided into five distinct groups. Least frequent of them comprised the only two cases in which the perforation was not achieved. Both of them occurred in the lowest initial velocity group and were beneficial for the determination of the ballistic limit velocity V_{bl} . As per [3], the V_{bl} may be found as the average between the highest velocity not providing perforation and the lowest

velocity under which the perforation of the target was achieved. In Table 2, the penetration process outcome for the first group of firings can be found. It is important to note that although the perforation was achieved in three out of five firings from the Group I, the residual velocity was not measured. During the analysis of the target plate it was discovered that the diameter of the openings created by those firings was between 4.7 and 5.1 mm which, having in mind that the diameter of the penetrator's cylindrical section is 6 mm, led to conclusion that the penetrator itself didn't pass through the target. This conclusion was verified by the finding of penetrators in the area between the barrel and the target. Although the fragments were ejected from the target plate, they were either not sufficiently big to achieve the contact between the foils or were ejected at an angle that would make them miss the contact screens thus preventing the residual velocity measurement.

Table 2. Ballistic test results for the Group I

No.	Initial velocity $V_{2.5}$ [m/s]	Impact velocity V_i [m/s]	Opening in the target plate
I-1	427.0	414.9	No
I-2	433.5	421.3	Yes
I-3	436.7	424.4	No
I-4	437.0	424.7	Yes
I-5	447.0	434.4	Yes

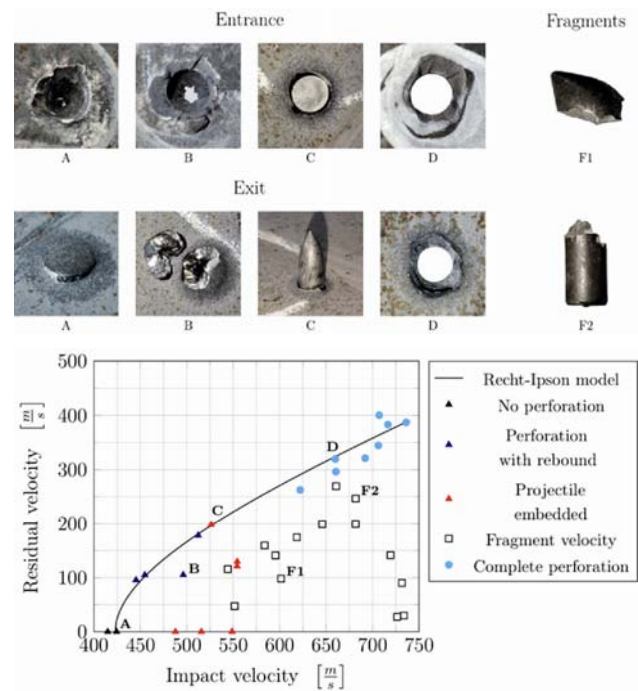


Figure 5. Impact and rear surfaces of several representative firings and the experimental residual versus impact velocity curve based on a best fit to the modified Recht-Ipson model

Based on the results presented in Table 2, the ballistic limit velocity has been found to be equal to $V_{bl} = 422.8$ m/s. Relationship between the impact

velocity and residual velocity can be established by using the well-known model of Recht-Ipson [10], which in the case of the perforation of a plate by a penetrating projectile has the following form:

$$V_r = (V_i^2 - V_{bl}^2)^{0.5} \quad (1)$$

However, it was found that the Eq. 1 may not provide a perfect fit with the experimental results in a number of cases, e.g. when the projectile's deformation cannot be considered small [3], when the friction is not taken into account [11] and when the mass of the ejected target material may not be considered negligible. In order to provide a better fit with the experiment, the modification which includes the empirical coefficients may be used:

$$V_r = \alpha(V_i^p - V_{bl}^p)^{1/p} \quad (2)$$

where the α and p are fitting parameters. In Fig. 5, the curve representing the best fit of the residual versus impact velocity data and the proposed empirical model is shown. The values of fitting parameters are found to be $\alpha = 0.68$ and $p = 1.8$. It may be seen that the curve represents the data in the lower impact velocity zone with almost no deviation, while with the increase of the impact velocity the deviation between the model and data also increases. The residual versus impact velocity curve has a relatively high gradient in the vicinity of the ballistic limit velocity which is in agreement with the experiment results, as it was seen that a small change in the impact velocity near the V_{bl} may cause great variation in the value of residual velocity and the outcome of the penetration process.

In the lower range of the observed impact velocities, apart from the aforementioned group in which the perforation was not achieved, two more groups were noticed. Four firings resulted in a perforation with a projectile rebound, with the size of the created openings ranging from 1.6 mm to 5.2 mm. Residual velocities of the ejected fragments were measured for all of those cases and good match with the Recht-Ipson curve was achieved (Fig. 5). Six firings in the impact velocity range from approximately 490 m/s up to 550 m/s have resulted in the penetrator embedment in the target plate. The zone of impact velocities in which this group of firings is located partially overlaps with the zone in which the perforations with rebound are placed. Identification of the projectile sticking phenomenon indicates the significance of the friction between the penetrator and the target during the penetration process, which can amount up to three per cent of the projectile's kinetic energy loss [12]. Highest measured value of residual velocity in the group of embedded projectiles is in a close match with the residual versus impact velocity curve, while the two other measured values greatly deviate from the empirical model. In those cases, fragments from both the target plate and the penetrator were collected. As it may be seen from Fig. 5, there are two more firings nearby for which the fragment velocities were detected, but although the measured velocities are similar in value, outcome of the penetration process is different as in the two firstly

described firings the penetrator was embedded while in latter two the complete perforation was achieved. Detection of this transition is significant as it indicates which value of impact velocity is sufficiently high to provide complete perforation and passage of penetrator through the target plate.

With the further increase of the projectile impact velocity, two different outcomes were observed. Penetrator achieved complete perforation either without breaking or it was fragmented during the penetration process. As shown in Fig. 5, first case of complete perforation for which no fragmentation of the penetrator was observed appeared at the impact velocity of 622 m/s, indicating that there is a zone of velocities starting at around 525 m/s

with the width of 100 m/s in which all of the firings have resulted in penetrator fragmentation with residual velocities significantly lower than predicted by the empirical model. On the other hand, with the impact velocities greater than 622 m/s the penetrator had achieved the equal number of complete perforations with and without its fragmentation. Residual versus impact velocity curve had become significantly less steep in the zone of higher impact velocities as the level of kinetic energy converted to the work during the projectile/target interaction had decreased. Deviation between the experimental results and the empirical model had increased for the higher velocity impacts which can be attributed to the observed penetrator fragmentation and severe projectile deformation.

3.2. Failure mechanisms

Three modes of material failure known as ductile failure, adiabatic shear plugging and discing have been identified as most common in the penetration of metallic armor [5]. Due to the anisotropy of the target material and the non-ideal impact conditions, mixed modes of failure may be expected in practical cases of penetration rather than the ideal ones [4]. In the present study, influence of the impact velocity on the target plate failure mode was investigated.

In the vicinity of the ballistic limit velocity, two cases of partial shear plugging were observed where one of them is shown in Fig. 5 as A. Asymmetric bulges were formed on the rear surface with the maximum heights of 1.3 mm and 1.5 mm and diameters of 5.6 mm. On the impact surface, the indentations were formed with the penetrator-shaped cavities being 5.2 mm and 5.5 mm deep. As stated in [13], in any penetration process it is energetically favorable for the first part of penetration to be achieved through the ductile hole formation which will then be followed by the plugging mode upon sufficient reduction of the target thickness. Described behavior was observed in the aforementioned partial shear plugging cases where ductile hole enlargement preceded shear plugging. Similar behavior was seen in three other firings from the Group I in which the plug ejection was achieved and the target was perforated even though the projectile was rebounded. Several cases of rear surface bulging and brittle failure were observed during the second stage of the penetration (Fig. 5(B)) in the transition zone where the projectile

embedment was seen. Still, majority of the impacts in that zone resulted in shear plugging during the second stage of penetration. For the highest values of impact velocities, ductile failure modes become predominant modes of material failure in both the initial and final stages of penetration and the plugs weren't recovered for the impact velocities greater than 690 m/s.

4. CONCLUSIONS

Ballistic performance of the ARMOX 500T high-hardness steel plate under the impact of 7.62x39 mm armor-piercing incendiary projectile was experimentally investigated. Impact velocity has been varied in a range from the ballistic limit velocity to the nominal projectile's velocity. Some of the important conclusions and observations are:

- Analytical model for the calculation of impact velocity has been verified experimentally. Deviation between the model and the test results has been found to be sufficiently small on the observed range of velocities,
- Experimental set-up and utilized instruments were able to provide the initial and residual velocity data
- Empirical model of Recht-Ipson can provide accurate prediction of the residual velocity, especially in the lower range of the observed impact velocities, although the deviations have increased with the occurrence of penetrator fragmentation,
- Impact velocity increase results in reduction of the slope of the residual versus impact velocity curve. Also, it results in the increased chance for the penetrator fragmentation,
- Transition zone with the high probability of penetrator embedment in target plate was observed indicating the zone in which the friction and elastic recovery of the target material have great influence on the penetration
- Relatively wide zone of intermediate impact velocities was observed for which the target perforation is accompanied with the penetrator fragmentation. This has led to the decrease in residual velocity which indicates that additional effort needs to be put with the aim to improve penetrator's mechanical properties.

Future work will be focused on the utilization of the acquired experimental data in the development of the numerical model for the observed penetration process.

Acknowledgement

The authors gratefully acknowledge the support provided by the SSAB Special Steels, Sweden.

References

- [1] АБДУЛЛИН, И.А.: *Бронебойно-зажигательные боеприпасы к стрелковому оружию*, КНИТУ, (2013)
- [2] HAZELL, P.: *Armour: Materials, Theory and Design*, CRC Press, (2015)
- [3] BORVIK, T. ET AL.: *Effect of target thickness in blunt projectile penetration of Weldox 460 E steel plates*, International Journal of Impact Engineering, 28, (2003), 413-464
- [4] ZUKAS, J. ET AL.: *High velocity impact dynamics*, New York: Wiley, (1990)
- [5] WOODWARD, R.: *The interrelation of failure modes observed in the penetration of metallic targets*, International Journal of Impact Engineering, 2, (1984), 121-129
- [6] BORVIK, T. ET AL.: *Normal and oblique impact of small arms bullets on AA6082-T4 aluminium protective plates*, International Journal of Impact Engineering, 38, (2011), 577-589
- [7] FIKUS, B. ET AL.: *Preliminary comparative investigations on ballistic properties of intermediate cartridges*, Problemy Mechatroniki, 11, 4 (42), (2020)
- [8] BURIAN, W. ET AL.: *Protection effectiveness of perforated plates made of high strength steel*, International Journal of Impact Engineering, 126, (2019), 27-39
- [9] JINZHU L. ET AL.: *Perforation experiments of concrete targets with residual velocity measurements*, International Journal of Impact Engineering, 57, (2013), 1-6
- [10] RECHT, R., IPSON, T.: *Ballistic perforation dynamics*, Journal of Applied Mechanics, 30, (1963)
- [11] ROSENBERG, Z., VAYIG, Y.: *On the friction effect in the perforation of metallic plates by rigid projectiles*, International Journal of Impact Engineering, 149, (2021)
- [12] WOODWARD, R.: *The penetration of metal targets by conical projectiles*, International Journal of Mechanical Sciences, 20, (1978)
- [13] WOODWARD, R.: *The penetration of metal targets which fail by adiabatic shear plugging*, International Journal of Mechanical Sciences, 20, (1978)



DESIGN OF SUITABLE PYROTECHNIC DELAY COMPOSITION WITH WIDELY USED COMPONENTS

JELENA MOJSILOVIĆ

Military Technical Institute, Belgrade, mojsilovic.jeca@gmail.com

JELENA PETKOVIĆ-CVETKOVIĆ
Military Technical Institute, Belgrade

DRAGICA KOSTIĆ
TRAYAL Corporation AD, Kruševac

JOVICA NEŠIĆ
Military Technical Institute, Belgrade

JELA ILIĆ
Military Technical Institute, Belgrade

MIRJANA KRSTOVIĆ
Military Technical Institute, Belgrade

Abstract: The development of time delay pyrotechnic elements represents an important part of improving a new fuse and ammunition. This study aims to show an optimization of the ratio in the fuel oxidant mixture and how this ratio influences the burning properties of pyrotechnic compositions. In compositions observed in this research, sulfur and charcoal react as fuels, potassium nitrate reacts as an oxidant and phenol-formaldehyde resin operates as a binder. The stoichiometric ratios were determined by using the oxygen balance (OB) and pyro valence (PV) values. The linear burning rate was measured using a VOD 811 system for some typical compositions which were pressed into aluminium tubes. The calorimetric bomb was used in the experiments with an inert gas supply to determinate the heat of reaction and the closed-vessel test was used to measure the production of gaseous products.

Keywords: Pyrotechnic, time delay, charcoal, sulfur, burning rate,

1. INTRODUCTION

Among the variety of energy-intensive compositions, delay pyrotechnic compositions are of great interest, which serve to create time delays of the required duration. The need to ensure a time delay in the operation of pyrotechnic products arose with the appearance of black powder and the first powder bombs, hand grenades and rockets. The delay was necessary to have time to move away to a safe distance, and to detonate the charge at the right moment [1]. Pyrotechnic delay compositions can be considered gasless or gas-producing depending on the quantity of gas generated during the combustion. Typically, gasless delays are used in sophisticated projectiles and gas-producing delays are used for inexpensive munitions such as hand grenades and signal devices, considering the quantity of gas upon ignition (approximately 50% of the reaction products are gaseous) [2]. The advantages of gas producing delay compositions over gasless systems are their ability to provide accurate delay time, long-term storage stability, and available ingredients. The disadvantage of the system lies in the

effect of external pressure on their burning rate which can be overcome by providing an adequate design of a fuse [3]. Black powder composition designed in a manner of time delay device in this paper typically consists of 65-80 wt.% potassium nitrate, 5-25 wt.% charcoal, 5-10 wt.% sulfur with rest comprising of phenol-formaldehyde resin. Some of the important characteristics of these delay compositions are gaseous combustion behaviour, constant burning time, economically acceptable and widely used ingredients and long-term storage stability. Charcoal is a natural solid fuel. It is produced by pyrolysis or carbonization of wood. The precise definition of chemical composition and physical appearance is hard to define. It depends on the degree of carbonization, temperature and pressure in which the process takes place. This natural material contains carbon, moisture, ash-generating minerals, and a large number of different hydrocarbons that volatilize when combustion is initiated.[4] It has properties like large surface area, approximately 1-3m²/mg, heat conductivity and adsorption. [5] Thus, black powder has a high burning rate and charcoal is used as a catalyst. The pyrotechnic behaviour of charcoal may vary, depending on which wood is used to prepare the material.

[2,5] A similar observation has been reported previously by [2], [6-9] and thermodynamic code EXPLO5 has predicted charcoal formula as shown in Table 1. This implies that charcoal contains largely of carbon, and for easier determination of OB, PV and theoretical maximum density (TMD) in this paper was used carbon as an approximation in calculations. The charcoal used in this paper has a willow tree (*Salix*) origin.

Table 1. Charcoal formulations from different sources

Number	Charcoal formula	Source
1	C ₆ H ₂₀	Sidlovski [6]
2	C ₁₆ H ₁₀ O ₂	Maksimovic[7], Cokling[2]
3	C ₂₀ H ₇ O	Orbovic [8]
4	C ₄₂ H ₆₀ O ₂₈	Koch [9]
5	C _{7,2} H _{4,99} O _{0,52}	EXPLO5
6	C ₁₀ H _{4,77} N _{0,04} O _{1,23} Ca _{0,003}	EXPLO5

Eight compositions were selected to determinate OB, PV and TMD, and they are presented in Table 2. The $\Omega(\text{CO}_2)$ of all compositions lies in the range of -63.08% to +34.3%. Pyro valence was calculated for all compositions and it is noticeable that PV approach has a similar trend when it comes to assuming the products of reaction as OB method. The theoretical maximum density (TMD) is calculated using the mass fraction and density of each ingredient in the mixture.

Table 2. Selected formulations of time delay pyrotechnic compositions

	TD-1	TD-2	TD-3	TD-4	TD-5	TD-6	TD-7
KNO ₃	65	70	75	80	85	75	75
C	25	20	15	10	5	5	10
S	5	5	5	5	5	15	10
C ₁₃ H ₁₂ O ₂	5	5	5	5	5	5	5
OB[%]	-63.08	-52.6	-37.3	-12.55	+34.3	-9	-25.8
PV	+7.22	+5.05	+3.4	+1.47	-0.42	+1.36	+2.32
TMD [g/cm ³]	2.734	2.602	2.471	2.339	2.208	2.201	2.335

2. EXPERIMENTAL DETAILS

2.1. Ingredients and Preparation

2.1.1 Mixing process

The following substances were used to prepare the abovementioned formulations and perform the experimental study: potassium nitrate as an oxidizer, charcoal and sulfur as fuel and phenol-formaldehyde resin as a binder. The method of preparation consists of the following operations:

- 1) weighting of ingredients;
- 2) drying of oxidizer and fuels in an oven at 60°C for 3h;
- 3) dissolving the phenol-formaldehyde resin in a solvent;
- 4) dry homogenization is performed in several phases. The first phase was performed by mixing fuels until all components were evenly dispersed,

then was added oxidizer and all compounds were well-mixed together

- 5) wet homogenization was performed with well mixed ingredients from dry homogenization with the addition of dissolved binder
- 6) mashing phase consists of manual sieving of the wet mixture through a sieve
- 7) drying in an oven at 60°C for 4h to remove remaining moisture content
- 8) the last operation was packing into hermetic containers. [10]

The present study focuses on experimentally investigating the impact of the ratio in the fuel oxidant mixture and how this ratio influences the burning properties of pyrotechnic compositions with widely used components. All ingredients were delivered by Traylor Corporation AD (commercial quality) and formulations TD-1, TD-3, TD-4, TD-6 and TD-7 from Table 2 were selected to determinate linear burning rate, the heat of reaction and predict the burning behaviour of formulations by the closed-vessel system. These mechanical mixtures are used in powder form for calorimetric bomb and closed-vessel experiments. Further, these mechanical mixtures were pressed with a hydraulic press into aluminium tubes for burning rate tests.

2.2. Techniques

2.2.1 Heat of reaction

The calorimetric bomb analysis was performed using the IKA-Calorimeter C 2000 model. Experiments were performed in the absence of oxygen with an inert gas supply to determinate the heat of reaction value. A mechanical mixture of 3 g was used in powder form to determinate the value of heat released during the reaction. Heat of reaction is defined as the amount of heat released through the combustion of 1 g of pyrotechnic composition in an inert atmosphere.

2.2.2 Linear Burning rate

Burning characteristics of any multicomponent solid fuels depend on many significant parameters such as overall composition, fuel and oxidizer particle size, adequate inter-particle contacts between reactants, an adequate technique of mixing, bulk thermal conductivity and heat of reaction of the mixture, reaction rate progress, reaction zone temperature and pressure. [11] It is a self-propagating reaction in solid mixtures with a strongly exothermic reaction when a considerable amount of heat is evolved in the chemical charge. The linear burning rate can be determined based on the physicochemical property of the ingredients and their relative proportion. The purpose of this time delay composition is to be able to provide a specific time between two events and also has a role to ignite the next mixture in the pyrotechnic line. Therefore, it is important to define the precise time and flux of gaseous products so they can fulfil their required function. For each composition, five tubes were tested. A

specific amount of each pyrotechnic composition was measured and pressed into an aluminium alloy tube (height 15mm, radius 8mm and thickness of wall tube 2mm) with 20 MPa of pressure on the “DUNKES” hydraulic press (Figure 1.). The linear burning rate was determined with VOD 811 system with specially adjusted software for the correct display of lower combustion velocities.



Figure 1. “DUNKES” vertical press

2.2.3 Closed vessel system

The selection of an oxidizer, fuel and binder for pyrotechnic composition and their weight ratio determines the heat output as well as the gas output for the mixture under consideration. [2] For time delay compositions, considered in this paper, is very important to have first information on gas generating possibilities especially how many gas products are going to be produced in a function of time. The pressure of combustion products is a very distinctive characteristic of every pyrotechnic composition and it is strongly influenced by the nature of ingredient's oxygen/fuel ratio. The pressure of combustion products was measured in a closed vessel. Every sample prepared for the experiment consisted of 3g of pyrotechnic composition in powder form placed in polyethylene containers and fitted with an electric igniter. The polyethylene containers were then placed in a bomb and an electric igniter was connected onto connectors on the bomb cover. The Tektronix DPO 4054 Digital Phosphor Oscilloscope (500MHz-2ns) (Figure 2.) was used to measure data.



Figure 2. Tektronix DPO 4054 Digital Phosphor Oscilloscope

3. RESULTS AND DISCUSSION

3.1. Heat of reaction

For each pyrotechnic composition, three measurements were performed and an average value is presented in Figure 3. The first property to notice in Figure 3 is that the value of energy potential is the highest with the composition TD-4 (3051.8 J/g). It contains the highest content of oxidizer from 80 wt.% and OB has a -12.55% value. It is interesting to note that composition TD-6 has the second highest value of energetic potential, the highest content of sulfur and smallest OB value -9% of all compositions. This result can be explained by the dual nature of sulfur. Depending on conditions, sulfur can behave as an oxidizer or as a fuel in the combustion process.

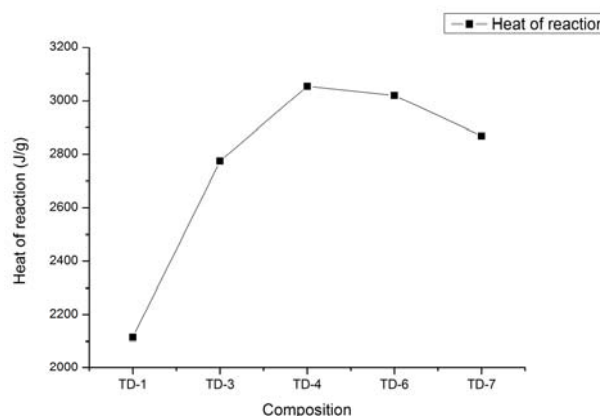


Figure 3. Selected compositions and their heat of reactions values

3.2. Determination of gas producing characteristic

The gas-producing characteristic was measured in a manometric bomb. For each composition, three measurements were taken and an average value was calculated. The results are shown in Figure 4.

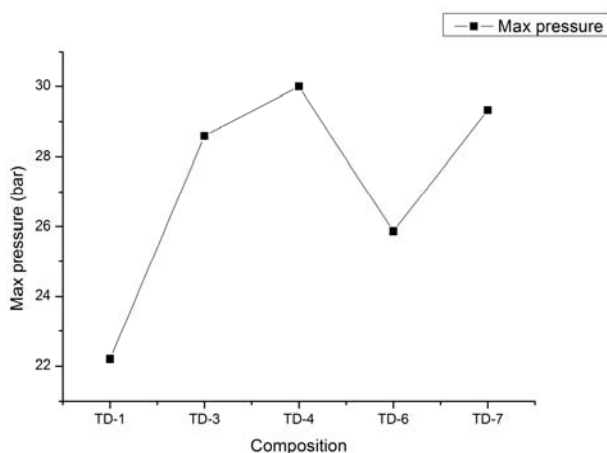


Figure 4. Selected compositions and their maximum pressure

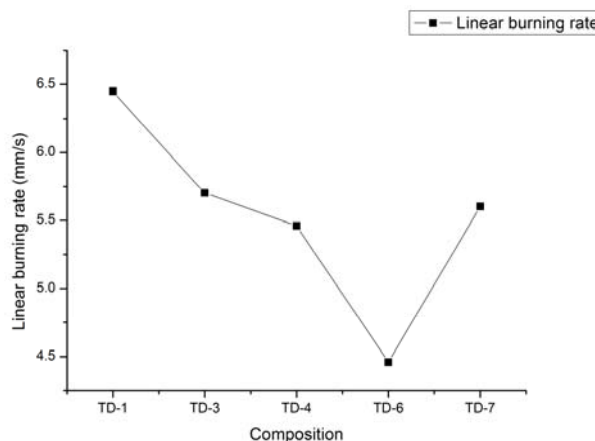


Figure 5. Average linear burning rate for selected pyrotechnic composition

Results in Figure 4 and Table 3 show that compositions TD-3, TD-4, TD-6 and TD-7 have relatively small scattering values in both maximum pressure of combustion products (P_{\max}) and time to reach P_{\max} (t_{\max}), so they have similar behaviour when it comes to gas-producing characteristic.

Table 3. Measured time (t_{\max}) to reach maximum pressure (P_{\max}) for selected compositions

Composition	TD-1	TD-3	TD-4	TD-6	TD-7
P_{\max} [bar]	22.2	28.6	30	25.87	29.33
t_{\max} [ms]	121.73	47.27	39.87	51.53	36.2

Pyrotechnic composition TD-1 has a huge drop compared to the four mentioned in both maximum pressure of combustion products (P_{\max}) and time to reach P_{\max} (lowest t_{\max}). This is attributed to the presence of a high mass percentage of charcoal which implies that due to its nature, charcoal has an affinity to “suffocate” combustion process. Furthermore, this implies that incomplete combustion has occurred with TD-1 composition.

3.3. Linear burning rate

Data from the linear burning test are shown in Figure 5. For each composition, five tubes were tested, and an average value was calculated. Results in Figure 5 reveal that the fastest burning belongs to composition TD-1 and from that point there is a decreasing trend of burning time which follows until composition TD-6. It is interesting to note that the pyrotechnic composition TD-1 has the highest OB value, the lowest value of heat of reaction and poorest, substandard values of gas-producing characteristic, this implies that burning characteristic depends on properties like inter-particle contacts between reactants, heat conductivity increases if the pyrotechnic composition is in compressed form.

4. CONCLUSION

The main focus of this work was to incorporate widely used and acceptable ingredients to produce desired time delay effect. In this work, a four-component pyrotechnic system of potassium nitrate (KNO_3), charcoal, sulfur and phenol-formaldehyde resin were analyzed and compared. Any change in the ratio of the pyrotechnic composition essentially affects the equilibria. For gaseous, time delay pyrotechnic composition is important to have a well-balanced combination of gaseous and condensed products of combustion. The obtained data shows that combustion of pyrotechnic compositions is a complex thermodynamic process and that it changes with a slight change in oxidant-fuel ratio. Therefore, the primary functions of gaseous time delay compositions are satisfied with compositions TD-3, TD-4, TD-6 and TD-7. Those pyrotechnic compositions can be used in different types of ammunition depending on the required effect. The composition TD-1 does not satisfy the minimum of performed tests. However, for a more precise determination of time delay compositions, more tests must be performed for full characterization. For some future work, it would be interesting to perform an analysis with active carbon and carbon black instead of charcoal.

References

- [1] S.E. GABDRASHOVA, M. I. TULEPOV, M. A. KORCHAGIN, L. R. SASSYKOVA, F. YU. ABDRAKOVA, ZH. B. BEXULTAN, Y. K. AITENOV, S. E. TOKTAGUL, D. A. BAISEITOV: *Development of pyrotechnic delay mixtures based on a composite material hardened with carbon nanotubes*, Journal of Nanomaterials and Biostructures Vol. 16 No4, p. 1341-1350, 2021.
- [2] JOHN A., CONKLING AND MOCELLA, *Chemistry of Pyrotechnic Basic Principles and Theory* Second Edition, CRC Press Taylor & Francis Group 2011
- [3] T.T. GRIFFITHS AND A. E. CARELL: *Delay Compositions Containing 1,2,4-Trihydroxyanthraquinone*, 48th International Annual Conference of ICT, June 27-30, 2017 Karlsruhe, Germany

- [4] I. GLASSMAN: *Combustion*, 3rd Edition, 1996
2.Auflage De Gruyter, pp.321
- [5] J.H. MC LAIN: *Pyrotechnic from the viewpoint of Solid State Chemistry*, Franklin Institute Press, 1980 USA
- [6] SHIDLOVSKY A.A.: *Fundamentals of pyrotechnic*, CFSTI, 1953, Moscow
- [7] MAKSIMOVIC P.: *Tehnologija eksplozivnih materija*, 1972, Belgrade
- [8] ORBOVIC N.: *Uvod u energetske materije*, KIZ „Centar“, 2020, Belgrade
- [9] E.C.Koch: *Sprengstoffe treibmittel pyrotechnika*, 2.Auflage De Gruyter, pp.321
- [10] PASAGIC S.: *Investigation of Pyrotechnic Charges for Base Bleed Projectiles*, Scientific Technical Review, Vol.61, No3-4, pp. 56-62
- [11] GANANAPRAKASH KANAGARAJ AND JACK J. YOH: *Burning Characteristics of Pyrotechnic Time-Delay Composition Subjected to Moisture and Heat* Journal of Propulsion and Power <https://doi.org/10.2514/1.B38215>



NUMERICAL ANALYSIS OF THE INHOMOGENEOUS OBSTACLE INFLUENCE ON THE PRECURSOR SHAPED CHARGE WARHEAD PERFORMANCE

MILOŠ MARKOVIĆ

University of Belgrade, Faculty of Mechanical Engineering, Belgrade, mdmarkovic@mas.bg.ac.rs

PREDRAG ELEK

University of Belgrade, Faculty of Mechanical Engineering, Belgrade, pelek@mas.bg.ac.rs

DEJAN JEVTIĆ

University of Belgrade, Faculty of Mechanical Engineering, Belgrade, djevtic@mas.bg.ac.rs

RADOVAN ĐUROVIĆ

University of Belgrade, Faculty of Mechanical Engineering, Belgrade, rdjurovic@mas.bg.ac.rs

IVANA TODIĆ

University of Belgrade, Faculty of Mechanical Engineering, Belgrade, itodic@mas.bg.ac.rs

Abstract: Purpose of the precursor shaped charge warhead is to initiate the Explosive Reactive Armor (ERA) and thus provide an unobstructed path to the jet of the main shaped charge. The precursor warhead is most commonly placed in the front of the missile where it is surrounded by other subsystems. All of the subsystems which lay on the path of the precursor warhead's shaped charge jet represent the obstacle that will decrease its efficiency. The goal of this paper is to analyze the precursor warhead's performance in a case where the inhomogeneous obstacle is placed in front of it. The numerical analysis of the obstructed formation process was performed in order to determine the properties of the formed jet using ANSYS AUTODYN 2D software. For the existing missile configuration, jet formation process and precursor warhead's performance against ERA were analyzed numerically. Significant differences in formed jet's properties were observed for the simulations with and without the inhomogeneous obstacles. In the case of inhomogeneous obstacle it is present decreasing of jet tip velocity for around 23%, decreasing of jet tip diameter for around 50% and jet time are delayed in contact with ERA front panel for around 10 μ s. Obtained results indicate that in the observed cases, formed jet has enough energy to initiate the explosive reactive armor.

Keywords: numerical analysis, shaped charge, precursor warhead, explosive reactive armor.

1. INTRODUCTION

In the early stages of missile design, it is highly important to determine payload subsystem's configuration and position. Antitank missile's design and its subsystems placement strongly depend on its tactical-technical requirements. In a case of a missile that contains a homing head, it will inevitably be placed in its front section where it will be surrounded with various electronic components, optical lenses, power supply etc. Majority of those parts will be placed in front of a precursor shaped charge warhead leading to the occurrence of their interaction during the jet formation process that will decrease jet's performance against the ERA. Due to that, it is highly important to clarify whether or not a precursor shaped charge will be able to penetrate all of the aforementioned obstacles and activate explosive reactive armor.

ANSYS AUTODYN software is widely used in the fields of warhead design [1], physics of explosion [1,2],

terminal ballistics etc. as it is able to successfully simulate blast, fragmentation and penetration processes [3-8]. Yanan et al. [9] have investigated penetration performance of the main shaped charge warhead in presence of other missile subsystems placed in front of it. Missile configuration in that research doesn't include precursor shaped charge warhead. Numerical model was developed in order to test different stand-offs for optimal solution determination. Chang et al. [10] have analyzed low-density jet penetration into the explosive reactive armor by the means of numerical simulation. For the ERA's explosive, COMP B with the Lee-Tarver's equation of state was selected as it is able to simulate the process of ignition and growth. Results indicate that the observed low-density jet has sufficient energy and is able to activate the explosive reactive armor. Liangliang et al. [11] numerically simulated jet formability and damage characteristics for the low-density liner material. Furthermore, theoretical and empirical initiation criteria of ERA was presented and the analysis of ERA's reaction degree coefficient was displayed. In the present research, numerical investigation was performed in ANSYS

AUTODYN software in order to determine to which degree the inhomogeneous obstacles in front of precursor warhead deteriorate its properties for the real missile configuration. All of the observed processes, including the detonation wave propagation, jet formation, penetration through the inhomogeneous obstacles and the interaction with ERA were simulated using the Euler 2D Multi-material solver. Shaped charge jet's properties were tracked using the fix gauge points placed along the symmetry axis. In addition, a simulation was performed without the obstacles to serve as a reference.

2. NUMERICAL ANALYSIS

2.1. Warhead and ERA configuration

Investigated precursor shaped charge warhead may be seen in Fig.1(a). It consists of a copper liner (pos.1), high explosive charge (pos. 2) and aluminum casing (pos.3).

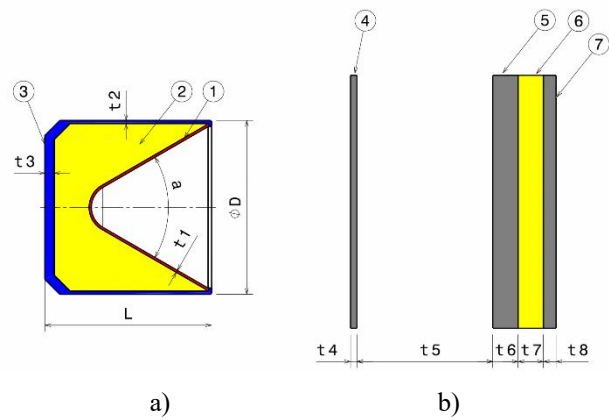


Figure 1. Configuration of the analyzed precursor shaped charge and ERA with main dimensions

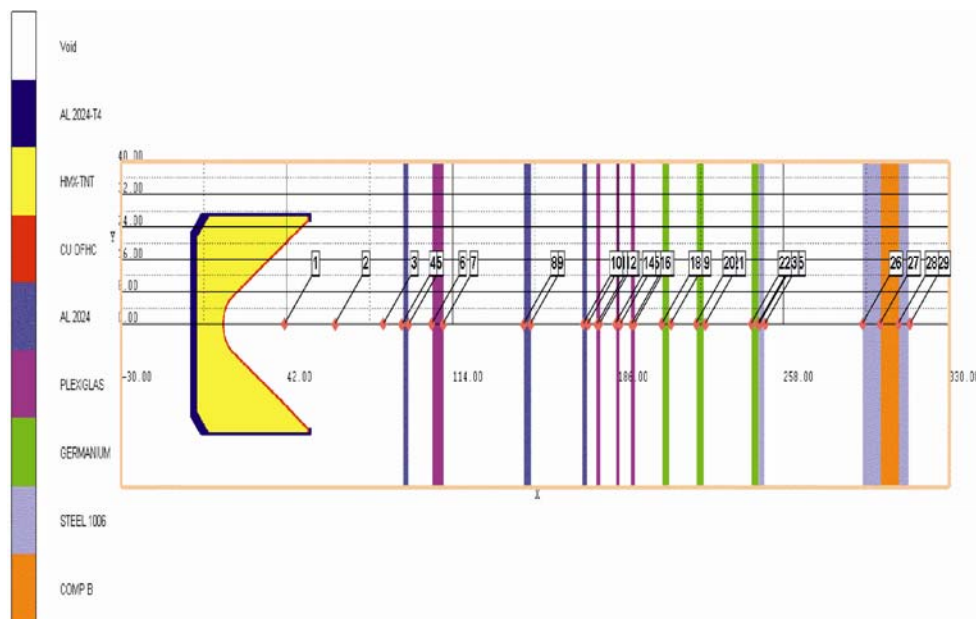


Figure 2. Geometry of the developed numerical model and the Euler domain

First generation of explosive reactive armor is investigated due to its extensive usage for the vehicle protection. As described in ref. [12], it comprises a steel container box (pos. 4) followed by a sandwich made from front steel panel (pos. 5), explosive charge (pos. 6) and rear steel panel (pos. 7) (Fig.1(b)). Dimensions of both the precursor shaped charge and the explosive reactive armor may be found in Table 1. Stand-off distance from the ERA's front metal plate was kept constant in both of the analyzed cases with its value being equal to 3.5 calibers.

Table 1. Shaped charge and ERA dimensions

Precursor shaped charge	
Length	L = 53 mm
Diameter	D = 55 mm
Liner thickness	t1 = 0.75 mm
Confinement thickness side	t2 = 1.5 mm
Confinement thickness bottom	t3 = 3 mm
Liner angle	a = 55°

Explosive reactive armor	
Container thickness	t4 = 2 mm
Distance	t5 = 45mm
Front panel thickness	t6 = 8 mm
Explosive charge thickness	t7 = 8 mm
Rear panel thickness	t8 = 4 mm

2.2. Numerical model setup

Two-dimensional axisymmetric numerical model was developed using the Euler, 2D Multi-material solver. In Fig.2, Finite Element model of the precursor shaped charge, inhomogeneous obstacles and the ERA is displayed. The model is mirrored about the symmetry axis for the better visualization. Dimensions of the rectangular domain are 360x40 mm and their selection was based on the two geometrical conditions. The first one is related to length of the missile's front section and the length of the ERA while the second one is related to the precursor

shaped charge warhead’s diameter. In order to avoid occurrence of the wave refraction, “flow out” boundary condition was set on the domain’s outer edges. Grade zoning was applied in the lower J-direction with fixed cell size of $dy=0.1\text{mm}$ and the $nJ=30$ times. There are several reasons for the implementation of the grade zoning: diameter of the formed jet is relatively small when compared to the diameter of the obstacles and ERA, jet formation and penetration processes are concentrated in the vicinity of the symmetry axis and it provides better mesh quality while keeping the number of elements unchanged. In the axial direction of the rectangular domain, constant element size of 0.2 mm was chosen. In total, 360000 mesh elements were created. Furthermore, 29 fixed gauge points were placed along the axis of symmetry in order to detect the changes in jet’s properties during its formation and throughout the process of interaction with the obstacles.

2.3. Material models

Liner of the investigated shaped charge was made from copper. Zerilli-Armstrong strength model was selected for its behavior modeling as it is advantageous when compared to the other strength models available in hydro-code numerical simulations [13]. Parameters for the equation of state and strength model were adopted from the AUTODYN material library and are given in Table 2.

Table 2. Material properties of OFHC cooper

Reference Density	8.96g/cm3
EOS	Linear
Bulk Modulus	1.29e+08 kPa
Ref. Temperature	295.149994 K
Specific Heat	383 J/kgK
Strength Model	Zerilli Armstrong
Shear Modulus	4.6e+07 kPa
Yield Stress	6.5e+04 kPa
Hardening Constant #2	8.9e+05 kPa
Hardening Constant #4	115e-04 (none)
Ref. Strain Rate (/s)	1

Explosives used in the simulations are HMX-TNT for the shaped charge and COMP B for the ERA. Both of them are available in the AUTODYN’s standard material library with the Jones-Wilkins-Lee (JWL) equation of state for which the parameters are given in Table 3. Initiation of the ERA’s explosive due to the impact of the shaped charge’s jet may be modeled using the complex Lee-Tarver model which describes initiation and growth of the detonation due to the occurrence of shock pressure. Nevertheless, similar results may be obtained by adding two more parameters to the JWL equation. Those parameters are known as burn on compression fraction and pre-burn bulk modulus for which the values can be found in available experimental reports for commonly used explosives.

Table 3. Properties of the implemented explosives

HMX-TNT	
Reference Density	1.776 g/cm3
EOS	JWL
Parameter A	7.0079E+08 kPa
Parameter B	1.2116e+07 kPa

Parameter R1	4.5
Parameter R2	1.1
Parameter W	0.3
C-J Detonation velocity	8.21e+03 m/s
C-J Energy/unit volume	8.89536e+06 kJ/m3
C-J Pressure	3.11e+07 kPa
COMP B	
Reference Density	1.776 g/cm3
EOS	JWL
Parameter A	5.2423e+08 kPa
Parameter B	7.678e+06 kPa
Parameter R1	4.2
Parameter R2	1.1
Parameter W	0.34
C-J Detonation velocity	7.98e+03 m/s
C-J Energy/unit volume	8.585e+06 kJ/m3
C-J Pressure	2.95e+07 kPa
Burn on compression frac.	0.8
Pre-burn bulk modulus	4.343697e+06 kPa

Equations of state and strength models for the materials of the obstacles which are located in front of the precursor shaped charge are given in Table 4, while their purpose, thickness and axial positions are enlisted in Table 5. Position of each obstacle was measured from the reference coordinate system placed on the rear edge of the precursor shaped charge warhead up to the component’s closest edge.

Table 4. EOS and strength models of the inhomogeneous obstacle materials

Material name	Equation of state	Strength model	Failure model
AL2024-T4	Shock	Steinberg Guinan	None
HMX-TNT	JWL	None	None
CU OFHC	Linear	Zerili Armstrong	None
AL 2024	Shock	None	None
PLEXIGLAS	Shock	None	None
GERMANIUM	Shock	None	None
STEEL 1006	Shock	Johnson Cook	None
COMP B	JWL	None	None

Inhomogeneous obstacles comprise elements of the missile’s autopilot (pos.1–3), TV homing head’s electromechanical components (pos.4–7), and TV homing head’s optics (pos. 8–10).

Table 5. Properties of the inhomogeneous obstacles

Pos.	Purpose	Material	Thickness [mm]	Position [mm]
1	Carrier	AL2024	2	93
2	PCB	PVC	5	105
3	Carrier	AL2024	3	145
4	Carrier	AL2024	2	170
5	PCB	PVC	2	176
6	PCB	PVC	1.5	185
7	PCB	PVC	3	191

8	Optic	Germanium	4	205
9	Optic	Germanium	4	220
10	Optic	Germanium	4	245

3. RESULTS AND DISCUSSION

Numerical simulation of the interaction between the shaped charge jet and inhomogeneous obstacle was performed using the previously described setup and material models. Furthermore, additional simulation without the inhomogeneous obstacle was conducted with the aim to obtain insight into the differences in performances and properties of the formed jets. Those simulations have also provided information about the detonation wave propagation process, jet formation process and explosive reactive armor activation.

3.1. Detonation wave propagation

Detonation wave propagation in precursor shaped charge warhead is same for both of the analyzed cases as the obstacles don't have the influence on it. Sequence of plots depicting the evolution of the detonation wave may be seen in Fig.3. Observed warhead does not contain a wave shaper and thus, the detonation wave propagates in a spherical form. Detonation point was placed on the symmetry axis, in the rear end of explosive charge. Time needed for the completion of the detonation process was 6.617 μ s. It is noteworthy to mention that the considered warhead is not designed optimally and that the jet and detonation properties could be enhanced.

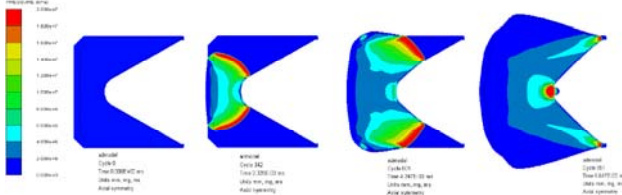


Figure 3. Detonation wave propagation in precursor shaped charge warhead

3.2. Jet formation process

Two simulation were performed: when the jet's path during the formation is unobstructed (Fig.4) and when the inhomogeneous obstacles are present (Fig.5).

In Fig.4 and Fig.5, sequences of jet formation process are displayed without the detonation products of the shaped charge's explosive and without the warhead's casing with the aim to provide better visualization of the jet.

Unobstructed jet had maintained approximately the same level of kinetic energy until it had achieved contact with the ERA's container when the minor drop of around 5% in its kinetic energy had occurred (Fig.6).



Figure 4. Jet formation process without obstacles

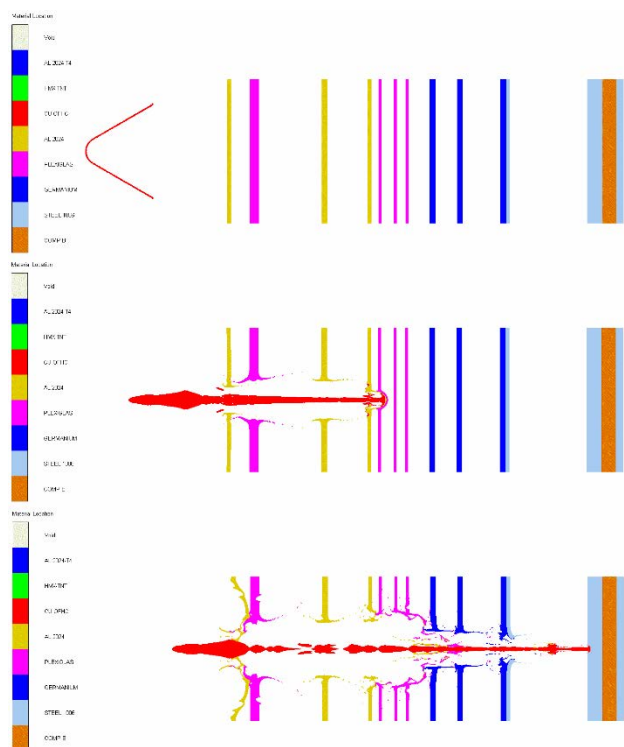


Figure 5. Jet formation process with inhomogeneous obstacle

In the case of the obstructed jet, jet formation process was characterized by several steep drops in the kinetic energy level and significant changes in the geometry of the primary jet due to the material bulking and localization that will lead to the jet particulation (Fig.5). Jet tip's encounter with each obstacle degrades the kinetic energy value in an approximately stepwise manner, as shown in Fig.6. It can also be noted that the time of the jet tip's impact into the ERA's front panel is not the same for both cases as there is a time delay in the obstructed case which is around 10 μ s. This time period is highly important when the activation of the the main shaped charge warhead is considered, as it has to be done at a desired time and stand-off distance.

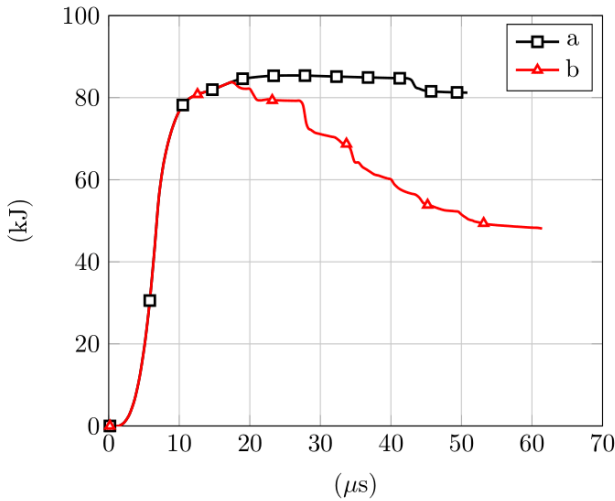


Figure 6. Cooper liner kinetic energy vs. time, a) without inhomogeneous obstacle, b) with inhomogeneous obstacle

By positioning the 29 fixed gauge points along the jet formation path, it was possible to observe jet’s dynamic characteristics. Figure 7 shows the change in the jet tip velocity over time for both of the observed cases.

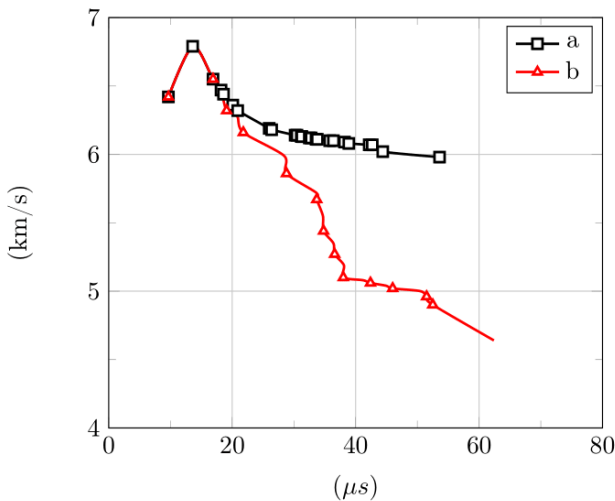


Figure 7. Jet tip velocity vs. time before impact into the ERA’s front panel, a) without inhomogeneous obstacle, b) with inhomogeneous obstacle

In the case of the unobstructed jet formation, the jet tip velocity slightly decreases. Value of the jet tip velocity at the moment of its encounter with the ERA’s front panel is 6km/s. On the other hand, in the case when the jet is obstructed by the inhomogeneous obstacles, jet tip’s velocity drops significantly over time and forms a stepped profile that may be seen in Fig.7(b). In the moment of its impact into the ERA’s front plate, velocity has the value of 4.6 km/s indicating the decrease of almost 25%.

Velocity gradient over the jet length is displayed in Fig.8 for both of the analyzed cases. For the unobstructed jet, its tip diameter is 5 mm and the maximum slug diameter is 10 mm. Total length of the jet in the moment of impact is 238.4 mm. For the case of the obstructed jet maximum jet tip diameter is 2.6 mm and maximum jet slug diameter is 11 mm, while the total length of the jet is 230 mm. As it may be seen, jet tip’s diameter was reduced in size for

almost 50%. On the other hand, change in the value of the jet’s length is minor. According to the theoretical and the empirical criteria [9-12,14], formed jet meets the initiation conditions, even though it was heavily influenced by the inhomogeneous obstacles that have reduced its dynamic properties.

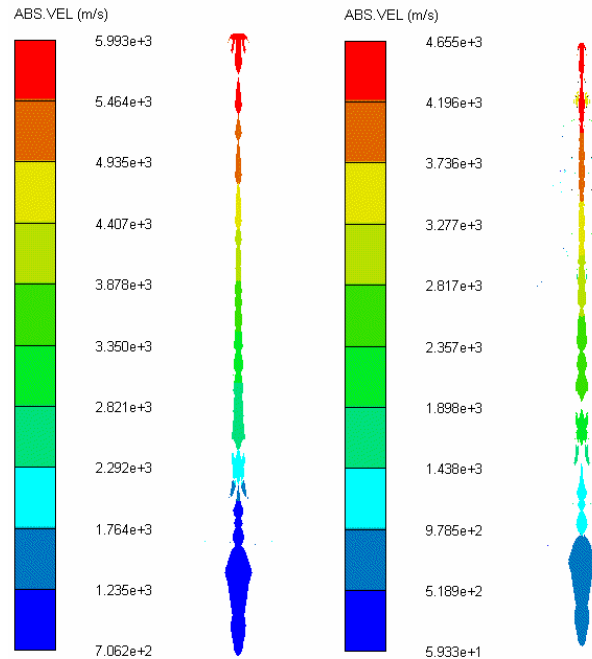


Figure 8. Velocity gradient in the jet at the moment of impact into the ERA’S front panel for the unobstructed (left figure) and obstructed (right figure) formation

3.2. Interaction of the jet and ERA

Upon the jet tip’s impact into the ERA’s front metal panel, large value of pressure was achieved in its material with the maximum of $3.086 \cdot 10^7$ kPa that was propagating towards the explosive. If the value of the shock wave pressure is smaller than Comp B’s pre-bulk modulus, sufficient initiation energy won’t be achieved. However, in the observed case the obstructed jet was able to induce the pressure of $5.2781 \cdot 10^6$ kPa in the Comp B which is enough to initiate explosive and create a hot spot at 65 μ s, before the jet’s tip had reached the front edge of the explosive. Figure 9 shows response of the ERA’s explosive to the influence of the obstructed jet throughout the processes of its ignition and detonation wave propagation.

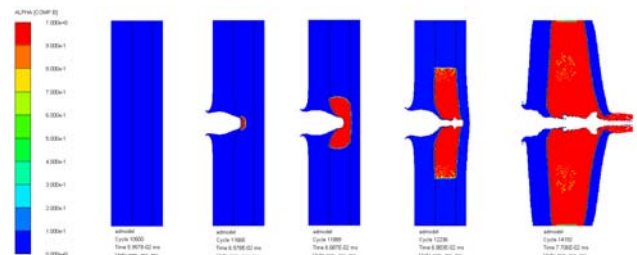


Figure 9. Sequences of ERA activation and change of the ALPHA coefficient

As an indicator of the explosive’s current state, the reaction degree APLPHA was observed. In a case of a

complete explosive reaction its value is $\text{ALPHA}=1$, while for the unreacted explosive it is equal to zero ($\text{ALPHA}=0$). Part of the explosive that has not yet reached state of complete detonation is located between those two values ($\text{ALPHA}=0-1$). From Fig.9, conclusion can be made that after the jet penetrates through the first steel plate and initiates the explosive in $65 \mu\text{s}$, the explosive continues to decompose and generates sufficient amount of energy which will lead to the initiation and growth of the explosive material in the radial direction. This is especially visible in the plots corresponding to the $66.87 \mu\text{s}$ and $68.83 \mu\text{s}$. Complete detonation of the Comp B appears at $77.06 \mu\text{s}$ where the transfer of the energy from the detonation products onto the steel plates is clearly visible through their acceleration and displacement.

4. CONCLUSIONS

Following conclusions may be derived from the conducted study and thus obtained results:

- Numerical analysis of the jet formation process indicates that the inhomogeneous obstacles decrease the jet performance by the deterioration of the velocity gradient over its length. This is clearly evident when the jet tip velocity is being considered as its value had decreased for around 23% when compared to the unobstructed jet formation process. Furthermore, size of the jet tip diameter has been reduced for almost 50%.
- Even after the jet had penetrated through all of the inhomogeneous obstacles, he had enough energy to initiate ERA's explosive.
- Instead of the complex Lee-Tarver ignition and growth model for which the material parameters are hard to find in the open literature, simulations were performed by the implementation of the burn on compression coefficient and pre-bulk modulus. Calibration of these two coefficients should be made through the comparison of the simulation results with the experimentally obtained results.
- Analyzing explosive reactive armor activation time is important information for the main shaped charge warhead initiation. Numerical simulation can provide complete interaction analyses of precursor-shaped charge, main shaped charge warhead and explosive reactive armor.
- For future work it is recommended to analyze different angle position between missile and explosive reactive armor to determine threshold detonation angle. For maximum performances of precursor shaped charge warhead it must be analyzed with embedded wave shaper. Finally, the experimental validation of the obtained results is also planned.

ACKNOWLEDGEMENT

This research has been supported by the Ministry of Education, Science and Technological Development of

the Republic of Serbia, through the subproject III-47029, in the 2022 year, which is gratefully acknowledged.

References

- [1] Орленко, Л.П. : Физика Взрыва, Главная редакция физико-математической литературы, Москва, (2004).
- [2] CORLEONE, J.: Tactical Missile Warheads, American Institute of Aeronautic and Astronautic, Washington, (1993).
- [3] UGRČIĆ, M. et al.: *Characterization of the natural fragmentation of explosive ordnance using the numerical techniques based on the FEM*, Scientific Technical Review, 65, (2015), 16-27.
- [4] UGRČIĆ, M. et al.: *Fem techniques in shaped charge simulation*, Scientific Technical Review, 59, (2009), 26-34.
- [5] MARKOVIĆ, M. et al.: *Numerical and analytical approach to the modeling of explosively formed projectiles*, 6th international scientific conference on defensive technologies, (2014), 1-7.
- [6] MARKOVIĆ, M. et al.: *Comparative approaches to the modeling of explosively formed projectiles*, Proceedings of Tomsk State University, 293, (2014).
- [7] MARKOVIĆ, M. et al.: *Simulation of changes in temperature and pressure fields during high speed projectiles forming by explosion*, Thermal science, 20, (2016), 1714-1752.
- [8] JEREMIĆ, O., et al.: *Analytical and numerical method of velocity fields for the explosively formed projectiles*, FME Transactions, 45, (2017), 38-44.
- [9] YANAN, DU. et al.: *Study on penetration performances of rear shaped charge warhead*, Materials, 14, (2021), 1-17.
- [10] CHANG, B.H. et al.: *Numerical simulation of modified low-density jet penetrating shell charge*, International journal of simulation model, 14, (2015), 426-437.
- [11] LIANGLIANG, D., et al.: *Simulation study on jet formability and damage characteristics of a low-density material liner*, Materials, 11, (2018), 1-17.
- [12] UGRČIĆ, M.: *Prilog teoriji interakcije eksplozivnog oklopa I kumulativnog projektila*, Doktorska disertacija, (1995).
- [13] PAPPU, S., MURR, L.E.: *Hydrocode and microstructural analysis of explosively formed penetrators*, Journal of Materials Science, (2002), 233-248.
- [14] UGRČIĆ, M., et al.: *Teorijski aspekti I numerička simulacija kumulativnog efekta*, Kumulativna naučnotehnička informacija, Vojnotehnički institut – Beograd, (2012).



NUMERICAL ANALYSIS OF THE TUNGSTEN CARBIDE-COBALT CORED BULLET PENETRATING THE HIGH-HARDNESS STEEL PLATE

RADOVAN ĐUROVIĆ

University of Belgrade, Faculty of Mechanical Engineering, Belgrade, rdjurovic@mas.bg.ac.rs

PREDRAG ELEK

University of Belgrade, Faculty of Mechanical Engineering, Belgrade, pelek@mas.bg.ac.rs

MILOŠ MARKOVIĆ

University of Belgrade, Faculty of Mechanical Engineering, Belgrade, mdmarkovic@mas.bg.ac.rs

DEJAN JEVTIĆ

University of Belgrade, Faculty of Mechanical Engineering, Belgrade, djevtic@mas.bg.ac.rs

MIHAILO ERČEVIĆ

Prvi Partizan, Užice, mihailo.ercevic@prvipartizan.com

Abstract: In the present study, penetration of a 6.5 mm Grendel armor-piercing projectile with a front tungsten carbide-cobalt core and rear lead-antimony core into the 8.5 mm PROTAC 500 high-hardness armor steel plate was analyzed both experimentally and numerically. Ballistic tests were performed in which the projectile's initial velocity had the value of 740 m/s. Experimental results have shown that the partial perforation with the projectile embedment was the most frequent outcome. Two-dimensional axisymmetric non-linear numerical model corresponding to the performed tests was developed in ANSYS AUTODYN software using the mesh based Lagrangian technique. Johnson-Cook strength and failure models were employed for the characterization of the material behavior. Developed numerical model was verified against the experimental results and the influence of the projectile's impact velocity on the parameters of the penetration was investigated. Rear lead alloy core was found to be able to provide significant enhancement of the projectile's efficiency.

Keywords: terminal ballistics, armor-piercing projectile, tungsten-carbide-cobalt, numerical analysis

1. INTRODUCTION

Small-arms armor-piercing (AP) ammunition is widely used for the perforation of light-armored targets owing to its high penetration efficiency. However, advances in the armor material technology and in the design of protective structures induce a continuous demand for the enhancement of the AP projectiles' ballistic properties.

It is known that increase in the impact velocity has the beneficial effect on the penetration efficiency which, for example, may be seen in the well-known models of Recht and Ipson [1] and Lambert and Jonas [2], and in numerous experimental studies. In order to increase the projectile's impact velocity and kinetic energy, it is necessary to increase projectile's initial velocity and/or to reduce velocity drop over the distance. During the development of the 6.5 mm Grendel bullet, both the gunpowder mass and the projectile's ballistic coefficient were optimized, resulting with the improvement in the bullet's internal and external ballistic properties. In an experimental research [3], performance of the 6.5 mm Grendel bullet was compared with that of the 5.56x45 mm SS109 and the 7.62x39 mm API bullets. Their velocities were measured over the range of 700 meters and based on the obtained

results, it was concluded that the projectile's kinetic energy is by far the highest in the case of 6.5 mm Grendel cartridge, exceeding that of the 7.62x39 mm for more than double on the medium and long ranges. Nevertheless, even though the increase in kinetic energy may provide increase in penetration, it may also lead to the loss of the projectile's integrity due to the high values of compressive and bending loads being exerted on it during the ballistic impact. Thus, it is highly important to conduct a thorough investigation of the projectile-target interaction which for the high velocity impacts may be done through experimental, analytical and numerical approaches [4]. Numerical simulations have shown to be a valuable tool in the design phase as their usage can lead to the shorter development time and to the reduced number of prototypes and ballistic tests, while providing accurate prediction of the complex physical phenomena during the ballistic impacts.

In the present study, ballistic testing of the 6.5 mm Grendel armor-piercing tungsten carbide-cobalt (WC-Co) cored projectile against PROTAC 500 high-hardness armor steel was conducted and corresponding two-dimensional numerical model was developed in the ANSYS AUTODYN software. Accuracy and utility of the

numerical models in the field of penetration mechanics are usually limited by the material behavior description [5], thus making it necessary to validate the developed model against the obtained experimental results. In the process of model validation, influence of the rear lead alloy core and its erosion criteria value on the penetration process was investigated. After the good agreement between the experimental results and the numerical model was achieved, additional simulations with the different values of impact velocities were conducted.

2. BALLISTIC TESTS

In a series of ballistic tests, 6.5x39 mm Grendel armor-piercing rounds (Fig. 1) were fired through a 415 mm long ballistic test barrel into the 8.5 mm thick PROTAC 500 high-hardness steel plate. Square-shaped plate with the edge size of 500 mm was mounted in the rigid frame and placed at the distance of 100 meters from the barrel muzzle. In order to enhance the credibility of the tests and to assure no reciprocal influence in the results, in-plane distance between adjacent shots and the boundaries was

kept greater than 100 mm [6]. During the tests, angle of incidence between the projectile and the target plate was kept normal.

In total, nine tests with the bullet's nominal initial velocity of 740 m/s were conducted. Its value was being monitored with the use of the infrared optical velocity measuring system. Based on the measured values and on the known projectile's ballistic coefficient of 0.540 (G1 drag function), the impact velocity was calculated and its average value was found to be equal to 702.1 m/s. Deviations from the average value were found to be minor and negligible. HPI B590 optical target system was used for the acquisition of the projectile's accuracy data.

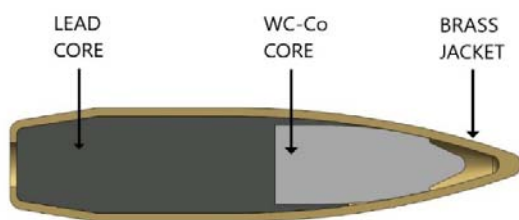


Figure 1. Cross-section of 6.5 mm Grendel AP projectile

As it may be seen in Fig. 1, observed armor-piercing projectile consists of front tungsten carbide-cobalt core and rear lead-antimony core which are both being encased in the brass jacket. Hard WC-Co core has the mass of 1.8 grams with the length of 11 mm and the diameter of its cylindrical section equal to 4.7 mm. Mass of the complete projectile is 7.8 grams and its length is 30.2 mm.

Results of the conducted firings have shown that the complete perforation wasn't achieved in any of the tests. In seven firings, partial perforation with the penetrator embedment was observed, while in the two firings no perforation was observed at all. Pictures of several distinct penetration process outcomes may be seen in Fig.

2. For the great majority of the conducted firings, ductile hole formation in initial stage and adiabatic shear plugging in the second stage of penetration was observed as the failure mechanism. Due to the fact that shear bands nucleate and propagate to the rear surface independently, plugging failure will generally lead to the asymmetric deformation and combination of adiabatic shear with the bending away and fracture of the plug from the target [7]. Side views in Fig. 2 clearly indicate that in the firings without the perforation (labeled A and B), the adiabatic shear plugging with the asymmetric plug formation had occurred but that the fracture and consequent ejection of the plug failed to happen. Inspection of the indentations created during those impacts has shown that the penetrator wasn't embedded in the target plate, indicating that its fragmentation had occurred during the process of penetration due to the high loads. Collapse of the penetrator material was also observed in several firings in which the partial perforation has been achieved (D in Fig. 2). Initial stage of penetration was identified as critical, as during this stage the core undergoes the maximum compressive and bending loads which often cause the collapse of the WC-Co composite due to its brittleness [8]. Frontal conical section of the WC-Co penetrator has shown to be particularly susceptible to the exerted loads, while the cylindrical section stayed intact and was found embedded in the target plate. In lesser number of firings, the whole penetrator was found intact and embedded in the target plate (C in Fig. 2).

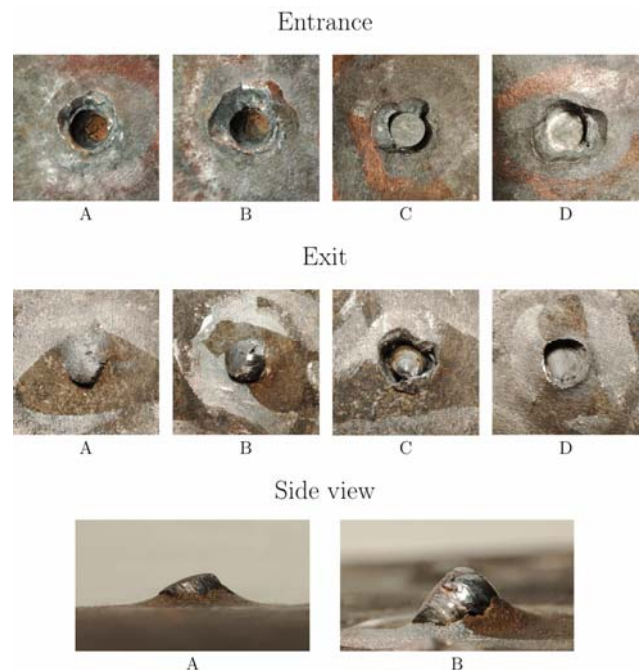


Figure 2. Target plate damage morphology

No evidence of the lead-antimony core and brass jacket embedment was recorded, indicating their complete destruction in the process of penetration. However, their influence may be seen in the zone of the hole entrance where the cratering was observed for all of the conducted firings. This behavior is characteristic in the penetration of metallic targets with a cored projectile that is achieved via the ductile hole formation mechanism [9]. On the rear surface of the target plate, bulges have been formed in

seven firings with partial perforation outcome. Their maximum heights were in the range from 1.1 to 1.8 mm while the diameters of the generated holes were in the range from 4.5 to 4.9 mm. Plugs created during the two firings without the achieved perforation have the maximum height of 2.2 mm (A in Fig. 1) and 3.6 mm (B), measured from the rear surface of the target.

Differences observed in the outcomes of the performed firings can be attributed to the stochastic nature of ballistic tests. During the research of Kilic et al. [10], it was found that only one of five shots has shown the perpendicular intrusion in the target material while in the remaining impacts the obliquity was detected. Based on the analysis of the target plate after the ballistic tests were performed, similar conclusion was made in the present research.

3. MATERIAL MODELS

High velocity impacts and penetrations are exceptionally complex processes and their numerical modeling represents a great challenge due to the occurrence of high strain-rates, large deformations, high temperatures etc. which make the characterization of material behavior and failure difficult. One of the most widely used constitutive models was developed by Johnson and Cook [11]. It is an empirical visco-plastic model which is suitable for the modeling of ductile metals and which takes into account strain hardening, strain rate and thermal softening effects. According to it, the equivalent stress may be expressed as:

$$\sigma_Y = [A + B\varepsilon_p^n][1 + C \log \dot{\varepsilon}_p^*][1 - T_H^m] \quad (1)$$

where ε_p is the equivalent plastic strain, $\dot{\varepsilon}_p^*$ is the dimensionless plastic strain rate for $\dot{\varepsilon}_0$, T_H is homologous temperature $T_H = (T - T_{room}) / (T_{melting} - T_{room})$, while A, B, C, n and m are material constants.

Apart from the material strength model, Johnson and Cook have also developed a ductile failure model which takes into account effects of strain rate, temperature and stress triaxiality on failure strain [12]. According to it, failure strain for metals increases with increase in temperature, while it decreases with increase in strain rate and stress triaxiality. The Johnson-Cook failure model is empirical cumulative damage – fracture model which assumes that damage is accumulated in the material during the plastic straining until a critical value is reached after which the material breaks immediately. Thus, the damage has no contribution on the stress field until the fracture occurs. Due to the J-C model being an instantaneous failure model, no strength of eroded material elements will remain after their erosion happens.

The damage to an element is defined by:

$$D = \sum \frac{\Delta \varepsilon}{\varepsilon^f} \quad (2)$$

where $\Delta \varepsilon$ is the increment of equivalent plastic strain and ε^f is the equivalent strain to fracture given by:

$$\varepsilon^f = [D_1 + D_2 \exp(D_3 \sigma^*)][1 + D_4 \ln|\dot{\varepsilon}_p^*|][1 + D_5 T_H] \quad (3)$$

Material parameters D_1 , D_2 and D_3 which represent the strain hardening are predominant when compared with

two other which represent the strain rate hardening (D_4) and thermal softening (D_5). The dimensionless pressure-stress ratio σ^* represents a measure of stress state triaxiality. The damage variable D may take values in a range from 0 to 1 where $D = 0$ represents undamaged material elements while in the elements in which D reaches 1 the fracture will occur, leading to their removal from the simulation. In order to implement the Johnson-Cook strength and fracture models in the numerical analysis, it is necessary to know the material parameters. PROTAC 500 was experimentally and numerically investigated in the study of Trajkovski et al. [13]. Its J-C model parameters were determined and are given in table 1, together with basic mechanical properties.

Table 1. PROTAC 500 basic mechanical properties and Johnson-Cook parameters [13]

Density		7.85 g/cm ³			
Hardness		470-540 HB			
Yield strength		1400 MPa			
Tensile Strength		1800 MPa			
Elongation A5		10 %			
Strain hardening			Strain rate hardening		Temperature softening
A [MPa]	B [MPa]	n	c	$\dot{\varepsilon}_0$ [s ⁻¹]	m
1380	948	0.2351	0.0035	0.001	1.087
D_1	D_2	D_3	D_4	$\dot{\varepsilon}_0$ [s ⁻¹]	D_5
0.0001	1.586	-1.718	0.00695	0.001	3.247

Lead being used for the production of bullet cores is generally alloyed with antimony with the aim to increase its hardness and strength [14]. Antimony content can range from 0.5 to 25 wt.-% and in the present study, it was equal to 8 wt.-%. Brass from which the jacket is made is widely used CuZn10 alloy, also known as red brass and tombac. Mechanical properties of both the lead alloy and the brass are relatively low when compared with those of tungsten carbide-cobalt and high hardness armor steel. Thus, severe deformation and distortion will appear in the jacket and soft core elements during the high-velocity impact. In order to avoid simulation interruption, Lagrange solver relies on a technique of numerical erosion for the deletion of highly strained elements. Several erosion criteria are available in AUTODYN software, including the erosion upon material failure and instantaneous geometric strain erosion. Johnson-Cook failure model was used as erosion criteria for brass, while in the case of lead alloy a preliminary value of 2.5 was chosen for the instantaneous geometric strain erosion [15]. Even though the latter one represents an ad hoc method that has no physical basis, knowledge of the ballistic test outcome makes it possible to determine the appropriate erosion criteria and the erosion strain value. In Table 2, Johnson-Cook model parameters for the jacket and the soft core materials are summarized.

Table 2. Johnson-Cook parameters for lead alloy and brass

Lead core [16]					
Strain hardening			Strain rate hardening		Temperature softening
A [MPa]	B [MPa]	n	c	$\dot{\epsilon}_0 [s^{-1}]$	m
10.3	41.3	0.21	0.00333	0.01	1.03
Brass jacket [16]					
Strain hardening			Strain rate hardening		Temperature softening
A [MPa]	B [MPa]	n	c	$\dot{\epsilon}_0 [s^{-1}]$	m
448.2	303.4	0.15	0.00333	0.01	1.03
D_1	D_2	D_3	D_4	$\dot{\epsilon}_0 [s^{-1}]$	D_5
2.25	0.0005	-3.6	-0.0123	0.01	0

Materials for armor-piercing projectiles' hard cores are often modeled as rigid, due to their high mechanical properties [17]. Tungsten carbide-cobalt (WC-Co) is a metal-ceramic composite characterized by high hardness, high density and relatively good compressive and bending strength values [8]. In the present study, WC-Co alloy (85% WC, 15% Co) with a hardness of 1090 HV and density of 14.08 g/cm³ was used as the core material and in the conducted simulations it was modeled as rigid.

4. NUMERICAL MODEL

Two-dimensional axisymmetric model corresponding to the conducted ballistic test was developed in ANSYS AUTODYN. Mesh based Lagrangian technique was employed during the model development as it is computationally efficient and provides insight into the material boundaries. Its downside is that it requires implementation of element erosion in order to handle severe mesh distortions which will inevitably appear during the ballistic impact simulations. Deletion of highly deformed cells will lead to the removal of internal material energy from the model which will result in reduced accuracy. Apart from the WC-Co penetrator that is modeled as rigid, other parts of the projectile and the target are prone to the element erosion and loss of internal energy, with the jacket and lead core being exceptionally susceptible to it as they are made from ductile materials which undergo large deformations during the penetration process. However, as it was concluded in the work of Borvik et al. [6], ballistic limit velocity was reduced by 3 to 5 % when only the hard core of the projectile was used indicating that the effect of the brass jacket and the lead cap on the penetration process is minor. Thus, it was concluded that the Lagrangian discretization may be used in the present research. Nevertheless, due to the large volume and mass of the lead alloy core when compared to the WC-Co core, additional simulations were conducted with the hard core as the only element of the projectile.

During the experiment, target plate with the impact area of 500x500 mm was used. However, in order to reduce the computational cost of the simulation target was modeled as a circular, axisymmetric plate with the radius of 100 mm which corresponds to the distance between adjacent shots. As the projectile's dimensions are considerably smaller when compared to the target radius, finer mesh was created in the central zone of the target plate and as a result, element size gradually increases in radial direction from 0.1 mm in the zone of impact to the 0.5 mm at the target's outer surface where the fixed boundary condition was applied. Element size in range from 0.1 mm to 0.15 mm was chosen for the meshing of the projectile and in total, around 26000 elements were formed for the purpose of target and projectile discretization. Created Finite Element model may be seen in Fig. 3, where the 2D model was rotated for 90° about the symmetry axis in order to provide a better representation of the model's geometry. Only a central zone of the target is shown due to its large radius.

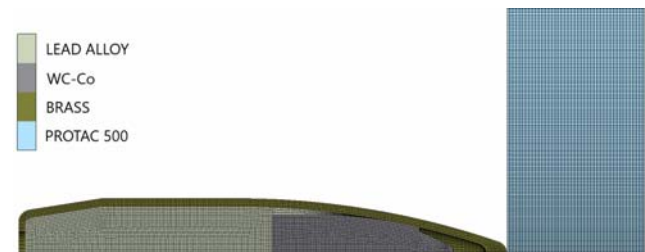


Figure 3. FE model of the projectile and the target

Geometry of the projectile's numerical model is identical to the geometry of the actual bullet. For the purpose of model validation, impact velocity and target thickness were same as in the ballistic test. Friction between the projectile and target was neglected as its influence is considered to be minor in the high velocity impacts.

5. RESULTS AND DISCUSSION

Using the presented numerical model, a simulation corresponding to the conducted experimental firings was performed. Furthermore, an additional simulation was conducted in which the brass jacket and the lead core were removed, thus making it possible to determine the degree of their influence on the penetration process parameters. As a result, profiles of WC-Co core's velocity over time (Fig. 4) and vs. its displacement (Fig. 5) were created for both of the observed cases. Reference coordinate system was set at the target plate's impact surface and the displacement of the hard core was measured from it after the contact with the target was achieved. For a better understanding of the presented velocity curves, a sequence of plots displaying the evolution of the penetration process is shown in Fig. 6.

In the simulation with the complete projectile, WC-Co core had to penetrate through the jacket tip (as it may be seen in plot for $t = 4.13 \mu s$ in Fig. 6), thus experiencing a drop in velocity prior to its contact with the target at $t = 4.78 \mu s$. However, by comparing the results from both of the conducted simulations it was found that the difference in velocity caused by this drop is less than 1%, indicating that the brass jacket may be neglected.

Furthermore, it may be seen in Fig. 6 that the erosion of the jacket material happens with almost no damage being generated in the target plate which additionally confirms the previously stated conclusion. On the other hand, numerical results show that the influence of the lead alloy core is significant and that it may not be neglected due to the great differences in the penetration process parameters which have been observed.

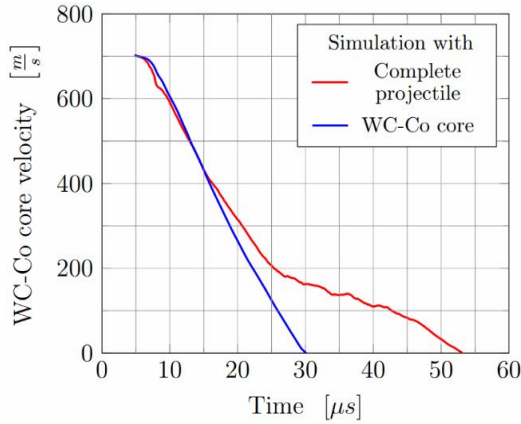


Figure 4. WC-Co core’s velocity over time for the simulations with the complete projectile and with the WC-Co core only

Upon the impact of the WC-Co core into the target plate and throughout the penetration, significant change of the velocity was observed in both of the simulations. However, character of that change greatly differs during the majority of the penetration process. Velocity vs. time curve for the simulation with only the WC-Co core has a steep gradient with the approximately constant value of the deceleration. Observed curves are similar only during the first 10 μs of the penetration, from the moment of impact to around 15 μs where they start diverging. This point represents the end of the first out of four sections which can be seen on the velocity vs. time curve for the complete projectile simulation. Second section is characterized by an increase in the slope and the decrease in deceleration by 31.8%. However, its value is still relatively high causing further velocity drop, although more moderate than in the case with the WC-Co core as the only part of the projectile.

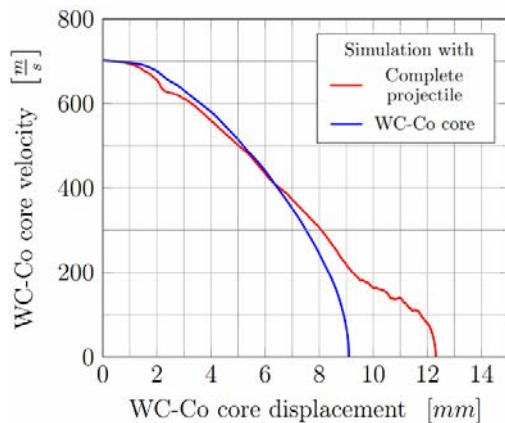


Figure 5. WC-Co core’s velocity vs. displacement for the simulations with the complete projectile and with the WC-Co core only

Simulation results have shown that first two sections are responsible for the majority of the WC-Co core’s penetration. In fact, 9.1 mm or 74% of the core’s total axial displacement of 12.3 mm had been accomplished during them while the first section alone is accountable for the 48.8% of the core’s total displacement (Fig. 5). By observing the plots for $t = 8.56 \mu s$ and $t = 16.37 \mu s$ shown in Fig. 6, it may be seen that during the first section there was no significant erosion of the lead alloy core. Thus, it may be concluded that the WC-Co core is able to provide relatively large penetration even though its mass represents only 23% of the complete projectile’s mass. However, enhancement of the WC-Co core’s penetration by the effect of the lead alloy core is significant and clearly visible, especially in the third section during which the additional displacement equal to 3.2 mm is achieved. In the observed case, 26% of the WC-Co core’s total axial displacement may be attributed to the lead alloy core.

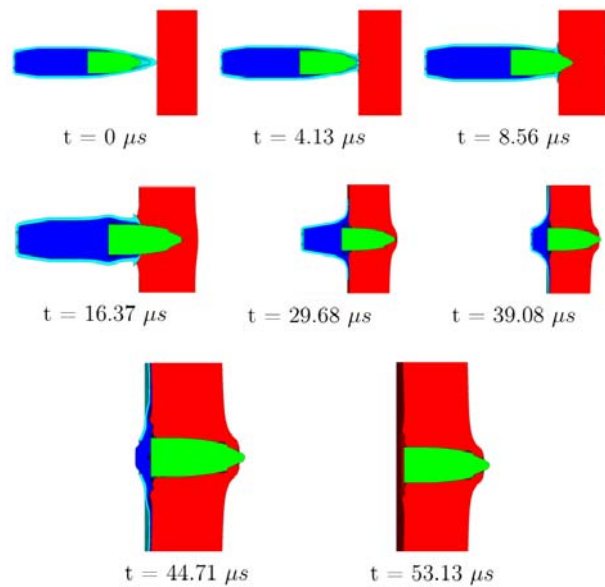


Figure 6. Evolution of the penetration process in the simulation corresponding to the performed experiment

Velocity drop during the third section is also heavily influenced by the lead alloy core, resulting in the considerably smaller deceleration. End of this section is characterized by the complete erosion of the lead core that had occurred at around 46 μs . Even though the WC-Co core still had a velocity of around 80 m/s in that moment, it was not able to provide any additional displacement during the fourth section (Fig. 5).

Based on the experimental results, it was concluded that the simulation with the complete projectile had provided better agreement than that with hard core only. Partial perforation with the projectile embedment was achieved which is in accordance with the majority of the conducted ballistic tests. Furthermore, a comparable value of penetration depth was achieved as in Fig 2, case C. Minor deviation between the model and the experiment may be seen on the target’s impact surface where the crater created during the simulation is considerably smaller in both the depth and the diameter than the experimental one. Also, ejection of the target plate’s material from its rear surface wasn’t reproduced properly. However, this

may be attributed to the changes in the material failure mechanisms between the initial and second stage of penetration and the transition from the ductile to brittle failure which may not be described accurately using the same material model. Ductile hole formation during the initial stage of the penetration was, on the other hand, successively simulated.

Due to the conclusion that the lead core may not be neglected, additional simulations have been performed with the values of erosion strain (ES_{IGS}) different from the preliminary value of 2.5 as the calibration of this erosion

criteria against the experimental results had to be done. Velocity and displacement histories for those simulations may be seen in Fig. 7. Acquired results have shown that the velocity vs. time curves significantly differ only in the fourth section and that the crucial changes in the hard core's displacement weren't observed. Best agreement with the experiment may be achieved with the ES_{IGS} values in range from 2.3 to 2.5 and in the following simulations, numerical model with the erosion strain of 2.5 was used.

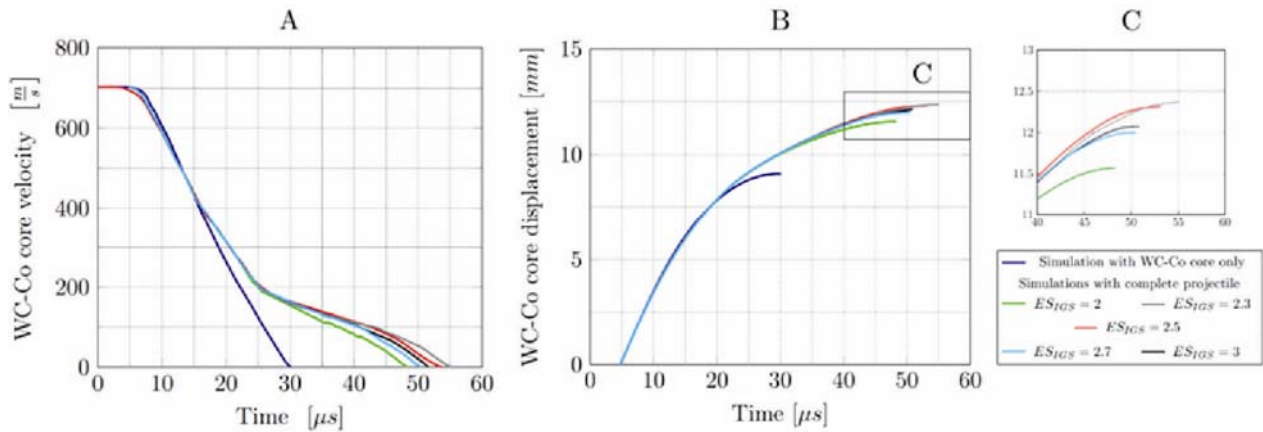


Figure 7. Velocity (A) and displacement (B) of the WC-Co core over time for the several values of ES_{IGS} erosion strain in the range from 2 to 3

Experimental results shown in Section 2 indicate that the observed impact velocity is in vicinity of the ballistic limit velocity for the observed projectile and target plate configuration. In order to determine the change in the parameters of the penetration process under the different impact velocities, additional numerical simulations were performed using the previously described and verified numerical model. WC-Co core's velocity vs. displacement curves for the impact velocities in range from 660 m/s up to 770 m/s are displayed in Fig. 8. In accordance with the obtained results, the projectile will be able to achieve complete perforation of the target under the impact velocities equal to 730 m/s and higher. Significant change in the value of residual velocity was observed even with the small increase in the impact velocity. This can be partially attributed to the observed change in the influence of the lead alloy core during the third section of penetration. As it may be seen in Fig. 8, value of the WC-Co core's velocity at which the third section starts increases greatly with the increase in impact velocity and that is accompanied with the increased slope for that section. This increase in the slope can even result in the positive value being achieved, meaning that the increase in the WC-Co core's velocity caused by the contribution of the lead core surpasses the decrease caused by the resistance of the target plate. Thus, velocity of the hard core may even increase during the penetration.

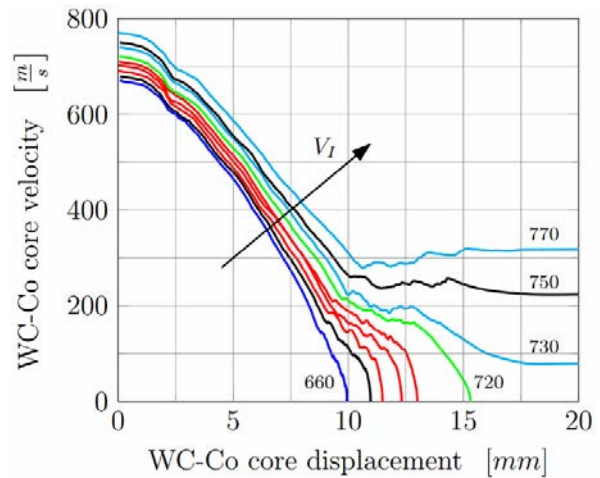


Figure 8. WC-Co core's velocity vs. displacement for the several values of the projectiles impact velocity V_I

Decrease in the value of the impact velocity will result in the increased deceleration in the third section; in the reduction of its duration and in the reduced contribution of the lead alloy core to the total axial displacement. For the lowest impact velocity considered in the present study, third section had almost been blended into the second section and the penetration achieved during it has been minimized. This may pose a risk to the efficiency and usability of the observed projectile on the mid and long ranges where a considerably lower values of impact velocities are to be expected. On the other hand, implementation of the rear core made from lead alloy had led to the significant enhancement of the projectile's ballistic properties in the cases of impact velocities above

the ballistic limit and this may be valuable on the short ranges. Main advantage of the lead is that is highly ductile when compared to the brittle tungsten carbide-cobalt alloy. By the utilization of the presented dual core configuration, same level of penetration could be achieved with the WC-Co core that is smaller in size and thus, less prone to the loss of integrity during the penetration process.

5. CONCLUSIONS

Ballistic tests and two-dimensional numerical simulations have been performed with the aim to investigate the high velocity impact of the dual-cored 6.5 mm Grendel AP projectile into the 8.5 mm thick high hardness steel plate. Some of the important conclusion and observations are:

- Experimental firings have shown that the partial perforation with the projectile embedment was the most common penetration process outcome. Also, in two out of nine firings perforation was not achieved at all indicating that the impact velocity is close to the ballistic limit velocity. During the tests, obliquity angle was kept normal and the average value of the projectile's impact velocity was 702.1 m/s. Tungsten carbide-cobalt core had lost its integrity in majority of the tests which can be attributed to its brittleness and the high compressive loads exerted on it during the penetration process. Ductile hole enlargement was identified as the main failure mechanism,
- Numerical model developed in ANSYS AUTODYN using the Lagrangian mesh based technique was able to provide a good agreement between the numerical and experimental results. WC-Co core was modeled as rigid while the other elements of the projectile and the target were modeled using the Johnson-Cook strength and failure models, with the exception of lead alloy core where the instantaneous geometric strain was applied as the failure and erosion criteria.
- Calibration of the erosion strain value was conducted against the experimental results by performing the simulations with the $\epsilon_{S_{TGS}}$ values in range from 2 to 3. With the exception of the lowest considered value, others were found to produce a similar outcome and the differences in the velocity and displacement curves between them were relatively small. However, best agreement was provided by the values of 2.3 and 2.5 and the latter one was adopted as the erosion strain value for the developed numerical model.
- Simulation results have shown that the brass jacket has a minor influence on the parameters of the penetration process and that it may be neglected. On the contrary, influence of the lead alloy core was found to be significant and non-negligible. For the simulation corresponding to the conducted firings, soft core was solely responsible for the 26% of the hard core's total axial displacement. Beneficial effects provided by the lead alloy core were found to increase with the increase in the projectile's impact velocity. For the values that are far enough from the BLV, WC-Co core's velocity even grew in value during one part of the penetration. However, even a small decrease in the value of impact velocity had

strongly reduced the projectile's penetration which may pose a threat to its efficiency and utility on the mid and long ranges.

- Although good agreement was achieved with the rigid model of the WC-Co, additional effort needs to be made in the implementation of the deformable model that will successfully model brittleness and failure.

References

- [1] RECHT, R., IPSON, T.: *Ballistic perforation dynamics*, Journal of Applied Mechanics, 30, (1963)
- [2] LAMBERT, J., JONAS, G.: *Towards standardization in terminal ballistics testing: velocity representation*, U.S. Army Ballistic Research Laboratory, (1976)
- [3] JOKIĆ, Ž. ET AL.: *Primena VIKOR metode prilikom izbora kalibra za automatske puške u cilju uvođenja u operativnu upotrebu u jedinicama Vojske Srbije*, Vojno delo, 71(6), (2019), 200-221
- [4] ZUKAS, J.: *Introduction to Hydrocodes*, Elsevier Science, (2004)
- [5] ZUKAS, J. ET AL.: *Impact dynamics*, Wiley, (1982)
- [6] BORVIK, T. ET AL.: *Perforation resistance of five different high-strength steel plates subjected to small-arms projectiles*, International Journal of Impact Engineering, 36, (2009), 948-964
- [7] WOODWARD, R.: *The interrelation of failure modes observed in the penetration of metallic targets*, International Journal of Impact Engineering, 2, (1984), 121-129
- [8] KOLMAKOV, A. ET AL.: *Materials for Bullet Cores*, Russian Metallurgy (Metally), (2021), 351-362
- [9] ME-BAR, Y.: *On the correlation between the ballistic behavior and dynamic properties of titanium-alloy plates*, International Journal of Impact Engineering, 19, (1997), 311-318
- [10] KILIC, N.: *Ballistic resistance of high hardness armor steels against 7.62 mm armor piercing ammunition*, Materials and Design, 44, (2013), 35-48
- [11] JOHNSON, G., COOK, W.: *A constitutive model and data for metals subjected to large strains, high strain rates and high temperatures*, Proceedings of the 7th international symposium on ballistics, (1983)
- [12] JOHNSON, G., COOK, W.: *Fracture characteristics of three metals subjected to various strains, strain rates, temperatures and pressures*, Engineering Fracture Mechanics, 21, (1985), 31-48
- [13] TRAJKOVSKI, J. ET AL.: *Flow and fracture behavior of high-strength armor steel PROTAC 500*, Materials and Design, 66, (2015), 37-45
- [14] PERONI, L. ET AL.: *Mechanical properties at high strain-rate of lead core and brass jacket of a NATO 7.62 mm ball bullet*, The European Physical Journal Conferences, 26, (2012)
- [15] TELAND, JAN: *Numerical Simulation of Light Armor-Piercing Ammunition Against Ceramics*, Norwegian Defence Research Establishment, (2004)

- [16] CARBAJAL, L. ET AL.: *Assault Rifle Bullet- Experimental Characterization and Computer (FE) Modeling*, Experimental and Applied Mech., (2011) 7.62 mm caliber projectiles, Procedia Engineering, 88, (2014)
- [17] MANES, A. ET AL.: *Ballistic performance of multi-layered fabric composite plates impacted by different*



INFLUENCE OF DIFFERENTLY CURED POLYMERIC BINDERS ON RHEOLOGY PROPERTIES OF PLASTIC EXPLOSIVES

DANICA BAJIĆ

Military Technical Institute, Belgrade, simic_danica@yahoo.com

IVAN DIMITRIJEVIĆ

MC Labor, Belgrade, ivandimitrijevic2801@gmail.com

SLAVICA TERZIĆ

Military Technical Institute, Belgrade, slavica@algodesk.com

Abstract: *Plastic Explosive Compositions consisting of HMX and liquid polyurethane binder were prepared in order to determine influence of differently cured polymeric binders on rheological properties of plastic explosives. First, a set of polymeric binders was prepared in polyaddition reaction between HTPB and IPDI, with varying NCO:OH ratio and examined through the standard and non-standard rheological tests on a dynamic rotational rheometer. Viscosity curves of polymeric binders show viscosity increase with NCO:OH ratio increase, as expected. Amplitude sweep tests reveal liquid-like structure of PEs, with structure strength increase with higher NCO:OH ratio of polymeric binder used, and limiting values of LVER vary from 10^{-3} to 10^{-2} strain. Results of creep test reveal that with increase of NCO:OH ratio of polymeric binder in PE zero-shear viscosity increase and viscous portion deformation decrease. Also, penetration decrease with increase of NCO:OH ratio. The obtained results indicate that initial rheology testing is crucial in plastic explosive formulation regarding their processability and physical properties.*

Keywords: *plastic explosive, polymer binder, rheology, creep.*

1. INTRODUCTION

Plastic explosives (hereinafter referred to as PE) are dispersions of crystalline explosives in polymer binders, with high content of explosive components. As a rule, polymer binders are in a liquid state. Thanks to the composition and characteristics of PE, after the action of force (shaping), they keep their shape. The mass fraction of the explosive component in PE is usually in the range of 70 wt.% to 90 wt.%. The binder gives the explosive mixture plastic properties, and at the same time phlegmatizes it (reduces the sensitivity of PE to the effect of unwanted external impulses). This type of explosive, due to its plastic behavior, is easily shaped in a wide range of temperatures, and is used above all for various types of engineering and sabotage demolitions (e.g. bridges, docks and railway tracks), is used in specific weapons such as reactive armor, and somewhat less often for the ammunition filling (such as booster charges, hand grenades, anti-tank and anti-personnel mines, anti-tank and anti-aircraft missiles) [1, 2]. The convenience of manual shaping is reflected in the fact that it is possible to quickly place various forms of PE on structures to be demolished, which can be located both on land and in water. In addition to the two mandatory, already mentioned components, various additives are added to PE compositions that modify detonation or physical properties (oxides, metal powders, antioxidants, bonding agents, plasticizers, etc.).

PEs have a high detonation velocity, a high destructive power, and at the same time a low sensitivity to external

impulses, which makes them safer to handle than some other explosive compositions and charges. If necessary, by increasing the content of the inert component and adding appropriate additives, PE compositions with low detonation velocities can be obtained, for specific use.

Given that PEs are primarily used in demolition and engineering actions, it is necessary that they possess appropriate physical characteristics in terms of plasticity, consistency, stickiness, etc. The science of rheology deals with examining those characteristics, which studies the behavior of matter under the influence of force [3]. In previous research in the field of PE in Military Technical Institute, the rheological characteristics of PE were, in the absence of appropriate equipment and testing methods, examined by very indirect and subjective methods. Thus, the consistency was determined by the "Bofors" method, which involves the assessment of manual shaping, retention of plasticity and retention of the original shape after PE has been standing for some time in a climate chamber at a certain temperature and air humidity [4]. Adhesion was determined by manual molding and assessment of PE adhesion to hands during molding [5]. Also, the old method for determining penetration is outdated nowadays. For the reasons mentioned above, and with the aim of following up current achievements in research in the field of PE, it is important to consider new methods for the adequate rheological characterization of PE and binders used for the production of plastic explosives. Establishing proper methodology would be significant from the aspect of standardizing the testing of the rheological characteristics of PE, and the data

obtained by testing different compositions of PE could be compared, and it could be unequivocally determined which of the mentioned compositions shows better consistency, greater stickiness and stability, etc.

As, by research in the field of PE from 2018 [6], liquid polyurethane binders obtained by the polyaddition reaction between hydroxyl-terminated poly(butadiene) prepolymer and isophorone diisocyanate crosslinker proved to be suitable for the production of PE, in this research the binders were also used based on those raw materials. Therefore, in order to gain methods for the rheological characterization of PE, four liquid polyurethane binders with different NCO:OH ratios were prepared from hydroxyl-terminated poly(butadiene) and isophorone diisocyanate. On the basis of these binders and the crystal explosive octogen, four PEs consisting of 85 wt. % of explosives and 15 wt. % binder were prepared. Due to the different NCO:OH ratio of the binder, the rheological characteristics of PE are different, and by examining these characteristics, the influence of differently cross-linked binder on the rheological characteristics of PE was observed. In this way, an insight into the validity of the applied rheological tests for testing PE was obtained. The rheological characterization of the produced binders and PE was performed on an Anton Paar rheometer MCR 302, and included [7]:

1. determination of the binder viscosity curve,
2. determination of the dependence of the dynamic rheological parameters of the binder and PE on the deformation amplitude,
3. determination of frequency dependences of dynamic rheological parameters of binder and PE,
4. PE creep test outside the linear viscoelasticity area, and
5. determining the penetration resistance and adhesiveness (stickiness) of explosives.

2. MATERIALS AND METHODS

2.1. Composition and production of binders for plastic explosives

As already mentioned in the introduction of this paper, the basic components of the binder are the prepolymer of hydroxyl-terminated poly(butadiene) and the isophorone diisocyanate crosslinker. In addition to this, the binders also contained the bonding agent triethylenetetramine and an antioxidant, N-phenyl-2-naphthylamine. The produced binders differ only in the NCO:OH ratio. The compositions of the binders are shown in Table 1. The binders are named PUPE (PolyUrethane for Plastic Explosive).

Table 1. Compositions of the binders

Binder label	NCO:OH	HTPB	IPDI	TETA	FβNA
		wt. %			
PUPE 1	0.2	96.00	1.60	0.48	1.92
PUPE 2	0.25	95.62	1.99	0.48	1.91
PUPE 3	0.3	95.24	2.38	0.48	1.90
PUPE 4	0.35	94.86	2.77	0.47	1.90

The used hydroxyl-terminated poly(butadiene) (HTPB, Shanghai Rongau Enterprises) was provided by the

company TRAYAL, Kruševac. The used isophorone diisocyanate (IPDI, Merck) is a mixture of cis and trans isomers, and has a purity greater than 99%; the triethylenetetramine (TETA, Sigma Aldrich) was of technical purity (60%), and the N-phenyl-2-naphthylamine (FβNA, Sigma Aldrich) had 97% purity. The binders were made in a vertical mixer DRAIS FH. The components HTPB, TETA and FβNA were homogenized for 5 minutes at atmospheric pressure and 30 minutes under vacuum at a temperature of 60°C. Then the IPDI was added and the mixture was mixed for 5 minutes at atmospheric pressure and 15 minutes under vacuum at the same temperature. The binders were poured into glass cups and left to crosslink for 96 hours at a temperature of 70°C in a drying oven with a water jacket.

2.2. Composition and production of plastic explosives

Plastic explosives were made from manufactured binders and octogen, HMX (class 1) purchased from the factory "Prva Iskra-Namenska" Barič. Each plastic explosive was made from 15 wt. % binder and 85 wt. % of octogen in a horizontal kneader, according to the established technological procedure [8]. Plastic explosives were named PE with suffixes from 1 to 4, depending on the binder used for their production (PE 1 from binder PUPE 1, etc.).

2.3. Rheological testing

All rheological tests were performed on a rheometer MCR 302 manufactured by Anton Paar (Figure 1).



Figure 1. Rheometer MCR 302, PE adhesion and penetration resistance test

2.3.1. Viscosity testing

The viscosity of the produced binders and the HTPB used for the production of the binder was tested by rotary tests using a cone-plate tool. The cone with a diameter of 25 mm and an angle of 1° was the moving part, and the plate with a diameter of 50 mm was stationary. Measurements were made at a temperature of 25 ± 0.5 °C. The shear rate was varied from 0.1 to 100 1/s (in order to obtain a value of zero viscosity and to simulate the technological process of kneading during which shear rates from 1 to 100 1/s occur) through 19 values equidistant on a logarithmic scale. In order to establish a laminar flow of the sample before reading the stress value, the length of the point measurements was also changed logarithmically from 60 s (how long the first point was measured at the lowest shear rate) to 10 s (how long the last point was measured at the highest shear rate). The distance between the tools was determined by the geometry of the tool and was 0.051 mm.

2.3.2. Examination of the dependence of the dynamic rheological parameters of binders and explosives on the amplitude of deformation

The dependence of the dynamic rheological parameters of binders, HTPB and explosives on the amplitude of deformation was examined using plate tools (upper movable plate with a diameter of 25 mm, lower stationary plate with a diameter of 50 mm), at a constant angular frequency of 10 rad/s and temperature of 25 ± 0.5 °C. After placement and removal of excess sample, and prior to testing, the samples were allowed to "recover" from the stresses applied during placement for 180 s. When testing the binder and HTPB, the deformation amplitude was varied from 10% to 1000% through 21 equidistant values on a logarithmic scale (10 points per decade), and the distance between the tools was 0.5 mm. When testing plastic explosives, the deformation amplitude was varied from 0.001% to 1% through 31 equidistant values on a logarithmic scale (also 10 points per decade), and the distance between the tools was 3 mm (to avoid the influence of large octogen particles on the measurement).

2.3.3. Examination of frequency dependences of dynamic rheological properties of binders and explosives

Frequency dependences of dynamic rheological properties of binders, HTPB and explosives under shear load in the area of linear viscoelasticity were examined to dependence on amplitude of deformation, at a temperature of 25 ± 0.5 °C. When testing the binder and HTPB, the angular frequency was varied from 628 rad/s to 1 rad/s through 28 equidistant values on a logarithmic scale (10 points per decade), the distance between the tools was 0.5 mm, and the measurement length of the points was left to the device. During the PE test, the angular frequency was varied from 10 rad/s to 0.01 rad/s through 31 equidistant values on a logarithmic scale, the distance between the tools was 3 mm, and the measurement length of the points was increased logarithmically from 20 s (how long the first point was measured at the highest angular frequency)

to 100 s (how long the last point was measured at the lowest angular frequency).

2.3.4. PE creep test outside the linear viscoelasticity region

The creep of PE outside the area of linear viscoelasticity was tested using tools used to determine the dependence of rheological parameters, at a temperature of 25 ± 0.5 °C. The samples were handled as in the the previously explained tests. The distance between the tools was 3 mm. A total of 67 points were read (the length of the point measurement was logarithmically increased from 0.1 s to 10 s) and in the recovery period 136 points (the length of the point measurement was also logarithmically increased from 0.1 s to 10 s).

2.3.5. Determination of penetration and adhesiveness of explosives

Determination of penetration resistance and adhesiveness of PE was performed at a temperature of 25 ± 0.5 °C, using the upper parallel plate with a diameter of 4 mm and a metal container with a diameter of 55 mm and a height of 35 mm. The mass of PE in the amount of 100 g was inserted into the container and leveled so that the height of PE in the container was about 28 mm, and the container was placed on the lower tool of the device (the lower stationary parallel plate with a diameter of 50 mm). The measurement consisted of 3 intervals, in each interval the head of the device (and thus the upper tool) moved at a constant set speed of 100 $\mu\text{m/s}$, only the direction of movement was changed. In the first interval, the direction was towards the sample (penetration interval) from the initial height of 20 mm to the final height of 10 mm. Then the direction was from sample (debonding interval), from a height of 10 mm to a height of 20 mm. The third interval was the same as the first (re-penetration). Each interval lasted 100 s, and during each interval 1000 normal force values were read.

3. RESULTS AND DISCUSSIONS

3.1. Viscosity of the binders

Figure 2 shows viscosity curves for HTPB and the prepared binders.

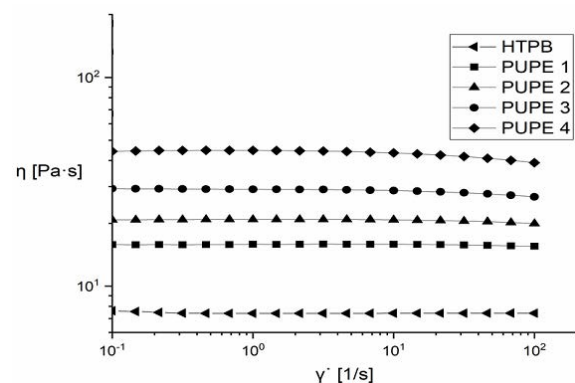


Figure 2. Viscosity curves for HTPB and binders

By analyzing the viscosity curves, it can be seen that HTPB and binders with a lower NCO:OH ratio behave almost like Newtonian fluids in the range of shear rates from 0.1 to 100 1/s, i.e. that pseudoplastic behavior becomes more pronounced with increasing NCO:OH ratio. This is in line with expectations, given that with an increase in the NCO:OH ratio, the length of the macromolecular chains, i.e. the molar mass of the binder, also increases. Increasing the molar mass increases the viscosity and pseudoplasticity of polymer fluids.

3.2. Dependence of dynamic rheological parameters of binders and explosives on deformation amplitude

Figure 3 shows the dependence of G' , G'' and $\tan\delta$ on γ on a graph with logarithmic scales for PUPE 4 binder, as a representative example. It can be seen that $G'' > G'$, i.e. that the binder behaves like a viscoelastic liquid, and that the limit value of the deformation is about 60%. The graphs of the dependence of G' , G'' and $\tan\delta$ on γ for all binders and HTPB look similar to this (all produced binders behave like viscoelastic liquids).

Figure 4 shows the dependence of G' on γ on a graph with logarithmic scales for all binders and HTPB, and it shows the above-mentioned: G' values increase with increasing NCO:OH ratio, i.e. pure HTPB has the smallest values of G' (where, conditionally speaking, the NCO:OH ratio is zero), while the binder PUPE 4, which is made with the largest amount of crosslinker, has the highest values. Also, it can be noticed that with an increase in the NCO:OH ratio, the value of G' leaves its plateau faster, i.e. that with an increase in the NCO:OH ratio, the area of linear viscoelasticity decreases. This can again be explained by the fact that with an increase in the NCO:OH ratio and an increase in the length of the polymer chains.

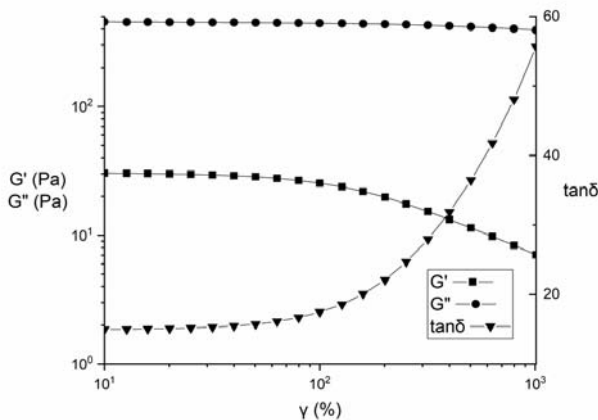


Figure 3. Graph of dependence of G' , G'' and $\tan\delta$ on γ for PUPE 4

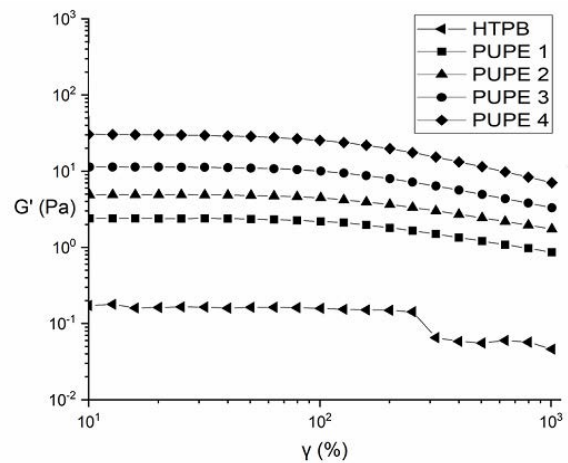


Figure 4. Graph of dependence of G' on γ for binders and HTPB

Figure 5 shows the dependence of G' , G'' and $\tan\delta$ on γ on a graph with logarithmic scales for plastic explosive PE 4. It can be seen that $G'' > G'$, like a binder

PUPE 4, PE behaves like a viscoelastic fluid. The other PE compositions also have graphs of the dependence of G' , G'' and $\tan\delta$ on γ similar to this, that is, all PE compositions behave as viscoelastic liquids. It reveals that there is no strong forces (in this case physical forces) in the structure of plastic explosives, i.e. good interactions between the binder and the octogen crystals. This could generally be expected considering that, due to the nature of the prepolymer, the macromolecular chains of the binder are mostly non-polar and there are not many possibilities for the formation of stronger physical forces (such as dipole-dipole interactions and hydrogen bonds) between the chains and the octogen crystals.

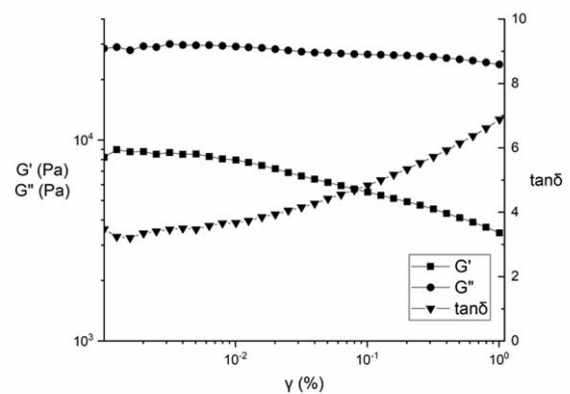


Figure 5. Graph of dependence of G' , G'' and $\tan\delta$ on γ for PE 4

Figure 6 shows the graph of the dependence of G' for all plastic explosives. Vertical displacement is a consequence of the binder used to make PE, i.e. rigidity, because with increasing rigidity, more energy was needed for deformation, so the modulus values are higher.

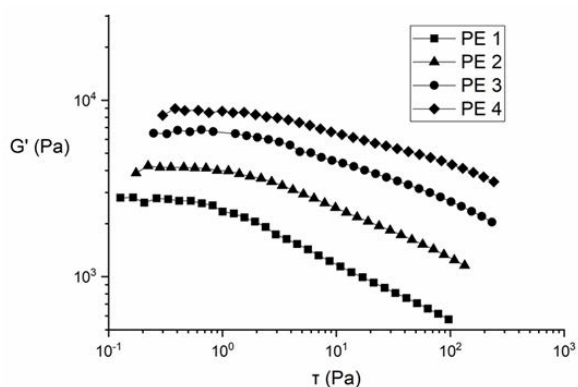


Figure 6. The dependence of G' for plastic explosives

3.3. Frequency dependence of dynamic rheological parameters of binders and explosives

Figure 7 shows the dependence of G' and G'' of PUPE 1 on ω on a graph with logarithmic scales.

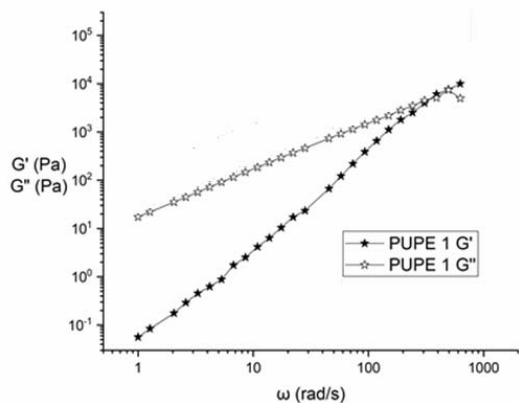


Figure 7. Graph of dependence of G' and G'' of PUPE 1 and PUPE 7 binders on ω

Due to the different molar mass of the binder, as well as differences in the chemical structure (concentration of hard segments) and interactions between macromolecular chains, the only thing that can be analyzed from the frequency dependence of the rheological quantities of the binder are the slopes of G' and G'' , that is, the distribution of molar masses.

Table 2 shows the slope values G' and G'' for HTPB and binders, obtained by linear regression of test results, as well as correlation coefficients.

Table 2. Values of slope G' and G''

	HTPB	PUPE 1	PUPE 2	PUPE 3	PUPE 4
Slope G'	1.931	1.979	1.955	1.773	1.617
Slope G''	0.998	0.962	0.954	0.926	0.896

The values of the slopes G' and G'' for HTPB, PUPE 1 and PUPE 2 are very close to two and one, respectively, which means that they have a narrow molar mass distribution. In the case of other binders, with increasing NCO:OH ratio, the slope values are further away from the values of two and one, and the molar mass distributions are also wider. A wide distribution of the molar mass of

the binder is not desirable, because it can be expected that during long-term standing there will be exudation of macromolecules of smaller molar masses from PE, which leads to a decrease in the binder content in PE and worse characteristics.

The frequency dependence of the dynamic rheological parameters of plastic explosives was determined for the compositions PE 1 and PE 4, Figure 8.

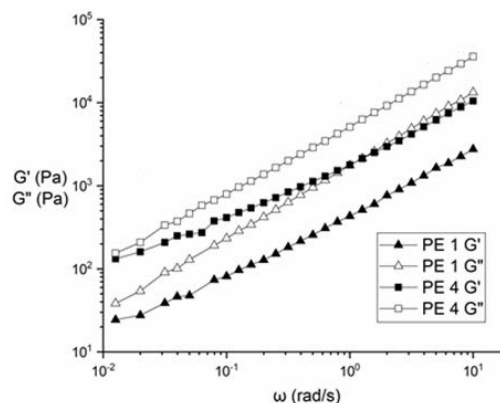
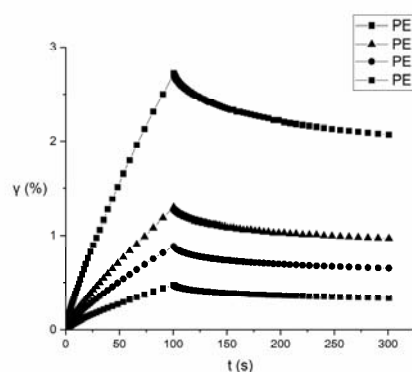


Figure 8. Graph of dependence of G' and G'' of PE 1, PE 4 on ω

As can be noticed, compositions PE 1 and PE 4 at values $\omega \rightarrow 0.01$ show $G'' > G'$. This means that these compositions do not have the appropriate consistency at rest, i.e. that their storage for a long period of time would cause undesirable phenomena such as phase separation and sedimentation. This can be concluded without testing for compositions PE 2 and PE 3.

3.4. Creep of plastic explosives outside the region of linear viscoelasticity

Figures 9 shows PE creep curves of the examined plastic explosives.



Figures 9. PE creep curves.

Due to the application of the same magnitude and duration of stress in all samples, samples with a weaker structure were deformed more and those with a stronger structure less. Considering that the total deformation in all samples γ_{max} is greater than the limit value of the linear region of viscoelasticity γ_1 , the basic laws of rheology cannot be applied to the obtained results. Nevertheless, the values of the return deformation γ_e and residual

deformation γ_v can be analyzed. Table 3 shows those values.

Table 3. Values of total, return and residual deformation of PE

PE	γ_{max} (%)	γ_e (%)	γ_v (%)	γ_e/γ_{max} (%)
PE 1	2.720	0.650	2.070	23.89
PE 2	1.290	0.319	0.971	24.73
PE 3	0.886	0.235	0.651	26.52
PE 4	0.474	0.140	0.334	29.54

From the value of the ratio γ_e/γ_{max} , it can be concluded that the recovery of PE after the end of the force increases from the composition of PE 1 to the composition of PE 7, i.e. the elastic response rises with increasing NCO:OH ratio of the binder used to make PE.

3.5. Penetration and stickiness of plastic explosives

Table 4 shows the work values performed by the rheometer tool during PE penetration (A_{p1} work during the first penetration interval, A_{p2} work during the second penetration interval), the work values performed by the rheometer tool during PE detachment (A_o) and the ratio A_{p2}/A_{p1} . Work values are calculated using the formula

$$A = \int F(h) * dh \quad (1)$$

where h is the path traversed by the tool during penetration or detachment.

The value of A_{p1} is determined by the strength of PE, the value of A_o by the stickiness of PE, and the ratio A_{p2}/A_{p1} by the ability of PE to return to its initial state after stress, Table 4.

Table 4. Values of penetration parameters for the examined explosives

PE	A_{p1} (mJ)	A_o (mJ)	A_{p2} (mJ)	A_{p2}/A_{p1} (%)
PE 1	0.239	0.218	0.117	48.95
PE 2	0.505	0.405	0.244	48.32
PE 3	0.726	0.620	0.370	50.96
PE 4	0.945	0.771	0.483	51.11

Based on the value of A_{p1} , it can be concluded that the composition of PE 4 is the strongest and most adhesive. The ability of PE to return to its initial state after stress is similar for all compositions, it is slightly better for compositions PE 3 and PE 4.

4. CONCLUSIONS

The presented results of this research are an attempt to validly characterize plastic explosives, given the possibility that they behave non-homogeneously during rheological tests. As the test results followed the trend

expected due to the different NCO:OH ratio of the binder, it can be argued that the measurements were valid.

As for the produced binders, they all behave as viscoelastic fluids, and with increasing NCO:OH ratios zero viscosity increases exponentially and the limiting value of the linear region of viscoelasticity decreases exponentially, which indicates an increase in the mean value of the molar mass by numerical representation; and that the distribution of binder molar masses is getting wider. Amplitude sweep tests of plastic explosives have shown that all plastic explosives behave like viscoelastic liquids, which means that the interaction between the binder and explosive particles is not strong, and that they do not show great consistency stability when standing.

Frequency sweeps tests of plastic explosives have shown that compositions of plastic explosives from PE 1 to PE 4 do not have a suitable consistency at rest, and would not be suitable for long-term storage.

The penetration and stickiness test showed that the PE 4 composition has the highest strength and the best stickiness, and overall it can be said that it is the best of the tested compositions.

In further work, it is necessary to improve the binder and the composition of the plastic explosive, in order for the plastic explosive to show better rheological characteristics, primarily in order to increase the stability during rest (long-term storage).

The composition, in order to achieve better rheological characteristics, could be improved by increasing the mass fraction of explosives. Of course, then some other problems related to the production technology and possible increase in sensitivity due to the lower binder content could occur. In addition, the use of finer granulation explosives, and thus a larger specific surface area, would enhance the explosive-binder interaction.

ACKNOWLEDGEMENT

The authors acknowledge the support of this research from the Serbian Ministry of Education, Science and Technological Development (grant-contract No. 451-03-68/2022-14/200325).

References

- [1] Cooper, Paul W. (1996). Chapter 4: Use forms of explosives. Explosives Engineering. Wiley-VCH. pp. 51–66. ISBN 0-471-18636-8.
- [2] Antic G. Overview of research and development of cast and plastic explosives at VTI, VTI 004-01-0488, Belgrade, 2007.
- [3] Jovanović S., Jeremic K. Characterization of polymers, Faculty of Technology and Metallurgy, Belgrade, 2007.
- [4] Minov G. Examination of the quality of plastic explosives during storage and the influence of atmospheric, stagnant and flowing water on its properties, ITI-175, Belgrade, 1997.
- [5] Minov G., Azdejković M. Investigation of the influence of river water on the rheological and

- explosive characteristics of plastic pentrite explosives, ITI-201, Belgrade, 1998.
- [6] Dimitrijević I., Simić D., Terzić S. Production and characterization of pentrite plastic explosives, VTI 04-01-1239, Belgrade, 2018.
- [7] Mezger T. The Rheology Handbook, 4th Edition, Vincentz Network, Hanover, 2014.
- [8] Minov G. General technological procedure for the production of plastic explosives, VTI 004-01-0421, Belgrade, 2005.

SYNTHESIS – THE CORE COMPONENT OF ENERGETIC MATERIALS RESEARCH

JASMIN T. LECHNER

Department of Chemistry, Ludwig Maximilian University Munich, Butenandtstr. 5–13, 81377 Munich, Germany
jalech@cup.uni-muenchen.de, <http://www.hedm.cup.uni-muenchen.de>

THOMAS M. KLAPÖTKE

Department of Chemistry, Ludwig Maximilian University Munich, Butenandtstr. 5–13, 81377 Munich, Germany
tmk@cup.uni-muenchen.de, <http://www.hedm.cup.uni-muenchen.de>

Abstract: The synthesis of new and novel energetic materials can be pursued with different interests. There is the pure academic interest, which consists, for example, of the complete characterization and analysis of already known compounds or the synthesis of exotic compounds with a nitrogen content above 90%. On the other hand, there is the industrial interest, which consists mainly in finding replacements for the currently used "state of the art" molecules that surpass them in their properties or at least do not have their disadvantages such as toxicity. In the synthesis of energetic compounds, various strategies can be used to achieve certain properties, such as increasing stability or energy content by addition of certain functional groups to the molecular backbone. When a new compound is prepared, which at best is a possible replacement, it is important to study the compound extensively. New materials are then chemically analyzed among other techniques by X-ray diffraction, NMR and vibrational spectroscopy. In addition, their physicochemical properties are determined in terms of impact sensitivity (IS), friction sensitivity (FS) and electrostatic discharge (ESD), as well as their thermal stability. In addition, the energetic properties are calculated using the EXPLO5 code and various tests such as SSRT (Small-scale Shock Reactivity Test) or Koenen tests are performed to get a sense for their energetic behavior.

Keywords: energetic materials, future energetics, nitrogen, performance, synthesis.

1. INTRODUCTION

Energetic materials are most commonly used in either high explosives or propellant formulations. Certain parameters are important in determining the effectiveness of new molecules in these formulations, including high densities (ρ), good oxygen balance (Ω) and high detonation/combustion temperatures and high specific impulses (I_{sp}) for rocket propellant formulations and lower combustion temperatures combined with a high force and pressure and a high N_2/CO ratio of the reaction gases for gun propellants. Figure 1 shows five of the most popular energetic compounds.[1-3]

Using the heat of explosion (Q), the detonation velocity (D) and the detonation pressure (P) as a measure for the performance of a high explosive, one can clearly see from Figure 2 that since the time TNT was taken into service the performance of chemical explosives has improved substantially.[1,2,4]

In spite of the many years of research, there are limited possibilities to realize a substantial increase in performance from conventional C-H-N-O explosives. Recent advances in energetics energy output have come in improved processing or inclusion of energetic binders to increase overall formulation energy, but limited success has been realized in the development of novel energetics. One reason for this is that conventional nitramine and nitroaromatic explosives such as TNT, RDX, HMX and

other similar molecules share the same three limitations (Table 1):

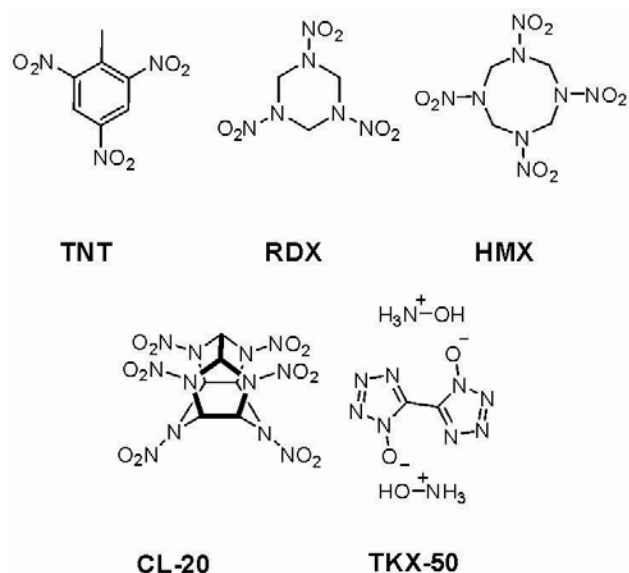


Figure 1. Chemical Structure of TNT (2,4,6-Trinitrotoluene), RDX (1,3,5-Trinitro-1,3,5-triazinane), HMX (1,3,5,7-Tetranitro-1,3,5,7-tetrazocane), CL-20 (Hexanitrohexaazaisowurtzitane) and TKX-50 (Dihydroxylammonium-5,5'-bitetrazole-1,1'-dioxide).

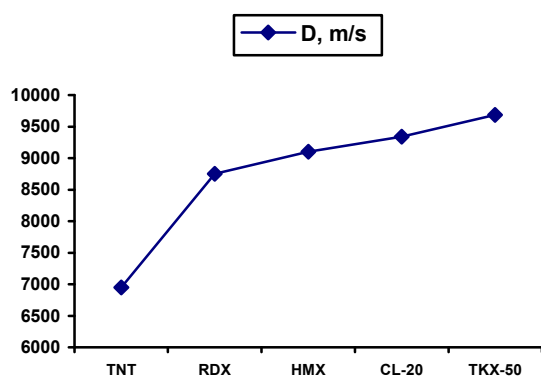


Figure 2. Detonation velocities (D) of chemical explosives.

- (i) they are not nitrogen-rich ($N \leq 50\%$);
- (ii) the oxygen-balance is not close to zero;
- (iii) formulations (mixtures of various HEs) are required to achieve a good oxygen balance.

Table 1. Nitrogen content (N) and oxygen balance regarding CO_2 (Ω) of conventional HEs.

	N [%]	Ω_{CO_2} [%]
TNT	18.5	-73.9
PETN	17.7	-10.1
RDX, HMX	37.8	-21.6

Nitrogen rich molecules are desired as energetics because of the high energy content in N-N bonds. Oxygen balance is defined as the percentage of used oxygen that remains or is needed after an oxidation reaction and can therefore be positive or negative. Materials with an oxygen balance close to zero are typically, but not always, more effective energetics since all of the oxygen is used up in reaction. An oxygen balance can be modified through formulation additions to bring the overall formulation oxygen balance close to zero.[1-3]

Interest of the synthesis of energetic materials

The synthesis of new energetic materials can be pursued with different interests. The interest of industry is mainly to find substitutes for the currently used "state of the art" molecules that surpass them in their properties or at least do not have their disadvantages, such as toxicity to humans and the environment. For the synthesis of new energetic compounds, different strategies can be used to achieve certain properties, e.g. increasing stability or energy content by adding certain functional groups to the molecular framework. As mentioned before, the strategy of a high nitrogen content in the compounds is desirable as it leads to good properties.

On the other hand, there is the pure academic interest, which consists for example in the synthesis of exotic compounds with an extremely high nitrogen content. A recent example is the synthesis of the extremely sensitive compound 2,2'-azobis-(5-azidotetrazole) (C_2N_{16}) as a

representative of binary CN-compounds with a nitrogen content of 90.3%. The chemical structure of C_2N_{16} is shown in Figure 3.[5]

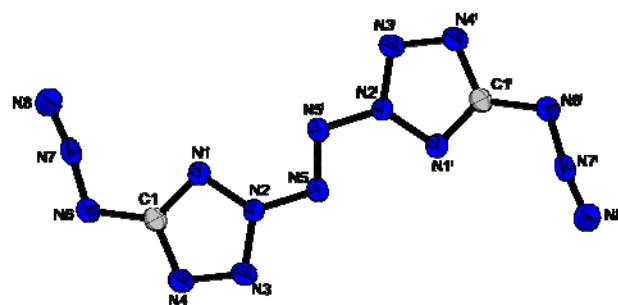


Figure 3. Crystal Structure of 2,2'-azobis-(5-azidotetrazole) (C_2N_{16}).

Alternatively, another example of the synthesis of new compounds with academic interest is the introduction of unusual elements or even isotopes into molecules. A recent example here is the synthesis of deuterated FOX-7 (1,1-diamino-2,2-dinitroethylene) and the comparison of its structural behavior and energetic properties with the hydrogenated homologues, you can see the chemical structures and some properties in Figure 4.[6]

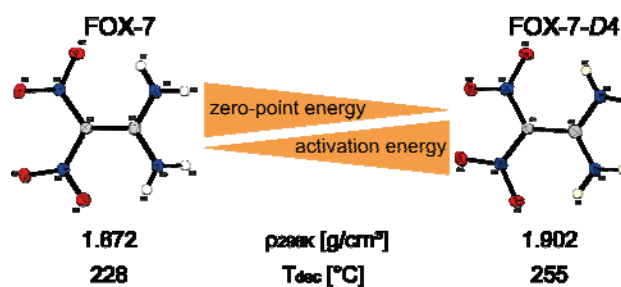


Figure 4. Chemical Structure of FOX-7 and FOX-7-D4 with some properties.

But not only the synthesis of such extraordinary compounds is of academic interest, it is also the complete characterization and analysis of already known compounds which is important. In order to better understand their structure-properties-relationship and possibly find new applications for them.

Replacements and future energetics

Researchers have already realized the energy content limit for CHNO based molecules. Research needs to expand beyond this way of thinking and increase efforts to explore different molecular structures and molecular make-up in order to realize the substantial increase in performance that will be required for future combat systems. Early research has shown that materials with a high nitrogen content offer many advantages to those with carbon backbones, including the potential for vastly increased energy content. Research into molecules with high nitrogen content (>50%) has shown potential for a substantial increase in available energy. The first generation of high-nitrogen compounds, such as hydrazinium azotetrazolate (HZT) and triamino-guanidinium azotetrazolate (TAGZT) (Figure 5), did indeed meet the criteria for being nitrogen rich and

proved to be very desirable ingredients in erosion-reduced gun propellants, however, due to the unfavorable oxygen balance such compounds are not suitable as energetic fillers in high explosive compositions.[1]

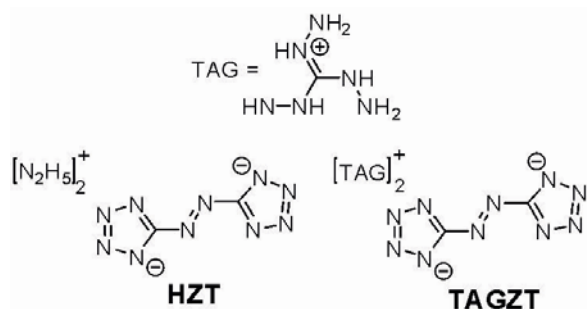


Figure 5. Chemical Structure for HZT (hydrazinium azotetrazolate) and TAGZT (triamino-guanidinium azotetrazolate).

The second generation of high-nitrogen compounds which have improved oxygen balances such as TKX-50 (Figure 1), combines desirable high nitrogen content with a good oxygen balance.[4] These compounds are therefore more suitable for use in high-explosive formulations. Moreover, materials with an oxygen balance close to zero are also suitable as powerful ingredients in solid rocket propellants. An increase of the I_{sp} of only 20 seconds would be expected to increase the payload or range by ca. 100%. Related to this, Figure 6 shows the computed performance parameters for conventional and high-N gun propellants.[1]

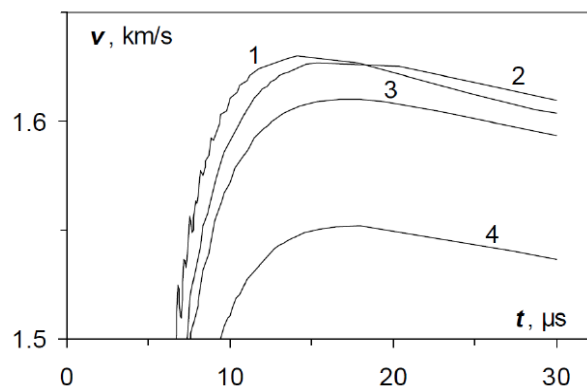


Figure 6. Acceleration of T_a cylindrical layers by TKX-50 (1), HMX (2) & RDX (4).

The computed and predicted performance values not only exceed the first generation of high-nitrogen compounds (e.g. HZT) but, in case of TKX-50, also the performance values of RDX and HMX (Fig. 2).[1]

LMU Munich is constantly researching possible better substitutes and environmentally friendly replacements. In the following you can find further areas of energetic materials research at LMU:

- High Explosives (HEDM, RDX replacements)
- Lead-free Primary Explosives
- High Oxidizers (HEDO)
- Nitrogen-rich Gun Propellants
- Visible Pyrotechnical Compositions & Smokes

- Flow chemistry for energetics
- NIR Illuminants
- Agent Defeat Weapons (ADW)
- Energetic Polymers & Reactive Struct. Materials

A promising RDX replacement is of course TKX-50, as already mentioned, but TKX-55 also has very good thermostable properties. Figure 7 shows the structures of both compounds.[4,7]

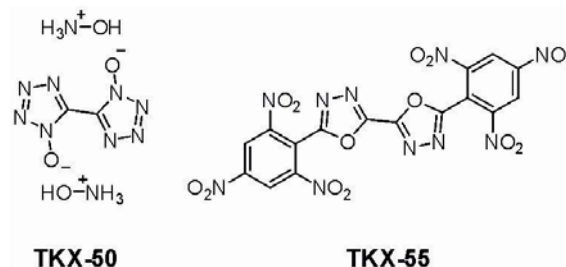


Figure 7. Chemical Structure of TKX-50 (Dihydroxylammonium–5,5′-bitetrazole-1,1′-dioxide) and TKX-55 (5,5′-bis(2,4,6-trinitro-phenyl)-2,2′-bi(1,3,4-oxadiazole)).

A possible lead-free primary is K_2 DABT, shown in Figure 8.[8]

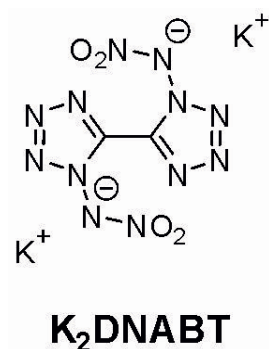


Figure 8. Chemical Structure of K_2 DNABT (Dipotassium dinitraminobistetrazolate).

A possible ammonium perchlorate replacement as a non-toxic oxidizer is TNEF (Figure 9).[9]

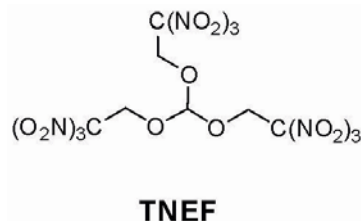


Figure 9. Chemical Structure of TNEF (2,2-trinitroethyl orthoformate).

Furthermore, promising visible pyrotechnical compositions & Smokes mixtures were developed based on TNEB and GZT, shown in Figure 10.[10,11]

Moreover our group at LMU has been working on TBX formulations with improved oxidizers and energetic fillers.[1]

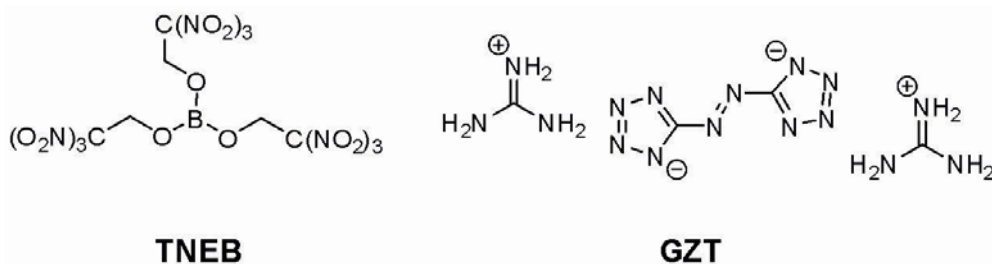


Figure 10. Chemical Structure of TNEB (tris(2,2,2-trinitroethyl)borate) and GZT (Guanidinium 5,5'-azotetrazolate).

Table 2. Comparison of the heat heats of reaction (Q_{ex}) of a conventional high-explosive HMX-based formulation and two thermobaric compositions.

	anaero ^b	aerob ^{a,b}	anaero ^b	aerob ^{a,b}	anaero ^b	aerob ^{a,b}
HMX	85	85	45	45	45	45
AP			10	10		
TNEF					10	10
Al			15	15	15	15
Mg			15	15	15	15
EXPLO5 V6.06.01						
$\Omega(\text{CO}_2) / \%$	-66.2	0	-77.4	0	-79.8	0
$\rho / \text{g cm}^{-3}$	1.63	1.63	1.68	1.68	1.67	1.67
$Q_{ex} / \text{kJ kg}^{-1}$	4878	13769	8301	18113	8539	18916
T / K	3158 ^d	6118 ^c	4583 ^d	7408 ^c	4705 ^d	7486 ^c
p_{C-J} / GPa	22.4		15.8		15.4	
D / m s^{-1}	7645		6443		6372	

a) Aerobic calculation done using isochoric combustion run, loading density 0.001 g/cm³; b) Al₂O₃ and MgO taken to be solid; c) Adiabatic combustion (with oxygen) temperature; d) Detonation temperature.

Ideal molecular high explosives (HE) such as TNT, RDX, PETN and HMX generate during detonation fast decaying blast waves of high peak pressure with very short duration and are designed to throw shrapnel, shatter structures or penetrate armors. However, they are lethal only within their immediate vicinity and show visible shortcomings for defeating hardened targets such as tunnels and caves. To overcome these shortcomings, great efforts have been focused on the development of new weapons able to generate higher impulse, higher blast and able to use its energy not to destroy corners or walls, but to travel around it efficiently and defeat hardened targets

Today, cast composite thermobaric explosives most often consist of a high explosive (RDX, HMX), polymeric binder (e.g. HTPB), fuel component (metal powder for enhancement of the blast effect, e.g. Al, Mg) and an oxidizer (AP or AN).

Table 2 shows a comparison of the detonation temperatures and combustion temperatures with afterburn of a conventional explosive formulation (HMX-HTPB) and a thermobaric composition.

References

- [1] T. M. Klapötke, *Chemistry of High-Energy Materials*, 6th edn., Walter de Gruyter, Berlin/Boston, 2022.
- [2] *Energetic Materials Encyclopedia*, T. M. Klapötke, De Gruyter, Berlin / Boston, 2018.
- [3] *Structure and Bonding*, Vol. 125/2007: High Energy Density Compounds, T. M. Klapötke (ed.), Springer, Berlin/Heidelberg, 2007.
- [4] N. Fischer, D. Fischer, T. M. Klapötke, D. G. Piercey, J. Stierstorfer, *J. Mater. Chem.*, 2012, 22, 20418.
- [5] M. Benz, T. M. Klapötke, J. Stierstorfer, M. Voggenteiler, *J. Am. Chem. Soc.*, 2022, 144, 6143 – 6147.
- [6] T. M. Klapötke, B. Krumm, J.T. Lechner, J. Stierstorfer, *Dalton Trans.*, 2022, 51, 5788 – 5791.
- [7] T. M. Klapötke, T. Witkowski, *Chem. Plus Chem.*, 2016, 81, 357 – 360.

- [8] D. Fischer, T. M. Klapötke, J. Stierstorfer, *Angew. Chem. Int. Ed.* 2014, 53, 8172 – 8175.
- [9] T. M. Klapötke, B. Krumm, R. Moll, S. F. Rest, *Z. Anorg. Allg. Chem.* 2011, 637, 2103 – 2110.
- [10] T. M. Klapötke, B. Krumm, M. Rusan, J. J. Sabatini, *Chem. Commun.* 2014, 50, 9581 – 9583.
- [11] T. Küblböck, G. Ange, G. Bikelyte, J. Pokorna, R. Skacel, T. M. Klapötke, *Angew. Chem. Int. Ed.* 2020, 59, 12326 – 12330.



DETONATOR TESTING SOFTWARE

VLADIMIR DRINCEVIC

Metropolitan University, Vlatacom Institute, Belgrade, vladimir.drincevic@vlatacom.com

PROF. DR DRAGAN DOMAZET

Metropolitan University, Belgrade, dragan.domazet@metropolitan.ac.rs

NIKOLA LATINOVIC

Vlatacom Institute, Belgrade, nikola.latinovic@vlatacom.com

Abstract: Trend in the modern military technology is usage of electric explosive devices. In domain of aerial bombs, modern fuzes use electric igniting devices, electric detonator devices and pyrotechnic components controlled by electronics. For safe and secure usage, these components must also be tested according to applicable military standards and these tests are of high interest. Due caps high sensitivity, all tests must be done with great care using very precise equipment.

This paper presents method of detonator testing using specially designed software. Special attention is given to Maximum No-Fire Current, Minimum All-Fire Current and Stray Voltage tests.

The software manages the test hardware, which is cheap and it consists of commercially available components. Those components can be easily changed in the hardware itself, thus providing a great opportunity to vary parameters and restrictions for caps testing.

Detonator testing software provides great advantages over classical testing methods primarily in terms of data acquisition speed and in terms of test price. Considering that's possible to use the software even with changes in hardware, which enables very fast and cheap modification of test parameters, this software can become an indispensable part of the equipment when testing the caps according to the requirements of military standards.

Keywords: Detonator; Testing software; Electronics; Pyrotechnic, EED.

1. INTRODUCTION

In aerial bomb fuzes, any explosive, if used correctly, applied in no matter how small quantity, can produce useful mechanical effect. For proper initiation the explosive needs some form of external stimuli [1]: mechanical force, heat energy or an electrical signal. In this paper the focus is on initiation via electrical signal.

When we talk about detonator, we are talking about electro-explosive devices or EED, as are known in the literature. EEDs must be determined before using any device that contains them and this is to be done with the help of suitable sensitivity tests as explained in [2]. Sensitivity testing must be made only by properly employed techniques in order to get accurate estimates of EED reliability and safety. Improperly applied, sensitivity testing can produce misleading data which may compromise mission success or result in rejection of reliable units [3].

For reliability determination of EEDs, their stimulus level is determined by suitable sensitivity tests. Published papers gives frequently used sensitivity test methods: Bruceton Method, Langlie Test, Neyer's Method, AD Optimal Method. Common to all tests is that they require

experiments with high testing cost and numerous statistical calculations. To reduce the manual error and the lengthy calculations which are consuming huge amount of time, user-friendly menu driven software has been developed. Software will process the entire experimental data, perform tedious and complicated statistical calculations, and give the optimal results in a few seconds.

Testing of EEDs involves the determination of various properties of the different energetic materials that are used in commercial, mining, and in military applications. It is highly desirable to measure the required conditions for several reasons, including: Safety in storage, Safety in handling, Safety in use.

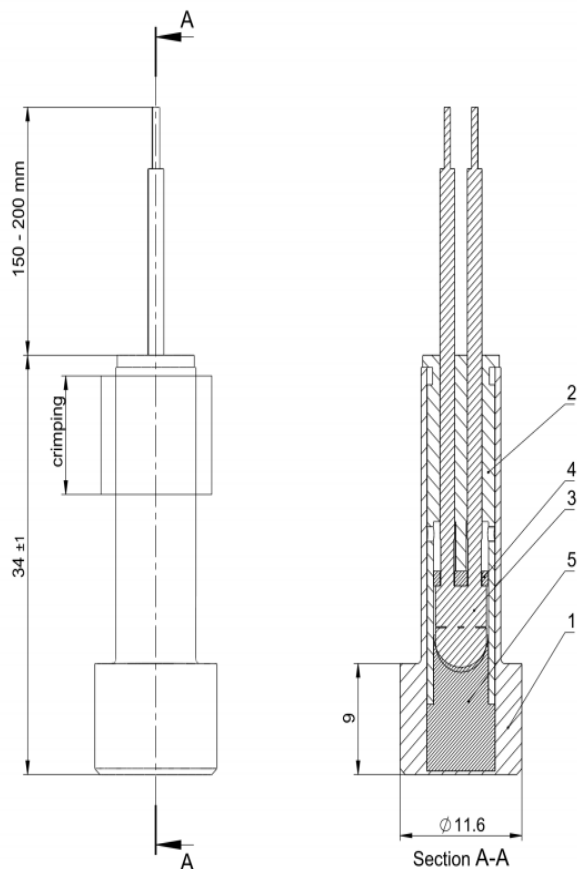
EEDs give consistent and repeatable performance and therefore are extensively used in aerial bomb fuzes.

1.1. Caps used for testing

Caps tested by the software are mostly used in aerial bomb fuzes. Models used are M-79 and ED-P2.

Many other caps can also be tasted by the software, like other detonators ED-DD, ED-P1 and M-84.

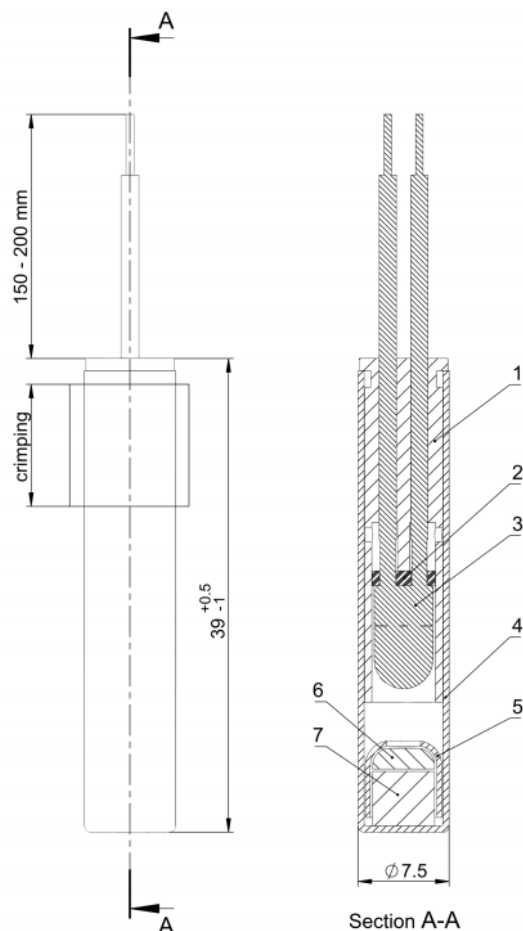
Figure 1 shows drawing of M-79 detonator with its elements and explosive filling quantity.



Pos.	Name, Description	Material	Qty
1	Aluminum housing	3.2315	1
2	ESD Protective rubber	P/N F300 esdpV	1
3	Bridge wire	NiCr thickness 30 μ m	1
4	Silicon plate 1.2mm 70 shore	Silicon VMQ70	1
5	Black Powder No.7 class	340 \pm 10mg	1

Figure 1. M-79 detonator drawing

Figure 2 shows drawing of ED-P2 detonator with its elements and explosive filling quantities.



Pos.	Name, Description	Material	Qty
1	ESD Protective rubber	3.2315	1
2	Silicon plate 1.2mm 70 shore	Silicon VMQ70	1
3	Bridge wire	NiCr thickness 30 μ m	1
4	Tube 7.5 mm diameter	AlMg2	1
5	Aluminum cup	AlMg2	1
6	Detonating charge 2 DLA	2DLA (40 \pm 5mg)	1
7	Primary charge PETN	PETN (100 \pm 5mg)	1

Figure 2. ED-P2 detonator drawing

2. METHODOLOGY

2.1. Tests of interest

Maximum No-Fire Current is the term for the maximum current that may be applied for a specified time period without firing the initiator or pyrotechnic device.

Minimum All-Fire Current is the minimum current that will always fire the initiator or pyrotechnic device.

Stray Voltage test determines whether the initiator or pyrotechnic device is capable of withstanding the effects of a stray voltage environment without firing.

2.2. Hardware

Hardware is implemented via 8-bit Arduino microcontroller [5], power supply LT3092 [6] and transistor switching logic for charging and discharging of 440µF capacitor (see block diagram on Figure 3).

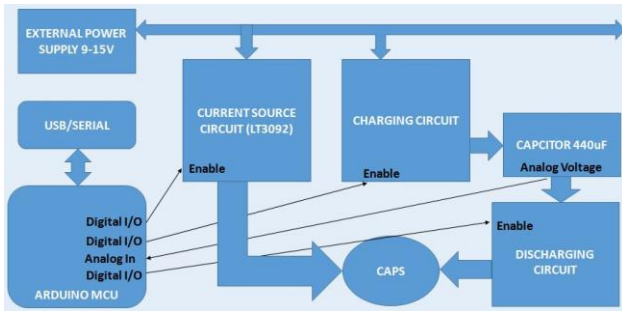


Figure 3. Block diagram

All these blocks are controlled from a microcontroller through digital input/output ports that receives commands via a graphical user interface from a PC. Also, on Analog Digital converter of microcontroller is connected circuit for measuring the voltage on the capacitor.

Following tests are enabled: Stray Voltage, Minimum All Fire Current and Maximum No Fire Current.

The Arduino microcontroller unit MCU is powered from a PC via a USB connection. The power supply for the current source, charging and discharging of capacitor is supplied externally and it should be in range of 9-15V DC. Arduino MCU is connected to a PC via a USB cable.

2.3. Software

The software is written in the LabView [7] programming environment using the Arduino MCU library. User interface with clarification of the commands can be seen on Figure 4.

For Stray Voltage test we set the duration of one and zero (x times 50 ms) and the duration of the test itself (in seconds) – by standard [4] it is 1000 s, namely 2000 impulse, where one lasts 300 ms and zero 200 ms, so we write in the boxes with following order 1000, 6, 4. The one corresponds to a direct current value of 100 mA.

For Maximum No-Fire Current the duration of the test is set – by standard [4] it is 5 min (300s). Current of 100 mA is released continuously in the detonator, after the end of the test, the indicator that the test is finished is activated and the power source is automatically turned off.

After entering the appropriate values for the tests, we activate and deactivate the specific test using the commands.

For Minimum All-Fire Current test, it is necessary to first define the voltage value of the capacitor based on the calculated minimum energy necessary to trigger the cap.

$$\frac{1}{2}CU^2 \tag{1}$$

In Equation (1) C stands for capacitance in Farads and U stands for potential difference or Voltage in Volts.

After determination of minimum activation energy, activate the capacitor charging circuit, and after indication that the capacitor is charged to the desired value, deactivate the capacitor charging circuit and activate the capacitor discharge circuit.

Moreover, within Graphical User Interface GUI, the user is enabled to follow the movement of the voltage value on the capacitor at any time through the graph.

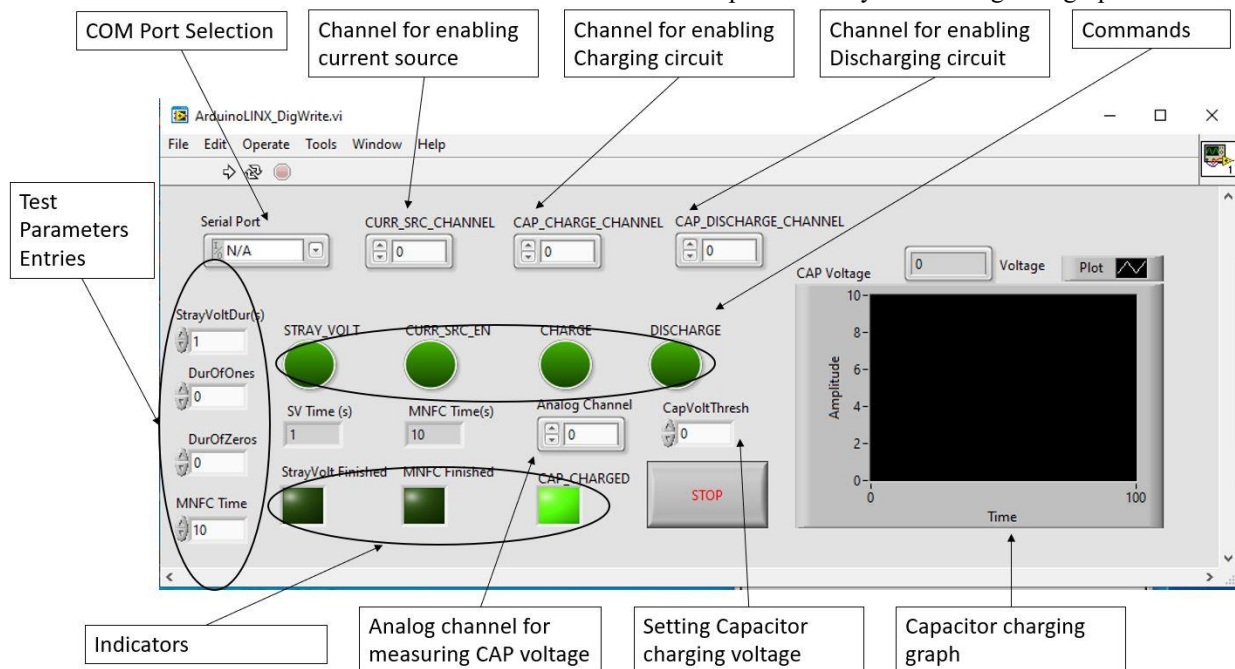


Figure 4. User interface with commands clarification

3. SOFTWARE POSSIBILITIES

Considering that test hardware consists of cheap and commercially available components, test setup can easily be adjusted to fulfill requirements of other sensitivity tests.

For calculation of Minimum All-Fire Current with Bruceton Method [9], test hardware does not need any change, the existing system can be used. This is due the fact that in the system we have the ability to define the charging voltage of the capacitor ourselves, so in software we just need to make it start from a given value and automatically raise/lower for a certain threshold that we set. To be very precise, by writing an additional software block of code and adding it to the existing one, Bruceton Method to determine Minimum All-Fire Current can be made.

There is a possibility to substitute existing microcontroller for a microcontroller with higher processing power, with support to perform even more complex mathematical operations.

Circuit diagram can be modified with addition of 1A current source. This enables execution of Bruceton Method not only by the capacitor discharge method but also by constant current test method.

4. DISCUSSION

4.1. Price

Classical testing methods, as the one shown in [8] whose no-fire current measurement schematic diagram is shown on Figure 5, requires expensive test hardware like special test chamber that can which can withstand detonator explosion.

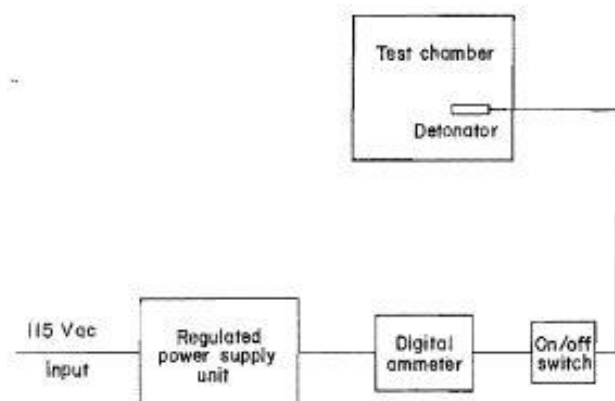


Figure 5. Schematic diagram of no fire current measurement

Presented detonator testing software manages test hardware which consists of cheap and commercially available components.

4.2. Time

Frequently used testing methods like Bruceton Method, Langlie Test or Neyer’s Method require experiments with

numerous lengthy statistical calculations which can lead to manual error and certainly are consuming huge amount of time.

Presented detonator testing software will process the entire data, performs all necessary calculations, and give the optimal results in a few seconds.

4.3. Component interchangeability

Experimental setup with expensive and rigid test hardware, positioned in specially designed laboratories obviously cannot be easily moved to different location, and as such is set for specific testing without much space for variation of the test and much less for expansion of the test.

Test hardware which is managed by the detonator testing software can easily be changed, thus providing a great opportunity to vary test parameters and restrictions and even expand the scope of testing with just a minor changes/addition in software. Complete test setup can easily be moved to desired location.

5. CONCLUSION

This paper presents user-friendly detonator testing software. Tested caps are mainly used in aerial bomb fuze. The software was created for Vlatacom Institute as a part of test equipment on the project 126.

Presented software clearly provides great advantages over classical testing methods primarily in terms of data acquisition speed and in terms of test price.

It is important to note that component interchangeability and easy portability of the test setup provides possibility to vary test parameters and even expand the scope of caps testing.

With all above-mentioned advantages over classical testing methods, this software can become an indispensable part of the equipment when testing the caps according to the rigorous requirements such as those from military standards.

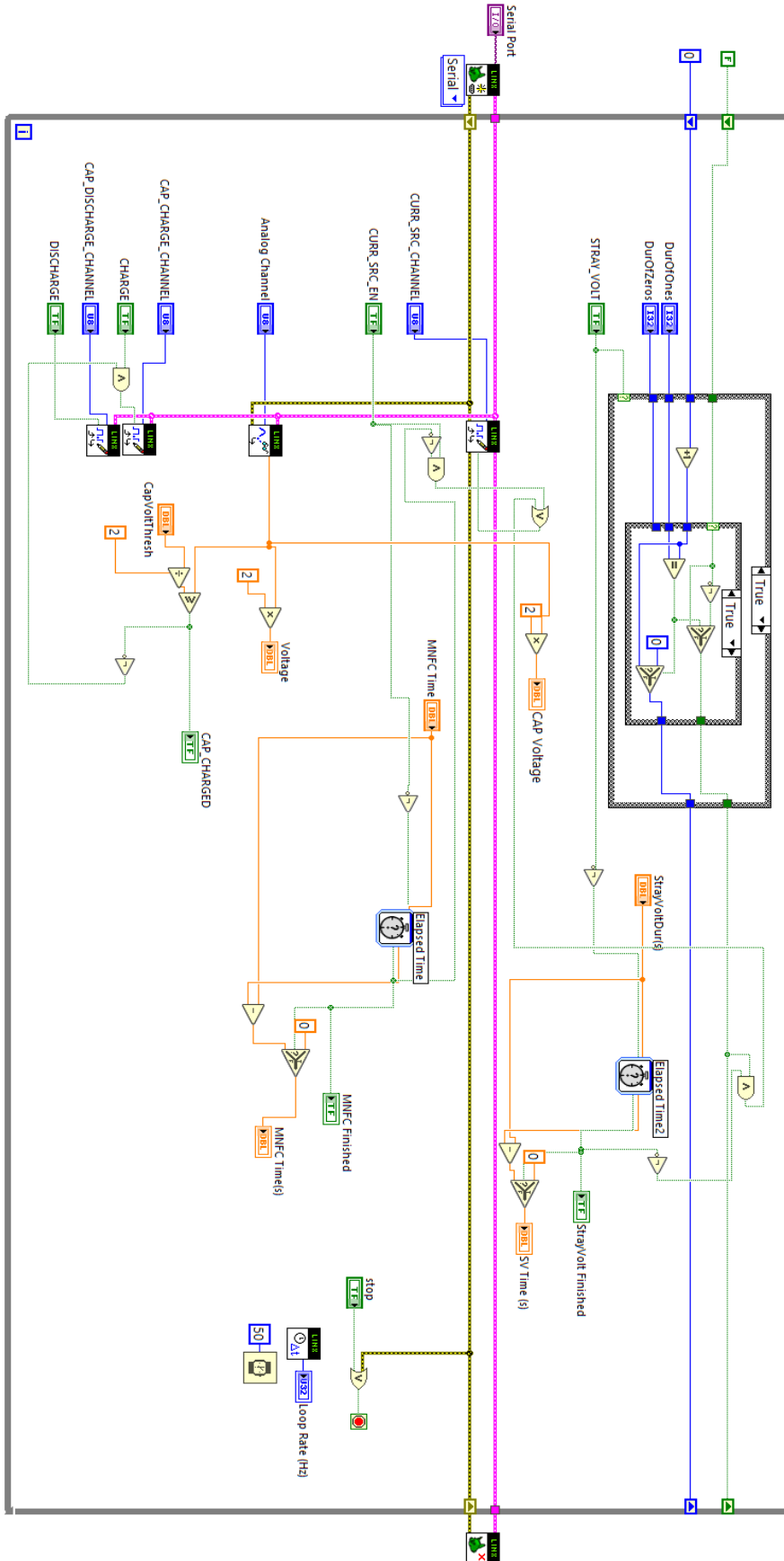
References

- [1] E.F. COOPER: *Electro-explosive devices*, IEEE Potentials (Volume: 19, Issue: 4, Oct/Nov 2000).
- [2] GURMEET SINGH, PRATIK KUMAR, RAGHUVENDRA SINGH CHAUHAN: *Sensitivity Analysis of Electro-Explosive Devices*, International Journal of Engineering Research & Technology (IJERT), Vol. 3 Issue 3, March – 2014.
- [3] HERBERT D. PECKHAM: *Problems in Sensitivity Testing of "One Shot" Electro-Explosive Devices*, IEEE Transactions on Aerospace (Volume: AS-3, Issue: 2, June 1965).
- [4] MIL-DTL-23659F, *DETAIL SPECIFICATION INITIATORS, ELECTRIC, GENERAL DESIGN SPECIFICATION FOR*, 10 June 2010.
- [5] ARDUINO. 2021. ARDUINO UNO R3.
- [6] ANALOG DEVICES. 2021. LT3092.

-
- [7] NATIONAL INSTRUMENTS. 2019. LabVIEW 2019 SP1.
- [8] T. S. BAJPAYEE, R. J. MAINIERO, J. E. HAY: *Electrostatic Sensitivity, Strength, and No-Fire Current of Short-Delay Detonators*, Report of investigations, 1985.
- [9] J. P. YRIBARREN, G. BENEDETTI: *Testing Electro Explosive Devices by the Bruceton Method with an APL Program for the Analysis of the Results*, European Space Research and technology Centre, 1976.

APPENDIX A

Source Code





INVESTIGATION ON THE DISTRIBUTION OF COMPONENTS IN RECYCLE DOUBLE BASED PROPELLANTS

ISKRA PIROEVA

Institute of Physical Chemistry, Bulgarian Academy of Sciences, Acad. G. Bonchev Str., bl.11, 1113 Sofia, Bulgaria,
ipiroeva@ipc.bas.bg

STELA ATANASOVA-VLADIMIROVA

Institute of Physical Chemistry, Bulgarian Academy of Sciences, Acad. G. Bonchev Str., bl.11, 1113 Sofia, Bulgaria,
statanasova@ipc.bas.bg

FEYZIM HODZHAOGLU

University of Structural Engineering & Architecture, Sofia, Bulgaria, feyzim@ipc.bas.bg

RADI GANEV

University of Structural Engineering & Architecture, Sofia, Bulgaria, radiganev@abv.bg

Abstract: The investigation proposes research on waste recycle double based propellants obtained from utilization, naturally aged in military storage facilities, because the overall effect of these reactions and processes are changes of physical, chemical, thermal, ballistic and mechanical properties with storage time, i.e. the reduction of the propellants performances and safe service life. Double based propellants have a single-channel cylindrical shape. With scanning electron microscopy and EDS microanalysis have been received photos and data on the distribution of the components of the double based propellants.

Keywords: double based propellants, utilization, SEM, EDS microanalysis.

1. INTRODUCTION

For a long time the double base propellants were made by directly mixing dry nitrocellulose (NC) with nitroglycerin (NG). It is extremely dangerous. The propellants mass is unevenly distributed. The swelling processes on the surface of sections of nitrocellulose fibers are important. This makes it difficult for nitroglycerin to penetrate into the depth of nitrocellulose fibers and its uniform distribution throughout the volume. [1,2]

The aim of this study is to investigate the distribution of components in double based propellants obtained from recycling. Samples of the double-base propellant were dissolved in acetone and pressed twice to obtain a cylindrical shape. They are then stabilized with dibutylphthalate (C₄H₂₂O₄), which remains in the same amount after processing (about 1%).

Propellant, known as a kind of energetic materials for launching, usually contains fuel and oxidizer components. It has widespread application in weapon equipment, space navigation, and industrial and agricultural production, so researches on propellant have received great attention for a long time. Double bases propellant usually consists of nitrocellulose (NC) and nitroglycerin (NG), to which a plasticizer is added.

2. RESULTS AND DISCUSSION

The double based propellants, produced in 1985, who are stored in unheated storage facilities in army were tested. After utilization, the propellants were dissolved by a standard method. With the help of rollers, a propellants cloth with a thickness of 5 mm is obtained to remove moisture. The next operation is pressing to obtain single-channel propellants.

Composition of the studied double based propellants (DB) by recipe.

Composition of coloxylin 57,6-59,6%

Nitroglycerin content 39.4-40.6%

The remaining additives up to 100% are stabilizing and technological additives.

We used scanning electron microscopy (SEM) JSM 6390 (Japan) in conjunction with energy dispersive X-ray spectroscopy (EDS, Oxford INCA Energy 350) in regimes of secondary electron image (SEI) and Backscattered Electron contrast (BEC). The accelerating voltage was 20 kV.

The distribution of the elements in wt% was done with the help of EDS detector. Energy-dispersive X-ray spectroscopy is an analytical technique that enables the elemental analysis of materials. A sample excited by an energy source (such as the electron beam of an electron

microscope) dissipates some of the absorbed energy by ejecting a core-shell electron. A higher energy outer-shell electron then proceeds to fill its place, releasing the difference in energy as an X-ray that has a characteristic spectrum based on its atom of origin. This allows for the compositional analysis of a given sample volume that has been excited by the energy source. The position of the peaks in the spectrum identifies the element, whereas the intensity of the signal corresponds to the concentration of the element. We used carbon tape to fix samples and after that we covered with gold, because the samples weren't conductive.

The SEM magnification is x 3000, x 10000 and x 15000, and shown in Fig. 1.

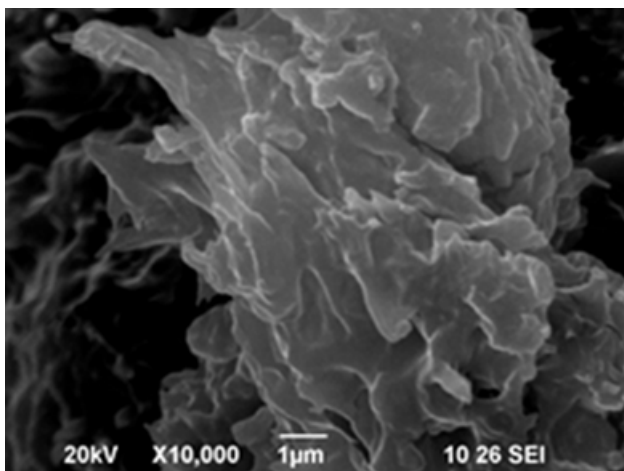
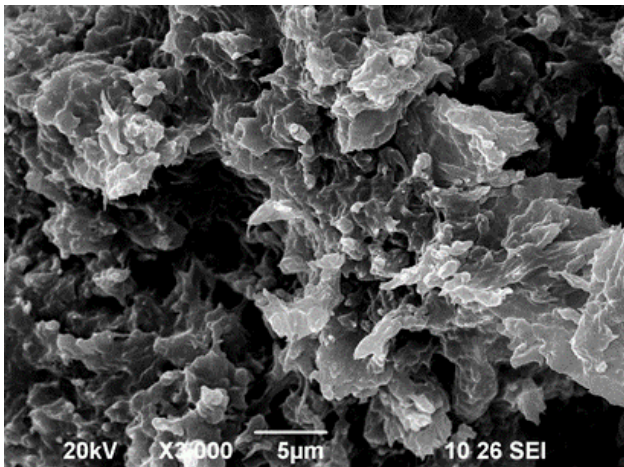


Figure 1. SEM photo of waste double based propellants after secondary processing.

In the Fig.1. are shown smooth and rounded areas, forming aggregates and can be seen the action of destruction in one hand and the action of hydrolysis on the other. It may be assumed that a process of denitration of the nitrocellulose from the propellants takes place, by a process of dissociation. Therefore, structures of hydrolytic origin are obtained [3,4].

The crystalline areas are in the form of lamellae, representing dendrites are visible. The formations are 1.61 by 1.04 μm and illustrate the crystal structure of nitrocellulose from propellants. This is probably due to the higher degree of inhomogeneous nitration and the

molecular-structural heterogeneity of nitrocellulose with nitroglycerin. In addition, it is possible to influence the degree of crystallinity of the cellulose from which the nitrocellulose was obtained, because it is also a non-constant value, Fig.2. [5]

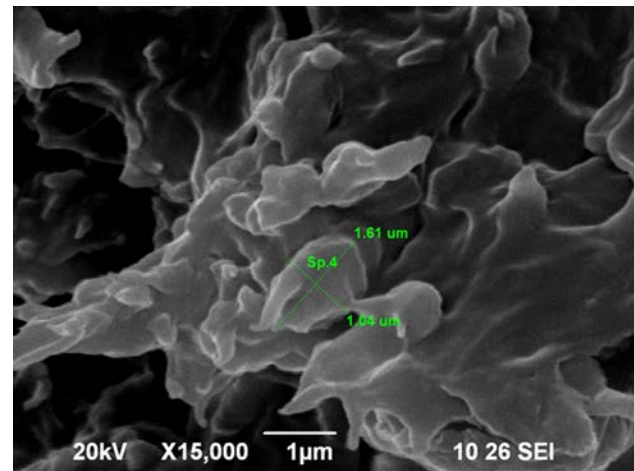


Figure 2. The dimensions of crystal

The double based propellants were done in four points and the results are shown in Table 1 and point 4 is given in Fig. 3.

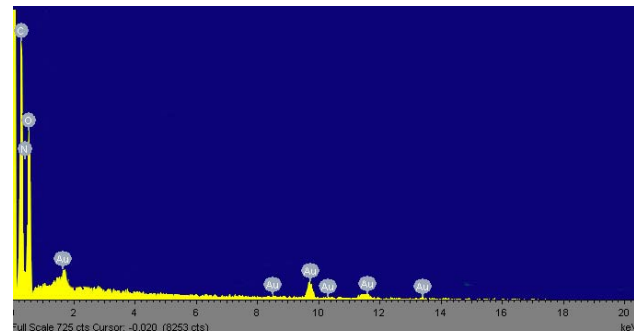


Figure 3. EDS microanalysis of the content of the major elements, in point four.

Table 1. Obtained results for C, N, O content at four points of the double based propellants

wt %	C	N	O	Total
Sp 1	36.72	14.33	48.95	100
Sp 2	26.31	10.35	65.35	100
Sp 3	50.71	0	49.29	100
Sp 4	41.61	19.85	38.54	100

In Table 1 is showing an uneven distribution of the C, N, O content. Even in point three, the nitrogen is absent. This is probably the result of the ongoing destruction processes in the double based propellants during long-term storage. As expected, the molecular weight of nitrocellulose decreases with increasing years of storage. These processes lead to an increase in the OH content, both from the hydrolyzed nitro groups and as end groups when the ether bond between the glycosidic rings is broken. [6,7]

3. CONCLUSIONS

Various processes take place in a double based rocket, propellants grain over time, even under ambient storage conditions. The overall effect of these reactions and processes are changes of physical, chemical, thermal, ballistic and mechanical properties of rocket propellants with storage time, i.e. the reduction of the propellants performances and safe service life. A greater homogenization of the propellant mass is required for the disposal of waste double based propellants than for the production of a new propellant. For the production process is necessary greater control and monitoring.

References

- [1] СМОРНОВ Л.А., КАЛАБУХОВ Г.В. *Создание смесевых твердых топлив: Учеб. пособие* МГАХМ.М., 1997, 112.
- [2] МАРЧЕНКО А. В., ЛЕОНТЬЕВА Л.М., ГАВРИЛОВА Л.А. *Ракетные твердые топлива смесевые, Краткий энциклопедический словарь. Энергетические конденсированные системы*, Под ред. Б.П. Жукова. М.: Янус-К, 1999, 483-486.
- [3] TAN D, WANG Y, GUO B, CHEN F, WEI X. *Application of Supercritical CO₂ Foaming Technology for Waste Double-Base Propellants*, ACS Omega, 2021, 45.
- [4] JUTIER J.J., HARRISSON Y., PEMONT S., *J. Appl. Polim. Sci.*, 1987, 33, 4, 1359-1375.
- [5] ЛУРЬЕ Б.А., НАМЕСТНИКОВ В.В., МАХОТКИН А.Ф. И ДР. *Высокомолекулярные соединения, серия А*, 1991, 33, 1683-1690.
- [6] ERGANG YAO, NINGNING ZHAO, ZHAO QIN, HAIXIA MA, HAIJIAN LI, SIYU XU, TING AN, JIANHUA YI, FENGQI ZHAO. *Thermal Decomposition Behavior and Thermal Safety of Nitrocellulose with Different Shape CuO and Al/CuO Nanothermites*. *Nanomaterials*, 2020, 10, 725.
- [7] WU DAI JIAN. *Rheological behavior of concentrated nitrocellulose solutions*, 2nd International Annual Conference. Germany, 1990, 50.

Acknowledgments: Research equipment of united research infrastructure INFRAMAT, supported by Bulgarian Ministry of Education and Science was used.



10th INTERNATIONAL SCIENTIFIC CONFERENCE
ON DEFENSIVE TECHNOLOGIES
OTEH 2022

Belgrade, Serbia, 13 – 14 October 2022



SECTION V

**INTEGRATED SENSOR SYSTEMS AND
ROBOTIC SYSTEMS - ISSRS**

CHAIRMAN

**prof. Stevica Graovac, PhD
Ilija Popadić, PhD
Nikola Zogović, PhD**



SLIDING MODE CONTROLLER DESIGN FOR DC MOTOR DRIVEN ELECTROMECHANICAL FIN ACTUATOR

ZLATKO PETRONIJEVIĆ

Military Technical Institute, Belgrade, zlatko970@gmail.com

PAVLE ADAMOVIĆ

Military Technical Institute, Belgrade, adamovic.pavle@gmail.com

NEBOJŠA JOVIČIĆ

Military Technical Institute, Belgrade, nesapz@yahoo.com

ALEKSANDAR STEFANOVIĆ

Military Technical Institute, Belgrade, stefanovicva@outlook.com

MILOŠ PAVIĆ

Military Technical Institute, Belgrade, mecelos.pavic@gmail.com

Abstract: *In this paper modelling and control of an electromechanical actuator (EMA) system for aerofin control (AFC) with brushed DC motor driven by motor driver using pulse width modulated (PWM) control signal are investigated. Model of system has been developed and experimentally verified in actuator test bench. Model has been used as the starting point for Sliding Mode position controller synthesis.*

Keywords: *Electromechanical actuator, Aerofin, DC motor, Sliding Mode*

1. INTRODUCTION

The use of electromechanical actuation has become increasingly popular, for a while now, in the aerospace industry as more importance is placed on maintainability. Main usage of electromechanical actuators (EMAs) is for actuation of flight critical control surfaces and thrust vector control as sad in [2].

The most commonly used actuators for actuation of aerodynamic surfaces are direct current (DC) motors. For that reason, research in this paper is based on application of electromechanical actuator system driven by permanent magnet brush DC motor for aerofin position control. Aerofin position control is achieved by creating position control feedback loop using contactless magnetic position encoder. PID controllers, fuzzy controllers, different non-linear controllers, etc. are used very often for either position or speed control of DC motors. Conventional PID controller tuning relies on some tuning method such as Ziegler-Nichols or simply on hit and trial. Reasonable response is provided as long as there are no significant disturbances or parameter variations. Fuzzy controllers offer better transient response than conventional PID controller, and should be preferred. Non-linear techniques such as sliding mode control produce good quality results and offer simple to implement control laws for uncertain or complicated model dynamics.

The proposed design will be based on sliding mode controller for position control. Sliding mode control has been treated as a powerful technique to cope with

complex systems with unmodelled dynamics due to its simplicity and strong robustness with respect to system parameter variations and external disturbances. The idea of sliding mode control is to employ different feedback control laws acting on opposite sides of a predetermined surface (often called sliding surface) in the system time space. Each of those control laws provides motion of the system states towards the sliding surface, and once system states reach the surface for the first time, they stay on it thereafter. The resulting motion of the system is confined to the surface, which can be interpreted as „sliding“ of the system states along the surface.

2. SYSTEM DESCRIPTION

2.1. Electromechanical aerofin system

Aerofin control (AFC) system, which is considered here, is control system of the missile using two pairs of fins, for pitch and yaw control of missile. Fin configuration is given in Figure 1. Deflecting each pair of fins result in formation of moment about the center of mass of missile, which generates rotation of missile body. The resulting orientation angle generates aerodynamic force, which accelerates missile in desired direction.

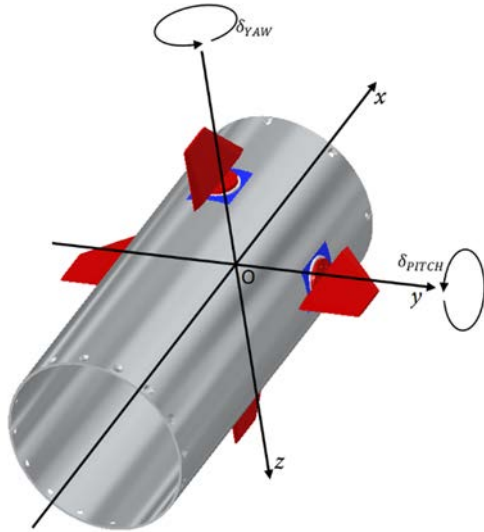


Figure 1. AFC system

2.2. Hardware and equipment

The actuator assembly, presented in Figure 2, consists of the Maxon RE 30 brushed DC motor with Maxon planetary gearhead GP 32 with reduction ratio of 1:1, which drives the screw shaft with ball nut. Output shaft with fin is connected to the ball nut through lever mechanism.

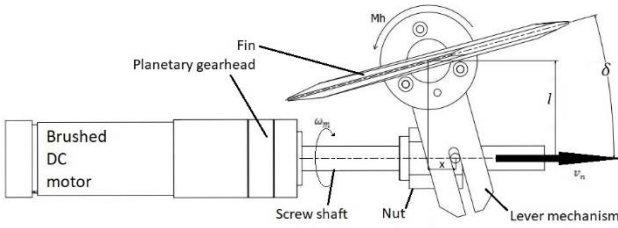


Figure 2. Actuator assembly

On the output shaft, an absolute encoder is mounted and fixed to the actuator systems body. Absolute encoder is AS5048A angle position encoder with resolutions of 14 bits. Sensor reading are forwarded to microcontroller using SPI communication protocol.

The microcontroller is ESP32 with Tensilica Xtensa LX6 microprocessor. Control loop is performed on 1 kHz sampling rate, while the serial communication with acquisition program on 500 Hz. Control signal is pulse width modulated and two control signals are forwarded to the motor driver.

The motor driver is IBT-2 H-bridge high power motor driver. In order to be controlled, it needs two pulse width modulated signals, for each rotation direction of motor. The principle of operation of the H-bridge is presented on Figure 3.

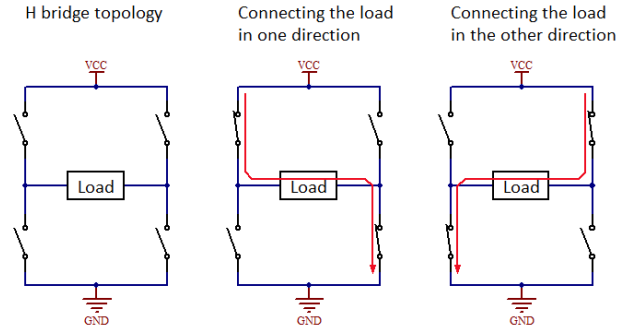


Figure 3. H-bridge operation principle

In order to simulate aerodynamic torque aerofin control system is mounted on the testing bench and equivalent torque load is applied using two stretched out springs mounted on bar which is placed instead of fin, as shown on the Figure 5.

3. SYSTEM MODELING

Mathematical model of brushed DC motor presented in this paper represents electromechanical part of the actuator assembly. Hence, torque of the motor shaft M_m is proportional to the magnetic flux, which is proportional to the armature current I_m

$$M_m = K_M I_a \quad (1)$$

where K_m is motor torque constant.

Due to rotation of motor shaft, back electromotor force E_m is induced in the motor coils. Back electromotor force is proportional to the rotor angular velocity ω_m

$$E_m = K_e \omega_m \quad (2)$$

where K_e is the motor electrical constant. Torque constant K_m and motor electrical constant K_e are equal for the ideal motor, but in case of real motor their values are similar.

Electrical equation of the rotor circuit is:

$$U_m = R_m I_m + L_m \frac{dI_m}{dt} + E_m \quad (3)$$

where R_m is electrical resistance and L_m is electrical inductance of the motor coils.

Combining equations (1), (2) and (3) yields:

$$\left(T_e \frac{dM_m}{dt} + M_m \right) \frac{R_m}{K_M} = U_m - K_e \omega_m \quad (4)$$

where T_e is electrical time constant of the motor:

$$T_e = \frac{L_m}{R_m} \quad (5)$$

It represents the time period necessary for the current to reach 63% of stall current value.

Angular velocity of the rotor depends on motor torque and load torque. The following equation describes dynamics of the motor:

$$J \frac{d\omega_m}{dt} = M_m + M_L \quad (6)$$

where J is equivalent moment of inertia $J = J_l + J_m$. Let θ_m be rotation angle of the rotor, then it yields:

$$J \frac{d\theta_m}{dt} = \omega_m \quad (7)$$

The total gear ratio of the ball screw drive is described by the following equation:

$$N = \frac{2\pi l}{\cos\delta h} \quad (8)$$

where l is normal distance between the ball nut and the output shaft axes, and h is the ball screw pitch. It is obvious that the gear ratio value depends on deflection angle of the fin.

Equations (1)-(8) are used to develop nonlinear simulation model of the EMA-AFC system. Still, model of the motor driver has not been modelled. Voltage motor drive can be modelled using $\text{sign}(\cdot)$ function with the gain of maximum voltage value V_{max} , that is time sampled with control frequency which was mentioned earlier. In the Figure 4. the output signal of the motor driver is shown.

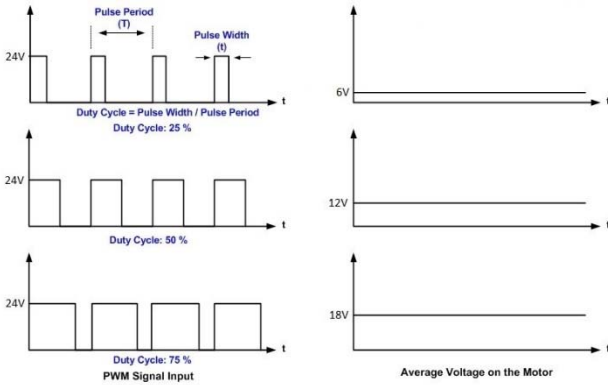


Figure 4. Motor driver output signal

The following parameters of the modelled system have been used: $J_m = 33,1 \times 10^{-7} \text{ kgm}^2$, $K_e = 0,0398 \text{ V/s}$, $K_M = 0,0398 \text{ Nm/A}$, $L_m = 0,281 \times 10^{-3} \text{ H}$, $R_m = 1,43 \Omega$, $U_{max} = 24 \text{ V}$, $\omega_{max} = 8590 \text{ min}^{-1}$.

4. CONTROLLER DESIGN

The state space of the brushed DC motor is described by following equation:

$$\begin{bmatrix} \dot{\theta}_m \\ \dot{\omega}_m \\ \dot{i}_a \end{bmatrix} = \begin{bmatrix} 0 & 1 & 0 \\ 0 & 0 & K_M/J \\ 0 & -K_e/L & -R/L \end{bmatrix} \begin{bmatrix} \theta_m \\ \omega_m \\ i_a \end{bmatrix} + \begin{bmatrix} 0 \\ 0 \\ 1/L \end{bmatrix} u \quad (9)$$

Let write $a_{23} = K_M/J$, $a_{32} = K_e/L$, $a_{33} = R/L$, and $b_3 = 1/L$, then equation (9) can be rewritten as:

$$\begin{bmatrix} \dot{\theta}_m \\ \dot{\omega}_m \\ \dot{i}_a \end{bmatrix} = \begin{bmatrix} 0 & 1 & 0 \\ 0 & 0 & a_{23} \\ 0 & -a_{32} & -a_{33} \end{bmatrix} \begin{bmatrix} \theta_m \\ \omega_m \\ i_a \end{bmatrix} + \begin{bmatrix} 0 \\ 0 \\ b_3 \end{bmatrix} u \quad (10)$$

As mentioned earlier sliding mode control is a powerful technique offering robust control of a system. Given below is a design of a sliding mode controller for brushed DC motor. The control law is derived from [3]:

$$u = -\frac{1}{L_g L_f^{\rho-1} h(x)} \left[L_f^\rho h(x) - r^{(\rho)}(t) + \sum_{i=1}^{\rho} c_i e_{i+1} \right] + v \quad (11)$$

where u represents the control law, L_f , L_g are Lie derivatives and ρ is the relative degree of the system. The reference value is given by r and the error states are given by e . Lastly, the switching function is given by v .

The state variables can be adopted as,

$$\begin{aligned} x_1 &= \theta_m \\ x_2 &= \omega_m = \frac{d\theta_m}{dt} \\ x_3 &= i_a \end{aligned} \quad (12)$$

As it is obvious relative degree ρ of the system is 3. From state space equation 10 yields:

$$f(x) = \begin{bmatrix} x_2 \\ a_{23}x_3 \\ -a_{32}x_2 - a_{33}x_3 \end{bmatrix}, \quad g(x) = \begin{bmatrix} 0 \\ 0 \\ b_3 \end{bmatrix} \quad (13)$$

For designing control law using (11) it is necessary to find Lie derivatives of $h(x)$ along the $f(x)$ and its Lie derivative along $g(x)$. These derivatives are given below:

$$\begin{aligned} L_f h(x) &= \frac{\partial h}{\partial x} f(x) = [1 \quad 0 \quad 0] \begin{bmatrix} x_2 \\ a_{23}x_3 \\ -a_{32}x_2 - a_{33}x_3 \end{bmatrix} \\ &= x_2 \end{aligned} \quad (14)$$

$$\begin{aligned} L_f^2 h(x) &= \left(\frac{\partial}{\partial x} L_f h(x) \right) f(x) \\ &= [0 \quad 1 \quad 0] \begin{bmatrix} x_2 \\ a_{23}x_3 \\ -a_{32}x_2 - a_{33}x_3 \end{bmatrix} \\ &= a_{23}x_3 \end{aligned} \quad (15)$$

$$\begin{aligned} L_f^3 h(x) &= \left(\frac{\partial}{\partial x} L_f^2 h(x) \right) f(x) \\ &= [0 \quad 0 \quad a_{23}] \begin{bmatrix} x_2 \\ a_{23}x_3 \\ -a_{32}x_2 - a_{33}x_3 \end{bmatrix} \\ &= -a_{23}(a_{32}x_2 + a_{33}x_3) \end{aligned} \quad (16)$$

$$\begin{aligned} L_g L_f^2 h(x) &= \left(\frac{\partial}{\partial x} L_f^2 h(x) \right) g(x) = [0 \quad 0 \quad a_{23}] \begin{bmatrix} 0 \\ 0 \\ b_3 \end{bmatrix} \\ &= a_{23}b_3 \end{aligned} \quad (17)$$

With $\rho = 3$ the control law defined in (11) becomes:

$$\begin{aligned} u &= -\frac{1}{L_g L_f^2 h(x)} [L_f^3 h(x) - \ddot{r}(t) + c_1 e_2 + c_2 e_3] + v \\ &= -\frac{1}{a_{23}b_3} [c_1 e_2 + c_2 e_3 - a_{23}a_{32}x_2 \\ &\quad - a_{23}a_{33}x_3 - \ddot{r}(t)] + v \end{aligned} \quad (18)$$

Variable v represents switching function here given by $v = -\beta(x)\text{sgn}(s)$ where $\beta(x)$ is found by finding the upper

bound of the uncertainties. The rest of parameters are defined earlier.

Tracking error is defined as:

$$\begin{aligned} e_1 &= r - x_1 \\ e_2 &= \dot{r} - x_2 \\ e_3 &= \ddot{r} - x_3 \end{aligned} \quad (19)$$

$$\begin{aligned} \frac{de_1}{dt} &= e_2 \\ \frac{de_2}{dt} &= a_{23}x_3 - \dot{r} \\ \frac{de_3}{dt} &= -a_{32}x_2 - a_{33}x_3 + b_3u - \ddot{r} \end{aligned} \quad (20)$$

The sliding surface is $s = c_1x_1 + c_2x_2 + x_3$, taking its derivative we have:

$$\begin{aligned} \dot{s} &= c_1\dot{e}_1 + c_2\dot{e}_2 + \dot{e}_3 \\ &= c_1e_2 + c_2a_{23}x_3 - c_2\dot{r} \\ &\quad - a_{32}x_2 - a_{33}x_3 + b_3u - \ddot{r} \end{aligned} \quad (21)$$

To find $\beta(x)$ it is necessary to find upper bound, as shown in [1] and [3]. The upper bound is:

$$\left| \frac{c_1e_2 + c_2a_{23}x_3 - a_{32}x_2 - a_{33}x_3 - c_2\dot{r} - \ddot{r}}{b_3} \right| \leq \rho(x) \quad (22)$$

$$\begin{aligned} \left| \frac{-(c_1 + a_{32})x_2 + (c_2a_{23} - a_{33})x_3 + c_1\dot{r} - c_2\ddot{r} - \ddot{r}}{b_3} \right| \\ \leq \rho(x) \end{aligned} \quad (23)$$

therefore

$$\begin{aligned} \beta(x) = \\ \left| \frac{-(c_1 + a_{32})x_2 + (c_2a_{23} - a_{33})x_3 + c_1\dot{r} - c_2\ddot{r} - \ddot{r}}{b_3} \right| + 1 \end{aligned} \quad (24)$$

From (23) the final control law becomes:

$$\begin{aligned} u = \\ -\frac{1}{a_{23}b_3} [c_1e_2 + c_2e_3 - a_{23}a_{32}x_2 - a_{23}a_{33}x_3 - \ddot{r}(t)] \\ + \left(\left| \frac{-(c_1 + a_{32})x_2 + (c_2a_{23} - a_{33})x_3 + c_1\dot{r} - c_2\ddot{r} - \ddot{r}}{b_3} \right| \right. \\ \left. + 1 \right) \text{sgn}(s) \end{aligned} \quad (25)$$

5. RESULTS

To verify design of control law system was simulated in MATLAB-Simulink environment and experimentally evaluated on testing bench with spring load that is shown in Figure 5.

Both in simulation and experimental evaluation of EMA-AFC system, as reference value, has been used step signal

with amplitude of $\pm 5^\circ$. Reference signal characteristics are given in following equation:

$$r(t) = \begin{cases} 0^\circ & \text{for } t \in [0,5[\cup]7,12[\cup]14,\infty[\\ \in [0^\circ, 5^\circ] & \text{for } t = 5 \\ 5^\circ & \text{for } t \in]5,7[\\ \in [0^\circ, -5^\circ] & \text{for } t = 12 \\ -5^\circ & \text{for } t \in]12,14[\end{cases} \quad (26)$$

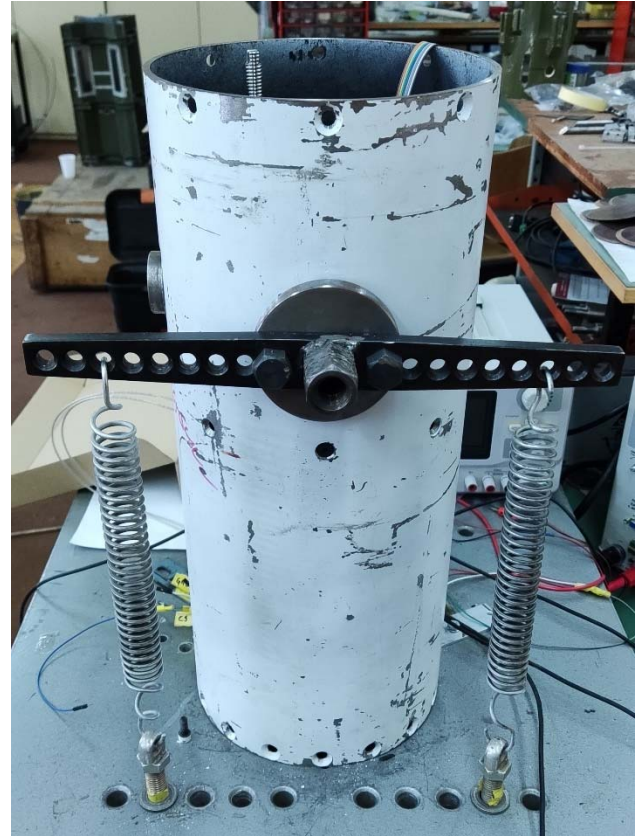


Figure 5. EMA-AFC system on the testing bench

A sliding mode controller based on the control law proposed in (11) and determined for EMA-AFC system in (22) has been implemented in simulation and microcontroller using parameters given in table 1.

Table 1. Sliding mode control law parameters

Parameter	Value
c_1	-141,597
c_2	0,4232282
β	150

Using hit and trial approach for finding best values of parameters given in Table 1. it has come to optimal output response for simulated and real system. Output signals of simulated and experimentally tested system are shown in Figure 6.

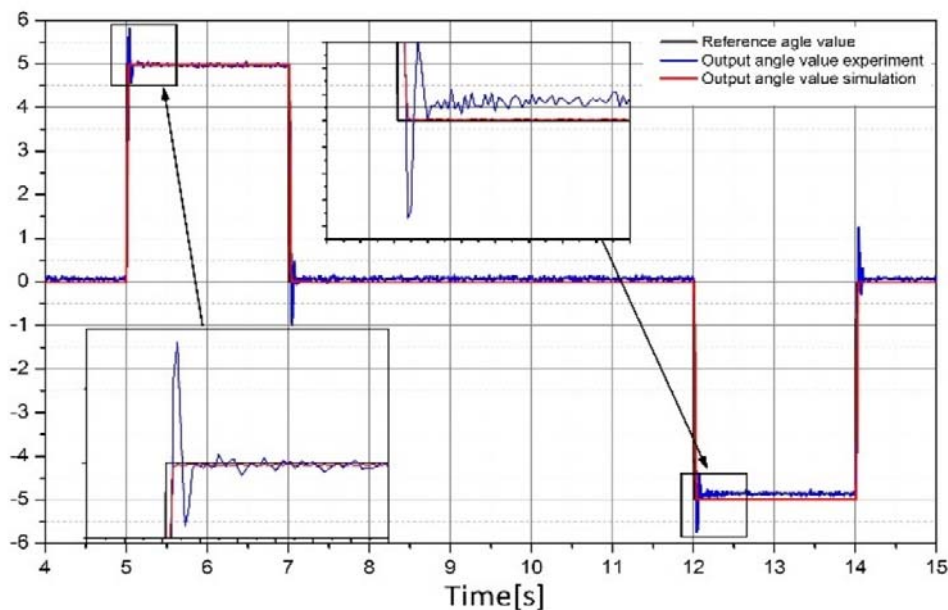


Figure 6. Reference and output signals from simulation and experiment

5. CONCLUSION

This paper presents solution for control electromechanical aerofin actuator system using sliding mode control. For this type of system robustness, disturbance rejection and low sensitivity to parameter variation is necessary which is provided using sliding mode control.

Modelling of dynamics of the system and design of the control law was given in this paper both in simulation and experimental environment. Given research could be used for obtaining robust control of EMA-AFC systems.

Reference

- [1] Khalil, H. K. (2002). *Nonlinear systems* (3rd ed.), Englewood Cliffs, New Jersey: Prentice-Hall
- [2] Milan Ristanović, Žarko Čojbašić, Dragan Lazić,

Intelligent control of DC motor driven electromechanical fin actuator, *Control Engineering Practice*, Volume 20, Issue 6, 2012, Pages 610-617, ISSN 0967-0661

- [3] J. Mehmood, M. Abid, M. S. Khan and A. Q. Khan, "Design of Sliding Mode Control for a Brushless DC Motor," *2020 IEEE 23rd International Multitopic Conference (INMIC)*, 2020, pp. 1-5
- [4] Utkin, V.I., 1993. Sliding mode control design principles and applications to electric drives. *IEEE transactions on industrial electronics*, 40(1), pp.23-36
- [5] A. Durdu and E. H. Dursun, Sliding mode control for position tracking of servo system with a variable loaded DC motor, *Elektronika ir Elektrotechnika*, vol. 25, no. 4, pp

LEAD COMPENSATOR DESIGN FOR DC MOTOR DRIVEN ELECTROMECHANICAL FIN ACTUATOR

PAVLE ADAMOVIĆ

Military Technical Institute, Belgrade, adamovic.pavle@gmail.com

ZLATKO PETRONIJEVIĆ

Military Technical Institute, Belgrade, zlatko970@gmail.com

NEBOJŠA JOVIČIĆ

Military Technical Institute, Belgrade, nesapz@yahoo.com

ALEKSANDAR STEFANOVIĆ

Military Technical Institute, Belgrade, stefanovicva@outlook.com

MILOŠ PAVIĆ

Military Technical Institute, Belgrade, mecelos.pavic@gmail.com

Abstract: This paper presents modeling, simulations and control of the ground-to-air missile fin actuation system, where brushed DC motors are used as actuators, which are driven using voltage regulation-Pulse Width Modulation (PWM). The mathematical model of the system was determined using the differential equations of behavior of the lowest order that was experimentally confirmed. This model was taken as a starting point in the synthesis of the Lead compensator, used to regulate the position of the missile's control surfaces. The trial and error method was used for the synthesis of Lead compensator, taking care to meet the required characteristics of the System, in form of bandwidth and gain. The improved transient process and behavior of the System have also been experimentally confirmed.

Keywords: Fin actuation system, DC motor, Lead compensator, control surfaces.

1. INTRODUCTION

By developing different forms of regulators, it was tried to obtain better static and dynamic properties of the system for fin control, but with the development there was generally an increased complexity of the regulator, which led to the difficulty of implementing it into the system and synthesizing it. When it comes to fin actuators in the form of DC motors with brushes, simple regulator solutions in the form of PID regulators or compensators with phase lag or lead are still showing enviable properties. Such regulators are simple to synthesize and implement and in most cases are used in today's systems.[1]

2. SYSTEM DESCRIPTION

Fig. 1. shows a block diagram of the VRVZ-200 rocket control rudder driver with positional feedback, which has the task of moving the missile rudder in accordance with the input control signal. The initial signal corresponds to the required (desired) value of the rudder deflection angle. The signal from the positional feedback loop is subtracted from the input signal and represents the system error which

is amplified and fed to the input of the phase lead compensator, which determines the required control of the DC motor. The motor torque is increased (angular velocity decreases) by means of a reducer, which is introduced into the servo system in the form of a reducer with a screw transmission and balls (spindle) and leads to fin - the rudder, under the influence of which the rudder rotates around its axis of rotation.

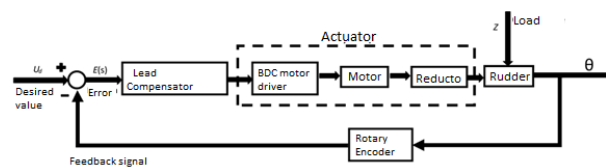


Figure 1. Block diagram of a rudder servo actuator

A direct current motor (DC motor) is often used to drive a fin actuator system.

Based on the equations that describe the behavior and dependence of certain quantities in the motor, the block diagram of the DC motor shown in Figure 2 can be drawn.

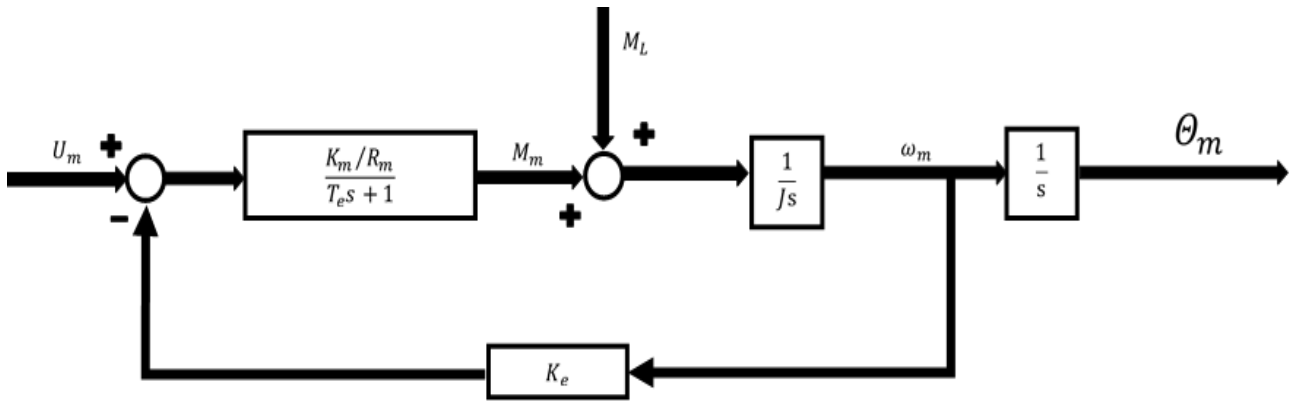


Figure 2. Block diagram of a DC motor

Where quantities are:

- U_m -stator power supply
- K_m - torque constant of the motor
- K_e - electrical constant of the motor
- R_m - motor winding resistance
- T_e -electrical time constant of the motor
- M_m -motor torque
- M_L - load torque
- θ_m - rotation angle of the rotor
- ω_m -angular velocity of the rotor
- J - moment of inertia

After the motor, there is a reducer with a ball-spindle screw transmission. The screw (spindle) transmission (bolt and nut, Figure 3.) transforms the fast rotational movement into a slower translational movement of the nut, which is transformed into the rotational movement of the rudder shaft by means of a lever mechanism. The bolt is attached to the motor shaft, and the nut to the rudder via the lever with slot and slide.

The advantage of this type of transmitter is the small overall dimensions of the system, simple construction and manufacturing. In order to reduce high friction and losses, a screw and a nut with balls were used.

The reducer with screw and nut with balls is used in actuators that require high positioning accuracy.

The efficiency coefficient of a reducer with a screw and a nut with balls can reach a value of 0.9. Frictional forces in the transmission are independent of speed. The gap can practically be completely eliminated.[1]

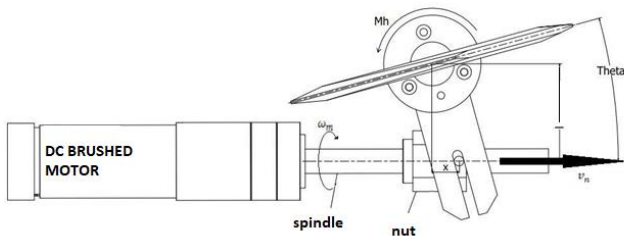


Figure 3. DC motor with screw gear

The transmission ratio of this reducer is obtained from the equation 1

$$i = \frac{2\pi l_\delta}{\cos \delta h} \quad (1)$$

3. ANALYSIS AND SYNTHESIS OF THE MISSILE RUDDER ELECTRO-SERVO DRIVE SYSTEM

Figure 4 shows a linear block diagram of a servo system without a synchronizer.

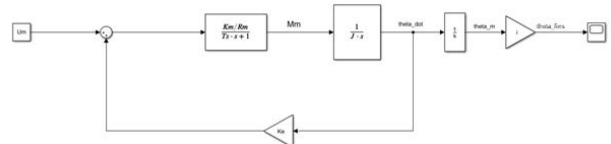


Figure 4. Block diagram of a uncompensated linear system with no load

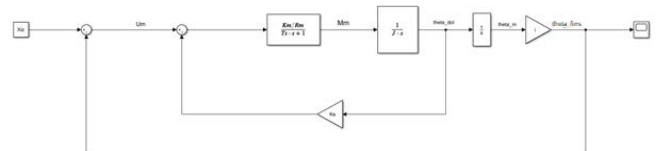


Figure 5. Block diagram of a uncompensated closed loop linear system with no load

After inserting the parameters of the reducer into equation 1., we get that the transmission ratio is the $i = 0.0074462$.

After entering the motor data taken from the catalog and the corresponding coefficients, the transfer function of the servo system of the given missile is obtained (equation (2)).

$$W_o = \frac{42790637.6665126 * 0.0074462}{s^3 + 5088.96797153025 * s^2 + 1702585.37 * s} \quad (2)$$

4. SYNTHESIS OF PHASE LEAD COMPENSATOR

The transfer function 2 was taken as a starting point in the synthesis of the phase lead compensator. The condition is given that the damping of the system is $\xi = 0.6$ and that the bandwidth is $\omega = 50.2 \frac{rad}{sec}$.

It must be taken into account that the nominal voltage of the selected motor is 36V, but the system will be powered by a 24V battery.

The phase lead compensator itself works on the principle of increasing the gain of the system for higher frequencies, thereby increasing the phase between its zeros and poles. The transfer function of the phase lead compensator is given in the form:

$$Wr = K \cdot \frac{s \cdot T1 + 1}{s \cdot T2 + 1} \tag{3}$$

where $T1 > T2$

Second form is:

$$Wr = K \cdot \frac{\frac{s}{\omega_z} + 1}{\frac{s}{\omega_p} + 1} \tag{4}$$

From which it follows that:

$$T1 = \frac{1}{\omega_z} \tag{5}$$

$$T2 = \frac{1}{\omega_p} \tag{6}$$

It is necessary to determine the coefficients T1 and T2, respectively the limiting frequencies ω_z and ω_p and the gain K so that the given criterion is satisfied. Determining the coefficients of phase lead or lag compensator is usually done by the Trial and Error method, but the number of possibilities is reduced by some additional condition during determination.

In this case, it was assumed that the ratio of coefficients T1:T2=10, which makes it easier to determine. The Matlab program was used as an helping tool.

After a certain number of attempts, the coefficients T1=150 and T2=15 were determined, but it is necessary to determine the gain K, since although we obtain a stable system according to the Bode criterion, which can be seen from Figure 6, the specified conditions are not met.

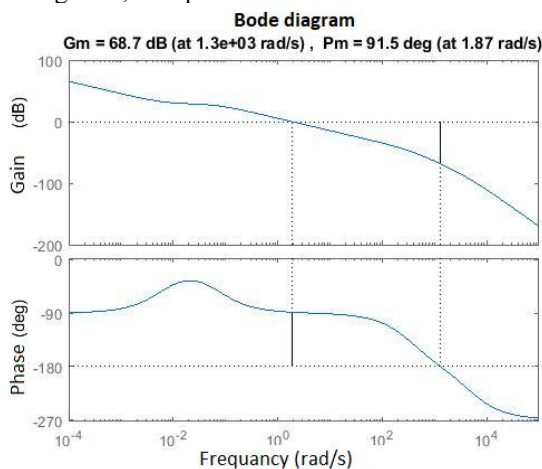


Figure 6. Bode diagram of system with phase lead compensator without gain

The gain K is determined by the RL graph in the figure 7. From the condition that the damping is $\xi = 0.6$, the amplification K=108 is determined.(Figure 8) By checking

the stability, we determine that the system with the given gain is stable, which can be seen in Figure 9.

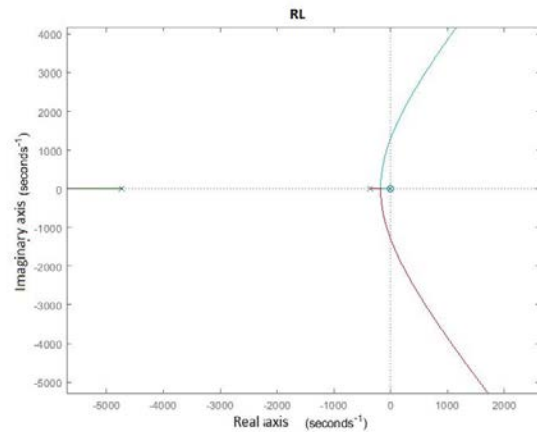


Figure 7. RL graph of a system with phase lead compensator without gain

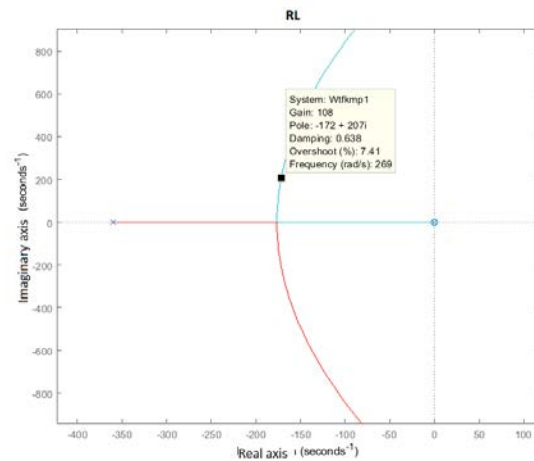


Figure 8. Adequate system gain with phase lead compensator

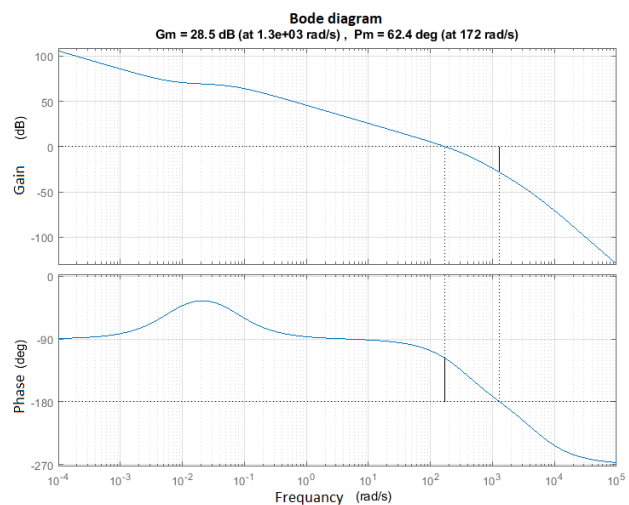


Figure 9. Bode diagram of a system with the adequate gain

On the Bode diagram of the closed circuit of the system with adequate coefficients, it can be seen that the bandwidth condition is also fulfilled. (Figure 10) For a

given frequency of 8Hz, which is about 50 rad/s , the gain of the system is 0.0344 dB, which corresponds to a limiting gain of 3dB. The bandwidth of this system is 283 rad/s , which is about 45Hz, of course this is impossible in a real case, due to the existence of the maximum possible control of 24V, friction, gaps and other elements that were included during the synthesis.

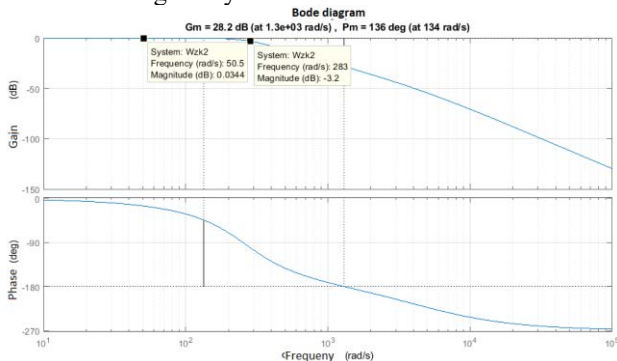


Figure 10. Bode diagram of a closed loop system with a adequate gain

5. ANALYSIS OF PHASE LEAD COMPENSATOR

After the synthesis of the compensator, it is necessary to perform an analysis of its operation, that is, to see to what extent the compensator itself improves the properties of the entire system and how the system will behave with different input signals.

Matlab's Simulink tool was used to analyze the system. The block diagram of a continuous system with a phase lead compensator is shown in Figure 11.

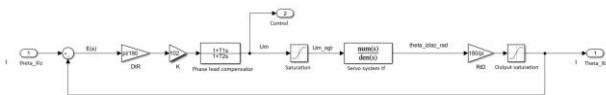


Figure 11. Block diagram of the system with phase lead compensator

In order to make the system simulation more realistic, output and control saturations were kept. The maximum angle at which the flaps can be turned is $\pm 20^\circ$, while the maximum voltage that can be supplied to the motor for maximum control is 24V DC.

The sine function, step function and quadrate function are supplied as system inputs.

Figure 12. shows the response of the system to the stepped function as a substitute for the step, since the middle position of the flaps is marked as 0° , so it is shown how the system behaves when the fins are rotated in both directions.

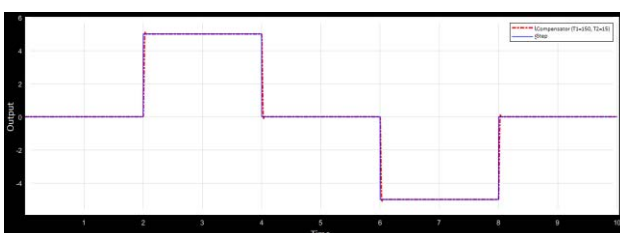


Figure 12. Continuous system output (step function)

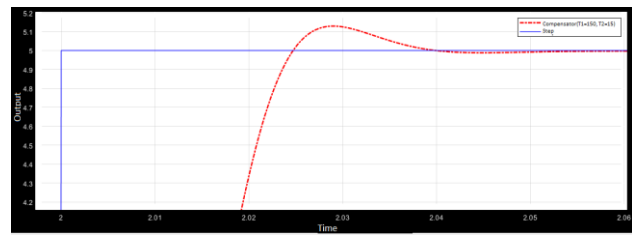


Figure 13. Output of continuous system (step function)-magnified

A better representation of the response can be seen in Figure 13, it can be said that the system follows the desired value well. The overshoot of the system is insignificant and amounts to about 3%, and the rise time is $t_u = 0.025s$, while the settling time is about $t_s = 0.05s$, the stationary error is almost completely removed.

Next, the response of the system to a periodic input is shown in the form of a sine function, which can be seen in Figure 14.

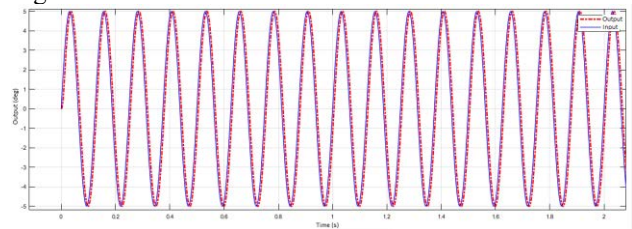


Figure 14. Continuous system output (sine function-8Hz)

In this case, the input signal frequency of 8Hz and amplitude of 5° is set, which corresponds to the initial requirements of the system characteristics. The output of the system closely follows the desired value, which corresponds to the indicators on the bode plot in Figure 10. As shown, the system gain is close to zero, while the phase lag is about 10° .

The bandwidth for this type of system model, if saturations are included, is around 15Hz. (Figure 15.)

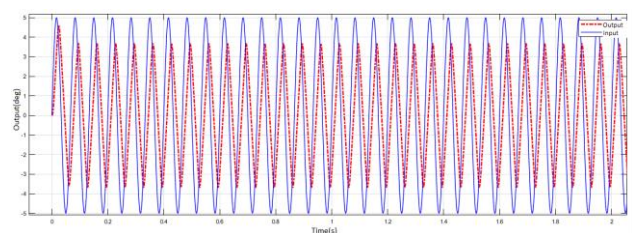


Figure 15. Continuous system output (sine function-15Hz)

The real system is not continuous, but discrete, so in order to perform the analysis of the system in full, it is necessary to first discretize the existing model of the continuous system and later to examine such a model.

Discretization was performed using the bilinear method or the Tusten method, and the sampling time is $T=1ms$ or $T=0.001s$.

The bilinear method is performed:

$$s = \frac{2(z-1)}{T(z+1)} \rightarrow W_s \quad (7)$$

Each complex s from the continuous transfer function W , is changed with Equation 7.

After the discretization, the transfer function of the phase lead compensator takes the form:

$$W_r = \frac{102 \cdot (9.999700009999666 \cdot z - 9.999633345555148)}{(z - 0.999933335555482)} \quad (8)$$

After discretization, the transfer function of the object takes the form:

$$W_o = \frac{(2.02664935e^{-5} \cdot z^2 + 3.391045e^{-5} \cdot z + 1.9056724e^{-6})}{(z^3 - 1.706487172 \cdot z^2 + 0.7126515508163 \cdot z - 0.006164378419)} \quad (9)$$

Discretization was performed using Matlab, with the command `c2d()`.

Figures 16. and 17. show a comparison of the output of a continuous and discrete system for a step input signal.

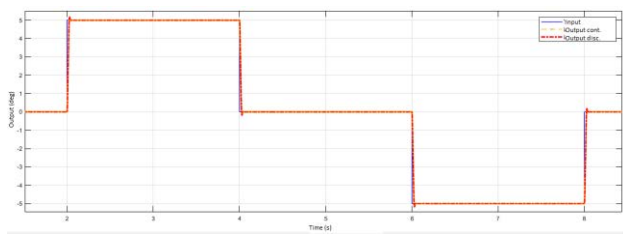


Figure 16. Comparison of response of discrete and continuous system to step input signal

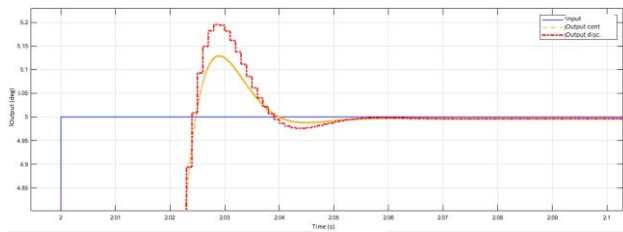


Figure 17. Comparison of response of discrete and continuous system to step input signal- magnified

It is noted that the deviations of the output of the discrete system from the continuous one are negligibly small, which means that the discretization was performed correctly, and the behavior of the real system should not have any major deviations from the behavior of the simulated system model.[3]

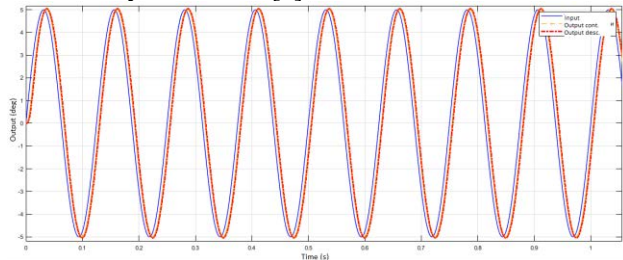


Figure 18. Comparison of the response of a discrete and continuous system to a sine input signal

With periodic inputs, it is also observed that the outputs of the discrete and continuous model of the system match,

which additionally confirms the quality of the modeled system. (Figure 18.)

With the real system, the problem is that it was not possible to achieve continuous control, instead pulse width modulation (PWM) of the controller's output signal was performed. An analysis of such a system was performed, and the matching of it and the pure continuous modeled system was verified.

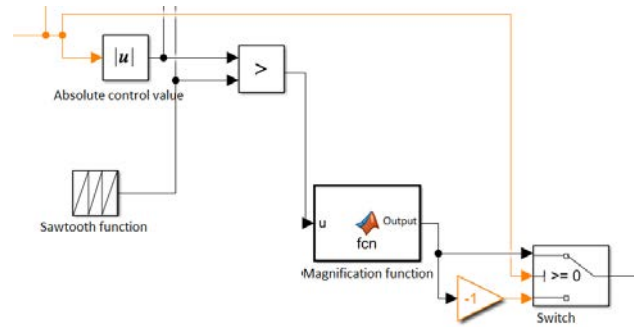


Figure 19. Block diagram of the PWM block in Simulink

The operation of the PWM block is based on the principle of comparing the absolute value of the continuous control and the sawtooth function has a peak at 1, if the control is greater than the current value of the sawtooth function, a 1 is sent from the comparator and vice versa, then in the magnification function if it is received as an input 1 at the output it sends 24 or if 0 is obtained, 0 is sent and finally, depending on the sign of continuous control, the function is exited with + or - and such a signal is further sent to the object. (Figure 19.[4])

It can be seen in Figure 20. that the outputs of the continuous system and the system with PWM almost overlap, except in the stationary state where the output of the system with PWM has small oscillations, but within the allowed limits (Figure 21).

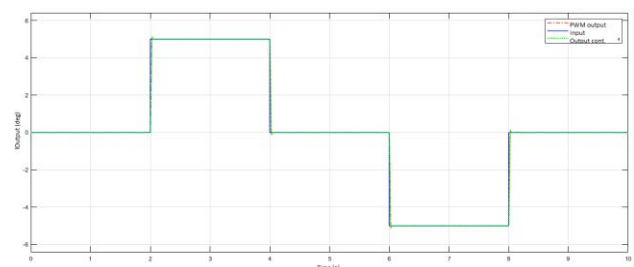


Figure 20. Comparison of the response of a PWM system and a continuous system to a step input signal

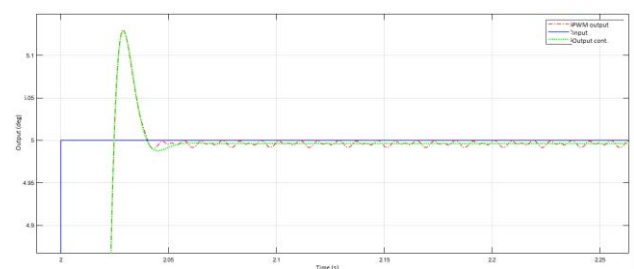


Figure 21. Comparison of the response of a PWM system and a continuous system to a step input signal- magnified

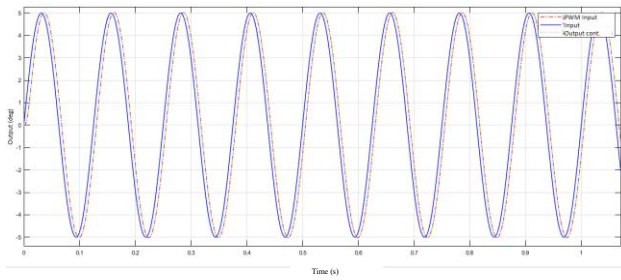


Figure 22. Comparison of the response of a system with PWM and a continuous system to a sinusoidal input signal

For testing of the real system, a special construction is made. The DC motor together with the spindle and the reducer and the handle for the fins is inside a steel tube. Instead of the flaps, a mechanism with a lever is attached to the supports, which is attached to the table through the ends, by means of a spring. This mechanism should simulate the moment that occurs when turning the wing and which tries to return the flap to the zero position (resistance moment) (Figure 23)



Figure 23. Resistance simulation mechanism

Figure 24 shows the response of the real system to the step input signal. It must be taken into account that the signal received from the sensor contains a lot of noise, as can be seen in the picture, and that the phase lead compensator has a very large differential effect and reacts quite aggressively to fast changes in the error, so the system will never remove the error completely. The static error is about 0.1° , which is not bad, if you take into account the characteristics of the system, while the overshoot is about 0.5° , or 8%.

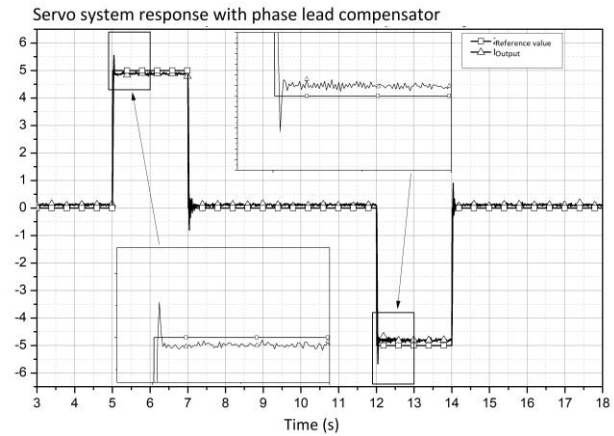


Figure 24. Response of a real system to a step input signal

6. CONCLUSION

With a good knowledge of the system's characteristics, that is, if the transfer function of the system is correctly determined, it is possible to simply synthesize a compensator with valid characteristics, which is easy to implement, which shows why it is still used today in the control of certain systems. The synthesis of the phase lead regulator was carried out, which managed to provide satisfactory dynamic characteristics.

References

- [1] RISTANOVIĆ, M., LAZIĆ, D, ČOJBAŠIĆ, Ž. : *Intelligent control of DC motor driven electromechanical fin actuator*. Control Engineering Practice, June 2012.
- [2] TENNAKON, W, MUNASINGHE, S.: *Design and Simulation of a UAV Controller System with High Maneuverability*, December 2008.
- [3] SHEIBANI, A., POURMINA, M.A: *Simulation and Analysis of the Stability of a PID Controller for Operation of Unmanned Aerial Vehicles*. Springer, Berlin, Heidelberg, 2012.
- [4] SHAO, P., ZHOU, Z., MA, S., BIN, L.: *Structural Robust Gain-Scheduled PID Control and Application on a Morphing Wing UAV*, Dalian, China, 26-28 July 2017.

UAV ENGINE SPEED CONTROLLER FOR HOVER PERFORMANCE MEASUREMENT

LAZAR PETROVIĆ

Military Technical Institute, Belgrade, lazar.petrovic.node@gmail.com

MARIJA SAMARDŽIĆ

Military Technical Institute, Belgrade, marija.samardzic.vti@gmail.com

UROŠ IVKOVIĆ

Military Technical Institute, Belgrade, uske80@gmail.com

SNEŽANA ZUROVAC

Military Technical Institute, Belgrade, zurovac@medianis.net

Abstract: This paper presents the characteristics of the interface for controlling the speed of each individual UAV engine using a computer, as well as the difficulties during its construction. The interface was designed and built in the Laboratory for Experimental Aerodynamics at the Military Technical Institute, Belgrade. The required engine speeds as well as its characteristics are set using a computer. Speed measurement is performed optically or by sampling the voltage on one phase of the motor. The ESC management protocol used is the 50 Hz PWM Standard. The communication protocol between the PC and the interface is RS485. The microcontroller used was PIC12F1572. The control program was written in the C programming language and a compiler from the microcontroller manufacturer was used.

Keywords: unmanned aircraft vehicle (UAV), electronic speed controller (ESC), standard PVM protocol, RS485, PIC microcontroller.

1. INTRODUCTION

The control of the number of revolutions of each drone engine is controlled by a central controller that receives data from sensors (GPS, electronic compass, altimeter, camera...), remote control and the current state of the engine and battery, and on the basis of that data determines whether the number of engine revolutions should be increased or decreased, Figure 1 [1].

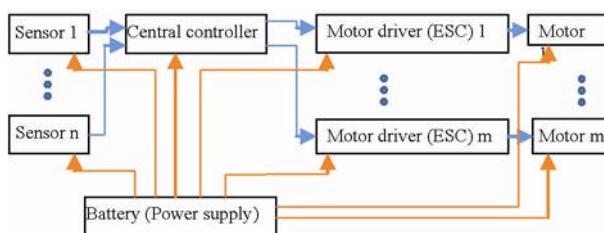


Figure 1. Block scheme UAV

Testing the characteristics of the drone implies a constant number of revolutions of the engine during the measurement. The number of revolutions of the engine is the result of the state of all sensors, so it is not possible to achieve a constant number of revolutions of the engine using the remote control. Simulating the data of all the sensors that affect the engine's behavior would be a more demanding task than creating a computer-controlled controller individually for each engine [2].

The diagram of computer-controlled drone motors is shown in Figure 2.

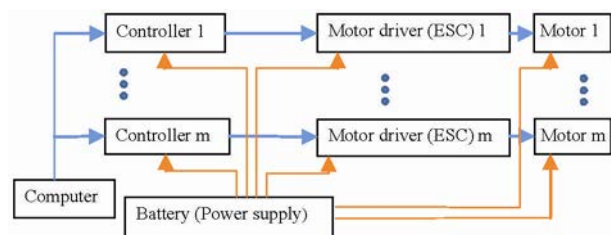


Figure 2. Computer-controlled drone motors

2. REQUIRED CHARACTERISTICS OF THE CONTROLLER

The controller should meet the following requirements:

- Use of standard engine speed control protocol
- Two-way communication between the controller and the computer
- Measuring the number of revolutions of the engine
- Supply voltage 6 – 24V
- Small dimensions of the controller so that it can be installed in the drone.

There are several protocols for controlling the speed of the drone's engine: Standard PWM, Oneshot125,

Oneshot42, Multishot, Dshot, ProShot,... The oldest and most universal is the PWM Standard. The disadvantage of this protocol is that the response of the drone engine is slower compared to other protocols. The difference in reaction time is measured in tens of milliseconds so it is not important for this test. The PWM period is 20 ms and can be changed if necessary, while the active part of the period lasts from 1 to 20 ms. The active part of the period less than 1 ms (with some ESC 2 ms) stops the motor, while for the maximum number of revolutions of the motor, the active part of the period is more than 2 ms. For the sake of simplicity and reliability of operation, the selected microcontroller (part of the controller) should have hardware PWM.

The communication between the computer and the controller should be reliable, resistant to induced interference, and the components needed to implement it (cables and electronic components) should be as small as possible. RS485 was chosen because only one pair is needed, it is possible to connect several devices, a minimum number of components is required, it is simple to implement both with the computer and with the controller, and it is resistant to interference caused by the operation of the motor. The communication speed is 9600 bps, which is sufficient for testing purposes. It is essential that the microcontroller has at least one serial communication port.

It is possible to perform three methods for measuring the number of revolutions: an optical sensor on the motor rotor, measuring the time between two rising edges on one phase of the motor and finding the dominant frequency of the signal on one phase of the motor.

The voltage supply of the microcontroller is in the range of 2 to 5V. The PWM output needs to be 3.3 or 5 V.

In order to reduce the number of components, the microcontroller is powered by a 5V stabilizer, so there is no need for a voltage translator for the ESC, whose PWM requires 5V. Drones powered by only one lithium cell are so small that it is not possible to place this controller inside the drone itself. It is necessary to make a suitable controller for such drones.

3. PROGRAM REQUIREMENTS

The functions to be performed by the controller are related to the number of required microcontroller pins. RS485 communication requires 3 pins (Rx, Tx and DE), one pin is used to measure the number of revolutions, one pin is PWM output and one pin is to control the operation mode (programming/normal operation). The minimum number of microcontroller pins is 6 + 2 for power (the programming pins are used as standard I/O pins during normal operation). The PIC12F1572 microcontroller was chosen as the most suitable [3].

Communication is done via the microcontroller's serial port (UART) which is connected to the RS232(TTL)/RS485 conversion IC, SN75176, which is always receiving except when it needs to send data [4]. The pins DE and RE of the circuit are controlled by the microcontroller. The microcontroller program should

continuously receive characters in the FIFO register and measure the time between receiving two characters. If the time between receiving two characters is longer than the time required to send two characters, then the FIFO register is emptied. The character reception is in the interrupt routine. If the number of characters in the FIFO register is equal to the length of the command, the contents of the FIFO register are analyzed and the contents are acted upon.

PWM with initial parameters is activated on the pin intended for PWM output immediately after starting the program. Changes of the period and the active part of the cycle are performed by commands without interrupting the operation of the PWM.

4. COMMANDS

Controlling the number of revolutions of the engine is done by sending commands through the serial port of the computer. The commands implemented are:

- Setting the period for PWM
- Setting the active part of the PWM cycle
- Setting the number of motor poles
- Setting the engine speed
- Setting the number of motor speed samples for averaging.

The command syntax is:

- Command code (1 byte)
- Engine address (1 byte)
- Command argument (2 bytes)
- End of command (1 byte)

After receiving a valid command (with the appropriate address, code and syntax and argument value), the controller responds with a message with the following syntax:

- Command confirmation code (1 byte)
- Engine address (1 byte)
- Last measured engine speed (2 bytes)
- End of command confirmation (1 byte)

The first two commands control the signal sent to the ESC. The transmission characteristic of each individual ESC - motor pair is different, so setting the same parameters will not result in the same number of revolutions on the drone's motors. Also, the number of revolutions of the engine depends on the voltage of the battery, the load on the engine, the temperature of the ESC itself and other parameters, so it is necessary to create a program feedback loop in the computer that gives the commands, based on the current number of revolutions of the engine. The program feedback loop should be tolerant to errors in the measurement of the number of revolutions of the engine both in terms of value and time (missing samples) [5].

The command for setting the motor poles is a number by which the measured number of pulses on one phase of the motor is divided to obtain the actual number of

revolutions of the motor. It is usual that the number of poles of the drone motor is seven, which is the initial value.

By setting the (target) number of engine revolutions, an internal program feedback loop is activated in the device itself so that the device changes the duration of the active part of the PWM cycle in order to achieve the set number of engine revolutions. This way of controlling the engine speed gives satisfactory results in the engine speed range of interest because the current control for each phase of the PWM motor is often more than an order of magnitude higher than the basic phase frequency. The band-pass filter at the input of the microcontroller for measuring the number of revolutions is adjusted to the expected range of frequencies, so that invalid measurements of the number

of revolutions are significantly more frequent outside the expected range.

4. REALIZATION OF THE DEVICE

The approximate dimensions of the double-sided printed circuit board of the first version of the device are 50x26x 10 mm, which is enough to install the device in the drone housing for each motor separately. The schematic is shown in Figure 3, and the appearance of the assembled device is shown in Figure 4.

By using components that are commercially available and smaller in size, as well as multilayer PCB, it is possible to significantly reduce the dimensions of the device.

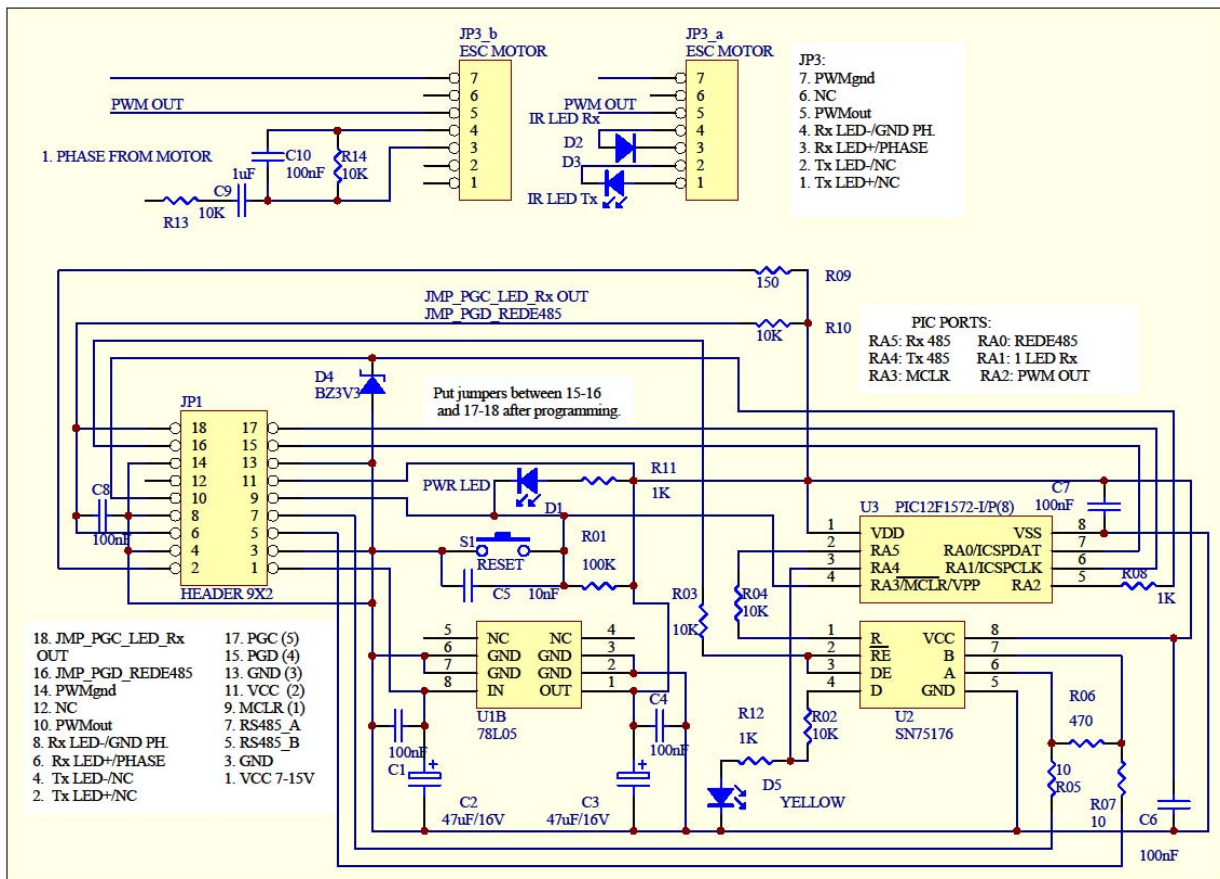


Figure 3. Controller's schematics

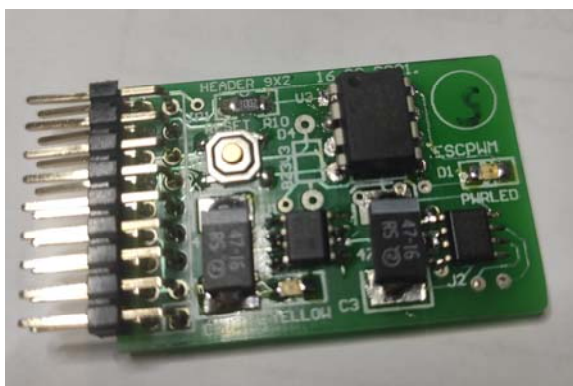


Figure 4. Assembled device

6. DEVICE TESTING

Program development and device testing was performed on an external ESC module and motor with similar characteristics as the drone that was tested. The difference between the ESC in the drone and the external ESC is in the voltage of the active level of the PWM signal. For the drone, that voltage is 3.3 V, while for the external ESC it is 5 V, which can be seen from the omitted Zener diode D4 of 3.3 V on the device.

The use of CRC was initially foreseen in the communication, but later it turned out that it was not necessary because during the development and testing

there was not a single case of error in the communication. The device communicates with the computer according to the command-response principle. The computer records the absence of a response from the device as an error and repeats the command. It was found that the optimal period for sending commands is about 0.5 seconds, because this way the trend of the change in the number of revolutions of the engine can be followed, and in case of a wrong measurement, that measurement can be omitted.

During testing, it was noticed that the device stopped working for an unknown reason and that, after the reset, it continued to work. A temporary solution to this situation was the introduction of WDT, which resets the device in such situations. Resetting the device takes a few seconds, which are critical during the measurement because the motor stops working. Later it was found that it was necessary to disable the interrupt until the processing of the previous interrupt was completed. After this program change, no reset due to WDT was observed.

After connecting the drone instead of one ESC to the motor, it was noticed that sometimes the device does not respond to the command. By increasing the time between the transitions from reception to transmission in the computer program, this deficiency was eliminated. The probable reason for this phenomenon is a longer communication wire and more participants in the communication.

7. CONCLUSION

The device for measurement of engine speeds performs its function, but it is necessary to increase its accuracy. One of the reasons of its low reliability is the lack of program memory space in the microcontroller itself. The program now occupies almost all available memory space, less than ten assembly instructions are not filled. Using another microcontroller (PIC16F18015 instead of PIC12F1572) would increase the program space by 4 times and it would be possible to implement an algorithm

for more reliable measurement of engine revolutions.

The dimensions of the device could be significantly smaller if SMD components of appropriate dimensions were used and if the connector for programming the microcontroller was eliminated. The programming connector could be replaced by contact pads on the PCB itself.

The command syntax could have been more adapted for this special case, but the syntax previously established for controlling the actuators on the model was respected.

ACKNOWLEDGEMENTS

This work was supported by the Ministry of Education, Science and Technological Development of the Republic of Serbia (Contract No. 451-03-68/2022-14/200325).

References

- [1] <https://oscarliang.com/> ESC Firmware and Protocols Overview
- [2] RUSSELL, C., WILLINK, G., THEODORE, C., JUNG, J., GLASNER, B.: *Wind Tunnel and Hover Performance Tests Results for Multicopter UAS Vehicle*, NASA/TM-2018-219758, Ames Research Center, 2018.
- [3] www.microchip.com, datasheet for PIC12 F1571/2, document DS40001723D.pdf
- [4] www.ti.com, datasheet for SN75176A Differential Bus Transceiver, document sn75176a.pdf
- [5] GHUDE, S., WEN, P.: *PID controller evaluation with missing samples in a networked control system using spline interpolation method*, International Conference on Computer and Automation Engineering (ICCAE 2009), 8-10 Mar 2009, Bangkok, Thailand



OPTIMIZATION OF THE ALGORITHM FOR ESTIMATING TIME OF ARRIVAL OF THE ACOUSTIC WAVE FRONT BY CHOOSING THE SIGNAL FILTERING METHOD

MIODRAG VRAČAR

Military Technical Institute, Belgrade, vracamiodrag@mts.rs

STEVO VRAČAR

Comtrade Technology Center, New Belgrade, office@its.edu.rs

Abstract: In this paper is described the optimization of the algorithm for determining the time of arrival (ToA) of the acoustic front of shock and detonation waves, which is not based on the application of cross-correlation analysis. In order to increase the signal-to-noise ratio in the initial phase of the algorithm, two approaches were used. The first is the wavelet decomposition of the signal, i.e. the Daubechies coefficient of the seventh order, or "db7", and the second approach in signal filtering is based on the use of the fourth order cumulants. Based on the obtained results, an assessment of the acceptability of the proposed solutions is given. Based on the obtained results, suggestions are given in which cases the use of a certain approach to increase the signal ratio is optimal and desirable to use.

Keywords: time of arrival, cumulants, algorithm, wavelets, muzzle wave, shock wave.

1. INTRODUCTION

The topic of this paper is optimization of the algorithm for determining the time of arrival (ToA) of the acoustic wave front by choosing the signal filtering method. It is well known that for finding efficient and precision methods for estimation of the ToA from acoustic signal significant attention has been paid to the last few decades. Wavefront travel time gives the range and direction of radiating target. In either case the estimation of these time delays is often corrupted by ambient and receiver generated noise, and multipath and finite length observation intervals. Undoubtedly, the application of any method for determining ToA will significantly depend on signal to noise ratio. Increasing the signal to noise ratio is achieved by some filtering method. In this paper, two signal filtering methods are considered. One is wavelet signal decomposition, and the other is based on the application of the fourth-order cumulants.

The algorithm for automatic ToA estimation is developed during past few years and tested and applied to various types of acoustic signals that come from firing from a rifle, mortar and cannon. The description of the algorithm is presented in several papers [1,3]. The concept of the algorithm consists of amplitude-time analysis in which statistical methods are included. The available literature describes several algorithms used for automatic estimation of ToA values from acoustic signal. Most of them is designed to overcome the limitation of traditional threshold method, the practicality of Hinkley criterion, cumulative energy, power curve, and Bai's CWT binary map method and others. Verification of these algorithms was done on the base of acoustic signals which originate from different explosion events such as firing from artillery weapons, and etc [4].

ToA is propagation time of the signal travelling between a source and a receiver in one way direction. Since in order to determine the location of the sound source, it is necessary to have information about ToA from several spatially distributed sensors, it is necessary to ensure the synchronization of the measured signals. A relatively common synchronization technique used in those cases is based on the use of GPS signals, whose accuracy is within limits of 20 ns. ToA multiplied with speed of sound gives mutual distance of the source and receiver. Position of the source in a two dimensional (2D) space is on the circle with the center at the receiver. The position of the sound source is located in the intersection of the circles defined by ToA values and positions of the receiving sensors [5,6].

The simplest procedure for determination the position of the sound source is based on the use of signals from minimum three receiving sensors and their positions. In other words, triangulation is the determination of an object's position based on simultaneous time of arrival (ToA) or range measurements from three stations at known locations. Four ToA measurements yield better position estimation without significant deviation. Namely algorithms based on three ToA measurements are faced with considerable difficulty in determination of the vertical component of the position of the sound source. This problem is possible to resolve if some information about the general location of the source is available, for instance is it below or above the measuring stations planes.

In the available literature are explained two common methods that normally being used to estimate ToA. The first is threshold method and the second cross-correlation method. The threshold method can be considered as the

simplest among these two techniques; however, it has poor accuracy of estimation. On the other hand, cross-correlation method gives a more accurate estimation than threshold, but it requires both transmitting signal and receiving signal to measure the time lag. Thus, the complexity increases.

Generally, the distance between source and receiver, using acoustic sensor, is measured based on time-of-arrival (ToA) and time difference of arrival (TDoA) which means time differences of estimated ToAs. A ToA measurement requires synchronization between source (transmitter) and receiver. TDoA only requires time synchronization among the receivers since it does not utilize the transmission time from the source [7].

Time of arrival estimation is significant in the field of Structural Health Monitoring (SHM) technique. This technique is used to perform continuous monitoring of structures to detect the presence of damage. The detection and location of damage by sensing acoustic signals could serve as a form of automated structural inspection. The location damage can be determined using measurements of Time Difference of Arrival (TDOA) of the signals detected at different sensors in an array [8].

In the time domain, Akaike [4] developed a statistical method to determine the transition point in a time series between noise and a coherent signal. This was achieved by using the Akaike Information Criterion (AIC) as expressed in Eq. (1).

$$AIC(t) = t \log_{10}(\text{var}(x[1;t])) + (N-t-1) \log_{10}(\text{var}(x[t;N])) \quad (1)$$

where $x(t)$ is time series signal, t – time, N length of the time window and var is variance function.

The signal $x(t)$ is partitioning into two sections at a point t and calculating the AIC value. This process is repeated for all points within a time window of length N and the minimum value of AIC indicates the estimated point of signal onset. Sedlak P. et al. [4] reported that the performance of this method is strongly dependent on the choice of the time window duration N . The window size N is determined by firstly using fixed threshold detection to obtain a ‘rough estimation’ of onset time, and then a portion of the signal-several hundred samples-is selected before and after this point as the window duration [4,6]. Improvements to the performance of this method have been demonstrated by firstly pre-processing the signal to increase the SNR and then shortening the duration of N to a smaller range. The criterion for choosing the new time window is however based on trial and error [4].

2. TIME-VARYING CORRELATION METHOD

Cross-correlation is a measure of the linear correlation (dependence) between two signals, giving a value between +1 and -1 inclusive, where 1 is total positive correlation, 0 is no correlation, and -1 is total negative correlation. The cross-correlation between two signals, U and V , can be calculated using the expression in Eq. (2).

$$r_{UV}(d) = \frac{\sum_{i=1}^n (u(i) - \bar{U})(v(i-d) - \bar{V})}{\sqrt{\sum_{i=1}^n (u(i) - \bar{U})^2} \sqrt{\sum_{i=1}^n (v(i) - \bar{V})^2}} \quad (2)$$

where \bar{U} and \bar{V} are the means of the signals U and V respectively, n is the number of samples, and $d = 0, 1, 2, \dots, n$ is the time delay. The magnitude of the cross-correlation function $r_{uv}(d)$ represents the level of similarity between these two signals with the time shift and the maximum value k , as expressed in Eq. (3), indicates the time when both signals are aligned with the most similar characteristics.

$$k = \arg \max_d (r_{uv}(d)) \quad (3)$$

Cross-correlation is a computationally intensive process and cross-correlation relies on a large section of acquired signal. This is fine in large open environments with no possibilities of reflections. However, reflections in the form of echoes and reverberations make cross-correlation methods somewhat in accurate.

3. WAVELET AND CUMULANT DECOMPOSITION

Wavelet is a windowing techniques with variable-sized regions. Wavelet analysis allows the use of long time intervals where is possible to get more precise low-frequency information and shorter regions where high frequency information is available. In our case de-noising of the signal is performed via wavelet decomposition by using of the seventh order Daubishies waveform, see Fig.1.

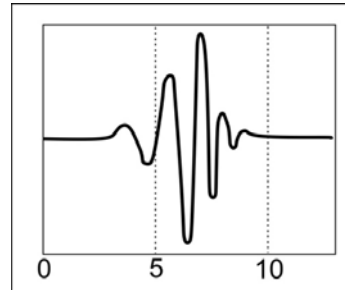


Figure 1. *db7* Daubechies waveform.

As shown in Fig.1, a wavelet is a waveform of effectively limited duration that has an average value of zero. Wavelet analysis means breaking up of a signal into shifted and scaled versions of the original (or mother) wavelet.

An algorithm for determining the time of arrival of an muzzle or shock wave, ToA, which originates from the firing of different types of infantry or artillery projectiles, has been developed in two variants. The first variant of the signal de-noising algorithm uses wavelet decomposition relying on *db7* Daubechies wavelet functions, see Fig.1.

The second variant of the acoustic signal de-noising algorithm is based on the use of the fourth order cumulants. The use of fourth order statistics (the kurtosis measure) can provide a way to distinguish speech or other

type of signals like explosions from noise. A Gaussian random process exhibit a cumulant with a zero value for any cumulant order higher than two. Estimation of higher order cumulants will in general eliminate Gaussian noise. The most real noise sources have a probability density function close to the Gaussian distribution, but sources of interest like explosions, firing from cannons or guns have different distributions [9]. The fourth order cumulant technique is used in other areas, such as for example the estimation of incoming direction of electromagnetic waves or direction of arrival (DoA) problem [10].

The application of such structured algorithms, based on wavelet or the fourth order cumulant, bypasses the need to use the cross-correlation method for estimating ToA, i.e. the use of two different acoustic signals, or, an acoustic signal and a pseudo signal to determine ToA. The application of wavelet decomposition of the signal gives good results and makes a relatively small error in estimation ToA. The application of the algorithm is illustrated by several examples. These examples originate from firing projectiles from a 122 mm caliber cannon.

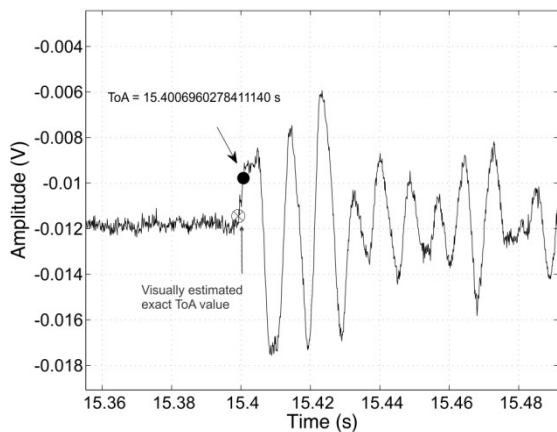


Figure 2. Visually estimated exact ToA value is designated with \otimes symbol, and ToA value which is algorithmically estimated, with wavelet de-noising of the signal, is designated with \bullet symbol.

The initial acoustic signal, before wavelet de-noising procedure and estimation of the ToA value, is shown in Fig.3.

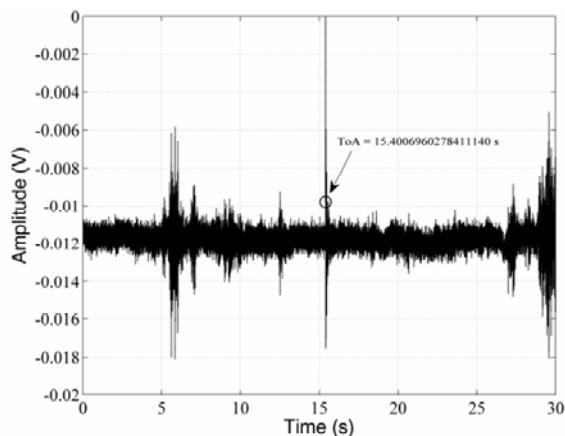


Figure 3. An unfiltered acoustic signal of a total duration of 30 s in which disturbances are expressed in the interval 5-13 s and finally in the interval 27-30 s.

The second example illustrates ability of the algorithm to recognize and estimate two close ToA values which originate from firing two artillery shells in short time interval, see Fig. 4.

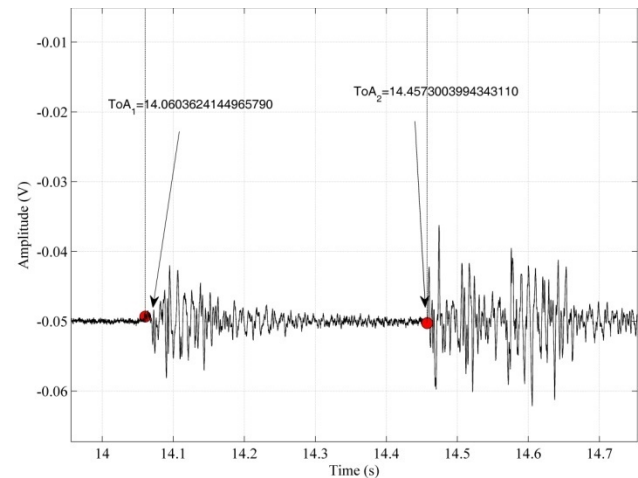


Figure 4. The algorithm with wavelet de-noising of the signal estimate two ToA values which originate from shot from two cannons.

In the case when the useful signal is very noisy or distorted due to the conditions under which it propagates, such as the configuration of the ground, long range, significant ambient noise, the state of the atmosphere and others, a different approach must be used in solving the problem of autonomous estimating ToA value. Using the fourth order cumulant analysis in de-noising of the signal is promising method. In Fig.5. is presented one such example.

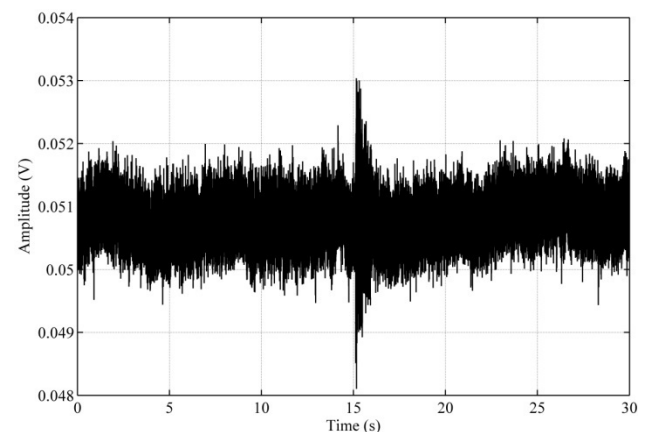


Figure 5. Example of the very noisy acoustic signal of the gun fire. Case when wavelet de-noising did not allow application of the algorithm for estimating ToA value.

In this case, see Fig.5, a more efficient method of de-noising the acoustic signal must be applied. Therefore the second variant of the acoustic signal de-noising algorithm based on the use of the fourth order cumulants is used. The result of applying this variant of the algorithm is shown in Fig 6. Application of the fourth order cumulant made it possible to significantly remove noise from the acoustic signal and significantly increase signal-to-noise ratio. After filtering, a clearly separated acoustic part was obtained, which is the result of shell fired from a cannon. If we apply an algorithm with adaptively adjustable

amplitude parameters on such a well-filtered acoustic signal for autonomous estimating ToA, and as result we get an almost accurate value of the moment when the signal occurs, see Fig. 7.

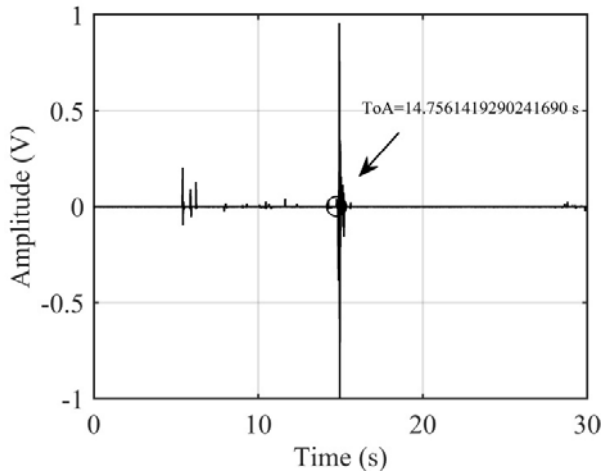


Figure 6. Filtered signal from Fig.5 using the fourth order cumulant and estimated ToA value.

When the Gaussian noise was previously removed from acoustic signal using the fourth order cumulant analysis, it was easy to apply the algorithm for autonomous estimation of the ToA value, as shown in Figures 5 and 6.

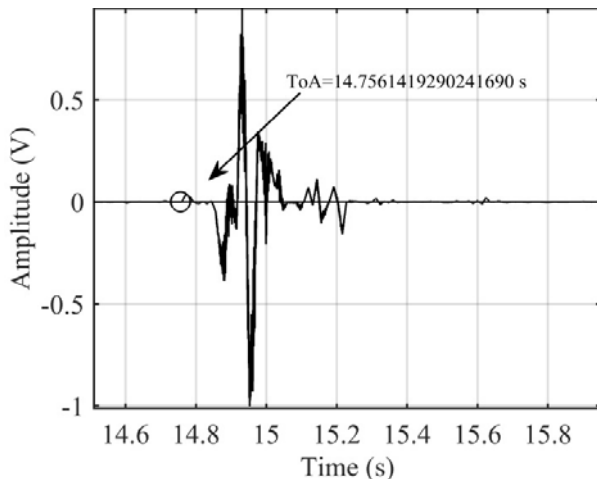


Figure 7. A zoomed-in part of the acoustic signal from Figure 6 that refers to the useful signal - the acoustic signal that is the result of a shell being fired from a cannon.

When looking more closely at the result shown in the diagram, see Figure 7, it can be seen that the moment of the beginning of the acoustic signal originating from the cannon shot is very precisely estimated.

4. ACHIEVED ACCURACY

The accuracy of the applied filtering methods and algorithm for autonomously estimating ToA values was checked as shown in Figure 2. After using a certain method of filtering of the signal and estimating ToA, the actual moment of beginning of the part of the acoustic signal related to the firing of the shell could be visually observed on the diagram, so ToA estimated value is marked with a symbol \otimes , and read its value with an

accuracy of the order of microseconds.

$$\Delta ToA = ToA_{exact} - ToA_{estimated} \quad (4)$$

The absolute error (ΔToA) of estimated ToA values is calculated according Eq. 4. Statistical analysis of absolute errors was performed on 155 samples when wavelet decomposition of the signal was applied and 41 signal analysis with signal filtering using the fourth order cumulant analysis.

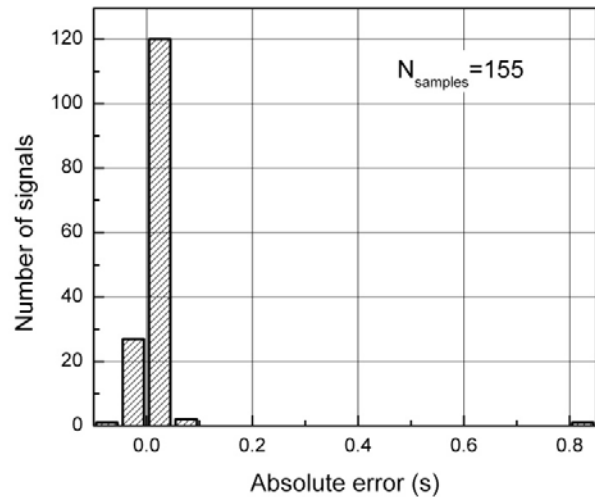


Figure 8. Histogram distribution of the absolute error of ToA estimated values when wavelet decomposition of the acoustic signal is used.

The absolute errors of the ToA values estimation when using wavelet decomposition of the acoustic signal are good grouped around zero, see Fig. 8. Relatively small absolute error was obtained in almost all cases. However, it should be noted that wavelet signal decomposition was applied only in those cases where there was a relatively high signal-to-noise ratio. The signal quality assessment was performed before applying the algorithm for estimating ToA value via the crest factor, so the signal is rejected if there was too much noise. The crest factor is a parameter of a waveform showing the ratio of peak values to the effective value.

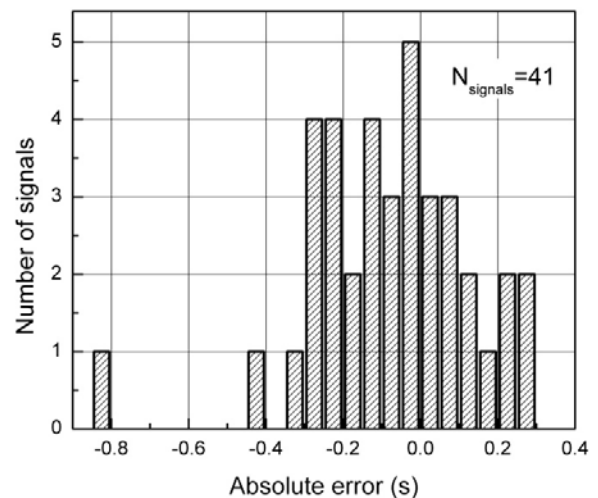


Figure 9. Histogram distribution of the absolute error of ToA estimated values when the fourth order cumulant decomposition of the acoustic signal is used.

The situation regarding accuracy when estimating ToA values is quite different compared to the previous case. The distribution of the absolute error is significantly wider, as are the values of the absolute errors are significantly bigger, see Fig. 9. The explanation of the results thus obtained consists in the following:

- the first, the fourth order cumulant filtering method was applied in all those cases when the signal is very noisy, so that the wavelet decomposition of the signal did not give any result and
- the second, the fourth order cumulant analysis was applied to windows of 200 points, which significantly reduced the time resolution of the filtered signal during ToA estimation process.

The explanation why such a coarse time resolution was used when using the fourth order cumulant method is that the average computer time for processing one acoustic signal is 13.38406027 seconds with standard deviation of 0.7021416 seconds. In contrast, the computer time when using the wavelet method is significantly less and amounts to around 0.4 seconds.

In order to better understand necessary computer time for estimating ToA, it is useful to specify the characteristics of the computer that was used for this analysis. During ToA time analysis a relatively outdated personal computer with a processor Intel(R) Core™ 2 Duo CPU E7500 2,93 GHz with 1,96 RAM was used.

5. CONCLUSION

The paper describes two methods of filtering acoustic signals for the purpose of applying an algorithm for the autonomous estimation of ToA shock or muzzle waves that occur when firing from artillery or personal weapons. It should be emphasized that it is not about competing methods that exclude each other. Rather, it could be said that they complement each other. The method based on the use of the fourth cumulant is applicable in all cases where the Gaussian noise is significantly present in the signal. However, the main disadvantage of using this method is the relatively large computer time required for signal processing, which temporarily excludes this method from being used for source localization using acoustic methods.

The future development of efficient and fast algorithms for calculating the fourth order cumulant, as well the realization of faster computers will bring this filtering method to the same position as wavelet signal decomposition. Also, it will enable the successful processing of signals that were generated at a greater distance and that are therefore significantly distorted.

The application of this new method of filtering acoustic signals will lead to a significant increase the range of locating the sources of shock or muzzle waves.

References

- [1] Miodrag S. Vračar, Ivan Pokrajac: Application of the algorithm for time of arrival estimation of N-waves produced by projectiles of different calibers, doi: 10.1121/2.0000648, Proc. Mtgs. Acoust. 30, 055008, 2017.
- [2] Ivan Pokrajac, Miodrag Vračar, Nadica Kozić, Radiana Brusin, Milan Stanojević,: Position Determination of Acoustic Source Using a Discrete Probability Density Method Supported by Joint Detection and Time of Arrival Estimation, Scientific Technical Review, Vol.67, No.1, pp.29-37, 2017.
- [3] Ivan P. Pokrajac, Miodrag Vračar, Tamara Šević, Vasilija Joksimović.: Position Determination of Acoustic Source Using Higher-Order, Spectral Analysis for Time of Arrival Estimation, Scientific Technical Review, Vol.69, No.3, pp.41-48, 2019.
- [4] F.Bai,D.Gagar, P.Foote,Y.Zhao, Comparison of alternatives to amplitude thresholding for onset detection of acoustic emission signals, ELSEVIER, Mechanical Systems and Signal Processing 84, pp 717-730, 2017.
- [5] RAVINDRA S. AND JAGADEESHA S. N., Time of arrival based localization in wireless sensor networks: a linear approach, Signal & Image Processing: An International Journal (SIPIJ) Vol.4, No.4, August 2013.
- [6] Mohamed Khalaf-Allah, Time of Arrival (TOA)-Based Direct Location Method, Conference Paper, DOI: 10.1109/IRS.2015.7226229, June 2015.
- [7] Chee Sheng Tan, Rosmiwati Mohd-Mokhtar, Mohd Rizal Arshad, Time of arrival estimation using fast Fourier transform overlap for underwater distance measurement, Indian Journal of Geo Marine Sciences, Vol. 48 (07), pp. 1070-1080, July 2019.
- [8] Lu Cheng, Hoahui Xin, Milan Veljkovic, Acoustic Emission Source Location on i girder based on Experimental Study and Lamb Wave propagation simulation, XII Conference on Steel and Composite Construction Coimbra, Portugal, 2019.
- [9] Mikael Swartling, Benny Sällberg, Nedeljko Grbić, Direction of Arrival Estimation for Speech Sources Using Fourth Order Cross Cumulants, IEEE, 978-I-4244-1684-4/08, pp 1696-1699, 2008.
- [10] P. Palanisamy and N. Rao, Direction of Arrival Estimation Based on Fourth-Order Cumulant Using Propagator Method, Progress In Electromagnetics Research B, Vol. 18, 83 (99), 2009.



CONTROL SYSTEM DESIGN AND INTEGRATION OF A BLOWDOWN WIND TUNNEL MODEL SUPPORT PITCH MECHANISM

BILJANA ILIĆ

Military Technical Institute, Belgrade, biljana.ilic@icloud.com

MIRKO MILOSAVLJEVIĆ

Military Technical Institute, Belgrade, mirko.milosavljevic.bgd@gmail.com

STEFAN KRSTIĆ

Military Technical Institute, Belgrade, stefankrstic18@gmail.com

GORAN OCOKOLJIĆ

Military Technical Institute, Belgrade, ocokoljic.goran@gmail.com

DIJANA DAMLJANOVIĆ

Military Technical Institute, Belgrade, didamlj@gmail.com

Abstract: Development of a novel system for automation of aerodynamic experiments in the VTI T-38 wind tunnel included control system design and integration of a wind tunnel model support pitch mechanism. Considering that even small errors in scaled-model pitch angle affect the final aircraft configuration, an extremely accurate position control servo system is needed, capable of positioning the model with no measurable overshoot, low settling times and very good repeatability. To study the performance of the mechanism under the extremely high aerodynamic loads acting on the wind tunnel model, a dynamic model that reproduces the behavior of the model support mechanism is developed. Then a closed-loop control system is designed, consisting of a major loop with position feedback, which is stabilized by an inner loop with velocity feedback. To compensate for the system steady-state error, a gain scheduling approach is applied by switching two linear controllers based on the system state. The pitch mechanism control system is integrated and tested covering the full wind tunnel operating envelope. It is capable of accurate trajectory control of $\pm 0.05^\circ$ throughout an entire move at speeds of up to $15^\circ/s$. The system accuracy at the endpoint is $\pm 0.01^\circ$ with no measurable overshoot.

Keywords: Wind tunnel, model support, pitch mechanism, system dynamics, position control, gain-scheduled control.

1. INTRODUCTION

Wind tunnel testing applications normally require positioning of the model in the airstream to simulate flight attitudes. For that reason, a standard wind tunnel design includes a positioning system which locates a model in the test section at a series of prescribed positions.

In most tests, it is required to place the model at various angles of attack for fixed sideslip angles or at various sideslip angles for fixed angles of attack. In blowdown wind tunnels, this type of positioning is usually accomplished by combining the actions of pitch and roll model support mechanisms. The problem of model positioning in the airstream is further complicated by deflections of the model support component parts caused by aerodynamic loads, which vary depending on the structure stiffness, model attitude, Mach number and dynamic pressure. Model support position achieved by the actions of the support mechanisms is therefore mathematically corrected, based on the previous experimental determination of the expected deflections, in order to establish the model position in the airstream. In

such circumstances, the extremely accurate control of model support position is of utmost importance.

Model support mechanisms are usually sturdy systems weighing up to several tons and having one or more degrees of freedom, with drives of hydraulic, electric or hybrid type. Advanced control systems are required to both control mechanisms such as these and provide synchronization with the overall wind tunnel control and data acquisition process [1]. In the past, such control systems were hardware-based, with the multitude of accessories, connection cables and software applications to support devices in use [2]. In recent years, costly and cumbersome process of integration and maintenance of hardware-based control systems is being replaced by the software approach to motion control [3], providing the user with an interactive, productive and cost-effective platform for automation, as well as superb precision performance.

In line with these trends, the traditional hardware-based control system for the VTI T-38 wind tunnel model support pitch mechanism is replaced with the software solution. A dynamic model of the pitch mechanism is

developed and used in the design of a double-loop control system that performs both velocity and position control. A compromise between several conflicting requirements, namely high position accuracy, precise reference tracking, low settling times and positioning without overshoot, is achieved using a gain scheduling method based on switching two linear controllers. The pitch control system is designed and integrated into the overall wind tunnel control system in such manner to operate both independently and in synchronization with other components during a test.

2. MODEL SUPPORT DESCRIPTION

Model support in the 1.5 m × 1.5 m VTI T-38 wind tunnel is a 2 DOF system consisting of two mechanisms: the hydraulically actuated pitch mechanism and the electrically driven roll mechanism. It permits movement of the model within ±20° in pitch and ±720° in roll. The main components of the model support are shown in Figure 1.

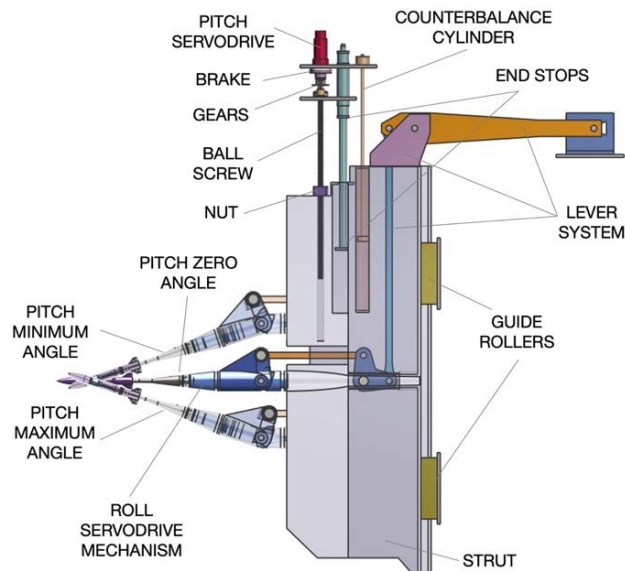


Figure 1. Model support in the VTI T-38 wind tunnel

The vertical strut is the most massive part of the pitch mechanism. Mass of the strut with linkage assembly is more than 3000 kg. Motion of the strut is restrained to vertical only by axial and side roller assemblies mounted in the wind tunnel structure. It is driven by a hydraulically powered ball screw and nut. Adjustable end stops with energy absorber and strut counterbalance cylinder are included in the system. Model pitching is accomplished by a lever system, parts of which are built into the body of the strut. The model support system is designed to withstand the maximum aerodynamic forces with suitable safety margins, that is, the normal force of 64 kN, the axial force of 18.3 kN and the pitching moment of 3.3 kNm.

Moog Series A084 hydraulic servodrive is used for the model support actuation, with a Moog 72-102 servovalve and a 9-piston, axial drive Moog-Donzelli servomotor. Around 90 percent of the mass of the model support system is pneumatically balanced via the counterbalance cylinder connected to the source of compressed air.

3. MATHEMATICAL MODEL EQUATIONS

The mathematical model of the electrohydraulic and mechanical components of the pitch mechanism is derived in order to obtain a physical model of the system.

A two-stage flow control servovalve uses an electrical torque motor, a double-nozzle pilot stage and a sliding-spool second stage. Electrical input current in the torque motor gives proportional displacement of the second stage spool, and hence, control flow proportional to the load. Control flow to the load will change with load pressure drop and electrical input, following the theoretical relationship for sharp-edged orifices, which is:

$$Q_L = C_d K_v i \sqrt{P_V} \quad (1)$$

where:

$$P_V = (P_S - P_R) - P_L \quad (2)$$

The two servovalve control ports connect to a fixed-displacement axial drive motor. An input current to the servovalve causes one control port to be connected to supply pressure, while simultaneously the other control port is connected to the return line. Pistons that are connected to supply pressure attempt to extend, so apply a force to the swash plate, resulting in a torque on the motor drive shaft. The overall result is motor shaft speed and direction proportional to the input current to the servovalve. The torque generated on the hydraulic motor shaft must overcome acceleration torque, torque due to viscous friction and load torque:

$$D_m P_L = J \alpha + B \omega + T_L \quad (3)$$

Moment of inertia on the motor shaft represents a sum of the moments of inertia of the main movable parts of the pitch mechanism:

$$I = I_m + I_s + I_L \quad (4)$$

The load torque comprises torque due to the mechanism mass unbalanced by the pneumatic system, torque due to friction and torque due to aerodynamic forces:

$$T_L = T_g + T_f + T_a \quad (5)$$

The electrohydraulic system is fully defined by adding to the relations (1) – (5) the continuity equation for the motor, assuming that the hydraulic fluid is incompressible:

$$Q_L = D_m \omega + Q_{fl} \quad (6)$$

Based on the mathematical model (1) – (6), it is possible to determine the control flow for the known load conditions, ie., the required input signal from the control system.

To fully describe the pitch mechanism, geometric description is needed for motion of mechanical components of the system. Rotational motion of the motor is converted to translational motion of the strut via leadscrew, based on the following kinematic relation:

$$\varphi = \frac{2\pi}{p} x \quad (7)$$

Kinematic relation for the strut translational motion and the mechanism pitch angle is the following:

$$x = 1.75s \sin \theta \quad (8)$$

System of equations (1) – (8) represents the mathematical model of the pitch mechanism.

4. PHYSICAL MODELLING AND SIMULATION

A physical model of the pitch mechanism is developed using Simscape in the Matlab-Simulink environment, as presented in Figure 2. The model is developed to be used in the simulations, with the aim to obtain the response of the pitch mechanism, and to use simulation data in control design and integration. The parameters of the components defined by model equations are coded into the Simscape model and presented in Table 1.

Table 1. System parameters

Parameter	Symbol	Unit	Value
System pressure	P_s	bar	130
Valve maximum opening	-	m	0.005
Flow discharge coefficient	C_d	-	0.7
Critical Reynolds number	-	-	12
Valve sizing constant	K_V	m ³ /sA	0.265
Valve maximum current	i_{max}	A	0.01
Motor displacement	D_m	m ³ /rad	12.88 10 ⁻⁶
Motor maximum velocity	ω_{max}	rad/s	146.6
Motor volumetric efficiency	-	-	0.92
Motor total efficiency	-	-	0.8
Motor moment of inertia	J_m	kg·m ²	0.06
Damping coefficient	-	Nm/(rad/s)	0.4
Ball screw lead	-	m	0.0254
Ball screw efficiency	-		0.9
Ball screw velocity threshold	-	m/s	0.6
Coulomb friction force	-	N	500

A fixed-displacement axial piston pump that is used as a source of hydraulic energy in combination with four accumulators is considered powerful enough to maintain required supply pressure at its outlet regardless of the load

and it is represented by an ideal hydraulic pressure source in the Figure 1. The flow from the pump supplies the flow control valve, which regulates the amount of fluid entering the hydraulic motor. The ball screw that is used to convert rotation of the motor shaft to translation of the vertical strut is modelled taking into account friction losses. The sensors for position and velocity are used in the model under assumption that their inertia, friction and delays can be neglected. The outputs of the sensors are coded as relative, with the possible ranges of [-1, 1].

The nonlinearity in this type of system can arise from different sources, including flow deadband and saturation, relation between pressure and flow, friction between moving parts or changes in supply pressure and load [5]. The response of the pitch drive mechanism is analyzed in order to determine if the system can be linearized in the entire position range. The analysis is done by presenting an impulse function to the input of the simulation model in Figure 2, assuming the maximum aerodynamic forces.

The nonlinearity in this type of system can arise from different sources, including flow deadband and saturation, relation between pressure and flow, friction between moving parts or changes in supply pressure and load [5]. The response of the pitch drive mechanism is analyzed in order to determine if the system can be linearized in the entire position range. The analysis is done by presenting an impulse function to the input of the simulation model in Figure 2, assuming the maximum aerodynamic forces.

Based on the simulation data, transfer function of the motor shaft angular velocity (AV) to the servovalve input current (I) is approximated by the second-order system (V) with 99.02% fit to estimation data, as is shown in (9).

$$V(s) = \frac{AV(s)}{I(s)} = \frac{43.06s + 800.9}{s^2 + 57.64s + 7481} \quad (9)$$

In addition, transfer function of the wind tunnel model angular position (AP) to the motor shaft velocity (AV) is represented by the first-order system (P) with 95.68% fit to estimation data, as is shown in (10).

$$P(s) = \frac{AP(s)}{AV(s)} = \frac{0.9316}{s} \quad (10)$$

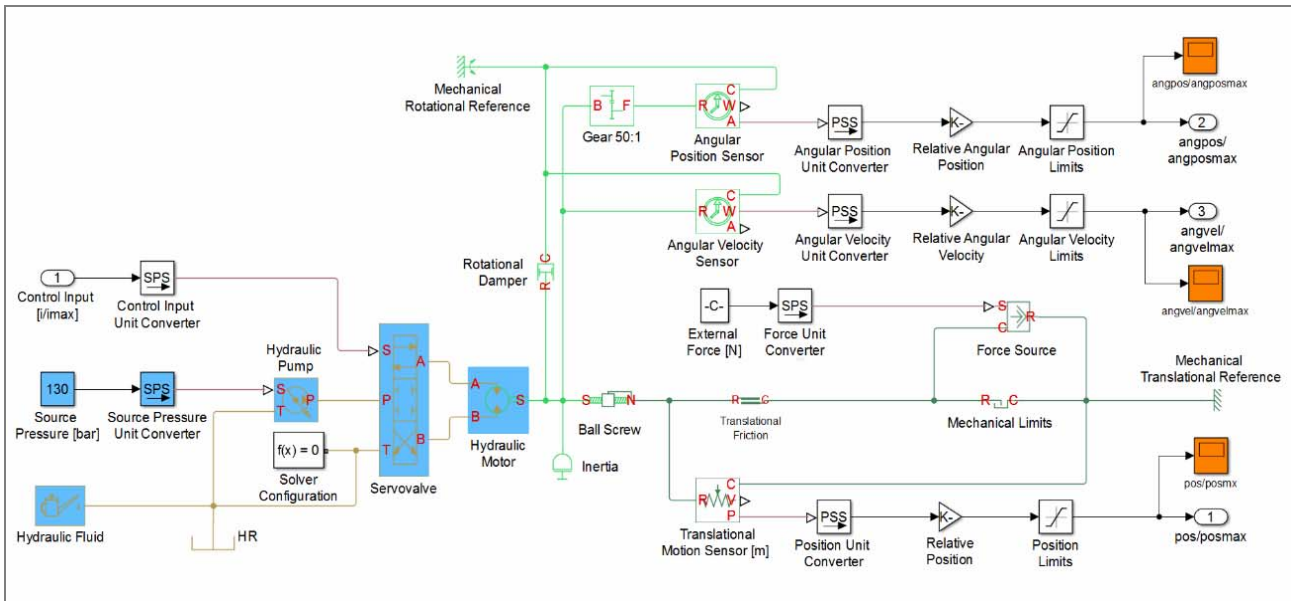


Figure 2. Simulink/Simscape model of the pitch drive mechanism

Equations (9) and (10) represent the linearized simulation model in Figure 2. Note that the motor and the load here are modelled separately. Since they are rigidly connected via the common shaft, it would be possible to develop a combined lumped parameter model and use the single transfer function of the angular position to the servovalve input current. However, due to highly variable nature of aerodynamic loads acting on the wind tunnel models it was decided to consider the motor and the load separately in control system design. This approach enables better capturing of how the dynamics of the motor and the load is distributed [6] and consequently, the more effective compensation by the control system.

4. CONTROL SYSTEM DESIGN

Control system for the pitch mechanism is designed based on the requirement to have precise model positioning in

all wind tunnel test conditions, including those with extremely high and very variable aerodynamic loads. Consequently, the torque required to move the load is also variable, and it needs to be generated while maintaining the desired shaft speed and the model support mechanism position. Such requirements imply the need for the multi-loop control system that would be able to provide both velocity control of the motor shaft and position control of the mechanism.

Based on the above reasoning, the cascade control system is designed, consisting of the inner loop for the motor shaft angular velocity control with a tachogenerator as a velocity feedback, and the outer loop for the mechanism position control with an encoder as a position feedback. Block diagram of the suggested cascade control system applied to the linearized dynamics of the motor (9) and the load (10) is presented in Figure 3.

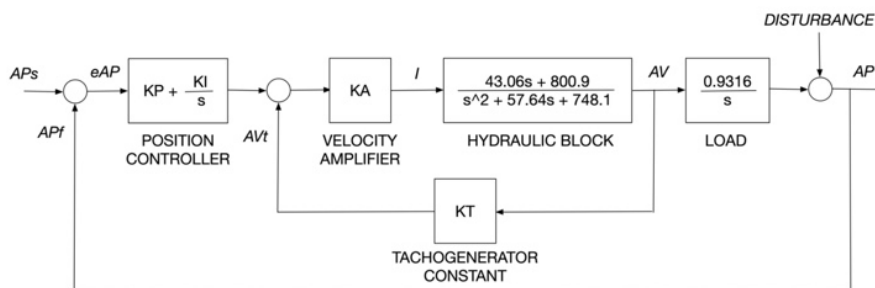


Figure 3. Block diagram of the pitch mechanism with cascade control

Both loops are tuned using Simulink linear analysis tool.

The tachogenerator constant $KT = 0.8$ is determined based on its relative output voltage relation to the relative motor shaft speed. The actual feedback and setpoint velocities in the inner loop are fed into the velocity amplifier. Any difference between the two velocities is amplified and the output serves as the relative current input to the hydraulic block. The amplifier gain is tuned to $KA = 4.671$. Figure 4 compares the motor shaft velocity frequency response of the system with inner loop

(red line) to the response of the system without inner loop (blue line).

Closed-loop control of motor shaft velocity apparently brings several benefits, the most important being the larger bandwidth. The cutoff frequency without speed control loop of 7.45 Hz is increased to 32.2 Hz in a closed-loop system, which increases bandwidth more than four times. The higher is the bandwidth of the velocity loop, the quicker system responds to changes in the velocity command [7]. For example, a load disturbance causing an acceleration or deceleration of the motor shaft

and the rise of velocity error can be compensated in the inner loop, which results in maintaining the motor speed without error propagation to the outer position loop.

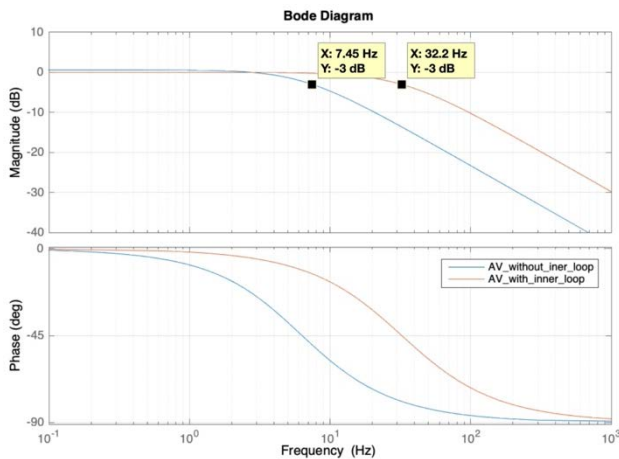


Figure 4. Bode plot of the motor shaft velocity responses without and with velocity loop

The position controller of the PI type selected for the outer loop was tuned using the previously determined parameters of the inner loop. In addition to high positioning accuracy and low settling times, the main requirement was to achieve positioning without measurable overshoot and with the maximum rise time, which amounts to ~ 0.85 s for the unit step response of the system (expressed as relative position, with step function from 0 to 1).

Figure 5 compares step responses of the system for several proportional (P-only) controllers, with $KP=1,2,3,4,5$.

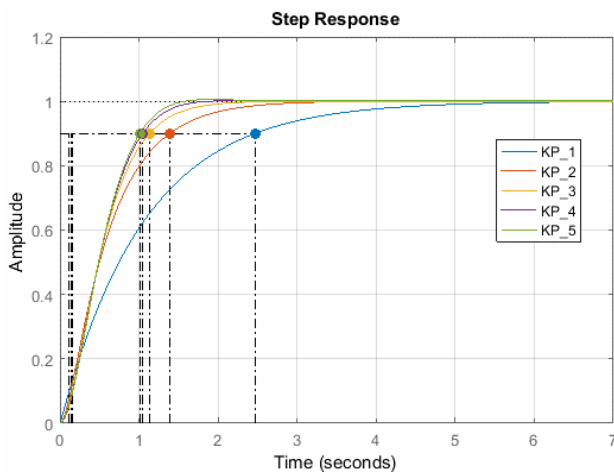


Figure 5. Step responses and rise times of the system position for several P-only controllers

The main characteristics of the system responses shown in Figure 5 are given in Table 2. Rise time is defined from 10% to 90% of the response, and settling time within 2% of the setpoint.

The rise time for $KP = 4$ is close to maximum for the system dynamics. Further increasing of KP does not bring a noticeable improvement of the rise time and settling time, and contrary to the control system design goals, it increases overshoot. Thus, the proportional $KP = 4$

controller appears to fulfil requirements concerning the rise time and settling time, but it still brings a mild overshoot and, as it is expected for this control method, results in a steady-state error. Since wind tunnel tests bring variable and frequent disturbances and the model support positioning application requires tighter set point tracking, proportional-only control does not appear to be sufficient.

Table 2. Step response characteristics

Controller	Rise time [s]	Settling time [s]	Overshoot [%]	Steady-state error [%]
$KP = 1$	2.35	4.19	0.00	0.02
$KP = 2$	1.25	2.28	0.00	0.00
$KP = 3$	0.98	1.70	0.00	0.01
$KP = 4$	0.88	1.44	0.16	0.08
$KP = 5$	0.85	1.34	0.56	0.30

The proportional-integral (PI) form of the controller provides correction for steady-state error and decreases rise time. However, adding integral term comes to the cost of introducing overshoot. In the case of the pitch mechanism, maximum physically possible rise time is achieved with P-only controller. Integral term thus cannot improve the system rise time. Tuning was attempted by adding relatively weak integral actions ($KI = 0.1$ and $KI = 0.01$) to two P controllers ($KP = 4$ and $KP = 2.5$), the idea being to avoid overshoot that would have been brought by higher values of the integral term. The step responses of the corresponding four PI controllers are given in Figure 6.

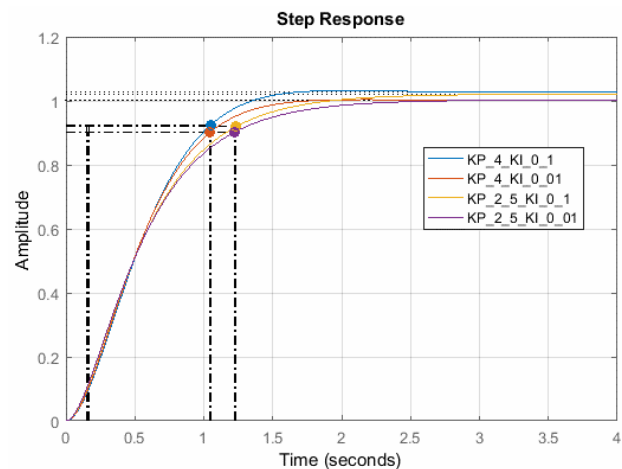


Figure 6. Step responses and rise times of the system position for several PI controllers

The main characteristics of the system responses shown in Figure 6 are shown in Table 3.

Table 3. Step response characteristics

Controller	Rise time [s]	Settling time [s]	Overshoot [%]	Steady-state error [%]
$KP = 4.0; KI = 0.1$	0.88	1.40	0.471	2.80
$KP = 4.0; KI = 0.01$	0.88	1.44	0.182	0.25
$KP = 2.5; KI = 0.1$	1.08	1.94	1.19	1.19
$KP = 2.5; KI = 0.01$	1.08	1.94	0.24	0.24

It is evident that adding integral action results in larger overshoots, without the effect on rise times. In fact, proportional term appears to have a dominant effect on the pitch system response, given that $KP = 2.5$, $KI = 0.1$ and $KP = 2.5$, $KI = 0.01$ controllers resulted in the increased rise times despite the integral terms. Larger overshoots brought by PI controllers are explained by the fact that the integral term action is proportional not only to the error, but also the time for which it has persisted. Thus, the error accumulation during the move causes overshoots even for very low values of integral coefficients. In addition, since the performance of the pitch system are close to maximum with P-only controller, adding integral action does not have an expected effect to steady-state error, which is even higher with PI controllers.

In order to entirely eliminate overshoot and achieve steady-state error below 0.01%, the attempt was made with gain-scheduling approach. The idea was to use P-only controller during the pitch move, and switch to PI controller only when position is within narrow range around the setpoint. The final gain-scheduled controller obtained by the tuning procedure as the best fit is the following:

$$|eAP| > 2\%: KP = 4.5; KI = 0$$

$$|eAP| \leq 2\%: KP = 4.5; KI = 0.01 \quad (11)$$

Thus, the integral action is triggered only when angular position error (eAP) is within $\pm 2\%$ of the setpoint. Figure 7 presents the step response of the system position with the gain-scheduled controller defined by (11).

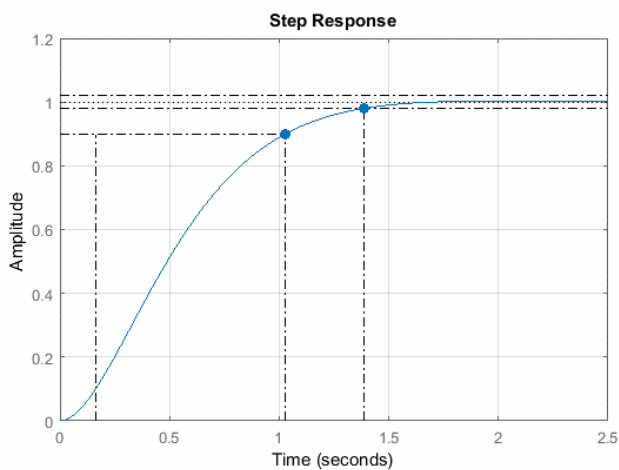


Figure 7. Step response of the system position with the final gain-scheduled controller

The response of the selected controller has the similar characteristics as for the $KP = 4$ controller. Its rise time is 0.88 s and the settling time is 1.44 s. However, it has not a measurable overshoot, and its steady state error is 0.008%, which is within required accuracy of 0.01%.

The frequency response of the outer position loop of the pitch system is presented in Figure 8. The outer position loop cutoff frequency is 0.386 Hz, which is two orders of magnitude smaller than the bandwidth of the inner velocity loop (see Figure 4). This bandwidth difference is

an indicator of the quality of the cascade control design.

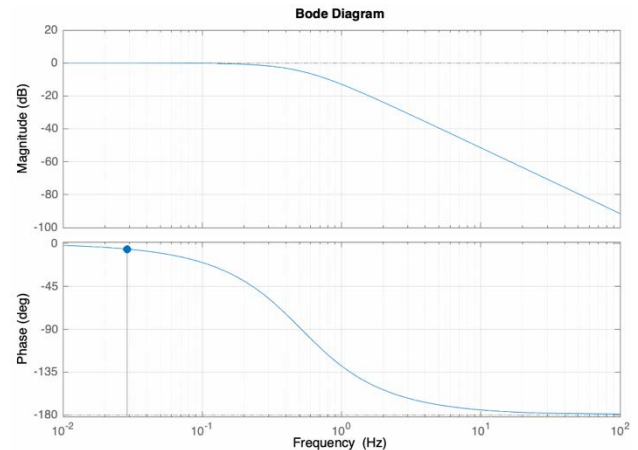


Figure 8. Bode plot of the position loop response

In addition, the closed-loop system appears stable, with phase margin of 174 degrees at 0.029 Hz.

4. CONTROL SYSTEM INTEGRATION

The pitch mechanism cascade controller is integrated in the VTI T-38 wind tunnel overall system for automation of aerodynamic experiments. It is implemented using the LabVIEW development environment on the NI CompactRIO hardware platform. The loops are closed on the FPGA level of the CompactRIO, at a fixed frequency of 1 kHz. A resolver that was previously used as position sensor is replaced by a 14-bit digital encoder, giving a position resolution of 0.002° .

Typical pitch movement profiles of a model, sampled with frequency 1 kHz, in several wind tunnel tests at Mach 2 are shown in Figure 8. After the flow is established, the model is moved from zero to the initial pitch position (-5° in these tests) at maximum speed ($15^\circ/s$), then it is swept at the desired speed (from $2^\circ/s$ to $12^\circ/s$) to the final pitch position (19°), and in the end, it is moved to the zero-pitch position at maximum speed before the flow is stopped.

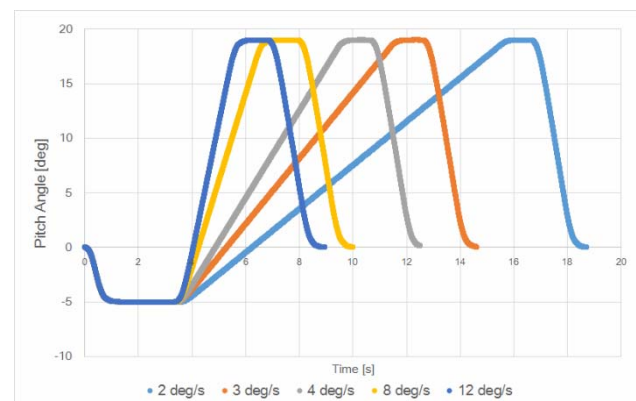


Figure 8. Typical pitch movement of the model in several wind tunnel tests

Reference tracking for all pitch speeds was within $\pm 0.05^\circ$ throughout an entire move, with the accuracy at the endpoint within $\pm 0.01^\circ$ in all wind tunnel tests.

The pitch mechanism can be operated both independently

and in synchronization with other wind tunnel components during a wind tunnel run.

5. CONCLUSION

The pitch mechanism in the T-38 wind tunnel is an electro-mechanical system which is intended for high-accuracy positioning of the model in the airstream. Due to massive aerodynamic forces, the power amplification is realized through a spool valve and a hydraulic motor. In this paper, design and integration of a highly accurate gain-scheduled cascade control system for the pitch mechanism is described. It is capable of trajectory control within $\pm 0.05^\circ$ throughout an entire move at speeds of up to $15^\circ/\text{s}$. The steady-state accuracy is better than $\pm 0.01^\circ$ with no measurable overshoot. Since its integration, the system is successfully used in several wind tunnel test campaigns.

Symbols

B	[Nms]	motor viscous friction
C_d	[-]	flow discharge coefficient
D_m	[m ³ /rad]	motor displacement
i	[A]	input current
J	[kg·m ²]	moment of inertia on the motor shaft
J_L	[kg·m ²]	moment of inertia of the load
J_m	[kg·m ²]	moment of inertia of the motor
J_s	[kg·m ²]	moment of inertia of the ball screw
K_v	[m ³ /sA]	valve sizing constant
p	[m]	lead of the ball screw
P_L	[Pa]	load pressure drop
P_R	[Pa]	return pressure
P_S	[Pa]	supply pressure
P_V	[Pa]	valve pressure drop
Q_{in}	[m ³ /s]	motor internal leakage
Q_L	[m ³ /s]	control flow
T_a	[Nm]	torque due to aerodynamic forces
T_g	[Nm]	torque due to the unbalanced mass

T_f	[Nm]	torque due to friction
T_L	[Nm]	load torque
x	[m]	strut position
α	[rad/s ²]	motor angular acceleration
φ	[rad]	motor angular position
θ	[rad]	pitch angle
ω	[rad/s]	motor angular speed

References

- [1] CRAWFORD, B.L., SPELLS, C.: *Increasing Efficiency at the NTF by Optimizing Model AoA Positioning*, Proceedings of the 44th AIAA Aerospace Sciences Meeting and Exhibit, Reno, Nevada, 2006.
- [2] HAGAR, H.D., BUTLER, R.G.: *Design Philosophy for Wind Tunnel Model Positioning Control Systems*, Proceedings of the 38th International Instrumentation Symposium, Las Vegas, Nevada, 1992.
- [3] ILIC, B., MILOSAVLJEVIC, M.: *FPGA-based Embedded System for Wind Tunnel Variable-Geometry Nozzle Positioning*, Scientific Technical Review, 69(1) (2019) 3-9.
- [4] ILIC, B., MILOSAVLJEVIC, M.: *FPGA-based Embedded System for Wind Tunnel Variable-Geometry Nozzle Positioning*, Scientific Technical Review, 69(1) (2019) 3-9.
- [5] OLABANJI, O.M., MPOFU, K.: *Physical Modelling, Simulation and Experimental Analysis for Synchronizing Multiple Hydraulic Actuators*, International Journal of Mechanical and Mechatronics Engineering IJMME-IJENS, 19(04) (2020) 122-136.
- [6] QIAN, Y., OU, G., MAGHAREH, A., DYKE, S.: *Parametric Identification of a Servo-Hydraulic Actuator for Real-Time Hybrid Simulation*, Mechanical Systems and Signal Processing, 48(1-2) (2014) 260-273.
- [7] BOBROW, J., LUM, K.: *Adaptive, High Bandwidth Control of a Hydraulic Actuator*, Journal of Dynamic Systems, Measurement, and Control, 118 (1996) 714-720.



MILITARY PROVING GROUND ELECTRO-OPTICAL SURVEILLANCE SYSTEM DESIGN

SAŠA VUJIĆ

Vlatacom Institute, Belgrade, sasa.vujic@vlatacom.com and Belgrade Metropolitan University

MILOŠ RADISAVLJEVIĆ

Vlatacom Institute, Belgrade, milos.radisavljevic@vlatacom.com and Belgrade Metropolitan University

BRANKO LIVADA

Vlatacom Institute, Belgrade, branko.livada@vlatacom.com

BRANKO TOMIĆ

Vlatacom Institute, Belgrade, branko.tomic@vlatacom.com

DRAGANA PERIĆ

Vlatacom Institute, Belgrade, dragana.peric@vlatacom.com

DRAGAN DOMAZET

Belgrade Metropolitan University, Belgrade dragan.domazet@metropolitan.ac.rs

Abstract: Military proving ground is a common facility for testing of broad spectrum of military equipment, where safety of people, area security, presentation of results during the shooting tests, and general surveillance are very important. In order to obtain safety, security, efficient presentation of results during the shooting tests, and general surveillance, a surveillance system for such proving ground should be provided. Important properties of the proving ground are analysed and system requirements are defined. Based on these requirements the surveillance system is designed and implemented. The created surveillance system comprises the number of imaging sensors, including thermal and visible imaging sensors, communication network, control center and software for monitoring and control. The use of this surveillance system can have an important effect on how proving ground will be used with more efficient use and higher safety and security. Furthermore, with established surveillance system additional advancements are possible including the implementation of artificial intelligence algorithms for easier and more reliable use.

Keywords: Surveillance, imaging sensors, thermal imager, software, military proving ground.

1. INTRODUCTION

The multi-sensor surveillance system is an adaptable modular system for managing distributed imaging sensors using human observed command and control station. Current advances in imaging sensors technology and manufacturing volume provides wider application in the security related multi sensor systems [1-4].

Video surveillance technology has been used in many civil and military applications for decades. There are many known military applications including patrolling national borders, measuring the flow of refugees in troubled areas, monitoring peace treaties, and providing secure perimeters around bases and embassies [5,6], and often combined with other sensors [7].

It is important to understand system requirements and limitations to optimize surveillance system architecture according to aimed application and budget, and design system control and command software [8].

There is a widely available literature in a field of civil video surveillance, including intelligent video surveillance [9], critical asset protection, perimeter monitoring, and threat detection [10], real time surveillance of people and their activities [11]. There are also applications in combined military civil environments [12]. However, there are specific requirements for surveillance of a military proving ground, which are not widely available in literature.

A military proving ground is an outdoor area, with specially built objects, used for firing, exercises (training range) or testing of weapons and military equipment (test range). For such area there is a need not just for general surveillance but also to obtain safety, security and more efficient presentation of results during the shooting tests.

In this paper some key design decisions are discussed. The main objective of this paper is to analyze the technological and application limits of the advanced video based surveillance systems generated by specific system mission

and application environment as military proving ground is.

As a starting point we presented a basic properties of the selected proving ground facility that causes some limitation in the system architecture and generates basic requirements for system control and command software design. After that we described surveillance system architecture and application software requirements. As a final point we described software application structure and functions. All system components are manufactured and software application is tested in laboratory. The most of the hardware is deployed in the field, but some structural changes in the proving ground are not still finalized so system is not completely integrated and tested in the field. According to the results of the laboratory testing results and our previous experiences with complex electrooptical systems instalations in the field we do not expect problems.

2. THE MILITARY PROVING GROUND BASIC PROPERTIES

In order to design a surveillance system for such complex area it was necessary to perform a detail site survey. After the survey it was possible to analyze the properties of the proving ground and to define system requirements.

A satellite image of military proving ground with labeled areas and objects is shown in Figure 1.

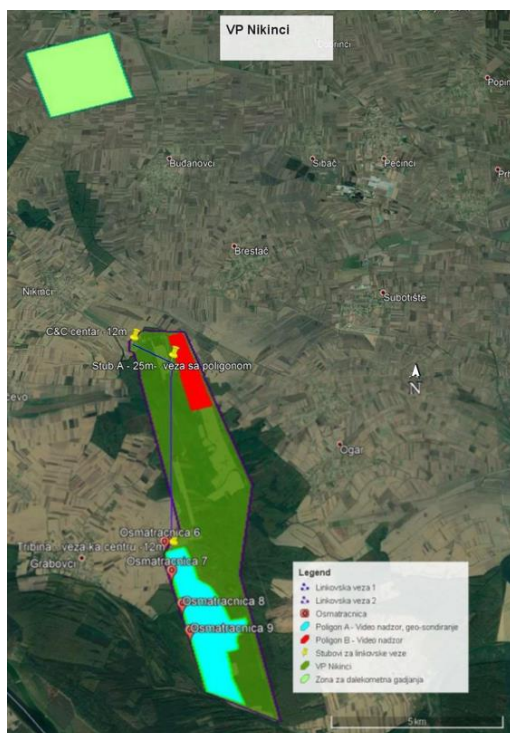


Figure 1. A satellite image of military proving ground with labels of internal areas and objects.

The military proving ground is a complex area consisting of a group of administrative buildings, and the rest is a combination of forests and meadows, where all the shooting and equipment testing is carried out, and additional objects like watchtowers. The forest is planted, about 10-15 meters high, quite dense. Meadows are used for agriculture, where wheat, corn and other agricultural crops are cultivated.

There is a need for military proving ground surveillance with combination of visible and thermal sensors, with three main purposes:

- during the shooting tests to spot a person in the area of the proving ground,
- to show the shooting to clients/visitors of the proving ground, during the shooting tests,
- security surveillance around a clock in order to detect unauthorized intrusions into the area of the proving ground.

If the person is spotted in the restricted area during the shooting, the shooting will be immediately stopped. It is not necessary that this person recognition is done automatically, but it would be sufficient for the operator in the monitoring room to see the person in the restricted area.

Safety of people is the most important, and even though there are already defined procedures and measures related to safety, it is always good to have additional insight during the firing tests provided with the surveillance system, especially having in mind that not only military proving ground employees and other people who are involved in tests, but also other people who work in the fields are expected within the area.

Military proving ground security is the next important topic, and similarly like with safety aspect, there are already defined procedures and measures related to security, however it is always good to have additional insight provided with the surveillance system, not only during the firing tests but also in any other time.

During the shooting tests there is a need to present results and real time insight is very valuable and helps to improve efficiency. With the designed solution, it will possible to achieve a significant improvement in operability and control at the proving ground itself, in a quick and effective way, which was the basic requirement.

Based on the collected information, the locations of special interest for the implementation of video surveillance project are defined and for all these locations the coverage zones for cameras are defined. Furthermore, other system requirements are defined.

3. SYSTEM ARCHITECTURE AND DESIGN

The main system components are sensors, communication network, control center and software for monitoring and control, as shown in Figure 2.

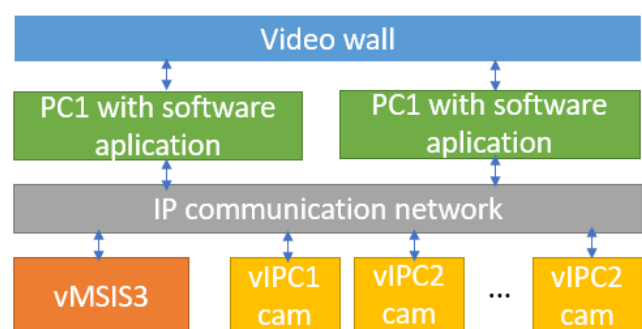


Figure 2. Main system components

The selected sensors for this application are one multisensory imaging system with thermal infrared imager and visible imager integrated on a moving positioner, and a number of fixed CCTV IP cameras. All sensors are connected to the control center through the IP network.

3.1 Imaging sensors

The multisensory imaging system with thermal infrared imager and visible imager integrated on a moving positioner, with integrated automated tracking, is custom designed for this application in order to provide optimal solution for this particular application. The thermal imager is uncooled 640x480, 17 μm pitch, LWIR detector coupled with 28-225mm focal length continuous zoom lens, providing a field of view in range from 22,26° in the wide field of view, to 2,77° in the narrow field of view. The visible imager is a color CCD sensor coupled with 23-506mm focal length continuous zoom lens, providing a field of view in range from 11,92° in the wide field of view, to 0,53° in the narrow field of view. The implemented system is shown in Figure 3.



Figure 3. vMSIS3-USD2-C225 electro-optical system with thermal and visible imagers integrated on a pan tilt positioner.

Figure 4 shows coverage zones of vMSIS3-USD2-C225 electro-optical system with 2,77° narrow field of view shown with blue, and 180° area highlighted.



Figure 4. Coverage area with vMSIS3-USD2-C225 in patrol mode of operation

The fixed CCTV IP cameras are vCAM vIPC-3M1 camera modules. The vCAM vIPC-3M1 model is a compact camera designed for indoor and outdoor use. The basic function of this camera is to capture images of the scene, convert them into video content or a series of images, and then send them via the selected telecommunications network and/or save them in the local memory (SD card).

The vCAM vIPC-3M1 camera module is shown in Figure 5.



Figure 5. vCAM vIPC-3M1 camera module

The camera modules are integrated within a standard outdoor enclosure with IP66 protection, as shown in Figure 6.



Figure 6. An IP camera in an outdoor enclosure during the installation

As in this case observation of areas at longer distances is required, the VIPC-3M1 camera is configured to be used with a viewing angle of 30°, for which a human recognition range of up to 400m is expected.

Figure 7 provides coverage zones of fixed vCAM vIPC-3M1 cameras from planned locations.



Figure 7. Area coverage with vCAM vIPC-3M1 cameras configured with 30° field of view

3.2 Network parameters configuration

The communication network is reliable IP network based on fiber optical physical layer and standard passive and active equipment configured for particular need. In Figure 8 is shown block schematic of communication network.

In order to use the network bandwidth in optimal way, all equipment, including the cameras is configured to operate in broadcast mode of operation.

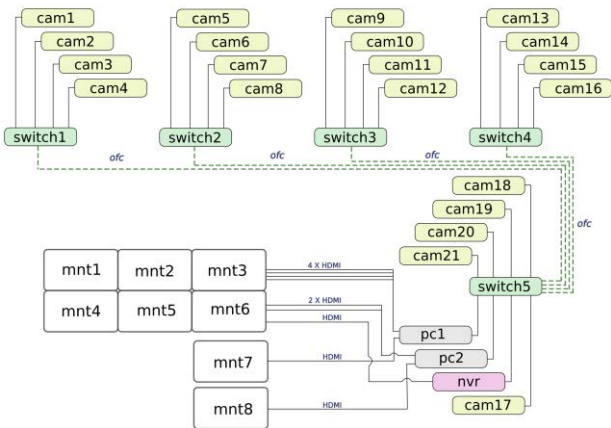


Figure 8. IP communication network

All IP camaras are configured in line with defined IP address plan as shown in Figure 9.

ip/adress	Proizvodjac	Model	oznaka	s/n	IP addr	Subnet	Gateway
...	...	ME5288P	switch1	PM28004258	10.10.10.10	255.255.255.0	10.10.10.01
...	...	vGm VPC-3M2	cam01	DSLR-4031017	10.10.10.11	255.255.255.0	10.10.10.01
...	...	vGm VPC-3M2	cam02	DSLR-4031020	10.10.10.12	255.255.255.0	10.10.10.01
...	...	vGm VPC-3M2	cam03	DSLR-4031021	10.10.10.13	255.255.255.0	10.10.10.01
...	...	vGm VPC-3M2	cam04	DSLR-4031022	10.10.10.14	255.255.255.0	10.10.10.01
...	...	ME5288P	switch2	PM28004125	10.10.10.20	255.255.255.0	10.10.10.01
...	...	vGm VPC-3M2	cam05	DSLR-4031023	10.10.10.21	255.255.255.0	10.10.10.01
...	...	vGm VPC-3M2	cam06	DSLR-4031024	10.10.10.22	255.255.255.0	10.10.10.01
...	...	vGm VPC-3M2	cam07	DSLR-4031027	10.10.10.23	255.255.255.0	10.10.10.01
...	...	vGm VPC-3M2	cam08	DSLR-4031029	10.10.10.24	255.255.255.0	10.10.10.01
...	...	ME5288P	switch3	PM28003211	10.10.10.30	255.255.255.0	10.10.10.01
...	...	vGm VPC-3M2	cam09	DSLR-4031087	10.10.10.31	255.255.255.0	10.10.10.01
...	...	vGm VPC-3M2	cam10	DSLR-4031046	10.10.10.32	255.255.255.0	10.10.10.01
...	...	vGm VPC-3M2	cam11	DSLR-4031065	10.10.10.33	255.255.255.0	10.10.10.01
...	...	vGm VPC-3M2	cam12	DSLR-4031012	10.10.10.34	255.255.255.0	10.10.10.01
...	...	ME5288P	switch4	PM28007053	10.10.10.40	255.255.255.0	10.10.10.01
...	...	vGm VPC-3M2	cam13	DSLR-4031013	10.10.10.41	255.255.255.0	10.10.10.01
...	...	vGm VPC-3M2	cam14	DSLR-4031014	10.10.10.42	255.255.255.0	10.10.10.01
...	...	vGm VPC-3M2	cam15	DSLR-4031015	10.10.10.43	255.255.255.0	10.10.10.01
...	...	vGm VPC-3M2	cam16	DSLR-4031019	10.10.10.44	255.255.255.0	10.10.10.01
...	...	ME5288P-AC	switch5	E532012754	10.10.10.50	255.255.255.0	10.10.10.01
...	...	vGm VPC-3M2	cam17	DSLR-4031045	10.10.10.51	255.255.255.0	10.10.10.01
...	...	vGm VPC-3M2	cam18	DSLR-4031031	10.10.10.52	255.255.255.0	10.10.10.01
...	...	vGm VPC-3M2	cam19	DSLR-4031030	10.10.10.53	255.255.255.0	10.10.10.01
...	...	vGm VPC-3M2	cam20	DSLR-4031011	10.10.10.54	255.255.255.0	10.10.10.01
...	...	vMSIS3-USD-C225-S2	cam21	DS-4X909C1001	10.10.10.55	255.255.255.0	10.10.10.01
...	...	Intel® E 2800/2658	pc1		10.10.10.56	255.255.255.0	10.10.10.01
...	...	Intel® E 2800/2658	pc2		10.10.10.57	255.255.255.0	10.10.10.01
...	...	Intel® V919222-4MS2E	nvr	7E077FPAZ70B27	10.10.10.58	255.255.255.0	10.10.10.01
...	...	servisni recunov			10.10.10.100	255.255.255.0	10.10.10.01

Figure 9. IP address plan

3.3 Control center

The control center comprises number of video monitors and PC computers with installed software applications for particular application. PC computers are connected and configured to the same network as shown in Figure 8. In order to provide users with more convenient and user-friendly environment a video wall is implemented containing 6 monitors in two rows and three columns as shown in Figure 10. Two monitors will be used for two video streams from multisensor imaging system vMSIS3-USD2-C225, and four monitors will be used for presentation of video streams from fixed vCAM vIPC-3M1 cameras.



Figure 10. Assembling of monitors for 2x3 video wall

For this application a software application with graphical user interface is designed to be able to effectively use a number of IP cameras, which will be described in more details in the following section.

4. SOFTWARE ARCHITECTURE AND DESIGN

As part of this military proving ground video surveillance, it was necessary to develop a software application with a graphical user interface, for the simultaneous display of a number of video streams on one or more monitors. Based on system requirements the software application requirements are defined. The software application is designed to work with video streams using the RTSP protocol and with h.264 compression. The number of simultaneously accepted and displayed streams should be limited only by hardware resources (network, processor, memory, number and size of monitors), and not by the software application implementation. The software application should be designed so that it does not impose an exact limit on the number of video streams. Special attention should be on design of graphic user interface, and it is assumed that a single operator should serve the software application at runtime.

The software application should run on a standard desktop PC running Windows 10 or later. The existence of at least one network adapter with speed of 100Mbps or more is expected. For the display of video streams, it is assumed that a maximum of four monitors per computer will be used. Under one instance of the operating system, it will be possible to run only one instance of the software application at a time.

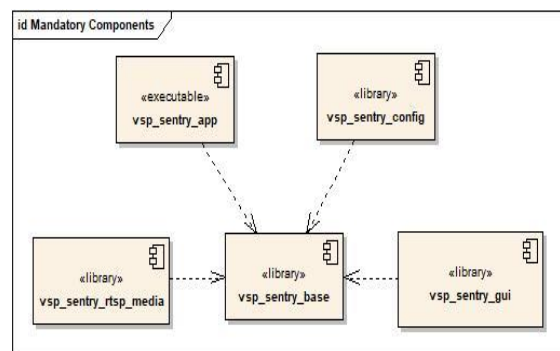


Figure 11. Mandatory components of the software application.

Based on system requirements the software requirements are defined in Vlatacom Institute document “VSP Sentry Functional Specification”, and the technical specification was created in Vlatacom Institute document “VSP Sentry Technical Specification – version 1.0.0.”.

The main functionality of the software application is presentation of video streams. The screens for displaying video streams are arranged on the layout space in a matrix form with cells of equal size. The number of types and columns of that matrix depends on the number of open screens for displaying video streams. The number of species is always equal to, or one less than, the number of columns. Some examples of the dimensions of this matrix depending on the number of video streams are given in the **Table I**.

Table I. Examples of the dimensions of this matrix depending on the number of video streams.

Number of video streams	Dimension of the matrix display
1	1x1
2	1x2
3, 4	2x2
5, 6	2x3
7, 8, 9	3x3

Opening a new screen to display the stream redistributes depending on the number of open screens and the current dimension of the matrix view. If necessary, a new column or type is added to the matrix display, and the newly opened screen is displayed in the first free cell. The content of the empty cells of the screen layout for displaying video streams should be designed according to the marketing aspect of the application.

The implemented software application consists of several executable components – the software application itself and several shared libraries. The software application is developed within a WPF application project. Other projects are standard Windows dynamic linked libraries. The project is structured this way in order to obtain modularity to the software application, and to be able to easily add a set of features to the software application, or to remove it. Therefore, related features are grouped closely in a single library that may or may not be incorporated into the final configuration of the software application. Some libraries are mandatory to be included in whatever configuration. Minimal set of components is shown in Figure 11.

5. RESULTS AND DISCUSSION

The multisensory imaging system with thermal infrared imager and visible imager integrated on a moving positioner has been implemented and tested in laboratory conditions. In Figure 12 image taken with thermal imager with laboratory collimator is shown, and in Figure 13 image taken with thermal imager at narrow field of view (2,77°) with scene of building at 4km distance.

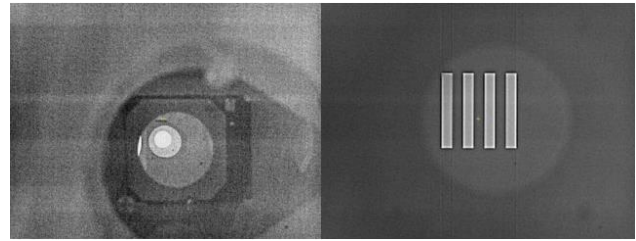


Figure 12. Wide and narrow field of view in laboratory



Figure 13. Narrow field of view (2,77°) – scene with building at 4km distance

The camera modules integrated within a standard outdoor enclosure with IP66 protection are installed on watchtowers. Examples of the camera installations are shown in **Figure 14**. and **Figure 15**.



Figure 14. Cameras installed on the watchtower



Figure 15. View from watchtower with installed cameras

Software application is implemented and tested in laboratory conditions (with outdoor view of cameras) and proved that it is ready for test on the field.

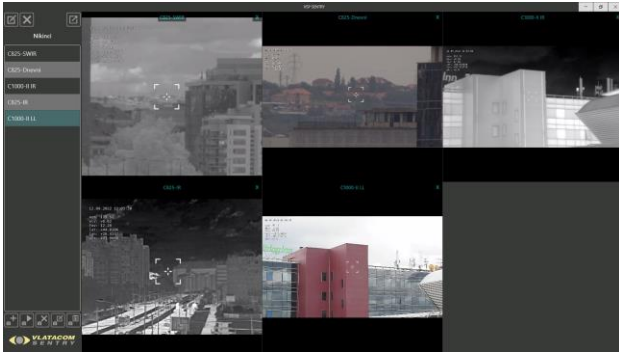


Figure 16. Screenshot of software application GUI during the development and tests

6. CONCLUSION

The surveillance system has been designed and implemented, and partially deployed in the field. In order to put it in full production additional infrastructure work at the military proving ground needs to be done. With the system implemented on the military proving ground, the users will be able to perform testing of military equipment with improved safety and security, and more efficiently. They will be able to monitor and present the results during the shooting tests in a way that was not possible before implementation of this system.

Further development can be focused on the introduction of the additional software application functions:

1. Situational overview of surveillance system cameras.
2. Interactive situational overview of cameras that allows opening and arranging streams for display.
3. Support for recording video streams directly from the software application, or using external accessories and software (NVR).
4. Introduction of alarms based on video analysis - motion detection
5. Classification of detected objects - human, vehicle, animal...
6. Expanding the ability to arrange streams on stream control panels.

Acknowledgment

Authors would like to thank Vlatacom Institute for equipment and support which enabled continuous work and improvements in the field of electro-optics. This work was undertaken within the Vlatacom Institute project P145.

References

- [1] PERIĆ,D., LIVADA,B.: *Technical, technological and application limitations of the electro-optical surveillance systems*, 8th International Conference on Defensive Technologies, OTEH 2018, Belgrade, Serbia, 11-12 October 2018
- [2] GREIFFENHAGEN,M., COMANICIU,D., NIEMANN,H., RAMESH,V.: *Design, analysis and engineering of video monitoring systems: an approach and case study*, The Proceedings of the IEEE, vol. 89, no. 10, pp. 1498- 1517, October 2001
- [3] TSAKANIKAS,V., DAGIUKLAS,T.: *Video surveillance systems-current status and future trends*, Computers & Electrical Engineering, Volume 70, 2018, Pages 736-753, ISSN 0045-7906,
- [4] REGAZZONI,C.S., FABRI,G., VERNAZZA,G. (Editors): *Advanced video-based surveillance systems*, Springer Science+Business Media, New York, 1999
- [5] COLLINS,R., et al.: *A system for video surveillance and monitoring*, VSAM Final Report, Technical Report, CMURI-TR-00-12, May 2000
- [6] FORESTI,G.L., MÄHÖNEN,P., REGAZZONI,C.S. (Editors), *Multimedia video-based surveillance systems: Requirements. Issues and Solutions*, Springer Science+Business Media New York, 2000
- [7] FARINA,A., ORTENZI,L., RISTIC,B., and SKVORTSOV,A.: *Integrated Sensor Systems and Data Fusion for Homeland Protection*, Chapter 22 in Academic Press Library in Signal Processing, 2014; 2: 1245–1320, doi: 10.1016/B978-0-12-396500-4.00022-3.
- [8] PERIĆ,D., VUJIĆ,S., LIVADA,B.: *Multi-sensor system operator's console: Towards structural and functional optimization*, 7th International Conference on Defensive Technologies, OTEH 2016, Belgrade, Serbia, 6-7 October 2016
- [9] DUFOUR,J.Y.(Editor): *Intelligent Video Surveillance Systems*. ISTE Ltd. London and John Wiley & Sons Inc., New York, 2013
- [10] LIPTON,A.J., HEARTWELL,C.H., HAERING,N., and MADDEN,D., *Critical Asset Protection, Perimeter Monitoring, and Threat Detection Using Automated Video Surveillance*, white paper, ObjectVideo
- [11] HARITAOGU,I., HARWOOD,D. and DAVIS,L.S., *W4: Real time surveillance of people and their activities*, IEEE Trans. Pattern Anal. Machine Intell., vol. 22, no. 8, pp. 809–830, Aug. 2000.
- [12] SKINNER,C.J., COCHRANE,S., FIELD,M., JOHNSTON,R.: *Defence Against Terrorism: The Evolution of Military Surveillance Systems into Effective Counter Terrorism Systems Suitable for Use in Combined Military Civil Environments. Dream or Reality?*, DTIC ADA460826, NATO Conference paper MP-SCI-158-25, October 2004



10th INTERNATIONAL SCIENTIFIC CONFERENCE ON DEFENSIVE TECHNOLOGIES OTEH 2022

Belgrade, Serbia, 13 – 14 October 2022



APPLICATION OF INFRARED THERMOGRAPHY IN MONITORING OF PETROL ENGINE WITH AIR COOLING

LJUBIŠA TOMIĆ

Technical Test Center, Belgrade, ljubisa.tomic@gmail.com

GORDANA MAJSTORVIĆ

Military Academy, University of Defence in Belgrade, majstor1962@gmail.com

NENAD MUNIĆ

Technical Test Center, Belgrade, nenadmunic@yahoo.com

NENKO BRKLJAC

Technical Test Center, Belgrade, brkljacnenko@gmail.com

ALEKSANDAR KOVAČEVIĆ

Faculty of technical sciences, B University of Kragujevac, Čačak, aleksandarkovacevic1962@yahoo.com

DARKO VASILJEVIĆ

Institute of Physics, University of Belgrade, darko@ipb.ac.rs

Abstract: *Infrared thermography has emerged, over the past few years, as an attractive and reliable technique of non-destructive testing in cases such as testing different materials and monitoring the operation of complex systems. The paper presents the possibilities of wide application of infrared thermography for monitoring the operation of a four-stroke petrol engine BMW and a three-cylinder petrol engine OPEL CORSA 1.0. A quantitative analysis of the temperature of parts of the engine made of different materials was carried out during the operation of the open engine with air cooling.*

Keywords: *pulsed thermography, non-destructive testing, infrared thermography, petrol engine.*

1. INTRODUCTION

Infrared thermography (IRT) based on infrared radiation, provides particular advantages in different fields, as it is non contact, non invasive technique [1]. Any object which has a temperature above the temperature of absolute zero (i.e., $T > 0\text{K}$) emits infrared radiation (spectral range $> 0.7 \mu\text{m}$) [2, 3]. Measuring devices acquire infrared radiation emitted by an object and transform it into an electronic signal producing a detailed infrared image of the scene, since the human eye cannot see this type of radiation. Infrared camera detects the radiations emitted by the heated object and presents it in the form of a thermogram.

Thermographic testing may be used to record of the operating temperature distribution on the certain visible parts of engine. It is known that not all parts of the engine are made of the same material, and hence the exposure of materials of a particular engine to a higher temperature. The deviation of the measured temperature from the referent range one indicates the malfunction of the discharge of the cooling water supply hose, combustion of seals made of rubber and other poles, etc., as well as permanent damage to engines requiring general overhaul.

In this paper, we present the results of using IRT technique for temperature monitoring of parts of four-stroke petrol engine BMW 325i and a three-cylinder petrol engine OPEL CORSA 1.0. The thermal imaging are used for calculation and estimation temperatures of chosen parts of the engine.

2. THE TEMPERATURE MONITORING OF ENGINE HEATING BY TERMOVISION CAMERA

In the following text, an attempt were made to measure the thermogram of the engine in operation and investigate the possibilities of using an infrared (IC) camera to monitor the operation of the engine heating. The thermograms of temperature distributions on the surface of the engine in function of time were used for calculation and estimation temperatures of chosen parts of the engine.

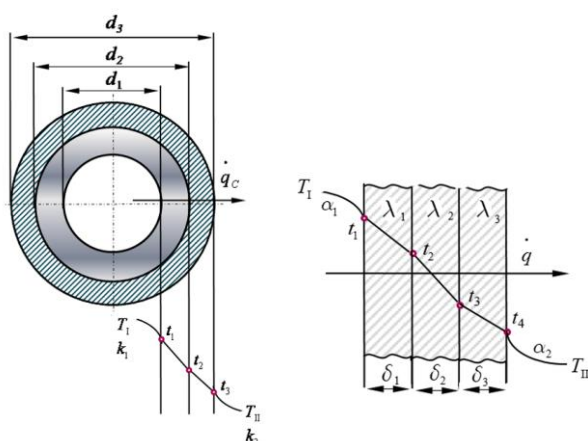
2.1. Description of engine and his parts to be monitored

Depending on the types of energy that motor drive machine converted into mechanical work exist:

- electric,
- thermal, hydraulic,
- pneumatic motors, etc..

Especially, internal combustion engines belong to the group of heat engines, which are used in everyday use for mastering an external resistance and the realization of a work. This type of engines are used in land, water and air transport, agricultural and heavy machinery, industrial and aggregate application and others.

Some description of parts that are observed by thermal imaging camera we will only give in this text. Recordings were made on: electromagnetic valve and cooling pipe tube which enters the engine.



a) b)

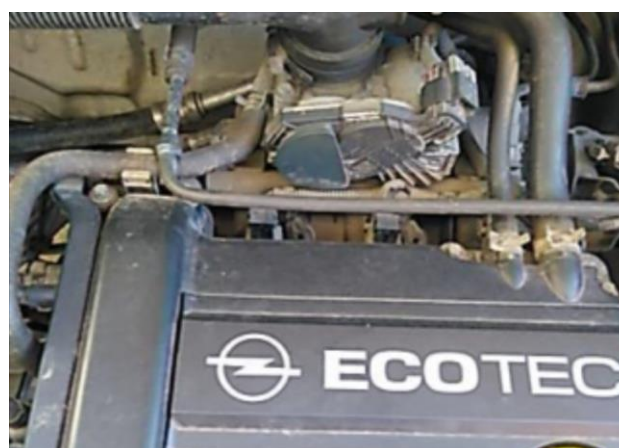
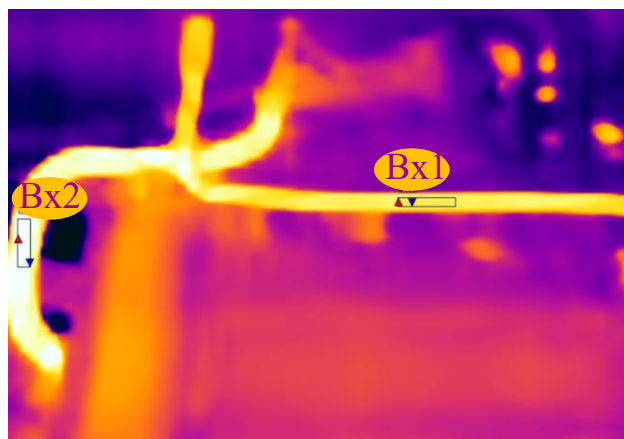
Picture 1. Example of: a) radial heat flow in a cylinder and b) heat flow through a $n=3$ parallel layers flat wall.

2.2. Thermographic testing of the engine heating

Observed parts with different geometries that are made of materials of different thermal conductivity and corresponding temperatures of the points were obtained by analyzing the thermogram of these parts. Further, temperatures of the interior wall of the depicted parts can be calculated.

The selected engine regions are the cooling pipe tube which enters the engine (Bx1 and Bx2, respectively) of the CORSA 1.0 ECOTEC engine. Further, selected region is electromagnetic valve of the BMW 325i (Bx3). Thermograms of the chosen parts of engine during heating and photography of the engines with those areas are shown in Pictures 2. and 3.

The process of heat transfer between two fluids separated by a solid wall, when there is simultaneous heat transfer by convection and conduction, is called heat passage. The heat transfer from the internal fluid to the wall of the tube and from the outer surface of the tube to the other fluid is via convection, while the heat exchange through the layers of the tube is conduction.



Picture 2. The upper part: infrared image acquired during operation and heating of the engine and lower part: photography of the engine CORSA 1.0 ECOTEC.

The specific heat flux in the case of a heat passage through an n parallel layers flat wall, see part b) in Picture 1, is given [5]:

$$\dot{q} = k (T_I - T_{II}) \quad (1)$$

while resistance to heat transfer generally is calculated by the equation:

$$\frac{1}{k} = \frac{1}{\alpha_I} + \sum_{i=1}^n \frac{\delta_i}{\lambda_i} + \frac{1}{\alpha_{II}} \quad (2)$$

where is: \dot{q} - specific heat flux; k - coefficient of heat transfer through a flat wall, in general, for a multi-layer wall; $1/k$ - resistance to heat transfer from convection and conduction; λ - coefficient of heat conductivity; δ - wall thickness; α - heat transfer coefficient.

The specific heat flux \dot{q}_C (per unit length of the tube) in the case of a heat transfer through the wall of an infinite tube, see part a) in Picture 1, is given [5]:

$$\dot{q}_C = k (T_I - T_{II}) \quad (3)$$

Resistance to heat transfer (per unit length of tube) in generally case is given:

$$\frac{1}{k_C} = \frac{1}{d_1 \pi \alpha_1} + \frac{1}{2 \pi \lambda_i} \sum_{i=1}^n \ln \frac{d_{i+1}}{d_i} + \frac{1}{d_{i+1} \pi \alpha_{II}} \quad (4)$$

where is: q_C - specific heat flux per unit length of tube; k_C - coefficient of heat transfer through wall per unit length of tube; d - tube diameter.

The interior wall temperatures of the designated parts, see upper parts of Picture 2. and Picture 3., with different geometries and materials, applying equations (1) – (4) are estimated with coefficient values listed in Table 1.

Table 1. Thermal properties of some materials [5].

Material	Coefficient of heat conductivity λ [W/m·K]	Heat transfer coefficient $\frac{1}{\alpha}$ [W/m ² ·K]
Aluminum	229.111	-
Brass	102.3	-
Isolation	0.05	-
Plexiglas	0.195	-
Fuel mixture	-	5000

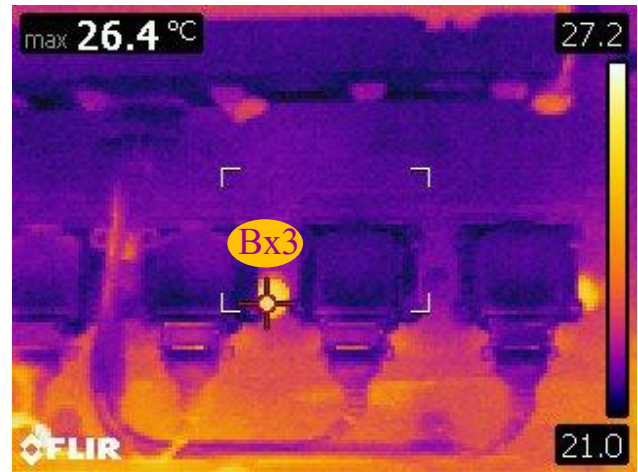
The term oil vapor in Table 1. is heat transfer coefficient from the oil vapor to the interior surface of the tube. The wall of the syringe is heat transfer coefficient from the wall of the syringe to the surrounding air and fuel mixture is heat transfer coefficient from the fuel mixture to the interior surface of the flat wall.

3. RESULTS

Thermograms that are recorded corresponds heating engine operation. Thermogram of the engine during heating and photography of the engine are shown in upper and lower parts of Picture 2. and Picture 3.

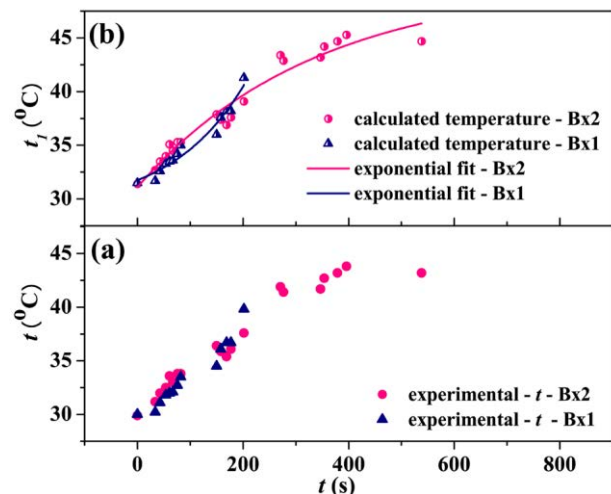
Temperature distributions on the surface of the engine (average temperature value of all pixels in corresponding areas while the surrounding temperature during experiment was 22°C) [6, 7, 8] as a function of time were obtained and analyzed, see Picture 4 and Picture 5. The temperature of outer wall of depicted areas in the mentioned cases, randomly increases with time.

The temperature of interior wall of electromagnetic valve is calculated by equations (3) and (4) with constants of thermal properties listed in Table 1. In this case temperature difference between outer and interior wall is different, see parts (a) and (b) in Picture 5. This can be explained by the existence of isolation materials in this case.



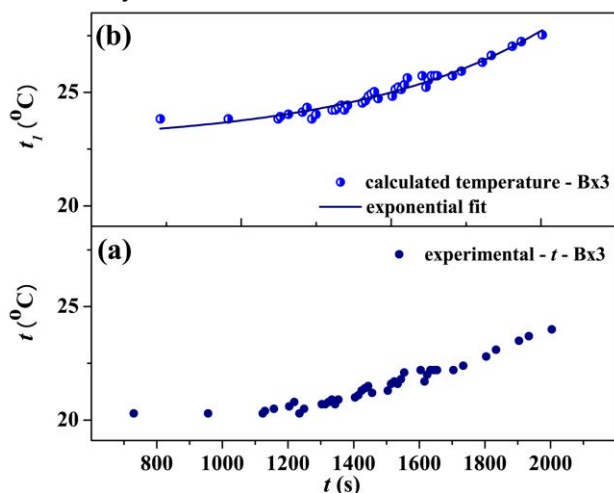
Picture 3. The upper part: infrared image acquired during operation and heating of the engine and lower part: photography of the engine BMW 325i.

In the case of thinner brass cooling tube, for Bx1, model function of temperature distribution as a function of time is: $t_1 = 2.8135 \exp(-t/ -141.636)) + 28.926$ while the model function of temperature distribution as a function of time



Picture 4. The dependence upon time of (a): temperature of outer walls of thinner brass cooling tube Bx1 and thicker Bx2 and (b): calculated temperatures (t_1) of interior walls of regions Bx1 and thicker Bx2.

for thicker brass cooling tube Bx2 is: $t_1 = -19.1179 \exp(-t/-336.387) + 50.206$. The temperature of interior and outer wall are similar because of good thermal conductivity of material.



Picture 5. The dependence upon time of (a): temperature of outer wall, Bx3 (b) temperature distributions of the interior wall.

In the case of a heat transfer through a flat wall with parallel layers, Bx3, temperature of interior wall of this case is estimated using equations (3) and (4) with constants values listed in Table 1. Temperature distribution as a function of time of Bx3 are modeled by: $t_1 = 0.2185 \exp(-t/-639.3) + 22.17$.

There are temperature difference of outer and interior wall in the case of Bx3, see parts a) and (b) in Picture 5. The lower temperature correspond the outer wall.

4. CONCLUSION

The paper gives a description of thermovision temperature distribution on certain parts of the motor. Considering the type of materials as well as geometry of the parts and based on thermodynamic constants and available data, the thermodynamic characteristics of these chosen parts are calculated. In the case of brass cooling tube, temperature difference between outer and interior wall isn't significant. This can be explained by the good thermal conductivity of material. The temperature of interior and outer wall in the case of electromagnetic valve are more significant because of the existence of isolation materials in this case.

In the further work iteration, and on the basis of the obtained results, certain conclusions can be drawn about the associated load of these operations in the same way as the occurrence of any damage as a result of the occurrence of unauthorized temperature loads. This procedure gives great importance to the thermal imaging surveillance of their results and processing them are coming in fast and easy way.

References

- [1] Vollmer, M., Möllmann, K.P., *Infrared Thermal Imaging: Fundamentals, Research and Applications*, Wiley: Weinheim, Germany, 2011.
- [2] Barbarić, Ž., *Termovizija formiranje i primena termovizijske slike*, Akademska Misao, Beograd, 2014.
- [3] Usamentiaga R., Venegas P., Guerediaga J., Vega L., Molleda J. and Bulnes F. G., *Infrared thermography for temperature measurement and non-destructive testing*, Sensors, 2014, pp.12305-12348, 14.
- [4] Pešić, Z., Muždeka, S., Perić, S., Krsmanović, M., Grkić, A., Rakić, S., *Motori i motorna vozila*, Ministarstvo odbrane VS, Beograd, 2009.
- [5] Kozić Đ., Vasiljević B., Bekavac V., *Priručnik za termodinamiku*, Mašinski fakultet, Univerzitet u Beogradu, Beograd, 1987.
- [6] Tomić Lj. D., Elazar J. M., *Pulse thermography experimental data processing by numerically simulating thermal processes in a sample with periodical structure of defects*, NDT & E International, Volume 60, December 2013, Pages 132-135
- [7] Tomić Lj., Jovanović D., Jovičić S., Karkalić R., Dikić G., *The Aircraft Structural Elements Corrosion Study Using Strain Gauge Method and Pulse Video Thermography*, Scientific Technical Review, 2015, Vol.65, No.4, pp. 55-61
- [8] Janković D., Vasiljević D., Majstorović G., Tomić Lj., Kostić I., Perić S. and Dikić G., *Application of infrared thermography in monitoring of diesel engine with air cooling, 8th International scientific conference on defensive technologies*, 2018, (OTEH 2018), Belgrade, Serbia, 11-12 October 2018., pp. 60-63



PERFORMANCE COMAPRISON OF METALLIC REFLECTOR AND PRINTED PLANAR ANTENNAS FOR MOBILE INFANTRY RADARS

BORO RELJIC

Institute RT-RK Computer based systems, Novi Sad, Serbia, bora_relic@hotmail.com

ZORAN GOLUBICIC

Institute RT-RK Computer based systems, Novi Sad, Serbia, golubicic.zoran@gmail.com

IGOR DOTLIC

Institute RT-RK Computer based systems, Novi Sad, Serbia, dotlic@gmail.com

SVETISLAV MARIC

University of California San Diego, Division of Extended Studies, La Jolla, CA, USA, email@domen.com

MARIJAN HERCEG

RT-RK Institute for Computer Based Systems, Osijek, Croatia, email@domen.com

Abstract: *The paper analyzes performances of metallic reflector and printed planar antennas aimed for application in modern mobile ground based infantry radars. It is known that metallic reflector antennas might generally have better gain comparing to classical printed planar antenna solutions. The paper however shows that when all major parameters are taken into account for both antenna classes in this kind of application including electrical, mechanical, and economical - conclusion is that printed planar antennas that employ modern technologies and design approaches on one side could realize gain figures that are close to metallic reflector antenna ones while on the other side overall performances push them considerably above metallic reflector antennas and make them better and more effective solution in such applications.*

Keywords: *Sensor, Radar, Infantry radar, Antenna, Printed Antenna, PCB antenna, Reflector antenna.*

1. INTRODUCTION

Surveillance radars now days represent common equipment used by defense forces, various governments security agencies and even for some civil applications as they have various advantages over optical/IR systems and other methods.

Today's trends for portable radars/sensors implicate the following performance requirements:

- Mobility (even handling by a single person)
- Lightweight
- Small size
- Longer detection ranges
- Higher resolution
- Low transmitting power
- Low radio siginture
- Powerfull processing of raw data to achieve:
- intelligent detecion, classification and target activity analysis
- High reliability in various environments.

All these requirements have implication to various elements of the radar system. One of them is antenna that is at common infantry radar frequencies usually largest

and block of considerable importance as it establishes several major radar parameters, e.g.: bearing/angular resolution, available S/(N+I) level, sensitivity, maximal target detection range, mass, size, mobility, required output power levels, etc.

This article analyzes performance and compares two antenna classes:

- classical metallic parabolic reflector antenna and
- planar printed antenna arrays

from the perspective of integrability and system performances of infantry surveillance radar IP-15 which design is described [1], [2].

2. CURRENT SOLUTION, REQUIREMENTS OF NEW GENERATION

Original version of IP-15 radar uses metallic (parabolic) reflector antenna and it is realized in waveguide technology. On one side its 3d shape do not enable integration (for that - planar structures are required) and on the other side its depth is too big and causes additional difficulties. Also waveguide technology, though it offers low losses, is cumbersome and doesn't enable easy integration of an antenna into a compact system.

So the new solution generally needs planar antenna design as it directly help to improve: size, mass, mobility, and achieve high level of integration of all radar components, improve reliability and achieve cost effective solution. Though planar antenna could be realized in various technologies – here PCB technology is considered as a most effective one to achieve set goals.

In Table 1 comparison of major parameters are listed for two antenna classes for portable radar/sensor applications: reflector antennas and planar flat panel PCB antenna arrays [3], [4], [5] and [6]. PCB antenna arrays properties listed in the column 3 represent current state of the art without novel technologies and solutions proposed in the paper. Performances that could be achieved with that novel technologies applied to PCB antennas (based on experience and various antenna experiments) are listed in the column 4.

Table 1. Comparison of Reflector and PCB antennas

ANTENNA PROPERTIES			
ELECTRICAL:	Metallic reflector antenna	Flat Panel PCB array, Current SoA 1)	Flat Panel PCB array, Novel 2)
Gain (G)	High, very High	Medium	High 3)
Directivity (D)	High, very High	High, Very High	High, Very High
3dB Beam Width, Azimuth	Narrow, very Narrow	Narrow, Very Narrow	Narrow, Very Narrow
Efficiency (η)	High, very High	Medium	High 3)
Side Lobe Level (SLL)	Low, very Low	Medium	Low 3)
Front / Back (F/B)	High, very High	High, Very High	High, Very High
Return Loss (RL)	High	Medium	High
Frequency (Fc)	Low, High, very High	Low, Medium	Low, High 3)
MECHANICAL			
Size	Big	Medium, Small	Medium, Small
Depth	Big	Thin, Very Thin	Thin, Very Thin
Technology	Metallic parabolic reflector W/G/CX port	PCB, Planar/ Flat Panel W/G/CX port	PCB, Planar/ Flat Panel W/G/CX port
No. elements	Single antenna	Antenna array (>200 antenna elements)	Antenna array (>200 antenna elements)
Mass	Bulky, Considerable	Lightweight, Compact	Lightweight, Compact
Cost	Medium, High	Low, Medium	Low, Medium
Rigidity, compactness	Medium, High	Low, Medium	Medium, High

- 1) current State of the Art (SoA), classical approaches
- 2) with new technologies and solutions applied by the authors
- 3) limits are not established

Note: for metallic reflector antennas - parameter ranges that are considered here represent only what is reasonable to fit within portable infantry radar size constraints. It is well known that parabolic reflector antennas could achieve very high levels of directivity and gain with appropriate big reflectors size. However it is obvious that size of the reflector that is in the ranges of 1m and above is completely impractical for these applications.

3. PCB PLANAR ANTENNA SOLUTIONS

3.1. State of the art

General block scheme and various elements of Flat panel PCB antenna for radar applications is show in Fig.1.

Based on Table 1 (column Current State of the Art, SoA) conclusion is that PCB antennas can not compete reflector antennas in several major parameters. As a result PCB antenna arrays have not been used much for these applications though there were some attempts even at lower microwave frequencies (e.g. X band) however without much success. One very promising and advanced approach would be to use Boro arrays [6] (as of their inherent low losses and reduced feeding network) – however up to now no specific project for that have been launched.

Essentially major reason why PCB antenna cannot compete reflector ones is so called “gain saturation effect” combined with some mechanical issues.

As it is known when size of PCB antenna array is increased (to increase aperture of the antenna, directivity and gain) – gain and directivity are also increasing. However at some point (depending on frequency, losses, etc.) – when antenna size increases further - gain initially begin to saturate and by going further it starts even to decrease (while directivity still increases). That “gains saturation effect” is direct consequence of increased losses in feeding network.

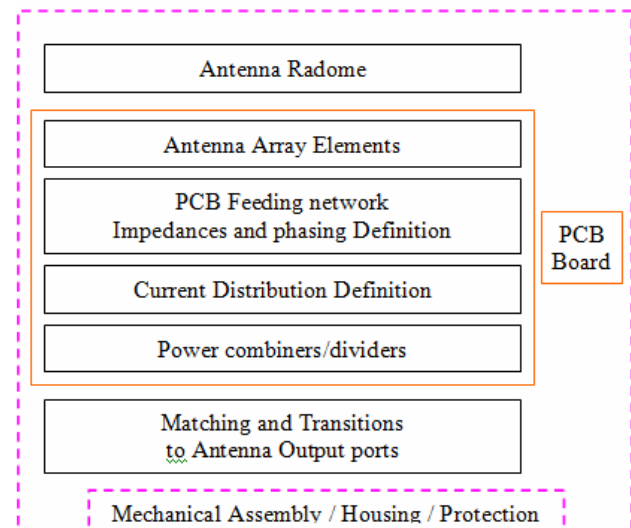


Figure 1. General block diagram of PCB antenna.

As of gain saturation effect - up to now current state of the art has enabled manufacturing of flat panel PCB antennas only with medium gain levels at microwave frequencies however that is not enough for portable radar applications. Generally speaking gain levels above ~25dBi were practically impossible to achieve at microwave frequencies (especially higher ones) with high efficiency and decent antenna size.

3.2. Advanced design approaches

By working extensively on various PCB antenna classes and by analyzing major drawbacks of current state of the art and PCB antenna solutions it has been concluded that considerable advances and breakthrough could be achieved with PCB antennas however with novel concepts and technologies.

In Figure 1 it is shown general block diagram of radar antenna that employs PCB technology. For this application particular attention has to be devoted to rigidity, mechanical construction, radome and environmental protection as equipment is normally deployed in harsh environment. This is also important as it is known that PCB antenna core itself is quite fragile.

Major new technological elements and solutions for PCB based antennas that could considerably boost up their performances are:

1. Antenna element design and performances
2. Connection of antenna elements to feeding network
3. Current distribution type
(currently Uniform and Binomial are generally used, however more efficient ones like Dolph-Chebyshev are not used probably as there were no solutions for implementation of such current distribution scheme)
4. Current distribution implementation
(i.e. physical definition of amplitudes and phases of required current distribution in chosen technology)
5. Feeding network and losses reduction
6. Solutions less sensitive to production tolerances
7. Power combining of subarrays to ensure high efficiency and reduce losses
8. Implementation of required output ports, interfaces between PCB and Front End block
9. Design of necessary transitions with high efficiency
10. Combining optimal transmission lines in antenna system, etc

Technologies and solution under listed points above are new ones and not previously used and published in open literature (except perhaps couple, however only partially and at basic level without deeper analysis). Extensive research and necessary experiments have been performed to confirm viability and quality of such technologies and solutions. Based on simulation and experimental results it is concluded that approach that includes above listed technologies offers considerable performance improvements and realization of high efficiency PCB antennas. And also major electrical performances (e.g. gain) of such PCB antennas could definitely satisfy requirements for portable radar application and could be comparable to or better than reflector antenna ones.

4. PCB ANTENNA - ADVANCED SOLUTIONS

4.1. Antenna design

Based on the analysis initial task is set to design a PCB antenna for initial feasibility analysis and compare its performances with reflector antenna from IP-15 radar system.

This feasibility model includes only few elements from the previous list with the goal to check general performances i.e., beam width, side lobe levels (SLL), size, mass etc and compare with the reflector antenna. Etc As only few elements (1, 2, 3, and partially 4, 5) of previously listed improvements are applied and also as of production tolerances expectation is that some parameters (e.g. realized gain level) of this breadboard model would not show maximal figures (and get close to reflector antenna), however plan is to tackle maximum gain level in the next step.

Major goal of this prototype is just to asses overall electro-mechanical performances, confirm it has potential to replace reflector antnena and confirm that gain could be further improved considerably at the next step.

The PCB antenna arrays consist of 256 antenna elements with Dolph-Chebyshev current distribution implemented. In Fig. 2 PCB antenna array with reflector plate and some mechanical supporting element is shown. As of clarity radome is not shown.

Simulated model with 3d radiation pattern is shown in Fig.2.

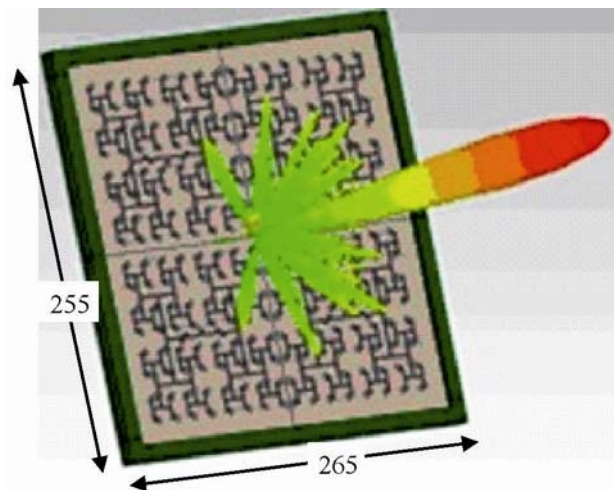


Figure 2. 3d model of prototype antenna (radome is not shown)

Radiation patterns, 2d plots, of the PCB antenna are shown in Fig. 3 (E plane) and in Fig.4 (H plane).

Simulation shows that PCB antenna has high directivity ($\sim 30.5\text{dBi}$) and gain ($\sim 28.5\text{dBi}$) with side lobe level (SLL) $\sim 20\text{dB}$.

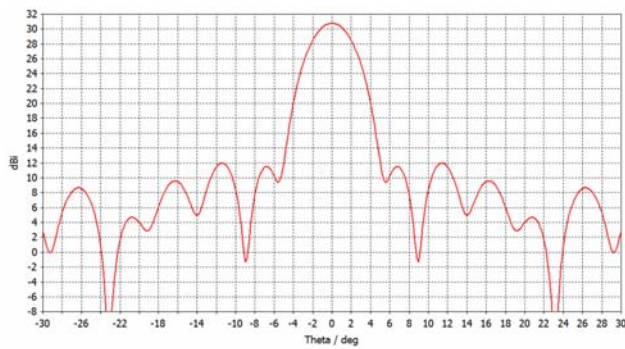


Figure 3. Radiation pattern of the PCB antenna, E plane.

Comparing radiation patterns of both antennas (PCB and reflector) conclusion is that both antennas practically have identical main lobe (that could be easily concluded by comparing 3dB beam width of both antennas, see Table 2 as well). In addition maximum side lobe levels are also quite similar (~20dB).

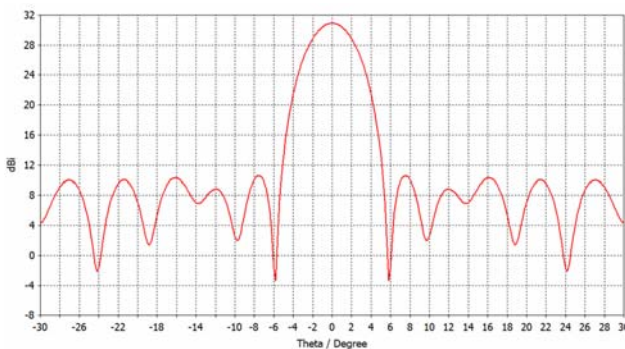


Figure 4. Radiation pattern of the PCB antenna, H plane.

For comparison - radiation pattern of parabolic reflector antenna IP-15 is shown in Fig. 5.

Table 2 also shows that both antennas have similar directivity as well (PCB antenna ~30.5dB).

Simulated gain of the feasibility model is $\sim 2 \div 2.5$ dB below parabolic antenna reflector antenna. Though smaller this figure is in fact quite good result having in mind smaller size and aperture of the PCB antenna (lateral size ~25% smaller), see Table 2.

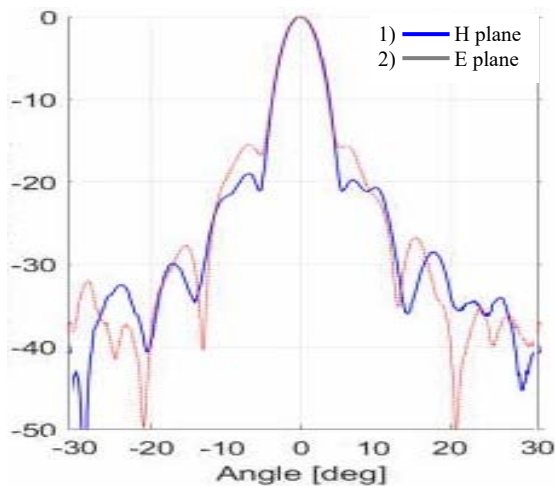


Figure 5. Radiation pattern of the reflector antenna.

PCB antenna gain level is again direct consequence of losses in feeding network and the fact that not all improvements are applied. The goal of this breadboard model is just to assess initial electrical and mechanical performances and see what capacity it has to get electrical parameters close to reflector antenna ones.

Simulated Return Loss of the PCB antenna is shown in Fig. 6. As it can be seen levels between 15-20dB could be achieved in decent band width (~5%) around center frequency of the antenna without additional matching elements.

It is worth to note that active area of PCB antenna (i.e. area occupied by antenna elements without mechanical fixtures) is 17% smaller than aperture of reflector antenna (without fixture elements as well) - so achieved results is considerable breakthrough.

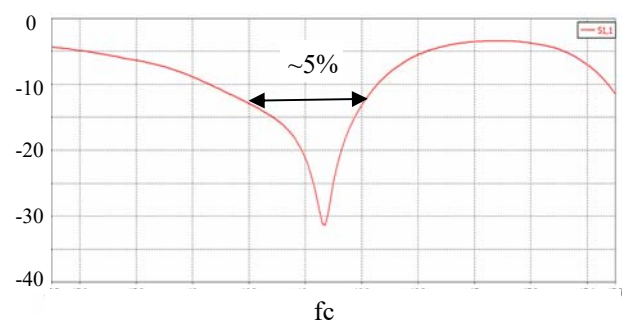


Figure 6. Return loss of the PCB antenna.

On the other side comparing this PCB antenna to current state of the art PCB antenna performances – conclusion is that this novel solution have higher performances and gain saturation issue has been pushed further which gives performances suitable for radar applications.

In the Table 2 performances of realized PCB antenna and reflector antenna are summarized.

Table 2. Comparison of realized performances of novel PCB antenna array and original radar reflector antenna

Antenna Parameter:	PCB Flat panel array	Metallic reflector	Unit
Gain (G)	~ 28.5	~ 30.5	dBi
Directivity (D)	~ 30.5	~ 31	dBi
3dB Beam Width, Azimuth	~ 4.85	~ 4.80	°(degrees)
Efficiency (η)	~ 66.5	~ 88.8	%
Side Lobe Level (SLL)	~ 20	~ 20	dB
Front / Back (F/B)	> 35	> 35	dB
Return Loss (RL)	15 - 20	> 20	dB
Frequency (Fc)	Ku band ~15	Ku band ~15	GHz
Size, Lateral	~270	~350	mm
Size, Depth	~30	~180	mm
Mass	~1	~3	kg
Technology	PCB, Planar	Parabolic reflector	
No. elements	256	Single ant	
Note: All parameters include radome, for both antennas			

Overall results show that presented feasibility prototype and proposed approach are viable and such PCB antenna has potential to get electrical performances close to reflector antenna while based on size, mass and geometry it has number of advantages over reflector antenna.

Also novel PCB antenna with presented performances will have enough capacity to cover near and medium ranges for detection. Apart from smaller gain level (which will be improved at prototype stage) PCB and reflector antennas have similar other electrical performances. At the same time PCB antenna is smaller more compact and with reduced profile and mass comparing to original reflector antenna and enables better integration of components.

5. CONCLUSION

Overall performances of novel PCB antenna where apart from electrical we have to consider also integrability and mechanical and economical parameters – show that PCB could be more effective solution and is in line with modern trends of miniaturization of radars with increased mobility and functionality. Novel PCB antenna is ~25% smaller (front profile) and has ~4 times smaller depth than reflector antenna. Directivity is similar to reflector antenna while gain is around 2-2.5 dB smaller than reflector antenna. Smaller gain is result of losses in feeding network and smaller aperture size of PCB antenna. The next step is to assemble and measure the PCB antenna and compare measured results with simulated ones and with reflector antenna ones as well. Also after measurement of this feasibility model the plan for the future antenna prototypes is to apply few

additional (of 1-10) listed technologies. That will aim to realize prototype PCB antenna with all electro-mechanical-environmental features that will have higher gain and closer to the reflector antenna one - so it could completely replace reflector antenna in the radar system.

References

- [1] Simic S., Golubicic Z., Zejak A.J., “Design of High Resolution, Coded, Portable Battlefield Surveillance Radar PR-15”, Proc. of 4th International Conference
- [2] Simic S., Zejak A.J., Golubicic Z., “PR-15 Radar Signals: Measurements And Analysis”, Proc. of 6th International Conference OTEH 2014, Belgrade, Serbia, October, 2014.
- [3] Constantine A. Balanis, Antenna Theory: Analysis and Design, JWS, 1996
- [4] John D. Kraus, Antennas. McGraw-Hill Book Company, 1988
- [5] Richard C. Johnson, Henry Jasik, Antenna engineering handbook, 3rd edition
- [6] Dr Boro M. Reljic, Dr Aleksa J. Zejak, Dr Zoran Golubicic, Dr Slobodan Simic, Combining linear Boro arrays into complex planar arrays to achieve high gain and efficiency printed antenna arrays, 2018 EUCAP International Conference, EurAAP.



SIMPLE RADAR SYSTEM FOR DRONE SURVEILLANCE AND ACQUISITION

ZORAN GOLUBIČIĆ

Institute RT-RK Computer based systems, Novi Sad, Serbia, golubicic.zoran@gmail.com

SLOBODAN SIMIĆ

Military Academy, Belgrade, Serbia, slobodan.simic@va.mod.gov.rs

SVETISLAV MARIĆ

University of California, San Diego, USA, smaric@ucsd.edu

BOJAN ZRNIĆ

Military Academy, Belgrade, Serbia, zrnice_bojan@yahoo.com

BOGDAN PAVKOVIĆ

Institute RT-RK Computer based systems, Novi Sad, Serbia, bogdan.pavkovic@rt-rk.com

Abstract: This paper is dedicated to drone surveillance system taking into account main drone characteristics – low RCS and limited vehicle speed. As a nominal values maximum drone speed of 100m/s (360km/h) and RCS of $10^{-3}m^2$ are assumed. Radar system has to fulfill two main requirements. Drone has to be detected at the distance longer than it is the drone missile operating range (about 20km max) and price of the radar component should be significantly lower than it is the price of antiradar missile. As a solution quasi bi static system is proposed. Low RCS target is detected by the long energy integrated during the relatively long time (0.25s). Beam width is optimized according the drone dynamic. System with 10 beam width is obtained as the optimal solution. Required power for continuous wave radar operation was 5W. Maximum distance for drone detection was 30km. System operate at Ku band require parabolic antenna of 1.5m. Systems operating at other bands need proportionally larger or smaller antennas. In order to surveillance certain solid angle sector few Tx antenna are necessary. Exact number is discussed in the paper.

Keywords: quasi bistatic radar, continuous wave radar, COTS technology, Doppler processing

1. INTRODUCTION

Massive application of drones in the recent wars generates mythology about drone efficiency in the combat environment. Drones were applied successfully against non-prepared and non-protected artillery and armored vehicle. Massive drone attacks had the surprising effect typical for the new system application. Systems that were used for defense were classic anti-aircraft system. These systems were used more or less successfully. These systems are many times more expensive than attacking drones. Surveillance and acquisition system of these systems are not optimized for anti-drone operation. Target of this design is to design the cheap systems capable to detect drones at the distances where usual attacking arm (missile) is useless. Price of the radar system is significantly below the one missile carried by drone. Main performances of the drones are low RCS and low flying speed. Second performance offers possibility to radar to accumulate lot of reflected energy in the long time. Reflected energy should be accumulated during the target illumination and pulse Doppler radar is not adequate for this application. For that reason quasi-bi-static radar should be applied.

2. TYPICAL SCENARIO

Typical parameters relevant for drone detection are as follows:

- Drone RCS $10^{-3}m^2$ (it is assumed that RCS is constant over the frequency of 7.5GHz i.e. 4cm wavelength)
- Drone maximum speed 100m/s (360km/h)
- Radar radial resolution 50m
- Radar frequency between 7.5GHz and 18GHz
- Radar wavelength 1.5cm to 4cm
- Tx power 5W
- Antenna gain 42dB to 46dB
- Parabolic dish antenna diameter 1.3m to 3m
- Beam width 1°
- S/N 14dB
- Equivalent bandwidth 4Hz

According the previous data maximum radar range should be (3cm wavelength is used as example but other wavelength, using the proper antenna, shall give the same results):

$$R = \sqrt[4]{\frac{P_t G^2 \lambda^2 \sigma}{(4\pi)^3 B \left(\frac{S}{N}\right) k T F}} = \sqrt[4]{10^{18}} = 30 \text{ km} \quad (1)$$

According the previous calculation during the time of 1s radar can surveillance angular space of $2^\circ \times 2^\circ$. During 100s drone can pass maximum 10km radial distance. For 100s radar can cover $20^\circ \times 20^\circ$ angular spaces.

These data can be used as the starting point for the particular design.

For example, in the case that 50W amplifier is available (typical for communication purpose) bandwidth could be amplified to 40Hz. It means that solid angle of $60^\circ \times 60^\circ$ could be illuminated in 100s.

3. RADAR ARCHITECTURE

Radar is based on two antennas (Tx and Rx) separated few tents of meters and central unit. In this way

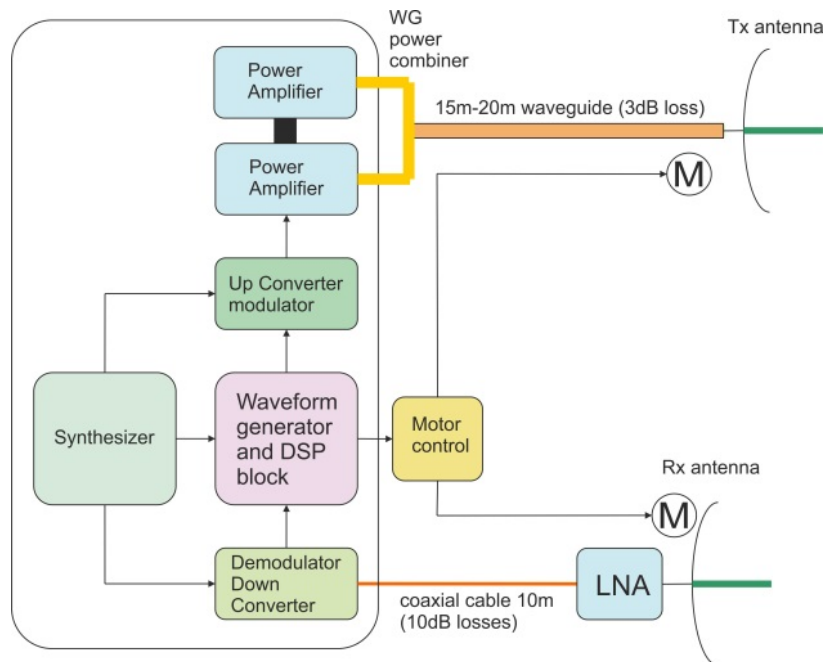


Figure 1. Radar block diagram

Key radar component is the power amplifier. Availability of this component is the problematic for all radar manufacturers, except for the some of them situated in the most powerful countries. For that reason, in the case of unavailability, power amplifiers based on the powerful RF electronic tubes or semiconductors usually used in other fields of application (industrial or scientific equipment etc.) could be applied. As an example, tubes or semiconductors applicable in different microwave transmitter or plasma heating devices could be useful. Separation of power amplifier position from the Tx antenna significantly increase the probability of amplifier survivability. Sometimes two parallel amplifiers could be combined in order to compensate waveguide losses. Taking into account problems with amplifier availability this unit can be accommodated in the armored box (in order to survive missile attack).

simultaneous signal transmission and reception are enabled. Rx antenna integrates LNA stage. LNA stage is connected to central unit via coaxial cable. Tx antenna is connected with the central unit via waveguides providing low losses between central unit and transmission antenna. Inside the central unit power amplifier, synthesizer with frequency converters, waveform generator and signal sampler are accommodated. Signal processing should be performed off line by the classic host computer. General schematic is presented at the Fig. 1.

Because Tx antenna is the most susceptible to anti-radar missile attack it is practically impossible to protect this antenna from the destroying by anti-radar missile. But the price of this antenna (parabolic dish with rotating mechanism) is many times below anti-radar missile and technology required for these antenna fabrications is not high and it is available for almost all countries.

In the cases when attack of anti-radar missile is not expected (or amplifier unit is available by the domestic production) power amplifier could be joint to Tx antenna and flexible coaxial cable could be applied for the connection between amplifier and the rest of the radar.

Because Rx antenna doesn't radiate electromagnetic power radar central unit could be associated to the Rx antenna. This antenna is protected from the anti-radar missile but it could be recognized by the optical equipment. It means that this antenna should be the protected by the classical masking methods.

3.1. Synthesizer with up/down converters

Basic component of the synthesizer presents commercially available crystal oscillator operating with the frequency about 100MHz (with low phase noise).

Frequency of this signal could be multiplied between 8 and 20 times by the commercially available UHF transistors or Schottky diodes used in usual mobile communication equipment. Obtained signal could be multiplied 9 times ($\times 3$ and $\times 3$) by the low power transistors (usually applied in LNB blocks for satellite signal receivers) or by Schottky diodes used in the LNB mixers. Similar component could be applied for the receiver low noise amplifier and mixer. All these components are in the mass production with low price. Low frequency mixer/modulator could be realized by the Schottky diode applied for the LO signal synthesizer design. Purpose of these architectures is to enable signal processing part independent of radar operating frequencies.

Important components in the synthesizers design and fabrication are filters. Frequency plan assume application of commercially available SAW filters at 1070MHz (SSR) and 70MHz is usual IF frequency for telecommunication equipment. Frequency distances between components in the multipliers, modulators and demodulators are enough that microstrip filters (with IQ modulators and demodulators) can select desired frequencies.

Example of the block diagram of the synthesizer with up/down converter (for X-band radar) is presented at the Fig. 2. Presented synthesizer is only example. Depending of the available power amplifier frequency plan could be adopted but cheap and commercially available component should be applied.

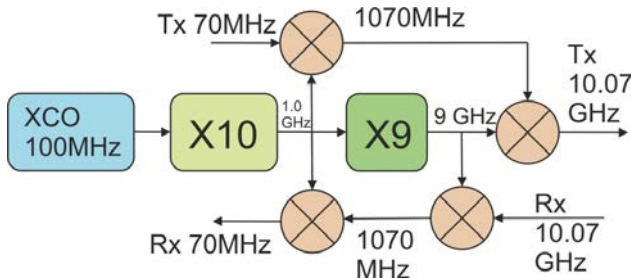


Figure 2. Block diagram of the synthesizer

3.2. Waveform generation and signal sampling

Because maximum drone speed is 100m/s and signal integration time is 250ms drone can pass 25m during the integration time. In order to enable high probability to detection distance resolution should be 50m. Signal bandwidth should be 3MHz. In order to fulfill under sampling condition with sufficient guard band for signal filtering RF bandwidth should be extended to 5.64MHz and IF frequency to 70.5MHz. Sampling frequency should be 11.28MHz (available by the cheap AD converter).

BPSK Tx signal should be generated by modulated periodic bit stream of 141Mbit/s (01010101...). This stream is modulated by 3Mbit/s (47bits 010101... are included in the one information bit). Generation of Tx signal is possible by simple FPGA circuit or standard microcontroller.

Sampling rate of 11.28MSPS could be performed by the AD converters with serial outputs. Even that signal is coded with 16bits output stream has bit rate below 200Mbit/s. This velocity is compatible with standard microprocessor or FPGA devices.

Block schematic of the generation and sampling signal is presented at the Fig. 3.

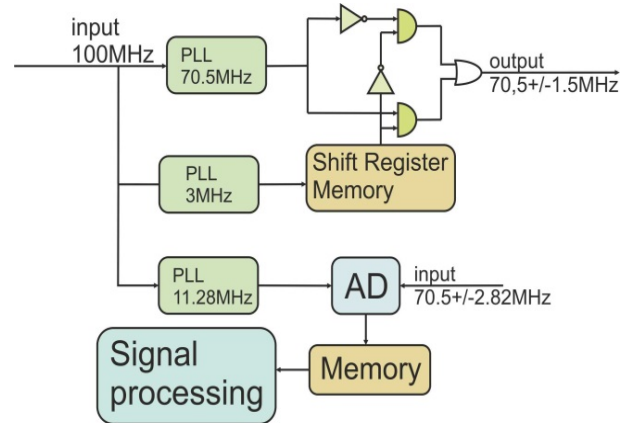


Figure 3. Frequency plan for signal generation and sampling

3.3. Signal processing

First step in the signal processing part is IQ signal forming. Pair and impair samples are separated as I and Q samples. Impair samples in I and Q streams are multiplied by -1 and two components of base band signal are obtained [1]. Fir filter is used to reject all image bandwidth in the under sampling process. Signal is correlated with the long sequence. Because integration time is long, bank of the matched filters should be applied. FFT processor is optional.

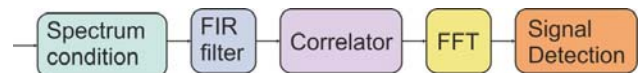


Figure 4. Off-line processing

4. POINTING CALIBRATION

One of the main problems in the bi static radar operation is the antenna pointing synchronization. This problem could be resolved using own drone transmitting the signal from the far field distance (250m or more). Both antennas Tx and Rx has to have small monopulse receivers for initial position calibration. These antennas could be used for passive drone detection in the case that drone radiate some signals. Pointing system can operate at the different frequency than radar.

In the case that spillover problem could be solved at the small distance between Tx and Rx antenna both of them could be positioned at the one rotating platform. Availability of low noise amplifier is not problematic i.e. destroying of both (Tx and Rx) antenna is not critical damage.

To prove concept, an experiment was done with available hardware. Experimental setup is shown on Fig. 5.



Figure 5. Experimental setup



Figure 6. Corner reflector used for calibration

Two ground surveillance radars PR-15 [2], and one corner reflector [3], shown on Fig. 6, were used. The radar on the left in Fig. 5, with parabolic antenna were illuminating the target, while the radar on the right, with flat printed antenna, was passive and used as receiver. Considering that PR-15 radar

- has antenna with gain of 30 dB which is quite smaller than that one proposed in Section 2,
- cannot work continuously without hardware adaptation, so it can give maximum average power of 600 mW which is quite smaller than that one proposed in Section 2,

experiment was done at smaller distance (5 km) than requested in Section 2 (30 km) and with the target quite bigger than drone. The distance between Tx and Rx antenna was small, but their positions and orientations were fixed, so it was possible to place them in such a way as to avoid the spillover problem.

The results are shown on Fig. 7. Methodology was the same as in [4]. The time – Doppler signal representation is shown. The complex signal with duration of 13 seconds measured by receiving PR-15 radar (top), spectrogram of this signal (centre) and its projections on Doppler axis (left) are shown.

Pedestrian was walking away of radar. After 10 seconds, he stopped and started to wave with a corner reflector. The signal originates from the range cell at distance of 4.9 km of the radar. Bi-phase coded radar pulse with duration of 19.2 μ s is applied in transmitter. Golay complementary sequences lengths of 64 are used for coding.

As there is noticeable variation in the amplitude of its real (blue) and imaginary (red) parts we can conclude that signal is above the noise. However, that variation is slow, indicating that it is caused by strong ground clutter. It is better shown in spectrogram, in the middle at zero Doppler. We can see one non-stationary component corresponding to moving person and his activities with the corner reflector in the range cell.

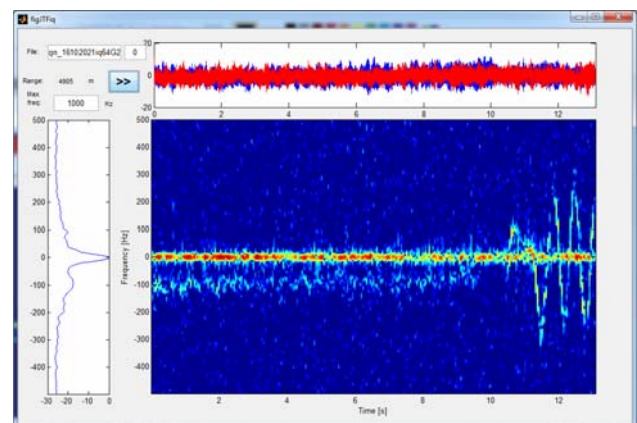


Figure 7. Time – Doppler signal representation

5. CONCLUSION

Concept of drone surveillance radar system taking into account main drone characteristics – low RCS and limited vehicle speed is presented. Calculation shows that small

drone with RCS of 10^{-3}m^2 can be detected at maximum distance at 30km, with continuous wave radar power of 5W, with parabolic antenna of 1.5m at Ku band. Experimental verification of the concept at smaller distance of 5 km was done with two ground surveillance radars PR-15 and one corner reflector.

References

- [1] GOLUBIČIĆ Z., SIMIĆ S., ZEJAK A.J., “Design and FPGA implementation of digital pulse compression for band-pass radar signals”, *Journal of Electrical Engineering*, Vol. 64, No. 3, 2013, pp. 191–195.
- [2] SIMIĆ S., GOLUBIČIĆ Z., ZEJAK A.J., “Design of High Resolution, Coded, Portable Battlefield Surveillance Radar PR-15”, *Proc. of 4th International Conference OTEH 2011*, Belgrade, Serbia, October, 2011.
- [3] ZEJAK A.J., ZEJAK R., SIMIĆ S., RELJIĆ B., DOTLIĆ I. “Design, Fabrication and Performance evaluation of Passive Corner Reflector for Ground Surveillance Radar Testing”, *Proc. of 10th International Conference OTEH 2022*, Belgrade, Serbia, October, 2022. (*submitted*)
- [4] SIMIĆ S., ZEJAK A.J., GOLUBIČIĆ Z., “PR-15 Radar Signals: Measurements and Analysis”, *Proc. of 6th International Conference OTEH 2014*, Belgrade, Serbia, October, 2014.



DESIGN, FABRICATION AND PERFORMANCE EVALUATION OF PASSIVE CORNER REFLECTOR FOR GROUND SURVEILLANCE RADAR TESTING

ALEKSA ZEJAK

Institute RT-RK Computer based systems, Novi Sad, Serbia, aleksa.zejak@rt-rk.com

RADULE ZEJAK

Peripolis Elektronika, Belgrade, Serbia, aleksa.zejak@rt-rk.com

SLOBODAN SIMIĆ

Military Academy, Belgrade, Serbia, simasimic01@gmail.com

BORO RELJIC

Institute RT-RK Computer based systems, Novi Sad, Serbia, bora_relic@hotmail.com

IGOR DOTLIĆ

Institute RT-RK Computer based systems, Novi Sad, Serbia, igor.dotlic@rt-rk.com

Abstract: Ground surveillance radars are intended for the detection of moving targets on the ground, from the ground. This implies a significant impact of relief, vegetation and infrastructure facilities on radar performance. Therefore, when evaluating the performance of these radars, it is important to have objects with a large radar reflex surface, which can move, in order to create more or less controlled test conditions. One solution may be an off-road vehicle. But, this solution is expensive if the tests are frequently conducted and short-lived, which is exactly the case in the development phase. A much more cost-effective solution is a man equipped with a passive radar reflector. The passive radar reflector should be clearly visible for radar from a wide range of angles in both azimuth and elevation planes. Also, it should be light and comfortable to be carried by one person. This paper presents the design, fabrication and performance evaluation of one such reflector intended for testing ground surveillance radar in the Ku band.

Keywords: radar, corner reflector, radar testing .

1. INTRODUCTION

Every radar aim, object, from which the emitted electromagnetic wave is reflected, is basically a radar reflector. However, in general sense, specific geometry structure created to have desired radar reflexive surface and predefined reflexivity diagram, will be considered a reflector. [1, 2]

Radar reflectors can be used for different [3], mutually opposed, purposes. For example, they can be used for enlarging of radar visibility of small vessels at sea and for marking the sea coast for navigation safety. They can be used and for numerous radar testings (as in our case). Opposing purpose is considered to be use of reflectors in electronic war (EW), when, using the reflector, false aims, targets, baits are formed for deceiving purposes. We needed reflectors for testing of small infantry radars [4], border protection radars. Problems and solutions are similar to those applied for increasing of radar visibility of small vessels at sea and for marking the sea coast, so they are applicable for those purposes also.

2. RADAR CROSS SECTION

Term target cross section is easiest to explain by radar equation. The radar range equation (or shorter: the radar

equation) represents the physical dependences of the transmit power, which is the wave propagation up receiving the echo signal. Below is one of the more basic forms for a single antenna system. The maximum radar detection range is

$$R_{\max} = \sqrt[4]{\frac{PG^2\lambda^2\sigma}{(4\pi)^3 S_{\min}}}, \quad (1)$$

Where P = transmit power, S_{\min} , minimum detectable signal, G antenna gain, λ transmit wavelength, σ target cross section.

The radar cross section of a target is a fictitious, but useful, characteristic of the body. The RCS of all but the simplest of objects varies by orders of magnitude as the viewing angle changes, sometimes over as little as a fraction of a degree. This being the case, we almost always measure our target echo characteristics as functions of aspect angle.

The result is a set of RCS patterns with the amplitude of the echo, usually in the decibel scale, charted along the ordinate and the aspect angle along the abscissa.

3. RADAR CORNER REFLECTOR

Corner reflector is a structure that is used as a radar target, often in calibrating test equipment. Corner reflectors are used for many reasons: they have very high radar-cross-section (RCS) for a small size, the high RCS is maintained over a wide incidence angle, and an exact solution is known for their RCS. Corner reflectors are easy to make from sheet metal such as aluminum and they are robust enough to maintain good flatness.

There are two main types of corner reflectors, dihedral and trihedral. The dihedral has two surfaces that are on orthogonal planes, the trihedral has three. Sketches of the two are shown in figure 1 (b and c) below, along with generally used coordinate systems.

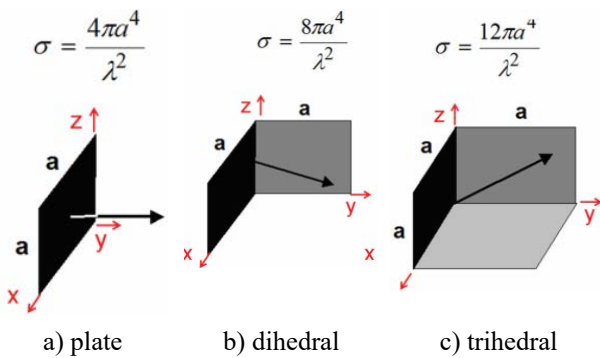


Figure 1. Planar test targets.

Table 1. shows RCS of standard objects

Table 1. RCS of standard objects

Target	Dimensions	Max RCS
Sphere	D : diameter	$\sigma = \pi D^2 / 4$
Plate	a, b : length, width	$\sigma = 4\pi a^2 b^2 / \lambda^2$
Cylinder	r : radius, L : length	$\sigma = 2\pi r L^2 / \lambda$
Dihedral Reflector	a, b : length, width	$\sigma = 8\pi a^2 b^2 / \lambda^2$

Figure 2 shows geometric model of the triangular pyramidal trihedral corner reflector: θ is incident angle and ϕ is azimuthal angle.

4. NEW CORNER REFLECTOR CLUSTERS

For obtaining the desirable reflexivity diagram it is necessary to construct complex structure which we will name reflector cluster. In horizontal plane it is desirable that reflexivity diagram is approximately omnidirectional.

In horizontal plane we need reflector clusters that have reflexivity diagrams suitable for specific situations in the field. For example, when radar is on lower position than the surveilled field, it is necessary that the diagram is directed downwards, and when opposite situation, upwards. It is similar with the application on buoys at sea or marking of sea coast.

In this article we will not elaborate theoretical and constructional details but it will be the theme of the other articles to follow. We will show the realization of two types of reflector clusters and their measured reflexivity diagrams.

In new reflector cluster constituent elements are triangular trihedral corner reflectors (Figure 2). Base are the equilateral reflectors with 90° angle. Rest of the reflectors are construed to optimize space and obtain the simplicity of construction.

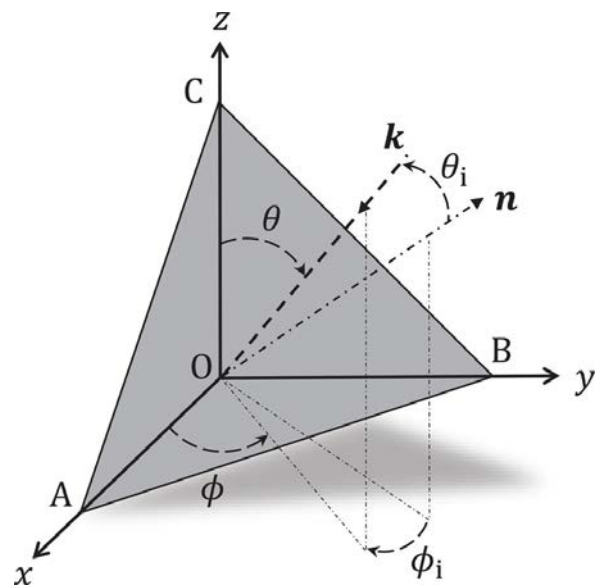


Figure 2. Geometry of the trihedral corner reflector.

We combined two different groups of reflectors and selected two types of clusters: Type 1 and Type 2 (Figure 3, and Figure 4).

Measures are performed in the Ku band. In Figure 5. reflexivity diagram in horizontal plane cluster type 1 is shown. Maximum reflexivity measured is 43.85 dB, the mean is 39.5 dB.

In Figure 6. reflexivity diagram in vertical plane is shown. Maximum reflexivity measured is 44.25 dB, the mean is 38.8 dB.

In Figure 7. reflexivity diagram in horizontal plane cluster type 2 is shown. In all the figures, as a reference, metal disc reflexivity diagram is shown.

Also, these clusters showed good performances and on the radar field testing, which is their final purpose.

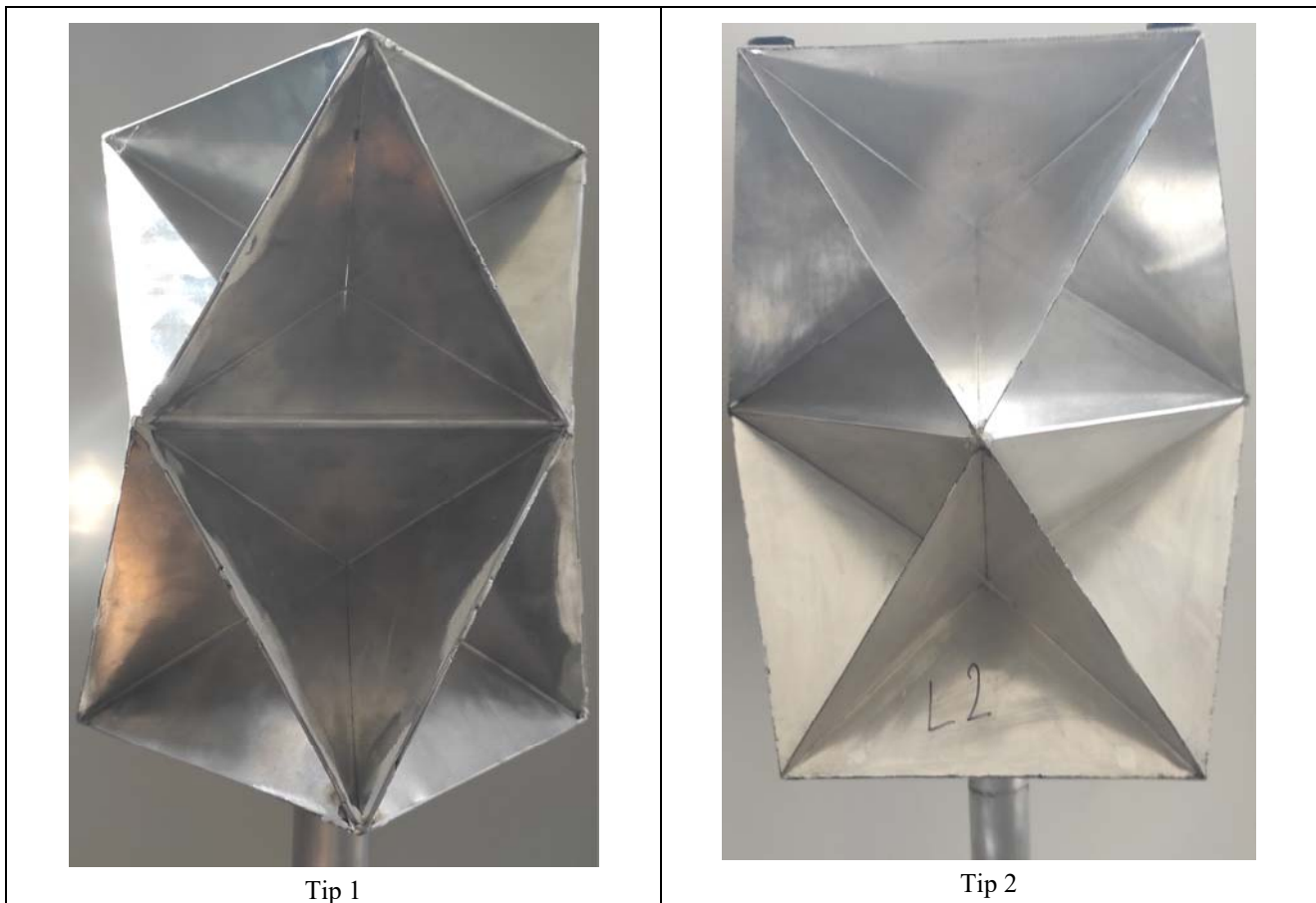


Figure 4. Cluster configuration Tip 1 and Tip 2.

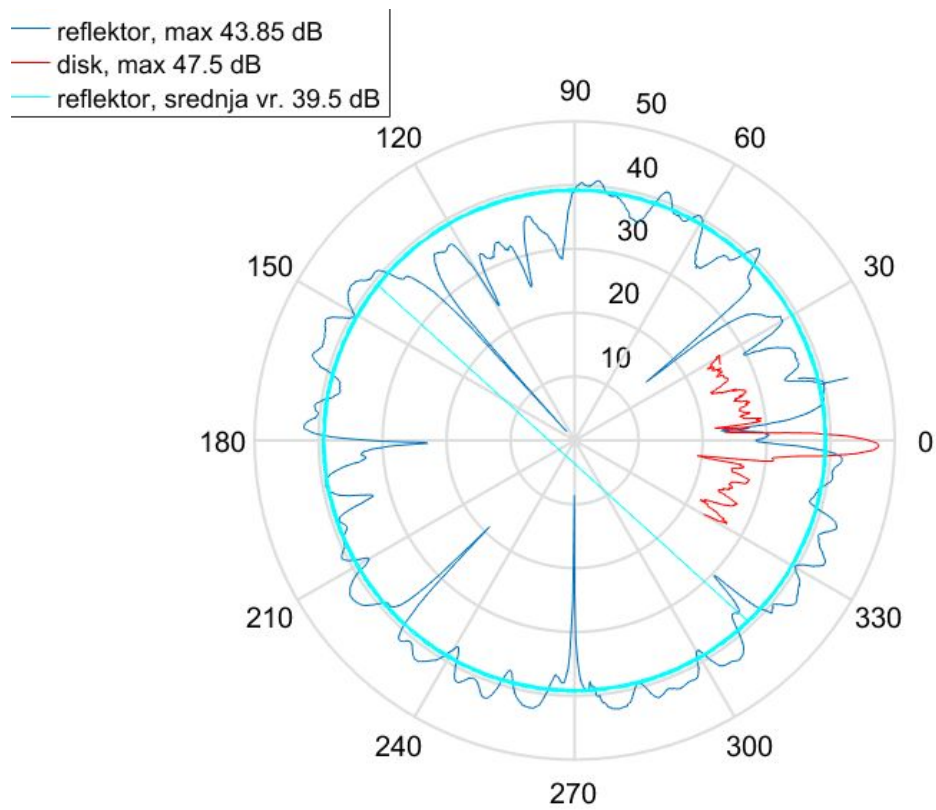


Figure 5. Cluster Type 1 – measured reflexivity diagram in horizontal plane.

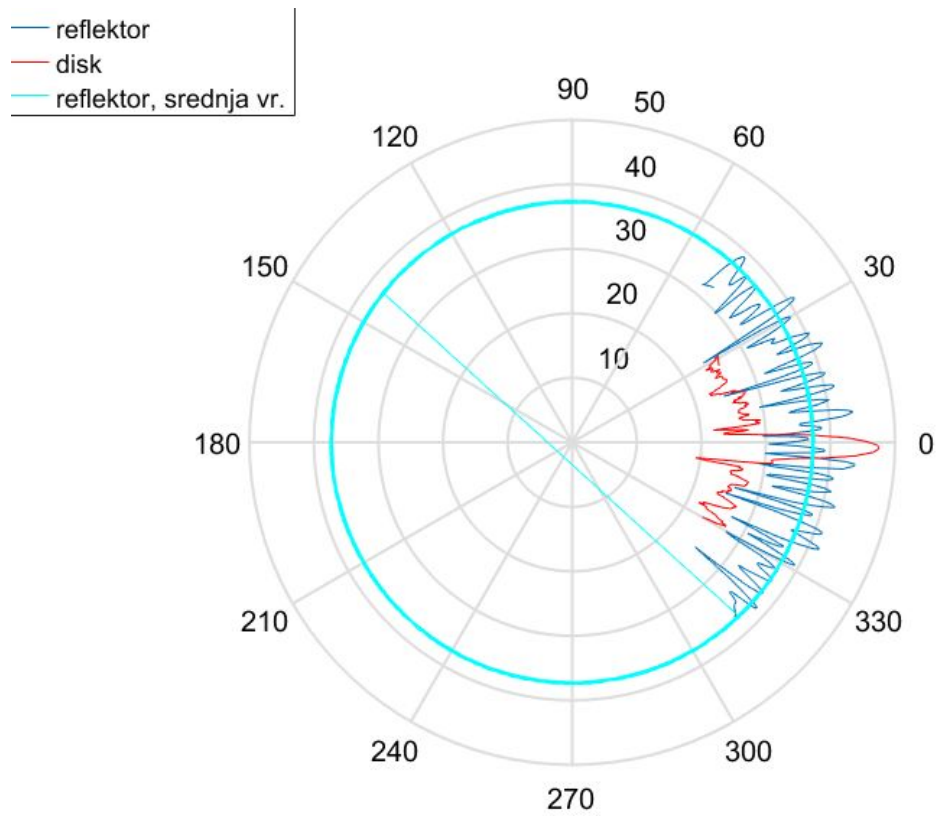


Figure 6. Cluster type 1 – measured reflexivity diagram in vertical plane

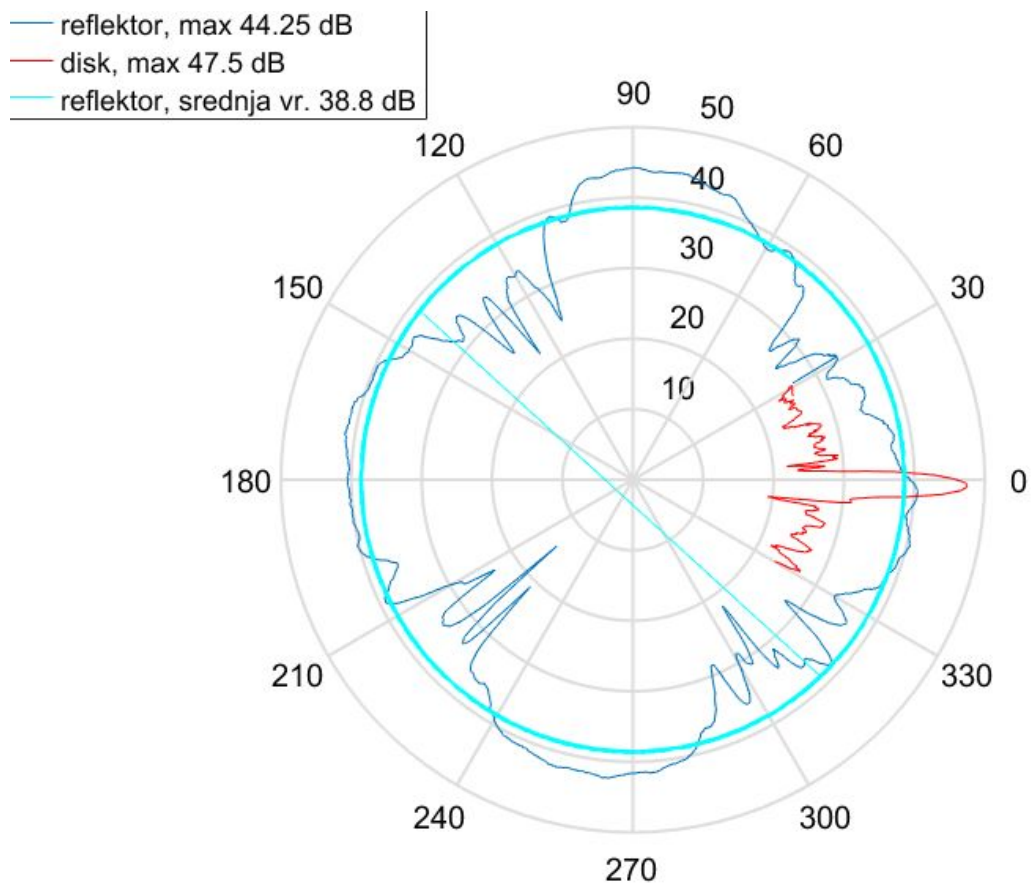


Figure 7. Cluster type 2 – measured reflexivity diagram in horizontal plane

5. CONCLUSION

First developed, and later on constructed reflector clusters, have excellent reflexivity diagrams in both planes (horizontal and vertical).

These specific examples are made to be suitable for manual use. They are made of aluminum sheet 0.5mm thickness. The whole construction with the axis, longed to be suitable for holding, weighs less than 2kg. However, in field testing it turned out to be too heavy for longer carrying, so we made a version with aluminum sheet 0.2 mm thickness. Aluminum sheet that thin is shown to be impossible to affix by usual techniques, so we developed special manufacturing procedure.

In next step, we will develop the clusters adapted to be mounted on the off road vehicle. Those solutions will be suitable for applications on the ships, for marking the sea coast and for geodesic testing.

References

- [1] KNOT, E. F., SHAEFFER, J. F., TULEY, M. T., "Radar Cross Section," Artech House, Norwood, MA, 1985.
- [2] SKOLNIK, M. I., "Radar Handbook," McGraw Hill, NY, 1990.
- [3] SUKHAREVSKY, OLEG, SERGEY NECHITAYLO, and VITALY VASILETS. "Using Corner Reflectors to Increase Backscattering of Radar Targets." In 2020 IEEE Ukrainian Microwave Week (UkrMW), pp. 207-212. IEEE, 2020.
- [4] SIMIĆ S., GOLUBIČIĆ Z., ZEJAK A.J., "Design of High Resolution, Coded, Portable Battlefield Surveillance Radar PR-15", Proc. of 4th International Conference OTEH 2011, Belgrade, Serbia, October, 2011.
- [5] Goble, A.T. "Confusion reflectors." Electronic Countermeasures (1978): 18_1-18_23.



SIDE LOOKING DRONE RADAR FOR BURIED VEHICLES IN THE FORESTALL ENVIRONMENT

SLOBODAN SIMIĆ

Military Academy, Belgrade, Serbia, slobodan.simic@va.mod.gov.rs

ZORAN GOLUBIČIĆ

Institute RT-RK Computer based systems, Novi Sad, Serbia, golubicic.zoran@gmail.com

ALEKSA ZEJAK

Institute RT-RK Computer based systems, Novi Sad, Serbia, aleksa.zejak@rt-rk.com

BORO RELJIĆ

Institute RT-RK Computer based systems, Novi Sad, Serbia, boro.reljic@gmail.com

EUGEN ŠIMARA

RT-RK Institute for Computer Based Systems, Osijek, Croatia, simara.eugen@gmail.com

Abstract: Surveillance of artillery and blinded vehicle by the drones is usually based on the optical devices mounted on the drone platforms. This method has the problem to detect arms buried in the forestall environments especially if the vehicles are masked by different methods. In this paper simple side locking radar mounted at the drone bottom side is proposed. This radar is intended to detect artillery and blinded vehicle masked in the forestall environment. One dimensional antenna array is proposed to avoid aerodynamic disturbance. Antenna operates at UHF frequency and can penetrate through the woods and similar environments. Because target dimensions are in order of few meters radar operates in optical zone. Eight radiating elements with 10W output power should be enough to cover the distances in the range of 1.5km to 15km. Length of the antenna is 2m and height 30cm. Radial resolution is 1.5m. Angular precision is obtained by the low frequency narrowband filter. It depends from the radial distance but average value of tents of meter could be assumed as the initial value.

Keywords: Linear array, SAR imaging, UHF radar.

1. INTRODUCTION

Typical method for artillery system masking assumed protection in optical spectrum. For that reason drones guiding the own artillery cannot detect the target and cannot sent to own center precise coordinates of the enemy troops. Artillery or armored vehicles are covered with masking reds or are buried in the woods. Solution for detecting masked arms should be found in radar device application.

Detection and tracking are the functions most-commonly associated with radar. Increasingly, however, radars are being used to generate two-dimensional images of an area. Such images can be analyzed for intelligence and surveillance purposes, for elevation/topology mapping, or for analysis of earth resources issues such as mapping, land use, ice cover analysis, deforestation monitoring, and so forth. While radar images have not achieved the resolution of optical images, the very low attenuation of electromagnetic waves at microwave frequencies gives radar important advantage of seeing through clouds, fog, precipitation and vegetation very well. Consequently, imaging radars generate useful imagery when optical instruments cannot be used at all [1].

Especially in recent years, along with the SAR (synthetic aperture radar) imaging technology has been great focused, many experts and scholars have shifted their research focus to achieve the high-quality imaging both in efficiency and resolution. These studies can be departed to three parts: the SAR imaging technology, real-beam scanning imaging technology and mono-pulse imaging technology. These research results have greatly improved the imaging quality, but for e.g. the missile borne detector, these algorithms seem too complex. On the other hand, the limited space in the novel optional burst height proximity fuze require the complexity of signal processing algorithm and imaging strategy, therefore, in [2] authors propose a novel monopulse forward-looking high-resolution imaging algorithm based on adaptive iteration. In this type of radar, the antenna is mounted in the nose of the missile, which limits its dimensions, and thus the gain. Concept is proven experimentally by drones.

In our previous work [3] linear array antenna mounted along the missile body is presented. Linear array consists of patch type radiating elements. The array has maximum gain at the plane orthogonal to the missile, so it is optimal for side looking.

In this paper, we were looking for a radar concept that would be airborne, have a high-gain antenna (for good resolution and range) and a simple processing method (for high efficiency). The choice fell on a side looking radar that would be mounted below drone body.

2. RADAR CHARACTERISTICS

Radar has to operate at low frequency enabling electromagnetic propagation through the natural protections including the short propagation through the ground. Taking into account dimensions of the artillery or armored vehicle radar can operate in optical zone (RCS independent of wavelength) at the UHF frequencies (between 0.7m and 0.3m). Penetration through the ground should be better if the radar operates in the resonant zone i.e. VHF band (wavelength between 1.5m and 0.7m). Application of VHF band radar requires higher Tx power for the same antenna dimension as it is applied at the UHF radar. Dimension of the radar antenna has to be in accordance with drone capability and aerodynamic requirement. As an example, UHF radar (with VHF intermediate signals) is proposed. Radar antenna should be realized as the linear array of 16 horizontal dipoles. Horizontal dipoles are selected because artillery tubes are mainly positioned in the horizontal direction and polarization losses are minimized. Brewster angle enables that lot of energy reflected from the ground shouldn't be reflected to the radar increasing the signal clutter.

In order to determine enemy artillery position, position of drones and drones trajectory should be known with high precision. For that reason pitch, roll, yaw (especially) component of the drone flight should be known for the calculation process.

Example of the useful radar characteristics are presented below:

- Operating frequency UHF band 675MHz
- Wavelength 45cm
- Linear array - number of elements 16
- Antenna gain 20dB
- $RCS > 1m^2$
- $P_t > 100W$
- $NF < 2dB$
- Antenna length 5m
- Antenna height 0.3m
- Beam width in azimuth 6° .
- Beam width in elevation 50° .
- Pulse duration $50\mu s$ (blind zone 7.5 km)
- PRI – $200\mu s$ (unambiguous range 30km).
- PRF 5kHz
- S/N 20dB
- Effective bandwidth 100Hz
- Coherent integration time 40ms.
- Drone speed 200m/s
- Drone flight height 7km

According previous data radar range is:

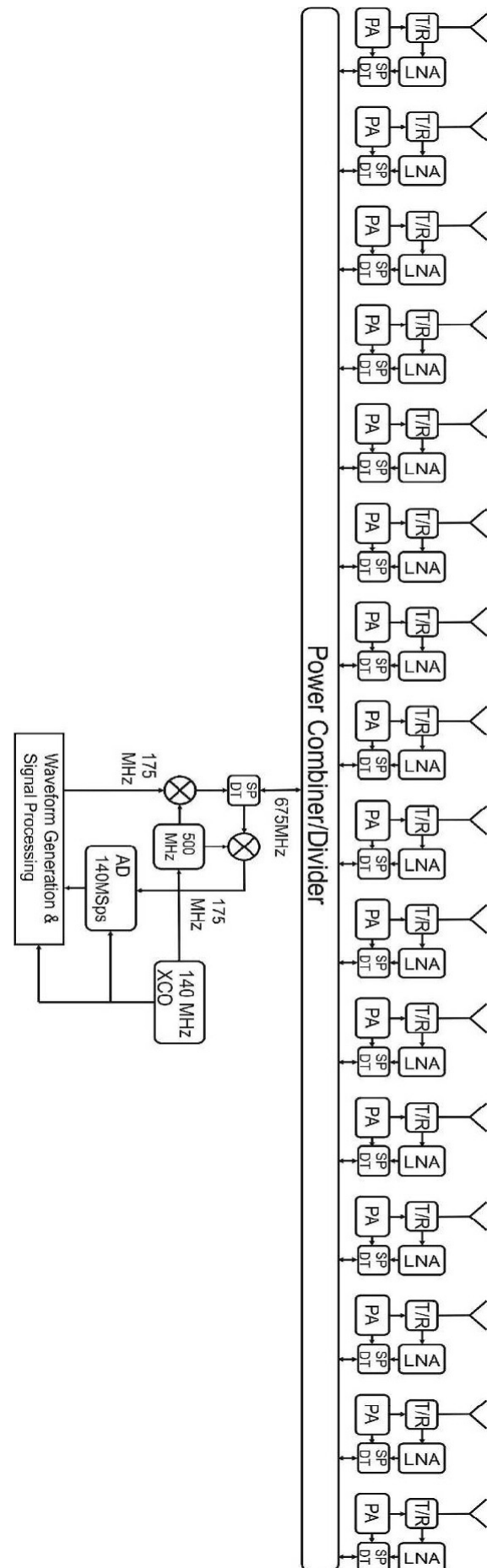


Figure 1. Radar block diagram

$$R = \sqrt[4]{\frac{P_t G^2 \lambda^2 \sigma}{(4\pi)^3 \left(\frac{S}{N}\right) kTF}} = \sqrt[4]{10^{18}} = 30 \text{ km} \quad (1)$$

Distance resolution should be 3m. It means that signal bandwidth is 50MHz. Chip period is 20ns. During the time of 50 μ s sequence has 2500chips i.e. processing gain is 34dB.

Block schematic of the radar is presented at the Fig. 1. Radar is based on active linear array consists of dipole type radiating elements and T/R modules. The T/R module includes power amplifier, LNA stage, circulator and T/R switch. Because antenna operates at low frequencies, price of transmitter/receiver is low and availability of component is not limited.

Waveform generator and signal processing unit can be realized as in [4].

3. PERFORMANCE ASSESSMENT

Spot illuminated by the radar depends of the distance between radar and target. As a rough estimation width of the illuminated spot is 10% of the distance. For example, width of the spot at 30km is 3km. Unfortunately, operating frequency has to be low and Doppler frequency of the reflected object at the edge of the spot is low. Target selection based on the Doppler shift can reduce the spot width to half (1.5km at 30km distance). Even that obtained S/N is 20dB precision of the target position should be limited to 150m.

There are two options for better precision in target location process. First is to apply synthetic radar principle to determine target position [5] and second is to determine target position by two drones flying over orthogonal (or nearly orthogonal) trajectory as it is illustrated on Fig. 2.

Synthetic radar technique is based on coherent integration

of the energy reflected from the target. Delay of the reflection from the particular target is equalized for different radar position. In order to equalize these delays radar need significant processing power. Powerful signal processor could be situated at the drone or reflected signal could be transferred to ground for further processing.

In the case of two drone application information about target position is obtained almost immediately. Both drones measure radial distance with high radial resolution and precision. Target position is obtained in the cross section of the axial resolution lines.

Taking into account flying speed of 200m/s and integration time of 40ms drone will pass 8m illuminating target. In that case resolution cell of 3 \times 8m could be assumed as the maximum resolution area. Time of 40ms could be assumed as the Doppler resolution cell of 25Hz. Maximum Doppler frequency is generated by the targets at the edge of radar spot. In the case that beam width is 6 $^\circ$ maximum radial velocity of target should be:

$$v_{rad \max} = v_{drone} \sin(3^\circ) = 0.05v_{drone} = \frac{10m}{s} \quad (2)$$

Then, the maximal Doppler frequency is:

$$f_{d \max} = \frac{2v}{c} f_c = 45Hz \quad f_{d \max} = \frac{2v}{c} f_c = 45Hz \quad (3)$$

In the case that drone velocity is halved (100m/s) Doppler shifts should be negligible. In the case of VHF antenna with the similar dimension beam width should be 4 times wider and radial velocity of the target should be four times higher. As the central frequency is four times lower Doppler shifts should be the similar as it is in the UHF band. For Doppler shifting elimination, only two times longer antenna or two times lower drone speed could be useful.

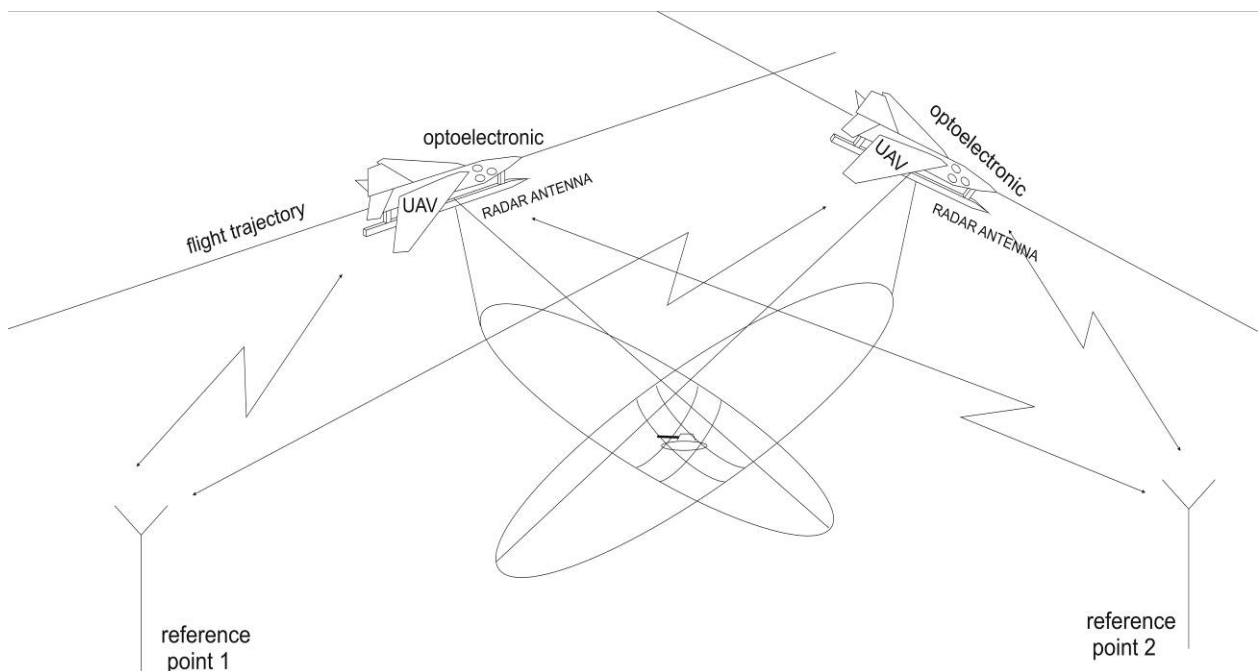


Figure 2. Double drone observation concept

In the first phase of the signal processing response from different range gates are obtained. Targets with Doppler frequency should be reject what means that simple integration of the received signal should during the 40ms should be performed. In this way reflected signals from all range gates (7500) are obtained.

Next step in the signal processing should be SAR integration process. All response corresponding to one resolution cell should be integrated during the illumination time period. This process could be numerically too complex for simple on board computer and should be performed at the ground.

Numerically complicated process could be replaced by double drone observation.

4. CONCLUSION

Concept of side looking radar for buried vehicles in the forestall environment is presented. Antenna operates at UHF frequency and can penetrate through the woods and similar environments. The initial calculation shows that even when the S/N of 20dB is obtained, the accuracy of the target position is limited to 150m, which is not enough to guide one's own artillery.

Two options for better precision (of order 3×8 m) in target location process are considered. First of them is to apply synthetic radar principle to determine target position and the second one is to determine target position by two drones flying over orthogonal (or nearly orthogonal) trajectory.

The first method is computationally complex and requires a powerful processor, situated either on the drone's board or on the ground, but with fast communication link to drone in addition. The second method is computationally much simpler, but requires two drones.

References

- [1] RICHARDS M., *Fundamentals of Radar Signal Processing*, McGraw-Hill, New York, 2005.
- [2] CHENG C., ZHOU X.D., ZHU-LIN M.G., at all, *Research on monopulse forward-looking high-resolution imaging algorithm based on adaptive iteration*, Defence Technology, 16(1), (2020), 158-171.
- [3] GOLUBIČIĆ Z., SIMIĆ S., ZEJAK A., *Multi-beam receiving antenna at the missile lateral structure*, Proc. of 6th International Conference OTEH 2014, Belgrade, Serbia, October, 2014.
- [4] GOLUBIČIĆ Z., SIMIĆ S., MARIĆ S., ZRNIĆ B., PAVKOVIĆ B., *Simple Radar System for Drone Surveillance and Acquisition*, Proc. of 10th International Conference OTEH 2022, Belgrade, Serbia, October, 2022. (submitted)
- [5] ANTONIJEVIĆ G., SIMIĆ S., BUJAKOVIĆ D., *Improving the azimuth resolution of strip-map SAR image using Adaptive Weighted Norm Extrapolation*, 25th Telecommunication Forum (TELFOR), Belgrade, Serbia, November, 2017

DEVELOPMENT OF THE DEVICE BASED ON THE DSPIC30F6014A MICROCONTROLLER FOR MEASUREMENT OF AXLE POSITION ANGLE

VLADIMIR LAPČEVIĆ

Military Technical Institute, Belgrade, vladimirlapcevic@mts.rs

Abstract: Development of the device for measurement of axle position angle is presented in this paper. In many cases where the motors are used there is a need for measurement of axle position angle. This document presents the detailed development of hardware and software which provide precise measurement of axle position angle. Created device is based on the microcontroller dsPIC30F6014A. Transducer of angle which is used is absolute encoder.

Keywords: microcontroller dsPIC30F6014A, encoder, hardware, software .

1. INTRODUCTION

Electric motors are used in servo controlling very often. In that case working body on the motor's axle is settled and it is necessary to be positioned very precisely. Sensor of angle has to precisely set working body in the determined position. The encoder is a sensor of angle which gives information of the position of working body. Electronic device is connected to an encoder and takes values from the encoder and sends data to the computer. This paper presents the development of the device which takes serial data from encoder, then it does digital processing of data, where serial bits are packed into the

digital word, and then this device sends digital word to computer by serial interface RS232. Communication between the device and the encoder is realised by RS485 serial interface. Complete electronics of the device is presented in this paper. Microcontroller dsPIC30F6014A [1] is used inside the device. Program for microcontroller dsPIC30F6014A [2] is written in C program language. The size of written program for microcontroller is 4 KB. Application program, which is installed on the computer and which enables communication with the device is written in C# program language. Development board of device is shown in the figure 1.

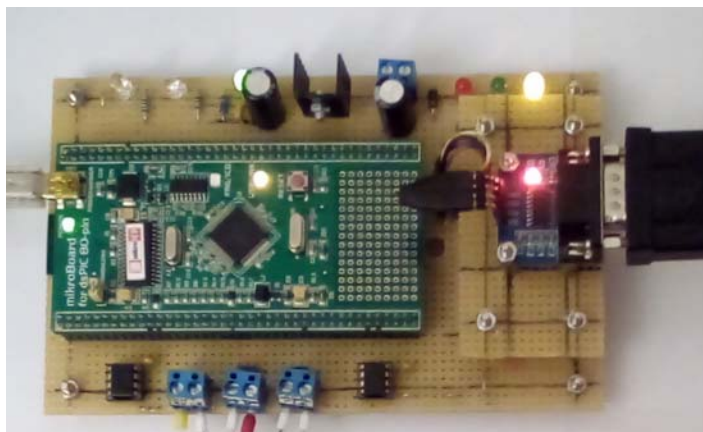


Figure 1. Development board of the device

2. ELECTRONICS OF DEVICE

2.1. Microcontroller dsPIC30F6014A

A microcontroller dsPIC30F6014A is the microcontroller which belongs to the family of digital signal controllers [3]. A digital signal controller is the microcontroller which is much better than the ordinary microcontroller because it has a digital signal processor (DSP) besides the microcontroller. The digital signal processor provides computing complex mathematical operations for a very short time: multiplying two 16-bits numbers, shifting 32-

bits number and adding two 32-bits numbers. The digital signal processor enables multiplying two 16-bits numbers in one instruction's cycle. The digital signal controller is used in the real time system because of its speed. The digital signal controller reads signal from input sensors, processes all input signals and then generates control signals on its output. The digital signal controller must do all these operations in the defined time because only in that case a system is a real time system. The microcontroller dsPIC30F6014A and its connections to the rest of electronics inside the device is shown in the figure 2.

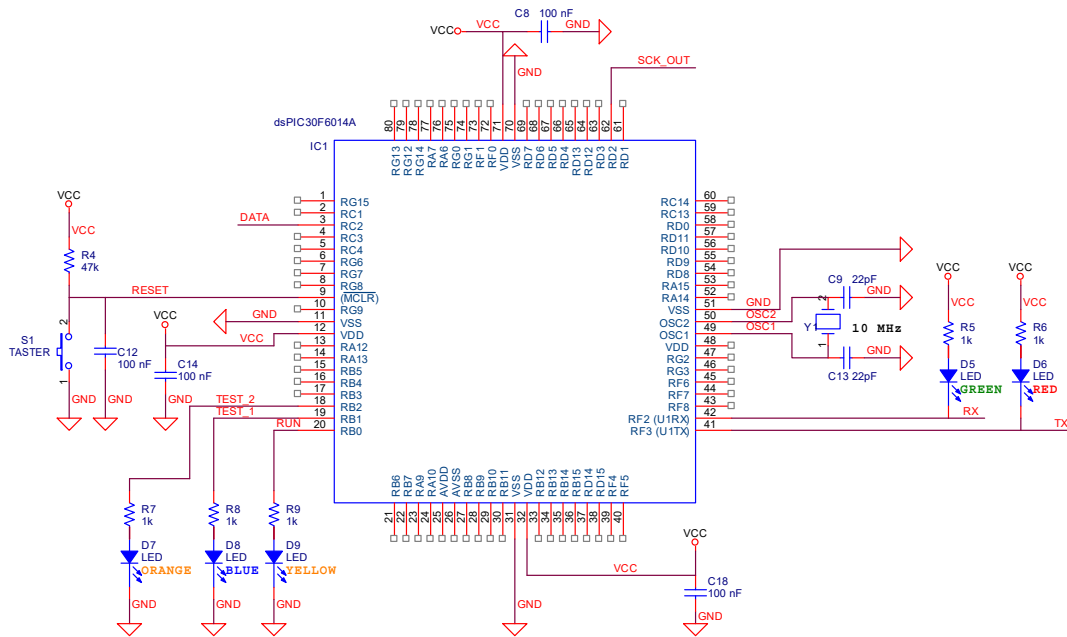


Figure 2. Microcontroller dsPIC30F6014A and its connections to the rest of electronics in the device

PLL oscillator is integrated into the microcontroller dsPIC30F6014A. It is possible to change the frequency of a microcontroller in reference of crystal quartz frequency, which is connected to the microcontroller, by this PLL oscillator. Frequency, on which microcontroller dsPIC30F6014A works, can be computed by next equation:

$$F_{CY} = \frac{K_P \cdot f_Q}{4} \quad (1)$$

where is:

f_Q – frequency of crystal quartz

K_P – coefficient of PLL oscillator (4, 8, 16)

Coefficient of PLL oscillator has one of the next values: 4, 8 or 16. The value of this coefficient is asserted during setting configuration bits of a microcontroller. It can be seen from equation (1) that choosing value of coefficient K_P can achieve that frequency of microcontroller which can be equal or higher in reference of crystal quartz frequency. In this case it is chosen that the value of coefficient $K_P = 8$. In that way the results is two times higher frequency of the microcontroller than the frequency of a crystal quartz. As the frequency of crystal quartz $f_Q = 10$ MHz, then the frequency of a microcontroller $F_{CY} = 20$ MHz. The microcontroller dsPIC30F6014A sends clock to encoder and gets serial digital data from it. Communication between the microcontroller and the encoder is realized by serial RS485 interface. The maximum value of pulse and pause for this encoder is $12.4 \mu s$. A clock, which the microcontroller sends to the encoder, has equal values of pulse and pause and they have the value $10 \mu s$. Timer T1, which is integrated into microcontroller dsPIC30F6014A, is used for realization of the clock. Since pulse and pause of the clock are equal and have value of $10 \mu s$, it is necessary that interruption of the routine of a timer occurs

every $10 \mu s$. Period of the interrupt routine occurrence is computed by next equation:

$$T_{INT} = n \cdot T_{CLK} \quad (2)$$

Where is:

n – number of ticks of timer until interruption occurs

T_{CLK} – period of a timer's clock

Number n is the difference between the value of a register PR1 and the starting value of a timer TMR1. The starting value of a timer TMR1 is asserted to the zero. The timer counts ticks. The interruption occurs when the value of a timer is equal with the value of a register PR1. Period of timer's clock is equal to the reciprocal value of frequency of timer's clock:

$$T_{CLK} = \frac{1}{f_{CLK}} \quad (3)$$

where is:

f_{CLK} – frequency of timer's clock

The value of the prescaler K_S of the timer T1 is asserted in the control register T1CON. Fourth and fifth bit in the control register T1CON are dedicated for setting the value of the prescaler K_S . These bits are called TCKPS bits. The value of the prescaler K_S can be: 1, 8, 64 and 256. In table 1 values of TCKPS bits and values of the prescaler are shown.

Table 1. Values of TCKPS bits and values of the prescaler

TCKPS<1:0>	K_S
00	1
01	8
10	64
11	256

Frequency of timer's clock is got as a divider of frequency of microcontroller F_{CY} and the value of prescaler K_S of that timer.

$$f_{CLK} = \frac{F_{CY}}{K_S} \quad (4)$$

Where is:

F_{CY} – frequency of the microcontroller

K_S – value of the prescaler of a timer T1 (1, 8, 64, 256)

Expression for time period repeating interrupt routine is based to equations (2), (3) and (4):

$$T_{INT} = \frac{n \cdot K_S}{F_{CY}} \quad (5)$$

The frequency of the timer's clock f_{CLK} is equal to the frequency of the microcontroller F_{CY} if the value of the

prescaler K_S is asserted to 1 in the control register T1CON. As a result, last expression can be written:

$$T_{INT} = \frac{n}{F_{CY}} \quad (6)$$

The variable n must have the value 200 because the frequency of the microcontroller $F_{CY} = 20$ MHz and the interruption routine of a timer occur every $10 \mu s$. It can be realized if the value of the register PR1 is 200 and the starting value of the timer T1 is asserted to zero every time when entrance to interruption routine occurs.

2.2. Serial interface RS485 through encoder

The encoder, which is used, has integrated RS485 interface. The signals from the encoder are differential signals. The connection between the microcontroller and the encoder is realized by RS485 interface. In the figure 3 serial interface RS485 is shown.

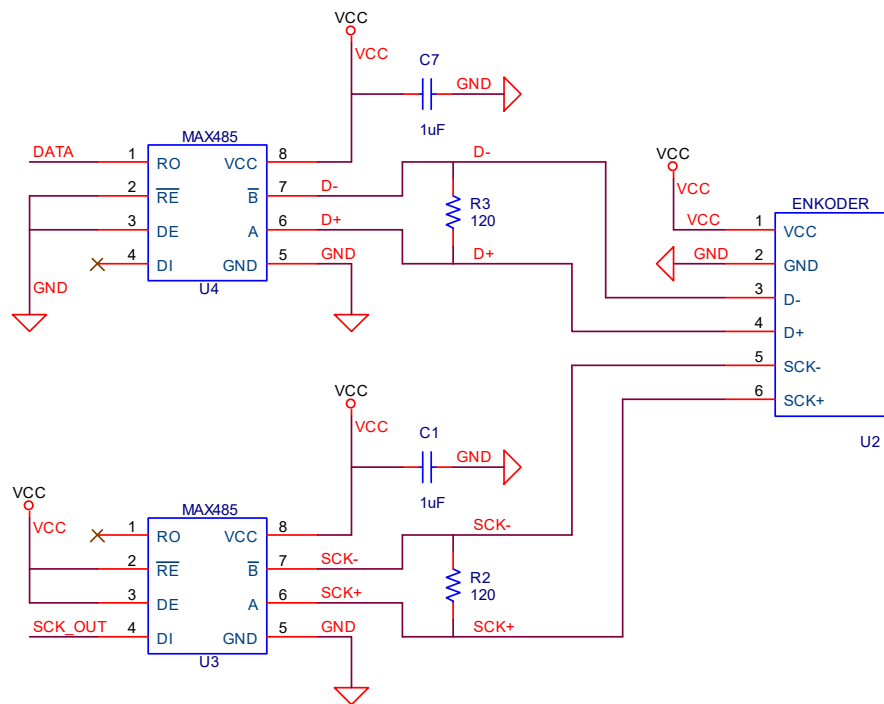


Figure 3. The serial interface RS485 between the microcontroller and the encoder

The integrated circuit MAX485 [4] is used for RS485 serial interface in this device. One integrated circuit MAX485 is used for transferring the signal of clock and the other integrated circuit MAX485 is used for transferring signal of data. The signal of clock is the output signal of the microcontroller. Integrated circuit MAX485, which is used for transferring the signal of clock, is configured as a transmitter. It is done by its second and third pin. These pins define the direction of transfer and they are connected to the high logic level and that is the voltage of 5 V. The signal of data is the input signal of the microcontroller. The integrated circuit MAX485, which transfers the signal of data, is configured as a receiver. Its second and third pin is connected to the low logic level and that is the voltage of 0 V. The

microcontroller generates the signal of clock and reads serial data from the encoder. The encoder sends serial data bit by bit. The microcontroller reads input bit on the falling edge of a clock [5]. Data reading from encoder is done periodically with the period of 10 ms. The microcontroller generates signal of clock on every 10 ms. The signal of clock exists during the reading data from encoder. The duration time of pulse and pause of the clock is equal and has the value of $10 \mu s$. It means that the period of clock is equal to $20 \mu s$. Data length from encoder is 14 bits. A few clocks are necessary for the initialization of reading from encoder, 14 clocks for reading 14 bits from encoder and one clock after the reading is ended. The maximum 18 clocks are needed for reading position from encoder. It means that the

maximum time needed for reading data from encoder is equal to $360 \mu\text{s}$, if period of clock is $20 \mu\text{s}$. Every 10 ms the microcontroller generates pulses for the reading data from encoder. The signal from encoder is at the high logic level in the beginning. The encoder sets the data on the low logic level when the encoder receives a clock from the microcontroller. In that way the encoder sends confirmation to the microcontroller that it receives pulses of a clock. This low logic level of data presents the message of acknowledgement. Then the encoder raises the signal of data on the high logic level. In that way the encoder reports to the microcontroller that it is ready for sending data. The microcontroller reads logic one on its input on the falling edge of a clock. In that way the microcontroller understands that the encoder is ready for sending serial data of 14 bits. This higher logic level from the encoder presents starting message. The microcontroller reads bit by bit serial data of 14 bits and packs them in the digital word. The microcontroller raises the signal of clock on the high logic level after reading of 14-bits is ended. The data from the encoder have the length of 14-bits and they are presented in the form of complement of two. This data must be shifted 2 bits in left in order to enable the operation subtraction. In that way

the data of 16-bits in the form of complement of two is obtained. The next operation is the subtraction between measured value of position and zero position value. The difference between these two numbers is a number which is also in form of the complement of two. It can be positive or negative number. The values are positive in the first half of a circle and they can be in range from 0 to 32768. They respond to the value of an angle from 0 to 180° . The values are negative in the second half of circle and they can be in range from 0 to -32768 . They respond to the value of angle from 0 to -180° . The value of zero position is taken during setting parameters. This value should be shifted for 2 bits in left and after that put in the EEPROM memory of the microcontroller. Every shifting digital number for 2 bits in left presents multiplying with 4. After digital data transferring from a device to a computer, it is necessary to have that number divided by 4. In that way the value of an angle from 0 to 180° responds to a number from 0 to 8192. The value of angle from 0 to -180° responds to a number from 0 to -8192 . The time diagram of the signals from the encoder during data reading is shown in the figure 4. The upper signal presents the clock and the lower signal presents the data.

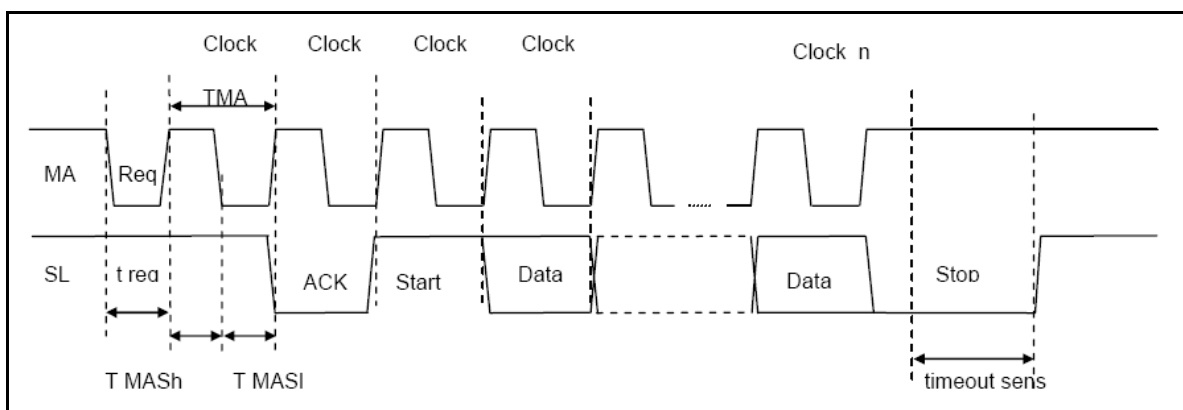


Figure 4. The time diagram of the signals from the encoder

2.3. Serial interface RS232 through computer

Communication between a device and a computer is realized by the serial RS232 interface at the baud rate of 115200 bits in seconds. This baud rate is the maximum baud rate because it is the maximum baud rate of the integrated circuit MAX232. The integrated circuit MAX232 is used for the translation of voltage levels from TTL level to RS232 level. The converter RS232/USB is used only in the case when computer does not have the RS232 interface. For serial communication it is very useful for a device to have 2 LED diodes (figure 2). The red LED diode is used for showing the data sending from

a device to a computer. The red LED diode blinks during data sending. The green LED diode is used for showing data receiving from a computer to a device. The green LED blinks during data receiving. These LED diodes are very useful because in the case of some malfunction it is very easy to determine the existence of data transfer. These LED diodes are connected to the cathode with the pins of microcontroller dedicated to receiving and sending data. These LED diodes are connected to the anode with pull up resistors. The electronics for the realization of RS232 interface are presented in the figure 5.

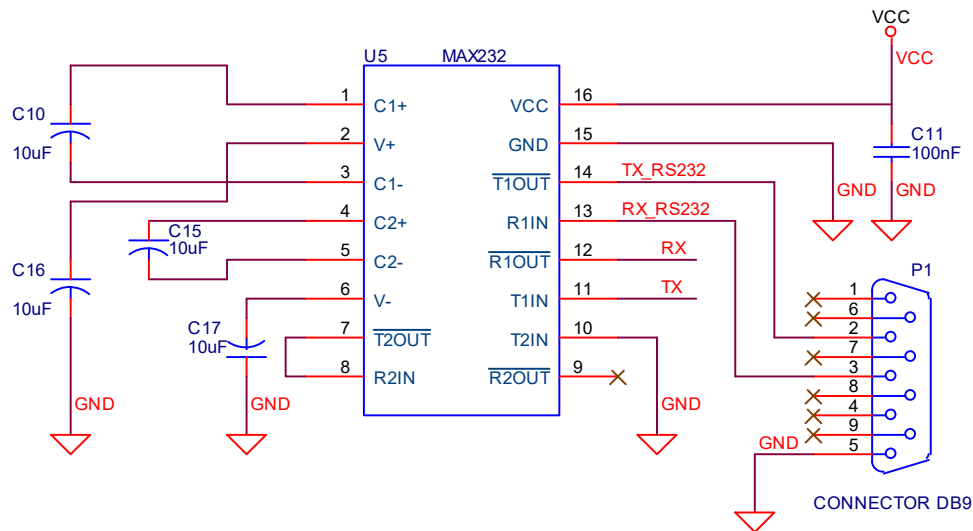


Figure 5. Serial interface RS232

Serial communication on the baud rate of 115200 is realized by writing value in the U1BRG register which is obtained by the next equation:

$$U1BRG = \frac{F_{CY}}{16 \cdot B} - 1 \quad (7)$$

where is:

F_{CY} – frequency of microcontroller

B – baud rate of RS232 interface

If the frequency of the microcontroller $F_{CY} = 20$ MHz and if the baud rate $B = 115200$ bits in seconds then the value of the $U1BRG = 10$.

2.4. Power supply

The microcontroller and the integrated circuits which are used in this device demand the voltage of 5 V for their

work. The power supply of the device can be realized in two ways. The first way is that the device is power supplied by a USB port. The development board which is used in this device has the USB port. This USB port is dedicated to programming microcontroller, but it can also be used for power supply of the device. Nominal voltage of power supply of USB port is 5 V. Voltage from the USB port, according to the standard, must be in range from 4.4 V to 5.25 V [6]. The current consumption of this device from the voltage source of 5 V, which is USB port, is 270 mA. The second way of power supplying is using extern voltage source of 9V and linear regulator LM7805 which is resided on the board. Linear voltage regulator LM7805 is used for getting voltage of 5 V. The figure 6 shows the electronics for power supply of a device.

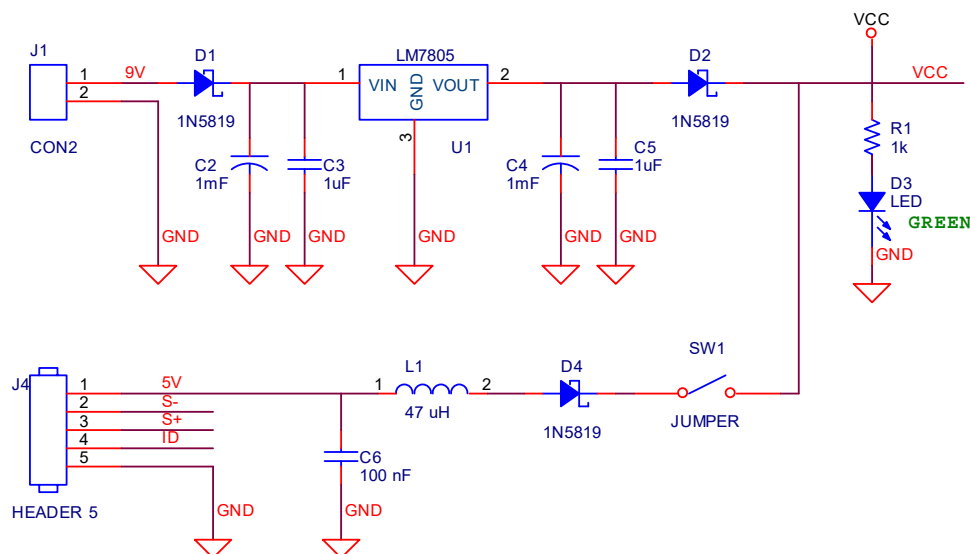


Figure 6. Power supply of the device

Microcontroller dsPIC30F6014A has integrated Brownout detector which can be turned on by configuration bits. The brownout detector is an electronic circuit which measures the voltage of power supply of the microcontroller. If voltage of power supply of the microcontroller drops below defined value, the brownout detector resets the microcontroller and keeps it in the reset state until the power supply voltage of the microcontroller rises above the defined value. The minimum voltage of the power supply is asserted by the configuration bits. It is very useful to turn on Brown detector because in that way innacuarate performance of the microcontroller is avoided. In this case, the minimum voltage of power supply is asserted to 4.2 V.

3. SOFTWARE APPLICATION

Software application for communication between a device and a computer is written in C# program language. The execute program is run by clicking on the file "Encoder.exe". After that the main window is opened. The window for setting parameters of serial port is opened by pressing on the button "Open connection". The window for setting parameters of the serial port is shown in figure 7.

The screenshot shows a Windows-style dialog box titled "ConnectionForm". It contains several input fields and dropdown menus for configuring a serial port connection. The fields are: "Address of encoder" with the value "255" and a range indicator "<0..255>"; "Port" with a dropdown menu showing "COM1"; "Baudrate" with a dropdown menu showing "115200"; "Data bits" with a dropdown menu showing "8"; "Parity" with a dropdown menu showing "nema"; "Stop bits" with a dropdown menu showing "1"; and "Flow Control" with a dropdown menu showing "nema". At the bottom right, there are "OK" and "Cancel" buttons.

Figure 7. Setting parameters of the serial port

In this window a user only chooses the name of a serial port "COM". It is predicted that every device has its own address which can be in range from 0 to 254. The address which is equal to 255 is the common address for all devices and it is used if a user forgets the address of a device. The main window for communication with the device is shown after opening of a serial port. There are 5 commands which can be used for communication. At the beginning, it is necessary to determine if the communication between a computer and a device exists. It can be checked by command "LINK RESET". The device gets this command and sends a message of

acknowledgement by which the device informs the user that the communication between the device and the computer exists. The computer waits for the device to send the acknowledgement message. If the device does not send the acknowledge message in 1 second, then the computer will write the message "timeout" on the monitor. This case can happen only if the wire between the device and the encoder is cut off. By pressing the button "SET PARAMETERS" a window is opened for setting the address of a device and zero position of the encoder. The window for parameters setting is shown in the Figure 8.

The screenshot shows a Windows-style dialog box titled "SetupForm". It contains two input fields. The first is "Address of encoder" with the value "1" and a range indicator "<0..254>". The second is a field for zero position with the value "0" and a range indicator "<0..1>". Below the second field, there is a legend: "1 - Taking zero position" and "0 - Non taking zero position". At the bottom right, there are "OK" and "Cancel" buttons.

Figure 8. The window for setting the parameters of a device

The choice for setting zero position is given. The address of a device will be set in every case, but a user can decide if they want to set zero position. The address of a device and the zero position of the encoder are written in the EEPROM memory of the microcontroller which means that they remain even after the power is turned off. The zero position of the encoder is set only at the beginning of measuring. Firstly it is necessary to set the encoder in the zero position. Then it is necessary to choose an option for setting zero position of the encoder in the application program. The device reads value from the encoder and puts it in the EEPROM memory of the microcontroller during setting zero position of the encoder. The device resets itself after the parameters are written in EEPROM memory. Then the program goes in the infinite "while" loop from which can not go out until the watchdog timer does not reset the device. The timeout of watchdog timer is set to 128 ms. The instruction for clearing of watchdog

timer is written in the main program on the beginning of the main "while" loop. The watchdog timer works on the frequency of the RC oscillator which is integrated into the microcontroller. During the program installation, which occurs after reset, the value of parameters is read from EEPROM memory and they are written in variables which occur in RAM memory. The main program works with these variables from RAM memory. At every time a user can read the asserted address of the device by clicking on the button "READ PARAMETERS". A user can reset the device by clicking on the button "RTU RESET". A user can read the position from encoder by pressing button "READ DATA". By pressing on the button "HELP" a manual for work with the application is opened. A user should press the button "Close connection" after the work is finished and then the serial port is closed. The main window of application is shown in the figure 9.

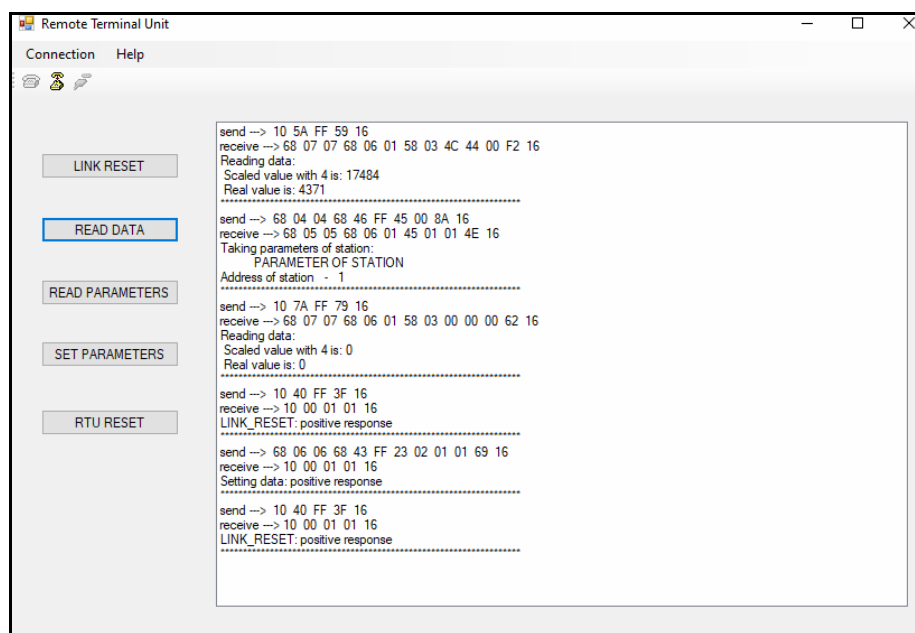


Figure 9. The main window of application

4. CONCLUSION

In the most cases the resolution of 14 bits of angle is quite satisfactory. It means that the minimum change of angle, which can be detected, is equal to 0.022 degrees or 1.32 minutes. The reason for this is that the angle of 360 degrees, which is a full circle, is presented with the data which is equal to 16384. The number 16384 is got as 2^{14} . This device offers further development in the way of serial communication. The serial communication RS232 becomes absolute, because a very small number of desktop computers have the interface RS232. Today it is very hard to find a laptop computer which has the interface RS232. The converter from RS232 to USB must be used if a computer does not have the interface RS232. Further improvement can be done in the way of developing a device with the USB interface. In that case the converter RS232/USB should not be used which brings low cost of device.

References

- [1] MICROCHIP: *dsPIC30F6014A Datasheet*, Microchip Technology, 2011.
- [2] MICROCHIP: *dsPIC30F Family Reference Manual*, Microchip Technology, 2006.
- [3] MICROCHIP: *dsPIC30F Digital Signal Controllers*, Microchip Technology, 2005.
- [4] MAXIM INTEGRATED: *MAX485 Low Power RS-485/RS-422 Transceivers*, datasheet, Maxim Integrated Products, 2014.
- [5] HENGSTLER: *ACURO – SSI/BISS*, Technical Datasheet Interface.
- [6] AXELSON, J.: *USB Complete*, page 436, 2005.

ACTIVE DISTURBANCE REJECTION CONTROL OF UNMANNED TRACKED VEHICLE

GORAN BANJAC

Military Academy, Belgrade, gbbanjac@yahoo.com

MOMIR STANKOVIĆ

Military Academy, Belgrade, momir_stankovic@yahoo.com

STOJADIN MANOJLOVIĆ

Military Academy, Belgrade, colemanojle@yahoo.com

Abstract: Significant improvement of the unmanned vehicles possibility has achieved by increasing its autonomy, i.e. by excluding the human operator from the guidance loop. In this paper is considered the autonomous control of the unmanned tracked vehicle (UTV) in the presence of the unknown caterpillar tracks slippage. The longitudinal and lateral control model for the UTV path following problem are developed. To handle unknown uncertainties and slippage disturbances, the design of active disturbance rejection control (ADRC) for both, longitudinal and lateral control channels, are proposed. ADRC strategy is enabled that all the control channel uncertainties and disturbances are treated as one lumped (total) disturbance, which is defined as an extended system state and estimated by appropriate extended state observer (ESO). Further, applying the appropriate closed-loop control laws, based on the total disturbance estimation, the complex longitudinal and lateral control problems are reduced to disturbance-free model control. The numerical simulations for the different path following scenarios and caterpillar tracks slippage dynamics are given to verify effectiveness of the proposed UTV control.

Keywords: Unmanned Tracked Vehicle, Active Disturbance Rejection Control, Extended State Observer.

1. INTRODUCTION

In recent years, autonomous unmanned vehicles have received significant attention. They are used for a wide variety of both civilian (transporting, assistance to disabled people, fumigation, harvesting, patrol monitoring and detection, investigation, exploration and inspection at tunnels, buildings, etc...) and military applications (as weapons platforms, logistics carriers, and surrogates for reconnaissance, surveillance, and target acquisition). Generally, the autonomous movement of vehicles requires integration of subsystems for navigations, guidance and control [1]. The navigations subsystem provides a data related to vehicle position in the space, using the different types of sensors (camera, radar, laser sensors...) and/or global navigation system such (GPS, GLONASS, QZSS, Galileo, etc...). On the other hand, the guidance system provides the desired path of the vehicle, whose way of realization depending on the level of autonomy of the vehicle. It can be generated directly by a human (lowest level of autonomy) or by using self-governing subsystems for path planning (higher levels of autonomy). However, regardless of the chosen navigation and guidance system, from the control point of view, their outputs can be considered as feedback and reference signals for control system. Then, control system by appropriate control algorithms generates signals to vehicle driving actuators. The graphical presentation of autonomous vehicles structure is shown in Fig.1.

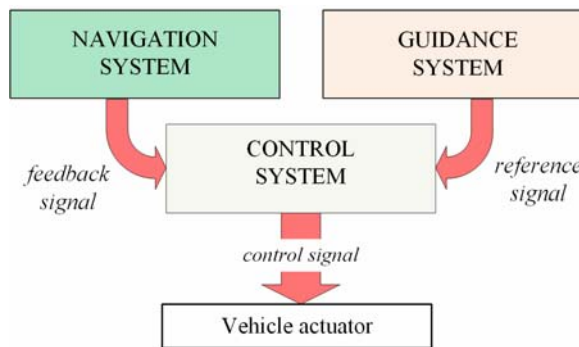


Figure 1. Structure of autonomous vehicles system

The control algorithm should ensure the robustness and stability of the movement, taking into account the dynamic behaviour and constructive limitations of the vehicle itself as well as influences of external disturbances, such as unknown slipping dynamics or the variable vehicles load. Therefore, the applications of the conventional control strategy, such as PI/PID structures, are usually limited [2], [3]. Among the many robust control approaches, active disturbance rejection control (ADRC) concept is standing out with a good trade-off between high control performances on the one side, and relative low complexity, on the other side. This algorithm has proven to be very robust, effective and practical in suppressing both external (environmental) disturbances and internal disturbances, such as vehicle unmodeled

dynamics, system internal uncertainties and nonlinearities [3],[4],[5],[6]. The main advantages of ADRC is that all system uncertainties and disturbances treats as one total disturbance, which can be estimated by extended state observer (ESO) and then rejected in real-time using appropriate control law.

This paper proposes the application of ADRC-based control structure to enable complex path following of the unmanned tracking vehicle (UTV), in the presence of variable slippage dynamics. To handle unknown uncertainties and slippage disturbances, the design of ADRC, for both semi-coupled longitudinal and lateral control channels, are introduced. ADRC strategy is enabled that all the control channel uncertainties and disturbances are treated as one lumped (total) disturbance, which is defined as an extended system state. Total disturbance in both channels are estimated by appropriately designed ESOS, and then rejected by ADRC control laws. The efficiency of the proposed control strategy is tested through different simulation scenarios in complex path following problem in presence of the variable slippage dynamics.

2. UTV MOTION MODEL

The motion model of the UTV can be described as:

$$\begin{bmatrix} \dot{x}(t) \\ \dot{y}(t) \\ \dot{\theta}(t) \end{bmatrix} = \begin{bmatrix} \cos(\theta(t)) & 0 \\ \sin(\theta(t)) & 0 \\ 0 & 1 \end{bmatrix} \begin{bmatrix} v(t) + v_d(t) \\ \omega(t) + \omega_d(t) \end{bmatrix}, \quad (1)$$

where coordinate $x(t)$ and $y(t)$ denotes vehicle position in the inertial coordinate system, $\theta(t)$ is angle orientation of UTV, $v(t)$ and $\omega(t)$ are longitudinal velocity and angular speed, respectively, both considered as the system control inputs. The uncertainties in the linear and angular velocity, caused by unknown track friction, i.e. track slippage, are represent with $v_d(t)$ and $\omega_d(t)$, respectively.

Including the dynamic model of UTV [5], the control inputs $v(t)$ and $\omega(t)$ can be defined as:

$$v(t) = \frac{a}{2} (\omega_R(t) + \omega_L(t)), \quad (2)$$

$$\omega(t) = \frac{a}{2} (\omega_R(t) - \omega_L(t)), \quad (3)$$

where m is the wheel radius, b is the normal distance between the right and left track, and (ω_R, ω_L) are the angular velocities of the right and left track wheel. In should be noted that ω_R and ω_L represents the control input of the real vehicle, both determined based on the designed control signals $v(t)$ and $\omega(t)$.

In the presence of the track slippage, (2) and (3) should be modified as:

$$v(t) + v_d(t) = \frac{m}{2} (a_R \omega_R(t) + a_L \omega_L(t)), \quad (4)$$

$$\omega(t) + \omega_d(t) = \frac{m}{b} (a_R \omega_R(t) - a_L \omega_L(t)), \quad (5)$$

where (a_R, a_L) are unknown friction coefficients of the right and left track, which are in the range $[0,1]$.

From the previous analyses, one can see that UTV motion control involves design of subsystems for longitudinal velocity control (longitudinal controller) and for angular speed control (lateral controller).

3. LONGITUDINAL CONTROL DESIGN

To govern vehicle velocity in the presence of the slippage $v_v(t) = v(t) + v_d(t)$, longitudinal model of the UTV is formulated as:

$$\dot{v}_v(t) = a(t) + \dot{v}_d(t), \quad (6)$$

where $a(t) = \dot{v}(t)$ is control signal, which should be design to enable that $v_v(t)$ track the desired velocity $v_r(t)$ in the presence of the disturbance $v_d(t)$.

Applying ADRC concept for the first order system, the (6) can be represent in the state-space form as:

$$\begin{bmatrix} \dot{v}_v(t) \\ \dot{f}_v(t) \end{bmatrix} = \begin{bmatrix} 0 & 1 \\ 0 & 0 \end{bmatrix} \begin{bmatrix} v_v(t) \\ f_v(t) \end{bmatrix} + \begin{bmatrix} 1 \\ 0 \end{bmatrix} a(t) + \begin{bmatrix} 0 \\ 1 \end{bmatrix} \dot{f}_v(t), \quad (8)$$

where $f_v(t) = \dot{v}_d(t)$ represents the unknown the longitudinal channel total disturbance, which can be estimated by appropriate extended state observer:

$$\begin{bmatrix} \dot{\hat{v}}_v(t) \\ \dot{\hat{f}}_v(t) \end{bmatrix} = \begin{bmatrix} 0 & 1 \\ 0 & 0 \end{bmatrix} \begin{bmatrix} \hat{v}_v(t) \\ \hat{f}_v(t) \end{bmatrix} + \begin{bmatrix} 1 \\ 0 \end{bmatrix} a(t) + \begin{bmatrix} l_1 \\ l_2 \end{bmatrix} e_v(t), \quad (10)$$

where $e_v(t) = v_v(t) - \hat{v}_v(t)$ is observer error and (l_1, l_2) are observer gains.

Active rejection of the total disturbance $f_v(t)$ can be realized by its estimation $\hat{f}_v(t)$ applying control law:

$$a(t) = \dot{v}_r(t) + k_p (v_r(t) - v_v(t)) - \hat{f}_v(t), \quad (11)$$

where k_p is adjustable controller parameters.

Assuming $\hat{f}_v(t) \approx f_v(t)$ and substituting (11) into (6) follows:

$$\dot{v}_v(t) + k_p v_v(t) \approx \dot{v}_r(t) + k_p v_r(t), \quad (12)$$

where one can see that desired control performances could be adjust by the appropriate selecting parameters k_p .

4. LATERAL CONTROL DESIGN

To define lateral control model, consider the UTV path following problem shown in Fig. 2, where the desired

path is defined by moving of the virtual target:

$$\begin{aligned}\dot{x}_r(t) &= v_r \cos(\theta_r) \\ \dot{y}_r(t) &= v_r \sin(\theta_r)\end{aligned}\quad (13)$$

where (x_r, y_r) are coordinates of the virtual target, v_r is the virtual target velocity (i.e. reference velocity of the vehicle) and θ_r is angle orientation of the virtual target in inertial coordinate system. Path following error vector $e(t)$ is defined in path-bound coordinate system by two components: lateral error $e_d(t)$ and along-track error $e_s(t)$, obtained as [2]:

$$e(t) = \begin{bmatrix} e_s(t) \\ e_d(t) \end{bmatrix} = \begin{bmatrix} \cos(\theta_r) & \sin(\theta_r) \\ -\sin(\theta_r) & \cos(\theta_r) \end{bmatrix} \begin{bmatrix} x(t) - x_r(t) \\ y(t) - y_r(t) \end{bmatrix}, \quad (14)$$

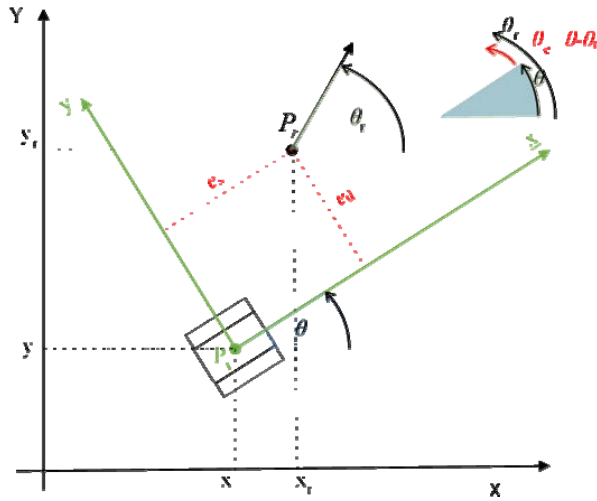


Figure 2. UTV path following problem

Denoting the course error angle as $\theta_e(t) = \theta(t) - \theta_r(t)$ and differentiating (7) follows:

$$\begin{aligned}\dot{e}_s(t) &= \dot{\theta}_r(t)e_d(t) + v_r(t) + (v(t) + v_d(t))\cos(\theta_e(t)), \\ \dot{e}_d(t) &= (v(t) + v_d(t))\sin(\theta_e(t)) + \dot{\theta}_r(t)e_s(t), \\ \dot{\theta}_e(t) &= \omega(t) + \omega_d(t) - \dot{\theta}_r(t)\end{aligned}\quad (15)$$

As in practice the lateral error is main concern [4], lateral subsystem control can be formulated as a regulation control of the $e_d(t)$. Actually, the aim of the lateral subsystem control is to minimize $e_d(t)$ by the control input $\omega(t)$ in the presence of disturbances $v_d(t)$ and $\omega_d(t)$. Therefore, the lateral model can be reformulated in the form:

$$\begin{aligned}\dot{e}_d(t) &= v(t)\sin(\theta_e(t)) + d_1(t), \\ \dot{\theta}_e(t) &= \omega(t) + d_2(t),\end{aligned}\quad (16)$$

where $d_1(t) = v_d(t)\sin(\theta_e(t)) + \dot{\theta}_r(t)e_s(t)$ and $d_2(t) = \omega_d(t) + \dot{\theta}_r(t)$ are system disturbances. It should be noted that $d_1(t)$ represents mismatched uncertainty because it does not affect on the same input as control

signal $\omega(t)$.

By differentiating and substituting, the model (16) can be presented in the more compact ADRC form as:

$$\ddot{e}_d(t) = v(t)\cos(\theta_e(t))\omega(t) + f_d, \quad (17)$$

where $f_d(t) = \dot{v}(t)\sin(\theta_e(t)) + v(t)d_2(t)\cos(\theta_e(t)) + d_1(t)$ is the “total disturbance” of the lateral subsystem control, which is in the matched channel with the control signal $\omega(t)$. Also, it is evident that, even without system disturbances ($d_1(t) = d_2(t) = 0$), (11) has nonlinear dynamic that considered control problem makes challenging.

In the same as in longitudinal controller structure, the system (11) can be represent in the ADRC-based state-space model as:

$$\begin{bmatrix} \dot{e}_d(t) \\ \dot{e}_d(t) \\ \dot{f}_d(t) \end{bmatrix} = \begin{bmatrix} 0 & 1 & 0 \\ 0 & 0 & 1 \\ 0 & 0 & 0 \end{bmatrix} \begin{bmatrix} e_d(t) \\ \dot{e}_d(t) \\ f_d(t) \end{bmatrix} + \begin{bmatrix} 0 \\ v(t)\cos(\theta_e(t)) \\ 0 \end{bmatrix} \omega(t) + \begin{bmatrix} 0 \\ 0 \\ 1 \end{bmatrix} f_d(t) \quad (18)$$

Total disturbance can be estimate by extended state observer:

$$\begin{bmatrix} \hat{e}_d(t) \\ \hat{e}_d(t) \\ \hat{f}_d(t) \end{bmatrix} = \begin{bmatrix} 0 & 1 & 0 \\ 0 & 0 & 1 \\ 0 & 0 & 0 \end{bmatrix} \begin{bmatrix} \hat{e}_d(t) \\ \hat{e}_d(t) \\ \hat{f}_d(t) \end{bmatrix} + \begin{bmatrix} 0 \\ v(t)\cos(\theta_e(t)) \\ 0 \end{bmatrix} \omega(t) + \begin{bmatrix} l_{d1} \\ l_{d2} \\ l_{d3} \end{bmatrix} e(t) \quad (19)$$

where $e(t) = e_d(t) - \hat{e}_d(t)$ is observer error and (l_{d1}, l_{d2} and l_{d3}) are observer gains. Utilizing a controller with disturbance rejection and estimated variables

$$\omega(t) = \frac{-k_{pl}\hat{e}_d(t) - k_{dl}\dot{\hat{e}}_d(t) - \hat{f}_d(t)}{v(t)\cos(\theta_e(t))}, \quad (20)$$

where k_{pl} and k_{dl} are adjustable controller parameters.

Assuming $\hat{f}_d(t) \approx f_d(t)$, $\hat{e}_d(t) = e_d(t)$, $\dot{\hat{e}}_d(t) = \dot{e}_d(t)$ and substituting (20) into (17) follows:

$$\ddot{e}_d(t) + k_{dl}\dot{e}_d(t) + k_{pl}e_d(t) \approx 0, \quad (21)$$

where one can see that desired control performances could be adjust by the appropriate selecting parameters k_{pl} and k_{dl} . As a result, creating a control signal that assures the error accurately follows the provided dynamics (21) is the problem of following a certain path.

It should be noted longitudinal channel output $v(t)$ affects the UTV lateral control, but not vice versa. Therefore, the motion control of the UTV should be considered as the control problem of two semi-couple subsystems. Consequently, the architecture of the proposed two channel based UTV control is shown in Fig.3.

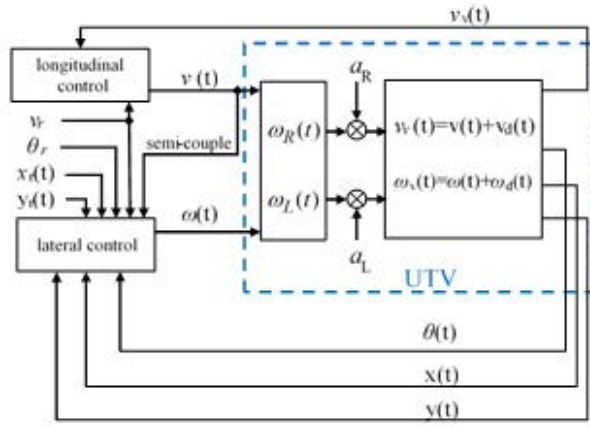


Figure 3. Control architecture of UGV

5. SIMULATION RESULTS

To verify the effectiveness of the proposed control algorithms the numerical simulations are performed based on considered UTV model with parameters $m=0.1\text{m}$ and $b=1.4\text{m}$ in presence of track slipping dynamics as $a_R = 0.15 \sin(5t) + 0.65$ and $a_L = 0.85$. Two different simulations scenarios are assumed and that is presented in the following.

A. Simulation scenario 1: The straight-line reference trajectory tracking

In this scenario the given path represents straight line with $\theta_r = \pi/4$ and $v_r = 1\text{m/s}$. It is assumed that initial UTV coordinates are $x(0) = 0$, $y(0) = 0$ and $\theta(0) = 0$. The longitudinal controller coefficients are tuned based on pole placement method [7] as $\omega_{cv} = k_p$, and $l_1 = 2\omega_{ov}$, $l_2 = \omega_{ov}^2$, where $\omega_{cv} = 3\text{rad/s}$ and $\omega_{ov} = 9\text{rad/s}$ are longitudinal closed-loop system and observer bandwidth, respectively. Similarly the lateral controller coefficients are tuned as $k_{pl} = \omega_{cl}^2$, $k_{dl} = 2\omega_{cl}$, $l_{1l} = 3\omega_{ol}$, $l_{2l} = 3\omega_{ol}^2$, $l_{3l} = \omega_{ol}^3$, where $\omega_{cl} = 9\text{rad/s}$ is lateral closed-loop system bandwidth and the observer bandwidth is change through three cases:

$$\text{C1: } \omega_{ol} = 3\omega_{cl},$$

$$\text{C2: } \omega_{ol} = 6\omega_{cl},$$

$$\text{C3: } \omega_{ol} = 9\omega_{cl}.$$

The tracking results and the cross-track errors for all three cases are presented in Fig. 4 and Fig. 5. From Fig.4 one can see that the tracking performance is highly consistent with the reference path, despite the presence of the track slippage. The high accuracy in following the reference path can also be seen by the cross-track error in Fig 5, but it is evident that system with the larger value of ω_{ol} achieves the better tracking performance in both transient steady-state (see zooming part of Fig.5).

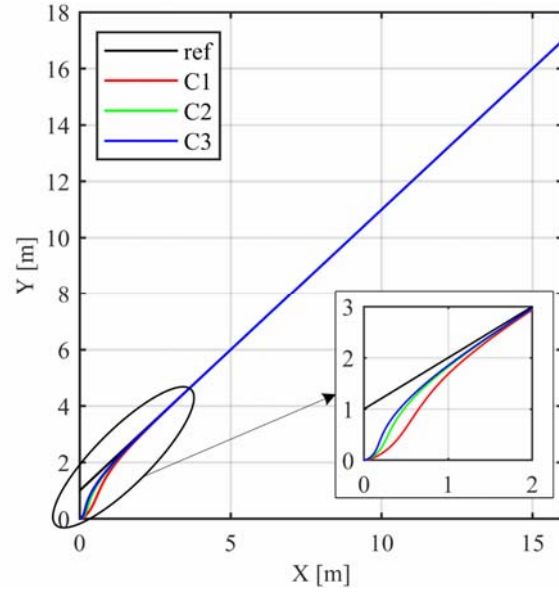


Figure 4. Tracking results of the UTV

The total disturbance estimation error $f_{ed}(t) = f_d - \hat{f}_d$ in lateral channel in steady state is gathered in Fig.6. It can be observed that all cases of ESO tuning provide reliable estimations performances which conduce to the strong capability of disturbance rejection. As it is expected, the better estimation quality and consequently the better tracking performance enables case C3. However, it is paid by larger value of the actuators control signals in transient depicted in left side of Fig.6, while the control signals for C2 and C1 are significantly lower in the transient and smoother in the steady state (right side of Fig.6).

B. Simulation scenario 2: The complex reference trajectory tracking

In this simulation scenarios the complex octagon path tracking is analyzed. Lateral closed-loop system and observer bandwidth are chosen as follows, $\omega_{cl} = 3\text{rad/s}$, $\omega_{ol} = 9\text{rad/s}$, and for the longitudinal controller closed-loop system bandwidth is set as $\omega_{cv} = 3\text{rad/s}$, while following three cases of the observer bandwidth of longitudinal are considered:

$$\text{C1: } \omega_{ov} = 3\omega_{cv},$$

$$\text{C2: } \omega_{ov} = 6\omega_{cv},$$

$$\text{C3: } \omega_{ov} = 9\omega_{cv}.$$

Additionally, a noise is introduced into the measurement of both output signals, for lateral controller (e_d) and for longitudinal controller (v_v), after tenth seconds of simulation.

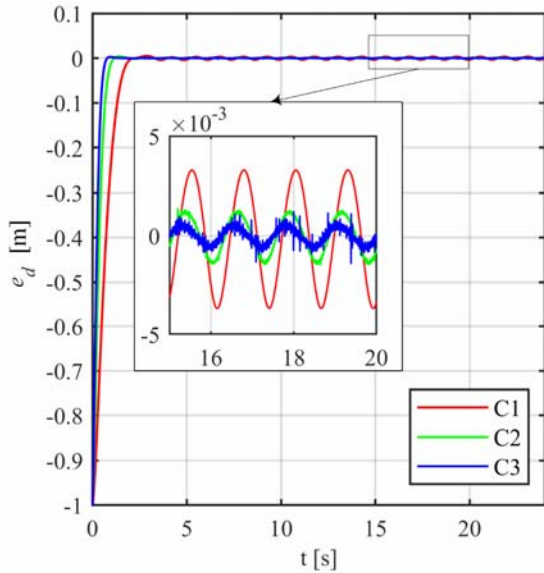


Figure 5. Cross-track errors of the AGV

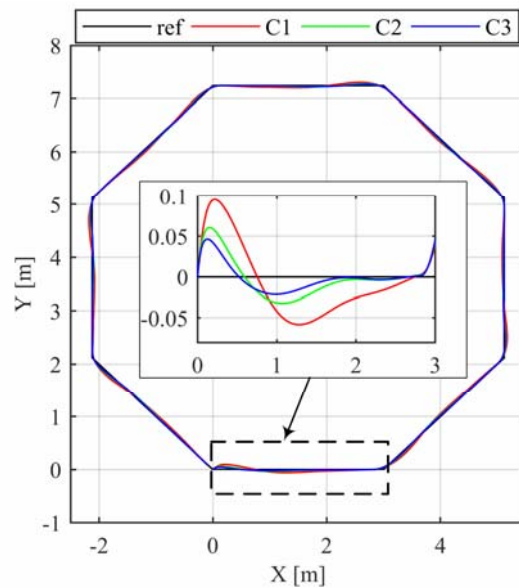


Figure 7. The octagon reference trajectory tracking results for three cases of longitudinal controller observer bandwidth (C1, C2, C3)

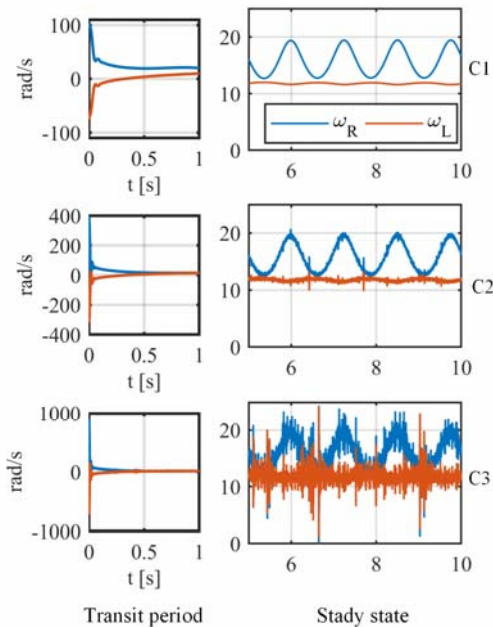


Figure 6. Actuator control signals for cases C1, C2 and C3 in transient (left) and steady state (right)

The obtained UTV octagon trajectory tracking and cross track errors are shown in Fig.7 and Fig.8, where one can note that the proposed control approach provides satisfied tracking performance for the octagon path, regardless of the variable track slipping and noise in measured feedback signals. Similarly as in previous simulation scenario, it is evident that the case C3, with the larger value of observer bandwidth, provides the better tracking accuracy

The total disturbance estimation signal in the longitudinal channel is presented in Fig. 9. It can be seen that the measurement noise has the larger influence on systems with larger value of ω_{ov} (case C3), due to large value of observer gains in that case.

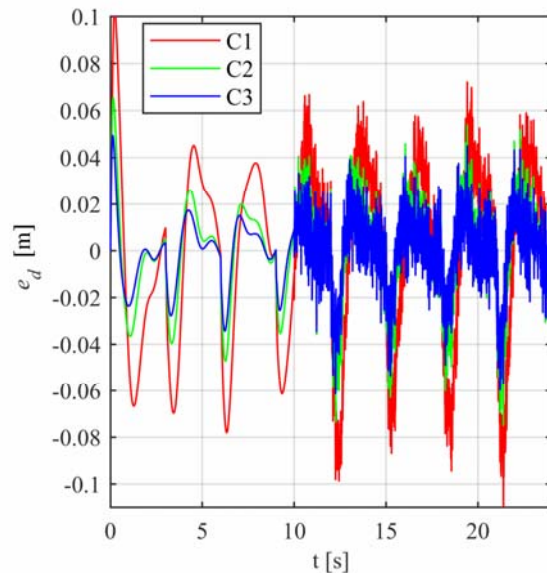


Figure 8. The octagon reference trajectory cross-track errors for three cases of longitudinal controller observer bandwidth (C1, C2, C3)

The results from Fig. 10, shows the efficiency of the longitudinal controller, which enables satisfied control of the real vehicle speed v_r (hold it approximately equal to the speed of the reference point $v_r = 1\text{m/s}$), by its output v in the presence disturbance v_d the reference. To avoid redundancy the results are presented only for case C3.

The actuator control signals are gathered in Fig.11, and it should be noted that these signals are similar. However, one can see that in the case C3 the signals reach the larger peak values, which is the influence of the parameters varying and the measurement noise in the longitudinal channel.

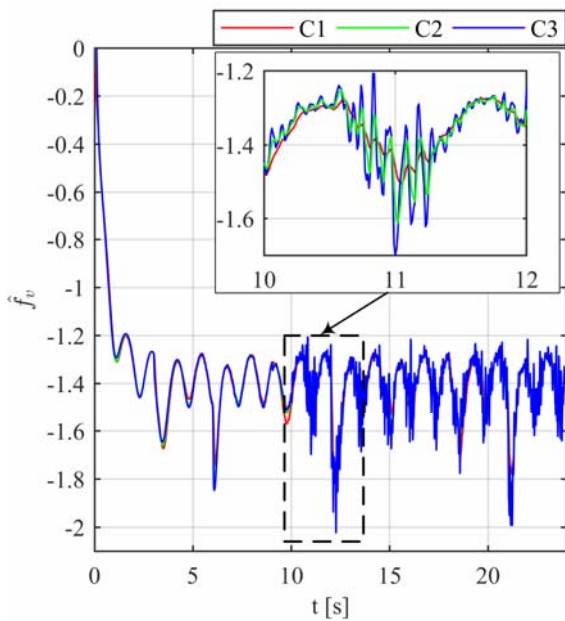


Figure 9. Longitudinal channel total disturbance estimation for three cases of longitudinal controller observer bandwidth (C1, C2, C3)

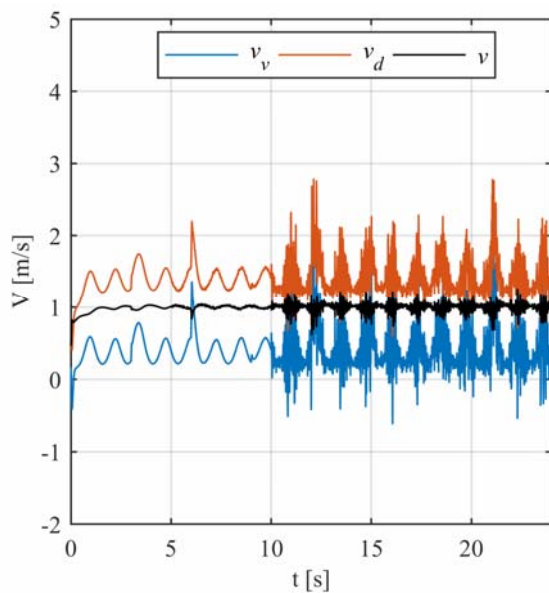


Figure 10. The real speed of the UTV (v_v), output of the longitudinal controller (v) and longitudinal disturbance (v_d) for C3 case of longitudinal controller setup

6. CONCLUSION

The new UTV control strategy based on ADRC longitudinal and lateral controllers are proposed. The appropriately designed forms of ESOs and control laws are enabled estimation and rejection of the internal and external disturbances in the control channels and consequently high path following system performances. The proposed control structure is tested by Matlab/Simulink numerical simulations through two scenarios of path following problem in the presence of variable track slippage dynamics. The achieved results have validated the suggested UTV control solution, and

the further work will be focused to implementation of the designed controllers to real UTV and experimental verifications.

ACKNOWLEDGMENT

The research is extensively supported by University of Defence in Belgrade, Military Academy, Belgrade, Serbia, under grant VA-TT/1/21-23.

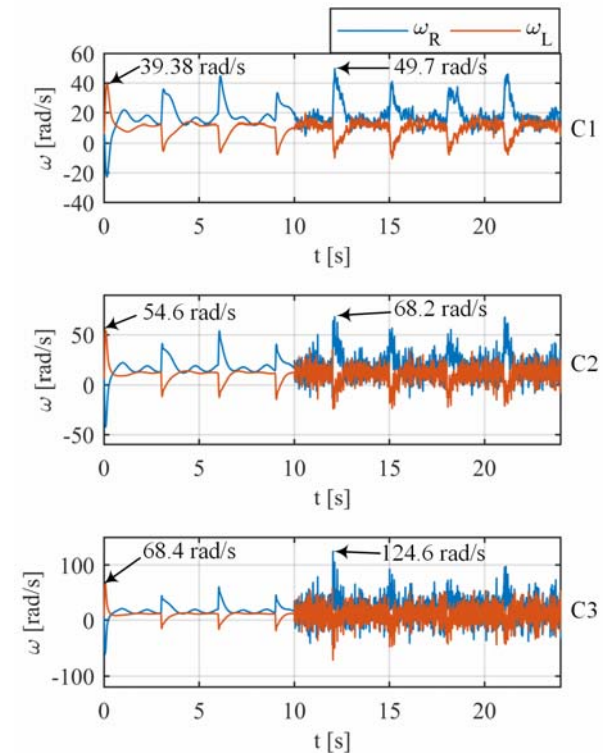


Figure 11. Actuator control signals for the case C1, C2 and C3

References

- [1] NONAMI, K., KARTIDJO, M., YOON: *Autonomous Control Systems and Vehicles*, Intelligent Systems, Control and Automation: Science and Engineering, 2013.
- [2] CHEN S., WENCHAO X., ZHIYUN L., YI H.: *On Active Disturbance Rejection Control for Path Following of Automated Guided Vehicle with Uncertain Velocities*, American Control Conference (ACC) Philadelphia, pp.2446-2451, July, 2019.
- [3] CHEBLY, A., TALJ, R., & CHARARA, A.: *Coupled longitudinal/lateral controllers for autonomous vehicles navigation, with experimental validation*, Control Engineering Practice, 88, 79–96., 2019
- [4] CHEN S., XUE W., LIN. Z., HUANG Y.: *On active disturbance rejection control for path following of automated guided vehicle with uncertain velocities*, In 2019 American Control Conference (ACC), pp. 2446-2451, IEEE, 2019.
- [5] STANKOVIĆ M. i MANOJLOVIĆ S.: *Autonomno kretanje besposadnog vozila po zadatoj putanji primenom algoritma sa aktivnim potiskivanjem poremećaja*, ETRAN, Republika Srpska, Stanišić, 2021.

- [6] WANG H., ZUO Z., WANG Y., YANG H., CHANG S.: *Composite nonlinear extended state observer and its application to unmanned ground vehicles*, Control Engineering Practice 109, 2021.
- [7] GAO Z.: *Scaling and bandwidth-parameterization based controller tuning*, Proceedings of the 2003 American Control Conference, 2003.



SOFTWARE FOR VIDEO STREAMS SYNCHRONIZATION IN LONG RANGE SURVEILLANCE SYSTEMS

ALEKSANDAR SIMIĆ

Vlatacom Institute, Belgrade, aleksandar@vlatacom.com and Belgrade Metropolitan University

TAMARA PAROJČIĆ

Vlatacom Institute, Belgrade, tamara.parojcic@vlatacom.com

MIROSLAV PERIĆ

Vlatacom Institute, Belgrade, miroslav.peric@vlatacom.com

DR DRAGAN DOMAZET, EMERITUS

President of Belgrade Metropolitan University, dragan.domazet@metropolitan.ac.rs

Abstract: Long range surveillance systems are imaging systems used for military or law enforcement applications which include different types of imaging sensors like thermal camera, visible light camera and SWIR camera that are installed on common pan-tilt positioner. Video signals from these sensors propagate to command center through communication network in compressed form (e.g. using H264 video compression) that degrades image quality. In order to perform further signal processing of these stream, like multi-modal target detection using artificial intelligence EDGE processing platforms, these streams should be synchronized in time domain and in observation field of view. In this paper we present new solution for this problem which uses embedding metadata information into video frames on the host side in a manner that this information can be reconstructed on the receiver side. The problem is solved by embedding text and markers at special positions in a frame that keeps information about current azimuth, elevation, field of view of each stream together with frame sequencing marking. The solution also exploits the fact that all streams have in one moment, determined by time synchronization of each stream's frame sequence, the same azimuth and elevation. We present measurement results in urban environment using Vlatacom Institute's multi-sensor imaging systems class VMSIS3.

Keywords: Surveillance, multi-spectral imaging systems, video stream, synchronization

I. INTRODUCTION

In order to achieve its mission in the majority of day/night and meteorological conditions long range surveillance systems – LRSS incorporate multi spectral cameras from various ranges like visible light, thermal in long range infrared – LWIR or medium range infrared MWIR or short range infra-red SWIR. Some early-days solution could be found in [1] and [2], while the more detailed description of one of the world-class solution, denoted as Vlatacom Multisensor Imaging System, third generation, VMSIS3 is presented in [3]. The most important component of LRSS which should be carefully tailored for systems' mission is presented in [4] and [5]. Apart from installed cameras, video signal processing

elements are crucial for overall long-range surveillance system performance [6]. One typical application is target tracking [7]. In order to activate target tracker, various modes of target detection system are utilized ranging from manual, via motion detection to artificial intelligence- AI based modules.

Modern surveillance system utilizes several thousands of cameras to cover area of interest. This yields to camera networks. Some basic principles are described in [8] and [9]. Video stream from multiple cameras in LLSS are transmitted to command and control – C2 center usually in digitalized and compressed form. In order to efficiently utilize transmission network bandwidth video stream is compressed. One of the most popular video compression algorithms is H.264 [10]. This algorithm is lossy type, which means that video quality is degraded in comparison to uncompressed raw video. The algorithm is optimized for

visible color image and its performance comparison to other video compression algorithm are investigated in [11] and [12]. Unfortunately, the algorithm is not equally optimized for thermal images, which are intensity only, especially in the cases when image is not focused enough or too noisy. Tailoring algorithm parameters for this use case is usually proprietary by LLSS manufacturers.

Unlike CCTV type of cameras that have fixed position and thus can be easily integrated into advanced video analytics applications like pedestrian monitoring [13] and [14], LLSS video stream has additional parameters like camera position specified by pan (azimuth) and tilt (elevation) angles and zoom (field of view – FOV). This information cannot be accurately embedded into a compressed video stream. Since in a LLSS multiple cameras share the same positioning platform, denoted as a pan-tilt positioner, in this paper we utilize this fact and explore how to embed this information in efficient way in video stream so video analytics software in a C2 center can utilize acquired information more efficiently. The paper is structured as follows: In section II we give system description, in section III we give detailed description of the algorithm in section IV we give measurement results and in section V we give conclusion

II. SYSTEM DESCRIPTION

Overlaid text detection and embedded marker detection was researched/analyzed with the idea of later using it for synchronization of three different cameras- SWIR, Thermal and Low Light. In figure 1 are shown examples of frames from all three cameras.

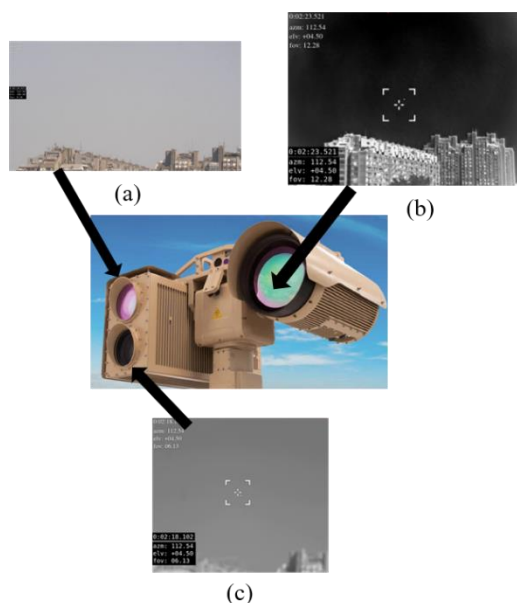


Figure 1. Examples of frames with embedded text from all three cameras: (a) Low Light, (b) Thermal, (c) SWIR

Information about azimuth, time, elevation and field of view is overlaid on videos for testing methods used for character recognition. Also, two types of markers were embedded in videos, blinking and moving marker. Blinking marker is one pixel that appears every 30 frames

at the same position for every video, and the idea is to use this marker for camera synchronization. Moving markers are one pixel information moved throughout first row of video, moving its position one pixel per frame. This marker carries analogue information- its position- and this can be used for encrypting any kind of information that user needs. In figure 2 is shown an example of frame which has moving, blinking markers and overlaid text information.

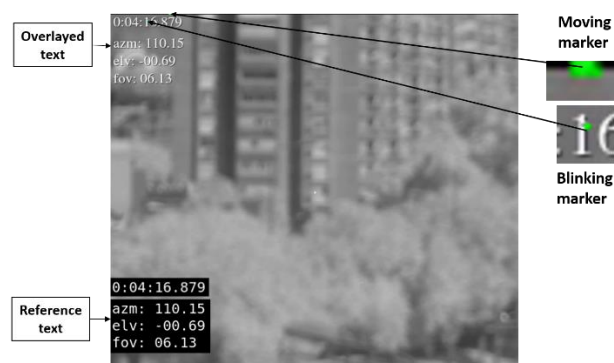


Figure 2. Example of frame with blinking, moving marker, and overlaid text

Analysis was done on 27 videos, nine videos for each channel (SWIR, Thermal, Low Light). Videos were recorded using Vlatacom vMSIS C-825 camera.

The nine videos included recording of three different surroundings/scenes, text written in two different fonts, and text written with or without homogenous background, every video included two types of embedded markers.

III. DESCRIPTION OF THE ALGORITHM

Environment used for data processing is *Python ver. 3.8* (Python Software Foundation, open source) in Spyder (Python Software Foundation, open source). The used libraries were: numpy [15], openCv [16], matplotlib [17], pandas [18], pytesseract [19].

Blinking marker is placed at the same positions in frames from all three cameras thus, the information about marker position was available and its detection was simplified.

Detection of blinking marker was performed by checking if the value of weight function, defined by equation (1) (sum of absolute differences between red, green and blue channels) is greater than threshold value T_{HF} , in the area near/around the previously determined position.

$$f = \sum |R-G| + |R-B| + |B-G| \quad (1)$$

where

- R – pixel value of red channel,
- G – pixel value of green channel, and
- B – pixel value of blue channel.

Threshold value is determined by comparing values of weight function for every video. We found that value of $T_{th}=300$ is the optimal value. Moving marker is always placed in the first row so its detection implied finding the y-coordinate (x-coordinate was always 0) of the maximum value of weight function.

For text detection two approaches were used *Tesseract* and template matching method.

We use open-source OCR (Optical Character Recognition) engine *Tesseract* [20]. *Tesseract* uses trained LSTM (Long short-term memory) models to extract and interpret information from a variety of documents.

Preprocessing for *tesseract* included cropping text parts of images and converting them to grayscale. We have tested OCR algorithms with two types of fonts (*DejaVu Sans Mono* and *Nimbus Roman No9 L*), with and without homogenous background. *Tesseract* was configured to treat the image as a single word and to read only digits, it takes image and converts it to string. The main downside of using OCR engines is that they are time-consuming, when using *Tesseract* process time per frame was around 0,5 seconds. Beside of being time-consuming *Tesseract* accuracy was low thus other method was proposed.

Template matching is a fast process that moves the template over the entire image and calculates the similarity between the template and the covered window on the image. It is implemented via two-dimensional convolution function from OpenCV framework. Since the font and the position of text were known/predetermined it was possible to use the template matching method. First, it was necessary to make templates of digits, plus and minus signs for two fonts. Template matching was implemented on parts of images that contained information about time, azimuth, elevation and field of view. A threshold value of 0,9 was used to determine if the similarity between the window of the image and the template is high enough.

IV. MEASUREMENT RESULTS

Marker detection was successful for both moving and blinking markers. In figure 3 are shown graphs for y coordinate of moving marker for one video of different types of cameras. On these graphs we can see that y-coordinate has linear trend in range from zero to the maximum width of image. The difference between y-coordinates in adjacent frames can't be easily observed from these graphs so in figure 4 are shown graphs of differences between neighboring frames.

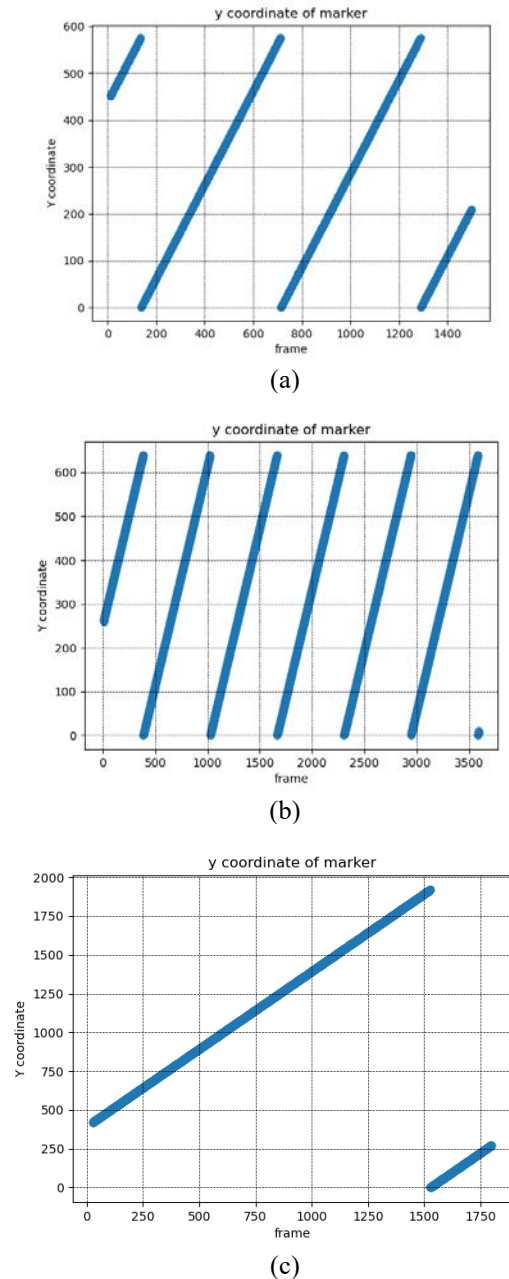
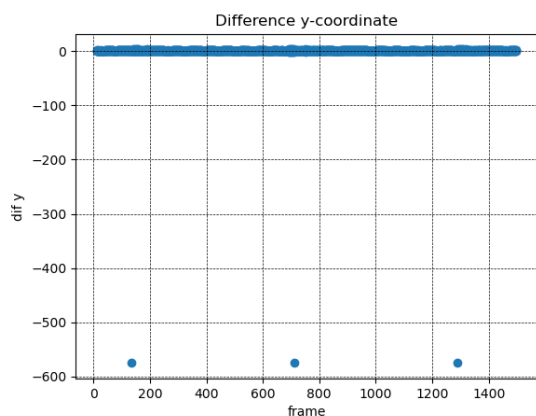
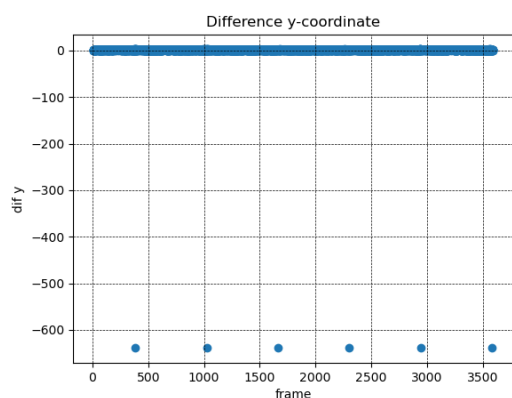


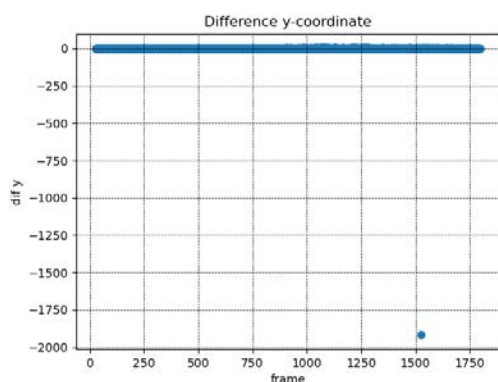
Figure 3. Graphs for y coordinate of moving markers: (a) SWIR, (b) Thermal, (c) Low Light



(a)



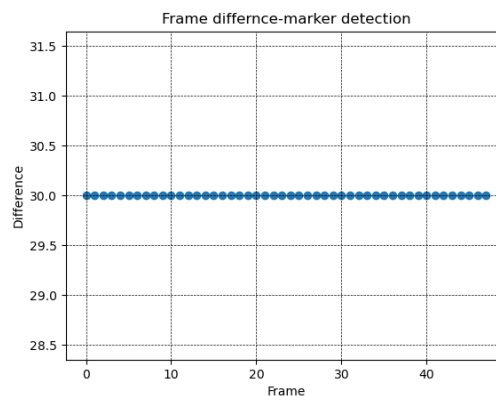
(b)



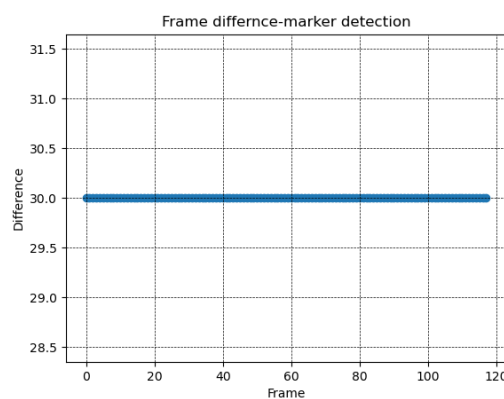
(c)

Figure 4. Difference between y coordinate of moving marker of adjacent frames: (a) SWIR, (b) Thermal, (c) Low Light

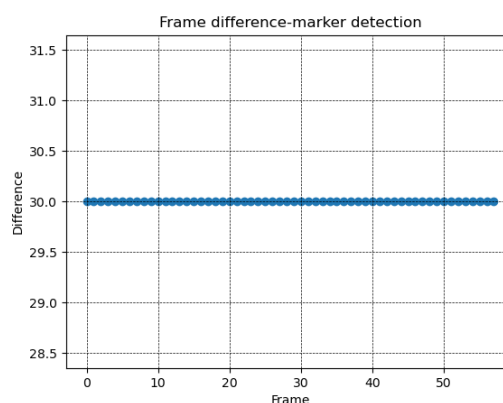
In figure 5 are shown differences between frames in which blinking marker was detected. Since this value is always the same, marker detection was successful.



(a)



(b)



(c)

Figure 5. Difference between frames where blinking marker was detected: (a) SWIR, (b) Thermal, (c) Low Light

Text detection

Tesseract

Using *Tesseract* included lot of fine tuning of crops of image, the results obtained weren't consistent even for the same video where value of azimuth, elevation and field of view is same throughout frames. The execution was slow, per video time of execution was in average around 20 minutes. Resolution of characters, which was 10x14 pixels, represented main issue for *Tesseract* since it has higher accuracy when using images with larger resolution. However increasing resolution of characters would make

the characters too big for overlaying in videos from the end user perspective.

Template Matching

In order to overcome these issues the Template Matching was subsequently applied. Percentages of frames in which text was wrongly read are given in tables 1-3. Text written using DejaVu Sans Mono font with homogenous black background (in a bottom left corner) was used as a reference, because acquired values were equal to true values..

First column of tables represents ordinal number of video, in videos from 1 to 3 *Nimbus Roman No9 L* font without homogenous background was used for text in upper left corner, in videos from 4 to 6 *Nimbus Roman No9 L* font with homogenous background was used also for text in upper left corner, and for videos from 7 to 9 *DejaVu Sans Mono* font without homogenous background was used for upper left corner. Videos S1, T1, V1, S4, T4, V4 and S7, T7, V7 are recordings of sky in the background; S2, T2, V2, S5, T5, V5 and S8, T8, V8 are recordings of with building in background, while S3, T3, V3, S6, T6, V6 and S9,T9,V9 are recordings of traffic intersection in background. Letter S in video indexing represents videos recorded using SWIR camera, letter T in video indexing represents videos recorded using Thermal camera while letter V in video indexing represents videos recorded using LowLight camera.

Table 1. Percentage of wrongly read text for SWIR camera, using template matching method

Videos	Azimuth (%)	Elevation (%)	Field of view (%)	Time (%)
S1	0.20	2.48	3.78	1.32
S2	0.61	4.56	2.68	2.19
S3	2.96	3.57	2.38	3.03
S4	0	0	0	0.68
S5	0.07	0	0	0
S6	0.14	0	0	0.04
S7	2.80	2.45	1.95	1.04
S8	0.34	0	0	0
S9	0.81	0.27	0.20	0.45

Table 2. Percentage of wrongly read text for Thermal camera, using template matching method

Videos	Azimuth (%)	Elevation (%)	Field of view (%)	Time (%)
T1	0.20	2.48	3.78	2.32
T2	0.61	2.56	2.74	2.19
T3	1.96	4.57	3.38	2.03
T4	0	0	0	0.06
T5	0.07	0	0	0
T6	0.14	0	0	0.24
T7	3.80	2.05	5.95	3.64
T8	0.34	0	0	0
T9	0.81	0.27	0.20	0.56

Table 3. Percentage of wrongly read text for Low Light camera, using template matching method

Videos	Azimuth (%)	Elevation (%)	Field of view (%)	Time (%)
V1	34.12	26.78	19.66	17.76
V2	19.34	22.57	18.36	19.49
V3	5.67	10.12	11.47	16.9
V4	0.17	0	0	0.25
V5	0.06	0	0	0.16
V6	0.11	0	0	0.16
V7	12.56	22.47	18.72	18.44
V8	16.67	55.46	29.49	40.88
V9	13.28	10.05	12.06	41.11

Since the lowest error values were for videos 4, 5 and 6 it can be concluded that text recognition is more accurate when text is written with homogenous background, which was anticipated. Also by comparing the error percentages from the tables it can be observed that text detection had higher error percentage for LowLight videos. By analyzing tables for SWIR and Thermal videos it can be interpreted that text was wrongly read for videos where it wasn't overlaid on homogenous background and the scene behind it wasn't homogeneous.

The templates that were used had white characters written on black background. They are the reason for lower accuracy for LowLight videos and text written without homogeneous backgrounds. Examples of the templates that were used are shown in Figure 6.

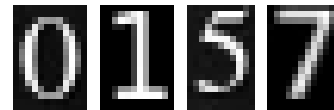


Figure 6. Example of templates used for OCR

In Figure 7 are represented examples of text overlaid without homogenous background and with homogenous background.

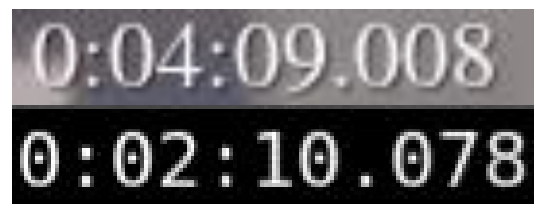


Figure 7. Text overlaid without and with black homogenous background

Impact on the results of text detection and recognition also has H264 compression. In figure 8 is given an example where before mentioned compression had affected text by smearing it in some frames.

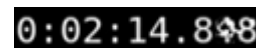


Figure 8. Example of smeared time stamp

Synchronization of two rtsp streams using embedded markers

Video signal propagates from camera to client through frame grabber, enters processing module (JetsonTX2) where it is compressed (H264 compression) and after that, using rtsp server, rtsp stream is generated which further propagates through network infrastructure and finally it is received on the client side using rtsp client software. Every element in this path affects latency of video signal, which can be variable. Most impact of latency variability comes from propagation through network. So, in general case, two video streams received on client side are not in synchronization. Signal processing chain is shown on figure 9.

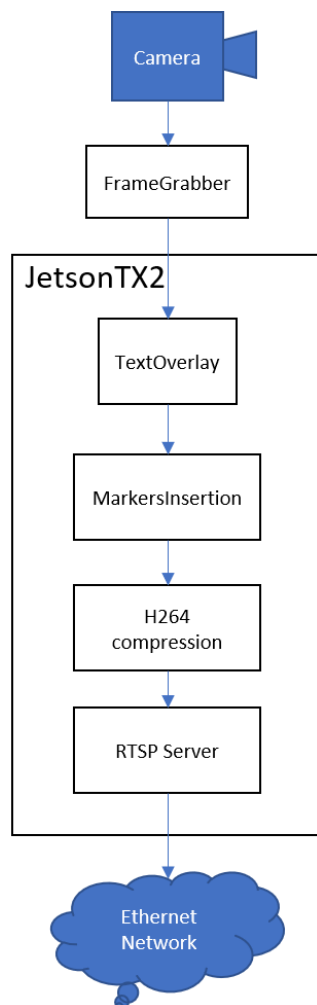


Figure 9. Signal processing chain on single channel

We embedded synchronization markers on every 2 seconds on both video streams (Thermal and LowLight). Markers are embedded just before H264 compression. It is considered that latency of signal through frame grabber is fixed. When we detect these markers on frames received on client side, and offset them with that fixed latency amount, streams are synchronized. Results are shown on following images.

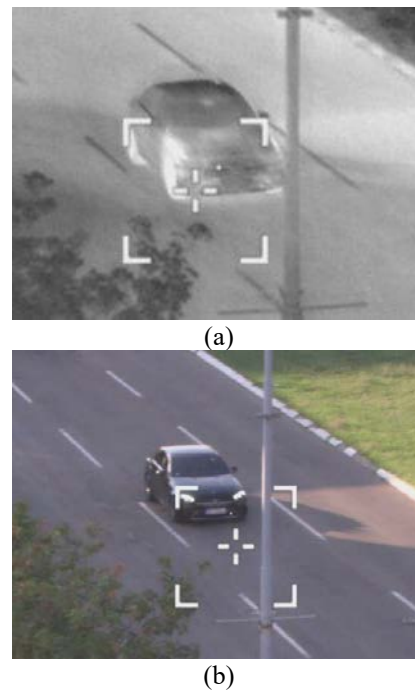


Figure 10. Unsynchronized stream from (a) Thermal and Visible (b) camera

Figure 10 shows two frames received from both cameras without synchronization. Traffic pole is used as reference and we can see that car approaching pole is not on the same place on two images. Measuring time difference between two frames where the object of interest (car) is on the same place we can find out fixed latency between video signals which is 99ms in this case. After that, we simulated network latency of 100ms (with „latency“ parameter of gstreamer pipeline which is used as rtsp client). On Figure 11 we can see larger synchronization issue caused by this latency.

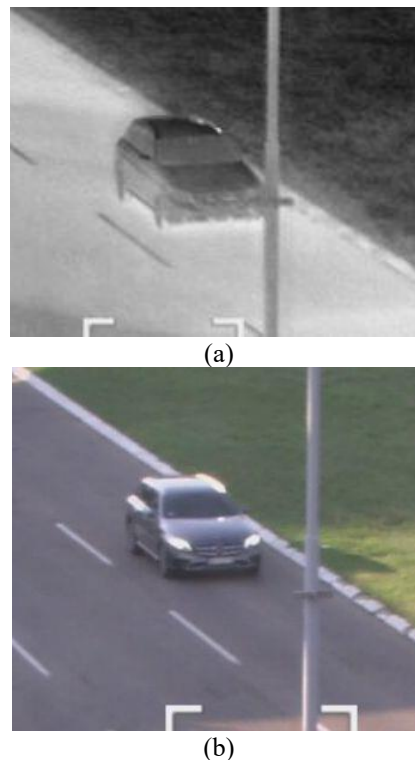


Figure 11. Unsynchronized stream from (a) Thermal and Visible (b) camera with network latency of 100 ms

After detection of embedded markers on both streams on Figure 12 is shown that two streams are well synchronized.

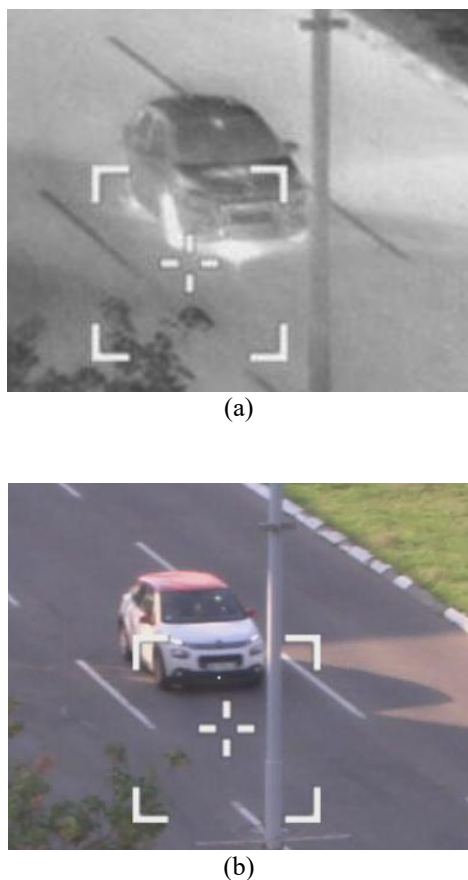


Figure 12. Synchronized streams from (a) Thermal and Visible (b) camera

Synchronization of azimuth and velocity data with video frames

Meta data relevant for optical systems are propagated through independent RTSP stream (azimuth, velocity, field of view, digital zoom value, etc.). There is a need to synchronize this data with video frames. Overlaying textual information on video stream (before H264 compression) and taking into account fixed amount of latency between actual scene and this data we can synchronize data with appropriate video frame.

Further investigation proposals

Proposed methodology enables data transfer through overlaid text on the image and also using markers which are embedded on first line of the frame. Embedded markers on first line of the image transfer information which has precision determined with image size. In VGA image it is 1/640, HD image 1/1280, FullHD image 1/1920. Markers that we used transfer binary information, but it can be investigated how to achieve larger precision. There can be used, for instance, markers with different illuminance, or

we can use larger number of markers with appropriate coding.

V. CONCLUSION

Proposed methodology using information embedded into compressed video stream and its reconstruction on client side can be used for solving synchronization problem of rtsp streams in multisensors optical systems and also for data synchronization (azimuth, elevation, field of view...) with video frames. Result for text recognition on thermal and SWIR channel give satisfactory results, while for low light channel, methodology can be used only if overlaid text has fixed (e.g. black) background. On the other hand, synchronization by embedded markers proves reliable on all channels, so the idea of using azimuth and elevation info for one, the most reliable channel to all available video channels is feasible.

References

- [1] TRZASKAWKA,P., KASTEK,M., ŻYCZKOWSKI,M., DULSKI,R., SZUSTAKOWSKI,M., CIURAPIŃSKI,W., BAREŁA,J.: *System for critical infrastructure security based on multispectral observation-detection module*, Proceedings of the SPIE, Volume 8896, 2013.
- [2] SZUSTAKOWSKI,M., ŻYCZKOWSKI,M., KAROL,M., KASTEK,M., DULSKI,R., SZUSTAKOWSKI,A.,M., BAREŁA,J., MARKOWSKI,P., KOWALSKI,M.: *Ultra long range surveillance camera for critical infrastructure protection research range*, SPIE Security + Defence, Dresden, Germany, 2013.
- [3] CIZELJ,V.: *Vlacom Institute of High Technology—Ten Years since the First Accreditation*, Belgrade, 2021; ISBN 978-86-7466-891-7.
- [4] PERIĆ,D., LIVADA,B., PERIĆ,M., VUJIĆ,S.: *Thermal Imager Range: Predictions, Expectations, and Reality*, Sensors 2019.
- [5] KURODA,T.: *Essential principles of image sensors*, Boca Raton, Florida, CRC Press, 2015.
- [6] LATINOVIĆ,N., POPADIĆ,I., TOMIĆ,B., SIMIĆ,A., MILANOVIĆ,P., NIJEMČEVIĆ,S., PERIĆ,M., VEINOVIĆ,M.: *Signal Processing Platform for Long-Range Multi-Spectral Electro-Optical Systems*, Sensors, 2022.
- [7] STOJANOVIĆ,M., VLAHOVIĆ,N., STANKOVIĆ,M., STANKOVIĆ,S.: *Object Tracking in Thermal Imaging using Kernelized Correlation Filters*, Proc. of 17th International Symposium INFOTEH, Jahorina, March 2018.
- [8] AGHAJAN,H., CAVALLARO,A.: *Multi-Camera Networks: Principles and Application*, Academic Press, 2009.
- [9] WANG,X.: *Intelligent multi-camera video surveillance: A review*, Pattern Recognit. Lett. 2013.
- [10] ITU-T REC. H.264.: *SERIES H: AUDIOVISUAL AND MULTIMEDIA SYSTEMS, Infrastructure of audiovisual services – Coding of moving video, Advanced video coding for generic audiovisual services*, revision 08/2021.

- [11] KHAN,I,U., ANSARI,M.,A., YADAV,A., SAEED,S.,H.: *Performance analysis of H.264 video decoder: Algorithm and applications*, 2015 International Conference on Energy Economics and Environment (ICEEE), 2015.
- [12] LAYEK,A.: *Performance analysis of H.264, H.265, VP9 and AV1 video encoders*, 2017 19th Asia-Pacific Network Operations and Management Symposium (APNOMS), 2017.
- [13] DIMITRIEVSKI,M., VAN HAMME,D., VEELAERT,P., PHILIPS,W.: *Cooperative Multi-Sensor Tracking of Vulnerable Road Users in the Presence of Missing Detections*, Sensors 2020.
- [14] NEFF,C., MENDIETA,M., MOHAN,S., BAHARANI,M., ROGERS,S., TABKHL,H.: *REVAMP2T: Real-Time Edge Video Analytics for Multicamera Privacy-Aware Pedestrian Tracking*, IEEE Internet of Things Journal, vol. 7, no. 4, pp. 2591-2602, April 2020.
- [15] HARRIS,C.,R., MILLMAN,K.,J., VAN DER WALT,S.,J.: *Array programming with NumPy*, Nature 585, 357–362, 2020.
- [16] BRADSKI,G.: *The OpenCV Library*, Journal of Software Tools, 2000.
- [17] HUNTER J.,D.: *Matplotlib: A 2D Graphics Environment*, Computing in Science, Engineering, vol. 9, no. 3, pp. 90-95, 2007.
- [18] MCKINNEY,W.: *Data structures for statistical computing in python*, Proceedings of the 9th Python in Science Conference. p. 51–6, 2010.
- [19] DOCSUMO: *10 Best OCR software in 2022*, https://docsumo.com/blog/best-ocr-software_2022.
- [20] GITHUB INC: *Tesseract OCR* <https://github.com/tesseract-ocr/tesseract>, 2022.

DESIGN OF CONTROL SOFTWARE FOR EXTREME PERFORMANCE GYRO-STABILIZED PAN TILT POSITIONER FOR ELECTRO-OPTICAL SYSTEMS

MILOŠ RADISAVLJEVIĆ

Vlatacom Institute, Belgrade, milos.radisavljevic@vlatacom.com

MILOŠ STANKOVIĆ

Vlatacom Institute, Belgrade, milos.stankovic@vlatacom.com

DORĐE VULOVIĆ

Vlatacom Institute, Belgrade, djordje.vulovic@vlatacom.com

DRAGAN DOMAZET

Metropolitan University, Belgrade, dragan.domazet@metropolitan.ac.rs

Abstract: In this paper a design of control software for extreme performance gyro-stabilized pan tilt positioner for electro-optical systems is presented. This control software is designed to achieve desired extreme performance based on the selected sensors and actuators. The short review of the structure of the gyro stabilized positioners is presented. For pan tilt positioners for EO (electro-optical) systems, special attention must be paid to the dynamic performance of the positioner in order to meet the high demands arising primarily from the need to stabilize LOS (line of sight) due to disturbances to which the EO system is exposed, especially at small FOVs (field of view). The generalized structure of the control software is defined and the parameters and functions of the key components are discussed.

Keywords: Pan Tilt positioner, electro-optical systems, gyro stabilization.

1. INTRODUCTION

In this paper, a software structure for a pan tilt positioner with extreme performance is proposed. Pan-tilt positioners are used in many areas where the goal is to precisely point the object of interest. The use of pan-tilt positioners in electro-optical (EO) systems arises as a result of the need to move the same optical system to cover a larger part of the space, without losing the performance of the optical system itself (resolution, field of view...).

There are articles related to these topics in the available literature [1]–[6], however, details on how to determine the structure and input parameters of the control software used in the devices are not readily available. Similar principles are applied in this article, but the main contribution of the research lies in the use of specifics related to the selection of hardware and the analysis of the required performance as basic inputs for the design of controllers for the target group of EO systems. The paper combines analyzes for an adequate understanding of control system design problems, such as the analysis of required performance and the right choice of hardware structure and components.

After the introduction, the basic concepts of the system and its use in electro-optic devices are given. In the third chapter, the hardware structure of pan tilt is described with the given basic parts. In addition to the general structure of pan tilt, both the choice of the shape of the PT and its basic hardware parts are described. At the end of the chapter, there is an overview of the influence of the control method on the selection of the components as well as the method of

selecting the performance of the system. Then, in the next chapter, the structure of the control software is described. In addition to the software architecture diagram, both the mechanism and the way of controlling the actuators are described. In the fifth chapter, the description of the model in Simulink is given and the results of the simulations are presented. At the end of the paper, a conclusion can be found with the direction of further research.

2. BASIC CONCEPTS OF THE SYSTEM AND ITS USE IN ELECTRO-OPTIC DEVICES

The proposed gyro-stabilized pan-tilt platform is a platform with two degrees of freedom [7] consisting of an inner axis (elevation axis) with a limited rotation angle ($\pm 90^\circ$) and an outer axis (azimuth axis) with an unlimited rotation angle ($N \times 360^\circ$).

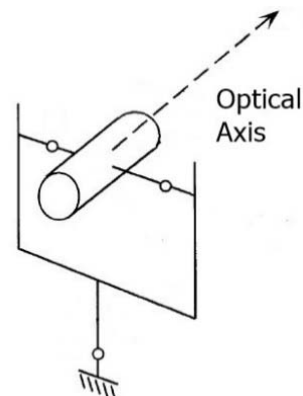


Figure 1. Platform with two degrees of freedom

The basic parts are the mechanical frame that provides the ability to move in both axes, then the motors with their motor drivers and the controllers.

The basic block diagram of one-axis control is shown in

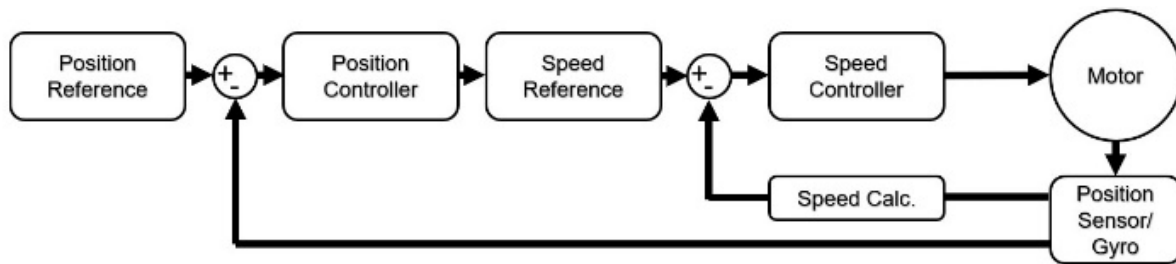


Figure 2. Block diagram of the system model

EO systems generally consist of one or more sensors and are intended for observing objects or areas of interest. In order to achieve observability in different conditions (day, night, fog...), such systems are equipped with image sensors in using different EM spectral wavelength mounted on a pan tilt platform. In addition to cameras in the visible part of the spectrum, cameras in the MWIR or LWIR spectral range or in some cases also in the SWIR part of the spectrum are most often added. Also, in addition to these cameras, other sensors can be added, such as sensors for geolocation of the system (GPS, compass) as well as a device for measuring the distance to the observed target (LRF). Fig. 1 shows an example of an EO System on a pan tilt platform, which consists, beside a camera in the visible part of the EM spectrum, a MWIR camera and an LRF.



Figure 3. vMSIS-EO system with visible light camera, MWIR camera and laser rangefinder on pan tilt positioner

The performance of the pan-tilt positioner is particularly important in systems with a small FOV, less than a degree, where precise positioning is required. Agility, speed of movement of the system, stems from the need to move from one scene to another in the shortest possible time with same FOV (narrow viewing angle).

During work with EO systems as one of the key components that affects the perception of the observer, in addition to precise positioning, in order to observe objects of interest, image stabilization was also identified, especially in systems with a long detection range where viewing angles are very narrow. Disturbances occurring in the image of the EO system can be roughly divided into low frequency

Figure 2. As can be seen from the diagram, actuator control is performed through two loops, the inner one for motor speed control and the outer one for position. The design of the control software includes both control loops and it is similar for both axis, azimuth and elevation.

disturbances (up to 10Hz) and higher frequency disturbances (>10Hz). By implementing different types of electronic stabilization such as IMU [8] or video stabilization implemented on a signal processing platform [9], higher frequency disturbances are successfully suppressed, so one of the main challenges is the successful elimination of low frequency disturbances. In EO systems with LRF, where it is necessary to determine the distance of the target, the absence of a stabilized platform in case of disturbances, makes the distance measurement very difficult because the target moves in relation to the beam of the LRF, so it is difficult to hit it. As another example where gyro stabilization is necessary is the use of an EO system on a moving vehicle or vessel where it is necessary for the observed target to remain in the field of view even during movement.

These and similar types of disturbances that occur in EO systems can be successfully eliminated by using a gyro-stabilized pan-tilt platform.

3. STRUCTURE OF GYRO STABILIZED PAN TILT

The design of the pan tilt mechanical frame is one of the important elements for system performance in terms of accuracy, durability, reliability, speed, size, weight and cost. Due to the diversity of optical components within the EO system, (dimensions, mass distribution, shape, etc.) the very arrangement of the center of mass (CM) of the equipment as a whole is of big importance. It is very important that all components behave as one body with CM in the axes of rotation. If there is a small imbalance of the equipment, depending on the distance from the axis of rotation, the pan-tilt performance can be degraded. Disadvantages in the CM layout are reflected in the pan-tilt design, engine selection, shape and robustness of the structure, etc. Imbalances caused by inadequate arrangement of equipment require motors with higher torque, which increases the size of the motor itself and the whole system.

A "U"-shaped platform was proposed in order to achieve better dynamic performance, a smaller moment of inertia of the entire system, which is very important on platforms mounted on a moving vehicle or vessel. Additionally, experiences with T-shape platforms mounted on a telescopic

pole show that the T-shape approach has major drawbacks. Due to the large moment of inertia of the system, which is a consequence of its shape (mass distributed on the larger arm), problems arise in the stability of the system on an insufficiently rigid base such as a telescopic pole.

Pan-tilt architecture with the equipment inside the structure, U shape pan-tilt enables the manipulation of heavier equipment. In U shape pan-tilt, due to the layout of the equipment within the system structure, it is possible to better arrange the CM equipment, which, as already stated, is of great importance for the performance of the whole system. Motors with smaller dimensions and a larger number of poles provide the possibility of high-resolution stabilization.

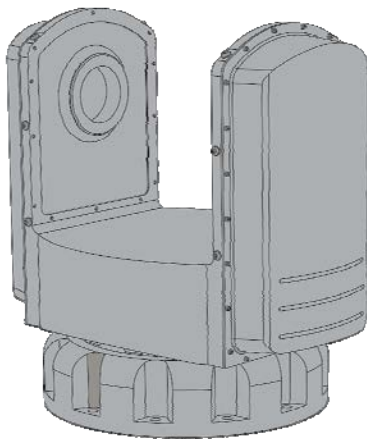


Figure 4. U-shape pan-tilt example

Within the axle driving system, there are several ways to transfer torque from the engine to the drive axles. Belt or gear transmission applications are common. The disadvantage of such a transmission is the delay caused by the elasticity of the material from which the transmissions are made, as well as gaps. As a solution, we come across with the latest generation of direct drive motors. Direct drive motors have a great advantage over other motors in

that they are directly connected to the torque transmission, to the shaft.



Figure 5. Direct Drive motor

In order to avoid the influence of the drift of the gyroscope [10] and to maintain the level of accuracy of the positioning of the platform in both axes, it was foreseen that there are two operating modes of the platform, with gyro stabilization on and off. In the operating mode with the gyro stabilization off, the position is maintained using a high-resolution and accurate encoder. In the mode with gyro stabilization on, maintenance of the set position is performed using the gyroscope added on encoder position. Therefore, two position sensors, a gyroscope for operation in stabilized mode and a precision encoder for operation in non-stabilized mode, are required.

A complete block diagram of the motor control and controlling hardware is presented in the following figure

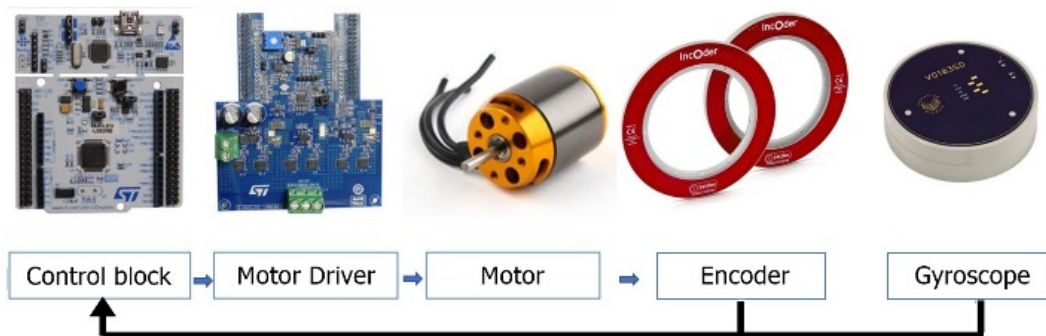


Figure 6. Block diagram of components along one axis of rotation

For the necessary signal passage of both power supply and communication through the azimuth axis, and since it is necessary to ensure $N \times 360^\circ$ rotation, a slip ring is necessary [11].

The stabilization performance must be defined so that the stabilization error does not affect the characteristics and performance of the EO system itself.

Observing the LRF, in order to ensure accurate measurement of the target distance by the LRF, it is necessary that the stabilization error be smaller than the beam divergence of the LRF itself so that the target remains within the given beam.

As for cameras, in order to avoid blur caused by the movement of the scene during the exposure of a single

frame, the movement of the scene must be less than 1/3 of the visual angle of one pixel.

For the simulation, the load in the elevation axis is approximated by a cube with a mass of $m_e=5 [kg]$ and a side of $a=0.1 [m]$, which, according to (1), gives elevation moment of inertia I_e :

$$I_e = \frac{1}{8} m_e a^2 = 0.00833 [kgm^2] \quad (1)$$

Considering that it is proposed the U shape pan tilt, we can consider that from the point of view of the azimuth axis, the load can be approximated by a cylinder with total mass and dimensions equivalent to the sum of the masses and dimensions of the payload itself and the mechanical construction of the elevation axis, including the motor and sensors (encoder, FOG...). Therefore, the total mass for the azimuth axis is taken as $m_a=12 [kg]$ and the radius of $R=0.2 [m]$ which, according to the (2) for the moment of inertia of the cylinder, gives:

$$I_a = \frac{1}{2} m_a R^2 = 0.24 [kgm^2] \quad (2)$$

4. CONTROL SOFTWARE STRUCTURE

Typical embedded system software consists of several modules, most often implemented in C or C++. C/C++ lends itself well to hardware modules such as peripherals such as motor drivers or position sensors. These modules are usually universal and are only tied to the specific hardware being used.

On the other hand, control algorithms as software modules are specific to a given system and must be simulated and verified in order to achieve the best possible performance.

The block diagram of the firmware for the controller [12] is given in the following figure:

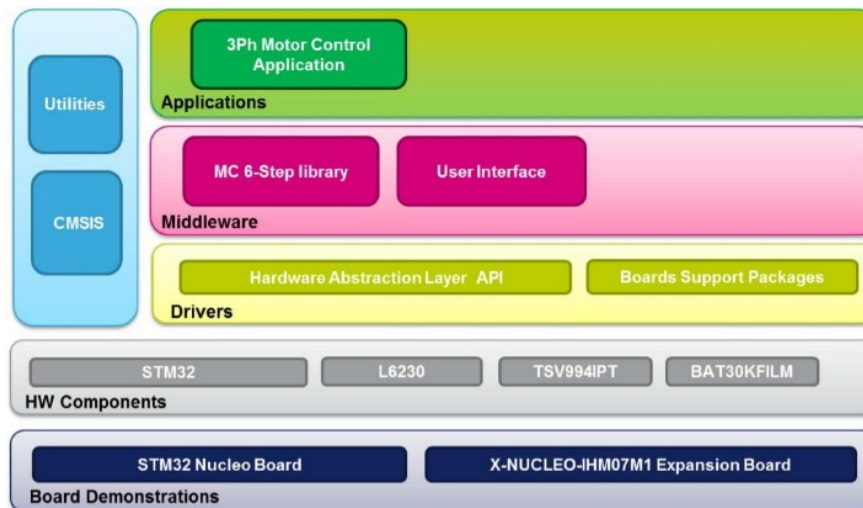


Figure 7. FW controller architecture

At the bottom is the Board demonstration and HW Components layers, which contain drivers for the hardware components of the system, both on the controller board itself and on additional external boards.

Above that are Drivers which contain low-level drivers and hardware interface methods for interacting with higher layers.

Middleware contains components and libraries that are used both for management and for other higher layer functions such as USB Host, FreeRTOS, UART...

On top is a global application layer that enables real-time interaction and serves all lower layers.

In the application layer, communication with the operator is implemented according to a specially defined protocol. Through the communication protocol, it is possible to set the desired azimuth and elevation position both in stabilized and non-stabilized mode (absolute movement) as well as continuous speed along both axes with and without stabilization (continuous movement). It is also possible to

change the operating mode from stabilized to non-stabilized and vice versa. As feedback from the system, the protocol can read the current azimuth and elevation angles as well as the operating mode (stabilized or non-stabilized). Communication with the operator takes place via the serial communication channel.

The implementation of management algorithms is in the middleware and application layer

Direct drive motors are controlled using FOC (Field Oriented Control) control [13] [14]. The implementation of FOC control allows the BLDC (BrushLess Direct Current) motor to operate more efficiently, with less torque ripple. The basis of such control is the placement of the stator magnetic field orthogonal to the rotor field, which achieves the biggest force. The position of the rotor is determined by a precise encoder. In order to implement this control method, a motor with a sinusoidal bEMF (back Electro Motor Force) or a PMSM [7] motor (Permanent Magnet Synchronous Motor) is a prerequisite.

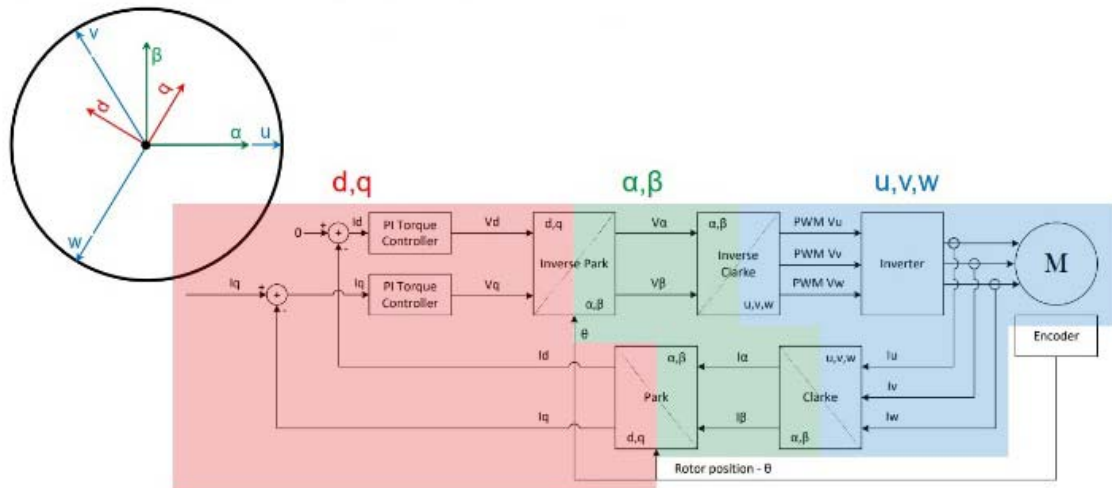


Figure 8. FOC control of a three-phase PMSM motor

In the picture you can see the block diagram of FOC control operation, where different vector spaces are marked with colors. The three-phase rotating vector space is indicated in blue, which is transferred to a rotating vector space with two orthogonal vectors (green) using the Clark transformation, which is transferred to a static orthogonal vector space (red)

using the Park transformation. Then the control signals are returned to the vector space of the motor by inverse transformations.

The architecture of the system envisages the existence of several control loops for the one axis as shown in the figure.

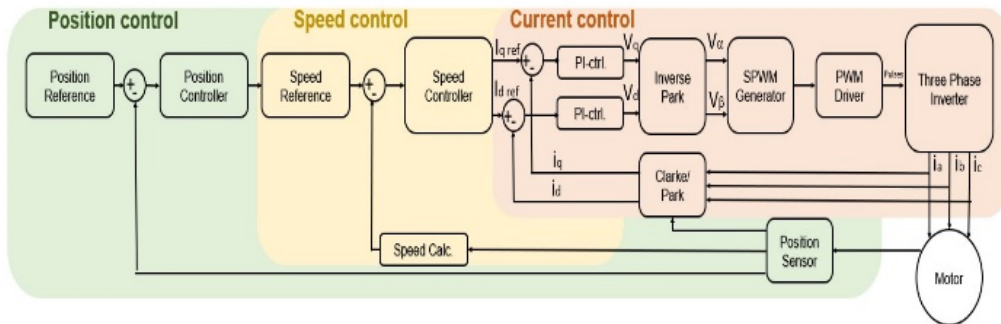


Figure 9. Control system design

5. SIMULATION RESULTS

As a basis for the simulations for validation of proposed control loops, the control model of the PMSM motor was taken in Simulink, to which control loops were added, as well as the simulation of the behavior of the gyroscope. It

was considered that the axes are mutually independent, so simulations can be performed on each of the axes individually with modified load parameters as well as differently configured PID controllers.

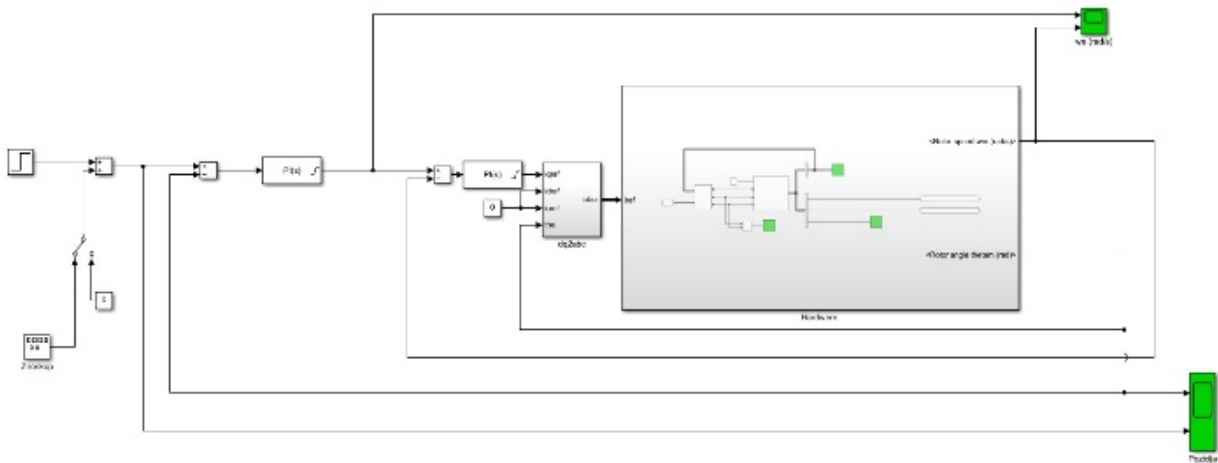


Figure 10. One axis control loop in Simulink

Where the hardware part is isolated and its block diagram is given in the following figure:

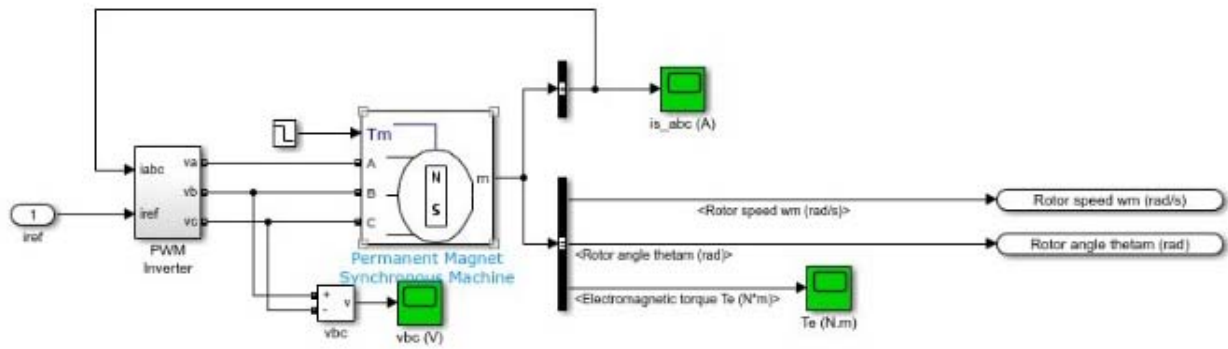


Figure 11. HW part of the model

The obtained responses to the step excitation are shown in the following figures. The motor parameters were taken as default from Simulink, while the PID controllers parameters got initially using the Ziegler Nichols method [15] and adjusted in order to get better performance.

The input is marked in red, while the response is given in blue.

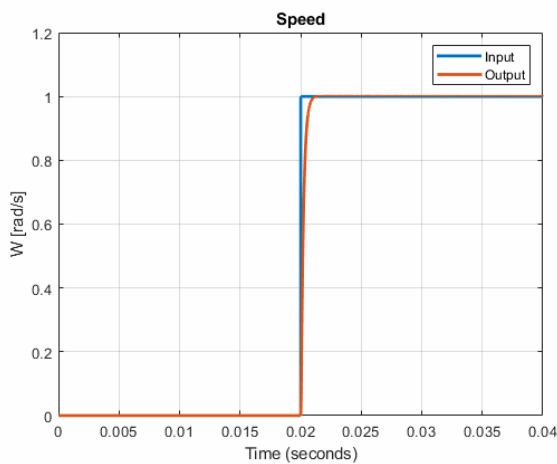


Figure 12. Step response to set speed - elevation

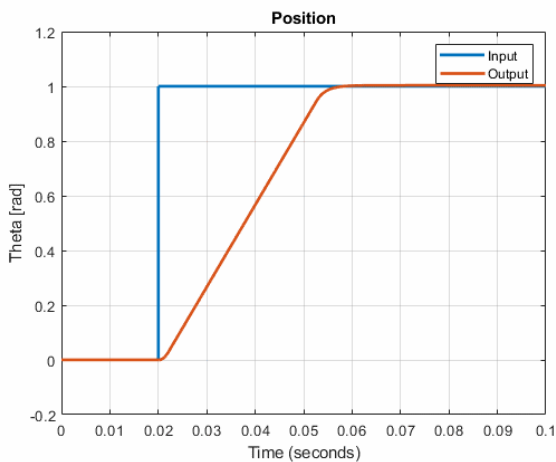


Figure 13. Step response to set position-elevation

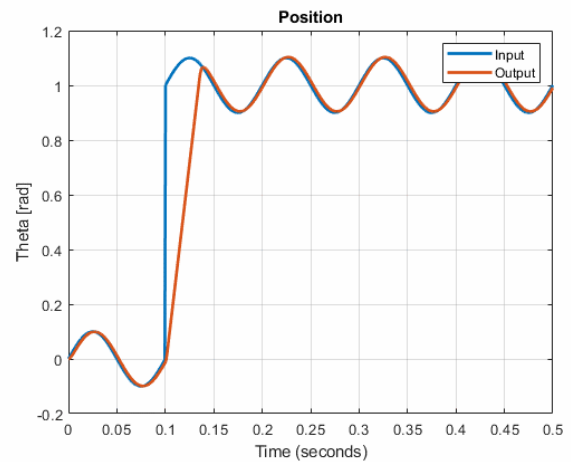


Figure 14. Position step response with gyroscope - elevation

As can be seen from the images, the system reaches the set position and speed and successfully follows the disturbances caused by the gyroscope. A frequency of 10Hz was taken as the disturbance of the gyroscope. The signal from the gyroscope can be considered as superimposed on the input reference.

In next figures step responses in azimuth axis are presented.

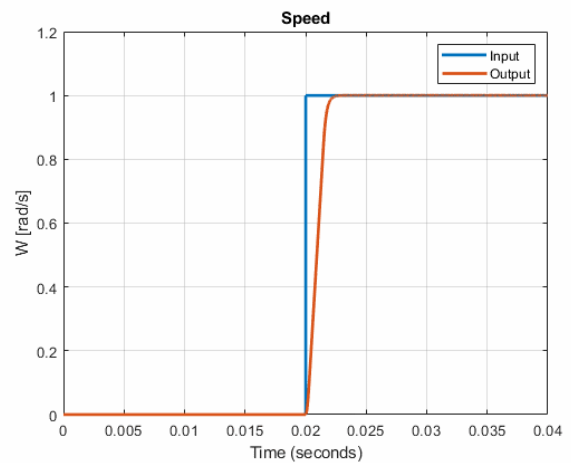


Figure 15. Speed step response - azimuth

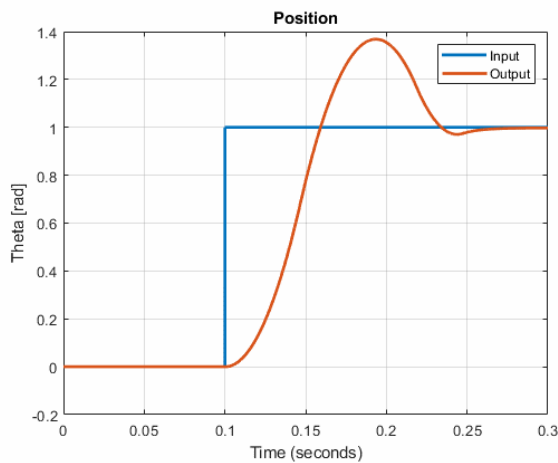


Figure 16. Position step response -azimuth

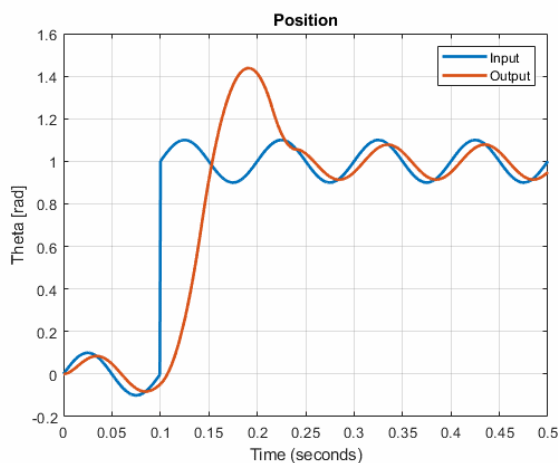


Figure 17. Position step response with gyroscope - azimuth

In position step response in azimuth axis overshoot is present which is consequence of “faster” PID controller because of bigger moment of inertia in azimuth axis, so that the system could suppress the disturbance from the gyroscope. By using ramp instead step, this issue can be overcome.

6. CONCLUSION

This paper presents the design of a control software for new two-axis gyro-stabilized pan-tilt positioner. The presented architecture enables positioning and response to challenging performance both in terms of position and gyro stabilization, which was demonstrated by modeling in the Simulink software package.

Further research on this topic will deal with the implementation of the architectures themselves and focus on the optimization of both the hardware part and the software part, primarily control loops and control methods. Also, cross-coupling between axes should be entered in calculations.

ACKNOWLEDGMENT

The authors would like to thank the Vlatacom Institute for the equipment and support that enabled continuous work

and improvement in this area. This work was undertaken within the Vlatacom Institute project P171.

References

- [1] KENNEDY, P. J., KENNEDY, R.: *Stabilizing the Line of Sight*, Photonics Media Press p. 210, 2014.
- [2] VAN NISPEN, S.H.M. (STEPHAN), PROF. WANG, L., PROF. DR. NIJMEIJER, H.: *Design and control of a three-axis gimbal*, TU/e - Department of Mechanical Engineering, May, 2016.
- [3] NEGRO, J., GRIFFIN, S.: *Inertially Stabilized Platforms for Precision Pointing*, BOEING - SVS ALBUQUERQUE NM, 2006.
- [4] JIA, R., NANDIKOLLA, V. K., HAGGART, G., VOLK, C. AND TAZARTES, D.: *System Performance of an Inertially Stabilized Gimbal Platform with Friction, Resonance, and Vibration Effects*, J. Nonlinear Dyn., vol. 2017, pp. 1–20, 2017, doi: 10.1155/2017/6594861.
- [5] SKOGLAR, P.: *Modelling and control of IR / EO-gimbal for UAV surveillance applications*, Electr. Eng. Linköping Inst. Technol. Linköping, Sweden, 2002
- [6] ANDRÉN, W., HJERTBERG, E.: *Gyro Stabilization of a Positioning Unit*, 2019,
- [7] EKSTRAND, B.: *Equations of motion for a two-axes gimbal system*, IEEE Trans. Aerosp. Electron. Syst., vol. 37, no. 3, pp. 1083–1091, 2001, doi: 10.1109/7.953259.
- [8] MILANOVIĆ, P. D., POPADIĆ, I. V., KOVAČEVIĆ, B. D.: *Gyroscope-based video stabilization for electro-optical long-range surveillance systems*, Sensors, vol. 21, no. 18, pp. 1–23, 2021, doi: 10.3390/s21186219.
- [9] LATINOVIĆ, N., POPADIĆ, I., TOMIĆ, B., SIMIĆ, A., MILANOVIĆ, P., NIJEMČEVIĆ, S., PERIĆ, M., VEINOVIĆ, M.: *Signal Processing Platform for Long-Range Multi-Spectral Electro-Optical Systems*, Sensors, vol. 22, no. 3, 2022, doi: 10.3390/s22031294.
- [10] COWAN, M. K.: *Laser Gyroscopes*, pp. 1–10, 2010.
- [11] BRAKE, N. J.: *Control System Development for Small Uav Gimbal*, Zhurnal Eksp. i Teor. Fiz., August, 2012.
- [12] STMICROELECTRONICS: *User manual Getting started with STM32 Motor Control Nucleo Packs*, September, 2016.
- [13] YESILBAG, E., ERGENE, L. T.: *Field oriented control of permanent magnet synchronous motors used in washers*, 16th Int. Power Electron. Motion Control Conf. Expo. PEMC 2014, pp. 1259–1264, 2014, doi: 10.1109/EPEPEMC.2014.6980685.
- [14] VUKOSAVIC, S. N.: *Electrical Machines*, Springer, 2013, doi: 10.1007/978-1-4614-0400-2.
- [15] ZIEGLER, J. G., NICHOLS, N. B.: *Optimum settings for automatic controllers*, J. Dyn. Syst. Meas. Control. Trans. ASME, vol. 115, no. 2B, pp. 220–222, 1993, doi: 10.1115/1.2899060.

AUTONOMOUS ROBOT EXPLORATION IN GAZEBO SIMULATOR

NOVAK ZAGRADJANIN

University of Belgrade, School of Electrical Engineering, Belgrade,
Material Resources Sector, Ministry of Defence, Belgrade, zagradjaninnovak@gmail.com

NIKOLA KNEZEVIC

University of Belgrade, School of Electrical Engineering, Belgrade, knezevic@etf.rs

KOSTA JOVANOVIC

University of Belgrade, School of Electrical Engineering, Belgrade, kostaj@etf.rs

BOJAN PAVKOVIC

Military Technical Institute, Belgrade, bjnpav@gmail.com

Abstract: An autonomous robot is often in a situation to perform tasks or missions in an initially unknown environment. A logical approach to doing this implies discovering the environment by the incremental principle defined by the applied exploration strategy. A large number of exploration strategies apply the technique of selecting the next robot position between candidate locations on the frontier between the unknown and the known parts of the environment using the function that combines different criteria. In this paper, an architecture is proposed that in Gazebo, using ROS and Matlab, can test different exploration strategies in order to build map of the environment. Besides, proposed architecture allow improving the exploration strategy's adaptability to different situations.

Keywords: robot path planning, frontier-based exploration of environment, Gazebo, ROS.

1. INTRODUCTION

Autonomous exploration of the environment is an important area of study in robotics. In the literature, it is most often defined as a combination of mapping of the environment (in which the robot moves) and robot path planning, Fig. 1 [1].

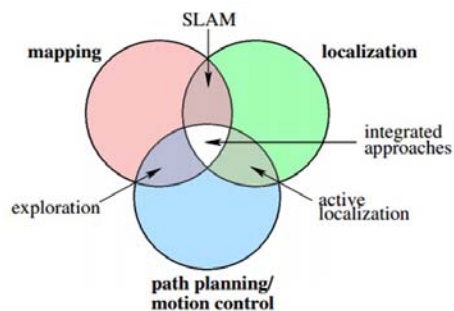


Figure 1: The basic tasks of the autonomous robot

Mapping is the problem of integrating the information gathered with the robot's sensors aiming to construct a map of an unknown environment. In order to form a map of the entire environment, it is necessary for the robot to go from one position to another (along a path defined by a planner) and from those positions to successively observe the environment, collect data and integrate them, until the task is completed. To perform this task reasonably, it is necessary to define an appropriate exploration strategy.

Generally, the environment exploration is not limited to

the environment mapping, but is defined as a set of actions taken by an autonomous mobile robot in accordance with a previously defined strategy, with the aim to discover the characteristics of the environment that are of importance to the operation. Hence, exploration is the basis of numerous real-world applications of robotics, such as, in addition to the environment mapping [2], search and rescue operations [3], space missions, visual inspections, mining, robotic vacuum cleaners, etc. For example, in search and rescue operations, the goal is to locate injured persons or victims of natural disasters, fires or other accidents. There are frequent situations that in parallel or just before the basic operation, a mapping of the environment has to be performed, so that the operation can be accomplished. Similar scenarios of the exploration, combined with several types of tasks, can be seen in practice in other robotic applications.

Exploration can be broadly classified into two distinct approaches [4]. The first approach involves a prior knowledge of the environment, based on which off-line algorithms are used to define the exploration strategy. In this approach, the path of the robot is determined in advance (a predefined path). The second approach is applied when the environment is completely unknown or when there is not enough information for efficient application of off-line algorithms. In that case, the exploration is much more challenging and involves an online incremental exploration principle. If so, after collecting data from the current position, the robot selects the next position, moves to it, observes the environment from the new position and repeats this process until it

completes the task or completes the operation [5]. The main problems, when using this exploration concept, is choosing the next position and planning the path. Most of the strategies for the exploration are based on choosing the next robot position out of the set of "candidate positions" that are on the frontiers between the explored free space and the unexplored parts of the environment, applying some criteria for their evaluation. These are so-called frontier-based strategies. The concept of frontier-based exploration of the environment was first officially presented in the *Yamauchi's* paper in 1997 [6].

Apart from frontier-based, other types of strategies are used to explore the environment. Some strategies, for example, involve human participation in the loop of choosing the next robot position, then applying a probability analysis of various benefits in the selection process between candidate positions or simply choosing the next position by random selection, etc. What is common to all classic environmental exploration strategies is that they aim to do the exploration in the shortest possible time or in the shortest possible total distance traveled by the robot.

Fig. 2. shows a Carnegie Mellon University study that explains that frontier-based strategies perform better than the other two analyzed types of environmental exploration strategies.

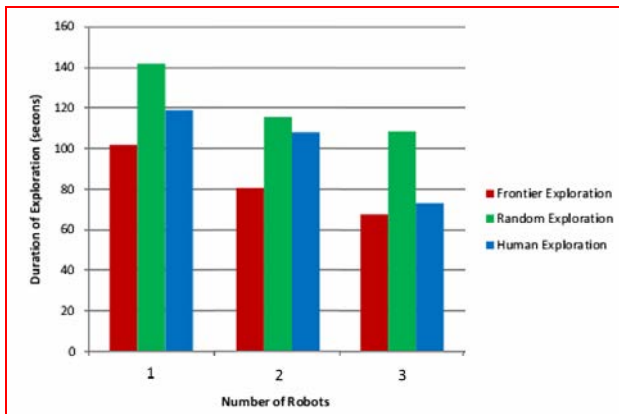


Figure 2: Different concepts of exploration

2. THE CONCEPT OF FRONTIER-BASED EXPLORATION

As already stated in Section 1, most exploration strategies belong to the group of frontier-based family. Even today it is one of the basic directions of research in the field of autonomous exploration of the environment.

The main steps of frontier-based exploration are presented in Fig. 3 and can be defined as follows [7]:

1. The selection of the next observation location according to an exploration strategy;
2. The reaching of the observation location selected in previous step. This step requires the planning and following a path, that goes from the robot's current position to the chosen location;
3. The acquisition of a partial map from the observation location, using data collected by the robot's sensors;

4. The integration of the partial map within the global map.

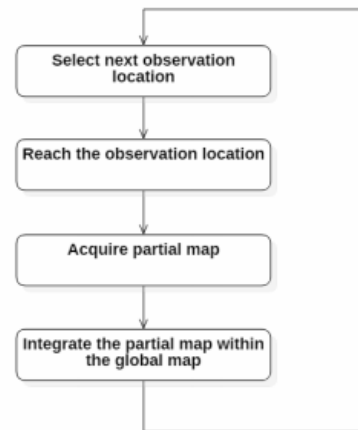


Figure 3: The main steps of the exploration process

The frontier determination techniques usually implies the environment representation in the form of an occupancy grid map. The boundary of the robot's field of view defined by the range of its sensors can be divided into free, obstacle and frontier arcs, Fig. 4. [8]. Free arcs are parts of the border to the explored part of the environment, whereas obstacle arcs are parts of the border to locally detected obstacles. Any arc that is neither obstacle nor free is a frontier arc and is, in fact, part of the border to the unexplored part of the environment. The fact that each frontier arc is actually one frontier can be adopted. Allow us also to take that the middle point of each frontier represents one candidate for the next robot position, which is a common approach in the papers [4,5,8] dealing with this topic.

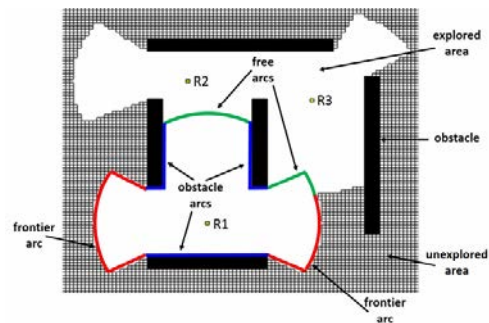


Figure 4: Free, frontier and obstacle arcs in exploration

When the robot reaches the selected location, it observes the surroundings, improves the knowledge of the environment and also updates the frontier list [8].

3. FRONTIER-BASED EXPLORATION STRATEGIES

To evaluate the candidate p in order to select the next robot position in frontier-based exploration strategies, different criteria are proposed in the literature. The following criteria are most commonly used [9]:

- $L(p)$, the minimum length of a collision free path or the minimum path cost from the current robot position to r usually calculated by using a path planner,

- $A(p)$, the expected information gain obtained by simulating the robot's perception from the location p ; it is calculated or estimated based on the size of the unexplored area that would be explored from that location, given the current status of the occupancy grid map and the robot's sensing range,

- $P(p)$, the probability that the robot, if it arrives at the location p , will be able to communicate with the base station and send the collected data; this probability generally directly depends on the distance of p from the base station.

- Classic exploration strategies

There are various approaches using one of the above-mentioned criteria or a larger number of them in the form of the function that uniquely describes each candidate p . The classic exploration strategies are summarized in [9].

The first strategy is trivial and it chooses for the next robot position the one up to which the path planner, in relation to the current robot position, calculated the minimum length or cost of the path, counting all candidate positions. It is usually denoted by Dist Min. In the next strategy, $L(p)$ is combined with $A(p)$ in the form of the linear function (1):

$$u(p) = A(p) - L(p) \quad (1)$$

The parameter β regulates the influence of the criterion $L(p)$ versus $A(p)$.

Another approach describes the candidate p as the following exponential function (2):

$$u(p) = A(p) \cdot \exp(-\lambda \cdot L(p)) \quad (2)$$

The parameter λ is greater than zero and weights both included criteria. This strategy is named after the authors as the GBL strategy. The GBL strategy is most often proposed in the literature as a good enough choice. It can be considered as a classic strategy and has been used as a reference strategy in a significant part of the relevant literature that studies the subject area [8,9].

These exploration approaches are mainly used for the map building process. In this process and especially in the case of search and rescue missions, however, it is usually important to introduce a criterion related to the probability of establishing communication between the robot from the location p and the base station ($P(p)$), so that the information can be forwarded as soon as possible to be further used. The introduction of this criterion was proposed in the form of the following function (3) [9]:

$$u(p) = (A(p) \cdot P(p)) / (L(p)) \quad (3)$$

On the other hand, different additional criteria for the selection of the next robot position are proposed in the literature. For example, the overlap ($O(p)$) of the current environment map and the part of the environment visible from p can be proposed as an additional criterion [8,9]. In addition to the path cost, the criteria such as the recognition of the uncertainty of a landmark, the number of the features visible from the location, the length of the

visible free edges, and the number of the rotations and stops required from the robot to reach a location can be considered, also [8,9]. Criteria selection depends on the mission specifics and the exploration goals. In this context, the introduction of the criteria that (if possible) will take into account the types of facilities for each candidate location is proposed in the paper [5] (which considers exploration in search and rescue missions) in order to initially direct a mission to the residential area, where the largest number of the victims of a disaster are logically expected.

- MCDM-based exploration strategies

Taking into account the above-mentioned, a more recent direction of research in this area includes the implementation of different MCDM methods in MCDM-based exploration strategies. MCDM provides a broad and flexible approach to the selection of the utility function that can be used to evaluate candidates for the next observation location. In [4,9], for example, the Choquet fuzzy integral is proposed. This approach enables a researcher to take into account the relative relationship between criteria, such as redundancy and synergy, which is its main characteristic. The experimental results in those papers show that respectable results are obtained by using MCDM-based exploration strategies compared to the classic exploration strategies. In [5], the proposed approach to the selection of the next location from a set of

candidates within the exploration strategy uses a standard MCDM method—PROMETHEE II. Here, an attempt is made to take advantage of the characteristic of this method referring to the fact that, in addition to weights, preference functions are used as additional information for each criterion. Autonomous robot navigation strategy based on MCDM Additive Ratio ASsessment (ARAS) method is proposed in [10]. The greedy area exploration approach is suggested, while the criteria list consists of: battery consumption rate, probability to collide with other objects, probability to yaw from course, probability to drive through doors, probability to gain new information, length of the minimum collision-free path. In [11], the implementation of the on-line MCDM-based exploration strategy that exploits the inaccurate knowledge of the environment (information obtainable from a floor plan) is proposed. The results of the experiment show that the proposed approach has a better performance in different types of environments with respect to the strategy without prior information. Although the use of more accurate prior information leads to a significant improvement in performance, the use of inaccurate prior information could lead to certain advantages also, managing to reach the high percentages of the explored area travelling a shorter distance, with respect to the strategy not using any prior information.

This paper generally belongs to the above-mentioned direction of autonomous exploration research, bearing in mind the fact that this issue is not sufficiently considered in the existing literature.

The exploration strategies based on MCDM in this paper are using the standard SAW, COPRAS and TOPSIS methods proposed in [9].

- Determination of criteria values

The criteria $L(p)$, $A(p)$ and $P(p)$ are used for candidate selection in this paper. To determine the value of criterion $L(p)$, the powerful D* Lite algorithm is used [8,12]. The criterion value $P(p)$ illustrates the Euclidean distance p from the base station [8,9].

The value of the criterion $A(p)$, which actually illustrates the pre-estimated gain of data about the environment that the robot can "see" with its sensors if it reaches the position p , is calculated in the manner described below [11]. How candidate positions are defined in the frontier-based environment exploration is described in Section 2. In order to evaluate the visibility of the point s with the robot sensor of the range r from the point p (in the case of positioning the robot at the point p), it is necessary to check whether the point s belongs to the corresponding line of sight. Fig. 5. illustrates the assessment of information potential for three different candidate positions.

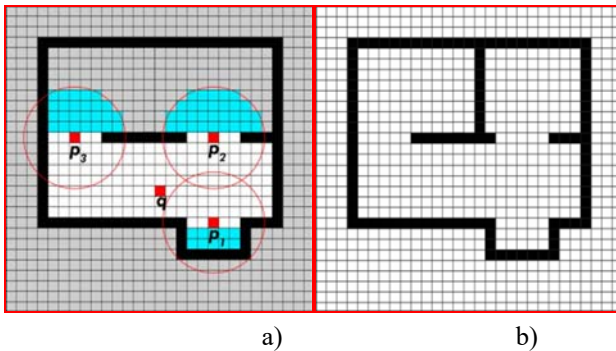


Figure 5: Evaluation of the information potential value (cells marked in blue) of candidate positions p_1 , p_2 and p_3 . The current position of the robot is q (a) map of the explored part of the environment, (b) real map of the environment).

In Fig. 5. it can be seen that there was an error in the assessment of the informative potential for the candidate position p_2 , because in the unexplored part of the environment there is another partition wall which, if the robot chooses that position, will reduce the actual perception by the sensor compared to the assessment performed based on its maximum ability.

4. MAP BUILDING EXPLORATION IN GAZEBO 3D SIMULATOR

Gazebo is a specialized environment for 3D robot simulation. It enables credible testing of robots and their activities in 3D scenario simulations and can be used as a plausible substitute for testing on real robots.

In the present case, the virtual model of *Turtlebot 3* robot was used. The specified robot model for mapping environment as a sensor used *LIDAR LDS-01*, range 3.5m and angle resolution 1° . Packages operating under Robot Operating System (ROS) were used to control the robot, odometry and SLAM function, i.e. to integrate data collected with a robot sensor, forming a map of the environment and simultaneously determining the position of the robot in relation to that map. ROS provides a

collection of tools and libraries for the development and optimization of robotic systems, which is especially suitable in combination with other specialized software packages intended for robotics such as *Gazebo*, but also in combination with *Matlab*, etc.

Notably, the following packages were used in this approach: *turtlebot3_gazebo* and *turtlebot3_gmapping*. these packages use the following types of messages: */odom* (for information on the robot's position obtained by odometry), */scan* (for information collected from *lidar* sensor), */map* (data to map the environment), */cmd_vel* (linear and rotational speed of the robot), */tf* (describes the relationship between the coordinate system of maps and coordinate systems of the robot), */joint_states* (information on robotic actuators), */hack_scan* (modified */scan* data). The ROS architecture used with the nodes displayed, the package names and the data flows is shown in Fig. 6.

Gazebo communicates as a simulator with ROS, and ROS sends data about the map to *Matlab* where strategies are executed for the selection of the following exploration position and planning robots to that position. After that, the algorithm was performed in *Matlab*, which regulates the control of the robot movement to monitor the calculated path. Specific challenges represented the following:

- Adjusting the map view from ROS in *Matlab* in order to comply;
- Customize the map from *Matlab* to select the next robot position and planning robot paths. It was necessary to form a buffer zone (several rows of artificially blocked fields) around obstacles to prevent physical contact of the robot with the same;
- Adaptation of LIDAR data so that the algorithm can do the mapping of open space according to line-of-sight. The physical sensor is designed in such a way, when an obstacle is much further than its range, the feedback signal is not registered. For such situations, it is defined that there are no obstacles in the range of sensors.

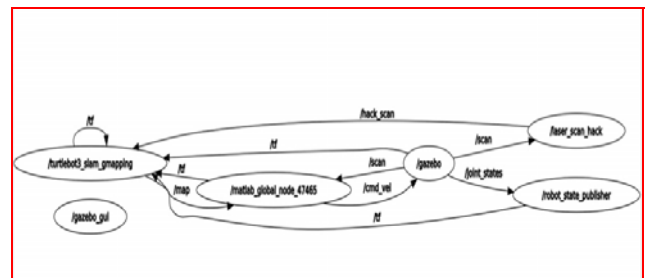


Figure 6: The ROS architecture using nodes, package names and data streams

For testing, two test environments were created in *Gazebo*. The first environment (environment A, Fig. 7.) had dimensions 10mx10m, while the second environment (environment B, Fig. 8.) is more complex and had dimensions 30mx30m. The both environments were 2D discretized into 0.2mx0.2m cells.

All the MCDM methods were tested with two

combinations of criteria weights: 0.7, 0.2, 0.1 (Strategy 1) and 0.5, 0.4, 0.1 (Strategy 2), for the criteria $L(p)$, $A(p)$ and $P(p)$, respectively. The Strategy 2 can be characterized as more aggressive, because it gives more importance to the criterion of the expected information gain, forcing the robot to take more risks and to travel greater distances in order to explore more space, regardless of the complexity of the environment [8]. By changing the weights during exploration, we can switch between different behaviors, varying the criteria's importance that drive robot decisions. This is a significant advantage of MCDM-based exploration strategies over other approaches. In order to test different approaches, GBL strategy was also tested (expression (2), where $\lambda = 0.2$, the same value reported in the papers [8,9]).

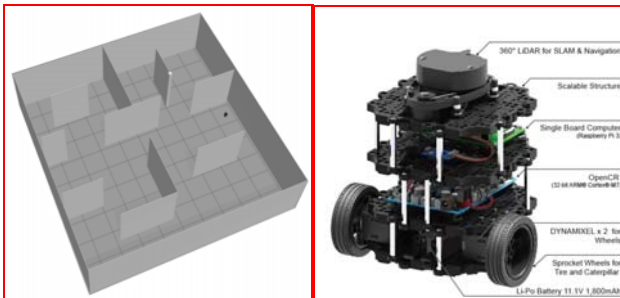


Figure 7: Map A created in Gazebo simulator for the purposes of testing exploration strategies, the black dot illustrates the robot (left side). Turtlebot 3 robot and its basic components (right side).

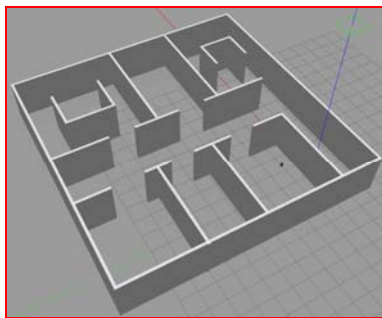


Figure 8: Test environment B created in Gazebo simulator for the purposes of testing exploration strategies.

The exploration results using the TOPSIS 1, COPRAS 2 and GBL strategies, the corresponding robot paths generated by the D* Lite algorithm in the test environment A for the starting location $x=13$ and $y=7$, are shown in Fig. 9, 10 and 11, respectively.

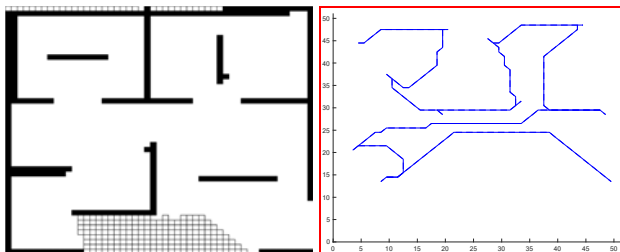


Figure 9: Map A built after exploration and the robot path generated by the D* Lite algorithm in the Gazebo with the implemented COPRAS 2 exploration strategy.

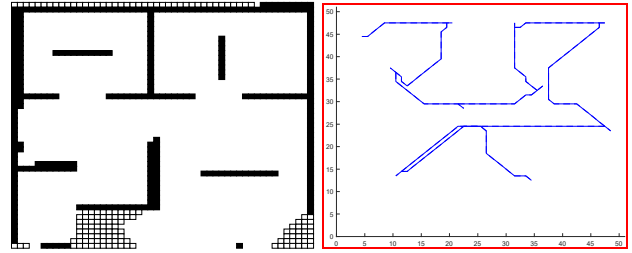


Figure 10: Map A built after exploration and the robot path generated by the D* Lite algorithm in the Gazebo with the implemented TOPSIS 1 exploration strategy.

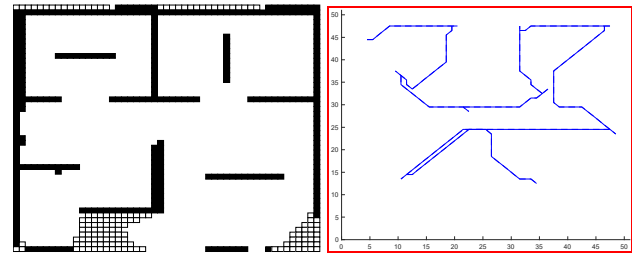


Figure 11: Map A built after exploration and the robot path generated by the D* Lite algorithm in the Gazebo with the implemented GBL exploration strategy.

The exploration results using the TOPSIS 1, COPRAS 2 and GBL strategies, the corresponding robot paths generated by the D* Lite algorithm in the test environment B for the starting location $x=7$ and $y=7$, are shown in Fig. 12, 13 and 14, respectively.

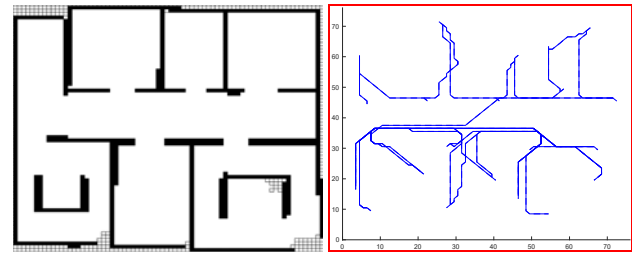


Figure 12: Map B built after exploration and the robot path generated by the D* Lite algorithm in the Gazebo with the implemented TOPSIS 1 exploration strategy.

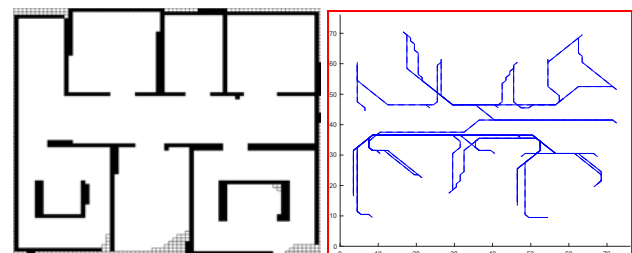


Figure 13: Map B built after exploration and the robot path generated by the D* Lite algorithm in the Gazebo with the implemented COPRAS 2 exploration strategy.

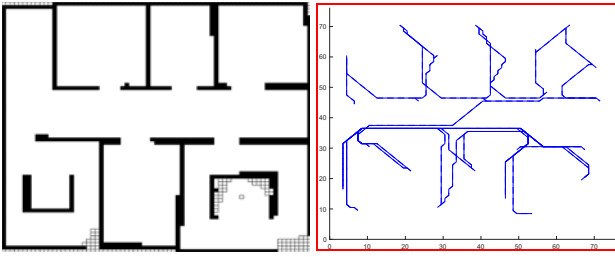


Figure 14: Map B built after exploration and the robot path generated by the D* Lite algorithm in the Gazebo with the implemented GBL exploration strategy.

Table 1. The average exploration results in terms of the travelled distances for the environment

Exploration strategy		Travelled distance	
		Environm. A	Environm. B
MCDM	SAW 1	251.45	1.097,2
	SAW 2	258.36	1.102,1
	COPRAS 1	240,29	1.050,8
	COPRAS 2	247,52	1.078,9
	TOPSIS 1	216,52	1.024,3
	TOPSIS 2	218,93	1.036,1
GBL		216,52	1.032,1

Analyzing Table 1, the TOPSIS method had the best results, but additional research is needed, bearing in mind that the results also depend on the starting positions [8].

5. CONCLUSION

In paper, an architecture is proposed that in Gazebo, using ROS and Matlab, can test different strategies for exploration in order to build map of the environment. It can also be used to determine the optimal mission plan to improve the exploration strategy's adaptability to different situations (limited exploration time, the need to change the exploration direction in different parts of environment during the mission, etc.).

References

- [1] C. Stachniss, "Robotic mapping and exploration," Springer, 2009.
- [2] C. Gomez, A. C. Hernandez and R. Barber, "Topological frontier-based exploration and map-building using semantic information," *Sensors*, vol. 19, no. 20, pp. 4595, 2019.
- [3] S. Kohlbrecher, J. Meyer, T. Graber, K. Petersen, O. von Stryk et al., "Hector open source modules for autonomous mapping and navigation with rescue robots," in *RoboCup: Robot World Cup XVII*, ser. Lecture Notes in Artificial Intelligence (LNAI). Berlin: Springer, pp. 624–631, 2013.
- [4] N. Basilico and F. Amigoni, "Exploration strategies based on multi-criteria decision making for an autonomous mobile robot," in *Proceedings of the 4th European Conf. on Mobile Robots*, Mlini/Dubrovnik, Croatia, pp. 259–264, 2009.
- [5] P. Taillandier and S. Stinckwich, "Using the PROMETHEE multi-criteria decision making method to define new exploration strategies for rescue robots," in *Proceedings of the IEEE Int. Sym. on Safety, Security, and Rescue Robotics*, Kyoto, Japan, pp. 321–326, 2011.
- [6] B. Yamauchi, "A frontier-based approach for autonomous exploration," in *Proceedings of the IEEE Int. Sym. On Computational Intelligence in Robotics and Automation*, Monterey, California, USA, pp. 146–151, 1997.
- [7] M. Kulich, T. Juchelka and L. Preucil, "Comparison of exploration strategies for multi-robot search," *Acta Polytechnica*, vol. 55, no. 3, pp. 162–168, 2015.
- [8] N. Zagradjanin, D. Pamucar, K. Jovanovic, N. Knezevic and B. Pavkovic, "Autonomous exploration based on multi-criteria decision-making and using D* Lite algorithm," *Intelligent Automation & Soft Computing*, Special Issue: Soft Computing Methods for Intelligent Automation Systems, pp. 1369-1386, 2021.
- [9] N. Basilico and F. Amigoni, "Exploration strategies based on multi-criteria decision making for search and rescue autonomous robots," in *Proceedings of the 10th Int. Conf. on Autonomous Agents and Multiagent Systems*, Taipei, Taiwan, pp. 99–106, 2011.
- [10] R. Semenas and R. Bausys, "Autonomous navigation in the robots' local space by multi criteria decision making," *Open Conf. of Electrical, Electronic and Information Sciences*, Vilnius, Lithuania, pp. 1–6, 2018.
- [11] M. Luperto, D. Fusi, N. Alberto Borghese and F. Amigoni, "Exploiting in accurate a priori knowledge in robot exploration," in *Proceedings of the 18th Int. Conf. on Autonomous Agents and MultiAgent Systems*, Montreal, Quebec, Canada, pp. 2102–2104, 2019.
- [12] S. Koenig and M. Likhachev, "D* Lite," in *Proceedings of the Eighteenth National Conf. on*
- [13] *Artificial Intelligence*, Edmonton, Canada, pp. 476–483, 2002.

DESIGNING THE CONTROLLED GENERATOR OF A HOMOGENOUS MAGNETIC FIELD

RADOSLAV SURLA

Faculty of Technical Sciences, University of Kragujevac, Svetog Save 65, Čačak, Serbia, ekorade@gmail.com

NEBOJŠA MITROVIĆ

Faculty of Technical Sciences, University of Kragujevac, Svetog Save 65, Čačak, Serbia,
nebojsa.mitrovic@ftn.kg.ac.rs

PAVEL CRNOMARKOVIĆ

Military Technical Institute, Ratka Resanovića 1, Belgrade, Serbia, pavel@ptt.rs

Abstract: The paper describes a design of a generator of a homogenous magnetic field by two pairs of Helmholtz coils and related calculations. The paper presents software that performs the calculation, as well as the proof of results using two magnetometers. Simulated results completely correspond to the experimental results. Therefore, the presented software can be used for designing the generator of the homogenous magnetic field of different magnetic field strengths, as well as different dimensions. The presented generator enables an easy positioning of a magnetic element into the generated homogenous magnetic field.

Keywords: Helmholtz coils, solenoid, coil, magnetic field generator.

1. INTRODUCTION

A controlled generator of a homogenous magnetic field produces a magnetic field of high homogeneity in the axis direction along which magnetically sensitive elements are installed [1]. High homogeneity is achieved along the axis between a pair of the Helmholtz coils [1-3]. This enables an easy positioning of magnetic elements into a homogenous field. These magnetic elements are analyzed with the additional tools from the aspect of change of electromagnetic performances under the influence of the homogenous magnetic field [4]. Homogeneity of the magnetic field along the axis of coils may be increased by adding more pairs of the Helmholtz coils [3]. The homogenous magnetic field enables considering the change of other physical characteristics (such as impedance, electrical resistance, pressure, etc.) depending on the change of the magnetic field [5, 7].

2. THEORETICAL BACKGROUND

2.1. Field along the solenoid axis

Let us assume that the solenoid consists of a large number of coils of a thin conductor which is tightly and evenly wound on a cylinder of a diameter r and length L (Fig. 1) [1, 2]. If the coil consists of a large number of N turns, then Ndx/L is the number of turns on the element of a length dx of a solenoid axis.

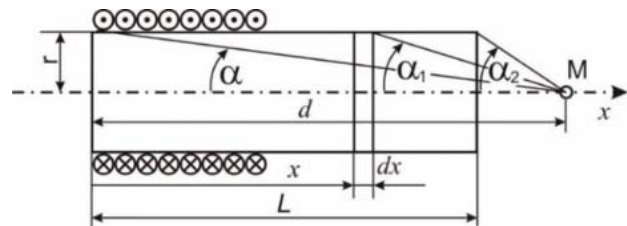


Figure 1. A solenoid with induction in point M.

If one presents a current in a solenoid, made of a group of turns on the element dx , it may be treated as a helical current contour where the value of current is $(NI/L)dx$, and the complete solenoid could be considered as a series of equivalent helical current contour with mutual distance dx . Since in solenoid axis points the elementary inductions by certain current contours have only axial component, we may add them algebraically, so the total induction in point M is [1]:

$$B = \int dB = \mu_0 \frac{NI}{2L} \int dx \frac{\sin^3 \alpha}{r}, \quad (1)$$

where x is a distance of elementary current contour from the left solenoid end, and d is a distance from the point M, where the following relations are valid: $d - x = ctg\alpha$ and $dx = (r/\sin^3 \alpha) d\alpha$. If one counts an integral in the interval from α_1 to α_2 , the next equation is satisfied:

$$B = \mu_0 \frac{NI}{2L} \int_{\alpha_1}^{\alpha_2} \sin \alpha d\alpha = \mu_0 \frac{NI}{2L} (\cos \alpha_1 - \cos \alpha_2). \quad (2)$$

Observing the point M in the center and on the edge of the solenoid, we get the expressions for induction in the center of the solenoid:

$$\alpha_2 = \pi - \alpha_1 \Rightarrow B = \mu_0 \frac{NI}{2L} 2 \cos \alpha_1 = \mu_0 \frac{NI}{2L} \frac{1}{\sqrt{1+(r/L)^2}}, \quad (3)$$

whereby, if L is much larger than r, it follows: $B = \mu_0 NI/L$, and according to the same principle, when $\alpha_2 = \pi/2$, the induction at the solenoid end is: $B = \mu_0 NI/2L$, i.e., twice lower regarding the solenoid center.

2.2. Field along the coil axis

The coil may be observed as a certain number of solenoids wound to each other, where the diameter of each following solenoid increases by the thickness of a wire regarding the previous one (in case of ideal contours) (Fig.2 a) [2].

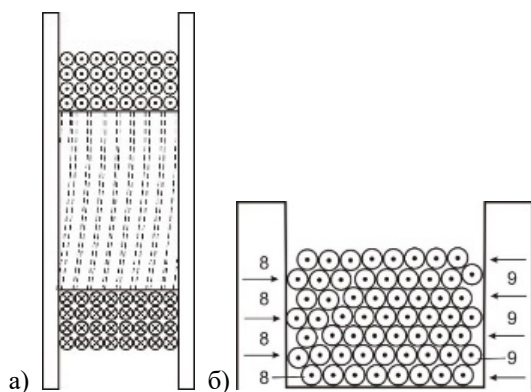


Figure 2. Wiring into a coil: a) ideal contours, b) real contours.

For thinner cross sections of lacquer isolated wire, it is difficult to ideally arrange each following row of wire precisely one onto another, so that the coil in each following row (solenoid) in the circular transducer falls into grooves between two previous windings (Fig. 2 b) [2]. In that case, the increase in the diameter of each following solenoid in the coil is determined as a relation to the thickness of coils and the number of wound solenoids, which is a lower value than the total wire thickness (with isolation). For thicker cross sections of the wire and precisely dimensioned width of the coil frame, it is possible to achieve that each row of coils has an identical number of windings. However, if that condition is not fulfilled, each second row of coils usually has an identical number of windings, and the neighboring ones differ for one winding (Fig. 2 b). Therefore, the field in the solenoid axis is calculated according to the formula (2), and the field in the coil axis is calculated as an algebraic sum of all individual results.

2.3. Field along the axis of the pair of coils (Helmholtz coils system)

If one applies the previously description on a pair of coils where L is significantly smaller regarding r, and if they are arranged at a mutual distance a, and if fulfilled a condition that $a = r$, the magnetic field between these coils will be approximately homogenous along the axis x [2,4]. This coils system is known as ‘‘Helmholtz coils’’,

according to the scientist who constructed them. In case ($a > r$) or ($a < r$) the homogeneity of the field is lost, and the field lines are convex or concave, respectively (Fig. 3).

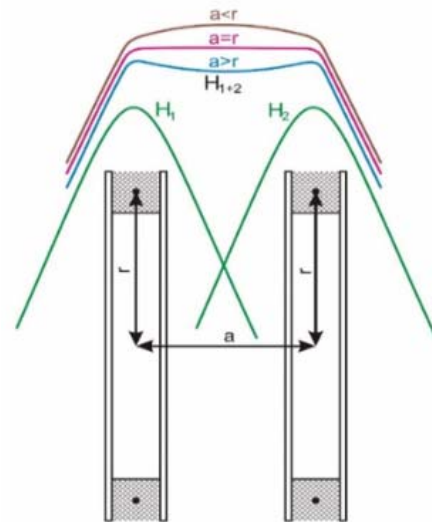


Figure 3. Helmholtz coils for different relations of the parameters a and r.

3. CALCULATION OF FIELD ALONG THE PAIR OF COILS

Parameters for the calculation of the field in a point along the x-axis of the pair of coils:

$$H = H_1 + H_2 = \frac{NI}{2k} (\cos \alpha_1 - \cos \alpha_2 + \cos \beta_1 - \cos \beta_2)$$

$$\alpha_1 = \arctg(a/x), \quad \text{for } 0 < x < c$$

$$\alpha_2 = \pi - \arctg(a/(L-x)), \quad \text{for } 0 < x < L$$

$$\alpha_2 = \pi/2, \quad \text{for } x = L$$

$$\beta_1 = \pi - \arctg(a/(b-x)), \quad \text{for } 0 < x < b$$

$$\beta_1 = \arctg(a/(x-b)), \quad \text{for } b < x < c$$

$$\beta_1 = \pi/2, \quad \text{for } x = b$$

$$\beta_2 = \pi - \arctg(a/(c-x)) \quad \text{for } x < c$$

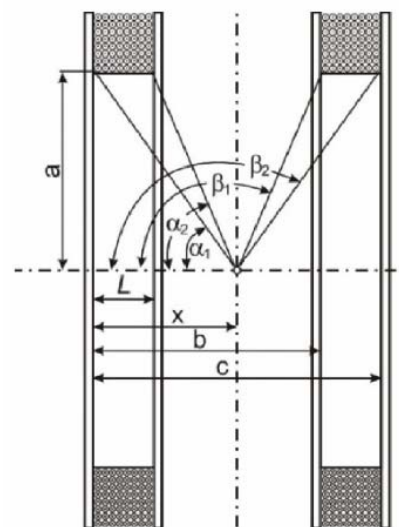


Figure 4. Helmholtz coils with the parameters for the calculation

Figure 4. shows the parameters for calculation of the field in the axis of coils, with individual cases of the position of the parameter x .

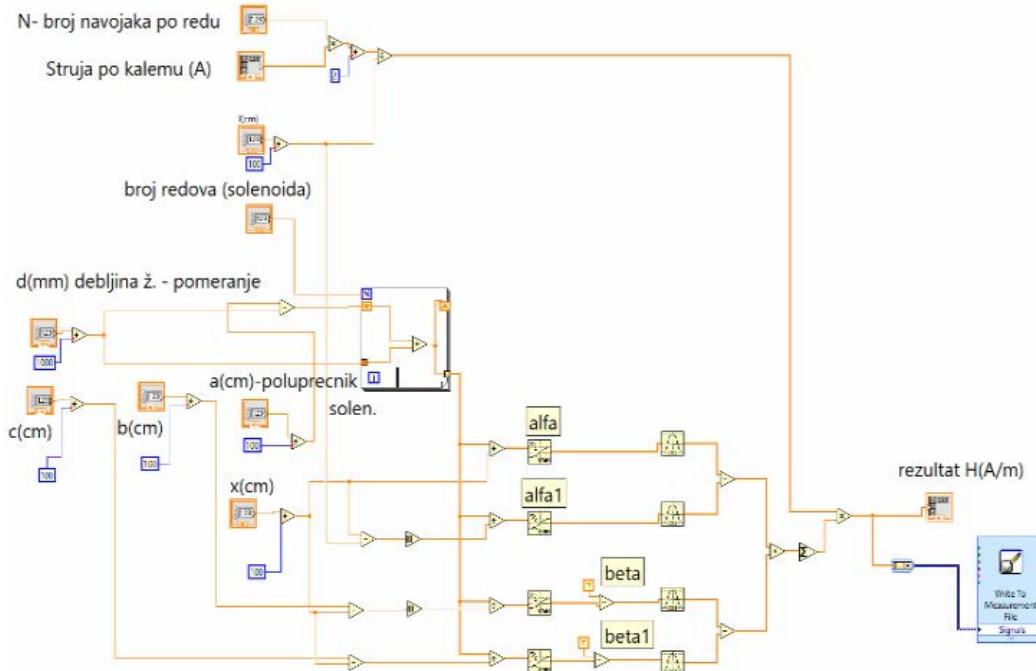


Figure 5. A block diagram of the “G” software for relation $L < x < b$

A block diagram of the “G” software that is performed in the “Labview” software package for the case, i.e. $L < x < b$ is shown in Fig 5. When the value x is out of these limits, it is also necessary to adjust the software code by creating the sub-software for each case shown in Fig 4. Based on geometry and data on the thickness of the wire we determine the number of turns along the solenoid, as well as several rows (solenoids) in the coil. Using the “movement” parameter, close to the value of the thickness of the wire “ d ”, we define the change of the parameter “ a ” while performing each software loop (“FOR loop”) in “G” software, and several solenoids define how many software loops will be performed. The software code is started, after entering the parameters in the front panel of the program code, for calculating the field in the axis of the Helmholtz coils (Fig. 6). The set parameters in the Front panel (Fig. 6) are executed in the background through "G software" (Fig. 5). The results obtained from the front panel (Fig. 6) are shown in the diagrams in Figures 9 to 11.

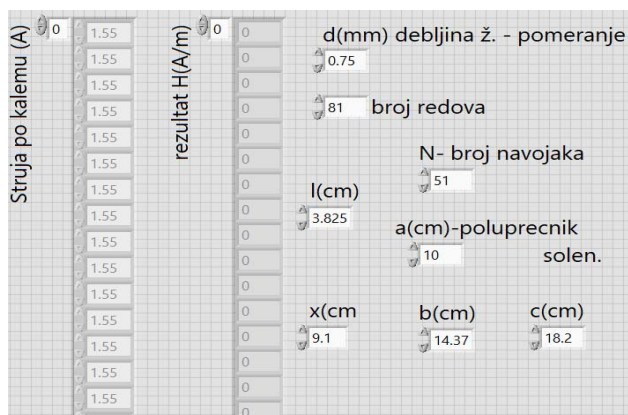
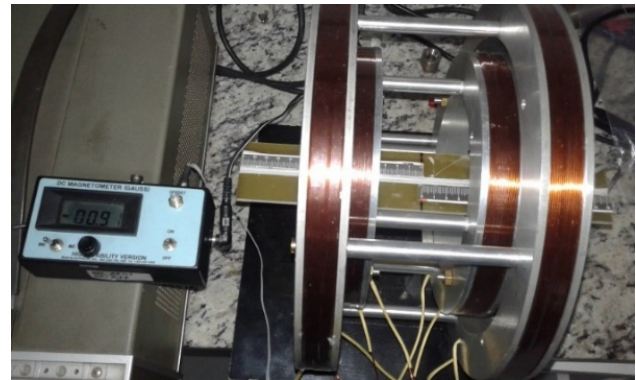


Figure 6. The Front panel of the software for the

calculation of the magnetic field

4. TESTING HOMOGENEITY OF SIMULATED AND MEASURED VALUES OF MAGNETIC FIELD GENERATOR

By applying the two pairs of Helmholtz coils, the homogeneity between the coils is increased (Fig. 7).



Small coils	Large coils
$x = 5.75$ cm	$x = 7.75$ cm
$L = 2$ cm	$L = 2$ cm
$a = 8.5$ cm	$a = 13$ cm
$b = 9.5$ cm	$b = 13.5$ cm
$c = 11.5$ cm	$c = 15.5$ cm
$N = 377$	$N = 367$
$d = 0.95$	$d = 0.95$
number of rows = 21	number of rows = 21
$R_{Small} = 5.5 \Omega \times 2$	$R_{Large} = 7.7 \Omega \times 2$

Figure 7. The generator of the homogenous magnetic field made of two pairs of Helmholtz coils with coils parameters

Testing the homogeneity of the generator of the magnetic field from Figure 7 is realized by two magnetometers: *AlphaLab Inc* (Fig. 8 a) and *Metrolab* (Fig. 8 b). For a precious movement of a sensor, a slider with a brake has been designed (Fig. 8 c).



Figure 8. Equipment for testing homogeneity of the magnetic field, magnetometers: a) “AlphaLab Inc.” and b) “Metrolab” and c) slider with brake

The results of testing the homogeneity of the generator of the homogenous magnetic field from Fig. 7 are shown in Figures 9 – 11.

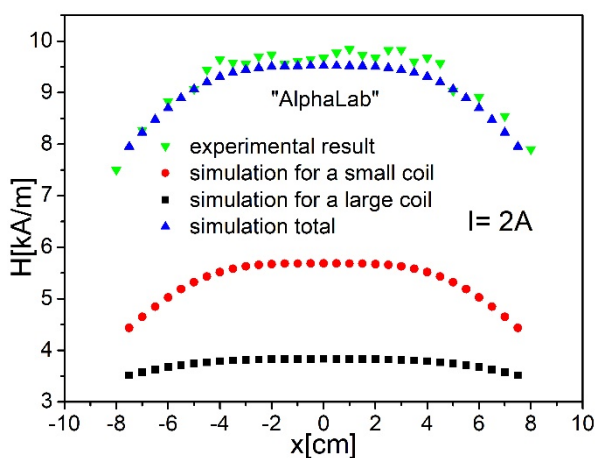


Figure 9. Testing the homogeneity of the generator of the magnetic field with the “AlphaLab Inc.” instrument

Fig. 9. shows the diagrams obtained by the experimental

results and calculated values of the magnetic field along the x-axis which has been measured by the “AlphaLab Inc” instrument, while Fig. 10 shows the results obtained by the “Metrolab” instrument.

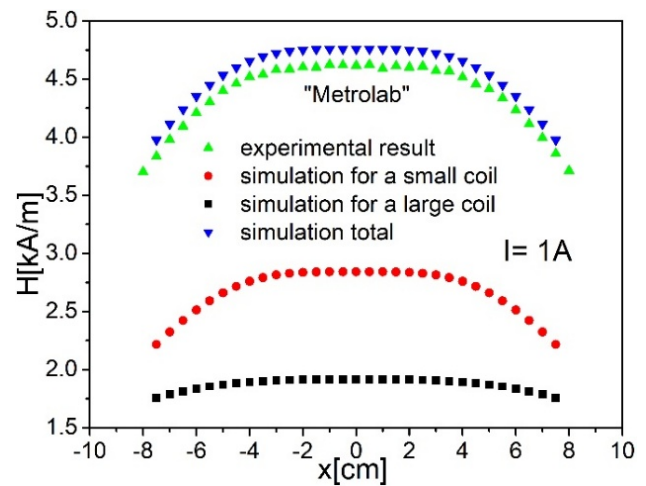


Figure 10. Testing the homogeneity of the generator of the magnetic field with the “Metrolab” instrument.

The magnetic field is extremely homogeneous in a length of 6 cm in the axis of the coils (from -3 cm to +3 cm) (Fig. 11). The maximum deviation of the results obtained by the “AlphaLab” instrument is: +4% (at +3cm), while this value for the results measured by the “Metrolab” instrument is: -3.6% (at +3cm). It is important to note that the measurement error was significantly reduced by using a slider that accurately move the sensor along the axis of the coils. The value of the calculated magnetic field in the x-axis of the coils is extremely close to the values of the arithmetic mean of the results obtained with two different magnetometers.

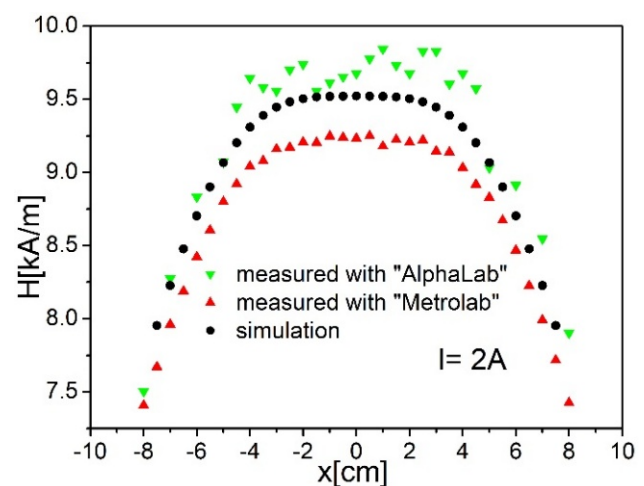


Figure 11. Comparison of the simulated result with experimental results obtained with various instruments.

One pair of the Helmholtz coils can be set at an angle 90° to the second pair (Fig. 12), and in that way, it is possible to test the magnetocrystalline anisotropy of the magnetic element [3].



Figure 12. Arranging coils for testing the magnetocrystalline anisotropy of the magnetic element.

5. CONCLUSION

By applying two pairs of Helmholtz coils to one axis we achieve a remarkable homogeneity of the magnetic field between the coils arranged along the central axis. The simulated result of the magnetic field obtained by the “Labview” software package corresponds to a real value of the magnetic field that is generated by coils with a *dc* current flow. The described method can be applied for the design and calculation of the coils with various dimensions, depending on the required intensity of the magnetic field of high homogeneity.

References

[1] BRUCE, R. M., ARTHUR, A. P., MICHAEL W. S., Electromagnetic Fields Induced by Helmholtz

Aiding Coils Inside Saline-Filled, Boundaries, *Bioelectromagnetics*, 4 (1983), 357-370

- [2] RUARK, A. E., PETERS, MELVILLE F.: Helmholtz coils for producing uniform magnetic fields, *Journal of the Optical Society of America*, 13 (1926) 205-212.
- [3] GUENDOUZ, L., SIDI M. GHALY, A. O., HEDJIEDJ, A., ESCANYÉ, J-M, CANET, D., Improved Helmholtz-type magnetic resonance imaging coils with high-B1 homogeneity—Spherical and ellipsoidal four-coil systems, *Concepts in Magnetic Resonance Part B: Magnetic Resonance Engineering*, 33 (2008) 9-20.
- [4] TROUT, S.R., Use of Helmholtz coils for magnetic measurements, *IEEE Transactions on Magnetics*, 24 (1988) 2108-2111,
- [5] HERZER, G., Nanocrystalline soft magnetic alloys in *Handbook of Magnetic Materials*, Buschow, K., H., (edit.), 10 (1997), 415-462
- [6] SURLA, R., MITROVIĆ, N., VASIĆ, M., MINIĆ, D., The Inverted hysteresis loops and exchange bias effects in amorphous/nanocrystalline Fe₇₂Cu₁V₄Si₁₅B₈ ribbons at room temperature, *Science of Sintering*, 52 (2020) 283-298,
- [7] SURUTKA, J. V.: *Elektromagnetika*, osmo izdanje, Akademska misao, poglavlje 9.6.5., Polje u osi solenoida, 2006.
- [8] SURLA, R.: *Doktorska disertacija: Uticaj odgrevanja na strukturne transformacije i magnetna svojstva legure Fe₇₂Cu₁V₄Si₁₅B₈*, FTN Čačak, Univerzitet u Kragujevcu (2021).



A NEW INFRARED RADIATION DETECTION SYSTEM AS AN INSPIRATION FOR THE POTENTIAL CONSTRUCTION OF A RADIOMETRIC DETECTOR

MARINA SIMOVIĆ-PAVLOVIĆ

Faculty of Mechanical Engineering, University of Belgrade, Kraljice Marije 16, 11000, Belgrade, Serbia,
*corresponding author email: simovicmarina99@gmail.com

LJUBIŠA TOMIĆ

Technical Test Center, Vojvode Stepe 445, 11000, Belgrade, Serbia,
email: ljubisa.tomic@gmail.com

BRANKO KOLARIĆ

Institute of Physics, University of Belgrade, Pregrevica 118, 11000, Belgrade, Serbia,
email: branko.kolaric@umons.ac.be

DARKO VASILJEVIĆ

Institute of Physics, University of Belgrade, Pregrevica 118, 11000, Belgrade, Serbia,
email: darko@ipb.ac.rs

Abstract: *In the search for new detection systems that are of great importance in various fields, physical phenomena play a major role. The radiometric detector relies on a powerful combination of the thermophoretic effect and the holographic observation method. When we use holography to record the deformation of the nanometer structure caused by the effect of infrared radiation, we only have to measure the mechanical deformation and convert it into an output signal. The perfection of modern solutions lies in the simplicity of the applied technology.*

Keywords: *Detectors, Infrared radiation, Holography.*

1. INTRODUCTION

In modern times, infrared detectors are widely used in various fields. [1] Thermal cameras form an image using infrared radiation, and this kind of imaging has a particular application for military purposes. The main advantage of thermography is the possibility of night observation without the need for additional lighting. This property is a consequence of the property of all objects with a temperature above absolute zero to emit infrared radiation. These features are of great importance for military purposes, since thermal imaging devices are especially effective at night and in low visibility conditions.

There are two significant groups of infrared detectors, thermal and quantum. Each group has its advantages and disadvantages in terms of effect, working conditions, production price, etc. However, there is a constant need to find new mechanisms, which will overcome the current limitations in the detection of thermal radiation. A new way to detect thermal radiation described in this paper is based on the radiometric effect. [2] The radiometric effect is a thermo-mechanical phenomenon caused by temperature gradient formed on the piece of material after this material absorbed some electromagnetic radiation. Parallel to the existence of a temperature gradient, the

material has such a structure that its characteristic dimension is of the order of the mean free path of the surrounding gas molecules.

The radiometric effect essentially refers to the action of a force that leads to material deformation. This force is called the radiometric force and is formed when the molecules of the surrounding gas carry much more mechanical impulse from one side of the material, from warmer side.

The energy of the invisible parts of the electromagnetic radiation spectrum is converted in motions of submillimeter size particles. The conversion of the energy of invisible electromagnetic radiation into mechanical displacement is detected by the holographic method. [2, 3]

2. EXPERIMENTAL

Different butterflies' wings were examined to propose a new infrared sensory system. The change of the color spectrum on the natural structure of the butterfly's wings was used, caused by thermal influence, and thermophoretic effect as a consequence of the process. [4]

Different physico-chemical parameters that could have an influence on the thermophoretic effect on the wing were investigated. The analysis of the obtained results definitely showed that the main parameter of influence

classic metal processing step by step according to the technologies developed for each part separately.

4. CONCLUSION

In accordance with modern military technologies, and from the aspect of optics, the need to find new infrared detection mechanisms was recognized. In this sense, the thermophoretic effect was identified as interesting and of potential importance and the study of it was done using the holographic method. The price reduction and simpler maintenance technologies represent the main advantage of this type of system. The goal for further improvement is to define the final solution with the smallest possible dimensions and to test the efficiency of the final product.

References

- [1] HE, Y., DENG, B., WANG, H., CHENG, L., ZHOU, K., CAI, S., & CIAMPA, F.: *Infrared machine vision and infrared thermography with deep learning: a review*, *Infrared Physics & Technology*, vol. 116, p. 103754, 2021.
- [2] OSTROVSKY, Y.I., SHCHEPINOV, V.P., YAKOVLEV, V.V.: *Holographic Interferometry in Experimental Mechanics*, Volume 60, Springer, 2013.
- [3] SIMOVIC-PAVLOVIC, M., PAGNACCO, M.C., GRUJIC, D., BOKIC, B., VASILJEVIC, D., MOUCHET, S., VERBIEST, T., KOLARIC, B.: *Uncovering Hidden Dynamics of Natural Photonic Structures using Holographic Imaging*. *J. Vis. Exp.* (), e63676, doi:10.3791/63676 (2022).
- [4] SIMOVIĆ-PAVLOVIĆ, M.: *Radiometarski detector baziran na biološkim strukturama – MEMS/NEMS*, Doktorska disertacija, Mašinski fakultet – Univerzitet u Beogradu, Beograd, 2022.
- [5] CHEN, Y. P., YANG, M. D.: *Micro-scale manufacture of 3D printing*, *Applied mechanics and materials*, Vols. 670-671, pp. 936-941, 2014.
- [6] SIMOVIC-PAVLOVIC, M., BOKIC, B., VASILJEVIC, D., KOLARIC, B.: *Bioinspired NEMS - Prospective of collaboration with nature*, *MDPI - Applied Sciences*, vol. 12, no. 905, 2022.



10th INTERNATIONAL SCIENTIFIC CONFERENCE
ON DEFENSIVE TECHNOLOGIES
OTEH 2022

Belgrade, Serbia, 13 – 14 October 2022



SECTION VI

**TELECOMMUNICATION AND INFORMATION
SYSTEMS - TIS**

CHAIRMAN

prof. Milorad Obradović, PhD
assoc. prof. Vladimir Mladenović, PhD



NOVEL APPROACH TO RECONFIGURATION POWER LOSS REDUCTION PROBLEM BY SIMULATED ANNEALING TECHNIQUE

BRANKO STOJANOVIĆ

Tehnički opitni centar, Beograd, stojanovic.branko@rocketmail.com

TOMISLAV RAJIĆ

Elektrotehnički fakultet, Beograd, rajic@etf.rs

ALEKSANDAR KOVAČEVIĆ

Fakultet tehničkih nauka u Čačku, Univerzitet u Kragujevcu, aleksandar.kovacevic@ftn.kg.ac.rs

Abstract: The network reconfiguration is done by changing the status of the switches, mainly for two reasons: an active power loss reduction and load balancing attracting the attention of distribution engineers for quite a long period of time. In this article solving method for the active power loss reduction is given. Searching for the relevant radial configurations is done by a simulated annealing technique. To aid the search, a programme for checking the connectivity of the power system, with imposed radiality constraint, is presented enhanced by a new approximate power flow method. The applied power flow programme is very efficient and fast but can be used only as an indication for the loss estimation because of the insufficient method accuracy. At the end of algorithm it is necessary to run efficient power flow programme to determine the real situation concerning the loss reduction. A numerical example for Baran and Wu network is analyzed. The developed method converges to the global optimum given in a numerical example. The time duration of the used method is of an hour order and does not depend on the fast manipulation of incoming data files. This advantage makes the method interesting in the planning stage as well as the application in real time. Main contribution of this paper is a novel approach which exploits mostly the following mechanisms: network connectivity checking matrix, Lavorato et al. criterion for imposing radiality constraint and efficient power flow algorithm combined with precise power flow for exact loss calculation.

Keywords: network configuration, active power loss, connectivity, radial configuration, power flow algorithm, simulated annealing.

1. INTRODUCTION

Network reconfiguration requires determination of the best combination of branches, one from each loop, to be switched out so that resulting radial distribution system incurs minimal kW losses. Reconfiguration of network is obtained by changing the status of sectionalizing (normally closed) and tie line (normally open) switches. Since the statuses of the tie switches and sectionalizing switches are binary (open or closed), the solution space is discontinuous. Owing to the discontinuous and discrete nature of the problem, classical techniques are rendered unsuitable and the use of global search techniques is warranted.

Network reconfiguration belongs to “minimum spanning tree” problems (network looks like a spanning tree) known as NP - combinatorial optimization problems. Algorithm should find minimum loss configuration, system constraints being satisfied.

Numerous methods have been reported in the literature for radial distribution systems (RDS) reconfiguration. A branch exchange type algorithm has been proposed in [1] that suggests a formula for determination of change of

power loss due to branch exchange. In [2] a different method for branch exchange using a heuristic approach is proposed. Most of these methods depend on some heuristics. Another limitation of these algorithms is that they give only a local minimum solution and the global optimum solution may not be found.

In [3] the authors start from network where all switches are closed and then they successively open them to eliminate loops regarding which switch to open, after an optimal flow pattern application. Using DISTOP programme the authors come to an interesting and true conclusion that weakly meshed configurations are with the lowest power loss. The implemented efficient power flow algorithm requires the reenumeration of nodes in levels that is not solved accurately when there are a large number of configurations.

In [4] a new algorithm is constructed with no need of matrix operation, only building of network graph from no branch configuration. One-source node networks are studied. Approach to the optimal solution is direct, radial configuration is maintained during the whole process, voltage and current constraints are easily satisfied, initial feasible configuration is not necessary and optimal one with minimal losses can be achieved.

The heuristic method is described in [5] for obtaining minimum loss configuration. Merlin and Back approach is adopted. A fast and reliable new efficient power flow algorithm is applied for searching through feasible configurations applicable for real networks.

Systematic method in [6] for reconfiguration power loss reduction problem is suggested. Methodology has three basic parts. Load estimation in real time, building of minimum loss configuration and cost and benefit estimation. The authors conclude that reconfiguration on a daily basis is not economically justified. It is justified on seasonal level with each month small correction. In this sort of planning, a lot can be saved in price.

Simulated annealing is used for the first time to solve reconfiguration power loss reduction problem in [7, 8]. It is presented as a non-differentiable multiple objective function combinatorial optimization problem with constraints.

In [9] authors also apply simulated annealing for reconfiguration solution and discrete optimization algorithm for capacitor placement.

Authors in [10] use only simulated annealing for solving reconfiguration and capacitor placement.

In [11] sophisticatedly based simulated annealing method is presented (with special cooling and perturbation mechanism) for the large-scale systems reconfiguration problem. Authors in [12] use a combined simulated annealing method with taboo search for minimization of the losses in distribution systems.

Distribution system minimum loss reconfiguration in the Hyper-Cube Ant Colony Optimization framework is presented in [13].

In recent years, evolutionary computational algorithms such as genetic algorithm (GA) [14] and evolutionary programming have been proposed for distribution system reconfiguration, with encouraging results. At every generation of the evolution, the chromosome structure must satisfy the radial property of the network without islanding any load point. The problem is highly significant since there is every probability that the genetic operators might disrupt the radial nature of the chromosome.

Only two works [15 and 16] analyze unbalanced networks. Borozan considers unbalanced Skoplje network and applies heuristics and Zimmerman solves unbalanced network with 144 branches, 9 normally closed and 3 tie switches by means of simulated annealing.

In all stated literature complicated software is applied that is not presented and is run on fast PC-s (Pentium-IV), especially in recent references.

As a cornerstone of this paper, the article of Nahman and Perić [17] is used. Connectivity check criterion (presented in Section 2) that was refined and efficient power flow algorithm also modified with basic ideas in [17]. Fundamentals for simulated annealing algorithm programming are borrowed from Masters work [18].

Although in recent time distribution engineers turn to

more complicated problems such as simultaneous reconfiguration and capacitor switching in the presence of renewable generation [19, 20] and not only minimization of losses bases for methods in mentioned references are laid out in this paper.

2. NETWORK CONNECTIVITY CHECK

Power network is connected if there is a path between any pair of its nodes. This means that all load nodes are connected to the source node and can be supplied from that node. Network connectivity can be easily checked by means of matrix (NC) defined as [21]:

$$(NC) = (B) \exp(n-1), \quad (2.1)$$

where n is the number of network nodes and (B) is $n \times n$ system connectivity matrix with elements $B(i,j)$ equal to 1 if there is a line between nodes i and j , and 0 otherwise. When $i=j$ in accordance with convention [21] $B(i,j)$ equals 1. Network is connected if all (NC) matrix elements equal 1 [21]. Arithmetic operations in (2.1) are Boolean, what means:

$$0+0=0;$$

$$0+1=1+1=1;$$

$$0*0=0 \text{ and}$$

$$1*1=1.$$

One of applications of matrix B is to check if the distribution system is connected.

Distribution system topology can be presented by graph with m branches and n nodes (buses) [22]. It can be stated that distribution network topology is radial if it satisfies the following two conditions [22]:

- 1) configuration must have $n-1$ branches;
- 2) configuration must be connected.

3. MODIFIED EFFICIENT POWER FLOW ALGORITHM

Modified efficient power flow algorithm was borrowed from [17].

Many problems related to the distribution system real application as optimization, capacitor placement, voltage regulation, planning, restoration, state estimation, and so on, seek efficient power flow algorithm for network voltage (branch current) and loss calculation.

Widely adopted is the forward/backward sweep method where cumbersome input data feeding for level drawn network is exploited. The biggest drawback of these procedures is that data input must be generated and fed all the time, for each new configuration, which makes them practically useless for dynamic problems such as network reconfiguration and expansion planning.

Algorithm proposed in this paper is novel and classical.

It involves the building of network node admittance matrix which is only input parameter that changes with reconfiguring while all other incoming data remain the

same and no reenumeration of nodes is necessary. Analyzed network can be radial or weakly meshed. The proposed method is robust but demands efficient power flow to be applied in the end [23] because of insufficient preciseness.

Applied programme is analyzed in [24]

4. THE BLOCK DIAGRAM

The block diagram of the proposed algorithm is given on Figure 1.

Programme starts with any initial feasible configuration. Adopted cooling schedule can be expressed as $T=0.95*T$, initial temperature T being 5000.

New feasible configuration is generated by means of random number generator.

Let E_i be the current solution and E_j a neighbor solution. $\Delta E_{ij} = E_i - E_j$.

If $\Delta E_{ij} < 0$ replace the solution j by solution i , if not find $\exp(-\Delta E_{ij}/T)$. If $\exp(-\Delta E_{ij}/T)$ is greater than the random number uniformly distributed in segment $[0,1)$ replace the solution j by solution i . If not retain current solution j .

The algorithm stops in two cases, whichever occurs first:

1. The length of Markov chain at a certain temperature becomes greater than 3000 counted configurations.
2. Acceptance rate becomes less than 0.001.

The following data are in programme output file.

E- losses for the last generated configuration by simulated annealing (kW).

EOLD- losses for the last accepted configuration by simulated annealing (kW).

EOLDD- losses that are minimal during the whole procedure of performing simulated annealing (greedy search of all generated configurations) in kW.

niz- vector denoting open branches for the last generated configuration.

nizOLD- vector denoting open branches for the last accepted configuration.

nizOLDD- vector denoting open branches linked with EOLDD losses.

IMIN- number of generated minimal configurations (by monitoring greedy search) in descending order.

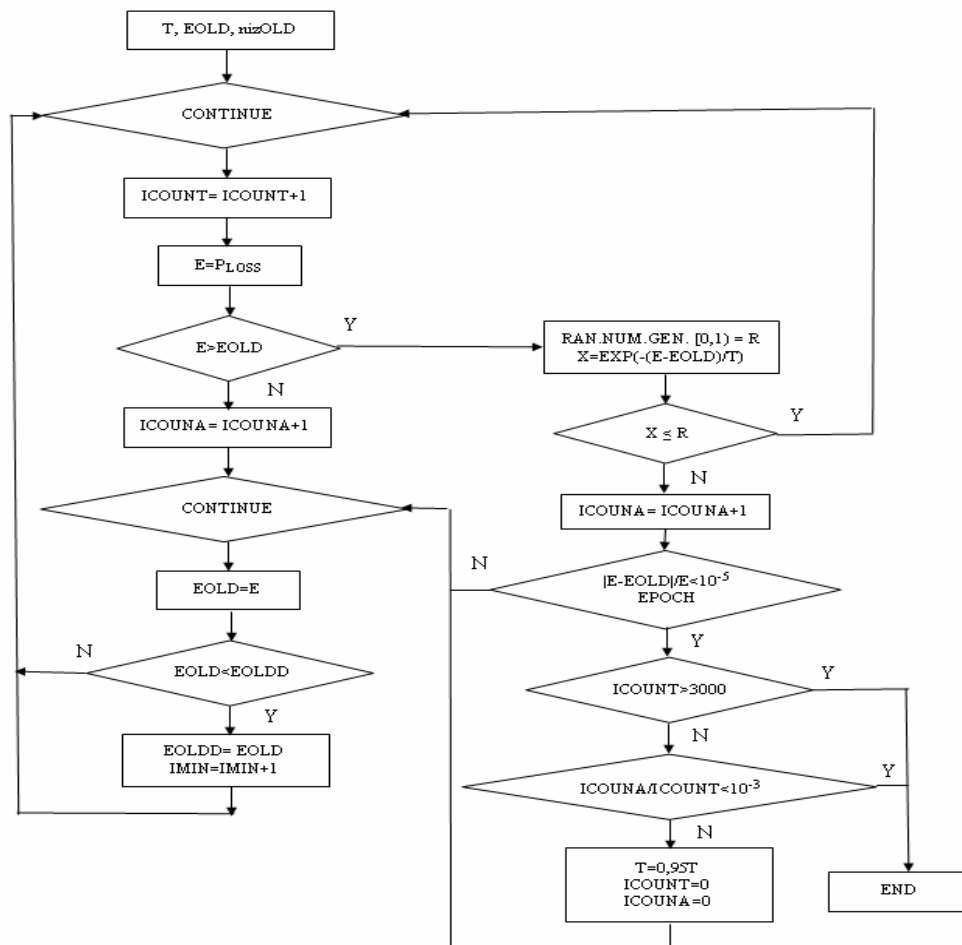


Figure 1. The programme block diagram

5. NUMERICAL RESULTS

Tested system is hypothetical 12.66 kV system [2] (given in Figure 2) comprising of 32 branches and 5 tie switches forming 5 different loops when closed. System data are given in Table 1. The summary of losses with data for open branches is given in Table 2. Total active and reactive load of tested network amount to 3715 kW and 2300 kVar respectively. Initial system active power loss is 202.675 kW (precise power loss [3, 23]) which is 5.5 % of total active power demand. The lowest voltage of the initial configuration is 0.9131 p.u. It is also supposed that each branch can be open or closed by the means of sectionalizing switch. Shaded figure in |V| p.u. column denotes the lowest node voltage.

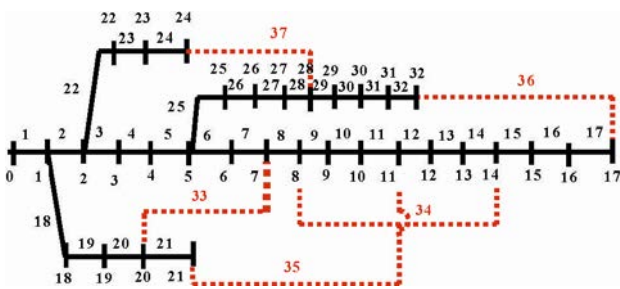


Figure 2. Network Baran and Wu [2]

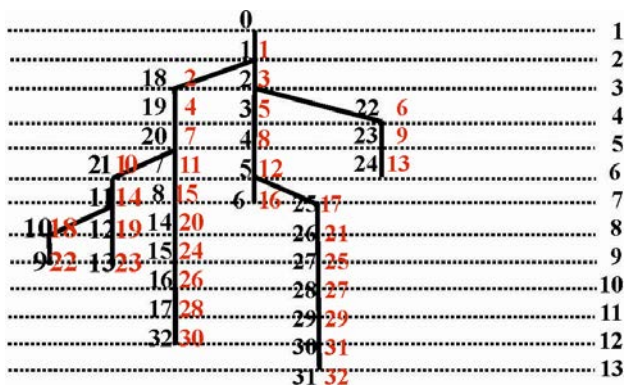


Figure 3. The optimal configuration

6. DISCUSSION AND CONCLUSIONS

1) In this example target optimum is reached in the following manner. Of all programme runs select lowest suboptimum. Open branches are 7, 9, 13, 32 and 37. On

network figure close branch 13 and perform branch exchange by opening branch 14 which is the adjacent one. The target optimum is achieved.

2) The lowest voltage of the target optimum configuration is 0.938 p.u. which is better than the previous value 0.913 p.u. of initial configuration. The same applies for suboptimal configurations, so that with reconfiguration the voltage picture is only improved.

3) Currents of branches 15, 16, 17, 18, 19, 20 and 21 of the target optimum configuration are higher than in initial configuration. That shows that conclusion of Padilha Feltrin [25] is only partly true. The target optimum currents are mainly lower than in initial configuration but for minimum incremental loss branches. By rising losses of these branches and lowering losses of high current branches optimal configuration is achieved. Similar applies for suboptimal configurations.

Voltage and current constraints are not incorporated in authors' programme.

4) Second duration execution time of reconfiguration problems is ridiculous. In such cases the time for preparation of input data is of greater importance. In this example CPU time is of an hour order. With rising complexity of the system the time increases. With more rigorous parameters of simulated annealing time rises as well. Sometimes the quality of solution with moderate demands (epoch < 0.001, a.r. < 0.001 and ICOUNT=3000) gives for an acceptable time (2 hours) the best result. The reason for this is that obtained suboptimum is the result of hybrid and not alone simulated annealing algorithm. Suboptimum of implemented algorithm is more than desirable when having in mind that obtaining target optimum lasted several months, for example, in question in [26].

5) The CPU time can be less without improving of optimum when switched to inhomogeneous algorithm which decreases temperature after each transition (before applying Metropolis criterion).

6) Besides the fact that many algorithms are applied for the reconfiguration in distribution networks traceability and repeatability of the method exposed in this paper make it different and unique.

Table 1 - Input data and results of precise power loss programme (Ploss=202.6 kW) for the initial configuration 33, 34, 35, 36 and 37 branches open (zeros in A, kW and kVar column)

branch	R (Ω)	X (Ω)	PLoad (kW)	QLoad (kVar)	V p.u.	Ibranch module (A)	Branch Ploss (kW)	Branch Qloss (kVar)
0-1	0.0922	0.0470	100.00	60.00	0.9970	364.3	12.2	6.2
1-2	0.4930	0.2511	90.00	40.00	0.9829	324.1	51.7	26.3
2-3	0.3660	0.1864	120.00	80.00	0.9755	233.1	19.9	10.1
3-4	0.3811	0.1941	60.00	30.00	0.9681	221.5	18.6	9.5
4-5	0.8190	0.7070	60.00	20.00	0.9497	216.1	38.2	33.0
5-6	0.1872	0.6188	200.00	100.00	0.9462	101.1	1.9	6.3
6-7	0.7114	0.2351	200.00	100.00	0.9413	82.4	4.8	1.5
7-8	1.0300	0.7400	60.00	20.00	0.9351	63.7	4.1	3.0
8-9	1.0440	0.7400	60.00	20.00	0.9292	58.4	3.5	2.5
9-10	0.1966	0.0650	45.00	30.00	0.9284	53.0	0.5	0.1
10-11	0.3744	0.1238	60.00	35.00	0.9269	48.5	0.8	0.2
11-12	1.4680	1.1550	60.00	35.00	0.9208	42.6	2.6	2.0

12-13	0.5416	0.7129	120.00	80.00	0.9185	36.6	0.7	0.9
13-14	0.5910	0.5260	60.00	10.00	0.9171	24.5	0.3	0.3
14-15	0.7463	0.5450	60.00	20.00	0.9157	19.4	0.2	0.2
15-16	1.2890	1.7210	60.00	20.00	0.9137	13.9	0.2	0.3
16-17	0.7320	0.5740	90.00	40.00	0.9131	8.5	0.05	0.04
1-18	0.1640	0.1565	90.00	40.00	0.9965	31.3	0.1	0.1
18-19	1.5042	1.3554	90.00	40.00	0.9929	23.5	0.8	0.7
19-20	0.4095	0.4784	90.00	40.00	0.9922	15.6	0.1	0.1
20-21	0.7089	0.9373	90.00	40.00	0.9916	7.8	0.04	0.05
2-22	0.4512	0.3083	90.00	50.00	0.9794	83.9	3.1	2.1
22-23	0.8980	0.7091	420.00	200.00	0.9727	75.6	5.1	4.0
23-24	0.8960	0.7011	420.00	200.00	0.9694	37.9	1.2	1.0
5-25	0.2030	0.1034	60.00	25.00	0.9477	113.1	2.6	1.3
25-26	0.2842	0.1447	60.00	25.00	0.9452	108.2	3.3	1.6
26-27	1.0590	0.9337	60.00	20.00	0.9337	103.3	11.3	9.9
27-28	0.8042	0.7006	120.00	70.00	0.9255	98.6	7.8	6.8
28-29	0.5075	0.2585	200.00	600.00	0.9220	87.6	3.8	1.9
29-30	0.9744	0.9630	150.00	70.00	0.9178	40.4	1.5	1.5
30-31	0.3105	0.3619	210.00	100.00	0.9169	26.2	0.2	0.2
31-32	0.3410	0.5302	60.00	40.00	0.9166	6.2	0.01	0.02
7-20, 33	2.000	2.000				0	0	0
8-14, 34	2.000	2.000				0	0	0
11-21, 35	2.000	2.000				0	0	0
17-32, 36	0.500	0.500				0	0	0
24-28, 37	0.500	0.500				0	0	0

Table 2 - Results of precise power loss programme calculating Ploss for the initial, suboptimal and optimal configuration

Configuration	Initial	Suboptimal	Optimal
Open branch	33, 34, 35, 36 and 37	7, 9, 13, 32 and 37	7, 9, 14, 32 and 37
Ploss	202.6 kW	143 kW	139.5 kW

References

- [1] Civanlar S, Grainger JJ, Yin H, Lee SSH. Distribution feeder reconfiguration for loss reduction, IEEE Transactions on Power Delivery, Vol.3, No.3, July 1988; 1217-1223.
- [2] Baran ME, Wu FF. Network reconfiguration in distribution systems for loss reduction and load balancing, IEEE Transactions on Power Delivery, Vol.4, No.2, April 1989; 1401-1407.
- [3] Shirmohammadi D, Hong HW. Reconfiguration of electric distribution networks for resistive line losses reduction, IEEE Transactions on Power Delivery, Vol.4, No.2, April 1989; 1492-1498.
- [4] Glamočanin V. Optimal loss reduction of distribution networks, IEEE Transactions on Power Systems, Vol.5, No.3, August 1990; 774-782.
- [5] Borozan V, Rajčić D, Ačkovski R. Improved method for loss minimization in distribution networks, IEEE Transactions on Power Systems, Vol.10, No.3, August 1995; 1420-1425.
- [6] Borozan V, Rajaković N. Application assessments of distribution network minimum loss reconfiguration, IEEE Transactions on Power Delivery, Vol.12, No.4, October 1997; 1786-1792.
- [7] Chiang HD, Jumeau RJ. Optimal network reconfigurations in distribution systems: part 2: Solution algorithms and numerical results, IEEE Transactions on Power Delivery, Vol.5, No.3, July 1990; 1568-1574.
- [8] Chiang HD, Jumeau RJ. Optimal network reconfigurations in distribution systems: part 1: A new formulation and a solution methodology, IEEE Transactions on Power Delivery, Vol.5, No.4, November 1990; 1902-1909.
- [9] Jiang D, Baldick R. Optimal electric distribution system switch reconfiguration and capacitor control, IEEE Transactions on Power Systems, Vol.11, No.2, May 1996; 890-897.
- [10] Su CT, Lee CS. Feeder reconfiguration and capacitor setting for loss reduction of distribution systems, Electric Power Systems Research 58 (2001) 97-102.
- [11] Jeon YJ, Kim JC, Kim JO, Shin JR, Lee KY. An efficient simulated annealing algorithm for network reconfiguration in large-scale distribution systems, IEEE Transactions on Power Delivery, Vol.17, No.4, October 2002; 1070-1078.
- [12] Jeon YJ, Kim JC. Application of simulated annealing and tabu search for loss minimization in distribution systems, Electrical Power and Energy Systems 26 (2004) 9-18.
- [13] Carpaneto E, Chicco G. Distribution system minimum loss reconfiguration in the hyper-cube ant colony optimization framework, Electric Power Systems Research 78 (2008) 2037-2045.
- [14] Stojanović M, Tasić D, Vučković M, Ristić A. Optimal distribution network evaluation by genetic algorithm, CIRED National Committee Serbia, Vrnjačka banja 23-28.09.2012 (paper in Serbian)

- [15]Borozan V, Rajičić D, Ačkovski R. Minimum loss reconfiguration of unbalanced distribution networks, IEEE Transactions on Power Delivery, Vol.12, No.1, January 1997; 435-442.
- [16]Zimmerman RD. Network reconfiguration for loss reduction in three-phase power distribution systems, Masters thesis, Cornell University, May 1992, 60 pages.
- [17]Nahman JM, Perić DM. Optimal planning of radial distribution networks by simulated annealing technique, IEEE Transactions on Power Systems, Vol. 23, No. 2, May 2008; 790-795.
- [18]Stojanović B. Simulated annealing method and its application to capacitor placement problem in radial distribution networks, Masters thesis in Serbian, University of electrical engineering, Belgrade, 1997, 96 pages (basic part).
- [19]Stojanović B, Tomislav R. Distribution network reconfiguration and capacitor switching in the presence of wind generators, Electrical Engineering, 2022, pp 1-18.
- [20]Stojanović B, Tomislav R, Šošić D. Distribution network reconfiguration and capacitor switching in the presence of wind generators and solar panels, ENERGETIKA 2022, 21-24 June, Zlatibor, Serbia (paper in Serbian)
- [21]Heydt GT. Computer analysis methods for power systems, Purdue University, Macmillan Publishing Company, New York, Copyright 1986. 359 p. (pp. 11-15)
- [22]Lavorato M, Franco JF, Rider JM, Romero R. Imposing radiality constraints in distribution system optimization problems, IEEE Transactions on Power Systems, Vol. 27, No. 1, February 2012; 172-180.
- [23]Stojanović B. Efficient automatic programme for voltage and current calculation in large scale radial balanced distribution networks without transformers, International scientific conference on defensive technologies, OTEH 2011, Belgrade, Serbia, October 2011.
- [24]Stojanović B, Moskovljević M, Rajić T. Modified efficient power flow algorithm Nahman and Perić, OTEH (International scientific conference on defensive technologies, Belgrade, VTI) 2016.
- [25]Carreno EM, Romero R, Padilha-Feltrin A. An efficient codification to solve distribution network reconfiguration for loss reduction problem, IEEE Transactions on Power Systems, Vol. 23, No. 4, November 2008; 1542-1551.
- [26]Stojanović B. Branch exchange approach to power loss reduction in reconfiguration problem of balanced distribution networks, Vol.2, No.3, 2015, IJMEA, 142-149.



BIRDS AND DRONES SPECTROGRAMS AND HOW TO DIFFER THEM

JOVAN RADIVOJEVIĆ

IRITEL a.d., Belgrade, jovan.radivojevic@iritel.com

DEJAN STANOJEVIĆ

IRITEL a.d., Belgrade, dejan.stanojevic@iritel.com

ALEKSANDAR LEBL

IRITEL a.d., Belgrade, lebl@iritel.com

Abstract: FMCW radar spectrograms are powerful technique for malicious drones detection and identification. But, there is a high risk that drones are replaced by birds and vice versa. The original analytical procedure for birds spectrogram calculation is presented in this paper. The developed expressions are similar to the known corresponding expressions for drones. These expressions are suitable to hovering drones and birds whose only movement is related to flapping wings. It is analyzed how physical characteristics and motion performances of both targets influence their spectrogram appearance. The obtained spectrograms for drones and birds are mutually compared and some recommendations for their distinguishing are emphasized.

Keywords: FMCW radar, birds and drones spectrograms, wings flapping, drones rotors movement.

1. INTRODUCTION

Today the importance of malicious drones detection grows every day. Various sensor types may be utilized for this task. A comprehensive survey of applied detection techniques is given in [1]. Among the detector types radars are unavoidable choice and an integral part of nearly all practical solutions.

Frequency Modulated Constant Wave (FMCW) radars are powerful device to detect and classify different objects. Such identification is based on the whole object movement or, at least, on some parts of object micro motion. These micro motions produce specific radar echo and, as a consequence, specific radar spectrograms depending on the characteristics of the observed object. For example, the obtained spectrograms as the result of drones' rotors rotation may be used for drones detection.

The spectrograms produced by drones' rotors rotation are often very similar to the spectrograms produced by birds' wings motion. Both directions in the sense of false detection are possible: 1. wings motion is detected as rotors rotation – false alarm, or 2. rotors rotation appears as wings motion – alarm miss. When drone presence is detected, its operation has to be jammed. Such scenario of jamming is called reactive jamming. (The other possible scenario is that jamming is performed continuously, regardless of drone detection process – this is active jamming [2], [3]).

Distinguishing drones and birds according to their spectrograms is subject of significant number of analysis. In fact, FMCW radar effectiveness in birds detection and classification was noticed even 50 years ago [4]. Such

investigation is further expanded in [5] where it is presented a classification algorithm aimed at automatic recognition of bird targets using Artificial Neural Networks (ANN) (machine learning) principles. ANNs (i.e. its class Convolutional Neural Networks) have been analyzed in a mission of drones and birds distinguishing. Such solutions have proved high reliability in birds' and drones' targets differentiation with error probability in some scenarios significantly lower than 10% [6]. In contribution [7] micro-Doppler signatures are filtered to compensate Doppler shift caused by target (drone or bird) motion and to get only the spectrogram caused by micro motions as this is very powerful base for targets classification. The authors in [8] prove this statement, i.e. why it is worth to filter Doppler shift due to the whole target motion: the probability of successful detection drops down for moving objects caused both by their velocity and acceleration or, in other words, detection must take longer time for such objects. The most often applied frequency for FMCW radar realization is 24GHz (our analysis in this paper is limited to this frequency), but better quality spectrograms are usually obtained using higher radar frequencies (for example 94GHz in [9]). The lower frequencies are also applicable (9.6GHz in [8]). FMCW radars are not the only one to exploit Doppler-effect to obtain drones or birds spectrograms. They may be also obtained by pulsed-Doppler radars [10] although the appearance of spectrograms is different than in the case of FMCW radars application.

Analytical models of birds and drone flight are presented in the sections II and III. The spectrograms according to these models are drawn in the sections IV and V. The main suggestions how to distinguish birds and drones from the presented spectrograms are emphasized in the section VI. Finally, conclusions are in the section VII.

2. BIRD FLIGHT MODELLING

Wings motion is the cause of birds' micro-Doppler signatures. Depending on the view direction towards the FMCW radar, the wing motion may be modelled as flapping (Figure 1a), twisting (Figure 1b) or sweeping (Figure 1c). When a view is from the front or back side, besides only flapping, the wing may have one movement more, meaning that folding wing is obtained (Figure 1d) [11]. Generally, the view at the flying bird is not strictly according to the one of the positions from figures 1a, 1b or 1c. The method for spectrogram determination in such general case is presented in [12].

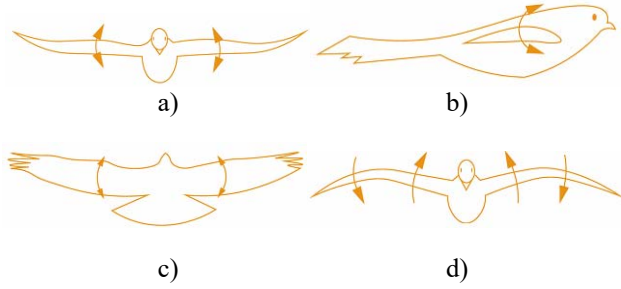


Figure 1. Modelling wings motion: a) flapping; b) twisting; c) sweeping; d) folding

Our contribution in this paper is to develop in a closed analytical form the expression for bird micro-Doppler signature. In the analysis we are limited to the case from the Figure 1a. The only bird motion is its wings flapping, the bird is nearly not flying.

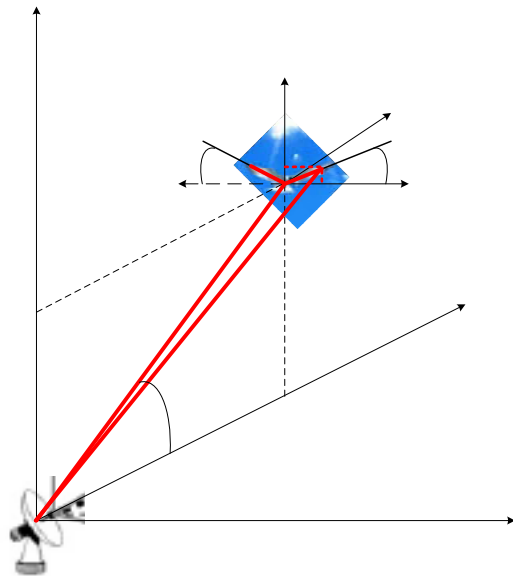


Figure 2. Parameters to determine bird micro-Doppler signature

We start from the sketch in the Figure 2. FMCW radar is located at the origin point of coordinate system xyz . The centre of the bird body is at the point where it is $x_l=0$ and the two remaining coordinated may be expressed as:

$$y_1 = R_0 \cdot \cos \beta \tag{1}$$

$$z_1 = R_0 \cdot \sin \beta \tag{2}$$

where R_0 is the distance between radar and the bird body central point A and β is the bird central point elevation towards the horizontal plane.

According to our model, flapping of wings is realized in the plane parallel to xz plane at the distance y_l . We shall suppose that the bird is located in the new coordinate system $x_a y_a z_a$ whose origin point has coordinates $x_l=0$ while y_l and z_l are expressed by (1) and (2). The wings angle φ during flapping may be modelled as

$$\varphi(t) = \varphi_{\max} \cdot \sin(2\pi \cdot f_{fl} \cdot t + \varphi_0) \tag{3}$$

where φ_{\max} is the maximum flapping angle, f_{fl} is the flapping rate and φ_0 is the initial flapping angle. Without loss in generality we shall suppose that $\varphi_0=0$.

Let us now consider some point B on the bird wing at the distance l_p from the bird central point A. The coordinates of this point are expressed as:

$$x_2 = l_p \cdot \cos \varphi \tag{4}$$

$$z_2 = l_p \cdot \sin \varphi \tag{5}$$

The distance of point B from the FMCW radar may be now calculated as

$$\begin{aligned} OB &= R_p = \sqrt{x_2^2 + y_1^2 + (z_1 + z_2)^2} = \\ &= \sqrt{l_p^2 \cdot \cos^2 \varphi + R_0^2 \cdot \cos^2 \beta + (R_0 \cdot \sin \beta + l_p \cdot \sin \varphi)^2} \tag{6} \\ &= \sqrt{l_p^2 + R_0^2 + 2 \cdot R_0 \cdot l_p \cdot \sin \beta \cdot \sin \varphi} \approx \\ &\approx R_0 + l_p \cdot \sin \beta \cdot \sin \varphi \end{aligned}$$

because it is

$$\left(\frac{l_p}{R_0}\right)^2 \approx 0 \tag{7}$$

and it is valid, generally

$$\sqrt{1 + 2 \cdot q} \approx 1 + q \tag{8}$$

for low values of q .

Now the radar received signal as a consequence of reflection from the point B is

$$\begin{aligned} s_R(t) &= \exp\left\{-j \cdot \left[2\pi \cdot f \cdot t + \frac{2\pi \cdot f}{c} \cdot 2 \cdot R_p(t)\right]\right\} = \\ &\exp\left\{-j \cdot \left[2\pi \cdot f \cdot t + \frac{4\pi}{\lambda} \cdot (R_0 + l_p \cdot \sin \beta \cdot \sin \varphi)\right]\right\} \tag{9} \end{aligned}$$

where f is the radar frequency, λ is its wavelength and the reflected signal passes the distance R_p two times. It is supposed that total transmitted signal is reflected towards radar.

The total reflected signal from one bird wing is obtained after integrating the reflected signal over the whole wing length L :

$$s_L(t) = \exp\left(-j \cdot \frac{4\pi}{\lambda} \cdot R_0\right) \cdot \int_0^L \exp\left\{-j \cdot \left[\frac{4\pi}{\lambda} \cdot (l_p \cdot \sin \beta \cdot \sin \varphi)\right]\right\} \cdot dl_p \quad (10)$$

Replacing (3) to (10) it is obtained

$$s_L(t) = \exp\left(-j \cdot \frac{4\pi}{\lambda} \cdot R_0\right) \cdot \int_0^L \exp\left\{-j \cdot \left[\frac{4\pi}{\lambda} \cdot \left(l_p \cdot \sin \beta \cdot \left(\sin(\varphi_{max} \cdot \sin(2\pi \cdot f_{fl} \cdot t + \varphi_0))\right)\right)\right]\right\} \cdot dl_p \quad (11)$$

If we now introduce the replacement

$$K = -\frac{4\pi}{\lambda} \cdot \sin \beta \cdot \sin(\varphi_{max} \cdot \sin(2\pi \cdot f_{fl} \cdot t)) \quad (12)$$

it is obtained

$$s_L(t) = \exp\left(-j \cdot \frac{4\pi}{\lambda} \cdot R_0\right) \cdot \int_0^L \exp\{j \cdot K \cdot l_p\} \cdot dl_p = L \cdot \exp\left(-j \cdot \frac{4\pi}{\lambda} \cdot R_0\right) \cdot e^{\frac{j \cdot K \cdot L}{2}} \cdot \text{sinc}\left(\frac{K \cdot L}{2}\right) \quad (13)$$

where it is $\text{sinc}(q_l) = \sin(q_l)/q_l$.

The movement of two bird's wings is symmetric towards the yz plane i.e. towards the radar meaning that both wings produce the same effect when considering spectrogram. Thus the total reflected signal from both wings is

$$s_{Ltot}(t) = 2 \cdot s_L(t) \quad (14)$$

or the magnitude of this signal is

$$|s_{Ltot}(t)| = \left| 2 \cdot L \cdot \exp\left(-j \cdot \frac{4\pi}{\lambda} \cdot R_0\right) \cdot e^{\frac{j \cdot K \cdot L}{2}} \cdot \text{sinc}\left(\frac{K \cdot L}{2}\right) \right| \quad (15)$$

The standard procedure to calculate spectrogram is based on Short Time Fourier Transform (STFT) calculation of the considered signal according to the equation [13]:

$$STFT(S_n(m, \omega)) = \sum_{n=-\infty}^{\infty} S_n \cdot w_{n-m \cdot R} \cdot \exp(-j \cdot \omega \cdot t_n) \quad (16)$$

where R is the number of samples between two successive segments of Fourier transform calculation, m is the ordinary number of a segment and w_n is the Hanning window defined by [14]:

$$w_n = \frac{1}{2} \cdot \left(1 - \cos\left(\frac{2 \cdot \pi \cdot n}{N}\right)\right) \quad (n = 0, 1, 2 \dots N) \quad (17)$$

If we now analyze the expression (15) and, related to it, the expression (12), we conclude that four elements contribute to the birds micro-Doppler signature appearance: the elevation angle β , the maximum flapping

angle φ_{max} , the flapping rate f_{fl} and the wings length L .

3. DRONE FLIGHT MODELLING

Method for drone micro-Doppler signature calculation has been already developed in [12], [15]. The developed model considers separately single rotor and multirotor drones. On the base of these contributions we have already performed the analysis of various drone micro-Doppler signatures in [16]. This analysis is limited to hovering drones, i.e. drones which are not flying. In order to consider a higher number of spectrograms and the influence of wider range of characteristic parameters change, we have developed our original calculation program [17]. Here we only repeat the formula for the magnitude of the single rotor drone echo signal:

$$|S_{\Sigma}(t)| = \left| L \cdot \exp\left(-j \cdot \frac{4 \cdot \pi}{\lambda} \cdot (R_0 + z_2 \cdot \sin \beta)\right) \cdot \sum_{k=0}^{N-1} \text{sinc}(\Phi_k(t)) \cdot \exp(-j \cdot \Phi_k(t)) \right| \quad (18)$$

as well as for multi rotor drone echo signal:

$$|S_{\Sigma}(t)| = \left| \sum_{i=1}^{N_r} \sum_{k=0}^{N-1} s_{ik}(t) \right| = \left| \sum_{i=1}^{N_r} L \cdot \exp\left(-j \cdot \frac{4 \cdot \pi}{\lambda} \cdot (R_{0i} + z_{2i} \cdot \sin \beta_i)\right) \cdot \sum_{k=0}^{N-1} \text{sinc}(\Phi_{ik}(t)) \cdot \exp(-j \cdot \Phi_{ik}(t)) \right| \quad (19)$$

where it is

$$\Phi_{ik}(t) = \frac{4 \cdot \pi}{\lambda} \cdot \frac{L}{2} \cdot \cos \beta_i \cdot \cos\left(\Omega_i \cdot t + \varphi_{0i} + \frac{2 \cdot \pi \cdot k}{N}\right) \quad (k=0, 1, 2, \dots, N-1) \quad (20)$$

The meaning of the new variables in (18)-(20) comparing to the previous formulas is:

- N - the number of blades in each rotor;
- Ω - rotor angular rotation speed;
- N_r - the number of drone rotors.

The maximum Doppler shift may be calculated as [12]

$$f_{Dmax} = \frac{4 \cdot \pi \cdot \Omega \cdot L}{\lambda} \cdot \cos \beta \quad (21)$$

4. BIRDS' SPECTROGRAMS CAUSED BY FLAPPING WINGS

Several birds spectrograms, obtained when four already cited parameters in the Section 2 are varied are presented in the figures 3-X. The graphs in these figures are now obtained starting from the echo magnitude expressed by (15) which is then modified using (16) and (17) to give the desired time-frequency shape. All spectrograms in the paper are presented for FMCW radar operating frequency $f=24\text{GHz}$ and digital sampling rate $f_{step}=20\text{kHz}$. Generally, all spectrograms have the similar describable

appearance: the parts with higher echo (wider brown, red, orange and yellow areas) are periodically followed by the parts with lower echo where brown, red, orange and yellow areas are narrower. The rate of these areas in spectrogram corresponds to the bird wings flapping rate. The frequency bandwidth of the wider areas depends on the concrete values of four parameters.

The influence of β is obvious according to the figures 3 and 4. The values of four variable parameters are presented by different colour ink for each parameter in the figures' legend. The bandwidth of wider frequency areas is increased when β , i.e. $\arcsin(\beta)$ is increased. An explanation of such behaviour follows from the fact that bird wings are flapping in yz plane. Thus the variation of their distance from radar is maximum when it is $\beta=90^\circ$. When it is $\beta=0^\circ$, this variation practically does not exist.

The influence of wings length may be analyzed comparing figures 4 and 5. It is obvious the logical conclusion that longer wings lead to wider frequency area with brown, red, orange and yellow colour.

Influence of maximum flapping angle follows from the comparison of figures 4 and 6. The greater flapping angle also means that frequency area with brown, red, orange and yellow colour will be wider.

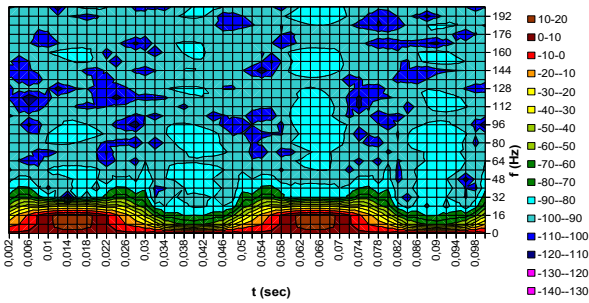


Figure 3. Spectrogram of bird with flapping wings, the wing length $L=0.24\text{m}$, wing flapping rate $f_{fl}=20\text{flaps/s}$, maximum flapping angle $\varphi_{max}=40^\circ$, bird height $z_f=30\text{m}$, bird distance from radar $R_0=100\text{m}$, bird elevation angle towards radar $\beta=\arcsin(0.3)$.

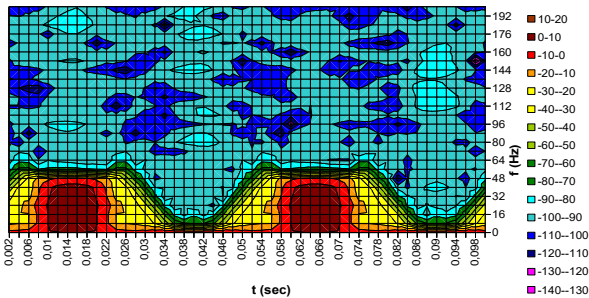


Figure 4. Spectrogram of bird with flapping wings, the wing length $L=0.24\text{m}$, wing flapping rate $f_{fl}=20\text{flaps/s}$, maximum flapping angle $\varphi_{max}=40^\circ$, bird height $z_f=70\text{m}$, bird distance from radar $R_0=100\text{m}$, bird elevation angle towards radar $\beta=\arcsin(0.7)$.

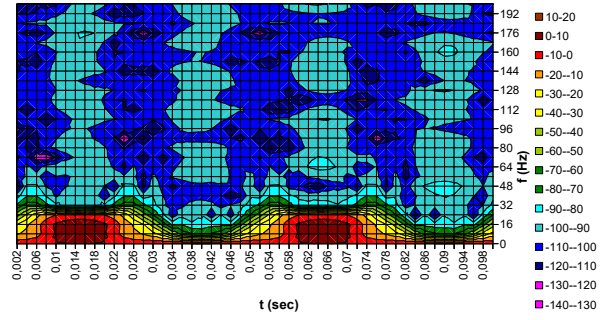


Figure 5. Spectrogram of bird with flapping wings, the wing length $L=0.12\text{m}$, wing flapping rate $f_{fl}=20\text{flaps/s}$, maximum flapping angle $\varphi_{max}=40^\circ$, bird height $z_f=70\text{m}$, bird distance from radar $R_0=100\text{m}$, bird elevation angle towards radar $\beta=\arcsin(0.7)$.

Variation of flapping rate has twofold effect onto spectrogram as may be concluded after the comparison of figures 6 and 7. The number of spectrogram figures repetitions equals the flapping rate, but also the bandwidth of brown, red, orange and yellow colour area increases when the flapping rate increases.

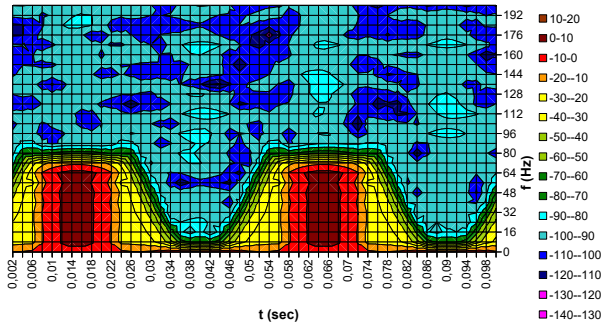


Figure 6. Spectrogram of bird with flapping wings, the wing length $L=0.24\text{m}$, wing flapping rate $f_{fl}=20\text{flaps/s}$, maximum flapping angle $\varphi_{max}=60^\circ$, bird height $z_f=70\text{m}$, bird distance from radar $R_0=100\text{m}$, bird elevation angle towards radar $\beta=\arcsin(0.7)$.

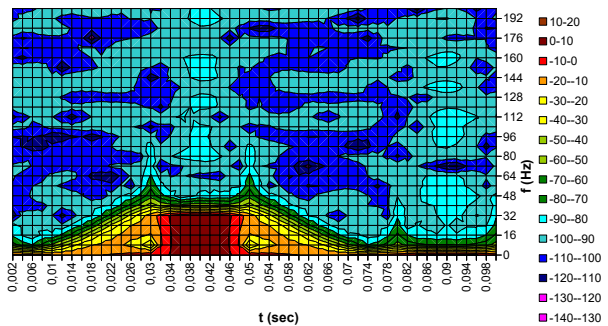


Figure 7. Spectrogram of bird with flapping wings, the wing length $L=0.24\text{m}$, wing flapping rate $f_{fl}=10\text{flaps/s}$, maximum flapping angle $\varphi_{max}=60^\circ$, bird height $z_f=70\text{m}$, bird distance from radar $R_0=100\text{m}$, bird elevation angle towards radar $\beta=\arcsin(0.7)$.

5. DRONES' SPECTROGRAMS CAUSED BY ROTORS MOVEMENT

Drones spectrograms are obtained using equation (18) or (19) depending on the number of drone's rotors. As for birds, the applied equation is then translated to time-frequency field by (16) and (17).

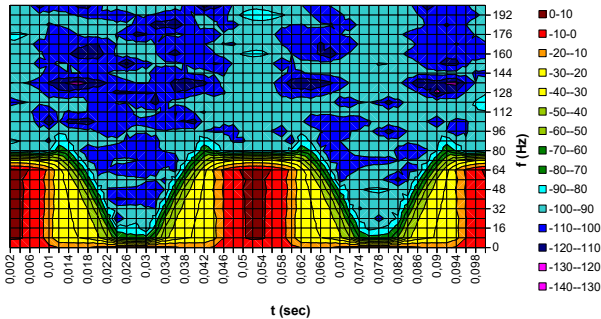


Figure 8. Drone spectrogram for one rotor with one blade, the blade length $L=0.24m$, blade rotation speed $\Omega_{rot}=20rotations/s$, drone height $h=70m$, drone distance from radar $R_0=100m$, drone elevation angle towards radar $\beta=arcsin(0.7)$.

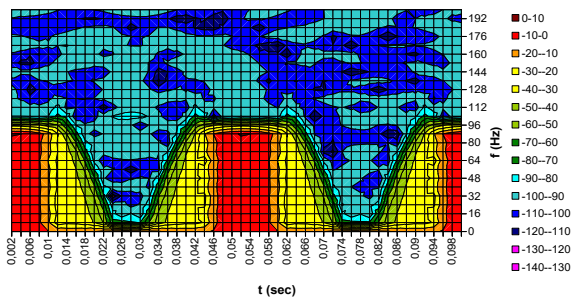


Figure 9. Drone spectrogram for one rotor with one blade, the blade length $L=0.24m$, blade rotation speed $\Omega_{rot}=20rotations/s$, drone height $h=30m$, drone distance from radar $R_0=100m$, drone elevation angle towards radar $\beta=arcsin(0.3)$.

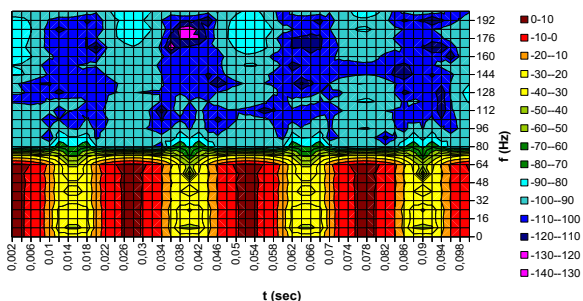


Figure 10. Drone spectrogram for one rotor with two blades, the blade length $L=0.24m$, blade rotation speed $\Omega_{rot}=20rotations/s$, drone height $h=70m$, drone distance from radar $R_0=100m$, drone elevation angle towards radar $\beta=arcsin(0.7)$.

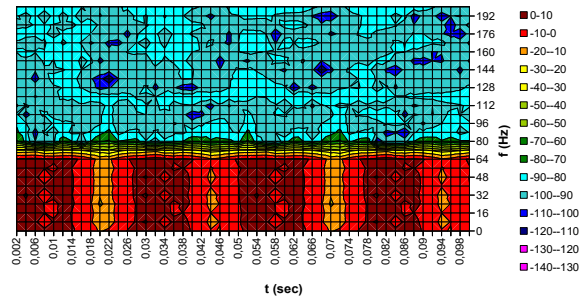


Figure 11. Drone spectrogram for four rotors with one blade, the blade length $L=0.24m$, blade rotation speed $\Omega_{rot}=20rotations/s$, drone height $h=70m$, drone distance from radar $R_0=100m$, drone elevation angle towards radar $\beta=arcsin(0.7)$.

The influence of elevation angle β is opposite than in case of birds. It is illustrated by the spectrograms in the figures 8 and 9. The bandwidth of wider frequency areas is decreased when β , i.e. $arccos(\beta)$ is increased. An explanation of such behaviour follows from the fact that drone rotors are rotating in xy plane. Thus the variation of their distance from radar is maximum when it is $\beta=0^\circ$. When it is $\beta=90^\circ$, this variation practically does not exist.

Characteristics of drone spectrograms are modified in the same way when rotor blades length and their rotation rate are varied as when bird wings length and flapping rate are changed. That's why these characteristics are not presented in this paper.

When rotor drone has two blades, the frequency of repeated areas with wider brown, red, orange and yellow parts is doubled, as presented in the Figure 10. If the number of rotors is increased instead of the number of rotor blades (quadcopters are very often applied), spectrogram changes its appearance. It has one more uniform area, without separated brown, red, orange and yellow parts. This is presented by the Figure 11.

6. DRONES AND BIRDS DETECTION FROM THEIR SPECTROGRAMS

The following steps about drone or birds target presence may be defined on the base of investigation presented in this paper:

1. spectrograms of multirotor drones (quad or more) are highly different and the possibility of false detection is very small. Hovering quadcopter's spectrogram more looks like one surface of uniform bandwidth (brown, red and orange surface in the Figure 11). All spectrograms of birds with flapping wings have sinusoidal repetition of such surfaces (for example, the spectrogram in the Figure 4 is for the same β , same L and the value of f_{fl} is the same as the value of Ω_{rot} for the drone in the Figure 11);
2. if difference may not be made according the step 1, i.e. if the drone target is of helicopter type, it is necessary to go to the further steps. The second step in the decision algorithm is to determine the rate of spectrogram repetitions. The drones' rotors rotation

rate is usually higher than the birds' wings flapping rate [15]. In the case that helicopter's rotor has more than one blade, the rate of spectrogram repetitions is even obtained by the multiplication of the rotation rate and the number of blades (Figure 10 for two blades). Such behaviour means that the probability of false detection when it is necessary to distinguish birds and helicopter drones with the rotor having more than one blade is further decreased;

3. the third criterion of decision could be implemented for helicopter drones having only one blade in their rotor (which is very rare case). It is necessary to consider in the same time the target elevation angle β and the bandwidth of the spectrogram part in brown, red, orange and yellow colour. Our investigation has proved that this bandwidth increases when birds are considered, but decreases when drones are considered, as a function of β increasing (figures 3 and 9). We have explained that the difference of plane where micro motions is performed is the cause of this characteristic behaviour. As a consequence, it is possible to make a reliable decision about the detected target when β is gradually increased (as a consequence of target approaching at nearly same height) or decreased;
4. it remains now to analyze the situation when the target is moving directly towards radar. In this case detection reliability may be improved by considering maximum flapping angle φ_{\max} . According to [12], the typical value of this angle is 40° and with such angle the obtained bandwidth of brown, red, orange and yellow surface is lower than for drone spectrogram (figures 4 and 8).

The elevation angle β may be determined by the implementation of some algorithm on FMCW radar [17].

The possibilities for reliable distinguishing of birds from drones are here analyzed in a qualitative sense.

7. CONCLUSION

The main objective of this paper has been to define the algorithm to differ drones from birds when a target is detected. The decision is made based on the difference in the appearance of spectrograms collected by FMCW radar. The analysis is limited to hovering drones and birds with flapping wings. The obtained results, i.e. obtained spectrograms for drones may be easily compared to the corresponding recorded spectrograms presented in literature [12], [15]. The spectrogram shape dependence is based on the same drone construction and flight characteristics (number of blades in rotors, blades length, rotors rotation rate, etc.) and the spectrograms appearance is very similar in our paper as in this emphasized literature. Instead of practical measuring and recording, we have used our original calculation method to obtain the spectrograms based on varying the parameters of drones' and birds' flight. We have developed the expressions for modelling the bird moving and have used the already existent expressions for the drone. The results of our investigation show that there is possibility to easily distinguish birds from multicopter drones. In the case of drones with only one rotor (helicopter), differences in spectrograms are very clear when the drone has more than

one blade and if its elevation angle is not in the area about 45° . There is only very low possibility of false detection when helicopter rotor has one blade and a drone is positioned near $\beta=45^\circ$. The quantitative values for the decision algorithm and the collection of results by calculation and real-life recording will be the subject of future development.

References

- [1] MATIĆ,V., KOSJER,V., LEBL,A., PAVIĆ,B., RADIVOJEVIĆ,J., *Methods for Drone Detection and Jamming*, 10th International Conference on Information Society and Technology (ICIST), Kopaonik, in: ZDRAVKOVIĆ, M., KONJOVIĆ, Z., TRAJANOVIĆ, M., Proceedings 1 (2020) 16-21.
- [2] RADIVOJEVIĆ,J., PAVIĆ,B., LEBL,A., PETROVIĆ,M., *Sweep Jamming with Discrete Subbands – an Advanced Strategy for Malicious Drones Missions Prevention*, Scientific Technical Review, 71(2), (2022) 46-52, ISSN: 1820-0206, UDK: 355.43:623.624.449.8, COSATI: 03-10, 14-04-01, DOI: 10.5973/str2102046R.
- [3] RADIVOJEVIĆ,J., LEBL,A., MILEUSNIĆ,M., VUJIĆ,A., ŠEVIĆ,T., JOKSIMOVIĆ,V., *Multichannel Radio-jammer Development Considerations for prevention of Illicit Drone Missions*, 9th International Scientific Conference on Defensive Technologies OTEH 2020., Belgrade (2020) 270-275, ISBN 978-86-81123-83-6.
- [4] MARTISON,L.W., *A Preliminary Investigation of Bird Classification by Doppler Radar*, RCA Government and Commercial Systems, Missile and Surface Radar Division, Moorestown, NJ, NASA Wallops Station, Wallops Island, (1973).
- [5] ZAUGG,S., SAPORTA,G., VAN LOON,E., SCHMALJOHANN,H., LIEHTI,F., *Automatic identification of bird targets with radar via patterns produced by wing flapping*, Journal of the Royal Society, 5, (2008) 1041-53, DOI: 10.1098/rsif.2007.1349.
- [6] CHEN, X., ZHANG, H., SONG, J., GUAN, J., LI, J., HE, Z., *Micro-Motion Classification of Flying Bird and Rotor Drones via Data Augmentation and Modified Multi-Scale CNN*, Remote Sensing, 14, 1107, (2022) 1-25, <https://doi.org/10.3390/rs14051107>.
- [7] MOLCHANOV,P., HARMANY,R.I.A., DE WIT,J.J.M., EGIAZARIAN,K., ASTOLA,J., *Classification of small UAVs and birds by micro-Doppler signatures*, International Journal of Microwave and Wireless Technologies, 6(3-4) (2014) 435-444.
- [8] YOON,S.-W., KIM,S.-B., JUNG,J.-H.,CHA,S.-B., BACK,Y.-S., KOO,B.-T., CHOI,I.-O., PARK,S.-H., *Efficient Classification of Birds and Drones Considering Real Observation Scenarios Using FMCW Radar*, Journal of Electromagnetic Engineering and Science, 21(4) (2021) 270-281., ISSN: 2671-7255., <https://doi.org/10.26866/jees.2021>.
- [9] RAHMAN,S., ROBERTSON,D.A., *Radar micro-Doppler signatures of drones and birds at K-band*

- and W-band, Scientific Reports, (2018) 1-11, DOI: 10.1038/s41598-018-35880-9.
- [10] RITCHIE, M., HORNE, C., PETERS, N., *Radar UAV and Bird Signature comparisons with Micro-Doppler*, Chapter 1, pp. 1-33.
- [11] SONG, B., LANG, X., XUE, D., YANG, W., *A review of the research status and progress on the aerodynamic mechanism of bird wings*, Scientia Sinica Technologica, (2021) 1-18, DOI: 10.1360/SST-2020-0515.
- [12] CHEN, V. C., *The Micro-Doppler Effect in Radar*, Artech House, Second Edition, 2019., ISBN: 978-1-63081-546-2.
- [13] AHMADIZADEH, M., *An Introduction to Short-Time Fourier Transform (STFT)*, Sharif University of Technology, Department of Civil Engineering, (2014).
- [14] GABERSON, H. A., *A Comprehensive Windows Tutorial*, Sound and Vibration, Instrumentation Reference Issue, (2006) 14-23.
- [15] ZHAO, C., LUO, G., WANG, Y., CHEN, C., WU, Z., *UAV Recognition Based on Micro-Doppler Dynamic Attribute-Guided Augmentation Algorithm*, Remote Sensing, Article 1205, 13(6), (2021) 1-17., DOI: <https://doi.org/10.3390/rs13061205>.
- [16] LEBL, A., MILEUSNIĆ, M., MITIĆ, D., RADIVOJEVIĆ, J., MATIĆ, V., *Verification of Calculation Method for Drone Micro-Doppler Signature Estimation*, accepted for publication in Facta Universitatis, Series: Electronics and Energetics, ISSN: 0353-3670.
- [17] RADIVOJEVIĆ, J., PETROVIĆ, P., LEBL, A., MILEUSNIĆ, M., *Initial Development of a Program for Drone Micro-Doppler Signature Modelling*, on the review for the IXth IcETRAN Conference, Novi Pazar (2022).



SOFTWARE ALGORITHM FOR DRONE PRESENCE DECISION ON THE BASE OF RADAR SPECTROGRAMS

DEJAN STANOJEVIĆ

IRITEL a.d., Belgrade, dejan.stanojevic@iritel.com

JOVAN RADIVOJEVIĆ

IRITEL a.d., Belgrade, jovan.radivojevic@iritel.com

ALEKSANDAR LEBL

IRITEL a.d., Belgrade, lebl@iritel.com

Abstract: *FMCW radars and spectrograms obtained by its implementation are very powerful and reliable technique for malicious drones' detection and identification. But, the challenge is to differentiate drone and birds spectrograms which are very similar. The most often applied software algorithms to achieve this functionality are based on artificial intelligence implementation principles. The special problem when these algorithms are practically applied is to previously make a huge data base of spectrograms with flying drones and other targets. Our objective was to develop a software algorithm with only limited set of decision criteria which would analyze maximum simplified spectrograms without the need to have spectrograms base. Our decision program implements only four decision criteria and in a great majority of situations allows drones detection from only one spectrogram of an appreciated target. The limitation in this first variant of software algorithm is that it is limited to distinguishing hovering drones from flapping wing birds.*

Keywords: *FMCW radar, birds and drones spectrograms, software algorithm, decision criteria.*

1. INTRODUCTION

Various sensor types are applied in modern solutions for malicious drones' detection. Among these sensors the most often we find radars, RF detectors, acoustic detectors and optical and thermal cameras. Each of these sensors has its benefits and drawbacks. In the case that radar detection is considered, the benefits are very important for the final solution reliability. These benefits comparing to other sensor types may be summarized in several points: 1) when implemented in environment without obstacles, radar is suitable for long range detection, at higher distance than other sensor types, especially cameras or acoustic sensors; 2) it is possible to detect drones, which are autonomous when they are moving, i.e. when there is no their communication with a pilot or supervisory centre, thus overcoming the possibilities of RF detectors which are effective only in detecting this communications between drone and its controller; 3) the satisfactory drone detection is possible in bad weather conditions and in low or no light conditions – such degree of independence of weather conditions is not evident at acoustic or optical sensors [1]. The benefits of radar implementation for drone detection are also emphasized in [2]. As a consequence of these benefits, radar sensors are usually a part of each multisensor drone detection system. Frequency Modulated Constant wave (FMCW) radars are usually applied for this purpose [3].

A great challenge in radar detection of malicious drones is to reliably separate drones from other targets, especially

from birds. This is, in some way, the drawback of radar sensors comparing to thermal and, even more, optical cameras, but this drawback may be significantly mitigated by precise and comprehensive definition of drone detection software algorithm. In many applied solutions different artificial intelligence algorithms are used to increase detection reliability, especially related to deep neural networks [4]. The main objective of this paper is to present our originally developed software algorithm for drone detection, identification and localization. The paper is the logical extension of the contribution [3].

The section II of this paper presents several drones and one bird spectrogram. Two spectrogram variants are considered: in six colours and in two colours, the second one being very suitable for software analysis. Initial definition of software algorithm for drone presence decision is described in the section III including a survey of situations when each one of the four decision criteria is suitable for the right decision. At the end, conclusions are in the section IV.

2. SPECTROGRAMS PREPARATION FOR SOFTWARE ANALYSIS

Spectrograms for the analysis by our software decision algorithm are a little bit modified spectrograms presented in [3], [5], [6]. They are obtained implementing our original calculation program developed in Excel. The whole area of possible signal levels in a spectrogram is divided into six sub-areas. The shape of higher level sub-areas is used for decision making. That's why these sub-

areas cover lower width of spectrum. For the spectrograms in figures 1-8 the highest level sub-area has the designation 1 (i.e. 0.5-1.5) and its level spectrum is 10dB wide. The sub-areas with the designation 2 (i.e. 1.5-2.5) and 3 (i.e. 2.5-3.5) are two steps below the first area, also 10dB wide each one. The next two sub-areas with the designation 4 and 5 are 20dB and 40dB wide, respectively, while all the lower signal levels are covered by the sub-area 6.

The other implemented way of spectrograms presentation is with only two areas. The area with higher signals level (designation 1, i.e. 0.5-1.5 on the black-white spectrogram) covers the areas with designations 1-3 according to the first presentation style on the coloured spectrograms while the area with lower signals level (designation 2, i.e. 1.5-2.5 on the black-white spectrogram) covers the areas with designations 4-6 on the coloured spectrograms. Thus obtained graphs in the black-white style are also presented. Spectrograms in both styles are presented for all analyzed situations, but decisions may be made according to black-white spectrograms.

The spectrograms in the figures 1-7 correspond to hovering drones while the spectrogram in the figure 8 is for the bird whose only movement is wings flapping. Each spectrogram is presented in two shapes with the designations a and b. The figures with designation a are in six colours while figures with designation b are "black" - "white" where brown, red and orange parts in the "a" figures are replaced by black parts in the "b" figures and yellow, green and turquoise parts in the "a" figures are replaced by white parts in the "b" figures. The physical and movement characteristics of a target are emphasized in the figures legends. The most important parameters are written in different colour letters in the legend of each figure. When considering birds spectrograms, data dealing the birds flapping rate are limited to maximum 20flaps/s according to [7]-[9] with only one exception non-important for our development [9] (Figure 8). On the other hand, the minimum multicopter drone propellers rotation rate is about 30rotations/s (2000rotations/min) [10] (as in Figure 2). In our analysis we are going to even lower value of 20rotations/s (figures 1, 3, 4, 7), equal to the number of birds flaps/s, or even lower at 10rotations/s (Figure 6). The spectrograms in this paper are the further insight into the spectrograms recorded in [3]. They are the valuable support to define concrete values of four decision algorithms described qualitatively in [3].

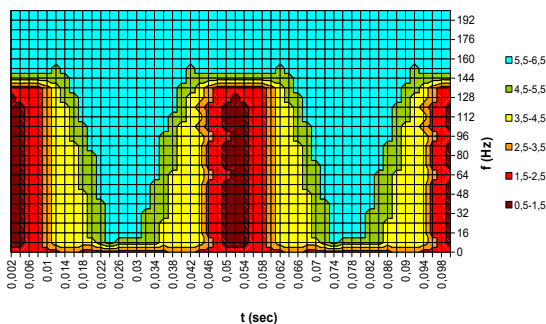


Figure 1a.

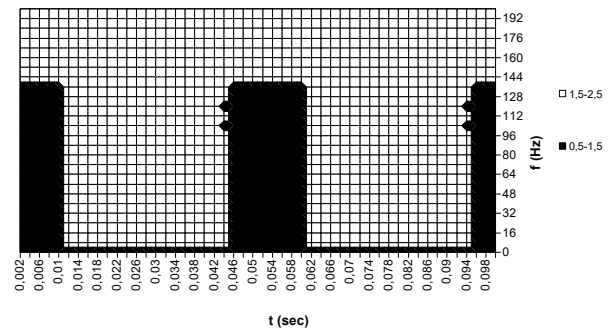


Figure 1b.

Figures 1a and 1b. Drone spectrogram for **one rotor** with **one blade**, the blade length $L=0.48m$, blade rotation speed $\Omega_{rot}=20rotations/s$, drone height $h=70m$, drone distance from radar $R_0=100m$, drone elevation angle towards radar $\beta=arcsin(0.7)$.

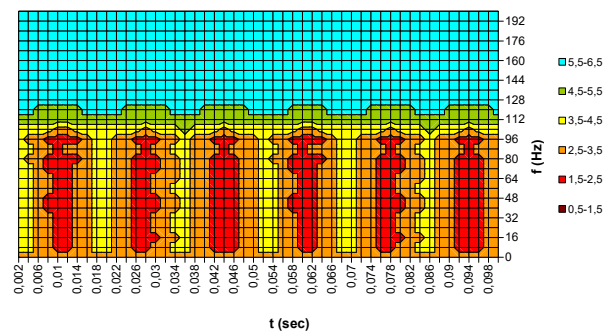


Figure 2a.

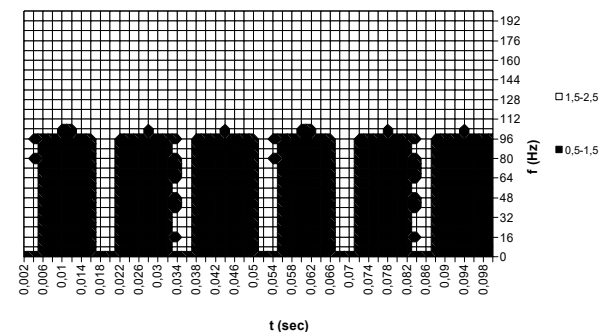


Figure 2b.

Figures 2a and 2b. Drone spectrogram for **one rotor** with **one blade**, the blade length $L=0.12m$, blade rotation speed $\Omega_{rot}=60rotations/s$, drone height $h=70m$, drone distance from radar $R_0=100m$, drone elevation angle towards radar $\beta=arcsin(0.7)$.

The spectrograms in the figures 1-6 are for helicopter type drones having only one rotor. The rotors of helicopters have 2-7 blades where 2, 3 and 5 are the most often found number [11]. We haven't found data about aircrafts of helicopter type with only one blade in their rotor, but such a case is also analyzed in this paper due to the fact that it would be the most demanding task to distinguish these drones from birds. The spectrograms in the figures 1 and 2 are for such a hypothetical case that helicopter has only one rotor. The figures 3, 5 and 6 are for the two-blade rotor and Fig. 4 corresponds to the three-blade rotor. The spectrogram in the Figure 7 is for a quadcopter (which has

four rotors). The majority of presented examples consider the spectrograms when 20 repeatable parts appear in one second because this is the maximum expected bird wings flapping rate i.e. the distinguishing threshold between drones and birds. The number of repeatable parts in drone spectrograms is directly proportional to the number of blades in each rotor (comparing figures 1 and 4), then to the rotors rotation rate (comparing figures 3 and 6), while the width of important frequency components (black spectrogram parts) is proportional to the blades length and the rotors rotation rate (comparing figures 2 and 5).

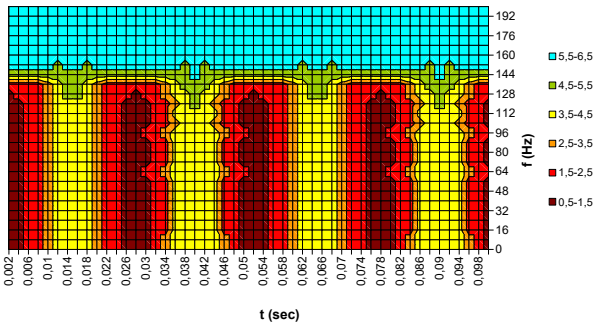


Figure 3a.

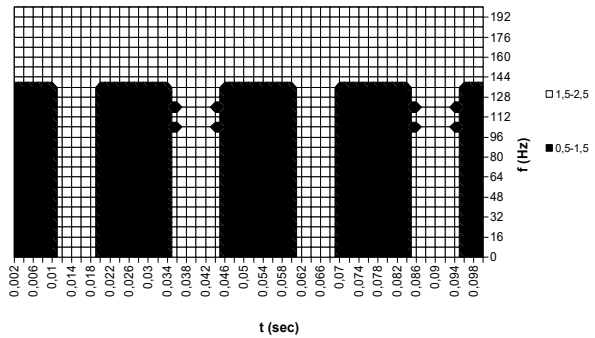


Figure 3b.

Figures 3a and 3b. Drone spectrogram for **one rotor** with **two blades**, the blade length $L=0.48m$, blade rotation speed $\Omega_{rot}=20rotations/s$, drone height $h=70m$, drone distance from radar $R_0=100m$, drone elevation angle towards radar $\beta=arcsin(0.7)$.

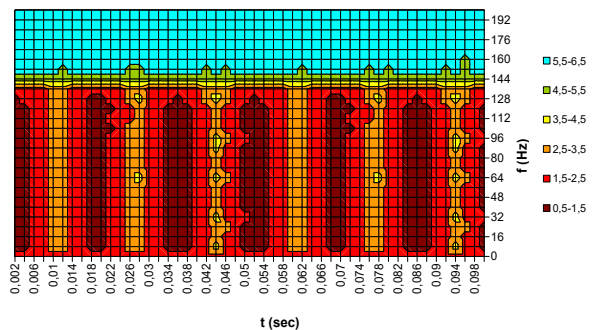


Figure 4a.

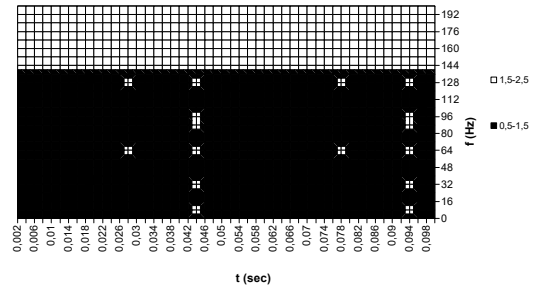


Figure 4b.

Figures 4a and 4b. Drone spectrogram for **one rotor** with **three blades**, the blade length $L=0.48m$, blade rotation speed $\Omega_{rot}=20rotations/s$, drone height $h=70m$, drone distance from radar $R_0=100m$, drone elevation angle towards radar $\beta=arcsin(0.7)$.

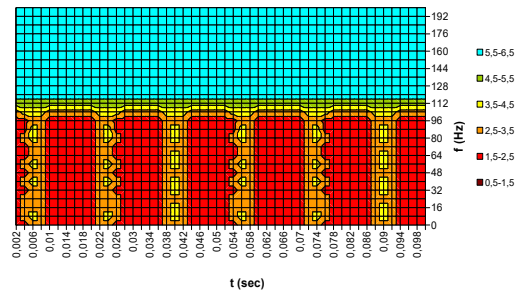


Figure 5a.

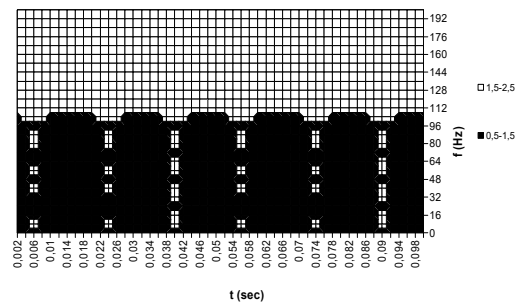


Figure 5b.

Figures 5a and 5b. Drone spectrogram for **one rotor** with **two blades**, the blade length $L=0.24m$, blade rotation speed $\Omega_{rot}=30rotations/s$, drone height $h=70m$, drone distance from radar $R_0=100m$, drone elevation angle towards radar $\beta=arcsin(0.7)$.

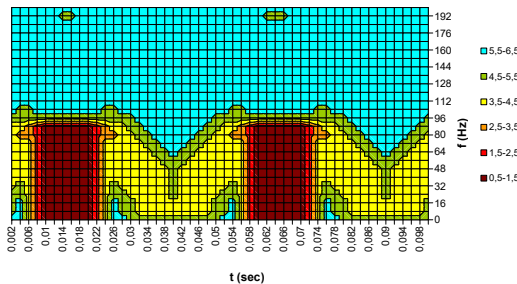


Figure 6a.

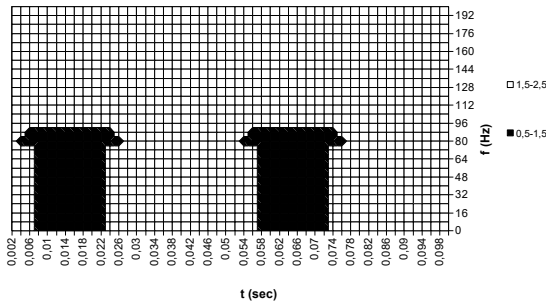


Figure 6b.

Figures 6a and 6b. Drone spectrogram for **one rotor** with **two blades**, the blade length $L=0.64\text{m}$, blade rotation speed $\Omega_{rot}=10\text{rotations/s}$, drone height $h=70\text{m}$, drone distance from radar $R_0=100\text{m}$, drone elevation angle towards radar $\beta=\arcsin(0.7)$.

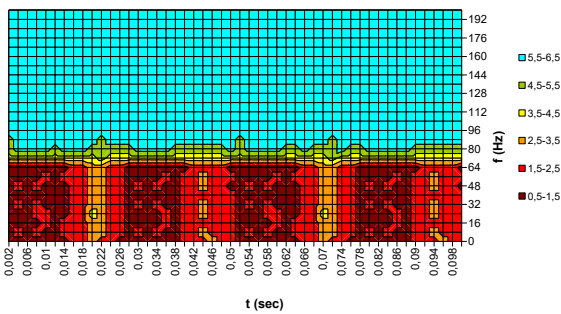


Figure 7a.

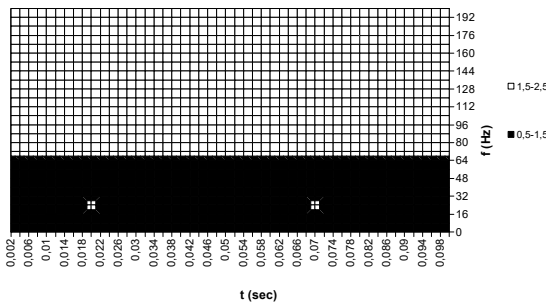


Figure 7b.

Figures 7a and 7b. Drone spectrogram for **four rotors** with **one blade**, the blade length $L=0.24\text{m}$, blade rotation speed $\Omega_{rot}=20\text{rotations/s}$, drone height $h=70\text{m}$, drone distance from radar $R_0=100\text{m}$, drone elevation angle towards radar $\beta=\arcsin(0.7)$.

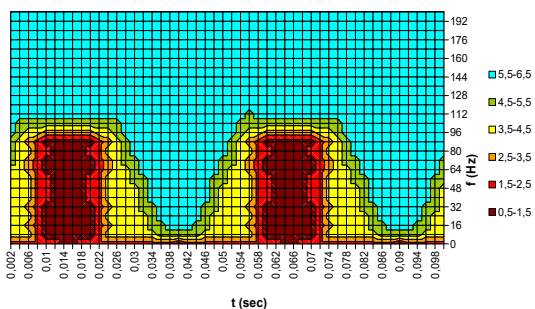


Figure 8a.

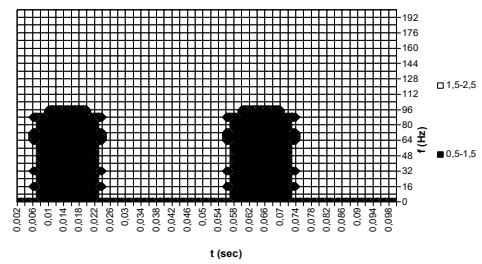


Figure 8b.

Figures 8a and 8b. Spectrogram of bird with flapping wings, the wing length $L=0.48\text{m}$, wing flapping rate $f_{fl}=20\text{flaps/s}$, maximum flapping angle $\varphi_{max}=40^\circ$, bird height $z_f=70\text{m}$, bird distance from radar $R_0=100\text{m}$, bird elevation angle towards radar $\beta=\arcsin(0.7)$.

3. PROGRAM FOR SPECTROGRAM ANALYSIS

The first step in spectrogram analysis is to process it in a suitable sense to allow reliable decision making. Black-white variant of spectrograms is processed. The flow-chart of the program for spectrograms analysis is presented in the Figure 9.

The spectrogram graphs are 2D pictures of the dimension $M \times N$ where M and N are the number of time samples for any frequency value and frequency samples for any time moment, used for the presentation. The first step in the program flow is to read the values for M and N . After that follows the input of black-white samples: $S(i,j)=1$ for black and $S(i,j)=0$ for white samples. The values of i are changed from 1 to M to cover all time samples and j is changed from 1 to N to cover all frequency components.

The principle in the spectrogram analysis is to first consider each row of data, i.e. the samples value during time for each frequency. It is necessary to determine the period of this signal and the time interval while the signal is $S(i,j)=1$ and while it is $S(i,j)=0$. The signal processing starts in the moment when the instantaneous signal value is changed from 0 to 1. According to the Figure 9, it is when the answer to both questions “ $S(i,j)=1?$ ” and “ $S(i-l,j)=0?$ ” is “yes”. Considering time domain, it is when signal sample from “white” goes over to “black”. The register k with the number of periodic time cycles is increased for 1 and the register $T_1(k,j)$ intended to follow the duration of the state $S(i,j)=1$ is initiated to 0. After that the register $T_1(k,j)$ is incremented after each time interval when it is $S(i,j)=1$. The similar processing is performed when signal goes over from “black” to “white” (the answer to the first question “ $S(i,j)=1?$ ” is “no” and the answer to the second question “ $S(i-l,j)=1?$ ” is “yes”) and while it is in the state “white” with the exception that the value of register k is not changed and that the values of the register $T_2(k,j)$ is varied instead of $T_1(k,j)$.

It is already proved by spectrogram in the Figure 4 that “white” areas are very narrow considering variation in time already at 20rotations/s for helicopter type drones when the rotor has 3 blades. When the rotor has 2 blades, such behaviour is obvious at only bit higher rotations speed of 30rotations/s (Figure 5). The similar behaviour is

obvious when helicopter type drones are replaced by quadcopters (Figure 7). Such types of spectrograms as in the figures 5, 6 and 7 are characteristic for the great majority of situations and the last software processing in the Figure 9 is intended to separate these spectrograms. According to the last decision block, whenever the time interval of “white” part is lower than the minimum threshold T_{min} and the duration of $T_2(k,j)$ interval is lower than interval $T_1(k,j)$, this “white” interval is eliminated ($T_2(k,j)=0$), the number of signal periods for the further evaluation is decreased and the duration of “white” interval is added to the “black” interval $T_1(k,j)$. The value of T_{min} according to graphs in the figures 4a and 5b is 4ms. In this way it is allowed that spectrograms may be further easily processed according to the step 1 from [3] if they satisfy conditions of this step.

The flow-chart of a program for drone presence decision is presented in the Figure 10. The decision is the result of four criteria implementation according to [3]. The analysis is performed separately for each of N frequencies in the spectrogram to investigate whether it is candidate to be a part of drone spectrogram.

The decision about the first criterion separates multicopter drones from other targets (birds or non-drones objects and slow rotating helicopter type drones) – spectrogram in the Figure 7. This criterion also distinguishes helicopter type drones when they have three or more blades – spectrogram in the Figure 4 or when helicopter type drones have two blades which rotate at a bit higher rate than the minimum 20rotations/s – spectrogram in the Figure 5. In this case the number of repeatable parts in each frequency line is always $k=1$ as the result of processing in the last part of the flow-chart according to the Figure 9. If a spectrogram consists of a single “black” part (i.e. $k=1$ and T_1 area exists – $\sum T_1 > T_{min}$), the value of register dec is increased. Such processing is performed for each frequency line in a spectrogram. If the final value of register dec is higher than the minimum value dec_{min} , the decision about drone presence is positive. There is no one unique value dec_{min} because the spectrogram frequency bandwidth depends both on blades length and rotors rotation rate. That’s why it is necessary first to determine rotors rotation rate from the spectrograms periodicity, if it is possible. After that, for example, in the case of 60rotations/s, the dec_{min} would be about 140Hz for very short 0.12m blades (example in the Figure 2).

The criterion 2 separates helicopter type drones when they have two blades rotating at low rate (10-20rotations/s – Figure 3) and the hypothetical helicopter drone with only one blade rotating at higher rate than 20rotations/s – Figure 2. In this case there are $k > k_{min}(=20)$ alterations of “black” and “white” parts and vice versa during time interval of 1s. The following processing in this case is the same as for the criterion 1.

The difference between criteria 1 and 2 from the criterion 3 is that criterion 3 does not allow decision on the base of only one spectrogram. It is necessary consider at least two time-lagged spectrograms. The results of decisions for each frequency line in spectrogram for the criterion 3 is accumulated in the separate register $decl_l$, in a similar way as it is in the register dec for the first two criteria.

Then the decision about a drone presence depends on the relation between the elevation angle β_l in some moment l and the value obtained in $decl_l$. The drone is detected if the increase in β_l value ($\beta_l > \beta_{l-1}$) causes decrease of $decl_l$ value ($decl_l < decl_{l-1}$). The same decision is also in the case of opposite combination of values ($\beta_l < \beta_{l-1}$ and $decl_l > decl_{l-1}$). In the remaining two combinations the considered target is a bird, not a drone. The criterion 3 is used to define a target when the spectrogram as the one presented in the figures 1, 6 and 8 is recorded. It is important to emphasize, as in [3], that elevation angle is determined using some other algorithm on FMCW radar.

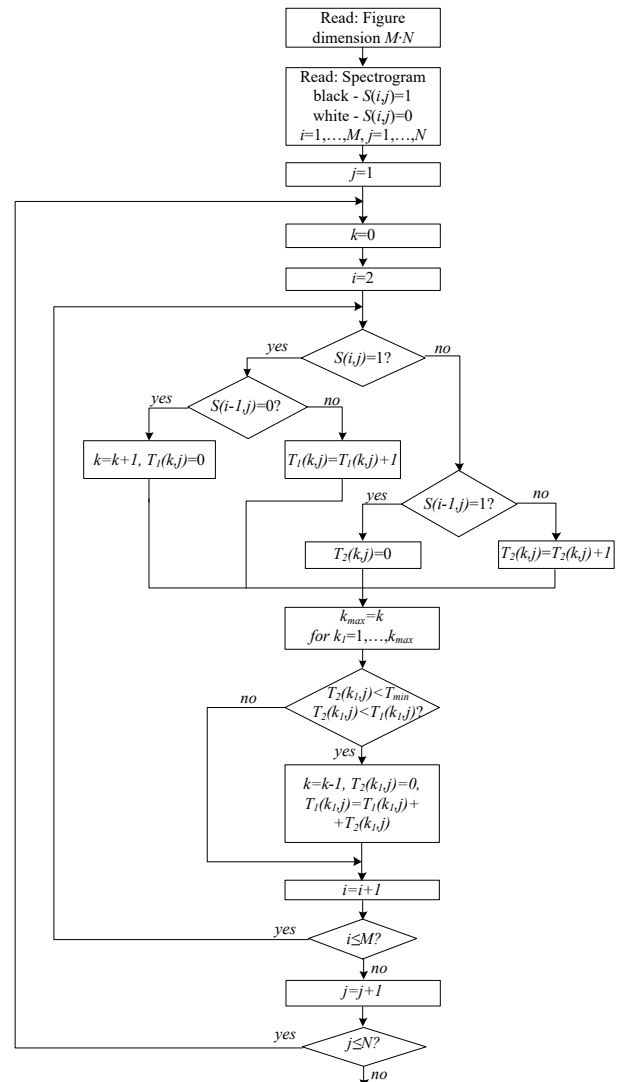


Figure 9. The flow-chart of a program for spectrograms processing

The criterion 4 follows after the criterion 3 if the elevation angle β is approximately not changed with time, i.e. for $\beta_l \approx \beta_{l-1}$ (the target is moving directly towards radar or directly away from radar). In this case the decision follows from the fact that birds’ higher wing flapping rate means that the birds’ wings length is lower. Among the birds’ species and their characteristics important for our analysis which are presented in [12], there is only one example where the flapping rate is a little higher than 20 flaps/s and the wings length in this case is only 0.09m. The bird species with the nearest flapping rate to 20

flaps/s from the lower side has wing length 0.164m. Both these wing lengths are lower than it is usual for helicopter drone causing the lower value in the register $decI_1$. The other important conclusion follows from the comparison of spectrograms in the figures 1 and 8. All parameters for these spectrograms are the same including drone blade length in the Figure 1 and the wings length in the Figure 9, but about 25% lower value in the register $decI_1$ follows from the fact that wings maximum flapping angle is 40° and the rotor makes full rotations. In this way both factors contributing to the value of $decI_1$ are higher in the case of drone presence i.e. the minimum threshold $decI_1$ may be determined for each specific rotation (flapping) rate and elevation angle.

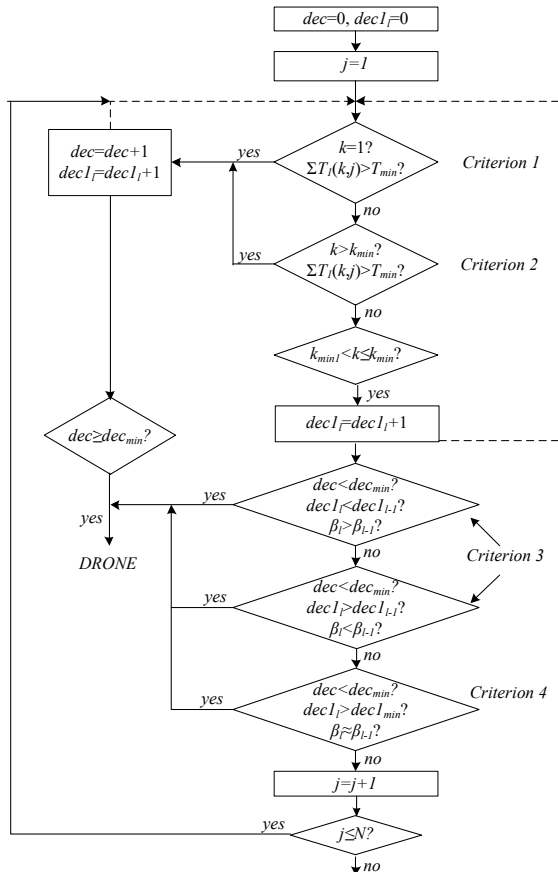


Figure 10. The flow-chart of a program for drone presence decision

4. CONCLUSION

This paper presents original software algorithm to reliably distinguish spectrograms of drones and flying birds. The spectrograms are obtained by FMCW radar. In this program development phase we have limited ourselves to hovering drones and birds with only flapping wing movements. The paper is logically an extension of the contribution [3]. The spectrograms obtained by the implementation of our original calculation program in [3] are partially simplified in two steps: first to six signal level areas and after to only two areas. The variant with only two areas (“black” - “white” spectrograms) are used for software analysis to decide about the drone presence. The decision program is relatively simple. It is not necessary to have huge data base with previously

recorded spectrograms of various drone types and flying birds’ species to allow decisions making using artificial intelligence principles. In the great majority of situations it is enough to analyze only one spectrogram to make a decision. Only in very rare cases when helicopter type drones have low rotation rate or are flying directly towards or away from radar it is necessary to consider several spectrograms separated by some time interval.

The developed software algorithm is verified only on calculated spectrograms for hovering drones and birds with flapping wings. Our developed algorithm was able to distinguish that spectrograms in figures 2-7 from this paper (“black” - “white” versions) belong to drones and that the spectrogram in the figure 8 is for a bird. The algorithm has also successively distinguished spectrograms from [3]. In the future it is necessary to test it in real applications and to modify it to allow differentiation of flying drones and birds, not only hovering drones and flapping wing birds.

References

- [1] ERIKSSON, N., *Conceptual study of a future drone detection system Countering a threat posed by a disruptive technology*, Master thesis in Product Development, Chalmers University of Technology, Gothenburg, Sweden (2018).
- [2] MATIĆ, V., KOSJER, V., LEBL, A., PAVIĆ, B., RADIVOJEVIĆ, J., *Methods for Drone Detection and Jamming*, 10th International Conference on Information Society and Technology (ICIST), Kopaonik, in: ZDRAVKOVIĆ, M., KONJOVIĆ, Z., TRAJANOVIĆ, M., Proceedings 1 (2020) 16-21.
- [3] RADIVOJEVIĆ, J., STANOJEVIĆ, D., LEBL, A., *Birds and Drones spectrograms and how to differ them*, paper on the review for the 10th International Scientific Conference on Defensive Technologies OTEH 2022., Belgrade (2022).
- [4] MENDIS, G. J., WEI, J., MADANAYKE, A., *Deep learning cognitive radar for Micro UAS detection and classification*, Cognitive Communications for Aerospace Applications Workshop (CCAA), 27-28. June 2017., Cleveland, Ohio, USA, IEEE, 1-5., DOI: [10.1109/CCAAS.2017.8001610](https://doi.org/10.1109/CCAAS.2017.8001610).
- [5] LEBL, A., MILEUSNIĆ, M., MITIĆ, D., RADIVOJEVIĆ, J., MATIĆ, V., *Verification of Calculation Method for Drone Micro-Doppler Signature Estimation*, accepted for publication in Facta Universitatis, Series: Electronics and Energetics, ISSN: 0353-3670.
- [6] RADIVOJEVIĆ, J., PETROVIĆ, P., LEBL, A., MILEUSNIĆ, M., *Initial Development of a Program for Drone Micro-Doppler Signature Modelling*, on the review for the IXth IcETRAN Conference, Novi Pazar (2022).
- [7] BLAKE, C. H., *More Data on the Wing Flapping Rates of Birds*, The Condor, 50(4) (1948) 148-151, <https://doi.org/10.2307/1364930>.
- [8] PENNYCUICK, C. J., *Speeds and wingbeat frequencies of migrating birds compared with calculated benchmarks*, The Journal of Experimental Biology, 20 (2001) 3283-3294.

- [9] Birds of a feather, Wildcare, 1-2, http://support.wildcarebayarea.org/site/DocServer/BF_PRE_Grades_2-6_Wing_Rates.pdf.
- [10] NOWICKI, N., *Measurement and Modeling of Multicopter UAS Rotor Blade Deflection in Hovering*, KTH – Royal Institute of Technology, Degree project, (2016) 1-45.
- [11] TATIĆ, B., BOGOJEVIĆ, N., TODOSIJEVIĆ, S., ŠOŠKIĆ, Z., *Analysis of Noise Level Generated by Helicopters with Various Numbers of Blades in the Main Rotor*, 4th International Conference Noise and Vibration, Niš (2012) 249-253.
- [12] VAN DEN BERG, C., RAYNER, J. M. V., *The Moment of Inertia of Bird Wings and the Inertial Power Requirement for Flapping Flight*, The Journal of Experimental Biology, 198 (1995) 1655-1664.

ANALYSIS AND DESIGN OF HIGH GAIN FLAT PATCH ANTENNA

SAŠA GUNDELJ

Military Technical Institute, Belgrade, gundelj@yahoo.com

ALEKSANDAR STEFANOVIĆ

Military Technical Institute, Belgrade, stefanovicva@outlook.com

SAŠA ANTONOVIĆ

Military Technical Institute, Belgrade, sale.antonovic82@gmail.com

IGOR GORŠIĆ

Military Technical Institute, Belgrade, gorsic@gmail.com

Abstract: This paper demonstrates an enhanced version of a high gain flat patch antenna which provides a gain of 8 dBi. This commercial antenna has a resonant frequency of 1.2 GHz and is considered as a reference antenna in this analysis. The simulations of the reference antenna and the proposed one were carried out using the 3D Full-Wave Finite Element Method (FEM) electromagnetic simulator, Ansys HFSS. The simulation results have a good agreement. The proposed antenna has achieved the main goal of a 1.32 GHz resonant frequency with an increased gain of 9.5 dBi. The effects of the different parameters like SWR, S11 parameter, radiation patterns, bandwidth are analyzed. The proposed antenna is manufactured, measured and tested in real-world conditions. The proposed antenna can be efficiently used in applications such as video signal transmission.

Keywords: equivalent model, patch antenna, antenna radiation pattern, directional antenna, HFSS.

1. INTRODUCTION

For wireless communication systems, the antenna is one of the most critical components. A good design of the antenna can relax system requirements and improve overall system performance [1].

The flat patch antenna is a directional low-profile antenna which belongs to the class of resonant antennas. It is characterized by low manufacturing costs and easy design due to its simple structure, with the drawback of a narrow bandwidth. In essence it is comprised of the upper plate and ground plate with a dielectric substrate in between, as shown in *Figure 1.1*. The ground plane serves as a conductive plate while the upper radiating patch functions as a wave-generating element.

The design outline of the flat patch antenna results in a maximized radiation pattern with a right angle against the upper patch and simultaneously minimized under the lower, ground plate. With this design approach a directional radiation pattern was achieved in the upper half of the sphere, therefore increasing gain.



Figure 1.1. Side view of the flat patch antenna

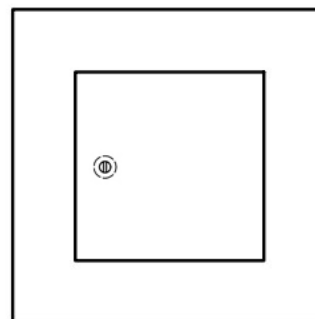


Figure 1.2. Top view of the flat patch antenna

Highly directional antennas are essential for more sophisticated missions, goals, decreased instrument's complexity, large amounts of scientific data handling, higher data rate links, and for better signal to noise ratio [4] [5].

2. REFERENCE ANTENNA ANALYSIS

In this paper we consider a commercial antenna as the reference one with a nominal resonant frequency of 1.14 GHz. The simulations of reference antenna were carried out using the 3D Full-Wave Finite Element Method (FEM) electromagnetic simulator, Ansys High Frequency Structure Simulator - HFSS. Ansoft HFSS can be used to calculate parameters such as S-Parameters, Resonant Frequency, and Fields.

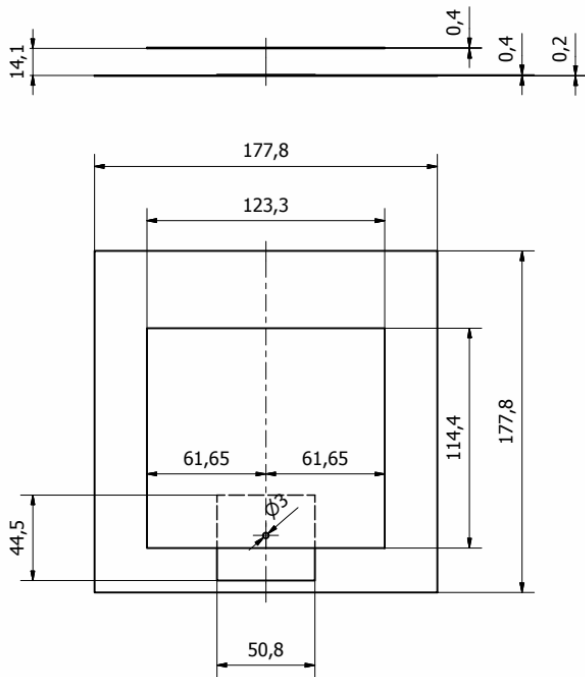


Figure 2.1. Geometry of the reference antenna, side and top view

The geometry of the reference antenna is shown in *Figure 2.1.* and consists of three elements, in contrast to the theoretical antenna described in the introduction. The ground plate is comprised of two elements from different materials, the larger being an aluminum square with dimensions of $a = 177.8 \text{ mm}$ and a thickness of 0.2 mm , while the smaller brass rectangle measures $a_2 = 44.5 \text{ mm}$ and $b_2 = 50.8 \text{ mm}$, 0.4 mm thick. The material used for the upper patch was brass as well, with dimensions $w = 123.3 \text{ mm}$ width and $l = 114.4 \text{ mm}$ length, 0.4 mm thick. The feed point for the upper plate i.e., the wave emitting element is located 6.5 mm from the edge of the plate, whereas widthwise it is positioned at the value midpoint $w = 123.3 \text{ mm}$ which totals 61.65 mm . The height between panels equals $h = 14.1 \text{ mm}$.

Modeling this data through the HFSS simulation program yields results corresponding to the factory specifications of this reference antenna.

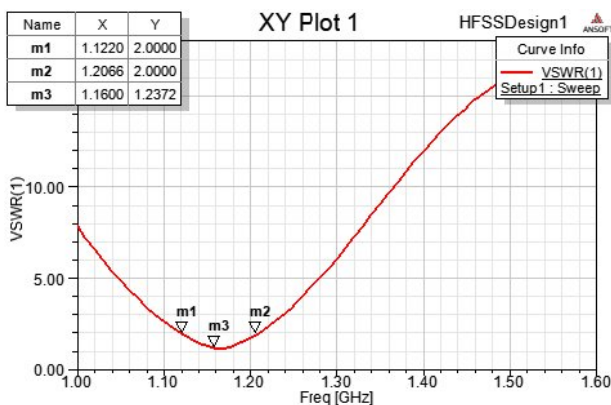


Figure 2.2. Standing Wave Ratio of the reference antenna

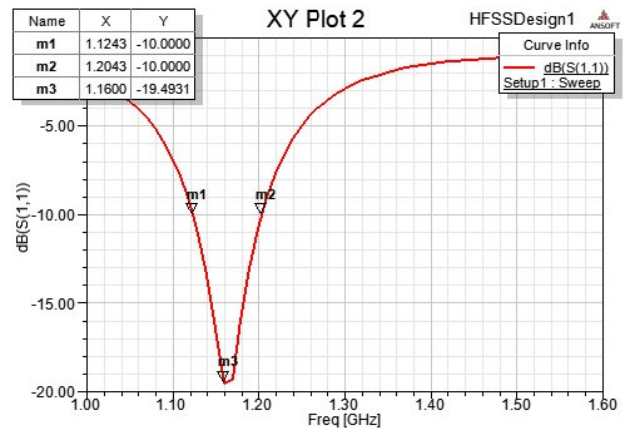


Figure 2.3. S11 – reference antenna parameter

Through a simulation we obtained results for the VSWR shown in *Figure 2.2* and the S11 parameter from *Figure 2.3* from which we can affirm the 1.16 GHz resonant frequency of the reference antenna. Examination of the reference antenna factory specifications defines its resonant frequency of 1.14 GHz , while its bandwidth ranges from 1.08 GHz to 1.2 GHz .

The existence of these minor differences between the simulated antenna and its factory specifications may be attributed to approximations done during the simulation setup, as well as potential imperfections in the antenna's manufacturing. In either case we can attest that the simulation data is credible enough for the same simulation principle to be used on our proposed antenna.

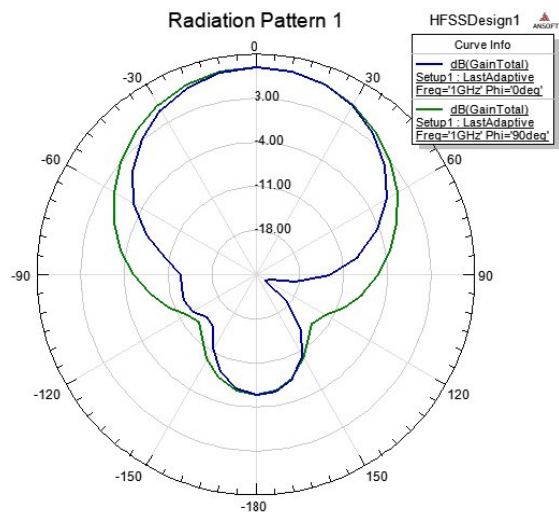


Figure 2.4. Radiation patterns of the reference antenna

Radiation patterns of the simulated reference antenna are shown in *Figure 2.4*. Maximum antenna gain at the frequency of 1 GHz for $\varphi = 0^\circ$ and $\varphi = 90^\circ$ is 8.0284 dBi , matching factory specifications of 8 dBi . *Figure 2.5* displays the 3D simulated reference antenna gain.

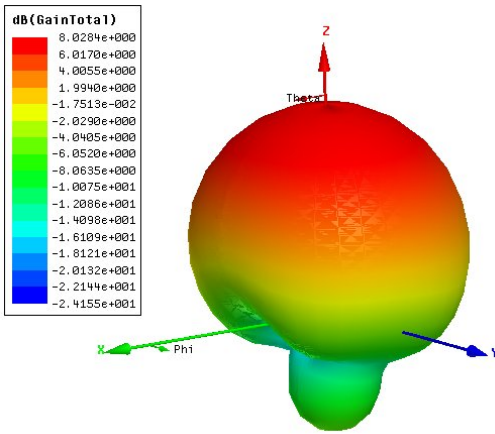


Figure 2.5. 3D Radiation pattern of the reference antenna

3. ANALYSIS AND DESIGN OF THE PROPOSED ANTENNA

Starting from the reference antenna analysis, we set forth to create an antenna which would meet our needs for a resonant frequency of 1.32 GHz. For a quicker and simpler design all the established elements of the reference antenna were used with the exception of switching from a brass wave-emitting element to a copper one.

Optimized dimensions of the suggested antenna’s upper radiating plate, after a number of simulations are as follows: $w = 123.3 \text{ mm}$ and $l = 100 \text{ mm}$, while the thickness 0.4 mm remains unchanged, with the height decreasing from 14.1 mm to $h = 11.3 \text{ mm}$.

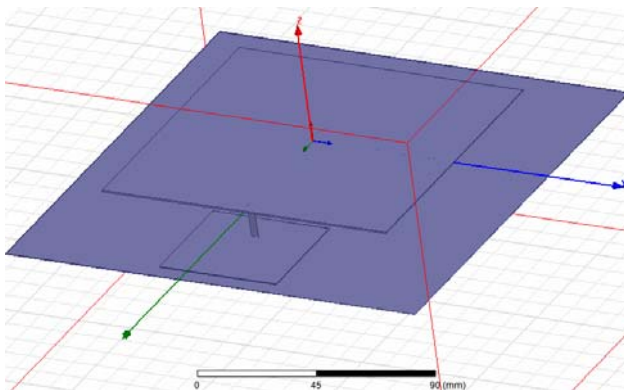


Figure 3.1. Simulation model in Ansys HFSS

The antenna met our goals in various other combinations, e.g, with the retained height of $h = 14.1 \text{ mm}$, the dimensions of the transfer plate would be: $w = 118 \text{ mm}$ and $l = 98 \text{ mm}$, however this solution was dismissed due to a slightly inferior Standing-wave ratio (SWR) parameter.

The SWR and S11 parameters of the simulated antenna represented in Figures 3.2 i 3.3 were defined by the dimensions of the upper antenna plate and height between plates. With the antenna geometry we reached the desired resonant frequency of 1.32 GHz.

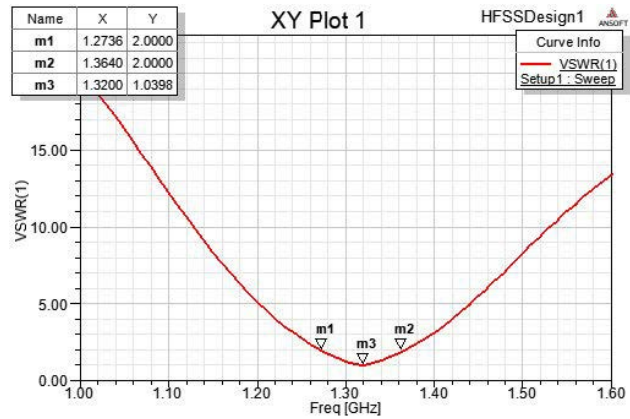


Figure 3.2. Standing Wave Ratio of the proposed antenna

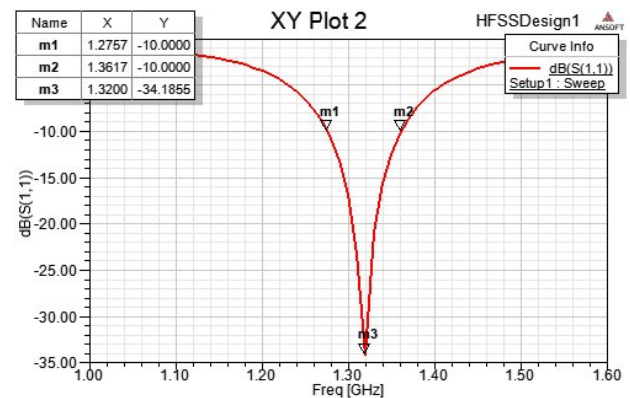


Figure 3.3. S11 – parameter of the proposed antenna

Based on the S11 parameter simulation data bandwidth a range from 1.2757 GHz to 1.3617 GHz can be infer, we conclude that the proposed antenna has a very wide bandwidth.

The radiation pattern of the simulated proposed antenna is shown in Figure 3.4. for $\phi = 0^\circ$ and $\phi = 90^\circ$.

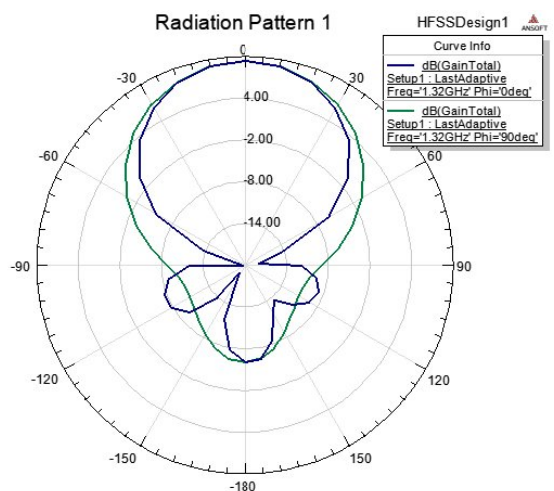


Figure 3.4. Radiation pattern of the proposed antenna

Figure 3.5. represents the 3D simulated gain of the proposed antenna. Gains in the direction of propagation amount to 9.4364 dBi.

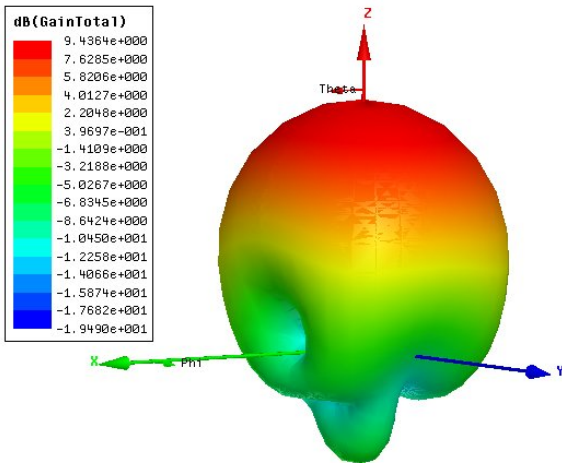


Figure 3.5. 3D radiation pattern of the *proposed* antenna

The results were verified with laboratory measuring in which the prototype of the proposed antenna had a resonant frequency of 1.3154 GHz . Agilent HP 8753ES RF Vector Network Analyzer was used during laboratory testing.

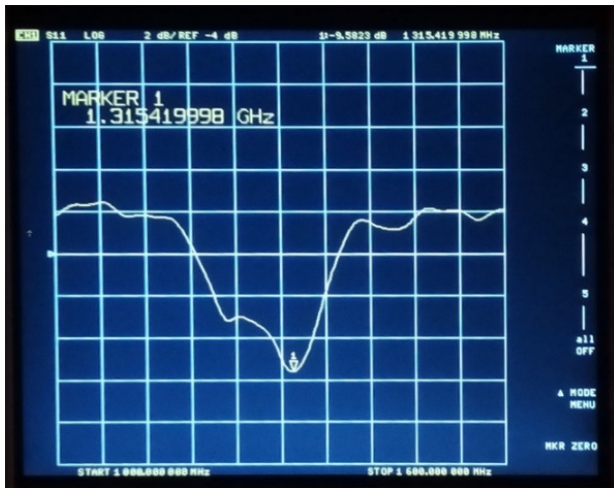


Figure 3.6. The result of the proposed antenna laboratory test.

The proposed antenna was subject to real world testing where optical visibility was achieved. With a transmitter strength of $P_t = 5\text{ W}$, a transmission antenna gain of $G_t = 7\text{ dBi}$, receiver sensitivity of $P_r = -70\text{ dbm}$, at a frequency of $f_c = 1.32\text{ GHz}$, the antenna achieved video signal transmission from a distance of $R = 26\text{ km}$. Using the Friis equation:

$$P_r = \frac{P_t G_t G_r \lambda^2}{(4\pi R)^2} \quad (1)$$

we can get confirmation of the proposed antenna gain of close 9.5 dBi , as predicted by the simulation.

4. CONCLUSION

From the commercial high gain flat patch antenna and the simulation performed using the 3D Full-Wave Finite Element Method (FEM) electromagnetic simulator, Ansys HFSS, we obtained results very similar to the factory specification of a 1.2 GHz resonant frequency and an antenna gain of 8 dBi . Based on the commercial antenna analysis results, which was used as a reference one, we modeled our own antenna. The manner in which we achieved that involved minimal interventions regarding the reference antenna elements i.e., changing the geometry of the wave-emitting element as well as the height between the elements. This whole process underwent with the help of the HFSS software. Simulations were repeated until a desired result was reached. The parameters of our proposed antenna consist of a 1.32 GHz resonant frequency and a gain of 9.5 dBi which fully completed the task at hand. This process proved it is possible to achieve a desired result and build a prototype based on a series of simulations. Respectively, laboratory and real-world testing only confirmed the data obtained in the simulation. In the absence of laboratory confirmed antenna characteristics, simulated results can be used with a great degree of certainty in the production of a desired antenna. The proposed antenna can efficiently be used in applications like video signal transmission.

References

- [1] BALANIS, C. A.: Antenna Theory: Analysis and Design. Third ed., Hoboken, 2005.
- [2] GARG, R., BHARTIA, P., BAHL, I., ITTIPIBOON, A.: Microstrip Antenna Design Handbook, Boston, London, 2001.
- [3] MRABET, EL, O.: High Frequency Structure Simulator (HFSS) Tutorial, Rennes, 2005 – 2006.
- [4] HEIDT, H., PUIG-SUARI, J., MOORE, A., NAKASUKA, S. and TWIGGS, R.: CubeSat- A new generation of picosatellite for education and industry low-cost space experimentation, 2000.
- [5] SAMSUZZAMAN, M., ISLAM, M.T., NAHAR, M.K., MANDEEP, J.S., MANSOR, F., ISLAM, M.M.: Circularly polarized high gain S band antenna for nanosatellite, Amsterdam, 2015.



DRONE CLASSIFICATION BASED ON RADIO FREQUENCY: TECHNIQUES, DATASETS, AND CHALLENGES

BOBAN SAZDIĆ-JOTIĆ

Military Academy, University of Defence, Belgrade, boban.sazdic.jotic@vs.rs

BOBAN BONDŽULIĆ

Military Academy, University of Defence, Belgrade, bondzulici@yahoo.com

IVAN POKRAJAC

Military Technical Institute, Belgrade, ivan.pokrajac@vs.rs

JOVAN BAJČETIĆ

Military Academy, University of Defence, Belgrade, bajce05@gmail.com

MOHAMMED MOKHTARI

Military Academy, University of Defence, Belgrade, mokhtari.med91@gmail.com

Abstract: *This research article presents a comprehensive review of current literature on drone classification (detection and identification) in the radio-frequency domain. The usage of unmanned aerial systems or drones, both for commercial (amateur or civilian) and functional (military or industrial) purposes, has multiplied numerous times over in the last decade. Drones have undergone great improvement, and at the same time, they have become low-priced and easier to manipulate, but on the contrary, they come to be more adaptable to illegal actions. Due to the scope of the subject matter, the review included only the classification of drones via passive, radio-frequency sensors with a description of the classification techniques (set of algorithms, methods, and procedures) and the datasets used for performance testing. Moreover, the challenges of drone classification based on radio-frequency were presented in this work. The general outcome of this study shows that deep learning techniques are currently the best solution for solving the issue of drone classification. However, it should be noted that most modern research is experimental and that there are only limited practical implementations. A particular problem is the lack of a general specification for radio-frequency drone classification that must be based on requirements defined from everyday experience.*

Keywords: *Deep learning algorithm, drone, detection, classification, identification, radio-frequency.*

1. INTRODUCTION

Unmanned aerial systems (UAS), especially commercial off-the-shelf (COTS) ones, become less expensive, equipped with better optoelectronic sensors (daily and night cameras), easier to fly, and have attracted increasing attention due to their boundless applications. However, such imminent technological improvements contribute that UAS being more adaptable for crime, terrorism, or military purposes. Moreover, this caused security forces to be increasingly challenged by the need to quickly detect and identify UAS, especially in security-sensitive areas. With such a huge expansion of UAS applications, which can be harmful, there is a prerequisite to protect sensitive areas and critical points of the vital infrastructure by using specific means, i.e. anti-drone (ADRO) systems. Various ADRO systems can be found on the market presently, and all of them have one important characteristic in common: the usage of several different (optoelectronic, acoustic, radar, and radio-frequency) sensors. Additionally, it can be noted that every ADRO system consists of the following core

subsystems: monitoring (sensing), mitigation, and command and control (C2) subsystem [1]. Based on this, the modern ADRO system needs to incorporate different procedures against UAS: detection, spoofing, jamming, and mitigation procedures [2], [3].

Detection or warning procedures are based on various detection devices (sensors) to perform early warning on the presence of any UAS (set of drones with their ground controller and equipment). The additional function of these procedures is the identification and localization (optionally, tracking) of detected drones in order to provide inputs for the next stage of the ADRO system. The spoofing procedure is involved in the next phase but it is not compulsory. With this procedure, the ADRO system deceives drones by sending false radio signals (GPS spoofing is a typical example of an emergency landing). If the spoofing procedure fails, the ADRO system can engage the jamming procedures, where the drone's control and navigation signals are disturbed by posing strong artificial interference. Finally, the ADRO system can use the mitigation procedure, to destroy or capture malicious drones. Although ADRO systems

comprise diverse procedures and sensors, practical implementations mainly rely on radar and radio-frequency (RF) sensors, rather than optoelectronic or audio sensors for primary drone detection.

The main advantage of RF sensors is zero irradiated power, a longer detection range, an association with procedures against UAS (especially jamming), and usage of various techniques for exploiting the intercepted RF signal. RF sensor is a passive device that only receives RF signals from UAS (both drone and ground controller) which are present in almost every situation. Contrary to that, radar is an active device that irradiates electromagnetic energy, thus it can be a constraint because it can not be used in every possible scenario. The detection range of RF sensors depends on the surroundings and transmitter power of UAS but usually is comparable with the radar range. Another interesting fact in favor of the RF sensors is a possible connection between the receiver and jammer. Parameters obtained from the UAS detection stage can be used for spoofing and jamming if this is requested. Additionally, an RF receiver is a very resourceful sensor in contrast to the others. The received RF signals can be used for different purposes such as communication protocol detection, drone MAC address detection, feature extraction, or for direct use with some classification algorithms.

The ADRO systems can extract useful information from intercepted RF signals between the drone and the ground controller to resolve communication protocol or the MAC address. Drones use specific protocols for communication which can be used for detection and identification purposes. Additionally, the IEEE 802.11 (Wi-Fi) standard can be exploited to trace the MAC addresses of the specific drone model. However, a major drawback of such ADRO systems is the a priori knowledge of communication protocols and MAC addresses, which in some situations may not be the case (hand-made drones can also have custom-made protocols). Furthermore, the ADRO system can extract some features from intercepted RF signals for detection purposes. In addition, the ADRO system exploits frequency or joint time-frequency signal representation (TFSR) of I/Q data (raw RF signal), to prepare inputs to some classification algorithm.

The disadvantage of RF-based drone detection is ambient RF noise, multipath, and the fact that customized UAS can operate autonomously, without an active communication link between drone and ground controller. Additionally, real-time RF monitoring is a cumbersome process, due to the very specific conditions of the RF domain. It is important to note that all drone RF communication can be organized into three main categories of communications: command and control (uplink), telemetry and video (downlink), and guidance communications. The first two groups are using a wide range of frequencies (between 400 MHz and 6 GHz), while guidance communications use global navigation signals (GPS L1/L2/L2c/L5, Glonass, Beidou, or Galileo). In such a complex environment, RF sensors must be very agile with high-speed scanning performance, highly sensitive, and with a high dynamic range across the whole frequency range.

The rest of the paper is organized as follows: section 2 is a categorization and overview of relevant studies, section 3 describes the comparison of classification techniques, the results of comparative analysis of the most relevant papers are presented in section 4, and finally, the conclusion is given in section 5.

2. CATEGORIZATION AND REVIEW OF LITERATURE

To the best of our knowledge, available studies introduced different classification techniques (approaches) based on the RF sensors. We created a new categorization of these classification techniques according to:

- the method of processing input data:
 - classic engineering techniques that require prior feature extraction in combination with a simple decision threshold mechanism,
 - advanced engineering techniques that do not require prior feature extraction with complex learning procedures for classification purposes (feature extraction is implemented in deep learning algorithms together with the learning process), and
 - hybrid engineering techniques that present a combination of previous ones.
- the type of input data:
 - techniques with classification algorithms that use the MAC address information as input data,
 - techniques with classification algorithms that use the protocol information as input data,
 - techniques with classification algorithms that use features of RF signals as input data, and
 - techniques with classification algorithms that use the entire received I/Q RF signal as input data.

It is important to note that one technique can be categorized by both rules, i.e. some approach is a classic engineering technique that uses protocol information as input data. The categorization presented in this research paper is based on the most relevant research papers that are available in the literature in the last five years. A total of 96 research papers, that are dealing with RF classification (detection and identification) of drones, were incorporated into this research.

2.1. RF techniques according to the method of processing input data

When it comes to input data preparation and processing method, classical engineering techniques require a mandatory step to extract features from intercepted RF signals. This is an important step because only extracted features with a decision threshold mechanism can be used for classification. The main disadvantage of the classic engineering techniques is the complex process of feature extraction which must be adopted according to the nature of input data. This implies that feature extraction is a very demanding and time-consuming process that requires profound engineering skills. Authors in [4] used the standard deviation analysis, maximum slope analysis, and

accumulation in azimuth direction as statistical features for drone detection and direction finding. Moreover, the principal component analysis and the empirical mode decomposition (EMD) based wavelet transform (WT) methods were engaged to cope with additive Gaussian white noise. Furthermore, the cyclostationarity signature of the drone RF signal and pseudo-Doppler principle was presented in [5] for the classification issue with a single-channel universal software radio peripheral (USRP) receiver. In [6], the authors described an innovative passive drone detection system (Matthan), based on two key physical signatures of the drones (body shifting and vibration). However, the Matthan approach is challenged with the range constraint, so did not find any practical implementation up till nowadays.

Alternatively, artificial intelligence (AI) algorithms, especially deep learning (DL), approach the problem of classification without prior extraction of features. Advanced engineering techniques use the entire received I/Q RF signal, perform some preprocessing steps and send all data to the learning process. The advantage, compared to the classical engineering techniques is the more robust and scalable approach. However, a huge amount of input data is required for the training process which can be a disadvantage in some cases. Fully connected deep neural networks (FC-DNN) were engaged in [7]–[9] to classify drones. Similarly, convolutional neural networks (CNN) as one of the prominent DL algorithms were used in [10]–[14] for the same purpose.

The quantitative comparison of the techniques that exploit RF sensors according to the method of processing input data is presented in Figure 1.

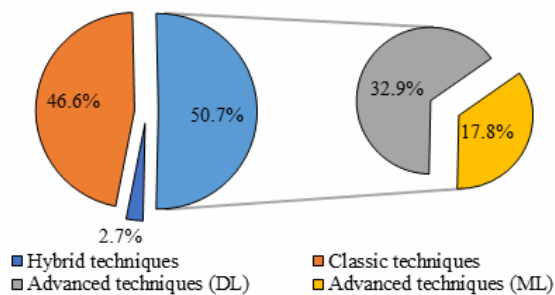


Figure 1. Quantitative comparison of RF techniques according to the method of processing input data.

It should be noted that 50.7% of all research papers rely on advanced techniques compared to 46.6% of classic engineering techniques. This result is not surprising because the analysis included only works in the last five years when advanced techniques began to be widely applied. This also means that classical engineering techniques are being given up in favor of advanced ones. Furthermore, DL and ML algorithms participate with 32.9% and 17.8%, respectively, in advanced engineering techniques.

It is also worth mentioning that the authors in [15]–[20] present classical and advanced engineering techniques in combination with direction-finding (DF) methods. However, the specific hardware and software implementation of the RF-based DF of UAS is presented in [20] because the authors used a single-channel RF

sensor and a four-element antenna array, in combination with a sparse denoising autoencoder that is based on a deep neural network (SDAE-DNN). Although, it is important to notice that some authors in [21]–[24] use a hybrid engineering technique or a combination of classical and advanced techniques. In [21] authors used extracted features (the slope, kurtosis, and skewness) of the drone RF signal as input for an FC-DNN. Moreover, in [23], the authors performed feature extraction and used ML algorithms (Logistic Regression). On contrary, authors in [25] used deep learning algorithms (ResNet50) for feature extraction together with ML classifier Logistic Regression. An interesting approach was presented in [24] where authors extracted fifteen statistical features from the UAS RF signal and engaged them with five different machine learning (ML) classifiers at different SNR levels.

2.2. RF techniques according to the type of input data

RF sensors receive an RF signal from a UAS, which can be exploited for different purposes. There are four different techniques for detecting and identifying drones according to the type of input data. The first group includes techniques that use classification algorithms for the detection and identification of the MAC address of the transceiver device in a drone. The second group includes techniques that exploit classification algorithms for the detection and identification of the protocol of communication between drones and ground control devices. These two techniques are the least represented in the available literature because they have major limitations and shortcomings. The main characteristic of both approaches is the use of received and demodulated RF signals for finding information about the MAC address of the RF transceiver installed in the drone and about the type of communication protocol that is unique for certain types of drones. Such obtained information is afterward used for the detection and identification of drones. However, to the best of our knowledge, the technique with classification algorithms based on protocol recognition is more efficient than the previous. Furthermore, there are more practical hardware implementations of ADRO systems based on this technique. Authors in [26] performed device and protocol identification throughout the data format analysis. In [27], features such as packet inter-arrival time and size were analyzed, while in [28] authors studied eight protocols to classify UAS.

Moreover, techniques with classification algorithms that use features of RF signals as input data are more present in the literature. We have mentioned some important studies that exploited features because this is a mandatory step for classical engineering techniques. Nevertheless, more and more research papers are appearing in the literature dealing with the entire intercepted I/Q RF signal. The faster hardware and improved computing power are the reason and the possibility to exploit the full power of DL algorithms which are created for a huge amount of data. Because of that, the techniques with algorithms that perform classification with the entire received I/Q RF signal as input data are becoming widely present solutions providing excellent results. The main

characteristic of this approach is the use of RF sensors to record the raw RF signal, followed by different pre-processing steps in order to prepare input data for the classifier. Some authors in [7]–[9] performed magnitude or phase spectrum calculations to obtain 1-D (vector) data with corresponding labels. Others in [12]–[14] used more complex TFSRs such as spectrograms or scalograms to obtain 2-D (image) representations of intercepted I/Q RF signals with corresponding labels for classification purposes. The illustration of one 2-D TFSR obtained from RF activities in the 2.4 GHz is presented in Figure 1. This TFSR is a spectrogram of RF signal when two drones operate simultaneously at 2.4 GHz. It is important to note that two emissions are visually distinctive in Figure 2: the command and control (fixed frequency) and telemetry and video (frequency hopping) emission.

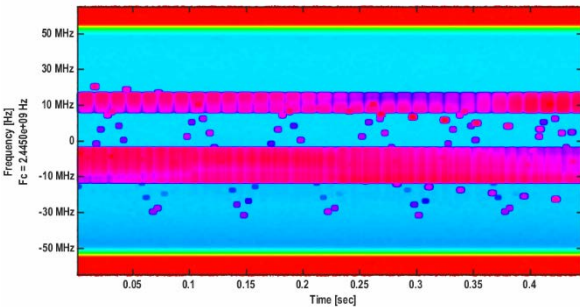


Figure 2. Spectrogram of two RF drone signals.

Depending on the method of preparation of input data, different DL models are used. In [8], [29] authors used an FC-DNN and CNN for single drone classification (detection and type identification) and multiple drone detection. Moreover, in [12] authors examined CNN accuracy with SNR dependency showing that classification is feasible. The quantitative comparison of the techniques that exploit RF sensors according to the type of input data is presented in Figure 3.

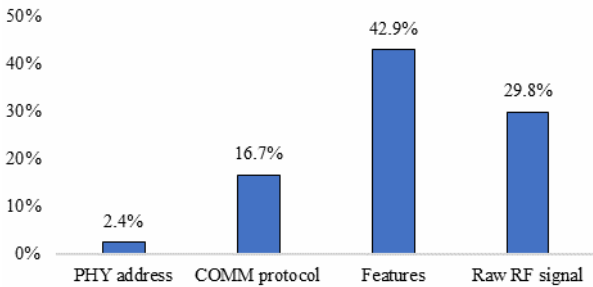


Figure 3. Quantitative comparison of RF techniques according to the type of input data.

It is important to note that techniques with classification algorithms that use features of RF signals as input data are the most exploited with 42.9%, followed by the techniques with classification algorithms that use the entire received I/Q RF signal as input data with 29.8%. More interesting is the fact that 95.9% of all papers that use the entire received I/Q RF signal as input data are used advanced engineering techniques.

3. COMPARISON OF DETECTION TECHNOLOGIES

An extensive comparative analysis of all literature was performed in order to support the proposed categorization and to emphasize the best RF-based drone detection technique. The most relevant research papers were used for this purpose. The comparison was done according to the used dataset and engineering techniques. The publicly available studies whose results were verified on the “DroneRF dataset” and the “VTI_RF_Dataset” was presented. Additionally, these studies were classified according to our categorization, together with results from three different experiments. This was done intentionally as it is the only way to compare different approaches according to the detection or identification of the same number of classes.

It is important to notice that there are very few publicly available datasets that contain RF signals from drones. It should be emphasized that only two datasets have records of RF signals from both industrial, scientific, and medical (ISM) radio bands, but just one has multiple drones. Additionally, some authors in [30] and [31] used ground controllers for classification which can be valuable in various researches. Moreover, RF receivers generate a vast amount of data during the recording process, which leads to huge datasets. This can be a disadvantage in some situations because of the prerequisite for superb computers, storage, and GPUs. The list of publicly open datasets that contains RF signals from UAS is presented in Table 1.

Table 1. The RF drone publicly available datasets.

Reference	Number of UAS	Multiple drones	2.4 GHz	5.8 GHz
[32]	3	-	+	
[33]	3	+	+	+
[30]	17	-	+	
[34]	NaN	-	+	
[35]	7	-	+	
[31]	10	-	+	+

Authors in [32] presented a “DroneRF” dataset that incorporated three different drones, recorded in four different operating modes in only one ISM band (2.4 GHz). This dataset was used in over 60% of reviewed literature which is an impressive result. Analogous, authors in [33] introduced a similar dataset with three drones, recorded in four different operating modes in two ISM bands (2.4 and 5.8 GHz). Moreover, this dataset contains records of multiple (two and three) drones operating at the same time simultaneously. This makes “VTI_RF_Dataset” unique because to the best of our knowledge there is no such dataset in the available literature.

4. RESULTS

The main goal of this research was to review and categorize all available RF-based drone classification research papers and datasets. The studies whose results were verified on the “DroneRF dataset” are presented in Table 2.

Table 2. Comparative analysis of publicly available studies verified on the “DroneRF dataset”.

Reference	1 st	2 nd	Drone detection	Type identification	Flight mode identification
[7]	A	R	99.7	84.5	46.8
[10]	A	R	<u>100.0</u>	94.6	87.4
[25]	H	F	-	-	91.0
[11]	A	R	99.8	85.8	59.2
[36]	A	R	<u>100.0</u>	<u>99.6</u>	<u>99.3</u>
[37]	A	F	<u>100.0</u>	98.6	95.1
[38]	H	F	-	-	99.2
[39]	A	R	99.8	98.5	95.3

The notation “H” stands for hybrid and “A” for advanced engineering techniques. The notation “F” stands for features and “R” for raw I/Q RF signal. It is important to note that the best results were achieved in [36] with multistage DNN and CNN algorithms. More important, there are no classic engineering techniques employed on the “DroneRF dataset”. Additionally, some of the studies whose results were verified on the “VTI_RF_Dataset” are presented in Table 3.

Table 3. Comparative analysis of publicly available studies verified on the “VTI_RF_Dataset”.

Reference	1 st	2 nd	Drone detection	Type identification	Multiple drone detection
[8]	A	R	<u>99.8</u>	96.1	<u>97.2</u>
[29]	A	R	-	<u>100.0</u>	-
[40]	A	F		99.9	

It is worthy of mention that “VTI_RF_Dataset” provides multiple drone detection on real RF signals, rather than simulated RF signals.

5. CONCLUSION

This study set out to establish the new categorization and provided a deeper insight into the publicly available drone classification techniques in the radio-frequency domain. Overall, the following conclusions can be pointed out: the proposed categorization provides a useful tool for a literature review, the comparative analysis shows that deep learning techniques are currently the best solution for solving the issue of drone classification, and there is a little number of publicly available datasets with radio signals from drones. The main strength of this study is that it represents the first comprehensive review of publicly available datasets with RF signals from drones.

Further research should focus on determining an approach to merge two or three datasets or to test the classification techniques on different datasets. Additionally, it is important to examine the new multimodal deep learning algorithm which will incorporate different features and raw radio signals for solving the classification issue.

References

[1] V. U. Castrillo, A. Manco, D. Pascarella, and G. Gigante, “A review of counter-UAS technologies for cooperative defensive teams of drones,” *Drones*, vol. 6, no. 3, 2022, doi: 10.3390/drones6030065.

[2] G. Ding, Q. Wu, L. Zhang, Y. Lin, T. A. Tsiftsis, and Y. D. Yao, “An amateur drone surveillance system based on the cognitive Internet of Things,” *IEEE Commun. Mag.*, vol. 56, no. 1, pp. 29–35, 2018, doi: 10.1109/MCOM.2017.1700452.

[3] M. Hassanalian and A. Abdelkefi, “Classifications, applications, and design challenges of drones: A review,” *Prog. Aerosp. Sci.*, vol. 91, no. 2017, pp. 99–131, May 2017, doi: 10.1016/j.paerosci.2017.04.003.

[4] X. Lv and Z. Wang, “An improved RF detection algorithm using EMD-based WT,” *KSII Trans. Internet Inf. Syst.*, vol. 13, no. 8, pp. 3862–3879, 2019, doi: 10.3837/tiis.2019.08.003.

[5] H. Fu, S. Abeywickrama, L. Zhang, and C. Yuen, “Low-complexity portable passive drone surveillance via SDR-based signal processing,” *IEEE Commun. Mag.*, vol. 56, no. 4, pp. 112–118, 2018, doi: 10.1109/MCOM.2018.1700424.

[6] P. Nguyen, H. Truong, M. Ravindranathan, A. Nguyen, R. Han, and T. Vu, “Cost-effective and passive RF-based drone presence detection and characterization,” *GetMobile Mob. Comput. Commun.*, vol. 21, no. 4, pp. 30–34, 2018, doi: 10.1145/3191789.3191800.

[7] M. F. Al-Sa’d, A. Al-Ali, A. Mohamed, T. Khattab, and A. Erbad, “RF-based drone detection and identification using deep learning approaches: An initiative towards a large open source drone database,” *Futur. Gener. Comput. Syst.*, vol. 100, pp. 86–97, Nov. 2019, doi: 10.1016/j.future.2019.05.007.

[8] B. Sazdić-Jotić, I. Pokrajac, J. Bajčetić, B. Bondžulić, and D. Obradović, “Single and multiple drones detection and identification using RF based deep learning algorithm,” *Expert Syst. Appl.*, vol. 187, Jan. 2022, doi: 10.1016/j.eswa.2021.115928.

[9] S. Yang, Y. Luo, W. Miao, C. Ge, W. Sun, and C. Luo, “RF signal-based UAV detection and mode classification: A joint feature engineering generator and multi-channel deep neural network approach,” *Entropy*, vol. 23, no. 12, p. 1678, Dec. 2021, doi: 10.3390/e23121678.

[10] M. S. Allahham, T. Khattab, and A. Mohamed, “Deep learning for RF-based drone detection and identification: A multi-channel 1-D convolutional neural networks approach,” in *2020 IEEE International Conference on Informatics, IoT, and Enabling Technologies (ICIoT)*, Feb. 2020, pp. 112–117. doi: 10.1109/ICIoT48696.2020.9089657.

[11] S. Al-Emadi and F. Al-Senaid, “Drone detection approach based on radio-frequency using convolutional neural network,” in *2020 IEEE International Conference on Informatics, IoT, and Enabling Technologies (ICIoT)*, Feb. 2020, no. December, pp. 29–34. doi: 10.1109/ICIoT48696.2020.9089489.

[12] E. Ozturk, F. Erden, and I. Guvenc, “RF-based low-SNR classification of UAVs using convolutional neural networks,” *arXiv Signal Process.*, pp. 1–18,

- Sep. 2020, Accessed: Nov. 23, 2020. [Online]. Available: <http://arxiv.org/abs/2009.05519>
- [13] S. Basak, S. Rajendran, S. Pollin, and B. Scheers, "Drone classification from RF fingerprints using deep residual nets," in *2021 International Conference on COMMunication Systems & NETWORKS (COMSNETS)*, Jan. 2021, pp. 548–555. doi: 10.1109/COMSNETS51098.2021.9352891.
- [14] H. N. Nguyen, M. Vomvas, T. Vo-Huu, and G. Noubir, "Spectro-Temporal RF Identification using Deep Learning," *CoRR*, vol. abs/2107.0, Jul. 2021, [Online]. Available: <https://arxiv.org/abs/2107.05114>
- [15] S. Basak and B. Scheers, "Passive radio system for real-time drone detection and DoA estimation," *2019 Int. Conf. Mil. Commun. Inf. Syst. ICMCIS 2019*, pp. 1–6, 2019.
- [16] X. Shi, C. Yang, W. Xie, C. Liang, Z. Shi, and J. Chen, "Anti-drone system with multiple surveillance technologies: architecture, implementation, and challenges," *IEEE Commun. Mag.*, vol. 56, no. 4, pp. 68–74, 2018, doi: 10.1109/MCOM.2018.1700430.
- [17] U. Bhattacharjee, E. Ozturk, O. Ozdemir, I. Guvenc, M. L. Sichitiu, and H. Dai, "Experimental study of outdoor UAV localization and tracking using Passive RF Sensing," *WiNTECH 2021 - Proc. 15th ACM Work. Wirel. Netw. Testbeds, Exp. Eval. Charact. Part ACM MOBICOM 2021*, no. September, pp. 31–38, 2022, doi: 10.1145/3477086.3480832.
- [18] D. Shorten, A. Williamson, S. Srivastava, and J. C. Murray, "Localisation of drone controllers from RF signals using a deep learning approach," *ACM Int. Conf. Proceeding Ser.*, pp. 89–97, 2018, doi: 10.1145/3243250.3243272.
- [19] I. Bisio, C. Garibotto, H. Haleem, F. Lavagetto, and A. Sciarone, "On the localization of wireless targets: A drone surveillance perspective," *IEEE Netw.*, vol. 35, no.5, pp.249–255, 2021, doi: 10.1109/MNET.011.2000648.
- [20] S. Abeywickrama, L. Jayasinghe, H. Fu, S. Nissanka, and C. Yuen, "RF-based direction finding of UAVs using DNN," in *2018 IEEE International Conference on Communication Systems (ICCS)*, Dec. 2018, pp. 157–161. doi: 10.1109/ICCS.2018.8689177.
- [21] H. Zhang, C. Cao, L. Xu, and T. A. Gulliver, "A UAV detection algorithm based on an artificial neural network," *IEEE Access*, vol. 6, pp. 24720–24728, 2018, doi: 10.1109/ACCESS.2018.2831911.
- [22] C. J. Swinney and J. C. Woods, "RF detection and classification of unmanned aerial vehicles in environments with wireless interference," in *2021 International Conference on Unmanned Aircraft Systems (ICUAS)*, Jun. 2021, pp. 1494–1498. doi: 10.1109/ICUAS51884.2021.9476867.
- [23] O. O. Medaiyese, M. Ezuma, A. P. Lauf, and I. Guvenc, "Wavelet transform analytics for RF-based UAV detection and identification system using machine learning," *Pervasive Mob. Comput.*, vol. 82, 2022, doi: 10.1016/j.pmcj.2022.101569.
- [24] M. Ezuma, F. Erden, C. Kumar Anjinappa, O. Ozdemir, and I. Guvenc, "Detection and classification of UAVs using RF fingerprints in the presence of Wi-Fi and bluetooth interference," *IEEE Open J. Commun. Soc.*, vol.1, pp.60–76, 2020, doi: 10.1109/OJCOMS.2019.2955889.
- [25] C. J. Swinney and J. C. Woods, "Unmanned aerial vehicle operating mode classification using deep residual learning feature extraction," *Aerospace*, vol. 8, no.3, p.79, Mar. 2021, doi: 10.3390/aerospace8030079.
- [26] M. Haluza and J. Cechak, "Analysis and decoding of radio signals for remote control of drones," *NTSP 2016 - Proc. Int. Conf. New Trends Signal Process.*, 2016, doi: 10.1109/NTSP.2016.7747781.
- [27] S. Sciancalepore, O. A. Ibrahim, G. Oligeri, and R. Di Pietro, "PiNcH: An effective, efficient, and robust solution to drone detection via network traffic analysis," *Comput. Networks*, vol. 168, p. 107044, 2020, doi: 10.1016/j.comnet.2019.107044.
- [28] P. Stoica, S. Basak, C. Molder, and B. Scheers, "Review of counter-UAV solutions based on the detection of remote control communication," *2020 13th Int. Conf. Commun. COMM 2020 - Proc.*, no. July, pp. 233–238, 2020, doi: 10.1109/COMM48946.2020.9142017.
- [29] M. Mokhtari, J. Bajcetic, B. Sazdic-Jotic, and B. Pavlovic, "RF-based drone detection and classification system using convolutional neural network," in *2021 29th Telecommunications Forum (TELFOR)*, Nov. 2021, pp. 1–4. doi: 10.1109/telfor52709.2021.9653332.
- [30] MartinsEzuma, "Drone remote controller RF signal dataset," *IEEE-Dataport*, 2021. <https://iee-dataport.org/open-access/drone-remote-controller-rf-signal-dataset> (accessed Jul. 22, 2022).
- [31] M. Vuorenmaa, J. Marin, M. Heino, M. Turunen, T. Riihonen, and K. Pärlin, "Radio-frequency control and video signal recordings of drones," *Zenodo*, 2020. https://zenodo.org/record/4264467#.Ytrq_7ZBxD8 (accessed Jul. 22, 2022).
- [32] M. S. Allahham, M. F. Al-Sa'd, A. Al-Ali, A. Mohamed, T. Khattab, and A. Erbad, "DroneRF dataset: A dataset of drones for RF-based detection, classification and identification," *Data Br.*, vol. 26, p. 104313, Oct. 2019, doi: 10.1016/j.dib.2019.104313.
- [33] B. Sazdic-Jotic, "VTI_RF_DroneDataset," *Mendeley Data*, 2020. <https://data.mendeley.com/datasets/s6tgnnp5n2/1> (accessed Jul. 22, 2022).
- [34] Olusiji Medaiyese, "Cardinal RF (CardRF) dataset," *IEEE-Dataport*, 2022. <https://iee-dataport.org/documents/cardinal-rf-cardrf-outdoor-uavuasdrone-rf-signals-bluetooth-and-wifi-signals-dataset> (accessed Jul. 22, 2022).
- [35] C. J. Swinney, "The DroneDetect dataset," *IEEE-Dataport*, 2022. <https://iee-dataport.org/open-access/dronedetect-dataset-radio-frequency-dataset-unmanned-aerial-system-uas-signals-machine> (accessed Jul. 22, 2022).
- [36] Y. Mo, J. Huang, and G. Qian, "Deep learning approach to UAV detection and classification by using compressively sensed RF signal," *Sensors*, vol. 22, no. 8, 2022, doi: 10.3390/s22083072.
- [37] R. Kılıç, N. Kumbasar, E. A. Oral, and I. Y. Ozbek, "Drone classification using RF signal based spectral features," *Eng. Sci. Technol. an Int. J.*, vol. 28, p. 101028, Apr. 2022, doi: 10.1016/j.jestch.2021.06.008.
- [38] I. Nemer, T. Sheltami, I. Ahmad, A. U. H. Yasar, and

- M. A. R. Abdeen, "RF-based UAV detection and identification using hierarchical learning approach," *Sensors*, vol. 21, no. 6, pp. 1–23, 2021, doi: 10.3390/s21061947.
- [39] T. Huynh-The, Q. V. Pham, T. Van Nguyen, D. B. Da Costa, and D. S. Kim, "RF-UAVNet: High-performance convolutional network for RF-based drone surveillance systems," *IEEE Access*, vol. 10, pp. 49696–49707, 2022, doi: 10.1109/ACCESS.2022.3172787.
- [40] M. Mokhtari, J. Bajčetić, B. Sazdić-Jotić, and B. Pavlovic, "Developing a convolutional recurrent neural network for drone classification," in *Proceedings of the 9th Small Systems Simulation Symposium 2022*, 2022, no. March, pp. 85–89.



TDOA BASED APPROACH FOR ACCURATE TARGET LOCALIZATION BASED ON HYBRID GENETIC ALGORITHM

MAJA ROSIĆ

Faculty of Mechanical Engineering, University of Belgrade, Belgrade, mrosic@mas.bg.ac.rs

MILOŠ SEDAK

Faculty of Mechanical Engineering, University of Belgrade, Belgrade, msedak@mas.bg.ac.rs

MIRJANA SIMIĆ

School of Electrical Engineering, University of Belgrade, Belgrade, mira@etf.rs

PREDRAG PEJOVIĆ

School of Electrical Engineering, University of Belgrade, Belgrade, peja@etf.rs

Abstract: Accurate localization of target based on time difference of arrival (TDOA) measurements is of crucial importance in a large number of different military and civil applications, especially in security systems, radars, sonars etc. This paper focuses on the determining the position of a target from a set of TDOA measurements obtained on several receivers whose positions are known. The considered target localization problem is formulated as the optimization problem, where the corresponding objective function is obtained based on least squares (LS) method. Due to the complexity of the considered problem, the resulting objective function is highly nonlinear and multimodal. Therefore, to solve this complex optimization problem this paper proposes the hybridization of Genetic Algorithm (GA) with well-known Gauss-Newton (GN) method. The performance of considered hybrid algorithm is investigated and compared to well-known conventional optimization algorithms in solving the considered TDOA based localization problem. The simulation results of the proposed optimization method indicate a significant improvement in localization accuracy compared to well-known algorithms.

Keywords: Localization, Optimization, Least Squares, Time Difference of Arrival, Wireless Sensor Networks.

1. INTRODUCTION

The problem of determining the unknown location of a target based on TDOA measurements from a set of receivers, whose positions are known, is an essential problem in many applications such as military target tracking, environmental monitoring, telecommunications, security systems, wireless sensor networks, and many others [1-2]. In each of these applications, the key requirement is determining the accurate location of a target from a set of noisy measurements.

In general, localization algorithms use various techniques such as the time of arrival (TOA), the time difference of arrival, the received signal strength (RSS), or the angle of arrival (AOA), depending on the available hardware to locate the targets [1]. This paper focuses on a target localization problem based on the TDOA measurements due to its high ranging accuracy and relatively simple required hardware structure.

The target location can be estimated based on the least squares and the maximum likelihood (ML) as a powerful methods which can be employed successfully in a practical application [3]. Hence, due to the TDOA measurement errors, the considered localization problem is formulated as an optimization problem known as least-squares problem. The LS problem is based on the

minimization of the sum of squared errors between the estimated and the measured distances. Generally, the LS estimator can be divided into two classes: linear least squares (LLS), which can provide closed-form solution, and nonlinear least squares (NLS). In this paper, the NLS estimator is employed to accurately estimate the target location based on the noisy TDOA measurements. Due to the complexity of the considered problem, the objective function of the NLS estimator is highly nonlinear and multimodal [3]. Therefore, it is difficult to obtain the global optimal solution with a conventional optimization algorithm, where the convergence of these algorithms mainly depends on the appropriate choice of initial solution and thus may not always converge to the global optimal solution. In order to overcome this difficulty, in this paper the hybridization between Genetic Algorithm and a local search Gauss-Newton method is proposed, due to the individual efficiencies of these algorithms [4, 5]. The proposed hybrid GA-GN algorithm goes through two phases during the optimization process. In the first phase, the GA is employed to explore the search space, with the aim to find the region of the global optimal solution. Then, in the second phase, the solution obtained in the first phase is used as the initial solution and improved using the GN local search method.

The target location is usually obtained by the linear

estimator as algebraic closed-form solutions and in this case, avoid the selection of initial solution [3, 6]. The weighted least square (WLS) algorithm for estimation of the target is presented in this paper due to its computational efficiency and the linear closed-form solution in the WLS sense [6]. This approach linearizes the nonlinear TDOA measurement equations by introducing an additional variable in order to minimize the weighted sum of the squared residuals.

The Cramer–Rao Lower Bound (CRLB) of the TDOA measurements from all receivers provides a lower bound on the variance of any unbiased estimator [7] and it is a very useful tool for evaluating the localization accuracy.

The paper is organized as follows: the target localization problem based on the TDOA measurements from a set of receivers whose positions are known is stated in Section 2. Section 3 describes target localization problem which is modeled as a least-squares estimation problem with NLS and WLS approaches. In Section 4, the hybrid GA–GN method is presented. The CRLB is given in Section 5. Section 6 gives the simulation results of the proposed hybrid optimization algorithm against the conventional approaches. Finally, conclusion and future work are presented in Section 7.

2. PROBLEM FORMULATION

In this section, the two-dimensional (2D) target localization problem using TDOA measurements under the line-of-sight (LOS) environment is presented. To determine the unknown position of a target, the considered localization problem requires a measurement from at least three receivers, $N \geq 3$, whose locations are known, placed at coordinates $\mathbf{x}_i := [x_i \ y_i]^T \in \mathbb{R}^2$, $i \in \{1, 2, \dots, N\}$ as shown in Fig. 1.

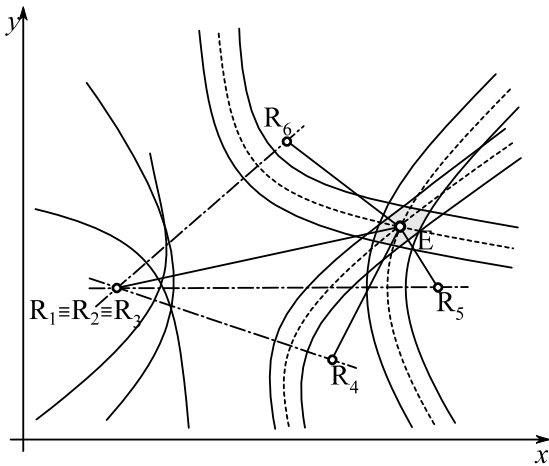


Figure 1. Geometrical model based on TDOA.

Here, we assume that the range difference errors $\{n_i\}$ can be modelled as independent Gaussian random variables with zero mean and variance σ_i^2 , i.e., $\mathcal{N}(0, \sigma_i^2)$. We can set the first receiver R_1 to be the reference receiver, without loss of generality of considered localization problem.

Using geometrical relationships between a target and the receivers R_i , $i \in \{2, 3, \dots, N\}$, the target's unknown location is determined. Unknown distances denoted by $\{r_{i,1}\}$ are produced by multiplying the calculated times with the speed of light. These lengths may be calculated using the formula

$$r_{i,1} = d_{i,1} + n_{i,1}, \quad i \in \{2, \dots, N\}, \quad (1)$$

where $d_{i,1} = d_i - d_1$. Here, distances between the target and the receiver pair R_i and R_1 can be expressed as follows

$$\begin{aligned} d_1 &= \sqrt{(x - x_1)^2 + (y - y_1)^2}, \\ d_i &= \sqrt{(x - x_i)^2 + (y - y_i)^2}. \end{aligned} \quad (2)$$

where $\mathbf{x} := [x \ y]^T \in \mathbb{R}^2$ is the unknown position of a target.

As a result, the hyperbola is defined by the fact that, as shown in Fig. 1, the difference $d_i - d_1$, between any point on it and the two foci R_i and R_1 , respectively, is constant.

The intersection of two 2D hyperbolas, as shown in Fig. 1, provides the geometric model for finding the target's unknown actual coordinates using TDOA data in the absence of noise.

More than two hyperbolas do not meet at the same spot in real-world settings when noise is present, necessitating the use of an appropriate optimization technique to reduce the localization error.

3. LEAST SQUARE METHODS

This section presents the formulation of the LS method for the considered target localization model, using the obtained TDOA measurements, as described in previous section. In general, the formulation of the NLS problem comes first when formulating the LS problem. Here, the objective function $J_{NLS}(\tilde{\mathbf{x}})$ is defined as the sum of squared residuals between the estimated and the measured TDOA values, which can be written as

$$J_{NLS}(\tilde{\mathbf{x}}) = \min \sum_{i=1}^N R_{es,i}^2(\tilde{\mathbf{x}}), \quad (3)$$

where $\tilde{\mathbf{x}}$ denoted the vector of decision variables and residual $R_{es,i}(\tilde{\mathbf{x}})$ is calculated as

$$R_{es,i}(\tilde{\mathbf{x}}) = \tilde{r}_{i,1} - r_{i,1}. \quad (4)$$

Therefore, from the minimization problem in Eq. (3), the appropriate optimal solution $\hat{\mathbf{x}}$ can be obtained as

$$\hat{\mathbf{x}} = \arg \min_{\mathbf{x} \in \mathbb{R}^2} J_{NLS}(\tilde{\mathbf{x}}), \quad (5)$$

It has been previously shown that the formulation of TDOA problem provides nonlinear equations of hyperbolas. Therefore, the following steps must be taken

in order to transform the nonlinear equations into the proper set of linear equations. Firstly, the Eq. (2) is substituted into the Eq. (1), which results in the following expression

$$r_{i,1} + \sqrt{(x-x_1)^2 + (y-y_1)^2} = \sqrt{(x-x_i)^2 + (y-y_i)^2} + n_{i,1}, \quad i \in \{2,3,\dots,N\}. \quad (6)$$

Eq. (6) is squared on both sides, and a new variable is added

$$R_1 = d_1 = \sqrt{(x-x_1)^2 + (y-y_1)^2}, \quad (7)$$

and using some algebraic techniques, we can demonstrate that

$$(x_i - x_1)(x - x_1) + (y_i - y_1)(y - y_1) + r_{i,1}R_1 = 0.5 \left[(x_i - x_1)^2 + (y_i - y_1)^2 - r_{i,1}^2 \right] + d_i n_{i,1} + 0.5 n_{i,1}^2, \quad (8) \quad i \in \{2,3,\dots,N\},$$

Then, the obtained system of equations in Eq. (8) is linearized by

$$(x_i - x_1)(x - x_1) + (y_i - y_1)(y - y_1) + r_{i,1}R_1 = 0.5 \left[(x_i - x_1)^2 + (y_i - y_1)^2 - r_{i,1}^2 \right] + m_{i,1}, \quad i \in \{2,3,\dots,N\}, \quad (9)$$

where the second-order term $n_{i,1}^2$ is neglected and $m_{i,1} = d_i n_{i,1}$. Hence, the system in Eq. (9) is linear and can be written in the following matrix form

$$\mathbf{A}\boldsymbol{\theta} = \mathbf{b} + \mathbf{m}, \quad (10)$$

in which

$$\mathbf{A} = \begin{bmatrix} x_2 - x_1 & y_2 - y_1 & r_{2,1} \\ x_3 - x_1 & y_3 - y_1 & r_{3,1} \\ \vdots & \vdots & \vdots \\ x_N - x_1 & y_N - y_1 & r_{N,1} \end{bmatrix}, \quad (11)$$

$$\boldsymbol{\theta} = [x - x_1 \quad y - y_1 \quad R_1]^T, \quad (12)$$

$$\mathbf{b} = 0.5 \begin{bmatrix} (x_2 - x_1)^2 + (y_2 - y_1)^2 - r_{2,1}^2 \\ (x_3 - x_1)^2 + (y_3 - y_1)^2 - r_{3,1}^2 \\ \vdots \\ (x_N - x_1)^2 + (y_N - y_1)^2 - r_{N,1}^2 \end{bmatrix}, \quad (13)$$

$$\mathbf{m} = [m_{2,1} \quad m_{3,1} \quad \dots \quad m_{N,1}]^T. \quad (14)$$

Based on the linear-matrix form, given in Eqs. (10)-(14), the following WLS objective function can be defined as follows

$$J_{WLS}(\boldsymbol{\theta}) = (\mathbf{A}\boldsymbol{\theta} - \mathbf{b})^T \mathbf{W}(\mathbf{A}\boldsymbol{\theta} - \mathbf{b}). \quad (15)$$

where $\mathbf{W} = (E\{\mathbf{m}\mathbf{m}^T\})^{-1}$ is the weighting matrix. Therefore, the considered localization problem can be written as the following localization problem

$$\min_{\mathbf{x} \in R^2} J_{WLS}(\mathbf{x}). \quad (16)$$

The formulated linear LS problem, given in Eq. (16) provides algebraic closed-form solution, which for WLS method is denoted as $\hat{\mathbf{x}}_{WLS}$. This solution provides the minimum of linearized objective function $J_{WLS}(\boldsymbol{\theta})$. It can be shown that $\hat{\mathbf{x}}_{WLS}$ can be obtained from Eq. (16) by the following equation [6]:

$$\hat{\mathbf{x}}_{WLS} = (\mathbf{A}^T \mathbf{W} \mathbf{A})^{-1} \mathbf{A}^T \mathbf{W} \mathbf{b}. \quad (17)$$

The WLS method's main advantages are its simple implementation and high computing efficiency, however it does not achieve adequate accuracy for handling extremely nonlinear and complicated problems.

4. HYBRID GA-GN METHOD

The proposed hybrid GA-GN is described in this section in the context of its application to the problem of locating emitting sources using TDOA measurement. The basic purpose of hybridizing several optimization algorithms is to establish the most effective technique for solving the considered optimization problem. As a result of hybridizing the algorithms, it is possible to combine the benefits of each algorithm while avoiding their disadvantages [4, 5]. As a powerful stochastic global optimization method, the GA explores the search space by randomly generating starting solutions within boundary restrictions and finds the global or near-global optimal solution. By utilizing the neighborhood of the initial solution found by the GA, a local search algorithm is used to identify the best global optimal solution of the considered problem.

In this paper, the GA algorithm and the efficient GN local search method are merged to generate the hybrid GA-GN algorithm, which improves the efficiency and accuracy of the GA solution. As a result, the GA and GN methods are introduced in this section, and afterwards the appropriate hybridization procedure is introduced.

4.1. Genetic algorithm

The genetic algorithm is a widely applied metaheuristic optimization method that is based on genetics and natural selection mechanisms found in nature [4], and may be used to tackle NLS minimization problems effectively. Therefore, to apply the GA to NLS problem, the stated minimization problem in Eq. (3) may be altered by adding bound-constraints, which can be stated as

$$\min_{\mathbf{x}^l \leq \mathbf{x} \leq \mathbf{x}^h} J_{NLS}(\mathbf{x}), \quad (18)$$

where \mathbf{x} denotes a vector of decision variables, \mathbf{x}^l and \mathbf{x}^h are introduced as the minimum and maximum bounds

of \mathbf{x} respectively. The bound-constraints are provided to prevent the objective function from being evaluated for infeasible solutions during the search process.

The optimization procedure of GA begins with a population of N_p individuals chosen at random from the feasible solution space. In contrast to gradient-based optimization processes, where potential solution is directly drawn from the solution space, in GA each individual is represented by a chromosome, which is encoded as a fixed length vector of binary values. The length of this vector is determined by the number of optimization parameters employed and the required encoding precision. According to the evolutionary operators, the suggested GA procedure may be separated into selection, crossover, and mutation.

The process of selection uses the fitness values of chromosomes to determine which individuals are chosen for the mating, and eliminates the chromosomes which don't have necessary attributes for the efficient solving of the optimization problem. Chromosomes are selected according to roulette wheel selection, so individuals with lower objective function values, which is desired for minimization problems, are more likely to be selected. The probability of selecting an i -th individual is proportional to the quality of its original fitness, which can be formulated as a probability of selection P_i formulated as follows

$$P_i = \frac{F_i}{\sum_{j=1}^{N_p} F_j}, \quad i \in \{1, \dots, N_p\}, \quad (19)$$

where F_i denotes the corresponding fitness value of the chromosome. Therefore, the appropriate cumulative probability C_i of the i -th individual is determined according to the following expression

$$C_i = \sum_{j=1}^{N_p} F_j. \quad (20)$$

After all of the individuals in the population have been assigned a cumulative probability, they are subjected to a selection procedure in which an appropriate individual is picked based on a random number r that must satisfy the following expression

$$C_{i-1} < r \leq C_i, \quad i \in \{1, 2, \dots, N_p\}, \quad (21)$$

where r denotes the random number generated between 0 and 1.

The crossover operator, one of the most important parts of GA, combines and exploits the available information, stored in chromosomes, to influence the search direction during the optimization process. The crossover operator combines the information of two individuals, previously chosen in the selection process, to create an offspring that shares both individuals positive traits. Such offspring could potentially have necessary abilities to successfully solve the optimization problem. As shown in Fig 2, two-

point crossover is performed by selecting two random crossover points along the chromosome length, denoted as c_1 and c_2 . As a result, the encoded binary values enclosed by these points are interchangeably exchanged between selected individuals.

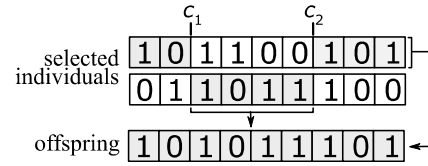


Figure 2. The illustration of two-point crossover operator

Mutation is a GA operator that introduces new unexplored solutions into the GA population and prevents the algorithm from becoming stuck in the local optima, allowing it to achieve better results faster. Only a small percentage of the population is mutated in order to avoid destroying valuable information for the optimization process. The mutation rate is defined as the percentage of a population's total number of genes whose values have changed. Mutation happens when a chromosome undergoes random binary changes. Each digit of the gene being mutated is changed to either 0 or 1 to express the randomness of the changes. The mutation rate must be small, for if it is large, a good chromosome might accidentally mutate into a bad one by chance.

The process of selection, crossover, and mutation is repeated, and the population evolves over successive iterations towards the global optimal solution of the given optimization problem until the termination criterion is satisfied. Although most evolutionary algorithms use the maximum number of iterations as a termination criterion, the relative error between two consecutive iterations of the average population fitness is also used. Therefore, the execution of algorithm can be stopped by comparing the population fitness in consecutive iterations when it becomes smaller than a certain threshold, which is expressed in the following expression

$$\left| \frac{f_{avg}^{(k)} - f_{avg}^{(k-1)}}{f_{avg}^{(k)}} \right| \leq \varepsilon, \quad (22)$$

where ε is a small positive real number, in which

$$f_{avg}^{(k)} = \frac{1}{N_p} \sum_{i=1}^{N_p} f_i, \quad (23)$$

represents the average fitness value of the entire population in k th iteration.

4.2. Gauss-Newton method

The Gauss-Newton method is widely applied method for solving the LS problems [8]. In comparison to the Newton-Raphson method, which requires the Hessian matrix to be calculated. The Gauss-Newton method requires only the first derivative of the objective function $J_{NLS}(\mathbf{x})$, making it computationally less expensive in each iteration. It is now a widely used method for

minimizing objective functions that are represented as the sum of squares of nonlinear functions. The solution is iteratively obtained using the following expression

$$\mathbf{x}^{(k+1)} = \mathbf{x}^{(k)} - \left[\mathbf{J}(J_{NLS}(\mathbf{x}^{(k)}))^T \cdot \mathbf{J}(J_{NLS}(\mathbf{x}^{(k)})) \right]^{-1} \cdot \mathbf{J}(J_{NLS}(\mathbf{x}^{(k)}))^T \cdot \mathbf{e}(\mathbf{x}^{(k)}), \quad (24)$$

where $\mathbf{e}(\mathbf{x}^{(k)})$ is a residual vector and $\mathbf{J}(J_{NLS}(\mathbf{x}^{(k)}))$ is the Jacobian matrix evaluated at $\mathbf{x}^{(k)}$, which can be expressed as

$$\mathbf{J}(J_{NLS}(\mathbf{x})) = \begin{bmatrix} \frac{\partial \|\mathbf{x}_1 - \mathbf{x}\|_2}{\partial x} & \frac{\partial \|\mathbf{x}_1 - \mathbf{x}\|_2}{\partial y} \\ \vdots & \vdots \\ \frac{\partial \|\mathbf{x}_N - \mathbf{x}\|_2}{\partial x} & \frac{\partial \|\mathbf{x}_N - \mathbf{x}\|_2}{\partial y} \end{bmatrix}. \quad (25)$$

Once the gradient of the objective function $J_{NLS}(\mathbf{x})$ is sufficiently close to zero, the iteration process is stopped, e.g. when

$$\|\nabla J_{NLS}(\mathbf{x}^{(k+1)})\| \leq \varepsilon, \quad (26)$$

where the gradient is measured in a suitable norm and ε is a given threshold.

5. CRAMER-RAO LOWER BOUND

The Cramer-Rao Lower Bound is a theoretical lower bound on the covariance matrix, which is obtained from the Fisher information matrix (FIM) of the unbiased estimator [7]. As a result, the connection between the CRLB and the variance is as follows:

$$E[(\hat{\mathbf{x}} - \mathbf{x})(\hat{\mathbf{x}} - \mathbf{x})^T] \geq \text{CRLB}(\mathbf{x}) = \text{trace}\{\mathbf{I}(\mathbf{x})^{-1}\} \quad (27)$$

where $E[\cdot]$ denoted the expectation operator and $\mathbf{I}(\mathbf{x})$ is FIM given by

$$\mathbf{I}(\mathbf{x}) = -E\left[\frac{\partial^2 \ln(f(\mathbf{r}|\mathbf{x}))}{\partial \mathbf{x} \partial \mathbf{x}^T}\right], \quad (28)$$

The probability density function $f(\mathbf{r}|\mathbf{x})$ can be defined as

$$f(\mathbf{r}|\mathbf{x}) = \frac{1}{(2\pi)^{(N-1)/2} |\mathbf{C}|^{1/2}} \cdot \exp\left(-\frac{1}{2}(\mathbf{r} - \mathbf{d}(\mathbf{x}))^T \mathbf{C}^{-1} \left(-\frac{1}{2}(\mathbf{r} - \mathbf{d}(\mathbf{x}))\right)\right), \quad (29)$$

where \mathbf{C} is covariance matrix is given as

$$\mathbf{C} = \begin{bmatrix} \sigma_1^2 + \sigma_2^2 & \sigma_1^2 & \cdots & \sigma_1^2 \\ \sigma_1^2 & \sigma_1^2 + \sigma_3^2 & \ddots & \sigma_1^2 \\ \vdots & \ddots & \ddots & \vdots \\ \sigma_1^2 & \sigma_1^2 & \cdots & \sigma_1^2 + \sigma_N^2 \end{bmatrix}. \quad (30)$$

After performing differentiation on the natural logarithm of (29) with respect to \mathbf{x} , the FIM can be obtained as

$$\mathbf{I}(\mathbf{x}) = \left[\frac{\partial \mathbf{d}(\mathbf{x})}{\partial \mathbf{x}} \right]^T \cdot \mathbf{C}^{-1} \cdot \left[\frac{\partial \mathbf{d}(\mathbf{x})}{\partial \mathbf{x}} \right] \quad (31)$$

where $\mathbf{d}(\mathbf{x}) = [d_1, d_2, \dots, d_N]^T$ the true distance vector.

5.SIMULATION RESULTS

This section presents the results of the numerical simulation performed in order to compare the localization performance of the proposed hybrid GA-GN method, with the well-known WLS method and derived CRLB. The considered simulation environment includes, five receivers which are position at known coordinated $[200,300]^T$ m, $[1500,100]^T$ m, $[120,1500]^T$ m, $[1510,1500]^T$ m and $[700,900]^T$ m

It is assumed, that for simulation purposed the true position of the target is placed at $[300,500]^T$ m. To evaluate and compare the localization performance of different considered algorithms the root mean square error (RMSE) measure is employed, which can be defined as

$$RMSE = \sqrt{\frac{1}{N} \sum_{n=1}^N \|\hat{\mathbf{x}}(n) - \mathbf{x}\|_2^2}. \quad (32)$$

where \mathbf{x} and $\hat{\mathbf{x}}(n)$ are the true and estimated positions of the target, respectively, and $N=1000$ is a number of Monte Carlo simulation runs.

Firstly, the accuracy of the localization of different considered algorithms is evaluated depending on the level of TDOA measurement noise. Therefore, on Figure 3 the RMSE of the GA-GN and WLS methods is plotted as a function of SNR, with the appropriate calculated value of CRLB.

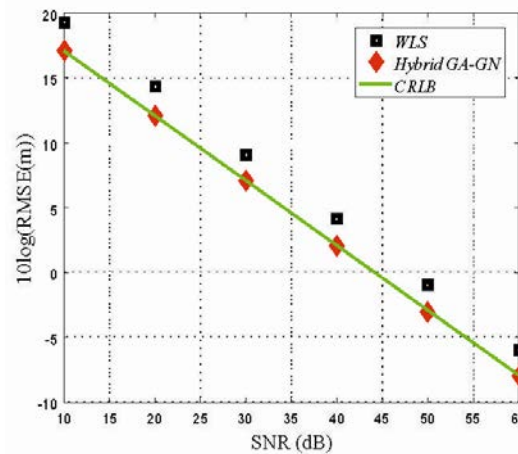


Figure 3. Comparison of RMSE versus SNR levels for different considered algorithms

According to the findings in Fig. 3, the proposed hybrid GA-GN technique can achieve the CRLB for a wide

range of SNR, demonstrating the robustness of the hybrid GA-GN algorithm in various noisy measurement situations. Furthermore, the suggested hybrid GA-GN algorithm consistently outperforms the current WLS method.

Next, in order to assess the localization performance, the CRLB is compared with the cumulative distribution functions (CDFs) of the hybrid GA-GN and WLS localization methods, at different SNR levels. Here, the SNR is used in simulations at two distinct levels, 10 dB and 50 dB, respectively.

The proposed hybrid GA-GN method and the WLS CDFs are shown in figure 4, with the SNR level set to 10 dB.

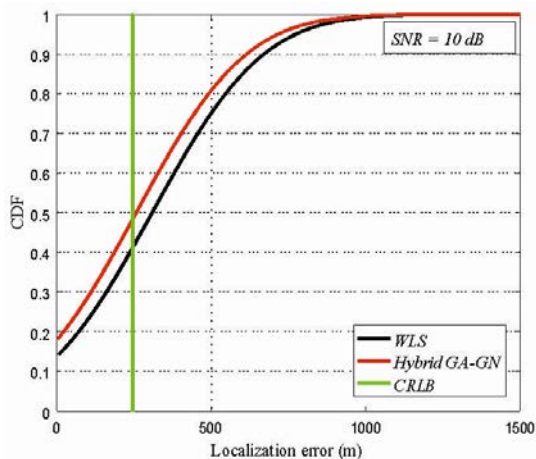


Figure 4. CDFs of the localization error of different localization algorithms for SNR = 10 dB.

According to Fig. 4, the hybrid GA-GN technique outperforms the WLS estimator with localization errors in more than 50% of the simulated runs near to the CRLB.

Fig. 5 depicts the CDFs for the case when the SNR = 50 dB.

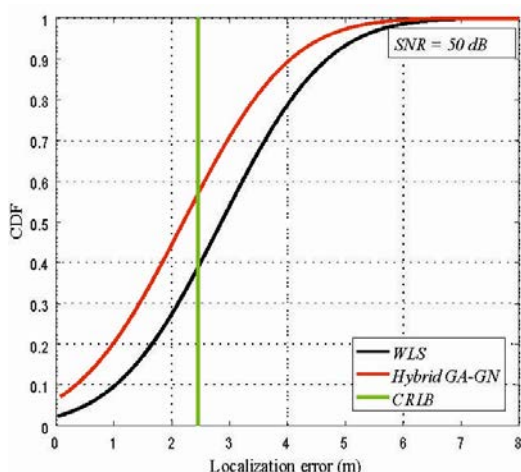


Figure 5. CDFs of the localization error of different localization algorithms for SNR = 50 dB.

When comparing the numerical results from Figures 4 and 5, it is clear that the hybrid GA-GN method performs better in terms of localization accuracy than the WLS

estimator, particularly at high SNR values. These findings are in correlation with the conclusions drawn from the Figure 3.

6. CONCLUSION

This paper considers the localization problem based on a set of TDOA measurements obtained on several receivers whose positions are known. The paper provides the definition of the TDOA localization problem, which is formulated as an optimization problem, where the corresponding objective function is obtained based on the least squares (LS) method. To solve the complex optimization problem, this paper proposes a hybridization between genetic algorithms and the conventional gradient-based Gauss Newton method. Furthermore, in order to compare the localization performance, the CRLB is derived for the considered localization problem. Simulation results show that the proposed nonlinear optimization methods outperform the WLS method and can achieve higher localization accuracy over a wide range of SNR values.

In future work, the developed optimization models can be further extended with the additional energy efficiency criterion, which can be solved by multi-objective optimization.

AKNOWLEDGMENT

The research of M. Rosić was supported by the Serbian Ministry of Education and Science under Grant TR35029. The research of M. Sedak was supported by the Serbian Ministry of Education and Science under Grant No. TR35006. The work of M. Simić was supported in part by Serbian Ministry of Education and Science under Grant TR32028.

References

- [1] Figueiras, J., Frattasi, S., Mobile Positioning and Tracking, John Wiley & Sons, United Kindom, 2010.
- [2] Chalise, B., Zhang, Y., Amin, M., Himed, B., "Target localization in a multi-static passive radar system through convex optimization", Signal Processing, 102 (2014) 207-215.
- [3] R. Zekavat and R. M. Buehrer, Handbook of Position Location: Theory, Practice and Advances, John Wiley & Sons, 2011.
- [4] J. Wang, J. Guo, "Research on the base station calibration of multi-station and time-sharing measurement based on hybrid genetic algorithm," Measurement, vol. 94, pp. 139-148, Dec., 2016.
- [5] V. R. Kulkarni, V. Desai, and R. V. Kulkarni, "A comparative investigation of deterministic and metaheuristic algorithms for node localization in wireless sensor networks," Wireless Networks, vol. 25, no. 5, pp. 2789–2803, 2019.
- [6] Einemo, M., So, H. C., "Weighted least squares algorithm for target localization in distributed MIMO radar", Signal Processing, 115 (2015) 144-150.

- [7] M. Laaraiedh, S. Avrillon, B. Uguen, "Cramer-Rao lower bounds for nonhybrid and hybrid localisation techniques in wireless networks," *European Transactions on Telecommunications*, vol. 23, pp. 268-280, Apr., 2012.
- [8] Gratton, S., Lawless, A.S. and Nichols, N.K., 2007. Approximate Gauss-Newton methods for nonlinear least squares problems. *SIAM Journal on Optimization*, 18(1), pp.106-132.



GNS3 SIMULATION OF IS-IS PROTOCOL IN NETWORK COMPOSED OF JUNIPER ROPUTER

PAVEL CRNOMARKOVIĆ

Military Technical Institute, Ratka Resanovića 1, Belgrade, Serbia, pavel@ptt.rs

RADOSLAV SURLA

Faculty of Technical Sciences, University of Kragujevac, Svetog Save 65, Čačak, Serbia, ekorade@gmail.com

Abstract: This paper presents the use of free software (GNS3) in a computer network simulation, with an emphasis on the IS-IS protocol. Without the use of hardware such as router, switches and other network equipment, as well as the analysis of the obtained results.

Keywords: Juniper, free software, GNS3, simulation, IS-IS protocol.

1. INTRODUCTION

These days, the Internet is widely used by multimillions of people all over the world, with a variety of applications, such as e-commerce and multimedia streaming requiring guaranteed speed and sufficient bandwidth. Furthermore, communication networks are growing rapidly to meet the increasing needs for file transfer, video conferencing etc. With this rapid network expanding, engineers are tasked to find solution for efficient data forwarding through the network.

Network is a connection of multiple hosts which exchange information among each other. The Open Systems Interconnection (OSI) model was developed in order to achieve the compatibility between them [1]. This model contains 7 (seven) layers, Physical, Data-Link, Network, Transport, Session, Presentation and Application. Routing protocols are mainly applied in the network layer. These protocols are used to provide the data traffic path from source to destination host.

Among other routing protocol, Intermediate System to Intermediate System (IS-IS) protocol recently took attention because of the large scalability of network, fast convergence and an additional advantage of not needing the IP connectivity to communicate with neighbours, so is more and more popular with service providers [2][3].

In this paper is shown a simulation of computer network using multiple routers and a free software. IS-IS protocol is set on routers and also all settings and readings according which it can be concluded that network is fully operational are given.

2. IS-IS PROTOCOL OVERVIEW

IS-IS protocol is developed by Digital Equipment Corporation, in 1980, originally standardized by ANSI, as International Organization for Standardization (ISO) protocol. IS-IS protocol is a routing protocol, primarily designed to efficiently forward data within computer

networks or groups of physically connected computers.

IS-IS protocol is an internal gateway protocol, designed primarily for the use within an autonomous system.

IS-IS is a link state protocol, which operates by sending link state information via a router. Each router independently creates a network topology, aggregating the obtained network data.

The IS-IS router runs the Dijkstra shortest-path first calculation to determine the shortest path to each destination in the network. Each router executes the Dijkstra algorithm independently, and each router has an identical database as a result.

Packets are then sent through the network to the destination via the calculated best route.

Unlike other IP routing protocols, IS-IS is directly applicable to data link layer (the second layer of OSI model), and does not require an address in every interface, but only on the router. This makes the configuration simpler.

IS-IS protocol is designed as part of the OSI network protocol, and not as a part of the TCP/IP protocol. It uses a different network address record. Instead of 32-bit addresses, IS-IS protocol uses a 10-bit Network Entity Titles (NET) in next format:

49.0040.0172.0016.0005.00

The first three bytes (49.0040) represent an area identifier. In this case, the area 40 is defined, while 49 represents Address Family Identifier (AFI) are used for private addresses. The next six bytes represent the system identifier of the router on the network. Finally, the last two bytes must be 00 to denote this system.

The IS-IS protocol divides each autonomous system into several smaller segments, so called areas. Each area is a collection of networks and hosts administratively brought together. Routers in one area use the link state algorithm in parallel, and store the results in their database. Routers,

within one area, exchange this information with each other and have an identical link-state database. In addition, routers can forward a list of routes in their area to routers of the other areas.

Routers within one area that use IS-IS protocol, are divided into two types. Level 1 routers route traffic within the same area, while Level 2 routers route traffic between different areas [4].

3. PROJECT

This chapter describes what hardware and software configuration is needed to simulate the routing protocol for computer network, as well as a brief overview of software installation.

3.1. Hardware requirement

A personal computer (PC) will be required for the simulation.

Minimum required configuration:

- CPU: Dualcore 1.7GHz
- Memory: 4GB Ram 800MHz
- Hard drive: 20GB free space or more

Recommended configuration:

- CPU: Intel i5 1.7GHz
- Memory: 8GB Ram 1600Mhz
- Hard drive: 40GB free space or more or higher.

3.2. Software requirement

The work is based on usage of free software (software for which is not required to purchase a licence), which can be downloaded for free from developer’s websites.

Used platform is the operating system Linux- Ubuntu [5], which can also be used under a virtual machine Oracle „VM VirtualBox“ [6].

Remaining required software:

Oracle VM VirtualBox – intended for virtualization [6]

QEMU – software intended for emulation [7]

GNS3 (Graphic Network Simulator 3) – software intended for simulation of network devices [8].

FreeBSD – Unix version of operating system [9]

Junos Olive – operating system of generic Juniper router [10]

Wireshark – software intended for monitoring traffic between network devices [11]

3.3. Software installation

As previously stated, the operating system used for simulation is Linux Ubuntu. After that, the GNS3

software package is installed, and also additional software as QEMU and VPC.

In order to add Juniper router in the GNS3 software package within the installed QEMU emulator, FreeBSD is installed, and at the end Juniper Olive software.

After all the installation is finished, GNS3 is started and the software is ready for creating certain network topology, simulation - test and performing further settings of routers, virtual PCs, links etc.

Using the GNS3 software, computer network is created. It consists of five routers, one switch and two Virtual Computers (VPC), whose appearance from the GNS3 software is given in Figure 1.

The system is divided into three autonomous areas. The first autonomous area (area20) - consists of routers R1 and R2, connected by a link 10.0.0.0/24. The second autonomous area (area30) - consists of router R3 and R4, connected by a link 10.0.0.0/24. The third autonomous area (area40) - consists of router R5, connected with a link 15.0.0.0/24 with first autonomous area (area20), and with link 14.0.0.0/24 with second autonomous area (area30).

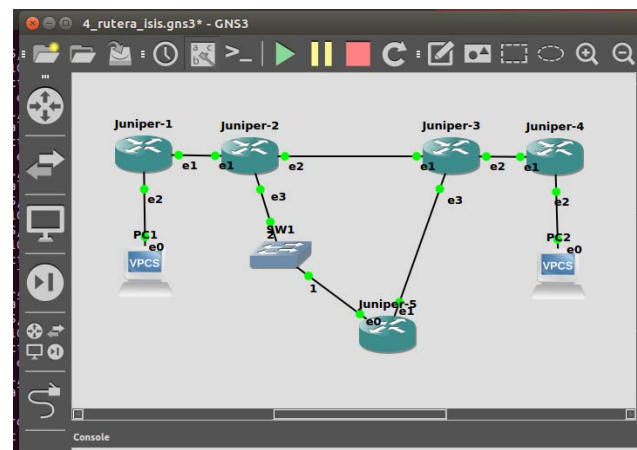


Figure 1. Network topology

The first and second autonomous area (area20) and (area30), respectively, are connected by link 100.0.0.0/24.

The switch located on the link between the routers R2, and R5, enables the use of the Wireshark software in order to monitor and analyse packets.

VPC1 is connected to the router R1, and VPC2 is connected to the router R4. The function of these virtual machines is to finally check if the network is really working. Table 1 shows the port settings of the routers.

Table 1. Port settings on routers: R1, R2, R3, R4, R5

	R1	R2	R3	R4	R5
em0	-	-	-	-	15.0.0.6
em1	10.0.0.5	10.0.0.6	100.0.0.6	11.0.0.6	14.0.0.6
em2	13.0.0.5	100.0.0.5	11.0.0.5	12.0.0.5	-
em3	-	15.0.0.5	14.0.0.5	-	-
lo0	172.16.1.1	172.16.2.1	172.16.3.1	172.16.4.1	172.16.5.1

Table 2 shows the interface settings of the VPCs.

Table 2. Interfaces setting on VPC1 and VPC2

	VPC1	VPC2
ip address	13.0.0.6	12.0.0.6
gateway	13.0.0.5	12.0.0.5

3.4. IS-IS protocol setting

The IS-IS protocol setting is shown through the following three steps:

Interfaces that use the IS-IS protocol are defined as well as the level. These settings are configured in the menu [edit interfaces]

The ISO family protocol is activated in the interface in the menu [edit interfaces]

The NET address is configured (in loopback interface).

In Table 3 are given the NET addresses for the routers R1, R2, R3, R4, and R5.

Table 3. Settings of the - NET address on routers: R1, R2, R3, R4, R5

Router	NET address
R1	49.0020.0172.0016.0001.00
R2	49.0020.0172.0016.0002.00
R3	49.0030.0172.0016.0003.00
R4	49.0030.0172.0016.0004.00
R5	49.0040.0172.0016.0005.00

3.5. Reading the results

Wireshark software package is used for the results analysis.

The results of above performed configuration and settings, is a configured network model with five routers, which work according to the IS-IS protocol, switch and two virtual computers. On one link in the branch with the switch, we activate the recording of the package via the software tool Wireshark. In Figure 2 are shown Hallo ISIS packets first level.

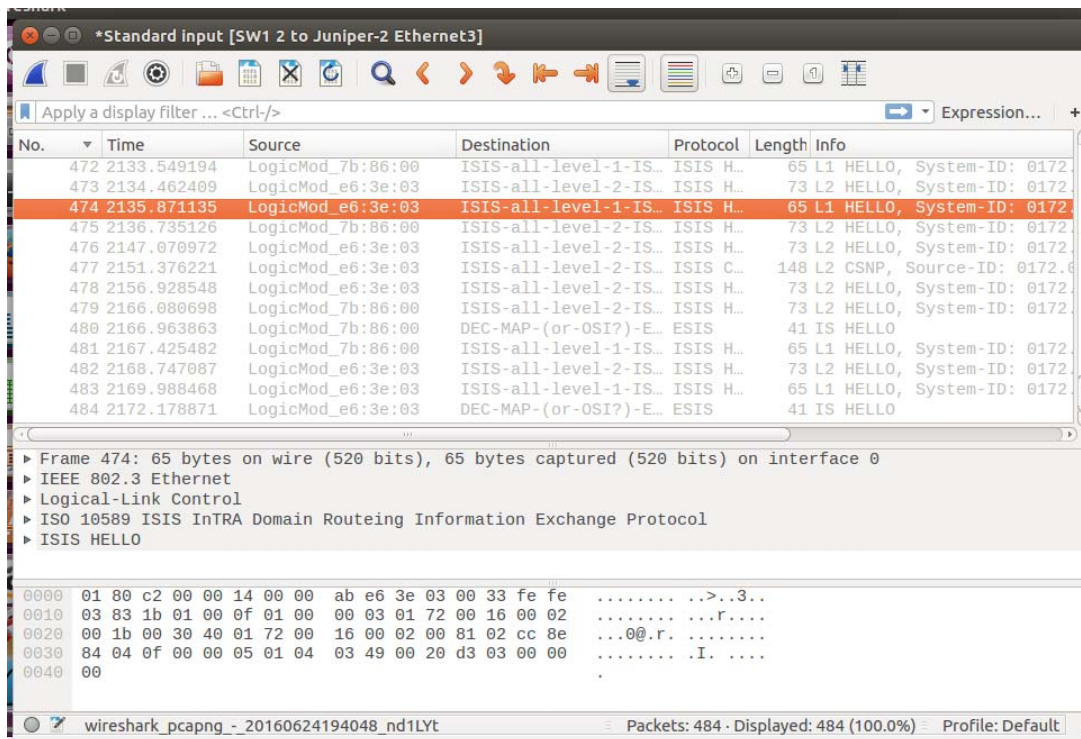


Figure 2. Hallo packets level 1

These are Hallo packets that are exchanged within an area. Their role is to exchange information about routes, inside one, specified area.

These are packets that are exchanged between different areas. Their role is ability to see routes from one area, and beyond this area.

In Figure 3 are shown Hallo ISIS packets second level.

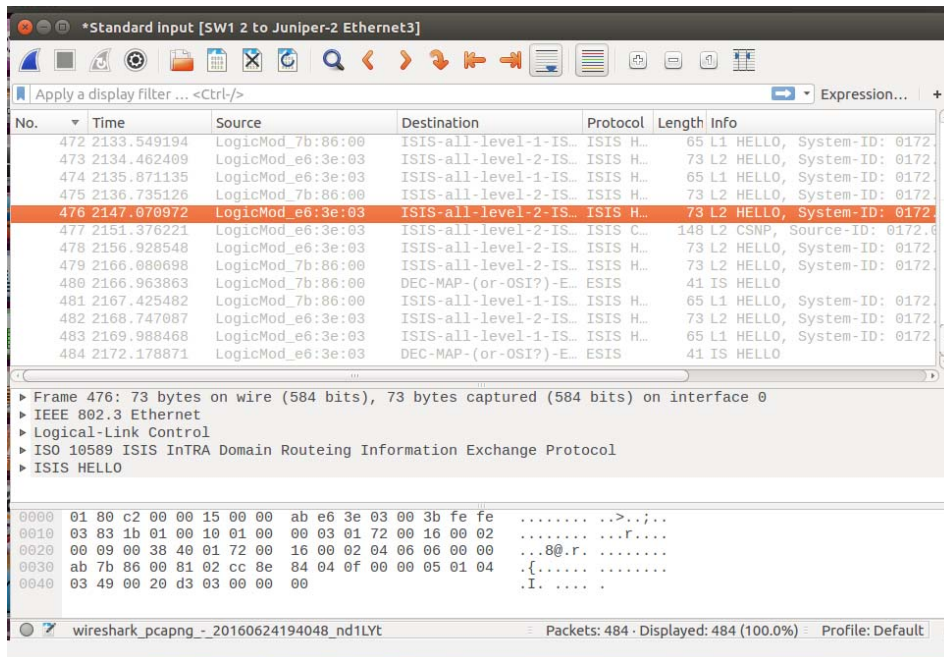


Figure 3. Hallo packets level 2

3.6. Checking network functionality

In this section, the emphasis will be on checking network functionality. Certain commands from the terminal are used for checking on certain router or VPC, which would be otherwise used to work on real routers and computers.

3.6.1. Router check

In edit mode, from the terminal, on specified router, in the case router 4 (R4), it is typed **show route**, and gotten the

printout as shown in the Figure 4.

Figure 4 representation tells us that we have routes created via the protocol IS-IS on the router 4 (R4).

Also in same mode, with command **show isis adjacency**, gotten printout is shown in Figure 5.

In the same picture (Figure 5), can be notice that the router 4 (R4) is directly connected to the router 3 (R3), via interface **em1.0**, and also that the link is active.

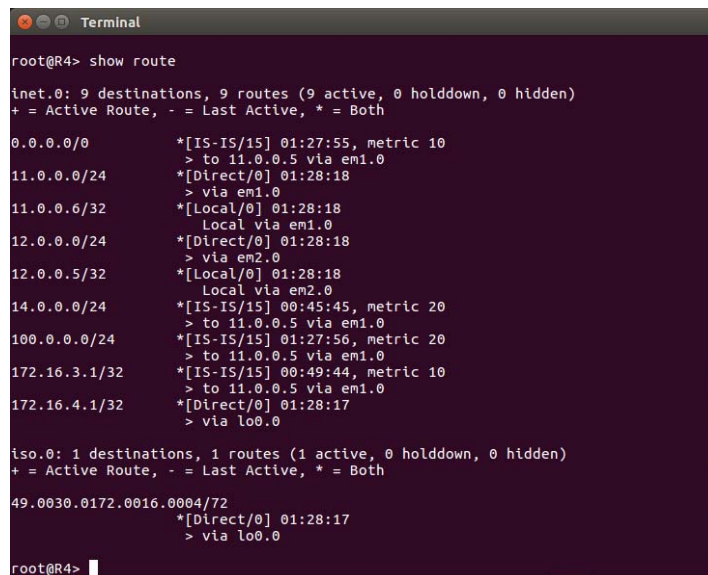


Figure 4. Shows of routes on router 4 (R4)

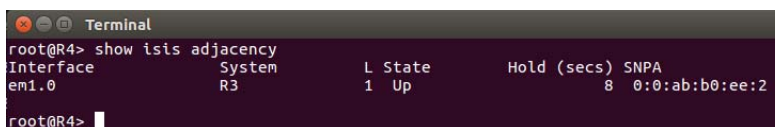


Figure 5. Shows of router 4 (R4) adjacency

By analogy, it is possible to check other routers, which is not given here due to the conciseness of the presentation.

3.6.2. Network check

To check overall functionality of the network, two VPCs are used. They are located on opposite sides of the network, so that communication between them involves

the flow of data, through almost all routers (Figure 1).

The check is also performed from the terminal of VPC using the **ping** command, followed by the ip address of the other VPC. The results obtained, when the VPC2 was pinged from VPC1 and conversely, are given in the Figure 6.

```

Terminal
PC1> ping 12.0.0.6
84 bytes from 12.0.0.6 icmp_seq=1 ttl=60 time=3.325 ms
84 bytes from 12.0.0.6 icmp_seq=2 ttl=60 time=2.964 ms
84 bytes from 12.0.0.6 icmp_seq=3 ttl=60 time=3.096 ms
84 bytes from 12.0.0.6 icmp_seq=4 ttl=60 time=3.578 ms
84 bytes from 12.0.0.6 icmp_seq=5 ttl=60 time=3.108 ms
PC1>

Terminal
PC2> ping 13.0.0.6
84 bytes from 13.0.0.6 icmp_seq=1 ttl=60 time=3.301 ms
84 bytes from 13.0.0.6 icmp_seq=2 ttl=60 time=3.169 ms
84 bytes from 13.0.0.6 icmp_seq=3 ttl=60 time=2.948 ms
84 bytes from 13.0.0.6 icmp_seq=4 ttl=60 time=3.543 ms
84 bytes from 13.0.0.6 icmp_seq=5 ttl=60 time=3.302 ms
PC2>

```

Figure 6. Pinging VPCs

Figure 6 shows that the network is functional that the routing system (routing protocol) is fully operational, since the expected answers to the given command are obtained.

4. CONCLUSION

This paper presents the possibility of performing the network simulation, in this case with IS-IS protocol, traffic flow monitoring using free software, without purchasing expensive hardware or testing on an already existing active network, where routing problem could occur due to certain settings, which could be entered into the routers in the testing process, and which could turn out to be wrong.

Upon successful completion of the test, the router parameters can be implemented on routers in the real network.

References

- [1] J. F. Kurose, K. W. Ross, "Computer Networking: A Top-Down Approach", Boston, Pearson Education Inc., 2010.
- [2] A. Baba-Ali, M. Tabassum, K. Mathew, "Performance Analysis of Interior Gateway Protocols across Different AS", Journal of Computer Science & Computational Mathematics, Volume 4 Issue 4, December 2014.
- [3] A. Sillame, A. Abo-Jreeda, M. Hasaneen, "Evaluating the Fast Rerouting with MPLS Network as a Fault tolerance Mechanism with OSPF and IS-IS routing protocols", International Conference on Advances in Electrical, Electronic and Systems Engineering (ICAEEES), 2016
- [4] A. Garrett.: "JUNOS Cookbook", O'Reilly Media, Inc., 1005 Gravenstein Highway North, Sebastopol, CA 95472, 2006.
- [5] <https://ubuntu.com>
- [6] <https://www.virtualbox.org>
- [7] <https://www.qemu.org>
- [8] <https://www.gns3.com>
- [9] <https://juniperolive.blogspot.com>
- [10] <https://www.wireshark.com>
- [11] <https://www.wireshark.com>



SIGNAL CONSTELLATION DISTORTION AND ITS IMPACT ON CUMULANT-BASED AMC PERFORMANCE

VLADIMIR D. ORLIC

Vlatacom Institute of High Technologies, Belgrade, vladimir.orlic@vlatacom.com

RADE R. BOZOVIC

Faculty of Information Technologies, Alfa BK University, Belgrade, rade.bozovic@alfa.edu.rs

Abstract: Automatic modulation classification (AMC) is of crucial importance for a variety of both military and commercial communications, where signal constellation is not a priori known at the receiver. Due to their simplicity, among many AMC algorithms developed so far, the algorithms based on higher-order cumulant structures remain competitive in terms of practical applicability and thus being in focus of authors worldwide. Still, most of research addressing these algorithms particularly is focused on only additive white Gaussian noise, multipath and interference as sources of signal degradation, and corresponding AMC performance. In this paper a set of practical sources of signal constellation distortion is analyzed in context of AMC for the first time, namely: amplitude imbalance, phase imbalance and the presence of phase jitter. Impact of these effects is presented on AMC performance in the cases of standard fourth-order cumulants, standard sixth-order cumulants and unbiased sixth-order cumulants, in noisy environment, with considerations verified via a number of Monte-Carlo simulations.

Keywords: automatic modulation classification, cumulants, phase jitter, amplitude imbalance, phase imbalance.

1. INTRODUCTION

Automatic modulation classification (AMC) has been in focus of many researchers worldwide for around three decades. Being of crucial importance for a variety of both military (electronic warfare, spectrum surveillance) and commercial applications (intelligent radio, cognitive systems, IoT), it represents an important tool for processing a priori unknown communication signal, logically placed between the points of signal detection within receiver and its further demodulation, i.e. before the extraction of the very information carried by the signal itself [1-3].

There are many AMC algorithms developed so far. Although not being very much new as a concept, due to their extreme simplicity – algorithms based on specific higher-order statistics (HOS) features of the signal, such as moments and cumulants, still remain quite competitive in terms of practical applicability, and “still be considered as state-of-the-art in AMC” [4]. Fourth-order cumulants [5,6] and sixth-order cumulants [7-9] structures are the most frequently considered for this purpose, although other HOS-based solutions can be found in literature as well, nowadays often additionally equipped with complex and powerful classifiers, like neural networks and deep learning engines [10,11].

When it comes to the issue of realistic propagation conditions in published AMC research, it can be easily concluded that mostly additive white Gaussian noise (AWGN) was considered as the source of signal degradation. In addition to AWGN, effects of multipath

propagation and interference were considered by some authors, while the structure of normalized higher-order cumulants makes them „naturally“ resistant on effects of flat fading (i.e. fixed amplitude attenuation) and fixed-value phase mismatch – which thus have no relevance for performance of corresponding AMC algorithms. Still, there is a number of sources of signal degradation, quite present in practice, which to the best of our knowledge have not been addressed in AMC research so far.

In this paper a set of practical effects of signal constellation distortion is analyzed in context of AMC, for the first time. Amplitude imbalance, phase imbalance and the presence of phase jitter [12,13] have been set up in context of modulation classification performance, in an AMC problem observed through higher-order cumulants.

2. SIGNAL CONSTELLATION DISTORTION

One typical constellation diagram of a signal modulated according to Quadrature Phase Shift Keying - QPSK scheme is presented in Fig. 1: it is characterized by identical voltage level values which represent the signal amplitudes in both I and Q branch, with fixed phase spacing between branches of 90 degrees. Therefore, the constellation diagram has the shape of a regular square, and the positions of individual symbols within this square are marked by precisely grouped constellation points. Strong shape regularity of the formed figure points to conclusion that the presented diagram represents undistorted signal. At the same time, zero dispersion of the values of individual symbols means practically no presence of noise.

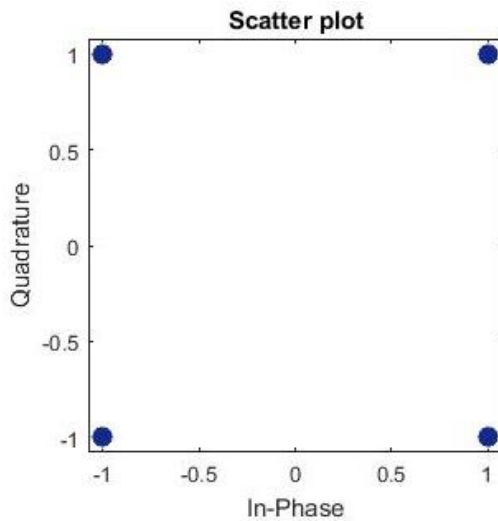


Figure 1. Ideal QPSK signal constellation diagram

Different impacts can result in disruption of the correct structure shown in Fig. 1, and based on the type of change to which the constellation diagram is exposed, the following phenomena can be distinguished:

1. Amplitude imbalance - appears as a consequence of different amplification of signal components in the I and Q branches. In the constellation diagram, amplitude imbalance is manifested by expansion of one of the components and / or simultaneous compression of the other component of the signal. The cause of this phenomenon lies in the fact that the automatic gain control (AGC) block in the receiver keeps the mean value of the signal level constant. An example of a signal constellation diagram, in which the amplitude imbalance is expressed, corresponding to the undistorted signal from Fig. 1, is shown in Fig. 2.

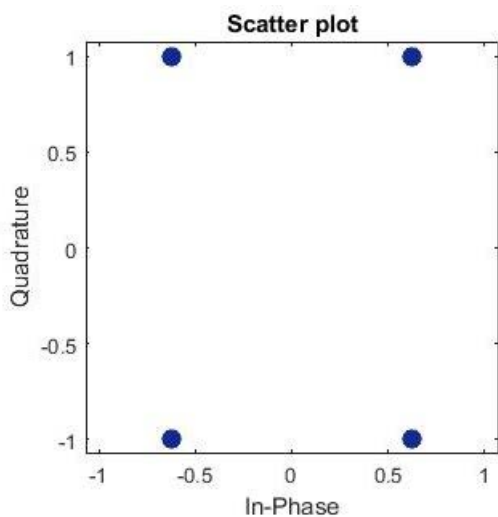


Figure 2. QPSK signal with amplitude imbalance, constellation diagram

2. Phase imbalance - represents the deviation of the angle between the I and Q components of the signal, from the (ideal) value of 90 degrees. On the constellation diagram, it is manifested through the loss of orthogonality of the figure, i.e. it can be noticed that points of the constellation are not simultaneously parallel with both x and y axes of

the diagram. The occurrence of phase imbalance comes as a direct consequence of the imperfection of the phase shifter of the I/Q modulator. An example of signal in which a phase imbalance is present, corresponding with undistorted signal from Fig. 1, is shown in Fig. 3.

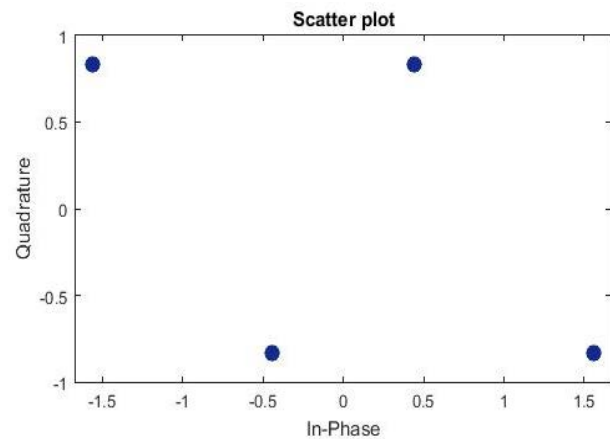


Figure 3. QPSK signal with phase imbalance, constellation diagram

3. Phase jitter - which arises as a consequence of the action of transponders present on the signal route, or within the I/Q modulators. It can also come as a result of inadequate regeneration of the carrier within the receiver. Unlike phase imbalance, this phenomenon captures the signal in both branches equally, and is manifested through the occurrence of rotation of constellation points around the center of the IQ plane. An example of this phenomenon is shown in Fig. 4.

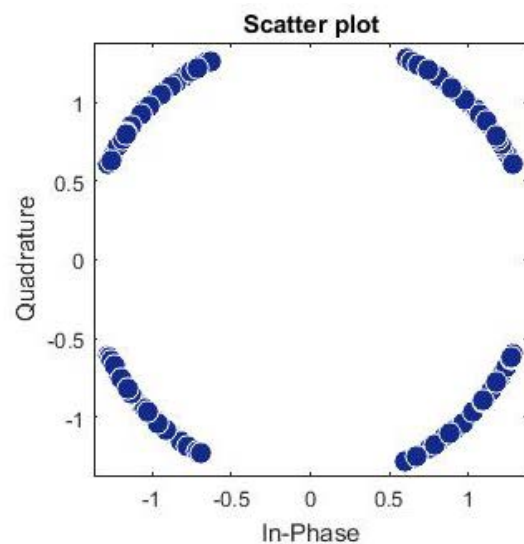


Figure 4. QPSK signal with strong phase jitter, constellation diagram

In addition to the mentioned above, in practice there is also distortion phenomena like: amplitude error (free deviation of symbol amplitudes from their nominal values), phase error (rotation of all constellation points around the center for some fixed, the same angle value), DC offset (representing the translation of the diagram points for an identical, fixed vector value in the IQ plane), etc. Even more, in practice, it is realistic to expect even

the combined action of several different sources of signal degradation, simultaneously, which potentially affects the work of signal processing blocks within the receiver, thus also making an impact on AMC algorithms performances.

3. CUMULANT-BASED AUTOMATIC MODULATION CLASSIFICATION

The received signal sequence $y(n)$, corrupted by AWGN during propagation, can be represented by:

$$y(n) = x(n) + g(n), \quad (1)$$

with $x(n)$ standing for transmitted symbols (of an unknown modulation), and $g(n)$, representing zero-mean AWGN with variance of σ_g^2 . For zero-mean random variable x , associated with transmitted data sequence $x(n)$, the second-order cumulant is:

$$C_{21,x} = E(|x|^2). \quad (2)$$

where $E(\cdot)$ represents a mathematical expectation, realized as an average value over observed signal samples. The fourth-order cumulant and the normalized fourth-order cumulant of the same variable are given as:

$$C_{42,x} = E(|x^4|) - |E(x^2)|^2 - 2E^2(|x^2|), \quad (3)$$

$$\hat{C}_{42,x} = C_{42,x} / (C_{21,x})^2. \quad (4)$$

The standard (classical) sixth-order cumulant and its corresponding normalized value of the same random variable x are given as:

$$C_{63,x} = E(|x|^6) - 9E(|x|^4)E(|x|^2) + 12|E(x^2)|^2 E(|x|^2) + 12E^3(|x|^2), \quad (4)$$

$$\hat{C}_{63,x} = C_{63,x} / (C_{21,x})^3. \quad (5)$$

Apart from standard, the following formulas are used for general and unbiased sixth order cumulant [7], along with its corresponding normalized value:

$$C_{63,x_UNB} = E(|x|^6) - 9E(|x|^4)E(|x|^2) + 18|E(x^2)|^2 E(|x|^2) - 6|E(x^2)| E(x^2|x^2) + 12E^3(|x|^2), \quad (6)$$

$$\hat{C}_{63,x_UNB} = C_{63,x_UNB} / (C_{21,x})^3. \quad (7)$$

For random variable y associated with received sequence $y(n)$, normalized higher-order cumulants can be expressed in the following manner:

$$\hat{C}_{42,y} = \frac{C_{42,y}}{(C_{21,y} - \sigma_g^2)^2}, \quad (8)$$

$$\hat{C}_{63,y} = \frac{C_{63,y}}{(C_{21,y} - \sigma_g^2)^3}, \quad (9)$$

$$\hat{C}_{63,x_UNB} = \frac{C_{63,y_UNB}}{(C_{21,y} - \sigma_g^2)^3}. \quad (10)$$

Equations (8) - (10) describe the AMC execution within the receiver. While noise power is commonly considered to be known, it was shown that the same can be easily estimated also, without relevant loss in performance [14].

The decision-making process for modulation recognition is based on a comparison of obtained values of normalized cumulant estimates with predefined thresholds. It was shown, on the basis of intensive computer simulations, that optimal comparison threshold values are positioned at the middle of intervals between expected (theoretical) values corresponding with particular modulation formats [15].

While cumulant's estimates of complex constellations are strictly unbiased, lower Signal-to-Noise (SNR) values introduce stronger bias for real signal's cumulant's estimates, for standard sixth-order cumulant structure, specially. Some theoretical values for normalized cumulants' values, for BPSK and QPSK constellations, are shown in Table 1.

Table 1. Theoretical values of normalized cumulants

Constellation	\hat{C}_{42}	\hat{C}_{63}	\hat{C}_{63_UNB}
BPSK	-2.0000	16.0000	16.0000
QPSK	-1.0000	4.0000	4.0000

4. SIMULATIONS

In channel with AWGN only, distinguishing BPSK from QPSK signals is reported to be superior with standard sixth-order cumulants, when compared to fourth-order and unbiased sixth-order cumulants. As previous researches showed, this comes due to a strong bias in \hat{C}_{63} values of BPSK signal, representing an interesting specific phenomena present in standard sixth-order cumulants only. For the basic reference, simulation with 2,000 Monte Carlo experiments is carried out, $N=250$ symbols are generated from the set of signal constellations {BPSK, QPSK} in each trial, with noise variance considered to be known, and probability of correct classification values P_{CC} for all considered AMC algorithms was calculated in a wide range of SNR values, from -10dB to 20dB. Results obtained from these simulations are shown in Fig. 5.

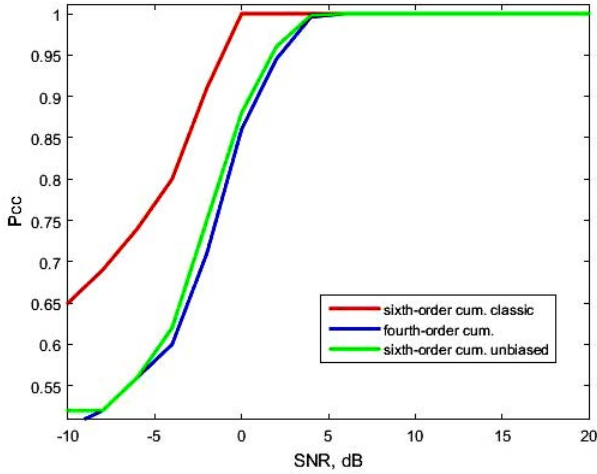


Figure 5. Correct classification probability in {BPSK, QPSK} scenario, $N=250$, AWGN channel

4.1. Amplitude imbalance

In order to evaluate classification performance in the presence of amplitude imbalance, corresponding distortion was introduced into the samples of $x(n)$ in eq. (1): like in a manner shown in Fig. 2, the I component of each sample was limited on amplitude value of $(1-a)$, $a < 1$, while Q component preserved its unit value. As the boundary case, scenario with $a_{\text{lim}} = 0.41485$ was recognized, when $P_{CC} = 0.75$ for all AMC algorithms in noiseless conditions. Even the slight introduction of noise further has the impact on performance of standard sixth-order cumulants, since its specific bias in this boundary scenario reflects negatively on decision making. Simulations were carried out under the same conditions as presented at the beginning of this section, now with amplitude imbalance a_{lim} introduced, and resulting values of P_{CC} are presented in Fig. 6. For comparison of effects, scenarios with less rigid values of $a = 0.5 * a_{\text{lim}}$ and $a = 0.75 * a_{\text{lim}}$ are included in the same figure.

From Fig. 6 it can be noticed that strong amplitude imbalance a_{lim} , from the point of AMC, introduces more “BPSK-like” properties into the imbalanced QPSK signal, causing the bias of \hat{C}_{63} to start reflecting on QPSK signals also, thus significantly degrading the performance of this particular algorithm. On the other side, performance of \hat{C}_{42} and \hat{C}_{63_UNB} , although degraded by amplitude imbalance a_{lim} , remains stable. For SNR values lower than -2dB approximately, the effect of noise becomes dominant. While small imbalance $a = 0.5 * a_{\text{lim}}$ introduces almost no degradation in performance of algorithms, somewhere around the imbalance value of $a = 0.75 * a_{\text{lim}}$, performance of all three considered cumulant structures becomes approximately equal, until the point of SNR when noise effect becomes dominant.

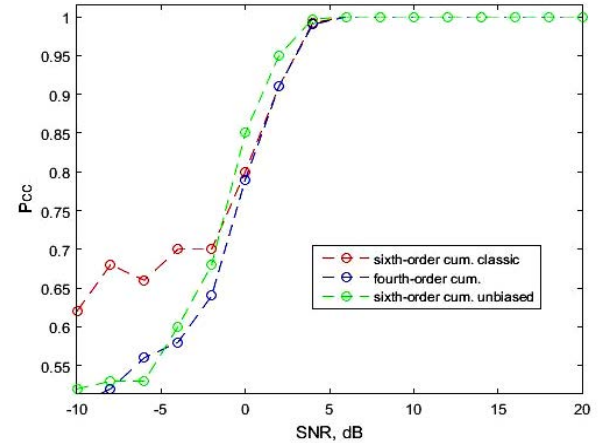
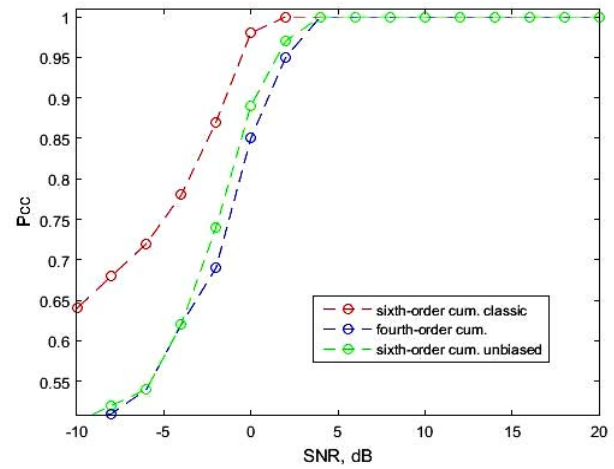
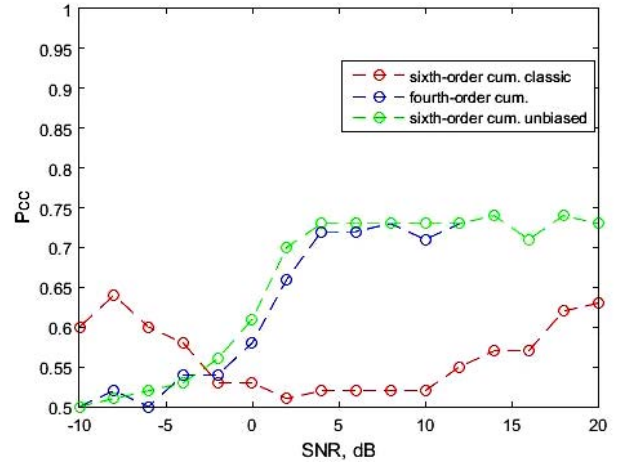


Figure 6. Correct classification probability in {BPSK, QPSK} scenario, $N=250$, AWGN channel with amplitude imbalance a_{lim} (top), $a = 0.5 * a_{\text{lim}}$ (middle) and $a = 0.75 * a_{\text{lim}}$ (bottom)

4.2. Phase imbalance

As illustrated in Fig. 3, phase imbalance was introduced via the angle shift of α between I and Q components of signal samples $x(n)$ in eq. (1), as a measure of violation of two branches’ mutual orthogonality. As the boundary – case, scenario with $\alpha_{\text{lim}} = 3\pi/8$ was recognized, since then P_{CC} becomes < 1 for standard sixth-order cumulants

even in noiseless channel conditions. Simulations were carried out with phase imbalance α_{lim} introduced, and resulting values of P_{CC} are presented in Fig. 7. For comparison, scenario with $\alpha = 0.5 * \alpha_{lim}$ is also included.

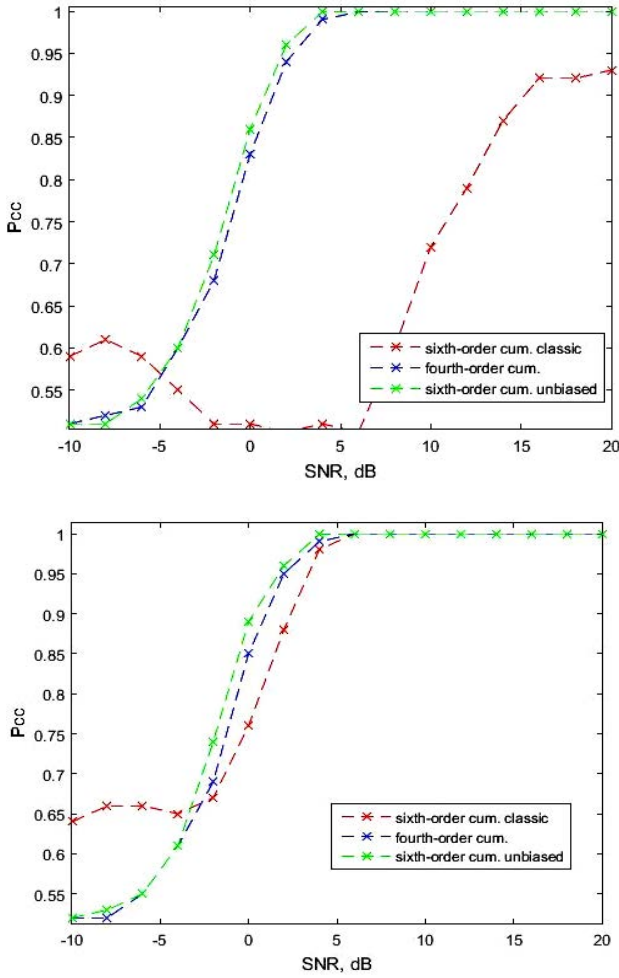


Figure 7. Correct classification probability in {BPSK, QPSK} scenario, $N=250$, AWGN channel with phase imbalance α_{lim} (top) and $\alpha = 0.5 * \alpha_{lim}$ (bottom)

From Fig. 7 it can be noted that strong phase imbalance α_{lim} , similarly like strong amplitude imbalance, makes significant impact on properties of the imbalanced QPSK signal, causing the bias of \hat{C}_{63} to start reflecting on QPSK signals and violating the decision making whose decision thresholds are derived from theoretical cumlants' values, thus significantly degrading the performance of standard sixth-order cumulants algorithm. On the other side, it is very much interesting to note that performance of \hat{C}_{42} and \hat{C}_{63_UNB} seems not affected by phase imbalance at all, and keeps the value of $P_{CC} \approx 1$ for higher values of SNR. Again, for SNR values lower than -2dB approximately, the effect of noise becomes dominant, in comparison with effects of phase imbalance. Lighter phase imbalance $\alpha = 0.5 * \alpha_{lim}$, as expected, introduces almost no degradation in performance of two unbiased algorithms, while this phase imbalance value approximately brings the AMC algorithm based on standard (i.e. biased) sixth-

order cumulants to the same order of P_{CC} values, making the performances of all three considered cumulant structures (more or less) equal, down to the point when noise effect becomes dominant.

Obtained results under amplitude and phase imbalance are potentially important since, to the best of our knowledge, they represent the first examples published so far where classification in {BPSK, QPSK} scenario shows as being not superior with standard (biased) sixth-order cumulants.

4.3. Phase jitter

The presence of phase jitter was introduced into the $x(n)$ samples via the random values of phase offset per each particular sample, generated with equal probability from the interval of angles $[-\varphi, \varphi]$. Here as the boundary case, value of $\varphi_{lim} = 2\pi/9$ was selected, when $P_{CC} = 0.75$ for all observed AMC algorithms in noiseless conditions. Simulations were executed for phase jitter under limits of φ_{lim} , with resulting values of P_{CC} presented in Fig. 8, along with results achieved in scenario with $\varphi = 0.5 * \varphi_{lim}$ included in the same figure.

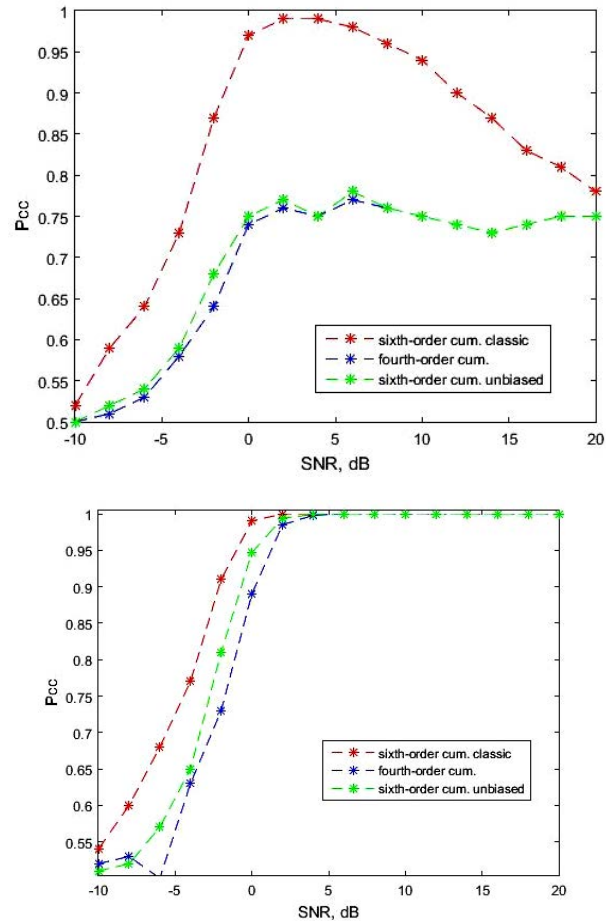


Figure 8. Correct classification probability in {BPSK, QPSK} scenario, $N=250$, AWGN channel with phase jitter under φ_{lim} (top) and $\varphi = 0.5 * \varphi_{lim}$ (bottom)

In contrary to effects of amplitude imbalance, from Fig. 8 it can be noted that strong phase jitter φ_{lim} introduces

more “QPSK-like” properties to the imbalanced BPSK signal, which then gets compensated by the bias of \hat{C}_{63} with moderate SNR, in manner contributing to successful classification. Performance of \hat{C}_{42} and \hat{C}_{63_UNB} , both degraded by presence of phase jitter, remains stabile, while smaller jitter limits of $\varphi = 0.5 * \varphi_{lim}$ introduce only slight loss in performance of all considered AMC algorithms, down to the point when noise effect becomes dominant.

4.4. Combined distortion

Finally, simulations have been repeated for scenario of combined joint effect of all previously discussed sources of signal degradation: with samples $x(n)$ corrupted by amplitude imbalance with parameter $a = 0.75 * a_{lim}$, phase imbalance of $\alpha = 0.5 * \alpha_{lim}$ and phase jitter within the boundaries $[-\varphi, \varphi], \varphi = 0.5 * \varphi_{lim}$, simultaneously. As an illustration of this joint degradation effect, resulting QPSK signal is presented in Fig. 9, while classification performance of considered cumulants-based AMC algorithms is given in Fig. 10.

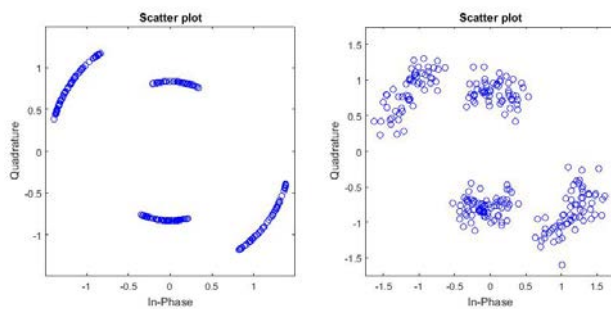


Figure 9. QPSK signal constellation diagram in combined presence of phase jitter, amplitude and phase imbalance: without noise (left) and at SNR=20dB (right)

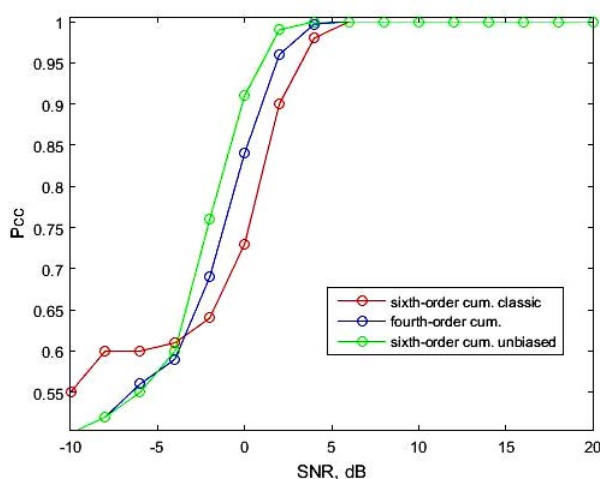


Figure 10. Correct classification probability in {BPSK, QPSK} scenario, $N=250$, AWGN channel with amplitude imbalance $a = 0.75 * a_{lim}$, phase imbalance $\alpha = 0.5 * \alpha_{lim}$ and phase jitter under $\varphi = 0.5 * \varphi_{lim}$

Simulations show that effects of amplitude imbalance

and, especially, phase imbalance, dominate over the impact of phase jitter in overall performance, for combined presence of different sources of signal degradation. Bias introduced for BPSK signals by classical sixth-order cumulants-based AMC algorithm no longer brings outstanding success in classification. Even in contrary: it accelerates the effects of imbalance, resulting with lower performances in terms of AMC for standard sixth-order cumulants, when compared with fourth-order and unbiased sixth-order cumulants used as features of interest.

5. CONCLUSION

In this paper well known AMC algorithms based on higher-order cumulants are observed in context of various effects of signal degradation, and their performances were evaluated in intensive computer simulations. Several specific effects of degradation were explained, with boundary – value parameters thereof reported, in an AMC application. It was shown that presence of amplitude and phase imbalance cannot be successfully compensated with bias introduced by standard sixth-order cumulants, which still works well under the terms of phase jitter. Nevertheless, in scenario with combined presence of various signal degradation sources, unbiased (fourth and sixth-order) cumulants-based AMC algorithms show as more reliable and better performed, which makes them a solution of choice, for any application where presence of discussed signal degradation sources seems unavoidable.

References

- [1] DOBRE,O.A.: *Signal identification for emerging intelligent radios: Classical problems and new challenges*, IEEE Instrumentation & Measurement Magazine, 18(2) (2015) 11-18.
- [2] ELDERMERDASH,Y.A., DOBRE,O.A., ONER,M.: *Signal identification for multiple-antenna wireless systems: Achievements and challenges*, IEEE Commun. Surv. Tutor., 18(3) (2016) 1524–1551.
- [3] PAJIC,M.S., VEINOVIC,M., PERIC,M. et al.: *Modulation order reduction method for improving the performance of AMC algorithm based on sixth order cumulants*, IEEE Access, 8 (2020) 106386-106394.
- [4] PENNACCHIO,A.A, LUCTOSA da COSTA, J.P.C., BORDINI, V. M. et al.: *Eigenfilter-based automatic modulation classification with offsets for distributed antenna systems*, Simposio Brasileiro de telecomunicacoes e processamento, Sinais, Brasil, (2016) 260-261.
- [5] SWAMI,A., SADLER,B.M.: *Hierarchical digital modulation classification using cumulants*, IEEE Trans. Commun., 48(3) (2000) 416-429.
- [6] WU,H., SAQUIB,M., YUN,Z.: *Novel automatic modulation classification using cumulant features for communications via multipath channels*, IEEE Trans. Wirel. Commun., 7(8) (2008) 3098-3105.
- [7] SIMIC,M., STANKOVIC,M., ORLIC,V.D.: *Automatic modulation classification of real signals in AWGN channel based on sixth order cumulants*,

- Radioengineering, 30(1) (2021) 204-214.
- [8] PAJIC,M.S., VEINOVIC,M., ORLIC, V.D.: *Complex signal constellations in cumulants-based AMC: Statistics and performance*, Telfor Journal, 13(2) (2021) 63-68.
- [9] BOZOVIC,R.R., ORLIC,V.D.: *Estimation of bias in numerical values of normalized sixth-order cumulants' structures for various signal constellations*, 2021 International Conference on Computational Performance Evaluation (ComPE), (2021) 410-414.
- [10] LI,X., DONG,F., ZHANG,S. et al.: *A survey on deep learning techniques in wireless signal recognition*, Wireless Comm. and Mobile Computing, (2019).
- [11] MENG,F., CHEN,P., WU,L., et al.: *Automatic modulation classification: A deep learning enabled approach*, IEEE Transactions on Vehicular Technology, 67(11) (2018) 10760-10772.
- [12] SIMROCK,S., GENG,Z.: *RF Detection and Actuation*. In: *Low-Level Radio Frequency Systems. Particle Acceleration and Detection*, Springer, Cham, (2022) 149-182.
- [13] ERGEN,M.: *Basics of cellular communication*. In *Mobile Broadband*, Springer, Boston, MA, (2009) 19-65.
- [14] NERANDZIC,M., BOZOVIC,R.R., ORLIC,V.D.: *Impact of AWGN estimation on classification performance of AMC algorithms based on higher order cumulants*, 2021 29th Telecommunications Forum (TELFOR), (2021) 1-4.
- [15] ORLIC,V.D., DUKIC,M.L.: *Setting the optimal decision threshold and analysis of impact of sample size on automatic modulation classification based on sixth-order cumulants*. In Proc. Int. Sci. Conf. Defensive Technol. OTEH, (2012) 511-515.



DESIGNING THE PORTABLE BIOMETRIC STATION FOR MILITARY APPLICATION

DEJAN ĆIPROVSKI

Metropolitan University, Vlatacom Institute, Belgrade, dejan.ciprovski@vlatacom.com

BOŠKO BOŽILOVIĆ

Vlatacom Institute, Belgrade, bosko@vlatacom.com

SAŠA BOŽINOVIĆ

Vlatacom Institute, Belgrade, sasa.bozinovic@vlatacom.com

DRAGAN DOMAZET

Metropolitan University, Belgrade, dragan.domazet@metropolitan.ac.rs

Abstract: Identification and verification of authorised users in a military context can sometimes be a matter of life or death and it is therefore essential for systems to be accurate, reliable and robust. In order to fulfill requirements for secure collection of military personnel biometric data for an African country, Vlatacom Institute has developed the Portable Biometric Station (PBS). Portable Biometric Station consists of rugged case with integrated devices for acquiring biometric data and a laptop which runs the Enrolment Station software application. The military application of PBS stress its hardware ruggedisation and software reliability. This paper describes in details implemented software application that collects data such as facial image, digital signature as well as fingerprints. The PBS is easy to handle, and portable which means it can be moved easily to the different remote locations. PBS can operate in both online and offline modes. The data collected during the enrolment process are, uploaded to the server application in order, their validity to be approved/rejected. The acquired data, later, can be used for military base access control, soldier identity verification, and/or in production of the officer electronic identification (eID) cards.

Keywords: military, portable biometric station, vlatacom, enrolment, software.

1. INTRODUCTION

Typically utilized in security protocols, biometric techniques can ascertain the identity of individuals via the examination of specific physiological and behavioral identifiers. The six most commonly used forensic biometric identifiers are finger, face, voice, hand geometry, iris, and signature. These biometrics are measurable, unique characteristics that are used to identify both living and/or deceased individuals [1].

Many organizations, ranging from small companies to governmental and international institutions, may run some kind of electronic personal identification system, based on human biometric data. Usually, the organisation issues a document containing biometric data to the person and keeps track of that document in its biometric information system.

A biometric system can be used for verification or identification. Verification refers to validating a person's identity by comparing the captured biometric data with their own biometric template(s) stored in the system database [2]. This is a one-to-one process that answers the question of whether the person concerned is who they claim to be. Identification refers to recognizing an individual by searching the templates of all the users in the database for a match. Identification is a one-to-many

comparison to establish an individual's identity without the person concerned having to claim an identity.

2. RELEATED STUDIES

The term biometrics strictly relates to the statistical analysis of biological phenomena and measurements, but has become widely accepted within the security profession to describe technologies used for personal identity verification [3].

The conflicts in Iraq and Afghanistan have prompted the widespread use of biometrics in the field. In many circumstances, accurate identification becomes a matter of life or death [4]. The first large-scale use in these theatres was in 2004, at Falluja, Anbar Province. A major stronghold for insurgents and the scene of some the fiercest fighting in the whole campaign, Falluja was surrounded and contained by the US Marine Corps. No-one was allowed in or out without having their biometric details captured.

The use of biometrics was given even greater impetus later that year when an Iraqi suicide bomber gained access to a US base in Mosul and killed 22 personnel. This spurred greater efforts at positively proving the identities of anyone gaining access to US facilities, which resulted in the Biometric Identification Systems for Access

(BISA). This provided every foreign national who needed to enter a US military facility with a biometric ID card. The data was checked against two databases, Automated Biometric Identification System (ABIS) and the FBI's Integrated Automated Fingerprint Identification System (IAFIS).

The value of biometrics became most readily apparent in April 2011 when 475 prisoners tunneled their way out of the Saraposa prison in Kandahar, Afghanistan. Around 35 escapees were back in jail within a few days by being identified at checkpoints, routine traffic stops and borders. Less dramatically, but perhaps more significantly, some 20-25 suspects are apprehended each week as a result of routine biometric checks.

While much biometric research involves authenticating the identity of living individuals by comparing them with who they claim to be, postmortem applications of biometrics often involve the identification of an unknown individual [5]. Therefore, postmortem biometrics such as fingerprints, irises, and facial recognition may be a useful approach toward establishing a positive identification of unknown human remains in forensic settings. With improved digital imaging capabilities that have led to more efficient capturing of biometric data, along with the increased use of biometrics as part of identity profiles, it is becoming more practical to consider these data as part of the biological profile of human remains.

In December 2001, U.S. military forces detained Mohamed Al Kahtani as an enemy combatant on the field of battle in Southwest Asia. During repeated interrogations Kahtani denied being a combatant and offered an innocent explanation for his presence in the region. While Kahtani was in military custody, the FBI team fingerprinted him in much the same way law-enforcement officials routinely fingerprint criminal suspects in the United States. They took Kahtani's 10 "rolled" fingerprints. This collection of biometric data eventually led U.S. investigators to believe Kahtani was the missing 20th hijacker in the terrorist attacks of 11 September 2001 [6].

3. PORTABLE BIOMETRIC STATION

The Vlatacom product, Portable Biometric Station (PBS) enables government agencies to implement large-scale identity management, including biometric data, to enhance process security and protect the identity of each registered individual.

The authority performs biometric data acquisition on easily accessible sites, where the applicants apply for a personal identity documents. The collected data should finally end up at the central site, where the main databases and servers reside.

Enrolment Station is designed to collect the data, create the electronic application record and send it to a central location (online mode), or store them on the local storage device (offline mode). Upon successful submission of the application record, processing of the applicant is finished and the new enrolment process can proceed. Enrolment Station supports submission of application records to

several kinds of storages, but in most cases, this storage is local enrolment server, residing on the same site as the Enrolment Station, often in the same local area network. Application records can be stored locally so that it can be transferred to the central location when it is convenient.

3.1. Components of the Portable Biometric Station

The PBS integrates all devices needed for the enrolment process into the rugged case. It includes fingerprint scanner, camera for capturing facial images, signature pad, laptop which runs the Enrolment Station application software, battery for independent power supply, cables and charges for battery and laptop.

Ruggedized case provides durable protection from impacts and environmental factors for the internal devices.

3.2. Components of the Enrolment Station

The Enrolment Station is a client-server application, where the server part runs all necessary hardware devices for capturing biometric data and the client part controls the workflow of the enrolment process, prepares the application records and submits it to the enrolment server or stores them locally.

The Enrolment Station consists of two applications. The first application is the Biometric Service Station (BSS) which initializes and runs all hardware components needed for acquiring applicant's data.

The other one is Enrolment Control Station (ECS) that is front-end application which controls the enrolment process.

3.3. Preparing Portable Biometric Station for Use

Rugged case and interior design provide protection and shock absorption to keep internal components safe from impacts and environmental factors. Portable Biometric Station is equipped with laptop, signature pad, fingerprint scanner and camera. Battery provides up to 8 hours autonomy for Portable Biometric station. It is equipped with power bar with built-in surge protection for battery and laptop charger.

Closed case ready for transport is shown in the Figure 1.



Figure 1. Closed PBS



Figure 2. PBS ready for Use

Devices integrated into the Portable Biometric Station are shown in the Figure 3:

1. Upper additional lighting for taking facial images
2. Camera for taking facial images
3. Lower additional lighting for taking facial images
4. Fingerprint scanner
5. Passive pen for signature pad
6. Signature pad



Figure 3. PBS components

4. ENROLMENT STATION APPLICATION

The Enrolment Station is an application software capable of acquiring biometric, and demographic data, for each person that is going to be introduced in the system. In the context of biometric system and Enrolment Station, the person whose biometric and other data are captured is an applicant, and in the forthcoming text, this person shall be referred as such.

Basically, there are two kinds of enrolment processes, attended and unattended. Attended process requires a trained officer who is going to guide the applicant through the process and who will guarantee that the process is performed correctly. Unattended process is self service

process, where the applicant follows the instructions presented on the visual interface and all the actions are performed in an automated manner. The Enrolment Station operates in attended way. In this paper, the person who is leading attended enrolment process will be referred as the enrolment officer.

4.1. Starting the application

For the operation of the Enrolment Station, few preconditions must be met. After the Portable Biometric Station is prepared for use as described in the previous chapter, the laptop battery has to be charged and the Windows operating system on the laptop should be ready for use. Next step is starting the Biometric Service Station application. Biometric Service Station is application which configures and initialize all devices for acquiring biometric data from applicant. Biometric Service Station is running in the Console mode.

After the Biometric Service Station is successfully started, it is ready to receive requests from the Enrolment Control Station. Next step is to start the Enrolment Control Station.

When the connection between Enrolment Control Station and Biometric Service station is established, the Enrolment Control Station is started and application is ready for use.

4.2. Enrolment Process Workflow

Acquiring biometric and other data necessary for introducing the applicant to the biometric information system runs in a pre-determined workflow. The enrolment process workflow consists of several steps performed in a single pass. The enrolment officer can go back and forth among steps in order to create enrolment record. What must be fulfilled in order to create enrolment record is that each step is completed correctly and without errors. The workflow can be cancelled at any time, but with the loss of previously collected data. The workflow steps are:

- General data step
- Facial image data step
- Signature data step
- Fingerprint data step

Passing from one step to another will not lead to the loss of the previously captured data. After successful submission of the record, all captured data are cleared and the first step is displayed again, ready for the next applicant's enrolment process.

4.2.1. General data step

General data step provides form for the enrolment officer to enter demographic and additional data. Step with demographic data is shown in the Figure 4.

Every piece of demographic data has its graphical field on the screen for entering the actual data. The type of the field depends on the type of the data.

Figure 4. General data step window

Simple textual fields, where the officer can type in arbitrary text are aimed for entering following data:

- First Name
- Last Name
- Date of Birth
- Place of Birth
- Personal ID Number
- Blood type
- Height
- Color of eyes
- Address
- Phone number

Fields containing lists with predefined values of the data that can be selected are aimed for entering following data:

- Blood type
- Color of eyes

There is also field for entering only date:

- Date of Birth

All of the fields are marked as mandatory and they are in red color. That means that field must be filled before submitting enrolment record. When the enrolment officer enters correct value in the field which is marked as red, the field will change its color to black.

4.2.2. Facial image step

Facial image step screen is shown in the Figure 5. This screen presents live preview from the camera on the left

side of screen. The enrolment officer is able to see the position and expression of applicant placed in front of the camera and guide him/her to the correct position. Live preview is started and enrolment officer captures the facial image of the applicant. Live preview is stopped and captured image of applicant is displayed on the right side of the screen.

The software then tries to automatically crop the facial image according to the standards and if succeeds the cropped photo is displayed on the screen and the corresponding value is shown below the picture representing the quality of the image. If the automatically crop fails then the enrolment officer can do it manually using the green rectangle shown on the screen and adjusting the appropriate size.

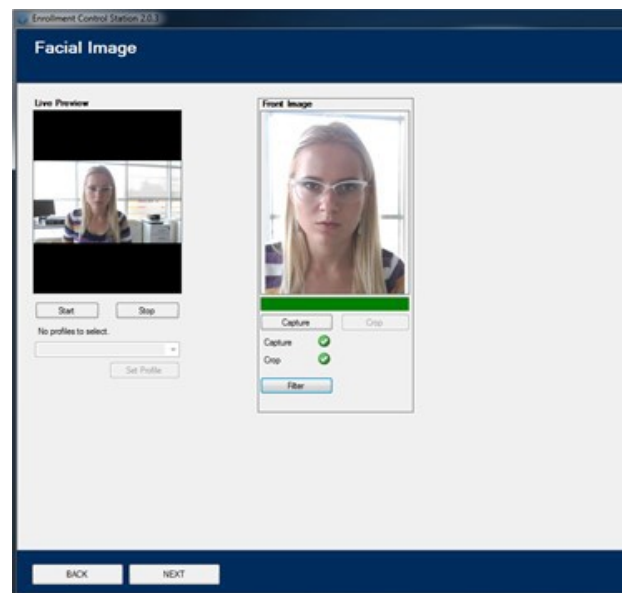


Figure 5. Facial image step window

After cropping the facial image, the enrolment officer optionally can select 1 out of 10 available filters. Each filter contains different values of brightness and contrast (Figure 6).

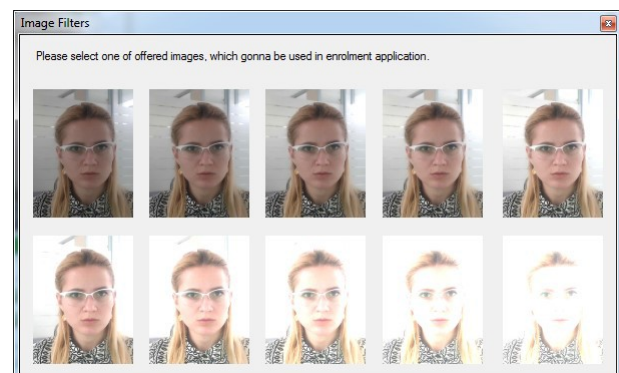


Figure 6. Available Image filters

4.2.3. Signature step

When Signature step is shown on the screen, the signature pad device is automatically set to capture applicant's signature. The enrolment officer should instruct the

applicant to sign on the pad, and when the process is done, the officer should capture the signature. The signature image is displayed on the screen (Figure 7).



Figure 7. Available step window

4.2.4. Fingerprint step

Fingerprints are captured using the fingerprint scanner. There are numerous types of scanners. The one used on the Portable Biometric Station provides capturing multiple fingerprints simultaneously. Left little finger, ring finger, middle finger and index finger are all together make the left slap and, accordingly, the same fingers of the right hand make the right slap. Both thumbs together are thumbs slap.



Figure 8. Fingerprint step window

To scan a slap, the officer should guide the applicant to put the fingers correctly on the scanner. First, the officer should perform the action for capturing the slap image. When the scanner is ready for scanning the applicant should put its fingers on the scanning area. After a few moments, slap image is displayed in the corresponding image box. The software automatically segments slap images extracting fingerprint images of each of the fingers and determines the quality of the images. This quality is important because the higher the quality is, the more accurate results of the later matching are. If the quality is above predefined threshold, the fingerprint is accepted. The slap segmentation and quality assessment are in progress after the slap image is displayed and the officer should wait for the results. Once the results are ready, each segmented fingerprint is displayed on corresponding image box below the slap image and the quality level is displayed.

If the quality of each finger is good enough the background of the quality result is green. Otherwise, the dialog with info message will be displayed and officer should repeat capturing procedure. Capturing the slap fingerprint image can be repeated as many times as

needed in order to get a good quality of the fingerprints. Below the fingerprint image box there are additional information about the fingerprints which are requested by the enrolment process.

Applicant can have some of the fingers missing, or temporarily unavailable for scanning. In that case the exemptions have to be assigned for each unavailable fingerprint with the reason of exemption.

4.2.5. Submitting enrolment record

After all data are acquired, enrolment application record is ready to be submitted. Before the enrolment officer submits enrolment record, completeness and correctness of the data should be checked, especially the demographic data since typographic mistakes are very common in this case.

After the process is successfully submitted, officer is presented with confirmation window that contains the application number assigned to the submitted record, which can be used in searching for the application across the system (Figure 9). After the process is submitted, the enrolment data are cleared and the first step is displayed ready for the new enrolment process.

If submission fails, message is displayed informing about the failure and the reason that caused it.

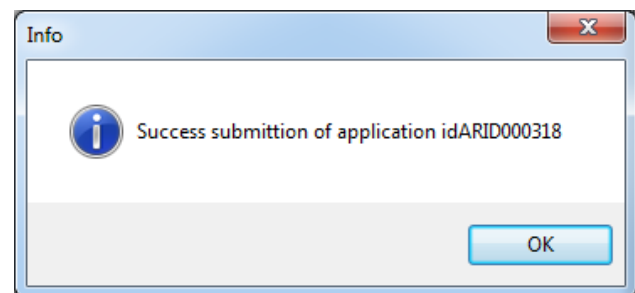


Figure 9. Submit done

4.2.6. Cancelling the enrolment process

The current enrolment process of an applicant can be cancelled at any time but any previously captured data will be lost. If the officer chooses to cancel the process, for any reason, all the data previously acquired are deleted.

5. PORTABLE BIOMETRIC STATION UPGRADES

The acquired data can be used for soldier identification system using the Automated Biometric Identification System (ABIS). The ABIS is a highly specialized system for identification which compares templates generated from probe biometric data (raw biometric data acquired from a person or another source) with templates of previously acquired biometric data stored in the database. Biometric modalities used for comparison can be physical, such as facial, iris, fingerprint, and hand geometry; or behavioral like gait, keystroke, signature, etc. Some modalities, like the voice, can be considered



INTERCEPT PROBABILITY ANALYSIS OF WIRELESS SENSOR NETWORKS WITH OPTIMAL SENSOR SCHEDULING

ALEKSANDRA S. PANAJOTOVIĆ

University of Niš, Faculty of Electronic Engineering, Niš, aleksandra.panajotovic@elfak.ni.ac.rs

DEJAN N. MILIĆ

University of Niš, Faculty of Electronic Engineering, Niš, dejan.milic@elfak.ni.ac.rs

IVICA B. MARJANOVIĆ

Republic of Serbia Ministry of Defense, Belgrade, ivica.marjanovic@mod.gov.rs

JELENA A. ANASTASOV

University of Niš, Faculty of Electronic Engineering, Niš, jelena.anastasov@elfak.ni.ac.rs

NIKOLA M. SEKULOVIĆ

College of Applied Technical Sciences, Niš, nikola.sekulovic@akademijanis.edu.rs

DANIELA M. MILOVIĆ

University of Niš, Faculty of Electronic Engineering, Niš, daniela.milovic@elfak.ni.ac.rs

Abstract: *In this paper, we investigate physical layer intercept probability of the wireless sensor networks with arbitrary number of sensors. Intercept behavior analysis is performed assuming a presence of an active eavesdropper. This authorized node tries to overhear the confidential data between a scheduled sensor and a sink. In the analysis that follows, we derive the probability of intercept utilizing the optimal scheduling scheme and the round robin scheduling scheme as a benchmark, over the composite α -F fading environment. According to the analytical results, numerical results are also shown. The impact of the number of sensor nodes, the average signal-to-noise ratios over the main/wiretap channel as well as the impact of the fading and shadowing shaping parameters on the intercept probability is analysed. The overall analysis and the obtained results have a high level of generality and also a high level of competency while the device-to-device (D2D) communication channels are described by α -F distribution, which is proposed in open technical literature as the best fitting distribution for the D2D channel characterization.*

Keywords: *intercept probability, optimal sensor scheduling, physical layer security, α -F fading, wireless sensor networks.*

1. INTRODUCTION

Wireless Sensor Networks (WSNs) are playing a key role in several application scenarios such as healthcare, agriculture, environment monitoring, and smart metering [1]. The WSN consists of many small sensor nodes, spatially distributed, that work cooperatively to communicate information gathered from the monitored field through wireless links. This network is exposed to constraints such as the device design, low power consumption, low production cost, and self-operation [2]. In addition, many challenges span all the conceptual communication layers, from the physical to the applicational. The massive deployment of WSNs provokes an increase of cybersecurity risks. Traditional cryptographic schemes may not be sufficient to prevent attacks encountered in WSNs. Providing satisfactory security protection in WSNs has always been a challenging task. A less complex alternative to cryptography, more suitable for WSN security enhancement, is a physical layer security (PLS). Namely,

cryptographic methods are inefficient in terms of energy consumption as they require extra resources for performing computations [3].

The PLS is based on the concept of information-theoretic security proposed by Wyner [4]. The concept of PLS describes communication over the main channel, between two authorized users, observed by unintended user by modeling a discrete memory-less wiretap channel [5]. Beside all of the benefits which PLS brings, it manifests some drawbacks. For example: it can not provide maximal security since PLS technique relies on the average information [6]; the PLS schemes mainly assume the knowledge of the eavesdropper's wiretap channel, which is not real scenario in practical applications [3]; moreover, the PLS requires a high data rate to ensure security. Therefore, the PLS should be combined with other higher-layer security techniques to achieve security and robustness of wireless communication networks [7,8].

The α -F distribution encounters two important effects, the shadowing and the non-linearity of the propagation medium [9]. Moreover, the α -F distribution is quite

general and encompasses, as particular cases, the well-known distribution, such as F distribution (Nakagami-m, Rayleigh, one-sided Gaussian), or α - μ distribution [10, 11]. This novel composite fading distribution yields a better fit to empirical data of device-to-device (D2D) communications, compared with k - μ shadowed, α - μ , and K distribution.

The authors in [12] have utilized the F fading model in the secrecy performance analysis for the basic Wyner's wiretap channel consisting of a source, destination, and an eavesdropper. Furthermore, achievable PLS over mixed fading channels, including the F, such as Nakagami-m/F channels, is analysed in [13]. The probability of intercept of the cascaded F fading links in a presence of randomly distributed eavesdroppers, has been determined in [14]. In [15], the optimal sensor scheduling (OS) scheme is adopted for selecting the sensor with the highest signal-to-noise ratio (SNR) for confidential transmission over Nakagami-m fading channels. The results showed the intercept probability decreasing for OS criterion in comparison to the conventional round-robin scheduling (RRS) scheme criterion. An indepth analysis of the WSN intercept behaviour in the presence of an attacker over F fading channels employing RRS, OS and cumulative distribution function-based scheduling scheme, is shown in [16].

In this paper, we derive the intercept probability of a WSN that contains an arbitrary number of sensors, a single sink and an eavesdropper. Two scheduling schemes, the conventional RRS and OS schemes, are applied in sensore selection. The main and wiretap links are modeled by composite α -F fading. The various systems' parameters influence on analyzed performance metric is discussed.

2. SYSTEM AND CHANNEL MODEL

The system under consideration, for the analysis that follows, is shown in Fig 1. We assume that the WSN has an arbitrary number of sensors, and that the selection of sensor for confidential data transmission to the sink is performed recalling OS scheme notation. A presence of an attacker trying to eavesdrop the communication can be noticed.

The received signal-to-noise ratio (SNR) from the i th main (sensor-sink) or wiretap (sensor-eavesdropper) link can be formulated as

$$\gamma_{*i} = \frac{|h_{*i}|^2 P_i}{\sigma_{*i}^2}, \quad i = 1, \dots, N, \quad (1)$$

where the subscript, *, denotes either the main (M), either the eavesdropper's (E) channel index; h_{*i} is a channel coefficient, σ_{*i}^2 denotes a variance of the zero-mean additive white Gaussian noise and P_i denotes the i th sensor's emitted power.

Following the assumption that the main and wiretap channels are corrupted by α -F fading, the probability density function (PDF) of the instantaneous SNR, over

both channels, corresponding to i -th node, has the following form [9, Eq. (3)]:

$$p_{\gamma_i}(\gamma) = \frac{\alpha_{*i}}{2B(\mu_{*i}, m_{s*i})} \left(\frac{(m_{s*i} - 1) \bar{\gamma}_{*i}^{\frac{\alpha_{*i}}{2}}}{\mu_{*i} \lambda_{*i}^{\frac{\alpha_{*i}}{2}}} \right)^{m_{s*i}} \gamma^{\frac{\alpha_{*i} \mu_{*i} - 1}{2}} \times \left(\gamma^{\frac{\alpha_{*i}}{2}} + \frac{(m_{s*i} - 1) \bar{\gamma}_{*i}^{\frac{\alpha_{*i}}{2}}}{\mu_{*i} \lambda_{*i}^{\frac{\alpha_{*i}}{2}}} \right)^{-(\mu_{*i} + m_{s*i})}, \quad (2)$$

$$\lambda_{*i} = \left(\frac{m_{s*i} - 1}{\mu_{*i}} \right)^{\frac{2}{\alpha_{*i}}} \frac{\Gamma(\mu_{*i} + \frac{2}{\alpha_{*i}}) \Gamma(m_{s*i} - \frac{2}{\alpha_{*i}})}{\Gamma(\mu_{*i}) \Gamma(m_{s*i})}$$

with $m_{s*i} > \frac{2}{\alpha_{*i}}$. In Eq. (2), $B(\cdot, \cdot)$ denotes Beta function [17], $\bar{\gamma}_{*i}$ is the average SNR, m_{s*i} is the shadowing severity parameter, $m_{s*i} > 1$, μ_{*i} is the fading depth parameter, $\mu_{*i} \geq 0.5$, α_{*i} is the parameter that defines non-linearity of the propagation medium, $\alpha_{*i} > 0$.

Utilizing the specific features of Meijer's G function relying on [18, Eq. (07.34.03.0271.01)] and additionally the form of the argument simplification [18, Eq. (07.34.16.0001.01)], the previous analytical expression of the PDF can be rewritten as:

$$p_{\gamma_i}(\gamma) = \frac{\alpha_{*i}}{2\Gamma(\mu_{*i})\Gamma(m_{s*i})\gamma} G_{1,1}^{1,1} \left(\frac{\gamma^{\frac{\alpha_{*i}}{2}}}{a_{*i} \bar{\gamma}_{*i}^{\frac{\alpha_{*i}}{2}}} \middle| \begin{matrix} 1 - m_{s*i} \\ \mu_{*i} \end{matrix} \right), \quad (3)$$

with $a_{*i} = \frac{(m_{s*i} - 1)}{\mu_{*i} \lambda_{*i}^{\frac{2}{\alpha_{*i}}}}$ and $G_{p,q}^{m,n}(\cdot)$ denoting the univariate Meijer's G function [17, Eq. (9.301)].

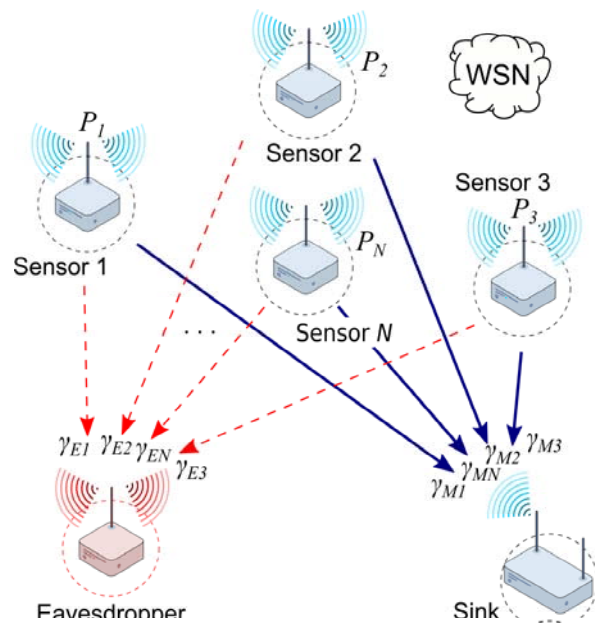


Figure 1. System model

The cumulative distribution function (CDF) of the instantaneous SNR over channels, can be determined with the help of [19, Eq. (26)], in the following form:

$$F_{\gamma_i}(\gamma) = \frac{1}{\Gamma(\mu_{s_i})\Gamma(m_{s_i})} G_{2,2}^{1,2} \left(\begin{matrix} \gamma^{\frac{\alpha_{s_i}}{2}} \\ \alpha_{s_i} \gamma^{\frac{\alpha_{s_i}}{2}} \end{matrix} \middle| \begin{matrix} 1 - m_{s_i}, 1 \\ \mu_{s_i}, 0 \end{matrix} \right). \quad (4)$$

3. INTERCEPT PROBABILITY EVALUATION

The intercept probability is one of the fundamental metrics for determining the system's PLS. It is a probability that the secrecy capacity, defined as difference

$$P_{\text{int}}^i = \frac{\alpha_E^{\mu_{M_i} + m_{s_{M_i}} - 1} \alpha_M^{\mu_{E_i} + m_{s_{E_i}} - 1}}{(2\pi)^{\alpha_{E_i} + \alpha_{M_i} - 2} \Gamma(m_{s_{E_i}}) \Gamma(m_{s_{M_i}}) \Gamma(\mu_{E_i}) \Gamma(\mu_{M_i})} \times G_{2\alpha_{E_i} + \alpha_{M_i}, 2\alpha_{E_i} + \alpha_{M_i}}^{\alpha_{E_i} + \alpha_{M_i}, 2\alpha_{E_i} + \alpha_{M_i}} \left(\begin{matrix} (m_{s_{E_i}} - 1)^{\alpha_{M_i}} \mu_{M_i}^{\alpha_{E_i}} \lambda_{M_i}^{\frac{\alpha_{E_i} \alpha_{M_i}}{2}} \\ (m_{s_{M_i}} - 1)^{\alpha_{E_i}} \mu_{E_i}^{\alpha_{M_i}} \lambda_E^{\frac{\alpha_{E_i} \alpha_{M_i}}{2}} \rho^{\frac{\alpha_{E_i} \alpha_{M_i}}{2}} \end{matrix} \middle| \begin{matrix} \frac{1 - m_{s_{M_i}}}{\alpha_{E_i}}, \dots, \frac{1 - m_{s_{M_i}} + \alpha_{E_i} - 1}{\alpha_{E_i}}, \frac{1}{\alpha_{E_i}}, \dots, \frac{\alpha_{E_i}}{\alpha_{E_i}}, \frac{1 - \mu_{E_i}}{\alpha_{M_i}}, \dots, \frac{\alpha_{M_i} - \mu_{E_i}}{\alpha_{M_i}} \\ \frac{\mu_{M_i}}{\alpha_{E_i}}, \dots, \frac{\mu_{M_i} + \alpha_{E_i} - 1}{\alpha_{E_i}}, \frac{1 - (1 - m_{s_{E_i}})}{\alpha_{M_i}}, \dots, \frac{\alpha_{M_i} - (1 - m_{s_{E_i}})}{\alpha_{M_i}}, 0, \dots, \frac{\alpha_{E_i} - 1}{\alpha_{E_i}} \end{matrix} \right) \quad (6)$$

where α_{M_i} and α_{E_i} are integers; and $\rho = \bar{\gamma}_M / \bar{\gamma}_E$ determines the average main-to-eavesdropper's channel power ratio (MER).

According to the OS criterion, the specific sensor is scheduled relying on the optimal secrecy capacity, which is determined as [15]:

$$C_{\text{secrecy}}^{\text{optimal}} = \max_{i \in N} \log_2 \left(\frac{1 + \gamma_{M_i}}{1 + \gamma_{E_i}} \right). \quad (7)$$

To maximize the secrecy capacity of the system under consideration, a sensor with the highest secrecy capacity should be chosen and scheduled to transmit its data to the sink. This algorithm is known as optimal [15].

We assume that each sensor estimates its own channel state information (CSI) and sends it to the sink. The sink collects all the sensors' CSI and determines the optimal one for communication. Thus, the OS intercept probability can be expressed as:

$$P_{\text{int}}^{\text{OS}} = \Pr \left[\max_{i \in N} \log_2 \left(\frac{1 + \gamma_{M_i}}{1 + \gamma_{E_i}} \right) < 0 \right]. \quad (8)$$

For different sensors, random variables γ_{M_i} and γ_{E_i} are independent of each other, so the previous equation can be rewritten as:

between the channel capacities of M and E paired channels, as $C_{s_i} = R_{M_i} - R_{E_i} = \log_2 \left(\frac{1 + \gamma_{M_i}}{1 + \gamma_{E_i}} \right)$, becomes

non-positive, i.e.:

$$P_{\text{int}}^i = \Pr[\gamma_{M_i} < \gamma_{E_i}] = \int_0^\infty F_{M_i}(\gamma_{E_i}) p_{E_i}(\gamma_{E_i}) d\gamma_{E_i}. \quad (5)$$

By substituting (3) and (4) in previous formula, we derive the intercept probability, recalling [18, Eq. (07.34.21.0013.01)], in the following form:

$$P_{\text{int}}^{\text{OS}} = \prod_{i=1}^N \Pr \left[\log_2 \left(\frac{1 + \gamma_{M_i}}{1 + \gamma_{E_i}} \right) < 0 \right] = \prod_{i=1}^N \Pr[\gamma_{M_i} < \gamma_{E_i}] = \prod_{i=1}^N P_{\text{int}}^i, \quad (9)$$

and the intercept probability of the scheduled link can be evaluated as a product of all N individual intercept probabilities.

For the conventional RRS scheme, N sensors take turns in accessing a given channel having an equal chance to transmit the sensed data to the sink. When RRS scheme is applied, the intercept probability can be obtained as the mean of all N intercept probabilities, in the following way:

$$P_{\text{int}}^{\text{RRS}} = \frac{1}{N} \sum_{i=1}^N P_{\text{int}}^i. \quad (10)$$

4. NUMERICAL RESULTS

In this section, numerical results of the intercept probability are presented to approve the mathematical analysis proposed in the paper. Numerical results are obtained using *Mathematica* and graphs have been drawn in *Origin* software package.

For the sake of simplicity, we assume that both the main

as well as the wiretap channels are independent and identically distributed, i.e. $\alpha_{M_i} = \alpha_{E_i} = \alpha^*$, $m_{sM_i} = m_{sE_i} = m_{s^*}$ and $\mu_{M_i} = \mu_{E_i} = \mu^*$.

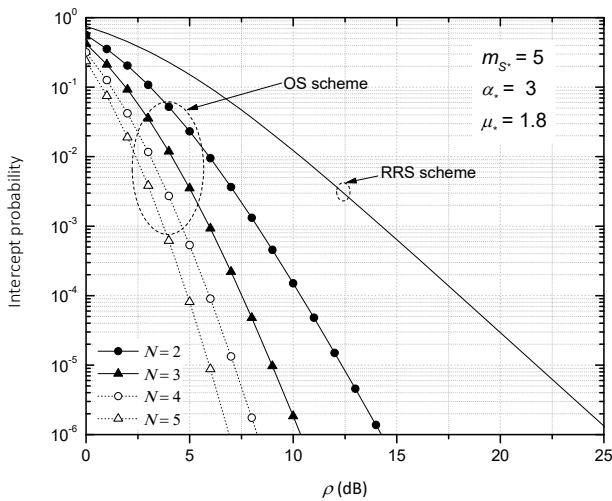


Figure 2. Intercept probability versus the average MER for different number of sensors

Figure 2 illustrates the intercept probability versus the average MER, ρ , for different number of active sensors. Two considered scheduling algorithms are analyzed. For the OS scheme, larger number of sensors provides more secure transmission. Degree of security does not increase linearly with increase in sensor number, so some trade-off should be made since the largest decline in the intercept probability occurs when two sensors are used. On the contrary, the obtained intercept probabilities with the RRS scheme are independent on the number of sensors.

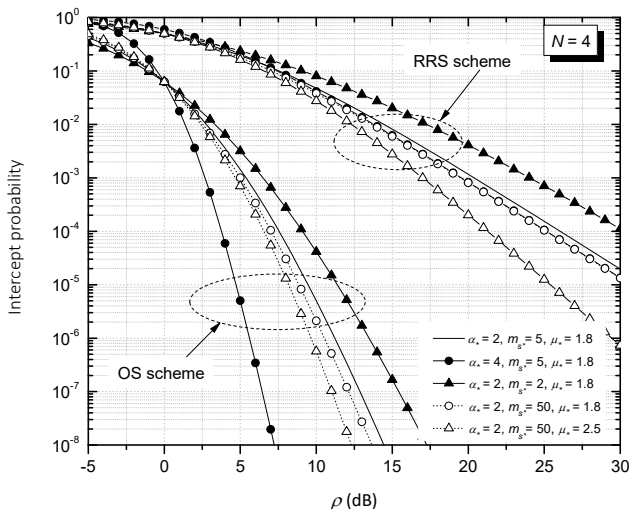


Figure 3. Intercept probability versus the average MER for various channel parameters

The influence of the fading shaping parameters, as well as the impact of the medium nonlinearity is analyzed in Fig. 3. It is assumed that wireless network is equipped with four sensors. Presented results show stronger influence of the variation in channel parameters on the transmission security when sink communicates with the best selected sensor, i.e. with the optimal scheduled sensor, but the communication is more secured. For the OS algorithm,

the change in medium nonlinearity brings the highest improvement in performance metric, while for RRS scheme the strongest influence is noticed for the change in both, the nonlinearity of the propagation medium and the shadowing severity.

5. CONCLUSION

In the paper, we have analysed the physical layer security of a sensor network employing the round-robin scheduling and the optimal sensor scheduling schemes over α -F fading environment. We have derived the closed-form expression for the intercept probability for both considered scheduling schemes. Presented results showed that increasing number of WSN sensors benefits only when the optimal sensor scheme is applied. Moreover, higher values of fading parameter and nonlinearity parameter, i.e. favorable channel conditions do improve the secrecy in sensor-sink communication, especially for moderate-to-high SNR regime.

Acknowledgment

This work has been supported by the Ministry of Education, Science and Technological Development of the Republic of Serbia.

References

- [1] MAINETTI, L., PATRONO, L., VILEI, A.: *Evolution of wireless sensor networks towards the internet of thing: A survey*, 19th International Conference on Software, Telecommunications and Computer Network - SOFTCOM 2011, Split, Croatia, (2011).
- [2] GUREWITZ, O., SHIFRIN, M., DVIR, E.: *Data gathering techniques in WSN: A cross-layer view*, Sensors, 22 (7) (2020) 2650.
- [3] SANENGA, A., MAPUNDA G.A., JACOB T.M.L., MARATA L., BASUTLI B., CHUMA J.M.: *An overview of key technologies in physical layer security*, Entropy, 22 (11) (2020) 1261.
- [4] WYNER, A.D.: *The wire-tap channel*, The Bell System Technical Journal, 54 (8) (1975) 1355-1387.
- [5] LI, J.: *A Critical Review of Physical Layer Security in Wireless Networking*, Master's Thesis, University College London, UK, 2015.
- [6] BLOCH, M., BARROS, J.: *Physical-layer Security: From Information Theory to Security Engineering*, Cambridge University Press, Cambridge, UK, 2011.
- [7] ROHOKALE, V.M., PRASAD, N.R., PRASAD, R.: *Cooperative wireless communications and physical layer security: State-of-the-art*, Journal of Cyber Security and Mobility, 1 (2012), 227-249.
- [8] CHEN, Y., YANG, Y., YI, W.: *A cross-layer strategy for cooperative diversity in wireless sensor networks*, Journal of Electronics, 29 (2012), 33-38.
- [9] BADARNEH, O.S.: *The α -F composite fading distribution: Statistical characterization and applications*, IEEE Transactions on Vehicular

- Technology, 69 (8) (2020), 8097-8106.
- [10] YOO, S.K., COTTON, S.L., SOFOTASIOS. P. C., MATTHAIYOU, M., VALKAMA, M., KARAGIANNIDIS, G.K.: *The Fisher–Snedecor distribution: a simple and accurate composite fading model*, IEEE Communication Letters, 21 (7) (2017), 1661-1664.
- [11] YACOUB, M.D.: *The α - μ distribution: a physical fading model for the stacy distribution*, IEEE Transactions on Vehicular Technology, 56 (1) (2007), 27-34.
- [12] KONG, L., KADDOUM, G.: *On physical layer security over the Fisher-Snedecor F wiretap fading channels*, IEEE Access, 6 (2018), 39466–39472.
- [13] BADARNEH, O.S., SOFOTASIOS, P.C., MUHAIDAT, S., COTTON, S.L., RABIE, K.M.; ALDHAHIR, N.: *Achievable physical-layer Security over composite fading channels*, IEEE Access 8 (2020), 195772–195787.
- [14] KONG, L., AI, Y., HE, J., RAJATHEVA, N., KADDOUM, G.: *Intercept probability analysis over the cascaded Fisher-Snedecor F fading wiretap channels*, 16th International Symposium on Wireless Communication Systems (ISWCS), Oulu, Finland, (2019), 672–676.
- [15] ZOU, Y., WANG, G.: *Intercept behavior analysis of industrial wireless sensor networks in the presence of eavesdropping attack*, IEEE Transactions on Industrial Informatics, 12 (2) (2016), 780-787.
- [16] MARICIC, S., MILOSEVIC N., DRAJIC D., MILIC D., ANASTASOV J.: *Physical layer intercept probability in wireless sensor networks over Fisher–Snedecor F fading channels*, Electronics, 12 (10), (2021), 1368.
- [17] GRADSHTEYN, I.S., RYZHIK, I.M.: *Tables of Integrals, Series, and Products*, fifth edition, New York, Academic Press, 1994.
- [18] The wolfram functions site, URL: <http://functions.wolfram.com>.
- [19] ADAMCHIK, V.S., MARICHEV, O.I.: *The algorithm for calculating integrals of hypergeometric type functions and its realization in reduce system*, International Symposium on Symbolic and Algebraic Computation - ISAAC'90 Minsk, USSR, (1990), 212-224.



EVALUATION OF LORA WIRELESS TECHNOLOGY FOR MILITARY APPLICATIONS

UROŠ PEŠOVIĆ

Faculty of technical sciences Čačak, University of Kragujevac, uros.pesovic@ftn.kg.ac.rs

SLAĐANA ĐURAŠEVIĆ

Faculty of technical sciences Čačak, University of Kragujevac, sladjana.djurasevic@ftn.kg.ac.rs,

MIHAILO KNEŽEVIĆ

Faculty of technical sciences Čačak, University of Kragujevac, mihailo.knezevic@ftn.kg.ac.rs

Abstract: *The modern military relies on broad information exchange to maintain military competitive advantage, where information is in most cases carried wirelessly, due high mobility of the field units. Among many low-power wireless communication technologies, LoRa (Long Range) wireless technology with high immunity to interference makes it prospecting for use in military applications, such as battlefield monitoring, friendly force identification, field unit localization, etc. LoRa technology is based on a CSS (Chirp Spread Spectrum) which makes it resilient to the Doppler Effect frequency shift caused by the movement of field units. Furthermore, the variable spreading factor makes this technology adaptable to various interference levels present in the channel. In this paper, we evaluated the properties of the Semtech SX1278 LoRa compliant module to implement frequency hopping spread spectrum operation. Obtained results show that LoRa technology can be successfully adopted for use in a wide range of low-power military applications.*

Keywords: *wireless, low-power, LoRa, CSS, FHSS.*

1. INTRODUCTION

Military innovations for a long time have been the primary driving force for mankind's technological advancements. In recent decades rapid revolution in the field of information communication technology became attractive for the military to increase battlefield information awareness [1]. Shared situational awareness is a requirement for efficient decision-making for military forces operating at the tactical level. Collection of information about the friendly force identification, field unit localization, battlefield monitoring and detection of enemy troops is a key enabler for achieving such shared situational awareness [2]. This information is collected using wearable electronic devices that can be worn as accessories or embedded in clothing, or by the sensors planted on the battlefield [3]. Due to mobility requirements, wireless technology is the only practical solution for such devices. Among many design requirements which include low power, low dimensions, security, etc, low-power wireless transmission is the most appropriate. The current low-power wireless transmission provides different modulation schemes, but all of them are limited to short-distance communication. The only way to increase communication distance is the use of a spread spectrum which enables the reception of signals whose power is near or below the channel noise level.

LoRa represents a spread spectrum modulation scheme derived from Chirp Spread Spectrum modulation (CSS)

which trades data rate for sensitivity within a fixed channel bandwidth. LoRa provides significant advantages over conventional modulation techniques, solving the traditional design compromise between long-range, immunity to interference and energy consumption.

In this paper, we presented the upgrade of LoRa modulation using the frequency hopping modulation scheme, which further increases interference immunity and adds another level of security that makes this solution practical for military use.

2. LORA MODULATION

LoRa represents Semtech's proprietary spread spectrum modulation scheme which is derived from Chirp Spread Spectrum modulation (CSS) [4]. CSS modulation is based on the generation of chirps, a signal which varies continuously in frequency. This signal property eliminates phase and frequency offset between transmitter and receiver, which makes the receiver design very simple since it doesn't require complex synchronization algorithms. LoRa modulation is highly adaptable to various channel conditions thanks to three configurable modulation parameters: Spreading Factor (SF), Bandwidth (BW), and Coding Rate (CR) which define data rate and receiver sensitivity.

LoRa modulation offers configurable forward error correction (FEC) encoding which for every 4-bit data adds a certain number of redundant bits which significantly increases interference resistance. The

number of redundant bits is defined by the Coding Rate (CR) parameter, which ranges from 1 to 4 and is adjusted according to the conditions of the channel used for data transmission. In the case of the coding rate of 1, one redundant bit is added to 4 data bits which reduce the useful data rate to 80%. In the case of 4 redundant bit bits, the data rate is reduced to 50%. The coded data blocks are then grouped to form symbols that are SF-bit long. Symbols are represented by an up-chirp signal, which frequency linearly changes in the range starting from f_{min} to f_{max} with supported the chirp bandwidth (BW) up to 500 kHz. The spreading Factor (SF) represents an exponential factor of 2 which defines how many chirps are used to represent one symbol and defines symbol duration. In case of the LoRa modulation Spreading Factor is taking values in the range {7; 8; 9; 10; 11; 12}. Symbols are modulated in the way that symbol value is used to cyclically-shift chirp starting frequency. In the case of the symbol with value 0, starting frequency is equal to f_{min} , while with the maximum symbol value of $2^{SF}-1$, starting frequency is equal to f_{max} .

The receiver uses unmodulated down-chirp signals, which frequency linearly changes in the range starting from f_{max} to f_{min} , to mix with the received up-chirp signals in order to demodulate coded encoded symbols as shown in Fig 1. The longer the chirp duration defined by the spreading factor, the receiver has more processing gain to decode symbols from the received signal with a negative SNR value or in the presence of narrowband interference.

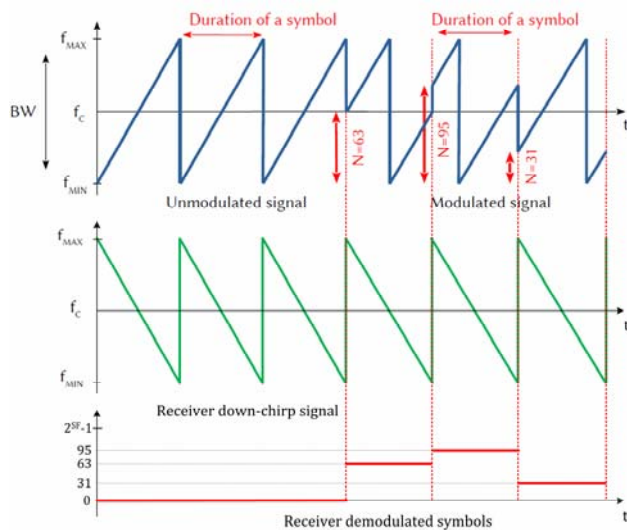


Figure 1. LoRa modulation

The duration of a symbol, known as symbol period is dependent on chirp bandwidth and spreading factor as defined by equation 1. The data rate is defined as the symbol rate multiplied by SF bits which represent one symbol. Furthermore, due to the use of FEC effective data rate is dependent on the used coding rate as shown by equation 2.

$$T_s = \frac{2^{SF}}{BW} \tag{1}$$

$$R_b = \frac{4}{4 + CR} \cdot SF \cdot \frac{BW}{2^{SF}} \tag{2}$$

Table 1. presents expected data bitrates which can be achieved for different channel bandwidths, with a maximum spreading factor of 12, and 4/5 coding rate. The LoRa packet format consists of the preamble, optional header which is only used in explicit mode, and the data payload as shown in Fig 2. The preamble field is used to synchronize the receiver with the incoming data packet and by default, is configured to the length of 12 symbols. The preamble length is configurable and may be extended up to 65539 symbols in case of the receive intensive applications, but its default value is sufficient for the most typical communication scenarios. The explicit mode uses the short header which is transmitted with a maximum error correction code (4/8). It contains information about the number of bytes, coding rate and whether a CRC is used in the packet and has its own CRC to allow the receiver to discard invalid headers. The packet payload contains actual data coded at the user-selected coding rate and its length is variable with a maximum packet length of 256 bytes. An optional CRC is appended to the end of the payload to check received data for errors at reception.

Table 1. LoRa expected bitrates

Bandwidth (kHz)	Spreading Factor	Coding rate	Data bitrate (bps)
7.8	12	4/5	18
10.4	12	4/5	24
15.6	12	4/5	37
20.8	12	4/5	49
31.2	12	4/5	73
41.7	12	4/5	98
62.5	12	4/5	146
125	12	4/5	293
250	12	4/5	586
500	12	4/5	1172

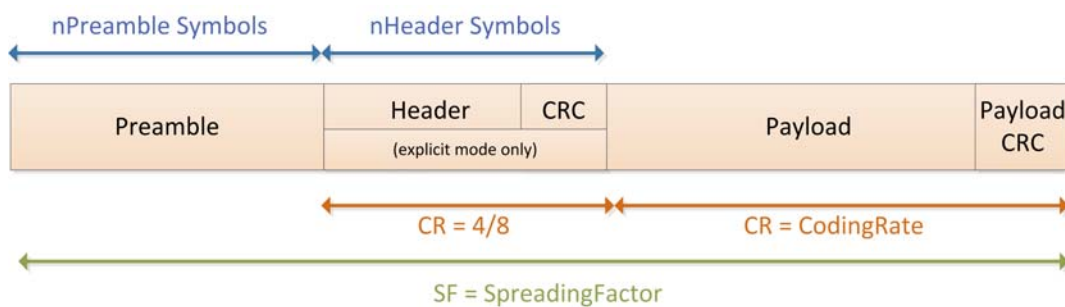


Figure 2. LoRa packet format

The total transmission (on-the-air) time of a LoRa packet is dependent on packet length, spreading factor (SF), coding rate (CR) and signal bandwidth (BW). In the case of long data packets transmitted with a high spreading factor, packet transmission could last in order of a second. In this case, LoRa could exceed regulatory requirements relating to the maximum permissible channel dwell time. This is most notably the case in US operations where the 902 to 928 MHz ISM band makes provision that the average time of occupancy at any frequency (dwell time) must not be larger than 0.4 seconds within a 20-second period [5]. To meet these requirements, FHSS (Frequency Hopping Spread Spectrum) is used where a portion of each LoRa packet is transmitted on a separate hopping channel from a look-up table of frequencies managed by the host microcontroller. After a predetermined hopping period has expired the transmitter and receiver change to the next channel in a predefined list of hopping frequencies to continue transmission and reception of the next portion of the packet, as shown in Figure 3. The hopping period is required to be shorter than the maximum channel dwell time and is represented as an integer multiple of symbol periods.

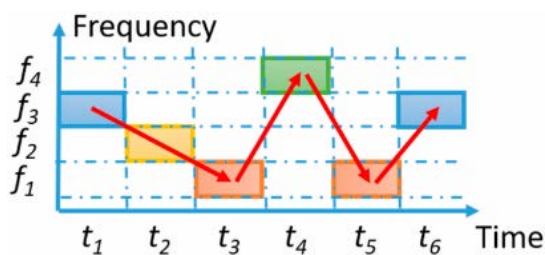


Figure 3. FHSS operation

3. LORA FHSS TRANSCEIVER

Semtech's SX1278 LoRa transceiver provides long-range communication and high interference immunity with minimized current consumption [6]. The transmitter part of this chip has a maximum transmitting output power of +20 dBm (100 mW), while receiver sensitivity of -148dBm provides a 168 dB maximum link budget making it optimal for any application requiring range and/or robustness. The main field of applications is automated meter reading, home and building automation, wireless alarm and security systems, industrial monitoring and control, and long-range irrigation systems. SX1278 transceiver is designed for battery-powered devices operating at 3.3V, with 12 mA current consumption in reception mode and 200 nA consumption in low-power register retention mode. Transmitter current consumption for different output power levels is shown in Table 2.

Table 2. Current consumption in transmit mode

Transmitting power	Current consumption
+ 20 dBm	120 mA
+ 17 dBm	87 mA
+ 13 dBm	29 mA
+ 7 dBm	20 mA

Besides LoRa modulation this transceiver also supports FSK, GFSK, MSK, GMSK, and OOK modulation. It can operate in the frequency range from 137 to 525 MHz, concerning the country's regulatory constraints on the permissible occupied bandwidth. For maximum flexibility the user may decide on the LoRa spread spectrum modulation bandwidth (BW), spreading factor (SF) and error correction rate (CR). The SX1278 chip offer bandwidth options ranging from 7.8 kHz to 500 kHz with spreading factors ranging from 6 to 12. Using the higher spreading factors will increase receiver capability to demodulate very low SNR signals, as shown in Table 3.

Table 3. LoRa Demodulator SNR

Spreading factor	Chirps per symbol	LoRa Demodulator SNR (dB)
6	64	-5
7	128	-7.5
8	256	-10
9	512	-12.5
10	1024	-15
11	2048	-17.5
12	4096	-20

The SX1278 transceiver is equipped with a 256-byte dual port data FIFO buffer which is accessible through an SPI interface. The content of the packet is written to the FIFO buffer by the host microcontroller after which the transceiver is switched to transmit mode, and automatically adds the preamble, and header to the packet, after the successful packet transmission the content of FIFO is cleared. In case the transceiver is in reception mode, any valid packet after reception will be stored in FIFO and the host microcontroller will be informed using the appropriate interrupt line.

SX1278 transceivers are connected to their host microcontrollers which are programmed to periodically exchange data, using regular LoRa modulation operating in the fixed channel in 433 MHz band, with 125 kHz channel bandwidth, spreading factor set to 12 and coding rate of 4/8. Figure 4, represents the spectral waterfall diagram of occupancy of the 433 MHz band during the data exchange between transmitter and receiver where modulated frequency chirps can be observed.

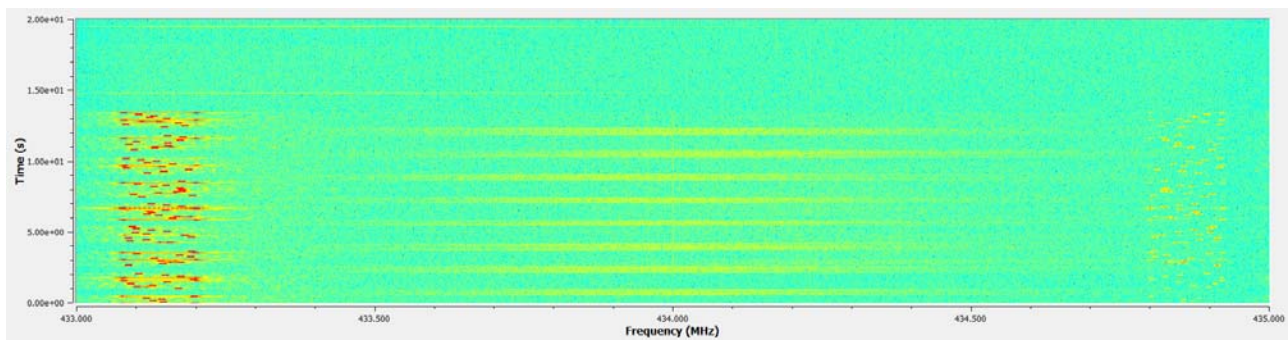


Figure 4. Regular LoRa modulation transmission in 433 MHz band

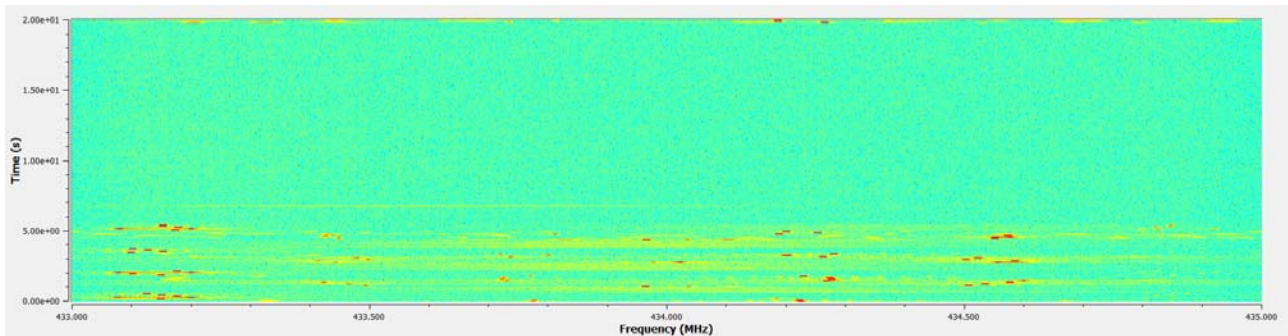


Figure 6. LoRa FHSS modulation transmission in 433 MHz band

The frequency hopping operation of LoRa modulation is managed by the host microcontroller which generates a channel look-up table using the pseudorandom generator fed by the pre-shared 32-bit key which is the same for the transmitter and the receiver. The frequency hopping mode starts at channel 0 from the look-up table, as shown in Figure 5. The transmitter sends the preamble and header on channel 0, while the receiver waits for a valid preamble detection at the same channel 0. At the beginning of each hopping period, the channel counter register in the transmitter and receiver is incremented and the interrupt signal is generated. Host microcontroller needs to service generated interrupt within the hopping period, where it programs new channel frequency from the look-up table to ensure it is taken into account for the next hop and clears generated interrupt.

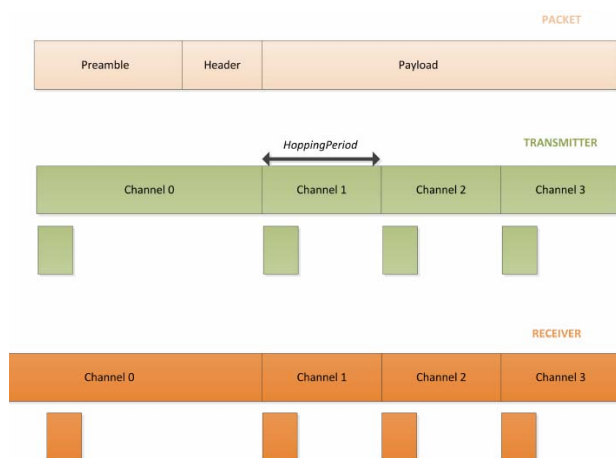


Figure 5. LoRa FHSS operation

SX1278 transceivers are configured by their host microcontrollers to a frequency hopping period of 10

symbols. At the beginning of every hopping period, the transceiver will generate an interrupt using digital pin DIO2, which will be processed by the host microcontroller in an interrupt service routine. The microcontroller will read the index of the next operating channel from the FhssPresentChannel register, and it will set the transceiver center frequency by the value indexed in the channel look-up table. Figure 6, represents the spectral waterfall diagram of occupancy of the 433 MHz band during the data exchange between transmitter and receiver with employed FHSS where we can observe chirp distribution to the entire 433 MHz band.

5. CONCLUSION

The modern military relies on robust wireless communication technologies to improve situational awareness on the battlefield. In this paper, we presented the use of frequency hopping spread spectrum implemented on regular LoRa modulation. By using a 32-bit shared key, security and resistance to jamming are significantly improved compared to the original LoRa modulation. Further research will be focused on LoRa communication based on FHSS between multiple nodes in a wireless sensor network.

ACKNOWLEDGEMENTS

The research in this paper is part of the project 451-03-68/2022-14/200132 funded by the Ministry of Education, Science and Technological Development of the Republic of Serbia.

References

- [1] SONDROL, T., JALAIAN, B., SURIN, N.: *Investigating*

- LoRa for the Internet of Battlefield Things: A Cyber Perspective*, MILCOM 2018 - 2018 IEEE Military Communications Conference (MILCOM), DOI: 10.1109/MILCOM.2018.8599805
- [2] LANGLEITE,R., GRIWODZ,C., JOHNSEN,F.: *Military Applications of Internet of Things: Operational Concerns Explored in Context of a Prototype Wearable*, International Command and Control Research and Technology Symposium (ICCRTS) proceedings 2021
- [3] JOHNSEN,F., BLOEBAUM,T., PUENTE,P.: *Towards friendly force tracking with MQTT over LoRa*, International Command and Control Research and Technology Symposium proceedings 2019
- [4] Semtech Corporation, *LoRa Modulation Basics, Application note AN1200.22*, 2015
- [5] LOY,M., KARINGATTIL,R., WILLIAMS,L.: *ISM-Band and Short Range Device Regulatory Compliance Overview, Application Report SWRA048*, Texas Instruments 2005
- [6] *SX1276/77/78/79 - 137 MHz to 1020 MHz Low Power Long Range Transceiver*, Datasheet Rev. 7, Semtech Corporation 2020



FLIGHT PLAN PREPARATION FOR POINT CLOUD DATA COLLECTION UTILIZING THE LASER SCANNER ALS80HP

DEJAN ĐORĐEVIĆ

Military Geographical institute “General Stevan Bošković”, Belgrade, dejandjordjevic.vgi@gmail.com

IVAN POTIĆ

Military Geographical institute “General Stevan Bošković”, Belgrade, ipotic@gmail.com

ZLATAN MILONJIĆ

Military Geographical institute “General Stevan Bošković”, Belgrade, zlatan.milonjic@gmail.com

MILOŠ BASARIĆ

Military Geographical institute “General Stevan Bošković”, Belgrade, m-basaric@protonmail.com

SAŠA BAKRAČ

Military Geographical institute “General Stevan Bošković”, Belgrade, sbakrac2017@gmail.com

Abstract: *This article describes the production of a flight plan to acquire point cloud data with a Leica ALS80 laser scanner to produce a high-resolution digital terrain model (DTM) as part of the IPA2014 project. When planning the flight, it is vital to examine the project tasks, the aircraft's technical prerequisites, and the laser scanner's characteristics, all of which influence the completion of the study. The initial part of the IPA2014 project, which intends to develop flood risk maps, entails creating a flight plan to scan the area of interest.*

Consequently, a summary of the project's structure, technical circumstances, and implementation requirements is provided through the planning of the flight plan. The objective, which is reflected in the effective flight planning and meteorological events, has been fully attained, indicating the successful preparatory research that preceded the planning and execution of the flight using the available aircraft and laser scanner Leica ALS80HP.

Keywords: *LiDAR, point cloud collection, remote sensing, MissionPro, DTM*

1. INTRODUCTION

In the past ten years, laser scanning has become an increasingly popular technique for collecting geospatial data, particularly the data necessary to generate a digital terrain model and other derivatives that provide a three-dimensional view of space. In conjunction with other geospatial data and research results derived from remote sensing techniques, a geospatial image is created that best portrays a terrain's geographic and topographical aspects. Collecting such data by laser scanning from airplane platforms involves careful planning that considers the sensor's features and the aircraft's performance. When planning a flight, it is essential to know the characteristics of the terrain that will be flown over, the project task, the desired outcome, and the final product resulting from the entire project. In the case of this paper, this meant the creation of vulnerability and flood risk maps through hydraulic modeling. This whole procedure represents a significant challenge for those who plan to implement such a task, not only in a professional sense but also involves additional research to satisfy all needs. The procedure was carried out without difficulty and simultaneously respecting the economy and productivity.

Part of the research was conducted prior to the actual acquisition of the equipment, i.e., the laser sensor, to evaluate the correctness of the permitted equipment in conjunction with the current equipment and, most importantly, the available aircraft.

The flight and laser scanning must be conducted in specified weather circumstances to avoid obtaining or collecting data that cannot be used appropriately and is valueless. Ideal weather conditions do not last long enough, so time and meteorological conditions contribute to the complexity. Satisfying all conditions established during the formulation of the flight plan for laser scanning data collecting is mandatory. This article will propose a flight planning solution utilizing a Leica ALS80HP laser scanner for the IPA2014 project to produce LiDAR point cloud, DTM, flood vulnerability and risk maps.

2. MATERIALS AND METHODS

Laser terrain scanning is a modern technique for collecting spatial data in the form of coordinates of points in space. In terms of recording type, laser recording might be either terrestrial or aero-photogrammetric. In both instances, data is collected that can be utilized to create digital two-dimensional drawings or three-dimensional

models, whether a digital terrain model or a model of a distinct object. The most significant benefit of this approach is its precision and rapidity. Laser surveying of the ground can be conducted using an aerial platform, such as a helicopter, an airplane, or an unmanned aerial vehicle. The value of geographical data and its applications continues to rise. This is particularly true for building 3D city models, numerous engineering projects, gathering DTM data for orthophoto production, and developing large- and medium-scale geodetic base maps [1].

LiDAR is synonymous with laser technology for recording topography. The name LiDAR is derived from the phrase "Light Detection and Ranging," which describes a remote sensing method used to examine the surface of the Earth. With this technique, distances are measured using light or laser pulses, where, in conjunction with data from the platform's system and orientation, precise three-dimensional data about forms on the Earth's surface and their features are generated, and a digital terrain model (DTM) is created [2].

The fundamental components of the LiDAR system consist of a) a laser scanning unit, b) GPS receivers on the platform and the ground station, c) an inertial navigation system unit with an inertial measurement unit (IMU), and d) a data storage and processing unit [2].

In the name of the laser scanner used for the IPA2014 project (Leica ALS80HP), the ALS80 designation represents an airborne laser scanner, i.e., a laser scanner designed for imaging from an aerial platform, whereas the HP designation denotes a general-purpose model for imaging at heights up to 3,500 meters above the ground [2].

2.1. Flight plan

With digital sensors, there are three fundamental forms of aerial photogrammetric surveying: 1) single line surveying, 2) corridor surveying, and 3) interest area or block surveying. Therefore, flight plans are established to execute aerial photography in which the flight lines have a specific correlation.

1) A unique line is only defined by its starting and stopping points. This is a practical method for recording a profile. Figure 1 depicts a flight plan for capturing a mountain profile using a line sensor.

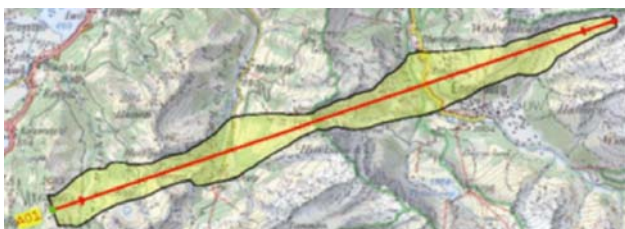


Figure 1. Illustration of the single-line recording

2) A corridor is a defined polyline that is formed of lines in varying forms with a specific width zone along a predetermined buffer zone. This mode is appropriate for surveying specific corridor directions and transportation

routes (Figure 2).

3) The Area Of Interest (AOI) is defined by polygons that are required to be covered by parallel flight lines. It is utilized for zonal recording and to produce DTM. For precautionary purposes, this zone is extended during the software computation.

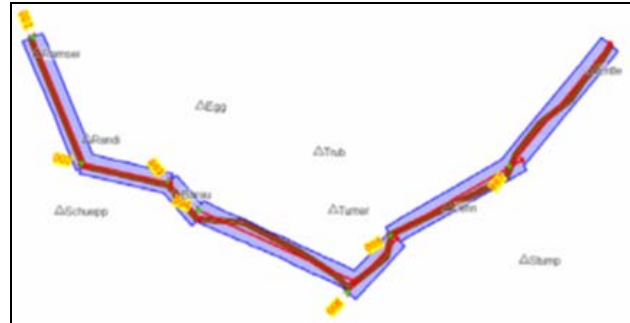


Figure 2. Illustration of a corridor recording

Due to the development requirements of flood risk maps, this form is utilized for the IPA2014 project (Figure 3).

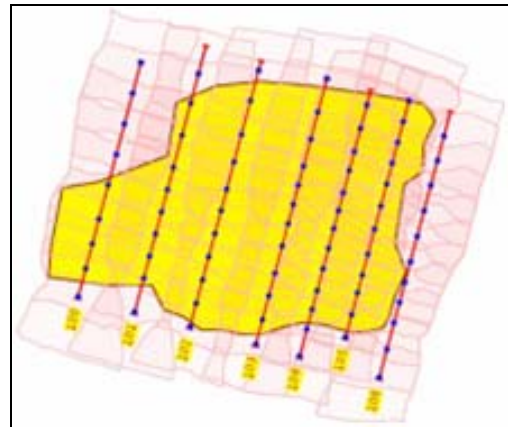


Figure 3. Illustration of an AOI recording

2.2. LiDAR recording requirements defined by the IPA2014 project

The IPA2014 project is an initiative of the European Union (EU) and the Republic of Serbia for the remediation of consequences that occurred after catastrophic floods that struck the western part of Serbia due to heavy rainfall in the third week of May 2014 and to prevent future floods [3].

The EU Directive on flood risk assessment and management, in conjunction with directive 2007/60/EC [4], reduces flood risk management activities to three procedures: preliminary flood risk assessment, risk assessment in which vulnerability maps are created, and flood risk maps and flood risk management plans [3]. The project's goal is to create flood vulnerability and risk maps. It is predicated on creating a DTM surrounding the defined flood zones with a horizontal accuracy of up to 0.5 meters and a vertical accuracy of up to 0.3 meters [5]. We refer to sensors mounted on aerial platforms when focusing on aerial photogrammetry and LiDAR recording technology. These platforms can be airplanes,

helicopters, satellites, drones, or other aircraft. As it is planned to conduct LiDAR surveys using the Piper Seneca V aircraft as part of the IPA2014 project, the explanation of the flight planning concept will continue on such an example [2].

The following requirements are defined for LiDAR scanning of approximately 9,427 km² by the IPA2014 project:

- a) The point density must be more than or equal to 5 points per square meter for flat regions and greater than or equal to 8 points per square meter for mountainous areas. To maintain homogeneity of gathered data, the ratio between the average distance of points in the direction of the flight line (dx , Along-track mean spacing) and the average distance of points perpendicular to the direction of flight (dy , Cross-track mean spacing) must not exceed 2 to 3;
- b) Perform laser scanning with a planned 30 percent transverse overlap of the scanning lines. The variation between the actual and planned transverse overlap of the scanning lines shall not exceed one-third of the transverse overlap;
- c) Utilize the GNSS station's "AGROS" network maintained by Republic Geodetic Authority for LiDAR scanning. At each scanning point, the distance between the aircraft and the permanent (or virtual) GNSS station must not exceed 30 kilometers (including the aircraft's turn). Utilize at least two permanent (or virtual) GNSS stations for LiDAR scanning;
- d) To prevent an unfavorable satellite constellation, the aircraft's inclination during the turn to scan the following row must not exceed 25 degrees;
- e) When collecting data, the "8" flying method must be applied before and after the LiDAR scanning [5].

2.3. Technical requirements for flight plan preparation

The DTM base is a crucial component for flight planning. It is always recommended to utilize the most precise DTM of the mapped region, but if one is unavailable, the global DTM - Shuttle Radar Topography Mission (SRTM) - may be used instead. SRTM is substantially less accurate than national and local digital terrain models, although it may still be used for flight planning.

The flight planning criteria having the most significant impact have been identified from aerial photogrammetry surveys conducted for Military Geographical Institute (MGI) projects. These include point density, Delta Scan, Range Gate, and the aircraft's minimum safe speed.

Point cloud density is the number of laser reflections measured per square meter. In LiDAR-based research, the outcomes are determined mainly by the density of points [6].

As illustrated in Figure 4, the point cloud density relies on the number of return signals per scan line (Sweep) and the number of scan lines that may be acquired in a given moment (Run) [7].

A correctly defined Delta Scan parameter will prevent the occurrence of duplicate points and the creation of the commonly named false point cloud density. To prevent the mentioned phenomena, the value of this parameter should be close to 0.5.

Factors that affect this parameter and must be corresponding are the flight speed, the angular range of the recording, the flight altitude, and the number of pulses of the laser sensor per second.

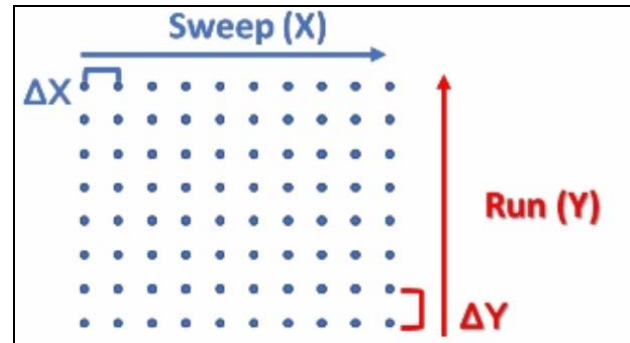


Figure 4. Factors affecting point cloud density [7]

The Range Gate explains the altitude during flight and the altitude change allowed during flight, so the highest peaks of the AOI are captured. The most common mistake when planning a flight is neglecting the height of objects. For example, if the lowest altitude at the AOI is 0 meters above sea level, the highest altitude is 150 meters above sea level, and the relative height of the building is 100 meters, this would mean that if the terrain recording is planned in the range from 0 to 150 meters above sea level, then there would be no data for a building located on the ground at the altitude of 100 meters because its top would be at an altitude of 200 meters (Figure 5).

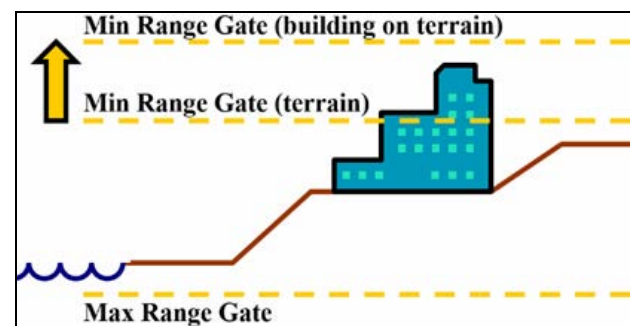


Figure 5. The problem of neglecting building height during flight planning

During laser scanning, it is essential to maintain the slowest feasible airplane speed. Light aircraft that fit this condition is thus used for this purpose. However, while discussing the aircraft's lowest speed, it must be kept in mind that this speed must be safe and sustainable for operation. Specifically, this value for the Piper SENECA V aircraft held by the MGI is 90 knots (1 knot = 1.85 km/h), whereas the recording speed ranges from 90 to 145 knots. Lower speeds are avoided as a safety precaution because they may result in engine cooling.

On the contrary, higher speeds would not have a beneficial impact on the density of points. This

characteristic is highly affected by wind speed. For instance, the aircraft is flown at around 150 knots to achieve the desired speed if the wind in the opposite direction of the aircraft's movement is projected to be 40 knots. Due to the engine cooling, such an approach would be impossible in the reverse direction of the aircraft. It states that the lowest safe speed of the airplane is a relative element that depends on the variables.

2.4. Flight plan production

In the MissionPro software environment, the flight plan is developed by defining the parameters based on automated calculations, which generate the project as a flight plan for a specific set of parameters. In order for the aircraft navigation system and the operational controller to read the project, it is exported in a format with the extension *.fpd2. Furthermore, MissionPro includes the possibility of the flight review, which addresses the issue of whether the actual flight followed the schedule, considering costs and quality. This software's application areas are all related and dependent on each other to operate.

MissionPro is a planning tool that allows the scheduling of scanning jobs from all aerial platforms' sensors, including LiDAR, line, and frame sensors. It is completely interoperable with all other Leica services, tools, and equipment. This program combines all earlier products of the same type within the company. Two- and three-dimensional spatial assistance is provided by MissionPro for the display of flight planning concepts.

The initial step in using the LiDAR system is to design the flight plan in this program. Figure 6 depicts how the LiDAR system and the software provided for the Leica company's models are used.

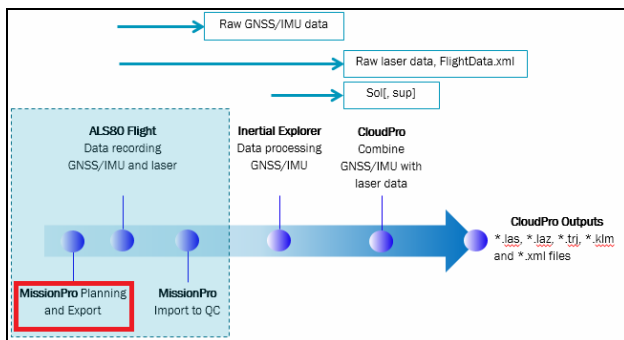


Figure 6. LiDAR system workflow

Both single-sensor and multi-sensor recording planning are targeted uses for the program. Multi-sensor imaging is typical for LiDAR recording, which requires simultaneous imaging with a digital aerial photogrammetry camera in addition to a laser sensor. In contrast, if recording from both sensors simultaneously is not feasible, each sensor must record the data separately within 15 days. This is the IPA2014 project requirement for data collection, so recording with an aerial photogrammetry camera and flight planning are performed separately.

The project requirement specifies that the transverse overlap along the flight lines must be recorded at a rate of

30%. However, the excess overlap, or the safety factor (minimum percentage of overlap under recording settings), is also established for precautionary purposes. In other words, depending on the circumstances during the actual flight, the flap will change and sometimes be less than the predetermined one. There could be issues with future data processing if this decrease is substantial, so the transverse overlap is not wide enough. As a result, a minimal overlap is defined that must be met and whose value will not interfere with further data processing.

While recording, the level of autonomy in adjusting the aircraft's flying altitude is determined by altitude parameters. Making as many favorable working environments is crucial. This also implies that the flight should be planned in line with the pilot's abilities and talents. Piloting is made simpler by avoiding rigorous maintenance of the plane's altitude.

The point density is defined as 5 per square meter for plain areas and 8 for mountainous areas, and within the flight plan preparation, it can be defined as the mean desired average point density and the worst-case average point density. The first value is entered as the density of points, which will be the average value of the density of points per square meter on the entire AOI, while the second value defines the worst possible density acceptable during recording and under the requirements of the project.

3. RESULTS

The division of the recording area carries out flight implementation and topography recording into polygonal "strips." A flight line in the center of each strip may be drawn to represent each flight plan graphically. The order of recording is determined by the flight lines, with the aircraft turning after each recorded line to record the following line in the opposite direction. Transversely, the recorded region on two adjacent flight lines overlaps by 30 percent following the angular range of sensor recording since it is required to preserve the integrity of the recording and the unity of the recorded information. The flight plan also specifies the manner of turning to the following flight line, the aircraft's turning angle, and the system startup procedure for the beginning and end of the recording. As stated, for the project's goals, the tilt during the turn for scanning the next row must not exceed 25 degrees to prevent an undesirable satellite constellation [2].

The "8" procedures are developed as integral components during the flight plan preparation. Method "8" is a required pre- and post-LiDAR scan procedure initialization, i.e., begins and stops operation of the IMU subsystem of the laser scanner during imaging based on the aircraft's typical figure-eight turn.

Additionally, the flight plan is constructed so that the distance between the aircraft and the permanent (or virtual) GNSS station at each scanning point (including the aircraft's turn) does not exceed 30 kilometers. As assistance for accurate positioning, these stations of the Active Geodetic Reference Base of Serbia ("AGROS")

were constructed within the territory of the Republic of Serbia. It comprises 30 permanent GNSS stations from which continuous GNSS observations are produced, located at an average distance of around 70 kilometers and mostly mounted on local cadaster structures.

The scanner manufacturer recommends that the distance between first turns and permanent stations should not exceed 20 kilometers (Figure 7). The image depicts the draft of the flight plan and the maximum distance of 50 kilometers between the final point of the AOI and the station, which is 30 kilometers in the project task.

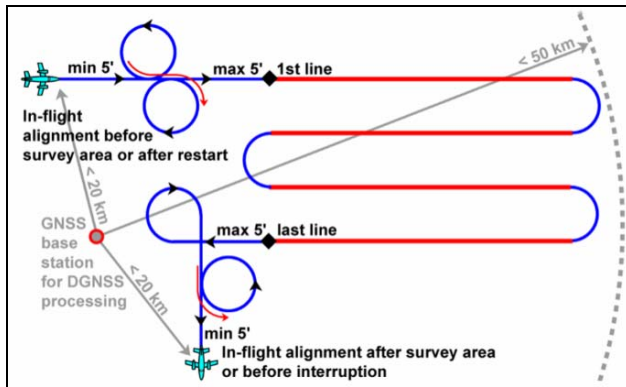


Figure 7. The draft of the flight plan concerning the position of the permanent stations

The Kolubara river basin's region is given as a LiDAR point cloud recording example. A large number of tributaries in its basin and the meanderings of the Kolubara River have impacted the decision to perform a segmentation recording. This requires recording the Kolubara River in seven sections, so its tributaries were recorded independently. The division of the recording territory is depicted in Figure 8 by flight lines for each territorial unit. Considering the various angles of each territorial unit's flight routes, the image illustrates the complexity of planning the recording of the entire region [2].

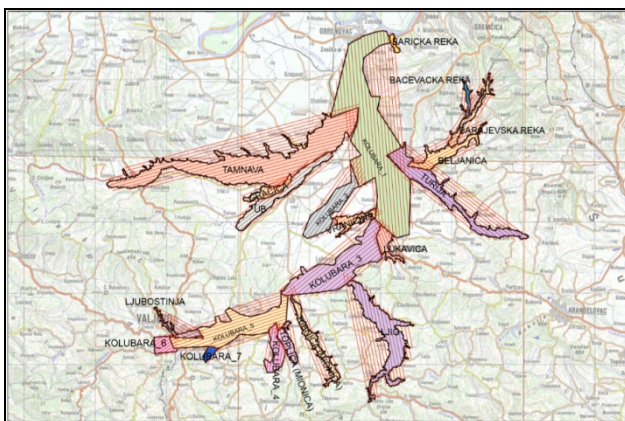


Figure 8. Kolubara River zones and flight lines

4. CONCLUSION

The article describes the complete process of the LiDAR survey flight plan for the area of interest, which is one of the phases of data collecting and processing for creating a flood risk map. The primary objective of this research was achieved, signifying that the flight preparation planning was carried out successfully and realized, facilitating data processing and the completion of subsequent phases of the project. It has been demonstrated that it is feasible to develop a flight plan that meets all the project's criteria as well as the technical capabilities of the aircraft (Piper SENECA V) and the laser sensor (Leica ALS80).

Part of the study was conducted prior to the actual acquisition of the equipment, i.e., the laser sensor, to assess the appropriateness of the equipment selection in conjunction with the current equipment and, most importantly, the available aircraft.

In general, LiDAR data collecting costs are less than aerial photo data collection, and processing times are shorter.

References

- [1] CVIJETINOVIĆ, Z.: Terrain digital modeling, University of Belgrade, Faculty of Civil Engineering, Belgrade, 2008.
- [2] SEKULOVIĆ D., BASARIĆ M., GARIĆ I.: The flood threat mapping of the Kolubara river basin using the Leica ALS80HP laser scanner, International conference on contemporary theory and practice in construction XN (Stepgard), University of Banja Luka, Banja Luka, pp. 99-112, 2020.
- [3] Official Gazette of the Republic of Serbia – "International agreements", no. 19 (29. december 2014), Action document for flood consequences relief, within the Instrument for Pre-Accession Assistance of the EU – IPA2014.
- [4] Directive 2007/60/EC of the European Parliament and of the Council of 23. October 2007. on the assessment and management of flood risks, Official Journal of the European Union L288, 6.11.2007, pp. 27-34.
- [5] Project task for collecting data with LiDAR technology in a purpose of creating digital terrain model of significant flood areas, Republic Geodetic Authority, 95-252/2015.
- [6] DEMIR, N.: Various Building Detection Methods With The Use Of Image And LIDAR Data, Technical Gazette, Vol. 21, No 2 (2014) 341-349
- [7] LiDAR flight planning. Available at: <https://www.slideshare.net/modusrobotics/lidar-flight-planning> [Accessed 11.06.2022]



10th INTERNATIONAL SCIENTIFIC CONFERENCE
ON DEFENSIVE TECHNOLOGIES
OTEH 2022

Belgrade, Serbia, 13 – 14 October 2022



SECTION VII

Materials and technologies - MT

CHAIRMAN

Dragomir Glišć, PhD
Maja Vitorović-Todorović, PhD
Jelena Gržetić, PhD
Danica Bajić, PhD



SOLVING MILITARY-TECHNICAL PROBLEMS USING INVENTOLOGY

DUSAN RAJIĆ

Innovation Centre of the Faculty of Technology and Metallurgy, University of Belgrade, Serbia

drajic@tmf.bg.ac.rs

Abstract: According to inventology, there are contradictions in the basis of every military-technical problem. They arise when weapons and military equipment (WME) are to be innovated. With the improvement of one WME parameter, the other, which is generically related to it, automatically deteriorates. In order to overcome the contradictions, it is necessary to rename the selected tactical and technical parameters of the WME that are being improved into the most similar mathematical-physical parameters that are in the Spatial-temporal LT-contradiction matrix. The most relevant contradiction in the problem is calculated by the modelling method, using tensor mathematics. Based on the principle of similarity with the X-element, the search of a real X-resource begins. The greater the similarity between the X-element as the basic LT-parameter and the X-resource as an expression of the state, the closer the obtained solution to the military-technical problem is to the notion of ideality.

Keywords: military-technical problems, inventology, equipment.

1. INTRODUCTION

Military-technical problems (MTP) are problems that arise during the research, development and exploitation of weapons and military equipment (WME). Experts who deal with these problems usually try to solve them using methods that belong to the inventive field. However, complex problems such as MTP require individual knowledge from multiple fields of study or a team interdisciplinary approach to be solved. In an effort to improve the creative ability of the person for effective inventive creation, between the 50s and 80s of the XX century, a number of different methods of active creative thinking appeared around the world, such as brainstorming, morphological analysis, synectics, lateral thinking, mind maps and numerous others [1]. In essence, all these techniques are reduced to the method of trial and error, because they allow a large number of different variants of possible solutions to the problem to be reviewed in a unit of time. That's why they lost their effectiveness when solving complex problems like MTP, but they remained good forgetting ideas [2].

The theory of solving inventive tasks (Russian abbr. TRIZ) is more effective than the mentioned psychological methods in the case of solving MTP because it is based on a scientific, not a psychological approach [2]. It is a heuristic methodology that relies on extracted know-how that exists in the world's patent documentation [3]. TRIZ contains an algorithm that, on a dialectical basis, directs the creative process in the direction of finding the ideal final solution (IFS) of the problem. However, TRIZ very often results in optimal and not desired IFS of problems [4,5]. The reason for this lies in the fact that heuristics are based on empirical, logically described knowledge based

on the laws of evolution of technical systems (TS), and not on exact calculation [6]. This means that there is a significant factor of subjective decision-making when choosing an IFS problem.

On a dialectical basis, but completely independently of TRIZ, the spatio-temporal LT-system was developed [7]. Within it, Bartini's LT-table was published as the most famous tool for solving MTP [8,9]. This system is based on the use of natural physical laws, and the solution of MTP is tried to be reached using a mathematical-physical approach. However, the main drawback is the incompleteness of this system, especially in terms of its practical application. Various authors have tried to compensate for this weakness [10-16], but the process has not yet been completed.

Through a critical review of TRIZ and LT-system, a spatial-temporal LT-matrix of contradictions [6, 17-21] was developed with an inventory, as a new tool that can be used to successfully solve various MTP by discovering their cause.

From the point of view of inventology, all three types of mentioned MTP can be put under the same category as inventive problems, but of different inventive level [22]. They can be classified as MTP of the first, lowest inventive level, to which functional tasks belong. In essence, these are technical improvements, which are achieved without the help of science.

The second category of inventive problems includes MTP related to the development of WME resources. They comprise the second and third inventive level and are arrived at using a heuristic methodology. In the third category of inventive problems belong MTP related to applied research. They contain the fourth or fifth, the

highest level of inventiveness that represents a scientific-technological breakthrough in a certain field of science and technology.

The aim of this work is to show that MTP can be solved more successfully using inventology and eco-inventology as a science of innovative creativity [3,4,23,24], than in a classical way or using methods of active creative thinking. This means shortening the time necessary for research and development, the expressed need for smaller material and financial investment and the achievement of better tactical and technical characteristics of newly acquired WME agents.

2. PHASES IN SOLVING MILITARY-TECHNICAL PROBLEMS

Each WME agent has its own life cycle. It consists of origin, growth, climax and obsolescence. This process can be represented by Gaussian curvatures (Fig. 1) [4]. In Phase I, while the growth rate of the new TS is hampered by the old system as its predecessor in the market, there are strong contradictions between them. In that phase, the TS is designed, refined, prototyped, and prepared for mass production. In phase II, the contradictions were overcome, which is why the accelerated growth of the new system occurs. In this phase, the "flourishing" of the TS occurs, during which it becomes more and more powerful and productive. Such TS enters the phase of serial production, its quality improves and the demand for it grows rapidly. In phase III, the system becomes older, and growth slows down. After some time, the improvement of TS becomes more and more difficult and it less and less meets the growing needs of man. At that stage TS starts doing more harm than good. This means that it is necessary to switch to the new system as soon as possible. The transition to a new TS at the end of the III phase can be viewed from a mathematical point of view as a disaster [4]. Disaster prevention can be temporarily postponed by technical improvement of TS (further movement along branch 3) or by shifting the sigmoid curve in the direction of innovative processes and technologies (movement along branch 1-2). In this way, new features of the TS will be obtained, which are at a significantly higher production and economic level than the old TS. Then with the new TS, the life cycle is repeated in the same way from beginning to end.

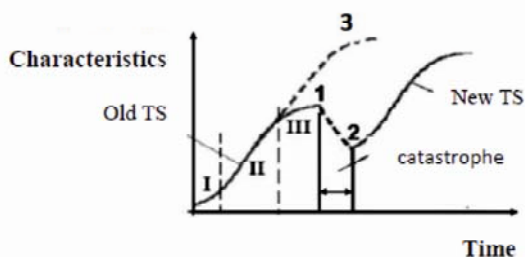


Figure 1. Life cycle of a WME agent

2.1. Functional problems or technical improvement of WME agents

One of the best systems of technical improvement in the

world is implemented within a process called kaizen (Japanese for continuous improvement). Kaizen management represents an element of comprehensive management quality control, and refers to a continuous long-term approach to changes, with respect for human needs and quality [25]. If the problem is not recognized, there is no recognition of the need for improvement. Once identified, the problem must be solved. Kaizen requires the use of a variety of tools to solve problems. After each solved problem, the upgrades reach higher levels. Improvement must be standardized to establish a new level. Kaizen, therefore, requires standardization. The word quality can be interpreted in many different ways and there is no agreement on the content of this term. In the broadest sense, quality is anything that can be improved. This means that quality can be associated not only with products and services, but also with how people work, how machines work and how work systems and procedures are implemented. It includes all aspects of human behavior. The Western expression of improvement more often refers to the improvement of devices and equipment. In contrast, kaizen is a generic term that can be used in any aspect, in any activity, including in the field of technical improvement of WMEs.

2.2. Developmental problems

A technical system can produce a useful function, while simultaneously creating a harmful function. The goal is to eliminate the negative characteristic. Based on the analysis of hundreds of thousands of patents, the TRIZ contradiction matrix was derived, with 40 inventive principles that are most likely to solve the formulated technical contradiction (TC). Although not all cells of the matrix are filled, the matrix contains principles for solving more than 1.200 different types of TC. This significantly reduces the scope of research and it is reduced only to appropriate concepts of possible solutions. For users of the matrix, it is therefore recommended to formulate several TCs for one problem situation [1, 3-5]. The next step is to use those principles that have been recommended 3 or more times. The principle that is recommended only once should be ignored. In any case, this approach helps to understand and document a number of basic TCs in the system that can be of great importance for problem analysis.

In addition to the described TRIZ contradiction matrix, a contradiction matrix based on TRIZ standards was developed within inventory [4]. Also, there are other heuristic tools such as the Algorithm for Solving Inventive Tasks (Russian abbr. ARIZ), Functionally Oriented Search (FOS) and others, which can also be used to find the MTP solution on a heuristic basis.

2.3. Research problems

Within the search for a solution to research MTP, the goal is to discover the cause or mechanism of the occurrence of a phenomenon or process. This can be done using ARIZ or relying on some other scientific methods. As part of the inventory, for this purpose a space-time LT-matrix of contradictions was developed, which can be used to solve over 3.000 different TC. It was designed by

combining TRIZ's contradiction matrix and Bartini's LT-table [20]. Thus, 64 parameters were obtained in the LT-matrix of contradictions. Each of them can be seen as a parameter that is fixed, corrupted, and can also represent a solution of the TC. If the obtained LT-parameter is not among the 64 listed LT-parameters (e.g. $L^{20}T^{-17}$), then this value L^mT^n shows that the solution to the contradiction is in the genetic trend whose value is 3 ($m+n=20-17=3$) and IFS of the problem in the form of the required X-element can be any member of that genetic group. Parameters belonging to a special genetic group are indicated by the sum of exponents ($m+n$): -3, -2, -1, 0, 1, 2 and 3.

3. CASE ANALYSIS

The Serbian Armed Forces has adopted the Filterable Protective Suit (FPS), which is intended to protect soldiers from highly toxic substances (HTS) or chemical (C) agents. It consists of a blouse and trousers (Fig. 2). The calculated ideality of this WME agent is 69% [26]. This means that there is a lot of room for improving its design in terms of approaching ideality. One of the goals of this paper is to propose a new FPS design whose ideality would be higher than the one mentioned.



Figure 2. Constituent parts of FPS

If the purpose of FPS-C is expanded so that it effectively protects not only from chemical (C) agents, but also from radioactive (R) and biological (B) agents, but with the same production cost, then it is obvious that this will achieve a higher ideality. The need for FPS-RCB construction is evident. Nowadays, insulating agents are most often used to protect the body from radioactive contaminants such as depleted uranium, as well as biological agents such as the coronavirus. These are different types of overalls. However, wearing them for longer periods of time can cause physiological unfitness, including heat stress, and even death in the user. However, since the FPS-RCB is expected to protect the soldier simultaneously from RCB agents, it is obvious that this increased level of protection will adversely affect his physiological suitability. Namely, it is assumed that due to the provided protection against RCB agents, it is necessary to insert additional protective layers into the FPS-C design, which would increase its mass. This would have a negative impact on the physiology of the user. This situation leads to the emergence of an inventive problem that requires an adequate solution. Details on the structure and design of the outer and inner layers of FPS-C, as well

as on the mechanism of protection against C agents are given in the literature [27, 28]. The decisive factor for the comfort of FPS-C is the water vapor permeability. In the case of spherical carbon materials, water vapor permeability is good, and water vapor molecules in spherical adsorbers are weakly bound. Therefore, a slight desorption occurs and a normal pressure gradient is established relatively quickly as soon as the relative humidity on the outside of the FPS-C decreases. In addition, thin-film spherical carbon materials possess good flexibility, which gives them good load-bearing properties.

4. RESULTS AND DISCUSSION

The main problem is how to make an FPS-RCB from the existing, two-layer FPS-C, without increasing its mass. In order to design a two-layer FPS-RCB, it is essential to consider the interrelationships of the following physical parameters: permeability, stationary object mass loss, absorption rate, and stationary object mass. All those parameters are listed in the segment of the space-time LT-matrix of contradictions (tab. 1) [20].

The technical contradiction (TC) that is created by crossing parameter no. 42 – Mass of a stationary object (x) and parameter no. 29 – Loss of mass of a stationary object (y) is represented by the following expression [21]:

$$x = \begin{bmatrix} L^3 & 0 \\ 0 & T^{-2} \end{bmatrix}, y = \begin{bmatrix} L^3 & 0 \\ 0 & T^{-2} \end{bmatrix}$$

TC in the form of a product xy is obtained using the expression:

$$TC_{(x,y)} = xy = \begin{bmatrix} L^3 & 0 \\ 0 & T^{-2} \end{bmatrix} \times \begin{bmatrix} L^3 & 0 \\ 0 & T^{-3} \end{bmatrix} = \begin{bmatrix} L^6 & 0 \\ 0 & T^{-5} \end{bmatrix} \quad (1)$$

The resulting product is called the determinant $D_{(x,y)}$, and is displayed using the expression:

$$D_{(x,y)} = L^6 \times T^{-5} \quad (2)$$

Power $TC_{(x,y)}$ is calculated using the expression:

$$R_{(x,y)} = \sqrt{(6)^2 + (-5)^2} = \pm\sqrt{61} = \pm 7.81 \quad (3)$$

If TC is created by transforming the expression $\frac{x}{y}$, then it follows:

$$TC_{(x-y)} = \frac{x}{y} = \begin{bmatrix} L^3 & 0 \\ 0 & T^{-2} \end{bmatrix} \times \begin{bmatrix} L^3 & 0 \\ 0 & T^{-3} \end{bmatrix}^{-1} = \begin{bmatrix} L^0 & 0 \\ 0 & T^1 \end{bmatrix} \quad (4)$$

Determinant $D_{(x-y)}$ is obtained by the expression:

$$D_{(x-y)} = L^0 \times T^1 \quad (5)$$

Power $TC_{(x-y)}$ is calculated using the expression:

$$R_{(x-y)} = \sqrt{(0)^2 + (1)^2} = \sqrt{1} = \pm 1 \quad (6)$$

Physical contradiction $PC_{(x,x)}$ for parameter x is obtained like this:

$$PC_{(x,x)} = x \times x = x^2 = \begin{bmatrix} L^3 & 0 \\ 0 & T^{-2} \end{bmatrix}^2 = \begin{bmatrix} L^6 & 0 \\ 0 & T^{-4} \end{bmatrix} \quad (7)$$

Its determinant $D_{(x,x)}$ is achieved using the following expression:

$$D_{(x,x)} = L^6 \times T^{-4} \quad (8)$$

Power $PC_{(x,x)}$ is obtained with the expression:

$$R_{x,x} = \sqrt{(6)^2 + (-4)^2} = \sqrt{52} = \pm 7.21 \quad (9)$$

Given that TC contains PC , their power ratio can be calculated via the ratio of the determinants given in the expressions:

$$D_{(x,x)} - D_{(x,y)} = x + x - (x + y) = D_{(x-y)} = x - y \quad (10)$$

By introducing a standardized value R_n of the relationship intensity between $TC_{(x-y)}$ and $TC_{(x,y)}$ a more objective assessment of the state of the forces that exist in TC are achieved:

$$R_n = \frac{R_{(x-y)}}{R_{(x,y)}} = \frac{1}{7.81} = 0.128 \quad (11)$$

From tab. 1 can be seen to be the greatest intensity is in the contradiction of R_n in TC which consists of parameters no. 42 and 29 with value $R_n = 0.128$ This means that in the case of a reduction in the mass of a stationary object (FPS-RCB), there is inevitably a loss of the mass of the stationary object. Since FPS-C consists of an inner layer impregnated with spherical granules of activated carbon, and an outer layer of woven material with an impregnated protective layer showing oleophobicity and hydrophobicity, this means that the thickness of the inner layer is reduced. This will weaken the FPS's protection against RCB agents. The structure of the contradiction is such that the intensity of the contradiction $R_{(x,y)} = 7.81$, which was obtained by multiplying two chosen parameters of $TC_{(x,y)}$, displays a stronger intensity than $R_{(x-y)} = 1$, which is obtained by dividing two parameters of $TC_{(x-y)}$. By multiplying parameters 42x29, parameter no. 39 is achieved - Using the energy of a moving object (L^6T^{-5}). That moving object that releases energy could be the Sun that releases heat and electromagnetic radiation. That energy should somehow be used at FPS-RCB. If we assume that the FPS-RCB should have two layers (inner and outer), then the inner layer should remain unchanged, i.e. it should retain a layer of spherical activated carbon that will absorb the C agent that penetrates to it in vapor form. The outer layer of FPS-CB should be made of woven material on which a thin layer of TiO_2 (alternatively: Ag) is applied. In contact with sunlight, the decontamination of C and B agents that reach the surface of FPS-RCB occurs.

In this way, this outer layer becomes a mechanical obstacle for the passage of contaminant droplets, but also a reactive layer. The external resource is the Sun, which enables this outer layer to turn from passive protection to active protection.

It was established that by modifying standard military textiles with TiO_2 nanoparticles, textile substrates with self-decontamination properties are obtained [26-28]. To solve the problem of protection against aerosol B and R agents, Functional Oriented Search (FOS) was used as one of the most powerful TRIZ tools for solving innovation problems on a heuristic basis [4].

Table 1. Calculation of the strength of contradictions R_n , $R_{(x,y)}$, $R_{(x-y)}$ respectively, in the inventive FPS-RCB design problem

Improvement	22	Permeability ($L^{-2}T^1$)	PC	2.864; 2.236; 6.403	3.606; 1; 3.606	4.135; 1.41; 5.831
	29	Loss of mass of a stationary object (L^3T^{-3})	PC	2.864; 2.236; 6.403	0.499; 5.657; 2.828	0.128; 7.81; 1
	31	Speed (L^1T^{-1})	PC	3.606; 1; 3.606	0.499; 5.657; 2.828	0.447; 5; 2.236
	42	The mass of a stationary object (L^3T^{-2})	PC	4.135; 1.41; 5.831	0.128; 7.81; 1	0.447; 5; 2.236

The main idea of FOS is to use existing technology from a different field of science and engineering to solve a specific innovation problem, in relation to the field to which the initial problem belongs. As it was determined in research [29-31] that the materials from which the protective half-masks are made successfully protect the respiratory organs from the aerosols of B agents, and the filter of the protective mask M3 from the aerosols of depleted uranium [32], then by analogy it was concluded that the same will apply and in the case of percutaneous protection of the human body. Namely, the structure of filters used in respiratory protection is in principle similar to the structural design of FPS-RCB, as respiratory protection is largely similar to percutaneous body protection. Therefore, it was concluded that the conceptual design of the double-layer FPS-RCB will effectively protect the user from all three types of contaminants, which should be confirmed experimentally. In wartime conditions, especially in conditions of imminent RCB danger, instead of wearing the classic war uniform, it is suggested to wear only the FPS-RCB.

5. CONCLUSION

Inventology combines functional, developmental and research problems treating them as inventive military technical problems from the first to the fifth level of inventiveness. At the same time, when searching for the ideal final solution to military technical problems, inventory relies on dialectics, mathematical-physical modeling and heuristics.

Functional problems are problems of technical improvement, and they are solved without the help of science and are of the first inventive level. A significant role in overcoming them is played by the application of

kaizen and standardization.

Development problems are successfully solved by applying heuristic scientific methodology. They contain a second or third level of inventiveness. When solving them, the tools of inventory and TRIZ are used.

Research problems are solved by the combined application of mathematical-physical modeling in order to determine the cause of the problem and heuristics in order to find an adequate resource, the introduction of which in the system results in solving the problem. They contain a fourth or fifth level of inventiveness. To solve them, inventory tools such as the LT-matrix of contradictions and TRIZ tools are used in combination.

On the example of the new conceptual design of the FPS-RCB filtering protective suit that should successfully protect against radioactive, chemical and biological (RCB) agents, the successful application of inventory to solve the military technical problems that arise was demonstrated.

ACKNOWLEDGEMENTS

This work was supported by the Ministry of Education, Science and Technological Development of the Republic of Serbia (Contract No. 451-03-68/2022-14/200287).

References

- [1] Rajic, D., Kamberovic, Z., Zakula, B., *Creative Engineering*, IC TMF, Belgrade, 2016. (In Serbian).
- [2] Очнев, А. В., *Курс ТРИЗ для оружейников*, Тула, 2004. <http://www.twirpx.com/file/158229> (11. 05. 2022).
- [3] Rajic, D., *Inventology*, Author's edition, Belgrade, 2017. (in Serbian).
- [4] Rajić, D., *Eco - inventology*, Author's edition, Belgrade, 2019. (in Serbian).
- [5] Rajic, D.: *Creative Ecology*, Author's edition, Belgrade, 2016. (In Serbian).
- [6] Rajic, D., "Compatibility between TRIZ - contradiction matrix and LT-unit system", *FME Transactions*, 48(2)(2020) 460-467.
- [7] Bolshakov, B. E., Petrov, A. E., "Algorithm of Multidimensional Space and Time Values Interrelation the in System of LT Dimension Coordinates by B. Brown, R. O. Bartini, P. G. Kuznetsov", *Journal of Engineering and Applied Sciences* 12 (3)(2017) 6620-6627.
- [8] Bartini, R., "Some relationships between physical quantities", *Dokl. Akad. Nauk SSSR, Ser. Fiz.* 163 (1965) 861-864 (in Russian).
- [9] Bartini, R. O., Kuznetsov, P. G., "On the multiplicity of geometries and the multiplicities of physical sciences", *Problems and Features of Modern Scientific Methodology*, (1978) 55-65.
- [10] Chujev, A. S., "On existing and theoretically possible force laws found in a system of physical quantities", (In Russian), (2003). <http://www.sciteclibrary.ru/rus/catalog/pages/5811.html> (05.01.2022).
- [11] Chujev, A. S., "About a multilevel system of physical quantities expressing the laws of nature, in particular, the structure and relationships of electromagnetic quantities", (2004). (In Russian) [http://www.sciteclibrary.ru/rus/catalog/pages/7335.html/\(05.01.2022\)](http://www.sciteclibrary.ru/rus/catalog/pages/7335.html/(05.01.2022)).
- [12] Chujev, A. S., "Physical picture of the world in the dimension length-time", *Series Informatization of Russia on the threshold of the XXI century. - M., SINTEG*, Also Natural kinematic system of dimensions, (1999) 96. (In Russian), <http://www.chuev.narod.ru/> (05.01.2022).
- [13] Bushuev, A. B., Petrov, V. A., Simulation modeling of control systems in the LT basis, Proceedings of the Eighth All-Russian Scientific and Practical Conference on Simulation Modeling and its Application in Science and Industry "Simulation. Theory and Practice "(IMMOD-2017) section 1. St. Petersburg, October 18-20, (2017) 88-93 (In Russian).
- [14] Bushuev, A. B., Search for quantitative estimates of resources in the Bartini basis / Collection of reports of the VII international conference "TRIZ: application practice and development problems", Moscow, (2015) 221-225 (In Russian).
- [15] Bushuev, A. B., High-speed innovation in the framework of the theory of disasters and TRIZ, "TRIZ in development" / Collection of research papers, TRIZ Developers Summit Library. Issue 9. St. Petersburg, Russia, (2017) 41 - 54 (In Russian).
- [16] Wei Z., Li Q., Wang D., Tian Y., The Application of LT-Table in TRIZ Contradiction Resolving Process. In: Tan R., Cao G., León N. (Eds) *Growth and Development of Computer-Aided Innovation. IFIP Advances in Information and Communication Technology*, 304 (2009) 266-275, Springer, Berlin, Heidelberg.
- [17] Rajic, D., Innovative synergism as a result of TRIZ and LT-system synthesis, In book: *Innovation as an Initiator of the Development "Innovations - Development Prospects"*, International Thematic Monograph - Thematic Proceedings, Publisher: University Business Academy in Novi Sad, Faculty of Applied Management, Economy and Finance, Belgrade, (2019) 226-242.
- [18] Rajic, D., Application of LT-contradiction Matrix in Development of Weapons and Military Equipment. 9th International Scientific Conference on Defensive Technologies, OTEH 2020, Belgrade, (2020).
- [19] Rajic, D., Application of LT-Contradiction Matrix in Innovation Development. International Thematic Monograph - Thematic Proceedings "Innovations - Development Prospects", Belgrade, (2020) 329-346.
- [20] Rajic, D., "LT - Contradiction Matrix", *FME Transactions*, 49 (1)(2021) 95-102.
- [21] Rajic, D., "Mathematical - Physical Model of Solving Inventive Problems". *FME Transactions*, 49 (3) (2021) 726-733.

- [22] Rajic. S. D., "Inventive Level as a Basic for the Assessment of Scientific Contribution of Inventors", *FME Transactions*, 47 (1) (2019) 76-82.
- [23] Rajić, D., Contribution of eco-inventology to the concept of sustainable development. Thematic proceedings Innovation as an initiator of the development "Innovations – basis for development", Belgrade, Serbia, (2019) 259-276.
- [24] Rajić, D., Eco-inventology. Thematic proceedings Innovation as an initiator of the development „Innovations – basis for development“, Belgrade, Serbia, (2018) 138-153.
- [25] Masaki, I., *Kaizen – ključ japanskog poslovnog uspeha*, Mono i Manjana, Beograd, 2008.
- [26] Rajic, D., Karkalic, R., Ivankovic, N., Otrisal, P., Florus, S., "Defining Filtering Protective Suit Ideality Using a Mathematical-Modeling Method", *AATCC Journal of Research*, 6 (6)(2019) 18-24.
- [27] Senic, Z., Bauk, S., Vitorovic-Todorovic, M., Pajic, N., Samolov, A., Rajic, D., "Application of TiO₂ Nanoparticles for Obtaining Self- Decontaminating Smart Textiles", *Scientific Technical Review*, 61 (3-4) (2011) 63-72.
- [28] Senic, Z., Bauk, S., Simic, D., Vitorovic-Todorovic, M., Markovic, T., Radojkovic, A., Rajic, D., "The Preliminary Comparative Analysis of Different Routes for TiO₂ Nanoparticles Synthesis and Their Deposition on Textiles", *Digest Journal of Nanomaterials and Biostructures*, 8 (2) (2013) 711-719.
- [29] Ivankovic, N., Rajic, D., Ilic, M., Vitorovic-Todorovic, M., Pajic, N. "Testing of the efficiency of military devices for personal respiratory protection in relation to sub-micron particles of biological agents", *Dig. J. Nanomater. Bios.* 7, (2012) 1089–1095.
- [30] Ivanković, N., Rajić, D., Karkalić, R., Jovanović, D., Radovanović, Ž., Stupar, S., Janković, D., "Influence of the aerosol flow and exposure time on the structural changes in the filtering half masks material", *J. Serb. Chem. Soc.* 83 (4) (2018) 463-471.
- [31] Rajic, D., Ivankovic, N., "Contributions of Impregnated Silver Nanoparticles to Ideality Increase of Filtration Material in Human Respiratory Protection", *Material Protection*, 60 (4)(2019) 360-368.
- [32] Rajić, D. S., Ivanković, N. D., Ivanković, N. D., Ilić, M. S., Senić, Ž. B., Pajić, N. D., "Testing the Protective Efficiency of Personal Respiratory", *Nuclear Technology & Radiation Protection*, Vol. 28 (1) (2013) 102-107.



CHARACTERIZATION AND HEAT TREATMENT OF ARMOUR STEEL OF NEW GENERATION

JURE BERNETIČ, MATJAZ MARČETIČ

SAAT, d.o.o., C. na Lipce 4, 4260 Bled, Slovenia, jure.bernetic@saat.si, matjaz.marctic@saat.si

DOMEN P. KOSEC, MIRKO SOKOVIĆ

University of Novo mesto, Faculty of Mechanical Engineering, Na Loko 2, 8000 Novo mesto, Slovenia, domenpk@gmail.com, mirko.sokovic@gmail.com

BORUT KOSEC, BLAŽ KARPE, ALEŠ NAGODE

University of Ljubljana, Faculty of Natural Sciences and Engineering, Aškerčeva cesta 12, 1000 Ljubljana, Slovenia
University of Ljubljana, Faculty of Mechanical Engineering, Aškerčeva cesta 6, 1000 Ljubljana, Slovenia, borut.kosec@ntf.uni-lj.si, blaz.karpe@ntf.uni-lj.si, ales.nagode@ntf.uni-lj.si

ZIJAH BURZIĆ, IGOR RADOSAVLJEVIĆ

Military Technical Institute, (MTI), Ratka Resanovića 1, 11030 Belgrade, Serbia, zijah.burzic@vti.rs; igor.radosavljevic@vti.rs

GORAZD KOSEC

SIJ ACRONI, d.o.o., C. B. Kidrica 44, 4240 Jesenice, Slovenia, gorazd.kosec@acroni.si

Abstract: Armour steel plate is intended for ballistic protection of military and civilian vehicles and structures, parts of machines and devices.

The work includes heat treatment and characterization of mechanical, microstructural and thermal properties of new generation of armour steel with internal code SA600.

Steel is the result of the development and knowledge of firm SAAT, d.o.o. in collaboration with scientific institutions and industry partners, produced in an industrial environment. The results of the research confirmed that the optimal austenitization temperature for steel SA600 is 870 °C, and the tempering temperature is 150 °C. Under these conditions, the hardness of the steel is 632 HV10, which means that it is suitably high. The yield strength is 1640 MPa and the tensile strength is 2052 MPa. The ratio $R_{p0.2}/R_m$ is equal to 0.799 and is correspondingly low.

The thermal conductivity increases with temperature and is equal to 28.33 W/mK at ambient temperature (approx. 22 °C) and 39.67 W/mK at 400 °C.

Keywords: armour steel, protection, heat treatment, characterization, production, testing.

1. INTRODUCTION

Steel armour plates are intended for ballistic protection of military and civilian vehicles and structures, parts of machines and devices. When selecting or developing the appropriate materials for the armour it is necessary to achieve the best possible compromise between the required mechanical properties of materials, its density and the final price of the product [1]. With the appropriate production technology, which includes casting, hot forming, heat treatment, etc. [2], high strength low alloy steel of good functional properties at affordable prices can be produced. By improving the strength and toughness of the steel, the required thickness and the weight of the armour can be reduced.

New steel for ballistic protection with internal code SA600 belongs to the group of high strength low alloy (HSLA) steels [3]. Steel is the result of the development and knowledge of SAAT, d.o.o. in collaboration with scientific institutions and industry partners, produced in

an industrial environment of VOEST Alpine GmbH. Table 1 shows the mass percentages of the elements that make up SA600 steel in addition to iron. The optimal chemical composition enables the achievement of the desired mechanical and physical properties and the planned microstructure.

The relevant mechanical properties are achieved by quenching and tempering [4].

Table 1. Indicative chemical composition of SA600 steel (in m.%)

C	0.43
Si	0.80
Mn	0.70
Cr	0.80
Ni	0.30
P	0.015
S	0.003
B	0.005
Fe	rest

The first and most important purpose of SA600 steel is resistance to the penetration of projectiles from small arms. The resistance depends mainly on the following mechanical properties: hardness, yield strength, tensile strength, plastic deformation capabilities, impact and fracture toughness, and stretching [5].

With the alloying elements silicon, chromium, molybdenum and boron, the appropriate manufacturing technology and heat treatment, all the desired mechanical properties can be achieved.

Table 2 shows the approximate values of the mechanical properties of SA600 sheet steel.

Table 2. Mechanical properties of SA600 steel

Hardness	590 – 640 HB
Yield strength	1600 MPa
Tensile strength	2050 MPa
Elongation	7.5 %
Impact toughness (at -40°C)	15 J

2. EXPERIMENTAL

The experimental work includes heat treatment and characterization of new generation armour steel with internal code SA600.

In Figure 1 is testing SA600 steel plate from which samples were cut to perform heat treatment, mechanical tests, microstructure analysis and thermal properties description.

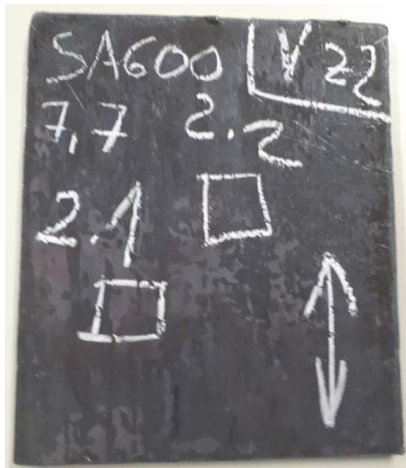


Figure 1. Testing SA600 steel plate

Samples from the supplied plates with a water jet for heat treatment and investigations of microstructure and mechanical properties (Figure 2) were cut.

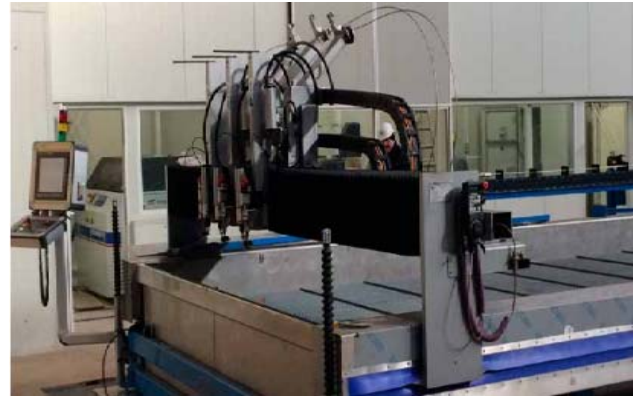


Figure 2. Water jet cutting machine Water Jet NC 2525 D in SIJ ACRONI d.o.o.

We performed heat treatment of steel SA600 in the delivered state, which consisted of hardening and tempering.

Based on experience and previous preliminary research, we determined a temperature of 870 °C for the optimal austenitization temperature, i.e. the temperature at which the original crystal grains of austenite do not grow more noticeably, and at which high hardness is obtained after quenching. The tempering was performed at temperatures of 150, 200, 300 and 400 °C.

In the Metallographic Laboratory of the Department of Engineering Materials, Faculty of Natural Sciences and Engineering, University of Ljubljana, samples cut from SA600 steel in the supplied and heat treated state were examined and analyzed with an OLYMPUS BX61 optical microscope, and a scanning electron field emission microscope Thermofischer Quattro S (Figure 3).

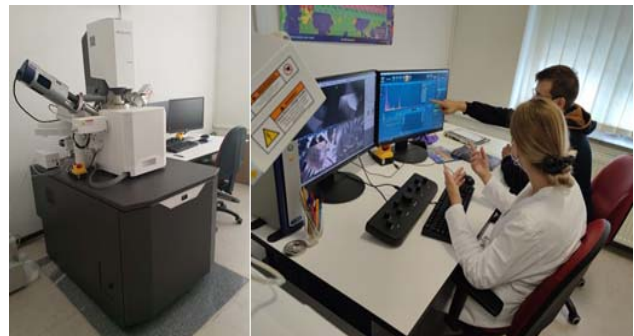


Figure 3. Scanning electron field emission microscope Thermofischer Quattro S

For the optimal austenitization temperature 870 °C was determined, i.e. the temperature at which the original austenite crystal grains do not yet grow more noticeably and at which high hardness is obtained after quenching. When examining the microstructure, the size of the original austenite crystal grains was measured.

Hardness measurements were performed with an instrument dynATESTOR 10, and a load of 100 N was used. Hardness was measured on all four samples heat treated samples, and on the fifth sample immediately after the first phase of heat treatment - quenching. Hardness with tempering temperature decreases from initial (immediately after quenching) hardness of 671 HV, to 632 HV at tempering at 150 °C / 1 h, and up to 455 HV at tempering at 400 °C / 1 h. Based on the results of hardness measurements, the temperature of 150 °C was chosen as the optimal temperature for the tempering.

The tensile tests were performed on a universal tensile testing machine INSTRON 1255 in accordance with the standard ISO 6892-1: 2009 [6].

3. RESULTS AND DISCUSSION

At temperature 150 °C temperature, SA600 steel achieves the most suitable combination of mechanical properties for armour steels.

Microstructure of SA600 steel hardened from 870 °C and hardened and tempered are shown in Figures 4 and 5. The grains grow more noticeably at temperatures above 870 °C (Figure 4).

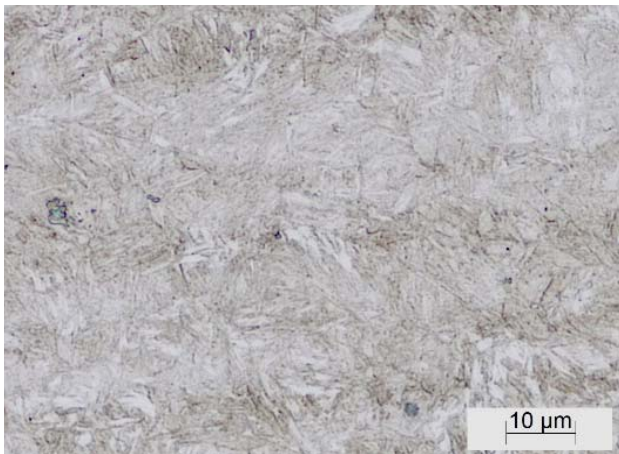


Figure 4. Microstructure of SA600 steel hardened from 870 °C; (OM)

Figure 5 shows the microstructure after tempering at 150 °C. At this tempering temperature, the first stage of tempering takes place, which involves the elimination of i.e. transition ε-carbides of formula Fe_{2,4}C. Elimination takes place by lowering the carbon content of martensite to form low-carbon martensite. In Figure 5, these carbides are very fine and in the form of thin needles. At this magnification, they are barely noticeable. They are excreted on the cubic planes of the martensite nut and on dislocations [3].

The hardness in our case is high and amounts to 632 HV (580 - 640 HV is prescribed).

Results of tensile tests are presented in Figure 6. The Rp_{0,2}/Rm ratio is the lowest at this temperature (0.7992). A low Rp_{0,2}/Rm ratio means higher resistance to local steel flow and thus better armour protection. The elongation at this temperature is 7.5% and thus reaches the required elongation value for armour steel.

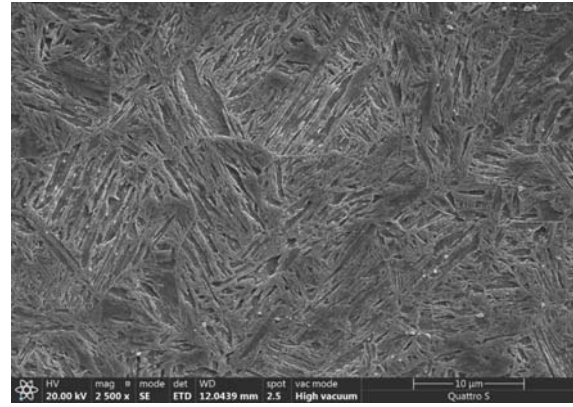


Figure 5. Microstructure of SA600 steel, hardened at 870 °C and tempered at 150 °C/ 1h; etched with Nital, (SEM).



Figure 6. Results of tensile test

Measurements and analysis of thermal properties of testing samples from the steel SA600 were performed in accordance with the standard ISO 22007-2 [7,8]. For determining the thermal properties, one of the most advanced instruments Hot Disk TPS 2200 (Figure 7), a product of Hot Disk AB company, Gothenburg, Sweden [9] was used.



Figure 7. Instrument Hot Disk TPS 2200

In Figure 8 are presented results of thermal properties measurements and determination at ambient temperature.

Row	St...	Description	Heating Power	Meas...	Sam...	Senc	Thermal Conductivity	Thermal Diffusivity	Specific Heat
0	C...	jeko SA 600_1	500 mW	5s	209 °C	5082	38,49 W/mK	8,748 mm ² /s	4,400 MJ/m ³ K
1	C...	jeko SA 600_2	500 mW	5s	209 °C	5082	37,45 W/mK	8,511 mm ² /s	4,400 MJ/m ³ K
2	C...	jeko SA 600_3	500 mW	5s	209 °C	5082	37,13 W/mK	8,439 mm ² /s	4,400 MJ/m ³ K
3	C...	jeko SA 600_4	700 mW	5s	209 °C	5082	36,56 W/mK	8,308 mm ² /s	4,400 MJ/m ³ K
4	C...	jeko SA 600_5	700 mW	5s	209 °C	5082	36,46 W/mK	8,286 mm ² /s	4,400 MJ/m ³ K
5	C...	jeko SA 600_6	700 mW	5s	209 °C	5082	36,40 W/mK	8,274 mm ² /s	4,400 MJ/m ³ K
6	C...	jeko SA 600_7	500 mW	5s	306 °C	5082	40,42 W/mK	8,421 mm ² /s	4,300 MJ/m ³ K
7	C...	jeko SA 600_8	500 mW	5s	306 °C	5082	39,57 W/mK	8,244 mm ² /s	4,300 MJ/m ³ K
8	C...	jeko SA 600_9	500 mW	5s	306 °C	5082	38,85 W/mK	8,094 mm ² /s	4,300 MJ/m ³ K
9	C...	jeko SA 600_10	700 mW	5s	306 °C	5082	38,74 W/mK	8,037 mm ² /s	4,300 MJ/m ³ K
10	C...	jeko SA 600_11	700 mW	5s	306 °C	5082	38,68 W/mK	8,118 mm ² /s	4,390 MJ/m ³ K
11	C...	jeko SA 600_12	700 mW	5s	306 °C	5082	40,54 W/mK	8,446 mm ² /s	4,300 MJ/m ³ K

Figure 8. Results of thermal properties measurements

In Table 3 are presented thermal properties (thermal conductivity, specific heat and temperature diffusivity) of steel at ambient temperature (approx. 22 °C). The thermal conductivity increases with temperature, and is equal to 28.33 W/m·K at ambient temperature, and 39.67 W/m·K at 400 °C.

Table 3. Thermal properties of steel SA600 at ambient temperature (approx. 22 °C)

Steel SA600	
Thermal conductivity	28.33 W/m·K
Specific heat	4.44 MJ/m ³ K
Temperature diffusivity	6.37 mm ² /s

3. CONCLUSIONS

The work includes heat treatment and characterization of mechanical, microstructural and thermal properties of new steel for armour protection with internal code SA600. Steel is the result of the development and knowledge of firm SAAT, d.o.o. in collaboration with scientific institutions and industry partners, produced in an industrial environment.

The results of the research carried out as part of the investigation confirmed that the optimal austenitization temperature for SA600 steel is 870 °C and the tempering temperature is 150 °C. Under these conditions, the hardness of the steel is 632 HV10, which means that it is suitably high. The yield strength is 1640 MPa and the

tensile strength is 2052 MPa. The Rp_{0.2}/Rm ratio is equal to 0.7992 and is correspondingly low.

The thermal conductivity increases with temperature and is equal to 28.33 W/m·K at ambient temperature, and 39.67 W/m·K at 400 °C.

ACKNOWLEDGEMENT

The authors want to thank dr. Slavko Ažman⁺ (SIJ ACRONI d.o.o.), professor Ladislav Kosec (University of Ljubljana), professor Franc Vodopivec⁺ (Institute of Metals and Technology, Ljubljana), dr. Milenko Rimac (Metallurgical Institute K. Kapetanovic, Zenica), and professor Anton Smolej (University of Ljubljana) for mentorship at study armoured steels.

References

- [1] CROUCH, I. G.: The Science of Armour Material. Amsterdam: Elsevier, 2017.
- [2] DOBRZANSKI, L.A.: *Technical and Economical Issues of Materials Selection*, Silesian Technical University, Gliwice, 1997.
- [3] TOTEN, G. E.: *Steel heat treatment: equipment and process design*. Boca Raton: CRC Press, Taylor & Francis Group, 2006.
- [4] BERNETIČ, J.: *Development of model for predicting hardenability of high strength low alloy steels*: (B. Kosec, A. Smolej), Doctoral Thessys, University of Ljubljana, Ljubljana, 2013.
- [5] BERNETIČ, J., KOSEC, G., KOSEC, B.: *Steel of new generation PROTAC 500*, IRT 3000, 8 (2013) 48, 30-31.
- [6] Slovenian standard SIST EN ISO 6892-1:2010: Metal Materials – Tensile Testing Part 1: *Testing Methods at Room Temperature* (01 – march- 2010).
- [7] International standard ISO 22007 (2009). *Plastics – Determination of thermal conductivity and thermal diffusivity – Part 1: General principles*. Reference: ISO 22007:2009(E).
- [8] BERNETIČ, J., KOSEC, B., KOSEC, G., GOJIĆ, M., BURZIĆ, Z., NAGODE, A., SOKOVIĆ, M., BIZJAK, M.: *A new generation of armoured steel plate*. Contemporary materials, 7 (2016) 2,137 – 141.
- [9] KOSEC, B., KARPE, B.: Instrument for the thermal properties analysis Hot Disk TPS 2200, IRT3000, 1 (2017), 67.



DIMETHOATE AND OMETHOATE HYDROLYSIS IN AQUEOUS SOLUTIONS AND THE ASSESSMENT OF THEIR NEUROTOXIC EFFECTS

DRAGANA D. VASIĆ ANIĆIJEVIĆ

University of Belgrade, “VINČA” Institute of Nuclear Sciences - National Institute of the Republic of Serbia, Mike Petrovica Alasa 12-14, 11000 Belgrade, Serbia, draganav@vin.bg.ac.rs.

VLADAN J. ANIĆIJEVIĆ

University of Belgrade, Faculty of Physical Chemistry, Studentski Trg 12, 11000 Belgrade, Serbia, anicijevicj.v@gmail.com.

TAMARA D. LAZAREVIĆ-PAŠTI

University of Belgrade, “VINČA” Institute of Nuclear Sciences - National Institute of the Republic of Serbia, Mike Petrovica Alasa 12-14, 11000 Belgrade, Serbia, lazarevictlj@yahoo.com.

Abstract: Organophosphates are widely used nowadays. They have applications as pesticides, drugs, plasticizers, flame retardants or chemical warfare agents. Their acute toxicity is ascribed to the inhibition of acetylcholinesterase, a key enzyme in the transmission of nerve impulses in animals. Their toxic effects manifest by acetylcholine accumulation in the nerve synapses and can lead to paralysis or death. Dimethoate, a systemic and contact organophosphate insecticide, has been registered for use since 1962. Its oxo-analog omethoate also can be found in the environment due to oxidation. Under environmental conditions, dimethoate and omethoate undergo chemical transformations and decomposition. However, systematic data about dimethoate and omethoate hydrolysis are scarce. We systematically analyzed dimethoate and omethoate hydrolysis under different pH conditions and estimated their neurotoxic effects. Dimethoate and omethoate hydrolyzed fast in alkaline aqueous solutions (half-lives 5.7 ± 1.4 and 0.89 ± 0.21 days) but were stable in acidic solutions (half-lives 124 ± 18 and 104 ± 9 days). The toxicity of these pesticide solutions decreases over time, indicating that more toxic products were not formed.

Keywords: dimethoate, omethoate, pH stability, toxicity.

1. INTRODUCTION

Dimethoate (DMT, Figure 1a) is an organophosphorus pesticide (OP) with contact and systemic action. It is in use against many insects in the agriculture and the housefly's control. DMT is known for its moderate toxicity to mammals. The US EPA classified it as a possible human carcinogen based on tumor occurrence in exposed mice [1]. Like other OPs, the acute toxicity of DMT is caused by its inhibition of acetylcholinesterase (AChE) [2]. The oxidation of DMT leads to the formation of its oxo-analog, omethoate (OMT, Figure 1b), which is more toxic to acetylcholinesterase than the respective parent compound. Besides it is one of the metabolites of DMT, OMT may also be found in the environment due to different oxidizing agents in water and soil [2]. Therefore, it is important to have a thorough understanding of the environmental fate of DMT and its analog OMT to mitigate the negative impacts on the environment and their non-target species.

Due to the high water solubility and low soil persistence of DMT, its potential to runoff into surface waters and leach into groundwater is high [3]. At the same time, it is not expected to adsorb to suspended solids and sediment [4].

The most important degradation pathways of DMT in the environment are hydrolysis, photolysis, and microbiological degradation [3]. The photocatalytic oxidation and microbial metabolism of DMT often have OMT as the final product, which is not desirable due to its extreme toxicity [5]. On the other hand, hydrolytic degradation is the main inactivating pathway of DMT in the environment and typically gives no OMT as the final product [6]. The hydrolysis of DMT is mostly dependent on the temperature and pH [7].

Thus, the aim of the present work is to investigate the kinetics of DMT and OMT hydrolysis in aqueous media in the pH range from 3 to 9 and explain the observed trends. In addition, the present work thoroughly addresses the evolution of toxicity of DMT and OMT solutions over time, which is essential for tailoring efficient strategies for DMT and OMT removal from water. Toxicity is assessed using AChE inhibition measurements to provide a broader context of the work and fill the identified gap in the literature. Namely, AChE inhibition is a common biomarker for environmental monitoring [8] which targets the overall eco-neurotoxicity of cholinesterase-inhibiting compounds.

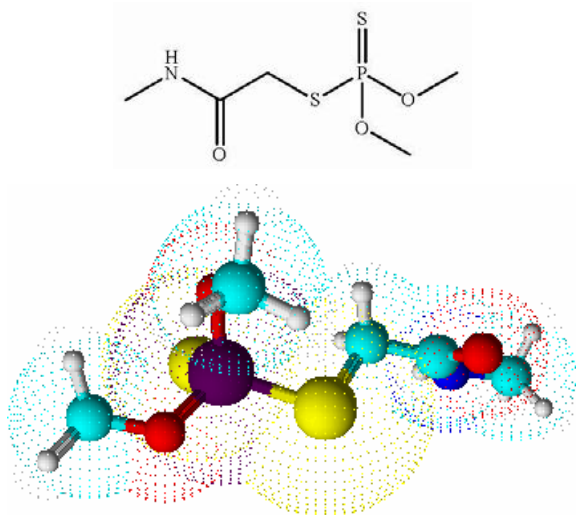


Figure 1a. The structure of DMT.

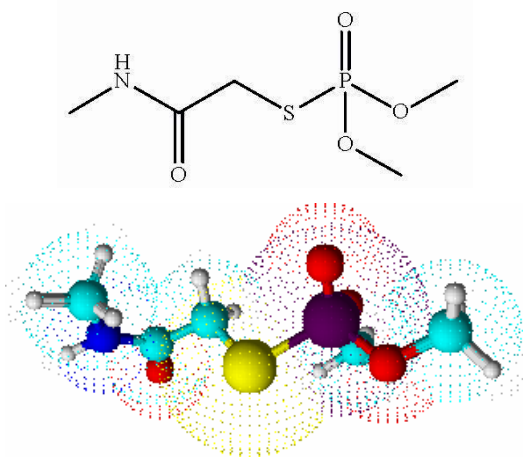


Figure 1b. The structure of OMT.

2. EXPERIMENTAL

2.1. Chemicals

Acetylcholinesterase from electric eel (AChE), acetylthiocholine iodide (ASChI), and 5,5'-dithio-bis-(2-nitrobenzoic acid) (DTNB) were purchased from Sigma-Aldrich St. Louis, MO, USA. Potassium-hydrogen phosphate ($K_2HPO_4 \cdot 3H_2O$) and acetonitrile were purchased from Merck KGaA, Germany. DMT and OMT (>98% purity) were purchased from Pestinal®, Sigma-Aldrich, Denmark. The pesticide working solutions were prepared by diluting the $1 \times 10^{-1} \text{ mol dm}^{-3}$ stock solutions in water. The pesticide stock solutions were held in the refrigerator until used. All chemicals were used without further purification. Deionized water was used throughout.

2.2. Stability of dimethoate and omethoate in aqueous buffer solution

The stability of DMT and OMT on different pH was investigated in 50 mmol dm^{-3} phosphate buffer solution (made using deionized water) with pH ranging from 3 to 9. The solutions of $1 \times 10^{-4} \text{ mol dm}^{-3}$ OPs were incubated

at a temperature of 25 °C and 35 °C in a laboratory orbital shaker-incubator (Orbital Shaker-Incubator ES-20, Grant-bio) for 10 days. The concentrations of investigated OPs were measured as described below in aliquots taken at relevant time points. In addition, the decomposition of $1 \times 10^{-4} \text{ mol dm}^{-3}$ DMT and OMT is analyzed in spiked tap water samples in order to link the results with a realistic scenario. All the measurements were done in triplicate, and the uncertainties were propagated using the least significant differences test (LSDs) at a 95% significance level.

2.3. UPLC analysis

For measuring the concentration of DMT and OMT, Waters ACQUITY Ultra Performance Liquid Chromatography (UPLC) system, coupled with a tunable UV photodiode array (PDA) detector controlled by the Empower software, was used. Chromatographic separations were run on an ACQUITY UPLC™ BEH C18 column with the dimensions $1.7 \mu\text{m}$, $100 \text{ mm} \times 2.1 \text{ mm}$ (Waters). DMT and OMT solutions were analyzed under isocratic conditions with a mobile phase consisting of 10% acetonitrile and 90% water (v/v). The eluent flow rate was $0.25 \text{ cm}^3 \text{ min}^{-1}$, and the injection volume was 5 mm^3 . Optical detection for both OP was done at 200 nm. Under described conditions, retention times of DMT and OMT were $(2.65 \pm 0.05) \text{ min}$ and $(1.12 \pm 0.05) \text{ min}$, respectively. DMT and OMT concentrations in the analyzed samples were determined using the linear calibration curves constructed using standard pesticide solutions in a wide concentration range. The described method was previously optimized and cross-validated using the in-house developed protocols and, as such, used in this and our previous works on DMT/OMT determination.

2.4. Neurotoxicity of DMT and OMT solutions over time

AChE inhibition measurements were performed to follow and quantify changes in the toxicity of DMT and OMT and investigate if there are any transformations of OPs into more toxic forms upon hydrolysis at different pH. These transformation products could exert harmful effects at concentrations below the detection limits of UPLC. AChE activity was assayed according to modified Ellman's procedure. The method is described in detail in our previous work [9], and here we provide a description for completeness. The *in vitro* experiments were performed by exposure of 0.5 IU commercially purified AChE from electric eel to OP solutions obtained in adsorption experiments at 37 °C in 50 mmol dm^{-3} PB pH 8.0 (final volume 0.650 cm^3). The enzymatic reaction was started by adding acetylthiocholine-iodide (ASChI) in combination with DTNB as a chromogenic reagent and allowed to proceed for 8 min until stopped by 10% sodium dodecyl sulfate (SDS). The enzymatic reaction product, thiocholine, reacts with DTNB and forms 5-thio-2-nitrobenzoate, whose optical absorption was measured at 412 nm. It should be noted that in these measurements, the enzyme concentration was constant and set to give an optimal spectrophotometric signal. Physiological effects

were quantified as AChE inhibition given as:

$$\text{inhibition}_{\text{AChE}} = 100 \times \frac{A_0 - A}{A_n} \quad (1)$$

where A_0 and A stand for the AChE activity in the absence of OP and the one measured after the exposure to a given OP. DMT solutions of initial concentration 1×10^{-4} mol dm^{-3} were left in phosphate buffers (pH ranging from 3 to 9, 25 °C and 35 °C) and in tap water for ten days to monitor the toxicity of the spontaneous hydrolysis products.

3. RESULTS AND DISCUSSION

3.1. Stability of dimethoate and omethoate in aqueous buffer solution and decomposition over time

The concentration of DMT and OMT was monitored in tap water and phosphate buffers with pH ranging from 3 to 9, as described in Section 2.2. for 10 days using UPLC analysis.

The time dependence of DMT concentration is presented in Figure 2. It was shown that the spontaneous concentration decay at 25°C (Figure 2a) and 35 °C (Figure 2b) over time is rather fast in buffers with neutral and alkaline pH and tap water (pH 6.5). On the other hand, in buffers with acidic pH, the decrease of OPs concentrations was also noticeable but at a lower rate. Different rate orders for the hydrolysis process were checked. However, in all the cases, the decay of DMT concentrations fitted the best to the exponential one and followed the pseudo-first-order kinetics.

Hence, the hydrolysis rate constants (k_h) were obtained by direct fitting the experimental data into the equation:

$$C_t = C_0 e^{-k_h t} \quad (2)$$

where C_t and C_0 are the remaining OPs concentrations at a given time (t) and the initial OPs concentration.

The results presented in Figure 2 show that with increasing pH value, i.e., the basics of the solution increase the degradation efficiency nonlinearly. The half-life of dimethoate with a concentration of 1×10^{-4} mol dm^{-3} at pH 9 at 25 °C is 8 days, and at 35 °C, it is 1.5 days, while in 9 days, it decomposes to $(3.5 \pm 0.5)\%$ of initial concentration. An increase in temperature of 10 °C accelerates degradation three times.

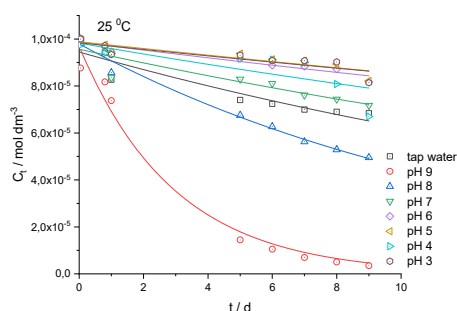


Figure 2a. Dependence of DMT concentration over 10 days at pH from 3 to 9 (25 °C).

Less efficient degradation to pH 8 at 35 °C shows that the half-life is 8.5 days, which means that reducing the pH by 1 increases the degradation length by 3.5 times. It applies to reducing the pH from 9 to 8. For other pH changes, the degradation takes more time.

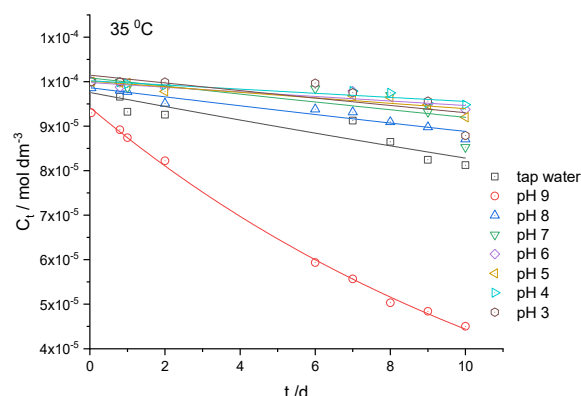


Figure 2b. Dependence of DMT concentration over 10 days at pH from 3 to 9 (35 °C).

The obtained hydrolysis rate constants for DMT and OMT were further used to determine the half-life ($t_{1/2}$) of these OPs under the given experimental conditions. As a result, the half-lives were estimated as:

$$t_{1/2} = \frac{\ln 2}{k_h} \quad (3)$$

The results are presented in Figure 3.

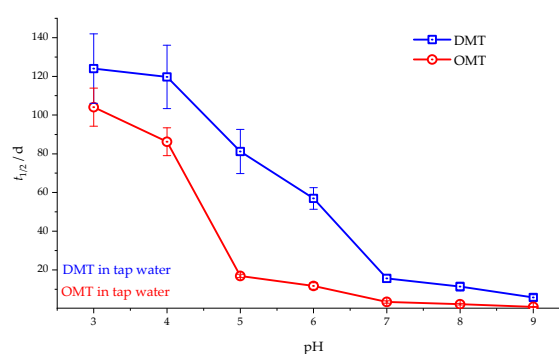


Figure 3. Estimated half-lives ($t_{1/2}$) for DMT and OMT in aqueous solutions as a function of pH (25 °C). The half-lives for spiked tap water are indicated using horizontal lines.

3.2. Neurotoxicity of DMT and OMT solutions over time

In this work, we are primarily interested in reducing DMT solutions toxicity and confirming that no OMT is formed, while the hydrolysis products are not specifically identified. The toxicity of DMT solutions was estimated via the AChE inhibition test as described in Section 2.4. The aliquots for AChE inhibition testing were taken at the start and after 1, 2, 6, and 10 days. The results are given in Figure 4. Toxicity measurements data showed that there is no formation of more toxic products during hydrolysis under the given experimental conditions in all cases.

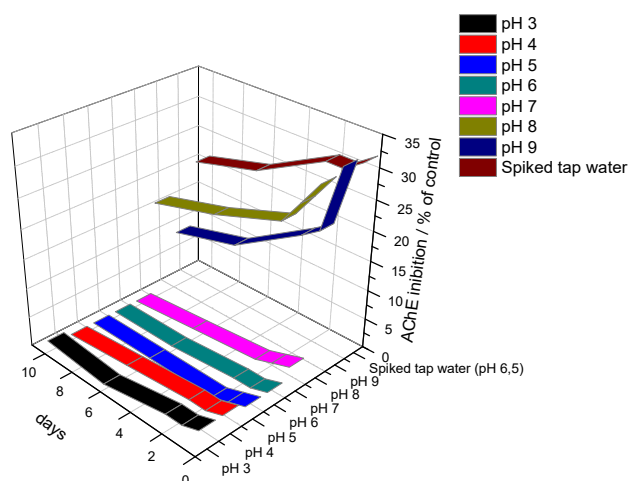


Figure 4. Toxicity of DMT solution over 10 days at pH from 3 to 9. The initial concentration of DMT was 1×10^{-4} mol dm⁻³ (25 °C)

5. CONCLUSION

DMT and OMT hydrolyze at different rates, and OMT hydrolysis is faster than the hydrolysis of DMT. During hydrolysis, there is no accumulation of OMT, which is much more toxic than DMT. As the rate constants of DMT and OMT hydrolysis rapidly increase with pH in alkaline media, it is suggested that alkaline hydrolysis is a suitable way to remove DMT from water. Namely, in contrast to some cases of microbial degradation and photocatalytic oxidation, alkaline hydrolysis does not lead to the accumulation of more toxic products during the degradation process. Hence, if alkaline hydrolysis is used for DMT (and OMT) removal, no special care should be taken to monitor the degradation process as the risk for the formation of toxic products is minor. The matrix effects in tap water were found to have a negligible impact on DMT and OMT hydrolysis rate, so the presented data can be safely used to estimate DMT and OMT half-lives in contaminated water. Toxicity measurements data showed that there is no formation of more toxic products during hydrolysis under the given experimental conditions in all cases. Moreover, the toxicity data can be used to evaluate acute toxicity upon water contamination, measured as the AChE inhibition.

The estimations for longer periods (beyond ten days) can be done using the combination of the stability data and the AChE inhibition curve for DMT. However, the results should be used with care, and it is suggested that general systematic work on OPs stability assessment is needed.

Acknowledgments

The research was funded by the Ministry of Education, Science and Technological Development of the Republic of Serbia.

References

- [1] https://www3.epa.gov/pesticides/chem_search/reg_actions/reregistration/ired_PC-035001_20-Aug-07.pdf
- [2] LAZAREVIC-PASTI, T., D., PASTI, I., A., JOKIC, B., BABIC, B., M., VASIC, V., M. (2016). *Heteroatom-doped mesoporous carbons as efficient adsorbents for removal of dimethoate and omethoate from water*. RSC Advances, 6 (67), 62128-62139. doi:10.1039/c6ra06736k
- [3] VAN, SCOY, A., PENNELL, A., ZHANG, X. (2016). *Environmental Fate and Toxicology of Dimethoate*. Rev Environ Contam Toxicol, 237, 53-70. doi:10.1007/978-3-319-23573-8_3
- [4] <https://pubchem.ncbi.nlm.nih.gov/source/hsdb/1586>
- [5] PAVLIC, M., HAIDEKKER, A., GRUBWIESER, P., RABL, W. (2002). Fatal intoxication with omethoate. Int J Legal Med, 116 (4), 238-241
- [6] <https://pubchem.ncbi.nlm.nih.gov/source/hsdb/1586>
- [7] https://www.who.int/water_sanitation_health/WHS_WWD2010_guidelines_2010_6_en.pdf?ua=1
- [8] MINEAU, P. (1991). *Cholinesterase-inhibiting insecticides : their impact on wildlife and the environment*. Elsevier, Amsterdam
- [9] LAZAREVIC-PASTI, T., COLOVIC, M., SAVIC, J., MOMIC, T., VASIC, V. (2011). *Oxidation of diazinon and malathion by myeloperoxidase*. Pesticide Biochemistry and Physiology, 100 (2), 140-144. doi:https://doi.org/10.1016/j.pestbp.2011.03.001



WASTE-DERIVED CARBON MATERIAL FOR MALATHION ADSORPTION

VLADAN J. ANIĆIJEVIĆ

University of Belgrade, Faculty of Physical Chemistry, Studentski Trg 12, 11000 Belgrade, Serbia, anicijevic.v@gmail.com

KATARINA KOKANOV

University of Belgrade, Faculty of Physical Chemistry, Studentski Trg 12, 11000 Belgrade, Serbia, kokanov.kaca@gmail.com

TAMARA TASIĆ

University of Belgrade, "VINČA" Institute of Nuclear Sciences - National Institute of the Republic of Serbia, Mike Petrovica Alasa 12-14, 11000 Belgrade, Serbia, tamara.tasic@vin.bg.ac.rs

VEDRAN MILANKOVIĆ

University of Belgrade, "VINČA" Institute of Nuclear Sciences - National Institute of the Republic of Serbia, Mike Petrovica Alasa 12-14, 11000 Belgrade, Serbia, vedran.milankovic@vin.bg.ac.rs

TAMARA LAZAREVIĆ-PAŠTI

University of Belgrade, "VINČA" Institute of Nuclear Sciences - National Institute of the Republic of Serbia, Mike Petrovica Alasa 12-14, 11000 Belgrade, Serbia, lazarevictlj@yahoo.com

Abstract: Widespread use of toxic organophosphate malathion raises the need to develop efficient procedures for its elimination from the environment. The acute neurotoxicity of malathion is associated with irreversible inhibition of acetylcholinesterase, the enzyme involved in signal transduction in the nervous system. Its inhibition leads to different neurological disorders. Various methods have been applied for the removal of malathion from water, but one of the most promising is adsorption. We used waste-derived activated carbon material as an adsorbent for malathion. It was shown that 1 g of investigated material is capable of adsorbing 5.514 mg of malathion at 25°C. The toxicity of all samples was decreased after the treatment with the adsorbent. The kinetics of the batch adsorption removal of malathion from aqueous solutions was also investigated. Results showed that malathion adsorption onto activated carbon followed the pseudo-first-order kinetics model most appropriately under the given experimental conditions, with the constant rate value of 0.56248 mg g⁻¹ min⁻¹.

Keywords: malathion, activated carbon, kinetics, toxicity.

1. INTRODUCTION

Organophosphate pesticides (OPs) are phosphoric acid esters and are commonly used as insecticides to control pests. Unfortunately, OPs are highly toxic to humans and animals because they inhibit the enzyme acetylcholinesterase (AChE) [1].

Malathion is a broad-spectrum organophosphate insecticide for agricultural, industrial and domestic use. People could be exposed to malathion by inhalation, dermal contact, diet, and water. In addition, oxidative desulfurization in the liver converts malathion to malaaxon, further resulting in acetylcholinesterase inhibition in nervous tissue [2]. At the same time, malaaxon is considered 22 times more toxic than its thio-analog malathion during acute dietary exposure and 33 times more toxic by all routes of exposure in short- and medium-term exposure [3].

To reduce the impact of OP on health and the environment, there are various methods to eliminate them. These include biodegradation, photocatalysis, electrochemical treatment, membrane separation, oxidation, and adsorption. Among the mentioned methods, adsorption is especially attractive for research and application because it is simple and economically acceptable [4]. Various materials can be used to remove pesticides, such as mesoporous monetite, mineral surfaces, activated carbon and zeolites, carbon-based materials, graphene, and others [5]. However, activated carbon is the most commonly used adsorbent to remove OP compounds due to its large specific surface area, porosity, thermal stability, and low acid/base reactivity. To use different carbon materials for the adsorption of OP, special attention is paid to those obtained by the carbonization of waste materials from agriculture, industry or biomass [6].

This paper aims to examine the adsorption kinetics of malathion on porous waste-derived carbon material. Also, the toxicity of malathion solution after the treatment over time has been investigated. It is of interest to create useful solutions for its removal from water. In addition, AChE activity in malathion solution before and after adsorbent treatment was monitored.

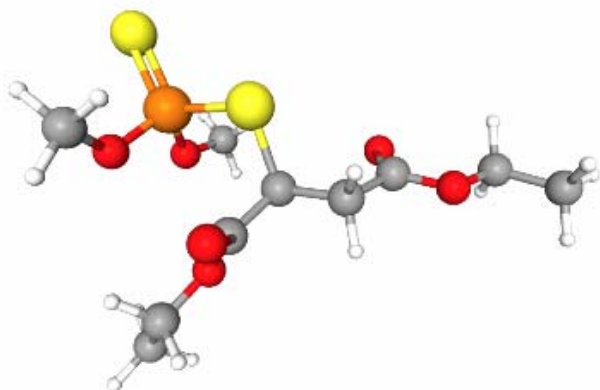


Figure 1. The structure of malathion.

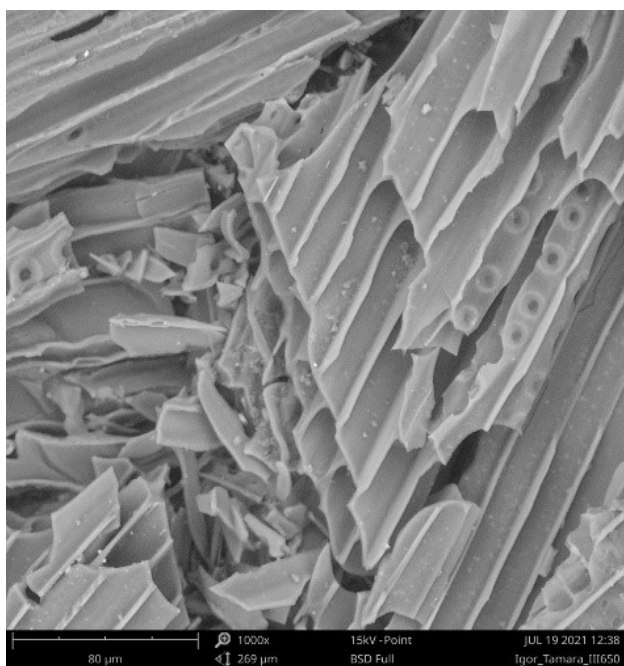


Figure 2. SEM micrography of investigated adsorbent.

2. EXPERIMENTAL

2.1. Chemicals

Acetylcholinesterase from electric eel, acetylthiocholine iodide (ASChI), and 5,5'-dithio-bis-(2-nitrobenzoic acid) (DTNB) were purchased from Sigma-Aldrich St. Louis, MO, USA. Potassium-hydrogen phosphate ($K_2HPO_4 \cdot 3H_2O$) and acetonitrile were purchased from Merck KGaA, Germany. Malathion (> 98% purity) was purchased from Pestinal®, Sigma-Aldrich, Denmark. The working pesticide solutions were prepared by diluting the

$1 \times 10^{-4} \text{ mol dm}^{-3}$ stock solutions in water. The pesticide stock solutions were held in the refrigerator until used. All chemicals were used without further purification. Deionized water was used throughout.

2.2. Material synthesis and adsorption experiments

Used rodent litter was dried for 24 h at 90 °C. Then, it was carbonized in a chamber furnace under a nitrogen atmosphere with a heating rate of 5.0 °C min⁻¹ and held isothermal for 60 min at 650 °C. The obtained carbon material was dispersed in double-distilled water (2 mg cm⁻³), and the desired amount of malathion stock solution was added to provide the targeted concentration of adsorbent and OP. Then, the vessel containing the adsorbent + malathion mixture was placed on a laboratory shaker and left for 1, 3, 5, 7, 10 min at 25 °C. After incubation, the mixture was centrifuged for 10 min at 14 500 rpm, and the supernatant was filtered through a nylon filter membrane.

2.3. UPLC analysis

For measuring the concentration of malathion, Waters ACQUITY Ultra Performance Liquid Chromatography (UPLC) system, coupled with a tunable UV photodiode array (PDA) detector controlled by the Empower software, was used. Chromatographic separations were run on an ACQUITY UPLC™ BEH C18 column with the dimensions 1.7 μm, 100 mm × 2.1 mm (Waters). Malathion solutions were analyzed under isocratic conditions with a mobile phase consisting of 60% acetonitrile and 40% water (v/v). The eluent flow rate was 0.20 cm³ min⁻¹, and the injection volume was 5 mm³. Optical detection for malathion was done at 200 nm. Under described conditions, the retention time of OP was (3.15±0.05) min. Malathion concentration in the analyzed samples was determined using the linear calibration curves constructed using standard pesticide solutions in a wide concentration range. The described method was previously optimized and cross-validated using the in-house developed protocols and, as such, used in this and our previous works on malathion determination.

2.4. SEM analysis

The waste-derived activated carbon material morphology was studied using a scanning electron microscope (SEM) JEOL JSM-5800 (JEOL, Ltd., Akishima, Tokyo, Japan). The sample is placed on carbon tape (which is adhesive on both sides - on one of the adhesive side of the tape with tweezers, powder of homogenized sample is applied). The other side of the adhesive tape is glued to the sample carrier, and then the sample carrier, together with the sample, is placed in the chamber SEM, and then the appropriate measurement is performed.

2.5. Neurotoxicity of malathion solutions

AChE inhibition measurements were performed to follow and quantify changes in the toxicity of malathion solutions before and after the adsorption. Also, this allows

us to investigate if there are any transformations of malathion into more toxic forms upon hydrolysis. These transformation products could exert harmful effects at concentrations below the detection limits of UPLC. AChE activity was assayed according to modified Ellman's procedure. The *in vitro* experiments were performed by exposing 1 U cm^{-3} AChE to malathion solutions before and after the adsorption experiments at 37°C in 50 mmol dm^{-3} PB pH 8.0 (final volume 0.650 cm^3). The enzymatic reaction was started by adding acetylcholine-iodide in combination with DTNB as a chromogenic reagent and allowed to proceed for 8 min until stopped by 10% sodium dodecyl sulfate (SDS). The enzymatic reaction product, thiocholine, reacts with DTNB and forms 5-thio-2-nitrobenzoate, whose optical adsorption was measured at 412 nm. Physiological effects were quantified as AChE inhibition given as:

$$\text{inhibition}_{\text{AChE}} = 100 \times \frac{A_0 - A}{A_0} \quad (1)$$

where A_0 and A stand for the AChE activity in the absence of malathion and the one measured after the exposure to malathion, respectively.

3. RESULTS AND DISCUSSION

3.1. SEM analysis

To examine the three-dimensional structure of the selected adsorbent, SEM micrography was taken and shown in Figure 2. From Figure 2, it can be seen that despite carbonization, the investigated material retained its primary structure. The roughness of the material can also be seen in the picture.

3.2. Kinetics of adsorption removal of malathion from aqueous solutions

To determine the kinetic parameters of malathion adsorption on investigated carbon material, the tested adsorbent at a concentration of 1 mg cm^{-3} was incubated with malathion at a concentration of $5 \times 10^{-5} \text{ mol dm}^{-3}$ at 25°C for 1, 3, 5, 7 and 10 min. The concentration of adsorbed malathion was calculated as the difference between its initial concentration (C_0) and the equilibrium concentration (C_e) of malathion measured by UPLC after removing the adsorbent. The obtained data were used to assess the kinetic parameters by the three kinetic models: pseudo-first-order model, pseudo-second-order model and interparticle diffusion model. The results are shown in Figure 3 and Table 1.

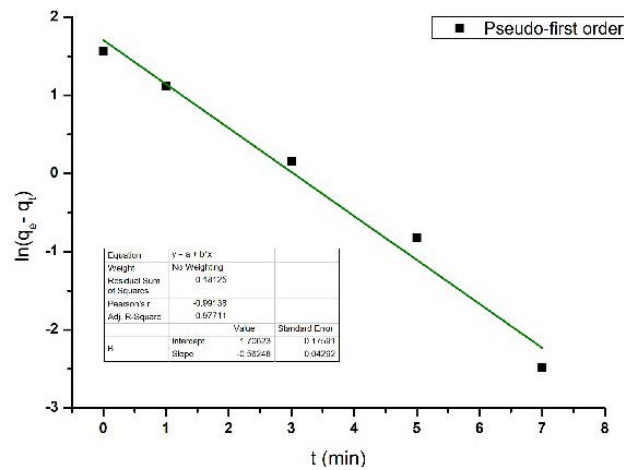


Figure 3a. The plot of pseudo-first-order for $5 \times 10^{-5} \text{ mol dm}^{-3}$ malathion and 1 mg cm^{-3} of adsorbent.

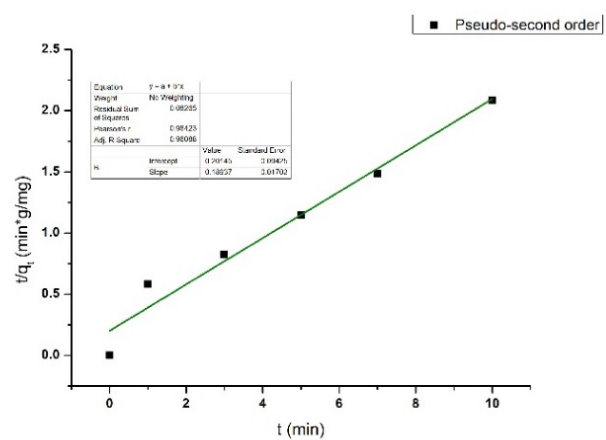


Figure 3b. The plot of pseudo-second-order model for $5 \times 10^{-5} \text{ mol dm}^{-3}$ malathion and 1 mg cm^{-3} adsorbent.

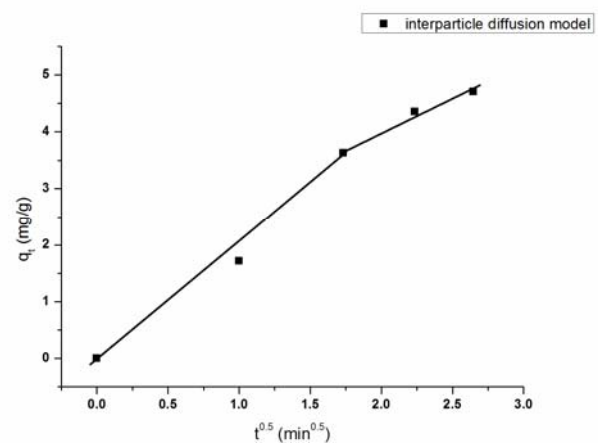


Figure 3c. The plot of the interparticle diffusion model for $5 \times 10^{-5} \text{ mol dm}^{-3}$ malathion and 1 mg cm^{-3} adsorbent.

Table 1. Kinetic parameters of the pseudo-first-order, pseudo-second-order and interparticle diffusion models for 5×10^{-5} mol dm⁻³ malathion and 1 mg cm⁻³ of investigated adsorbent

Parameters	Pseudo-first order	Pseudo-second order	Interparticle diffusion model
k^*	0.56248	0.17801	1.87393
R^2	0.97711	0.96088	0.97829

* (min^{-1}) for pseudo-first order, ($\text{mg g}^{-1} \text{min}^{-1}$) for pseudo-second order and ($\text{mg g}^{-1} \text{min}^{-1/2}$) for interparticle diffusion model

Based on the presented results, it was found that 1 g of test material is capable of adsorbing 5,514 mg of malathion. Besides, the obtained results showed that the adsorption of malathion on the selected adsorbent follows the pseudo-first-order kinetic model under the given experimental conditions with a rate constant of 0.56248 min^{-1} . Also, the interparticle diffusion kinetics model was applied to elucidate the diffusion mechanism. The two divided linear plots suggest the diffusion process occurs via two steps. The first segment of the plot denotes boundary layer diffusion, in contrast to the second segment representing interparticle diffusion of malathion throughout the open cavities of the adsorbent. The value for constant was $1,874 \text{ mg g}^{-1} \text{min}^{-1/2}$ at 25°C .

3.3. Neurotoxicity of malathion solutions

The toxicity of the malathion solution was assessed by the AChE inhibition assay as described in section 2.5. The results are given in Figure 4. Toxicity measurement data showed that under the given experimental conditions, in all cases, there is a decrease in the toxicity of the malathion solutions after the adsorption treatment. This process does not fabricate more toxic products that would more strongly inhibit AChE.

5. CONCLUSION

Activated carbon obtained from waste was used to remove malathion from the water. Based on the presented results, it was found that 1 g of test material is capable of adsorbing 5,514 mg of malathion. Also, the results showed that the adsorption of malathion on the corresponding adsorbent follows the pseudo-first-order kinetic model under given conditions, with a rate constant of 0.56248 min^{-1} . Furthermore, toxicological analysis of aqueous malathion solutions after the treatment with adsorbent showed descending trend, which means no more toxic products are formed during this process. Therefore, the removal of malathion using the tested adsorbent was successful.

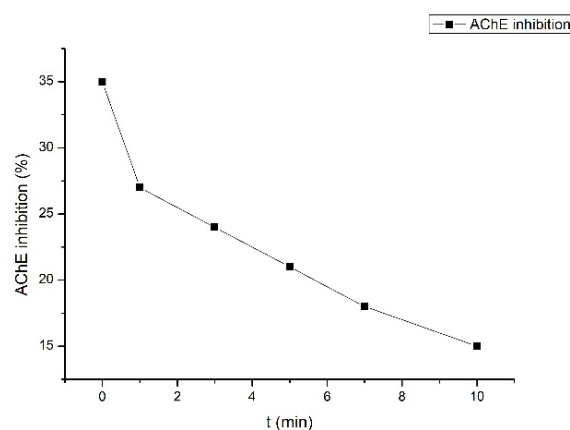


Figure 4. Toxicity of malathion solution after 0, 1, 3, 5, 7 and 10 min of contact with adsorbent. The initial malathion concentration was 5×10^{-5} mol dm⁻³.

Acknowledgments

This work was partially supported by the Ministry for Science of the Republic of Serbia (Grant no. 451-03-9/2022-14/200017).

References

- [1] LIM, L. and H.M. BOLSTAD, Organophosphate Insecticides: Neurodevelopmental Effects☆, in Encyclopedia of Environmental Health (Second Edition), J. Nriagu, Editor. 2019, Elsevier: Oxford. p. 785-791.
- [2] REED, N.R. and A.L. RUBIN, Malathion, in Encyclopedia of Toxicology (Third Edition), P. Wexler, Editor. 2014, Academic Press: Oxford. p. 133-137.
- [3] U.S. Government Printing Office: Washington, D., (2009). Revised Reregistration Eligibility Decision (RED) for Malathion; EPA 738-R-06-030; U.S. Environmental Protection Agency, Office of Prevention, Pesticides and Toxic Substances, Office of Pesticide Programs.
- [4] LIU, G., et al., Adsorption and removal of organophosphorus pesticides from environmental water and soil samples by using magnetic multi-walled carbon nanotubes @ organic framework ZIF-8. Journal of Materials Science, 2018. **53**.
- [5] LAZAREVIĆ-PAŠTI, T., et al., The impact of the structure of graphene-based materials on the removal of organophosphorus pesticides from water. Environmental Science: Nano, 2018. **5**(6): p. 1482-1494.
- [6] LAZAREVIĆ-PAŠTI, T., et al., Esters of Organophosphorus Acids - Toxicity, Application and Removal from the Environment. 2019.



THE DESIGN AND SYNTHESIS OF THE THREE NOVEL DUAL REVERSIBLE INHIBITORS OF ACETYLCHOLINESTERASE BASED ON THE TACRINE AND AROYLACRYLIC ACID PHENYLAMIDE SUBSTRUCTURES

TAMARA B. VUJATOVIĆ-VELIMIROV
Military Technical Institute, Belgrade, tamara.vujatovic@gmail.com

MILAN R. NIKOLIĆ
University of Belgrade - Faculty of Chemistry, Belgrade, mnikolic.chem@gmail.com

MAJA D. VITOROVIĆ-TODOROVIĆ
Military Technical Institute, Belgrade, mvitod@chem.bg.ac.rs

Abstract: Organophosphorous chemical warfare agents (i.e., nerve agents) exhibit toxic effects mainly through covalent, irreversible inhibition of acetylcholinesterase (EC 3.1.1.7), an enzyme that terminates cholinergic neurotransmission, by hydrolyzing acetylcholine at nerve and nerve-muscle junctions. The reversible inhibition of AChE was suggested as the pre-treatment option against nerve agents' intoxications. Aiming to investigate novel pre-treatment options, we designed and synthesized the three novel compounds consisting of tacrine and aroylacrylic acid phenylamide moieties, connected via a long methylene chain to target two distinct topologically separated anionic sites on the AChE. The inhibitory activity of the compounds toward the Electric eel AChE's was determined by the Ellman assay. The designed compounds may represent a new class of promising leads for developing more effective pre-treatment options.

Keywords: Acetylcholinesterase, dual-binding inhibitors, nerve agents, pre-treatment, tacrine, aroylacrylic acid derivatives.

1. INTRODUCTION

Acetylcholinesterase (AChE, EC 3.1.1.7.) is a carboxylesterase which terminates cholinergic neurotransmission by hydrolyzing the neurotransmitter acetylcholine (ACh) in a synaptic cleft of nerve- and nerve-muscle junctions [1]. Organophosphorus compounds are serine esterase and protease inhibitors widely used in agriculture as insecticides and acaricides, in industry and technology as softening agents and additives to lubricants. Some of them are declared chemical warfare agents. Organophosphorous pesticides are considered trialkyl esters of orthophosphoric acid, i.e. organophosphates. Nerve agents have a structure which can be derived from phosphonic acid, i.e. they are organophosphonates. They are divided according to the nature of the leaving group directly attached to the phosphorous atom into two groups: G-agents (alkyl methylphosphonofluoridates) and V-agents (alkyl dialkylaminophosphonotiolates) [2-3]. They rapidly inactivate AChE by binding to the catalytic Ser203 leading to the accumulation of ACh in the synaptic cleft. In the peripheral nervous system, acetylcholine accumulation leads to persistent muscarinic receptor overstimulation that triggers various symptoms, including miosis, profuse secretions, bradycardia, bronchoconstriction, hypotension, and diarrhea. It also leads to

overstimulation of nicotinic receptors, causing severe skeletal muscle fasciculation and subsequent weakness. Central nervous system-related effects include anxiety, restlessness, confusion, ataxia, tremors, seizures, cardiorespiratory paralysis, and coma. Organophosphate binds to catalytic Ser 203 residue, making a covalent complex similar to the acetylated enzyme formed during hydrolysis of the ACh. Hydrolysis of the formed complex is an extremely slow process, and in some instances, depending on the structure of the nerve agent bound to AChE, dealkylation, i.e., leaving of alkoxy group from AChE-nerve agent phosphate, occurs, resulting in a negatively charged dealkylated AChE-OP complex [4]. This process is called 'aging'. Before aging, therapeutic intervention is possible, and the organophosphate can be removed from the active AChE center by an oxime (pralidoxime or obidoxime). Still, AChE is permanently inhibited if aging occurs and cannot be recovered by any means [5].

Treatment for OP intoxication consists of an anticholinergic drug, such as atropine, which relieves the muscarinic symptoms, an oxime, which is able, to some extent, to reactivate the irreversibly inhibited AChE and restore its activity, and an anticonvulsant drug (diazepam or its pro-drug avizafone) which can block nerve agent-induced seizures. This treatment is not fully effective under life-threatening conditions. Oximes are considered

ineffective in the case of soman poisoning, mainly due to the rapid aging process, which prevents enzyme reactivation. The current therapy does not block efficiently nerve-agent induced seizures, which may lead to severe and prolonged brain injury. This treatment must be administered as soon as possible after exposure has happened, which can be complicated in battlefield conditions or any case of massive casualties (accidents, terrorist attacks) [6-7]. Given the drawbacks of the above described standard treatment, the so-called 'pre-treatment' option was proposed. The pre-treatment is given to healthy individuals when there is a higher probability of a chemical attack. The role of reversible AChE inhibitor in the pre-treatment mixture is to temporarily inhibit the fraction of the enzyme and protect it from irreversible, permanent inhibition by OP's. This might be especially important in the case of soman intoxications, where reactivation of AChE is impossible due to a rapid aging reaction.

The efficiency of reversible inhibitors against nerve agent toxicity was examined in several *in vitro* studies. Green was the first to propose that kinetic factors of the reactions between AChE with pre-treatment drug and the nerve agent govern the protective action of carbamates against the toxic action of the nerve agents. He found good qualitative agreement between the proposed theoretical model and *in vivo* experimental results [8].

Petroianu et al. investigated the effects of several moderately potent reversible AChE inhibitors on the rates of irreversible inhibition by organophosphate pesticides paraoxon and mipafox [9]. *In vitro* studies have shown that ranitidin can grant some protection against inhibition of cholinesterases by paraoxon. The results of *in vivo* studies were consistent with *in vitro* results. Administration of ranitidine before exposure to paraoxon increases the number of rats surviving an acute paraoxon exposure and protects the cholinesterases from organophosphate inhibition [10].

Eckert et al. developed a dynamically working *in vitro* model to estimate the protective effects of reversible inhibitors. They proved that pre-treatment with reversible inhibitors results in higher residual AChE activity during the presence of an irreversible inhibitor. Also, they showed that different kinetic behavior of reversible inhibitors determines the level of AChE residual activity and, therefore, the protection [11,12].

Few studies designed novel reversible, highly potent AChE inhibitors and tested *in vitro* their protective potential. Lenina et al. proposed that slow-binding reversible AChE inhibitors, with the slow dissociation from the enzyme and longer residence times in the micro-anatomical compartments such as neuromuscular junctions, may display better protective action compared to other reversible AChE inhibitors [13]. They examined *in vitro* and *in vivo* effects of compound C547, which was found to be a nanomolar reversible inhibitor in *in vitro* studies. Mice treated with C547 before exposure to paraoxon had a higher survival rate than untreated mice. The authors concluded that long-lasting slow-binding reversible AChE inhibitors could be considered new

potential drugs to increase the duration of pre-exposure treatment of OP poisoning.

Based on the previously derived 3D-QSAR model, in our previous work we designed and synthesized three novel dual binding AChE inhibitors. All three compounds were highly potent low nanomolar inhibitors of three cholinesterases (*HuAChE*, *HuBChE*, and *EeAChE*). The experiments revealed that the compounds were able to protect AChE from inhibition by nerve agents partially at compound concentrations higher than their IC_{50} values [14-15].

In this work, we continued the previously described studies and present synthesis, NMR characterization, and anticholinesterase activity of three novel nanomolar dual-binding reversible inhibitors of AChE, differently substituted at aroylphenyl and amidophenyl rings.

2. MATERIALS AND METHODS

2.1. Chemistry

All chemicals were purchased from Sigma Aldrich or Merck, and were used as received. The 1H and ^{13}C NMR spectra were recorded in $CDCl_3$ or d_6 -DMSO on Bruker AVANCE400/101 MHz instrument. Chemical shifts are reported in parts per million (*ppm*) relative to solvent shift. Spin multiplicities are given as follows: *s* (singlet), *d* (doublet), *t* (triplet), *m* (multiplet). Synthetic procedures for aroylacrylic acid amides were previously described in the literature [16].

Synthetic procedure for **9-chloro-1,2,3,4-tetrahydroacridine (3)**: 2-aminobenzoic acid (2.1 g, 15.3 mmol) and cyclohexanone (1.86 mL, 18 mmol) were added to the round bottom flask and placed in ice-bath, then phosphoryl chloride (16 mL) was added drop wise to the reaction mixture. After adding phosphoryl chloride, the reaction mixture was stirred and heated at the reflux temperature for 2,5^h. The reaction solution was then concentrated under reduced pressure (30 °C/560 mmHg, about half of the solution, was removed) and poured into a mixture of ice, deionized water, and acetone. The pH of the solution was set between 8 and 9 by adding potassium carbonate. Crude, solid compound was obtained from solution by filtration and purified by crystallization from acetone. Pure compound was obtained as a yellow solid substance with a reaction yield of 82%. 1H NMR (400 MHz, $CDCl_3$) δ 8.16 (*d*, $J = 8.4$ Hz, 1H, *o*-CH), 8.00 (*d*, $J = 8.4$ Hz, 1H, *o*-CH), 7.66 (*t*, $J = 7.7$ Hz, 1H, *m*-CH), 7.53 (*t*, $J = 7.6$ Hz, 1H, *m*-CH), 3.13 (*t*, $J = 6.2$ Hz, 2H, *o*-CH₂), 3.01 (*t*, $J = 5.9$ Hz, 2H, *o*-CH₂), 2.04 – 1.87 (*overlapped m*, 4H, *m*-CH₂). ^{13}C NMR (101 MHz, $CDCl_3$) δ 159.60, 146.62, 141.82, 129.50, 129.06, 128.64, 126.70, 125.56, 123.85, 77.16, 34.22, 27.64, 22.76.

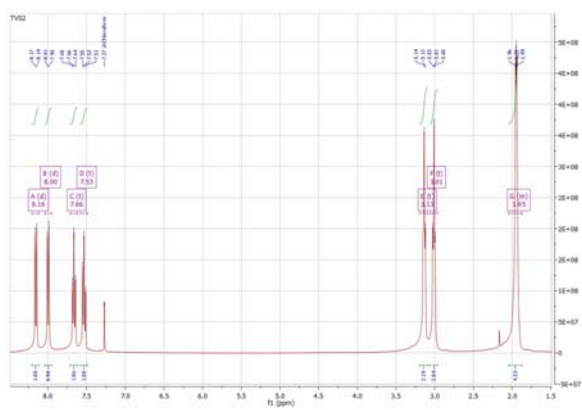


Figure 1. ^1H NMR spectrum of 9-chloro-1,2,3,4-tetrahydroacridine.

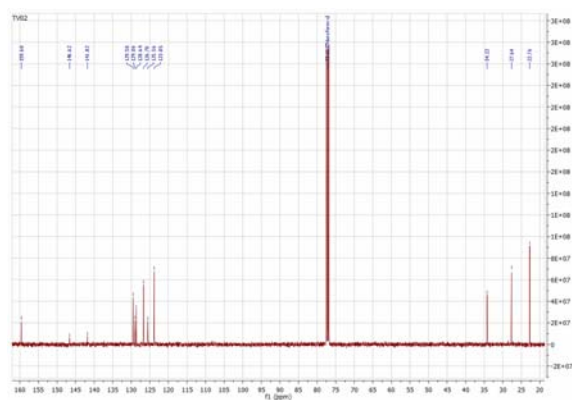


Figure 2. ^{13}C NMR spectrum of 9-chloro-1,2,3,4-tetrahydroacridine.

Synthetic procedure for **N1-(1,2,3,4-Tetrahydro-9-acridinyl)-octane-1,8-diamine(4)**: 1,8-diamino octane (0.99 g, 6.9 mmol), 9-chloro-1,2,3,4-tetrahydroacridine (0.5 g, 2.3 mmol) and 2 mL of 1-pentanol were added to the stainless-steel reactor. Reactor was sealed and heated to 160-165 °C for 8^h. After that, reaction mixture was transferred into separation funnel, diluted with ethyl acetate and washed with 10% aqueous solution of sodium hydroxide, deionized water and saturated aqueous solution of sodium chloride. Organic layer was dried over anhydrous magnesium sulphate and filtered. Solvents were removed under reduced pressure. Crude compound was purified using *dry-flash* chromatography with solvent system $\text{CHCl}_3/\text{MeOH}/\text{Et}_3\text{N}=7/3/0.07$. Pure compound was obtained as yellow semi-solid with reaction yield of 70%. ^1H NMR (400 MHz, CDCl_3) δ 7.94 (*d*, $J = 8.5$ Hz, 1H, *tacrine-o-CH*), 7.89 (*d*, $J = 8.5$ Hz, 1H, *tacrine-o-CH*), 7.53 (*t*, $J = 7.6$ Hz, 1H, *tacrine-m-CH*), 7.32 (*t*, $J = 7.6$ Hz, 1H, *tacrine-m-CH*), 3.46 (*t*, $J = 7.1$ Hz, 2H, linker *NH-CH2*), 3.04 (*s*, 2H, *tacrine-CH2*), 2.72 – 2.62 (*overlapped m*, 4H, *tacrine-CH2*, linker *NH2-CH2*), 2.17 (*br*, 3H, linker *NH* and *NH2*), 1.90 (*s*, 4H, *tacrine-CH2*), 1.63 (*quint*, $J = 14.4$, 7.1 Hz, 2H, linker *NH-CH2-CH2*), 1.50 – 1.23 (*overlapped m*, 10H, linker *CH2*). ^{13}C NMR (101 MHz, CDCl_3) δ 158.42, 150.98, 147.44, 128.67, 128.42, 123.68, 122.97, 120.26, 115.85, 49.58, 42.15, 34.02, 33.55, 31.85, 29.43, 29.39, 26.96, 26.84, 24.87, 23.14, 22.86.

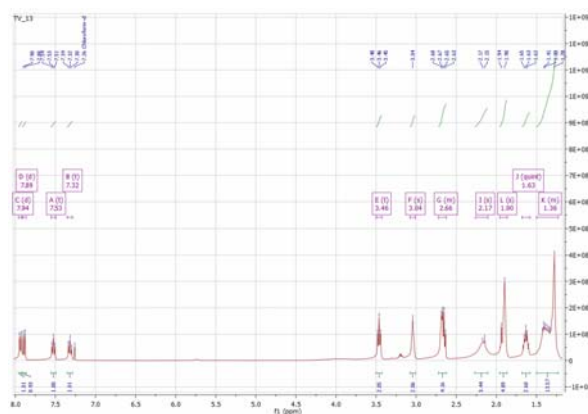


Figure 3. ^1H NMR spectrum N^*1^* -(1,2,3,4-Tetrahydroacridin-9-yl)-octane-1,8-diamine.

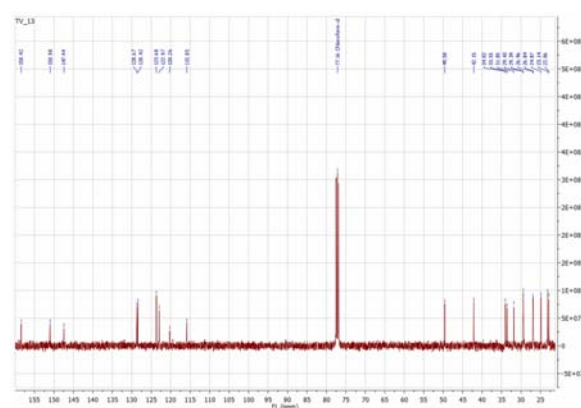


Figure 4. ^{13}C NMR spectrum $\text{N}1$ -(1,2,3,4-Tetrahydroacridin-9-yl)-octane-1,8-diamine.

General synthetic procedure for compounds **8-10**: $\text{N}1$ -(1,2,3,4-Tetrahydro-9-acridinyl)-octane-1,8-diamine was dissolved in DCM and then chosen aroylacrylic acid phenylamide was added. Molar ratio of $\text{N}1$ -(1,2,3,4-Tetrahydro-acridin-9-yl)-octane-1,8-diamine /aroylacrylic acid phenylamide used for synthesis was 1/1. The reaction mixture was stirred at room temperature for 24^h. Reaction progress was monitored by TLC (solvent system $\text{Tol}/\text{EA}/\text{MeOH}/\text{Et}_3\text{N}=2/2/1/0.05$). Crude compounds were obtained by solvent evaporation and purified by *dry-flash* column chromatography on silica gel using the solvent system $\text{Tol}/\text{EA}/\text{MeOH}/\text{Et}_3\text{N}=2/2/1/0.05$.

Synthetic procedure for **N-(3,5-Dimethoxyphenyl)-4-(4-methoxyphenyl)-4-oxo-2-[8-(1,2,3,4-tetrahydro-9-acridinylamino)-octylamino]-butyramide(8)**: Following the described general synthetic procedure, compound was obtained as yellow semi-solid with the reaction yield of 70%. ^1H NMR (400 MHz, CDCl_3) δ 9.58 (*s*, 1H, amido-*NH*), 8.07 – 7.92 (*overlapped m*, 4H, aroyl-*o*-phenyl and *tacrine-o-CH*), 7.57 (*t*, $J = 7.6$ Hz, 1H, *tacrine-m-CH*), 7.35 (*t*, $J = 7.6$ Hz, 1H, *tacrine-m-CH*), 6.93 (*d*, $J = 7.6$ Hz, 2H, aroyl-*m*-phenyl), 6.85 (*d*, $J = 2.1$ Hz, 2H, amido-*o*-phenyl-*CH*), 6.25 (*t-like*, 1H, amido-*p*-phenyl), 4.16 (*br*, 1H, linker *NH*), 3.86 (*s*, 3H, aroyl-*p-OCH3*), 3.78 (*d*, $J = 1.1$ Hz, 6H, amido-3,5-phenyl-diOCH3), 3.65 (*dd*, $J = 8.6, 2.4$ Hz, 1H, ABX), 3.59 (*dd*, $J = 17.3, 2.4$ Hz, 1H, ABX), 3.53 (*t*, $J = 6.8$ Hz, 2H, linker *NHCH2*), 3.24 (*dd*, $J = 17.3, 8.6$ Hz, 1H, ABX), 3.10 (*s*, 2H, *tacrine-CH2*),

2.75 – 2.65 (overlapped *m*, 3H, *tacrine-CH2* and linker **CH2**), 2.61 – 2.52 (*m*, 1H, linker-**CH2**), 2.17 (*s*, 1H, linker-**NH**) 1.92 (*s*, 4H, *tacrine-CH2*), 1.67 (quintet, $J = 14.0, 6.9$ Hz, 2H, linker-**CH2**), 1.50 (quintet, $J = 12.3, 6.4$ Hz, 2H, linker-**CH2**), 1.44 – 1.25 (*m*, $J = 33.7, 16.3$ Hz, 8H, linker-**CH2**). ^{13}C NMR (101 MHz, CDCl_3) δ 197.12, 172.20, 164.09, 164.04, 161.28, 139.70, 130.67, 129.49, 128.94, 127.89, 123.89, 123.12, 114.05, 97.73, 96.71, 59.83, 55.64, 55.52, 49.53, 48.55, 39.98, 33.41, 31.79, 31.00, 30.30, 29.42, 27.25, 26.98, 24.73, 23.04, 22.64.

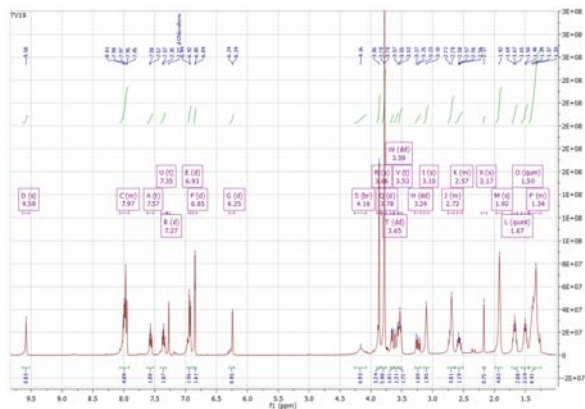


Figure 5. ^1H NMR spectrum of N-(3,5-Dimethoxyphenyl)-4-(4-methoxyphenyl)-4-oxo-2-[8-(1,2,3,4-tetrahydro-acridin-9-ylamino)-octylamino]-butyramide.

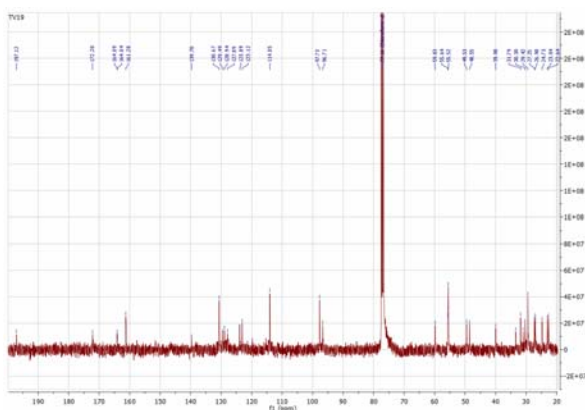


Figure 6. ^{13}C NMR spectrum of N-(3,5-Dimethoxyphenyl)-4-(4-methoxyphenyl)-4-oxo-2-[8-(1,2,3,4-tetrahydro-acridin-9-ylamino)-octylamino]-butyramide.

Synthetic procedure for N-(3,5-Dimethoxyphenyl)-4-(3,4-methyl-phenyl)-4-oxo-2-[8-(1,2,3,4-tetrahydro-acridin-9-ylamino)-octylamino]-butyramide(9): In addition to described general synthetic procedure reaction mixture was heated to reflux and catalytic amount of Et_3N was added. Compound was obtained as yellow semi-solid with the reaction yield of 17%. ^1H NMR (400 MHz, CDCl_3) δ 9.59 (*s*, 1H, amido-**NH**), 7.95 (*d*, $J = 8.3$ Hz, 1H, *tacrine-CH*), 7.89 (*d*, $J = 8.4$ Hz, 1H, *tacrine-CH*), 7.74 (*s*, 1H, aroyl-*o*-phenyl**CH**), 7.70 (*d*, $J = 7.7$ Hz, 1H, aroyl-*o*-phenyl**CH**), 7.53 (*t*, $J = 7.5$ Hz, 1H, *tacrine-CH*), 7.33 (*t*, $J = 7.6$ Hz, 1H, *tacrine-CH*), 7.25-7.15 (*m*, 2H, aroyl-*m*-phenyl-**CH**), 6.84 (*d*, $J = 2.1$ Hz, 2H, amido-*o*-phenyl-**CH**), 6.23 (*t*, $J = 2.0$ Hz, 1H, amido-*p*-phenyl-**CH**), 3.77 (*s*, 6H, amido-*m*-phenyl-**OCH3**), 3.72 – 3.55 (overlapped *m*, 2H, ABX), 3.47 (*t*, $J = 7.2$ Hz, 2H, linker-

NH-CH2-), 3.25 (*dd*, $J = 17.3, 8.7$ Hz, 1H, ABX), 3.05 (*s*, 2H, *tacrine-CH2-*), 2.74 – 2.63 (*m*, 3H, *tacrine-CH2-* and linker-**NH-CH2-**), 2.59 – 2.51 (*m*, 1H, linker-**NH-CH2-**), 2.30 (overlapped *m*, 6H, aroyl-**CH3**), 1.90 (*s*, 4H, *tacrine-CH2-*), 1.68 – 1.60 (*m*, 2H, linker-**NH-CH2-CH2-**), 1.53 – 1.44 (*m*, 2H, linker-**NH-CH2-CH2-**), 1.42 – 1.25 (*m*, 4H, linker-**CH2-**). ^{13}C NMR (101 MHz, CDCl_3) δ 198.50, 172.21, 161.25, 158.38, 151.04, 143.46, 139.67, 137.24, 134.32, 130.09, 129.43, 129.15, 128.50, 128.34, 126.06, 123.72, 123.01, 120.24, 115.83, 97.68, 96.70, 59.71, 55.50, 49.60, 48.51, 40.20, 33.95, 31.86, 30.32, 29.45, 27.27, 27.01, 24.87, 23.14, 22.85, 20.16, 19.86.

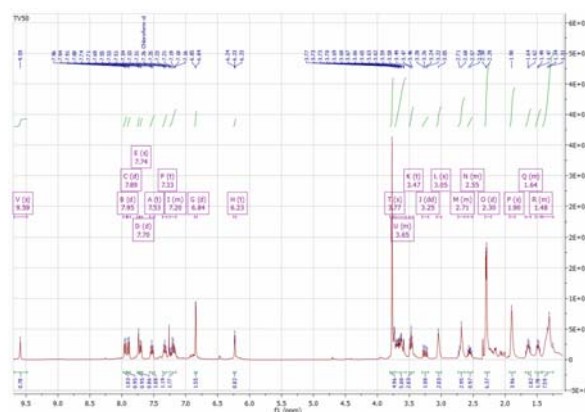


Figure 7. ^1H NMR spectrum of N-(3,5-Dimethoxyphenyl)-4-(3,4-methyl-phenyl)-4-oxo-2-[8-(1,2,3,4-tetrahydro-acridin-9-ylamino)-octylamino]-butyramide.

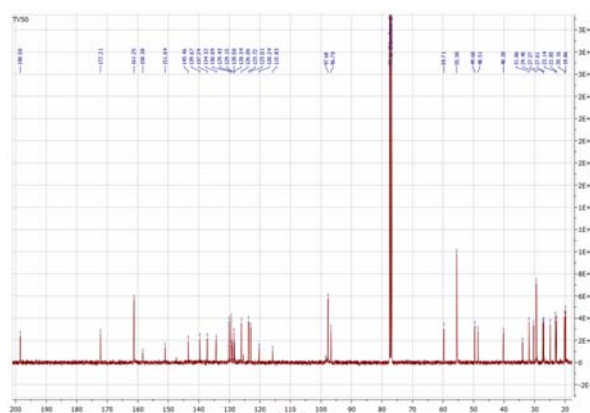


Figure 8. ^{13}C NMR spectrum of N-(3,5-Dimethoxyphenyl)-4-(3,4-methyl-phenyl)-4-oxo-2-[8-(1,2,3,4-tetrahydro-acridin-9-ylamino)-octylamino]-butyramide.

Synthetic procedure for N-(3,5-Dimethoxyphenyl)-4-(2,5-methyl-phenyl)-4-oxo-2-[8-(1,2,3,4-tetrahydro-acridin-9-ylamino)-octylamino]-butyramide(10): In addition to described general synthetic procedure reaction mixture was heated to reflux and catalytic amount of Et_3N was added. Compound was obtained as yellow semi-solid with the reaction yield of 26%. ^1H NMR (400 MHz, CDCl_3) δ 9.55 (*s*, 1H, amido-**NH**), 7.95 (*d*, $J = 8.3$ Hz, 1H, *tacrine-o-CH*), 7.90 (*d*, $J = 8.5$ Hz, 1H, *tacrine-o-CH*), 7.53 (*s*, 1H, aroyl-*o*-phenyl**CH**), 7.33 (*t*, $J = 7.6$ Hz, 1H, *tacrine-m-CH*), 7.28 – 7.23 (overlapped *m*, 2H, *tacrine-m-CH* and solvent), 7.21 – 7.11 (overlapped *m*, 2H, aroyl-*m* and aroyl-*p-CH*), 6.84 (*d*, $J = 2.2$ Hz, 2H, amido-*p*-phenyl-**CH**), 6.23 (*t*, $J = 2.1$ Hz, 1H, amido-*p*-

phenyl-CH), 3.78 (s, 6H, amido-*m*-phenyl-diOCH₃), 3.66 (dd, *J* = 8.6, 3.1 Hz, 1H, ABX), 3.59 – 3.51 (m, 1H, ABX), 3.49 (t, *J* = 7.3 Hz, 2H, linker-NH-CH₂-), 3.24 (dd, *J* = 17.5, 8.6 Hz, 1H, ABX), 3.05 (s, 2H, tacrine-CH₂-), 2.77 – 2.63 (overlapped m, 3H, tacrine-CH₂- and linker NH-CH₂-), 2.58 (dt, *J* = 18.4, 6.1 Hz, 1H, linker NH-CH₂-), 2.46 (s, 1H, linker-NH-), 2.35 (s, 3H, aroyl-CH₃), 2.34 (s, 3H, aroyl-CH₃), 1.91 (s, 4H, tacrine-CH₂-), 1.70 – 1.58 (m, 2H, linker-NH-CH₂CH₂-), 1.56 – 1.46 (m, 2H, linker-NH-CH₂CH₂-), 1.44 – 1.21 (m, 4H, linker-CH₂-). ¹³C NMR (101 MHz, CDCl₃) δ 202.39, 172.12, 161.26, 139.68, 136.79, 135.58, 132.84, 132.22, 129.77, 129.17, 128.59, 128.36, 125.43, 123.77, 123.03, 97.69, 96.67, 59.84, 55.53, 49.62, 48.47, 42.73, 31.89, 31.05, 30.37, 29.49, 27.31, 27.03, 24.87, 23.14, 22.84, 21.58, 21.25, 21.02.

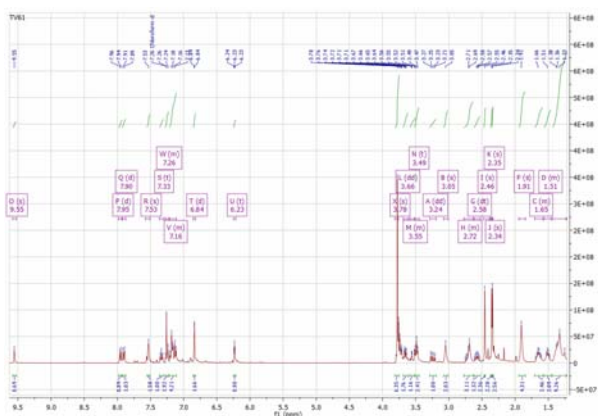


Figure 9. ¹H NMR spectrum of N-(3,5-Dimethoxyphenyl)-4-(2,5-methyl-phenyl)-4-oxo-2-[8-(1,2,3,4-tetrahydro-acridin-9-ylamino)-octylamino]-butyramide.

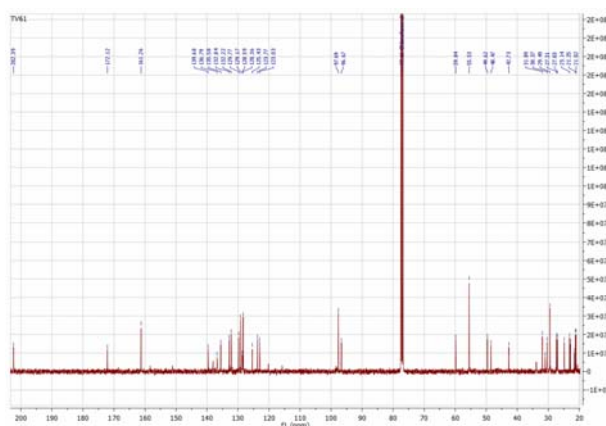


Figure 10. ¹³C NMR spectrum of N-(3,5-Dimethoxyphenyl)-4-(2,5-methyl-phenyl)-4-oxo-2-[8-(1,2,3,4-tetrahydro-acridin-9-ylamino)-octylamino]-butyramide.

2.2. Biology

The inhibition potency of the compounds **8–10** toward E. Eel AChE was evaluated by Ellman assay [20], using the type VI-S enzyme (Sigma) and acetylthiocholine iodide (in final concentration 0.28 mM) as a substrate. The measurements were done on Epoch Microplate Spectrophotometer (Biotek Instruments, USA). A broad range of concentrations, which produce 20–80% of enzyme activity inhibition, were used for each compound.

The reaction took place in the final volume of 0.2 mL of 0.1 M potassium phosphate buffer, pH 8.0, containing 0.02 U of AChE and 0.3 mM of 5,5-dithio-bis(2-nitrobenzoic)acid (DTNB), used to produce yellow anion of 5-thio-2-nitrobenzoic acid in reaction with thiocholine released by AChE. The tested compound (5 μL) was added to the enzyme solution (95 μL) and preincubated at 25 °C for 10 min, followed by the addition of DTNB (95 μL) and substrate (5 μL). The reaction was monitored for 3 min (absorbance was measured every 30 s), and the color production was measured at 412 nm. Determination of inhibition curves was performed at least in triplicate. One triplicate sample without a test compound was always present to yield 100% of AChE activity.

3. RESULTS AND DISCUSSION

3.1. Chemistry

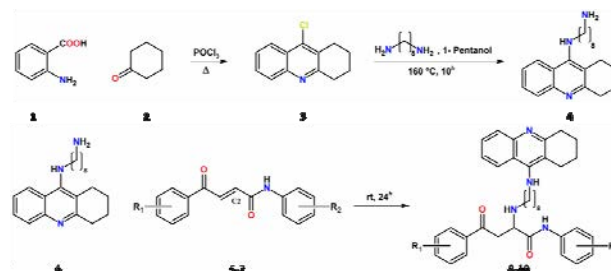
The synthetic path for compounds **8–10** is given in **Scheme 1**, and structures of synthesized compounds and corresponding reaction yields are presented in **Table 1**.

Table 1. Reaction yield of compounds 8-10.

Com. No.	R1	R2	Yield (%)
8	p-OMe	3,5-OMe	74
9	3,4-diMe	3,5-OMe	17
10	2,5-diMe	3,5-OMe	27

The Niementowski reaction between 2-aminobenzoic acid **1** and cyclohexanone **2** proceeded smoothly to give **3**. The procedure was slightly changed in accordance with the previously used procedure. During the process of purification, acetone was added to the mixture of water and ice, which made it possible for the compound to better distribute through the solution and facilitated neutralization. Compound **4** was obtained in the nucleophilic aromatic substitution (S_NAr) reaction of compounds **3** and 1,8-diaminooctane (linker). The reaction took place in a sealed stainless steel reactor. Although a triple amount of linker was used, a considerable amount of tacrine homodimer¹ was formed as a by-product, and it was separated from the targeted compound **4** by *dry-flash* column chromatography.

Michael's addition of **4** and substituted aroylacrylic phenylamides **5–7** was used to obtain the final products, compounds **8–10**. Procedures for the synthesis of aroylacrylic phenylamides are described in the previous work [16].



Scheme 1. Synthetic path for compounds 8-10.

¹ N,N'-Bis-(1,2,3,4-tetrahydro-acridin-9-yl)-octane-1,8-diamine.

The final synthetic step for compound **8** went smoothly with adequate reaction yield. However, compounds **9** and **10** were obtained in significantly lower reaction yields of 17% and 27%, respectively. In the case of compounds **9** and **10**, 24^h from the beginning of Michael's addition, we still noticed the presence of reactants on the TLC plates. To move the reaction equilibrium on the product's side, reaction mixtures were heated for a few hours, and then a catalytic amount of Et₃N was added. This did not increase the reaction yields. The effect of solvent on Michael's addition was examined by replacing DCM with MeOH. The decision to take this step was based on previous work that studied the kinetics of the reaction of Michael's addition using methanol as solvent [17]. However, this also did not increase the reaction yields nor reduce the reaction time needed to obtain the products.

Structures of the compounds differ only in substitution at aroyl ring (R1). In the case of compound **8**, corresponding aroylacrylic phenylamide **5** contains an electronegative atom in the *para* position (R1= *p*-O-CH₃) which can withdraw electron density from the conjugated system, making C2 more partially positive and promoting its electrophilic character. In opposition, corresponding aroylacrylic phenylamides **6** and **7** of compounds **9** and **10** are substituted with -CH₃ group as R1 in positions 3,4- and 2,5- respectively. The methyl group has an electron-donating inductive effect, which increases electron density on the aroyl ring.

Because the electronegative atom is present as an R1 substituent in the structure of compound **5**, the electron density is shifted toward the -OMe group, which results in an easier nucleophilic attack of compound **4**. This effect may explain the faster reaction rate in the case of compound **8** compared to compounds **9-10**.

3.2. Biology

Inhibition potency of compounds **8-10** was determined toward *EeAChE*. The results are shown in **Table 2**. All three compounds are highly potent low nanomolar inhibitors of *EeAChE*. The most potent compound is **8**, and the compound with the lowest inhibition potency is compound **10**.

Table 2. Inhibitory activity of compounds 9-10 toward AChE expressed as IC₅₀ value.

Com. No.	R1	R2	AChE IC ₅₀ ±SEM (nM)
8	<i>p</i> -OMe	3,5-OMe	5.56±0.34
9	3,4-diMe	3,5-OMe	6.97±0.50
10	2,5-diMe	3,5-OMe	25.13±0.27

It has been proven in several previous studies that dual AChE inhibitors bind in the way in which the tacrine substructure is oriented toward the bottom of the active site gorge, interacting with Trp86 and Tyr337 residues. In contrast, the other, a usually aromatic and polycyclic fragment of the molecule, is oriented toward the entrance of the active site gorge and interacts with amino acid residues that belong to the peripheral anionic site (PAS), namely Trp286, among others. PAS area of AChE is very wide and can accommodate a variety of highly

voluminous molecular fragments.

All three compounds are low nanomolar inhibitors of AChE. The difference in inhibitory activity of compounds **8** and **9** toward AChE is negligible, and it seems that methyl substitution at positions 3 and 4 of the aroylphenyl ring does not influence the IC₅₀ values. However, in compound **10**, the methyl substitution at positions 2 and 5 on the aroylphenyl ring notably increased the IC₅₀ values, i.e., reduced inhibitory activity. This may be due to the possible steric hindrance occurring at the PAS site. Still, it is also possible that conformational changes induced by R1 and R2 are responsible for different inhibitory activity toward AChE. To confirm this theory, further examination is needed.

4. CONCLUSION

Three novel dual-binding reversible inhibitors of AChE were synthesized, and their inhibitory activity toward *EeAChE* was examined. The synthesis path included the reaction of Niementowski, nucleophilic aromatic substitution, and Michaelis' addition. Compound **8** had the greatest overall reaction yield and the lowest IC₅₀ of 5.56 nM. Compounds **9** and **10** were obtained in lower yields, and compound **10** was the least active with an IC₅₀ value of 25 nM. All three compounds exhibited low nanomolar activity toward *EeAChE* and are considered good leads for further research.

References

- [1] TÖUGU, V.: *Acetylcholinesterase: Mechanism of Catalysis and Inhibition*, Curr. Med. Chem. – Central Nervous System Agents, 1 (2) (2001) 155-170.
- [2] COSTA, L. G.: *Current issues in organophosphate toxicology*, Clin. Chim Acta, 366 (1-2) (2006) 1-13.
- [3] SZINCZ, L.: *History of chemical and biological warfare agents*, J. Tox., 214 (3) (2005) 167-181.
- [4] KOVACH, I. M.: *Structure and dynamics of serine hydrolase-organophosphate adducts*, J Enzyme Inhib, 2 (3) (1988) 199-208.
- [5] Levy, A., G. Cohen, E. Gilat, R. Duvdevani, N. Allon, S. Shapira, S. Dachir, E. Grauer, Y. Meshulam, I. Rabinovitz, *Therapeutic versus prophylactic treatment strategies against nerve-agent induced brain injuries*, Proc. Med. Def. Biosci. Rev. (2000) 280-290.
- [6] McDONOUGH, J. H., McMONAGLE J., COPELAND T., ZOEFFEL D., SHIH T.: *Comparative evaluation of benzodiazepines for control of soman-induced seizures*, Arch of Toxi, 73 (1999) 473-478.
- [7] PETRAS, J. M.: *Neurology and neuropathology of Soman-induced brain injury: an overview*, J Exp Anal Behav, 61(2) (1994) 319-329.
- [8] GREEN, A.L.: *A theoretical kinetic analysis of the protective action exerted by eserine and other carbamate anticholinesterases against poisoning by organophosphorus compounds*, Biochem Pharmacol, 32 (11) (1983) 1717-1722.

- [9] PETROIANU G., *Weak inhibitors protect cholinesterases from strong inhibitors (paraoxon): in vitro effect of ranitidine*, J. Appl. Toxicol., 25 (1) (2005) 60–67.
- [10] PETROIANU G., HASAN M., NURULAIN S., SHAFIULLAH M., SHEEN R., NEGELKERKE N., *Ranitidine in acute high-dose organophosphate exposure in rats: effect of the time-point of administration and comparison with pyridostigmine*, Basic & Clinical pharmacology & toxicology 99 (4) (2006) 312-316 .
- [11] ECKERT S., EYER P., WOREK F.: *Reversible inhibition of acetylcholinesterase by carbamates or huperzine A increases residual activity of the enzyme upon soman challenge*, Toxicology, 233 (1) (2006) 180-186.
- [12] ECKERT S., EYER P., MÜCKETER H. WOREK F.: *Kinetic analysis of the protection afforded by reversible inhibitors against irreversible inhibition of acetylcholinesterase by highly toxic organophosphorus compounds*, Biochem. Pharmacol. 72 (3) (2006) 344-357.
- [13] LENINA, K. A.; ZUEVA, I. V.; ZOBOV, V. V.; SEMENOV, V. E.; MASSON, P.; PETROV, K. A.: *Slow binding reversible inhibitor of acetylcholinesterase with long lasting action for prophylaxis of organophosphate poisoning*, Sci. Rep., 10 (2020) 16611.
- [14] VITOROVIĆ-TODOROVIĆ, M. D.; CVIJETIĆ, I. N.; JURANIĆ, I. O.; DRAKULIĆ B. J.: *The 3D-QSAR study of 110 diverse, dual binding, acetylcholinesterase inhibitors based on alignment independent descriptors (GRIND-2). The effects of conformation on predictive power and interpretability of the models*, J Mol Graph Model, 38 (2012) 194-210.
- [15] VITOROVIĆ-TODOROVIĆ, M. D.; WOREK, F.; BAUK, S. Đ.; VUJATOVIĆ, T. B.; CVIJETIĆ, I. N: *The in vitro protective effects of the three novel nanomolar reversible inhibitors of human cholinesterases against irreversible inhibition by organophosphorous chemical warfare agents*, Chem. Biol. Interact., 309 (2019) 108714.
- [16] VITOROVIĆ-TODOROVIĆ, M. D.; ERIĆ-NIKOLIĆ, A.; KOLUNDŽIJA, B.; HAMEL, E.; RISTIĆ, S.; JURANIĆ, I. O.; DRAKULIĆ B. J.: *(E)-4-aryl-4-oxo-2-butenic acid amides, chalcone-arylacrylic acid chimeras: design, antiproliferative activity and inhibition of tubulin polymerization*, Eur J Med Chem, 62 (2013) 40-50.
- [17] CVIJETUĆ, N. I.; VITOROVIĆ-TODOROVIĆ, M. D.; JURANIĆ, I. O.; NAKARADA, Đ. J.; MILOSAVLJEVIĆ, M. D.; DRAKULIĆ, B. J.: *Reactivity of (E)-4-aryl-4-oxo-2-butenic acid and phenylamides with piperidine and benzylamine: kinetic and theoretical study*, Monatshefte für Chemie, 145 (8) (2014) 1297-1306.



HIGHLY EFFECTIVE NANOFIBERS WITH CATALYTIC CWA DEGRADATION ACTIVITY FOR CHEMICAL PROTECTION – CURRENT STATE-OF-THE ART

MAJA D. VITOROVIĆ-TODOROVIĆ

Military Technical Institute, Belgrade, mvitod@chem.bg.ac.rs

SONJA Đ. BAUK

Military Technical Institute, Belgrade, zsenic1@gmail.com

TAMARA B. VUJATOVIĆ-VELIMIROV

Military Technical Institute, Belgrade, tamara.vujatovic@gmail.com

Abstract: Current protective materials used for the development of CBRN protective suits and over garments need to fulfill two conflicting requirements: excellent protection that lasts at least 24 hours, but also high breathability and lightness. Currently employed materials, usually based on activated carbon materials, meet to some extent, these criteria. However, they still pose significant physiological burden to soldiers, and there are problems related to the secondary contamination and disposal of the used protective items. In this comprehensive review, we thoroughly analyzed recent developments regarding electrospun nanofibers and their combinations with nanoparticles that exert degradation efficiency toward chemical warfare agents. We briefly discussed various resulting protecting materials obtained in this way, compared their protective, mechanical and physiological properties and estimated their potential to be developed on an industrial scale.

Keywords: chemical warfare agents, protective materials, nanofibers, protection time, degradation efficacy.

1. INTRODUCTION

Engineered materials capable of capture and removal of chemical warfare agents (CWA), toxic industrial chemicals (TICs) and biological agents (bacteria, fungi and viruses) are highly desirable for protective textile applications. The very recent events in the beginning of the 2020, regarding the highest air pollution in Europe in the past ten years and unprecedented Covid-19 pandemics, as well as recent events in Syria regarding usage of CWA's, more than ever increased the need for the enhancement and/or development and implementation of the new types of the efficient protective materials which can be incorporated in the protective overgarments that serve to maintain the exposure to these agents as low as possible. Therefore, one of the main objectives in future will be the design of the lightweight protective composite fabrics, based on the nano-scaled supramolecular entities (particles and fibers) which will meet the following performance requirements:

- 1) Lightweightness and breathability – the resulting material should maintain or increase the overall comfort comparing to materials which are used in the current protective overgarments and protective suits;
- 2) Incorporation of active chemistry – the material should incorporate the possibility not only to retain CBW agents but also to destruct (decontaminate and disinfect) the agents in efficient manner and on the

reasonable time-scale. This will provide additional protection for the users, reduce the possibility of the cross-contamination and resolve the problems of the secondary waste storage and post-use decontamination procedures.

- 3) Reusability and durability – the resulting nano-engineered material should enable multiple usage and should possess optimal physical and mechanical properties to ensure its durability.
- 4) The material should be eco-friendly *i.e.* biodegradable and/or recyclable.

Traditional protective clothes comprise suits and over garments based on permeable materials, usually made of activated carbon liners or based on insulating materials (depending on the application rubber or other plastic and polymers). Although this kind of protective gear affords excellent protection against different kinds of toxic chemicals (especially CWAs) and biological agents, it has some major drawbacks. Some of them are bulk, increased weight and, consequently, the lack of breathability, which induces heat stress in soldiers, medical staff and other users. Moreover, these kinds of materials represent only a physical barrier against CW agents: the toxic chemicals or are retained within the material, so further steps of post-use decontamination procedures and adequate disposal are needed. Because of all stated above, there is an increasing need for the development of more effective protective materials for these purposes, which will not only represent a physical barrier against toxic chemicals, but will also perform decontamination (decomposition) of

toxic chemicals and meet all the requirements given above at the highest possible level. These kinds of products are often called “smart textiles.”

The design of the lightweight, highly breathable and self-decontaminating durable and eco-friendly material for protective suits and overgarments is achievable through the specific combination of the two main nano-scaled entities: (a) incorporation of the nanoparticulates as a carriers of active chemistry which would ensure the degradation of toxic chemicals and disinfection of pathogenic microorganisms and (b) nanofibers which would act as carriers for chemically active nanoparticles and which can be suitably modulated to ensure the optimal breathability in combination with good filtration efficiency and necessary mechanical properties of the materials.

Several chemically active nanoparticles might be useful for chemical and biological decontamination: titanium-dioxide, silver nanoparticles, magnesium-oxide aerogels, zirconium-hydroxide and cerium-oxide. Antibacterial action of the silver nanoparticles is undoubtedly and unequivocally proved in numerous studies. Titanium-dioxide is photoactive material which under UV irradiation is capable of destruction of any organic material, including both toxic chemicals and microorganisms. Beyond that, it is relatively cheap and readily available and also nontoxic [1]. But the major drawback of the TiO₂ is the necessity of the using UV light for its activity. Also, it has relatively low surface area and adsorption capacity comparing to for instance activated carbon which is traditionally used in the chemical protective clothing. Magnesium-oxide aerogel does not need UV irradiation for the destruction of the toxic chemicals and has relatively higher adsorption capacity, but antimicrobial activity is relatively low [2]. It was shown also that zirconium-hydroxide almost instantaneously decomposed several chemical warfare agents and also several nanocomposites based on Zr(IV) compounds exerted satisfactory antimicrobial activity [3].

Electrospun nanofibers are being designed and prepared for a variety of applications where modulation of their unique properties is used to tailor functionality of different products. Those unique properties of nanofibers include high surface area, small fiber diameter, potential to incorporate active chemistry, exceptional filtration properties, layer thinness, high permeability and breathability, and low weight. In electrospinning, a high voltage is applied to a polymer solution or melt, which overcomes the surface tension to form a charged jet. The ejected charged polymeric chains repel each other during the travel to the grounded collector and solidify in the form of thin fibers after solvent evaporation. By controlling the spinning conditions (concentration of polymeric solution, voltage, etc.), ultrafine fibers including microfibers (>1 μm) or nanofibers (<100 nm) can be produced. In this way relatively quickly and simply a variety of different polymer materials into nanofibrous structure can be fabricated.

In this comprehensive review, we thoroughly analyzed recent developments regarding electrospun nanofibers and their combinations with nanoparticles that exert

degradation efficiency toward chemical warfare agents. We briefly discussed various resulting protecting materials obtained in this way, compared their protective, mechanical and physiological properties and estimated their potential to be developed on an industrial scale.

2. CHEMICALLY ACTIVE ELECTROSPUN NANOFIBERS

There are several examples of the nanofibers which bear different chemical functionalities on its surface capable of destruction of various CWA's. For instance, Ramaseshan et al. [4] produced four different types of polyvinyl chloride (PVC) nanofibers with various carriers of active chemistry including: β-cyclodextrine (BCD), o-iodobenzoic acid (IBA), and newly synthesized compound 3-carboxy-4-iodobenzoyloxy-β-cyclodextrine (3CIB). It was shown that BCD possesses high hydrolytic activity toward phosphate alkyl esters, since their hydrophobic cavity mimics the catalytic activity of hydrolase enzymes. IBA is another example of detoxification agent for organophosphorous compounds and it acts as an anionic nucleophile. In reaction with OP compounds, IBA gets converted into o-iodobenzoate anion. Oxidants such as sodium-periodate or magnesium-peroxophthalate can be used to regenerate IBA into active form. Moreover, IBA is also known to be good oxidizing agent for sulfur mustard. The PVC nanofibers were obtained by electrospinning, with the addition of BCD, IBA and 3CIB into solution. Produced nanofibers had diameters between 300 and 450 nm, and the porosity of all membranes was greater than 80% which show that membranes would allow moisture exchange. Hydrolytic activity of the nanofibers was tested using spectrophotometric method and paraoxon as a model compound. The highest activity toward paraoxon hydrolysis showed membrane with 3CIB derivative incorporated, and it removed paraoxon 11.5 times faster than activated carbon by adsorption, which is promising result.

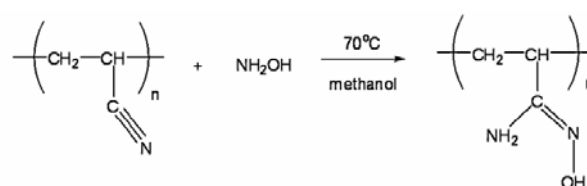


Figure 1. Oximation of PAN fibers.

Chen et al. [5] produced polyacrylonitrile nanofibers (PAN) and modified them by oximation with hydroxylamine to produce polyacrylamidoxime (PAAO) nanofibers as detoxifying protective fabrics, Figure 1. The obtained fibers had diameters from 250 to 500 nm. The hydrolytic activity of the nanofibers was investigated using ³¹P MAS NMR and diisopropylfluorophosphate (DFP) as a model compound. The apparent second-order rate constant, for the DFP hydrolysis was 10⁻⁶ s⁻¹mg⁻¹. The hydrolytic degradation of DFP occurs only in the presence of water, since dried fibers did not degrade DFP. The authors concluded that water serves as a medium to promote the nucleophilic action of the amidoxime groups

in the fibers by facilitating proton transfer and stabilizing the transition state.

Maddak and Azimi [6] produced nanofibers by combining the two polymers, *N,N*-dichloropolystyrene, as a donor of active chlorine species and polystyrene by electrospinning. The *N,N*-dichloropolystyrene was synthesized from polystyrene in five steps, that included sulfonation of polystyrene by sulfuric acid, chlorination with POCl_3 , amidification and chlorination by hypochlorite (Figure 2). The obtained nanofibers had diameters between 160 and 300 nm. The decomposition reaction of 2-CEES on the nanofibers was monitored by GC-MS. Very fast decomposition reaction of 2-CEES on the nanofibers was observed – the total amount of 2-CEES was decomposed in the timeframe of 7 minutes, with the main products of decomposition being ethyl vinyl sulfone, (2-chloroethyl)ethyl sulfone, (2-chloroethyl)ethylsulfoxide, depending on the ratio between 2-CEES and active chlorine species. The amount of active chlorine species in the nanofibers did not varied significantly during six months after production, yielding the stable protective materials.

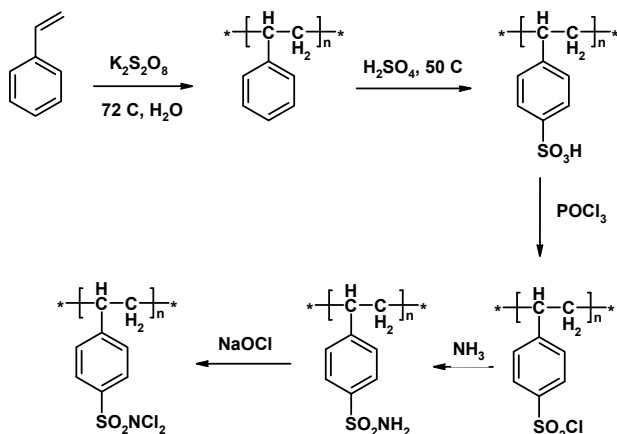


Figure 2. Synthesis of *N,N*-dichloropolystyrene sulfonamide.

Ying and coauthors made a versatile nanofibers combined of guanidine functionalized poly(2-(3-butenyl)-2-oxazoline and Nylon-6,6 polymers by coelectrospinning [7]. Nylon was chosen as a versatile material which is thin and flexible, and also has a high durability and toughness. However, it has a difficulty of introducing functional groups and therefore has a limited application in various specialized fields. Polyoxazolines were chosen because they represent a structural variant of nylon with amide functional groups in the side chains, which can be easily functionalized. Firstly, the poly(2-(3-butenyl)-2-oxazoline was synthesized, then amine groups were introduced using thiolene click chemistry, followed by guanidization, Figure 3. Guanidine as functional reactive group was chosen, due to its strong basicity, with pK_a around 13.6, and can be used as a catalyst for decomposition of organophosphates. Although functionally very reactive, the G-PBuOxz polymer has poor physical properties, forming a gel which is not able to yield nanofibers upon electrospinning.

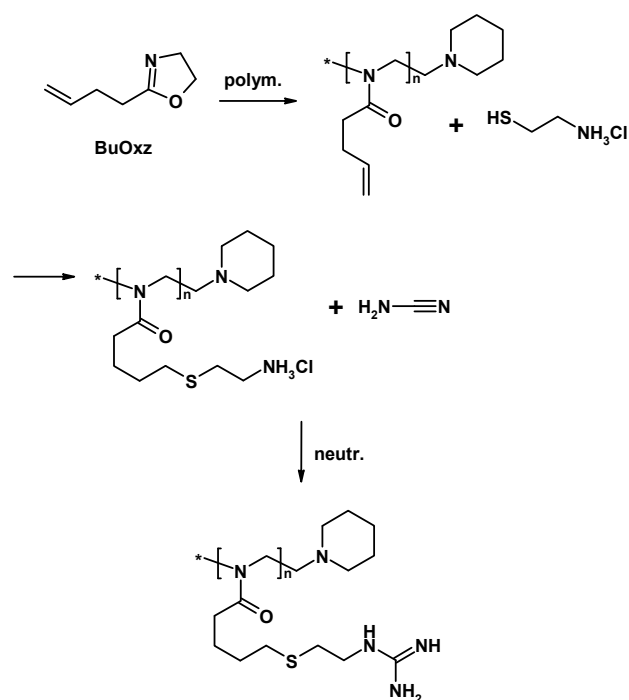


Figure 3. Preparation and guanidization of poly(2-(3-butenyl)-2-oxazoline

However, the mixture of Nylon-66 and G-PBuOxz was electrospun successfully yielding the nanofibers without any notable phase separation. The obtained nanofibers were very effective for the destruction of DFP.

In another work, non-woven nanofiber webs were produced using polyacrylonitrile (PAN) suitably modified by ethylenediamine using chemical vapor deposition process (CVD) to introduce available and hydrolytically active amino-groups into polymer [8]. CVD method may provide several benefits over solvent based treatment of the substrates, because it creates no waste and residues, and it doesn't affect the target material during modification. It is also able to produce uniform coating on the various substrates. In this case, by using various amines, such as ethylenediamine, diethylenetriamine, triethylenetetramine, and ethanolamine and various temperatures for CVD process, several amino-modified PAN nanofibers were produced. Their ability to degrade DFP was investigated by NMR spectroscopy. The fibers which were produced with CVD treatment of PAN with ethylenediamine at $120\text{ }^\circ\text{C}$ showed the best DFP degradation efficiency.

3. ELECTROSPUN NANOFIBERS WITH CHEMICALLY ACTIVE NANOPARTICLES

Many studies investigated the usage of magnesium-oxide (MgO) nanoparticles as carriers of active chemistry in permeable protective materials. They are cheap, easily made and non-toxic and above all, don't require the presence of UV/Vis light to initiate decomposition reaction, which is needed in case of titanium-dioxide nanoparticles.

Sundarrajan and Ramakrishna [9] prepared nanofibers based on the three different polymers: polyvinylchloride (PVC), poly(vinylidene fluoride-co-hexafluoropropylene (PVDF) and polysulfone (PS) and MgO nanoparticles. Firstly, they prepared nanocrystalline MgO and dispersed into solution of polymers for the electrospinning process. The loading of the MgO nanoparticles in the resulting nanofibers was around 30 wt %. The hydrolytic activity of the nanofibers with MgO nanoparticles was investigated by UV-Vis spectrophotometric method using paraoxone as a model compound. The order of reactivity of the membranes was PVC-MgO < PVDF < PSU < PVDF-MgO < PSU-MgO. The PSU-MgO nanoparticles were around two times faster in decomposition of paraoxone, comparing to the activated carbon for the adsorption. Yet the MgO nanoparticles tested in bulk were more active comparing to the PSU-MgO nanofibers which contained the same amount of MgO. The complete decomposition of paraoxone with PSU-MgO nanofibers was achieved after 200 minutes.

In another work by Liu et al. [10], the MgO nanoparticles were *in situ* grown on the surface of poly(m-phenylene isophthalamide), (PMIA), producing a flexible and breathable fabric for CWA's detoxification. The percentage of MgO on PMIA nanofibers was around 11%. The electrospun PMIA nanofibers were dipped into solution of MgSO₄, which was hydrolyzed to Mg(OH)₂, and the fibers were subsequently annealed at 350°C. The PMIA polymer has a high glass transition temperature, so it would not decompose or carbonize below this temperature used for annealing. The functional groups of PMIA would also easily form weak intermolecular interactions with MgO due to the lone pairs on oxygen atoms of PMIA. The degradation efficiency was tested using 2-CEES, a sulfur mustard surrogate by GC-MS. The degradation ability was obvious but relatively slow: around 70% of the 2-CEES was destructed after 20 h of reaction time.

Dadvar et al. [11] investigated the ability of activated carbon nanofibers embedded with MgO or Al₂O₃ nanoparticles to decompose 2-CEES. They used commercially available nanoparticles; MgO was in crystalline form, with particle size of 4-8 nm, while Al₂O₃ was amorphous. The specific surface area of both types of nanoparticles was between 200 and 600 m²/g. Firstly, they made MgO or Al₂O₃ polyacrylonitrile nanofibers by electrospinning and subjected them further to the process of carbonization and activation. The nanofibers with MgO and Al₂O₃ which had higher surface area showed better decontamination efficiency. Around 80% of 2-CEES was removed after 120 minutes of reaction time. Authors concluded that faster decontamination and a higher decomposition yield is related to both higher amounts of nanoparticles embedded in the nanofibers, but is also related with increase in the available reactive sites as a result of higher number of bigger pores.

Ramaseshan and Ramakrishna [12] made polyvinyl-pyrrolidone nanofibers (PVP) incorporated with zinc-titanate nanoparticles for the destruction of CWA's. They produced zinc-titanate nanofibers with sol-gel approach using a polymer binder PVP. The precursors for ZnO and

TiO₂ were titanium-tetraisopropoxide and zinc-acetate, dissolved in ethanol and in the presence of acetic acid the PVP polymer was dissolved. Different ratios of zinc and titanium were used. This mixture was electrospun to obtain the corresponding nanofibers. The nanofibers collected as random mats were annealed at different temperatures ranging from 300 to 700 °C, and cooled with the controlled temperature rate. The BET surface area of the annealed nanofibers was 90-130 m²/g. The only drawback of this approach is that nanofibers became very brittle after annealing. The nanofibers with zinc/titanium ratio of 4:6 annealed at 700 °C showed the highest decomposition efficacy both for paraoxon and 2-CEES; around 87 % of paraoxon was degraded in the first 50 minutes of the reaction, while 67% of 2-CEES was degraded in the first 10 minutes of the reaction. The products of reaction of zinc titanate against the simulants are identified and are found to be relatively harmless. The possibility of replacement of conventional-activated carbon by electrospun ceramic nanofibers for face masks and protective clothing is proposed.

Ryu et al. produced lightweight nanofibrous assemblies with high protection ability against CWA's using laminated outer and inner layer based on nanofiber composite materials [13]. The outer layer was composed of meta-aramid (Nomex) nanofibers and CWA commercially available adsorbents, MgO fine powder of 325 mesh (Sigma Aldrich) and polyoxometalate ammonium phosphomolybdate hydrate, (NH₄)₃PMo₁₂O₄₀ x nH₂O. These adsorbents were added to the electrospun Nomex nanofibers by electrospraying process. The fibers were then thermally treated at 300 °C, above the glass transition of NOMex, then treated with Unidyne to obtain oleophobic properties. The inner layer was made from polyamide 66 nanofibers and also included above mentioned sorbents for CWA's. The outer layer possessed high mechanical strength and an amphiphobic surface, capable of repelling liquid CWA's. The inner layer exhibited low permeability to gaseous CWA's and a high permeability to water vapour. Several combination of inner and outer layers were merged by glue spraying to produce different protective materials which contained 1 to 7 different layers. The permeability of the assembled protective materials were tested according to TOP 08-2-501 standard procedure which determines the permeability for challenge agents DMMP and 2-CEES. The highest protective ability had the material which consisted of 2 outer and 4 inner layers and exhibited permeability of 362.53 μg/cm² for 2-CEES and 126.30 μg/cm² for DMMP which is comparable to the permeability of conventional protective clothes. Authors concluded that these results indicate that the assemblies based on nanofibrous composites can be used to make lighter protective clothing materials than those currently available. Furthermore, the assembly with two outer and six inner sheets, which had comparable weight density to that of the reference protective clothing, exhibited improved protection ability against the simulants.

Many studies investigated the usage of metal organic frameworks (MOF) as carriers of active chemistry on different types of nanofibers for the destruction of toxic chemicals. The vast majority of materials in this area

focus on attaching MOF particles on fibers through covalent attachment or electrospinning polymers containing MOFs in the bulk solution. More recent efforts have focused on *in situ* techniques, where MOF particles are directly grown on the surface of the polymer rather than processing a polymer mixture containing preformed MOF powders into fibers.

Table 1. Novel nanofibers for CWA protection.

Ref.	Nanofiber	Active group	Test agent	Activity/protection
[4]	PVC	BCD, IBA	Paraoxon	11.5 x faster than active carbon
[5]	PAN	-oxime	DFP	$10^{-6} \text{ mg}^{-1} \text{ s}^{-1}$
[6]	PS, N,N-diCIPS	N-chloro	2-CEES	Total decomposition in 7 min
[7]	Guanidine functionalised polyoxazoline	-guanidin	DFP	approx. 60% removal in 2h
[8]	PAN	Ethylene Diamine	DFP	Total decomposition in 24 h
[9]	PVC, PVDF, PS	MgO, 30%	Paraoxon	2x faster than active carbon
[10]	PMIA	MgO, 11%	2-CEES	70% for 20h
[11]	PAN	MgO, Al ₂ O ₃ carbonisation	2-CEES	80% for 120 min
[12]	PVP	ZnTiO ₃	Paraoxon 2-CEES	87% in 50 min 67% in 10 min
[13]	Nomex Polyamide 66	MgO, POM	DMMP 2-CEES	Similar to available PPE

4. CONCLUSION

In the Table 1, all that was discussed above is summarized. It seems that nanofibers with organic functional groups reactive toward CWA's are good strategy for designing smart protective materials. Nanofibers with incorporated IBA and also dichloro modified polystyrene showed exceptional activity for destruction of the nerve and blister agents' simulants. On contrary, majority of nanofibers with nanoparticles incorporated whether in bulk or on their surface showed comparatively lower, but still promising degradation of the challenge agents. However, they have the advantage of reusability comparing to the nanofibers which directly react with the agents. In conclusion, both types of nanofibers show promising potential for the development of novel protective materials and personal protective equipment, and we should expect design of novel promising materials in the foreseeable future.

References

- [1] SENIĆ, Ž., BAUK, S., SIMIĆ, D., VITOROVIĆ-TODOROVIĆ, M., MARKOVIĆ, T., RAJIĆ, *The preliminary comparative analysis of different routes for TiO₂ nanoparticles synthesis and their deposition on textiles. The methyl-orange degradation and VX detoxication study*, Digest Journal of Nanomaterials and Biostructures, 8 (2013) 711-719.
- [2] RAJAGOPALAN, S., KOPER, O., DECKER, S., KLABUNDE, K.J., (2002) Chem. Eur J 8: 2602.
- [3] BANDOSZ, T. J. et al.: *Reactions of VX, GD, and HD with Zr(OH)4: Near Instantaneous Decontamination of VX*, J. Phys. Chem. C, 116 (2012) 11606-11614.
- [4] RAMASESHAN, R., et al.: *Functionalized polymer nanofibre membranes for protection from chemical warfare stimulants*, Nanotechnology 17 (2006) 2947-2953.
- [5] CHEN, L. et al.: *Chemical protection fabrics via surface oximation of electrospun polyacrylonitrile fiber mats*, J. Mater. Chem. 19 (2009) 2432-2438.
- [6] MADDAH, B., AZIMI, M.: *Preparation of N,N-dichloropolystyrene sulfonamide nanofiber as a regenerable self-decontaminating material for protection against chemical warfare agents*, Int. J. Nano Dim. 2 (2012) 253-259.
- [7] YING, W. B. et al.: *Toward a detoxification fabric against nerve gas agents: guanidine-functionalized poly[2-(3-butenyl)-2-oxazoline]/Nylon-6,6 nanofibers*, RSC Adv., 7 (2017) 15246.
- [8] LEE, J. et al.: *Preparation of non-woven nanofiber webs for detoxification of nerve gases*, Polymer 179 (2019) 121664.
- [9] SUNDARRAJAN, S. and RAMAKRISHNA, S.: *Fabrication of nanocomposite membranes from nanofibers and nanoparticles for protection against chemical warfare stimulants*, J Mater Sci 42 (2007) 8400-8407.
- [10] LIU, Y. et al.: *High Efficient Detoxification of Mustard Gas Surrogate Based on Nanofibrous Fabric*, J. Hazard. Mat, 347 (2018) 25-30.
- [11] DADVAR, S. et al.: *The Removal of 2-Chloroethyl Ethyl Sulfide Using Activated Carbon Nanofibers Embedded with MgO and Al₂O₃ Nanoparticles*, J. Chem. Eng. Data 57 (2012) 1456-1462.
- [12] RAMASESHAN, R. AND RAMAKRISHNA, S.: *Zinc Titanate Nanofibers for the Detoxification of Chemical Warfare Simulants*, J. Am. Ceram. Soc., 90 (2007) 1836-1842.
- [13] RYU, S. Y.: *Tunable multilayer assemblies of nanofibrous composite mats as permeable protective materials against chemical warfare agents*, RSC Adv., 7 (2017) 9964.



ASSESSMENT OF THE EFFECTIVENES OF PERSONAL PROTECTION AGAINST THE EFFECTS OF RADIOLOGICAL CONTAMINANTS

SRETEN ILIĆ

Military Tehnical Institute, Belgrade, Belgrade, sreten.iz@orion.rs

NATAŠA PAJIĆ

Military Tehnical Institute, Belgrade, natasa.pajic969@gmail.com

ŽELJKO SENIĆ

Military Tehnical Institute, Belgrade, Belgrade, zsenic1@gmail.com

TATJANA GOLUBOVIĆ

Faculty of Occupational Safety, University of Niš, Niš, acinos2002@gmail.com

Abstract: *The study displays results of examining decontamination efficiency of 1% detergent solution as a formation agent and efficiency of DECON gel decontamination on samples of materials used in manufacture of formation and non-formation means of personal protection. The examination showed that applied radioactive contaminant alters physical properties of the materials used in manufacture of the light protective coat M4 and that radioactive decontamination thereof is not purposeful. It also indicated that DECON GEL decontamination reaches the highest efficiency on samples of rubber located on cheeks of protective mask M3 (95.4%) and rubber of protective boots M4 (95%). Lower percentage of decontamination efficiency was achieved by the 1% detergent solution, and it reached the best results on samples of rubber. DECON GEL can be used more efficiently in radioactive decontamination of protective mask M3 than the formation 1% detergent solution.*

Keywords: *means of protection, contamination, decontamination efficiency*

1. INTRODUCTION

The Earth has been constantly exposed to natural radiation from cosmic sources, as well as the widespread natural active radionuclides. Natural radiation has existed from the very beginning of the Earth. This group includes cosmic radiation, as well as cosmogenous radionuclides resulting from the interaction of cosmic radiation with the atmosphere.

Technological sources are the result of human activity [1]:

- in industry (coal combustion, mining and construction activities, radionuclides in artificial fertilizers...),
- in medicine (for diagnostics and therapy),
- in public use (lightning rods, fire detectors),
- in nuclear facilities.

Radioactive contamination is the undesirable presence of radioactive substances in quantities that may be harmful to the health and dangerous to the life of people. Means of personal protection are intended to protect people against radioactive, chemical and biological contamination. They can be either formation (those present among the Serbian Army weapons) or non-formation (those not present among the SA formation, but with the same purpose). Radioactive decontamination is the procedure of removing radioactive substances from contaminated surfaces. Internal contamination implies entry of the contaminant into human organism through inhalation,

ingestion, or through human skin and mucosa, and chemical matter called radioprotectors is used in such cases. Radioactive material, removed from the contaminated surface by decontamination, is being treated as radioactive waste, and is being processed further, stored and kept in places where it will not represent hazard.

2. PERSONAL PROTECTION

In order to reduce the the impact of radioactive contamination on man it is necessary for individuals, as well as entire companies, to undertake protective measures that can be active or passive [1]. Radioactive protection may be said to represent a series of measures undertaken in order to avoid the consequences of radioactive contamination. Personal protection implies use of formation and non-formation means of protection. Means and equipment for personal protection at work, in terms of Rule Book on preventive measures for safe and healthy work using means and equipment for personal protection at work, includes all means and equipment that an employee wears, holds or otherwise uses at work, for the purpose of protecting themselves from one or more simultaneously arising hazards or damages, that is, to eliminate the risk of injury occurrence and health damage. Means of personal protection play a very important part, and can be divided into general (belonging to each individual) and specific (intended for protection of

personnel performing tasks under increased contamination conditions). General means of protection consist of means of respiratory organs' protection and means of body protection. Respiratory organs' protection employs formation protective masks operating on the principle of filtration or insulation and various non/formation means [1].

2.1. Formation personal protection means

Formation means of personal protection include: Protective mask M3, Protective gloves M4, Light protective coat M4, Protective socks M3, Protective overalls M5, Protective filtering suit M2 and Protective boots M4.

Protective mask M3 (PM M3) is intended for protection of respiratory organs, face and eyes against radioactive particles, poisonous gas (hereinafter as: PGa) and biological agents, as well as other harmful matter in the atmosphere where the percentage of oxygen is not lower than 17%.

Protective overalls M5 (PO M5) is intended for personal protection under considerable droplet contamination (e.g. during decontamination procedure). Provides a high level of protection, but represents a considerable heat burden to the wearer. Apart from chemical protection, PO also protects against radioactive and biological effects and, to a certain extent, against effect of thermal impulse of nuclear explosion (TINE) and burning napalm mixture. PO is produced in one-piece option. There used to be a two-piece option of PO (M3). It can be manufactured with a smaller surface mass, representing a physiologically somewhat more convenient option, as well as performing of some longer lasting activities (e.g. scouting in droplet contaminated zone). The hood is an integral part of the PO. The elements of PO manufactured from butyl rubber are sewn, and butyl strips are attached over the seams. The PO is opened and closed by a zipper located in the front. Ends of the sleeves and trouser legs have rings embedded, allowing firm tightness with

PG and PB. The overalls are decontaminated with the purpose of removing and neutralizing the PGa, biological agents and radioactive contaminants.

Light protective coat M4 (LPC M4) is intended for protection against liquid agents of PGa, contact with PGa droplets, as well as dust and other impurities. It also protects against radioactive precipitation, effect of burning napalm mixture and TINE. By placing personal weapons under LPC M4 they are protected against possible radioactive, chemical and biological contamination. LPC M4 can serve as cover or bolster. The hood is an integral part of LPC M4. It is manufactured in the shape of a cape and primarily in the form of a poncho. Construction solution of PC includes „Velcro“ strips, zippers and side holes with the purpose of obtaining multifunctionality (improvised tent, canopy, etc.). LPC M-4 is manufactured in forms of lighter and heavier type, that is, with lower and higher surface mass of coated butyl rubber. LPC M4 can be manufactured with one-sided or both-sided coating of butyl rubber. It is made in green colour or multicoloured camouflage option.

Protective gloves M4 (PG M4) are intended for protection of hands against effect of vapours, droplets and aerosols of PGa, radioactive precipitation, effects of burning napalm mixture and TINE. They are manufactured on the basis of butyl rubber. For specific purposes they can be manufactured on the basis of neoprene, natural rubber, nitrubber, Viton polymers, latex, etc. They are anatomic in shape and fove-fingered. Soldiers of some armies wear cotton pads underneath PG M4 to collect produced sweat and thus enable easy handling. PG M4 are manufactured from butyl rubber by the technological process of dipping (very seldom pressing). Thickness of PG M4 of 0,7 mm is customary with the mass of 170 t per pair. Specific tasks and special units require thinner or thicker PG, and they are therefore manufactured in material thickness of 0.5 mm to 0.9 mm. PG M4 have solid flexibility even at low temperatures. PG are decontaminated. PG M4 are decontaminated by dry and wet tampons (tampon soaked in soap or detergent solution).

Protective boots M4 (PB M4) are based on butyl rubber with the purpose of protecting the users' feet, primarily against effects of droplet contamination by PGa. PB M4 also protect against radioactive precipitation, effects of burning napalm mixture and TINE. They are used when performing RCB decontamination, RCB scouting, or another activity on contaminated ground.

Protective socks M3 (PS M3) are intended for protection of feet from radioactive, biological and chemical (CBR) contamination. They can decontaminate by the same method as the protective overalls, and can be disposed of and destroyed after use.

2.2. Non-pharmaceutical means of personal protection

Non-pharmaceutical means are not included among weapons of Serbian Army, but can be used for protection. The overalls based on TychemR F is similar in construction to PO M5 based on butyl rubber, with certain specifics concerning this material. Protective overalls based on TychemR F can be decontaminated, but also disposed of due to more accessible price. The suit weighs 450 g. [2]. All the modern armies of the worlds are equipped with protective coat, more precisely, the light type with the mass range of approximately 600 g. Lower mass enables easy movement, also providing lower thermal load. Protection by the coat of lighter type is lower than the protection by coat of heavier type. Generally speaking, protective coat is decontaminated, and the multicoloured camouflage PC unilaterally coated on the interior side is not. Almost all of the world armies are equipped with PS, but there is no such diversity in construction of any other protective means as there is in PS, which clearly indicates that concept solutions differ from army to army. PS are manufactured from very light and simple material of polyethylene type with slight protection, up to PS of heavy type from butyl rubber with high degree of protection against the effect of PGa. Construction solutions also differ. PS can also be coated with layers of various thicknesses, and the degree of achieved protection depends on the type of material and

applied protective layer. They can be monochrome or camouflage multicoloured.

3. MATERIALS USED IN MANUFACTURE OF PERSONAL PROTECTION MEANS

3.1. Insulating materials

Insulating materials are based on elastomer or plastomer. They are manufactured as relatively thick films, applied to the basic textile material based on polyamide, polyester or cotton. These materials are used to manufacture the protective overall, coat, gloves, socks and boots. Generally speaking, there are two basic types of material [2]:

- multilayer sandwich and
- coated textile material.

Du Pont has projected Tychem^R F army material with excellent protective features against the contaminating effect. Tyvek^R F base is Tychem^R C (Tyvec^R, non-woven fibres manufactured from high density polyethylene and polymer layers). The result is Tychem^R C (Figure 1), with firstly the barrier and then the polymer film applied to it, in order to obtain Tychem^R F (Figure 2).

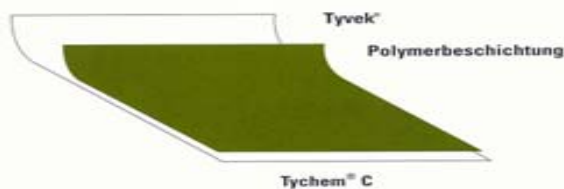


Figure 1. Tychem^R C material [2]

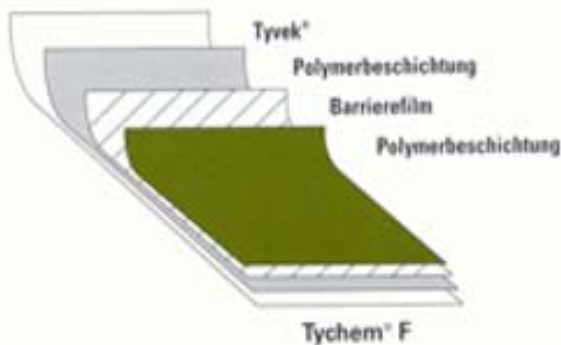


Figure 2. Tychem^R F material [2]

The overalls manufactured from Tychem^R F material protects extremely well against effect of many chemicals, which is very important in certain incident situations. Protection time while under effect of chemical and biological agents is higher than 48 hours. After contamination Tychem^R F either decontaminates or is rejected and destroyed. Tychem^R F is not resistant to effect of thermal impulse of nuclear explosion (TINE) and effect of napalm mixture, does not have camouflage features and is coloured green or white.

3.2. Filtering materials

Filtering materials are primarily used in manufacture of protective filtering suits (PFS) [2], consisting of inner and outer layer (Figure 3).

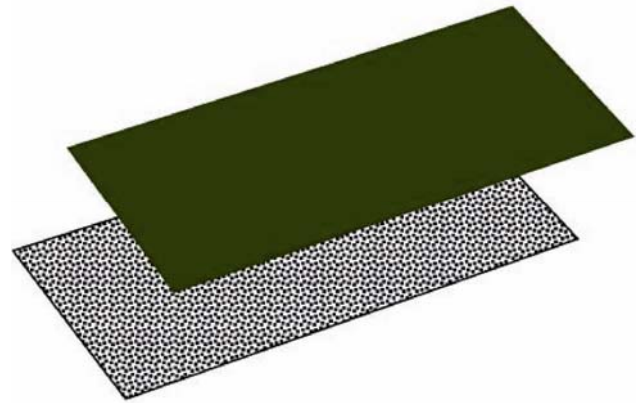


Figure 3. Construction of permeable CBR protective material [2]

Outer layer of filtering material represents woven textile material based on polyamide, polyester, cotton or polyacrylonitrile, which, depending on the required degree and selected mechanism of protection against the effect of PGa, can be processed or unprocessed. The processing refers to obtaining the quality of oleophobicity and fire resistance. Inner layer of filtering materials consists of the filtering layer, constituting of the holding fabric, and the sorption layer of active carbon material. Nowadays active coal is the basic component of permeable PFS. It is used in three basic forms [2]: granules or powder, spheres and carbon fibrous material. The active coal powder is applied to the woven textile material or thrown into the structure of non-woven textile material and polyurethane foam and is used in manufacture of the inner layer of PFS.

4. BASIC TERMS OF RADIOACTIVE CONTAMINATION AND DECONTAMINATION

4.1. Radioactive contamination

Radioactive contamination is defined as undesirable presence of radioactive materials in quantities exceeding permissible limits [3]. A radioactive contaminant that a surface can come in touch with may appear in solid, liquid or gaseous states. A contaminant dissolved in water can have an ionic or neutral form, while those that are not dissolved in water comprise a wide range of disperse states, form molecular aggregates, colloidal particles, and particles ranging from submicron to macroscopic in dimensions.

The strength of an established bond between contaminants and a surface depends of the nature of the contaminants and nature of the force surface established in contaminating can be of [3]:

- electrostatic nature;
- physical nature, excluding electrical;
- chemical, with the reaction between the contaminants and the surface producing new chemical compounds, and
- mechanical.

Depending on the character of forces acting in the contamination process, there is a possibility of occurrence of equivalent (molecule) adsorption, ion exchange adsorption and specific adsorption, also chemisorption and action of physical forces, as well as mechanical process.

Equivalent or molecule adsorption is based on equivalent action of cations and anions, with the electrolyte molecules adsorbing as a unity in such cases. If surface of the adsorbent, which had previously adsorbed an ion, contains an ion of the same charge, exchange between these two ions may occur, such form of adsorption being the ionic exchange adsorption. Specific adsorption occurs in case an adsorbent more strongly adsorbs one ion in the solution than the other, with resulting difference in potential between the bordering surfaces of the adsorbent and the solution. If a new chemical compound is created during the contamination process of a surface, such form of adsorption is named chemisorption. Mechanical procedure results from capturing of minute particles of the contaminant by a surface which is not ideal in the actual case and contains various defects, pores and cavities that the contaminant can penetrate.

Contamination also occurs through activation of the given material, if it entered a field of the corresponding radiation and thus got contaminated by their isotopes [4].

4.2. Radioactive decontamination

The term radioactive decontamination indicates a series of actions or processes eliminating contamination from surfaces. Decontamination of people, devices, technical instruments, facilities and land ought to stop spreading of contamination and reduce it to a permissible level where it had already occurred. Processes and procedures of decontamination include washing, heating, chemical or electrochemical action, as well as mechanical removing of contamination from certain surfaces. Generally speaking, multiple diversified methods or combination thereof, are necessary in each decontaminating procedure.

While implementing decontamination procedures one can encounter a problem of detecting low concentrations of contaminants and verifying reduction of their concentration to a permissible level, that is, determining of decontamination efficiency.

4.3. Radioactive decontamination methods

Methods of radioactive decontamination can be divided into dry and wet ones. The term wet methods imply that the procedures are based on chemical and physicochemical processes of eliminating radioactive contaminants from contaminated surfaces using water, detergents, solutions and solvents. The decontamination process itself occurs in the liquid stage, with particles of a contaminant separating from the surfaces on account of reduction in adhesion force [3].

Dry decontamination methods include the procedures of collecting and eliminating radioactivity by mechanical actions in absence of liquid environment (using lasers, vacuum and ultrasound, scraping, wiping, brushing,

peeling and other procedures). Loosely bound contamination is subjected to use of vacuum decontamination instruments, equipped with filters absorbing and retaining the radioactive material. Loosely bound and extensive contamination (thick layer of radioactive dust) is subjected to special varnishes that are applied to a contaminated surface, that dry very quickly and thus firmly bind the contaminant. After a while the varnish layer is peeled off together with the contaminant, after which additional decontamination procedures are implemented. Relatively bound contamination is mostly eliminated by wet methods. The most difficult contaminant to remove is the one bound to the surface by adsorbing chemical forces. The first level of decontamination includes removing of loosely bound contaminants. The remaining contamination is removed in the next step by decontaminating solutions containing complexing agents with the purpose of preventing resedimentation of the contaminants. If there is residual contamination after completing decontamination, abrasive agents are used.

4.4. Radioactive decontamination efficiency

The decontamination process comes down to breaking up the bond between the contaminant and the surface. The capacity of a surface to bind to itself and retain a certain contaminant is called contaminability, and its capacity to loosen and break up the bond between the contaminant and the surface under an influence (decontamination agent) – decontaminability. At the same time, contaminability also serves to compare different materials in terms of their susceptibility to contamination, as well as compare efficiency of different means of decontamination in relation to the same contaminated surface. Contaminability of a surface, relative to the given radionuclide, is expressed in percentages of residual activity at a surface ZA (%), representing the ratio between residual activity A after decontamination and initial activity A₀ [5]:

$$ZA (\%) = A/A_0 * 100 \quad (1)$$

The percentage of withdrawn activity SA (%) can be reached through the ratio between the withdrawn activity A₀-A and initial activity A₀ [5]:

$$SA (\%) = ((A_0 - A) / A_0) * 100 \quad (2)$$

The measure of decontamination efficiency is the decontamination factor F_d, defined as the ratio between initial activity A₀ and residual activity A after completion of decontamination, an can be expressed in equation:

$$F_d = A_0/A \quad (3)$$

It is evident that, the higher the decontamination factor, the more efficient will the decontamination process be, the higher the percentage of withdrawn activity, and the lower the percentage of the residual activity.

Decontamination efficiency represents the ratio between the decontamination factor (F_d) and the percentage of removed activity (% R), as defined in the following equations:

$$\% R = (1 - A / A_0) * 100 \quad (4)$$

$$F_d = A_0 / A$$

where A_0 is radioactive activity off the surface prior to application of decontaminating technologies, and A is the radioactive activity off the surface after decontamination.

$$\% R = (1 - 1 / F_d) * 100$$

Decontamination factor of 10 results in 90% of removed radionuclides from a surface:

$$90\% = (1 - 1/10) * 100.$$

5. SAMPLING AND MEASURING METHODOLOGY

In the period from the beginning of January until the end of July 2021 a number of 10 material samples were obtained and used to manufacture formation and non-formation means of personal protection (Figure 4a and 4b).

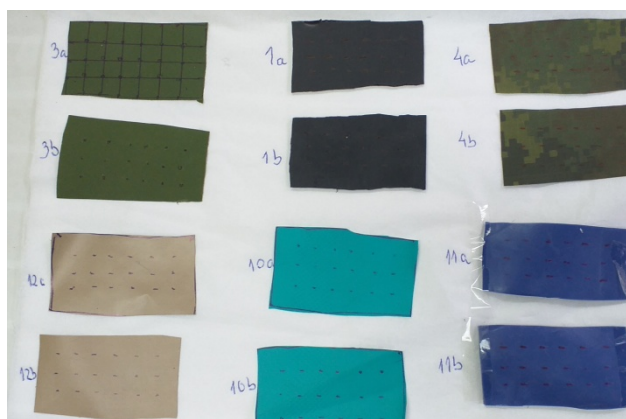


Figure 4a. Protective means material samples
(Photo: N. Pajic)

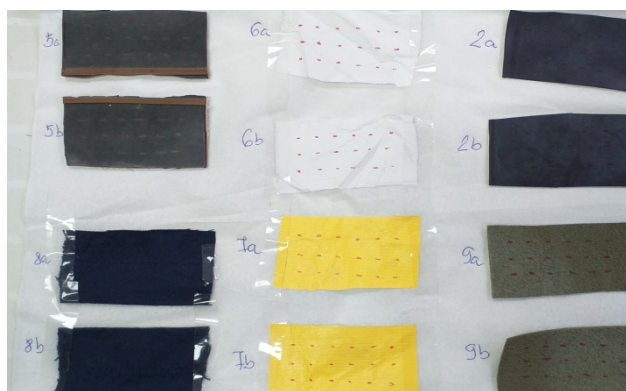


Figure 4b. Protective means material samples
(Photo: N. Pajic)

Out of the formation ones a number of 5 material samples were obtained that are used to manufacture 7 formation means of personal protection, namely: Protective mask M3, Protective gloves, Protective coat light M4, Protective socks M3, Protective overalls M5, Protective filtering suit M2 and Protective boots M4. 4 material samples were also obtained that are used to manufacture non-formation means of personal protection, namely: Tyvek overalls, Tychem overalls, Protective socks heavy

type, NITRAS gloves and samples of materials used to manufacture the protective hood (brown colour material from figure 4a). Two rectangles were cut out from each of the material samples of 3x5 cm dimensions, marked, amounting to the total of 20 material samples (Picture 4a and 4b). After that the samples were contaminated by the contaminating solution of specific activity of 1.23×10^4 Bq/mL and $\text{pH} = 2.5$, representing the diluted mixture of liquid samples of radioactive isotopes ^{60}Co (964.56 Bq/ml) in form of CoCl_2 , ^{133}Ba (515.79 Bq/ml) in form of BaCl_2 , ^{152}Eu (9496.12 Bq/ml) in form of EuCl_3 and ^{241}Am (1321.47 Bq/ml) $\text{Am}(\text{NO}_3)_3$. Marked area of sample of 15 cm^2 , (50 × 30) mm, was contaminated by applying 18 drops of solution of 10 μl volume in homogenous layout. Contaminated samples were dried in a digester in standard laboratory conditions.

Thus prepared material samples were measured on a semiconductor HPGe spectrometre, produced by „AMETEK-ORTEC“, of the resolution (FWHM) of 1.78 keV and of relative efficiency of 56.2 % for ^{60}Co at 1332 keV [6,7], thus obtaining the initial activity (A_0).

The detector was placed within a special low-pitched lead protection with 12 cm thick walls and 5 mm thick copper inner layer. All of the samples were measured for 10000 seconds, in order to obtain appropriate statistics of counting speed in the spectre.

Efficiency calibration of the detector was performed by a radioactive standard in a Marineli dish of 1000 ml, type MBSS, Inspectorate for ionizing radiation of the Czech metrolorical institute (certificate no: Cert.No: 9031-OL-159/08), the matrix of which is the sylicone resin of density with radionuclides: ^{241}Am , ^{109}Cd , ^{57}Co , ^{139}Ce , ^{133}Ba , ^{113}Sn , ^{85}Sr , ^{137}Cs , ^{88}Y , ^{54}Mn and ^{60}Co . The spectrum analyses were done on the basis of present gamma lines [6]. Software pakage Gamma Vision 32 was used to determine specific activity [7]. Obtained values of countdown below peaks of observed lines were corrected to the fon measured at 250000 s.

6. RESULTS AND DISCUSSION

In all of the 20 material samples, after receiving the initial activity (A_0), decontamination was performed by 1% detergent solution on 10 samples, and decontamination by DECON gel was performed on the remaining 10 samples. Applied radioactive contaminant alters physical properties of materials used in manufacture of Protective coat light M4 (LPC M4) and Tyvek material, that is, it deforms them. After contamination of „b“ samples (displaying deformity), no contamination was performed of the „a“ samples (Table 1). After performed decontamination, the samples were subjected to new measuring and thus obtained sample activity (A). After this, the decontamination factor was calculated, as well as efficiency of decontamination (equations 3 and 4). Obtained results are displayed in Table 1.

Table 1. Efficiency of decontamination of material used in manufacture of means of personal protection

Sample type	Decontamination by DECON gel – samples a			
	A ₀ Bqcm ⁻²	A Bqcm ⁻²	F _d	%R
Rubber on cheeks PM M3	9023	418	21.6	95.4
Rubber PG M4	17020	3100	5.49	81.8
Rubberized canvas PO M5	11240	3716	3.02	67
Rubberized canvas LPC M4	11720	2513	4.66	78
Rubber PB M4	11800	633	18.63	95
Tyvek material	6240	1371	4.55	78
Tychem material	21010	1545	13.6	93
Rubber PS M3 heavy type	3485	1901	0.55	83
NITRAS gloves	1870	309	6.05	83
Sample type	Decontamination by 1% detergent solution – samples b			
	A ₀ Bqcm ⁻²	A Bqcm ⁻²	F _d	%R
Rubber on cheeks PM M3	24000	4002	6	83.3
Rubber PG M4	16660	3144	5.30	81.1
Rubberized canvas PO M5	18600	3710	5.01	80
Rubberized canvas LPC M4	/	/	/	/
Rubber PB M4	21200	3200	6.63	84.9
Tyvek material	/	/	/	/
Tychem material	/	/	/	/
Rubber PS M3 heavy type	/	/	/	/
NITRAS gloves	/	/	/	/
Protective hood material	1990	345	5.77	82.7
Protective hood material	12400	2351	5.27	81

The applied method has proven as successful in assessment of efficiency of decontamination of rubber and textile materials and can as such be applied to other surfaces. Earlier research has shown that retention time of contaminants on surfaces has strong impact on efficiency of decontamination. Much higher decontamination efficiency was observed in rubber material samples as opposed to samples of textile materials. Difference in efficiency of decontamination in the examined materials is increasing almost linearly with the increase of time of retaining contaminants on the samples. Analysis of obtained results, after contamination procedures, and subsequent decontamination of samples leads to the conclusion that the highest efficiency of decontamination is displayed by DECON GEL on samples of rubber in cheeks of the mask, with 95,4% and rubber PB with 95% decontamination efficiency. Lower decontamination percentage was achieved by 1% detergent solution,

obtaining best results on samples of rubber in mask cheeks with 95% decontamination efficiency. Next lower decontamination percentage was achieved by 1% detergent solution, scoring best on samples of rubber in mask cheeks with 83.3%, as well as rubber in PB M4 with 84.9%.

7. CONCLUSION

After use of radioactive contaminants, the decontamination of people, weapons, technical resources, facilities and land should prevent spreading of contamination and, where it has occurred – to reduce it to a permissible level. While reaching the decision on the resources and methods to be used in decontamination procedures it is important to determine the level of contamination and define the physicochemical form of the contaminant and the contaminated surface. While implementing decontamination procedures one can encounter a problem of detecting low concentrations of contaminants and verifying reduction of their concentration to a permissible level, that is, determining of decontamination efficiency.

This study has defined procedures of decontamination by modern means of decontamination, as well as the efficiency of decontamination on means of personal protection in use, accentuating the impact of ratio between the contaminants and the contaminated surface.

The study compares results obtained by measurements on the subject means of radioactive decontamination. In the following research we need to consider introduction of new means of radioactive decontamination, as modern technologies and methods have shown that there are much more efficient means in the market, as well as means with a wider scope of impact, both in radioactive and chemical decontamination.

References

- [1] Glišović, D., *Protivnuklearno, hemijsko i biološko obezbeđenje*, Beograd: SSNO, 1976.
- [2] Dobričanin, D.: *Zaštita tela*, Vojnotehnički institut, 2009.
- [3] Lazarević, N.: *Dekontaminacija radne i životne sredine*, Beograd, INN "Vinča", 2017.
- [4] INN Vinča, *Radioaktivni izotopi i zračenja, knjiga II-Radne tehnike*, Beograd: Institut za nuklearne nauke "Boris Kidrič", 1985.
- [5] Vujošević, S., *Obuka za rad sa otvorenim izvorima i osposobljavanje za sprovođenje mera zaštite u naučnoistraživačkoj delatnosti*, Beograd: Institut za nuklearne nauke "Vinča", INN "Vinča", 2017.
- [6] Slivka, J.: *Gama spektrometrija - specijalne metode i primene*, Novi Sad: Univerzitet u Novom sadu, Prirodno -matematički fakultet, 2000.
- [7] ORTEC Gamma Vision - 32, Gamma-Ray Spectrum Analysis and MCA Emulator for Microsoft Windows 95, 98, 2000. s.l. : Software User's Manual, 2002.



INFLUENCES OF ELECTROLYTE TYPE AND AGITATION REGIMES ON STRUCTURAL – MECHANICAL PERFORMANCE OF ELECTROLYTICALLY DEPOSITED COPPER COATINGS ON DIFFERENT CATHODES

IVANA MLADENović

Institute of Chemistry, Technology and Metallurgy, University of Belgrade, Njegoševa 12, 11 000 Belgrade, Serbia,
ivana@nanosys.ihtm.bg.ac.rs

NEBOJŠA NIKOLIĆ

Institute of Chemistry, Technology and Metallurgy, University of Belgrade, Njegoševa 12, 11000 Belgrade, Serbia,
nikolic@ihtm.bg.ac.rs

JELENA LAMOVEC

University of Criminal Investigation and Police Studies, Cara Dušana 196, Zemun, 11 000 Belgrade, Serbia,
jelena.lamovec@kpu.edu.rs

DRAGAN TANASKOVIĆ

Institute of Chemistry, Technology and Metallurgy, University of Belgrade, Njegoseva 12, 11000 Belgrade, Serbia,
dragant@nanosys.ihtm.bg.ac.rs

MILOŠ VORKAPIĆ

Institute of Chemistry, Technology and Metallurgy, University of Belgrade, Njegoseva 12, 11000 Belgrade, Serbia,
worcky@nanosys.ihtm.bg.ac.rs

VESNA RADOJEVIĆ

Faculty of Technology and Metallurgy, University of Belgrade, Karnegijeva 4, 11 000 Belgrade, Serbia,
vesnar@tmf.bg.ac.rs

DANA VASILJEVIĆ RADOVIĆ

Institute of Chemistry, Technology and Metallurgy, University of Belgrade, Njegoševa 12, 11000 Belgrade, Serbia,
dana@nanosys.ihtm.bg.ac.rs

Abstract Composite systems of electrodeposited 10 μm Cu coatings on Cu foils and 30 μm Cu coatings on brass foils were obtained in direct current regimes (DC) from electrolytes without/with additives. Different regimes of stirring electrolytes were investigated: stationary, magnetic, and ultrasonic. Also, multilayered Cu coating was successfully obtained by the electrodeposition with periodic ultrasonic/magnetic stirring of basic sulfate electrolyte. A bending test technique was used to assess the adhesive strength to the cathodes. Vickers indentation test machine was used for measuring composite hardness in the micro-range. The adhesion parameters named “the critical reduced depth” and “critical cycle number” for the Cu coatings proved suitable for assessing the adhesion behavior. Composite hardness models of Korsunsky and Chen-Gao were applied in order to calculate an intrinsic hardness of the coatings and for an assessment of adhesion performance. The corrosion resistance of the Cu coatings was investigated using the “static corrosion test.” A comparative study showed that the Cu coatings produced in ultrasonic agitation regime or in laminate form have better mechanical properties and better corrosion resistance. It has also been shown that Cu coatings synthesized from electrolyte with additives are structurally superior, but a “soft hardening effect” was observed.

Keywords: composite, soft hardening effect, adhesion, critical reduced depth, critical cycle number.

1. INTRODUCTION

In the field of surface engineering and materials engineering the copper coatings and multilayer copper structures had attracted great interest. Control of the microstructure of these materials in cost-effective manner enables the development of high-performance materials

[1]. Among various techniques to enhance coating properties, electrodeposition technique is simple, low-cost, eco-friendly, easy-controlled, and compatible with other deposition techniques, such as: physical vapour deposition (PVD), chemical vapour deposition (CVD), spraying and roll-to roll coating processes [2]. The properties of copper coatings are a key factor that

determines the reliability of interconnections because copper replaced aluminum as the interconnect material in VLSI technology [3]. Ultrasonic-electrodeposition has much attention recently. The ultrasonic-electrodeposition was used for dispersion of the second phase in copper matrix such as SiC nanoparticles [4], for increasing deposition rate, for improved density and uniformity of the coating or enhanced ion diffusivity of electroplating solution [5]. However, the roughness of copper coatings can be increasing with the application of the stronger intensity of ultrasound probe indicating a strong effect of ultrasound on hydrodynamic conditions in the near-electrode layer, which is manifested by the increase of share of the „activation control“ in the mixed „activation-diffusion control“ of electroplating process [6]. The beneficial impact on the micromechanical properties of copper coatings was shown during electrodeposition with the assistance of the ultrasound bath during mixing of the electrolyte [7-8]. Nowadays, with application of old technique with little modification, it is possible to replace conventional electrodeposition copper coating (ordinary) with new nanostructured coating (ultrasonically) or with superior multilayer (laminated) composite structures.

The surface hardness of the different forms of copper coating can be investigated using continually or discontinually indentation techniques such as: nanoindentation or microindentation hardness techniques with various application types of shape indenter (pyramid, cone, sphere etc.) [9]. However, with application of microindentation technique for very thin coating with an application of loads above some critical value, a substrate (cathode) commences to contribute to a composite hardness. Then, it is necessary to apply corresponding mathematical composite hardness model for a determination of the absolute (or real) hardness of coating [10-14].

The adhesion strength of thin coating to the substrate is very important, too. Poor adhesion leads to a reduction in mechanical structural performance [10-12]. Test methods for coating adhesion investigation are very different. Fast tests are often used in the industry, such as: knife, tape-test, pull-off adhesion test, scrape, scratch test and bending test [15]. An adhesion is also a measurable result of some hardness tests made by pencil hardness, gravelometer, impact, mandrel bend or indentation Rockwell technique [16]. However, there is no universal test for adhesion testing of all types of coatings. Most simple tests are not expressed in numerical values or SI units, but are given descriptively, terms like „film failed“ or „film passed“ [12]. The adhesion investigation for the type of composite system „soft film on a hard substrate“ was conducted by Chen and Gao through a composite hardness model application of microindentation Vicker's technique on the example of copper films/glass substrate adhesion behavior [10-12]. The bending test jig was applied to investigate the adhesion of the copper coating to the stainless steel substrate using bending method [3]. The bending times or number of cycles before first delamination (air bubble appear on the sample) were recorded as the adhesion criterion of the coating samples. In this investigation the adhesion of the coating to the substrate was measured by bending method using a special automatic bending test designed in our lab. The

idea is to compare the values of the adhesion parameter (b) and the values of the critical number of cycles (n). The adhesion parameter (b) or critical reduced depth of indentation was calculated based on composite hardness model applied to experimental value of composite hardness. The adhesion parameter (n) or critical cycle number was obtained by measuring the adhesion through the bending test on home-made devices. In the experimental part of the paper, the construction and fabrication of devices based on the Fused Deposition Modeling (FDM) procedure will be presented [17]. An additive manufacturing technology and biodegradable material (filament based on polylactic acid-PLA) were used for fabricated parts of the adhesion testing device.

2. EXPERIMENTAL

2.1. Synthesis of copper coatings

Copper coatings were produced using the direct current galvanostatic mode (DC regime), DC mode with an application of ultrasound mixing of electrolytes (DC/US regime) and DC mode with an application of magnetic mixing of electrolyte (DC/MS regime) at constant current densities ($j = 50 \text{ mA} \cdot \text{cm}^{-2}$). For processes of the electrodeposition, the following electrolytes were used: 240 g/l $\text{CuSO}_4 \cdot 5 \text{H}_2\text{O}$ in 60 g/l H_2SO_4 , *electrolyte I* and 240 g/l $\text{CuSO}_4 \cdot 5\text{H}_2\text{O}$, 60 g/l H_2SO_4 , 0.124 g/l NaCl, 1 g/l PEG 6000 (polyethylene-glycol), 0.0015 g/l MPSA (3-Mercapto-1-propane sulfonic acid), *electrolyte II* [6-8]. Also, multilayered Cu coating was successfully obtained by the electrodeposition with periodic ultrasonic/magnetic stirring of *electrolyte I*. The ultrasonic bath (Bransonic 220 Ultrasonic Cleaner), frequency at 40 kHz, was performed for mixing of electrolyte [8]. The electrolytes were also stirred by an application of magnetic stirrer (MS) (100 rpm, Heidolph Instruments GmbH & Co. KG, Schwabach, Germany).

Table 1. The conditions of electrodeposition applied for a formation of Cu coatings on different substrates from electrolytes *I* and *II*. In all experiments current density was $j = 50 \text{ mA} \cdot \text{cm}^{-2}$.

No.	Name	Regime	Substrate	Thickness, δ (μm)	El.
1.	Ordinary	DC	Brass	30	<i>II</i>
2.	Ultrasonically	DC/MS	Brass	30	<i>II</i>
3.	Magnetically	DC/US	Brass	30	<i>II</i>
4.	Ordinary	DC	Cu	10	<i>I</i>
5.	Ultrasonically	DC/US	Cu	10	<i>I</i>
6.	Laminated	DC+DC/US	Cu	10	<i>I</i>

The cathodes were brass foil (260 1/2 hard, ASTM B36, K&S Engineering, 250 μm thick) and polycrystalline (pc) copper foil (125 μm thick) polished mechanically. The copper plate, cylindrical in shape, was used as anode, polished chemically in acid solution before deposition ($\text{HNO}_3 : \text{H}_2\text{O} = 1:1 \text{ vol. } \%$). The temperature and pH-values were maintained at $22 \pm 0.5 \text{ }^\circ\text{C}$, 0.30 (for

electrolyte I) and 0.33 (for *electrolyte II*), respectively. The coating thickness were 10 μm and 30 μm . Deposition area was 2 cm^2 . The coating thickness is controlled by the mechanical comparator with electronic reader on display (model: Iskra, type: NP37 (Iskra Avtomatica, Ljubljana, Slovenia) with the accuracy of the vertical shift $\pm 1 \mu\text{m}$ [7]. All conditions of obtained Cu coatings are summarized in Table 1.

2.2. Realization of lab-made bending test machine for adhesion evaluation using additive technology

The photography of our lab-made device for testing of copper coatings on various metal and flexible substrates on non-standard test machine is shown in Figure 1. Certain elements of the prototype were realized on a 3D printer (WANHAO Duplicator i3Plus, desktop printer ID: SHBST15080055732341YER-3, China). The basic parameters of device are: build volume $200 \times 200 \times 180 \text{ mm}$; layer resolution 0.1-0.4 mm; print speed 10-100 mm s^{-1} and extruder temperature 240°C - 260°C . The following parameters were used during the fabrication of PLA elements: 1) printing nozzle temperature of 215°C , 2) build plate temperature of 60°C , 3) print speed of 50 mm s^{-1} , 4) travel speed of 70 mm s^{-1} , and 5) infill orientation 90/-45/0/+45 and the 100% infill.

In this technical solution, a bipolar stepper motor NEMA 17HS4401 is used as a power unit with a 1.80 angular pitch, holding torque of 40 N·cm, and 1.7 A of phase current. The stepper motor provides precise positioning of the timing belt. It is computer controlled via a microcontroller board connected to a stepper motor driver. The test parameters for cyclic adhesion test were the following: maximal number of cycles ($n_{\text{max}} = 1000$), speed of rotation of step motors ($w = 500 \text{ o}\cdot\text{min}^{-1}$), the pulling force ($F_c = 21 \text{ N}$), speed of timing belt ($v = 9 \text{ m}\cdot\text{s}^{-1}$) and dimension of sample was $110 \times 10 \text{ mm}^2$ with coating deposition area of $50 \times 4 \text{ mm}^2$ [7].

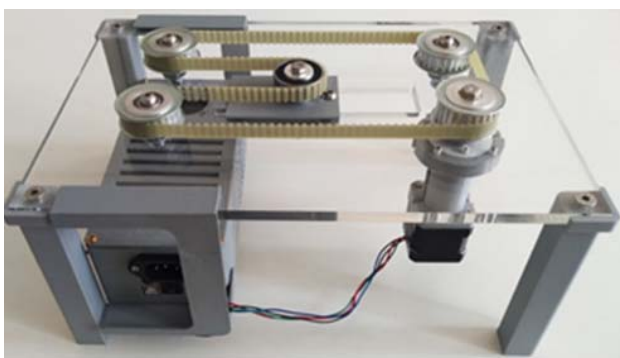


Figure 1. Appearance of the designed device for testing the adhesion by cyclic bending: real photography view.

2.3. Examination of the compactness of the copper coatings

The corrosion property and compactness of copper coatings obtained galvanostatic in different applied regimes and deposition times were investigated using static corrosion test. The nitric acid (20% HNO_3) was

selected as a corrosion medium, based on reference [3]. The experiment is based on weight losses of the copper samples in static corrosion test using acid solution. The corrosion start time of the sample (beginning of the etching reaction) is the moment when the first bubbles of gas (H_2) appear on the copper surface. The beginning of the reaction and the appearance of bubbles on the sample is shown in Figure 2.

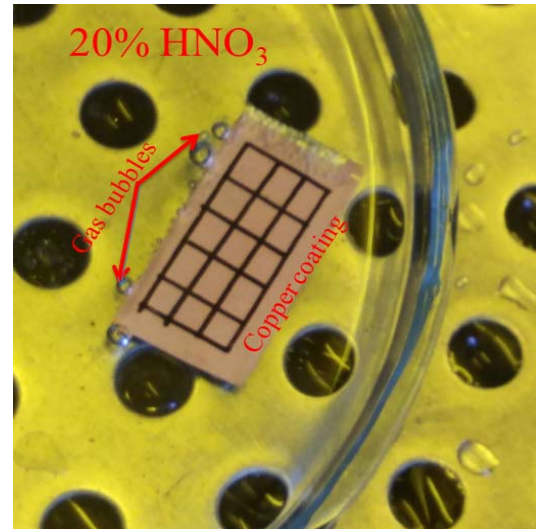


Figure 2. The appearance of the first gas bubbles as an indicator of the start of the reaction (etching start time).

2.4. Examination of the real hardness of the Cu coatings

Hardness analysis of the coatings was done by Vickers microindentation test machine. An applied loads were between 0.049 and 2.452 N, and a dwell time of 25 s. Vickers microhardness tester Leitz Kleinert Pruffer DURIMET I (Leitz, Oberkochen, Germany) was used for a determination of hardness. The measured Vicker's hardness of coating is defined by Eq. (1) [9]:

$$H_c = 0.01854 \cdot P \cdot d^{-2} \quad (1)$$

In Eq. (1), H_c (in Pa) is a measured or composite hardness, P (in N) is an applied load, and d (in m) is a size of diagonal made in a coating during indentation. Hardness of the substrates was determined by the PSR (Proportional Specimen Resistance) model, Eq. (2) [18]. The parameters a_1 and a_2 correspond to the elastic and plastic properties of the material.

$$\frac{P}{d} = a_1 + a_2 \cdot d \quad (2)$$

For electrolytically produced Cu/brass systems, the Chen-Gao (C-G) composite hardness model [10–12] was used for a determination of the absolute hardness of Cu coatings. This model was employed to evaluate the adhesion of Cu coatings on substrates, too. The following equations were used for the calculations: -equation (3) was used to fit the experimental data; -equation (4) was used to calculate coating hardness value (H_{coat}); -equation (5) was used to calculate adhesion parameter b :

$$H_C = A + B \cdot \frac{1}{h} + C \cdot \frac{1}{h^{m+1}} \quad (3)$$

where A , B and C are fitting parameters, calculated from curve fitting. Indentation depth (h) can be calculated as 1/7 of diagonal size as theoretical value according geometry of indenter [6-8, 10-12]. The value of m (power index) is found to be 1.8 for $H_{coat} < H_s$ ($m \rightarrow 2$; volume law of mixtures applies) or 1.2 ($m \rightarrow 1$; area law of mixtures applies) for $H_{coat} > H_s$ [10-12].

$$H_{coat} = A \pm \sqrt[m]{\frac{[m \cdot |B| / (m+1)]^{m+1}}{m \cdot |C|}} \quad (4)$$

The value of the adhesion parameter b is determined from the slope of the linear fit of the line $\Delta H = f(\delta/d)$:

$$\Delta H = \left[\frac{7 \cdot (m+1) \cdot (H_s - H_{coat})}{m \cdot b} \right] \cdot \frac{\delta}{d} \quad (5)$$

Model of Korsunsky (K-model) is suitable for the analysis of “hard film on soft substrate” composite systems [13-14] such as composite system Cu/Cu. The composite hardness, H_c according to this model, is expressed as equation (6):

$$H_c = H_s + \left[\frac{1}{1 + k' \cdot \left(\frac{d^2}{\delta} \right)} \right] \cdot (H_{coat} - H_s) \quad (6)$$

A dimensionless material parameter k' is related to the composite response mode to indentation.

3. RESULT AND DISCUSSION

3.1. Absolute hardness of cathodes (substrates)

Based on the PSR model, the absolute hardness of the selected cathode materials was estimated. The experimental points were given on Figure 3. By multiplying the value of the slope with the Vicker's constant, the absolute hardness of the substrate is calculated. The hardness of brass was 1.41 GPa [6], and hardness for copper substrate was 0.36 GPa. We can see that the hardness of brass substrate was $3.92 \times$ harder than copper substrate.

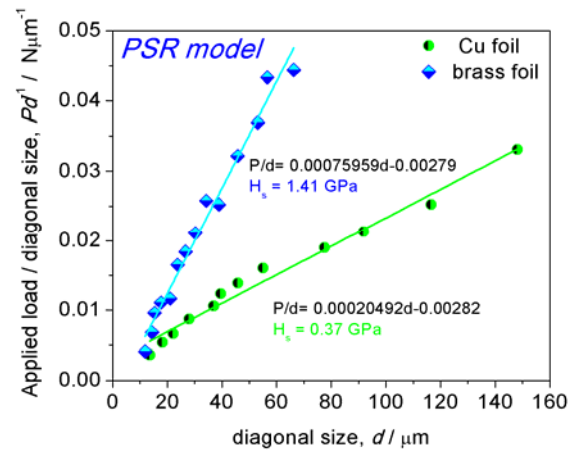


Figure 3. PSR model for calculated absolute hardness values of substrates without coatings.

3.2. Absolute hardness of the copper coatings

Figure 4 present fitting curves according to Chen-Gao model for electrodeposited 30 μm thick copper coatings on brass substrate. We can see from Figure 4 and Table 2 that the composite hardness and absolute hardness coating values obtained for the copper coatings in the DC/US regime were larger than those obtained in the DC/MS regime or DC regime.

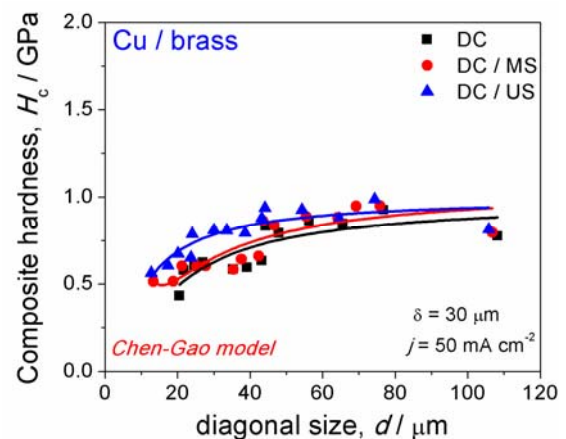


Figure 4. The dependencies of the composite hardness for 30 μm thick copper coatings electrodeposited on the brass substrate with variation current regime, on diagonal size calculated according to Chen–Gao model.

Figure 5 presents fitting curve according to Korsunsky model for electrodeposited 10 μm thick copper coatings on Cu substrate. Two current regimes were used: stationary DC regime without mixing of electrolyte I and DC/US regime with application of ultrasonic waves for mixing. The third sample was synthesized in the form of a laminate by deposition in a combination regime (DC+DC/US) with 1 μm thick and with 10 individual layers. The final layer was deposited in DC/US regime. The lowest value of an absolute hardness of Cu coating was shown by the sample deposited in the stationary mode, and the maximum by the laminate form of the coating.

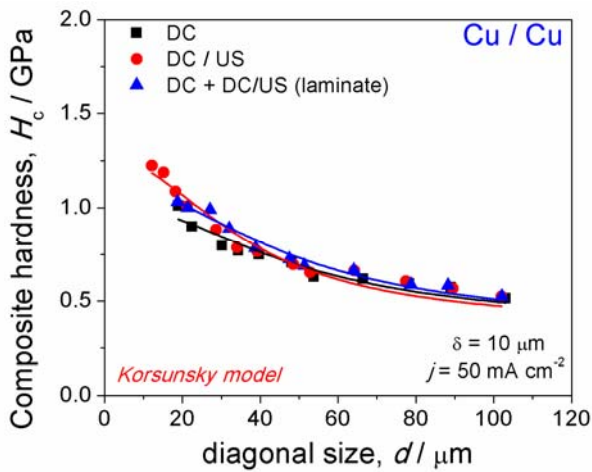


Figure 5. The dependencies of the composite hardness for 10 μm thick copper coatings electrodeposited on the copper substrate with variation current regime, on diagonal size calculated according to Korsunsky model.

Table 2. The results of the absolute hardness of the copper coatings with fitting errors. RMSE–Root mean square error and SE – Standard Error.

regime	Chen-Gao model				
30 μm Cu/brass	A	B	C	RMSE	H_{coat} /GPa
DC	0.99	-11.76	368.41	0.09	0.961
DC/MS	1.00	-6.73	83.78	0.06	0.953
DC/US	1.07	-14.06	718.78	0.08	1.043
regime	Korsunsky model				
10 μm Cu/Cu	k	SE	H_{coat} /GPa	SE	
DC	2.02E-4	3.94E-4	1.022	0.04	
DC/US	3.69E-4	5.72E-4	1.276	0.05	
DC + DC/US	2.15E-4	2.62E-4	1.296	0.03	

3.3. Adhesion properties of Cu coatings

The adhesion properties of different copper coatings were summarized according to Figures 6 and 7 and Table 3. Based on the values of the slopes of the lines in Figures 6 and 7, the parameter b was calculated and shown in Table 3, according to equation (5).

The larger value of the adhesion parameter b means the better adhesion of the coating with substrate [10-12]. From Table 3 we can see that the ultrasonic copper coating on brass has better adhesion strength. Although it was expected that the strongest adhesion exists between the same materials (Cu/Cu) the adhesion evaluation through the model did not show this. This behavior can be attributed to the influence of layer thickness and different microstructures of layers (deposition from two different electrolytes) during indentation. But it can be confirmed that the copper coating deposited using ultrasound shows better adhesion performance than the ordinary coating, deposited either on brass or copper substrates. The adhesion bending test results are shown in Table 3, too.

This test according to the value of critical cycle number (n) indicated that the thinner coating shows a better adhesion behavior [3]. This test also confirmed the better adhesion performance of the sample deposited in DC/US regime on both substrates.

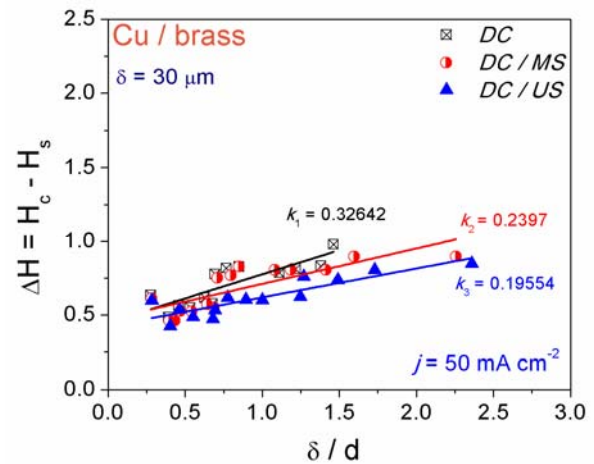


Figure 6. The hardness difference versus ratio between the coating thickness (30 μm) and the diagonal size for the Cu coatings electrodeposited on the brass substrate from electrolyte II.

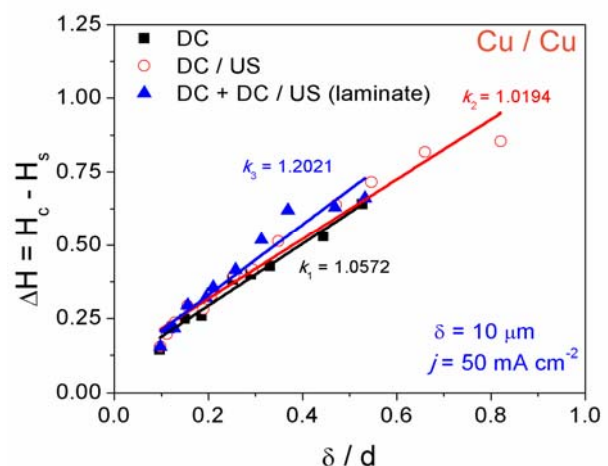


Figure 7. The hardness difference versus ratio between the coating thickness (10 μm) and the diagonal size for the Cu coatings electrodeposited on the copper substrate from electrolyte I.

Table 3. The results of adhesion properties of copper coatings on different substrates, b – critical reduced depth, N – critical cycle number.

substrate	δ	regime	el.	b	N
brass	30	DC	II	14.98	25.5
brass	30	DC/MS	II	18.76	32
brass	30	DC/US	II	20.44	41
copper	10	DC	I	7.07	114
copper	10	DC/US	I	11.53	130
copper	10	DC+DC/US	I	11.36	125

3.4. The compactness of the copper coatings

Figure 8 shows the average weight losses of the electrodeposited copper coatings samples obtained in different current regimes with/without mixing of *electrolyte II* on brass substrate. Figure 9 shows weight losses for Cu coatings deposited on copper substrate from *electrolyte I*. The laminate form of Cu coatings shows the better anticorrosion properties.

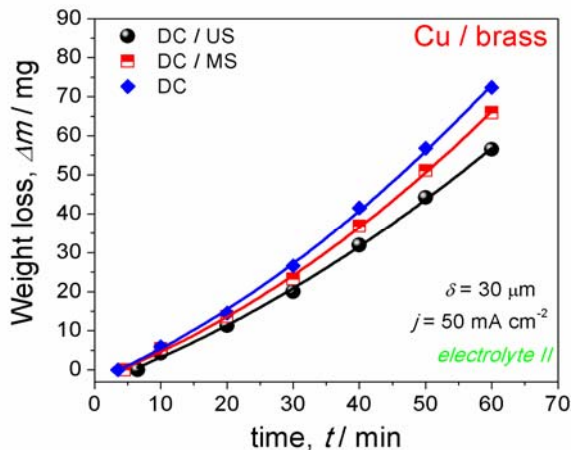


Figure 8. Weight loss of the copper coatings (30 μm) on brass substrates in static corrosion test.

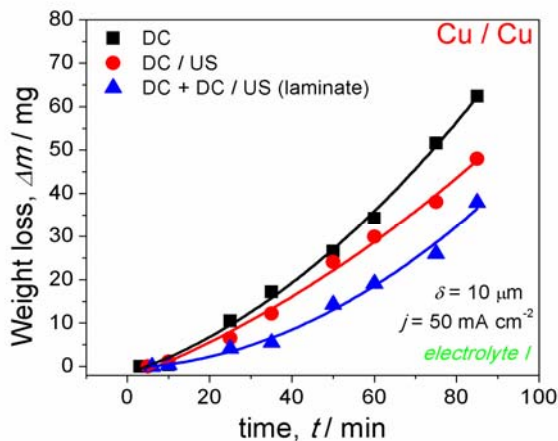


Figure 9. Weight loss of the copper coatings (10 μm) on Cu substrates in static corrosion test.

The first points of the curves are determined by the bubbling time of specimen (see Fig. 2). From Figure 8 we can see that corrosion rate of the DC/US sample is lower than DC/MS and DC samples. Copper coating obtained in stationary regime (DC) have higher corrosion rate than that of the ultrasonic electrodeposited copper coating or DC/MS sample. That means that its anticorrosion feature is worse. For the DC Cu sample, the bubbling time is 3' 27'', for DC/MS is 4' 24'' and for DC/US is 6' 32''. The longer starting time the etching in 20% HNO_3 means the better compactness of samples.

By comparing Figures 8 and 9, it can be concluded that copper samples electrodeposited from *electrolyte II* with additives show greater compactness and more chemical resistance to the HNO_3 acid.

4. CONCLUSION

A copper coating was obtained by different regime of electrodeposition technique: ordinary, magnetic, ultrasonic, and laminate form. The surface coating hardness of copper coating obtained in DC/US regime on brass substrate is 1.04 GPa, better than that in DC regime (0.961 GPa) or in DC/MS regime (0.953 GPa). The surface coating hardness of copper coating in combination regime (laminated form) on copper substrate is 1.296 GPa, better than ordinary copper (DC regime). The copper coatings obtained from *electrolyte II* have weaker mechanical properties, but it is more resistant to corrosion and more compact. The adhesion performance of the copper coating obtained in DC/US regime on brass substrate or laminated form of Cu on Cu substrate is better than Cu coatings obtained in DC regime. The corrosion rate of copper coatings from electrolyte with additives is obviously lower.

Acknowledgments

This work was funded by Ministry of Education, Science and Technological Development of Serbia (Grants No. 451-03-68/2022-14/200026 and 451-03-68/2022-14/200135).

References

- [1] ALIOFKHAZRAEI, M., WALSH, F.C. et al.: *Development of electrodeposited multilayer coatings: A review of fabrication, microstructure, properties and applications*, Applied Surface Science Advances, 6(1) (2021) 100141.
- [2] KHADAM, M., PENKOV, O.M., YANG, H.K. et al.: *Tribology of multilayer coatings for wear reduction: a review*, Friction, 5(1) (2017) 248-262.
- [3] CUI, R., HE, Y., YU, Z. et al.: *Preparation and Characterization of Ultrasonic Electrodeposited Copper Coating*, 11th International Conference on Electronic Packaging Technology & High Density Packaging, 16-19 Aug., 2010, 847-850.
- [4] HAN, L., WANG, J., GUO, S. et al.: *Fabrication and performance of SiC-reinforced Cu: Role of the aspect ratio of the SiC reinforcement phase*, Materials & Design, 220(1) (2022) 110869.
- [5] GONG, L., ZHAO, F., WANG, Z. et al.: *Preparation of cyanide-free gold-tin alloys by ultrasonic-assisted pulse electrodeposition*, Materials Letters, 317(1) (2022) 132029.
- [6] MLADENVIĆ, I., LAMOVEC, J., VASILJEVIĆ-RADOVIĆ, D. et al.: *Influence of intensity of ultrasound on morphology and hardness of copper coatings obtained by electrodeposition*, Journal of Electrochemical Science and Engineering, 12(0) (2022), In Press.
- [7] MLADENVIĆ, I., BOŠKOVIĆ, M., VUKSANOVIĆ, M. et al.: *Structural, Mechanical and Electrical Characteristics of Copper Coatings Obtained by Various Electrodeposition Processes*, Electronics, 11(3) (2022) 443.

- [8] MLADENOVIĆ,I., LAMOVEC,J., JOVIĆ,V. et al.: *Mechanical characterization of copper coatings electrodeposited onto different substrates with and without ultrasound assistance*, Journal of the Serbian Chemical Society, 84(7) (2019) 729-741.
- [9] BROITMAN,E.: *Indentation Hardness Measurements at Macro-, Micro-, and Nanoscale: A Critical Overview*, Tribology Letters, 65(1) (2017) 23.
- [10] CHEN,M., GAO,J.: *The adhesion of copper films coated on silicon and glass substrates*, Modern Physics Letters B, 14(3) (2000) 103-108.
- [11] HOU,Q., GAO,J., LI,S.: *Adhesion and its influence on micro-hardness of DLC and SiC films*, The European Physical Journal B - Condensed Matter and Complex Systems, 8(4) (1999) 493–496.
- [12] MAGAGNIN,L., MABOUDIAN,R., CARRARO,C.: *Adhesion evaluation of immersion plating copper films on silicon by microindentation measurements*, Thin Solid Films, 434(1-2) (2003) 100-105.
- [13] KORSUNSKY,A.M., MCGURK,M.R., BULL,S.J. et al.: *On the hardness of coated systems*, Surface & Coatings Technology, 99(1-2) (1998) 171-183.
- [14] TUCK,J.R., KORSUNSKY,A.M., BULL,S.J. et al.: *On the application of the work-of-indentation approach to depth-sensing indentation experiments in coated systems*, Surface and Coatings Technology, 137(2-3) (2001) 217-224.
- [15] <https://www.defelsko.com/resources/test-methods-for-coating-adhesion>.
- [16] KONURU,S.L. UMASANKAR,V., SARMA,A.: *A comparison of qualitative and quantitative adhesion analysis for a composite thin film system*, Materials Today: Proceedings, 46(PART II) (2021) 1243-1246.
- [17] CHALGHAM,A.,EHRAMANN,A.,WICKENKAMP,I.: *Mechanical properties of FDM printed PLA parts before and after thermal treatment*, Polymers, 13(8) (2021) 1239.
- [18] LI,H., BRADTH,R.C.: *The microhardness indentation load/size effect in rutile and cassiterite single crystals*, Journal of Material Science, 28(4) (1993) 917-926.



FIRE-RESISTANT COMPOSITES BASED ON ACRYLIC-FUNCTIONALIZED LIGNIN AND POLYESTER RESIN OBTAINED FROM WASTE POLY(ETHYLENE TEREPHTHALATE)

NATAŠA KNEŽEVIĆ

Faculty of Technology and Metallurgy, University of Belgrade, Belgrade, natasaknezevic94@gmail.com

ALEKSANDAR JOVANOVIĆ

Institute for Technology of Nuclear and Other Mineral Raw Materials, Belgrade, aleksandarjovanovic.tmf@gmail.com

JOVANA BOŠNJAKOVIĆ

Research and Development Institute Lola L.T.D., Belgrade, jovana.bosnjakovic@li.rs

MILENA MILOŠEVIĆ

Institute of Chemistry, Technology and Metallurgy, National Institute of the Republic of Serbia, University of Belgrade, Belgrade, milena.milosevic@ihtm.bg.ac.rs

MILICA RANČIĆ

Faculty of Forestry, University of Belgrade, Belgrade, milica.rancic@sfb.bg.ac.rs

ALEKSANDAR MARINKOVIĆ

Faculty of Technology and Metallurgy, University of Belgrade, Belgrade, marinko@tmf.bg.ac.rs

JELENA GRŽETIĆ

Military Technical Institute, Belgrade, jrusmirovic@tmf.bg.ac.rs

Abstract: This paper investigates the using potential of acryl-functionalized kraft lignin (AKL) in reducing the flammability of polymer composites based on recycled unsaturated polyester resins (UPR). Acryl functionalization of kraft lignin was performed by direct esterification of free polyphenolic groups with acryloyl chloride, after what, the AKL was blended in UPR resin synthesized from the polyols obtained by catalytic depolymerization of waste poly(ethylene terephthalate). The AKL was homogenized in UPR resin in different weight ratios: 2.5, 5.0, 7.5, and 12.5 wt.%. Structural and dynamic-mechanical characteristics of acryl-functionalized kraft lignin and composites were determined using FTIR spectroscopy, dynamic-mechanical analysis (DMA), and tensile tests. The influence of functionalization and mass fraction of AKL on tensile and thermal properties of UPR resin was studied. The thermal properties of the composite were tested according to the standard UL-94 method, based on which the highest category of heat-resistant materials is a composite with 12.5 wt.% acyl-functionalized lignin.

Keywords: Lignin modification, UPR-lignin composites, dynamic-mechanical testing, tensile testing, flame retardancy

1. INTRODUCTION

Polymers are widely used in various economy and defense sectors including housing, construction, transportation, rocket technology and aerospace due to their good mechanical and chemical properties and easy-processing. However, most industrial polymers (polyesters, epoxides, poly(ethylene), poly(propylene), etc.) are highly flammable and thermally unstable, which is especially expressed in hyperthermal conditions [1]. Due to the increasingly widespread use of such polymeric materials, fire resistance must be improved by the incorporation of different additives. Using-potential of some commonly applied flame retardants such as antimony trioxide and halogenated flame retardants is become limited due to environmentally issues. Nowadays, using non-toxic, biobased and environmentally friendly

fillers/additives and flame retardants in polymers increases the researcher's attention. Further, the increased daily consumption of polymers such as poly(ethylene terephthalate), PET, and increased amount of PET waste generated, imposes the development of new PET recycling methods, which give an applicable products. This achieves exceptional ecological and economic benefits, which are summarized in saving natural resources and reducing the consumption of water and energy [2,3]. The most significant recycling technique for waste PET is the chemical one, which involves depolymerization of the polymer chain to its basic structural/monomer units [4]. PET monomers, obtained by the glycolytic depolymerization process, can be used for the re-synthesis of PET, or the synthesis of alkyd, epoxy, and polyester resins as it is presented in this research.

Considering previous statements, the development of fire-resistant composites based on the unsaturated polyester resin, originated from recycled waste PET, and modified lignin as sustainable and renewable fire-resistant additive is shown. Lignin is widely used as filler/additive in composite production due to its chemical structure (natural aromatic polymer), which consists of three branched polyphenols/monolignols. Moreover, it is possible to perform chemical modification of the lignin surface to adjust its reactivity, surface and thermal properties [5,6,7]. Amount and type of the lignin functional groups depend on the source/feed and the process used for its extraction. Acrylic modification of kraft lignin to improve its functional properties is achieved by direct esterification of free polyphenolic groups with acrylic acid or acryloyl chloride.

This paper presents novel modification method for acrylic surface functionalization of the kraft lignin and investigates the using-potential of acrylic-functionalized lignin (AKL) as flame retardant in unsaturated polyester resin (UPR) based on waste PET.

2. EXPERIMENTAL PART

2.1. Materials

The UPR was synthesized from maleic anhydride and

products obtained by depolymerization of PET with propylene glycol (PG) in the presence of a tetrabutoxytitanate (TBT) catalyst. The molar ratio of PET and PG, used for glycolysis, was 1:2. The procedure of glycolysis was described earlier in the literature [8]. Kraft lignin with a low sulfonate content, tetrahydrofuran (THF), sodium hydroxide (97%, reagent grade), acryloyl chloride, isopropyl alcohol, methyl ethyl ketone peroxide (MEKP), cobalt octoate (Co-oct) were obtained from Sigma-Aldrich Company and are used as received.

2.2. Chemical modification of kraft lignin – AKL

Chemical modification of lignin was carried out by dissolving 5 g of kraft lignin in 21 cm³ of H₂O/NaOH/THF (3:1:3) mixture at room temperature in a 250 cm³ three-neck flask. After dissolving the lignin (30 min), acryloyl chloride (120 cm³) was added dropwise to the mixture over 1 h at -3 °C. After that, the contents of the flask were mixed for 2 hours at a temperature of 0 °C. After the reaction, the mixture was left overnight in cold deionized water and ice to precipitate the final product. The formed technical layer was decanted, and the precipitate was washed three times in isopropyl alcohol and three times in deionized water. The final product was separated by centrifugation and dried for 10 hours at 50 °C in a vacuum oven.

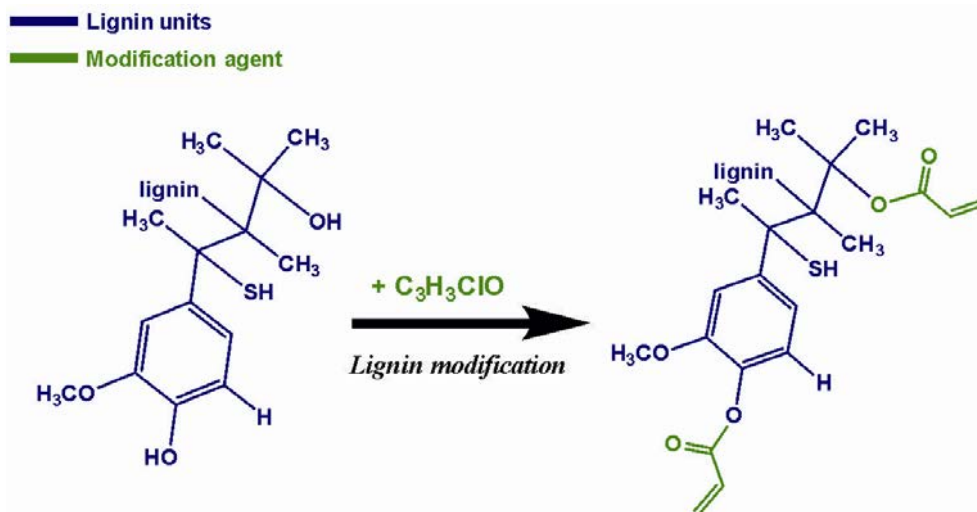


Figure 1. Schematic illustration of chemical modification of kraft lignin

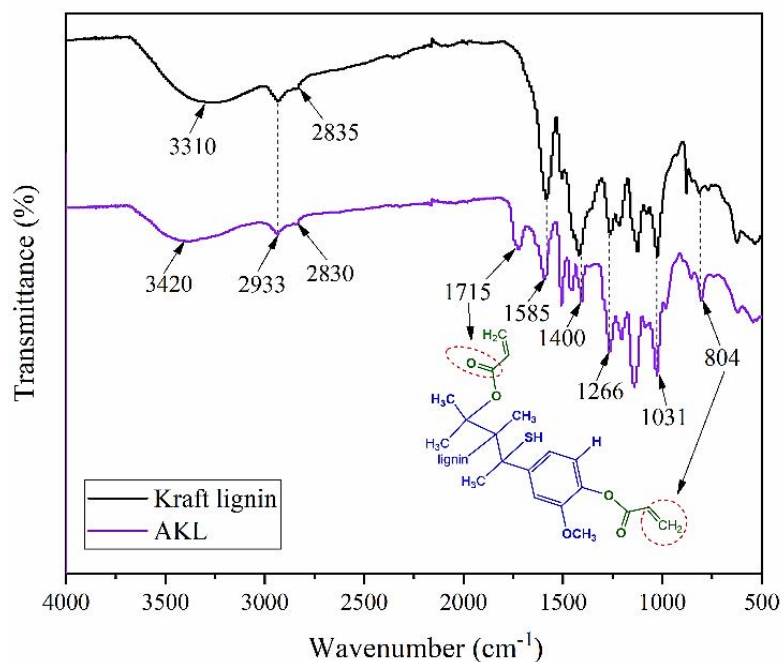


Figure 2. FTIR analysis of the kraft lignin (black line) and AKL (violet line)

The structural characterization of non-acrylate and acrylate kraft lignin was investigated by recording the FTIR spectrum (Figure 2). The analyzed spectra clearly show the success of the modification.

The bands at 3310 cm^{-1} and 3420 cm^{-1} belong to the O-H stretching vibration of a hydroxyl and phenolic groups in the kraft lignin and AKL. The region at $2933\text{--}2835\text{ cm}^{-1}$ is related to the C-H bending vibration of symmetric and asymmetric methyl and methylene groups in the unmodified and modified lignin. The new peak at 1715 cm^{-1} noticed after arylation process was assigned to the C=O stretching vibrations of acrylate group [9]. In the range of the stand spectrum between $1585\text{--}1400\text{ cm}^{-1}$ are assigned of aromatic skeletal vibrations of lignin [9]. The asymmetric and symmetric vibration of the C-O-C and C-O groups of in the structure of lignin appear in the region $1266\text{--}1031\text{ cm}^{-1}$. As a result of the successful acrylation, intensity of C-H deformation vinyl groups was noticed at 804 cm^{-1} .

2.3. UPR/AKL composites preparation

Waste PET-based UPR (2 g) was used as a polymer matrix for composites preparation. AKL was mixed in polymer matrix and the mass ratio varied from 2.5 wt.% to 12.5 wt.%. Homogenization of AKL with UPR was achieved using a modified laboratory homogenizer. MEKP (1.5 wt.%) and Co-oct (0.5 wt.%) were used as curing initiator and activator, respectively. After adding the initiator, the resulting dispersion was poured into molds for uniaxial tensile measurements (ASTM D882 test standard dimension $60\times 10\times 4\text{ mm}$ with narrowed neck area – $15\times 4\times 4\text{ mm}$) and for dynamic-mechanical analysis (standard dimension $60\times 10\times 4\text{ mm}$). The obtained cured neat UPR resin as well as UPR/AKL composites were presented in Figure 3.

Table 1. Compositions for preparation of neat UPR and UPR/AKL composites

Sample	UPR, g	AKL, g	MEKP, cm^3	Co-oct, cm^3
UPR		0 (0%)		
UPR/AKL	2	0.05 (2.5%)	0.350	0.150
		0.10 (5%)		
		0.15 (7.5%)		
		0.25 (12.5%)		

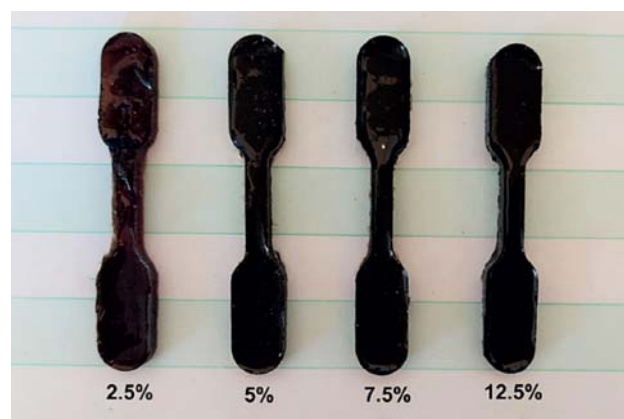


Figure 3. Standard test molds for uniaxial tensile measurements

2.4. Characterization methods

Recognition of existing functional groups in synthesized materials was obtained by Fourier transform infrared spectroscopy (FTIR). For this purpose, Nicolet™iSTM10 FTIR Spectrometer (Thermo Fisher SCIENTIFIC) with Smart iTR™ Attenuated Total Reflectance (ATR) was used. All spectrums are recorded between $4000\text{ and }500\text{ cm}^{-1}$.

Uniaxial tensile measurements of standard cured samples (ASTM D882) [11] were performed using an Instron tester 1122. All tests were performed at 20 °C and adjusted at a crosshead speed of 10 mm/min.

Optical micrographs of the cured composites after tensile tests were made using a BTC STM-8T Trinocular Stereo Microscope ZOOM with 50x magnification.

Dynamic mechanical analysis (DMA) study of the cured composite samples was performed in torsion deformation mode using the Modular Compact Rheometer MCR-302 (Anton Paar GmbH, Austria) equipped with standard fixtures (SRF12) for rectangular bars, temperature chamber (CTD-620) having high temperature stability (± 0.1). The standard sample of a rectangular bar shape (44×10×4 mm) was tested by using "temperature ramp test" at temperature range from 40 °C to 130 °C, the heating rate was 5 °C min⁻¹, the single angular frequency of 1 Hz and strain amplitude was 0.1%.

Flame-resistant properties were analyzed by the UL-94 flammability test [10].

3. RESULTS AND DISCUSSION

3.1. FTIR analysis

The FTIR spectra of the UPR/AKL composite and the pure resin are shown in Figure 4.

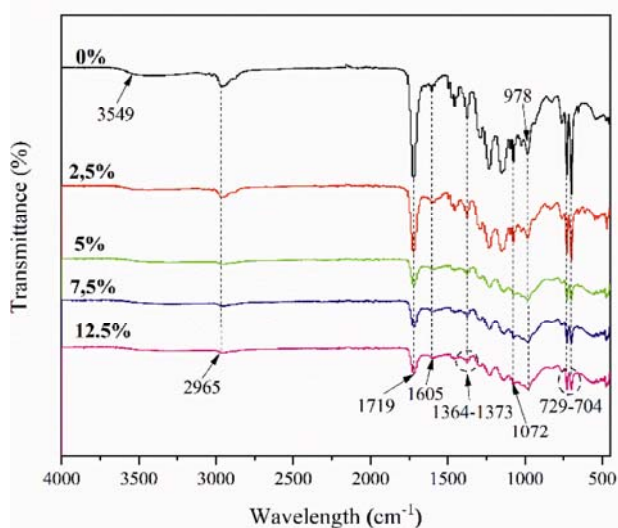


Figure 4. FTIR spectra of UPR and UPR/AKL composite (2.5 wt.%, 5 wt.%, 7.5 wt.%, 12.5 wt.%)

The peak around 3549 cm⁻¹ originates from the aliphatic and aromatic O-H vibration [12]. The intensity of this spectrum after the alkylation of lignin and incorporation into UPR is reduced. The wide peak at 2965 cm⁻¹ originates from the stretching vibration of the methyl or methylene group. In the region 1364-1373 cm⁻¹, asymmetric and symmetric C-H deformation vibrations of methyl and methylene groups can be observed. These vibrations overlap with the C-H stretching vibrations from the isopropyl moiety's methyl (CH₃) groups. The intense peak at 1719 cm⁻¹ is attributed to stretching vibrations of the ester C=O groups of UPR matrix. The narrow peaks identified at 729 cm⁻¹ and 704 cm⁻¹ are skeletal γ (CH) vibrations of the phenyl moiety. A lower intensity band

with an absorption maximum of 1072 cm⁻¹ originates from C-O valence vibrations. The consumption of the C=C bond in unsaturated polyesters was followed by the change in the peak area at 978 cm⁻¹. The spectrum at 1605 cm⁻¹ is due to the vibration of C=C group.

3.2. Tensile properties and microscopic fracture section of the investigated composites

In order to examine the contribution of AKL additives to the tensile properties of the UPR matrix, uniaxial tensile tests of cross-linked composites based on unsaturated polyester resins and acrylate lignin were performed. The obtained values are shown in the Table 2. The results show that σ and E increase with an increase in the proportion of acrylated lignin up to 7.5 wt.%, while an increase in AKL load leads to a decrease in the elongation value but a higher value of the elastic modulus, which can be associated with defects in the structure of AKL particles.

Table 2. The values of stress at break (σ), elongation at break (ϵ), tensile modulus (E) and energy adsorption

Sample	σ , MPa	ϵ , %	E , GPa
UPR	21.60	2.85	0.98
UPR/AKL 2.5%	9.16	4.72	0.140
UPR/AKL 5%	17.47	12.86	0.169
UPR/AKL 7.5%	19.19	7.16	0.289
UPR/AKL 12.5%	1.31	30.38	0.0084

The best results are given by the sample with 7.5 wt.% AKL as a result of good filler distribution and interfacial interactions between the UPR matrix and lignin particles. The deviation from the continuous growth of the value (12.5 wt.%) can be attributed to heterogeneity in the composite structure due to steric hindrance of the methylene group from the loose segment of the isopropyl alcohol, which requires additional optimization of the crosslinking conditions of polymer matrices with this modified lignin.

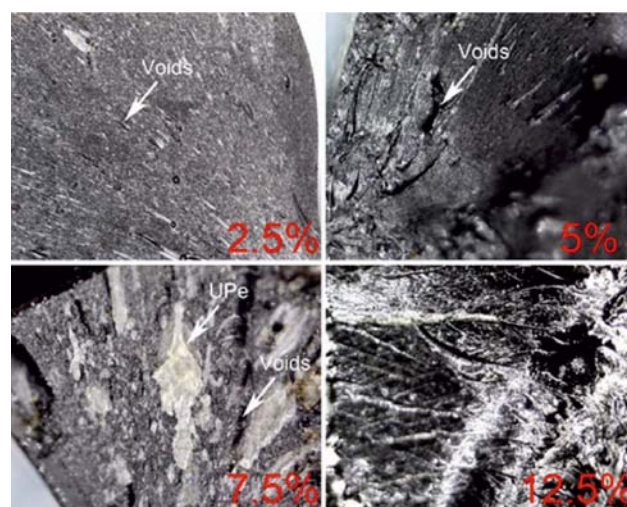


Figure 5. Microscopic view of broken test tubes with different parts AKL

The surface of the fracture, which was created by stretching the test tube, was recorded with an optical microscope with a magnification of up to 50x. Images of

the resulting fractures are shown in Figure 5. On the cross-sections of the samples with 2.5 wt.% and 5 wt.% AKL, the uniform distribution of the acrylate lignin into the UPR polymer matrix is clearly remarked. Compared to the higher loading of AKL (7.5 wt.% and 12.5 wt.%), segments of only cross-linked resin without AKL can be observed, which represent a weak segment in the structure and lead to poor mechanical properties, as confirmed by the values of σ and E in Table 2. Cracks on the sections of the 2.5 wt.% and 5 wt.% samples are caused by a mechanism that is characteristic of brittle polymers and polymer composites. Fractures on samples with 7.5 wt.% and 12.5 wt.% AKL in the matrix are more tough.

3.3. Dynamic-mechanical testing results

The rheological properties of cured polymeric composites are influenced by the polymer chain structure and its interactions with fillers. The results of the DMA properties of the UPR/AKL composites are presented as a temperature dependences of storage modulus (G'), loss modulus (G''), and their ratio (damping factor - $\tan\delta$) about temperature. The temperature increases from 40 °C to 130 °C during the DMA tests. Based on the obtained DMA diagrams, the glass transition temperature T_g ($\tan\delta$) was determined. Figure 6. shows the DMA diagrams of cross-linked UPR and UPR/AKL.

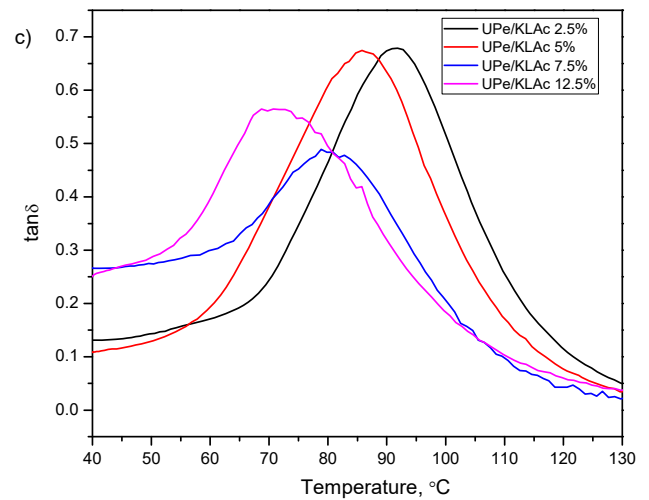
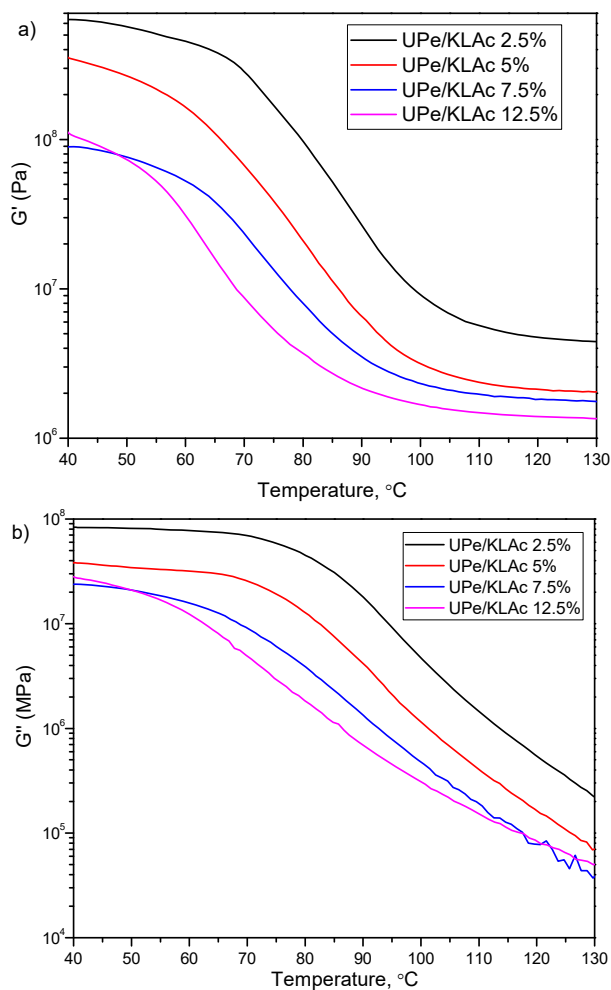


Figure 6. Temperature dependence of a) storage modulus (G'), b) loss modulus (G'') and c) $\tan\delta$ of cured UPR and corresponding composites

According to the DMA results presented in Figure 6. it can be concluded that T_g ($\tan\delta$) decreased with higher AKL content within the UPR matrix. Higher amount of filler particles creates agglomerates, which weakens interaction between polymer chains and reinforcements making macromolecule segments more movable. Moreover, the $\tan\delta$ peak height also decreased indicating more elastic response of materials with high amount of AKL.

3.4. Thermal stability testing results

The thermal stability of the formed composites was tested according to the standard flammability test method, known as UL-94V (flammability test of plastic materials for parts in devices and appliances). Test describes the material's tendency to extinguish or spread the flame after igniting the test tube. Samples can be classified as non-flammable (V-0), less flammable (V-1), explosive (V-2), and highly flammable (unclassified). The setup of the apparatus for the practical test is shown in Figure 7.

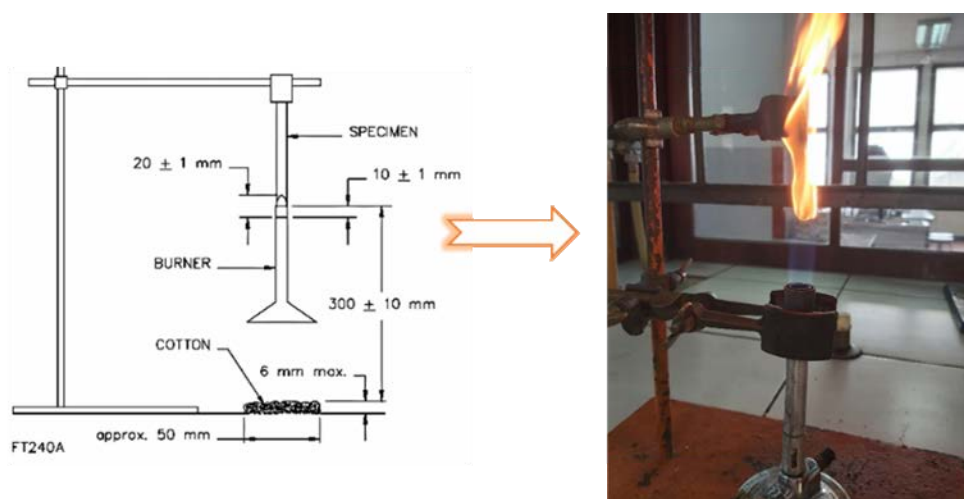


Figure 7. Standard and laboratory setup of apparatus (right) for vertical testing of thermal stability of samples[10]

Formed test tubes with dimensions of 60x10x4 mm were used to test the thermal properties. A blue flame of 20 mm height is placed on the lower edge of the vertically placed test tube for 10 s, after which the flame is removed, and the time is measured. The flame is applied again for another 10 s, and the time to extinction is recorded. It is expected that by increasing the mass fraction of modified lignin, the fire resistance of the material will also increase. After testing the flammability of all test tubes, the sample with 12.5 wt.% ALK was completely charred. Since there was no dripping/cracking of the sample and the flame extinguished itself after 25 s, according to the UL-94V test, this sample can be classified as the V-1 category. Samples with a smaller proportion of lignin started to crack after being exposed to the flame and extinguished faster, even in 100-120 s.

4. CONCLUSION

In this work, acrylic functionalization of kraft lignin was performed and its valorization as a flame retardant additive in recycled UPR was investigated. The structure of the formed UPR/AKL composites, as well as the pure resin, was analyzed using FTIR method. The effect of lignin in UPR matrix was studied by examining the thermal stability, flame resistance and mechanical properties of the prepared composites. Flame resistance is increased by cross-linking a larger amount of AKL, which is confirmed by the charring of the sample after exposure to fire. According to the standard flammability test, the sample with 12.5 wt.% lignin achieves the V-1 category, which makes it an extremely fire-resistant material. Contrary to this are the results of the mechanical properties (tensile strength and modulus of elasticity). The tensile properties of all composites based on UPR resin and modified lignin are improved compared to the tensile properties of pure resin, and the values of σ , ϵ and E increase with the increase of the lignin content up to 7.5 wt.%, after which they decrease due to the heterogeneous distribution of filler particles. These results confirm the application potential of the developed material as a fire-resistance material.

ACKNOWLEDGEMENTS

This work was supported by the Ministry of Education, Science and Technological Development of the Republic of Serbia (Contract Nos., 451-03-1270/2022-14/2685, 451-03-68/2022-14/200023, 451-03-68/2022-14/200066, 451-03-68/2022-14/200026, 451-03-68/2022-14/200169, 451-03-68/2022-14/200135, and 451-03-68/2022-14/200325).

References

- [1] Sherif Arabyabc, Brock Philipsa, Qingshi Mengd, Jun Maa, Tahar Laouie, Chun H.Wang, Recent advances in carbon-based nanomaterials for flame retardant polymers and composites, *Composites Part B: Engineering*, Volume 212, 2021.
- [2] Guo, C., Zhou, L., Lv, J., "Effects of expandable graphite and modified ammonium polyphosphate on the flame-retardant and mechanical properties of wood flour/polypropylene composites", *Polym. Compos.* 21 (2013) 449–456.
- [3] Al-Salem, S., Lettieri, P., Baeyens, J., Recycling and recovery routes of plastic solid waste (PSW): A review, *Waste Manag.* 29 (2009) 2625–2643.
- [4] Sinha V., Patel MR, Patel JV., Pet waste management by chemical recycling: A review. *Journal of Polymers and the Environment* 2010;18:8–25.
- [5] Prieur, B., "Modified lignin as flame retardant for polymeric materials", PhD Thesis, Universite Lille1 Sciences et Technologies France, 2018.
- [6] Ge, Y., Qin, L., Li, Z., "Lignin microspheres: An effective and recyclable natural polymer-based adsorbent for lead ion removal", *Materials and Design*, 95 (2016), pp. 141-147.
- [7] Liu, L., Qian, M., Song, P., Huang, G., Yu, Y., Fu, S., "Fabrication of green lignin-based flame retardants for enhancing the thermal and fire retardancy properties of polypropylene/wood composites", *ACS Sustainable Chemical Engineering*, 4 (2016), pp. 2422–2431.

- [8] Rusmirović, J., Trifković, K., Bugarski, B., Pavlović, V., Džunuzović, J., Tomić, M., Marinković A., "High performance unsaturated polyester based nanocomposites: Effect of vinyl modified nanosilica on mechanical properties", *eXPRESS Polymer Letters*, 10 (2) (2016), pp. 139–159.
- [9] Bykov I., „Characterization of Natural and Technical Lignins using FTIR Spectroscopy“, Master thesis, Luleå Univ. Technol, Luleå, 2008 Construction (2008).
- [10] UL 94V: Standard for tests for flammability of plastic materials for parts in devices and appliances, American National Standard (2001).
- [11] ASTM D882: Standard test method for tensile properties of thin plastic sheeting (2009).
- [12] Prieur, B., Meub, M., Wittemann, M., Klein, R., Bellayer, S., Fontaine, G., Bourbigot, S., "Phosphorylation of lignin to flame retard acrylonitrile butadiene styrene (ABS)", *Polymer Degradation and Stability*, 127 (2016), pp. 32-43.



SILVER COATED TEXTILES AS ELECTROCHEMICAL PSEUDOCAPACITIVE MATERIALS

STEVAN STUPAR

Ministry of Defense, Military Technical Institute, Ratka Resanovića 1, 11030 Belgrade, Serbia
stevan.stupar13@gmail.com

MIHAEL BUČKO

University of Defense, Military Academy, Pavla Jurišića Šturma 33, 11000, Belgrade, Serbia
mihaelbucko@yahoo.com

DUŠAN MIJIN

University of Belgrade, Faculty of Technology and Metallurgy, Karnegijeva 4, 11120 Belgrade, Serbia
kavur@tmf.bg.ac.rs

DENIS DINIĆ

University of Defense, Military Academy, Pavla Jurišića Šturma 33, 11000, Belgrade, Serbia
denis.dinic@yahoo.com

TANIĆ MILAN

University of Defense, Military Academy, Pavla Jurišića Šturma 33, 11000, Belgrade, Serbia
milantanic@yahoo.com

MARINA KNEŽEVIĆ

Ministry of Defense, Military Technical Institute, Ratka Resanovića 1, 11030 Belgrade, Serbia
katarinac2008@gmail.com

JELENA KARANOVIĆ

Ministry of Defense, Military Technical Institute, Ratka Resanovića 1, 11030 Belgrade, Serbia
jelenka74gmail.com

Abstract: Among numerous active electrode materials, silver is a promising electrode in electrochemical capacitors. In this work we investigate the electrochemical capacitance of two textile materials: polyester and cotton fabrics, coated with silver particles. The electrodes were prepared in a manner that the fabrics were immersed into a silver complex solution and subsequently dried in the air and heated to induce silver deposition by annealing. This synthesis method does not require the use of expensive and toxic chemicals or electricity, which makes the process more economically acceptable for production of lightweight and flexible conductive materials. The capacitance and energy density were measured in various electrolytes (KCl and NaOH), and for electrodes prepared by one, three, or five cycles of fabrics immersion in the silver solution. Characterization of the modified tissues was performed by scanning electron microscopy coupled with energy-dispersive spectroscopy (SEM-EDS). The capacitance was investigated by recording cyclic voltammograms, while the energy density was calculated from the recorded charge-discharge curves at the textile working electrodes. These findings promote the application of silver coated textiles as electrochemical pseudocapacitor materials.

Keywords: pseudocapacitor, textile electrode, silver deposition.

1. INTRODUCTION

Electrochemical capacitors, known also as supercapacitors and pseudocapacitors, are energy storage devices that store and release electric energy by electrostatic mechanism and through the Faradaic processes [1]. The first capacitors were based on high surface area carbon materials, yet these materials come with drawbacks like a large pore volume, which reduces

the conductivity and material density [2]. Later, transition metal oxides such as oxides of nickel, iron or ruthenium, had been introduced as pseudocapacitive materials to solve the problems observed with carbon-based electrodes, the RuO₂ oxide being the most successful [3]. However, the ruthenium materials come with issues such as high ecotoxicity and cost, and the quest for its replacement is ongoing.

Silver has been recognized as a transition metal that is very conductive, non-toxic to the environment, may

exhibit Faradaic redox reactions, with high surface area, reasonable wettability and low flammability, thus a desirable material for ruthenium replacement in supercapacitor applications. As a result, the electrochemical capacitors based on Ag wires, Ag dendrites, Ag thin films, Ag/graphene composites, etc., have already been reported [4].

This work aims to investigate the application of silver coating, applied with a special method on various fiber materials, as a novel supercapacitor material. Namely, textile capacitors are based on excellent textile characteristics demanded for a substrate: high toughness, strength and flexibility, low price and easy availability [5]. Most importantly for military application, due to their lightness, fiber-based supercapacitors are wearable and thus may be converted into wearable energy storage devices that may provide energy to a soldier when needed [6].

To prepare fiber-based capacitors in this work, a silver coating was applied to a textile substrate (cotton and polystyrene), by immersion and subsequent annealing. The electrochemical performance of the prepared capacitor materials was tested by cyclic voltammetry and chronoamperometry.

2. EXPERIMENTAL PART

2.1. Reagents and materials

Silver nitrate (AgNO_3 , 99.0 %) and ammonium hydroxide solution (NH_4OH , 30%) were produced by Carlo Erba Reagents (France). Sodium acetate (CH_3COONa) was obtained from Fisher Scientific (UK). The methanol and formic acid were produced by Sigma-Aldrich (USA). The used chemicals were of analytical grade or higher. The Arium® Pro Ultrapure Water System (Sartorius, Germany) provided deionized water. The polyester and cotton fabrics were obtained by YUMCO Company (Serbia). Ethanol ($\text{C}_2\text{H}_5\text{OH}$, 95%) was obtained from Zorka Šabac (Serbia) and used for sample rinsing.

2.2. Silver conductive complex synthesis

Synthesis of Silver Conductive Complex begins by dissolving 30 g of silver nitrate and 60 g of sodium acetate in 75 ml of deionized water in two separate systems. After complete dissolution of the salt, the solutions were combined and stirred vigorously at room temperature. In two separated systems, 30 g of silver nitrate and 60 g of sodium acetate dissolved in 75 ml of deionized water. After the complete dissolution of the salts, the solutions were merged and intensively mixed at room temperature. The synthesized silver acetate was filtrated and rinsed with deionized water and methanol. The rinsed filtrate was dried at room conditions for 24 hours without exposure to light.

The synthesis of the silver conductive complex is further performed by modified Tollens process. The synthesized silver acetate (20 g) was dissolved in 45 ml of ammonium hydroxide solution by mixing thoroughly at room temperature. After 20 minutes, 1 ml of formic acid was

added to the silver acetate and ammonium hydroxide solution. After adding the last drop of formic acid, the solution was mixed for 24 hours and filtrated through the 0.45 nm nylon syringe filter (Sartorius, Germany).

2.3. The textile surface modification by silver deposition

The metallization of fabrics was studied using the polyester and cotton fabrics. The synthesized conductive silver complex was applied by immersing onto one side of fabric in the dark at $\sim 21^\circ\text{C}$. All samples were set to air dry to evaporate the ammonia from the complex, changing the silver and formic acid complex solution from colorless to a silver-colored solution. After the evaporation of ammonia, fabrics with the applied silver complexes were heated for 40 minutes at 90°C in a thermostatic chamber (G209A, SDL Atlas, UK). By heating the fabric under the stated conditions, formic acid evaporates from the complex, and a film of elemental silver is firmly formed on the surface. After the heat treatment, the samples were rinsed using ethanol.

2.4. Textile surface characterization

The morphology, microstructure, and semi-quantitative elemental analyses of raw and modified textiles were determined using the scanning electron microscopy Energy-Dispersive X-ray Spectroscopy (20 kV, JEOL 6610LV, Japan).

2.5. Electrochemical characterization

The electrochemical characterization of silver/fiber electrodes was carried out using cyclic voltammetry (CV) and chronoamperometry measurements to investigate a specific capacitance and the charge-discharge ability of the prepared electrodes. These analyses were performed using a CH Instruments potentiostat, model 400C, with a typical electrochemical cell setup of the saturated Ag/AgCl reference electrode, Pt counter electrode, and the working electrode. The working electrodes were exposed to the two different electrolytes: 1.0 mol dm^{-3} KCl and 0.5 mol dm^{-3} NaOH aqueous solutions.

The specific capacitance analysis was conducted using CV at potential range of $\pm 400 \text{ mV}$ (depending on the electrode material) versus the open circuit potential, at several scan rates ranging from 50 to 500 mV/s.

3. RESULTS

3.1. SEM-EDS characterization of silver/textile electrodes

SEM-EDS was applied for analysis of the fabrics' morphological, structural, and semi-quantitative characteristics after the silver deposition process. The SEM microphotographs of the polyester and cotton fabrics modified by one cycle of silver deposition, the distribution of diameter of the particles, and silver coverage of the textile, are presented in Figure 1. In addition, the corresponding EDS spectrum is given.

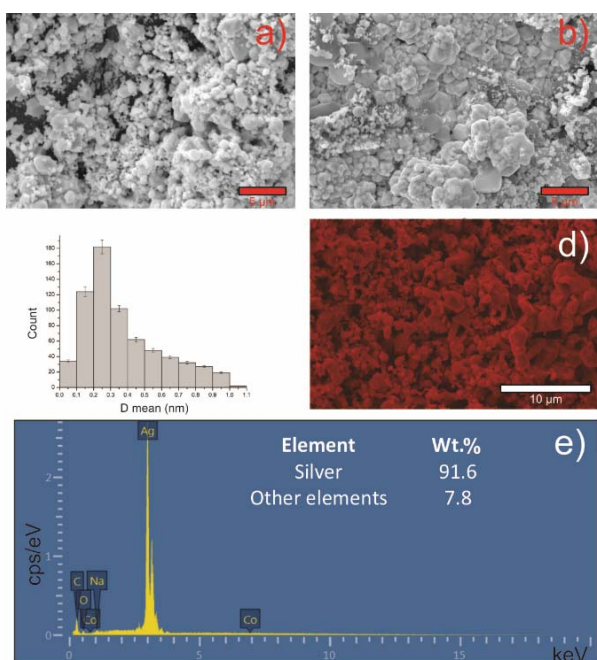


Figure 1. The SEM photographs of (a) polyester and (b) cotton fabrics modified by one cycle of silver deposition, (c) distribution of diameter of silver particles, (d) EDS mapping of the textile surface, and (e) EDS spectrum of the mapped area

The SEM microphotographs in Figure 1 show good coverage of the modified fabrics samples' surface after one silver deposition cycle. According to the determined distribution of the diameter of the particles, the average diameter of silver particles was between 0.2 and 0.3 μm . The distribution of silver particle sizes was obtained from the images where individual particles were distinguishable, and their diameters were measured using the image analysis software Image-pro. The SEM images also show the silver particles' agglomeration after the annealing treatment repetition. The porosity of multilayered silver particles is confirmed by SEM analysis and SEM micrographs of modified textiles shown. The complete mapping, obtained by energy-dispersive X-ray spectroscopy of the marked area of the SEM photograph, confirms the excellent coverage of the fabric by silver particles. The weight percentage (wt. %) of silver in polyester fabrics modified by one cycle of silver deposition, was 91.6%. The other elements exist as residuals from earlier textile industrial treatment.

3.2. Cyclic voltammetry

Among all the prepared and tested electrode materials, only some have shown a typical capacitive or pseudocapacitive behavior. Namely, independently on the electrolyte present in the cell (KCl whether NaOH), the electrode made of cotton with Ag deposit, shows only a purely Faradaic redox reaction, without any capacitive response, as demonstrated in Figure 2. The same stands for a polyester with Ag deposit, when only one immersion cycle is applied, as Figure 2 also shows. One may assume that the reason for the absence of a capacitive behavior in these samples, is such a silver deposit morphology that does not provide sufficient porosity and a sufficiently high surface area.

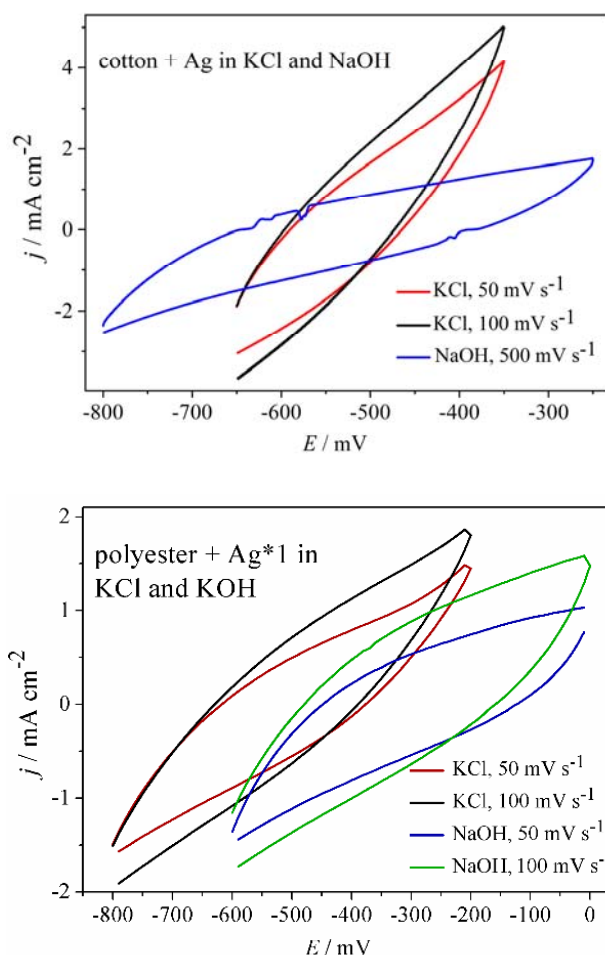


Figure 2. Cyclic voltammetry at various potential scan rates and in two different electrolytes, of cotton + Ag and polyester + Ag, after one immersion cycle

On the contrary, Figure 3 shows the cyclic voltammograms of the electrodes prepared by polyester modified by silver thin films, after three and five cycles of immersion. The diagrams recorded in NaOH show a purely capacitive response, with a square-like voltammogram and a significant gap between the positive and negative current, that increases with the scan rate. On the other hand, the voltammograms recorded in KCl contain one pair of peaks, placed in the potential range between -800 and -600 mV. The anodic and cathodic peaks are due to the oxidation and reduction of silver thin film by the chloride anion. These peaks are an indication of the pseudocapacitive behavior of polyester + Ag material in KCl solution.

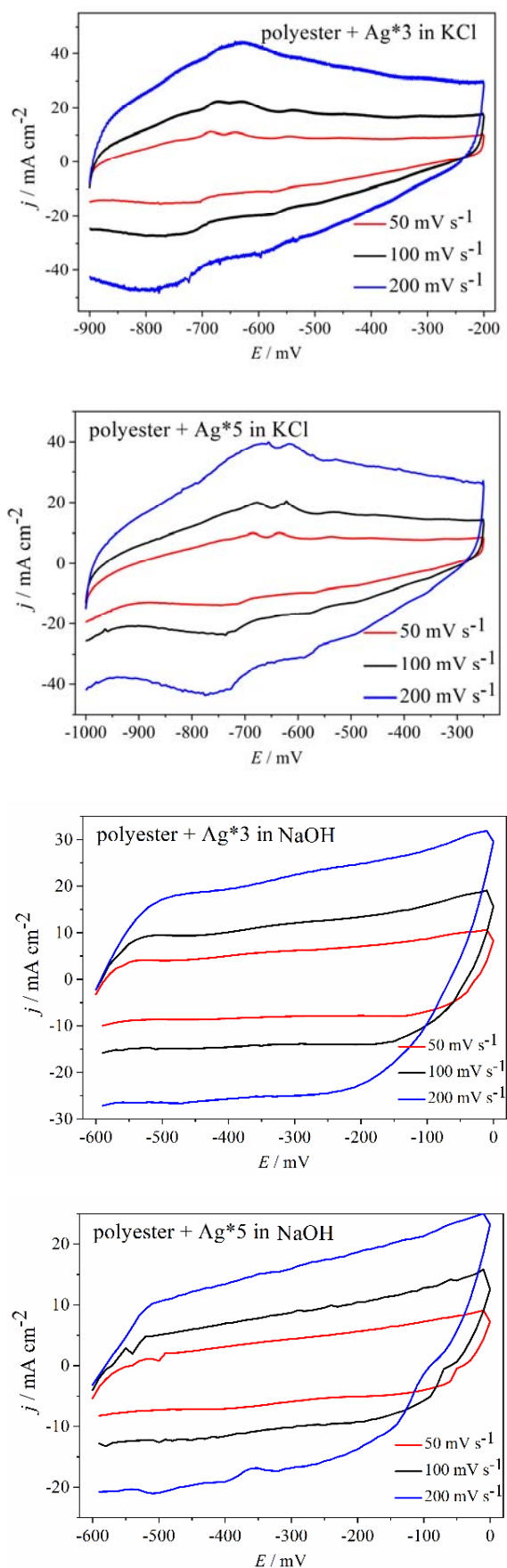


Figure 3. Cyclic voltammety at various potential scan rates and in two different electrolytes, of polyester + Ag, after three and five immersion cycles

The specific capacitance of the electrode surface was calculated from the CV curves using the equation:

$$C_s = \frac{\int I(V)dV}{m * \nu * \Delta V} \quad (1)$$

where C_s is the specific capacitance ($F g^{-1}$), ΔV is the scanning potential range (V), ν is the scan rate ($V s^{-1}$), m is the working electrode mass (g), and the $\int I(V)dV$ depicts an area of the CV curves [7].

The capacitance values, measured in the two electrolytes, from voltammograms recorded at $100 mV s^{-1}$, are presented in Table 1. Firstly, it is noticed that the fiber with three immersion cycles exhibits slightly higher capacitance in comparison to the samples obtained with five immersion cycles. It may be speculated that three immersion cycles are sufficient to form a silver layer of a sufficient thickness and compactness for capacitive behavior. And in case of five immersion cycles, the capacitive behavior is observed, but at the same time, the sample mass increases as well, which leads to the lower calculated capacitance. Secondly, the capacitance is higher in KCl solution, but this is probably the result of a Faradaic (pseudocapacitive) process involved, that increases the measured current.

The results obtained are quite lower than in earlier reports on similar, fiber-based electrodes, for example in [5, 8], yet still, the capacitive behavior is clearly present in our work.

Table 1. Specific capacitance of polyester + Ag samples, obtained after three and five immersion cycles in silver solution

	KCl, 3 cycles	KCl, 5 cycles	NaOH, 3 cycles	NaOH, 5 cycles
C_s , $F g^{-1}$	66	61	43	32

3.3. Chronoamperometry

To further investigate the application possibility of the synthesized materials as capacitors, the material performances were examined under potentiostatic conditions. As shown in Fig. 4, the current was quickly increased upon applying voltage of + 300 mV from the open circuit potential, denoting the charging of the capacitor. During the 10 s period of the applied positive potential, a slow current decay is observed, denoting the spontaneous capacitor discharging.

When the applied voltage was removed, the device current quickly decreased. Here, interestingly, the device current did not stop at 0 A after removing the applied voltage, but it did immediately overshoot to the negative direction. Furthermore, the negative current underwent a slow decay process after reaching the (negative) maximum values. This negative current part can be corresponded to the net charges stored by the previous potentiostatic charging operation [9].

The amount of charge (Q) stored can be calculated by integration of the area in the negative current part, and the integration results are shown in Table 2. Contrary to the CV results, the chronoamperometry evidences that polyester samples immersed in NaOH possess a much higher capacitance, i.e. the ability to store charges. This discrepancy is easy to understand. As explained, the voltammograms record both capacitive and pseudocapacitive response, while chronoamperometry, in the narrow potential range (up to 300 mV in this work), records only the purely capacitive response.

To conclude, the polyester modified with silver in three immersion cycles, when placed in NaOH electrolyte, is the best option for electric charge storage.

Table 2. The charge stored at the capacitor surface during the positive potentiostatic pulse in the two electrolytes, for polyester + Ag samples, obtained after three and five immersion cycles

	KCl, 3 cycles	KCl, 5 cycles	NaOH, 3 cycles	NaOH, 5 cycles
Q , mC cm ⁻²	10.9	8.4	119.8	37.0

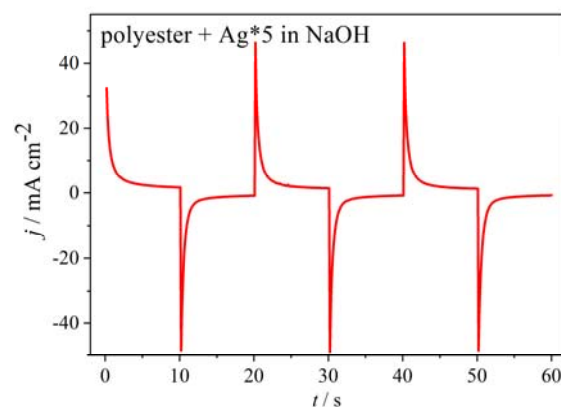
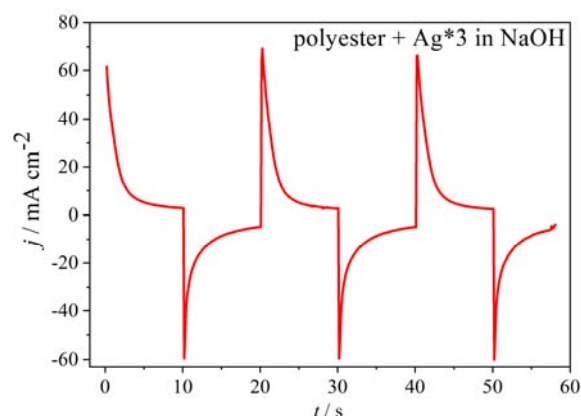
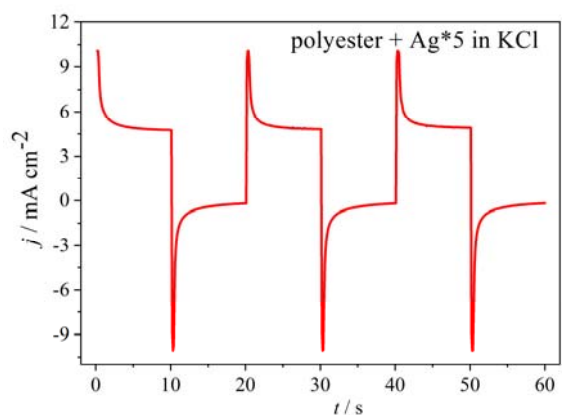
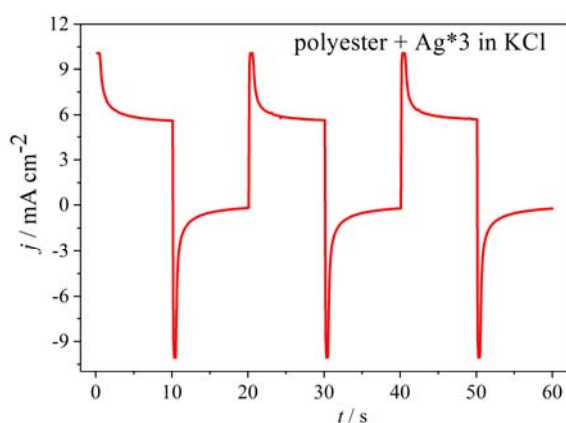


Figure 4. Repeated potentiostatic charge/discharge curves in two different electrolytes, for polyester + Ag electrode, after three and five immersion cycles in Ag solution

4. CONCLUSION

In this work, two different textile substrates were modified with a thin film of silver, by a novel immersion and annealing method. While the SEM shows excellent fiber coverage by silver particles even after the first immersion cycle, the electrochemical tests show significant differences between the samples. The cyclic voltammetry evidences that a cotton with silver deposit, and a polyester modified in only one immersion cycle in silver solution, do not exhibit any capacitive response. On the other hand, polyester modified with silver in three or five immersion cycles, shows a textbook-example of capacitive or pseudocapacitive behavior. This finding opens the door for production of wearable energy carriers, important in military applications.

As calculated from chronoamperometry measurements, the best charge carrying capacity shows polyester modified with silver in three immersion cycles, when placed in aqueous electrolyte containing 0.5 mol dm⁻³ NaOH.

ACKNOWLEDGMENT

The authors would like to acknowledge support from the scientific project of Military Academy, University of Defense in Serbia, "Research on influence of

characteristics of explosive ordnance on safety in Ministry of Defense and Army of Serbia” (VA-TT/1/22-24) and Ministry of Education, Science and Technological Development of the Republic of Serbia (Contracts No. 451-03-68/2021-14/200135, 451-03-9/2021-14/200017).

References

- [1] WANG, G., ZHANG, L., ZHANG, J.: *A review of electrode materials for electrochemical supercapacitors*, Chemical Society Reviews, 41 (2012) 797–828.
- [2] LUFRAÑO, F., STAITI, P.: *Mesoporous carbon materials as electrodes for electrochemical supercapacitors*, International Journal of Electrochemical Science, 5 (2010) 903–916.
- [3] LOKHANDE, C.D., DUBAL, D.P., SHIM JOO, O.H.: *Metal oxide thin film-based supercapacitors*, Current Applied Physics, 11 (2011) 255–270.
- [4] ALEX, O., OGWU, A., MIRZAEIAN, M., TSENDZUGHUL, N.: *Electrochemical energy storage of silver and silver oxide thin films in an aqueous NaCl electrolyte*, Journal of Electroanalytical Chemistry, 829 (2018) 59–68.
- [5] GAO, D., ZHAO, P., LIU, J., ZHOU, Y., LYU, B., MA, J., SHAO, L.: *Polyaniline/silver nanowire cotton fiber: A flexible electrode material for supercapacitor*, Advanced Powder Technology, 32 (2021) 3954–3963.
- [6] XU, H., ZHU, Y., ZHANG M., LI, Q., ZUO, S., CHEN, Y.: *Eigenstate PANI-coated paper fiber with graphene materials for high-performance supercapacitor*, Ionics, 26 (2020) 5199–5210.
- [7] KARAMI, Z., YOUSSEFI, M., RAEISSI, K., ZHIANI, M.: *An efficient textile-based electrode utilizing silver nanoparticles/reduced graphene oxide/cotton fabric composite for high-performance wearable supercapacitors*, Electrochimica Acta 368 (2021) 137647.
- [8] OJE, A., OGWU, A., MIRZAEIAN, M., OJE, A.M., TSENDZUGHUL, N.: *Silver thin film electrodes for supercapacitor application*, Applied Surface Science 488 (2019) 142–150.
- [9] LEE, H., KIM, J., KIM, H., KIM, Y.: *Strong photo-amplification effects in flexible organic capacitors with small molecular solid-state electrolyte layers sandwiched between photo-sensitive conjugated polymer nanolayers*, Scientific Reports 6 (2016), Article number: 19527.



INHIBITION OF ACID CORROSION OF MILD STEEL BY AQUEOUS EXTRACT OF OLIVE LEAVES

SOUAD TOUAZI

Laboratoire de Valorisation des Energies Fossiles (LAVALEF), Ecole Nationale Polytechnique d'Alger, Algeria
Laboratoire d'Electrochimie, Corrosion et de Valorisation Energétique (LECVE), Faculté de Technologie, Université de Bejaia, Algeria

souad.touazi@yahoo.fr

ADJOUATI BACHIR ABDERAOUF

Laboratoire de Valorisation des Energies Fossiles (LAVALEF), Ecole Nationale Polytechnique d'Alger, Algeria

bachir_abderraouf.adjouati@g.enp.edu.dz

ZIANE AYMENE

Laboratoire de Valorisation des Energies Fossiles (LAVALEF), Ecole Nationale Polytechnique d'Alger, Algeria

aymene.ziane@g.enp.edu.dz

NADIA ZAIDI

Laboratoire d'Electrochimie, Corrosion et de Valorisation Energétique (LECVE), Faculté de Technologie, Université de Bejaia, Algeria

zaidinadia06@gmail.com

MIHAEL BUČKO

University of Defense, Military Academy, Pavla Jurišića Šturma 33, 11000, Belgrade, Serbia

mihaelbucko@yahoo.com

telephone: 011 3603 464

LAID MAKHLOUFI

Laboratoire d'Electrochimie, Corrosion et de Valorisation Energétique (LECVE), Faculté de Technologie, Université de Bejaia, Algeria

laid_mak@yahoo.fr

Abstract: In this study, a green inhibitor of steel corrosion in acidic solution was prepared from an agricultural waste product based on olive leaves (*Olea Europaea Sylvestris*). The paper deals with the development of a method for extracting compounds from the plant, their use as corrosion inhibitors in acidic media and their mode of operation. The olive leaves extract, obtained by refluxed technique in water, was tested as a corrosion inhibitor for steel, using different electrochemical methods: open circuit potential monitoring and potentiodynamic (Tafel) curves, as the extract was added in various concentrations into the $0.1 \text{ mol dm}^{-3} \text{ HCl}$. The results obtained by various techniques showed that the extract acted as a mixed-type inhibitor. Several adsorption isotherms (Langmuir, Temkin and Frumkin) were evaluated to determine the effective adsorption isotherm. It was concluded that the adsorption of the inhibitor was spontaneous, through the mechanism of physical adsorption, and it obeyed the Langmuir adsorption isotherm. The highest corrosion inhibition efficiency of 66 % was obtained for $0.96 \cdot 10^{-3} \text{ g dm}^{-3}$ of inhibitor, as measured by potentiodynamic polarization method.

Keywords: corrosion inhibitor, green chemistry, olive leaves, steel.

1. INTRODUCTION

Corrosion inhibitors are compounds broadly used to prevent or completely inhibit metal corrosion in liquid or gaseous corrosion media. There are plenty of liquid media in military equipment where the application of corrosion inhibitors is mandatory, for example heating/cooling systems, lubrication systems, oils and fuels facilities, hydraulic systems in weaponry, vehicles and radar

systems, food processing, equipment decontamination and cleaning, preparation of ordnance for coating application and assembly, etc.

Corrosion inhibitors reduce the metal corrosion rate by various actions, such as adsorption of ions/molecules onto the metal surface, decreasing the diffusion of reactants and products of the corrosion process, or increasing the overpotential for anodic and cathodic reactions of the corrosion process [1].

A vast number of chemicals have been used as inhibitors. The most famous inhibitors in acidic media are nitrogen, oxygen and sulfur-based organic compounds and alkaloids, while in neutral media, chromates, benzoates, phosphates and nitrites are known as excellent corrosion inhibitors [2].

Many research groups have reported the successful use of green inhibitors, i.e. the naturally occurring chemicals that are easily biodegradable. Various natural compounds have been used for this purpose, such as honey, plant juice, oil, seeds and leaves, tree and fruit extracts, etc. [3].

As a continuation of previous efforts in this field, this paper aims to investigate the application of olive (lat. *Olea Europaea Sylvestris*) leaf extract as a corrosion inhibitor for mild steel corrosion in acidic medium. Steel equipment often comes in contact with acidic solutions, in processes like decontamination, acid cleaning, acid descaling, or acid pickling, and all these processes require the presence of corrosion inhibitors. Olive leaves are a cheap raw material, as a by-product in the olive grove farming and olive oil industry in the Mediterranean coastal zone [4].

The role of olive leaves extract in steel corrosion in HCl medium was investigated by the two electrochemical techniques: open circuit potential monitoring and potentiodynamic (Tafel) curves recording.

2. EXPERIMENTAL PART

2.1. Preparation of the corrosion inhibitor and the corrosion medium

The harvest of wild olive leaves was carried out at the National Polytechnic School of Algiers, in the northern Algeria during the flowering period in February 2020. The leaves were washed in distilled water, dried and grounded to obtain the powder. To obtain the extract, a sample of 10 g of olive leaves powder was mixed with 100 ml of distilled water, stirred and heated under reflux at 80 °C for 45 minutes. After extraction, the mixture was cooled and separated by filtration using a Büchner funnel and a water pump. The liquid phase was recovered, stored protected from light and subsequently used as a corrosion inhibitor.

The corrosive medium was 100 cm³ of 0.1 mol dm⁻³ HCl solution at 25 °C, without and with different concentrations of the olive leaf extract.

2.2. Electrochemical techniques

The working electrode in corrosion tests was mild steel, with the chemical composition shown in Table 1. The electrode was polished, degreased with acetone and rinsed in distilled water prior to the immersion in HCl.

Table 1. Chemical composition of steel, wt.%

C	0.15 – 0.26	S	< 0.040
Si	< 0.35	Mo	0.4 – 0.6
Mn	< 1.5	Fe	97 – 98
P	< 0.035		

Open circuit potential (OCP) and potentiodynamic polarization measurements were carried out using a PGZ100 type potentiostat-galvanostat controlled by a Voltmaster software. The reference electrode was K₂SO₄-saturated sulphate electrode (SSE) with an equilibrium potential of 0.655V vs. standard hydrogen electrode at 25 °C. Platinum mesh was used as counter electrode in the polarization experiments.

The potentiodynamic plots were obtained at a scan rate of 1 mVs⁻¹, over the respective OCP range between -250 mV and +250 mV, from cathodic to anodic end.

The results of the electrochemical measurements are the mean value of three runs, each with a freshly prepared steel sample and new acid solution. The percentage of inhibition efficiency was calculated using the equation below:

$$IE, \% = \frac{i_{corr} - i_{inh}}{i_{corr}} \quad (1)$$

where i_{corr} and i_{inh} are the corrosion current densities of steel, in the absence and presence of inhibitor, respectively.

3. RESULTS

3.1. Open circuit potential

Figure 1 depicts the evolution of the open circuit potential of the steel as a function of immersion time in 0.1 mol dm⁻³ HCl, with various concentrations of the aqueous extract of olive leaves. The curves obtained were compared with a reference curve obtained without the inhibitor.

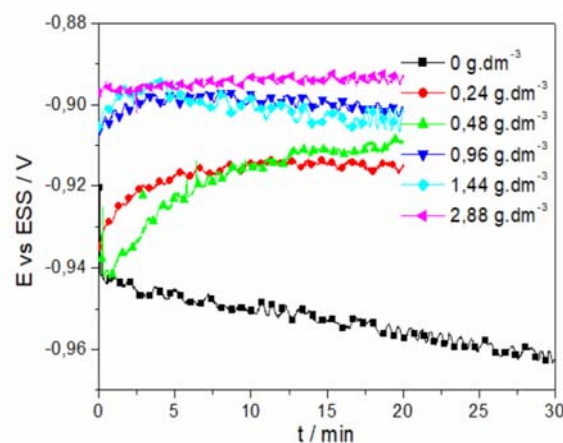


Figure 1. Monitoring of the open circuit potential of mild steel immersed in 0.1 mol dm⁻³ HCl at different concentrations of olive leaf extract

In the absence of the extract of olive leaves, it is noted that the evolution of the potential of steel tends towards more negative values, indicating the degradation of the metal. The stabilization of the OCP at a value of -0.96 V is achieved after 25 minutes of immersion. On the other hand, when the tests are conducted in the presence of the green inhibitor, a displacement of the potential towards more positive values is observed. This ennoblement of the potential indicates that there is a formation of a protective

layer on the metal surface, which can be attributed to the adsorption of the inhibitor on the active sites of the metal [4, 5].

It should be noted that the potential stabilization time decreases as the concentration of the extract increases, up to an added value higher than or equal to 0.96 g dm^{-3} . For these values of the inhibitor concentration, the value of the free potential stabilizes already in the first minutes of immersion.

3.2. Polarization curves

The potentiodynamic plots presented in Fig. 2, for various concentrations of the inhibitor added, show similar shape on both anodic and cathodic part, however the values of the corrosion potential and corrosion current density differ significantly.

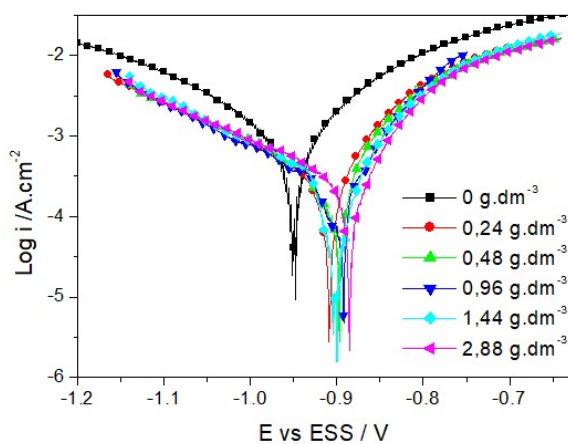


Figure 2. Cathodic and anodic polarization curves of steel in 0.1 mol dm^{-3} HCl with different inhibitor concentrations of olive leaf extract; potential sweep rate is 1 mV s^{-1}

The electrochemical parameters deduced from the potentiodynamic polarization curves, namely: corrosion current density (i_{corr}), corrosion potential (E_{corr}), cathodic and anodic slopes (β_c and β_a), polarization resistance (R_p) and the inhibition efficiency (IE), are grouped in Table 2. It may be deduced from the data that the increase in the concentration of the extract shifts the corrosion potential towards positive values, decreases the current densities of the anodic and cathodic branches.

Table 2. Electrochemical parameters of steel corrosion in HCl, extracted from the polarization curves

c , g dm^{-3}	E_{corr} , mV	i_{corr} , mA cm^{-2}	β_a , V dec^{-1}	β_c , V dec^{-1}	IE, %
0	-950	0.48	89	-110.3	-
0.24	-908	0.26	85.5	-179.1	45.9
0.48	-901	0.18	64.6	-140.6	61.4
0.96	-896	0.16	66.2	-141.1	65.9
1.44	-899	0.18	74.3	-134	61.8
2.88	-885	0.24	80	-189.5	50.4

The observation of the polarization plots shows that independently on the inhibitor concentration, the difference in corrosion potential (in the absence and in the presence of the inhibitor) is less than 85 mV and that the

two partial currents (anodic and cathodic) are almost equally reduced. These observations point to the mixed nature of the inhibitor [6] and clearly show that the olive leaf extract reduces both the rate of anodic dissolution of steel described by the reaction (Eq. 2)



and cathodic reduction of hydrogen protons (Eq. 3)



In view of the results obtained, one can also notice that the addition of the extract does not modify the shape of the anodic and cathodic branches, which reflects in an insignificant variation in the values of the Tafel coefficients (β_a and β_c). This result suggests that the adsorbed inhibitor acts by simple blocking of the cathodic and anodic sites. In other words, the inhibitor decreases the surface of the interface between the metal and the electrolyte, without affecting the corrosion mechanism [7].

The results obtained in Table 2 show clearly that the inhibition efficiency was improved with the increase in the concentration of the extract and reached a maximum value of 65.9% for an optimal concentration of 0.96 g.dm^{-3} . Beyond this concentration a decrease of the value of the inhibition efficiency is observed.

3.3. Adsorption isotherms and the inhibition mechanism

Several adsorption isotherms (Langmuir, Temkin and Frumkin) were evaluated to determine the effective isotherm that best describes the adsorption of olive leaves extract on the steel surface in HCl solution. The isotherms are described by the following equations [8]:

Langmuir:

$$\frac{C}{\theta} = \frac{1}{K} + C \quad (4)$$

Temkin:

$$\exp(-2a\theta) = KC \quad (5)$$

Frumkin:

$$\frac{\theta}{1-\theta} \exp(-2a\theta) = KC \quad (6)$$

where θ is the cover degree of the metal surface by the adsorbed inhibitor, defined by the following relationship

$$\theta = \frac{i_{\text{corr}} - i_{\text{inh}}}{i_{\text{corr}}} \quad (7)$$

where i_{corr} and i_{inh} are the corrosion current densities of steel, in the absence and presence of inhibitor, respectively.

The Figures 3, 4, 5 illustrate the three adsorption isotherms, while Table 3 shows the correlation coefficient obtained by the three different models:

Table 3. Coefficient of correlation, R^2 , between the data predicted by the adsorption model and the measured data

for the adsorption process of olive leaves extract on steel

Model	R^2
Langmuir	0.981
Temkin	0.680
Frumkin	0.299

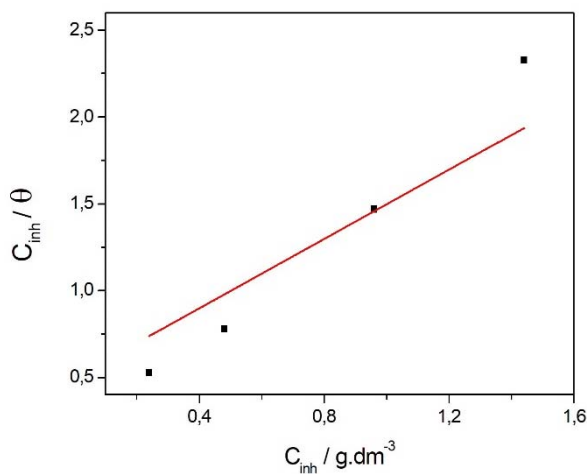


Figure 3. Langmuir adsorption isotherm of olive leaf extract on steel in 0.1 mol dm⁻³ HCl

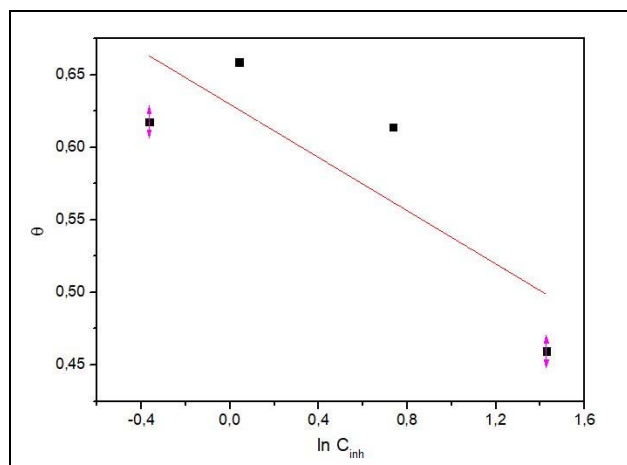


Figure 4. Temkin adsorption isotherm of olive leaf extract on steel in 0.1 mol dm⁻³ HCl

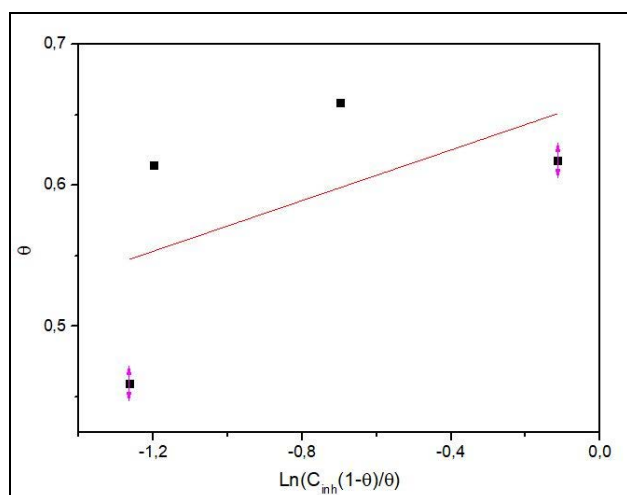


Figure 5. Frumkin adsorption isotherm of olive leaf extract on steel in 0.1 mol dm⁻³ HCl

Analysis of different figures, allows us to note that the only curve that shows linear behavior is the plot of (C_{inh}/θ) as a function of the concentration of inhibitor (Figure 3), presenting the highest correlation coefficient (Table 3). This leads to the conclusion that the adsorption of the olive leaf extract on the surface of mild steel in hydrochloric acid medium obeys the Langmuir adsorption isotherm. Thus, the equilibrium constant (K) can be calculated from the ordinate at the origin of the linear curve C/θ which gives the value ($1/K$). The parameter K is related to the free energy of adsorption (ΔG), the enthalpy of adsorption (ΔH) and the standard entropy of adsorption (ΔS)^o according to the equations (8 – 10):

$$K = \frac{1}{55.5} \exp\left(\frac{-\Delta G_{ads}^{\circ}}{RT}\right) \quad (8)$$

$$K = \exp\left(-\frac{\Delta H_{ads}^{\circ}}{RT}\right) \quad (9)$$

$$\Delta G_{ads}^{\circ} = \Delta H_{ads}^{\circ} - T\Delta S_{ads}^{\circ} \quad (10)$$

The values that describe the adsorption process for the organic molecules of the inhibitor are presented in Table 4:

Table 4. Thermodynamic parameters of the inhibitor adsorption on mild steel

Parameter	Value
ΔS° (J mol ⁻¹ K ⁻¹)	33.39
ΔH° (kJ mol ⁻¹)	-1.76
ΔG° (kJ mol ⁻¹)	-11.71

The negative value of the adsorption free energy indicates that the adsorption process is spontaneous. The value of the equilibrium constant K ($K = 2.04 \text{ dm}^3 \text{ kg}^{-1}$) is very low which indicates that the adsorption of the inhibitor on the steel surface is not strong. This result is in correlation with the result obtained during the kinetic study where the inhibition efficiency was not close to 1. Several researchers [6, 8] proposed that the values of the free energy of adsorption close to -20 kJ mol^{-1} , correspond to the electrostatic interactions between the charged molecules and the charges of the metal surface (physisorption), while on the other hand, when the free energy of adsorption is close to -40 kJ mol^{-1} , it corresponds to the transfer of charges between the molecules of the inhibitor and the surface of the metal and thus forming covalent bonds (chemisorption). In our case, the calculated values of the free energy of adsorption indicate that the process is characterized as a physisorption.

The negative values obtained for the enthalpy of adsorption show that the system studied is exothermic. As one can notice, there is an increase in the molecular disorder (ΔS°) with the adsorption of the inhibitor. We can therefore conclude that the phenomenon of adsorption disturbs the order of atoms on the surface of mild steel.

4. CONCLUSION

The scope of this work was to investigate whether the olive leaves extract may be applied as an inhibitor of mild steel corrosion in 0.1 mol dm⁻³ HCl solution. The open circuit potential monitoring and the potentiodynamic curves analysis clearly show that the steel corrosion rate

decreases as the extract is added to the solution in higher concentration. The extract acts as a mixed type inhibitor, since it retards both the anodic and cathodic process of corrosion. Based on the analysis of the adsorption isotherms, it may be concluded that the adsorption of the inhibitor is quite weak, as a result of the physisorption. The future research is going to be focused on the identification of active components in the olive leaves powder that are responsible for the observed inhibitive behavior of the extract.

Acknowledgment

One of the authors would like to acknowledge support from the scientific project of Military Academy, University of Defense in Serbia, "Research on influence of characteristics of explosive ordnance on safety in Ministry of Defense and Army of Serbia" (VA-TT/1/22-24).

References

- [1] AMITHA RANI, B.E., BAI J. BASU, B.: *Green inhibitors for corrosion protection of metals and alloys: An overview*, International Journal of Corrosion, (2012), Article ID 380217.
- [2] FATEH, A., ALIOFKHAZRAEI, M., REZVANIAN, A. R.: *Review of corrosive environments for copper and its corrosion inhibitors*, Arabian Journal of Chemistry, 13(1) (2020) 481-544.
- [3] KERAMATINIA M., RAMEZANZADEH, B., MAHDAVIAN, M.: *Green production of bioactive components from herbal origins through one-pot oxidation/polymerization reactions and application as a corrosion inhibitor for mild steel in HCl solution*, Journal of the Taiwan Institute of Chemical Engineers, 105 (2019) 134-149.
- [4] TABERA, J., GUINDA A., RUIZ-RODRIGUEZ A., SENORANS, F., IBANEZ, E., ALBI, T., REGLERO, G.: *Countercurrent supercritical fluid extraction and fractionation of high-added-value compounds from a hexane extract of olive leaves*, Journal of Agriculture and Food Chemistry, 52 (2004) 4774-4779.
- [5] BUČKO, M., TOMIĆ, M., STOJANOVIĆ, V., PAVLOVIĆ, M., BAJAT, J.B: *The electrochemical deposition and corrosion stability of Zn-Mn alloy coatings*, Materials Protection, 51 (2010) 105-110.
- [6] ZAABAR, A., BELHAMEL, K., SAIDANI, B.: *Inhibition of acid corrosion of mild steel by aqueous nettle extracts*, Pigment and Resin Technology, 43(3) (2014) 127-138.
- [7] GUPTA, N.K., VERMA, C., SALGHI, R., LGAZ H., MUKHERJEE A.K., QURAISHI M.A.: *New phosphonate based corrosion inhibitors for mild steel in hydrochloric acid useful for industrial pickling process: Experimental and theoretical approach*, New Journal of Chemistry, 41 (2017) 13114-13129.
- [8] AYAWEI N., EBELEGI A.N, WANKASI D.: *Modelling and interpretation of adsorption isotherms*, Hindawi Journal of Chemistry, Article ID 3039817.



AIR AND PRECIPITATION TESTING AS PART OF ENVIRONMENTAL RADIATION MONITORING IN THE VICINITY OF NUCLEAR FACILITIES

JOVANA KNEŽEVIĆ

PC „Nuclear Facilities of Serbia“, Mike Petrovića Alasa 12-14, Vinča, Belgrade, jovana.knezevic@nuklearniobjekti.rs

NATAŠA LAZAREVIĆ

PC „Nuclear Facilities of Serbia“, Mike Petrovića Alasa 12-14, Vinča, Belgrade, natasa.lazarevic@nuklearniobjekti.rs

SOFIJA FORKAPIĆ

Faculty of Sciences, University of Novi Sad, Trg Dositeja Obradovića 3, Novi Sad, Serbia, sofija@df.uns.ac.rs

KRISTINA BIKIT ŠREDER

Faculty of Sciences, University of Novi Sad, Trg Dositeja Obradovića 3, Novi Sad, Serbia, kristina.bikit@df.uns.ac.rs

VESNA RADUMILO

PC „Nuclear Facilities of Serbia“, Mike Petrovića Alasa 12-14, Vinča, Belgrade, vesna.radumilo@nuklearniobjekti.rs

DALIBOR ARBUTINA

PC „Nuclear Facilities of Serbia“, Mike Petrovića Alasa 12-14, Vinča, Belgrade, dalibor.arbutina@nuklearniobjekti.rs

Abstract: Public company „Nuclear Facilities of Serbia“ is the only operator of nuclear facilities and holder of licenses to perform nuclear activities in the country. By the current legislation, environmental radiation monitoring in the vicinity of nuclear facilities is performed to assess the level and control the external exposure of the population and environment to ionizing radiation due to the operation of nuclear facilities. This paper presents an overview of the representative environmental radiation monitoring results regarding radioactive contamination level and ambient gamma dose rate equivalent in air and precipitation for the year 2021. The obtained results show that there is no adverse influence on the population and environment and the radiation risk for individuals in the population is negligible.

Keywords: monitoring, environment, radioactivity, testing, nuclear facility

1. INTRODUCTION

Environmental radiation monitoring is a set of measurements, processing and interpretation of the results of measurements of radiation and meteorological parameters in order to assess the level and control the exposure of the population and the environment to ionizing radiation due to the operation of nuclear facilities. Systematic examination of radioactivity in the environment includes the following activities, according to the current legislation [1,2]:

- Measurements of radiation parameters, including:
 - o Control of the level of radioactive contamination in the environmental samples (air, precipitation, surface water, river sediment, potable water, ground water, soil, food);
 - o Examination the level of external radiation – measurements of ambient gamma dose

equivalent and continuous measurements of ambient gamma dose rate equivalent);

- Measurements of meteorological parameters;
- Mathematical modeling of the distribution of radionuclides in the boundary layer of the atmosphere.

In accordance with the national legislation [2], Public company „Nuclear Facilities of Serbia“ (PC NFS) conducts measurements of radiation parameters by examining the level of external radiation, measuring meteorological parameters and mathematical modeling. An independent authorized legal entity, in accordance with the [2], conducts measurements of radiation parameters by controlling the level of radioactive contamination of the environment. Radioactive contamination measurements are performed by Department of Physics, Faculty of Science, University of Novi Sad, Serbia. The sampling locations are shown in table 1 [3].

Table 1. Annual program of examination of the level of radioactive contamination and the level of external radiation in the environment in the vicinity of nuclear facilities in PC NFS [3]

LOCATION	FREQUENCY	TYPE OF ANALYSIS
RADIOACTIVE CONTAMINATION LEVEL CONTROL IN AIR SAMPLES		
<i>Reference point:</i> 1. Green hill, Environmental Protection Agency <i>Three sites at the location of PC NFS with the most frequent winds, which are directed towards Vinča settlement:</i> 1. Weather station mounting pole 2. Radioactive waste (RAW) storage 3. Elementary school (in the vicinity of PC NFS)	Continuous collection, cumulative monthly sample, monthly measurement, 12 times a year	Gamma spectrometric analysis
<i>Two sites at the location of PC NFS with the most frequent winds, which are directed towards Vinča settlement:</i> 1. RAW storage 2. Elementary school (in the vicinity of PC NFS)	Continuous collection – cumulative quarterly sample, quarterly measurements, 4 times a year.	Determination of ⁹⁰ Sr
RADIOACTIVE CONTAMINATION LEVEL CONTROL IN PRECIPITATION SAMPLES		
<i>Reference point:</i> 1. Green hill, Environmental Protection Agency <i>Two sites with the most frequent winds, which are directed towards Vinča settlement:</i> 1. Elementary school (in the vicinity of PC NFS) 2. Water station in Vinča settlement <i>Two sites at the location of PC NFS:</i> 1. Weather station mounting pole 2. „Vinča center“	Continuous collection, collected monthly sample, monthly measurement, 12 times a year	Gamma spectrometric analysis
<i>Reference point:</i> 1. Green hill, Environmental Protection Agency <i>One site with the most frequent winds, which are directed towards Vinča settlement:</i> 1. Water station in Vinča settlement <i>One site at the location of PC NFS:</i> 1. Weather station mounting pole	Continuous collection, collected monthly sample, monthly measurement, 12 times a year	Determination of ³ H
<i>Reference point:</i> 1. Green hill, Environmental Protection Agency	Continuous collection – cumulative quarterly sample, quarterly measurements, 4 times a year.	Determination of ⁹⁰ Sr
AMBIENT GAMMA DOSE RATE EQUIVALENT IN AIR		
1. Research nuclear reactor RA (PC NFS) 2. Water station in Vinča settlement 3. Weather station mounting pole (PC NFS) 4. RAW storage (PC NFS) – two measurement points 5. Secure storage of high activity sources (PC NFS) 6. Waste processing facility (PC NFS)	Continuous automatic measurement	Measurement of ambient gamma dose rate equivalent

This paper presents the representative environmental radiation monitoring results regarding radioactive contamination level and ambient gamma dose rate equivalent, in air and precipitation samples, for the year 2021.

2. METHODS AND MATERIALS

In following chapters, methods for determining the activity concentration of radionuclides, as well as ambient gamma dose rate equivalent are described. All the testing methods for determining the presence of radionuclides in air and precipitation samples are accredited according to the standard SRPS ISO/IEC 17025:2017 [4].

2.1 Determination of radioactive contamination in the air and precipitation

Air sampling from the ground layer of the atmosphere was carried out by continuous suction using constant flow air sampling pumps (50-80 m³/h). Monthly air samples collected on filter papers made of glass fibers (with pores of 1-2 μm) of high efficiency, by manufacturer F&J Specialty Products Inc., USA, were homogeneously packed in a cylindrical measuring vessel with dimensions 31 mm x 67 mm [5].

Precipitation samples were collected at the locations continuously with 25 m² surface samplers placed at a height of 0,8 m above the ground. Monthly precipitation samples were evaporated in dryers to a dry residue

according to the standard method [6].

Examination of gamma active radionuclides in air and precipitation samples was conducted by the gamma spectrometric method using High Purity Germanium (HPGe) detector according to [5]. Calibration of the HPGe detector was performed with certified reference material that contains mixture of gamma emitters in silica gel matrix of cylindrical geometry. Measurements of samples in contact geometry lasted for 80000 s. Detectors are connected to a digital spectroscopic processing using Canberra 1300 InSpector and multiport analyzer Canberra Multiport II. Gamma spectra were collected and analyzed using Canberra Genie 2000 Spectroscopy System software.

Examination of tritium ^3H in precipitation samples was performed in accordance with a validated method [7] on a liquid scintillation detector Quantulus 1220. This method involves mixing a distilled liquid sample with the scintillation cocktail in 8 ml : 12 ml ratio, in the original 20 ml measuring bottles. Quantulus 1220 has its own system of natural background radiation reduction consisting of active and passive protection. In order to determine „the window“ of ^3H in measured spectrum, the tritium standard with known activity concentration was measured as well as „background“ (distilled well water), and „the window“ was set to obtain the maximum figure of merit (FOM) factor. Preparation of the tritium standard, as well as „background“, was the same as preparation of the samples. Before the measurements were conducted, the samples were kept in a dark place for at least six hours to avoid the occurrence of luminescence.

Examination of strontium ^{90}Sr in air samples was performed as follows: the sample was dried at the temperature of 105°C . It was then homogenized with strong oxidizing agents and mineralized at the temperature of 600°C . The measured mass of mineral residue was dissolved in nitric acid with the addition of a known amount of inactive yttrium carrier. The separation of ^{90}Y from ^{90}Sr is based on a multi-stage extraction procedure with tri-butyl-phosphate, nitric acid and deionized water. The separated ^{90}Y was deposited as Y-hydroxide, which was transformed into yttrium oxide by annealing at the temperature of 900°C . The chemical yield of yttrium was calculated from the mass of obtained Y_2O_3 . The activity concentration was determined by measuring the activity concentration of the separated yttrium in an anti-coincidence counter of low beta activities „INC-Instruments“ USA.

Examination of ^{90}Sr in water samples was conducted by a validated method based on the detection of Cherenkov radiation on a liquid scintillation counter. Radioactive strontium ^{90}Sr decays by beta decay into its progeny yttrium ^{90}Y , emitting beta particles with maximum energy $E_{\text{max}} = 546 \text{ keV}$. ^{90}Y is also beta emitter with maximum energy of emitted beta particle $E_{\text{max}} = 2280 \text{ keV}$, and the half-life value of ^{90}Y is 64 h. Due to its short half-life, ^{90}Y is in radioactive equilibrium with the parent nucleus ^{90}Sr . In this way, by measuring the activity concentration of ^{90}Y in the sample, the activity concentration of ^{90}Sr in the sample is estimated. Fast electrons that are emitted by the

decay of ^{90}Y produce the Cherenkov radiation in water. Minimum energy that fast electrons need to have to produce the Cherenkov effect in water is 256 keV. The Cherenkov radiation belongs to visible and UV part of electromagnetic spectrum, so it can be identified by photomultiplier on a liquid scintillation detector. For detector calibration, a standard radioactive material (water solution $^{90}\text{Sr}/^{90}\text{Y}$) was used. The measurements were conducted on liquid scintillation detector Wallac 1220 Quantulus, that has high stability, good separation of alpha and beta signals based on the classification of pulse amplitudes based on their shape, passive protection made of lead and active protection against cosmic and other environmental radiation. Spectrum analysis was performed using Wallac WinQ 1220-307 Windows software, and for the data processing Wallac Easy View 1224-534 Spectrum analysis program.

2.2. Continuous measurements of ambient gamma dose rate equivalent

Continuous measurements of ambient gamma dose rate equivalent in the air were carried out to estimate the radiation field variations in the vicinity of nuclear facilities, as well as early warning of accidents. The ambient gamma dose rate equivalent in the environment generally depends on the geographical location as well as on the radioactive content of the local rocks and soil. In addition, these values also depend to a certain extent on different meteorological conditions (precipitation, humidity, wind, etc.). During the rainy season, there is a washing of radioactive elements from the atmosphere to the ground and an increase in the ambient radiation level in a short period of time. Therefore, there is justified to examine and determine the correlation between radiation and meteorological parameters, since from the point of view of radiation safety and radiation protection, it is very important to evaluate the influence of meteorological parameters and phenomena that can lead to changes in the values of radiation parameters, in order to unambiguously determine when detecting increased ambient gamma dose rate equivalent in the air, whether it is a potential radiation/nuclear accident, or an increase in the consequences of meteorological conditions in the environment at a given time.

Concentration of pollutants from artificial sources in the environment, in general, is monitored by a monitoring network with a limited number of discrete points. These measurements were performed with multifunctional gamma monitors. They are portable instruments, designed to automatically perform all necessary functions as independent local monitors. One monitor is connected to two energy-compensated Geiger-Miller counters (probes), with different sensitivities that can cover the range from natural background radiation to accidental levels (from 50 nSv/h to 1 Sv/h). These measurements were carried out according to the standard [8].

The data were collected continuously, during 24 hours and sent in half-hourly intervals to the database on the central computer in the control room where data acquisition, processing, storage, presentation and interpretation of obtained values were carried out. The

entire system is connected to the eEMIS application. With the help of the eEMIS application, data processing for the needs of operational tasks as well as for research purposes are performed [9].

The amount of precipitation, for the purpose of the correlation, was measured by an electric rain gauge with a heater, placed at a height of 1 m above the ground. Precipitation data is displayed on the central computer in the control room.

3. RESULTS AND DISCUSSION

3.1. Radioactive contamination in the air and precipitation

Figures 1 and 2 show the values of activity concentration of ^7Be and ^{210}Pb in air, respectively. Activity concentration of ^{137}Cs in air is below the value of minimum detectable activity (MDA), thus not presented as figure. Figure 3 shows the cumulative quarterly measurements of activity concentration of ^{90}Sr .

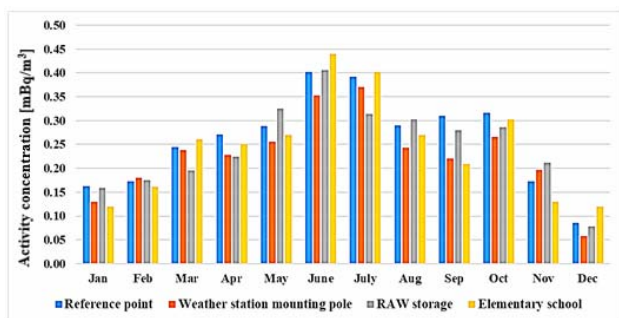


Figure 1. Activity concentration of ^7Be in air in mBq/m^3 for different locations during the year of 2021

It is known that production of cosmogenic radionuclide ^7Be depends on interaction between cosmic rays and upper layers of atmosphere. The production rate is varied by the solar modulation of galactic cosmic rays which is controlled by the solar magnetic field and, in turn, by solar activity [10], hence the seasonal variations of ^7Be be seen on figure 1. The highest values of activity concentration are in June and July, while lower values were obtained during winter months.

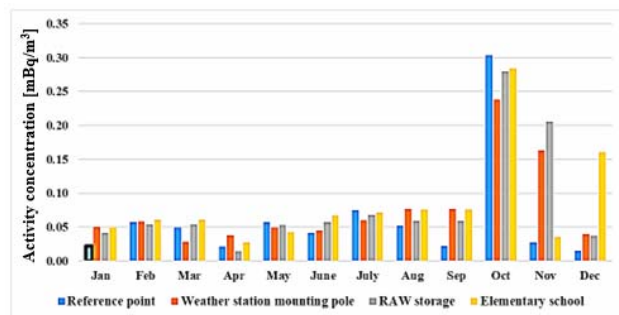


Figure 2. Activity concentration of ^{210}Pb in air in mBq/m^3 for different locations during the year of 2021. The framed bar (\square) represents MDA, since the value is below MDA

The observed increase in the activity concentration of

^{210}Pb in air in October 2021 is not due to operation of nuclear facilities, since the increase was also detected at the reference point with the highest value of activity concentration among all measurement points. The obtained value is in accordance with the results of environmental radioactivity monitoring in Serbia, where the activity concentration for the same measurement point is in interval $0,3 - 1,5 \text{ mBq}/\text{m}^3$ [11].

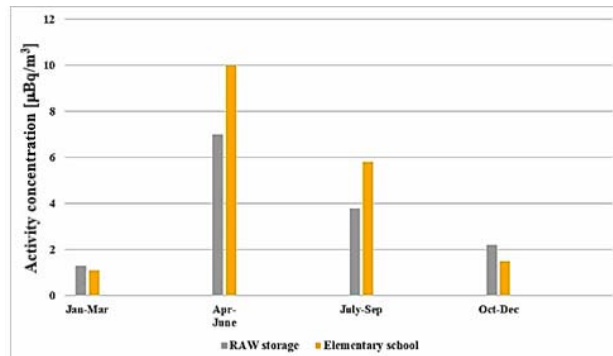


Figure 3. Activity concentration of ^{90}Sr in air in $\mu\text{Bq}/\text{m}^3$ for different locations during the four quarters of 2021

Figures 4, 5, 6 and 7 show the values of activity concentration of ^{226}Ra , ^{232}Th , ^{40}K and ^{238}U in precipitation samples, respectively. Activity concentration of ^{235}U , ^{137}Cs and ^3H in precipitation is mostly below MDA, thus not presented as figure. The cumulative quarterly values of activity concentration of ^{90}Sr in precipitation are below MDA.

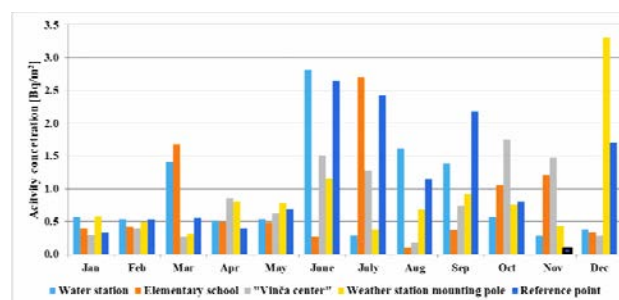


Figure 4. Activity concentration of ^{226}Ra in precipitation in Bq/m^2 for different locations during the year of 2021.

The framed bar (\square) represents MDA, since the value is below MDA

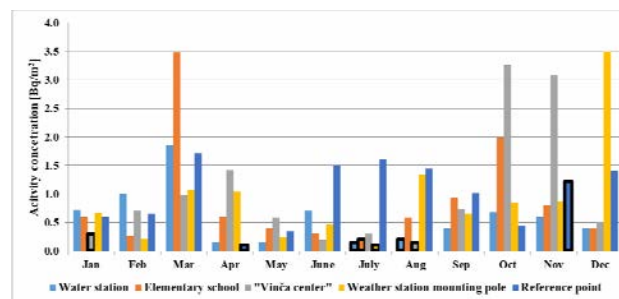


Figure 5. Activity concentration of ^{232}Th in precipitation in Bq/m^2 for different locations during the year of 2021.

The framed bars (\square) represent MDA, since these values are below MDA

It can be seen on figures 4 and 5 that values of activity

concentration of ^{226}Ra and ^{232}Th differ from one location to another. The existence of correlation between detected higher values and the position of the locations cannot be established, given the amount of data and parameters that influence the results (eg. geographic area/terrain, meteorological conditions of the location). Activity concentration of both radionuclides fluctuates in interval that is consistent with characteristic data for precipitation.

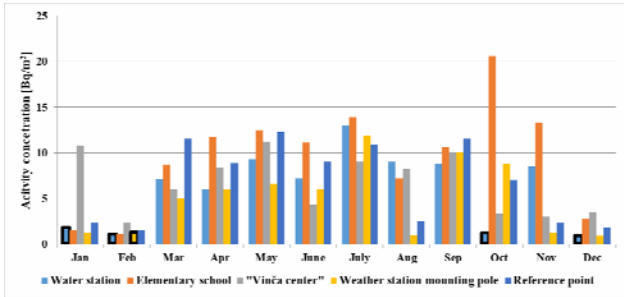


Figure 6. Activity concentration of ^{40}K in precipitation in Bq/m^2 for different locations during the year of 2021. The framed bars (\square) represent MDA, since these values are below MDA

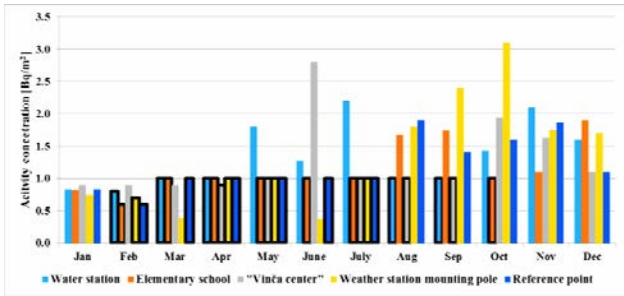


Figure 7. Activity concentration of ^{238}U in precipitation in Bq/m^2 for different locations during the year of 2021. The framed bars (\square) represent MDA, since these values are below MDA

The results for radionuclides ^{40}K and ^{238}U shown in figures 6 and 7, respectively, vary within the normal range for environmental samples.

3.2. Measurements of ambient gamma dose rate equivalent in the air

Figure 8 shows the monthly average values of ambient gamma dose rate equivalent in nSv/h for the measurement points according to table 1 in the vicinity of nuclear facilities. Figure 9 presents monthly variations of the daily mean values of ambient gamma dose rate equivalent for all six measurement points.

The obtained values of the ambient gamma dose rate equivalent in the air did not show any deviations from the mean values obtained by multi-year measurements on this site. The local maxima of ambient gamma dose rate equivalent in the air, which can be seen on the figure 9, are the result of intense precipitation with which there is a strong correlation. The characteristics of the measuring devices are such that even the slightest change of ambient gamma dose rate equivalent is registered due to washing of radioactive elements from the atmosphere during

precipitations. Figure 10 represents correlation between ambient gamma dose rate equivalent [nSv/h] and the amount of precipitation [mm].

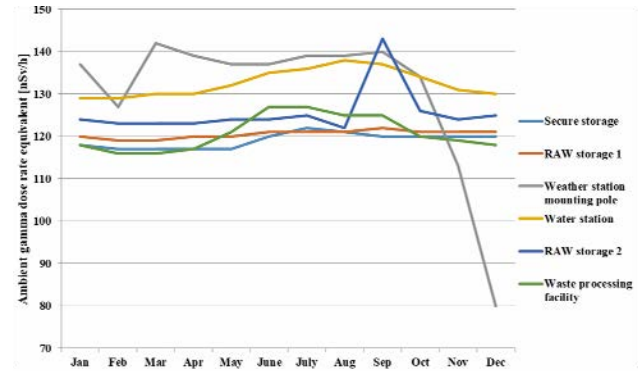


Figure 8. Monthly average ambient gamma dose rate equivalent in the air [nSv/h] for different locations for the year 2021

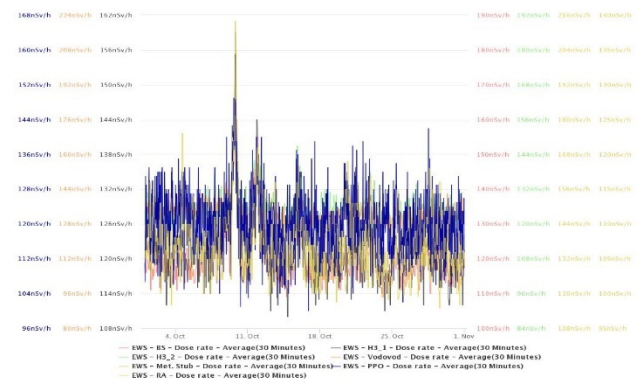


Figure 9. Monthly variation of the daily mean values of ambient gamma dose rate equivalent [nSv/h] at the PC NFS, October 2021

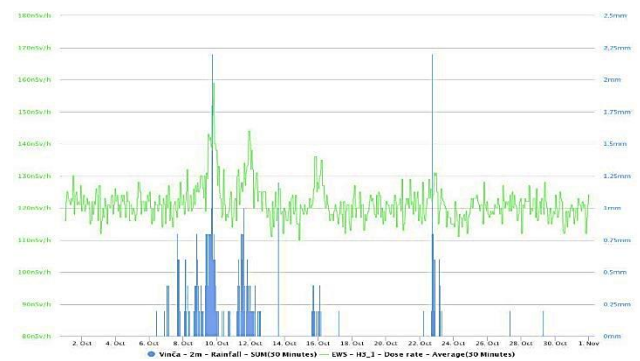


Figure 10. Correlation between ambient gamma dose rate equivalent [nSv/h] and precipitation [mm] for „Weather station mounting pole“ at PC NFS, October 2021

4. CONCLUSION

The presence of radionuclides of natural origin was detected in the samples, in activity concentration intervals that are characteristic for the investigated types of samples from the environment.

The activity concentration of artificial radionuclide ^{137}Cs is below MDA in both air and precipitation samples, for the examined period.

In precipitation samples, the activity concentration of radionuclide ^3H is below MDA, for the examined period.

The activity concentration of ^{90}Sr in air samples, for all four quarters of 2021, range from $1 \mu\text{Bq}/\text{m}^3$ to $10 \mu\text{Bq}/\text{m}^3$. The activity concentration of the produced radionuclide ^{90}Sr in precipitation is below MDA in all samples.

The values of ambient gamma dose rate equivalent in the air samples in the vicinity of nuclear facilities during 2021 are within the natural background radiation variation range. The increase of the values due to the atmospheric factors does not exceed the double value of natural background radiation (200 nSv/h).

The obtained values of activity concentration of radionuclides and ambient gamma dose rate equivalent show that the operation of nuclear facilities did not contribute to an increase in the level of exposure of the population and the radiation risk for individuals in the population is negligible. Along with this comes the fact that research nuclear reactor RA is out of operation mode for 30 years, fresh and spent nuclear fuel were repackaged and transported to the country of origin, the waste processing facility has not yet started its trial run, and both licenced RAW storage and secure storage for high activity sources are operating in safe and secure manner.

References

- [1] Law on Radiation and Nuclear Safety and Security (Official Gazette RS No. 95/18 No. 10/19).
- [2] Rulebook on Radioactivity Monitoring (Official Gazette RS No. 97/11).
- [3] Procedure on Radioactivity Monitoring QP.0565.1, Public Company „Nuclear Facilities of Serbia”, 2019.
- [4] SRPS ISO/IEC 17025:2017, General requirements for the competence of testing and calibration laboratories.
- [5] INTERNATIONAL ATOMIC ENERGY AGENCY, *Measurement of Radionuclides in Food and the Environment*, Technical Report Series No.295, IAEA, Vienna, 1989.
- [6] SRPS EN ISO 10703:2016, Water quality – Determination of the activity concentration of radionuclides – Method by high resolution gamma-ray spectrometry.
- [7] ASTM D4107–08, Standard Test Method for Tritium In Drinking Water, American Section of the International Association for Testing Materials, ASTM International, 2013.
- [8] EPA HASL 300, Radiometrology, US Environmental Protection Agency, Dept.of Homeland Security, In EML Procedures Manual, 28th Edition, Vol.I, Dept.of Energy Report, 1997.
- [9] User Manual for working with the eEMIS web application, Ames d.o.o, Ljubljana, Slovenia, 2019.
- [10] Lazarević,N., Senić,Ž. Rajić,D., Jevremović,M., Nouri,A., Jamhour,A.: *Activity of Be-7 in air in the city area Belgrade, Kumodraž*, International Scientific Conference on Defensive Technologies, 2009.
- [11] SERBIAN RADIATION AND NUCLEAR SAFETY AND SECURITY DIRECTORATE, *Report on the level of population exposure to environmental ionizing radiation in the Republic of Serbia in 2021*, Belgrade, July 2022.



DETERMINATION OF GAMMA PHOTON ATTENUATION COEFFICIENT OF LIGHTWEIGHT BUILDING AND INSULATION MATERIALS USED FOR OVERBUILDING IN SERBIA

MILAN TANIĆ

Military Academy, University of Defense, Belgrade, milantanic@yahoo.com

DENIS DINIĆ

Military Academy, University of Defense, Belgrade, denis.dinic@yahoo.com

STEVAN STUPAR

Military Technical Institute, Belgrade, stevan.stupar13@gmail.com

MIRJANA ČUJIĆ

Vinča Institute of Nuclear Sciences, University of Belgrade, Belgrade, cujicm@vin.bg.ac.rs

MARKO ANĐELKOVIĆ

CBRN Defense Centre, Kruševac, marko.andjelk@gmail.com

Abstract: Data on the protective properties of construction materials dwellings are being built of are among the most important ones to estimate consequences and risks to human health in nuclear and radiological emergencies. In this paper, building and insulation materials have been experimentally investigated in terms of mass attenuation coefficient for high-energy gamma photons of the cobalt-60 source. The lightweight autoclaved aerated concrete blocks known as Siporex blocks and stone wool slabs have been chosen for the research since they have been most commonly used for overbuilding of residential buildings in Serbian urban environments. Gamma radiation shielding capability of these materials was measured with the two different experiment designs: utilizing a gamma spectrometric system containing NaI(Tl) detector in narrow beam gamma-ray transmission geometry, and counter with pancake type Geiger-Muller probe in broad beam geometry. Linear attenuation coefficient, half-value, and tenth-value layer were also calculated. The results obtained indicated that the radiation protection properties of the materials investigated for high energy photon radiation are inferior in comparison to conventional building materials. Additionally, the data gained in this research could provide valuable information for practical shielding calculation.

Keywords: Gamma ray, radiation protection, half value layer, autoclaved aerated concrete, stone wool.

1. INTRODUCTION

Rapid urbanization and industrialization in modern days unavoidably lead to the migration of the population to urban environments. Urban environments are already densely populated and suffer from space deficiency. Overbuilding the existing residential buildings is an efficient way to overcome this lack, and consequently, cities are growing vertically, rather than outwards. Structures that are subject to overbuilding were constructed at different times, using different construction materials and applying different standards, therefore to preserve their static characteristics, lightweight construction materials accompanied by materials with good insulation properties are the first and logical choice to build dwellings over or on top of existed structures.

In comparison to conventional concretes, aerated autoclaved concrete (AAC) has many advantages such as lower density, higher strength-to-weight ratio, lower coefficient of thermal expansion as well as good acoustic

insulation. The AAC consisting of 80% air does not have coarse aggregates, and its main components are cement, sand, water, gypsum, lime, and expanding agents – Al or Zn powder. The chemical reaction of Al with $\text{Ca}(\text{OH})_2$ forms a gas that makes a porous inner structure of AAC, i.e. cementations mortar surrounding disconnected air voids and microscopic bubbles. This makes AAC a versatile lightweight material typically cast as blocks (lightweight concrete masonry units) used for exterior and interior construction [1].

If only AAC blocks were used for building, insulation standards in most European countries would require very thick walls. Therefore, an additional outer envelope of material with highly effective thermal and sound insulation and fire protection characteristics is needed. One of such materials is mineral wool.

Mineral wool is a generic term for a wide range of artificial non-metallic inorganic fibers. Stone wool (SW), known also as rock wool is a type of mineral wool produced from naturally occurring volcanic rocks

(diabase, basalt, or dolomite) and recycled of technological process waste with the addition of cement. The pulverized rock, limestone, and coke (as an energy source) are put in a cupola furnace where in the presence of oxygen, it is melted at a temperature of about 1500 °C. The most abundant chemical compounds in the composition of the raw materials are oxides of Si, Al, Ca, Mg and Fe. Fibers are created by projecting the molten mixture over a train of high-speed rotating disks. Resin binders, water repellents, and mineral oil are atomized over the fibers as they leave the discs. Formed and impregnated fibers go to a pressurized chamber where the primary SW sheet is formed. Such the sheet goes through the process known as batting creeping in order to increase the number of layers, after which a series of rollers compress the SW blanket to the desired thickness. After creeping, the oven blows air whose temperature is about 200 °C to polymerize the SW and the blanket gets its final thickness and consistency. Finally, the blanket is cut to a board of the required dimensions [2].

The construction industry is one of the fastest-growing branches of the Serbian economy. Statistical indicators showed that an increase in construction activity is quite remarkable in the most densely populated areas. For instance, the number of completed residential apartments in Vračar, the municipality of the City of Belgrade, where the population density is 19321 residents per km², increased from 9.6 completed apartments per 1000 residents in 2010 to 12.5 in 2020 [3].

Data on the protective properties of construction materials dwellings are being built of are among the most important ones to estimate consequences and risks to human health in nuclear and radiological emergencies. Those data are also needed for practical shielding calculation in sense of radiation safety. Attenuation data for commonly used building materials are available in many resources, but data on photon attenuation of previously described materials are very scarce. Therefore, the aim of this work was to experimentally determine mass attenuation coefficient and calculate linear attenuation coefficient, half and tenth-value layer for the lightweight AAC blocks known as Siporex blocks for exterior structures and SW slabs for ventilated façades most commonly used for overbuilding of residential buildings in Serbian urban environments and the most represented on the Serbian market.

2. MATERIALS AND METHODS

A collimated beam of mono-energetic gamma rays is attenuated in the matter according to the Lambert–Beer law, described by Eq. (1):

$$I_d = I_0 e^{-\mu_m d_m} \quad (1)$$

where I_d is radiation intensity after passing absorber with mass thickness d_m , and I_0 is incident intensity. I_d and I_0 are expressed as count rate I_R/s^{-1} .

Mass thickness, $d_m/kg m^{-2}$, is obtained by multiplying the linear thickness of the absorber, d_l/m , by the absorber density, $\rho/kg m^{-3}$, according to Eq. 2.

$$d_m = d_l \rho \quad (2)$$

Mass attenuation coefficient, $\mu_m/m^2 kg^{-1}$, is the most important quantity characterizing the transmission of gamma radiation, and for a given gamma-ray energy, the μ_m value does not vary with the physical state of a given absorber. The relationship between mass and linear attenuation coefficient, μ_l/m^{-1} is given by Eq. (3).

$$\mu_m = \frac{\mu_l}{\rho} \quad (3)$$

The thickness of any given material where 50 % and 90 % of the incident energy has been attenuated is known as the half-value layer ($d_{1/2}$) and tenth-value layer ($d_{1/10}$) thickness, respectively, both expressed in units of distance, and have been calculated applying Eq. (4) and (5):

$$d_{1/2} = \frac{\ln 2}{\mu_l} \quad (4)$$

$$d_{1/10} = \frac{\ln 10}{\mu_l} \quad (5)$$

Measurements were carried out using a gamma-ray source ⁶⁰Co with two lines with energies 1173.24 keV and 1332.50 keV. The activity of the source was 157 MBq. The source was enclosed in a 25 cm thick lead shield.

The geometry of AAC and SW absorber specimens was prism with the dimension of 20 × 20 × 10 cm³, and 20 × 20 × 12 cm³, respectively. The density of the AAC and SW absorbers was determined by the Archimedes method and were 0.50 g cm⁻¹ and 0.10 g cm⁻¹, respectively. AAC blocks and SW slabs were purchased from the local market by the authors based on pieces of advice they are given by construction engineers who lead overbuilding construction sites at the time when this research had been planned. The types of materials and their manufacturers are known to the authors.

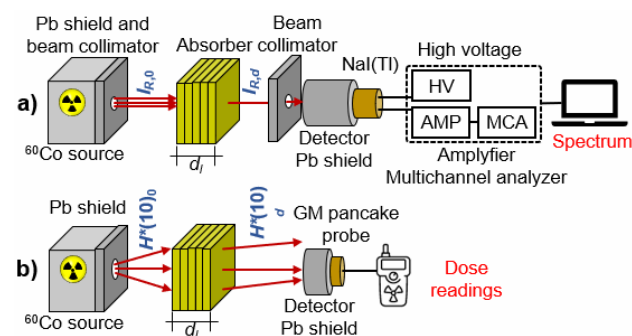


Figure 1. Experimental design for attenuation measurement: a) narrow beam geometry, b) broad beam geometry

The attenuation of gamma radiation was measured with the two different experimental setups illustrated in Figure 1. The narrow beam design depicted in Figure 1a) utilizes a well-collimated point ⁶⁰Co source collimated with the 10 cm lead panel with a 3 mm aperture placed after the source and in front of the detector. A 2" × 2"

NaI(Tl) detector system (Thermo Scientific RIIDEye M-GN) was used to measure two discreet ⁶⁰Co gamma energies for the unshielded source and 1 to 6 10 cm thick AAC layers and 1 to 8 12 cm thick SW layers. The detector's energy resolution was 7.5 % at 661.6 keV and was integrally coupled to a photomultiplier tube. The detector was shielded by lead bricks of approximately 5 cm thickness. The amplified signal from the detector is recorded by a 256-channel multichannel analyzer. Obtained spectra were processed in ScintiVision 32 software. Each measurement (spectrum acquisition) was performed three times per 3 min, and results were expressed as net count rate under photopeak at 1173.24 keV and 1332.50 keV energy. Those measurements do not account for any secondary or scattered gamma radiation.

The important feature of narrow beam geometry is that only gamma rays from the source that escape the absorber without any interaction can be counted by the detector. Real-life scenarios include more diffuse, non-collimated sources; hence it is needed to account for gamma rays emitted directly from the source as well as photons scattered in the absorber and other types of secondary photon radiation. In that sense, I_0 and I_d are more convenient to express in terms of dose rate, e.g., ambient equivalent dose rate, $H^*(10)/Sv h^{-1}$.

The broad-beam design given in Figure 1b) utilizes a non-collimated ⁶⁰Co source and dose rate meter (Thermo Scientific RadEye B20 with pancake type Geiger-Muller probe with dose equivalent filter) to measure $H^*(10)$ attenuation for AAC and SW layers. For each thickness of selected absorbers, ten measurements of 60 s were obtained. Data acquired with this arrangement accounts for attenuation of primary and any secondary radiation which passes through the AAC and SW absorbers. Those measurements are of greater importance and more indicative of many real-world applications of radiation sources and radiological and nuclear emergencies where the goal is to reduce the total dose to humans.

4. RESULTS AND DISCUSSION

4.1. Primary radiation attenuation

The dependence of the measured gamma count rate from the mass thickness of the AAC and SW absorbers at 1173.24 keV and 1332.50 keV is given in Figure 2. As expected, the count rate decreased exponentially with increased mass thickness. That decline was more notable for the AAC than for SW for the same linear thickness which is the consequence of a five times greater density of AAC material. Also, the decline in count rate was sharper at 1173.24 keV due to the slightly higher contribution of the photoelectric effect to total gamma-ray attenuation.

For both absorbers studied at both energies, fitting of experimentally obtained results with the exponential function given by Eq. (1) was satisfactory with the coefficient of determination R^2 greater than 0.999.

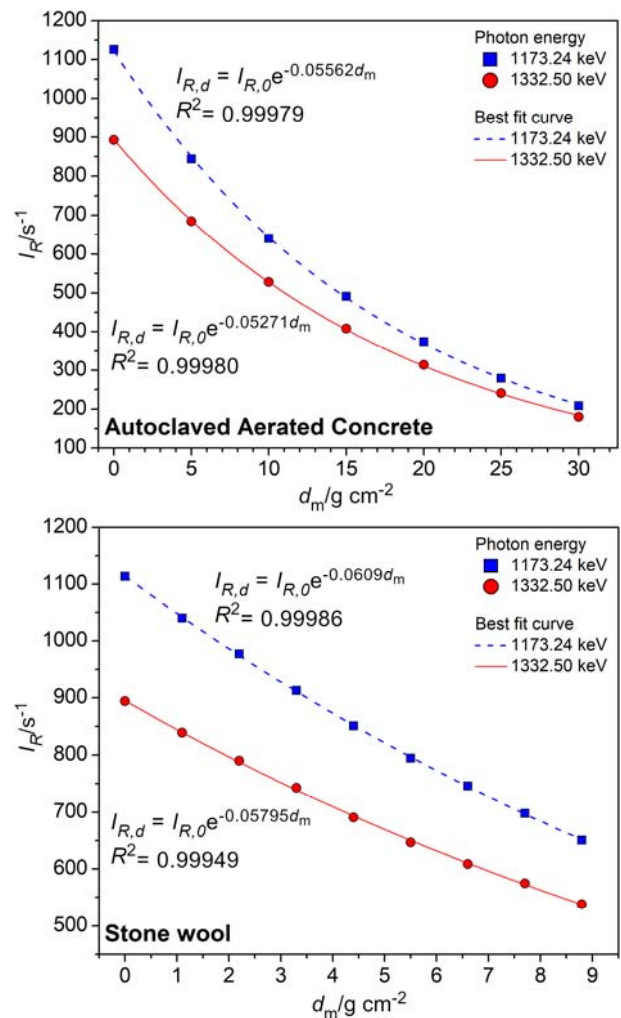


Figure 2. Count rate (I_R) as a function of the mass thickness (d_m) of the investigated absorbers at two ⁶⁰Co gamma energies

The experimental values of photon attenuation indices studied in this research for investigated building materials at two ⁶⁰Co energies are presented in Table 1.

Table 1. Gamma photon attenuation properties for absorbers of interest at two energies of ⁶⁰Co gamma rays

Energy	$10^{-2} \mu_m / cm^{-2} g$	$10^{-2} \mu_l / cm^{-1}$	$d_{1/2} / cm$	$d_{1/10} / cm$
Aerated autoclaved concrete				
1173.24	5.56 ± 0.04	2.78 ± 0.02	24.92 ± 0.16	82.8 ± 0.5
1332.50	5.27 ± 0.03	2.64 ± 0.02	26.30 ± 0.16	87.4 ± 0.5
Stone wool				
1173.24	6.09 ± 0.03	0.609 ± 0.003	113.8 ± 0.5	378.1 ± 1.6
1332.50	5.80 ± 0.05	0.580 ± 0.002	119.6 ± 0.9	397 ± 23

The most important mechanisms of interaction between gamma radiation and matter are photoelectric absorption, Compton scattering and pair production. Generally, at high energies, like energies of 1173.24 keV and 1332.50 keV, the Compton scattering mechanism, and pair production phenomena are dominant. In this case, this prevalence is a consequence not only of exposition to high-energy gamma-rays, but also of the low atomic

number of elements that are the most abundant in the AAC and SW materials (Si, Al, Ca, Mg, Zn, and Fe).

Gamma attenuation coefficients are inversely dependent on gamma energy and directly proportional to the atomic number of the elements shielding material are made of. For both materials, mass and linear attenuation coefficients were lower at 1332.50 keV. Despite cross-section for Compton scattering being approximately equal for two energies, the photoelectric absorption is a slightly more dominant way of interaction between gamma rays and atoms of the interacting materials at 1173.24 keV leading to somewhat greater absorption at that energy.

The lower the half and tenth-value layer values, the better the radiation shielding materials are in terms of the linear thickness requirements. Values of $d_{1/2}$ for AAC at 1173.24 keV and 1332.50 keV were 24.92 cm and 26.30 cm, respectively, while for the SW these values were about 4.5 times higher (113.8 cm and 119.6 cm).

Materials used widely in the construction industry such as concrete with different densities, bricks, pumice, and lightweight concrete blocks, have also been characterized in terms of shielding properties against photon radiation in numerous research. To put our results in perspective, the results obtained for half and tenth-value determined in this work have been compared to corresponding values for commonly used building materials that were determined in a similar experimental set-up applied in this research.

Table 2. Half and tenth-value layer thickness values for standard building materials

Material; $\rho/\text{g cm}^{-3}$	1173.24 keV		1332.50 keV		Ref.
	$d_{1/2}/\text{cm}$	$d_{1/10}/\text{cm}$	$d_{1/2}/\text{cm}$	$d_{1/10}/\text{cm}$	
Gas concrete (AAC); 0.40	31.4	104.2	32.2	107.1	[7]
Pumice; 0.85	14.7	49.0	15.8	52.3	
Brick; 1.50	14.7	29.1	15.7	27.1	
Concrete; 2.25	5.2	17.3	5.5	18.3	
Concrete; 0.6–1.5	6.86	22.79	7.70	25.58	[8]
Concrete; 1.4–2.0	6.03	20.02	6.36	21.12	
Concrete; 2.0–2.5	3.98	13.23	4.20	13.95	
Concrete; 2.5–3.0	3.96	13.15	4.15	13.78	
Concrete; 3.0–4.0	3.85	12.79	4.08	13.54	

By comparison with the data presented in Table 2. it can be noticed that for AAC and SW material investigated in this work, the $d_{1/2}$ and $d_{1/10}$ values were less than those of commonly used concrete of different densities, standard bricks, and pumice blocks. Published results for $d_{1/2}$ and $d_{1/10}$ of gas concrete (equivalent to AAC), but of lower density than AAC material of interest for this work, were 26 % and 23 % higher at 1173.24 keV and 1332.50 keV respectively, than the values determined here. Therefore, for a shielding effectiveness achieved with standard building materials, a larger thickness of the AAC blocks and SW slabs would be required.

4.2. Dose attenuation

The mass attenuation coefficient is independent of the density of the target material and depends on the

elemental composition of the material and photon energy [4]. Therefore, values of μ_m for a given photon energy are very similar, pointing out that equal masses of different materials should have nearly identical attenuation properties [5]. Nevertheless, the ratio of photoelectric absorption and Compton scattering varies in a different matter, therefore it is important to make difference between the attenuation of primary radiation (achieved in narrow beam geometry) and dose attenuation. The latter one involves the contribution of scattered photons and secondary radiation emitted at different angles and with various energies.

Scattered and secondary gamma radiation in some extent complicate the absorption law described by Eq. (1). The gamma photon attenuation coefficient calculated or experimentally determined for narrow (sometimes called “good” geometry) ignores the energy of secondary gamma radiation deposited in the detector. From the radiation protection point of view, it results in underestimation of shield thicknesses need to reduce dose to the desired level, especially for higher energy gamma radiation and lower atomic weight elements. In opposite to the well collimated beam, described situation is well characterized by broad beam or “bad” geometry.

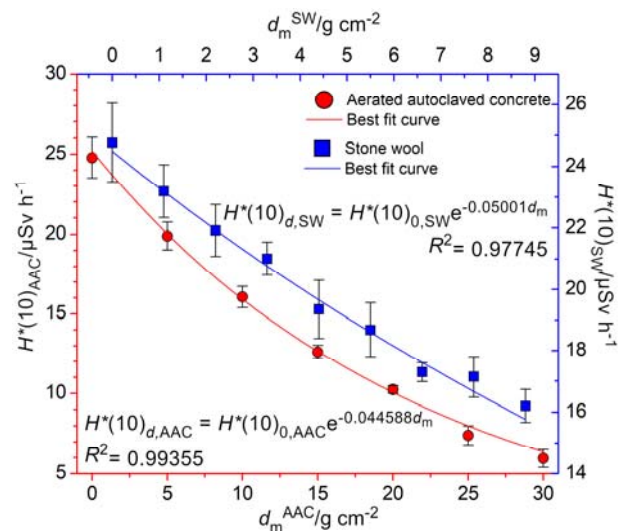


Figure 3. Ambient equivalent dose rate, $H^*(10)$, dependence on the mass thickness (d_m) of the investigated absorbers exposed to ^{60}Co gamma radiation

Figure 3. shows measured values of $H^*(10)$ as a function of different mass thickness of the absorbers of interest exposed to broad beam ^{60}Co gamma radiation along with exponential fitted function, while experimentally determined values of attenuation coefficient and half and tenth value layer thickness are listed in Table 3.

Table 3. Dose attenuation coefficients for absorbers of interest for ^{60}Co gamma rays

Absorber	$\mu_m/10^{-2} \text{ cm}^{-2} \text{ g}$	$\mu_l/10^{-2} \text{ cm}^{-1}$	$d_{1/2}/\text{cm}$	$d_{1/10}/\text{cm}$
AAR	4.59 ± 0.14	2.29 ± 0.07	30.2 ± 0.9	100 ± 3
Stone wool	5.00 ± 0.26	0.50 ± 0.03	139 ± 7	460 ± 23

As it is stated in the literature, the difference in

attenuation of primary radiation and dose attenuation is usually less than 10 to 15 % for high atomic number materials (Pb, Bi, etc.) and 30 to 40% for materials with a high abundance of elements with lower atomic number (e.g., Al, Fe). This is in consonance with the relative importance of the interactions based on photoelectric effect and Compton scattering in these different materials [6].

Experimentally determined values of mass and linear attenuation coefficient for dose reduction in this work were 15 % and 16 % lower than their values for primary radiation attenuation by AAC and SW, respectively, resulting in 18 % for AAC and 19 % for SW absorbers higher $d_{1/2}$ and $d_{1/10}$ values, respectively.

5. CONCLUSION

The gamma-ray shielding parameters such as half and tenth-value layer thickness, and linear and mass attenuation coefficients were experimentally determined for AAC and SW, two widely used lightweight building materials in Serbia, to define their effectiveness as gamma-ray shielding. The results gained in this study indicated that the shielding properties of the investigated materials against high-energy gamma radiation are inferior in comparison to conventional building materials. Most probably, in the case of nuclear or radiological emergencies involving photon radiation with energies greater than 1 MeV, AAC and SW materials would not provide adequate protection. Nevertheless, the data on their photon attenuation properties gained in this research could be used for practical shielding calculations necessary for establishing radiation safety program for authorized practices and sources within practices in premises already made with this type of materials.

References

- [1] KALPANA,M., MOHITH,S.: *Study on autoclaved aerated concrete: Review*, Materials Today: Proceedings, 22(3) (2020) 894-96.
- [2] GALLYER,F.,T.: *Insulation*, Plant Engineer's Handbook, Butterworth-Heinemann, Woburn, 2001.
- [3] GAVRILOVIĆ,D. (Ed.): *Municipalities and regions of the Republic of Serbia, 2021*, Statistical Office of the Republic of Serbia, Belgrade, 2021. (In Serbian)
- [4] KNOLL,G.,F.: *Radiation Detection and Measurement, 4th Edition*, John Wiley and Sons. Inc., New York, 2010.
- [5] HUBBEL,J.,H., SELTZER,S.,M.: *Tables of X-Ray Mass Attenuation Coefficients and Mass Energy-Absorption Coefficients (version 1.4)*. [Online] Available: <http://physics.nist.gov/xaamdi> [2022, June 30], National Institute of Standards and Technology, Gaithersburg, 2004.
- [6] McALISTER,D.,R.: *Gamma Ray Attenuation Properties of Common Shielding Materials*, PG Research Foundation, Inc., University Lane Lisle, 2018.
- [7] DOGAN,B., ALTINSOY,N.: *Investigation of photon attenuation coefficient of some building materials used in Turkey*, AIP Conference Proceedings, 1653 (2015) 020033.
- [8] AKKAS,A.: *Determination of the Tenth and Half Value Layer Thickness of Concretes with Different Densities*, Acta Physica Polonica A, 129(4) (2016) 770-72.



MANUFACTURING OF FIBER –REINFORCED POLYMER COMPOSITE THERMAL INSULATION BY VACUUM TECHNIQUE

MARICA BOGOSAVLJEVIĆ

Military Technical Institute, Belgrade, marica.radusinovic@gmail.com

JELENA GRŽETIĆ

Military Technical Institute, Belgrade, jrusmirovic@tmf.bg.ac.rs

SLAVKO MIJATOV

Military Technical Institute, Belgrade, slavko.mijatov@yahoo.com

SAŠA BRZIĆ

Military Technical Institute, Belgrade, sasabrzic@gmail.com

TIHOMIR KOVAČEVIĆ

Military Technical Institute, Belgrade, tkovacevic@tmf.bg.ac.rs

Abstract: *This study aimed to investigate the potential of application of vacuum technique for manufacturing of fiber-reinforced polymer composites used in military purpose as thermal insulation materials for solid rocket motor chamber. Vacuum technique without infusion of resin was utilized to produce different shapes of specimens. Such applied technique successfully resulted in obtaining rectangular plates for mechanical characterization and ablation test, as well as cylindrical motor chambers for inner ballistic examinations. Thermal insulation material was based on unsaturated polyester resin Dion FR 7721-00 which contained alumina tri-hydrate as fire-retardant. Carbon and glass fabrics were used as reinforcements. Rheological properties of the prepared composite were determined using dynamic-mechanical analysis, while the thermal properties were studied by ablation test. Obtained results indicated that vacuum technology was applicable and suitable for manufacturing of fiber-reinforced polymer composites. Developed materials show improved mechanical and thermal properties and could be used as thermal insulation/inhibitor of composite rocket propellant grains.*

Keywords: *Vacuum technique, carbon fabric, glass fabric, polyester resin*

1. INTRODUCTION

The thermal stability of a material is usually expressed in terms of ability to withstand specified conditions and still retain the physical properties required of the material in the given application. Determination of the structure of such materials for thermal protection plays an essential role in the designing of construction elements for rocket motors.

Polymeric ablation materials (PAMs) represent one of the most important parts of thermal protection system used in solid rocket motors (SRMs) [1]. In the most cases, PAMs should have a low density and thermal conductivity to achieve excellent thermal insulation, since SRMs generate significant amount of heat during their operation. PAMs should have good adhesion to propellant [2], and to protect the structural integrity of the SRMs during long-term storage and firing. During exposure of the propellant grain to extreme temperature and pressure, the PAMs decompose generating a protective char layer which has low thermal conductivity and high mechanical strength. Mechanical integrity gives the char layer resistance to the heat diffusion through it and to physico-chemical erosion caused by combustion gases [3].

Ablation materials, which are investigated in this study, are type of, fiber-reinforced polymer composites. There are various methods for producing selected type of composites, such as filament winding technique, blending, casting and vacuum techniques. Although the filament winding technique is commonly used for obtaining fiber reinforced composite materials used in rocket and aerospace industries [4], vacuum technique with (Figure 1) or without infusion of resin, shows its benefits related to the best fiber to volume ratio, ability to create light-weight materials with great mechanical strength.

Considering resin selection for the specified application, polyester, phenolic, vinyl ester, and epoxy resin proved to be the best choice for preparation of the PAMs [5]. Beside the listed, the unsaturated polyester (UPE) resins provide high protection in terms of severe conditions, such internal pressure, extreme temperature and corrosion [6], [7]. Consequently, UPE resins are widely used for impregnation of appropriate fiber reinforcements into multilayer structure of ablative material. Moreover, UPE resins are compatible with the commonly used reinforcement fibers (e.g. carbon, glass). Epoxy and UPE resins possess an appropriate temperature range

considering the processing conditions, which is crucial for its application in vacuum technique [4], [8].

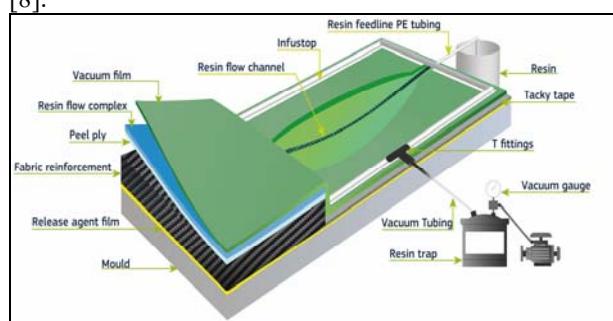


Figure 1. Schematic illustration of vacuum infusion process (reused from <http://sicomin.com/products/vacuum-and-infusion/infusion>)

Further, various ablative additives, such as fibers [9-12] and inorganic fillers [13-15], could be added to PAMs to improve mechanical properties and to reduce the oxidation rate of the char layer. It is considered that the usage of fibers transforms the polymeric matrix into conductive network, which facilitate the formation of numerous hot spots and accelerate heat diffusion [16-19].

Each component contributes in reaching desired properties in its own way. Therefore, the multilayer structure is preferable to achieve balanced ablation and thermal protective performances of PAMs. So far, the vacuum technique is proved and abundantly applied in manufacturing of insulations for various industrial applications, *e.g.* for hot water storages (thanks, boilers, heat pumps), industrial installations (heat shields, enclosures for valves, tanks), piping (district heating, process heating and cooling), laboratory devices (freezers, incubators, chromatographs, climatic chambers), ovens and dryers.

The main goal of this study was to estimate potential of application the vacuum technique for manufacturing thermal insulation materials for the rocket motor chambers. For that purpose, the self-extinguished UPe resin, which contained alumina tri-hydrate as fire-retardant, reinforced with carbon and glass fabrics was employed.

2. EXPERIMENTAL

2.1. Materials

Developed composites was based on self-extinguished UPe (Dion FR 7721-00, Reichhold, USA) mixed with initiator methyl ethyl ketone peroxide in toluene (MEKP, Sigma Aldrich, Germany) and carbon fabric (style 450-5 Aero, 200 g/cm², plain weave (Engineered Cramer Composites, Germany) and glass fabric (Interglas 05507, 200 g/cm², plain weave (Engineered Cramer Composites, Germany) as reinforcement.

2.2. Preparation of fiber-reinforced polymer composite

For the dynamic-mechanical and thermal properties

determination, the rectangular plate of 250x270 mm dimension was manufactured following the procedure: UPe was applied manually, by brush, over the carbon and glass fabric (in ratio 30 % resin to 70 % of reinforcement) The layers of fabrics were also arranged in two cycles – two layers of carbon, then two layers of glass fabric, and after repeating it twice, 5 layers of glass fabric were added on top of it. Vacuum was applied and enabled curing at room temperature without cavities in material. At the end of the process, extra resin was mechanically removed using lathe, thereby the fibers remained undestructed so this treatment did not affected mechanical characteristics of matherial. The final thickness of plate (determined with dimension of molde) was 5 mm (Figure 2).

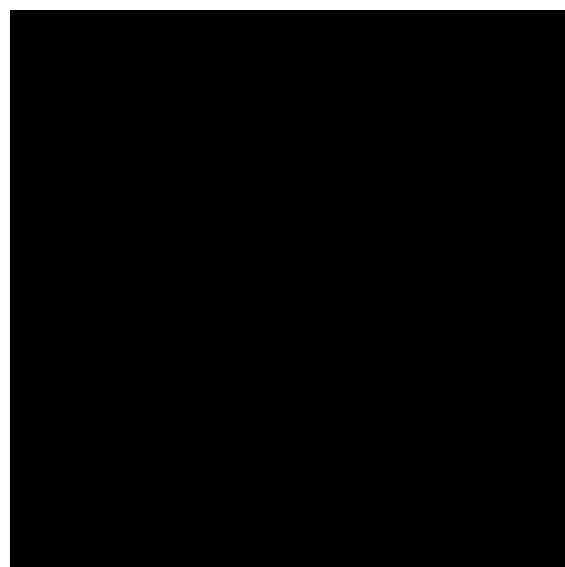


Figure 2. PAM in a shape of rectangular plate

In addition, to prove the potential of the vacuum technique for producing of cylindrical rocket chambers, a 2-inches motor, for inner ballistic characterization of rocket propellants, was manufactured. The 2-inches motor was also manufactured as a rectangular plate applying the UPe resin by brush on mandrel, over layers of carbon and glass reinforcements in the same ratio (70 to 30 % fibres to resin). When all set, vacuum was applied and left to cure at room temperature, constantly under vacuum conditions. Final external diameter was obtained applying mechanical processing (Figure 3). Furthermore, this technique is used for inhibiting double-base propellant grains (DBPG). Employed technique provided successfully coating of cylindrical specimens of DBPG, with and without calotte, which is great technological challenge for conventional techniques (Figure 3 (b)). In addition, satisfied bonding between propellant and composite inhibitor was achieved.

2.3. Characterization methods

Structural characterization of the cured composite was performed using Fourier transforms infrared spectroscopy (FTIR). FTIR spectra were recorded in absorbance mode using a Nicolet™ iS™ 10 FT-IR Spectrometer (Thermo Fisher SCIENTIFIC) with Smart iTR™ Attenuated Total Reflectance (ATR) Sampling accessories, within a range

of 400–4000 cm^{-1} , at a resolution of 4 cm^{-1} and in 20 scan mode.

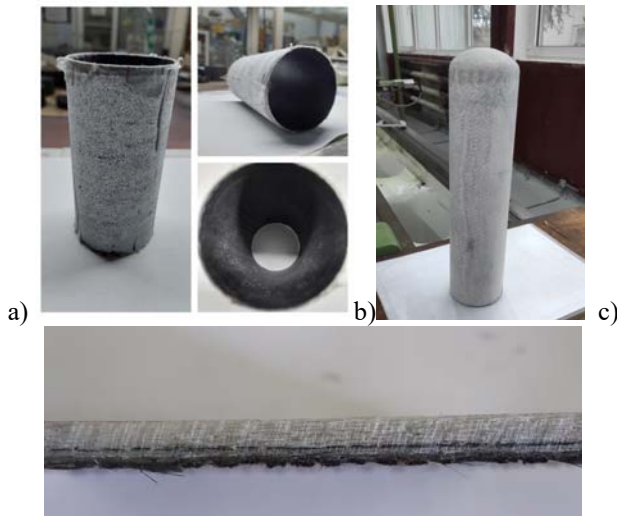


Figure 3. PAM in shape of cylindrical chamber for inner ballistic characterization (a), coated specimen with calotte (b), and cross section of the cured carbon/glass multi-layered composite (c)

Dynamic mechanical analysis (DMA) study of the cured composite samples was performed in torsion deformation mode using the Modular Compact Rheometer MCR–302 (Anton Paar GmbH) equipped with standard fixtures (SRF12) for rectangular bars, temperature chamber (CTD–620) having high temperature stability (± 0.1 $^{\circ}\text{C}$). The standard sample of a rectangular bar shape ($44 \times 10 \times 4$ mm) was tested by using "temperature ramp test" in temperature range from 40 $^{\circ}\text{C}$ to 170 $^{\circ}\text{C}$, the heating rate was 5 $^{\circ}\text{C} \cdot \text{min}^{-1}$, and the single angular frequency of 1 Hz, and strain amplitude was 0.1%.

The thermal properties of produced PAM plate based on the cured DION® FR 7721-00 resin as matrix were studied by a modified Oxyacetylene Ablation Testing of Thermal Insulation Materials [20] using an Extech High-Temperature infrared thermometer and an oxyacetylene flame. Samples of standard dimension ($100 \times 100 \times 6$ mm) were used (Figure 4).



Figure 4. Specimen for modified oxyacetylene torch test

3. RESULTS AND DISCUSSION

3.1. Structural characterization

FTIR spectra of uncured neat UPe resin and cured composite, CF and GF are presented in Figure 5.

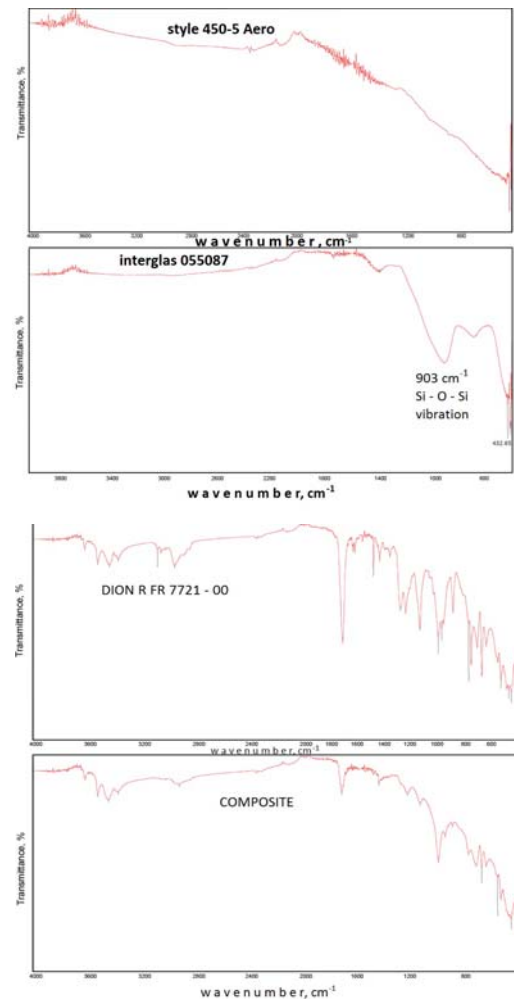


Figure 5. FTIR spectrum of the cured composite UPe_CGF, uncured UPe, carbon fabric (CF) and glass fabric (GF)

The peaks observed in the FTIR spectra of UPe and composite around 3616, 3525, 3444, and 3375 cm^{-1} and the low intensity peak at 697 cm^{-1} originate from hydroxyl (OH) and Al-OH groups stretching vibrations. Symmetric and asymmetric vibrations of CH_3 and CH_2 groups are observed around 3050, 2825, and 2840 cm^{-1} , while their bending vibrations are remarked at about 1454 cm^{-1} [21]. The intensity of these peaks is significantly reduced in FTIR spectrum of cured composite. The band at 1728 cm^{-1} in the FTIR spectrum of the composite originates from carbonyl C=O (ester) group present in the polyester resin [21]. This peak is shifted to a higher wavenumber compared to the neat UPe (1720 cm^{-1}) indicating interactions between UPe and carbon and glass fibers. The peak at 1490 cm^{-1} in UPe originates from the stretching vibration of the C=C and disappears after curing. Si-O-Si vibrations are observed as a broad peak at 903 cm^{-1} .

3.2. Dynamic mechanical analysis (DMA)

DMA is a standard technique abundantly used to examine viscoelastic properties of polymer materials in a wide temperature range. The temperature dependences of storage modulus (G'), loss modulus (G''), and loss factor ($\tan\delta$) of developed composite is shown in Figure 8. G' reflects elastic, while G'' reflects viscous behavior of polymer matrix. In addition, Table 1 shows comparison of some characteristics of analyzed sample, neat UPe resin and composite: storage modulus in glassy state and rubbery plateau (G'_{GS} and G'_{RP} , respectively), glass transition temperature (T_g) and $\tan\delta$ peak height.

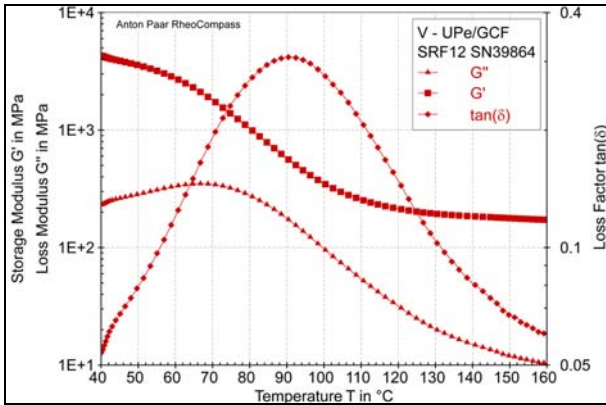


Figure 6. Temperature dependence of storage modulus (G') and loss modulus (G'') of cured UPe CG/FG composite

Table 1. DMA results of UPe and corresponding reinforced composites obtained by different techniques

Sample	G'_{GS} , MPa	G'_{RP} , MPa	T_g , °C	$\tan\delta$ peak height
UPe	1698	28.2	110.1	0.43
COMPOSITE	3260	190.2	91.0	0.32

It can be noted that PAM specimen shows higher values of the G' in glassy state compared to the neat UPe resin. Such a phenomenon is associated to the strength of fiber/matrix interactions and the way the polymer chains are packed. The temperature increase causes a decrease in G' for all samples, which is the consequence of greater movement of the polymer segments. The glass transition temperature (T_g) is determined from $\tan\delta$ peak position (Figure 6) and it reaches a value of 110.1 °C for UPe resin, and 91.0 °C for composite. The decrease in T_g for composite occurs due to the rigidity of the woven glass and carbon fibers.

3.3. Thermal properties

The thermal properties of developed composite are essential for its use as PAM, namely as thermal insulations in rocket motors. That is why modified ablation test is conducted and it is shown that composite sample has significantly greater thermal stability than the UPe resin. It is remarked that ignition temperature for neat UPe resin is 320 °C, while composite stayed stable even at the higher temperatures. Such phenomenon reflects the contribution of reinforcement to thermal

stability of the final material. The carbon and glass fibers transform the UPe matrix into conductive network, which facilitate the formation of numerous hot spots and accelerate heat diffusion. Contrary to this, fibers endothermically absorb heat and give mechanical strength to the charred/carbonaceous material.



Figure 7. Samples of cured composite after ablation test

4. CONCLUSION

The presented study investigates the potential of vacuum technique for manufacturing of fiber-reinforced polymer composites used in military purpose as thermal insulation materials for composite rocket propellants. Self-extinguish UPe resin, reinforced with carbon and glass fibers, prove themselves as adequate materials for processing by this technique. As results, different shapes of specimens, such as cylindrical motor chamber and rectangular plate, were obtained and used for characterization of composite. The vacuum technique is suitable for intended purpose, due to ease of use and economical and environment benefits since there is no waste generation.

The thermal properties of the prepared PAM were determined by modified ablation test, while viscoelastic properties were studied by dynamic-mechanical analysis. Ablative test indicates that vacuum technique is competitive with other similar techniques used for PAM preparation. Obtained material has significantly greater thermal stability than the UPe resin.

ACKNOWLEDGEMENT

The authors are grateful to the Ministry of Education, Science and Technological Development of the Republic of Serbia for the financial support provided, as part of the project: Contract No. 451-03-68/2022-14/200325.

References

- [1] Ji, Y.; Han, S.; Chen, Z.; Wu, H.; Guo, S. Understanding the role of carbon fiber skeletons in silicone rubber-based ablative composites. *Polymers* 2022, 14, 268.
- [2] George, K.; Panda, B.P.; Mohanty, S.; Sanjay, K.N. Recent developments in elastomeric heat shielding materials for solid rocket motor casing application for future perspective. *Polym. Adv. Technol.* 2019, 29, 8–21.
- [3] Ji, Y.; Han, S.; Xia, L.; Li, C.; Wu, H.; Guo, S. Synergetic effect of aramid fiber and carbon fiber to enhance ablative resistance of EPDM-based

- insulators via constructing high-strength char layer. *Compos. Sci. Technol.* 2021, 201, 108494.
- [4] J. Bassler, "Colorado State University Rocket team builds newly designed rocket fuselage with filament winding equipment provided by Prodigm, Lattice Composites resins, and Composites One carbon fibers," *Reinf. Plast.*, vol. 64, no. 2, pp. 92–96, 2020, doi: 10.1016/j.repl.2019.07.003.
- [5] M. Natali, J. M. Kenny, and L. Torre, "Science and technology of polymeric ablative materials for thermal protection systems and propulsion devices: A review," *Prog. Mater. Sci.*, vol. 84, pp. 192–275, Dec. 2016, doi: 10.1016/j.pmatsci.2016.08.003.
- [6] J. H. S. Almeida, M. L. Ribeiro, V. Tita, and S. C. Amico, "Damage modeling for carbon fiber/epoxy filament wound composite tubes under radial compression," *Compos. Struct.*, vol. 160, pp. 204–210, 2017, doi: 10.1016/j.compstruct.2016.10.036.
- [7] J. Bassler, "Colorado State University Rocket team builds newly designed rocket fuselage with filament winding equipment provided by Prodigm, Lattice Composites resins, and Composites One carbon fibers," *Reinf. Plast.*, vol. 64, no. 2, pp. 92–96, 2020, doi: 10.1016/j.repl.2019.07.003.
- [8] H. Boussetta, M. Beyaoui, A. Laksimi, L. Walha, and M. Haddar, "Study of the filament wound glass/polyester composite damage behavior by acoustic emission data unsupervised learning," *Appl. Acoust.*, vol. 127, pp. 175–183, 2017, doi: 10.1016/j.apacoust.2017.06.004.
- [9] Sun, H.; Yang, Y.; Ge, X. Effect of various fibers on the ablation resistance of poly(diaryloxyphosphazene) elastomer. *J. Appl. Polym. Sci.* 2020, 137, 48534.
- [10] Gao, G.; Zhang, Z.; Li, X.; Meng, Q.; Zheng, Y. An excellent ablative composite based on PBO reinforced EPDM. *Polym. Bull.* 2010, 4, 607–622.
- [11] Asghar, M.; Iqbal, N.; Iqbal, S.S.; Farooq, M.; Jamil, T. Ablation and thermo-mechanical tailoring of EPDM rubber using carbon fibers. *J. Polym. Eng.* 2016, 36, 713–722.
- [12] El-Dakhkhny, A.M.; Ahmed, A.F.; Rutkevicius, M.; El-Marsafy, S.; Abadeer, E. Effects of aramid fibers and colloidal particle fillers in composite ethylene propylene diene monomer rubber thermal insulators for rocket motor insulation. *J. Compos. Mater.* 2018, 52, 1989–1995.
- [13] Torre, L.; Kenny, J.M.; Boghetich, G.; Maffezzoli, A. Degradation behaviour of a composite material for thermal protection systems. Part III e char characterization. *J. Mater. Sci.* 2000, 35, 4563–4566.
- [14] Farajpour, T.; Bayat, Y.; Abdollahi, M.; Keshavarz, M.H. Effect of borax on the thermal and mechanical properties of ethylenepropylene-diene terpolymer rubber-based heat insulator. *J. Appl. Polym. Sci.* 2015, 132, 41936.
- [15] Dan, Z.; Zhang, C.; Hu, H.; Zhang, Y. Ablation behavior and mechanism of 3D C/ZrC composite in oxyacetylene torch environment. *Compos. Sci. Technol.* 2011, 71, 1392–1396.
- [16] Jaramillo, M.; Koo, J.H.; Natali, M. Compressive char strength of thermoplastic polyurethane elastomer nanocomposites. *Polym. Adv. Technol.* 2014, 25, 742–751.
- [17] Natali, M.; Koo, J.H.; Allcorn, E.; Ezekoye, O.A. An in-situ ablation recession rate sensor for carbon/carbon ablatives based on commercial ultra-miniature thermocouples. *Sens. Actuators B Chem.* 2014, 196, 46–56.
- [18] Ren, J.; Qin, Y.; Peng, Z.; Li, Z. Influence of composite structure design on the ablation performance of ethylene propylene diene monomer composites. *e-Polymers* 2021, 21, 151–159.
- [19] Liwei, Y.; Hao, Z.; Shengtai, Z.; Huawei, Z.; Yang, C.; Mei, L. Improving ablation properties of liquid silicone rubber composites by in situ construction of rich-porous char layer. *J. Appl. Polym. Sci.* 2021, 138, 50030.
- [20] [ASTM International, "Oxyacetylene Ablation Testing of Thermal Insulation Materials."
- [21] A. Drah et al., "Effect of surface activation of alumina particles on the performances of thermosetting-based composite materials," *J. Compos. Mater.*, p. 002199831983913, Mar. 2019, doi: 10.1177/0021998319839133.



DEVELOPMENT OF POLYMER COMPOSITE LINER AS INSULATION MATERIAL: RHEOLOGICAL, MECHANICAL AND THERMAL PROPERTIES

SLAVKO MIJATOV

Military Technical Institute, Belgrade, Serbia, slavko.mijatov@yahoo.com

SAŠA BRZIĆ

Military Technical Institute, Belgrade, Serbia, sasabrzic@gmail.com

TIHOMIR KOVAČEVIĆ

Military Technical Institute, Belgrade, Serbia, tkovacevic@tmf.bg.ac.rs

MARICA BOGOSAVLJEVIĆ

Military Technical Institute, Belgrade, Serbia, maricaradusinovic@gmail.com

JELENA GRŽETIĆ

Military Technical Institute, Belgrade, Serbia, jrusmirovic@tmf.bg.ac.rs

MLADEN TIMOTIJEVIĆ

Military Academy, Belgrade, Serbia, mladen.timotijevic@gmail.com

Abstract: The purpose of this study was to develop and analyze new composite material as a liner insulation material for rocket propulsion charges, hydroxyl-terminated polybutadiene (HTPB) based and reinforced with carbon fibers (CFs) and inorganic filler powders (IFPs). Novel material is an elastomeric adhesive, improving mechanical properties between the insulation/rocket motor chamber and the propellant and preventing heat penetration. Liner formulations were made for each material with a range of weight loadings of CFs and IFPs, and with different NCO/OH ratios of 0.85–1.5. Also, processability was observed by monitoring the change in viscosity during and immediately after mixing, depending on the composition and mixing parameters. Material rheological and mechanical characterization additionally contributed to the selection of a composition suitable for application to various geometric profiles. In order to offer more trustworthy information about the viscoelastic behavior of the liners, a dynamic-mechanical analysis (DMA) was performed and rheological measurements of uncured and cured materials were obtained. Small scale ablation testing was performed using an oxy-acetylene test as a significant factor in the material verification. The ablation results demonstrated that the prepared insulation materials could deliver good thermal ablative and insulative properties, also decrease in erosion rate. Therefore, developed polymer composite liners (PCL) could be an excellent heat-insulation and thermal-protection materials with applications in the field of rocket propulsion.

Keywords: HTPB, carbon fibers, liner, processability, ablation.

1. INTRODUCTION

The composite rocket propellant (CRP) is composed from elastomeric binder, plasticizer, bonding agents, ballistic modifiers and solids, metallic fuel and oxidizer. When ignited, CRP burns giving designed combustion profile, with the required thrust to launch rockets, missiles, and bullets. The elastomeric matrix with its carbon and hydrogen organic rich part binds the solids together and allows for the shaping and maintenance of the integrity of the propellant [1]. A combustion process of propellant is a complex process through which the system is subjected to highly severe conditions of temperature and pressure. A rocket motor is designed for enduring extreme conditions of temperature, pressure and turbulence during propellant combustion, so there is a need for some thermal insulation material between motor case and propellant, either for case bonded or cartridge loaded grains.

Case bonded systems use a thermal insulation lined inside the rocket motor, which protects motor case from high temperature during combustion of propellant. Contrary, cartridge loaded systems use inhibiting materials or inhibitors for case protection and maintaining the designed combustion profile. This helps to achieve the desirable pressure-time profile for a specific application and requirements. So, the performance of the propellant grain depends not only on the propellant but to an inhibition or insulation system [2].

Solid-propellant rocket motors consist of a motor case, igniter, propellant, nozzle, liner and/or insulator. Liner for solid propellants is an elastomeric adhesive, which amortizes difference in coefficient of linear thermal dilatation between steel or composite motor case and elastomeric propellant. In that way, the liner absorbs generated stress during prolonged storage and exploitation, providing good mechanical integrity of the

propellant. During combustion process the temperature can reach above 2.000 °C, pressure can exceed 10 MPa the velocity of the combustion gases can reach or exceed 0.2 Mach. These extreme conditions lead to eroding thermal insulation, which further can cause a failure of the rocket motor [3]. The selection of material for thermal insulation and liner is crucial to the design of the propellant grain.

Some of the requirements for solid rocket motor insulation are [4]:

- Low density (from 1.05 to 1.5 g cm⁻³);
- Sufficient tensile strength (0.5 MPa);
- Excellent bonding of the insulation material with propellant and motor case over the entire range of the working temperature;
- Low erosion rate (from 0.09 to 0.20 mm s⁻¹);
- Very low outer case temperature (<150 °C) over the entire range of working temperature;
- Low thermal conductivity (from 0.2 to 0.5 W m⁻¹K⁻¹);
- High specific heat (from 1000 to 2100 J kg⁻¹ K⁻¹); and
- Ability to resist mechanical and thermal stresses during storage, handling and curing operations.

Various inhibitor, insulation and liner compositions are developed with different polymers like epoxy, polyurethane, siloxanes and butadienes with incorporation of different fillers like silica, antimony trioxide, kaolin etc. for various applications [5], [6]. Out of these, a butadiene and Sb₂O₃ based composition is selected with the aim to enhance the integrated performance of elastomeric insulation material. These materials stand out on enhanced mechanical strength, thermal stability and barrier properties with ablation resistance [7]. For elastomers filled with carbon black, the ablation resistance is inadequate to withstand the high stresses and erosion rates resulting from the combustion gases [4]. Zirconium dioxide, a type of mineral oxide, has been tested as a filler for thermal insulation materials and it was found that it ensures the formation of a looser carbon–mineral coke structure in polyurethane materials during the ablation tests [5].

Commonly used insulators consist of either phenolic or some type of rubber and carbon black, asbestos, carbon fibers or aramid (Kevlar[®]) fibers as reinforcements [4]. It is desirable that liner and propellant have similar polymer basis to provide good compatibility *i.e.* adhesion between them. Appropriate modifiers or fillers form a protective layer *in-situ* at elevated temperatures to withstanding very high temperatures.

In this paper these characteristics were taken into account during the selection of three formulations based on polybutadiene resin with about 40-50% fillers. When fillers are added to polymeric matrices, they increase thermal stability and mechanical properties. Also, filled polyurethanes show pseudoplastic behavior, *i.e.* the shear rate has significant effect on viscosity [8]. In this contribution, we studied the effect of different reinforcements, *i.e.* chopped carbon fibers and inorganic powders onto the processability, mechanical, rheological and thermal properties of HTPB-based liners, with the ultimate and practical objective of determining its

application in solid rocket motors.

2. EXPERIMENTAL PART

2.1. Materials

Hydroxyl-terminated polybutadiene (HTPB) prepolymer resin in commercial grade (mean molar mass of 2900 g mol⁻¹, functionality 2.4) was obtained from Evonik, Germany.

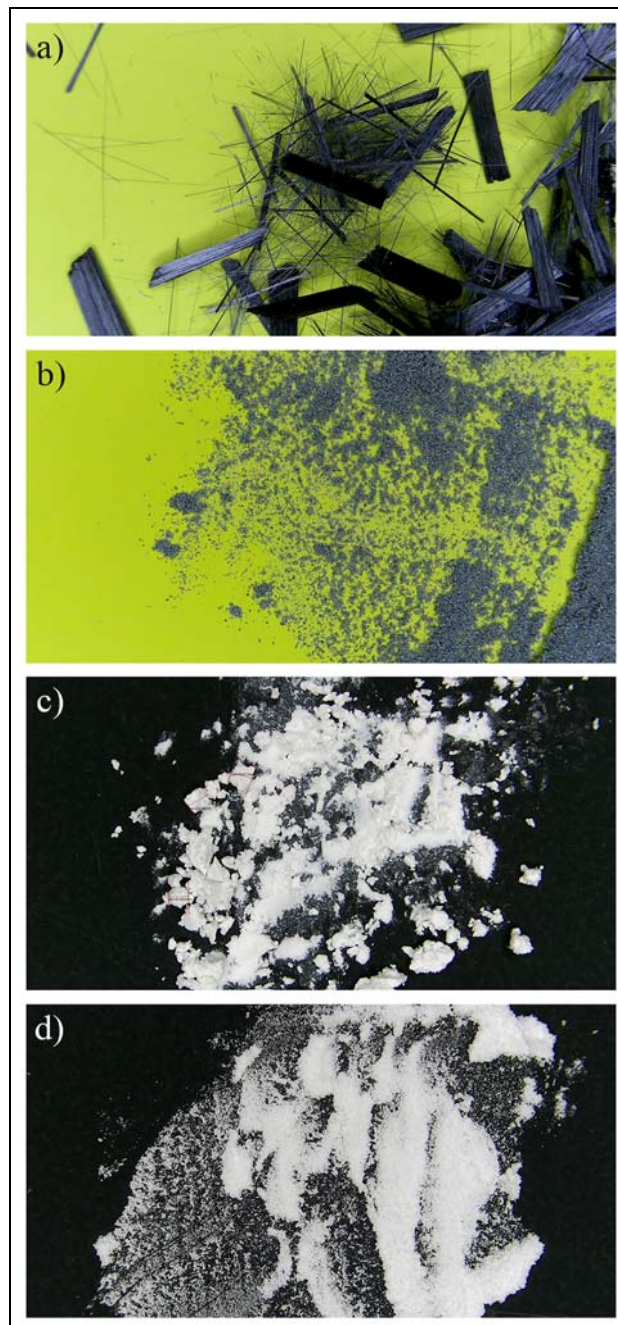


Figure 1. Carbon fibers (a) and inorganic filler powders: SiC (b), SiO₂ (c) and ZrO₂ (d)

Castor oil (CO), made by Interhem, Serbia, with mean molar mass 933 g mol⁻¹ and functionality 3.0, was used as reactive (cross-linkable) plasticizer and bonding agent. The curing agent for the described materials was isophorone diisocyanate (IPDI, Evonik, Germany), while

AO 2246, with N,N'-di-2-butyl-1,4-phenylenediamine as active component, was used as antioxidant. Materials, used for the preparation of thermally stable liner, were as follows: carbon roving (Tenax HTS40), which was cut in millimeter size before use, (Figure 1 (a)), aluminium trihydroxide (ATH, Technipur, Germany), catalyst ferric acetyl acetonate ($\text{Fe}(\text{AA})_3$) (Merck, Germany), SiC (97.5% 200 mech, Schnellendorf, Germany), SiO_2 (99.9% 325 mech, Cerac, UK) and ZrO_2 (99% 325 mech, Sigma Aldrich, USA) (Figure 1(b), (c) and (d), respectively). All solids were dried at 60 °C for three days to remove moisture before use.

2.2. Preparing of liner insulation materials

The homogenization of liner compositions was performed using laboratory mixer (LR 1000 B S099, Ika, Germany) at a temperature of 30 °C in two-step procedure. Firstly, the premix excluding $\text{Fe}(\text{AA})_3$ and IPDI (Table 1), was made by mixing HTPB, CO, AO2246, chopped carbon fibers and inorganic powders for 20 min under atmospheric pressure and 30 min under the vacuum. Afterwards, catalyst and curing agent were added in the obtained mixture and homogenization was continued for 5 min under atmospheric pressure and 10 min under the vacuum.

Table 1. Compositions of prepared insulation materials

Component	L4	L6	L10
<i>parts per hundred ratio (phr)</i>			
HTPB	100	100	100
CO	16.09	8.05	8.05
AO 22	0.5	0.5	0.5
$\text{Fe}(\text{AA})_3$	0.0075	0.0075	0.0100
IPDI	9.69	8.74	8.74
<i>mas.%</i>			
CFs	1.2	1.2	1.54
$\text{Al}(\text{OH})_3$	50	50	-
SiC	-	-	1.92
SiO_2	-	-	23.04
ZrO_2	-	-	13.44

Such obtained material was poured into the standard polytetrafluoroethylene (PTFE) molds and cured in the vacuum oven for the next four days at 60 °C. The specimens for the mechanical, rheological and thermal measurements were cut out from the cured material. The liner insulation materials are designed as follows: L4 and L6 contain chopped carbon fibers and aluminium trihydroxide, while L10 contains chopped carbon fibers, SiC, SiO_2 and ZrO_2 inorganic reinforcements. All these formulations were evaluated for their physical, mechanical, thermal and ablative properties.

2.3. Physical, rheological, mechanical and thermal analysis of materials

Shore A hardness (Sh A) of inhibitor samples was estimated by durometer (Zorn Stendal DDR testing device) according to the standard ASTM D2240 [9]. The five measurements were performed to determine mean values of Sh A hardness.

Density of prepared materials were obtained by a Mettler density kit at 25 °C, whereas isopropyl alcohol was used as a solvent [10]. The density, D , was determined according to the following Eq. 1:

$$D = \frac{m_0}{m_s} D_s \quad (1)$$

where D is the sample density (g cm^{-3}), m_0 is weight of the sample (g), m_s is weight of the sample in solvent (g) and D_s is the specific gravity of the solvent (g cm^{-3}). The five measurements were performed to determine mean values of liners density. Distribution of the filler particles within the polymer matrix after curing was determined using optical microscope (SMTV Visor Inspection System, Michael Bruch, Germany).

Dynamic mechanical analysis (DMA) study for cured materials was performed in torsion deformation mode using the Modular Compact Rheometer MCR-302 (Anton Paar GmbH), equipped with standard fixtures (SRF12) for rectangular bars, temperature chamber (CTD-620) with high temperature stability (± 0.1 °C), and automated cooling accessories using liquid nitrogen. The samples for the DMA tests were of a rectangular bar shape (44 mm \times 10 mm \times 4 mm). Dynamical-mechanical measurements were performed by using "temperature ramp test" and the following conditions: the temperature range from -80 °C to 40 °C, the heating rate was 5 °C \cdot min $^{-1}$ and the single angular frequency of 1 Hz. Strain amplitude was 0.1% (0.001), within linear viscoelastic region.

Viscosity is an easily measurable parameter to monitor curing and chemo-rheological properties of liners and propellants. As the cure proceeds, the molecular size increases, and so does the cross-linking density, which decreases the mobility of the molecules. Viscosity studies are worth to be continued to make compositions more process friendly, considering the technical difficulties involved in mixing during manufacturing. The rheological behaviors of the uncured liner formulations, before and 15 min after IPDI addition, were also investigated at shear rates ranging from 0.1 to 500 rad s $^{-1}$ at 25 °C. A series of measurements are performed in a cone-and-plate geometry with a diameter of 35 mm and a gap of 0.5 mm.

Uniaxial tensile measurements of samples cured for four days were performed using an Instron 1122 tester according to standard procedure [11]. All tests were performed at 20 °C adjusted at crosshead speed of 50 mm min $^{-1}$. Dumbbell-shaped specimens (100 mm \times 6 mm \times 3 mm) were used. The effective gauge length of the test samples was 46.5 mm. The tensile strength is calculated as $\sigma_m = F/S$ where F is the force, S is the transect area of sample at direction. Each value is an average of the five measurements with a relative standard deviation of $\pm 3\%$.

Flame resistance was evaluated using ASTM E285, Standard Test Method for Oxyacetylene Ablation Testing of Thermal Insulation [12]. The test equipment consists of an oxygen-acetylene control unit, gadget for data measuring (time, temperature) and a specimen-fixing unit (Figure 2).



Figure 2. Specimen-fixing unit for oxy-acetylene torch test

The size of the liner insulation material specimens was 100 mm × 100 mm and 3-4 mm thickness. The flame of 3000 °C was generated with a 1:1 oxygen-acetylene ratio and the distance between the specimen and torch was set at 60 mm. The erosion test lasted until the flame penetrated through the material. Additionally, the back surface temperature was measured using a mobile infrared thermometer (TFI 550, Xylem Analytics Germany, Ebro).

Samples were subjected to a flame torch of oxygen and acetylene and time to bore a hole in samples was recorded. The calculated parameter was erosion rate, Eq.2,

$$E = \frac{d}{t_b} \quad (2)$$

where E is the erosion rate (m s^{-1}), d is the thickness of panel (m) and t_b is the burn-through time (s).

3. RESULTS AND DISCUSSION

3.1. Physical and mechanical properties

Table 2 shows the mean Sh A and density, where a slight differences in resulting values is remarked.

Table 2. Hardness and density values for prepared insulation materials

Material	L4	L6	L10
Hardness (Sh A)	38	42	40
Density, D (g cm^{-3})	1.3517	1.3486	1.2853

Figure 3 shows the distribution of filler particles and carbon fibers in cured polymer matrix. Presence of copped carbon fibers is visible in the case of all samples, while in the case of the L10 material the presence of different powdered fillers is especially emphasized.

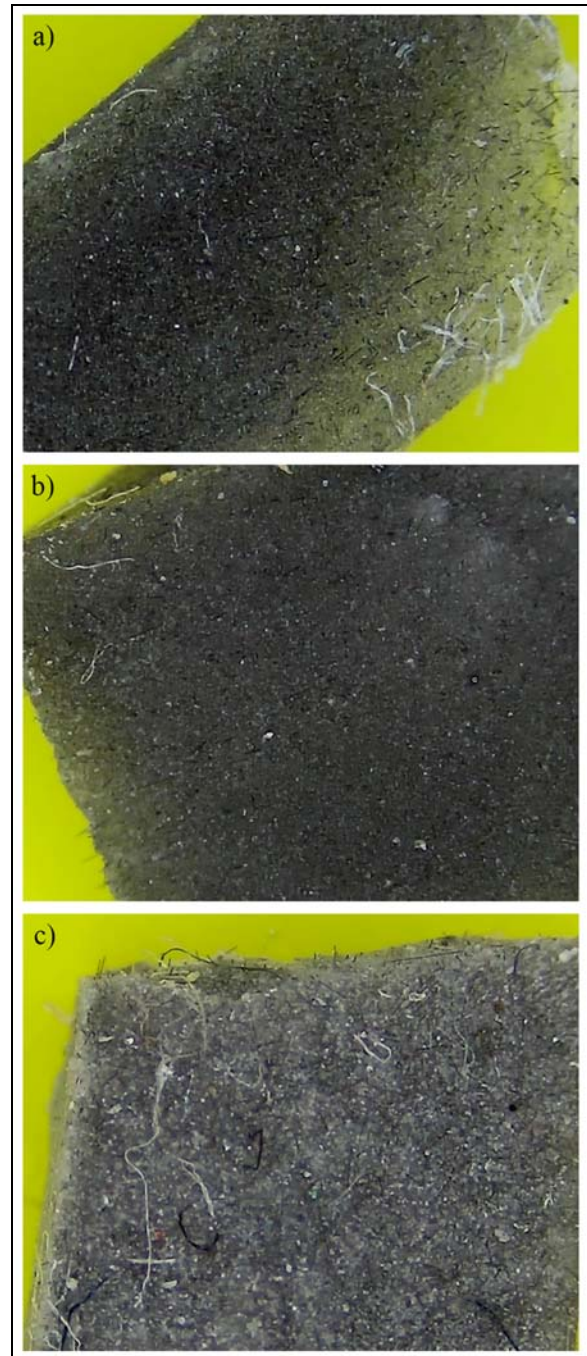


Figure 3. Distribution of reinforcements within the L4 (a), L6 (b) and L10 (c) by optical microscopy

Figure 4 shows the viscosity as a function of shear rate for the uncured liner insulation materials. It is obvious that viscosity increases with the decrease of CO content, in the case of L6. In addition, viscosity values less than 100.000 mPa·s are suitable in terms of composition processability, which means that L4 and L10 formulations could be suitable in liner insulation manufacturing process.

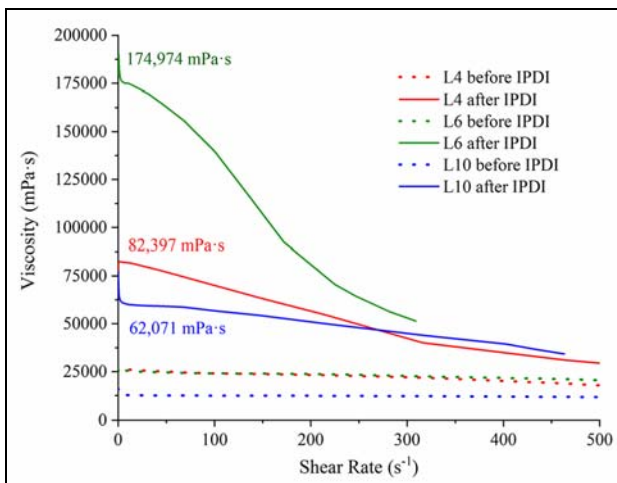


Figure 4. Viscosity versus shear rate of uncured material formulations

In the case of L10 material, due to carbon fibers lower content compared to other formulations, viscosity is lower, but requires a longer processing time.

Mechanical properties of HTPB-based liners mainly depend on the curing agent, NCO/OH ratio, chain extender nature, microstructure and crosslinkers [13]. Elasticity and high thermal resistance are required for the insulation layer of a propellant grain system. Tensile strength and elongation at break for prepared materials after curing at 60 °C for 96 hours were measured through maximum tensile strength (σ_m) until failure. Figure 5 shows comparison of tensile strength and elongation at break values (a) and the typical tensile stress-strain curves of the cured materials (b). L4 material has the highest elongation (759%) and correspondingly small tensile strength (0.358 MPa). In the case of L6 material, elongation was significantly reduced due to lowering of CO content, but conversely, tensile strength increased because of the higher NCO/OH ratio, which mostly affects mechanical characteristics [8], [13]. L10 shows high elongation value and the highest tensile strength among the tested materials, which is attributed to the greater carbon fibers content giving stiffness to the final material. In addition, it is well-known that the tensile strength of polymer composites strongly depends to the shape and content of the fillers, so L10 tensile strength value may arise due to diversity of inorganic particles in material formulation [14]. Also, it can be assumed that during combustion and high temperature pyrolysis it forms mostly ceramic layers which stick together and do not ablate in the current flow [15].

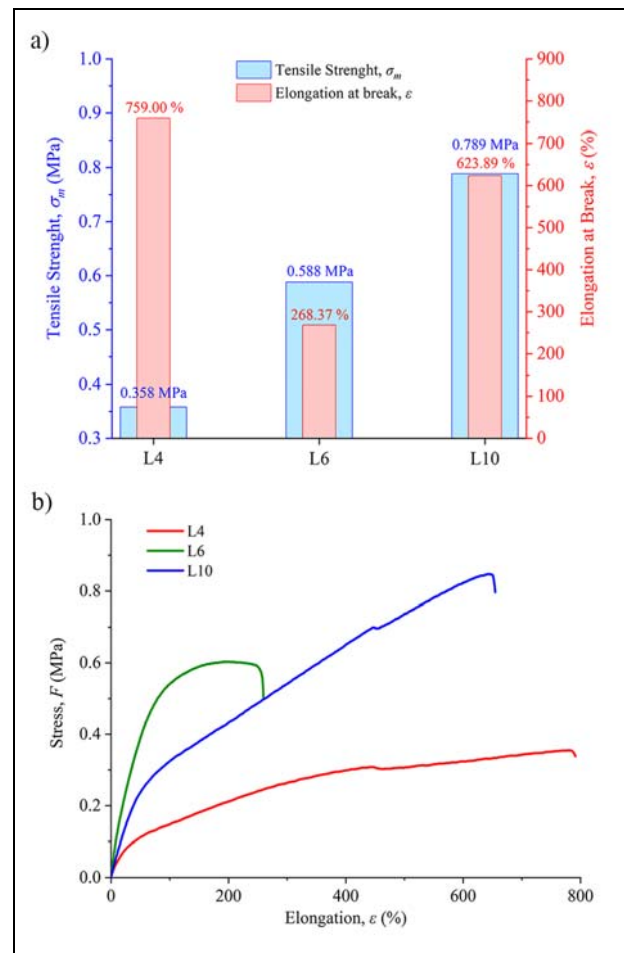


Figure 5. Comparison of tensile strength and elongation at break of samples (a) and tensile stress-elongation curves of the samples (b)

3.2. Rheological properties

Figure 6 shows the DMA curves of prepared liners as a function of different binder formulation and filler loading. The DMA curves provide specific information on the storage modulus, G' (elastic response), loss modulus, G'' (viscous component) and $\tan\delta$, within the applied temperature range. The G' reflects the elastic modulus of materials, G'' is related to the energy dissipation associated with the motion of polymer chains whereas $\tan\delta$ represents the phase delay between the applied force and the response of the material.

The resulting DMA curves are typical for elastomeric HTPB-based composites. Storage modulus decreases with temperature, from 1392, 2110 and 1726 MPa at -80 °C to 0.63, 0.81 and 0.62 MPa at 40 °C, for L4, L6 and L10, respectively. The maximum values are reached below the glass transition temperature zone (-80 °C to -60 °C). The L6 containing half as much CO in binder structure shows higher values of storage modulus in low temperature region due to the conspicuous chemical linkage in polymer network, but similar trend after glass transition zone, compared to L4 and L10.

Table 3. Glass transition temperatures of prepared insulation materials

Material	L4	L6	L10
T_g (°C)	-63.53	-60.61	-63.15

In all cases it is noticeable a double peak in the $\tan\delta$ curve, corresponding to alpha and beta transition of the polymeric matrix. The second peak is wide and has a lower intensity than the first peak. This behavior is related to the presence of hard and soft segments in polyurethane material.

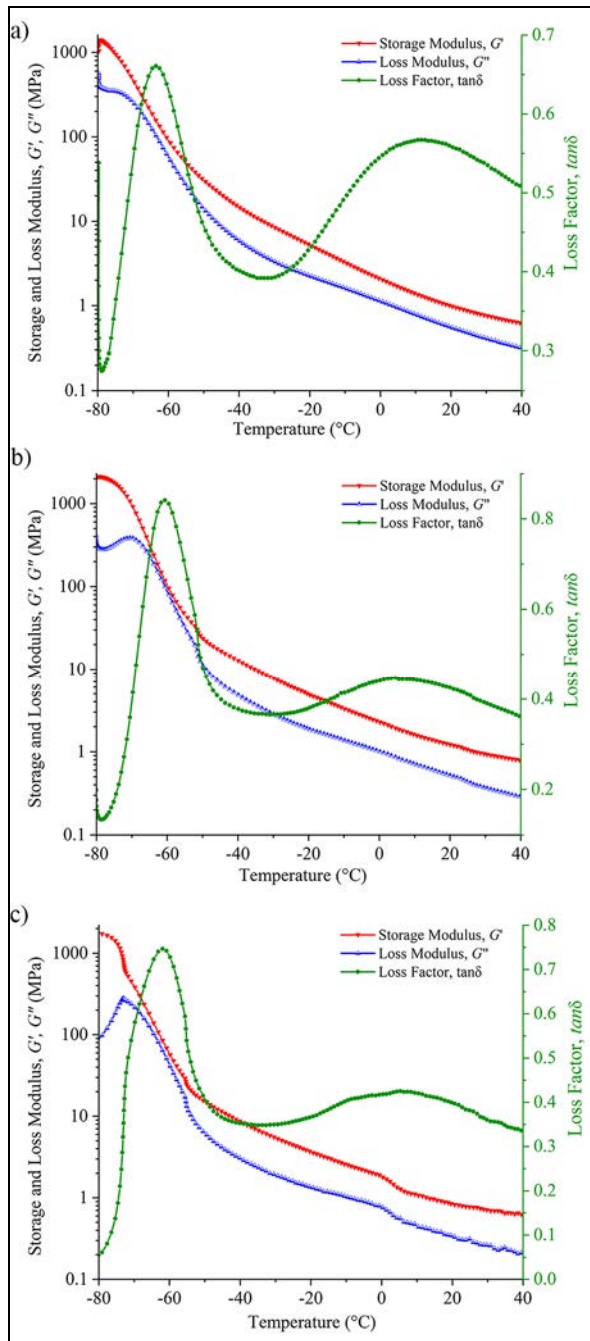


Figure 6. DMA curves of liner insulation material based on HTPB and CO: L4 (a), L6 (b) and L10 (c)

The first peak is a glass transition temperature of the soft segments (T_g), which determines the beginning or the end of the movement of the segments of the polymer backbone. Determined glass transition temperatures of L4, L6 and L10 cured materials are similar because of the

same binder bases, as presented in Table 3. The second peak is related to a complex process involving two mechanisms: the interactions of the polymer itself and the interactions of the matrix and solid phase. The mobility of macromolecule segments are significantly reduced due to solid content and interactions between the binding agent and the solids. Peak height in case of L4 is higher compared to L6 and L10 due to the higher amount of CO in material formulation, which segments remain unattached to polymer network and, thus are more movable.

3.3. Ablation testing

The oxyacetylene torch test results are summarized in Table 4. Exposing the liners to extreme temperatures leads to pyrolysis, which produces char on the material surface, acting as an insulating layer [16].

Table 4. Ablation test parameters and results

Material	L4	L6	L10
Length (mm)	100	100	100
Width (mm)	100	100	100
Thickness, d (mm)	3.90	3.82	2.93
Burning out time, t_b (s)	38	6	5
Burning out back-face temperature, T_b (°C)	102	44.0	56.9
E (m s ⁻¹)	1.0263×10^{-4}	6.3667×10^{-4}	5.8600×10^{-4}

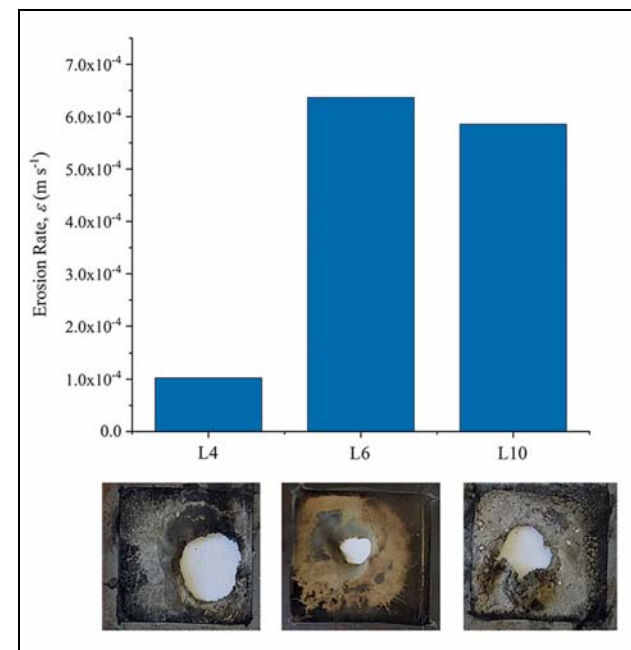


Figure 7. Comparison of erosion rates and appearance of liner insulation material samples after ablation testing

Back-face temperature for L4 reaches 102 °C when the surface temperature exceeds 3000 °C and linear erosion rate is 0.10263 mm s⁻¹, which is considerably lower than those observed for the other two samples (500% and 600%), as shown in Table 4 and Figure 7. These results

are mainly attributed to the higher char yield that can take away more heat to successfully insulate the material beneath the ablated surface.

Considering that the L4 material proved to be good in sense of casting viscosity (after IDPI addition in formulations), satisfactory mechanical characteristics and ablation resistance with small erosion rate, it can be concluded that this material completely meets the requirements of insulating material compared to other two.

5. CONCLUSION

In this work were developed three newly composite materials as a liners based on HTPB and reinforced with carbon fibers and inorganic filler powders, such as ATH, SiC, SiO₂ and ZrO₂. Prepared liner materials with a range of weight loadings of CFs and IFPs, with different NCO/OH ratios, were monitored for their processability and required rheological, mechanical and thermal properties. Prepared L4 material has the most desirable required properties for the majority of applied CRPs, *i.e.* adaptable mechanical properties, sufficient glass transition temperature and low erosion rate. Casting viscosity ensures good processability of the material while the density value corresponds to the general requirements. According to the same properties of studied L6 material, it is concluded that material formulation is adaptable in correlation to propellant properties and liner/insulation requirements. In addition, a special advantage of studied materials is that the binder has been based on the same polymer system as the composite solid propellant, thus it is considered reasonable to assume that the liner has the same mechanical properties as the propellant.

On the basis of such a composition, research should be continued and test methods should be expanded to optimize its application. In a specific case, complementary tests should be carried out with a proper rocket motor which should be stored at different temperatures and also test fired to secure no breakage at the long-duration stresses and strains that will occur during prolonged storage and firing. Some of the indispensable tests are the adhesion tests and examination of migration of individual components, depending on the correctly selected materials and construction of the rocket motor. Such studies of ablative and adhesive compositions of HTPB with novel additives, including different nanomaterials and particularly graphene oxide, emerge as novel and evolutionary SRM alternative research path.

ACKNOWLEDGEMENT

The authors thank to the Ministry of Education, Science and Technological Development of the Republic of Serbia for the support of the research through the Contract No. 451-03-68/2022-14/200325.

References

- [1] J. Deng, X. Wang, G. Li, and Y. Luo, "Effect of Bonding Agent on the Mechanical Properties of GAP High-Energy Propellant," *Propellants, Explos. Pyrotech.*, vol. 42, no. 4, 394–400, 2017.
- [2] K. Ghosh *et al.*, "Light weight HTPB-clay nanocomposites (HCN) with enhanced ablation performance as inhibition materials for composite propellant," *Def. Technol.*, vol. 17, no. 2, pp. 559–570, 2021.
- [3] A. Cosentino Garcia Miguel, F. C. Silva, G. Silva, J. Sciamareli, and E. Costa Mattos, "A Short Review about Aerospace Materials Characterization – Bonding Agents and Thermal Insulation," *Propellants, Explos. Pyrotech.*, vol. 45, no. 8, pp. 1175–1184, 2020.
- [4] A. F. Ahmed and S. V. Hoa, "Thermal insulation by heat resistant polymers for solid rocket motor insulation," *J. Compos. Mater.*, vol. 46, no. 13, pp. 1549–1559, 2012.
- [5] J. C. Q. Amado, P. G. Ross, N. B. Sanches, J. R. A. Pinto, and J. C. N. Dutra, "Evaluation of elastomeric heat shielding materials as insulators for solid propellant rocket motors: A short review," *Open Chem.*, vol. 18, no. 1, pp. 1452–1467, 2020.
- [6] H. Cheng, H. Xue, C. Hong, and X. Zhang, "Preparation, mechanical, thermal and ablative properties of lightweight needled carbon fibre felt/phenolic resin aerogel composite with a bird's nest structure," *Compos. Sci. Technol.*, vol. 140, pp. 63–72, 2017.
- [7] G. Latta, Q. Lineberry, R. Ozao, H.-Y. Zhao, and W.-P. Pan, "Thermal properties of ethylene octene copolymer (Engage)/dimethyldioctadecyl quaternary ammonium chloride-modified montmorillonite clay nanocomposites," *J. Mater. Sci.*, vol. 43, no. 8, pp. 2555–2561, 2008.
- [8] J. Quagliano, V. Wittemberg, J. Gonzalez, and A. Bacigalupe, "Mechanical and Rheological Properties of Polyurethane Elastomers from Hydroxy-Terminated Polybutadiene and Isophorone Diisocyanate Used as Liners for Composite Propellants," *J. Res. Updat. Polym. Sci.*, vol. 4, no. 1, pp. 50–55, 2015.
- [9] American Society for Testing and Materials, "ASTM D2240-15 Standard Test Methods for Rubber Property-Durometer Hardness," *Annu. B. ASTM Stand.*, pp. 1–13, 2015.
- [10] S. Brzić *et al.*, "Multi-component elastomeric composites based on castor oil/AgI/KI for cloud seeding: processing and modeling of reagent efficiency," *Polym. Bull.*, 2022.
- [11] American Society for Testing and Materials, "ASTM D412-15 Standard Test Methods for Vulcanized Rubber and Thermoplastic Elastomers - Tension," *Annu. B. ASTM Stand.*, pp. 1–14, 2002.
- [12] American Society for Testing and Materials, "ASTM E285–80 Standard Test Method for Oxyacetylene Ablation Testing of Thermal Insulation Materials," *Annu. B. ASTM Stand.*, 2008.
- [13] J. C. Quagliano Amado, P. G. Ross, L. Mattos Silva Murakami, and J. C. Narciso Dutra, "Properties of Hydroxyl-Terminal Polybutadiene

- (HTPB) and Its Use as a Liner and Binder for Composite Propellants: A Review of Recent Advances,” *Propellants, Explos. Pyrotech.*, vol. 47, no. 5, 2022.
- [14] J. Zhu, S. Wei, J. Ryu, L. Sun, Z. Luo, and Z. Guo, “Magnetic Epoxy Resin Nanocomposites Reinforced with Core–Shell Structured Fe@FeO Nanoparticles: Fabrication and Property Analysis,” *ACS Appl. Mater. Interfaces*, vol. 2, no. 7, pp. 2100–2107, 2010.
- [15] K. Menke, P. Gerber, E. Geißler, G. Bunte, H. Kentgens, and R. Schöffl, “Characteristic Properties of an End Burning Grain with Smoke Reduced Ferrocene Containing Composite Propellant,” *Propellants, Explos. Pyrotech.*, vol. 24, no. 3, pp. 126–133, 1999.
- [16] E. K. Allcorn, M. Natali, and J. H. Koo, “Ablation performance and characterization of thermoplastic polyurethane elastomer nanocomposites,” *Compos. Part A Appl. Sci. Manuf.*, vol. 45, pp. 109–118, 2013.



DIGITAL THREAD FOR ADDITIVE MANUFACTURING

SLOBODAN MALBAŠIĆ, MSC

Department for Defence Technologies, Belgrade, slobodan.malbasic@mod.gov.rs

SRDJAN ŽIVKOVIĆ, PHD

Military Technical Institution, Belgrade, srdjan.vti@gmail.com

VELJKO PETROVIĆ, MSC

Department for Defence Technologies, Belgrade, veljko.petrovic@mod.gov.rs

ALEKSA GRUBIĆ

Military Technical Institution, Belgrade, grubicaleksa8@gmail.com

Abstract: Additive manufacturing (AM) has been shaping the industrial manufacturing in recent decade due its high performance and benefits over the traditional technologies, especially in the field of prototyping and low volume production. AM transforms 3D models into the physical realm through the several steps know as digital thread, which explain the real digitization nature of this process. This paper intends to emphasis the benefits of AM approach, necessity for creating the digital thread for AM as well as to present some issues related to its applications. Also, some new trends in the development of AM production process (on-line platforms, Manufacturing Execution System, etc) will be briefly explained.

Keywords: Additive manufactuirng, 3D printing, digital thread, on-line AM platforms.

1. INTRODUCTION

In order to stay competitive at the global market companies around the world are trying to find feasibly solutions to improve their products, the way how perform their business, embrace new business models as well as new technologies. Product strategies and new technologies essentially change the process of developing and manufacturing the products.

Survey from [1] highlighted several strategies that companies can leverage to improve their competitiveness: advance product performance, increase product quality, make product smarter, lower cost of ownership for customers (maintenance and energy cost), lower product cost. Same survey further showed that 3D printing, use of new materials, ability to work with scanned data, cloud computing, IoT (Internet of Things), etc, are the technologies that will help companies to execute their strategies.

With previous in mind, it is becoming very clear that 3D printing technologies has taking an important role and this is the explanation why there are so many interests and activity about it. 3D printing or additive manufacturing (AM) are using synonymously but there are the differences. ED term was coin by MIT Institute and it is related to the fabrication of the object through the deposition of materials using print head, nozzle other printing technologies. This definition linking 3D process with binder and material jetting technologies as well as with material extrusion technology. Since the AM is a

process of joining material to make objects from 3D models usually layer by layer, it can be stated that 3D printing is sub group of AM technologies.

Starting from the 80-ies years of last century what is count as the appearance of the AM (companies Stratasys and 3D Systems are among the first to develop and apply AM technology), this technology keeps growing at record speed and its adaption increases. As it stated in [2] professionals use AM for two main purposes: 1) as prototyping solution for increase product development and 2) in manufacturing as low-run production.

Same authors further explain the benefits of this technologies are as follows: functional and accessible solution and effective design in prototyping phase, as well as fewer design restriction, on-demand production, mass customization, distributed manufacturing in production phase, AM processes enable minimization of material waste with direct manufacturing and no tooling needs. In addition to these benefits, it should be mentioned that prices of AM technologies are coming down while the speed of the manufacturing is increasing. These two elements have been seen as two main downsizes of AM.

There are the elements of disruption in the emerging of AM. Disruption is observed from the use of new process (adding material instead of subtraction), new services (on-line manufacturing platforms), use of information communication technologies (ICTs), and all together threaten to displace conventional methods (CM) of manufacturing in some fields. CM is not in position to create complex shapes (especially inside structure), there are limitations in use of materials and performances of

products, as well as limitation in further improvements in production process (lead time, cost reduction, quality, etc).

AM is one part of the new digital manufacturing production, and together with digital thread (or CAx chain), digital supply chains and smart factories, forming the new manufacturing landscape. With the embrace of new technologies, it is worth mentioning that many professionals choose on-line manufacturing platforms as the solution to fulfill their 3D printing requirements.

After the introduction that explains the market trends related to AM, next chapter is dedicated to the explanation of basic elements of additive manufacturing, while the 3rd chapter is dedicated to the main topic of this paper – digital thread for AM. The next chapter gives some basic information about new approaches and business models that support industrial/cloud application of AM. In conclusions, brief overview of presented information is given with suggestions for further research in this area.

2. THE BASICS OF ADDITIVE MANUFACTURING

In order to precisely define AM as well as to list the AM categories, almost all authors usually referring to the official statement and definitions from American Society for Testing and Materials (ASTM) group ASTM F42 and the ISO 17296 committee. With this in mind and according to [3] AM is ‘the process of joining materials to make objects from 3D model data, usually layer upon layer, as opposed to subtractive manufacturing methodologies.

Following the same referring methodology and authors, there are seven categories of AM technologies [3]: 1) vat photopolymerization including Stereolithography (SLA) and Direct Light Processing (DLP) 2) material jetting, 3) binder jetting, 4) material extrusion including Fused Deposition Modelling (FDM) and FFF (Fused Filament Fabrication), 5) Powder Bed Fusion (PBF) including Selective Laser Sintering (SLS), Selective Laser Melting (SLM) and Direct Metal laser Sintering (DMLS) 6) sheet lamination including Laminated Object Manufacturing (LOM) and 7) direct energy deposition including 3D laser cladding and Wire Arc Additive Manufacturing (WAAM).

AM technology is capable to produce fully functional parts using a wide range of materials: metal, ceramic, polymers and their combinations, composites or functionally graded materials (FGMs), [4]. For full functional production SLS, SLM and DMLS technologies are by far the best possible solution to do it.

AM technology is applied in various industries: aerospace and automotive industry, military industry, healthcare and medical industry, food industry, architecture, building, and construction industry, fabric and fashion industry, electric and electronic industry, etc.

Many companies’ sees in AM process as a replacement for conventional manufacturing process or in some cases

augmented it (technology process known as hybrid AM or the combination of conventional and AM techniques). So, at the first place, the advantage of AM is eliminating the tooling that goes with manufacturing and instead printing parts directly. This leads to the elimination of the time and costs linked with making this type of tool, [5].

AM gives new opportunity for designing of the products, with the introduction of the Design for the AM (DfAM) framework which deals with the design of the product, but at the same time focusing on manufacturing and assembly of that product. As it published in [6] and further explained in details, techniques for optimization of product geometry based on DfAM are: 1) Light-weight design (Complex design) including: topology optimization, application of bionic principles and transformation of shapes from nature and lattice and cellular structures, 2) Component consolidation (design of integrated geometries - several parts connected into one functional unit), 3) Design for functional integration - multifunctionality achieved by shape, 4) Design to improve the function and performance of the work, 5) Tool optimization and 6) Customization.

AM support traditional manufacturing process through the production of fixtures, jigs and tooling setups for machining and operations. These are low volume parts, but they are needed quickly and not need to be metal product (can be plastics, composite materials).

With the use of 3D models as a prerequisite for AM, and since the company beginning to explore what can be done with AM, digital inventories instead of physical ones came as good solution.

AM in form of DDM (Direct Digital Manufacturing) is part of the production of end-use components and products, and in most cases it is not just the extension of the rapid prototyping. With the advantage of the geometric complexity of the AM with DDM it can be produced parts with customized geometries.

3. THE DIGITAL THREAD FOR ADDITIVE MANUFACTURING

Due to the intensive technology development exchange of the information in manufacturing chain has become data intensive and digitalized. Digital thread is the communication framework that enables digitally connections among involved parties (designers, customers, AM providers, OEMs) providing material and manufacturing information, according to [7].

In digital thread information exchange are occurring in both directions, feed-forward and feed-back loops, and connects process stages from design, through simulation and build plan, process monitoring, control and verification [7]. All this information need to be a part of a single digital thread, accessible, traceable and interoperable with all machines within the process chain.

The typical information flow is presented on the Figure 1, (5). Each step uses a different piece of software (one software for design, other for simulation, then for printing, etc). Each of these software often requires a

different file formats, which later require file to be converted causing information to be lost. Beside these issues, researchers in the field of AM digital thread identifies some other challenges: lack of digital standards, disjointed digital thread that can cause the lost of information, etc.



Figure 1: Barriers to industrializing AM, [5]

With previous statement in mind, the importance of having an integrated end to end software solution, as unbroken digital thread of data, is becoming priority. Current markets are limited with new and powerful set of fully integrated solution for AM chain.

AM digital thread: The common vision for the digital, or CAX chain of AM is composed of five principal steps (Figure 2.).

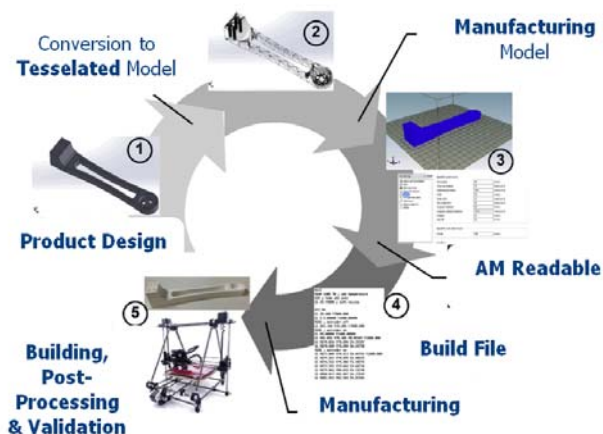


Figure 2: Typical AM digital thread, [3]

Process starting with the creation of a 3D model (by design or scanning) mainly using CAD software. After that, the 3D model is in most cases converted to an STL file format (first known AM format and accepted by almost all AM machine).

In order to overcome some lost of the information during the conversion to STL format, new formats have appeared: AMF (Additive Manufacturing Format) and 3MF (3D Manufacturing Format), Standard for the Exchange of Product model data (STEP), and STEP compliant Numerical Control (STEP-NC), [8, 9].

File in the appropriate format is then transferred to the slicing engine (or “CAM system”). After the part positioning/orientation at the build plate, slicing of the part into individual layers starting, with the manufacturing information settings and tool-paths generation (creation of

G-code that printer uses to print the file). In complex AM processes, like SLS, SLM, DMLS, all of these steps are processes in different software’s.

Post-processing can consist of several process which in basic include separating the print from the build plate and/or removing any support material (by melting or dissolving), and in some cases can comprise CNC machining and thermal treating.

Validation process is part of control, which helps to trace back the settings and conditions used throughout the design and build phase in order to compare it with initial data/design and make corrections.

4. NEW APPROACHES AND BUSINESS MODELS FOR SUPPORT INDUSTRIAL AM

This part is dedicated to the explanation of the Manufacturing Execution System as support for industrial AM production, as well as cloud-based solutions and new business models for AM.

Manufacturing Execution System: In the beginning of its appearance, AM was just a prototyping tool. Now days AM is a viable option for small serial production with intention to reach full serial production capacity in near future. To exploit the full potential of AM technologies and hardware/machines particularly in light of serial production, some issues still need to be resolved, like: organization of AM workflow and information movement, improvement of AM machine efficiency, optimization of AM process, etc.

Manufacturing Execution System (MES) is designed to address these challenges and help to run and monitor lot of more activities in production real time. MES offers running of several AM process simultaneously (even with different machine configuration), data acquisition and processing, scheduling of operation, handles management of the chain of process steps needed to create parts, control of resources and allocation, dispatching production to machines and workers, provides a bidirectional link between the enterprise planning layer and the shop floor, etc, [10].

Some MES solutions (instant quoting, 3D file optimization, and nesting) are specifically designed for additive manufacturing environments, and called Additive MES solutions.

MES features are serving as foundation for implementing Industry 4.0 concept providing manufacturer process to be smarter by supplying on-line data.

Cloud based solutions and new business models for AM: Additive manufacturing is a technology that changes engineering process and production, but also changes how the business is conducting. New business models, following the latest development in ICT technology, are now cloud-based collaboration platforms.

In order to make this business models works efficiently all relevant factors are included in its building and functioning: hardware and software vendors, material

vendors, part buyers, print SME, etc.

Idea behind this solution is to support the industrial business process, speed up the production as respond to customer request, organize the production close to the end user and reduce customer need for AM and IT infrastructure.

Manufacturing service providers and online manufacturing: According to [2] AM service provider sector is one of the fastest-growing sectors within the 3D printing industry, with its participation of 34% in total revenue.

AM service providers offer for businesses outsourcing of their AM production, helped further advancement of the technology, broaden the range of available applications, and provide more choices for OEMs to select AM manufacturers, [11].

World famous and leading hardware manufacturers, well known as the founder of AM technology Stratasys and 3D Systems, also offering AM services as part of their business model.

Particular opportunity for the AM services market is Metal additive manufacturing, and predictions for the revenue in this area is around 9.4 billion dollars by 2025, [11].

The new business models that provide manufacturing services are the “online manufacturing” or “MaaS – Manufacturing as a Services”. Beside AM services they also provide conventional manufacturing services as well as injection molding. This is the online platforms and on-demand services, connect world manufacturing suppliers with end users, and automate the procurement and sourcing process. As it stated in [11], 35-45% of AM service providers share can be attributed to “online manufacturing”.

5. CONCLUSIONS

Leading world companies in many industrial areas are discovering that the future of digital part production lies in adopting new technologies which transforming it and upgrading to a new capability. One of these technologies that create new and additional value to the product is the additive manufacturing.

Additive manufacturing technologies provide the creation of parts on totally new and innovative way (adding materials in layers), in contrast to traditional manufacturing process (subtractive approach), and with unique design, shape and parameters improvements (lightweight structure, strength and durability).

In order to connect various applications and processes within digital part production companies need to set up the digital thread. Basic frameworks for digital thread is presented in this paper.

Above mentioned parameters improvements can be achieved in digital thread through continuous digitalized communication feedback loop, which enables connection between shop floor, engineering and front-end design process. Digital thread with feedback loop provides data

transfer, elimination of duplication of data, inclusion of information from production to design stage, and in general offer the product with highest possible quality. This information exchange is very important in the process of development and production of complex combat systems.

But, with all its benefits and improvements, additive manufacturing technology is not being used to its full potential. Some barriers still exist and can be attributed to the limited know-how among designers, lack of understanding of benefits, price of machines and some type of materials, etc. As it already stated in the introduction of this work, the prices of the AM process are coming down while the speed of the process is increasing.

Nevertheless, there are several AM areas that are currently (and will be in future) subject of wide scientific research like materials, machine technologies, process parameter optimization, sustainable manufacturing, as well as business opportunities and solutions linked with these processes.

ACKNOWLEDGEMENT

This paper presents the results of research supported by the Ministry of Education, Science and Technological Development of the Government of the Republic of Serbia - Contract N°. 451-03-68 / 2022-14 / 200325.

References

- [1] Tech-Clarity Inc. - White paper: *How Top Manufacturers Are Planning for the Future*. <https://resources.sw.siemens.com/en-US/white-paper-3d-printing-techclarity>, 2017.
- [2] ROBERTS, T., BOURNIAS-VAROTSIS, A.: *3D printing trends 2020: Industry highlights and market trends*. https://downloads.hubs.com/3D_printing_trends_report_2020.pdf, (2020).
- [3] BONNARD,R., JEAN-YVES,H., MOGNOL,P., STROUD,I.: *STEP-NC digital thread for additive manufacturing: data model, implementation and validation*, International Journal of Computer Integrated Manufacturing, <https://www.researchgate.net/publication/327146163> August 2018, DOI: 10.1080/0951192X.2018.1509130
- [4] SHAHRUBUDIN, N., LEE,T.C., RAMLAN,R.: *An Overview on 3D Printing Technology: Technological, Materials, and Applications*. Procedia Manufacturing. 1286–1296, 2019.
- [5] ECKHOFF,A.: *(On demand webinar)*, 2020, <https://www.plm.automation.siemens.com/global/en/webinar/industrialize-additive-manufacturing/21293>.
- [6] D4AM Wiki – Open repository of design rules for AM, <https://www.mfkv.kg.ac.rs/d4am/>.
- [7] Bonham, E., McMaster, K., Thomson, E., Panarotto, M., Müller, J.R., Isaksson, O., Johansson, E.: *Designing and Integrating a Digital Thread System*

- for Customized Additive Manufacturing in Multi-Partner Kayak Production*, *Systems* 2020, 8, 43; doi:10.3390/systems8040043
www.mdpi.com/journal/systems, 2020.
- [8] NASSAR, A.R., REUTZEL, E W.: A proposed digital thread for additive manufacturing. Paper presented at 24th International Solid Freeform Fabrication Symposium - An Additive Manufacturing Conference, SFF 2013, Austin, TX, United States, 19-43.
- [9] Bonnard, R., Hascoët, J.Y., Mognolb, P., Zancul, E., J. Alvares, A.J.: Hierarchical object-oriented model (HOOM) for additive manufacturing digital thread, *Journal of Manufacturing Systems* 50 (2019) 3–52.
- [10] SHOJAEINASAB, A., CHARTER, T., JALAYER, M., KHADIVI, M., OGUNFOWORA, O., RAIYANI, N., YAGHOUBI, M., NAJJARAN, H.: *Intelligent manufacturing execution systems: A systematic review*, *Journal of Manufacturing Systems* 62 (2022) 503–522.
- [11] AKINSOWON, V., NAHIRNA, M.: *The Additive Manufacturing Landscape 2020*, <https://amfg.ai/whitepapers/the-additive-manufacturing-landscape-2020-report/>.



IMPACT OF THE DIFFERENT ACTIVE FILLING HEIGHT OF THE FILTER ON THE SORPTIVE CHARACTERISTICS OF FILTERING

MARINA ILIĆ

Military Technical Institute, Belgrade, marinailic1970@gmail.com

TATJANA MARKOVIĆ

Military Technical Institute, Belgrade, tanjin.mejl@gmail.com

BILJANA MIHAJLOVIĆ

TRAYAL Corporation, Kruševac, aktivni.ugljevi@gmail.com

VUKICA GRKOVIĆ

TRAYAL CorporaTion, Kruševac, vukica.g30@gmail.com

SONJA BAUK

Military Technical Institute, Belgrade, bauk.sonja@gmail.com

Abstract: This paper presents, in accordance with the defined requirements of the SRPS 8748 and SRPS EN14387 standards, the impact of the filter different active filling height, with activated carbon impregnated with the salts of Cu^{2+} , Ag^+ and Zn^{2+} instead of Cr^{6+} salt, on the filter sorptive characteristics. This work also investigates the sorptive characteristics of filters with the different active filling height, upon phosgene, chloropicrin, hydrogen cyanide, ammonia, sulphur dioxide, cyclohexane and carbon monoxide challenge at different testing conditions of concentrations and flow rates of the inlet gas mixture.

Keywords: active filling height, filters, sorptive characteristics of the filters and the efficiency of filtering.

1. INTRODUCTION

The Combined filter is a filtering device for respiratory protection which, together with the protective mask, makes up a complex device for the protection of eyes, face and respiratory organs against CBRN contamination in the form of gases, vapours, solid and liquid particles of aerosols.

The Combined filter can be used for the protection against the following contaminants:

- for dust, aerosols and smoke (anti aerosol filter),
- for vapours and gases (anti vapour filter),

in the way that the removal of the harmful substances is performed by mechanism of filtration or sorption.

The latest world trends, more frequent terrorist attacks or other potential forms of diversions, as well as accidents at the industrial plants, impose new requirements for the human protection.

Many toxic industrial chemicals used for the industrial purposes, due to their availability and low cost on the world market, can be used nowadays as chemical agents for causing the general threat to the people, with short-term effects or longterm effects.^[1]

Consequently, besides providing the CBRN protection against clearly defined chemical warfare, the Combined filter also serves to protect from toxic chemicals and industrial gases, especially from ammonia, sulphur dioxide, cyclohexane, carbon monoxide and hydrogen cyanide.

On the other hand, the requirements for the environmental protection bring restrictions regarding the use of chemicals being used for the impregnation of activated carbon in the filter. For this reason, the salts of six valent atom chrome are not used in many countries of Europe and worldwide due to their toxicity for humans and for the environment.^[3]

For this reason, this work emphasizes the change of the texture (activate carbon impregnated with the salts of Cu^{2+} , Ag^+ and Zn^{2+} instead of Cr^{6+} salt), as well as impact of the anti vapour active filling height, for the purpose of testing the sorptive properties of the filters against:

- Contaminants from the group of CBRN contaminants,
- Toxic industrial chemicals that can be used as contaminants.

Since the Filter M3 is official CBRN protection equipment of Serbian Armed Forces, experimental results for sorptive properties of the Filter M4 (changed impregnation and active filling height of 27 mm, 32 mm and 39 mm) are compared with the Filter M3 sorptive properties (standard impregnation and filling height of 27 mm).

The process of impregnation of the activated carbon is conducted in accordance with precisely defined parameters and conditions of application of impregnation compounds, and it is strictly monitored in each stage of the production, according to the prescribed monitoring procedures. After the thermal processing, the impregnated

carbon is sifted to be dust-free and brought to quality in accordance with prescribed technical characteristics.^[2]

The two batches of the impregnated activated carbon have been produced. The batch of the activated carbon impregnated with the salts of Cu^{2+} , Ag^+ and Cr^{6+} , according to the standard recipe for making of Filter M3, and the batch of the activated carbon impregnated with the salts of Cu^{2+} , Ag^+ and Zn^{2+} , instead of Cr^{6+} salt according to the altered recipe for the Filter M4. All the filters used for the purpose of testing the sorptive properties, are filled with batches of the impregnated activated carbon of both standard and altered impregnation.

2. EXPERIMENTAL PART

Testing the sorptive properties of the Filter M3 and Filter M4 are in accordance to two standards: SORS 8748 and SRPS EN 14387

2.1. Testing methods for the time of sorption properties for the Filter M3 and the Filter M4 with different active filling height, upon phosgene, chloropicrin and hydrogen cyanide challenge, according to the SORS 8748

2.1.1. Principle

The principle of the method consists of the monitoring and comparative analysis for the time of sorption properties of the Filter M3 (with standard impregnation and active filling height of 27mm) and the Filter M4 (with altered impregnation and filling height of 27 mm, 32 mm and 39 mm) upon phosgene, chloropicrin and hydrogen cyanide challenge at testing conditions of different concentrations, relative humidity and flow rates of the inlet gas mixture.

2.1.2. The activities sequence of methods for testing the time of sorption properties of the Filter M3 and the Filter M4 with different active filling height upon phosgene challenge.

The flow of the mixture of air and phosgene gas is to be set until the preset inlet concentration and relative humidity of gas mixture has been reached. The time is to be measured from the moment of introduction of the air and phosgene mixture into the filter till the change in colour of the indicator paper. The measured time indicates the protection time of the filter against phosgene.^[4]

2.1.3. The activities sequence of methods for testing the time of sorption properties of the Filter M3 and the Filter M4 with different active filling height upon chloropicrin challenge.

The flow of the mixture of air and chloropicrin gas to be set until the preset inlet concentration and relative humidity of gas mixture has been reached. The time is to be measured from the moment of introduction of the air and chloropicrin mixture into the filter, till the change in colour of the indicator paper.

The measured time indicates the protection time of the filter against chloropicrin.^[4]

2.1.4. The activities sequence of methods for testing of the sorption properties time of the Filter M3 and the Filter M4 with different active filling height upon hydrogen cyanide challenge

The flow of the mixture of air and hydrogen cyanide gas to be set until the preset inlet concentration and relative humidity of gas mixture has been reached. In this case the the sample of Filters M3 is not wetted to a constant mass.

The time is to be measured from the moment of introduction of the air and hydrogen cyanide mixture into the filter till the change in colour of the indicator paper.

The measured time indicates the protection time of the filter against hydrogen cyanide.^[4]

2.2. Testing methods for the time of sorption properties of the Filter M3 and the Filter M4 with different active filling height upon ammonia, sulphur dioxide, cyclohexane and carbon monoxide gas challenge, according to the SRPS EN 14387

2.2.1. Principle

The principle of the method consists of the monitoring and comparative analysis for the time of sorption properties of the Filter M3 (with standard impregnation and active filling height of 27mm) and of the Filter M4 (with altered impregnation and filling height of 27 mm, 32 mm and 39 mm) upon three test gases from the group toxic chemical, ammonia, sulphur dioxide, cyclohexane and carbon monoxide gas challenge, at testing conditions of different flows, constant concentrations and relative humidity of the inlet gas mixture.

2.2.2. The activities sequence of methods for testing of the time of sorption properties of the Filter M3 and the Filter M4, different active filling height upon ammonia challenge.

The flow of the mixture of air and ammonia gas to be set until the preset inlet concentration and relative humidity of gas mixture has been reached. The time is to be measured from the moment of introduction of the air and ammonia mixture into the filter till the change in colour of the indicator paper.

The time that has been measured indicates the protection time of the filter against ammonia.^[5]

2.2.3. The activities sequence of methods for testing the sorption properties time of the Filter M3 and the Filter M4 with different active filling height, upon sulphur dioxide challenge

The flow of the mixture of air and sulphur dioxide gas to be set until the preset inlet concentration and relative humidity of gas mixture has been reached. The time is to be measured from the moment of introduction of the air and sulphur dioxide mixture into the filter till the change in colour of the indicator solution. The time that has been measured indicates the protection time of the filter against sulphur dioxide.^[5]

2.2.4. The activities sequence of methods for the time of sorption properties testing of the Filter M3 and the Filter M4 with different active filling height upon cyclohexane challenge

The flow of the mixture of air and cyclohexane gas to be set until required inlet concentration, relative humidity of gas mixture in system of detection has been reached. The

time is to be measured from the moment of introduction of the air and cyclohexane gas mixture into the testing filter until the output concentration of cyclohexane of 10 ppm is detected.^[5]

2.2.5. The activities sequence of methods for the time of sorption properties testing of the Filter M3 and the Filter M4 with different active filling height upon carbon monoxide challenge

The gas analyzer and the artificial lungs are activated. The flow of the mixture of air and carbon monoxide gas is to be set until required inlet concentration, relative humidity and temperature of gas mixture in system of detection, has been reached. The time is to be measured from the moment of introduction of the air and carbon monoxide gas mixture into the testing filter until the output concentration of carbon monoxide of 100 ppm is detected on gas analyzer.^[5]

3. RESULTS AND DISCUSSION

In the aim of quality control of active filling for Filters M3 and Filter M4, two different produced batches of carbon were sampled for testing. The first batch used in Filter M3 is carbon impregnated according to standard recipe (activated with Cu^{2+} , Cr^{6+} and Ag^{+} salts). The second one used in Filter M4 is impregnated to altered recipe (activated with Zn^{2+} salt which serve as a substitute for Cr^{6+} salt).

Filter M3 is official CBRN protection equipment of Serbian Armed Forces, so experimental results for the Filter M4 sorptive properties are compared with the Filter M3 sorptive properties. Filters M4 are filled with active carbon, different filling heights of 27 mm, 32 mm and 39 mm and activated with Cu^{2+} , Zn^{2+} and Ag^{+} salts.

The samples from two above mentioned batches (with different impregnation of active carbon) were tested on the following quality parameters:

- - moisture content (according to SORS 8830/05),
- - apparent density (according to SORS 8830/05),
- - mechanical strength (according to SORS 8830/05),
- - grain size distribution (according to SORS 8830/05),

The results of testing are given in Table 1.

Table 1. Physical-mechanical properties of impregnated activated carbons for filters

Activated carbon type	Standard Impregnation for Filter M3	Changed Impregnation for Filter M4
Moisture content[%]	1.0	2.4
Apparent density [g/l]	536	570
Mechanical strength[%]	71	72
Grain size distribution		
> 1.6 mm	0.10 %	0.53 %
>1.4 mm	2.61 %	7.12 %
0.7-1.4 mm	95.01 %	91.82 %
0.5-0.7 mm	1.89 %	0.44 %
<0.5 mm	0.18 %	0.09 %

Before testing filters on CBRN gases, the Filters M3 and Filter M4 with different active filling height, were controlled according to the quality demands for following parameters:

- filter weight (according to SORS 8829),
- inhalation resistance (according to SORS 8829),
- filtration efficiency on paraffin aerosol mist (according to SORS 8829)

and the mean of obtained results are shown in Table 2.

Table 2. The values of mean weight, inhalation resistance and filtration efficiency for filters

Filter type	Weight [g]	Inhalation resistance [Pa]	Filtration efficiency [%]
Filter M3 (27 mm)	297.8	127	1×10^{-3}
Filter M4, (27 mm)	298	129	1×10^{-3}
Filter M4, (32 mm)	327	138	1×10^{-3}
Filter M4, (39 mm)	369	151.5	1×10^{-3}

The samples of impregnated activated carbons and Filters M3 and Filter M4 with different active filling height, were satisfied all the tested required parameters, that are shown in Tables 1 and 2.^{[6],[7]}

Mentioned testing parameters were main requirement for gas testing to be continued. Comparative testing for both type of filters on above mentioned test gases, were done with the aim to justify the idea to change the recipe of impregnation and active filling height, in order to expand the existing requirement for the protection provided by the official Filter M3.

3.1. The sorption properties of Filter M3 and Filter M4 with different active filling height upon pho-sgene, chloropicrin and hydrogen cyanide challenge

All the Filters M3 and Filters M4 that successfully passed the quality control on previous testing phase, were tested with CBRN gases. Wide range of conditions (inlet concentrations, flow rates and relative humidity of gas mixture), upon which the Filter M3 (with standard impregnation recipe and active filling height of 27 mm and the Filter M4 (with altered impregnation recipe and filling height of 27 mm, 32 mm and 39 mm) are tested, gives assurance that results obtained can be taken as representative for diverse exploitation conditions of filters.

The results of comparative testing of Filters M3 and Filter M4 with different active filling height, upon phosgene, chloropicrin and hydrogen cyanide challenge are shown in Tables 3, 4, 5, 6, 7 and 8.

3.1.1. Sorption properties of Filters M3 and Filter M4 with different active filling height upon phosgene challenge.

Filter M3 (with active filling height of 27 mm) and Filter M4 (with filling height of 27 mm, 32 mm and 39 mm) were tested upon phosgene challenge, under the following

conditions:

- inlet concentration of gas mixtures: 1000 ppm and 5000 ppm
- flow rate of gas mixtures: 30 l/min and 64 l/min
- relative humidity: 25 % and 80 %.

The results of protection time for Filter M3 and Filter M4 upon phosgene challenge, under different concentrations, flow rates and relative humidity of gas mixture are shown in Table 3 and 4.

Table 3. The protection time of filters against phosgene at flow rate of 30 l/min for different inlet concentration and relative humidity gas mixture

Inlet concentration [ppm]	Relative humidity [%]	Protection time [min] Filter M3 27 mm	Protection time [min] FilterM4		
			27 mm	32 mm	39 mm
1000	25	111	107		
			127		
			143		
1000	25	110	108		
			126		
			142		
1000	80	105	102		
			119		
			137		
1000	80	106	104		
			121		
			136		
5000	25	35	28		
			35		
			40		
5000	25	34	29		
			36		
			42		
5000	80	34	25		
			33		
			37		
5000	80	33	25		
			34		
			38		

Table 4. The protection time of filters against phosgene at flow rate of 64 l/min for different inlet concentration and humidity gas mixture

Inlet concentration [ppm]	Relative humidity [%]	Protection time [min] Filter M3 27 mm	Protection time [min] FilterM4		
			27 mm	32 mm	39 mm
1000	25	75	69		
			73		
			80		
1000	25	77	67		
			72		
			82		
1000	80	72	62		
			69		
			79		
1000	80	74	60		
			68		
			78		

5000	25	15	15
			17
			19
5000	25	16	15
			17
			21
5000	80	14	18
			19
			24
5000	80	13	19
			20
			22

The results show that the influence of active filling height on the protection time for Filter M4 (changed impregnation with Zn²⁺ salt) is significant. There is a noticeable increase in protection time with an increase in active filling height of Filter M4.

The influence of phosgene flow rates on protection time for the Filter M4 considerably high, because the filter time of protect directly proportional to contact time between filter adsorbens and test gas. At testing condition of lower flow rates gas mixture, the values of results in relation to high flow rates, for the Filters M4 times protection, are significantly higher, Figure 1.

For the same active filling height of 27 mm, the protection times upon phosgen challenge for Filters M3, has some advantages comparing to Filter M4. Since salt of chrome (VI)-chloride [2] are formed on active carbon, phosgene decomposition rate with Cr⁶⁺ ions (Filter M3) are considerably higher than rate with Zn²⁺ ions (Filter M4), Figure 1.

The differences between results in Filter M4, caused by relative humidity change (25% and 80%), are not as high as in case of flow rate, inlet concentration of gas mixture as well as recipe and height of active filling filters, Figure 2.

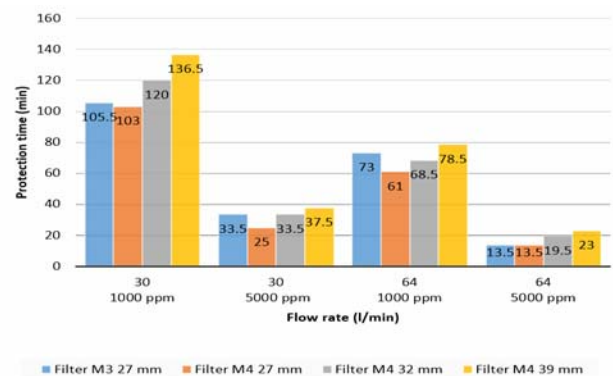


Figure 1. Influence of flow rates and inlet concentrations on protection time against phosgene for different filling heights filters at constant relative humidity of 80 %.

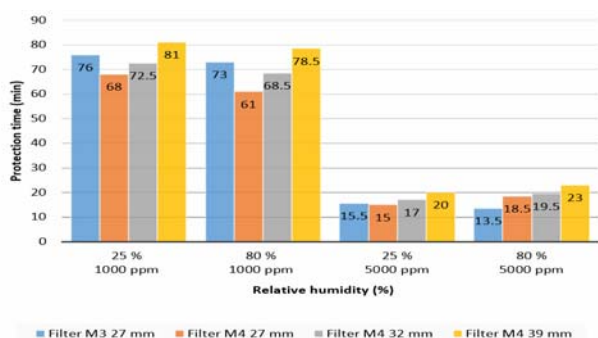


Figure 2. Influence of relative humidity and inlet concentrations on protection time against phosgene for different filling heights filters at constant flow rate of 64 l/min

3.1.2. Sorption properties of Filters M3 and Filter M4 with different filling height upon chloropicrin challenge

Filter M3 with active filling height of 27 mm and Filter M4 with height of 27 mm, 32 mm and 39 mm were tested upon chloropicrin challenge, under the following conditions:

- inlet concentration of gas mixture: 2200 ppm and 5000 ppm;
- flow rate of gas mixture: 30 l/min and 64 l/min and
- relative humidity: 25 % and 80 %.

The results of protection time for Filter M3 and Filter M4 upon chloropicrin challenge, under different concentrations, flow rate and relative humidity of gas mixture, are shown in Table 5 and 6.

Table 5. The protection time in filters against chloropicrin at flow rate of 30 l/min for different inlet concentration and relative humidity gas mixture

Inlet concentration [ppm]	Relative humidity [%]	Protection time [min] Filter M3 27 mm	Protection time [min] FilterM4				
			27 mm	32 mm	39 mm		
2200	25	26	32	38	117		
			32	40	115		
			22	36	103		
2200	80	21	20	33	102		
			32	34	48		
			5000	25	14	32	36
5000	25	14	22			26	43
5000			80			11	20
5000				80	10		20

Table 6 The protection time in filters against chloropicrin at flow rate of 64 l/min for different inlet concentration and relative humidity gas mixture

Inlet concentration [ppm]	Relative humidity [%]	Protection time [min] Filter M3 27 mm	Protection time [min] FilterM4				
			27 mm	32 mm	39 mm		
2200	25	10	12	15	20		
			11	17	19		
			2200	80	7	10	13
2200	80	7	11			14	16
5000			25			breakthrough	5
5000				25	breakthrough		5
5000	80	breakthrough					4
5000			80			breakthrough	4

The influence of relative humidity on adsorption of chloropicrin is greater than in the case upon phosgene challenge, Figure 4.

At condition of lower flow rates of gas mixture, the values of results for the Filters M4 times protection (filling height of 32 mm and 39 mm) are significantly higher. Under the extreme conditions at flow rate of 64 l/min and inlet concentration of 5000 ppm gas mixture, the value of the results for Filters M4 times protection (filling height of 32 mm and 39 mm) are some lower. However, the Filter M3 does not protect against chloropicrin Figure 3.

Decomposition and adsorption of chloropicrin on activated carbon is based on mechanism of physical adsorption (on the interfacial area) and partly by chemical decomposition of chloropicrin on impregnated carbon.

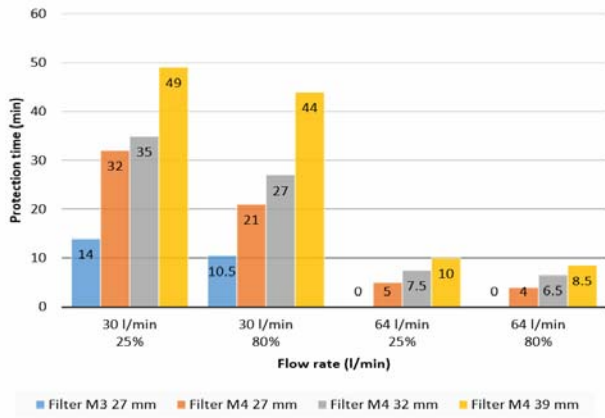


Figure 3. Influence of relative humidity and flow rate on protection time against chloropicrin for different filling heights filters at constant inlet concentration of 5000 ppm.

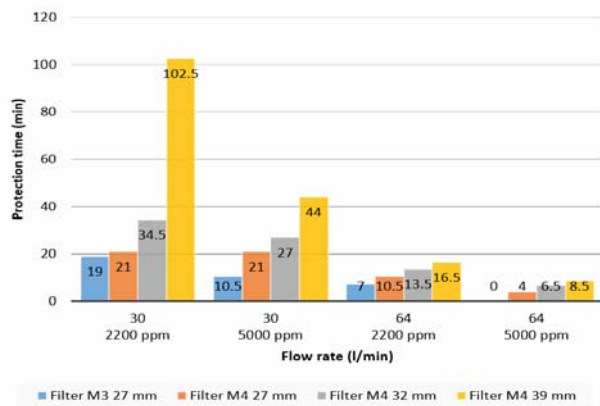


Figure 4. Influence of relative flow rate and inlet concentration on protection time against chloropicrin for different filling heights filters at relative humidity of 80 %.

3.1.3. Sorption properties of Filters M3 and Filter M4 with different filling height upon hydrogen cyanide challenge

Filter M3 with active filling height of 27 mm and Filter M4 with height of 27 mm, 32 mm and 39 mm were tested upon hydrogen cyanide challenge, under the following conditions:

- inlet concentration of gas mixture: 1000 ppm and 5000 ppm;
- flow rate of gas mixture: 30 l/min and 64 l/min and
- relative humidity: 25 % and 80 %.

The results of protection time for Filter M3 and Filter M4 upon hydrogen cyanide challenge, under different concentrations, flow rates and humidity of gas mixture, are shown in Table 7 and 8.

Table 7. The protection time in filters against hydrogen cyanide of flow rate of 30 l/min for different inlet concentration and relative humidity gas mixture

Inlet concentration [ppm]	Relative humidity [%]	Protection time [min] Filter M3 27 mm	Protection time [min] Filter M4		
			27 mm	32 mm	39 mm
1000	25	68	66	70	77
			68	72	76
			70	78	85
1000	80	72	73	77	83
			52	55	63
			55	54	64
5000	25	53	55	60	67
			58	67	73
			53	58	66

Table 8. The protection time in filters against hydrogen cyanide flow rate of 64 l/min for different inlet concentration and relative humidity gas mixture

Inlet concentration [ppm]	Relative humidity [%]	Protection time [min] Filter M3 27 mm	Protection time [min] Filter M4		
			27 mm	32 mm	39 mm
1000	25	34	33	38	45
			31	37	51
			36	45	53
1000	80	37	38	43	54
			23	27	29
			27	27	28
5000	25	26	29	31	32
			28	28	28
			29	28	29

Decomposition and adsorption of hydrogen cyanide on activated carbon is based on mechanism of chemical decomposition on impregnated active carbon (salts of cuprum (II)-cyanide are formed) and partly by physical adsorption. There is a noticeable increase in protection time with an increase in active filling height of Filter M4, Figure 5.

The differences between results in Filter M4, caused by relative humidity change (25% and 80%), are significant. At testing condition of higher relative humidity of gas mixture (80 %) the values of the Filter M4 time protection are some higher, Figure 6.

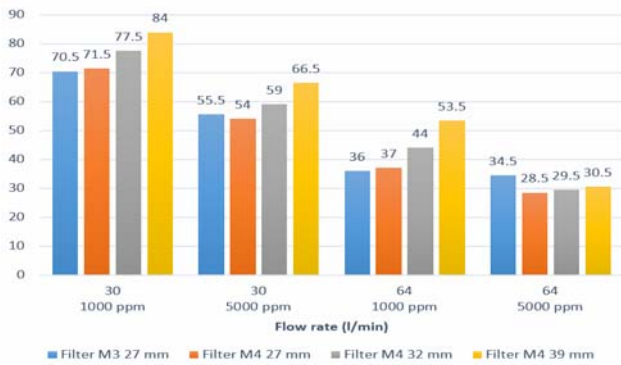


Figure 5. Influence of flow rate and inlet concentration on protection time against hydrogen cyanide for different filling height of filters at constant relative humidity of 80 %

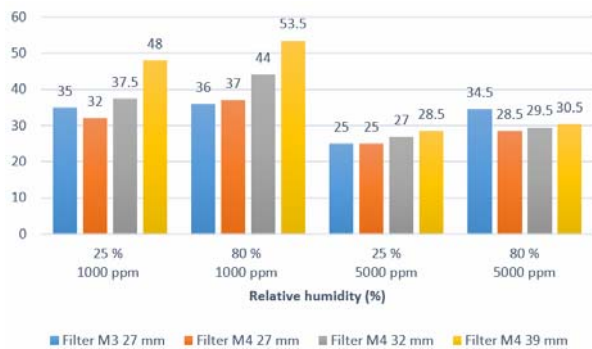


Figure 6. Influence of relative humidity and inlet concentration on protection time against hydrogen cyanide for different filling heights filters at constant flow rate of 64 l/min

3.2. The sorption properties of Filter M3 and Filter M4 upon ammonia, sulphur dioxide cyclohexane and carbon monoxide challenge

Testing methods for the time of sorption properties of the Filter M3 and the Filter M4 with different active filling height upon ammonia, sulphur dioxide, cyclohexane and carbon monoxide challenge, according to the SRPS EN 14387.

All the filters and activated carbons were satisfied required parameters of weight, inhalation resistance and filtration efficiency on paraffin aerosol mist.

The samples were tested to all above mentioned gases from SRPS EN14387 under the following test conditions.^[5]

- inlet concentration of gas mixtures: 5000 ppm

- flow rate of gas mixtures: 30 l/min and 64 l/min
- relative humidity: 70%

The obtained results are shown in Table 9. The expected the values of results for protection time for filters of two different types of impregnation, are achieved.

The results confirmed that both filter types protect against following toxic gases.

The Filter M3 did not protect against ammonia, while the Filter M4, with different active filling height, protects against ammonia. Therefore, Filter M4 with active filling heights of 32 mm and 39 mm, has slightly better protective properties then Filter M3 and Filter M4 with the same active filling heights.

Table 9. Protection time for filters against toxic compounds at flow rates 30 l/min and 64 l/min.

Inlet concentration [ppm]	Relative humidity [%]	Flow rate [l/min]	Test gas	Protection time [min] Filter M3	Protection time [min] Filter M4
5000	70	30	NH ₃	1	23
					35
					42
5000	70	30	NH ₃	1	22
					35
					43
5000	70	64	NH ₃	breakthrough	7
					17
					23
5000	70	64	NH ₃	breakthrough	8
					15
					22
5000	70	30	SO ₂	22	10
					20
					23
5000	70	30	SO ₂	22	10
					19
					25
5000	70	64	SO ₂	10	5
					11
					13
5000	70	64	SO ₂	8	4
					12
					14
5000	70	30	C ₆ H ₁₂	42,4	30
					48,6
					62
5000	70	30	C ₆ H ₁₂	43,6	26
					44,9
					59
5000	70	64	C ₆ H ₁₂	17,6	17
					21
					33
5000	70	64	C ₆ H ₁₂	16,3	18
					21
					31
5000	70	30	CO	0	0
					0
					0
5000	70	30	CO	0	0
					0
					0

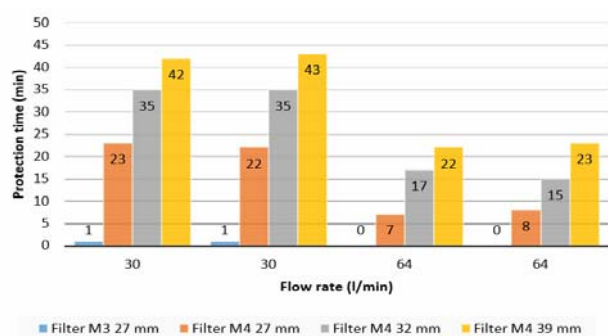


Figure 7. Influence of flow rate on protection time against ammonia for different filling heights of filters at relative humidity of 80 % and inlet concentration of 5000 ppm

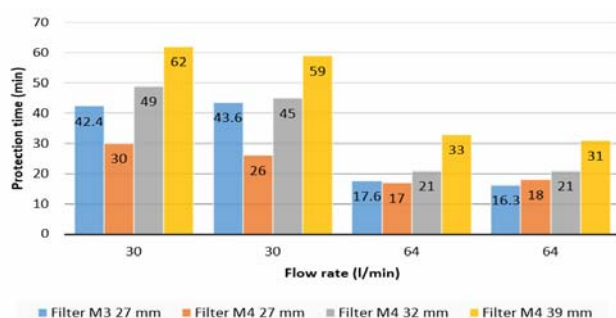


Figure 8. Influence of flow rate on protection time against cyclohexane for different filling heights filters at relative humidity of 80 % and inlet concentration of 5000 ppm

4. CONCLUSION

The aim of this work was to analyze the protection time of Filters M4 (loaded with Zn^{2+} impregnated activated carbon) with different filling height of 27 mm, 32 mm and 39 mm and official Filter M3 (loaded with Cr^{6+} impregnated activated carbon) against several different CBRN gases as well as industrial toxic chemical. Filters were tested upon gasses challenge, under the different conditions of inlet concentrations, flow rates and relative humidity of gas mixtures, in order to examine the validity of the idea replacing the active filling height of the official Filter M3 with the most optimal one (impregnated with Zn^{2+} salt instead Cr^{6+}) with the aim to expand the existing requirement for the protection provided by the Filter M3.

The obtained results have shown that there are differences in the protection time of Filter M4 with different filling height (of 27 mm, 32 mm and 39 mm) and official Filter M3. The influence of active filling height on the protection time upon all CBRN gasses challenge in Filter M4 is significant. There is a noticeable increase in protection time with an increase in active filling height of Filter M4, which is specifically expressed under conditions of lower values inlet concentrations and flow rates gas mixtures. This can be explained by the

mechanism of physical adsorption (on the interfacial area of active carbon) and partly by chemical decomposition.

Both filters were also examined against the toxic industrial chemicals according to SRPS EN 14387 standard, and proved that satisfactory protection was achieved upon sulphur dioxide and cyclohexane challenge, except upon carbon monoxide challenge.

It is especially important that protection against ammonia is provided by Filter M4, which is not the case by Filter M3. Ammonia is gas which is easily accessible, which makes it eligible for system paralyzing or provoking general danger against people.

Based on the tested and satisfied all required physical mechanical parameters for Filter M4 of filling height of 32 mm (mean weight and inhalation resistance) and taking into account the Filter M4 with mentioned filling height, provide protection against CBRN contaminants as well as industrial toxic chemicals, including the ammonia, we can reliably claim that Filter M4 (with filling height of 32 mm, impregnated with Zn^{2+} salt) has advantages compared to official Filter M3 (with filling height of 27 mm, impregnated with Cr^{6+} salt).

Based on the obtained results for protection time of the Filter M4 and Filter M3 against carbon monoxide gas (breakthrough), in the following period, work will be done on changing the composition of the active filling in the mentioned filters (based on hopcalite) with the aim to expand the existing requirement for the protection provided by the tested filters.

References

- [1] Impact of the altered texture of the active filling of the filter on the sorptive characteristics with the special reference to the efficiency of filtering, by Ilic M, SenicŽ, Petrović V, Mihajović B, Grković V
- [2] Adapted from Smisek, M. and Cerny, S., in *Active Carbon*, Elsevier Publ. Co., Amsterdam, 1970; and Jankowska H., Swiatkowski A., and Choma, J., in *Active Carbon*, Ellis Howard, England, 1991. With permission
- [3] Letal Mists, Eric. R.Tylor, An Introduction to the natural and Militar Sciences of Chemical, Biological Warfare and Terrorism
- [4] SORS 8748:2004, Personal CBRN protect device, Requirements and methods testing
- [5] SRPS EN 14387:2013, Respiratory protective devices- Gas filter(s) and combined filter(s)-Requirements, testing, marking, Institute for Standardization of Serbia.
- [6] SORS 8829:2005, Filter, Combined filter M3, Requirements and methods testing
- [7] SORS 8830:2005, Personal CBRN protect device, Active carbon KI M3 for combined filter, Requirements and methods testing

INFLUENCE OF PRODUCTION PARAMETERS ON THE QUALITY OF SEMIFINISHED RIFLED PISTOL BARRELS

MAJA MLADENović

Military Technical Institute, Belgrade, mmaja011@gmail.com

NADA ILIĆ

Military Technical Institute, Belgrade, nadalic67@vti.vs.rs

JOVANA MANDIĆ

Military Technical Institute, Belgrade, jmandic96@gmail.com

IGOR RADISAVLJEVIĆ

Military Technical Institute, Belgrade, radisavljevicigorbg@gmail.com

SLOBODAN ILIĆ

Directorate of Standardization, Codification and Metrology, Belgrade, slobodan.s.ilic@gmail.com

Abstract: In this paper several semi-finished rifled pistol barrels produced with different parameters were examined. The goal of the investigation was to determine the optimal production parameters for the barrels. Visual examination, microscopic analysis, SEM/EDS analysis and hardness tests were performed. The material of the barrels is 42CrMo4 steel. The caliber of the barrel is 9mm, and spiral grooves at the inside surface of the barrels were observed. Micro-cracks at the groove roots and geometrical deviances of the grooves were revealed in the specimens that were heat-treated by quenching and tempering. This indicates that improper rifling and/or heat treatment parameters were used during the production process for these specimens. On the specimen heat-treated by austenitization + continuous cooling no micro-cracks and geometrical deviances were observed, indicating that these heat treatment parameters are optimal for the subsequent process of rifling.

Keywords: pistol barrel, rifling, heat treatment

INTRODUCTION

Rifling is a process of making spiral-shaped grooves in the inside surface of a gun barrel [1]. The purpose of these helical grooves is to give a spin to the projectile, thus stabilizing it and improving accuracy of the gun. Technical drawing of the investigated barrels that shows the required geometry of the grooves is shown in Figure 1.

The main objective of this paper is to determine the cause of defects on the spiral grooves inside the pistol barrels, as well as to determine the optimal production parameters for the barrels, specifically in regard to the quality of the spiral grooves produced in the process of rifling.

1. EXPERIMENTAL WORK

1.1. Material and technology

Initial investigation was performed on three barrel specimens (specimens A, B and C), each in different stages of the production. A fourth barrel was produced after adjustments of production parameters and a specimen taken from this barrel was subsequently examined (specimen D). The specimens are shown in Figure 2. The examined semi-finished pistol barrels were made of steel 42CrMo4 / SRPS EN 10083-3. The heat treatment of the barrels A, B and C consisted of

austenitization at 850°C for 10 minutes, quenching in water, and tempering at 680°C for 1.5 hours. The heat treatment of specimen D consisted of austenitization at 850°C for 10 minutes and continuous cooling to 500°C for 10 minutes. The center of the barrels is drilled and rifled to a caliber of 9 mm.

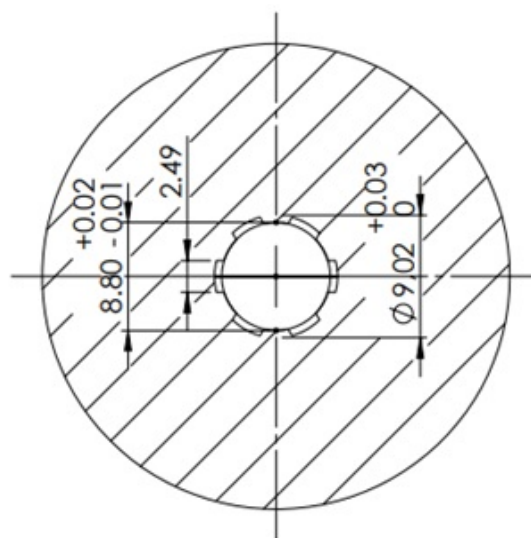


Figure 1. Technical drawing of the perpendicular plane projection of the pistol barrels.

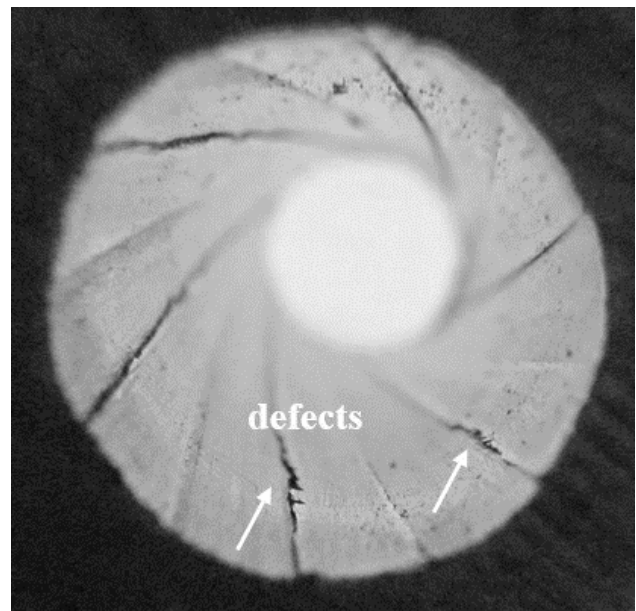
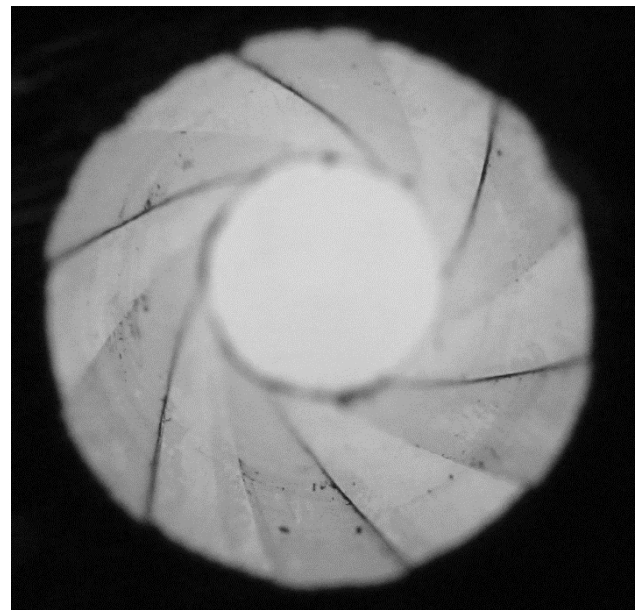
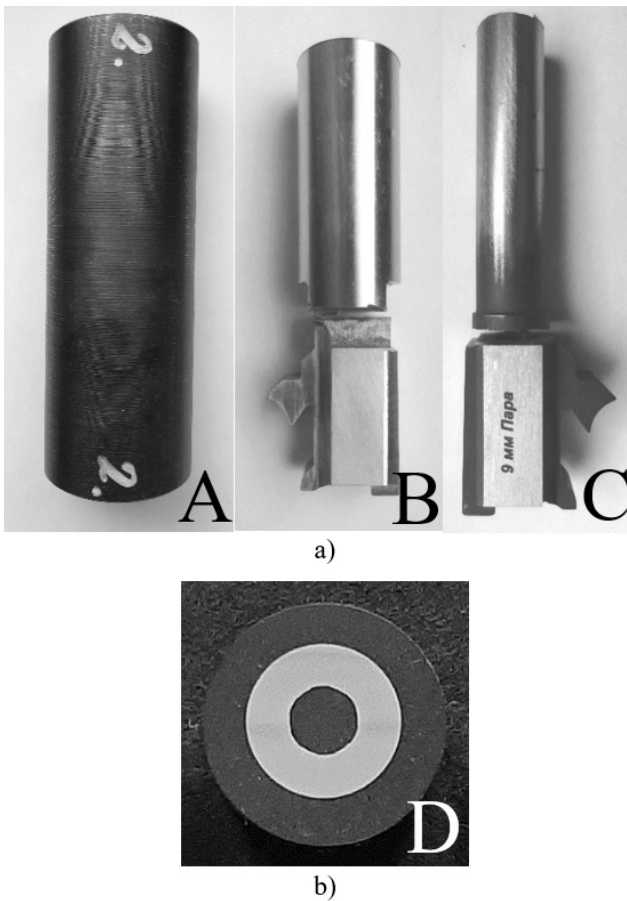


Figure 2. Pistol barrel specimens. (a) Initially examined pistol barrels A, B and C, in three different stages of barrel production. (b) Sample D cut in perpendicular direction from the subsequently produced pistol barrel.

a)

b)

b)

Figure 3. Inner surface of barrels (a) B without defects and (b) C with present defects.

1.2. Methods

Visual observation performed by naked eye and magnifying glass, and was documented with photographs.

The chemical composition of the pistol barrels A, B and C was analyzed by Optical Energy Spectrometer (OES) Belec Compact Port.

Hardness of all barrel samples was measured by Rockwell method (HRC), according to SRPS EN ISO 6508-1 [2].

In order to investigate the microstructure, samples were cut in perpendicular direction from the pistol barrels and prepared by grinding and polishing, followed by etching. A 3% nital etchant was used to reveal the microstructure. The polished and etched surfaces were examined using light microscopy, as well as scanning electron microscopy (SEM-JSM 6610 LV). An EDS analysis of an observed surface layer was performed on specimen C.

3. RESULTS

3.1. Visual examination

Visual examination of the inner surface of the barrels showed that the spiral grooves on the specimen C have defects. Such defects were not observed on specimens A, B and D. The spiral grooves as observed on specimens B and C are shown in Figure 3.

3.2. Chemical composition

The chemical composition of the specimens A, B and C are given in Table 1. Results showed that chemical composition of the pistol barrels is according to the chemical composition of steel 42CrMo4 as required by the standard SRPS EN 10083-3 [3].

Table 1. Chemical composition of the specimens A, B and C.

element	mass%		
	A	B	C
C	0.46	0.39	0.43
Si	0.24	0.24	0.23
Mn	0.84	0.78	0.78

P	0.017	0.013	0.011
S	0.027	0.007	0.003
Cu	0.25	0.17	0.18
Al	0.033	0.03	0.017
Cr	1.05	0.98	0.98
Mo	0.21	0.17	0.17
Ni	0.11	0.08	0.08
Fe	bal.	bal.	bal.

3.3. Hardness

Results of the hardness measurements of the specimens A, B, C and D are given in Table 2.

Table 2. Hardness of the pistol barrels, HRC.

specimen	Hardness, HRC			average
A	24.9	25.0	26.5	26
B	21.9	22.2	21.4	22
C	27.6	28.5	28.8	28
D	24.3	25.7	24.2	25

3.4. Microstructure

Micro-structural analysis of the specimens A, B and C as polished revealed cracks propagating from the sharp groove corner to the inner side of the barrels, Figure 4. Cracks length around 100 μm were observed on every groove on the specimens. The presence of cracks probably caused the macroscopic defects of the spiral grooves on specimen C. The angle of the groove corners is acute. It was also observed that the groove depth does not meet the requirements of the technical drawing of the barrels.

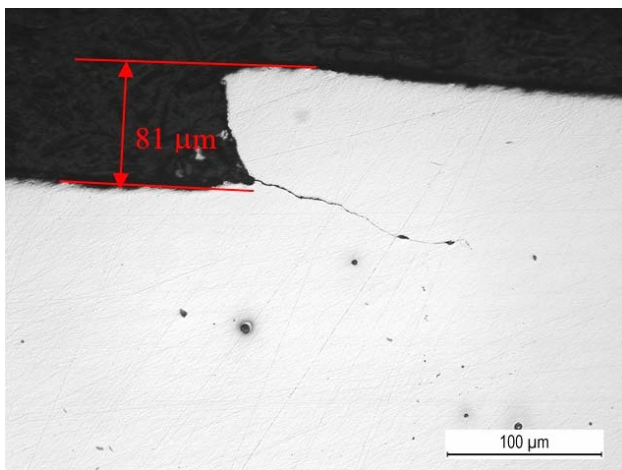


Figure 4. Microstructure of specimen A, as polished. Cracking at the groove corner.

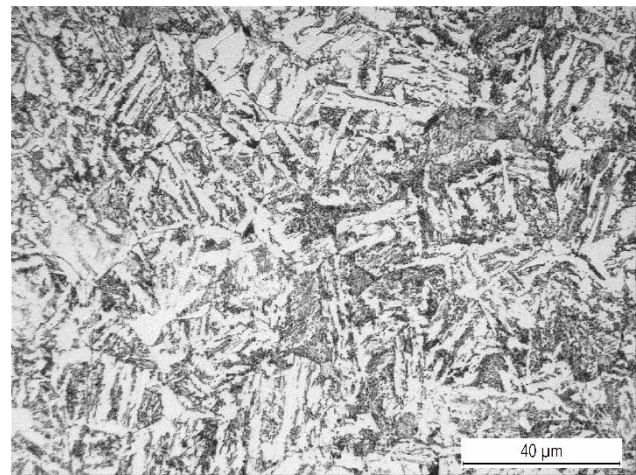


Figure 5. Microstructure of specimen B, etched.

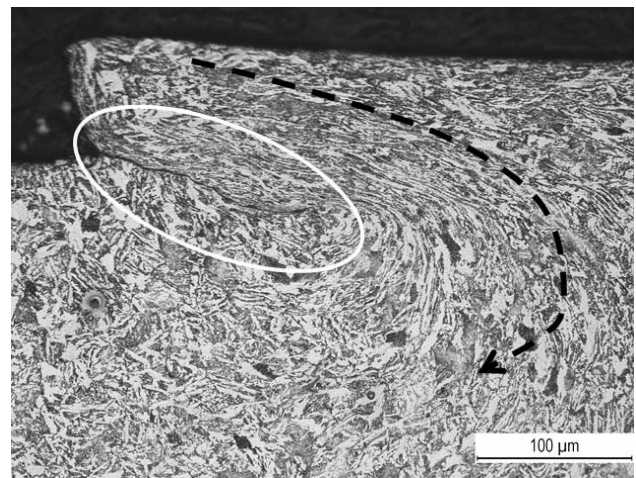


Figure 6. Microstructure of specimen A in the groove zone. The arrow indicates the material flow direction. Encircled is the crack at the groove corner.

Microstructure of the specimens A, B and C is tempered martensite, with a few visible ferrite grains. Figure 5 shows the microstructure of specimen C after etching.

Significant material flow in the groove zone was observed on specimens A, B and C, Figure 6. The cracks on the grooves appear to follow the material flow direction.

Presence of a surface layer was observed on specimen C, Figure 7. This layer is also present around the groove cracks.

Figure 8 shows the microstructure of specimen D, as polished. No cracks were observed at the grooves. The grooves are of sufficient depth, as required by the technical drawing of the barrels (Figure 1).

The microstructure of etched specimen D is shown in Figures 9 and 10. The microstructures consist predominately of fine pearlite and ferrite grains. The material flow around the groove corners is less pronounced than in specimens A, B and C.

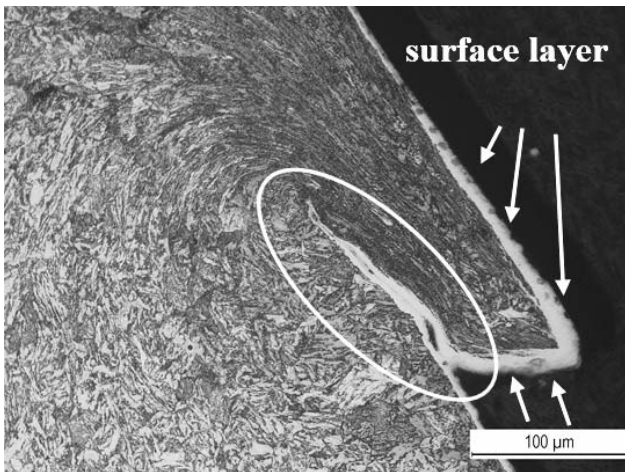


Figure 7. Microstructure of specimen C, etched. Encircled is the crack at the groove corner.

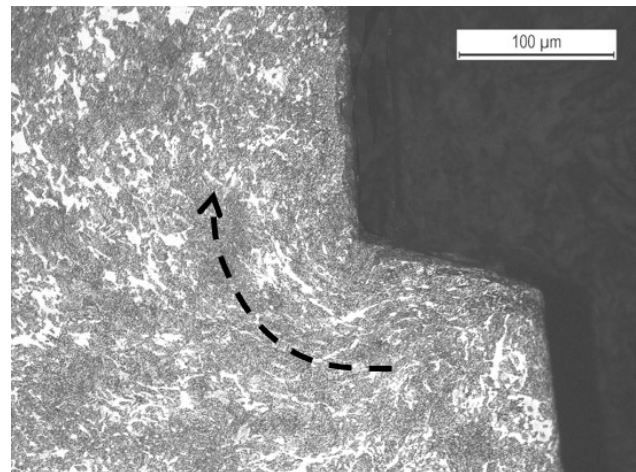


Figure 10. Microstructure of specimen D in the groove zone. The arrow indicates the material flow direction.

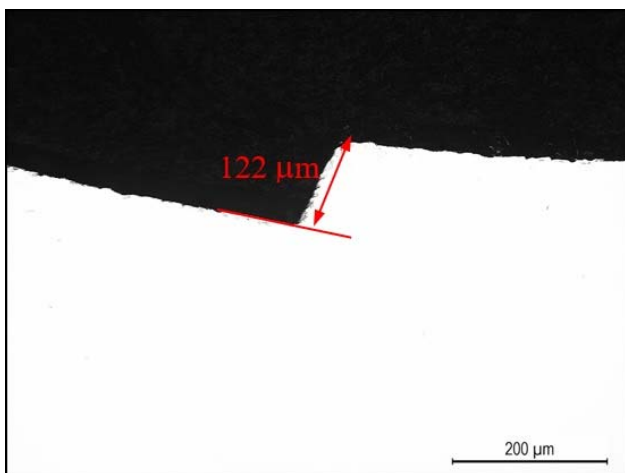


Figure 8. Microstructure of specimen D, as polished.

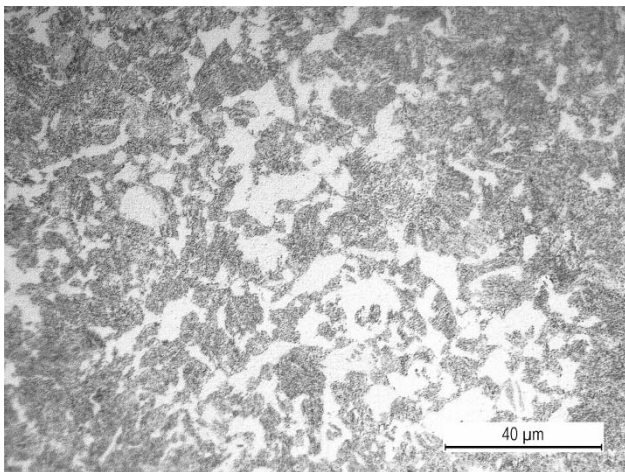


Figure 9. Microstructure of specimen D, etched.

3.5. SEM / EDS analysis

SEM and EDS analysis of specimen C identified the presence of a nitrogen-rich surface layer on the inner side of the pistol barrel, Figures 11 and 12. The nitride layer thickness is between 12 and 19 μm. The EDS analysis results are shown in Table 3.

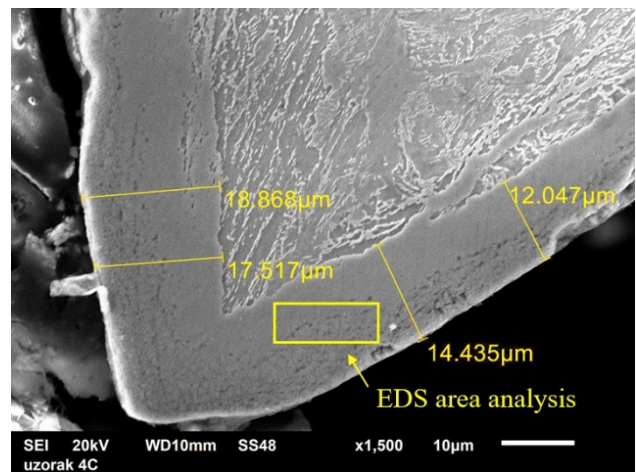


Figure 11. Microstructure of the groove tip zone on specimen C, as observed by scanning electron microscopy.

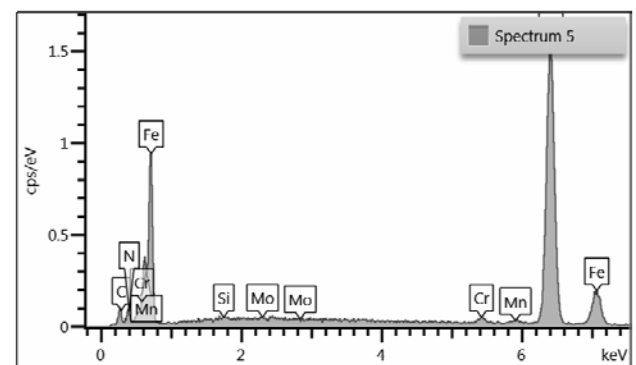


Figure 12. EDS analysis of the surface layer shown in Figure 11.

Table 3. Results of EDS analysis of the surface layer observed on specimen C.

Element	mass %
C	7.74
N	4.63
Si	0.07
Cr	0.87
Mn	0.62
Fe	85.65
Mo	0.41
total	100.00

4. DISCUSSION

The presence of cracks propagating from the spiral groove corners on each groove of specimens A, B and C, as well as the insufficient groove depth indicate that the material temper is not adequate for the rifling process. As a consequence, micro-cracks visible in early stages of production (specimens A and B) developed into macroscopic defects of the spiral grooves, as observed on specimen C. The acute angle of the grooves most likely contributed to the appearance of cracks [4].

The hardness of all specimens is in accordance with their respective microstructure [6]. A possible cause of the higher hardness of specimen C lies in the process of surface hardening that was performed on the specimen.

The microstructure of etched specimens A, B and C is in accordance with microstructure of steel 42CrMo4 in quenched and tempered condition [5,6]. There was significant material flow around the corners of the grooves, as a consequence of a rifling process involving cold deformation. The surface layer observed on specimen C is a consequence of a surface hardening process [7]. SEM/EDS analysis of specimen C confirmed the presence of a nitride layer on the barrel inside. This layer is also present around the groove cracks, indicating that the cracking occurred before the process of nitrating. The accicularity of the tempered martensite microstructure, as well as significant material deformation around the corners of the grooves, are factors that contributed to making the material more susceptible to cracking.

Microstructure of specimen D consisted of fine pearlite and ferrite grains [5,6]. Material flow in the groove zone

is less pronounced than on specimens A, B and C. No cracking was observed at the groove corners on specimen D. The groove shape and depth meet the geometrical requirements.

5. CONCLUSION

Micro-cracks at the groove roots and insufficient groove depth were revealed on 9mm cal. rifled pistol barrels that were heat treated by quenching and tempering prior the rifling process. This indicated that the material temper and its resulting microstructure is not adequate for the rifling process.

In order remedy the observed defects, a further barrel (specimen D) was produced with different heat treatment parameters (austenitization + continuous cooling) and examined. No fractures at the grooves were observed on specimen D, and the microstructural analysis showed less pronounced material flow on the barrel inside and a better geometry of the grooves than on quenched and tempered specimens. It can be concluded that the production parameters of pistol barrel D are appropriate for the process of rifling.

References

- [1] SUN J., CHEN G., QIAN, L., LIU, T., *Analysis of Gun Barrel Rifling Twist*, Materials Science, Energy Technology, and Power Engineering I, AIP Conf. Proc. 1839, 020096-1-020096-11, 2017.
- [2] SRPS EN ISO 6508-1 - *Metallic materials -- Rockwell hardness test -- Part 1: Test method (scales A, B, C, D, E, F, G, H, K, N, T)*.
- [3] SRPS EN 10083-3 - *Steels for quenching and tempering – Part 1: General technical delivery conditions*.
- [4] ASM Metals Handbook, *Failure Analysis and Prevention*, Vol.11, 9th Ed. ASM Metals Park Ohio, 1986.
- [5] ASM Metals Handbook, *Metallography and Microstructures*, Vol.9, 9th Ed., ASM Metals Park Ohio, 1985.
- [6] SCHRADER, A., ROSE, A., *De Ferri Metallographia II, Structure of Steels*, Verlag Stahleisen m. b. H., Düsseldorf, 1966.
- [7] ASM Metals Handbook, *Heat Treating*, Vol.4, ASM International Materials Park Ohio, 1991.



MECHANICAL CHARACTERISTICS OF ALUMINIUM SANDWICH PANELS WITH ALUMINIUM HONEYCOMB CORE

JELENA MARINKOVIĆ

Military Technical Institute, Belgrade, jecamarinkovic@gmail.com

IGOR RADISAVLJEVIĆ

Military Technical Institute, Belgrade, radisavljevicigorb@gmail.com

SRDJA PERKOVIĆ

Military Technical Institute, Belgrade, srdja.perkovic@vti.vs.rs

Abstract: The paper presents the results of testing the mechanical properties of aluminium sandwich panels with aluminium honeycomb core. The tests were performed under quasistatic conditions and monitored changes in mechanical characteristics at different crosshead speed rates. Determined mechanical characteristics were: FLATWISE Compressive Strength, EDGEWISE Compressive Strength and Flexural Properties of Sandwich Constructions (Flexural Stiffness and Core Shear Modulus). For tests were used aluminium panels different thicknesses (6,00 mm, 10,00 mm, 15,00 mm, 20,00 mm and 30,00 mm) and three test speeds were applied (6,00 mm / min, 200,00 mm / min and 400,00 mm / min). The results showed that there is no spread of deformation on the surface of the material and transfer along the core, so the deformation is exclusively of local character. This showed that the honeycomb core is an extremely good material in localizing deformation and has a positive effect on preserving the integrity of the remaining part of the structure that was not under the direct influence of external forces. It has been shown that in the case of deformation of the panel along the edge, the main load carrier is the surface sheet, while the core is a weak component of the system in the case when the sandwich panel is pressed or bent on the surface. Also, it was shown that between different test speeds applied on one panel thickness, there is no large deviation in the obtained maximum material strengths for a given mechanical characteristic.

Keywords: aluminium panel, honeycomb core, deformation.

1. INTRODUCTION

One of the composite structure types, aluminium sandwich panels with metal core in the form of honeycombs first appeared in the late 1940s for the needs of the aircraft industry. Adhesively bonded, aluminium sandwich panels with a honeycomb core provided designers with a lightweight, strong, fatigue-resistant and aerodynamic material. Today's application of aluminium sandwich panels in aircraft secondary structures has progressed from the trailing edges of control surfaces to the entire assembly, including cargo doors, engine buffers, etc. [1]. Besides aircraft industry, these panels are widely used in the automotive, civil engineering and military industries due to their high load capacity combined with excellent energy dissipation properties [2]. Because of their characteristics, they have outstanding potential for ballistic purposes because they can absorb strong shock waves, retain fragments, they are light and portable. Compared to common materials used for kinetic absorption, composite materials provide an extra lightweight modular solution with low space consumption [3]. In addition, they can be easily repaired and replaced, which is very important in the field. Besides, they should be resistant to fire, they must withstand greater loads or be able to absorb greater vibrations, etc. Sandwich

constructions, compared to conventional materials, provide the following key advantages: very low weight, high stiffness, durability, cost efficiency [4].

Sandwich construction generally consists of two facing sheets with a light core between them, Figure 1. These panels have the highest strength-to-weight ratio, unmatched by any other structural material. Their mechanical properties are controlled by the thickness of the facings and the characteristics of the honeycomb core (by the thickness the material foil from which core was made and also by the size and shape of the honeycombs themselves) [4]. As you can see in Figure 1, a sandwich panel with a honeycomb core consists of [2, 5]:

1. Face sheet – two thin plates,
2. Core – widely used honeycomb core – layer between two thin facings which also transfers the load from one to the other plate,
3. Adhesive - the primary role in joining the core and facings into a single structural unit and ensuring the rigidity and stability of the core.

Facing sheets are most often made of aluminium alloys, high strength steel, titanium alloys or composites [6]. The main role of the facings is to ensure the required strength and stiffness of the panel under conditions of axial loading, bending and shearing within it.

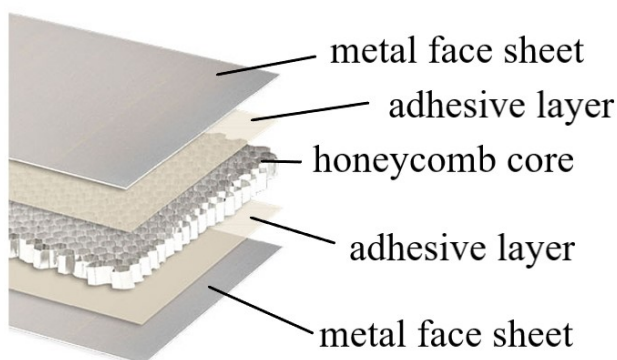


Figure 1. Layers of the aluminium sandwich panel

In order to meet the requirements and operating conditions for which facings are intended, it is also necessary to select adhesive in order to achieve a rigid connection between facings and the core. In addition to the basic load-bearing function, the selection of the facing material is also influenced by the required qualities for the surface of the panel itself. Accordingly, the given material must meet the requirements of roughness, wear resistance and corrosion resistance. In structural panels, both facing sheets usually have same thickness and such panels are called symmetrical sandwich panels. If the facings have different thicknesses (due to the requirement for different load on the panel itself), then they are asymmetric sandwich panels. Sheet thicknesses can range from 0,25 mm to 40,0 mm. In aluminium sandwich panels facing are usually made of high strength aluminium alloys from 7xxx and 2xxx series (alloys EN AW 7075, EN AW 2024, EN AW 2014,...), but also and from 5xxx series (EN AW 5083, EN AW 5754,...) [1, 3-6].

The core can be [3,6,7,8]:

1. The shape of honeycomb – made of thin foil strips in order to form a honeycomb. In the case of making a metal core, the most commonly used material is aluminium alloy EN AW 3003, but EN AW 5052, EN AW 5056, EN AW 2024 are also used. Honeycombs can be of different shapes, of which four are basic: hexagonal, circular, triangular and square. Conventional hexagonal honeycombs are commonly used for sandwich cores.
2. Foam or solid material as filling - cores made of these materials are cheap and involve the use of wood or some polymer foam.
3. Profiled core - these cores are made of some perforated profiled sheet.

In addition to connecting the core and surface sheets, the adhesive in sandwich panels also has the function of transferring shear and axial loads to and from the core. It should withstand the applied force and ensure that the connection between the core and the sheets does not break during exploitation. The adhesion for sandwich panels is chosen so that it has high strength and high binding power because it must bear a certain load. In most cases, when designing structures, core fractures (i.e., on the walls of the honeycombs themselves) represent more favorable

cases than fracture at the point of attachment of components (i.e., fracture on the bonding agent). In accordance to that, the type of binding core is chosen adhesive should require high strength and a strong bond with minimal surface contact at the ends of the core material [6,8].

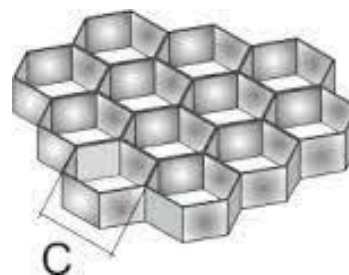
2. EXPERIMENTAL WORK

2.1. Material

For the purpose of testing were used "LARCORE" aluminium panels from the Spanish manufacturer "Alucoil". For tests were used aluminium panels in 5 different thicknesses (6,0 mm, 10,0 mm, 15,0 mm, 20,0 mm and 30,0 mm). The basic characteristics of the whole panel as well as its individual components (facings, core and adhesive) were obtained from the manufacturer [9]. Table 1 gives an overview of the dimensions of the used panels, while Figure 2 shows a schematic representation of the characteristic. As you can see in Figure 2, the mark "c" represents the size of the honeycomb, the mark "b" corresponds to the total thickness of the sandwich panel, while the marks "e₁" and "e₂" indicate the thickness of the surface sheets.

Table 1. Overview of aluminium panels with honeycomb core

Sandwich panel	Panel thickness, b	Facings thickness, mm	
		e ₁	e ₂
1	6,0 mm	1,0	0,5
2	10,0 mm	1,0	0,5
3	15,0 mm	1,0	1,0
4	20,0 mm	1,0	1,0
5	30,0 mm	1,0	1,0



a) honey comb



b) panel cross section

Figure 2. Dimensions of the panel

In accordance to manufacturer's specification:

- facings are made of aluminium alloy EN AW 5754
- honeycomb core is made of aluminium alloy EN AW 3005; foil thickness 70 μm; honeycomb size c=9,52 mm.

2.2 Mechanical tests

The tests were performed at room temperature on an electromechanical tension/pressure test machine "Schenck-Trebel RM100" with a maximum load of 100kN with a computer system for data acquisition. Four different mechanical tests were performed in quasistatic condition with constant speed. Applied crosshead speed rates were 6,0 mm/min, 200,0 mm/min and 400,0 mm/min. Test specimens for all tests were taken from a direction parallel to the long side of the panel. The dimensions of the test specimens are in accordance to the applied standard and depend on panel thickness.

2.2.1. Flatwise compressive test

The test method is used to determine the compressive strength of a sandwich panel in the direction normal to its surface. The test was performed in accordance with the standard ASTM C365 - Standard Test Method for Flatwise Compressive Properties of Sandwich Cores [10]. The test results represent the mean value of at least 3 test specimens.

2.2.2. Edgewise compressive test

The test method is used to determine the compressive strength of a sandwich panel in the direction normal to its edge. The test was performed in accordance with the standard ASTM C364 - Standard Test Method for Edgewise Compressive Strength of Sandwich Constructions [11]. The test results represent the mean value of at least 3 test specimens.

2.2.3. Three and four point bending tests

The bending test was performed using two different methods - 3-point bending (single-point midspan load) and 4-point bending (two-point load). The test method is used in order to evaluate the strength of the panel when the load is introduced locally on the sandwich panel. The test was performed in accordance with the standard ASTM C393 - Standard Test Method for Flexural Properties of Sandwich Constructions [12]. Unlike the previous tests, here the bending test was performed at only one applied crosshead speed rate, namely 6,0 mm/min. The test results represent the mean value of at least 3 test specimens.

The distance between the supports during the 3-point and 4-point bending tests was $L=130,0$ mm.

The 3-point bending test was performed by placing the support points according to the scheme given in Figure 3.

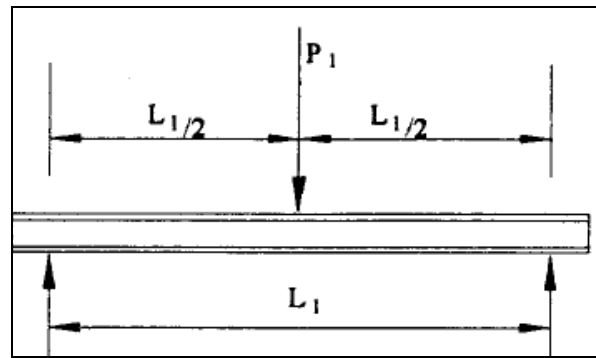


Figure 3. Schematic representation of 3-point bending – midspan loading

Based on the gain test results after 3-point test, calculation of flexural properties for sandwich panels and core materials can be written as follows [12]:

Core shear stress:

$$\tau = \frac{P}{(d+c) \cdot b} \quad (1)$$

where:

τ – core shear stress, MPa

P_{max} – max load, N

d – sandwich panel thickness, mm

c – core thickness, mm

b – sandwich width, mm.

Facing bending stress – calculate the facing bending stress as follows:

$$\sigma = \frac{P \cdot L}{2t \cdot (d+c) \cdot b} \quad (2)$$

where:

σ – facing bending stress, MPa

t – facing thickness, mm

L – span length, mm

Total sandwich beam deflection calculate as follows:

$$\Delta = \frac{P \cdot L^3}{48D} + \frac{P \cdot L}{4U} \quad (3)$$

where:

Δ – total beam midspan deflection, mm

G – core shear modulus, MPa

E – facing modulus, MPa

D – panel bending stiffness, N mm²

U – panel shear rigidity, N

Since facings were made of the same alloys but different thicknesses (at sandwich panels of 6,0 mm and 10,0 mm total thickness), this must be taken into account when calculating the coefficient D . Accordingly, to calculate D for sandwich panels:

1. for total thickness 6,0 mm and 10,0 mm

$$D = \frac{E \cdot t_1 E \cdot t_2 (d+c)^2 \cdot b}{4(E \cdot t_1 + E \cdot t_2)} \quad (4)$$

2. for total thickness 15,0 mm, 20,0 mm and 30,0 mm

$$D = \frac{E(d^3 - c^3) \cdot b}{12} \quad (5)$$

Panel rigidity calculate as follows:

$$U = \frac{G(d+c)^2 \cdot b}{4c} \quad (6)$$

The four-point bending test was performed by placing the support points according to the scheme given in Figure 4.

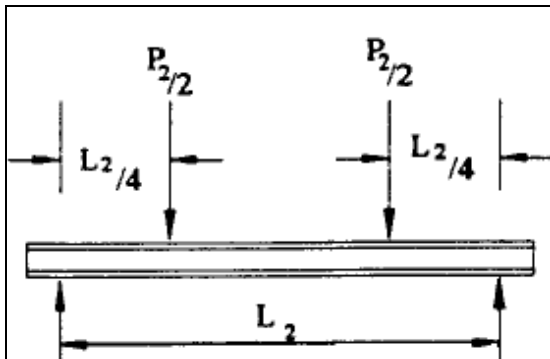


Figure 4. Schematic representation of 4-point bending – two-point loading

Calculation of flexural properties for sandwich panels and core materials after 4-point bending test can be written as follows [12].:

Core shear stress is calculate in accordance with equation 1.

Facing bending stress – calculate the facing bending stress as follows:

$$\sigma = \frac{P \cdot L}{4t(d+c) \cdot b} \quad (7)$$

Total sandwich beam deflection calculate as follows:

$$\Delta = \frac{11P \cdot L^3}{768D} + \frac{P \cdot L}{8U} \quad (8)$$

The determination of D and U values is performed in accordance with relations 4, 5 and 6.

If deflection of the same sandwich panel are determined under central load (3-point bending) and also under total load applied at 4-point bending, the flexural stiffness D and core shear modulus G may be determined from simultaneous solution of the deflection equation as follows:

$$D = \frac{P_1 L_1^3 \left[1 - \left(\frac{11L_2^2}{8L_1^2} \right) \right]}{48\Delta_1 \left[1 - \left(\frac{2P_1 L_1 \Delta_2}{P_2 L_2 \Delta_1} \right) \right]} \quad (10)$$

$$G = \frac{P_1 L_1 c \left[\frac{8L_1^2}{11L_2^2} \right]}{\Delta_1 b (+c)^2 \left[\left(\frac{16P_1 L_1^3 \Delta_2}{11P_2 L_2^3 \Delta_1} \right) - 1 \right]} \quad (11)$$

3. RESULTS AND DISCUSSION

During the tests it has been noticed that in the case of panels total thickness of 6,0 mm, a greater adhesive wetting on the walls of the honeycomb core compared to the other tested panel thicknesses. This was probably occurred during the panel production process itself. This is important because in case of panel 6,0 mm it cannot be precisely estimate what is the contribution to strength due to over wetting honeycomb core walls. It cannot be distinguished contribution of adhesive to strength of sandwich panel.

Also, it was shown that there is no great deviation in the obtained maximum strengths of the material for a given mechanical characteristic between different applied crosshead speed rates for the observed thickness of the panel. This confirms that the characteristics of sandwich panels are influenced by the mechanical characteristics of the alloy chosen for the facings because it is the carrier of strength. As mention above, facings at used sandwich panels, are made of aluminium alloys, which are known to be unaffected by deformation rates, so tacking that into account obtained results are expected.

3.1. Flatwise compressive test

Figure 5 shows the appearance of the specimen for flatwise compressive testing with the normal load to the surface of the aluminium sandwich panel.

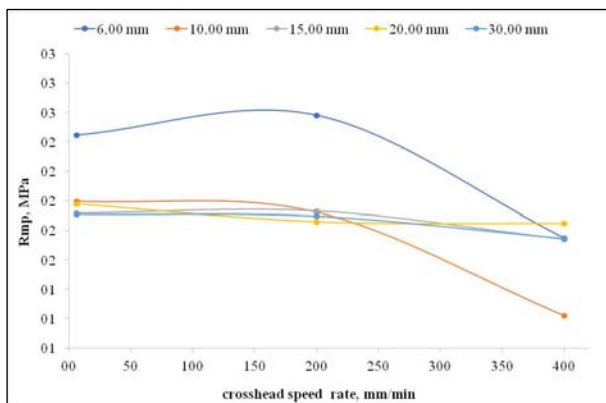
The test results are given in Table 2, while Figure 6 shows the dependence of the maximum compressive strength (Rmp) for different crosshead speeds.



Figure 5. Sample during the flatwise compression test

Table 2 Results from flatwise compressive test

Panel thickness, mm	Crosshead speed rate, mm/min	Fmp, kN	Rmp, MPa
6,0	6,0	17,7	2,4
	200,0	18,7	2,6
	400,0	12,6	1,7
10,0	6,0	14,4	2,0
	200,0	13,9	1,9
	400,0	8,8	1,2
15,0	6,0	13,9	1,9
	200,0	14,0	1,9
	400,0	12,6	1,7
20,0	6,0	14,3	2,0
	200,0	13,4	1,9
	400,0	13,4	1,8
30,0	6,0	13,8	1,9
	200,0	13,7	1,9
	400,0	12,6	1,7

**Figure 6.** The dependence of the maximum compressive strength (Rmp) for different crosshead speed rates for each panel thickness.

The obtained results indicate that the change in the crosshead speed has almost no effect on the compressive strength of sandwich panels. Also, the compressive strength does not depend on the change in the thickness of the sandwich panel. Based on the test results, it can be seen that the mean value of compressive strength for almost all thicknesses and crosshead speeds is about 1.9 MPa. The mean compressive strength for the 6.0 mm panel thickness is 2.4 MPa, 2.6 MPa and 1.7 MPa for 6.0 mm/min, 200.0 mm/min and 400.0 mm/min crosshead speed rates respectively. The given results are expected because it is a characteristic of the facing material itself [13]. Based on this, it can be concluded that the flatwise compressive strength of aluminium sandwich panels depends only on the mechanical characteristics of the alloy from which it is made. These results were also obtained by other authors [7,14,15].

In addition to the above, the tests showed that the core is the weakest part of the aluminium sandwich panel, because the yielding first occurred in it. Specimens inspection after test revealed yielding in an area that corresponds to half the height of the honeycombs themselves, figure 7. Yielding was observed between the honeycomb cell walls.

**Figure 7.** Appearance of the specimen after flatwise compression testing

3.2. Edgewise compressive test

Figure 8 shows the test specimen before edgewise compressive testing. The test results are given in Table 3, while Figure 9 shows the dependence of the maximum compressive strength (Rmpi) for different crosshead speed rates for each panel thickness.

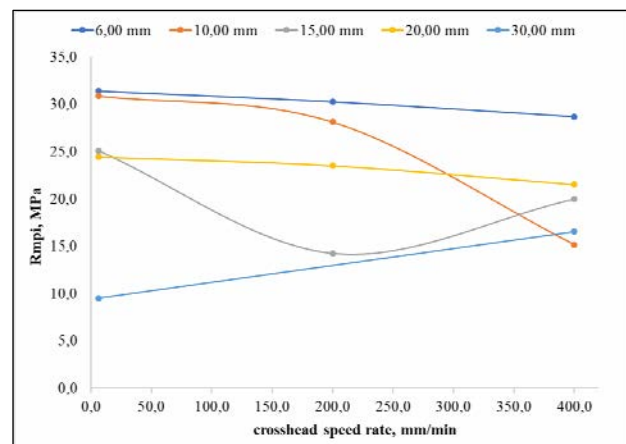
**Figure 8.** Sample before edgewise compressive test**Figure 9.** The dependence of the maximum compressive strength (Rmpi) for different crosshead speeds for each panel thickness

Table 3. Results from edgewise compressive test

Panel thickness, mm	Crosshead speed rate, mm/min	Fmpi, kN	Rmpi, MPa
6,0	6,0	9,4	31,4
	200,0	9,1	30,2
	400,0	8,6	28,7
10,0	6,0	15,4	30,9
	200,0	14,1	28,1
	400,0	7,6	15,1
15,0	6,0	18,8	25,1
	200,0	10,7	14,2
	400,0	15,0	20,0
20,0	6,0	24,4	24,4
	200,0	23,5	23,5
	400,0	21,5	21,5
30,0	6,0	14,2	9,5
	200,0	-	-
	400,0	24,8	16,5

Based on the obtained results, it can be seen that on the 6,0 mm panel thickness, change in the crosshead speed does not affect the value of the compressive strength. Also, this panel thickness gives the highest value of compressive strength (of about 30,0 MPa) compared to other thicknesses. However, taking into account the above, it is difficult to assess whether this is a real strength value or whether its contribution was influenced by the strengthening of the honeycomb walls due to the mutual reaction with the adhesive.

With other panel thicknesses, the strength does not have a constant change trend, its changes in relation to the applied test speeds. The greatest influence of the crosshead speed was observed in panels with a thickness of 10,0 mm, where at the lowest speed of 6,0 mm/min the compressive strength is 30,9 MPa, while at the maximum speed of 400,0 mm/min the compressive strength is 15,1 MPa. The 20,0 mm thick panel showed the least sensitivity to the applied crosshead speed, so the difference between the strength value at the minimum and maximum crosshead speed is about 12% (6,0 mm/min - Rmpi = 24,4 MPa; 400,0 mm /min - Rmpi = 21,5 MPa).

An important difference in relation to compress tests on the surface of the panel is that the compressive strength is up to 10 times higher in the case of the edgewise compressive test. This indicates that in the case of load along the edge of the panel, the strength depends mostly on the mechanical characteristics of the facing material, while in the case of load on the panel surface, the strength depended exclusively on the core. The impossibility of differentiating the main carrier to the strength contribution is reflected in the scattering of the strength results under conditions of the same test speeds, similar confirmations were also given by the authors [14, 15].

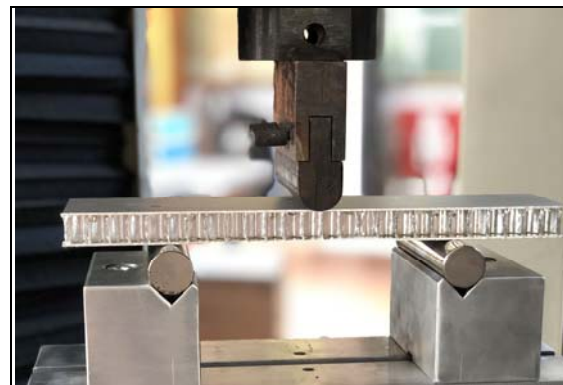
In addition to the above, the tests showed that when the maximum strength is reached, the material yield only in the places of contact with the pressure surfaces of the testing machine, i.e. places of load induction. Characteristic yielding takes place first by breaking the bond between facings and core, mainly by the bonding

agent, followed by local twisting or splitting of the panel. The given yielding of sandwich panels has also been observed by many authors [6,14-16]. Figure 10 shows the characteristic appearance of the specimen after testing.

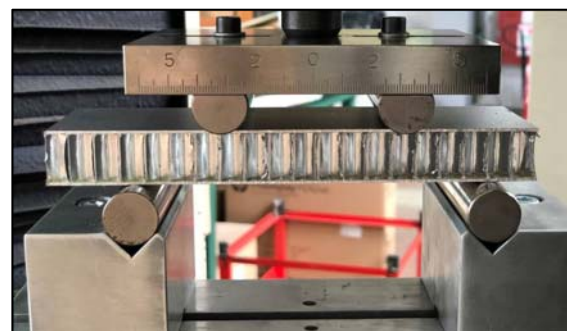
**Figure 10.** Appearance of the specimen after flatwise compression testing

3.3. Three and four point bending tests

Figure 11a shows the arrangement of the test specimen for 3-point bending tests, while Figure 11b shows the specimen for 4-point bending.



a) three point bending test



b) four point bending test

Figure 11. Appearance of the specimen before bending tests

The results obtained during bending tests are used to determine the bending stiffness of the sandwich panels, the shear resistance of the core and the shear modulus or the compressive and tensile strength of the facings. It is important to note that the mechanical characteristics of the core are most precisely determined in the case when the core is tested separately, as an independent component, in accordance with the methods defined within the MIL-STD-401 and ASTM C273 standards.

As within this test it is only possible to test the panel as a whole, the obtained results will be analyzed based on the precise relations given in the ASTM C393 standard.

An examination of the test specimen after applied bending test found that there is local deformation of the panels at the points of load induction, i.e. the contact of the mandrel on the panel, while the remaining ligament of the sample remains undeformed. This behavior of the same type of sandwich panel has been noted by several authors [6,7,15] and can be considered as one of the main characteristics of the panel.

In order to follow the influence of the thickness of the facings for panels of 6,0 mm and 10,0 mm thickness, tests were performed with a change in the position of the facings thickness in relation to the direction of load induction. Tests have shown that there is no influence of the orientation of the sides with a thinner or thicker facing. In both cases, changes in maximum force are negligible. Thus, in the case of panels marked 1, the mean value of F_{max} in the case of placing a surface with a thicker facing opposite to the direction of load induction is about 0,87 kN, while in the opposite case (thinner towards the direction of load induction) the mean value of $F_{max} = 0,84$ kN.



a) three point bending test



b) four point bending test

Figure 12. Appearance of the specimens after tests

The results of testing and calculation of the characteristic properties of the panels are given in tables 4, 5 and 6. Jung's

modulus of elasticity ($E=68$ GPa) of the facing material and shear modulus of the core material ($G=26$ GPa) are characteristics of the material itself and are taken from the manufacturer's specification. Figure 12 shows characteristic appearance of specimens after testing.

Table 4. Results from 3-point bending tests

Spec.	F_{max} , kN	τ_1 , MPa	σ_1 , MPa	D_1 , $\times 10^3$ GPa	U_1 , MN	Δ_1 , mm
1 TA*	0,87	1,38	119,68	37,49	9,56	1,07
1 TD**	0,84	1,33	115,56	37,49	9,56	1,03
2 TD	0,93	0,84	72,61	116,37	15,70	0,37
2 TA	0,98	0,88	76,52	116,37	15,70	0,39
3	1,31	0,78	50,68	400,52	23,52	0,15
4	1,74	0,76	49,61	737,12	31,29	0,11
5	2,05	0,59	38,29	1716,32	46,86	0,06

*TA - thicker facing up in the direction of the load induction

**TD - thinner facing up in the direction of the load induction

Table 5. Results from 4-point bending tests

Spec.	F_{max} , kN	τ_2 , MPa	σ_2 , MPa	D_2 , $\times 10^3$ GPa	U_2 , MN	Δ_2 , mm
1 TA*	1,22	1,94	83,92	37,49	9,56	1,03
1 TD**	1,14	1,81	78,41	37,49	9,56	0,96
2 TD	1,28	1,15	49,97	116,37	15,70	0,35
2 TA	1,33	1,20	51,92	116,37	15,70	0,36
3	1,72	1,02	33,27	400,52	23,52	0,14
4	2,08	0,91	29,65	737,12	31,29	0,09
5	2,92	0,84	27,27	1716,32	46,86	0,05

*TA - thicker facing up in the direction of the load induction

**TD - thinner facing up in the direction of the load induction

Table 6. Panel bending stiffness (D) and core shear modulus (G)

Specimen	D, $\times 10^3$ GPa	G, GPa
1 TA*	37	26
1 TD**	37	26
2 TD	116	26
2 TA	116	26
3	400	26
4	737	26
5	1716	26

*TA - thicker facing up in the direction of the load induction

**TD - thinner facing up in the direction of the load induction

Based on the obtained results, it can be seen that the shear stress of the core is higher in the case of 4-point bending, while the stress of the facings is higher in the case of 3-point bending.

The stiffness of the aluminium sandwich panel is the highest in the case of a panel with a thickness of 30,0 mm, 1716×10^3 GPa. Contrary, the panel with a thickness of 6.0 mm has the lowest stiffness 37×10^3 GPa.

As can be seen from the table 6, the shear modulus of the core (G) has the same value for all sandwich panel thicknesses, namely 26 GPa. As could be expected, shear modulus of the panel core is equal to the value for the core base material (alloy EN AW 3005, $G=26$ GPa). Taking all the previous tests and the analysis of the specimens after them, it can be said that during flatwise

compression tests and bending, the sandwich panel always first break in the core, which made it a weak component of the sandwich panel under the given conditions. Theoretical and experimental confirmations were also noted by other authors [17].

4. CONCLUSION

Tests at different crosshead speed rates showed that testing speed rates have no great effect on the obtained mechanical characteristics of aluminium sandwich panels. In case of panel deformation along the edge, the main load bearers are facings.

It was shown that during the load induction on the sandwich panel, the deformation is not transmitted through the entire system, but is exclusively of a local character, i.e. only at the places of the load induction.

The aluminium sandwich panel with a thickness of 6,0 mm has the lowest stiffness, of 37×10^3 GPa.

The aluminium sandwich panel with a thickness of 30,0 mm has the highest stiffness, of 1716×10^3 GPa.

Core shear modulus (G) for all sandwich panel thicknesses is 26GPa, which is equal to the shear modulus of the base core material, EN AW 3005 alloy.

The core is a weak component of the system in the case when the sandwich panel is subjected to compression or bending normal to its surface.

References

- [1] MIL.HDBK.349 – Manufacture and inspection of adhesive bonded, aluminum honeycomb sandwich assemblies for aircraft, 1994.
- [2] Chang Qi, Shu Yang, Dong Wang, and Li-Jun Yang, *Research Article - Ballistic Resistance of Honeycomb Sandwich Panels under In-Plane High-Velocity Impact*, Hindawi Publishing Corporation, The Scientific World Journal, Volume 2013, Article ID 892781, 20 pages, <http://dx.doi.org/10.1155/2013/892781>
- [3] <https://www.honeycombpanels.eu/en/ballistic-panels-new>
- [4] R. Huňady, *A Sensitivity Analysis of the Dynamic Behavior of Aluminium Honeycomb Sandwich Panels*, American Journal of Mechanical Engineering, 2016, Vol. 4, No. 7, 236-240. DOI:10.12691/ajme-4-7-1
- [5] D.L.Majid, Nor Hafiyah Manan, Yee Ling Chok, *Honeycomb Composite Structures of Aluminium Aerospace Applications*, Encyclopedia of Aluminium and Its Alloys, First Edition, Taylor&Francis, 2018, pp.1213-1243. DOI: 10.1201/9781351045636-140000279
- [6] Jeom Kee Paik, Anil K. Thayamballi, Gyu Sung Kim, *The Strength characteristics of aluminum honeycomb sandwich panels*, Thin-Walled Structures, 1999, Volume 35, Issue 3, pp 205-231. DOI:[10.1016/S0263-8231\(99\)00026-9](https://doi.org/10.1016/S0263-8231(99)00026-9)
- [7] QN Zhang, XW Zhang, GX Lu and D Ruan, *Ballistic impact behaviors of aluminum alloy sandwich panels with honeycomb cores: An experimental study*, Journal of Sandwich Structures and Materials, 2018, Vol. 20, Issue 7, pp. 861–884. DOI: 10.1177/1099636216682166
- [8] F. Tarlochan, *Sandwich Structures for Energy Absorption Applications: A Review*, Materials, 2021, Volume14, Issue 16, 4731 DOI:10.3390/ma14164731
- [9] Каталог произвођача - Aluminum honeycomb panels Larcore
- [10] ASTM C365 Standard Test Method for Flatwise Compressive Properties of Sandwich Cores
- [11] ASTM C364 - Standard Test Method for Edgewise Compressive Strength of Sandwich Constructions
- [12] ASTM C393 - Standard Test Method for Flexural Properties of Sandwich Constructions
- [13] Ђ. Дробњак, *Физичка металургија – Физика чврстоће и пластичности*, ТМФ, Универзитет у Београду, 1990, YU ISBN 86-7401-054-7.
- [14] M. K. Khan, *Compressive and lamination strength of honeycomb sandwich panels with strain energy calculation from ASTM standards*, Proceedings of the Institution of Mechanical Engineers, Part G: Journal of Aerospace Engineering, 2006, Volume: 220 issue: 5, pp. 375-386. doi.org/10.1243/09544100JAERO76
- [15] S.P.Zaoutsos, *Mechanical behavior of aluminum honeycomb sandwich structures under extreme low temperature conditions*, IOP Conference Series: Materials Science and Engineering, 2019, Vol 700, pp. 012017. DOI: 10.1088/1757-899x/700/1/012017
- [16] A. Jedral, *Review of testing methods dedicated for sandwich structures with honeycomb core*, Transaction on Aerospace Research, 2019, Volume 255, Issue 2, pp. 7-20. DOI: <https://doi.org/10.2478/tar-2019-0006>
- [17] M. Shaat, A.R. El Dhaba, *On the equivalent shear modulus of composite metamaterials*, Composites Part B, 2019, Vol. 172, pp.506–515. DOI:10.1016/j.compositesb.2019.05.056



PREPARATION AND CHARACTERIZATION OF HORSE SERUM BUTYRYLCHOLINESTERASE IMMOBILIZED ON PAPER-BASED CELLULOSE MATRIX

SONJA BAUK

Military Technical Institute, Belgrade, bauk.sonja@gmail.com

MAJA VITOROVIĆ-TODOROVIĆ

Military Technical Institute, Belgrade, majavitod@gmail.com

MARINA ILIĆ

Military Technical Institute, Belgrade, marinailic1970@gmail.com

TAMARA VUJATOVIĆ

Military Technical Institute, Belgrade, tamara.vujatovic@gmail.com

TATJANA MARKOVIĆ

Military Technical Institute, Belgrade, tanjin.mejl@gmail.com

Abstract: *The great importance of rapid detection and reliable quantification of toxic organophosphates (OPs) arose as a consequence of their widespread application, extreme toxicity and potential use as chemical warfare agents. The potency of OPs to inhibit enzymes of the cholinesterase family (ChEs) enabled the invention of various biosensors and disposable analytical devices able to provide simple, fast, sensitive, selective and low cost detection of OPs at low concentration. The effective immobilization of enzymes onto supporting material surfaces is an important step in design and fabrication of different bioassay devices, crucial for their performances. This work reports the immobilization of horse serum butyrylcholinesterase (BChE) on paper-based cellulose matrix and biochemical properties evaluation of the immobilized enzyme.*

Keywords: *butyrylcholinesterase, organophosphates, immobilization, cellulose, detection.*

1. INTRODUCTION

Acetylcholinesterase (AChE) and butyrylcholinesterase (BChE) are two main and closely related representatives of enzymes from the cholinesterase (ChEs) family, which play important roles in human and animal function and health [1][2]. Characteristic feature of ChEs is their inhibition by organophosphates (OPs), a group of highly toxic chemicals commonly used for agricultural, industrial, household and medical purposes, but also as nerve agents with dominant position in chemical warfare.

OPs, also known as anti-ChEs, exert their toxic action by covalently binding to the active site of AChE, one of the most crucial enzymes responsible for the normal functioning of the central and peripheral nervous system. The inhibition of AChE by OPs prevents the enzymatic breakdown of neurotransmitter acetylcholine, causing the overstimulation of acetylcholine receptors in the brain, skeletal and muscular systems, which results in convulsion, paralysis and finally death for insects and mammals [3]. Although the inhibition of BChE does not lead to mortality, it has a great toxicological and pharmacological importance as endogenous target susceptible to inhibition with high sensitivity [4][5].

The irreversible nature of ChEs inhibition by OPs permitted the development of many enzymatic methods for analysis and determination of those toxic compounds. Many research papers are focused on the applications of ChEs in different biodetection techniques, since the existence of rapid detection methods and reliable quantification of toxic OPs are of great importance. The potency of OPs to inhibit ChEs enabled the invention of simple detectors and disposable analytical devices for OPs assay, which are especially suitable for military, environmental and agricultural purposes. Many efforts have been focused on the construction of various dipsticks and strips, able to operate without any instrumental device, based on visible color change and applicable for semi-quantitative OPs assay [6][7][8].

Recently, paper has attracted considerable attention as a matrix for fabrication of low-cost analytical devices, owing to its unique features of being inexpensive, biodegradable, biocompatible and hydrophilic. The immobilization of ChEs on paper surface led to the invention of various fast-responding tools for rapid screening and early diagnosis in health and environmental applications [9][10]. Paper-based biosensors provide rapid detection of OPs with minimal equipment requirements

and with advantages of cost effectiveness, simple fabrication, disposability and stability.

Bioactive paper can be produced by various techniques of enzymes immobilization which can be broadly divided into covalent and physical methods according to the molecular forces between enzymes and support matrix. Physical methods are simple, have a wide range of applications and include adsorption and entrapment, but a combination of adsorption, covalent attachment and entrapment can also be found in literature. Adsorption is the simplest and most cost-effective immobilization method that barely affects enzyme activity due to weak interaction with the carrier.

In this work, the immobilization of horse serum butyrylcholinesterase (BChE) on paper-based cellulose matrix using the simplest and the most cost-effective method was examined, as well as the influence of stabilizers, organic solvents and elevated temperature on the properties of the obtained immobilizates.

2. MATERIAL AND METHODS

2.1. Material

Horse plasma butyrylcholinesterase (BChE, lyophilized powder, with the activity of ≥ 10 units/mg protein according to manufacturer's declaration), bovine serum albumin (BSA) and gelatin from porcine skin (high gel strength) were purchased from Sigma-Aldrich, as well as butyrylthiocholine iodide ($\geq 99.0\%$) and 5,5'-dithiobis (2-nitrobenzoic acid) (DTNB, $\geq 98\%$). All other reagents were of analytical grade. Whatman No. 1 filter paper manufactured as circular disks with a diameter of 15 mm (paper circles) was used as a support matrix for enzyme immobilization.

The enzyme stock solution (53 U/mL) was prepared by dissolving lyophilized BChE in phosphate buffer (PB, 50 mM, pH 7.4). Different volumes of enzyme stock solution were further diluted in PB to obtain working solutions with BChE concentrations in the range of 5-20 U/mL. Working solutions of BChE with albumin (1 - 5 %) or gelatin (0.5 - 1.5 %) were prepared according to the same procedure, by dilution of enzyme stock solution in PB containing the stabilizer in the amount required to achieve the final concentration.

2.2. Methods

2.2.1. Immobilization procedure

Working solutions of BChE were added to the paper circles in aliquots of 20 μ L and let to dry at 25 °C. The obtained immobilizates were stored in closed glass vessels and kept in the refrigerator until use.

The activity yield was calculated according to the following equation:

$$AY(\%) = \frac{A_i}{A_0} \times 100 \quad (1)$$

where A_0 is the total number of BChE units added to the support for immobilization (offered activity) and A_i is the number of BChE units detected in the support after immobilization under the conditions defined by the assay method described below (observed activity).

2.2.2. Activity assay

The BChE activity measurements were performed essentially according to the method of Ellman [12], using butyrylthiocholine iodide (2 mM) as the substrate and DTNB (0.32 mM) as the indicator (Ellman's reagent). Free enzyme (20 μ L) was added to a cuvette containing PB (2.64 mL) preincubated at 25 °C, followed by addition of DTNB (0.24 mL) and substrate (100 μ L). The formation of the yellow anion obtained from the reaction between Ellman's reagent and the thiocholine generated by enzymatic hydrolysis of the substrate was monitored by measuring the increase in absorbance at 412 nm for 3 min at 15 s intervals. The measurement of the immobilized enzyme activity was carried out as described above, except that corresponding amount of the immobilizate (one paper circle) was taken instead of free enzyme and placed in a dry cuvette before all others reagents. All results were obtained from measurements performed in triplicate.

One unit of enzymatic activity was defined as the amount of enzyme that catalyzes the hydrolysis of 1 μ mol of butyrylthiocholine per minute.

2.2.3. Thermal stability

Free enzyme (20 μ L) or immobilizate (one paper circle) was incubated at 55 °C for 4 h in a sealed cuvette with a portion of PB (1.5 mL). After incubation, the contents of the cuvette were diluted with another portion of cold PB from the refrigerator (1.14 mL) and the remaining activity in the cuvette was determined using a standard assay method. The contents of the cuvette were not previously equilibrated to a temperature of 25 °C.

The percentage of the residual activity for each sample was calculated considering its initial activity before heat treatment as 100%.

2.2.4. The effect of organic solvents

Free enzyme (20 μ L) or immobilizate (one paper circle) was incubated at 25 °C for 15 min in a sealed cuvette with PB (2.64 mL) containing 5 % organic solvent. After incubation, the remaining activity in the cuvette was determined using a standard assay method. The percentage of the residual activity for each sample was calculated considering its activity in the absence of organic solvent as 100%.

3. RESULTS AND DISCUSSION

3.1. The effect of enzyme concentration

The activities of the obtained immobilizates and the activity yields achieved using working solutions of BChE

with different enzyme concentrations in accordance with the described immobilization procedure are shown in **Table 1**.

Table 1. The influence of the enzyme concentration in working solution on the activity exerted by the immobilizate and achieved activity yield (the mean ± SD)

Working solution (U/mL)	Offered activity (mU)	Observed activity (mU)	AY (%)
5.0 ± 0.2	100 ± 4	28 ± 2	28 ± 2
10.0 ± 0.3	200 ± 5	64 ± 8	32 ± 4
14.9 ± 0.3	299 ± 7	127 ± 7	42 ± 3
19.9 ± 0.3	398 ± 5	172 ± 8	43 ± 2

Over the range of concentrations tested, the activity of immobilized BChE gradually increased, while the activity yield reached a plateau for enzyme concentrations above approximately 15 U/mL (**Figure 1**).

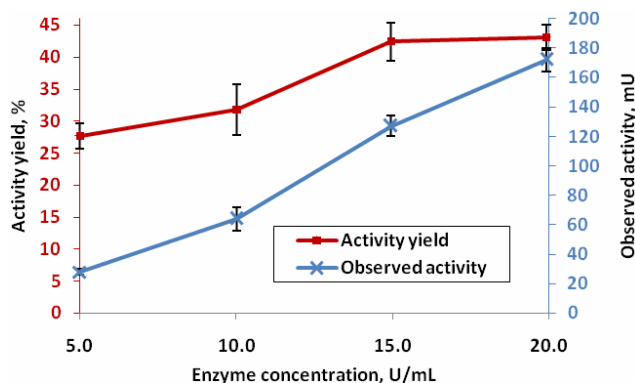


Figure 1. The observed activities of immobilized BChE and activity yields as a function of enzyme concentration

As the immobilization procedure did not include washing the immobilizates as an additional step that could remove unbound or loosely bound enzyme molecules from the support surface, enzyme leakage into the reaction solution during the activity assay was expected. However, control experiments in which the immobilizates were used for a second reaction cycle, after pre-washing traces of the reaction mixture from the first cycle, resulted in the activity drop below 5 % (data not presented) and revealed that the measured activity values, under the activity assay conditions, originated mostly from the action of enzyme molecules released from the surface into the reaction solution.

A working solution of BChE with the enzyme concentration of approximately 10 U/mL was chosen for further study.

3.2. The effect of stabilizers

Since BSA and gelatin were shown to have a stabilizing and protective effect on enzymes, working solutions of BChE with an enzyme concentration of approximately 10 U/mL and different concentrations of BSA or gelatin were

used in the immobilization procedure. The activities of the obtained immobilizates and the achieved activity yields are shown in **Table 2**.

The immobilization of BChE with 1 % BSA in working solution led to a higher observed activity of immobilizate **Im-A1** compared to **Im**. Consequently, this also meant an increased activity yield given the slight fluctuation of the offered activity between samples, possibly due to changes in the viscosity of the prepared enzyme solutions. A further increase of BSA concentration did not correspond to an increase in the observed activity of immobilizates (**Im-A2**, **Im-A3**), while the highest concentration tested led to a slight decrease in the activity yield (**Figure 2**).

Table 2. The influence of the type and amount of stabilizer in the working solution of BChE on the activity exerted by the immobilizate and achieved activity yield

	BSA (%)	Gelatin (%)	Offered activity (mU)	Observed activity (mU)	AY (%)
Im	-	-	200 ± 5	64 ± 8	32 ± 4
Im-A1	1	-	212 ± 3	90 ± 6	42 ± 3
Im-A2	3	-	194 ± 2	82 ± 5	42 ± 3
Im-A3	5	-	215 ± 3	80 ± 6	37 ± 3
Im-G1	-	0.5	202 ± 4	55 ± 7	27 ± 4
Im-G2	-	1	221 ± 5	31 ± 5	14 ± 2
Im-G3	-	1.5	226 ± 5	20 ± 4	9 ± 2

The presence of gelatin in the working solution of BChE gradually reduced the observed activity of immobilizates, with the most pronounced decrease in the activity yield at the highest tested concentration.

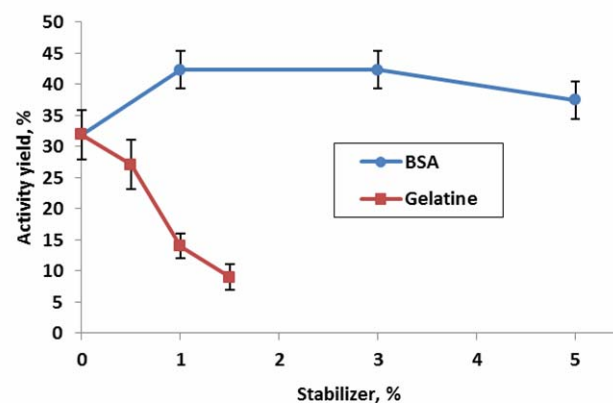


Figure 2. The activity yields as a function of the type and amount of stabilizer in the working solution of BChE used for immobilization

However, as the applied activity assay method hindered the true assessment of the overall immobilization efficiency and mainly reflected the amount of free enzyme in the solution, it is likely that both tested stabilizers had a different, but still beneficial effect on the immobilized BChE. A reasonable explanation for the diminishing effect of gelatin on the observed activities could rely on the fact that a higher concentration of

gelatin leads to a lower permeability and a higher diffusion resistance in immobilizates compared to the presence of BSA.

3.3. Thermal stability

The immobilizates prepared using working solutions of BChE with an enzyme concentration of approximately 10 U/mL without stabilizers or in the presence of three different BSA or gelatin amounts were subjected to thermal treatment at 55 °C for 4 h, as well as the free enzyme in solution without any additives. The measured activities before and after thermal treatment and calculated residual activities of all tested samples are shown in **Table 3**.

It should be emphasized that the obtained results do not reflect the true degree of temperature-induced effects on individual samples due to differences in the temperature conditions of initial and residual activity assay, but reflect the relative ratio of these effects among different samples.

Table 3. The activities of free enzyme and immobilizates before and after incubation at 55 °C for 4 h

	Initial activity (mU)	Activity after 4 h at 55 °C (mU)	Residual activity (%)
Free	172 ± 5	87 ± 4	51 ± 3
Im	54 ± 5	28 ± 2	52 ± 6
Im-A1	95 ± 5	74 ± 9	78 ± 10
Im-A2	69 ± 9	76 ± 7	110 ± 17
Im-A3	68 ± 8	78 ± 6	115 ± 16
Im-G1	58 ± 3	43 ± 3	74 ± 6
Im-G2	26 ± 2	52 ± 3	200 ± 19
Im-G3	17 ± 2	58 ± 3	341 ± 43

Two main trends can be observed from the data presented in **Table 3**.

First, the decrease in activity after thermal treatment was characteristic of the free enzyme, immobilizate prepared without stabilizers (**Im**) and immobilizates prepared with the lowest stabilizers concentrations in the range tested (**Im-A1** with 1 % BSA and **Im-G1** with 0.5 % gelatin).

Second, the increase in activity after thermal treatment was effect exerted by immobilizates prepared with two higher concentrations of stabilizers in the tested range (**Im-A2** and **Im-A3** with 3 % and 5 % BSA, **Im-G2** and **Im-G3** with 1 % and 1,5 % gelatin, respectively).

Denoted observations are visually more noticeable at **Figure 3**, where all activities are presented in normalized form, with a value of 100% assigned to the initial activity of free enzyme in the working solution tested.

Thermal treatment reduced the activities of free enzyme and immobilizate **Im** (prepared in the absence of any stabilizer) by the same extent, while the presence of stabilizers attenuated the temperature-induced inactivation and brought about activity changes in the other direction.

Higher activity values after thermal treatment in immobilizates prepared with stabilizers revealed higher enzyme loading and also leakage promoted under incubation conditions, the latter being more pronounced with gelatin. This is consistent with the fact that gelatin gels are not thermally and mechanically stable without additional cross-linking, since the gelation process is reversible with temperature.

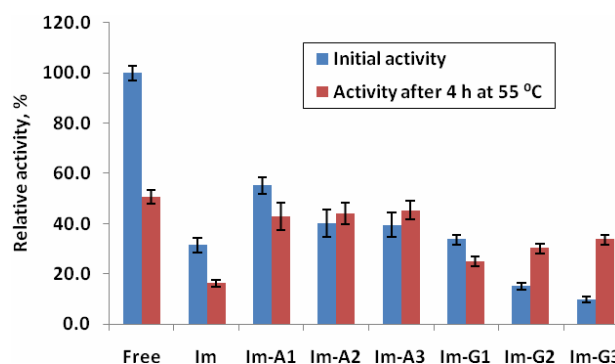


Figure 3. The activities of free enzyme and immobilizates before and after incubation at 55 °C for 4 h, relative to the initial activity of the free enzyme

3.4. The effect of organic solvents

The immobilizates prepared using working solutions of BChE with an enzyme concentration of approximately 10 U/mL without stabilizers or in the presence of 5 % BSA or 1.5 % gelatin were incubated in PB with 5 % of organic solvent (2-propanol, acetonitrile, acetone or DMSO), as well as the free enzyme in solution without stabilizers. The calculated residual activities of all samples examined are shown in **Table 4**.

None of the organic solvents altered the activity of free enzyme by more than 25% at the tested concentration. Besides, the action of all tested solvents on the free enzyme was inhibitory, with the exception of 2-propanol which had an activating effect.

A similar behavior was observed with the immobilizate **Im**, with a milder inhibitory and more pronounced activating effect that led to a 60 % increase in the observed activity.

Table 4. The residual activities of free enzyme and immobilizates after 15 min incubation at 25 °C in PB containing 5 % organic solvent

	Residual activity, %			
	2-propanol	acetonitrile	acetone	DMSO
Free	114 ± 6	81 ± 4	76 ± 5	94 ± 5
Im	160 ± 22	94 ± 13	91 ± 15	94 ± 14
Im-A3	174 ± 14	138 ± 11	135 ± 11	151 ± 15
Im-G3	301 ± 42	122 ± 22	154 ± 29	96 ± 21

Moreover, higher values of the observed activities after incubation in the presence of organic solvents relative to the initial activities were measured for immobilizates

prepared with stabilizers (**Im-A3** and **Im-G3**), with the exception of the slight decrease in the case of **Im-G3** in DMSO.

The results discussed are perceptible in the bar graph at the top of **Figure 4**. The significant increase in the activities of the immobilizates with stabilizers, similar as in the thermal stability test, again points to enzyme leakage during the incubation with organic solvent.

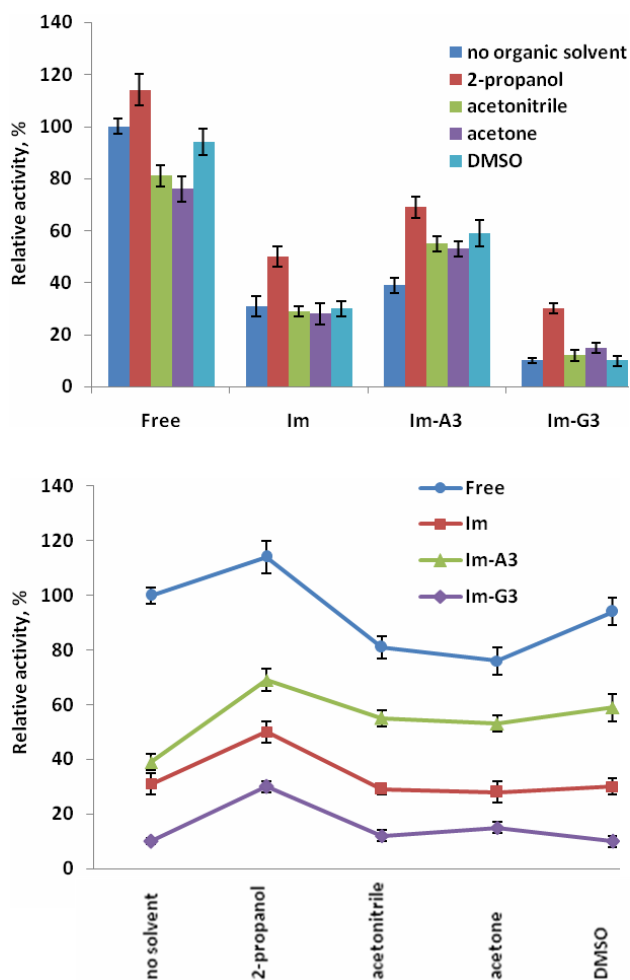


Figure 4. The effects of organic solvents on the activities of free and immobilized BChE relative to the initial activity of the free enzyme: graph in bar (top) and line form (bottom)

Apart from the fact that the applied treatment caused different changes in the magnitudes of the residual activities of different samples incubated in the presence of the same solvent, the spectrum of relative responses of free enzyme and immobilizates **Im** and **Im-A3** to the presence of different organic solvents have a similar profile, which corresponds well to the previous finding that the measured activity values in the activity assay conditions reflected particularly the action of the enzyme molecules released from the surface into the reaction solution. The similarity in the relative responses spectrum of free enzyme and immobilizates is more obvious from the line graph provided at the bottom of the **Figure 4**. A slightly different profile in the relative responses excreted by the immobilizate **Im-G3** implies the involvement of

additional processes in the obtained results, which probably arose from the extent and nature of organic solvents interactions with the porous structure of the gelatin film on the paper surface.

4. CONCLUSION

The immobilization of BChE was carried out by simple method consisting of applying equal aliquots of different enzyme solutions onto the surfaces of Whatman No. 1 paper circles. The influence of changing the applied enzyme solutions in terms of BChE concentration, the presence of stabilizers and their type and content on the observed activity of the obtained immobilizates, achieved activity yields, thermal stability and the effect of organic solvents was investigated. The performance assessment of different immobilizates were based on the measurements of their catalytic activity in a solution containing butyrylthiocholine iodide (2 mM) as a substrate and Ellman's reagent (0.32 mM) as an indicator.

In the range of BChE concentrations tested (5 – 20 U/mL), the immobilizates showed a gradual increase in the observed activity, while the activity yield reached a plateau of just above 40 % at an enzyme concentration of 15 U/mL. The immobilizates prepared in the absence of stabilizers had a similar response to the effect of thermal treatment (4 h at 55 °C) and organic solvents (5 %) as observed for the free enzyme. Immobilization in the presence of BSA or gelatin as stabilizers caused contrary effects on the observed activities of immobilizates and, consequently, the achieved activity yield, since BSA led to an increase, and gelatin to a significant and concentration-dependent decrease of these parameters. However, after thermal and organic solvents tests, both stabilizers contributed to higher values of the immobilizates residual activities that generally exceeded the initial ones, which revealed higher enzyme loading than obtained without stabilizers and also enzyme leakage from the carrier, the latter being in accordance with the used immobilization procedure.

It is known that the observed activity of an immobilizate is highly dependent on the activity assay used, which is mainly caused by diffusion limitations in the immobilization matrix. Accordingly, by examining the obtained immobilizates in a wider range of different conditions that allow a true assessment of their properties and overall immobilization efficiency, the possibilities and limitations of their application for the purposes of OPs detection would be more closely defined, which remains for further research.

References

- [1] Patočka, J., Kuča, K., Jun, D., "Acetylcholinesterase and butyrylcholinesterase – important enzymes of human body", *Acta Medica (Hradec Králové)*, 47(4) (2004) 215-228.
- [2] Pohanka, M., "Cholinesterases, a target of pharmacology and toxicology", *Biomedical Papers*, 155(3) (2011) 219-230.
- [3] Delfino, R.T., Ribeiro, T.S., Figueroa-Villar, J.D.,

- "Organophosphorus Compounds as Chemical Warfare Agents: a Review", *Journal of Brazilian Chemical Society*, 20(3) (2009) 407-428.
- [4] Holas, O., Musilek, K., Pohanka, M., Kuca, K., "The progress in the cholinesterase quantification methods", *Expert Opinion on Drug Discovery*, 7(12) (2012) 1207-1223.
- [5] Mehrani, H., "Simplified procedures for purification and stabilization of human plasma butyrylcholinesterase", *Process Biochemistry*, 39(7) (2004) 877-882.
- [6] Pohanka, M., Karasova, J.Z., Kuca, K., Pikula, J., Holas, O., Korabecny, J., Cabal, J., "Colorimetric dipstick for assay of organophosphate pesticides and nerve agents represented by paraoxon, sarin and VX", *Talanta* 81(1-2) (2010) 621-624.
- [7] Guo, X., Zhang, X., Cai, Q., Shen, T., Zhu, S., "Developing a novel sensitive visual screening card for rapid detection of pesticide residues in food", *Food Control*, 30 (2013) 15-23.
- [8] Pohanka, M., Vlcek, V., "Preparation and performance of a colorimetric biosensor using acetylcholinesterase and indoxylacetate for assay of nerve agents and drugs", *Interdisciplinary Toxicology*, 7(4) (2014) 215-218.
- [9] Wu, Y., Sun, Y., Xiao, F., Wu, Z., Yu, R., "Sensitive inkjet printing paper-based colorimetric strips for acetylcholinesterase inhibitors with indoxyl acetate substrate", *Talanta*, 162 (2017) 174-179.
- [10] Tsagkaris, A.S., Migliorelli, D., Uttl, L., Filippini, D., Pulkrabova, J., Hajslova, J., "A microfluidic paper-based analytical device (μ PAD) with smartphone readout for chlorpyrifos-oxon screening in human serum", *Talanta*, 222 (2021) 121535.
- [11] Li, J.-H., Deng, X.-L., Zhao, Y.-L., Zhang, X.-Y., Bai, Y.-P., "Paper-Based Enzymatic Colorimetric Assay for Rapid Malathion Detection", *Applied Biochemistry and Biotechnology*, 193 (2021) 2534-2546.
- [12] Ellman, G.L., Courtney, K.D., Andres Jr.V., Featherstone, R.M., "A new and rapid colorimetric determinaton of acetylcholinesterase activity", *Biochemical Pharmacology*, 7(2) (1961) 88-95.



INFLUENCE OF DIFFERENTLY CURED POLYMERIC BINDERS ON RHEOLOGY PROPERTIES OF PLASTIC EXPLOSIVES

DANICA BAJIĆ

Military Technical Institute, Belgrade, simic_danica@yahoo.com

IVAN DIMITRIJEVIĆ

MC Labor, Belgrade, ivandimitrijevic2801@gmail.com

SLAVICA TERZIĆ

Military Technical Institute, Belgrade, slavica@algodesk.com

Abstract: Plastic Explosive Compositions consisting of HMX and liquid polyurethane binder were prepared in order to determine influence of differently cured polymeric binders on rheological properties of plastic explosives. First, a set of polymeric binders was prepared in polyaddition reaction between HTPB and IPDI, with varying NCO:OH ratio and examined through the standard and non-standard rheological tests on a dynamic rotational rheometer. Viscosity curves of polymeric binders show viscosity increase with NCO:OH ratio increase, as expected. Amplitude sweep tests reveal liquid-like structure of PEs, with structure strength increase with higher NCO:OH ratio of polymeric binder used, and limiting values of LVER vary from 10^{-3} to 10^{-2} strain. Results of creep test reveal that with increase of NCO:OH ratio of polymeric binder in PE zero-shear viscosity increase and viscous portion deformation decrease. Also, penetration decrease with increase of NCO:OH ratio. The obtained results indicate that ininitial rheology testing is crucial in plastic explosive formulation regarding their processability and physical properties.

Keywords: plastic explosive, polymer binder, rheology, creep.

1. INTRODUCTION

Plastic explosives (hereinafter referred to as PE) are dispersions of crystalline explosives in polymer binders, with high content of explosive components. As a rule, polymer binders are in a liquid state. Thanks to the composition and characteristics of PE, after the action of force (shaping), they keep their shape. The mass fraction of the explosive component in PE is usually in the range of 70 wt.% to 90 wt.%. The binder gives the explosive mixture plastic properties, and at the same time phlegmatizes it (reduces the sensitivity of PE to the effect of unwanted external impulses). This type of explosive, due to its plastic behavior, is easily shaped in a wide range of temperatures, and is used above all for various types of engineering and sabotage demolitions (e.g. bridges, docks and railway tracks), is used in specific weapons such as reactive armor, and somewhat less often for the ammunition filling (such as booster charges, hand grenades, anti-tank and anti-personnel mines, anti-tank and anti-aircraft missiles) [1, 2]. The convenience of manual shaping is reflected in the fact that it is possible to quickly place various forms of PE on structures to be demolished, which can be located both on land and in water. In addition to the two mandatory, already mentioned components, various additives are added to PE compositions that modify detonation or physical properties (oxides, metal powders, antioxidants, bonding agents, plasticizers, etc.).

PEs have a high detonation velocity, a high destructive power, and at the same time a low sensitivity to external impulses, which makes them safer to handle than some other explosive compositions and charges. If necessary, by increasing the content of the inert component and adding appropriate additives, PE compositions with low detonation velocities can be obtained, for specific use.

Given that PEs are primarily used in demolition and engineering actions, it is necessary that they possess appropriate physical characteristics in terms of plasticity, consistency, stickiness, etc. The science of rheology deals with examining those characteristics, which studies the behavior of matter under the influence of force [3]. In previous research in the field of PE in Military Technical Institute, the rheological characteristics of PE were, in the absence of appropriate equipment and testing methods, examined by very indirect and subjective methods. Thus, the consistency was determined by the "Bofors" method, which involves the assessment of manual shaping, retention of plasticity and retention of the original shape after PE has been standing for some time in a climate chamber at a certain temperature and air humidity [4]. Adhesion was determined by manual molding and assessment of PE adhesion to hands during molding [5]. Also, the old method for determining penetration is outdated nowadays. For the reasons mentioned above, and with the aim of following up current achievements in research in the field of PE, it is important to consider new methods for the adequate rheological characterization of

PE and binders used for the production of plastic explosives. Establishing proper methodology would be significant from the aspect of standardizing the testing of the rheological characteristics of PE, and the data obtained by testing different compositions of PE could be compared, and it could be unequivocally determined which of the mentioned compositions shows better consistency, greater stickiness and stability, etc.

As, by research in the field of PE from 2018 [6], liquid polyurethane binders obtained by the polyaddition reaction between hydroxyl-terminated poly(butadiene) prepolymer and isophorone diisocyanate crosslinker proved to be suitable for the production of PE, in this research the binders were also used based on those raw materials. Therefore, in order to gain methods for the rheological characterization of PE, four liquid polyurethane binders with different NCO:OH ratios were prepared from hydroxyl-terminated poly(butadiene) and isophorone diisocyanate. On the basis of these binders and the crystal explosive octogen, four PEs consisting of 85 wt. % of explosives and 15 wt. % binder were prepared. Due to the different NCO:OH ratio of the binder, the rheological characteristics of PE are different, and by examining these characteristics, the influence of differently cross-linked binder on the rheological characteristics of PE was observed. In this way, an insight into the validity of the applied rheological tests for testing PE was obtained. The rheological characterization of the produced binders and PE was performed on an Anton Paar rheometer MCR 302, and included [7]:

1. determination of the binder viscosity curve,
2. determination of the dependence of the dynamic rheological parameters of the binder and PE on the deformation amplitude,
3. determination of frequency dependences of dynamic rheological parameters of binder and PE,
4. PE creep test outside the linear viscoelasticity area, and
5. determining the penetration resistance and adhesiveness (stickiness) of explosives.

2. MATERIALS AND METHODS

2.1. Composition and production of binders for plastic explosives

As already mentioned in the introduction of this paper, the basic components of the binder are the prepolymer of hydroxyl-terminated poly(butadiene) and the isophorone diisocyanate crosslinker. In addition to this, the binders also contained the bonding agent triethylenetetramine and an antioxidant, N-phenyl-2-naphthylamine. The produced binders differ only in the NCO:OH ratio. The compositions of the binders are shown in Table 1. The binders are named PUPE (PolyUrethane for Plastic Explosive).

Table 1. Compositions of the binders

Binder label	NCO:OH	HTPB	IPDI	TETA	FβNA
		wt. %			
PUPE 1	0.2	96.00	1.60	0.48	1.92
PUPE 2	0.25	95.62	1.99	0.48	1.91
PUPE 3	0.3	95.24	2.38	0.48	1.90
PUPE 4	0.35	94.86	2.77	0.47	1.90

The used hydroxyl-terminated poly(butadiene) (HTPB, Shanghai Rongau Enterprises) was provided by the company TRAYAL, Kruševac. The used isophorone diisocyanate (IPDI, Merck) is a mixture of cis and trans isomers, and has a purity greater than 99%; the triethylenetetramine (TETA, Sigma Aldrich) was of technical purity (60%), and the N-phenyl-2-naphthylamine (FβNA, Sigma Aldrich) had 97% purity. The binders were made in a vertical mixer DRAIS FH. The components HTPB, TETA and FβNA were homogenized for 5 minutes at atmospheric pressure and 30 minutes under vacuum at a temperature of 60°C. Then the IPDI was added and the mixture was mixed for 5 minutes at atmospheric pressure and 15 minutes under vacuum at the same temperature. The binders were poured into glass cups and left to crosslink for 96 hours at a temperature of 70°C in a drying oven with a water jacket.

2.2. Composition and production of plastic explosives

Plastic explosives were made from manufactured binders and octogen, HMX (class 1) purchased from the factory "Prva Iskra-Namenska" Barič. Each plastic explosive was made from 15 wt. % binder and 85 wt. % of octogen in a horizontal kneader, according to the established technological procedure [8]. Plastic explosives were named PE with suffixes from 1 to 4, depending on the binder used for their production (PE 1 from binder PUPE 1, etc.).

2.3. Rheological testing

All rheological tests were performed on a rheometer MCR 302 manufactured by Anton Paar (Figure 1).



Figure 1. Rheometer MCR 302, PE adhesion and penetration resistance test

2.3.1. Viscosity testing

The viscosity of the produced binders and the HTPB used for the production of the binder was tested by rotary tests using a cone-plate tool. The cone with a diameter of 25 mm and an angle of 1° was the moving part, and the plate with a diameter of 50 mm was stationary. Measurements were made at a temperature of $25 \pm 0.5^\circ\text{C}$. The shear rate was varied from 0.1 to 100 $1/\text{s}$ (in order to obtain a value of zero viscosity and to simulate the technological process of kneading during which shear rates from 1 to 100 $1/\text{s}$ occur) through 19 values equidistant on a logarithmic scale. In order to establish a laminar flow of the sample before reading the stress value, the length of the point measurements was also changed logarithmically from 60 s (how long the first point was measured at the lowest shear rate) to 10 s (how long the last point was measured at the highest shear rate). The distance between the tools was determined by the geometry of the tool and was 0.051 mm.

2.3.2. Examination of the dependence of the dynamic rheological parameters of binders and explosives on the amplitude of deformation

The dependence of the dynamic rheological parameters of binders, HTPB and explosives on the amplitude of deformation was examined using plate tools (upper movable plate with a diameter of 25 mm, lower stationary plate with a diameter of 50 mm), at a constant angular frequency of 10 rad/s and temperature of $25 \pm 0.5^\circ\text{C}$. After

placement and removal of excess sample, and prior to testing, the samples were allowed to "recover" from the stresses applied during placement for 180 s. When testing the binder and HTPB, the deformation amplitude was varied from 10% to 1000% through 21 equidistant values on a logarithmic scale (10 points per decade), and the distance between the tools was 0.5 mm. When testing plastic explosives, the deformation amplitude was varied from 0.001% to 1% through 31 equidistant values on a logarithmic scale (also 10 points per decade), and the distance between the tools was 3 mm (to avoid the influence of large octogen particles on the measurement).

2.3.3. Examination of frequency dependences of dynamic rheological properties of binders and explosives

Frequency dependences of dynamic rheological properties of binders, HTPB and explosives under shear load in the area of linear viscoelasticity were examined to dependence on amplitude of deformation, at a temperature of $25 \pm 0.5^\circ\text{C}$. When testing the binder and HTPB, the angular frequency was varied from 628 rad/s to 1 rad/s through 28 equidistant values on a logarithmic scale (10 points per decade), the distance between the tools was 0.5 mm, and the measurement length of the points was left to the device. During the PE test, the angular frequency was varied from 10 rad/s to 0.01 rad/s through 31 equidistant values on a logarithmic scale, the distance between the tools was 3 mm, and the measurement length of the points was increased logarithmically from 20 s (how long the first point was measured at the highest angular frequency) to 100 s (how long the last point was measured at the lowest angular frequency).

2.3.4. PE creep test outside the linear viscoelasticity region

The creep of PE outside the area of linear viscoelasticity was tested using tools used to determine the dependence of rheological parameters, at a temperature of $25 \pm 0.5^\circ\text{C}$. The samples were handled as in the previously explained tests. The distance between the tools was 3 mm. A total of 67 points were read (the length of the point measurement was logarithmically increased from 0.1 s to 10 s) and in the recovery period 136 points (the length of the point measurement was also logarithmically increased from 0.1 s to 10 s).

2.3.5. Determination of penetration and adhesiveness of explosives

Determination of penetration resistance and adhesiveness of PE was performed at a temperature of $25 \pm 0.5^\circ\text{C}$, using the upper parallel plate with a diameter of 4 mm and a metal container with a diameter of 55 mm and a height of 35 mm. The mass of PE in the amount of 100 g was inserted into the container and leveled so that the height of PE in the container was about 28 mm, and the container was placed on the lower tool of the device (the lower stationary parallel plate with a diameter of 50 mm). The measurement consisted of 3 intervals, in each interval the head of the device (and thus the upper tool) moved at

a constant set speed of 100 $\mu\text{m/s}$, only the direction of movement was changed. In the first interval, the direction was towards the sample (penetration interval) from the initial height of 20 mm to the final height of 10 mm. Then the direction was from sample (debonding interval), from a height of 10 mm to a height of 20 mm. The third interval was the same as the first (re-penetration). Each interval lasted 100 s, and during each interval 1000 normal force values were read.

3. RESULTS AND DISCUSSIONS

3.1. Viscosity of the binders

Figure 2 shows viscosity curves for HTPB and the prepared binders.

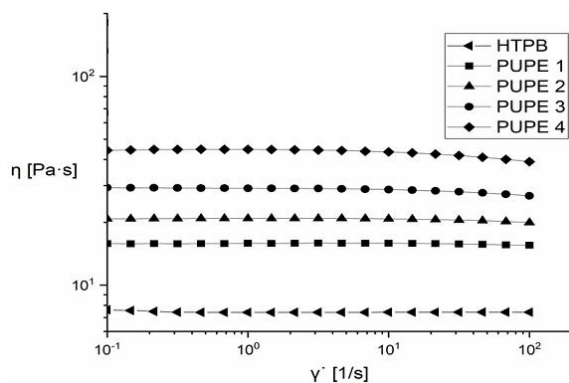


Figure 2. Viscosity curves for HTPB and binders

By analyzing the viscosity curves, it can be seen that HTPB and binders with a lower NCO:OH ratio behave almost like Newtonian fluids in the range of shear rates from 0.1 to 100 1/s, i.e. that pseudoplastic behavior becomes more pronounced with increasing NCO:OH ratio. This is in line with expectations, given that with an increase in the NCO:OH ratio, the length of the macromolecular chains, i.e. the molar mass of the binder, also increases. Increasing the molar mass increases the viscosity and pseudoplasticity of polymer fluids.

3.2. Dependence of dynamic rheological parameters of binders and explosives on deformation amplitude

Figure 3 shows the dependence of G' , G'' and $\tan\delta$ on γ on a graph with logarithmic scales for PUPE 4 binder, as a representative example. It can be seen that $G'' > G'$, i.e. that the binder behaves like a viscoelastic liquid, and that the limit value of the deformation is about 60%. The graphs of the dependence of G' , G'' and $\tan\delta$ on γ for all binders and HTPB look similar to this (all produced binders behave like viscoelastic liquids).

Figure 4 shows the dependence of G' on γ on a graph with logarithmic scales for all binders and HTPB, and it shows the above-mentioned: G' values increase with increasing NCO:OH ratio, i.e. pure HTPB has the smallest values of G' (where, conditionally speaking, the NCO:OH ratio is zero), while the binder PUPE 4, which is made with the largest amount of crosslinker, has the highest values.

Also, it can be noticed that with an increase in the NCO:OH ratio, the value of G' leaves its plateau faster, i.e. that with an increase in the NCO:OH ratio, the area of linear viscoelasticity decreases. This can again be explained by the fact that with an increase in the NCO:OH ratio and an increase in the length of the polymer chains.

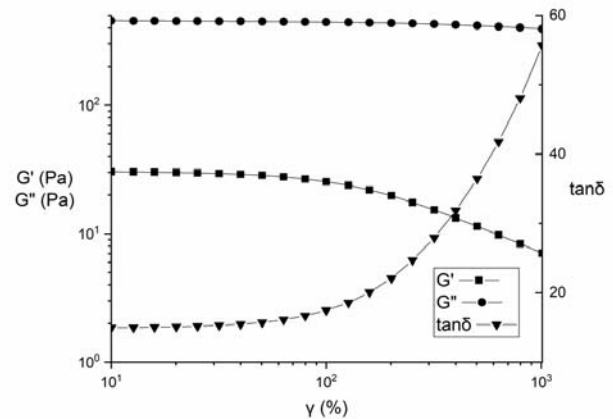


Figure 3. Graph of dependence of G' , G'' and $\tan\delta$ on γ for PUPE 4

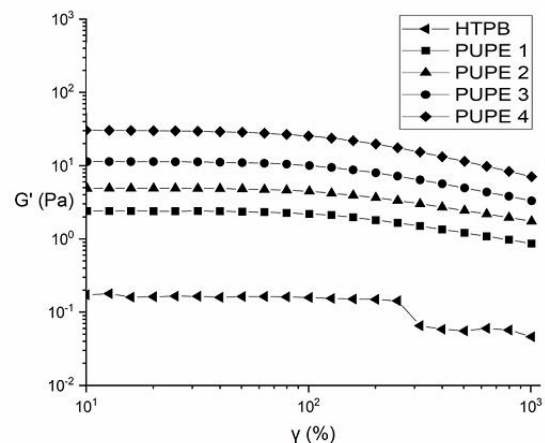


Figure 4. Graph of dependence of G' on γ for binders and HTPB

Figure 5 shows the dependence of G' , G'' and $\tan\delta$ on γ on a graph with logarithmic scales for plastic explosive PE 4. It can be seen that $G'' > G'$, like a binder

PUPE 4, PE behaves like a viscoelastic fluid. The other PE compositions also have graphs of the dependence of G' , G'' and $\tan\delta$ on γ similar to this, that is, all PE compositions behave as viscoelastic liquids. It reveals that there is no strong forces (in this case physical forces) in the structure of plastic explosives, i.e. good interactions between the binder and the octogen crystals. This could generally be expected considering that, due to the nature of the prepolymer, the macromolecular chains of the binder are mostly non-polar and there are not many possibilities for the formation of stronger physical forces (such as dipole-dipole interactions and hydrogen bonds) between the chains and the octogen crystals.

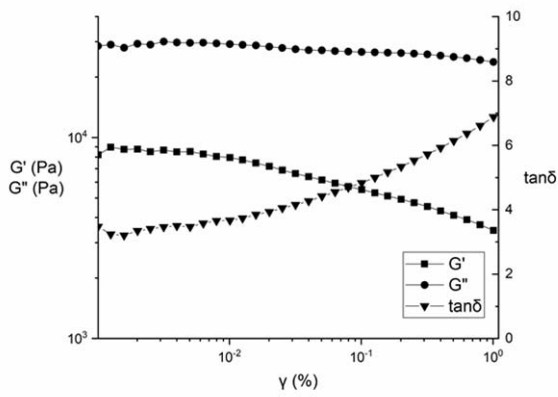


Figure 5. Graph of dependence of G' , G'' and $\tan\delta$ on γ for PE 4

Figure 6 shows the graph of the dependence of G' for all plastic explosives. Vertical displacement is a consequence of the binder used to make PE, i.e. rigidity, because with increasing rigidity, more energy was needed for deformation, so the modulus values are higher.

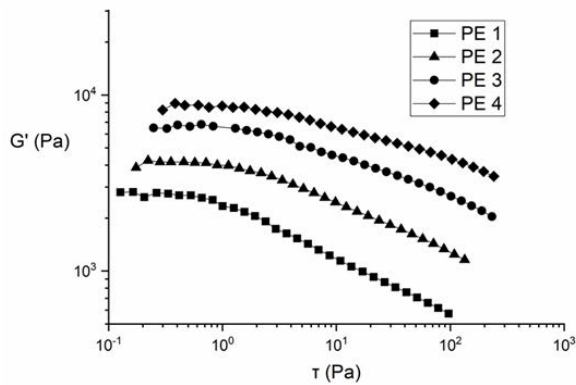


Figure 6. The dependence of G' for plastic explosives

3.3. Frequency dependence of dynamic rheological parameters of binders and explosives

Figure 7 shows the dependence of G' and G'' of PUPE 1 on ω on a graph with logarithmic scales.

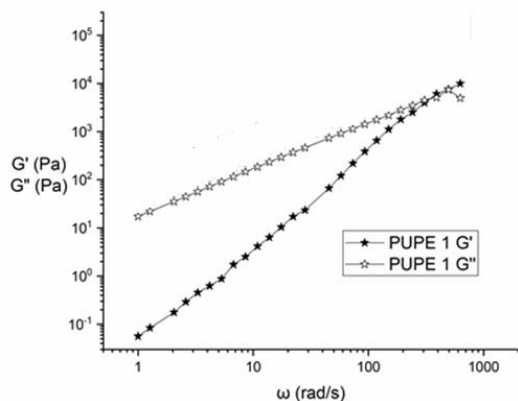


Figure 7. Graph of dependence of G' and G'' of PUPE 1 and PUPE 7 binders on ω

Due to the different molar mass of the binder, as well as

differences in the chemical structure (concentration of hard segments) and interactions between macromolecular chains, the only thing that can be analyzed from the frequency dependence of the rheological quantities of the binder are the slopes of G' and G'' , that is, the distribution of molar masses.

Table 2 shows the slope values G' and G'' for HTPB and binders, obtained by linear regression of test results, as well as correlation coefficients.

Table 2. Values of slope G' and G''

	HTPB	PUPE 1	PUPE 2	PUPE 3	PUPE 4
Slope G'	1.931	1.979	1.955	1.773	1.617
Slope G''	0.998	0.962	0.954	0.926	0.896

The values of the slopes G' and G'' for HTPB, PUPE 1 and PUPE 2 are very close to two and one, respectively, which means that they have a narrow molar mass distribution. In the case of other binders, with increasing NCO:OH ratio, the slope values are further away from the values of two and one, and the molar mass distributions are also wider. A wide distribution of the molar mass of the binder is not desirable, because it can be expected that during long-term standing there will be exudation of macromolecules of smaller molar masses from PE, which leads to a decrease in the binder content in PE and worse characteristics.

The frequency dependence of the dynamic rheological parameters of plastic explosives was determined for the compositions PE 1 and PE 4, Figure 8.

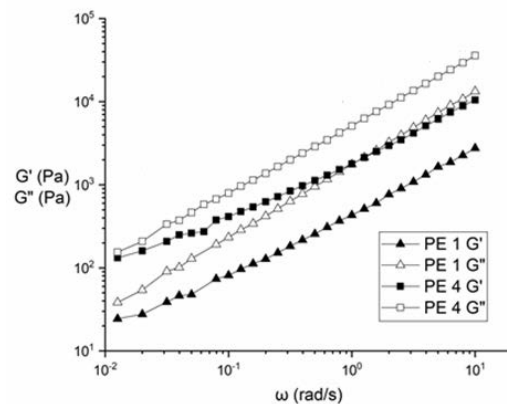
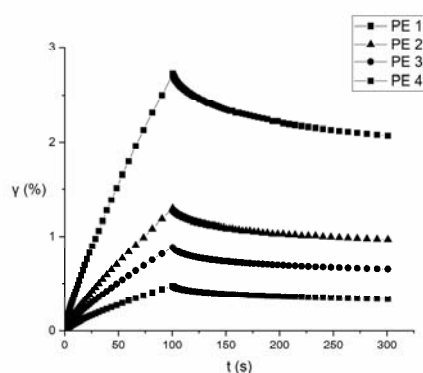


Figure 8. Graph of dependence of G' and G'' of PE 1, PE 4 on ω

As can be noticed, compositions PE 1 and PE 4 at values $\omega \rightarrow 0.01$ show $G'' > G'$. This means that these compositions do not have the appropriate consistency at rest, i.e. that their storage for a long period of time would cause undesirable phenomena such as phase separation and sedimentation. This can be concluded without testing for compositions PE 2 and PE 3.

3.4. Creep of plastic explosives outside the region of linear viscoelasticity

Figures 9 shows PE creep curves of the examined plastic explosives.



Figures 9. PE creep curves.

Due to the application of the same magnitude and duration of stress in all samples, samples with a weaker structure were deformed more and those with a stronger structure less. Considering that the total deformation in all samples γ_{max} is greater than the limit value of the linear region of viscoelasticity γ_b , the basic laws of rheology cannot be applied to the obtained results. Nevertheless, the values of the return deformation γ_e and residual deformation γ_v can be analyzed. Table 3 shows those values.

Table 3. Values of total, return and residual deformation of PE

PE	γ_{max} (%)	γ_e (%)	γ_v (%)	γ_e/γ_{max} (%)
PE 1	2.720	0.650	2.070	23.89
PE 2	1.290	0.319	0.971	24.73
PE 3	0.886	0.235	0.651	26.52
PE 4	0.474	0.140	0.334	29.54

From the value of the ratio γ_e/γ_{max} , it can be concluded that the recovery of PE after the end of the force increases from the composition of PE 1 to the composition of PE 7, i.e. the elastic response rises with increasing NCO:OH ratio of the binder used to make PE.

3.5. Penetration and stickiness of plastic explosives

Table 4 shows the work values performed by the rheometer tool during PE penetration (A_{p1} work during the first penetration interval, A_{p2} work during the second penetration interval), the work values performed by the rheometer tool during PE detachment (A_o) and the ratio A_{p2}/A_{p1} . Work values are calculated using the formula

$$A = \int F(h) * dh \tag{1}$$

where h is the path traversed by the tool during penetration or detachment.

The value of A_{p1} is determined by the strength of PE, the value of A_o by the stickiness of PE, and the ratio A_{p2}/A_{p1} by the ability of PE to return to its initial state after stress, Table 4.

Table 4. Values of penetration parameters for the examined explosives

PE	A_{p1} (mJ)	A_o (mJ)	A_{p2} (mJ)	A_{p2}/A_{p1} (%)
PE 1	0.239	0.218	0.117	48.95
PE 2	0.505	0.405	0.244	48.32
PE 3	0.726	0.620	0.370	50.96
PE 4	0.945	0.771	0.483	51.11

Based on the value of A_{p1} , it can be concluded that the composition of PE 4 is the strongest and most adhesive. The ability of PE to return to its initial state after stress is similar for all compositions, it is slightly better for compositions PE 3 and PE 4.

4. CONCLUSIONS

The presented results of this research are an attempt to validly characterize plastic explosives, given the possibility that they behave non-homogeneously during rheological tests. As the test results followed the trend expected due to the different NCO:OH ratio of the binder, it can be argued that the measurements were valid.

As for the produced binders, they all behave as viscoelastic fluids, and with increasing NCO:OH ratios zero viscosity increases exponentially and the limiting value of the linear region of viscoelasticity decreases exponentially, which indicates an increase in the mean value of the molar mass by numerical representation; and that the distribution of binder molar masses is getting wider. Amplitude sweep tests of plastic explosives have shown that all plastic explosives behave like viscoelastic liquids, which means that the interaction between the binder and explosive particles is not strong, and that they do not show great consistency stability when standing. Frequency sweeps tests of plastic explosives have shown that compositions of plastic explosives from PE 1 to PE 4 do not have a suitable consistency at rest, and would not be suitable for long-term storage.

The penetration and stickiness test showed that the PE 4 composition has the highest strength and the best stickiness, and overall it can be said that it is the best of the tested compositions.

In further work, it is necessary to improve the binder and the composition of the plastic explosive, in order for the plastic explosive to show better rheological characteristics, primarily in order to increase the stability during rest (long-term storage).

The composition, in order to achieve better rheological characteristics, could be improved by increasing the mass fraction of explosives. Of course, then some other problems related to the production technology and possible increase in sensitivity due to the lower binder content could occur. In addition, the use of finer granulation explosives, and thus a larger specific surface area, would enhance the explosive-binder interaction.

ACKNOWLEDGEMENT

The authors acknowledge the support of this research from the Serbian Ministry of Education, Science and Technological Development (grant-contract No. 451-03-68/2022-14/200325).

References

- [1] Cooper, Paul W. (1996). Chapter 4: Use forms of explosives. *Explosives Engineering*. Wiley-VCH. pp. 51–66. ISBN 0-471-18636-8.
- [2] Antic G. Overview of research and development of cast and plastic explosives at VTI, VTI 004-01-0488, Belgrade, 2007.
- [3] Jovanović S., Jeremic K. Characterization of polymers, Faculty of Technology and Metallurgy, Belgrade, 2007.
- [4] Minov G. Examination of the quality of plastic explosives during storage and the influence of atmospheric, stagnant and flowing water on its properties, ITI-175, Belgrade, 1997.
- [5] Minov G., Azdejković M. Investigation of the influence of river water on the rheological and explosive characteristics of plastic pentrite explosives, ITI-201, Belgrade, 1998.
- [6] Dimitrijević I., Simić D., Terzić S. Production and characterization of pentrite plastic explosives, VTI 04-01-1239, Belgrade, 2018.
- [7] Mezger T. *The Rheology Handbook*, 4th Edition, Vincentz Network, Hanover, 2014.
- [8] Minov G. General technological procedure for the production of plastic explosives, VTI 004-01-0421, Belgrade, 2005.



USING SELF-ADHESIVE CONDUCTIVE TEXTILE AND COPPER TAPE ON TEXTILE

DUŠAN NEŠIĆ

University of Belgrade, Institute of Chemistry, Technology and Metallurgy, Centre of Microelectronic Technologies, Belgrade, nesicad@nanosys.ihtm.bg.ac.rs

DRAGAN TANASKOVIĆ

University of Belgrade, Institute of Chemistry, Technology and Metallurgy, Centre of Microelectronic Technologies, Belgrade, dragant@nanosys.ihtm.bg.ac.rs

MILOŠ VORKAPIĆ

University of Belgrade, Institute of Chemistry, Technology and Metallurgy, Centre of Microelectronic Technologies, Belgrade, worcky@nanosys.ihtm.bg.ac.rs

Abstract: *The application of conductive layers on textiles is considered. Tapes or foils of conductive textile and thin copper tape were used. The good and bad characteristics of textiles as a substrate and conductive tapes on textiles are considered, especially during use. The method of cutting conductive tapes and transferring them to textiles by means of a special self - adhesive tape is shown. An example made in the microwave technique, which is important due to high frequencies, is also presented.*

Keywords: *electronic textile, conductive textile, microwaves.*

1. INTRODUCTION

Electronic textile is increasingly used in modern electronics [1-10]. The field developed very quickly and acquired a large number of applications from ordinary life to special medical controls. This substrate also has its limitations, which are reflected in the variation of up to 10% of the values of parameters such as dielectric constant and thickness [6].

In addition to the substrate, the use of conductive textiles as metallization is very actual [8-13]. It lags behind pure metal in conductivity but also has advantages. The advantage over the pure metal layer is primarily in the flexibility and mechanical resistance coupled with the use of textiles [9-11]. Despite this, the use of self-adhesive metal tapes, especially copper but also aluminum, are very current. The biggest advantage over conductive textiles is conductivity, but also easier bonding, especially copper with soldering. Both self-adhesive conductive textile and copper tape give the possibility of easy removal of the conductive structure and installation of a new one without damaging the substrate.

An important application of self-adhesive conductive textile with conductive adhesive is the creation of a multilayer structure of the conductive layer that increases the conductivity [11] or electrically connects parts of the structure [12-14].

One of the problems is the transfer of the formed conductive structure to a given textile substrate, which is a general issue with other bases as well. Complicated sacrificial layers or etching and cutting on the textile base itself are used, which is often demanding due to a possible

defect on the substrate. There is also the problem of large areas, such as clothes, as well as curved surfaces where it is impossible to easily cut.

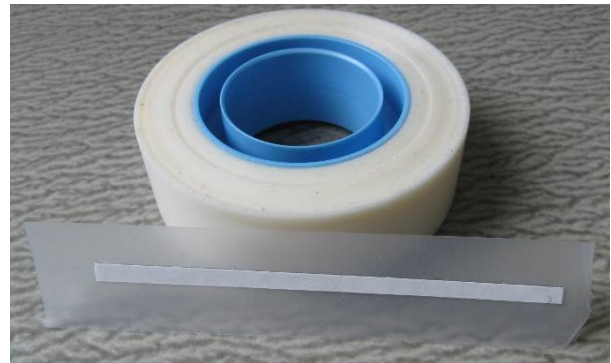
The application of electronic textiles in defense technology is also significant. It is at the forefront of new technologies in the application of textiles in defense [15-19]. Application for defense sector will hold nearly 45% of the conductive textile market by 2031 [17].

The example application is on microwave structures, like in [18,19] but can be also on lower frequencies. The microwave structure is taken as an example as the most demanding due to the high frequencies.

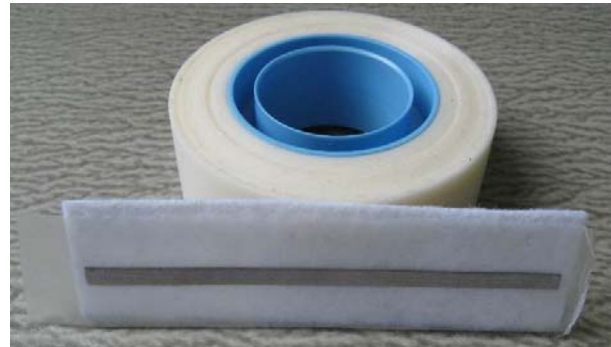
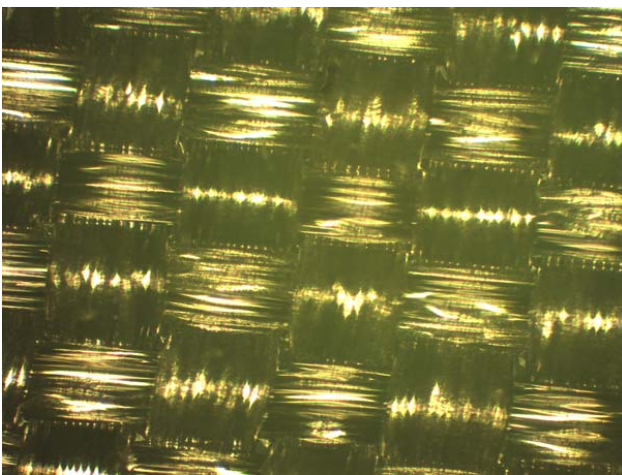
2. APPLICATION

Grid conductive cloth tape, *Xinst0402/12, Shenzhen Xinst Technology Co., Ltd*, total thickness (textile + conductive glue) 120 μm was used for conductive textiles with conductive adhesive. The conductivity of a given textile with a copper-nickel structure and polyester is about 10^5 S/m (copper bulk is $58 \cdot 10^6$ S/m, layer usually takes $18 \cdot 10^6$ S/m). A photograph of the surface and its photomicrograph is shown in Fig. 1. The disadvantage is the presence of plastic that makes it difficult to common soldering or bonding with silver epoxy paste.

The cutting was done by hand with a precision scalper given in [12]. In Fig. 2 are photographs from [12] of a cut structure on copper tape (copper 30 μm + non-conductive glue 30 μm) and of a cut structure on the given conductive textile. There is a tendency to wrinkle the copper tape while the conductive textile has remained flat.



a) Self-adhesive transparent tape (Scotch Removable) is glued to conductive textiles. Only supporting white paper carrying conductive textiles can be seen.



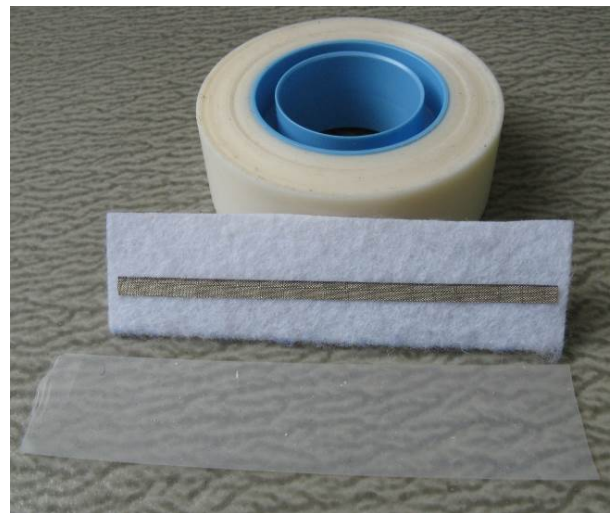
b) The supporting white paper was removed and the entire construction was glued to the substrate (felt). One can see the glued conductive textile and the self-adhesive transparent tape glued to it.

Figure 1. Photography and microscopic photography of conductive textiles (Motic 100x) [12].



Figure 2. Copper tape and conductive textiles cut with a precision scalper [12].

Using a special self-adhesive tape (*Scotch Removable*), as a sacrificial layer, the conductive structure is transferred to the textile. Fig. 3a, 3b and 3c show the procedures on the example with one strip of the sacrificial layer.



c) Removed self-adhesive transparent tape (below) as a sacrificial layer and only conductive textile remains on a felt substrate.

Figure 3. Using a special self-adhesive tape as a sacrificial layer

In Fig.4. photos from above and below of the filter with copper strip are given. You can see the use of short-circuited edges using conductive textiles with conductive glue. The use of short-circuiting at the edge is much closer to the definition of short-circuited branches than the usual conductive holes (via). Wrinkled copper surface can be seen.

In Fig. 5 is a photograph of the structures with conductive textiles from above using a short circuit at the edge. The application of conductive textiles with conductive adhesive can be seen here, similar to that in [11-14]. Even the author's work [12] was published before [14]. Fig. 6 presents SMA connectors details above and below. For better soldering next to the connector is copper, which is partly covered with the conductive textiles.

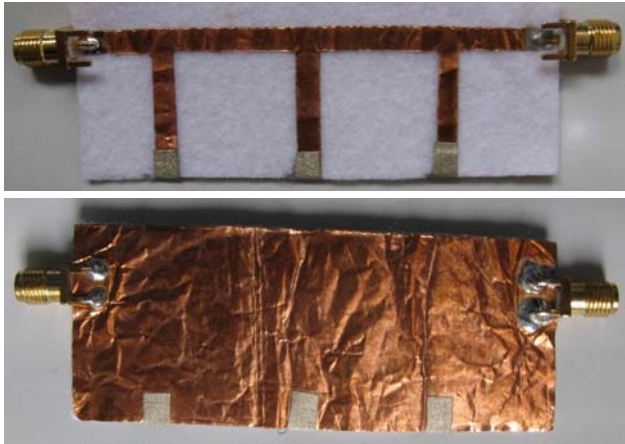


Figure 4. Structure with copper strip from above and below. You can see the use of short-circuited edges using conductive textiles with conductive glue.

Wrinkled copper surface can be seen.



Figure 5: Structure with conductive textiles from above.

One can see the use of shorting on the edge.



Figure 6: SMA connectors details above and below.

For better soldering next to the connector is copper, which is partly covered with the conductive textiles.

Both filters were made on a felt substrate with a thickness of about 0.85 mm, $\epsilon_r = 1.2$ and $\text{tg}(\delta)$ about 0.02. All microstrip lines are taken to be 50Ω . Since it was cut by hand, 3.5 mm was taken for the conductive textile and 4 mm for the copper strip. Stubs are 21.5 mm long. Simulation is in Program Package WIPL-D Microwave Pro v5.1 [20] for the metallized via holes. Models are in Fig. 7 for the conductive textile and in Fig. 8 for the copper tape. Corrections for the short-circuited edges (shorting on the edge) were done according to simulation and measurements. Simulated and measured S -parameters are given in Fig. 9. There are still needs for full wave EM-simulations.

It can be seen that conductive textiles have higher losses, which is logical. Without losses, the conductive textile would follow the copper tape filter.

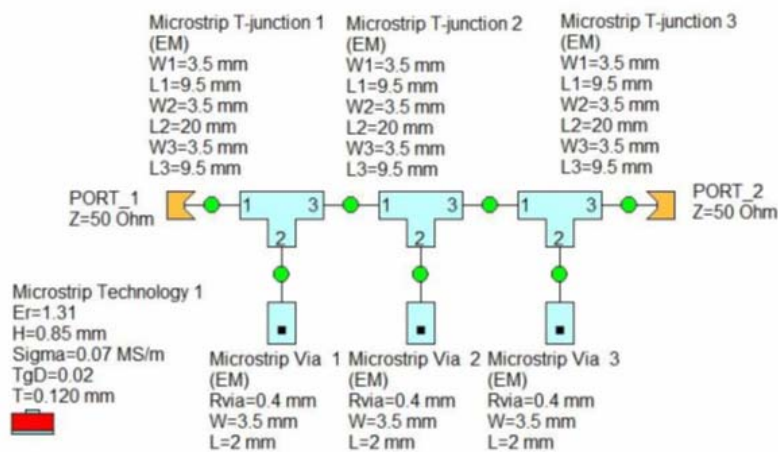


Figure 7: Simulation model with the conductive textile (including conductive adhesive in the metallization).

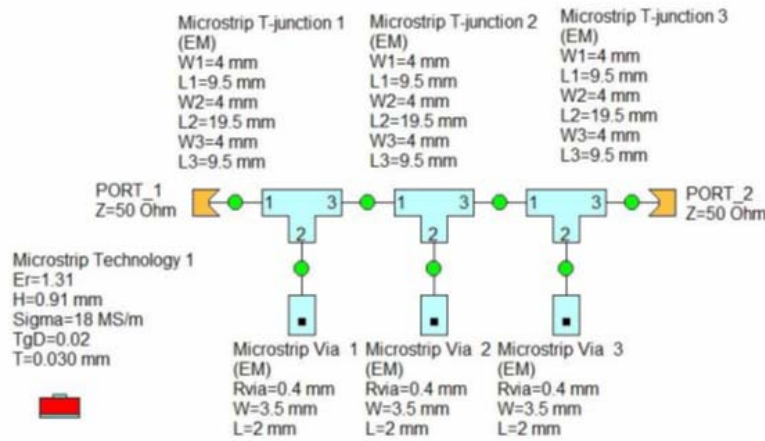


Figure 8: Simulation model with the copper tape (including nonconductive adhesive 2 x 0.030 mm).

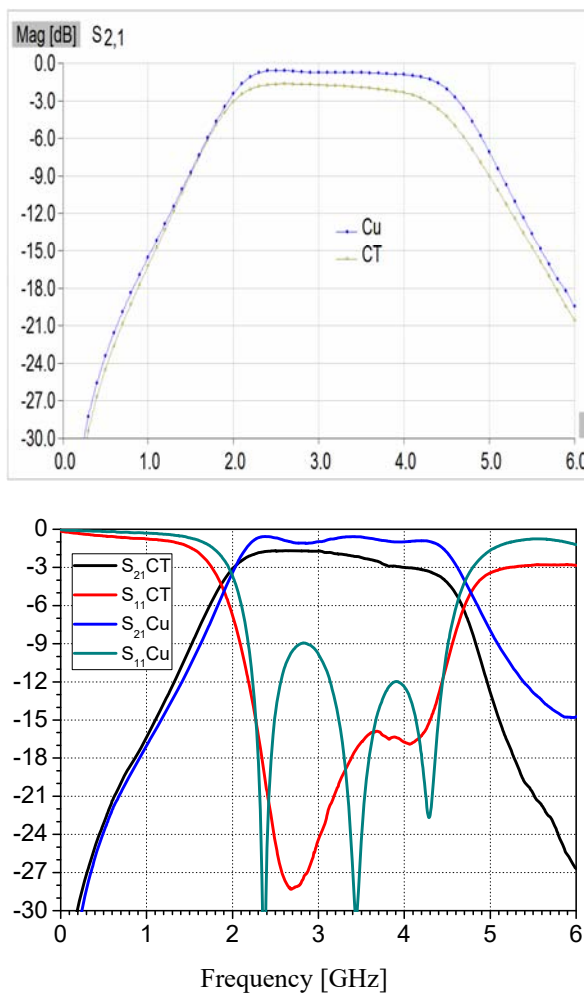


Figure 9. Simulation and measured S-parameters: CT-conductive textile; Cu-copper tape.

5. CONCLUSION

The advantage of conductive textiles is the applicability of electronics to clothes and other textile materials, while making them functional for use.

The lack is a textile material as a substrate that does not have a precisely defined thickness and dielectric constant. Some problems can be with washing and friction. It is

also problem with connector bonding due to the nature of the material (difficult bonding of textile conductor and low resistance to high temperatures of textiles and glue).

The microwave structure is taken as an example as the most demanding due to the high frequencies. The branches are short-circuited with a conductive strip on the edge (short-circuited edge) and not with conductive via.

The advantages over other techniques such as applying conductive ink or paste and embroidery with conductive thread are:

- By applying a special self-adhesive tape as a sacrificial layer, it is possible to transfer the formed conductive structure in the form of a self-adhesive conductive layer to surfaces where etching or other invasive shaping methods are difficult to perform.
- The definition of thickness of the conductive layer is like in common electronic structures (better simulations).
- The self-adhesive conductive structure allows removing or even repairing the conductive layer and forming a new one without damaging the substrate.

ACKNOWLEDGEMENT

The authors thank to V. Milosevic (Institute of Physics, Belgrade) for help in measuring and I. Mladenovic in microscope photography.

This work was financially supported by the Ministry of Education, Science and Technological Development of the Republic of Serbia (Grant No. 451-03-68/2022-14/200026).

References

- [1] EHRMANN,G., EHRMANN,A.: *Electronic Textiles*, Encyclopedia 2021, 1, 115–130.
- [2] RUCKDASHEL,R. R., VENKATARAMAN,D., PARK, J. H.: *Smart textiles: A toolkit to fashion the future*, J. Appl. Phys. 129, 130903 (2021)
- [3] ISMAR,E., BAHADIR,S.K., KALAOGLU,F., KONCAR,V.: *Futuristic Clothes: Electronic Textiles and Wearable Technologies*, Global Challenges

- 2020, 4, 1900092
- [4] KAN,C.-W., LA,Y.-L.: *Future Trend in Wearable Electronics in the Textile Industry*, Appl. Sci., 2021, 11, 3914.
- [5] VOLAKIS,J.L.: *Conductive Textile for Wearable Electronics*, IEEE Miami Section, March 23, 2021
- [6] CUPAL,M., RAIDA,Z.: *Frequency Limits of Textile-Integrated Components*, 2020, 23rd International Microwave and Radar Conference (MIKON)
- [7] CHOUDHRY,N.A., ARNOLD, L.N., RASHEED,A., KHAN, I. A., WANG,L.: *Textronics, A Review of Textile-Based Wearable Electronics*, Adv. Eng. Mater. 2021, 2100469
- [8] LUND,A., WU,Y., FENECH-SALERNO,B., TORRISI,F., CARMICHAEL,T.B., MÜLLER,C.: *Conducting materials as building blocks for electronic textiles*, MRS Bulletin, vol. 46, June 2021
- [9] MONTI,G., CORCHIA,L., TARRICONE,L.: *Fabrication techniques for wearable antennas*, 2013 European Microwave Conference
- [10] KRIFA,M.: *Electrically Conductive Textile Materials—Application in Flexible Sensors and Antennas*, Textiles, 2021, 1, 239–257
- [11] HA,H.: *Applying the Multilayer Textile Conductor Technique to Improve the Wearable Passive RF Devices*, Bachelor's Thesis, October 2020, Tampere University of Applied Sciences Energy and Environmental Engineering
- [12] NESIC, D.: *Examples of Wide Microwave Bandpass Microstrip Filters on Felt Substrate*, Proceedings of the International Conference on Microelectronics, ICM (MIEL), 2021
- [13] SEAGER,R.D., CHAURAYA,A., ZHANG,S., WHITTOW,W., VARDAXOGLU,Y.: *Flexible radio frequency connectors for textile electronics*, Electronics Letters, 2013 Vol. 49 No. 22 pp. 1371–1373
- [14] DANG,Q.H., CHEN,S.J., ZHU,B., FUMEAUX,C.: *Shorting Strategies for Wearable Textile Antennas*, IEEE Antennas Propagation Magazine, February 2022, 84-98
- [15] STEFFENS,F., GRALHA,S.E., FERREIRA, I.L.S., OLIVEIRA,F.R.: *Military Textiles – An Overview of New Developments*, Key Engineering Materials Online, Vol. 812, (2019) 120-126
- [16] PRADHAN,A., NAG,S.: *Smart Textiles for Defense Applications*, Conference: Texcreative 2019 By BIET, Davangere, India
- [17] <https://www.globenewswire.com/news-release/2022/02/24/2391760/0/en/Application-for-Military-Defense-Sector-to-Hold-Nearly-45-of-the-Conductive-Textile-Market-Demand-to-Grow-By-12-CAGR-Through-2031.html>
- [18] SPAHIU,N., MITILINEOSB,S., KAZANIC,I., AGASTRAD,E., VASSILIADISE,S., GUXHOF,G.: *A Textile RFID Meander Antenna for Military Application*, International Journal of Innovative Technology and Interdisciplinary Sciences, Vol. 4, Iss. 4, pp. 776-783, 2021
- [19] ÇELENK,E., TOKAN,N.T.: *All-Textile On-Body Antenna for Military Applications*, IEEE Antennas and Wireless Propagation Letters, Vol. 21, No. 5, 2022
- [20] Program Package *WIPL-D Microwave Pro v5.1* (WIPL-D d.o.o, Belgrade 2019. www.wipl-d.com)



POLYESTER KNITWEAR IMPREGNATED WITH PVB/IF-WS₂ SYSTEM AS POTENTIAL CAMOUFLAGE MATERIAL

ALEKSANDRA SAMOLOV

Military Technical Institute, Belgrade, Serbia, aleksandrasamolov@yahoo.com

DANICA BAJIĆ

Military Technical Institute, Belgrade, Serbia

KATARINA MIŠKOVIĆ

Military Technical Institute, Belgrade, Serbia

RADOSLAV SIROVATKA

Military Technical Institute, Belgrade, Serbia

MILAN M. STANOJEVIĆ

Military Technical Institute, Belgrade, Serbia

DRAGAN KNEŽEVIĆ

Military Technical Institute, Belgrade, Serbia

Abstract: This paper presents the results of research on the application of nanomaterials on knitwear intended for camouflage protection. Polyester fibers that had already been dyed in camouflage shades (light green, beige green and dark green) were additionally treated with poly(vinyl butyral) (PVB) with or without incorporated nanoparticles of tungsten disulfide (WS₂). This impregnation has proven to be successful in improving the camouflage characteristics of some other materials, like glass or cotton. For the prepared samples, the diffuse reflection, specular gloss and color coordinates of both treated samples and untreated samples were determined. Also, the samples were observed in the medium and long wavelength infrared spectrum using IR thermography. The obtained results indicated that there is a possibility of using this new impregnated knitwear in the wider area of the EMS.

Keywords: polyester knitwear, poly(vinyl butyral), tungsten disulfide nanoparticles, camouflage protection, IR thermography.

1. INTRODUCTION

In earlier research, the influence of tungsten disulfide structures on the physical-mechanical and spectrophotometric properties of polyurethane camouflage coatings was examined. Since the favorable influence of the nanoparticles and nanotubes of tungsten disulfide (IF-WS₂ and INT-WS₂, respectively) was proven, both on the mechanical and the camouflage characteristics [1-3], it was encouraging to use these particles on textile materials as well. First choice was to work with natural, cotton, textile materials and application to materials with a digital camouflage pattern that is already in use in the Serbian army. The results obtained at that time spoke in favor of the fact that the use of nanoparticles had a favorable effect on camouflage properties and on obtaining the so-called multispectrality, i.e. the possibility of this material for meeting the camouflage requirements in a wider area of the electromagnetic spectrum (EMS) [4].

In this research, analysis of the influence of tungsten disulfide nanostructures on the camouflage properties of a

synthetic fabric - polyester knitwear was performed. These nanostructures were previously dispersed in the chosen impregnating medium poly(vinyl butyral) (PVB). It is known that PVB as a thermoplastic elastomer is added to other polymer materials, brittle thermosetting resins such as epoxy and phenolic resin, to increase toughness [5]. PVB is a highly flexible material, compatible with numerous resins and additives, non-toxic, has very good adhesion to many substrates. PVB has very good impact resistance, tensile strength and elasticity, it is resistant to freezing and aging, it dissolves well in alcohols and organic solvents, it is transparent and colorless [6]. It releases solvents quickly so it is good for impregnation of materials, since it easily forms films and foils.

Dichalcogenides of transition metals (MoS₂, WS₂, NbS₂, etc.), thanks to their excellent mechanical properties, have a wide range of applications: to increase strength, reduce friction, as solid lubricants, in anti-corrosion and masking protection, etc. [3]. Due to these exceptional properties, tungsten disulfide, in the form of fullerene nanoparticles, IF-WS₂, and multilayer nanotubes, INT-WS₂, with a unique morphology and a spherical closed multilayer structure, i.e. a multilayer hollow nanotube structure, has

been recognized as a potential reinforcing filler for various composites. Nanoparticles of WS₂ reduce friction and heating, and thus mechanical wear. At the same time, contact pressure causes exfoliation (flaking off) of the nanospheres, releasing tribofilms that bind to surface irregularities and voids, smoothing them out and improving overall mechanical efficiency and extending the material's service life. These multi-layered IF-WS₂ nanospheres are known to withstand extremely low and high temperatures (-270 °C to 450 °C), and as they are resistant to impact and pressure, this makes them suitable for use in extreme conditions, from low to high temperatures, high pressure to high vacuum, under high loads and rotation speeds, at high radiation and in corrosive environments [5].

2. MATERIALS AND METHODS

2.1. Samples preparation

The following materials were used to make the samples in this research: polyester knitwear in three camouflage shades (dark green, beige green and light green) that correspond to the shades already in use in the Serbian army, manufactured by "Dunav" Grocka.

For the impregnation of selected knitwear, PVB Mowital B45H Kuraray was used and nanostructures of WS₂: IF-WS₂ nanoparticles, manufactured by NanoMaterials Ltd. - Nanotech Industrial Solutions Inc., Apnano Israel [7]. To disperse nanostructures and to dissolve PVB, 96% ethanol was used. The properties of the nanoparticles used are given in Table 1.

Table 1. Characteristics of IF-WS₂

Purity, %	>99
Particle density at 25 °C, g/cm ³	7,5
Apparent density, g/cm ³	0,7-1,1
Typical particle size, nm	40-300
Decomposition temperature, °C	1250
Oxidative stability in air, °C	>350
Oxidative stability in inert, °C	>1000
Molecular mass, g/mol	247,98

The samples were prepared as follows: first, powdered PVB was dissolved in ethanol, with or without fullerene particles of WS₂, by submerging the knitted fabric samples in the solution and evaporating the solvent. For

the sample without nanoparticles, PVB was dissolved in ethanol, in a mass concentration of 3 wt.%, and for the samples with nanoparticles, they were first dispersed in the solvent by an ultrasonic processor BadelinSonoPuls, and then, with vigorous mixing, PVB powder was added. The concentration of nanoparticles was 2 wt.%.

2.2. Camouflage efficiency characterization

Spectrophotometric properties were observed to evaluate the camouflage behavior by determining the following properties of the impregnated knitwear: specular gloss was measured at angle 85° with Elcometer 480 model T device, which is important feature for fabric materials in the field of military camouflage. Diffuse reflection was measured on UV/VIS/NIR spectrophotometer UV 3600 from a Japanese manufacturer Shimadzu with an integrating sphere in the 650 nm to 1000 nm wavelength area using UV Probe programme package [8] and color coordinates in CIE LAB system were determined as well using Color programme package with 10° and D65 observer [9].

2.3. IR Thermography

In the experiment, two measuring thermal imaging cameras operating in different ranges were used, FLIR SC620 and FLIR SC 7200. SC 7200 uses "Altair" software for data analysis and acquisition while SC 620 camera uses "ThermaCAM 2900" software package [10, 11]. The obtained images were analyzed with "ThermaCAM Researcher Professional" software [12]. In addition to the cameras, the black body TCB-4D, manufactured by Inframet, Poland, was also used in the experiment. Blackbody temperature values were controlled by the TCB TAS-T software [13]. The temperatures of the black body at which measurements were made were 45°C and 60°C. The sample was placed in front of the black body and the exposure time of the samples was 5 minutes. The goal of the experiment set up in this way was to make a comparison and insight into the process that takes place between the sample and electromagnetic energy in the MWIR and LWIR spectral range of EMS.

3. RESULTS

Diffuse reflection curves registered for the examined material are given in Figure 1.

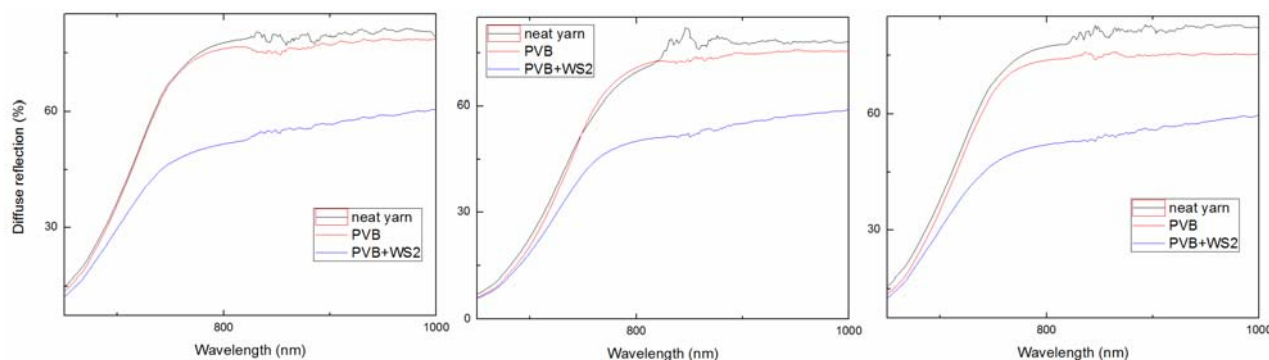


Figure 1. Diffuse reflection for: light green, dark green and beige green shade, from left to right

The results show that impregnation did affected camouflage behavior of the material and for the better. There can be observed a significant drop in values of the diffuse reflection. Before impregnation the diffuse reflectance values were very high but the IF-WS₂ changed these values resulting in obtaining lower diffuse reflectance curves. Moreover, visually the change was not observed, and that was confirmed by colour coordinates values, given in Table 2.

Table 2. Color coordinates

Shade	With PVB			With PVB/IF-WS ₂		
	L	a	b	L	a	b
Light green	45.3	-6.4	14.8	39.0	-4.4	11.3
Beige green	43.4	-2.6	13.5	37.3	-1.4	10.6
Dark green	33.6	-9.7	11.5	29.5	-8.1	10.1

Table 3 shows obtained values of specular gloss, which, as it may be observed, practically did not change. This means that PVB/IF-WS₂ could be used for the camouflage improvement not just for the natural fabrics but for the polymer threads and yarns as well.

Table 3. Specular gloss at 85°

Shade	With PVB	With PVB/IF-WS ₂
Light green	0.0	0.0
Beige green	0.0	0.2
Dark green	0.1	0.0

Temperature values were read from the obtained thermograms and used for comparison in order to determine relative temperature differences as a measure of the camouflage effect in the IR spectral range. Tables 4 and 5 show these results. The first column represents the ambient temperature, which ranged between 19°C and 21°C. The second and third columns represent the temperature of the material when the black body is heated to 45°C and 60°C, respectively. ΔT_1 represents the temperature difference of the material when the temperature of the black body was 45°C and when the black body was not heated while analogously ΔT_2 is the temperature difference when the black body was heated to 60°C and when it was not heated. The last two columns are the mutual quotients of these temperature differences obtained for the impregnated samples in relation to the non-impregnated sample that represents the reference sample.

Table 4. Results obtained with the FLIR SC620 camera

Sample	T _{amb} (°C)	T _{bb} (45°C)	T _{bb} (60°C)	ΔT_1 (°C)	ΔT_2 (°C)	$\Delta T_1/\Delta T_{ref}$	$\Delta T_2/\Delta T_{ref}$
dark green	19.43	31.93	38.99	12.50	19.56	1.00	1.00
dark green+PVB	20.27	29.27	35.1	9.00	14.83	0.72	0.76
dark green+PVB+ IF WS ₂	20.51	30.06	36.21	9.55	15.7	0.76	0.80
beige green	19.6	30.1	36.66	10.5	17.06	1.00	1.00
beige green +PVB	20.44	28.89	37.22	8.45	16.78	0.80	0.98
beige green +PVB+ IF WS ₂	20.77	31.11	37.66	10.34	16.89	0.98	0.99
light green	19.31	29.52	36.36	10.21	17.05	1.00	1.00
light green+PVB	20.36	31.91	39.61	11.55	19.25	1.13	1.13
light green+PVB+ IF WS ₂	20.51	30.44	37.97	9.93	17.46	0.97	1.02

Table 5. Results obtained with the FLIR SC7200 camera

Sample	T _{amb} (°C)	T _{bb} (45°C)	T _{bb} (60°C)	ΔT_1 (°C)	ΔT_2 (°C)	$\Delta T_1/\Delta T_{ref}$	$\Delta T_2/\Delta T_{ref}$
dark green	19,43	27,80	34,10	8,37	14,67	1,00	1,00
dark green+PVB	20,27	26,40	29,50	6,13	9,23	0,73	0,63
dark green+PVB+ IF WS ₂	20,51	27,20	30,10	6,69	9,59	0,80	0,66
beige green	19,6	28,00	31,30	8,40	11,70	1,00	1,00
beige green+PVB	20,44	26,70	31,30	6,26	10,86	0,74	0,93
beige green+PVB+ IF WS ₂	20,77	28,80	33,10	8,03	12,33	0,96	1,05
light green	19,31	26,50	31,60	7,19	12,29	1,00	1,00
light green+PVB	20,36	26,40	31,70	6,04	11,34	0,84	0,92
light green+PVB+ IF WS ₂	20,51	26,80	30,90	6,29	10,39	0,87	0,84

The results do not show consistent behavior. Namely, the results obtained with the FLIR SC620 camera show better suppression when the blackbody is heated to 45°C. Samples of light green color in this part of the spectrum, recorded by this measuring camera, do not behave in the manner required for camouflage protection. In contrast, dark green and beige green samples have better suppression when impregnated with PVB alone with similar percentage suppression.

On the other hand, the results obtained with the FLIR SC7200 camera show that the reduction of thermal reflection occurs in almost all treated samples. The reductions are larger and range up to almost 40%.

These results are quite different from the results obtained by measuring the diffuse reflectance in the VIS and NIR part of the EMS [4, 14]. Namely, it was shown that all three shades of green behave best when impregnated with

nanoparticles, lowering the reflection curve thus, improving the camouflage performance of the material. It remains to be seen why there were such results, that is, such differences in the behavior of samples. Performing additional analyzes (SEM, TEM, AFM, FTIR) could provide answers. It should also be emphasized that it is not unusual for the material to behave differently in different parts of the EMS, which is why obtaining the desired multispectrality is a demanding task.

5. CONCLUSION

Examination of the influence of tungsten disulfide nanostructures on the camouflage properties of polyester knitwear was conducted. Samples were prepared by impregnating polyester knitwear with camouflage pattern in PVB/IF-WS₂ from ethanol solution. The results show that impregnation has improved camouflage behavior of the material. The significant drop in values of the diffuse reflection was observed due to added IF-WS₂. Visual appearance of the samples did not change, what was confirmed by colour coordinates values. Specular gloss did not significantly change. In results obtained by recording with a FLIR SC620 camera, it was observed that the addition of nanoparticles in beige green and dark green shades, show better reduction of thermal reflection in knitted fabrics impregnated only with polyvinyl butyral. The behavior of the light green shade is not adequate for application in this part of the EMS. On the other hand, the results obtained with another type of measuring camera (FLIR SC7200) show a significantly greater drop in the temperature difference between treated and untreated samples. It was observed that almost all samples show a difference in behavior in this part of the EMS compared to untreated samples.

Overall, nanoparticle-impregnated polyester knitwear show potential for use in the field of multispectral camouflage protection. However, future research should encompass impregnation of more camouflage shades/colors, as well as other synthetic fabrics or knitweaves.

ACKNOWLEDGEMENT

The authors acknowledge the support of this research from the Serbian Ministry of Education, Science and Technological Development (grant-contract No. 451-03-68/2022-14/200325).

References

- [1] Dragana S. Lazić, Danica M. Simić, Aleksandra D. Samolov, Desimir Jovanović, Properties of standard polymeric and water-based coatings for military camouflage protection with addition of inorganic fullerene-like tungsten disulphide (IF-WS₂) nanoparticles, *Scientific Technical Review*, 2017, Vol. 67, No.1, pp.38-44.
- [2] Dragana S. Lazić, Danica M. Simić, Aleksandra D. Samolov, *Effect of IF-WS₂ nanoparticles addition on physical-mechanical and rheological properties and on chemical resistance of polymeric coating and polyurethane paint*, 7th International Scientific Conference on Defensive Technologies OTEH 2016, Belgrade, 6-7 October 2016. Proceedings, ISBN 978-86-81123-82-9, pp. 609-613.
- [3] Danica Simić, Milica Marjanović, Maja Vitorović-Todorović, Sonja Bauk, Dragana Lazić, Aleksandra Samolov, Novica Ristović: *Nanotechnology for Military Applications – a Survey of Recent Research in Military Technical Institute*, *Scientific Technical Review*, 2018, Vol.68, No.1, pp.59-72.
- [4] Aleksandra Samolov, Danica Simić, Bojana Fidanovski, Vera Obradović, Ljubiša Tomić, Dragan Knežević, Improvement of VIS and IR camouflage properties by impregnating cotton fabric with PVB/IF-WS₂, *Defence Technology*, 17 (6), pp. 2050-2056, 2021., ISSN 2214-9147, doi.org/10.1016/j.dt.2020.10.008.
- [5] Simić, D. M., Stojanović, D. B., Dimić, M., Mišković, K., Marjanović, M., Burzić, Z., Uskoković, P. S., Zak, A., Tenne, R. Impact resistant hybrid composites reinforced with inorganic nanoparticles and nanotubes of WS₂, *Composites Part B* 176, 107222, 2019. doi.org/10.1016/j.compositesb.2019.107222
- [6] <http://www.kuraray.eu/en/produkte/product-groups/polyvinyl-butylal>
- [7] R. Tenne, Inorganic fullerene-like structures and inorganic nanotubes from 2-D layered compounds, in *The chemistry of nanostructured materials*, editor: Peidong Yang, University of California, Berkeley, USA, World Scientific Publishing Co. Pte. Ltd. ISBN 981-238-405-7, ISBN 981-238-565-7 (pbk), 2003.
- [8] UV Programme package Tutorial, Shimadzu 2010.
- [9] Color programme package Tutorial, Shimadzu 2010.
- [10] Altair software Tutorial, https://www.altair.com/ThermaCAM_2.9_software_Tutorial, <https://www.flir.com/>
- [11] ThermaCAM 2.9 software Tutorial, <https://www.flir.com/>
- [12] ThermaCAM Researcher Professional software Tutorial, <https://www.flir.com/>
- [13] TCB software Tutorial, <https://www.inframet.com/>
- [14] Aleksandra Samolov, Danica Simić, PVB/IF-WS₂ system for impregnation of polyester knitwear, 9th European conference on protective clothing – ECPC, Stuttgart, 10-12 May, 2021.



DEVELOPMENT AND PRODUCTION OF ULTRA-HIGH-STRENGTH STRUCTURAL STEEL S1100QL

JAN FODER

R&D Engineer at SIJ Acroni d.o.o., Slovenia, tel.: +386 31 487 160, jan.foder@acroni.si

ANDREJ SKUMAVC

R&D Engineer at SIJ Acroni d.o.o., Slovenia, andrej.skumavc@acroni.si

Abstract: High-strength structural steels present the backbone for the design of the modern constructions, as they are incorporated in different components in transportation, mining, infrastructure and lifting industries. Various standards prescribe the specific requirements for mechanical properties, testing as well as limitations for chemical composition and production. Nowadays, as there are progressively stricter demands for lighter, stronger, and safer structural components, non-standardized steel grades are required. Prime example is quenched and tempered ultra-high-strength structural steel S1100QL with yield strength exceeding 1100 MPa. The main challenge when designing and producing such demanding steel grade is not the yield strength itself, but a combination of high-strength and toughness with good workshop properties like weldability and bendability. Only a specific combination of different metallurgical mechanisms, such as grain refinement, solid solution strengthening, work hardening and precipitation strengthening, can provide the desired properties. The paper presents crucial steps when developing S1100QL steel grade. Different microalloying additions in combination with lean chemical composition were first tested on the laboratory scale to set up optimal composition for the industrial production. Main challenges during the industrial production of quarto plates were addressed through carefully controlled steelmaking with steel scrap recycling, secondary metallurgy, continuous casting, thermo-mechanically controlled hot rolling, and heat treatment process. Final mechanical properties in quenched and tempered condition were tested and verified.

Keywords: S1100QL, ultra-high-strength steel, microalloying, mechanical properties, quarto plates

1. INTRODUCTION

Current and future trends for components made of high-strength structural steels follow the path of increasing material payload, durability and reducing the weight. Prime example is lifting industry, where the combination of high load-bearing capacity and low weight is crucial for safe and efficient operation of mobile, loader and tower cranes. Booms for such components are exposed to stresses which can exceed yield strength ($R_{p0.2}$) of common structural steels, resulting in catastrophic failure. This issue can be addressed by increasing either the thickness or the strength of the boom.

Nowadays, booms are made of high-strength structural steels in quenched and tempered (QT) condition, specified in standard EN 10025-6 [1], which entitles grades with $R_{p0.2}$ from 460 to 960 MPa. Generally, higher strength levels are used, namely 890 or 960 MPa, however, as there is ever growing need for lighter and stronger booms, non-standardized steel grades are being developed and used. Example of such steel grade is S1100QL, with $R_{p0.2}$ exceeding 1100 MPa. The term ultra-high-strength is not standardized and is used only to differentiate from high-strength steel grades specified in EN 10025-6. The biggest challenge when designing such steel grade is not high-strength alone, but the combination with toughness and workshop properties like weldability and bendability.

To obtain the desired properties, various metallurgical mechanisms are incorporated, like grain refinement, work hardening, solid-solution strengthening and precipitation strengthening [2]. All mentioned mechanisms depend on the chemical composition and production technology. Chemical composition should be as lean as possible to assure good weldability and bendability, however sufficient hardenability and grain size control shall be obtained. One way to obtain sufficient grain size control is with the use of the microalloying additions, especially Nb and Ti, which pin the prior austenite grain boundaries with nano-sized precipitates during reheating and hot rolling. Ti is also used for B protection, which is intentionally added for better hardenability, along with Cr, Mn and Mo. Ni addition is used to increase the low-temperature toughness, as it improves the mobility of dislocations within the iron lattice.

The aim of this paper is to present the concepts and challenges of designing ultra-high-strength steel grade S1100QL from laboratory to industry scale. Different alloying and microalloying additions were used and evaluated to set up the optimal chemical composition for industrial trials, where final mechanical properties in heat-treated condition were determined. Holding at various elevated temperatures for 1 h was done to determine maximum safe temperature, without degradation of mechanical properties.

2. EXPERIMENTAL

2.1 Laboratory scale

Production process

Three laboratory heats with different combinations of microalloying additions were produced in laboratory vacuum induction furnace with inert Ar atmosphere and deep vacuum. The main objective of the experimental heats was to determine the optimum microalloying additions for industrial trials on fixed alloying system. All three heats were Nb microalloyed, one was additionally alloyed with V and one with Ti. Logic behind the set-up composition was to examine if required mechanical properties could be achieved solely by Nb addition or if there is the need for V or Ti addition.

Steel was cast into 12 kg ingots and forged into 60 x 60 mm billets, which were then hot-rolled into 12 mm thick strips. Prior to rolling, billets were reheated to 1200 °C, which ensures full solubility of Nb(C,N) precipitates, to enable enhanced precipitation during the hot rolling. Precipitation phenomena was observed using calculated per pass mean-flow stresses, as it is described in paper [3]. Strips were air-cooled after hot rolling, followed by heat treatment consisting of water quenching and low-temperature tempering with air cooling.

Testing

Chemical composition was performed using optical emission spectroscopy (OES) ARL MA-310 for Si, Mn, Cr, Ni, Mo, Cu, Ti, Nb, V and B. Amount of C, S and N were determined with combustion method using LECO CS-600 for C and S and LECO TC-500 for N.

Specimens for evaluation of mechanical properties in quenched (Q) and QT condition were prepared, which included tensile test in accordance with EN ISO 6892-1 in longitudinal direction, and Charpy pendulum impact toughness (KV_2) at -40 °C in transverse direction in accordance with EN ISO 148-1.

Samples for metallographic examinations were prepared and Nital etched in order to compare prior austenite grain size (PAGS) and distribution between three experimental heats. Based on the results of mechanical testing and metallographic analysis, the most promising microalloying system was selected for further testing prior to industrial trials.

Samples for hot-compression testing on Gleeble 1500D were taken from plate and machined to cylindrical specimen with diameter and height of 10 and 15 mm, respectively. Plain hot compression and multi-stage tests were performed in accordance with scheme in Figure 1a and Figure 1b, respectively. Plain hot compression tests were conducted to study the dynamic recrystallization kinetics and the effect of thermomechanical parameters on grain size and distribution, in order to determine optimal parameters for hot rolling on industrial scale. Five-stage compression testing was done to determine the

non-recrystallization temperature (T_{nr}). First the average flow stress for each deformation stage was determined and plotted against inverse of the absolute temperature. Intersection between linear regression of two distinct linear regions represents T_{nr} .

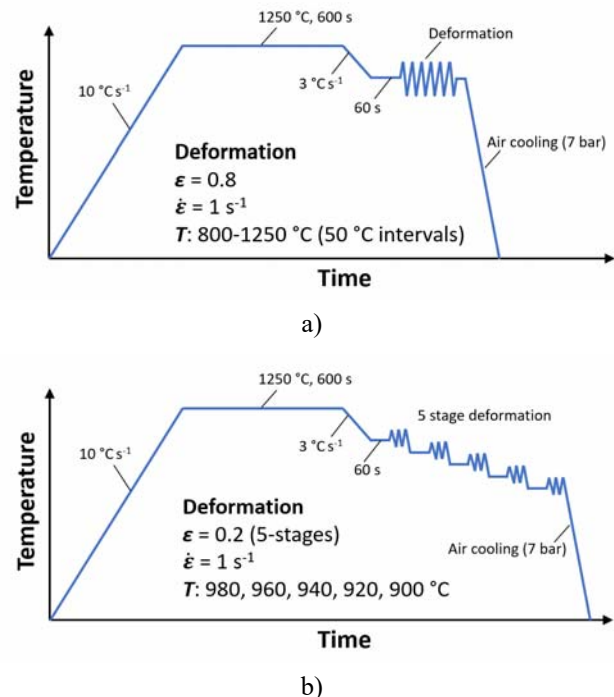


Figure 1. Schematic representation of a) plain hot compression test and b) multi-stage hot compression test.

Differential thermal analysis (DTA) was performed on cylindrical specimens with diameter and length of 4 and 3mm, respectively. Empty Al_2O_3 crucible cup was used as a reference. High-purity Ar 5.0 inert gas was used throughout the test to prevent oxidation. Three cycles of heating to 1550 °C and cooling to 1000 °C were performed, using heating/cooling rates of 20, 10 and 5 °C/min. Liquidus (T_{liq}) and solids temperature (T_{sol}) were determined on heating curves at 5 °C/min, using tangential method.

Dilatometric tests were done to study phase transitions in order to determine A_1 , A_3 and M_s temperatures, as also the necessary cooling rate to achieve fully martensitic microstructure after water quenching. Cylindrical specimens of diameter and length of 3 and 10 mm were used, respectively. Samples were heated with heating rate 1 °C/s to austenitizing temperature 900 °C and held for 15 minutes for homogenisation, followed by cooling using varying cooling rates from 0,1 to 100 °C/s.

2.2 Industrial scale

Production process

Based on the results of laboratory testing, slightly modified chemical composition of Nb-Ti steel was selected for industrial trials. Steel scrap with limited copper content was charged and melted in electric arc furnace (EAF). Special care was taken for optimal dephosphorisation by strict temperature control, slag

basicity and active oxygen content. Steel melt was tapped without carryover EAF slag to prevent P_2O_5 reduction.

Steel melt was fully killed and high basicity slag was formed with lime addition to ensure optimal cleanliness and low sulphur content. Prior to vacuum treatment, all alloying additions were added, slag composition and viscosity were adjusted and melt was reheated to correct temperature and homogenised using bottom Ar stirring. Vacuum degassing was conducted to reduce the hydrogen and nitrogen content. Due to intensive Ar stirring and high basicity slag, optimal conditions for desulphurisation were achieved, resulting in less than 10 ppm S in the final heat analysis. After degassing wires were injected to the melt, including CaSi cored wire for modification of non-metallic inclusions to ensure high cleanliness and prevent nozzle clogging due to clusters of Al_2O_3 inclusions.

Steel was cast into slabs on continuous caster, where special care was taken to prevent possible reoxidation. Based on T_{liq} determined on DTA, optimal casting temperature was chosen. Slabs were stack cooled prior to charging into reheating furnace and hot rolled into plates with thicknesses of 8, 10, and 15 mm. Rolling was divided into three phases, roughing, holding, and finishing. During roughing, the aim was to achieve grain refinement with static recrystallization between the passes. Holding was conducted so that finishing can be done in the temperature range where intense precipitation of Nb(C,N) occurs, resulting in refined PAGS. Plates were air cooled.

Last stage of the production process was the heat treatment consisting of water quenching after holding on austenitization temperature of 920 °C, which was selected based on results of dilatometric tests. Finally, low-temperature tempering at 180 °C was conducted.

Testing

Heat analysis was determined using OES and LECO and mechanical properties were evaluated in QT in Q condition. Additionally, effect of holding on elevated temperatures on mechanical properties was studied.

3. RESULTS AND DISCUSSION

3.1 Laboratory scale

Chemical composition of laboratory heats is presented in Table 1. The amount of alloying elements is fixed, so that the effect of microalloying addition can be studied. Relatively small amounts of microalloying addition were added to prevent possible segregation, which can result in

Table 1. Chemical composition of the experimental heats in mass. %.

Heat	C	Si	Mn	Cr	Cu	Ni	Mo	Ti	Nb	V	B	N
Nb	0,19	0,24	0,85	0,52	0,38	1,3	0,42	-	0,013	-	0,0011	0,0029
Nb-V	0,17	0,23	0,88	0,51	0,37	1,3	0,40	-	0,013	0,02	0,0011	0,0046
Nb-Ti	0,18	0,23	0,87	0,52	0,35	1,3	0,41	0,013	0,014	-	0,0011	0,0031

centreline formation of the Nb(C,N) eutectic [4]. Generally, alloying system C-Mn is set for sufficient strength, with additions of Cr, Mo, Ni and B for hardenability, Ni is also added for low-temperature toughness, as it improves dislocation mobility within the iron lattice, shifting ductile-to-brittle temperature to lower temperatures. Amount of Cu is increased to simulate the industrial condition where steel scrap is used, as Cu content is higher compared to iron ore-based steelmaking.

Mechanical properties in Q and QT condition in relation to microalloying elements used is presented in Figure 2. Increase in $R_{p0,2}$ and decrease in tensile strength (R_m) is observed after low-temperature tempering. All three microalloying systems achieve the minimum required $R_{p0,2}$ of 1100 MPa, as also KV_2 of 27 J at -40 °C in transverse direction. When it comes to elongation ($A_{5,65}$) and R_m , most of the producers guarantee $A_{5,65}$ of at least 10 %, which is the same as lower strength grade S960QL, whereas R_m is often in the range 1200-1550 MPa. In our case, $A_{5,65}$ of at least 11 % and R_m in the range between 1350 and 1400 MPa were achieved.

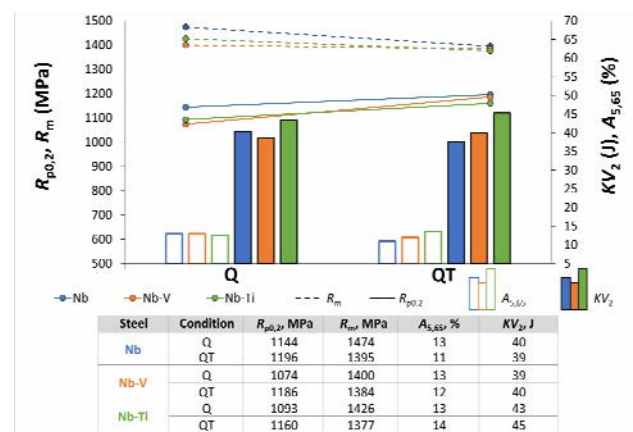


Figure 2. Mechanical properties of laboratory S1100QL heats in Q and QT condition.

PAGS distribution, expressed as equivalent circle diameter (ECD) calculated from individual grain area, is presented in Figure 3. Results are plotted against measured area and displayed in 15 area classes, which yields optimal results regarding possible bimodality, according to [5]. It is evident that the finest PAGS and narrowest distribution were achieved by Nb-Ti microalloyed steel, which explains highest $A_{5,65}$ and KV_2 values. Finer PAGS is the consequence of Ti addition, which forms small and stable TiN that pin austenite grains during reheating prior to hot deformation. Due to the finest PAGS, Nb-Ti microalloyed steel was chosen for industrial testing.

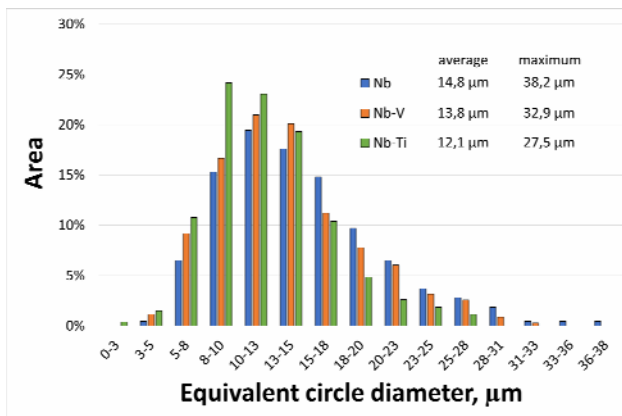


Figure 3. PAGS distribution in relation to microalloying system used.

For successful industrial implementation several parameters are critical, such as superheat before casting, thus T_{liq} of 1505 °C was determined from DTA heating curve. Optimal superheat was calculated to be 1530 °C. T_{sol} was determined to be 1473 °C.

Another critical process is hot rolling, where T_{nr} is crucial for the rolling schedule. It was determined to be 932 °C and practically matched the empirically determined T_{nr} , using widely accepted Boratto equation [6], calculated at 929 °C for a given chemical composition.

Results of the plain one-stage compressions tests, in terms of achieved microstructural evolution, are presented in Figure 4. PAGS increase with deformation temperature, due to enhanced mobility at elevated temperatures. First elongated grains are visible at 1000 °C, at 950 °C a combination of elongated and equiaxed grains is observed, while at 900 °C just a few equiaxed grains remain. Results are in accordance with calculated and experimentally determined T_{nr} .

For heat treatment, A_{c3} , A_{c1} and M_s temperatures were determined to be 800, 700 and 386 °C, respectively. Upper critical cooling rate, where fully martensitic microstructure is achieved, was determined to be 10 °C/s, which means, that water-quenching should result in martensitic microstructure, especially as the thicknesses of S1100QL plates are typically rather low.

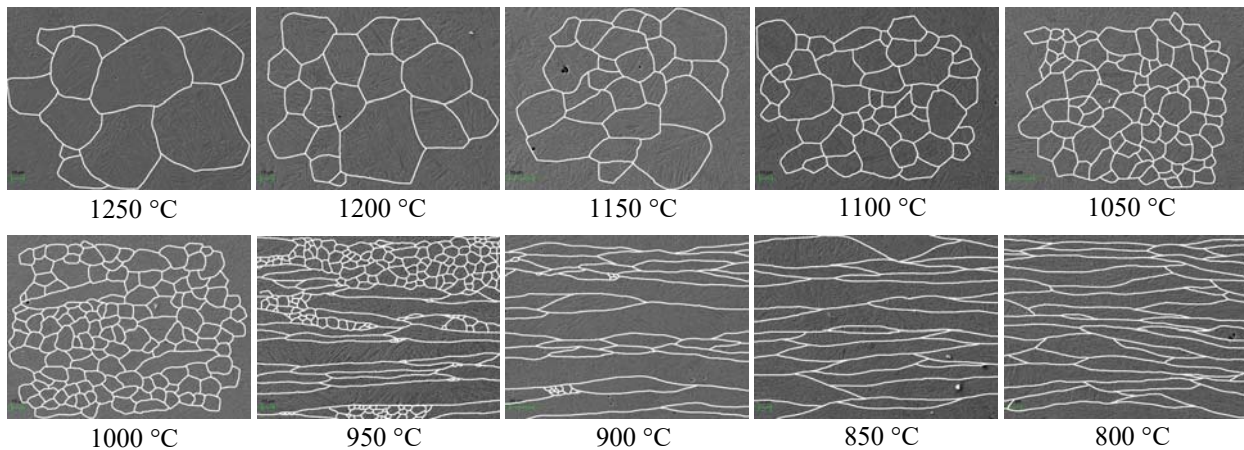


Figure 4. Evolution of microstructure in relation to deformation temperature of hot-compression tests.

3.2 Industrial scale

Heat analysis presented and compared to laboratory heat in Table 2. Some modifications were made, compared to laboratory heat, especially the increase of Mn and decrease of Ni content.

Quarto plates with thicknesses 8, 10 and 15 mm were produced as described in section 2.2. Microstructure in delivery QT condition is fully martensitic. Mechanical properties in Q and QT condition in relation to the plate thickness are presented in Figure 5. $R_{p0,2}$ increases with low-temperature tempering, providing a minimum of over 1100 MPa. All plates achieved over 10 % $A_{5,65}$ and KV_2 at

least 27 J at -40 °C in transverse direction. KV_2 increases with plate thickness, however one needs to notice that subsized Charpy V-notch specimens 7,5x10x55 were used for 8 mm thick plate, compared to standard 10x10x55 specimens used for 10 and 15 mm thick plate. Overall, all mechanical properties meet the requirements for S1100QL grade. Low-temperature tempering had a major contribution, especially in $R_{p0,2}$ increase, which could be due to the first stage of tempering by fine transition carbides precipitation and stress relaxation [7], [8]. Due to tempering at low temperatures, S1100QL has enhanced abrasion resistance, compared to lower strength grades.

Table 2. Chemical composition of the industrial heat and comparison with laboratory heat in mass. %.

Heat	C	S	P	Si	Mn	Cr	Cu	Ni	Mo	Ti	Nb	B	N	CEV
Industrial	0,17	0,0005	0,006	0,23	1,21	0,53	0,17	1,0	0,47	0,025	0,026	0,0016	0,0045	0,65
Laboratory	0,18	0,0005	0,007	0,23	0,87	0,52	0,35	1,3	0,41	0,013	0,014	0,0011	0,0031	0,62

Carbon equivalent was calculated according to the equation (1) of International institute of welding IIW.

$$CEV = C + Mn/6 + (Cr+Mo+V)/5 + (Ni+Cu)/15 \quad (1)$$

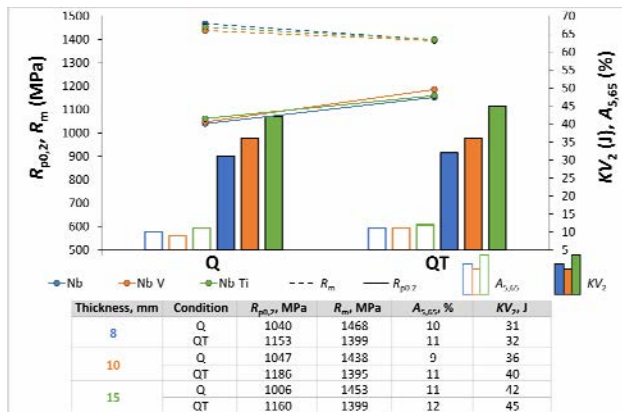


Figure 5. Mechanical properties of S1100QL plates in Q and QT condition.

S1100QL steel is often exposed to elevated temperatures, for example during preheating before welding. Figure 6 represents the effect of holding time at elevated temperatures on mechanical properties. KV_2 is stable up to 180 °C, which is the temperature used for low-temperature tempering. At 200 °C a drop occurs due to tempering embrittlement, typical for alloyed high-strength steels. Above 550 °C the KV_2 increases due to tempering of the martensite. $R_{p0.2}$ and R_m drop with increasing temperature, also the R_m to $R_{p0.2}$ ratio decreases. $A_{5.65}$ increases above 550 °C, similarly to KV_2 . Overall, maximum temperature which should not be exceeded is 180 °C.

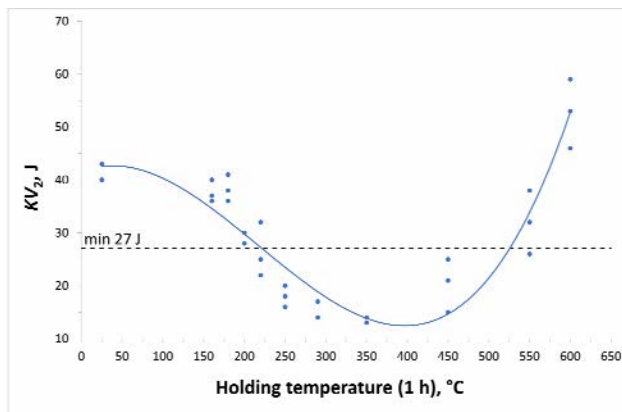


Figure 6. Effect of holding at elevated temperatures on impact toughness at -40 °C in transverse direction.

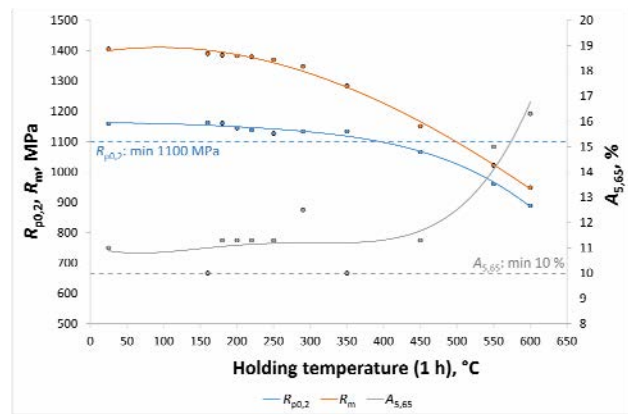


Figure 7. Effect of holding at elevated temperatures on tensile properties in transverse direction.

4. CONCLUSION

Laboratory test heats of ultra-high-strength S1100QL steel with different microalloying systems (Nb, Nb-V and Nb-Ti) were prepared and tested to determine optimal composition and processing parameters for industrial implementation. Based on the results, quarto plates were produced and tested to evaluate mechanical properties in final QT condition. The following results were obtained:

- Nb-Ti provided superior mechanical properties compared to Nb and Nb-V, especially in terms of KV_2 and $A_{5.65}$, due to pinning effect of small TiN precipitates, providing finer PAGs.
- Plates achieved the required mechanical properties in QT condition, where low-temperature tempering contributed to increase in $R_{p0.2}$, compared to Q condition.
- 180 °C was selected to be the maximum temperature which should not be exceeded as there is a drop of impact toughness, which occurs due to the tempering embrittlement.

References

- [1] Hot Rolled Products of Structural Steels-Part 6: Technical Delivery Conditions for Flat Products of High Yield Strength Structural Steels in the Quenched and Tempered Condition, EN 10025-6 Standard; European Committee for Standardization: Brussels, 2019.
- [2] ZHAO,J., JIANG,Z.: *Thermomechanical Processing of Advanced High Strength Steels*, Progress in Materials Science, 94 (2018) 174-242.
- [3] FODER,J., KLANČNIK,G., BURJA,J., KOKALJ,S., BRADAŠKJA,B.: *Mean-Flow-Stress Analyses of Laboratory Hot-Rolled S1100QL Steel with Minor Nb Addition*, Materiali in Tehnologije, 54(6) (2020) 901-908.
- [4] BERNETIČ,J., BRADAŠKJA,B., KOSEC,G., KOSEC,B., BRICELJ,B.: *Centreline Formation of the Nb(C,N) Eutectic in 0.15 % C; 0.0071 % N; 0.022 % Nb; 0.033 % Al and 0.003 % S Structural Steel*, Materiali in Tehnologije, 42 (2008) 291-294.

- [5] CHAKRABARTI,D., STRANGWOOD,M.: *Characterisation of Bimodal Grain Structures in HSLA Steels*, Materials Characterization, 58 (2007) 423-438.
- [6] BARBOSA,R., BORATTO,F., YUE,S.,JONAS,J.J.: *The influence of chemical composition on the recrystallisation of microalloyed steels*. Proceedings of the Processing, Microstructure and Properties of HSLA steels, Tokyo, (1988) 383-390.
- [7] KRAUSS,G., *Tempering of Lath Martensite in Low and Medium Carbon Steels: Assessment and Challenges*, Steel Research International, 88 (2017) 1-18.
- [8] FODER,J., BURJA,J., KLANČNIK,G. *Grain Size Evolution and Mechanical Properties of Nb, V-Nb, and Ti-Nb Boron Type S1100QL Steels*, Metals 11(3) (2021) 1-16.



FRACTURE ANALYSIS OF VEHICLE-MOUNTED TELESCOPING COMMUNICATIONS MAST

NADA ILIĆ

Military Technical Institute, Belgrade, nadalic67@vti.vs.rs

LJUBICA RADOVIĆ

Military Technical Institute, Belgrade, ljubica.radovic@vti.vs.rs

MAJA MLADENOVIĆ

Military Technical Institute, Belgrade, mmaja011@gmail.com

JOVANA MANDIĆ

Military Technical Institute, Belgrade, jmandic96@gmail.com

VESNA PEJOVIĆ

Military Technical Institute, Belgrade, vesna3393@gmail.com

Abstract: In this paper a fractured connector plate for a telescoping antenna mast made of aluminum alloy EN-AW 2007 was examined. The goal of the investigation was to determine the cause of fracture which occurred during attempting to raise the antenna. Specimens taken from the mast were visually examined, and the fracture surface was examined using a scanning electron microscope. Chemical analysis, microstructural analysis, electrical conductivity measurements, tensile test and hardness test were performed in order to investigate the properties of the material. Fracture occurred fast and visual and fractographic examinations showed that there is no visible plastic deformation near the fracture surface, which are characteristics of a quasibrittle fracture. It was shown that the mechanical properties of the examined specimens do not satisfy the minimal values defined in the standard for this material. All conducted tests indicated that the material had not been heat treated and mechanically worked, so applied stress during handling/raising the antenna led to the rapid quasibrittle fracture.

Keywords: alloy EN AW-2007, telescoping mast, fractography.

1. INTRODUCTION

One of the most effective and inexpensive radio antenna is a mast antenna that is mounted on the vehicle. It must be lightweight with high mechanical strength, mobile and allow easy mountings.

In spite of requirement for high material quality and calculation of stresses and strengths, several reports on antennas failure, with different reasons, were published [1-4]. That means that the mast's strength must be greater than the stress caused by the loads applied to it. The telescoping vehicle-mounted communications mast located on the PEBZOTS system fractured after attempting to raise the antenna. Further conditions under which the fracture occurred are unknown. The aim of this paper is to determinate the cause of fracture that occurred during handling/raising the antenna mast.

2. EXPERIMENTAL

The fractured antenna mast is made of aluminum alloy. The chemical composition is given in Table 1. The used material, is alloy EN AW-2007 (AlCu4PbMgMn),

according to SRPS EN 573-3 [5].

Table 1. Chemical composition of the antenna mast.

Element	Mass. %
Cu	4.51
Mg	0.65
Mn	0.60
Si	0.49
Fe	0.42
Zn	0.40
Bi	0.07
Pb	0.80
Sn	0.02
Al	bal.

A photograph of the base of the mast is shown in Figure 1. The cylinder and connector plate were machined from one round bar with a diameter of at least 370 mm.

After visual observation by the naked eye and by using magnifying glass, the macroscopic appearance of the fractured part was photographed.

Hardness was measured by Brinell method (HB 2,5/62,5), according to SRPS EN ISO 6506-1 [6].

Tensile tests were performed in accordance with SRPS EN ISO 6892-1 [7] on three tensile specimens taken in longitudinal direction from the cylindrical part of the mast, and three specimens taken from the connector plate of the mast, as shown in Fig. 1. The L_0 length of the short proportional round tensile samples was 30 mm at a sample diameter of 6 mm. The tensile test was performed at the strain rate of $\dot{\epsilon}=2.7 \cdot 10^{-3} \text{ s}^{-1}$.

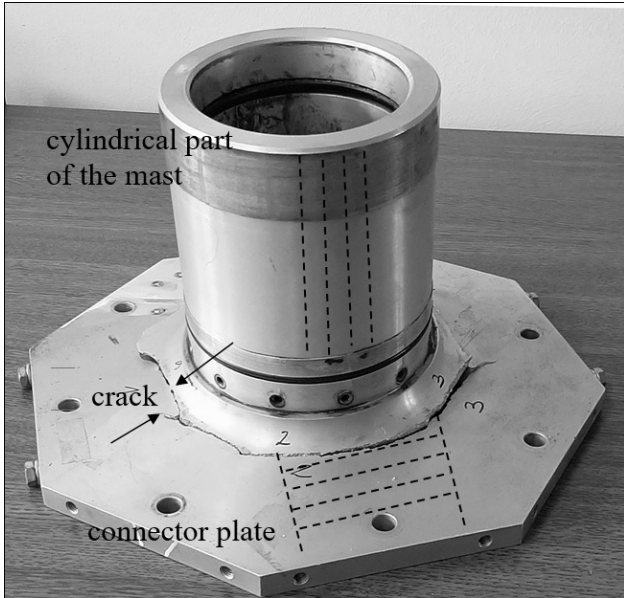


Figure 1. The fractured antenna mast. Dashed lines represent the location of samples for tensile testing.

The fracture surfaces of the tensile specimens were examined by scanning electron microscope JEOL 6010LV.

Electrical conductivity of the mast material was measured at 60kHz using Sigmatest D2.068.

Four specimens were taken from the mast in longitudinal and transverse direction from both the cylinder and connector plate, in order to examine the microstructure. The samples were prepared by grinding, polishing and electrochemical polishing in dilute perchloric acid, followed by electrochemical etching in Barker's reagent. The polished and etched surfaces were examined using light microscopy.

3. RESULTS

3.1 Visual examination

Visual examination of the fractured part showed that the fracture was initiated on the outer surface of the plate, close to the plate-to-cylinder radius, Figures 1 and 2. No visible plastic deformation near the fracture surface was observed. The fracture initiation point was identified by following the chevron pattern at the fracture surface, as shown in Figures 2 and 3. The chevron pattern pointing to the fracture initiation point is shown in Figure 3. Several secondary cracks were also visible, as shown in Figure 3. The crack propagated from the surface of the plate gradually in circumferential direction, around the

cylinder, as well as, throughout the plate.

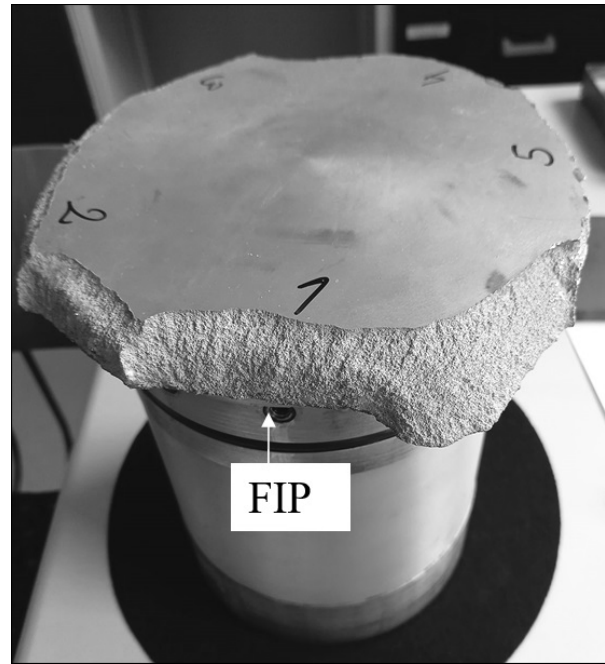


Figure 2. The fractured antenna mast, indicating the fracture initiation point - FIP.

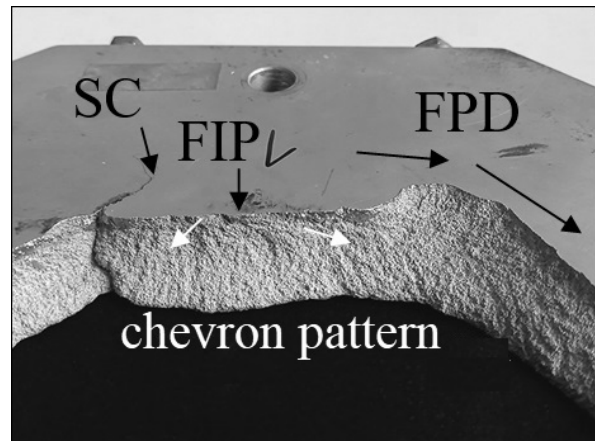


Figure 3. Plate-side fracture surface. FIP - fracture initiation point, FPD - fracture propagation direction, SC - secondary crack.

3.2 Hardness

Results of the hardness measurements of the antenna mast are given in Table 2.

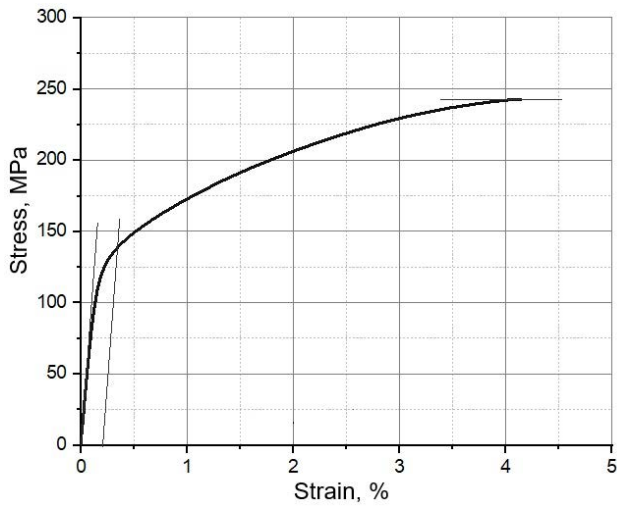
Table 2. Hardness of the antenna mast, HB

specimen	Hardness HB 2,5/62,5	Average
cylinder	85; 85; 87; 85; 85; 86	86
plate	85; 87; 86; 86; 87; 85	86

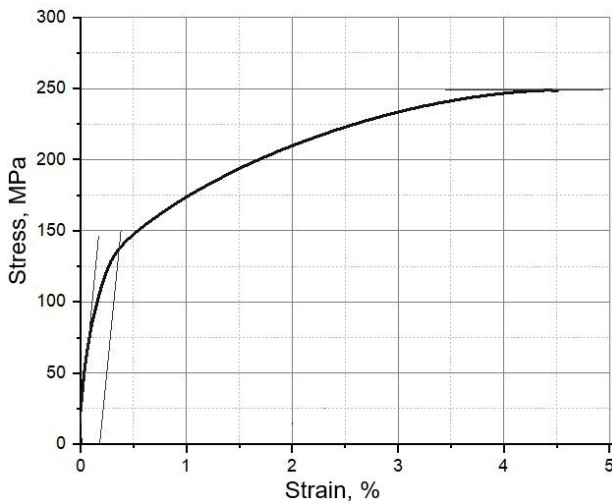
3.3. Tensile properties

The average values of the yield strength (YS), ultimate tensile strength (UTS) and elongation (A_5) observed during tensile testing of specimens taken from the antenna

mast are shown in Table 3. Characteristic stress-strain curves are shown in Figure 4. The diagrams indicate that the fracture occurs immediately after reaching the maximum force, with no posthomogenous elongation observed.



a)



b)

Figure 4: Characteristic stress-strain curves of tensile specimens taken from (a) the cylindrical part, (b) the connector plate of the antenna mast.

Table 3. Results of tensile tests.

specimen	YS [MPa]	UTS [MPa]	A ₅ [%]
cylinder	139	241	4.0
plate	138	249	3.9

3.4. Fractography

SEM analysis of the fracture surface of tested tensile samples revealed areas of transcrystalline fracture alongside with dimple areas, fractured coarse particles, as well as porosity with visible dendrites Figures 5, 6 and 7.

3.5. Electrical conductivity

The results of electrical conductivity measurements of the connector plate are given in Table 4.

Table 4. Electrical conductivity of the connector plate

%IACS					Aver. %IACS
41.10	40.93	40.78	40.72	40.74	40.85

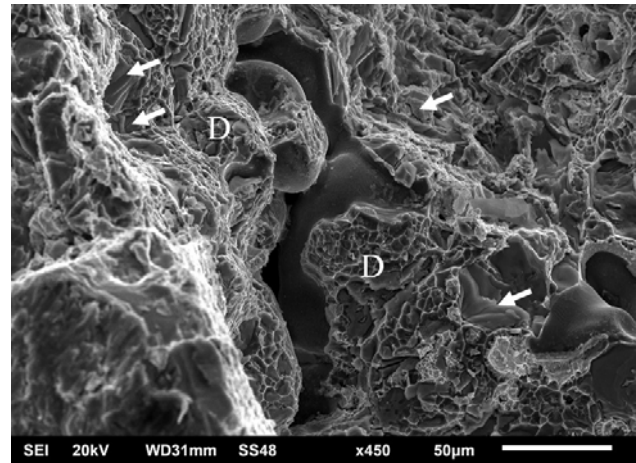


Figure 5. Fracture surface of tensile specimens as observed by scanning electron microscopy. Areas of dimpled fracture (D) Arrows indicate the fractured particles. Interdendritic porosity is visible in the middle of the microphotograph.

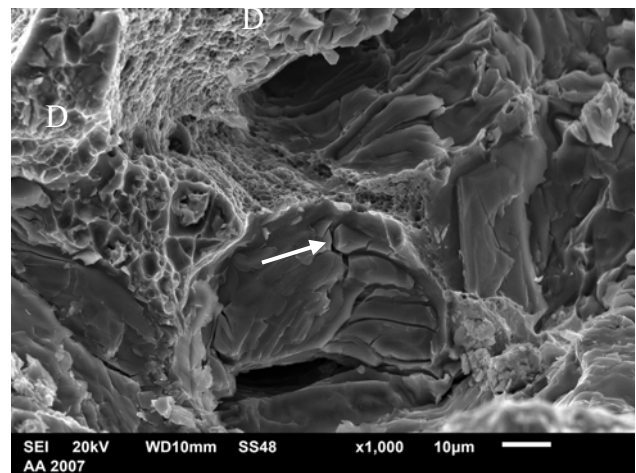


Figure 6. Fractured particles indicated by the arrow. Areas of dimpled fracture are also observed (D).

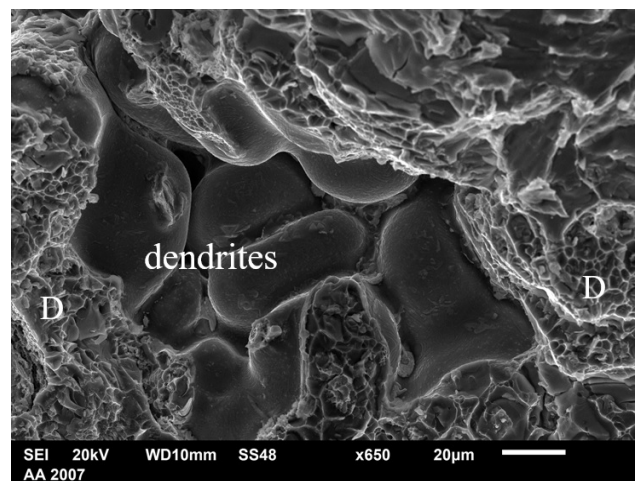


Figure 7. Fracture surface of the tensile specimens showing dimpled fracture (areas D) and exposed dendrites.

3.6. Microstructure

Figure 8 shows the microstructure of the specimens as polished. Large interdendritic porosity (IP), as well as large amount of shrinkage porosity (black spots) were observed in the cast microstructure. Figure 9 shows the microstructure as etched. A dendritic grain morphology was revealed.

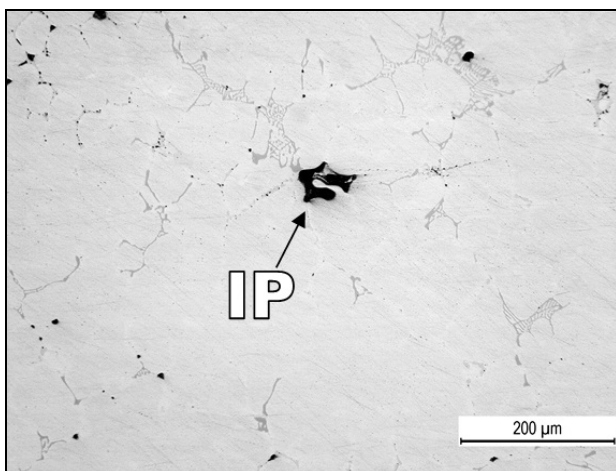
4. DISCUSSION

Visual examination of the fractured mast antenna revealed that crack was initiated on the outer surface of the plate, close to the plate-to-cylinder radius (Figure 1 and 2). It is evident that the crack was initiated in a region of high localized stress, and propagated circumferentially, around the cylinder, as well as, throughout the plate.

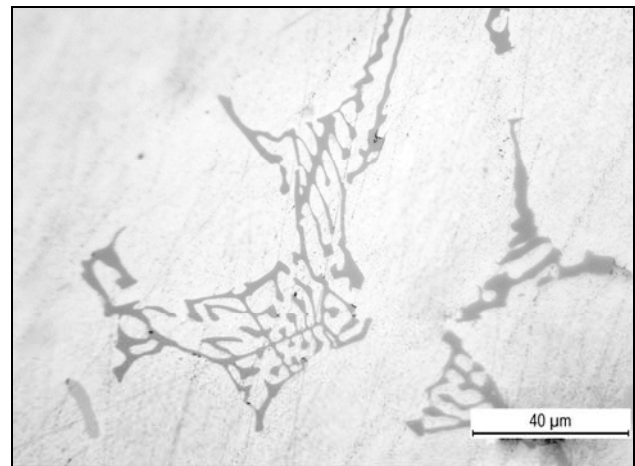
The observed chevron pattern on the fractured surface, pointing to the fracture initiation point is characteristic of macroscopic brittle behaviour of materials [8, 9].

Microstructural examination has shown that mast antenna was produced of cast material. Observed dendritic grain morphology is typical for alloys in as cast condition [10]. Interdendritic porosity was observed by the light microscopy (Figure 8), and by the SEM on the fracture surface of the tensile specimens (Figure 7).

Alloy EN AW-2007 [AlCu4PbMgMn] is a wrought type of aluminum alloy, and is not found in standards for aluminum alloy castings [5, 11, 12]. It is common that cast and homogenized bar subjected to a mechanical working, such as forging, rolling, extrusion, etc., result in uniform metallurgical structure. So, this aluminum alloy is intended to be used in form of wrought products, and it is very suitable for high machining speeds, due to Pb addition [13-16]. This alloy is not suitable to be used as cast, such as in this case. Additionally, the mechanical properties are defined for extruded bars of a maximal diameter of 250 mm [11]. The bar used to produce the mast exceeds this size limit, since it was not subjected to mechanical working.



a)



b)

Figure 8. Microstructure of the specimen, as polished: (a) Interdendritic porosity (IP) and shrinkage porosity (black spots), (b) shape of particles within the metal matrix. Light microscopy.

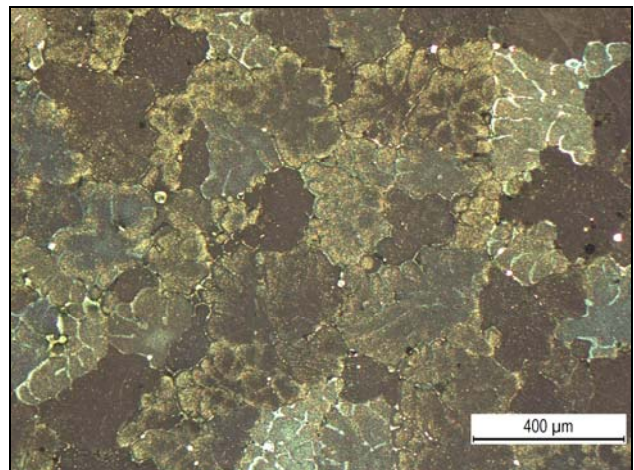


Figure 9. Microstructure of the specimen taken from the cylindrical part of the mast in perpendicular direction, etched. Dendritic grain morphology is present. Light microscopy under polarized light.

Therefore, it is expected that mechanical properties of the mast material were lower than required for extruded bars made of EN-AW 2007 [11]. It was confirmed by the mechanical testing (Tables 2 and 3). Hardness, as well as strength values were significantly lower than required by the standard for extruded bars (for maximal diameter of 250 mm). The results of tensile test were in accordance with the observed microstructure, as the presence of dendritic morphology and porosity contribute to the reduced mechanical properties, and the brittleness of the material.

The low tensile elongation and the lack of posthomogenous elongation (Table 3 and Figure 4), as well as the macroscopically brittle appearance of the fracture, all suggest that the material was not appropriately heat treated after casting. This is also supported by the higher electrical conductivity than the typical values given in literature for EN AW-2007 in T4 condition (18÷22 MS/m i.e. 30.96÷37.84 %IACS) [15, 16].

5. CONCLUSION

Fracture surface analysis showed macroscopic characteristics of quasibrittle fracture.

Crack initiated on the outer surface of the plate, close to the plate-to-cylinder radius.

The temper of the used EN AW-2007 alloy is not suitable for this application. The results suggest that material of the mast was not subjected to appropriate heat treatment and mechanical working, so, applied stress during handling/raising of the antenna mast, led to the rapid quasibrittle fracture.

References

- [1] Wulpi, D.J., *Understanding how components fail*, 3th Ed., ASM International, Metals Park Ohio, 2013.
- [2] List of catastrophic collapses of broadcast masts and towers, https://en.wikipedia.org/wiki/List_of_catastrophic_collapses_of_broadcast_masts_and_towers.
- [3] Dixon, B., *Military mast problems and solutions*, QST www.arrl.org, 2020.
- [4] Daso. D., *Antenna Masts: Safety and Selection*, <https://static.dxengineering.com>.
- [5] SRPS EN 573-3 - Aluminium and Aluminium Alloys – Chemical Composition and Form of Wrought Products – Part 3: Chemical Composition and Form of Products.
- [6] SRPS EN ISO 6506-1 – Metallic Materials – Brinell Hardness Test – Part 1: Test Method.
- [7] SRPS EN ISO 6892-1 – Metallic Materials – Tensile Testing – Part 1: Method of Test at Room Temperature.
- [8] ASM Metals Handbook, *Failure Analysis and Prevention*, Vol. 11, 9th Ed. ASM Metals Park Ohio, 1986.
- [9] ASM Metals Handbook, *Fractography*, Vol. 12, 2th Ed., ASM Metals Park Ohio, 1992, electronic files in 1998.
- [10] ASM Metals Handbook, *Metallography and Microstructures*, Vol. 9, 9th Ed., ASM Metals Park Ohio, 1985.
- [11] SRPS EN 755-2 – Aluminium and Aluminium Alloys – Extruded rod/bar, tube and profiles – Part 2: Mechanical Properties.
- [12] SRPS EN 1706 – Aluminium and Aluminium Alloys – Castings – Chemical Composition and Mechanical Properties.
- [13] JR Davis, *Aluminium and Aluminium alloys*, ASM International, 2001.
- [14] ASM Handbook, Vol. 16: *Machining*, ASM Metals Park Ohio, 1989.
- [15] Data Sheet: *Aluminium 3.1645 (AlCu4PbMgMn)*, Xometry, <https://xometry.eu/wp-content/uploads/2021/02/Aluminium-3.1645>.
- [16] https://www.leichtmetall.eu/site/assets/files/datenblatt/2007_Produktdatenblatt_A4-en_us.pdf



APPLICATION OF IT TECHNOLOGY IN WASTEWATER TREATMENT

MILJAN MILETIĆ

Technical College of Applied Studies in Kragujevac, section in Krusevac, Krusevac, mmelektronik1@gmail.com

MARINA ILIĆ

Military Technical Institute, Beograd, marinailic1970@gmail.com

TATJANA MARKOVIĆ

Military Technical Institute, Beograd, tanjin.mejl@gmail.com

BILJANA MIHAJLOVIĆ

Trayal, Krusevac, biljanamih037@gmail.com

Abstract: The paper that will be presented below deals with the application of modern information technology solutions in wastewater treatment and processing. Described solutions are applied to the treatment of water in the production process of the chemical industry, which deals with anodizing, galvanizing, nickel plating, chrome plating and cleaning of metal products. Microcomputers are also used to control the processing process, as well as an industrial server which parameters obtained from sensors and actuators are entered. This data is further processed to obtain relevant plant management data. The operation of the plant is fully automated with a minimum number of people who are now manipulating to add the raw materials necessary for the operation, as well as to take away the by-products created by the operation of the plant. All decisions and control are performed by a microcomputer and a PLC. The results obtained during the operation of the plant give up to 18% better results than the plants that are not fully automated. The results were verified in a certified laboratory. The following programming languages Java, C, C ++, PYTHON, MySQL, Ladder were used for the functioning of the existence.

Keywords: pH, sensors, PLC, microcomputer.

1. CHARACTERISTICS OF WASTEWATER QUALITY – UNPROCESSED

Significant characteristics of the quality of wastewater from chemical industry processes are:

- extremely high content of substances in the suspension, including fats and oils, which must be removed, because they would extremely quickly block - saturate the surface of activated carbon and prevent the access of dissolved and other substances that should be adsorbed.
- the content of H₂S - sulfides above MDK, which causes a very unpleasant smell of water and atmosphere in the premises of the chemical industry. H₂S originates from the extraction process, where sodium sulphide is used. It should be emphasized that hydrogen sulfide is treated as a dangerous industrial pollutant (of water and air) and as such is one of the test substances for assessing the quality of industrial protective agents. [1]
- high content of organic substances, dissolved in water, which cause high values of KMnO₄, HPK, BOD, etc.
- content of trivalent chlorine (Cr³⁺) above MDK originating from chemical industry processes. The quality characteristics of chemical industry process

wastewater are given based on average analyzes of water taken from several different chemical industry factories, as well as on the basis of data from the literature.

Table 1 gives a rough overview of the quality of waste water from chemical industry processes before treatment:

Table 1. Overview of the quality of waste water before treatment

TYPE OF ANALYSIS	VALUE
pH value	6,5 – 10
Water temperature	10 – 20 °C
Dry residue	6 – 10 g/l
Residue after annealing suspended matter	4 – 6 g/l
Electrical conductivity	above 2000 µS/cm
Turbidity (in degrees)	about 100
Color (in degrees)	400 – 50
Consumption of KMnO ₄	200 – 500 mg/l
HPK	100 – 300 mg/l
BPK	20 – 50 mg/l
Ammonia (N)	0,5 – 2 mg/l
The appearance of the water	partly cloudy
Sulfides (H ₂ S)	5 – 20 mg/l
Cr ³⁺ content	30 – 50 mg/l
Chloride content	10 – 30 mg/l
Nitrate content (N)	about 1,5 mg/l

3.2 Description of the technological stages of the water treatment process

The wastewater treatment process includes technological stages that are implemented as:

- pretreatment of water in basins into which water is introduced from chemical industry processes and
- final filtration and adsorption on granulated activated carbon.

It is planned that the wastewater treatment process is carried out 6-7 times during the month, depending of the intensity of work processing plant and the implemented processing processes.

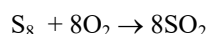
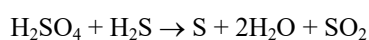
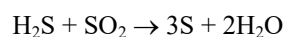
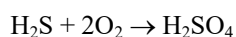
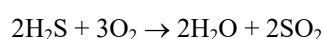
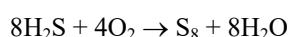
The pre-treatment of wastewater from pipeline I will be carried out in this department, in a pool divided into two chambers (the total volume of the pool is about 10 m³).

The characteristic of these waters is a high content of suspended matter (particles of dirty from washing leather, fat and oil, etc.) and a high content of H₂S, above the MDK value, which is separated from Na₂S.

In the first chamber of the pool, substances suspended in the water settle, which is enhanced by adding, dosing a certain amount of flocculant. By overflowing, the water from the first chamber of the pool passes into the second, where it is processed in order to effectively remove H₂S.

H₂S is, in principle, removed by adsorption on activated carbon but previously it is necessary to carry out a rapid pretreatment of water in order to oxidize H₂S. Oxidation of H₂S, which is dissolved in water, is often insufficient only by the aeration process (by blowing air with a compressor), but water must be pre-treated by adding a certain amount of Zavel water solution (sodium hypochlorite NaClO)₂ a very effective oxidizing agent for H₂S.

The mechanism of the H₂S oxidation process can be represented by the following equations:



For the adsorption of H₂S, i.e. sulfur and sulfur compounds, on granulated activated carbon, a layer of water film on the surface of activated carbon is required.

Oxidation of H₂S is additionally carried out in larger, coarser pores, followed by sulfur adsorption in micropores of activated carbon. In order to protect the adsorption capacity of GAU (granular activated carbon) and extend its service life, smaller doses of powdered

activated carbon can be used in water pretreatment, which is dosed together with flocculant.

The final elimination of H₂S, i.e. sulfur and sulfur compounds, is carried out by filtration on the GAU of the collected waste water from pipelines I and II, which are discharged into the second part of the pool with a volume of 50 m³.

3.2.1. Pretreatment of wastewater from pipelines II

The pre-treatment of this waste water is carried out by treatment with a special flocculant for the precipitation of trivalent chromium (Cr³⁺) at a certain pH value of the water, in the first of three water treatment basins.

Precipitation of trivalent chromium (Cr³⁺) can be carried out without adding flocculant if ferric hydroxide floc (Fe(OH)₃) is present. These waters also have an increased content of suspended matter, which settles after treating the water with flocculants and coagulants.

After the discharge of waste water from pipeline I, which are basic, into the same pool, the water is practically neutralized, so that a special adjustment of the pH value is not necessary.

Collective wastewater from the first basin is poured into the second basin, from where its further processing is carried out by filtration and adsorption on GAU.

3.2.2. Water treatment by filtration and adsorption on GAU

The final treatment of waste water is carried out by the processes of filtration and adsorption, whereby water is transported by a pump at a certain speed through two regularly connected filters, i.e. an adsorber filter.

Final water treatment is done 4-5 times a month, in batches of about 2-2.5 m³. Finishing capacity is 0.5 m³/h.

The first filter in the row is filled with hydroanthracite, type HYDRACIT M* (0.6-1.6), as a filtration material, up to about two-thirds of the height of the filter in order to ensure conditions for countercurrent washing of the filter filling. Filtration on a "mechanical filter" is necessary to eliminate residual substances in suspension and to protect the GAU filter.

The second filter has the role of filter adsorber. It is filled with granulated activated carbon (K-81/B or H-0.8) up to two-thirds of its height, in order to ensure countercurrent washing of the filter filling. It is intended for the adsorption of organic substances dissolved in water and H₂S oxidation products, which are also dissolved in water. [4]

The operating parameters of the filter adsorber are:

- dwelling time 15 – 20 minutes.
- filtration speed 4-6 m/h.

In any case, treated wastewater is discharged into the third pool with a volume of about 15 m³, so the chemical industry can operate for five months without releasing the treated wastewater or returning it to the process.

3.2.3. Sludge filtration

In the first chamber of the basin for waste water in pipeline I and the first basin for discharging water from pipeline II, after pre-treatment of water, sedimentation of suspended substances is carried out. Pool cleaning, sludge filtration, is done once a month, using a special sludge filter, which squeezes the sludge, keeping the sludge on a special filter cloth, from which it can be easily cleaned and separated. Sludge filtration separates sediment and filtrate. The separated sediment can be deposited in PE bags and deposited together with solid waste from chemical industry processes. The filtrate is, in principle, returned for reprocessing.

3.2.4. Example of a plant for the processing and purification of waste water in the chemical industry

Each of these species of wastewater has its own bathtub. In each tub there is a water level meter, a pump for transferring water to the collection tub located in the water treatment plant, a water flow meter (these water flow meters are a legal obligation to monitor the efficiency of the wastewater treatment plant). These meters are also located on the outlet tubs towards the recipient. At any moment, these flow parameters are recorded in the database, in order to create reports on the efficiency of the plant on a daily, monthly, and annual basis and calculate the payment for the discharge of wastewater into the recipient. The pump further uses a pipe to transfer water to the electromagnetic valve (it is transferred from tubs 1 and 2, i.e., the tub for acidic and basic water to the collection tub for acidic and basic wastewater located in the wastewater treatment plant), while from tub 3 a separate pipeline in particular, the water with heavy metals and chromium is transferred to the chromium collection tank. The purpose of the electromagnetic valve is to close the water supply in the sump - only one of the waste waters can come, either alkaline or acidic. In the collection tub for basic and acidic water, there is a pH meter whose role is to measure the pH value of waste water (picture no. 2)

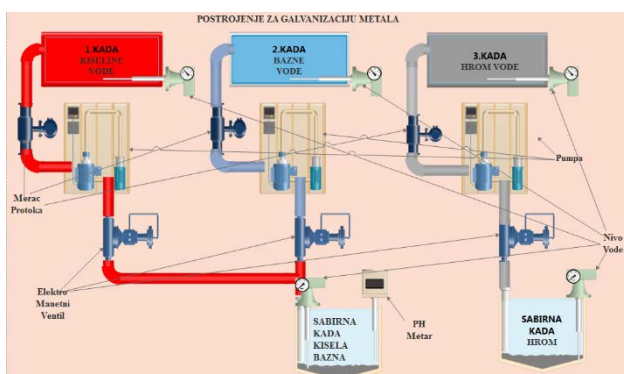


Figure 2. Wastewater processing processes

Waste water from the collection tub is transported to tanks (acid or base tanks) based on the pH value parameter (at 25°C water with a pH less than 7 is acidic, above 7 is basic). These tanks have mixers that maintain the concentration in a stable mode, without the possibility

of sedimentation. The water from one of these canisters is transported through a pipeline to a collection tank where the pH value is checked again. If the pH is less than 5, base from the base canister is added, otherwise, acid. This water is mixed and oxygen is pumped in. If the pH value of the water cannot be brought to a value of 6 to 8, concentrated acid is added, that is, prepared milk of lime, if basic water is needed. The water remains in this tank until its value is within the range of 6 to 8. Then the water is transported to the precipitator and after settling and checking the pH value, it is discharged into the recipient or returned for processing (picture no. 3).[5]

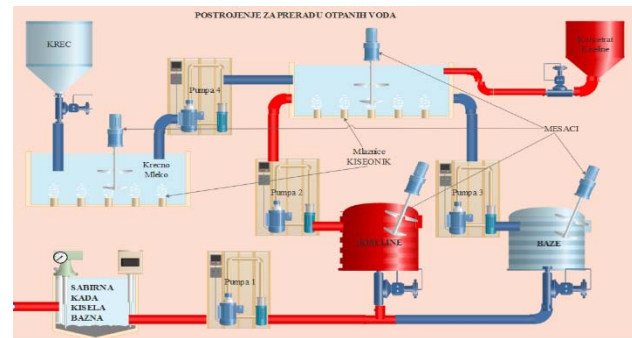


Figure 3. Processing of basic and acidic waste water

From the collection tank, chrome water is transported by pump to tank 2, where mixing, measurement of the water level in the tank, introduction of oxygen and introduction of thickener are carried out. The raw material is fed into the tank of the thickener. It is then transferred to tub 1 with a screw dispenser. A special mixer combines this thickener with clean water, and with the help of another dispenser, it is transferred to tub 2. After mixing for several hours, the water from tub 2 moves to tub 3, where the mixing of water continues and injection of oxygen. Then this water is transported by pump 2 to the filter press, where the collected heavy metals and thickeners are deposited on the filters, and the water obtained by pressing is returned to the precipitator tub 4 (picture no. 4).

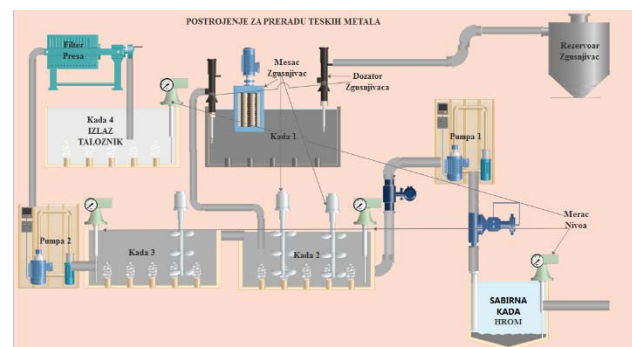


Figure 4. Separation of heavy metals from waste water

From the plant for the processing of basic and acidic waste water, water is delivered from sedimentation tank 1. It is then transported to sedimentation tank 2, where after measuring the pH value and temperature of the water, and in case the pH value is within the specified limits, the water is transported by pump 2 to the stabilization bath - laminator 1. This tub consists of numerous laminated

metal spirals. The dimensions of the bathtub are 10 m long, 2 m wide and 2 m high. By using the laminator, the water path through the tub was extended so that it now amounts to 100m. This leads to additional purification of water and in these laminators, oxygen is pumped in, thereby increasing the electroconductive potential of water. Pump 3 transfers water from stabilization tub 1 to stabilization tub 2, which has the same dimensions and the same operating principles.

From the plant for processing water with heavy metals (bath 4 - outlet settler), water is transferred by pump 4 to the stabilization bath of laminator 1. The process is the same as in the previously explained example. At the exit of the stabilization tub of laminator 2, there is an electromagnetic valve whose role is to prevent waste water from spilling into the recipient in the event that the values on the pH meter located in the recipient do not meet the set parameters, that is, the value of the redox potential is not within the limit values. This valve can be closed, so in case of weather events, when the level of the recipient rises suddenly, the plant is protected from flooding in this way (picture no. 5).

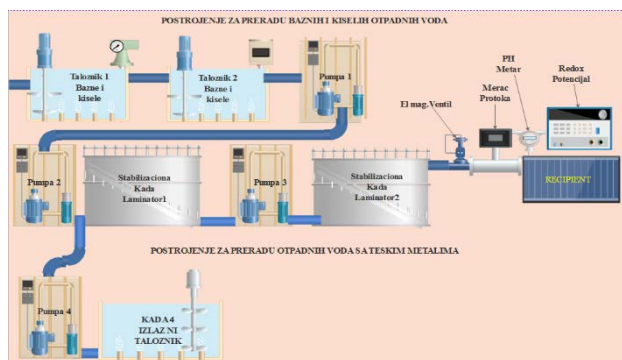


Figure 5. Discharge of treated water

4. VALUES MEASURED (VERIFIED) BY CHECKING IN AN AUTHORIZED (CERTIFIED) LABORATORY

By checking the value, which is carried out once a month in an authorized reference laboratory, exceptional results were obtained in which the values for the maximum allowed discharge from the plant are even 20% lower than the values prescribed by the legislator. In the tables below you can see the values for one month.

Table 3. Confirmed values of wastewater from an authorized laboratory

Parameters	Unit of measure	Processes											
		P1	P2	P3	P4	P5	P6	P7	P8	P9	P10	P11	P12
Aluminium	mg/l	2	-	2	-	-	-	-	-	1	2	1	2
Nitrogen from ammonia	mg/l	80	-	-	-	25	45	-	-	15	20	-	-
HPK	mgO ₂ /l	300	-	90	-	180	3500	-	-	90	300	320	200
Iron	mg/l	1	-	-	-	2	-	-	-	2	2	2	2
Fluorides	mg/l	40	-	40	-	40	-	-	-	40	20	-	-
Nitrogen and nitrates	mg/l	-	-	4	-	-	4	-	-	3	4	-	-
Hydrocarbons(III)	mg/l	8	-	9	-	7	9	-	-	8	8	7	9
Phosphor	mg/l	1	-	1	-	1	1	-	-	1	1	1	1
Toxicity to fish (TF)(IV)		5	-	1	-	4	5	-	-	3	4	4	5

Table 4. Confirmed values of wastewater from an authorized laboratory

Parameters	Unit of measure	Processes											
		P1	P2	P3	P4	P5	P6	P7	P8	P9	P10	P11	P12

AOH (adsorbing organic halogen)	mg/l	0,67	-	0,62	-	0,59	0,61	-	-	0,62	0,66	0,66	0,6
Arsenic	mg/l	0,06	-	-	-	-	-	-	-	-	-	-	-
Barium	mg/l	-	-	-	-	-	1,33	-	-	-	-	-	-
Lead	mg/l	0,33	-	-	-	0,32	-	-	-	0,34	0,33	-	0,33
Cadmium	mg/l	0,13				0,07			-	0,14	0,05		0,17
	kg/t	0,2							-				
Free chlorine	mg/l	0,33	-	-	-	-	0,32	-	-	-	0,33	-	-
Total chrome	mg/l	0,33	-	0,33	-	-	-	-	-	0,33	0,33	0,5	0,32
Chrome VI	mg/l	0,06	-	0,06	-	-	-	-	-	0,05	0,05	-	0,08
Cobalt	mg/l			0,65						0,66			
Cyanides	mg/l	0,13					0,66	-	-		0,14		
Copper	mg/l	0,33	-	-	-	-	-	-	-	0,33	0,33	0,5	0,31
Nickel	mg/l	0,33	-	-	-	-	-	-	-	0,33	0,34	0,5	0,32
Hydrargyrum	mg/l								-				
	kg/t								-				
Selenium	mg/l									0,67			
Silver	mg/l	0,06						-	-				
Sulfides	mg/l	0,67	-	-	-	-	-	-	-	0,67			
Tin	mg/l	1,33		1,38		1,31		-	-				
Zinc	mg/l	1,33	-	1,36		1,37		-	-	1,35	1,33	1,32	1,344

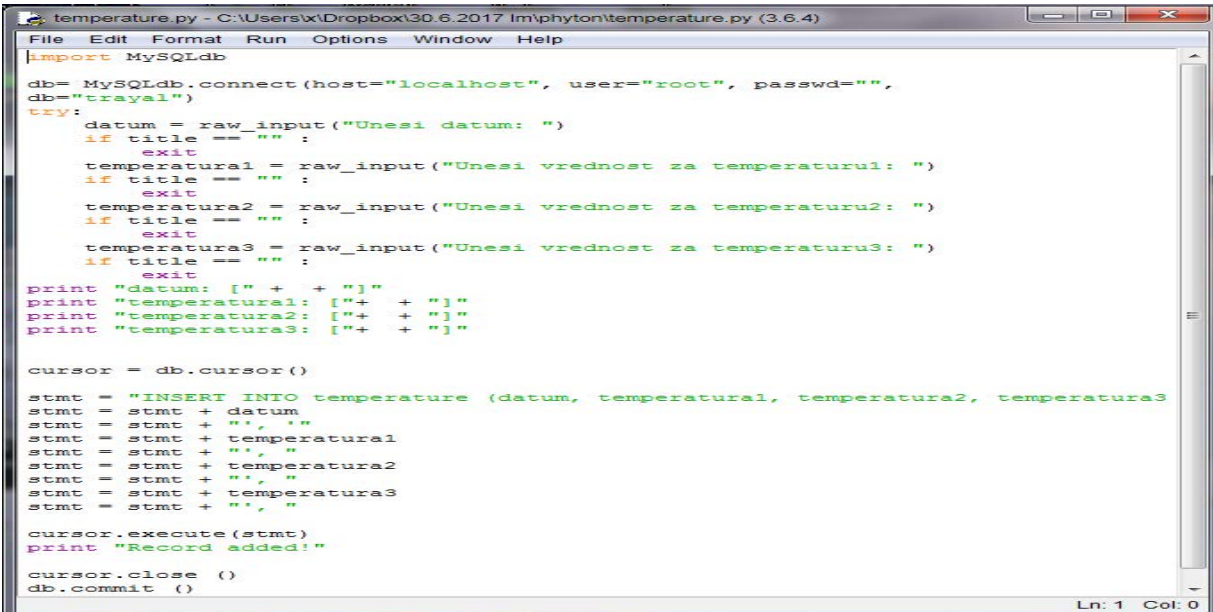
5. AUTOMATISATION AND DATA COLLECTION

Data collected from sensors and actuators (pH -meters, redox potentials, sensors for measuring temperature, water level, etc.) are necessary for the automated operation of wastewater treatment and purification plants.

The results of the measurements collected from the sensors after processing are forwarded by the PLC to the application in the programming language "PYTHON", which reads the values of voltage, current, frequency and converted scaled values from the communication ports and sends them to the application in the programming language "PHP", and then this application writes the data into the MySQL database . Figure 6 represents an

application written in the "PYTHON" program, which writes data into the MySQL database. The picture shows the connection string for connecting to the database, as

well as the fields that need to be entered in the database. [6]



```

import MySQLdb

db= MySQLdb.connect(host="localhost", user="root", passwd="",
db="trajal")
try:
    datum = raw_input("Unesi datum: ")
    if title == "" :
        exit
    temperatural = raw_input("Unesi vrednost za temperaturu1: ")
    if title == "" :
        exit
    temperatura2 = raw_input("Unesi vrednost za temperaturu2: ")
    if title == "" :
        exit
    temperatura3 = raw_input("Unesi vrednost za temperaturu3: ")
    if title == "" :
        exit
    print "datum: [" + + "]"
    print "temperatural: ["+ + "]"
    print "temperatura2: ["+ + "]"
    print "temperatura3: ["+ + "]"

    cursor = db.cursor()

    stmt = "INSERT INTO temperature (datum, temperatural, temperatura2, temperatura3
    stmt = stmt + datum
    stmt = stmt + ", "
    stmt = stmt + temperatural
    stmt = stmt + ", "
    stmt = stmt + temperatura2
    stmt = stmt + ", "
    stmt = stmt + temperatura3
    stmt = stmt + ", "

    cursor.execute(stmt)
    print "Record added!"

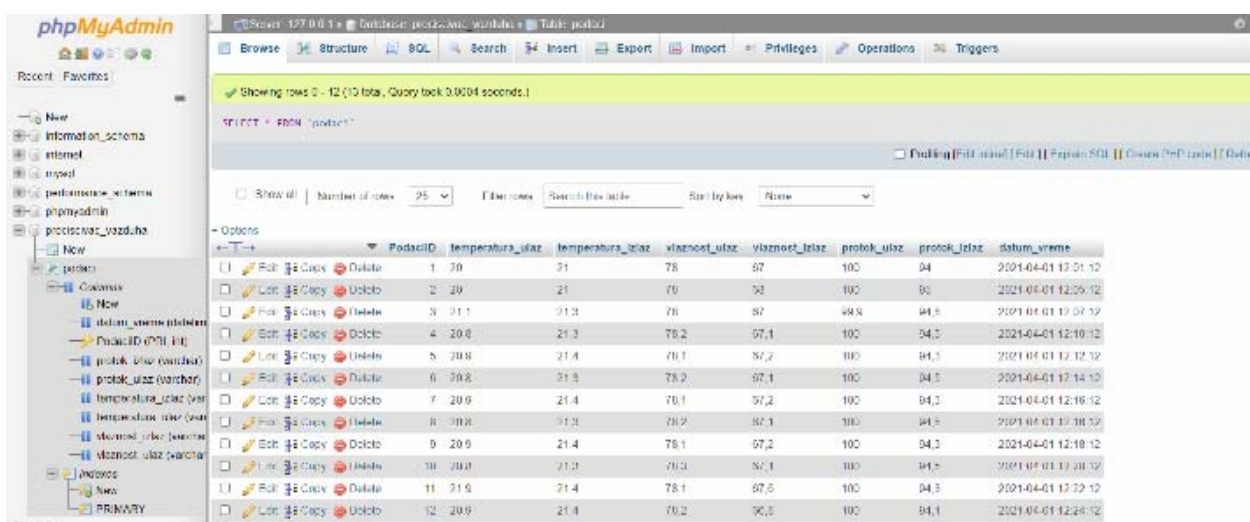
    cursor.close ()
    db.commit ()

```

Figure 6. Python application for entering data into the database

The "phpMyAdmin" database was used, the layout of the data table is shown in Figure 7. In the fields of the data table, enter the values of the temperature at the inlet and outlet of the purifier, the relative humidity of the air at the inlet and outlet, the air flow in front of the inlet and outlet filter of the air ionizer . The last field in this table is the date and time. Data is read from the sensor every 2 minutes and entered into the database. The time cycle between entries can be significantly longer, since the program continues to process the data, but due to data collection during the installation of the device, since each

room has different parameters, it initially starts with the entry for 2 minutes, but after establishing the balance and adjusting, this time will increase to 3 or 5 minutes. This significantly affects the required space occupied by the database and stored on the installed SSD disk on the microcomputer. In order to increase the space, the program generates tables with data after a month of operation, and deletes the data for that period. Based on these data, the program can continue working and setting up its output actions.[7]



PodaciID	temperatura_ulaz	temperatura_izlaz	vlaznost_ulaz	vlaznost_izlaz	protok_ulaz	protok_izlaz	datum_vreme
1	20	21	78	97	100	04	2021-04-01 12:21:12
2	20	21	70	93	100	00	2021-04-01 12:25:12
3	21.1	21.3	76	97	98.8	04.5	2021-04-01 12:27:12
4	20.8	21.3	78.2	97.1	100	04.2	2021-04-01 12:10:12
5	20.8	21.4	76.1	97.2	100	04.1	2021-04-01 12:12:12
6	20.8	21.3	78.2	97.1	100	04.3	2021-04-01 12:14:12
7	20.9	21.4	76.1	97.2	100	04.1	2021-04-01 12:16:12
8	20.8	21.3	78.2	97.1	100	04.5	2021-04-01 12:18:12
9	20.9	21.4	76.1	97.2	100	04.3	2021-04-01 12:18:12
10	20.8	21.3	76.0	97.1	100	04.5	2021-04-01 12:20:12
11	21.9	21.4	78.1	97.5	100	04.3	2021-04-01 12:22:12
12	20.9	21.4	76.2	97.3	100	04.1	2021-04-01 12:24:12

Figure 7. Table data phpMyAdmin

CONCLUSION

This paper shows the increase in the efficiency of waste water treatment in the chemical industry using filters with activated carbon, activated carbon powder. The goal of

introducing information technologies and artificial intelligence is to limit the human factor to the lowest possible level of decision making, and leave process management and processing management to automation. The man's role is to regularly supply the plant with the necessary chemicals, thickener, lime, activated carbon,

check the output parameters and empty the remains of the material created by the operation of the filter press, which extracts heavy metals in its filters. The facility has 24-hour monitoring of all parameters from the water level in all tubs, through pH and redox potential values, pressure, flow, and has an alarm system that is activated in the event of an accident. The system sends data on a daily basis to the plant manager who executes corrective measures in case of need. Based on the parameters saved on the PLC controller and the V BOX, reports are made on a daily, monthly and annual level, and the efficiency of the plant is checked by checking the values in the reference laboratory. This solution gives good results in practical use. Material savings (chemicals, thickeners) are achieved, because the PLC controller finds the ideal ratio. A significant increase in efficiency through the use of information technologies was shown, given that the microcomputer determines the optimal dosage of the necessary raw materials for obtaining water whose values are of the highest quality. The number of workers required for plant operation is also reduced. In addition to these economic results, the plant also produces better results in the quality of the water that is discharged into the recipient. This is the biggest contribution to the preservation of our waters.

References

- [1] Knetevic L.: Rekuperacija materijalnih resursa i z komunalnog cvrstog otpada-reciklata, Zbornik radova „Otpadne vode i ostali otpadi”, Vrnjaska Banja, 1995
- [2] Gaceša S.: Osnove tehnologije vode i otpadnih voda, Novi Sad, 1980
- [3] Ljubisavljević, D., Đukić, A., Babić, B. (2004). Prečišćavanje otpadnih voda, Građevinski fakultet Beograd.
- [4] Vučijak, B., Čerić, A., Silajdžić, I., Midžić Kurtagić, S. (2011). Voda za život: osnove integralnog upravljanja vodnim resursima, Institut za hidrotehniku Građevinskog fakulteta, Sarajevo.
- [5] Miljan Miletić, Bojan Milosavljević, Branko Grubić, „Informacione tehnologije za štiti životne sredine“, V nacionalna naučno-stručna konferencija sa međunarodnim učešćem „Trendovi u poslovanju“
- [6] Miljan Miletić, Radoje Cvejić, Velimir Dedić, „Napredne tehnike prečišćavanja otpadnih voda“, Peti naučno-stručni skup sa međunarodnim učešćem „Zaštita voda u zelenoj industrijskoj revoluciji“, Zbornik radova, Beograd, 2021. UDC: 628.31:004, ISBN 978-86-81400-60-9
- [7] Miljan Miletić, Radoje Cvejić, Velimir Dedić, „Information Technologies In Environmental Protection“, Sedma međunarodna konferencija “Pravo, ekonomija i menadžment u savremenim uslovima”, Lemima, 2021. Zbornik radova, knjiga II, Beograd, 2021. ISBN 978-86-81088-94-4



CHARACTERIZATION OF HETEROGENEOUS SENSING LAYERS IN GRAPHENE-BASED GAS SENSORS

STEVAN ANDRIĆ

University of Belgrade - Institute of Chemistry, Technology and Metallurgy - National Institute of the Republic of Serbia, Belgrade, Serbia, stevan@nanosys.ihtm.bg.ac.rs

IVANA JOKIĆ

University of Belgrade - Institute of Chemistry, Technology and Metallurgy - National Institute of the Republic of Serbia, Belgrade, Serbia, ijokic@nanosys.ihtm.bg.ac.rs

MILOŠ FRANTLOVIĆ

University of Belgrade - Institute of Chemistry, Technology and Metallurgy - National Institute of the Republic of Serbia, Belgrade, Serbia, frant@nanosys.ihtm.bg.ac.rs

KATARINA RADULOVIĆ

University of Belgrade - Institute of Chemistry, Technology and Metallurgy - National Institute of the Republic of Serbia, Belgrade, Serbia, kacar@nanosys.ihtm.bg.ac.rs

MARKO SPASENOVIĆ

University of Belgrade - Institute of Chemistry, Technology and Metallurgy - National Institute of the Republic of Serbia, Belgrade, Serbia, spasenovic@nanosys.ihtm.bg.ac.rs

Abstract: Graphene-based sensors have a great potential for applications in public and personal health protection, including defense and security fields. However, sensitivity and selectivity of such sensors are inherently dependent on adsorption properties of the graphene sensing layer, which is typically of heterogeneous morphology and/or of heterogeneous chemical composition due to intentionally introduced functionalizing elements or spontaneously adsorbed molecules during sensor fabrication or operation. Therefore, characterization and optimization of sensing layers is extremely important for achieving high sensing performance. In this work, we present a method for characterization of the heterogeneous sensing layer by using the frequency domain analysis of the sensor output signal. The method is based on the mathematical model we devised. Here, the model is presented in detail for the case of a surface with three types of adsorption sites, and then the method is applied for extraction of parameters that characterize adsorption properties of a graphene sensing layer.

Keywords: gas sensor, graphene, heterogeneous sensing layer, sensing surface characterization.

1. INTRODUCTION

Gas sensors are of vital importance for public and personal health protection, including defense and security fields. Graphene-based sensors have a great potential for such applications [1-4]. It stems from unique properties of graphene, such as a large specific surface area exposed to the adsorption of gas particles, and a pronounced change in its electrical, mechanical and optical parameters caused by gas adsorption, which results in a measurable sensor response even to extremely low adsorbed quantities [1]. The fast response of gas sensors based on graphene, and their applicability as low-power, miniature and portable monitoring devices, make them convenient for real time and in-situ gas detection. However, sensitivity and selectivity of such sensors (being adsorption-based) inherently depend on adsorption properties of the sensing layer, which is typically of heterogeneous morphology and/or of heterogeneous chemical composition due to

intentionally introduced functionalizing elements or spontaneously adsorbed molecules during sensor fabrication or operation. Therefore, characterization and optimization of sensing layers is extremely important for achieving high sensing performance.

Among graphene-based gas sensors, heterogeneity of the sensing surface morphology is especially pronounced in those with sensing layers obtained by the liquid phase exfoliation (LPE) method [5, 6]. LPE graphene consists of randomly arranged flakes with an abundance of highly reactive edges, which significantly increases graphene's capability for capturing of gas particles, and makes the material suitable for gas sensing. On the other hand, due to the existence of adsorption sites on both the edges and the basal planes of flakes, LPE graphene is a heterogeneous sensing material, which must be kept in mind during the evaluation and optimization of sensing performance, and the analysis of the measurement data.

In this paper, we present a method for characterization of the heterogeneous sensing layers of gas sensors. The method consists of the frequency domain analysis of the sensor output signal, and it is based on the mathematical model we devised [7, 8]. Here, we present in detail the model for the case of heterogeneous sensing layer with three types of adsorption sites. Then we illustrate the application of the model in the method for characterization of the surface of LPE graphene sensor for the detection of carbon-dioxide.

2. A MATHEMATICAL MODEL FOR THE FREQUENCY DOMAIN ANALYSIS OF A SENSOR OUTPUT SIGNAL

The sensing layer heterogeneity assumes that there is more than one type of adsorption sites, and that sites of different types differ in the affinities towards gas particles. When there are three types of adsorption sites, a sensor output signal is determined by

$$s = r_1 N_1 + r_2 N_2 + r_3 N_3 \quad (1)$$

where N_i (i is 1, 2 or 3) is the number of adsorbed particles on type i binding sites at the moment t , and r_i is the weight factor, representing the mean contribution to the sensor response of a single gas particle adsorption on a type i site. The output signal of resistive sensors is the change of the sensing layer conductance, which is proportional to the number of charge carriers, s_w , generated in the layer by gas adsorption, i.e. through the charge transfer between graphene and adsorbed gas particles. Therefore, Eq. (1) can be expressed as

$$s = u s_w = u(w_1 N_1 + w_2 N_2 + w_3 N_3) \quad (2)$$

w_i being the weight factor, equal to the mean number of charge carriers induced in a sensing material per a gas molecule adsorbed on a type i site, and u is the conversion factor of the total number of generated charge carriers to the resistance change.

The numbers of adsorbed particles changes through the processes of adsorption and desorption according to the equations [9]

$$\frac{dN_i}{dt} = k_{api} p (N_{mi} - N_i) - k_{di} N_i, \quad i \text{ is } 1, 2 \text{ or } 3 \quad (3)$$

where p is the gas pressure, N_{mi} is the number of type i adsorption sites on the sensing surface, and the corresponding adsorption and desorption rate constants for a given gas, k_{api} and k_{di} , equal

$$k_{api} = \frac{\alpha_i}{n_{mi}} \frac{1}{\sqrt{2\pi M k_B T}}, \quad k_{di} = \frac{1}{\tau_i} = \frac{1}{\tau_{0i} e^{E_{di}/(RT)}} \quad (4)$$

Here, α_i is the sticking coefficient, $n_{mi} = N_{mi}/A_i$ is the surface density of sites that cover the part of the sensing surface of the area A_i , M is the mass of a single gas particle, T is the temperature, τ_{0i} is the period of thermal vibrations of the adsorbed particle (typically of the order of 10^{-14} - 10^{-12} s), E_{di} is the desorption energy, k_B is the

Boltzmann constant, and R is the gas constant. Solving Eqs. (3) in the steady state ($dN_i/dt=0$) yields the expressions for the number of adsorbed particles on three types of sites

$$N_{si} = \frac{b_i p}{b_i p + 1} N_{mi} \quad (5)$$

and for the parameter

$$b_i = \frac{k_{api}}{k_{di}} = \frac{\alpha_i \bar{\tau}_i}{n_{mi}} \frac{1}{\sqrt{2\pi M k_B T}} \quad (6)$$

The frequency domain analysis of a sensor output signal starts from the Langevin equations which describe the fluctuations of the numbers of adsorbed particles ΔN_i around the corresponding steady-state values (these inevitable stochastic fluctuations are caused by the random nature of adsorption-desorption processes)

$$\frac{d\Delta N_i}{dt} = -\frac{1}{\tau_i} \Delta N_i + \xi_i \quad (7)$$

where

$$\tau_i = \frac{\bar{\tau}_i}{b_i p + 1} \quad (8)$$

and ξ_i is a random source function. Eqs. (7) are solved in the frequency domain in order to obtain the power spectral density (PSD) of fluctuations of the number of particles adsorbed on each type of sites

$$S_{Ni} = \frac{4N_{si} \tau_i^2 / \bar{\tau}_i}{1 + f^2 / f_i^2} \quad (9)$$

The characteristic frequencies of the spectrum are

$$f_i = \frac{1}{2\pi \tau_i} = \frac{1}{2\pi \bar{\tau}_i} \left(\frac{\alpha_i \bar{\tau}_i}{n_{mi}} \frac{1}{\sqrt{2\pi M k_B T}} p + 1 \right) \quad (10)$$

The PSD of fluctuations of the output signal equals

$$S = r_1^2 S_{N1} + r_2^2 S_{N2} + r_3^2 S_{N3} \quad (11)$$

since fluctuations of the number of adsorbed particles on different types of adsorption sites are statistically independent. Based on Eq. (2)

$$S = u^2 S_w = u^2 (w_1^2 S_{N1} + w_2^2 S_{N2} + w_3^2 S_{N3}) \quad (12)$$

where S_w is the PSD of the fluctuations of the number of carriers. After substituting Eqs. (9) in Eq. (12), and performing mathematical transformations, we obtain

$$S_w = S_{w,LF} \frac{(1 + f^2 / f_1^2)(1 + f^2 / f_2^2)}{(1 + f^2 / f_1^2)(1 + f^2 / f_2^2)(1 + f^2 / f_3^2)} \quad (13)$$

where the two remaining characteristic frequencies of the power spectrum are given by the system of equations

$$f_I^2 f_{II}^2 = \frac{(K_1 + K_2 + K_3) f_1^2 f_2^2 f_3^2}{K_1 f_1^2 + K_2 f_2^2 + K_3 f_3^2} \quad (14)$$

$$f_I^2 + f_{II}^2 = \frac{(K_1 + K_2) f_1^2 f_2^2 + (K_2 + K_3) f_2^2 f_3^2 + (K_1 + K_3) f_1^2 f_3^2}{K_1 f_1^2 + K_2 f_2^2 + K_3 f_3^2} \quad (15)$$

and the spectrum low frequency magnitude is

$$S_{w,LF} = K_1 + K_2 + K_3 \quad (16)$$

$$K_i = \frac{4w_i^2 N_{Si} \tau_i^2}{\bar{\tau}_i} \quad (17)$$

In order to obtain the expressions for the sensing layer parameters that determine its adsorption properties, we perform the following mathematical derivations. First, we introduce the designations

$$B_1 = \frac{f_I^2 f_{II}^2}{f_1^2 f_2^2 f_3^2}, \quad B_2 = f_I^2 + f_{II}^2 \quad (18)$$

After dividing both the numerator and the denominator of the expressions on the right side of Eqs. (14) and (15) by N_{m2} (here we have chosen N_{m2} , otherwise it can be any N_{mi}), and using Eqs. (18), we obtain

$$B_1 = \frac{K_{1p} v_{12} + K_{2p} + K_{3p} v_{32}}{K_{1p} v_{12} f_1^2 + K_{2p} f_2^2 + K_{3p} v_{32} f_3^2} \quad (19)$$

$$B_2 = \left[(K_{1p} v_{12} + K_{2p}) f_1^2 f_2^2 + (K_{2p} + K_{3p} v_{32}) f_2^2 f_3^2 + (K_{1p} v_{12} + K_{3p} v_{32}) f_1^2 f_3^2 \right] / (K_{1p} v_{12} f_1^2 + K_{2p} f_2^2 + K_{3p} v_{32} f_3^2) \quad (20)$$

where

$$K_{ip} = \frac{K_i}{N_{mi}} = 4w_i^2 \frac{b_i p}{b_i p + 1} \frac{\tau_i^2}{\bar{\tau}_i} \quad (21)$$

while v_{12} and v_{32} are the relative abundances of different types of adsorption sites on the sensing surface

$$v_{12} = \frac{N_{m1}}{N_{m2}}, \quad v_{32} = \frac{N_{m3}}{N_{m2}} \quad (22)$$

These parameters are used to characterize a sensing layer heterogeneity, and they are obtained from Eqs. (19) and (20) in the form

$$v_{12} = \frac{f_2^2 - f_3^2}{f_3^2 - f_1^2} \frac{f_1^2 + B_1 f_2^2 f_3^2 - B_2}{f_2^2 + B_1 f_1^2 f_3^2 - B_2} \frac{K_{2p}}{K_{1p}} \quad (23)$$

$$v_{32} = - \frac{f_2^2 - f_1^2}{f_3^2 - f_1^2} \frac{f_3^2 + B_1 f_1^2 f_2^2 - B_2}{f_2^2 + B_1 f_1^2 f_3^2 - B_2} \frac{K_{2p}}{K_{3p}} \quad (24)$$

The ratio of the number of type 1 sites and the number of

sites of the other two types is

$$v_1 = \frac{N_{m1}}{N_{m2} + N_{m3}} = \frac{v_{12}}{1 + v_{32}} \quad (25)$$

The total sensing area A consists of the parts A_i , containing different adsorption sites. Thus

$$A = A_1 + A_2 + A_3 = N_{m1} / n_{m1} + N_{m2} / n_{m2} + N_{m3} / n_{m3} \quad (26)$$

$$A_1 = \frac{v_{12} n_{m2} n_{m3}}{v_{12} n_{m2} n_{m3} + n_{m1} n_{m3} + v_{32} n_{m1} n_{m2}} A \quad (27)$$

$$A_2 = \frac{n_{m1} n_{m3}}{v_{12} n_{m2} n_{m3} + n_{m1} n_{m3} + v_{32} n_{m1} n_{m2}} A \quad (28)$$

$$A_3 = \frac{v_{32} n_{m1} n_{m2}}{v_{12} n_{m2} n_{m3} + n_{m1} n_{m3} + v_{32} n_{m1} n_{m2}} A \quad (29)$$

According to Eqs. (12) and (13), the PSDs S and S_w are proportional, and they have the same five characteristic frequencies (f_1, f_2, f_3, f_I and f_{II}). Thus, if these frequencies are used as a source of information of the sensing surface adsorption properties, it is convenient to use S_w instead of S in the analysis, because in that way it is not necessary to know the value of the parameter u , which depends on the geometric parameters of the sensing layer [10].

3. A METHOD FOR CHARACTERIZATION OF HETEROGENEOUS SENSING LAYERS

Characterization of a heterogeneous sensing layer encompasses the determination of the number and surface density of each type of sites on the sensing surface, which have a certain affinity for gas particles binding. These parameters, as well as the relative abundance of different types of adsorption sites, determine the dominant adsorption mechanism, and influence sensor characteristics such as the response magnitude, time response, sensor sensitivity and selectivity. The method that enables such characterization is based on the mathematical model presented in Section 2, and we describe its application for a LPE graphene sensor characterization, since the LPE graphene sensing layer naturally contains at least two types of adsorption sites.

For completely reversible adsorption, the site affinity for gas particles binding is described by the adsorption/desorption energy. Reversible adsorption is desirable in gas sensing applications, because it enables sensor reusability. The method we present, being based on the frequency domain analysis of sensor signal fluctuations, takes into account only the surface sites where the reversible adsorption occurs (the irreversible adsorption does not contribute to the fluctuations of the number of adsorbed particles, so it is not “visible” in the frequency domain after the establishment of the steady-state of all adsorption processes occurring on the sensing surface). Therefore, it is reasonable to assume the existence of three types of adsorption sites with reversible

adsorption processes on the LPE graphene surface: the sites on the edges of the graphene flakes (type 1 sites), and two types of functionalized sites on the basal planes of the flakes – those that are native, i.e. unoccupied by adsorbates (type 2 sites), and those that are already occupied by atoms/molecules of some reactive gas species from the environment (type 3 sites). Apart from the gas pressure and temperature values that are set and then kept constant, the characterization method uses the desorption energies and the weight factors for all types of adsorption sites as input parameters. In the case of 2D materials, the values of these parameters are usually obtained by the density functional theory (DFT) or other calculation methods [4, 11]. For the illustration of the method, we use the parameter values from the literature, which are obtained by DFT calculations for the reversible adsorption of CO₂ on the edges of graphene nanoribbons [12], and on Fe-functionalized graphene [13], where some of the functionalized basal plane sites are occupied by O₂ molecules, but they still can bind carbon-dioxide molecules: the desorption energies are $E_{d1}=19$ kcal/mol, $E_{d2}=12.5$ kcal/mol, and $E_{d3}=8.07$ kcal/mol, while the weight factors for a resistive sensor, expressed as the mean number of charge carriers induced in graphene per adsorbed CO₂ molecule, equal $w_1=0.9$, $w_2=0.02$, and $w_3=0.1$. Gas pressure $p=0.1$ Pa, the temperature $T=300$ K, and the sensing surface area $10\text{ mm} \times 10\text{ mm}$ are used in the analysis.

The method consists of the following steps:

1. When a sensor response reaches the steady state for a given gas pressure and temperature, the PSD of the sensor output signal is experimentally determined. Figure 1 shows the simulated PSD of fluctuations of the number of charge carriers in graphene for the above given parameter values.

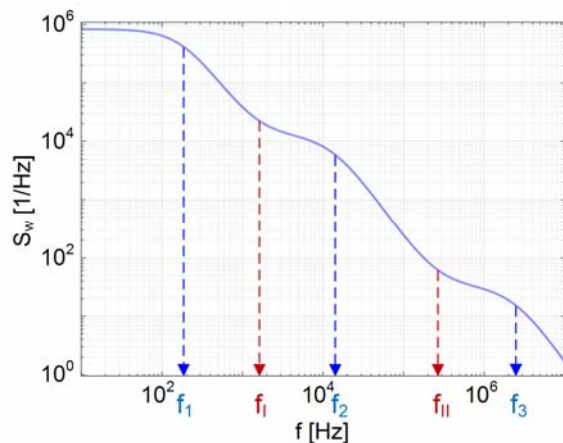


Figure 1. The power spectral density of the number of charge carriers in LPE graphene, caused by inherently random adsorption-desorption processes of carbon-dioxide molecules on the graphene sensing surface with three types of adsorption sites. The characteristic frequencies are shown.

2. The characteristic frequencies are determined from the experimentally obtained PSD, in accordance with Eq. (13), which for the example presented in Figure 1 yields $f_1=183$ Hz, $f_2=1.32 \times 10^4$ Hz, $f_3=2.35 \times 10^6$ Hz, $f_{i1}=1.65 \times 10^3$

Hz and $f_{i1}=2.62 \times 10^5$ Hz.

3. The surface density of each type of adsorption sites, n_{mi} , is uniquely determined by the frequency f_i , according to Eqs. (10), (8) and (6); thus, their values are obtained by using the experimentally obtained f_1 , f_2 and f_3 and the mentioned equations. For the given example: $n_{m1}=2 \times 10^{18}$ 1/m² and $n_{m2}=n_{m3}=4 \times 10^{17}$ 1/m².

4. The parameters B_1 and B_2 are calculated based on Eqs. (18) and the experimentally determined frequencies f_1 , f_2 , f_3 , f_{i1} and f_{i2} . The time constants τ_i and the parameters b_i are calculated after substituting the values for f_1 , f_2 and f_3 in Eqs. (10) and (8), respectively; then the parameters K_{ip} are calculated from Eq. (21). Consequently, the relative abundances of different types of adsorption sites are obtained by using Eqs. (23)-(25), which in our example yields $v_{12}=0.02$, $v_{32}=3$ and $v_1=0.005$.

5. The areas covered by each type of adsorption sites can now be obtained from Eqs. (27)-(29). In the analyzed example, $A_1=1 \times 10^{-7}$ m², $A_2=2.5 \times 10^{-5}$ m² and $A_3=7.49 \times 10^{-5}$ m², which means that the adsorption sites of the types 1, 2 and 3 occupy 0.1%, 25% and 74.9% of the total sensing surface, respectively.

6. Finally, the numbers of adsorption sites of different types are obtained as $N_{mi}=n_{mi}A_i$. Therefore, $N_{m1}=2 \times 10^{11}$, $N_{m2}=1 \times 10^{13}$ and $N_{m3}=3 \times 10^{13}$ in the given example.

The results of the sensing surface characterization by using the described method are summarized in Table 1.

Table 1. LPE graphene parameters describing heterogeneous adsorption properties of its surface towards CO₂; three types of sites are considered (A is the total sensing area, N_m is the total number of adsorption sites)

Site Parameter	Type 1 = Edge sites	Type 2 = Basal Fe sites	Type 3 = Basal Fe+O ₂ sites
Effective sensing area covered	1×10^{-7} m ²	2.5×10^{-5} m ²	7.49×10^{-5} m ²
% of A	0.1% A	25% A	74.9% A
Surface density of adsorption sites	2×10^{18} 1/m ²	4×10^{17} 1/m ²	4×10^{17} 1/m ²
Number of adsorption sites	2×10^{11}	1×10^{13}	3×10^{13}
% of N_m	0.497% N_m	24.876% N_m	74.627% N_m

4. CONCLUSIONS

The analysis of a gas sensor output signal in the frequency domain has been proven as an efficient tool for characterization of sensing layer adsorption properties. For the given adsorption/desorption energies for each type of adsorption sites, and the conversion factors that relate the binding of target molecules to the change of a sensor measurable parameter (which can be obtained by using the density functional theory or other calculation methods), the mathematical model and method presented

in this paper enable the characterization in terms of the abundance of various adsorption site types on the sensing surface, which is a unique property of a given sensor. It cannot be reliably predicted by other methods, so it must be determined experimentally. The significance of the model and method stem from the fact that real sensing layers (including those based on graphene) are not ideally homogeneous, which necessitates their characterization prior to their use for sensing, because the adsorption properties inherently affect gas sensor characteristics such as sensitivity, selectivity and the minimal detectable concentration.

ACKNOWLEDGMENT

This research was funded by the Science Fund of the Republic of Serbia, grant number 6057070, project Gramulsen, and by the Ministry of Education, Science, and Technological Development of the Republic of Serbia, grant number 451-03-68/2022-14/200026.

References

- [1] SCHEDIN,F., GEIM,A.K., MOROZOV,S.V., HILL,E.W., BLAKE,P., KATSNELSON,M.I., NOVOSELOV,K.S.: *Detection of individual gas molecules adsorbed on graphene*, 6 (2007) 652–655.
- [2] ZHANG,J., LIU,L., YANG,Y., HUANG,Q., LI,D., ZENG,D.: *A review on two-dimensional materials for chemiresistive- and FET-type gas sensors*, Phys. Chem. Chem. Phys., 23 (2021) 15420–15439.
- [3] WANG,T., HUANG,D., YANG,Z., XU,S., HE,G., LI,X., HU,N., YIN,G., HE,D., ZHANG,L.: *A Review on Graphene-Based Gas/Vapor Sensors with Unique Properties and Potential Applications*, Nano-Micro Letters, 8 (2016) 95–119.
- [4] CRUZ-MARTINEZ,H., ROJAS-CHÁVEZ,H., MONTEJO-ALVARO,F., PEÑA-CASTAÑEDA, Y.A., MATADAMAS-ORTIZ,P.T., MEDINA,D.I.: *Recent Developments in Graphene-Based Toxic Gas Sensors: A Theoretical Overview*, Sensors, 21 (2021) 1992.
- [5] RICCIARDELLA,F., MASSERA,E., POLICHETTI, T., MIGLIETTA,M.L., DI FRANCIA,G.: *A calibrated graphene-based chemi-sensor for sub parts-per-million NO₂ detection operating at room temperature*, Applied Physics Letters, 104 (2014) 183502.
- [6] TOMAŠEVIĆ-ILIC,T., JOVANOVIĆ,D., POPOV,I., FANDAN,R., PEDRÓS,J., SPASENOVIĆ,M., GAJIĆ,R.: *Reducing sheet resistance of self-assembled transparent graphene films by defect patching and doping with UV/ozone treatment*, Applied Surface Science, 458 (2018) 446–453.
- [7] JOKIĆ,I.: *Microfluidic Adsorption-Based Biosensors: Mathematical Models of Time Response and Noise, Considering Mass Transfer and Surface Heterogeneity*, In: Biosensors-Current and Novel Strategies for Biosensing, Villarreal-Gómez,L., Ed.; Intech Open: London, UK, 2021 1–25.
- [8] ANDRIĆ,S., JOKIĆ,I., STEVANOVIĆ,J., SPASENOVIĆ,M., FRANTLOVIĆ,M.: *Noise Spectrum as a Source of Information in Gas Sensors Based on Liquid-Phase Exfoliated Graphene*, Chemosensors, 10 (2022) 224.
- [9] LANGMUIR,I.: *The adsorption of gases on plane surfaces of glass, mica and platinum*, Journal of American Chemical Society, 40 (1918) 1361–1403.
- [10] LIANG,S.-Z., CHEN,G., HARUTYUNYAN,A.R., COLE,M.W., SOFO,J.O.: *Analysis and optimization of carbon nanotubes and graphene sensors based on adsorption-desorption kinetics*, Applied Physics Letters, 103 (2013) 233108.
- [11] MONTEJO-ALVARO,F., OLIVA,J., HERRERA-TREJO,M., HDZ-GARCIA,H.; MTZ-ENRIQUEZ, A.I.: *DFT study of small gas molecules adsorbed on undoped and N-, Si-, B-, and Al-doped graphene quantum dots*, Theor. Chem. Acc., 138 (2019) 37.
- [12] VANIN,M.: *First-principles calculations of graphene nanoribbons in gaseous environments: Structural and electronic properties*, Physical Review B, 82 (2010) 195411.
- [13] CORTÉS-ARRIAGADA,D., VILLEGAS-ESCOBAR,N., ORTEGA,D.E.: *Fe-doped graphene nanosheet as an adsorption platform of harmful gas molecules (CO, CO₂, SO₂ and H₂S), and the co-adsorption in O₂ environments*, Applied Surface Science, 427 (2018) 227–236.



POLYCHLOROPRENE BASED RUBBER COMPOSITIONS FOR GASKET PRODUCTION

MARIJA KLUZ

Military Technical Institute, Belgrade, marijakluz@gmail.com

JELA GALOVIĆ

Military Technical Institute, Belgrade, polimery04@gmail.com

ALEKSANDAR MILOJKOVIĆ

Military Technical Institute, Belgrade, zabackermi@gmail.com

LJILJANA JELISAVAC

Military Technical Institute, Belgrade, ljiljanajelisavac29@gmail.com

TANJA MILOŠEVIĆ

Military Technical Institute, Belgrade, tanjamilosevic993@gmail.com

Abstract: Comparison of physical and mechanical properties of four different polychloroprene-based vulcanized rubber compounds has been presented in this paper. Vulcanized rubber compounds containing different amounts of *N*-(1,3-dimethylbutyl)-*N*'-phenyl-1,4-benzenediamine (6PPD) as antiaging component (1 phr and 4 phr based on 100 weight of elastomer) and two types of plasticizers (phthalate free adipic acid ester mixture and ether tio ether) had been examined. Mechanical properties of elastomer materials are analyzed after vulcanization and after heat aging in a stream of hot air at 100°C for 70 hours to determine which rubber compounds would be suitable for non-standard gaskets. Rubber compound with the optimal mechanical properties, e.g. tensile strength is 17.9 MPa, and the optimal resistance against oxidizing agents has been selected as promising material for production of non-standard gaskets.

Keywords: elastomer materials, polychloroprene (CR), neoprene, vulcanization, physical and mechanical properties

1. INTRODUCTION

Due to the specific conditions of exploitation and the risk of fire, non-standard sealing elements made of suitable elastomeric material must fulfill the following requirements:

1. resistance to a very corrosive environment due to the presence of a strong powder oxidizer,
2. resistance to the action of oils, resins, crosslinkers, and alcohol,
3. appropriate physical and mechanical properties,
4. antistatic (in an explosive environment),
5. self-extinguishing,
6. durability at working temperatures up to 80°C
7. resistance to compressed air pressured up to 8.5 bar or vacuum.

In order to fulfill all of the above requirements, an elastomeric material based on polychloroprene rubber was developed.

2. THEORETICAL PART

2.1. Characteristics of polychloroprene based rubber compounds

Polychloroprene (CR), developed and sold under the trade name Neoprene by DuPont, was the first commercially successful synthetic elastomer. It is produced by free-radical emulsion polymerization of chloroprene (2-chloro-1,3-butadiene). The commercial material is mainly *trans*-1,4-polychloroprene, which is crystallizable [1, 2].

Its structure is shown in figure 1.

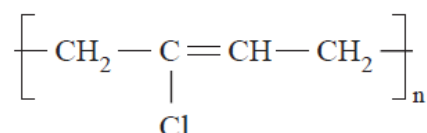


Figure 1. Structure of polychloroprene

Polychloroprenes are noted generally for their good resistance to abrasion, hydrocarbons, sunlight, oxygen, ozone, gas, weathering, and toughness. They have similar mechanical characteristics to natural rubber (NR), including good mechanical strength when it is compounded as a gum vulcanizate. It is more difficult to process than most other synthetic elastomers and has a high resistance to bending.

CR based rubber compound typically has tensile strength from 7 MPa to 17.5 MPa, elongation at break from 200% to 600% and hardness from 40 H ShA до 90 H ShA. Like all of the synthetic elastomers, CR is available in a number of grades to aid in compound mixing (blending the raw gum elastomer with a number of other ingredients to make the rubber compound) and to emphasize certain properties.

CR vulcanizates are usually intended for the production of rubber products that are resistant to the action of oxidizing agents (e.g. ozone) and resistant to wear. When aged at high temperatures, vulcanizates become hard and less flexible. With the addition of antioxidants, CR vulcanizates are resistant to aging in a stream of hot air at temperatures up to 90°C.

CR vulcanizates are stable and resistant to swelling in vegetable and animal oils, waxes and lubricants, as well as most aliphatic hydrocarbons, but swell on contact with aromatic hydrocarbons, ketones, esters and chlorinated organic solvents.

At low temperatures, polychloroprene becomes stiff, glass-like and brittle, and it also has tendency to crystallize. The glass transition temperature of CR rubbers and vulcanizates can be lowered using plasticizers, but they may increase the crystallization rate [3].

Since it contains chlorine, rubber products made of CR are self-extinguishing and very resistant to flame. That's why flammable ingredients (e.g. petroleum-based plasticizers) are not used in the production of CR vulcanizates in order to preserve their self-extinguishing.

Polychloroprene elastomers have wide range of applications, ranging from adhesives to wire insulation, depending on its overall durability. The main uses of polychloroprene elastomers are in the fabrication of mechanical rubber goods for automotive products; petroleum production; transportation, construction, and consumer products. The major uses include wire and cable insulation, industrial hoses, conveyor belts, diaphragms, seals, gaskets, O-rings, gasoline tubing, shoe heels, and solid tires. Neoprene latex is used in making gloves, adhesives, and binders.

Based on the above-mentioned properties, polychloroprene is a suitable elastomeric material for the production of non-standard gaskets. CR vulcanizates containing at least 10% carbon black with the addition of antioxidants are used for the production of sealing parts.

2.2 Determination of mechanical and rheological properties of raw gum elastomer and vulcanized rubber

Elasticity and plasticity occur when raw gum elastomer and vulcanized rubber are deformed. Elasticity is the basic property of vulcanized rubber and determines the conditions of exploitation of rubber products. Plasticity defines the technological properties and processability of raw rubber and rubber blends. Determining the mechanical characteristics of rubber is complex, because the character and size of the deformation depend on its amplitude and frequency, load rate and duration, and the ambient temperature. Elasticity includes a number of properties: the ability to retain dimensions and shape, the maximum degree of rubber deformation, the rate of elastic reversible deformation and the ability to reabsorb energy. In practice, it is necessary to evaluate the elastic and deformation properties of rubber. Due to their complex nature, the following elastic and deformation properties may be evaluated:

1. Relative elongation at break,
2. Young's modulus,
3. Moduli at given elongations,
4. Hysteresis losses,
5. Tear strength.

The level of viscoelastic deformations is determined by elongation or compression at a given load or tear. The rate of deformation is estimated based on the modulus (the stress at a given elongation). The ability to recover elastic deformation is determined by the amount of residual elongation or compression after removal of the load. The ability of rubber to reabsorb energy and the rate of reversible elastic deformation are determined based on the impact elasticity value and are used to characterize the elasticity of the rubber. The strength properties of rubber are most often related to tensile strength and tear resistance. In addition to the tensile strength, the elastic and deformation properties of the rubber are also determined, such as the relative elongation at break and as the moduli at a given elongations.

The hardness of the rubber refers to the resistance to the pressing of metal needles or balls into the rubber, under the action of the compression force of the spring or under the action of weight. To determine the hardness of rubber, Shore's hardness tester, which has a blunt needle connected to a spring, is most often used. The rubber, depending on its composition and degree of crosslinking, has a hardness in the range between 40 H ShA and 90 H ShA. It is known that with an increase in the content of fillers and the duration of vulcanization, hardness increases, while plasticizers decrease it.

Tearing strength (structural strength) is the resistance to the destruction (tearing) of rubber when stretched under conditions of stress concentration. It is determined as the ratio of the force at which the test piece splits and the original thickness of the sample.

Aging is an irreversible change in the properties of rubber under the influence of heat, oxygen, air, ozone, UV light, aggressive substances or constant flexing. After atmospheric aging or heat aging in a stream of hot air, test results are expressed by the aging coefficient, which represents the ratio of changes in tensile strength and relative elongation at the break before and after aging. The smaller change in properties during aging, the smaller aging coefficient. In order to estimate the service life of raw gum elastomer and vulcanized rubber, their properties are examined and compared before and after heat aging. Antioxidants and antiozonants protect rubber against oxidation, while carbon black protects it against UV light.

Based on the results of tests before and after heat aging, a suitable rubber mixture can be selected for the production of non-standard gaskets.

3. EXPERIMENTAL PART

3.1. Gasket properties

Figure 2. is showing the solid rubber polychloroprene ring.



Figure 2. O-ring made of polychloroprene

Based on the available technical documentation, it was determined that it is made of polychloroprene with a hardness of 60 ± 5 H ShA. Due to the aging process, a hardness of 80 H ShA was measured on it. The measured dimensions are $\varnothing 664/661$ mm (outer/inner diameter).

3.2. Samples of rubber compounds for non-standard gaskets preparation

Production of raw rubber compounds based on polychloroprene rubber (CR rubber) was carried out at the factory "Tigar Tehnička Guma" a.d. Pirot. Raw rubber compounds marked TG-1, TG-2, TG-3 and TG-4 were produced.

The raw rubber compounds marked TG-1 and TG-2 have the same amounts of *N*-(1,3-dimethylbutyl)-*N'*-phenyl-1,4-benzenediamine as antiaging component (1 phr or part per hundred rubber) and plasticizer (phthalate free adipate esters mixture). The composition of the third raw rubber mixture marked TG-3 has been changed, because it has a

higher content (4 phr) of anti-aging agents. The composition of the fourth raw rubber compound marked TG-4 has also 4 phr of anti-aging agents, but different plasticizer (ether tio ether) compared to the other raw rubber compounds. Rubber granulates are preheated on rollers with addition of other ingredients at temperatures between 40°C and 50°C for 30 minutes.

Vulcanization of raw rubber compounds was performed at a temperature of 170°C for 20 minutes. Vulcanizates in the form of plates and discs are made on a rubber press. Test pieces were cut from the plates and prepared for testing of mechanical properties before and after heat aging. The prepared discs were used as test pieces for testing permanent deformation by compression set at elevated temperature.

Mechanical properties of vulcanizates were tested: hardness, tensile strength, modulus at predetermined elongation, elongation at break and change in permanent deformation by compression set at elevated temperature [4]. For statistical analysis, tests were performed on 7 test pieces for each rubber compound. In addition, density at a temperature of 22°C and resistance to tearing were determined. The testing of vulcanizates was performed before and after heat aging in a stream of hot air at a temperature of 100°C for 70 hours, according to the standard requirements. The vulcanizates marked TG-1, TG-2, TG-3 and TG-4 were tested.

Test methods are listed in Table 1.

Table 1. List of test methods

Property	Test method
Density	SRPS ISO 2781:2019, method A [5]
Hardness	SRPS ISO 48-4:2019, type A hardness tester [6]
Tensile strength	SRPS ISO 37: 2019, type 1 dumb-bell test piece [7]
Modulus 200	
Modulus 300	
Elongation at break	
Tear strength	SRPS ISO 34-1: 2017 [8]
Permanent deformation after heat aging (compression set at 100°C for 70 h)	SRPS ISO 815-1: 2021 [9]

4. RESULTS AND DISCUSSION

It is known that vulcanizates based on CR rubbers are very resistant to atmospheric aging, the effect of ozone and other oxidizing agents. When examining the changes in mechanical properties after heat aging of the vulcanizate at a temperature of 100°C for 70 hours, results are compared with properties for standard quality rubber marked 60 CR.

Physical and mechanical properties of TG-1, TG-2, TG-3 and TG-4 vulcanizates before and after heat aging are presented in Table 2. Non satisfying values are shown in bold.

Table 2. Physical and mechanical properties of vulcanizates before and after heat aging

Physical and mechanical properties before aging	Requirements for 60 CR	Test results			
		TG-1 vulcanizate	TG-2 vulcanizate	TG-3 vulcanizate	TG-4 vulcanizate
Density (g/cm ³)	/	1.39	1.40	1.38	1.39
Hardness (H ShA)	60 ± 5	58	57	58	58
Tensile strength (MPa)	at least 12.0	20.8	18.7	17.9	16.7
Modulus at 200% deformation (MPa)	/	6.4	5.7	6.0	6.0
Modulus at 300% deformation (MPa)	/	12.4	11.3	11.4	11.7
Elongation at break (%)	at least 300	431	421	414	383
Tear strength (daN/cm)	/	45.5	42	48.6	43.3
Changes of mechanical properties after aging at 100°C for 70 hours					
Hardness (H ShA)	+ 5	+8	+6	+4	+ 2
Tensile strength (%)	± 15	-9	-4	0	+ 10
Elongation at break (%)	± 20	-32	-5	+6	+ 12.5
Tear strength (%)	/	+10	+1.5	+1.5	+ 10
Permanent deformation (%)	maximum 40	36	37	30	21

TG-1 vulcanizate has satisfying mechanical properties of initial quality according to the 60 CR quality requirements. After heat aging, this vulcanizate has a higher hardness and lower elongation at break than allowed. Therefore, it is suggested to the manufacturer of raw rubber compounds to prepare new samples in order to ensure better mechanical properties after heat aging, in order to achieve the optimal life cycle of the polychloroprene vulcanizate.

TG-2 vulcanizate has satisfying mechanical properties before and after heat aging. It satisfies 60 CR quality requirements. Changes in TG-2 vulcanizate properties show that the hardness is increased by 6 units and the tensile strength is reduced by 4%, which is satisfactory. Vulcanizates based on CR rubber are resistant to bending, so after testing the resistance to tearing before and after heat aging, results are in agreement with literature data for this type of elastomeric material. After heat aging, the resistance to tearing increased slightly (by 1.5%), which confirms high quality.

TG-3 vulcanizate has satisfying mechanical properties of the initial quality and their satisfactory change after heat aging, according to the standard for quality 60 CR. Its physical and mechanical properties are even better compared to the TG-2 vulcanizate. Higher content of the antiaging agent improved the mechanical properties of the tested vulcanizate after heat aging. Hardness is increased by 4 units, tear resistance by 1.5%, and tensile strength remained unchanged. Based on the obtained results, it was determined that the vulcanizate marked TG-3 has good physical and mechanical properties before and after heat aging. The content of added ingredients in this vulcanizate ensures that it has good mechanical properties after heat aging in air at temperatures up to 100°C.

TG-4 vulcanizate has satisfactory physical and mechanical properties of the initial quality and their satisfactory changes after heat aging, according to the requirements for 60 CR quality. Vulcanized TG-4 compound doesn't have better physical and mechanical properties compared to the vulcanizates TG-2 and TG-3. Higher content of antiaging agent did not significantly improve the mechanical properties of the tested vulcanizate after heat aging. It was found that the hardness increased by 2 units, and the tensile strength and resistance to tearing by 10%. The addition of a new plasticizer has reduced the change in permanent deformation by compression set at an elevated temperature, making this vulcanizate more flexible and tough. The obtained value of permanent deformation is about 21%.

5. CONCLUSION

The initial mechanical characteristics and their changes after heat aging were examined for four vulcanizates marked TG-1, TG-2, TG-3 and TG-4, which are made from raw rubber compounds based on polychloroprene. Based on the obtained test results, vulcanizate TG-3 has optimal mechanical properties before and after heat aging and fully meets the requirements defined by standard for 60 CR. It is shown that this vulcanizate can be a very good material for the production of solid rubber O-rings.

References

- [1] Milenko Plavšić, Radivoj Popović, Ružica Popović: Elastomerni materijali (kaučuk, guma i kompoziti), Naučna knjiga, Beograd 1995 (in Serbian)

- [2] Robert O. Ebewele, Polymer: Science and Technology, CRC Press, New York 2000.
- [3] Andrew Ciesielski: An Introduction to Rubber Technology, Rapra Technology Limited, 1999.
- [4] Roger Brown, Handbook of Polymer Testing, Rapra Technology Limited, 2002.
- [5] SRPS ISO 2781:2019 Rubber, vulcanized or thermoplastic — Determination of density
- [6] SRPS ISO 48-4:2019 Rubber, vulcanized or thermoplastic - Determination of hardness — Part 4: Indentation hardness by durometer method (Shore hardness)
- [7] SRPS ISO 37: 2019 Rubber, vulcanized or thermoplastic — Determination of tensile stress-strain properties
- [8] SRPS ISO 34-1: 2017 Rubber, vulcanized or thermoplastic — Determination of tear strength — Part 1: Trouser, angle and crescent test pieces
- [9] SRPS ISO 815-1:2021 Rubber, vulcanized or thermoplastic — Determination of compression set — Part 1: At ambient or elevated temperatures

THE INFLUENCE OF CHEMICAL COMPOSITION ON MECHANICAL PROPERTIES OF FLOW FORMED STEEL TUBES

IGOR RADOVANOVIĆ

Krušik Holding Corporation, radovanvic.igor931@gmail.com

SNEŽANA BLAGOJEVIĆ

Krušik Holding Corporation, Serbia, sneza.blago@gmail.com

LJUBICA RADOVIĆ

Military Technical Institute, Belgrade, Serbia, ljubica.radovic@vti.vs.rs

DRAGOMIR GLIŠIĆ

Faculty of Technology and Metallurgy, University of Belgrade, gile@tmf.bg.ac.rs

Abstract: The influence of chemical composition on mechanical properties of flow formed tubes were examined. Two medium carbon steels, 41Cr4 and 42CrMo4 were used. Flow forming was performed on industrial equipment in two passes, with total reduction of 75%. Strain hardening was evaluated by means of strength, elongation and hardness.

For both steels, yield strength increased from initial 756 MPa and 751 MPa to 1197 MPa and 1032 MPa, for 41Cr4 and 42CrMo4 steels, respectively, while ultimate tensile strength increased from initial 908 MPa and 857 MPa on 1308 MPa and 1210 MPa. Hardness, as illustration of strain hardening also increased from initial 275 HB and 274 HB to 380 HB and 362 HB, respectively. In both steels, elongation is greater than 12%, indicating that during flow forming, together with strain hardening, a restoration of deformed microstructure also occurred. Since applied flow forming is cold deformation process, it is assumed that dynamic recovery occurred during flow forming.

Keywords: flow forming, tube, 41Cr4 steel, 42CrMo4 steel.

1. INTRODUCTION

Flow forming is the most superior process of obtaining thin wall tubes with ratio length/diameter > 10 and diameter/wall thickness > 50 [1-3]. In this process preform, the most often cup or tube, is formed into hollow cylinder with the wall thickness reduction. The metal is displaced axially along a mandrel, increasing the length of the workpiece, while the internal diameter remains constant (Figure 1).

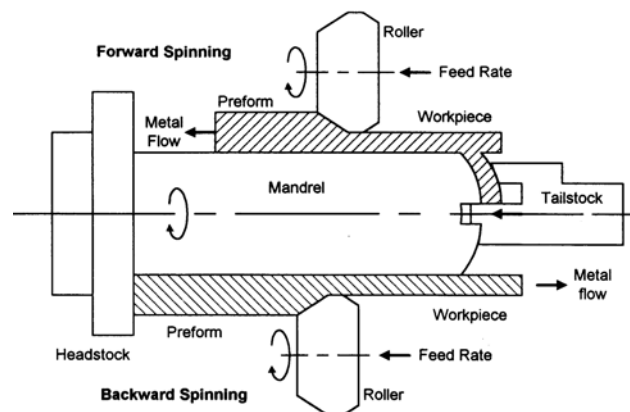


Figure 1. Forward and backward flow forming (tube spinning) [1].

Flow forming has significant advantages in comparison to conventional production technique, such as: high dimensional accuracy, quality of inner element surface, low tools price, high process rate, material savings, increasing in both strength and stiffness, etc. [1-3].

Among many factors that influence the process, the most important are selection of the type of steel and optimal heat treatment of the preform, partial and total deformation and gap between mandrel and preform [3-8]. Quality of the flow formed tubes is also influenced by design and dimension of the rollers, position during the forming, mandrel speed and axial roller feed rate [9].

Flow forming is suitable to deform large number of materials, soft materials, such as aluminum and copper, medium and very hard materials, even difficult-to-form metals be flow formed.

The aim of this work was to examine the influence of chemical composition on mechanical properties flow formed tubes, as well as strain hardening during the flow forming process.

2. EXPERIMENTAL

2.1. Material

Two medium carbon steels, 41Cr4 and 42CrMo4 were used, according to SRPS EN 10083-3 and SRPS EN 10083-3, respectively.

The chemical composition of used steel are given in Table 1.

Table 1. The chemical composition of the steels, mass. %

Steel	C	Cr	Si	Mn	P	S	V	Mo
41Cr4	0,406	1,009	0,131	0,660	0,014	0,004	/	/
42CrMo4	0,420	1,000	0,200	0,800	0,011	0,003	0,13	0,21

2.2. Flow forming

The sketch of preform for flow forming is given in Fig.2. It was made of hot rolled seamless steel tubes after machining and heat treatment.

The dimension and temper of hot rolled tubes are given in Table 2.

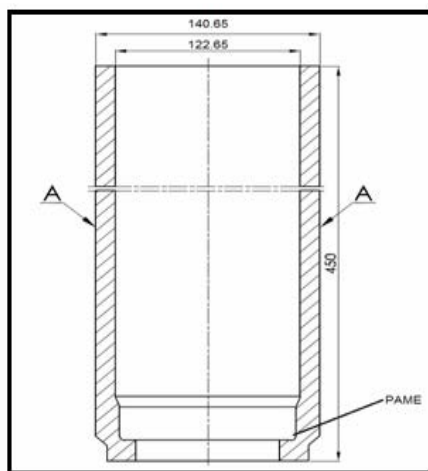


Figure 2. Preform for flow forming.

Table 2. Tubes dimension and temper

Steel	Hot rolled tube		Temper
	D_{out} (mm)	δ (mm)	
41Cr4	139	16	A
42CrMo4	127	17.5	Q+T

A-anneled

Q+T –quenched+tempered

The preforms for flow forming of 41Cr4 steel was proceed by:

- machining
- heat treatment Q+T
HT1: 840°C/3,5h/oil +600°C/4,5 h /air, or
HT2: 830°C/3.5 h/water +580°C/ 4,5h /air,
- final machining.

The preform of 42CrMo4 steel was produced by machining.

Forward flow forming was performed using LEIFELD ST 56-90 CNC - 10/1 machine, with three rollers. Tools, mandrel and rollers (Figure 3) were made of high quality tool steel and polished.

Preforms of both steels processed in two passes:

- from 9.0 mm up to 5,5 mm, and
- from 5.5 mm up to 2.2 mm,

where total reduction was 75 %. Mandrel speed was 270 rpm, and axial roller feed rate 300 mm/min.



a)



b)

Figure 3. Mandrels (a) and rollers (b) for flow forming.

2.3. Stress relieving

After flow forming, up to 4 hours after forming, stress relieving was performed at 280°C/5h/furnace cooling (5°C/min). EKP KCPH 200/300 furnace was used. Tubes are placed on vertical supports.

2.4. Testing methods

Visual examination, hydrostatic test and magnetic particle inspection were performed, as well as mechanical properties testing.

Hydrostatic test performed on 100 % specimens on SERVOTEH hydroequipment.

Ferromagnetic particle inspection performed on FEROFUX UNIVERSAL SW 3200 used.

Mechanical properties were determined by tensile tests and hardness measurement.

Brinell hardness measurement HB 2,5/187,5/15, according to SRPS EN ISO 6506-1, performed on SENSUS HBT-01 (Figure 3). Prepared tubes are fixed on support. Software SENSUSVMT-BHT used.

Tensile tests were carried at room temperature on WOLPERT 10-TUZ-745-100kN testing machines, using proportional squared specimens ($d=15$ mm, $b=2,2$ mm, $L_0=62$ mm), according to SRPS EN ISO 6892-1.3.

Three specimens were cut from each tube, at 120°.

3. RESULTS

The results of mechanical testing of the preforms are given in Table 3.

Table 3. Mechanical properties of the preforms

Steel	$R_{p0.2}$ [N/mm ²]	R_m [N/mm ²]	A_5 [%]	HB
41Cr4	756	905	18,30	275
42CrMo4	751	857	20,00	274

Non-destructive tests performed on the flow formed tubes, visual examination, hydrostatic test and magnetic particle inspection, did not show presence of the defects for both steels.

The results of mechanical testing of the flow formed tubes are shown in Table 4.

Table 4. Mechanical properties of the flow formed tubes

Steel	$R_{p0.2}$ [N/mm ²]	R_m [N/mm ²]	A_5 [%]	HB
41Cr4	1197	1308	12,8	380
42CrMo4	1032	1210	15,3	362

Mechanical properties of the preforms of both steels are similar. After flow forming, hardness and strength of the tubes increase with increasing strain, and more intensive increase was obtained for 41Cr4 steel (Figures 4 and 5).

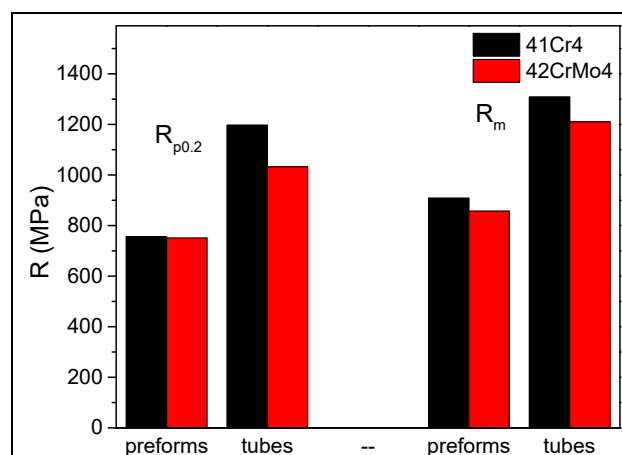


Figure 4. Effect of strain on $R_{p0.2}$ and R_m of flow formed 41Cr4 and 42CrMo4 steels.

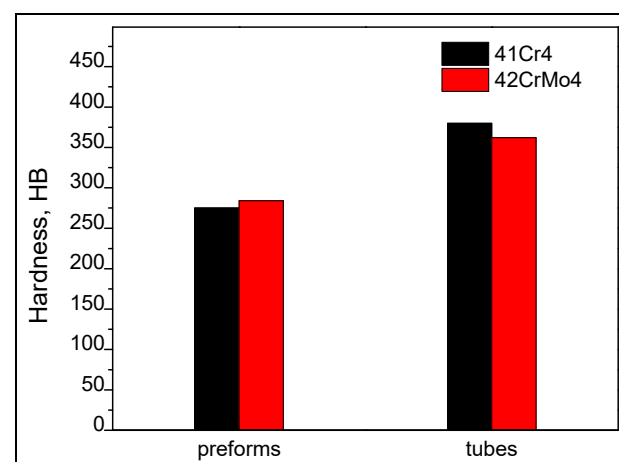


Figure 5. Effect of strain on hardness of flow formed 41Cr4 and 42CrMo4 steels.

4. DISCUSSION

During cold flow forming, it is expected that increase of dislocation density leads to strain hardening. Both steels were deformed in tempered state, i.e. starting microstructure consisted of tempered martensite with carbides (dominantly chromium carbides). It can be assumed that presence of Mo increases hardenability and increases the amount of martensite, i.e. carbon supersaturation will be higher. Therefore, driving force for precipitation will be increased, leading to, dominantly, higher nucleation rate for precipitation. Precipitation will start on grain boundaries, dislocation and twins formed during martensite transformation. Final result is that preforms made of CrMoV steel will have smaller precipitates on shorter distances.

The start of deformation is characterized with reactions of dislocations with coherent particles. Since particles are expected to be coherent in both steels, their response to applied stress, i.e. yield stress of both preforms/steels have similar values [10-12].

Flow forming technology was invented with aim to overcome very limited plasticity, since in uniaxial testing, plastic instability – necking appears at very small elongation. Introduction of additional compressive stresses due to use of mandrel and roller, provided delay of necking to considerably larger strains. The key is in presence of dynamic recovery. In this process, in dynamic conditions, present dislocations do not change their density, but only their distribution, i.e. large number of dislocations will be re-grouped to subgrain boundaries during deformation [10-12].

After flow forming, Yield stress and UTS of 41Cr4 steel have higher values in comparison to 42CrMoV4 steel. Higher strength means that higher dislocation density is present. It can be assumed that carbides in 41Cr4 steel are larger than in 42CrMo4 steel and that some of them are not only coherent, but also semi-coherent. This difference has two consequences: (i) longer distance between carbides and (ii) additional hardening due to formation of Orowan loops [13]. Both consequences lead to much pronounced dislocation reactions and final higher dislocation densities. In this respect, steel 41Cr4 exhibits higher strain hardening rate which lead to higher value of UTS. These results are in good agreement with previously published results on similar steels [4].

5. CONCLUSION

The influence of the chemical composition of the two medium carbon steels, 41Cr4 and 42CrMo4, on strain hardening of flow formed tubes was examined. Used steels contain 0.41 %C and 1 % Cr, with addition of 0.2 % Mo in 42CrMo4 steel. Hot rolled tubes after heat treatment and machining used as the preforms. The flow forming performed in two passes with total reduction of 75 %.

The non-destructive testing did not revealed the presence of defects, and hydrostatic test did not cause the occurrence of excessive dilatations.

After flow forming both steels exhibit large strain hardening. It was established that the yield strength

increased from 756 MPa and 751 MPa, to 1197 MPa and 1032 MPa, for 41Cr4 and 42CrMo4 steels respectively, while tensile strength increased from 908 MPa and 857 MPa to 1308 MPa and 1210 MPa. At the same time, hardness increased from 275 HB and 274 HB, to 380 HB and 362 HB. Hardening was more pronounced in 42Cr4 steel. It was assumed that presence of semicoherent particles enabled Orowan hardening and increased strength.

References

- [1] Wong, C.C., Dean, T.A., Lin, J., *A review of spinning, shear forming and flow forming processes*, International Int. J Mach Tools Manuf 43 (2003) 1419–1435.
- [2] Sivanandini M., Dhama S.S., Pabla, *Flow Forming of Tubes-A Review*, International Journal of Scientific & Engineering Research, Vol.3, Issue 5, 2012.
- [3] ASM metals handbook: *Forming and Forging*, Vol. 14. 9th ed. Ohio: ASM Metals Park, 1988.
- [4] Nikačević, M., Radović, Lj., *The influence of the heat treatment on the properties of flow formed rocket motor cases of 30CrMoV4 and 41Cr4 steels*, 6th Scientific Conference on Defensive Technologies, OTEH 2014, Belgrade, Serbia, 2014, 812-816.
- [5] Rajan, K.M., Deshpande, P.U., Narasimhan, K., *Effect of heat treatment of preform on the mechanical properties of flow formed AISI 4130 steel tubes - a theoretical and experimental assessment*, J Mat Proc Tech, 125-126, 2002, 503-511.
- [6] Tsivoulas, D., et al., *Effects of flow forming parameters on the development of residual stresses in Cr–Mo–V steel tubes*, Mat Sci Eng A624(2015)193–202.
- [7] Podder, B., et al., *Effect of preform heat treatment on the flow formability and mechanical properties of AISI4340 steel*, Mater Des 37 (2012) 174–181.
- [8] Gür C. H., Arda, E. B., *Effect of tube spinning and subsequent heat treatments on strength, microstructure and residual stress state of AISI/SAE type 4140 steel*, Mat Sci Tech, Vol. 19, 2003, 1590-1594.
- [9] Jahazi, M., Ebrahimi, G., *The influence of flow forming parameters and microstructure on the quality of a D6ac steel*, J Mat Proc Tech 103 (2000) 362-366.
- [10] Drobnjak, Dj., *Physics of strength and plasticity*, Faculty of Technology and Metallurgy, Belgrade, 2015.
- [11] Dieter, G., *Mechanical Metallurgy*, McGraw Hill-Book Company, Si Metric ed., London, 1988.
- [12] Smallman, R. E., Bishop, R.J., *Modern Physical Metallurgy and Materials Engineering*, Sixth ed. Butterworth-Heinemann, Oxford, 1999.
- [13] Bhadeshia, H.K.D.H., Honeycombe, R.W.K., *Steels Microstructure and Properties*, Third edition, Elsevier, Amsterdam, 2006.



EXPERIMENTAL INVESTIGATIONS OF THE INFLUENCE OF TEMPERATURE AND EXPLOITATION TIME ON THE FATIGUE CHARACTERISTICS OF X20 STEEL

DŽENANA GAČO

Technical faculty, University of Bihać, Bihać, Bosnia and Herzegovina, dzgaco@bih.net.ba

FADIL ISLAMOVIĆ

Technical faculty, University of Bihać, Bihać, Bosnia and Herzegovina, f.islam@bih.net.ba

SRĐA PERKOVIĆ

Military Technical Institute, Belgrade, Serbia, srdja.perkovic@vti.vs.rs

MIODRAG LISOV

Military Technical Institute, Belgrade, Serbia, miskolisov@gmail.com

RADICA PROKIĆ-CVETKOVIĆ

University of Belgrade, Faculty of mechanical engineering, Belgrade, Serbia, rprokic@mas.bg.ac.rs

Abstract: Research in this paper included the influence of the exploitation period and temperature on high-cycle fatigue properties, as well as fatigue crack growth parameters of the base material steel X20, by testing the new material and material after service for 116000 hours. The obtained test results and their analysis should provide a practical contribution to the assessment of the base material steel X20, thus enabling safety during exploitation of the thermal power plant components in variable load and high temperature conditions.

Keywords: high alloy steel X20, permanent dynamic strength, fatigue crack growth rate, fatigue threshold

1. INTRODUCTION

Exploitation life of the process equipment in the thermal power plants working in the high temperature conditions is up to 30 years, respectively 150000 working hours. Economic interests have influenced the design period, since exploitation life of the large number of components in power plants is usually longer than design life, which indicates the existence of conservatism in design. Due to this, the significance of the extension of the design life and revitalization of the thermal power plant components have increased, as a way to keep older power plants working for 40-50 years, and even longer [1]. Preliminary studies conducted at the Electric Power Research Institute (EPRI) [2], Centro Elettrotecnico Sperimentale Italiano (CESI) [3], and European Creep Collaborative Committee (ECCC) [4] show that the price of the revitalization of the typical thermal power plants can reach 20 to 30% of the price of the new power plant. In this case, revitalization indicates only insurance of the complete effectiveness of design life by means of selective substitution of the components with more modern ones. The basic approach in the revitalization process is the assessment of the remaining design life.

One of the most commonly used steel for operating at high temperatures and high pressures, and at the same time resistant to corrosion, is steel X20 CrMoV 12-1 (hereinafter: X20), primarily intended for the steam lines

and pipelines in the thermal power plants because of its strength and toughness at high temperatures. The tendency for the steam line wall to be as thin as possible for the required steam pressure, can only be achieved with the steel of the equivalent characteristics.

For construction exploitation safety of the process equipment in the thermal power plants, the most important characteristics are the ones that describe crack initiation and crack growth under variable load conditions. The occurrence of fatigue cracks on smooth and homogeneous construction shapes is still not describable with simple load and stress correlations, material characteristics and cross-section size, so that empirically deduced correlations have to be applied, conditioned by the extensive experimental and laboratory testing. Generally accepted characteristic in this case is fatigue strength that determines a stress level at which crack does not occur on the smooth test tube. Crack initiation and growth caused by the variable load, i.e. Paris crack growth law that establishes the correlation of the acting variable load, or equivalent stress intensity factor range and crack growth per cycles, is today generally accepted since it describes micro-mechanical behavior of the crack growth [1].

The effect of service conditions (service life and temperature) on high-cycle fatigue properties as parameters of fatigue crack growth in steel X20 was

analysed by testing the new material and material that had been in service for 116000 hours. Testing of new and used steel included determination of

- determining fatigue strength and design of the Veler curve, and
- determining fatigue crack growth parameters.

The results obtained by testing and their analysis should provide a practical contribution to assessment of quality of X20 steel, aimed at revitalisation and extension of service life of vital components in thermal power plants made of high alloy steel for elevated temperatures.

2. EXPERIMENT

2.1. Material

In order to assess the influence of the exploitation temperature and time on dynamic characteristics of the X20 steel intended for design of vital thermal power

plants components, we used new tube sample (N) and tube sample exploited for 116000 hours (S). Both samples were tubes with $\varnothing 450 \times 50$ mm size. The chemical composition of tested steel is given in Table 1, and mechanical characteristics are given in Table 2. [5].

3. TEST RESULTS

3.1. Testing with variable load

The influence of the exploitation conditions on the steel X20 base material in variable load conditions was performed on the sample of new material and material exploited for 116000 hours. These tests were performed in order to determine points in S-N diagram (Veler curve design) and dynamic strength S_f . Test specimens were shaped and sized according to the Standard ASTM E466 [6], Fig. 1. Testing was performed on the AMSLER high frequency pulsator.

Table 1. Chemical composition of the tested tube samples [5]

Batch	% mass								
	C	Si	Mn	P	S	Cr	Mo	Ni	V
Sample - N	0,21	0,27	0,563	0,017	0,006	11,70	1,019	0,601	0,310
Sample - S	0,22	0,31	0,539	0,019	0,005	11,36	1,033	0,551	0,314

Table 2. Mechanical characteristics of steel X20 [5]

Samples mark	Testing temperature, °C	Yield strength $R_{p0,2}$, MPa	Tensile strength R_m , MPa	Elongation A, %
New base material				
BM - 1 - 1N	20	521	742	17.3
BM - 1 - 2N		516	738	17.9
BM - 1 - 3N		513	734	18.2
BM - 2 - 1N	545	239	307	18.6
BM - 2 - 2N		231	302	19.2
BM - 2 - 3N		232	306	18.1
BM - 3 - 1N	570	191	249	22.3
BM - 3 - 2N		205	260	21.2
BM - 3 - 3N		196	255	22.7
Exploited base material				
BM - 1 - 1S	20	467	702	16.6
BM - 1 - 2S		471	709	16.4
BM - 1 - 3S		468	707	17.1
BM - 2 - 1S	545	224	281	18.4
BM - 2 - 2S		217	269	18.9
BM - 2 - 3S		220	275	18.1
BM - 3 - 1S	570	179	215	21.5
BM - 3 - 2S		188	231	21.7
BM - 3 - 3S		185	228	20.9

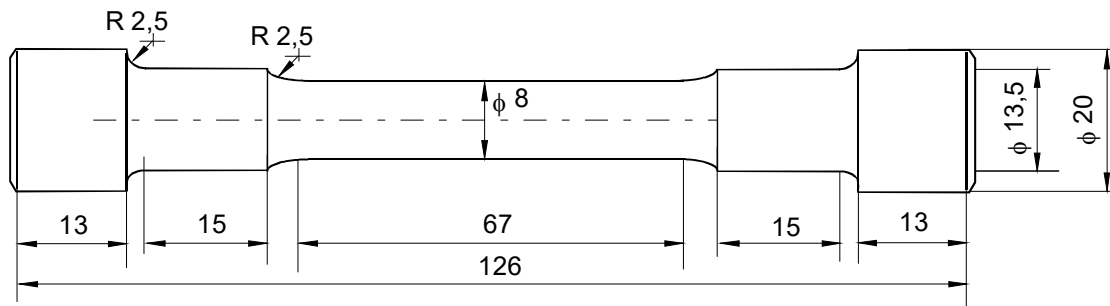


Figure 1. Test specimen for dynamic testing

High frequency pulsator can reach sinusoidal alternate variable load in range from -100 kN to +100 kN. Medium load and load amplitude is registered with precision ±50N. Reached frequency was in between 110-170 Hz, depending on the load quantity and tested temperature. In order to get the complete evaluation of the material behaviour in variable load conditions, and having in mind the test tube size, the most critical instance of variable load was performed, i.e. alternate variable load stress - pressure (R = -1).

The influence of these parameters on permanent dynamic strength values S_f , i.e. maximum dynamic stress at which crack initiation in smooth construction shapes does not occur, is shown in Veler curves (S-N diagrams) in Fig. 2 for new base material tubes, and Fig. 3 for exploited base material tubes.

This testing is determining the number of load changes until fracture occurs during constant range load. A standard demands the data on the size of the load, at which fracture does not occur after certain number of cycles (usually between 10^6 and 10^8 cycles). For steel materials Standard ASTM E468 [7] is defining permanent dynamic strength S_f , following 10^7 cycles. Due to this, the testing is very expensive, but also justified, when data are needed for designing, primarily from the viewpoint of fatigue and fracture mechanics; i.e. when designing components exposed to long-term variable load in total design life of the construction.

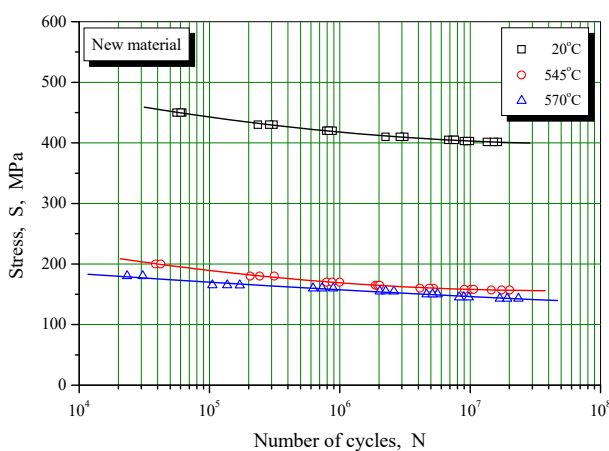


Figure 2. S-N diagram for the new X20 steel pipe base material [5]

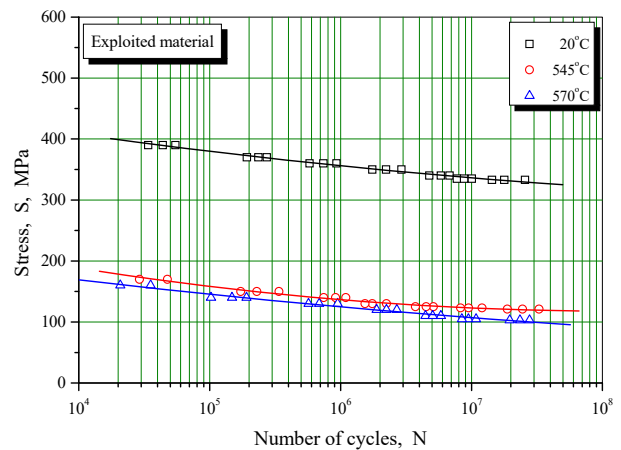


Figure 3. S-N diagram for exploited X20 steel pipe base material [5]

3.2. Determination of fatigue crack growth parameters

The basic progress that fracture mechanics has made in the material fatigue area is in the analytical analysis of the fracture phenomenon during fatigue initiation period in which fatigue crack occurs, but also during consequent growth and expansion period, in which crack grows to the critical size at which a sudden fracture appears. In this way the total number of cycles, N_u , after which fracture occurs, is divided on number of cycles required for fatigue crack initiation, N_i , and number of cycles required for crack to reach size critical for fracture, N_p .

$$N_u = N_i + N_p \tag{1}$$

Development in material behaviour evaluation in variable load conditions is enabled with parallel experimental and theoretical approach, since only theoretical approach can explain fatigue crack initiation and growth. The analysis of stress and strain at the tip of the fatigue crack growth with linear-elastic fracture mechanics (LEFM) resulted in Paris equation [8] that correlates fatigue crack growth rate and stress intensity factor range at the tip of the crack:

$$\frac{da}{dN} = C \cdot (\Delta K)^m \tag{2}$$

Although Paris equation of crack growth cannot be applied in the entire area, in between low rates near fatigue threshold (ΔK_{th}), and high rates (K_{Ic}), large linear

middle part of the curve covered by the Paris equation has proven to be the most important since it allows the difference between the fatigue crack initiation and growth.

In order to determine fatigue crack growth rate da/dN and fatigue threshold ΔK_{th} , research was performed on standard Charpy specimen tubes by tube bending method in three points on the resonant high frequency pulzator CRACKTRONIC. The testing was performed in the force control. Measuring tapes RUMUL RMF A-5 with 5 mm measuring length were affixed on the mechanically prepared test tubes that enabled measuring system FRACTOMAT to monitor the crack growth. As fatigue

crack grows under the measuring foil, the foil is split following the fatigue crack tip, thus changing electrical resistance of the foil linearly with crack length. Fatigue crack growth rate was determined on the basis of given correlation of the crack length a – number of cycles N . During the experiment number of cycles for each 0,05 mm of the crack growth was automatically recorded. The acquired correlation curves $a - N$, were used as a basis for the fatigue crack growth rate determination da/dN [8]. For easier comparison of the obtained results, Table 2 provides values of fatigue threshold ΔK_{th} , coefficient C and exponent m of the fatigue crack growth for all tested samples.

Table 3. Results of the fatigue crack growth parameters assessment [5]

Test mark	Testing temp. °C	Fatigue threshold ΔK_{th} , MPa m ^{1/2}	Coefficient C	Exponent m	da/dN, with $\Delta K=20\text{MPa m}^{1/2}$
N-1	20	8,1	$1.13 \cdot 10^{-15}$	4.689	$1.42 \cdot 10^{-09}$
N-2	545	6,9	$1.15 \cdot 10^{-13}$	2.933	$7.52 \cdot 10^{-10}$
N-3	570	6,8	$5.72 \cdot 10^{-15}$	3.828	$5.47 \cdot 10^{-10}$
S-1	20	7,2	$5.84 \cdot 10^{-15}$	4.852	$1.35 \cdot 10^{-08}$
S-2	545	5,8	$3.09 \cdot 10^{-13}$	3.065	$3.51 \cdot 10^{-09}$
S-3	570	5,7	$1.80 \cdot 10^{-13}$	3.286	$3.39 \cdot 10^{-09}$

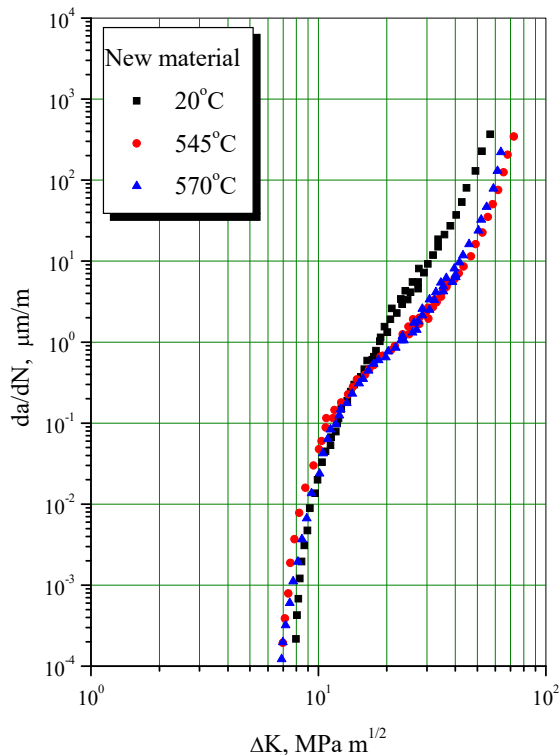


Figure 4. Dependency diagram $da/dN - \Delta K$ - test tube of the new steel X20 tube [5]

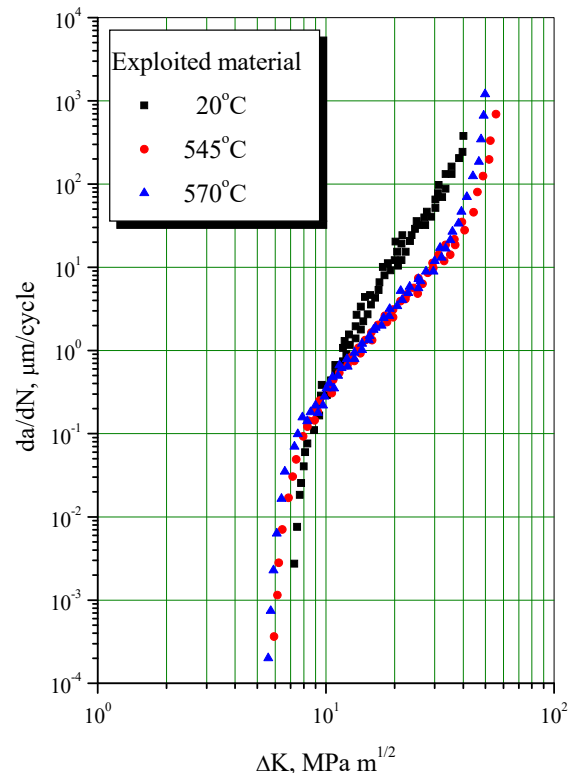


Figure 5. Dependency diagram $da/dN - \Delta K$ - test tube of the exploited steel X20 tube [5]

Dependency determination of the fatigue crack growth rate by cycle da/dN and stress intensity factor range ΔK can be reduced to determination of the coefficient C and exponent m in Paris equation. Fatigue crack growth rate requires current crack length, a , and stress intensity factor range, ΔK , that depends upon test tube geometry and crack length, and variable force range, $\Delta P = P_g - P_d$. Based on testing progress, outlined dependencies $\log da/dN - \log \Delta K$ were calculated. Typical dependency diagrams da/dN of ΔK are shown in Fig. 4, for test tubes extracted from new material X20, and Fig. 5, for test tubes extracted from exploited material X20.

4. RESULT ANALYSIS

By analyzing fatigue test results on smooth test tubes with the purpose of designing Veler curve and estimating permanent dynamic strength, we can see that exploitation time and testing temperature greatly affect obtained permanent dynamic strength values. Dependent on the testing temperature in new material tested at the room temperature, we can see that the obtained permanent dynamic strength value is 79% of the yield stress, and in exploited material 71%. During the testing at the operating temperature of 545°C, the obtained value for new material is 65%, and for exploited material 55% of the yield stress value, while at the maximum operating temperature permanent dynamic strength value is 64%, and for exploited material 53% of the yield stress value at the same temperature. If we observe the influence of the load type, we can see that influence of the exploitation time is much higher at dynamic testing, than at static testing [5].

As it is shown in the Table 2, exploitation time and testing temperature have a significant influence on the fatigue threshold values ΔK_{th} , and fatigue crack growth parameters. New material X20 has higher fatigue threshold value ΔK_{th} , i.e. better crack propagation resistance. If new material X20 contains crack of the same length as in the exploited material, its propagation in new material will require higher load (stress intensity factor range ΔK) in order to increase the crack [9].

The highest fatigue crack growth rates, that is, the least crack propagation resistance, have samples tested at the room temperature. Crack propagation resistance is increasing with samples tested at operating temperature of 545°C, while the highest crack propagation resistance can be found in samples tested at maximum operating temperature of 570°C. New material X20 obtained higher fatigue threshold value, and it also acquired lower fatigue crack growth rate in the same variable load conditions (stress intensity factor range ΔK) [10].

We can calculate fatigue crack growth rate for different values of the stress intensity factor range ΔK . The analysis required ΔK value of 20 MPa $m^{1/2}$. This stress intensity factor range can be found in the part of the curve in which Paris Law is applied. Fatigue crack growth rate, da/dN , is moving in the interval of $1.42 \cdot 10^{-9}$ for new material X20 sample, tested at the room temperature to

$5.47 \cdot 10^{-10}$ μm /per cycles, for sample tested at the maximum operating temperature of 570°C. The same tendency of the fatigue crack growth rate change can be found in the exploited material.

5. CONCLUSION

Based on the aforesaid, it can be concluded that:

- Exploitation period (new and exploited material) influences the values of the permanent dynamic strength by making new material more resistant to crack initiation in smooth construction shapes.
- Testing temperature also influences values of the permanent dynamic strength. Permanent dynamic strength value decreases with the increase of the testing temperature. Maximum fatigue crack growth rate, that is, the least crack propagation resistance, can be found in samples tested at room temperature. Crack propagation resistance is increasing as the testing temperature grows.

Maximum crack growth rate can be expected at the stress intensity factor range that is close to ductile fracture at flat strain ΔK_{Ic} , because brittle fracture can be achieved on this level. If we enter those values in the given diagrams $da/dN - \Delta K$, it is possible to estimate crack growth rate at which fatigue process gives way to development of the brittle fracture at various load levels.

References

- [1] SEDMAK,S., PRETROVSKI,B,: *Obezbeđenje kvalitetnih zavarenih spojeva i njihovog pouzdanog rada na parovodima termoelektrana ZEP-a*, Studija za potrebe Združene elektroprivrede Begrade, Contract no. 1093, TMF, 1988.
- [2] Project EPRI,: *The Grade 22 Low Alloy Steel Handbook*, Electric Power Research Institute (EPRI), EPRI Project Manager D. Gandy, Palo Alto, California, USA, 2005.
- [3] EC Project CRETE,: *Development and Harmonization of Creep Crack Growth Testing for Industrial Specimens*, A Root to a European Code of Practice, EC Project No. GRD2-2000-30021, 2001-2005.
- [4] EC Project Advanced Creep,: *WGI on Guidelines and Procedures*, European Creep Collaborative Committee (ECCC), European Technology Development (ETD) Ltd., EC Project No. G1RT-CT-2001-05042, 2001-2005.
- [5] GAČO,DŽ,: *Doctoral thesis (in Serbian)*, Mašinski fakultet u Beogradu, 2007.
- [6] ASTM E466-95, *Standard Practice for Conducting Constant Amplitude Axial Fatigue Tests of Metallic Materials*, Annual Book of ASTM Standards, Vol. 03.01, 1995.
- [7] ASTM E468-90,: *Standard Practice for Presentation of Constant Amplitude Fatigue Test Results for Metallic Materials*, Annual Book of ASTM Standards, Vol. 03.01, 2004.
- [8] PARIS,P.C., ERDOGAN,F,: *A Critical Analysis of Crack Propagation Laws*. Journal of Basic

Engineering, 85, 528-533, 1963.

- [9] DOGAN, B.: *High temperature defect assessment procedures*, International Journal of Pressure Vessels and Piping, No. 80, 2003, p. 149.
- [10] BURZIĆ, M.: *PhD Thesis*, University of Novi Sad, Department of Technical Faculty, Serbia, 2008.



THE INFLUENCE OF THE HEAT INPUT ON THE IMPACT ENERGY OF THERMALLY SIMULATED HSLA STEEL WELDMENTS

MERSIDA MANJGO

Faculty of Mechanical Engineering, Mostar, Bosnia and Herzegovina, mersida.manjgo@unmo.ba

TOMAŽ VUHERER

Faculty of Mechanical Engineering, Maribor, Slovenia, tomaz.vuherer@uni-mb.si

SRĐA PERKOVIĆ

Military Technical Institute, Belgrade, Serbia, srdja.perkovic@vti.vs.rs

MIODRAG LISOV

Military Technical Institute, Belgrade, Serbia, miskolisov@gmail.com

ZIJAH BURZIĆ

Military Technical Institute, Belgrade, Serbia, zijah.burzic@vti.vs.rs

Abstract: The paper presents the results of the influence of the amount of heat input during thermal simulation on the total impact energy, as well as the components energy of crack initiation and crack propagation energy of high-strength NIOMOL 490K steel. The influence of one-pass and two-pass HAZ simulation on the total impact energy of the tested steel was analyzed, as well as the change in the share of brittle and ductile components in the total impact energy.

Keywords: HSLA steel, Impact energy, Heat affected zone (HAZ), Welded Joint.

1. INTRODUCTION

The production of modern welded steel structures requires the use of steel of increased and high strength, with increased and high yield stress, stable toughness at low and elevated operating temperatures and good weldability. The successful application of high-strength steel, NIOMOL 490K, designed for heavily loaded welded structures, used at low temperatures, depends on the properties of the critical areas of the welded joint. Heat affected zone (HAZ) and weld metal (WM) can be places of reduced impact energy with transition temperature shifted towards higher temperatures [1-4].

Introducing a new approach in the design of welded structures, and for the sake of better test efficiency, the microstructure of the area of the heat-affected zone as the most critical place of the welded joint was simulated on the HAZ simulator. Through thermal simulation, heating to a certain temperature and programmed cooling, the microstructure of different areas of the HAZ is obtained on the samples. The influence of the amount of heat input during thermal simulation on the impact characteristics, as well as the change in the share of brittle and ductile components in the total energy of the impact, were experimentally determined and analyzed in this paper [1-4].

2. EXPERIMENTAL PART

2.1. Material

The influence of HAZ simulation regime and its influence on impact characteristics has been analysed in microalloy steel of increased strength NIOMOL 490K, produced in Steel factory "ACRONI" Jesenice [5]. The chemical composition and mechanical properties, according to manufacturer, are given in Tables 1 and 2 respectively.

2.2. Heat affected zone (HAZ) simulation

The production of complex and highly responsible welded constructions implies significantly sharper criteria for acceptance of errors. At the same time, due to the importance of such constructions, a few decades ago the need for a more reliable determination of the actual mechanical properties of all zones within the heat influence zone - HAZ was clearly recognized. For this purpose, welding simulators are used.

A welding simulator is a device that achieves controlled heating and cooling, similar to that of welding. The difference is that on a sample with maximum dimensions of 15x15x60 mm, i.e. on its middle part, a microstructure with a width of about 10mm is obtained, as a microstructure that corresponds to the zone from HAZ, which enables the determination of its basic mechanical properties [4]. A schematic representation of the simulation of the HAZ of the welded joint is given in Fig. 1.

Data on the maximum temperature and cooling time $\Delta t_{8/5}$, which represents the time it takes for the sample to cool from 800°C to 500°C, are important for the thermal cycle during heating during the simulation.

The procedure of HAZ simulation is done on simulator of

thermal cycle "SMITWELD". The test samples of quartile cross section, dimensions of 11x11x55mm are used in the simulation. Prior to heating thermo-couple Ni-NiCr had been welded at the middle of test sample, in order to monitor the temperature during the simulation.

Table 1. Chemical composition of steel NIOMOL 490K [5]

Chemical composition, mass %						
C	Si	Mn	P	S	Al	Cu
0,10	0,41	0,57	0,008	0,002	0,042	0,53

Table 2. Mechanical characteristics of steel NIOMOL 490K [5]

Direction of testing	Yield strength, $R_{p0,2}$, MPa	Tensile strength, R_m , MPa	Elongation A, %	Energy of impact, ISO-V, J
L - T	565	698	27.4	253, 259, 267
T - L	561	682	24.2	212, 206, 222

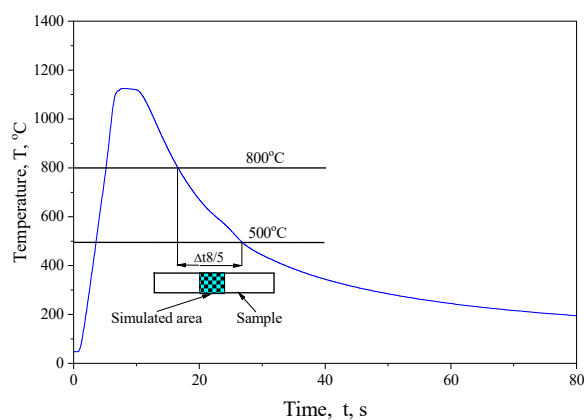


Figure 1. Simulation scheme of welded joint

Niomol 490K belongs to the group of microalloyed steels of high strength. This type of steel is welded within the cooling speed range of $8s \leq \Delta t_{8/5} \leq 15s$, where the lowest influence on decreasing of impact characteristics of sample with simulated HAZ microstructure is expected. The simulation of thermal conditions during welding is made by application of thermal cycles to samples of basic material [4]:

- One-pass influence with application of one cycle up to temperature $T_p \cong 1350^\circ\text{C}$ (grain growth HAZ)
- Two-pass influence with application of two cycles, the first one with temperature of $T_{p1} \cong 1350^\circ\text{C}$ (the grain growth HAZ is formed in such way) and the second one with temperature $700^\circ\text{C} \leq T_{p2} \leq 1100^\circ\text{C}$ (the resistance of output grain growth HAZ shall improve or fail by transformation, either partial or fully).

The heating rate for both cases was approx. $200^\circ\text{C}/\text{s}$. The temperature of heating was kept at maximum (T_p , T_{p1} , T_{p2}) during the time of 3s (in order to heat the whole cross section of sample), and cooling rate, i.e. $\Delta t_{8/5}$ was changed from 5s for group A, 10s for group B, 20s for group C, 40s for group D up to 80s for group E. The samples from group B (15 pieces) are tested at various temperatures, whilst other groups are tested at room temperature (20°C).

In all two-pass samples HAZ, the first thermal cycle was $T_{p1} \cong 1350^\circ\text{C}$, whilst for second group of samples F was

1100°C , for group of samples G was 980°C , for group of samples H was 880°C , for group of samples I was 780°C , for group of samples J was 700°C . The cooling time for groups of samples F, G and H was 10s for the first thermal cycle and 10s for the second thermal cycle, while in groups of samples I and J was 10s for the first thermal cycle and 20s for the second thermal cycle. Scheme of thermal cycle of one-pass HAZ is shown in Fig. 2., and two-pass HAZ in Fig. 3 [4].

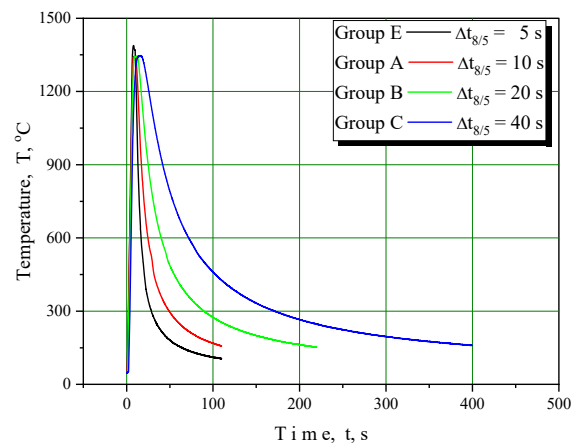


Figure 2. Thermal cycle of one-pass HAZ test samples A1, B1, C1 i D1.

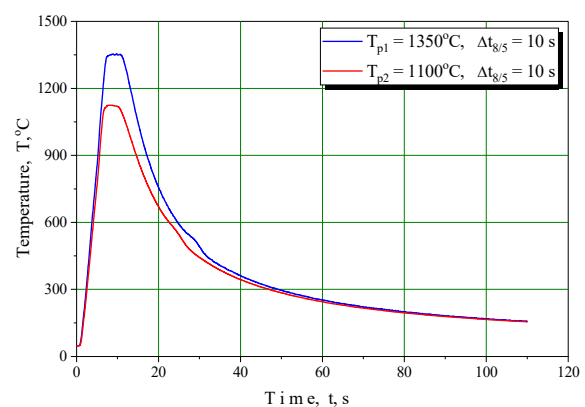


Figure 3. Thermal cycle of two-pass HAZ test samples F1.

2.3. Impact testing

Impact testing of samples is made in purpose of impact energy determination (resistance to impact). The process of testing is defined accordingly to EN ISO 148 [6] standard. Following completion of simulation the test samples dimensions of 11x11x55 mm, are processed on standard dimensions of 10x10x55 mm with V2 notch. The testing itself is done on pendulum hammer with modern instruments AMSLER 150/300 J.

3. RESULTS AND DISCUSSION

The results of impact tests are given in tab. 3 (one-pass HAZ) for test specimens of groups A, B, C, D and E that were tested at different cooling times and at a temperature of 20°C, tab. 4 (one-pass HAZ) for test specimens of group B, which were tested at different temperatures and the same cooling times, and tab. 5 (two-pass HAZ) for specimens of groups F, G, H, I and J.

Table 3. Impact testing results of test samples of one-pass simulated HAZ

Samples mark	Testing temp., °C	Cooling time $\Delta t_{8/5}$, s	Total impact energy, A_{tot} , J	Crack initiation energy, A_I , J	Crack propagation energy, A_P J
A1	+20	5	134	50	84
A2			108	48	60
A3			85	40	45
B7	+20	10	40	22	18
B8			33	20	13
B9			35	21	14
C1	+20	20	29	29	-
C2			24	24	-
C3			22	22	-
D1	+20	40	20	20	-
D2			22	22	-
D3			19	19	-
E1	+20	80	22	22	-
E2			16	16	-
E3			19	19	-

Table 4. Impact testing results of test samples of one-pass HAZ simulation

Sample mark	Testing temp., °C	Cooling time $\Delta t_{8/5}$, s	Total impact energy, A_{tot} , J	Crack initiation energy, A_I , J	Crack propagation energy, A_P J
B1	-20	10	14	14	-
B2			17	17	-
B3			19	19	-
B4	0	10	24	20	4
B5			27	21	6
B6			29	21	8
B7	+20	10	40	22	18
B8			33	20	13
B9			35	21	14
B10	+40	10	67	33	34
B11			59	30	29
B12			63	31	32
B13	+60	10	85	40	45
B14			82	39	43
B15			76	37	39

As the test was performed on an instrumented Charpy pendulum, it was possible to give an assessment of how the impact (impulse) effect affects the impact characteristics, and an assessment of the plasticity of the tested material.

Two dependencies were obtained by the test: force-time and energy-time. The influence of cooling time on impact characteristics is shown in fig. 4 to 8. Due to the scope of the experiment, only one diagram from each test group is shown.

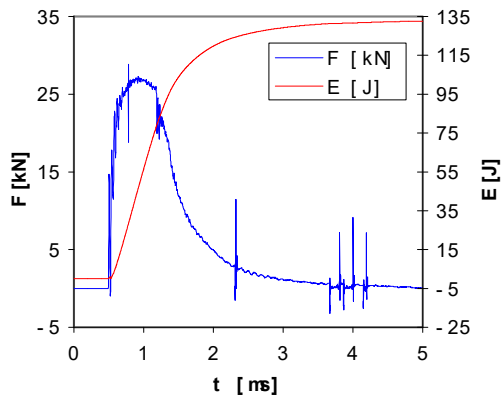


Figure 4. Specimen A1 - Simulation: $T_{p1} = 1350^{\circ}\text{C}$, $\Delta t_{8/5} = 5\text{s}$, Temp.: $+20^{\circ}\text{C}$, $A_{\text{tot.}}: 134\text{J}$

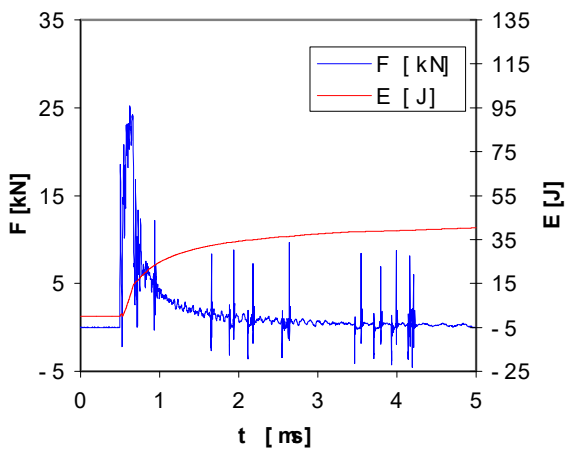


Figure 5. Specimen B1 - Simulation: $T_{p1} = 1350^{\circ}\text{C}$, $\Delta t_{8/5} = 10\text{s}$, Temp.: $+20^{\circ}\text{C}$, $A_{\text{tot.}}: 40\text{J}$

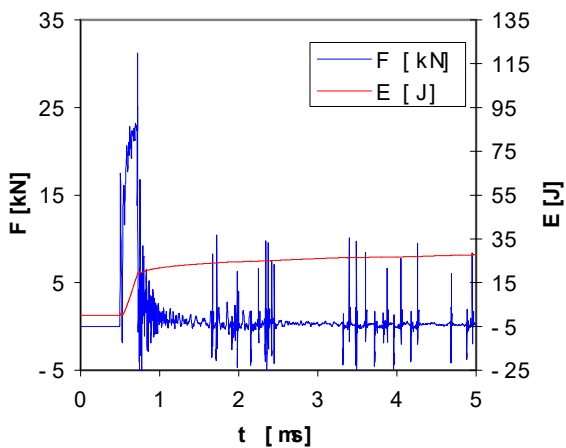


Figure 6. Specimen C1 - Simulation: $T_{p1} = 1350^{\circ}\text{C}$, $\Delta t_{8/5} = 20\text{s}$, Temp.: $+20^{\circ}\text{C}$, $A_{\text{tot.}}: 29\text{J}$

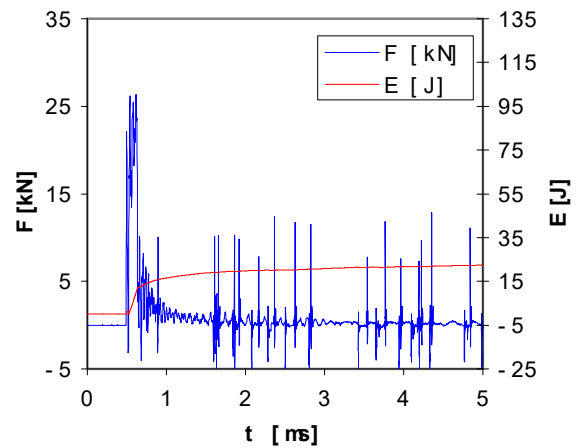


Figure 7. Specimen D1 - Simulation: $T_{p1} = 1350^{\circ}\text{C}$, $\Delta t_{8/5} = 40\text{s}$, Temp.: $+20^{\circ}\text{C}$, $A_{\text{tot.}}: 24\text{J}$

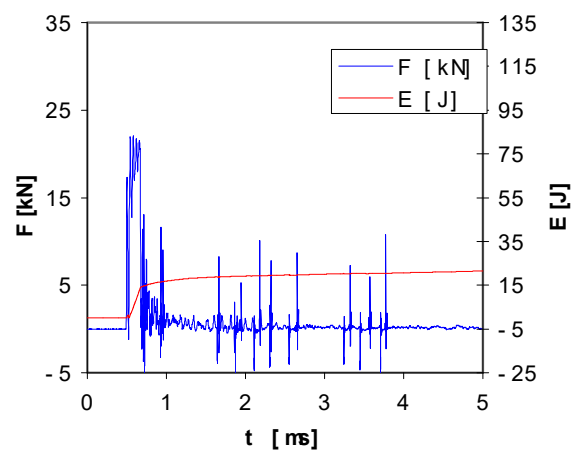


Figure 8. Specimen E1 - Simulation: $T_{p1} = 1350^{\circ}\text{C}$, $\Delta t_{8/5} = 80\text{s}$, Temp.: $+20^{\circ}\text{C}$, $A_{\text{tot.}}: 22\text{J}$

Graphics resulting from testing on instrumented Charpy pendulum enabled the analyses of testing results, first of all the evaluation of cooling time on the testing as well as temperature influence for total impact energy and its components, energy of crack initiation A_i and energy of crack propagation A_p .

The obtained test results show that at the same heating temperature (1350°C), the best values of the total impact energy have samples with the shortest cooling time (5s), Fig. 9. Total impact energy decreases while the cooling time increases up to 40s, and after that point stay on the same level. In other words, after $\Delta t_{8/5}$ 40s cooling time does not influence the value of total impact energy.

In most of cases nature of curves is principally identical differing only in value of maximum force P_{max} , and total impact energy A_{tot} . The total impact energy increases with increase of temperature ($\sim 14\text{J}$ at -20°C to $\sim 85\text{J}$ at 60°C), as shown in Figs. 10 to 14. That complies with data from literature for that type of steel [4].

Table 5. Impact testing results of test samples two-pass simulated HAZ

Sample mark	Testing temp., °C	Cooling time $\Delta t_{8/5}$, s	Total impact energy, A_{tot} , J	Crack initiation energy, A_I , J	Crack propagation energy, A_P J
F1	+20	10/10	88	65	23
F2			102	71	31
F3			62	42	20
G1	+20	10/10	108	71	37
G2			93	63	30
G3			88	60	27
H1	+20	10/10	57	20	37
H2			87	71	16
H3			75	55	20
I1	+20	10/20	34	20	14
I2			36	15	21
I3			36	14	22
J1	+20	10/20	18	9	9
J2			22	11	11
J3			17	9	8

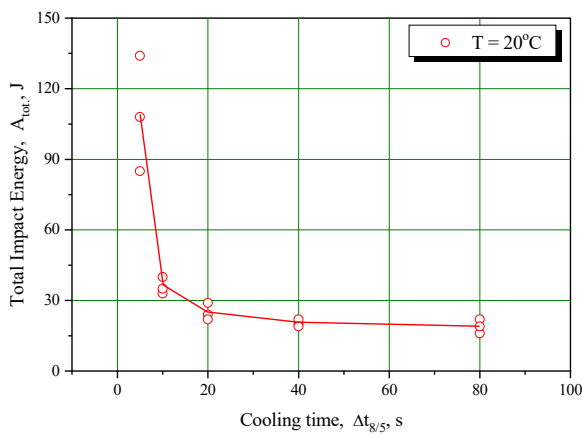


Figure 9. Diagram A_{tot} - $\Delta t_{8/5}$ to $T = 20^\circ\text{C}$

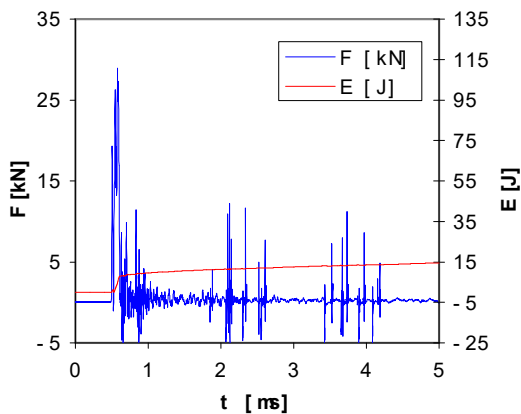


Figure 10. Specimen B1 - Simulation: $T_{p1} = 1350^\circ\text{C}$, $\Delta t_{8/5} = 10\text{s}$, Temp.: -20°C , A_{tot} : 14J

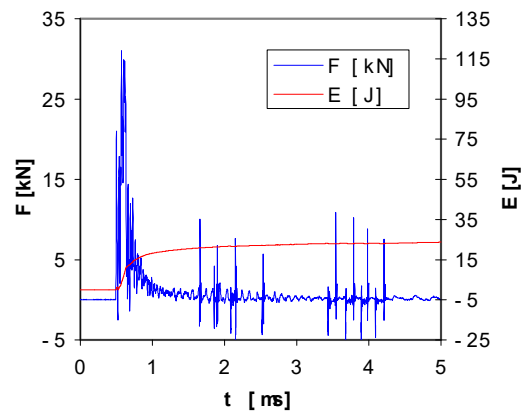


Figure 11. Specimen B4 - Simulation: $T_{p1} = 1350^\circ\text{C}$, $\Delta t_{8/5} = 10\text{s}$, Temp.: 0°C , A_{tot} : 24J

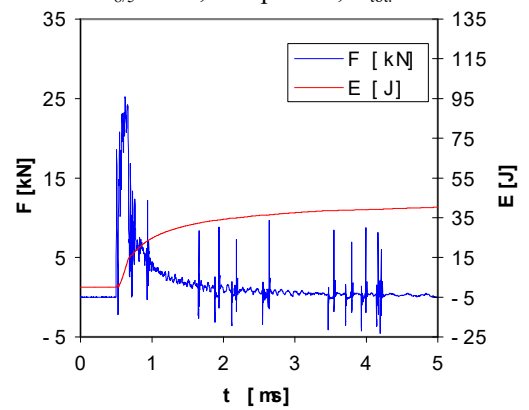


Figure 12. Specimen B7 - Simulation: $T_{p1} = 1350^\circ\text{C}$, $\Delta t_{8/5} = 10\text{s}$, Temp.: $+20^\circ\text{C}$, A_{tot} : 40J

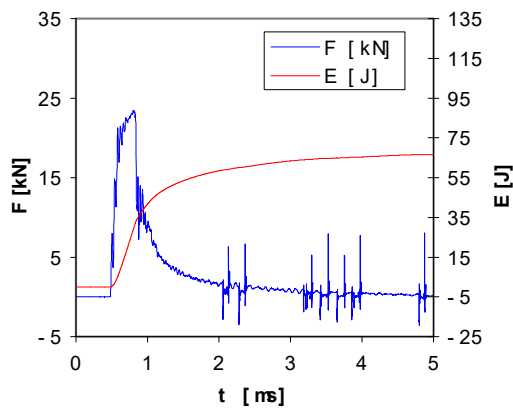


Figure 13. Specimen B10 - Simulation: $T_{p1} = 1350^{\circ}\text{C}$, $\Delta t_{8/5} = 10\text{s}$, Temp.: 40°C , $A_{\text{tot.}}: 67\text{J}$

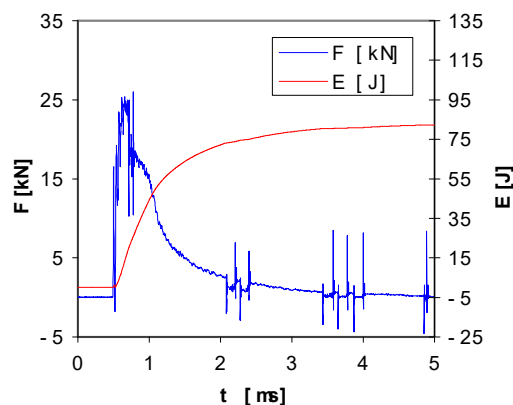


Figure 14. Specimen B13 - Simulation: $T_{p1} = 1350^{\circ}\text{C}$, $\Delta t_{8/5} = 10\text{s}$, Temp.: 60°C , $A_{\text{tot.}}: 85\text{J}$

Graphically, the dependence of the change in total impact energy with temperature is shown in fig. 15.

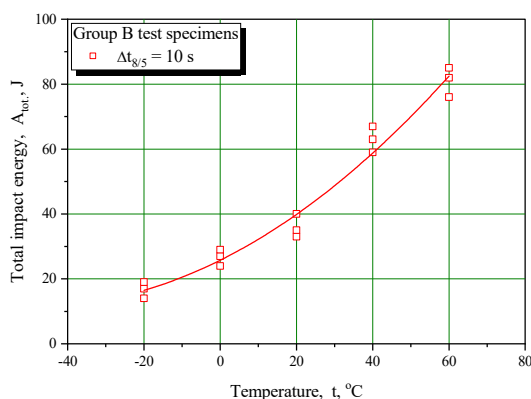


Figure 15. Diagram $A_{\text{tot.}}$ - temp. testing at $\Delta t_{8/5} = 10\text{s}$

The highest values of the total impact energy recorded in the two-pass HAZ, have the samples with the highest temperature of the second thermal cycle, Fig. 16. Thus, at the second thermal cycle of 1100°C and 980°C , the obtained impact energy values are on average value close to 90J , and at the second thermal cycle of 700°C , the total impact energy is around 20J [4].

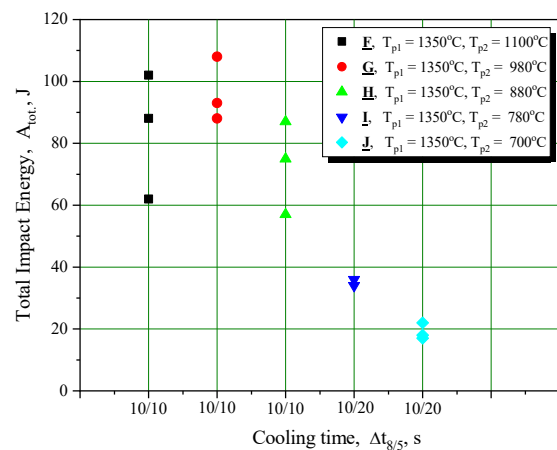


Figure 16. Diagram $A_{\text{tot.}}$ - cooling time $\Delta t_{8/5}$ at different t of the second thermal cycle

However, the interesting thing is that at -20°C the value of total impact energy decreases below impact energy of zero plasticity (transient temperature) that for HAZ NIOMOL-a 490K, in improved conditions, amounts to -27°C and at that temperature the value is 27J , based on data from literature and own research.

Decrease of participation of fracture plastic component, i.e. decrease of material plasticity is clearly reflected in the character of obtained curves, where the deflection value, D_f , decreases significantly with decrease of temperature. Dependence of deflection D_f is of the same character as dependence of total impact energy $A_{\text{tot.}}$, what means that deflection increases with increase of testing temperature.

4. CONCLUSION

The obtained results of the impact energy (impact toughness) of the simulated ZUT, microalloyed steel Niomol 490K, indicate that:

- In the case of one-pass ZUT, the best impact characteristics have samples with the shortest cooling time at the same temperature of the thermal cycle.
- In two-pass ZUT, the best impact characteristics have samples where the temperature of the second thermal cycle is the highest at the same cooling time.

References

- [1] MANJGO, M.,: *Kriterijumi prihvatljivosti prslina u zavarenom spoju posuda pod pritiskom od mikrolegiranih čelika*, Doctoral thesis (in Serbian), Mašinski fakultet u Beogradu, 2008.
- [2] BURZIĆ, M., MANJGO, M., VUHERER, T., PROKIĆ, R., POPOVIĆ, O., BURZIĆ, Z.,: *Sklonost ka krtom lomu simuliranog HAZ-a čelika povišene čvrstoće*, Zavarivanje i zavarene konstrukcije, vol. 60, br. 1, str. 7-14, Beograd, 2015,
- [3] GAČO, DŽ., BIŠĆEVIĆ, N., ISLAMOVIĆ, F., MANJGO, M., BURZIĆ, Z., BAJRAMOVIĆ, E.,: *The effect of cooling time on the values of total impact energy components*, Conference DIVK, Beograd, 2014
- [4] BURZIĆ, Z., PAŠIĆ, S., GLIHA, V., MANJGO, M., VUHERER, T.,: *An Influence of the Heat Input Onto the*

- Resistance to Cracks of Heat Affected Zone of High Strength Low Alloyed Steel*, 2nd DAAAM International Conference on Advanced Technologies Developing Countries, ATDC, Tuzla, 2003.
- [5] ACRONI: *High Strength Low Alloyed Steels*, Jesenice, 2002.
- [6] ISO 148-1: *Metallic materials - Charpy pendulum impact test - Part 1: Test method*, 2007



MIG WELDING PROCESS ON THE MECHANICAL PROPERTIES OF BUTT WELDED JOINTS OF DISSIMILAR ALUMINUM ALLOYS 2024-T351 /6082-T6

DRAGAN MILČIĆ

Faculty of Mechanical Engineering, University of Nis, Niš, Serbia

dragan.milcic@masfak.ni.ac.rs

TOMAŽ VUHERER

University of Maribor, Faculty of Mechanical Engineering, Maribor, Slovenia

tomaz.vuherer@um.si

LJUBICA RADOVIĆ

Military Technical Institute, Belgrade, Serbia

ljubica.radovic@vti.vs.rs

MIODRAG MILČIĆ

Faculty of Mechanical Engineering, University of Nis, Niš, Serbia

miodrag.milcic@masfak.ni.ac.rs

MAJA MLADENović

Military Technical Institute, Belgrade, Serbia

mmaja011@gmail.com

ANDREJA RADOVANOVIĆ

IMW Institut, Aleja Milanović bb, 34325 Lužnice, Kragujevac, Srbija

andreja.radovanovic@imw.rs

NENAD RADOVIĆ

Faculty of Technology and Metallurgy, University of Belgrade, Belgrade, Serbia

nenrad@tmf.bg.ac.rs

Abstract: The aim of this work was to present the effects of the MIG welding on the mechanical properties of a butt-welded joint of dissimilar aluminum alloys 2024-T351 and AA 6082-T6. Aluminum alloy 6082 T6 is well weldable by classical fusion welding processes (MIG and TIG), while aluminum alloy 2024-T351 is almost non-weldable. For the welding of these two Al alloys, the MIG welding on 8 mm thick sheets filler material 4043A (AlSi5) and a mixture of argon and helium as a shielding gas. The assessment of the mechanical properties of the welded joint of dissimilar Al alloys was performed by Vickers hardness testing, tensile and bending tests of the welded samples. The influence of MIG welding on the microstructure of the welded joint was analyzed by light microscopy (LM) and scanning electron microscopy (SEM). It was found that the fracture of the tensile test specimen occurred on the 6082-T6 aluminum alloy side. Tensile strength of the welded joint was 198 MPa, what was about 64 % of the tensile strength of the base metal, i.e. 6082-T6 alloy.

Keywords: Welded joints of dissimilar aluminum alloys, AA 2024-T351, AA 6082-T6, MIG welding process, Microstructure, Mechanical properties of welded joints.

1. INTRODUCTION

Aluminum structures are often used in transport technology, in the automotive industry, in the industry of rail vehicles, in shipbuilding, in the aviation industry and even in space technologies.

Constructions of cars, trains, ships, airplanes, spacecraft, which are made of different aluminum alloys, are most often joined by classic metal inert gas (MIG) and tungsten

inert gas (TIG) welding, friction stir, laser and electron beam welding. Fusion welding processes easily join materials that have good weldability. The material is well weldable if it is possible to make a welded joint without defects. The weldability of aluminum alloys is affected by a number of factors such as: oxygen affinity, high thermal expansion and thermal conductivity, high shrinkage during solidification, high solubility of hydrogen in the liquid phase, which decreases drastically during solidification. By welding aluminum alloys, mechanical

properties and corrosion resistance in HAZ are reduced, porosity, solidification and liquation cracks appear. Aluminum alloys are welded with additional material with increased content of Si or Mg [1].

Recently, leading manufacturers of welding equipment allow various modifications of MIG and TIG welding procedures, such as AC MIG with pulsing during welding with single or double pulse, or TIP TIG with automatic addition of hot wire.

If the technology of the welding procedure is not suitable, defects may appear in the area of the weld metal, which reduces the reliability of the welded structure. Weld defects such as porosity, cracks, lack of penetration or lack of fusion may appear [2].

Age-hardenable 2024 aluminum alloy belongs to the 2XXX alloy series where the main alloying element is copper. The mechanical properties of these alloys reach values similar to those of carbon steels. Such a high strength of the alloys is due to the precipitation of CuAl_2 particles during natural or artificial aging. As these alloys do not have good corrosion resistance, they are often coated (plated) with pure aluminum for corrosion protection. They are used for manufacturing parts in the aviation industry due to their high strength, good fatigue properties. With the addition of elements such as Mg and Li, it is possible to reduce the specific density and improve the performance of Al alloys for applications in the manufacture of parts in the aerospace industry [3]. Alloys of the 2XXX series, as a rule, have poor weldability with fusion welding (MIG, TIG), due to high crack sensitivity. Friction stir welding is mainly used for welding these alloys [4, 5].

Aluminum alloy 6082 belongs to the series of alloys age-hardenable 6XXX. Alloys where the alloying elements are silicon and magnesium. Alloys of the Al-Mg-Si system have moderate strength and good corrosion resistance, compared to other heat-treatable Al alloys. Typical of these alloys is that they have good formability and acceptable weldability.

Dissimilar aluminum alloys are being heavily used in the various fields of engineering due to its light weight and superior properties. In this paper, investigations of the mechanical behavior of the welded joint achieved by the MIG welding between dissimilar aluminum alloys 2024 T351 and 6082 T6 using the filler material S Al 4043A (AlSi5) are given.

2. MATERIALS AND METHODS

Experimental research was focused on determining the influence of the MIG welding process on the metallurgical and mechanical properties of welded joints of alloys 2024-T351 and 6082-T6.

The chemical and mechanical properties of the alloys 2024-T351 and 6082-T6 (according to standards), which are the subject of this research and joined by the MIG process, are given in Tables 1 and 2. The chemical properties of the additional material used during welding are given in Table 3.

The dimensions of the plates used for welding were 300 mm long, 125 mm wide and 8 mm thick. Welding machine was Fronius Transpuls Synergic 4000. Shielding gas was ISO 14175 – I3 –ArHe–30.

Table 1. Chemical composition of aluminum alloy 2024 T351 and 6082 T6 [6]

	Mn %	Fe %	Mg %	Si %	Cu %	Zn %	Ti %	Cr %	Al %
6082 T6	0.4-1.0	0- 0.5	0.6-1.2	0.7-1.3	0-0.1	0-0.2	0-0.1	0-0.25	Balance
2024 T351	0.65	0.17	1.56	0.046	4.7	0.11	0.032	-	Balance

Table 2. Mechanical properties of aluminum alloy 2024 T351 and 6082 T6 [6]

	Yield strength min R_{eh} (Mpa)	Ultimate tensile strength min R_m (Mpa)	Elongation at Break min A (%)	Hardness HV
2024 T351	310	425	10	137
6082 T6	260	310	10	95

Table 3. Chemical composition of the filler material of wire EN ISO 18273 S Al 4043A (AlSi5), mas. %

Mn %	Fe	Mg	Si	Cu	Zn	Ti	Be	Al
<0,15	<0,6	<0,2	4,5-5,5	<0,3	<0,1	<0,15	<0,0003	Balance

Table 4. Welding parameters for the MIG butt weld welding process for the material EN AW 2024-T351/EN AW 6082-T6

Run	Welding Process EN ISO 4063	Current I (A)	Voltage U (V)	Wire Feed Speed (m/min)	Welding Speed v (mm/s)	Heat input $H=I \cdot U \cdot \square/v$ (J/mm)
1	131	150	21	6,2	7	360
2	131	160	22	6,5	11,5	245
3	131	160	22	6,5	7,7	366

Vickers hardness was measured on a Willson VH1150 hardness tester. Tensile properties were determined at room temperature using a Shimadzu AG-X 300 kN tensile tester. Test specimens defined by the ASTM E8M standard obtained from welded samples perpendicular to the welded joint were used [7]. Specimens were cut from the welded samples using the water jet cutting process.

The bending tests were carried out on four specimens—in two the tensiled side was the face of the weld and in two the tensiled side was the root of the weld. The test was performed at room temperature using the three-point bending method.

A Leica Q500MC optical microscope (LM) was used to analyze the microstructure of the welded joint. The microstructure was examined on the cross-section of the samples after the usual metallographic preparation and etching in Keller's reagent. The tests were also carried out using the scanning electron microscope JOEL JSM-6610LV (SEM).

3. RESULTS

Figure 1 shows face side of a welded joint. Welded joint made with a backing material.

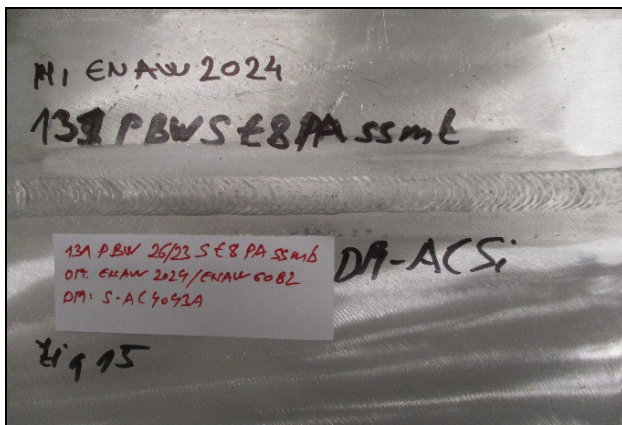


Figure 1. Face side of the welded joint.

3.1. Destructive Tests

3.1.1. Static Tensile Test

Figure 2 shows the specimen after breaking.

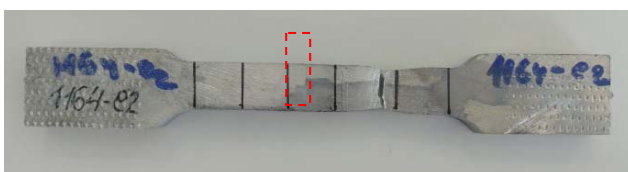


Figure 2. Specimen after a static tensile test.

Stress-strain curves is shown in Figure 3, and results are summarized in Table 5. The fracture was ductile and occurred in the 6082 base material (BM).

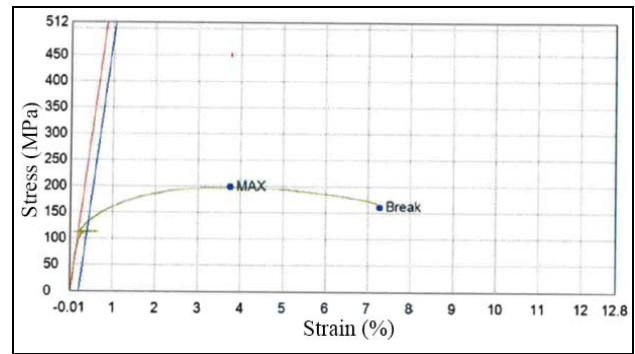


Figure 3. Stress-strain diagram.

Table 5. Tensile test results of welded joints

Cross-section area (mm ²)	Yield strength R_{eh} (MPa)	Ultimate tensile strength R_m (MPa)	Elongation at break A (%)	Place of fracture
80	113	198	7.3	BM 6082 T6

3.1.2. Bending Test

Root and face bending tests are given in Figure 4 and 5. The aim of this test was to investigate the plastic properties of the welded joint.



Figure 4. Root bend test.

The results shown small bending angle until the appearance of a crack in both root and face bend test. However, weld joint showed more ability to withstand deformation under face bend test.

Hardness measurements were made as shown in Figures 6 and 7.

The hardness of the weld metal, measured near the weld face and near the weld root, is about 80 HV, while hardness of base metals are about 90 HV and 150 HV for 6082-T6 and 2024-T351. The hardness of HAZ towards 6082-T6 and 2024-T351 is about 60 HV and 120 HV, respectively.

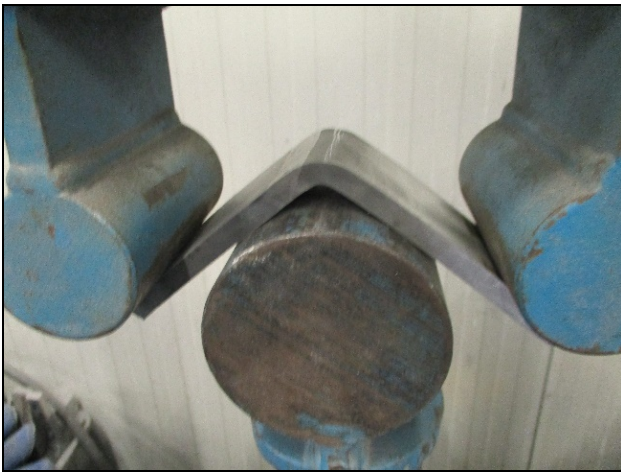


Figure 5. Face bend test.

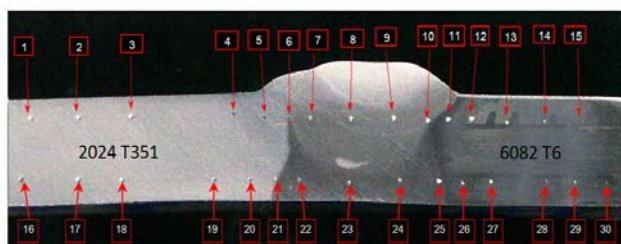


Figure 6. Hardness measurement of the joint.

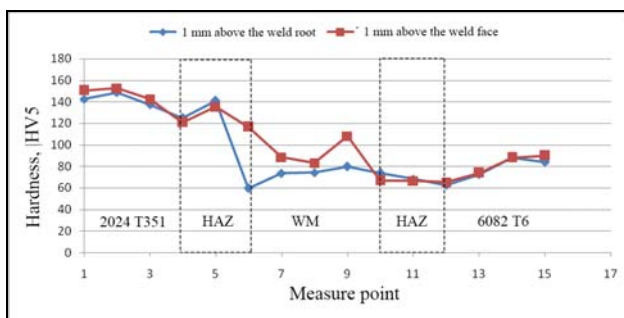


Figure 7. Hardness distribution of the joint.

3.1.3. Macro- and Microscopic Examinations

Figure 8 presents the macrostructure of the welded joint observed on the cross-section of the weld axis. The joint has a regular symmetrical shape with visible underfilling of the weld face, without visible pores.

Figure 9 and 10 shows the microstructure of base materials: 2024 T351 aluminum alloy and 6082 T6 aluminum alloy. Elongated grains in the rolling direction were observed on the sample of 2024-T351 alloy. SEM/EDS analysis identified coarse intermetallic particles Al-Cu-Fe-Mn-Si ($>10 \mu\text{m}$), finer Al-Cu-Mg, Al-Cu-Mn, Al-Cu-Mg-Si and Al-Si-Cu-Mg (Figure 11). The fine particles can be precipitates of alloys elements, Al-Cu and Al-Cu-Mg based.

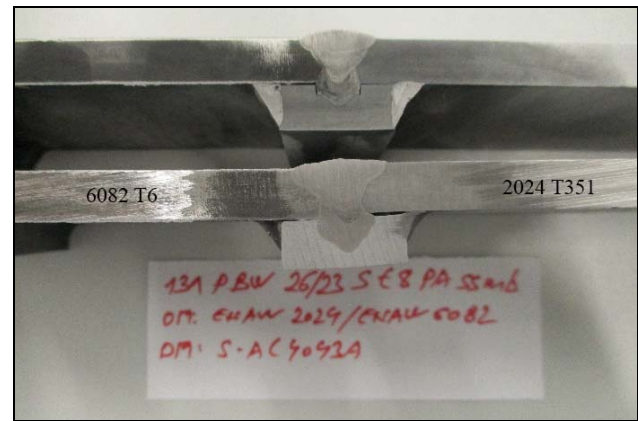


Figure 8. Macrostructure of a welded joint made with a backing material.

Microstructure of base metal – aluminum alloy 6082-T6, also consists of a wide range of intermetallic phases (IMP) formed during processing.

Larger particles in the direction of rolling Al-Fe-Mn-Mg-Si-Cr, Al-Mg-Si-Mn, Al-Mg-Si (Figure 12), and fine precipitate particles Mg-Si, formed during the artificial aging process were observed.

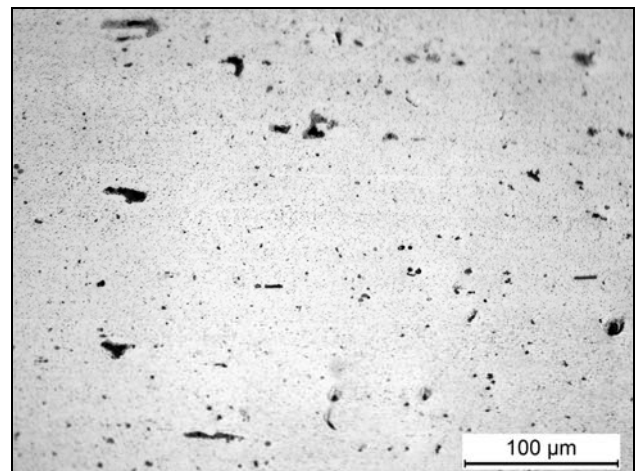


Figure 9. Distribution of second phase particles in 2024 T351 aluminum alloy. (LM).

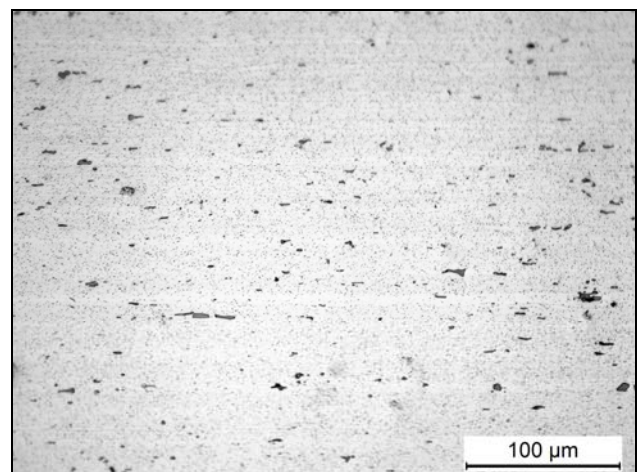


Figure 10. Distribution of second phase particles in 6082 T6 aluminum alloy. (LM).

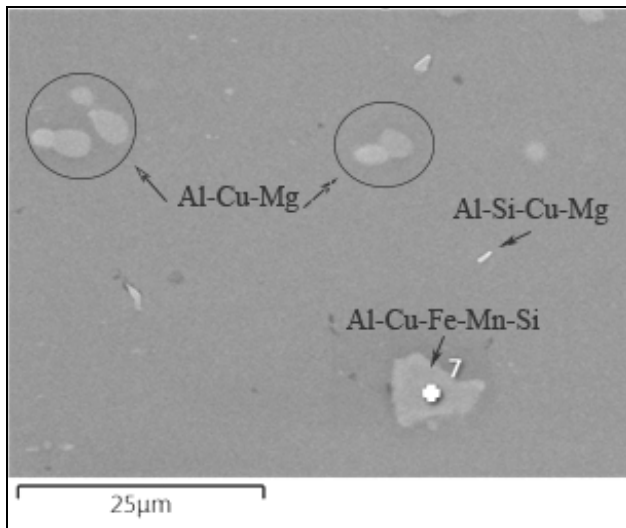


Figure 11. Second phase particles in 2024-T351 alloy. (SEM).

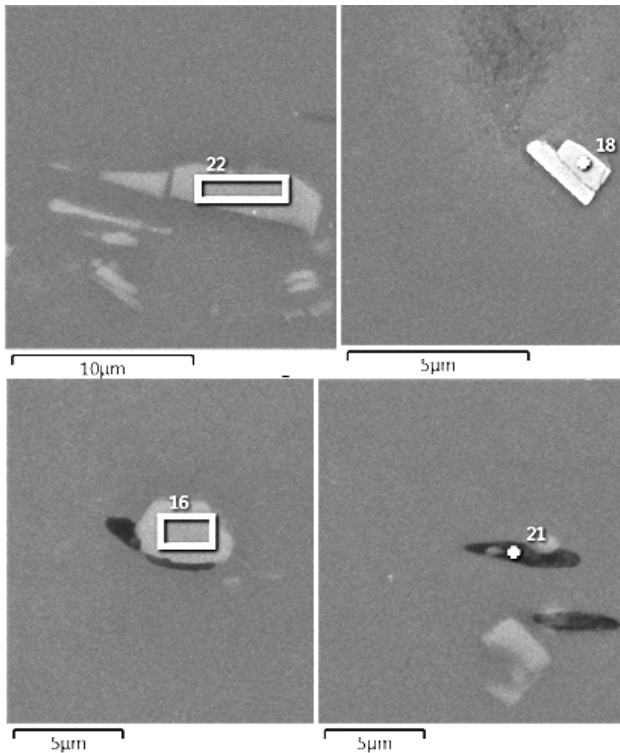


Figure 12. Second phase particles in 6082-T6 alloy. Al-Fe-Mn-Mg-Si-Cr, Al-Si-Mg, Al-Mg-Si-Mn, Al-Mg-Si., (SEM).

Figure 13 shows the microstructure of the heat affected zone (HAZ) between the weld metal (WM) and the 2024-T351 base metal. Lower density of the precipitates in the HAZ was observed.

Figure 14 shows the microstructure of the HAZ between the weld metal and the 6082-T6 base metal. A narrow zone of columnar crystals is present in the WM to the HAZ. The precipitates are formed along the grain boundaries and within the grains in coarse form. The precipitates in the HAZ distributed randomly as globular coarse particles, as well as, lower density of the fine precipitates in the HAZ was observed.

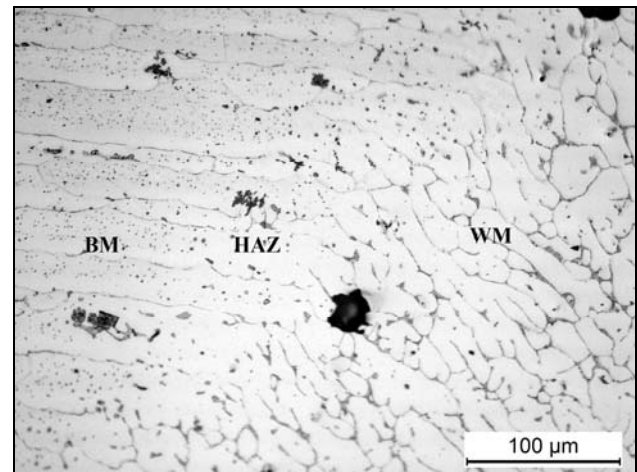


Figure 13. Heat affected zone in 2024 T351 alloy. (LM).

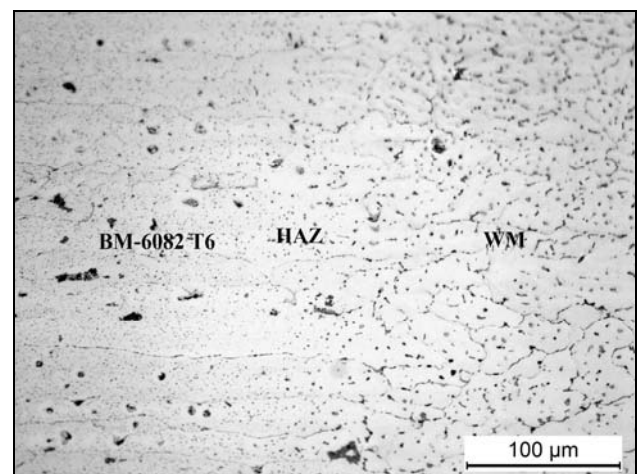


Figure 14. Heat affected zone in 6082 T6. (LM).

Figure 15 shows the microstructure of weld metal (WM) MIG joints for dissimilar aluminum alloys (2024-T351 and 6082-T6).

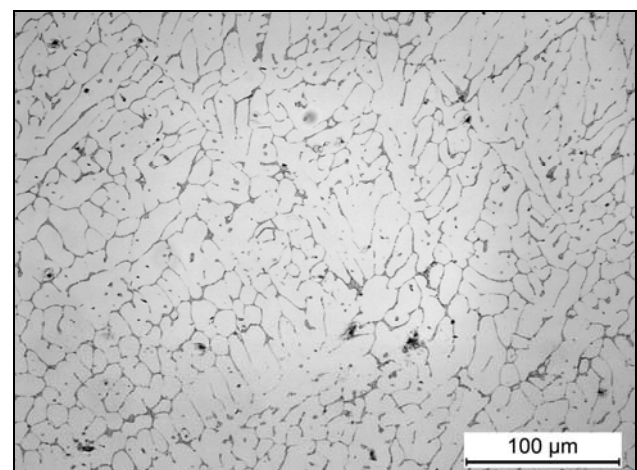


Figure 15. Microstructure of the weld metal. (LM).

4. DISCUSSION

The microstructure of the weld metal obtained by the MIG welding process is significantly different from the microstructure of the base metals, and accordingly, the

mechanical properties of the welded joint are lower than the mechanical properties of the base metals. A lower ductility was also observed during the tensile test.

The fracture location of specimen for tensile testing is in base metal – 6082-T6. The results of bending tests indicate poor technological properties of welded joints. A small bending angle until the appearance of a crack indicates that the welded joints are very brittle according to [8-11].

The hardness of the weld metal, measured near the weld face and near the weld root, is about 80 HV, which is less than the softer base metal 6082-T6, which has a hardness of about 90 HV, and significantly less than the base metal 2024-T351, which has a hardness of about 150 HV. The hardness of HAZ towards 6082-T6 is about 60 HV, lower than in the weld metal zone. HAZ towards 2024-T351 has a hardness of about 120 HV, but, also lower compared to 2024 base metal. Such hardness distribution (Figure 7) is obtained due to microstructural changes in HAZs in age-hardenable alloys (Figures 11 and 12). When the alloy is exposed to thermal cycle during welding, the hardening fine precipitates (dispersoids) dissolve, and at the same time the others overage. There is more coarse particles with decreasing amount of small dispersoids. Decrease density of smallest dispersoids lead to reduction of hardness/strength [12, 13].

The heat input of joints, the base metals and the filler metal create a zone of weld metal with a structure that is different from the structure of the base metals. A higher percentage of silicon (about 5%) in the filler material is useful for increasing the ductility of the welded structure and another benefits are low hot cracking sensitivity in most applications, excellent corrosion resistance, and low shrinkage rate/reduced distortion [14]. The melting zone, or weld metal area, is created by filling a previously prepared groove with molten filler material. After solidification, the weld metal has a characteristic casting structure (Figure 13). The layer that hardens last has a distinctly dendritic structure, which is characterized by the appearance of liquation, i.e. local chemical inhomogeneity, due to the lack of time for the diffusion of atoms of alloying elements. The grains are of different sizes and have a directional orientation [8].

5. CONCLUSION

Based on the above, it can be concluded:

- The tensile strength of the welded joint is (198 MPa) compared to (310 MPa) alloy 6082-T6 which is a weaker welded joint material, i.e. the reduction in strength is about (36%).
- The fracture of the tensile test specimen was found to occur on the 6082-T6 aluminum alloy side.
- Weld metal hardness is 55% lower than base metal hardness 2024-T351.
- To improve the performance of welded joints of different aluminum alloys 2024-T351 and 6082-T6, optimal welding parameters must be selected.

ACKNOWLEDGMENTS

This research work was financially supported by the Ministry of Education, Science and Technological Development of the Republic of Serbia (Contracts No. 451-03-68/2022-14/200109 and 451-03-68/2022-14/200325). This paper is the result of research within the bilateral project with the Republic of Slovenia "Providing high reliability of aluminum structures and their parts in transport technics" in the project cycle 2020-2022 (project no. 337-00-21/2020-09/48).

References

- [1] Metals Handbook, Vol. 6: *Welding, Brazing and Soldering*, ASM Metals Park, Ohio, 1997.
- [2] Molian, P. A., Srivatsan, T. S.: *Weldability of aluminium-lithium alloy 2090 using laser welding*, J. Mater. Sci., 25(7) (1990) 3347–3358.
- [3] Heinz, A., Haszler, A., Keidel, C., Moldenhauer, S., Benedictus, R. Miller, W.: *Recent development in aluminium alloys for aerospace applications*, Mater. Sci. Eng. A, 280 (2000) 1, pp.102–107.
- [4] Milcic, M., Vuherer, T., Radisavljevic, I., Milcic, D.: *Experimental Investigation of Mechanical Properties on Friction Stir Welded Aluminum 2024 Alloy*, Springer Nature Switzerland AG 2019, N. Mitrovic et al. (Eds.): CNNTech 2018, LNNS 54, pp. 44-58.
- [5] Milcic, M., Vuherer, T., Radisavljevic, I., Milcic, D., Kramberger, J.: *The influence of process parameters on the mechanical properties of friction stir welded joints of 2024 T351 aluminum alloys*, Materials and technology 53(6) (2019) 771–776.
- [6] ASM Handbook, Vol.2 - *Properties and Selection: Nonferrous Alloys and Special-Purpose Materials*, Edition Metals Handbook, ASM International 10th Ed. 1990.
- [7] ASTM E8M -Standard Test Methods for Tension Testing of Metallic Materials,
- [8] Nawres, N., J.: *Mechanical Properties of MIG Joints for Dissimilar Aluminum Alloys (2024-T351 and 6061-T651)*, Al-Khwarizmi Engineering Journal, 12(3) (2016) 121- 128.
- [9] Cavaliere, P., Nobile, R., Panella, F. W., Squillace, A.: *Mechanical and microstructural behavior of 2024-7075aluminum alloy sheets joined by friction stir welding*, International Journal of Machine Tools and Manufacture 46 (2005) 588-594.
- [10] Muafaq, M. S.: *Studying the effect of joint design, angle and heat treatment on mechanical properties of the aluminum alloy weldments (7020-T6) by MIG process*, Master Thesis, Technical College/Baghdad, 2005.
- [11] Missori, S., Sili, A.: *Mechanical behavior of 6082-T6 aluminum alloy welds*, Metallurgical Science and Technology, 18 (2000) 12-18.
- [12] Rakhmonov, J. et al. *Improving the Mechanical Response of Al–Mg–Si 6082 Structural Alloys during High-Temperature Exposure through Dispersoid Strengthening*, Materials 2020, 13, 5295.

- [13] Fang, X. et al., *Precipitation sequence of an aged Al-Mg-Si Alloy*, *J. Min. Metall. Sect. B-Metall.* 46 (2) B (2010) 171 – 180.
- [14] AMS 4190K Alloy 4043, <https://weldingwarehouseinc.com>



ANFIS FOR PREDICTING REMOVAL EFFICIENCY OF METHYLENE BLUE ONTO CORDIA MIXA-A

AHMED KHALEEL IBRAHIM

Depa. of Environmental Engineering / Faculty of Engineering / Tikrit University / Saladin / Iraq
ahmedkh71@tu.edu.iq

AMIR ALSAMMARRAI

Depa. of Mechanical Engineering / Faculty of Engineering / Tikrit University / Saladin / Iraq
amircratf@tu.edu.iq

SALWA HADI AHMED

Depa. of Environmental Engineering / Faculty of Engineering / Tikrit University / Saladin / Iraq
dr.salwahadi@tu.edu.iq

Abstract: In this study, *Cordia myxa* fruit (CM) was used as an adsorbent to remove methylene blue (MB) dye from industrial wastewater. Activated carbon was produced from (CM) by carbonization using a tubular furnace at temperatures of 400 °C and by passing nitrogen as inert gas for 2 hours. Appropriate tests were carried out for the biochar that was produced such as the effect of pH, adsorbent dose, adsorbate concentration and contact time on adsorption of MB on CM. The results also showed that the optimal pH was 7.5, the optimal dose of the adsorbent was 2 g/L, the optimal concentration of (MB) was 5 mg/L, and the contact time was 80 minutes. The removal efficiency of MB onto CM-A was modelled using Adaptive Neural Fuzzy Inference Systems (ANFIS). An MB-on-CM adsorption experiment was planned for ANFIS training. Using 40 experimental data sets, ANFIS was trained with gradient descent with momentum algorithm and averaged 0.52 per cent error. The testing accuracy was verified with 6 additional experimental data sets, and the average predicting error was 0.088%. The ANFIS model was used to discuss the effect of pH and contact time on MB removal from CM-B.

Keywords: Adsorption; biochar; *Cordia myxa*; Carbonization; ANFIS

1. INTRODUCTION

Environmental pollution and the problems resulting from it are among the important issues that have occupied the world since the beginning of the twentieth century [1]. Industrial, agricultural and population growth has made the water used for utilitarian purposes free of various types of pollutants in a continuous decrease [2]. It is known that the various industrial wastes, whether the petrochemical industries or the agricultural pesticide industry and other industries contain slow decomposing organic compounds and dyes that cannot be removed by traditional methods [3]. Dyes are considered dangerous industrial pollutants due to their large quantities in industrial wastewater, the difficulty of decomposition, hazardous effect and carcinogenicity, so it has become necessary to find methods to remove these pollutants [4]. Methylene blue MB is a basic dye and one of the dyes resulting from industrial waste is dangerous and cannot be removed by traditional methods [5]. The molecular formula of (MB) is $C_{37}H_{27}N_3Na_2O_9S_3$ and the molecular mass is 779.8 g mol^{-1} . (MB) is used as a disinfectant in pharmaceuticals, rubbers, varnishes, pesticides, dyestuff, colouring agents, and so on [6]. The discharging of (MB) into the water can significantly affect the food chain and aquatic life even in small concentrations [7]. (MB) shows

adequate resistance to oxidation by photodegradation, biodegradation and traditional chemical oxidation because of its complex aromatic structure [6]. Therefore, efficient decolorization treatment of (MB) from aqueous solutions has been gaining notice in recent years. Some adsorbents have been considered for the efficient removal of (MB) from water, such as magnesium carbonate hydroxide [8], activated carbons [9], silicon-carbon-nitrogen hybrid materials [10] and manganese dioxide [11]. It is not possible to remove (MB) by traditional methods, so adsorption is the appropriate method to remove this dye from the aqueous body [12].

Adsorption is one of the traditional methods of controlling the release of organic compounds [13]. Adsorption is primarily used to reduce organic discharges, although metal removal has been demonstrated in some wastewater applications. Adsorption is a mass transfer process that can generally be defined as the accumulation of substances at the interface between two phases [14]. In general, chemicals in the liquid phase preferentially accumulate on an unsaturated solid surface causing the chemical to be removed from the liquid phase. The substance on which the chemical (such as carbon) is absorbed is known as an adsorbent. The substance that gets absorbed (usually the contaminant) is known as an adsorbate [15]. There are two types of adsorption, physical and chemical. Physical

until the pH value became approximately 7 [29-31], then dried the product in an electric oven At a temperature of 105 °C for 2 hours and after taking it out of the oven, it is placed in a desiccator until its temperature becomes equal to the temperature of the laboratory. The resulting carbon from the Cordia myxa was activated with acid (CM-A), and then it is placed in a dark box for subsequent uses. The same procedure is repeated to produce activated carbon but at a temperature of 300 °C and 500 °C.

2.2. Tubular Furnace.

The tubular furnace of Chinese origin, is a Safftherm type, giving a temperature of from 30 to 3000 °C. It contains a quartz cylinder with a length of 800 mm, an inner diameter of 50 mm and an outer diameter of 60 mm, through which nitrogen gas passes, and it also includes a ceramic crucible bearing a temperature of 3000 °C placed in this cylinder.

2.3. Batch adsorption experiments.

The adsorption experiments were conducted in a 100 mL conical flask on a shaking water bath. All experiments were conducted three times and the average values were reported. The optimum pH was calculated by taking 4 samples of variable pH with a fixed concentration of the adsorbate (MB) and a fixed dose of the adsorbent (activated carbon), where the adsorbent concentration was 2 g/L and the adsorbate concentration was 5 mg/L. pH values were varied from sample to sample 3, 5, 7, and 9. The alkaline and acidic pH of the solution was maintained by adding amounts of HCl or NaOH solutions at a concentration of 0.1 mol/L at a mixing speed of 150 rpm and by taking a test for each sample every 10 minutes using a UV-VIS spectrophotometer. The optimal dose of CM-A was calculated by fixing the pH and the concentration of adsorbate. Conversely, the dose of the adsorbent was changed and the values were 1, 2, 5, 10, 15, and 20 g/L at a mixing speed of 150 rpm for 80 minutes. The effect of the initial concentration of MB was performed by varying the initial MB concentrations from 1 to 40 mg /L. CM was added to a 100 mL volume of MB solution. After different interval times, results from the reaction mixture were analyzed for residual MB concentration using a UV-VIS spectrophotometer at 638 nm wavelength. The effect of contact time was investigated using 2 g of CM, and 5 mg/L MB solution. The adsorbent dose was investigated using a 5 mg/L initial MB concentration with sorbent masses by varying from 0.5 to 3 g. The removal efficiency and amount of dye adsorbed at equilibrium onto CM were calculated by the equations 1 and 2.

$$R\% = \left(\frac{[C]_0 - C_e}{[C]_0} \right) \times 100 \quad (1)$$

Where R= Removal efficiency, C_0 (mg/L) = Initial concentration, C_e (mg/L) = effluent equilibrium concentration of MB.

$$q_e = \frac{(C_0 - C_e) \times V}{M} \quad (2)$$

Where q_e (mg/g) = adsorption capacity, M (g) = dosage of

activated carbon, V (L) = Volume of solution.

2.4. ANFIS Basics

Adaptive Neural Fuzzy Inference Systems (ANFIS) are AI modelling techniques with a structure akin to human brain cells. ANFIS combines the best qualities of Fuzzy Logic (FL) Systems and Artificial Neural Networks (ANN), *i.e.* it is one of a special ANN family components, utilized to define the approach of parameter approximation of Fatigue Life modelling based on experimental data in this study.

ANFIS' 5 layers (Fuzzification, Rule, Normalization, Defuzzification, Output summation node). MATLAB uses fuzzy iteration to train and evaluate ANFIS. Figure 1 shows a dual-input ANFIS network[37].

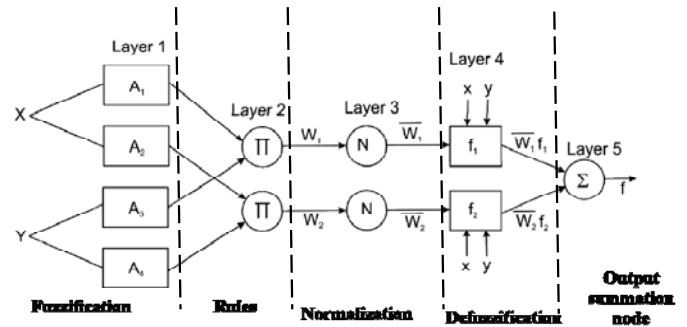


Figure.1. ANFIS structure.

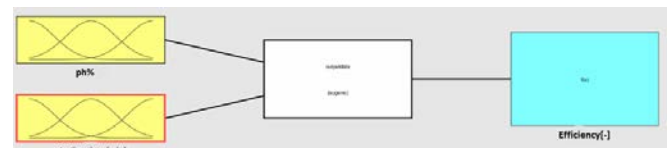
The model's performance was estimated using the RMSE statistical criterion, which is given in Equation 3: Root Mean Square Error:

$$RMSE = \sqrt{\frac{\sum_{i=1}^N (n_{ex} - n_{pr})^2}{N}} \quad (3)$$

Where n_{ex} is an Experimental number of the removal efficiency, n_{pr} is the Predicted number of the removal efficiency using the ANFIS model and N is the Data numbers This study used A Gaussian Membership function (GMFs).

2.5. ANFIS Model Design

Two neurons at the input layer (one for the testing time and one for pH on the adsorption of MB onto CM-A adsorbent), and one neuron at the output layer for calculating the removal efficiency in figure 2.



Figures 2..Fuzzy Inference System (FIS) modelling system

For fuzzy set input, the GMFs including pH and testing time variable is represented in Figure. 3a and b respectively.

3. RESULTS AND DISCUSSION

3.1. Effect of pH on the adsorption of MB onto CM-A adsorbent (Calculating the optimum pH).

The results showed that maximum removal efficiency calculated as in equations 1 was 65% at pH = 8 and contact time of 80 minutes as in Table 2 and Figure 5.

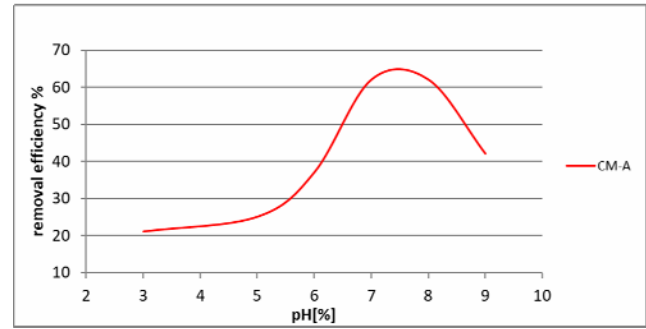


Figure 5. Effect of pH value on removal efficiency of MB onto CM-B

Table 2. The removal efficiency of MB by CM at various pH and times.

Time	Efficiency (%) (pH=3)	Efficiency (%) (pH=5)	Efficiency (%) (pH=7)	Efficiency (%) (pH=9)
0	0	0	0	0
10	10	14	33	31
20	16	25	44	35
30	21	27	47	39
40	22	29	49	44
50	23	30	50	46
60	23	31	52	48
70	24	33	53	50
80	25	33	54	51
90	25	33	54	51
100	25	33	54	51

3.2. Interchange effects of ANFIS

The results of the neural network were used to generate three-dimensional surface diagrams by taking into account the input parameters (test time and pH) as well as the output parameter (removal efficiency) as shown in Figure 6.

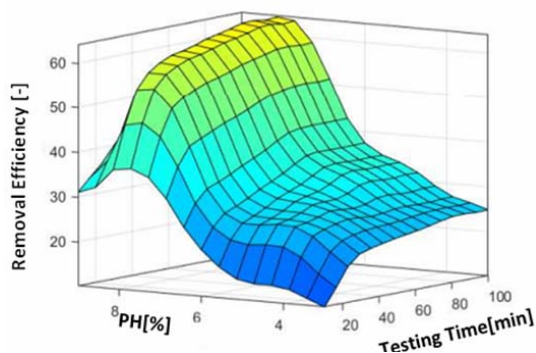


Figure 6. removal efficiency of MB onto CM-A are

affected by the interchangeability of pH and testing time.

3.3. Essential effect curves of ANFIS

To investigate and analyze the effect of pH and testing time on the MB removal from CM-A by changing one parameter at a time, while keeping all other parameters constant at the centre level Figure 7.

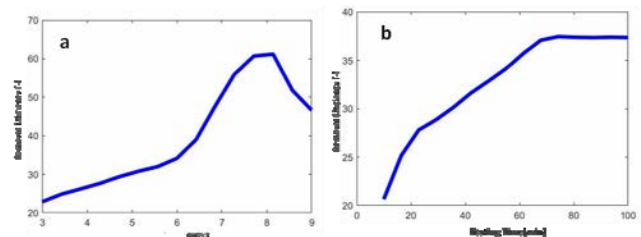


Figure 7. Affect MB removal from CM-A with a) pH, b) testing time

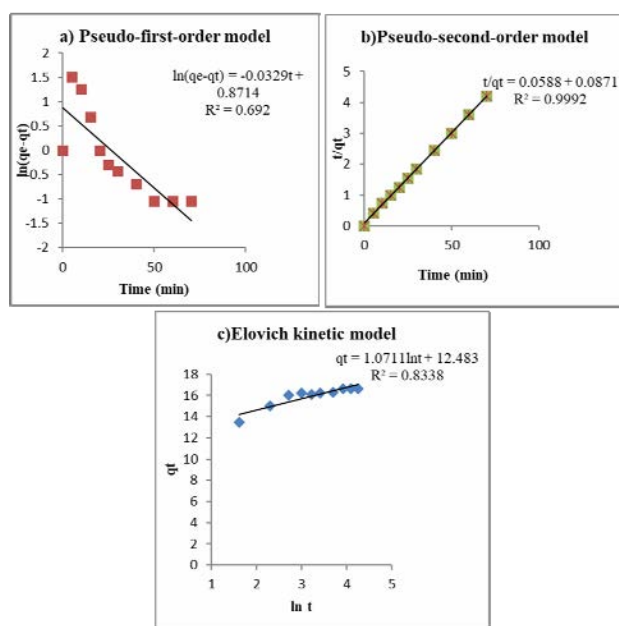


Figure 10. a) pseudo first order, b) pseudo-second order, c) Elovich, models to examine the adsorption behaviour of CM for MB.

and controlling mechanism for MB removal, the appropriate model is when the line of graph passes through all the points and the value of q_e (calculated by model) is close to q_e (experimental) and the value of R^2 is close to 1 [34]. The results showed that the pseudo-second-order is the best model to describe the experimental data Figure 10 a, b and c. Similar results have been previously reported in the kinds of literature for MB removal [21-23].

4. CONCLUSION

The study shows that CM-A is indeed a viable, cost-effective adsorbent material for the adsorptive removal of MB, where the process efficacy over 65% was achieved. The adsorption of MB dye onto CM-A was found to be highly dependent on pH, adsorbent dosage, initial dye concentration and contact time. The amount of dye adsorption was found to increase with the increase in its initial concentration. Percent MB dye removal was found to increase with the increase in dosage, adsorbent, and contact time. The rate of adsorption was found to conform to pseudo-second-order kinetics with a high correlation coefficient ($R^2 = 0.999$) for all studied concentrations.

Combining experimental results with the influencing modelling capabilities of ANFIS is a suitable approach to mathematical modelling and analysis of MB onto CM-A removal efficiency with practical applications in real manufacturing environments to define removal efficiency parameter settings to achieve desired performance.

The ANFIS model was trained with 40 basic experimental data sets and 6 additional experimental data sets. It was found that the mean prediction errors in the training and testing processes were 0.052% and 0.088%, respectively.

5. ACKNOWLEDGEMENT

Thanks to the laboratories in the College of Engineering at the University of Tikrit's Environmental Engineering and Chemical Engineering departments, we were able to finish this research.

References

- [1] Boisvenue, C., & Running, S. W. (2006). Impacts of climate change on natural forest productivity—evidence since the middle of the 20th century. *Global Change Biology*, 12(5), 862-882.
- [2] Bogardi, J. J., Leentvaar, J., & Sebesvári, Z. (2020). Biologia Futura: integrating freshwater ecosystem health in water resources management. *Biologia Futura*, 71(4), 337-358.
- [3] Rasheed, T., Shafi, S., Bilal, M., Hussain, T., Sher, F., & Rizwan, K. (2020). Surfactants-based remediation as an effective approach for removal of environmental pollutants—A review. *Journal of Molecular Liquids*, 318, 113960.
- [4] Lin, Y. T., Kao, F. Y., Chen, S. H., Wey, M. Y., & Tseng, H. H. (2020). A facile approach from waste to resource: Reclaimed rubber-derived membrane for dye removal. *Journal of the Taiwan Institute of Chemical Engineers*, 112, 286-295.
- [5] Abbas, M., & Trari, M. (2020). Removal of methylene blue in aqueous solution by economic adsorbent derived from apricot stone activated carbon. *Fibers and Polymers*, 21(4), 810-820.
- [6] Doma, A., Hassan, N., Abd-Elhamid, A. I., & Soliman, H. (2020). Adsorption of methylene blue dye on hydrothermally prepared tungsten oxide nanosheets. *Egyptian Journal of Chemistry*, 63(2), 483-498.
- [7] Moorthy, A. K., Rathi, B. G., Shukla, S. P., Kumar, K., & Bharti, V. S. (2021). Acute toxicity of textile dye Methylene blue on growth and metabolism of selected freshwater microalgae. *Environmental Toxicology and Pharmacology*, 82, 103552.
- [8] Song LM, Zhang SJ (2009) Direct synthesis of porous/hollow magnesium carbonate hydroxide spindle nanorods and their application in water treatment. *Colloids Surf A* 350:22–25
- [9] Zhang, Z., Xu, L., Liu, Y., Feng, R., Zou, T., Zhang, Y., ... & Zhou, P. (2021). Efficient removal of methylene blue using the mesoporous activated carbon obtained from mangosteen peel wastes: Kinetic, equilibrium, and thermodynamic studies. *Microporous and Mesoporous Materials*, 315, 110904.
- [10] Meng LL, Zhang XF, Tang YS, Su KH, Kong J (2015) Hierarchically porous silicon-carbon-nitrogen hybrid materials towards highly efficient and selective adsorption of organic dyes. *Sci.Reports* 5:7910
- [11] Diao, H., Zhang, Z., Liu, Y., Song, Z., Zhou, L., Duan, Y., & Zhang, J. (2020). Facile fabrication of carboxylated cellulose nanocrystal-MnO₂ beads for

- Agboola, P. O., & Waseem, M. (2020). Mesoporous silica prepared via a green route: a comparative study for the removal of crystal violet from wastewater. *Materials Research Express*, 8(1), 015005.
- [36] Youssef, H. F., Nasr, R. A., Abou El-Anwar, E. A., Mekky, H. S., & Abd El Rahim, S. H. (2021). Preparation and characterization of different zeolites from andesite rock: Product evaluation for efficient dye removal. *Microporous and Mesoporous Materials*, 328, 111485.
- [37]. Jang, J.S.R. (1993) ANFIS: Adaptive-Network-Based Fuzzy Inference System. *IEEE Transactions on Systems, Man, and Cybernetics*, 23, 665-685. <http://dx.doi.org/10.1016/j.apor.2003.06.001>



PREDICTION ON WEAR PROPERTIES OF PTFE AND PVC POLYMERS USING ANFIS

AMIR ALSAMMARRAI
amircratf@tu.edu.iq

SABAH MAHDI SAIH
sabahmahdi@tu.edu.iq

MALIK JUUMMA O.ZDANE
Depa. of Mechanical Engineering / Faculty of Engineering / Tikrit University / Saladin / Iraq
malk.j.mohammed43786@st.tu.edu.iq

Abstract: Superior strength in loading, wear resistance, environmental stability, insulating properties, and low cost are the main distinguishing properties of polymer materials, which encouraged many researchers to analyze the different behavior of these materials. In this work, a comparative study was conducted on the tribological behavior under dry sliding conditions of two pins of Teflon (PTFE) and Polyvinyl Chloride (PVC), both sliding on a steel disc. The study was conducted under different laboratory conditions to investigate the effect of normal load change, sliding time and roughness modulus on the wear rate. Sliding time minutes (10-60 min), three applied loads (5N, 10N and 15N), and two discs with different roughness coefficients of 0.611 μm and 2.394 μm were used, and the speed of rotation of the disc was constant (480 rpm) according to the specifications of the test device. These results showed that the wear degree depends on the nature and composition of the polymeric material. The material loss for both polymers increases with the applied load, but the loss of PTFE is greater for the same applied load than for PVC. The material loss for both polymers increases at the start of operation and then stabilizes to a specific value according to the applied load with the confirmation that the increase in the applied load decreases the volumetric wear coefficient k for both type specimens. It is a measure of the wear stability level of the composites. The ANFIS technique was used to study the predictability of the wear performances of PTFE and PVC and it was found that the developed ANFIS model showed promising results in predicting the wear coefficient of PTFE and PVC polymers that are subjected to different vertical loads, sliding time and change of the roughness coefficient.

Keywords:: wear, normal load, sliding time, roughness coefficient, ANFIS.

1. INTRODUCTION

Self-lubricating polytetrafluoroethylene composites run dry. Polytetrafluoroethylene composites have low water absorption and chemical resistance [1]. Wang et al. investigate a tribological behavior of a polytetrafluoroethylene (PTFE) disc and an AISI1045 steel screw in a straight line and torsional motion. The friction coefficients for one-directional rotation, linear frequency, and torsional motion were 0.1, 0.118, and 0.12. On PTFE's maximum linear-frequency wear-related mass loss was observed. Turning the object reduced wear. PTFE wore away by mild ploughing, substantial abrasive wear, and adhering together in unidirectional rotating, linear reciprocating, and torsional motion. Friction and wear experiments were completed on ultra-high molecular weight polyethylene with Hank's balanced salt solution lubrication using a stainless steel pin-shaped disc. As load grew, friction and wear rates dropped. Dry sliding friction coefficient and wear rate were higher for the measured sliding speeds and loads[2].

Low-dimensional fillers are essential for improving the tribological properties of PTFE-containing composites. Carbon nanotubes (CNT) and graphene-filled composites

exhibit substantially greater wear resistance than pure PTFE, and corrosion is reduced by 76.2% and 85.7%, respectively[3].

Soft PVC's tribological properties were tested under typical load and sliding speed. Infrared detected friction heating. PVC wears better under high speed and normal load due to friction heating during sliding[4].

PVC samples reinforced with CaCO_3 were tested for visibility. Also, examined are thermal ageing effects on pipe friction and wear. Several samples' wear was measured. Wear on composites and steel pins were studied [5]. The equipment were changed to research spherical-disc charge buildup and tribology. Positive and negative charges were tested using photoelectric nylon and electrostatic PVC. When there's no charge buildup at the friction interface, the friction pair has outstanding friction reduction, anti-wear performance, and stability. COF can be adjusted by altering Coulomb force charge accumulation. This study compares polymeric (PTFE and PVC) and steel wear (the revolving disk). [6].

Prediction of the frictional performances of T-BFRP using artificial neural networks was performed. Large amounts of experimental data were used to train the ANN

with varying loads and sliding distances. When the ANN model was trained using the Levenberg-Marquardt function, experimental and numerical findings were accurate[7]. ANFIS has been used to estimate hydraulic jumping in channels with varying bed conditions (that is, channels with different shapes and dependencies). 1700 experimental data were used to model hydraulic jump characteristics. The results showed that the approach accurately models hydraulic jump qualities. Channel expansion models with blocks were more successful than others[8]. The objective of the presented work is to apply the ANFIS method to predict the wear behavior of PTFE and PVC polymeric materials using a pin-on-disc type tribometer,

The main inputs affecting wear are the coefficient of roughness, sliding time and vertical load, and the sliding speed remains constant at 480 rpm.

$$\frac{V}{s \cdot A} = \frac{K}{H} \cdot \frac{F_N}{A} \xrightarrow{\text{yields}} \left\{ h = \frac{V}{A}, k = \frac{K}{H}, p = \frac{F}{A}, s = v \cdot t \right\} \xrightarrow{\text{yields}} \quad (1)$$

$$h = k \cdot p \cdot v \cdot t \quad (2)$$

or:

$$k = \frac{\Delta m}{F_N \cdot s \cdot \rho}, s = v \cdot t \quad (3)$$

where k is the volumetric wear rate [m³/Nm], p is the specific load [Pa], v is the sliding speed [m/s], t is the sliding time [s], and is the density of the softer material.

2.2. The Foundations of the ANFIS

Adaptive Neural Fuzzy Inference Systems (ANFIS) simulate human brain cells. ANFIS combines the fundamental properties of Fuzzy Logic (FL) and Artificial Neural Networks (ANN). Based on experimental data, ANFIS has been used to predict the tribological behavior of two thermoplastic polymers.

Fuzzification, Rule, Normalization, Defuzzification, and Output summation nodes were created in MATLAB to train and assess ANFIS. A dual-input ANFIS network is shown in Figure (1).

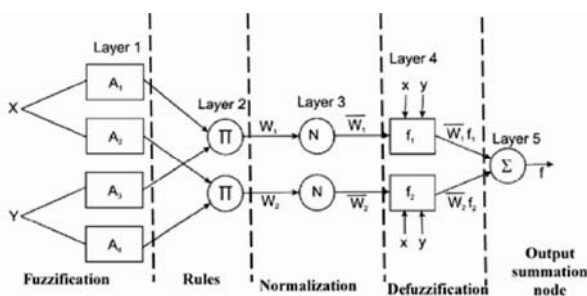


Figure.1. Design of a dual-input adaptive neural fuzzy inference system (ANFIS).

2. THEORETICAL METHOD

2.1. Loss of material (wear)

Wear is the slow removal of materials or the distortion of those materials that occurs on solid surfaces. The following is what we derive from the wear model, which is also often known as Archard's law of wear:

$$\frac{V}{S} = K \cdot \frac{F_N}{H} \quad (1)$$

where: V is the volume of the material that has been worn away due to wear [m³], F_N is the radial force operating on the bearing [N], s is the total sliding distance [m], and H is the hardness of the soft surface of the material that is being worn away [Pa].

For figuring out wear performances, it's best to use Archard's general wear law, which can be found by dividing equation (1) by the contact surface A:

The Gaussian Membership Function (GMFs) was used in this study. GMFs takes the highest value (1.0) and chooses the lowest value (0.0). The model's performance was evaluated using root mean square error (RMSE), which is given in equation 4:

$$RMSE = \sqrt{\sum_{i=1}^N \frac{(n_{ex} - n_{pr})^2}{N}} \quad (4)$$

where n_{ex} is the experimental number of the output, n_{pr} is the expected number of the output using the ANFIS model and N is the data numbers.

3. EXPERIMENTAL DESIGN AND PREDICTION METHOD

3.1. Experimental Design

Materials: Tests were done on samples made of PTFE and PVC, both of which are thermoplastics that are widely used in many fields as shown in Figure 2. the mechanical properties of both specimens test and test disc are listed in Table 1.

Test discs are made by heating stainless steel to 440°C. Fig. 3 shows the Surface roughness tester TR220, two discs with different roughness coefficients of 0.611 μm and 2.394 μm are used.

The test device (SHEMADZU/XDR-6000) (Fig. 4a) was used to calculate the material lost due to the vertical load and rotation of the test disc, according to the vertical load (5 N, 10 N and 15N) and the sliding time (10-60 min).



Figure 2. The tested PTFE and PVC specimens

Table 1. The mechanical properties of PTFE, PVC and Disc test

Property	PTFE	PVC	Disc test type grade 440C (440C stainless steel)
Density [kg/m ³]	2200	1300–1450	7800
Yield stress [MPa]	/	40.7–44.8	450-1900
Tensile Strength [MPa]	20.7–34.5	40.7–51.7	/
	0.6	/	0.27-0.30
Poisson's ratio	0.5	3.4	190-215
Young's modulus [GPa]	0.4 -0.55	2.4-4.14	200
Elasticity modulus [GPa]	327	400	1483

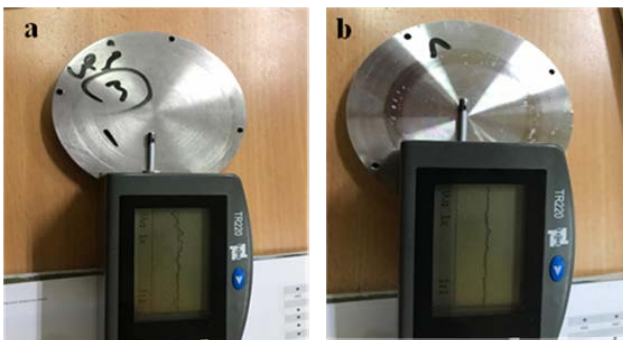


Figure.3 The device used to measure the surface roughness coefficient of the disc, a) the roughness coefficient disc 0.611, (b) the roughness coefficient disc 2.394 μm.

To ensure the accuracy of the results, the tests were repeated three times for each specimen, and the material loss (volumetric wear rate) was calculated by weighing the specimen before and after the test (for 10 minutes) and for 60 minutes using a digital sensitive balance (0.0001 mg) type (satorius-BL210s), (Figure.4b). All of the experiments were performed at ambient temperature.

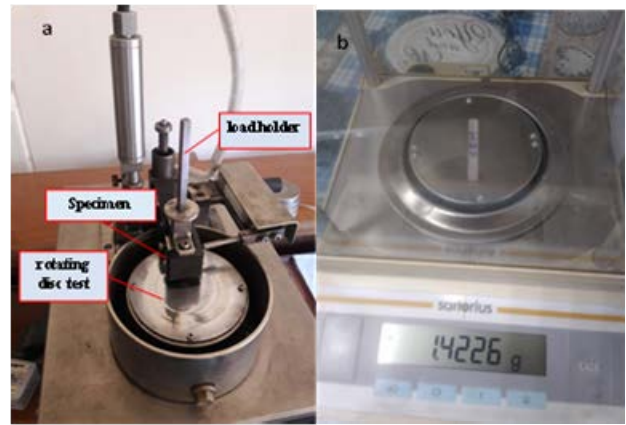


Figure 4: (a) Pin-on-disc tribometer type 'DUCOM's Wear Monitor, and (b) digital sensitive scale type (satorius-BL210s, 0.0001)

3.2. Prediction Method

The ANFIS network model was developed using PTFE and PVC wear rate data. Fig. 5 illustrates neural network predictions. The input layer represents the test disc roughness coefficient, sliding time of test specimens, and vertical load applied to test specimens and the output layer represents wear rate.

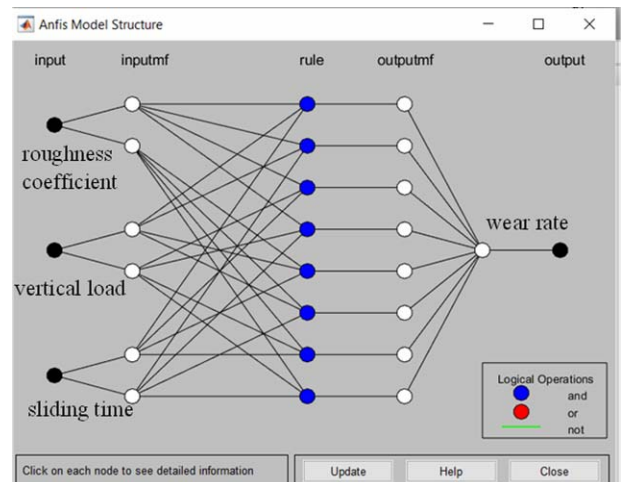


Figure 5. Generate ANFIS Model Predictive Wear Rate

Training error converges with ANFIS model iterations. In this model, 30 adaptive iterations were required to predict the wear rate of PTFE 0.0014 and 0.001 for PVC (Figure.6 a and b). The MF membership function type and options method was linear and mixed respectively.



Figure 6. ANFIS model iterations and error rate to predict wear rate, a) PTFE, b) PVC.

4. RESULTS AND DISCUSSION

4.1. Experimental results

PTFE and PVC specimens were tested, with an average of three specimens tested per material type to ensure reliable results. Therefore, wear test results were calculated as an average over a minimum of three samples.

In this study, the average value of local and total wear, as well as the load, roughness of the test disc, and sliding time were compared for PTFE and PVC materials, and it was found that the behaviour of the two materials is very comparable.

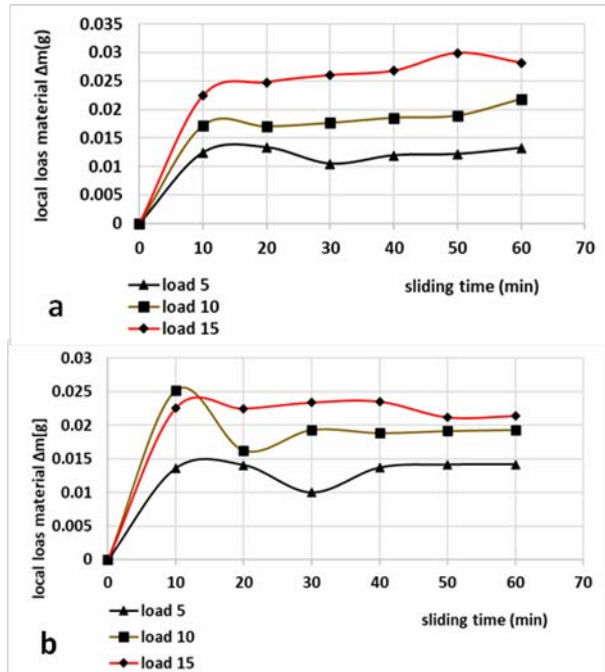


Figure 7. Effect of sliding time on the local lost material of disc roughness coefficient Ra 0.611 [µm], (a) PTFE (b) PVC

PTFE's wear rate was 0.015 g at a 5N load, whereas it reached PVC at the same load, sliding time, and roughness of 0.013 g, showing that as the vertical load increased, the number of lost materials increased, *i.e.* the wear rate. The data suggest that PVC can be used as a self-lubricating material with a lower wear rate than PTFE. This behavior is identical to the two vertical loads (10N and 15 N), however as shown in Figure. 7 a, b, the wear rate is precisely proportional to the increase in load.

Increasing the roughness coefficient (Ra) from 0.611 µm to 2.349 µm leads to an increase in the wear rates of PTFE more than PVC, and this is clear in comparison with the two figures (7 and 8)

The total wear rate is a linear function with the change of sliding time, and the PTFE specimens show a greater total wear rate than the PVC specimens when the sliding time, test disc roughness coefficient, and vertical load are all increased as shown in Figs. 9 and 10.

Due to the high temperature between the surface of the test disc and the selection specimen as a result of the interlocking of the microscopic peaks of both contact surfaces at the beginning of the running, which causes an increase in the ductility of the contact surface of the test specimen, and this, in turn, reduces the shear stress, which leads to abrasion of the specimen layer in contact with the hard surface, *i.e.* test disk.

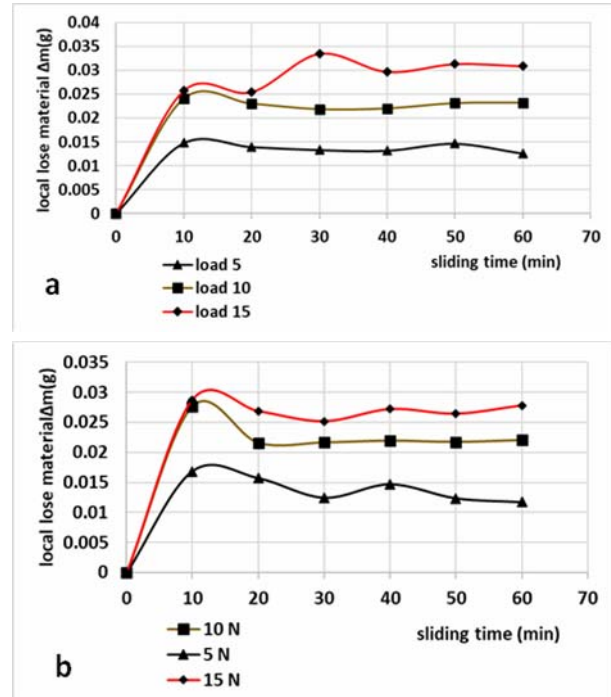


Figure 8. Effect of sliding time on the local lost material of disc roughness coefficient Ra 2.349 µm, (a) PTFE (b) PVC

The relationship between PTFE volumetric wear rate k and sliding time, normal load and coefficient roughness k can be separated into two regimes: transient wear and stable wear. The volumetric wear rate curve as a function of sliding time is depicted in Figure 10. The volumetric wear rate increases over the first 10 minutes of running to achieve the values load (15 N, 10 N and 5 N, respectively), suggesting that the transient wear system has the maximum values. As indicated in Fig. 8, it then declines and the period of steady wear system begins at 39 minutes of sliding time. Increasing the load causes the rate of volumetric wear to go up during the running period. However, as the sliding time goes by, the rate of volumetric wear stays stable, and the value of the wear rate converges during the stable period.

The same thing occurs when determining the relationship between volumetric wear rate k and sliding time of PVC specimens, as shown in Figure 11.

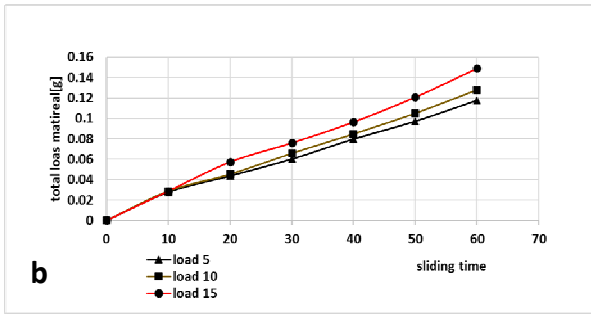
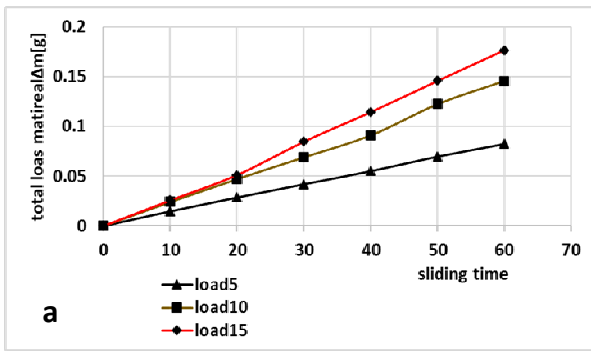


Figure 9. Effect of sliding time and vertical load on the total lost PTFE material of disc roughness coefficient Ra (a) 2.349 μm and (b) 0.611 μm

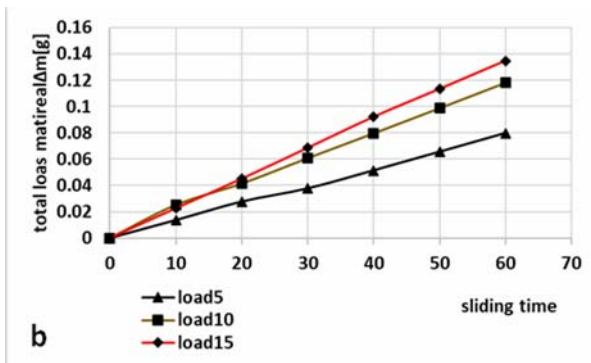
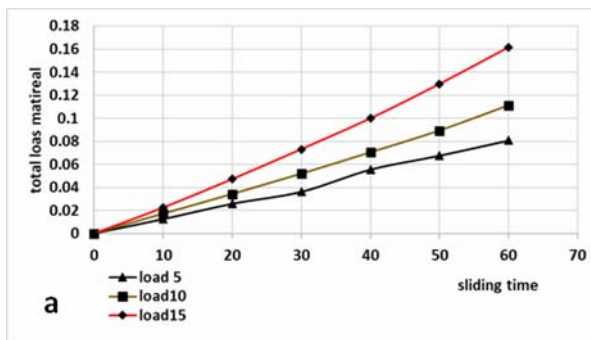


Figure 10. Effect of sliding time on the total lost PVC material of disc roughness coefficient Ra (a) 2.349 μm , (b) 0.611 μm

Figure 8 demonstrates that the change in the volumetric wear coefficient of PVC is more stable when the roughness coefficient of the test disc is less, and it increases with the decrease in the value of the vertical load, which indicates that the loss of the material becomes more stable at high loads. This behavior is similar to the PTFE samples as shown in Figure 11, which confirms

that the loss of material PTFE is more stable than the loss of material PVC.

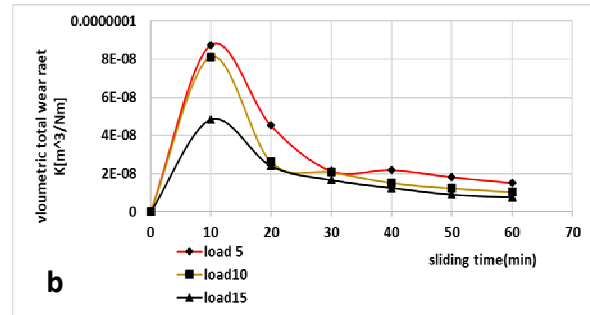
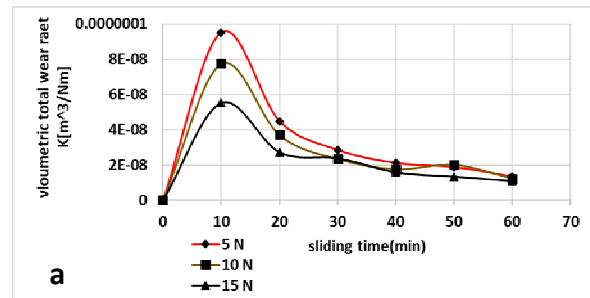


Figure 10. Effect of sliding time and vertical load on the volumetric wear rate k of PTFE material of disc roughness coefficient Ra (a) 2.349 μm , (b) 0.611 μm

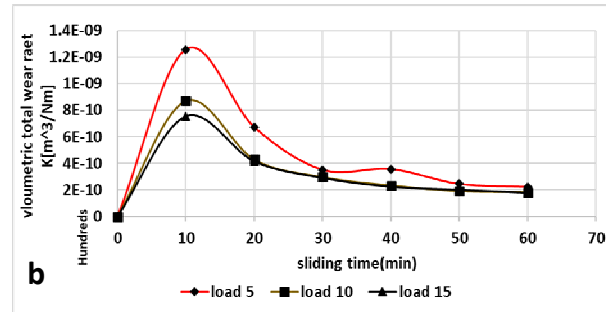
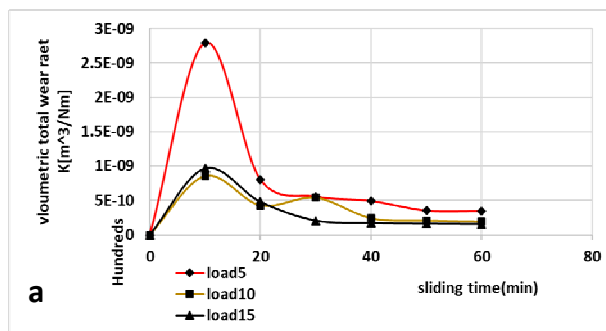


Figure 11. Effect of sliding time and vertical load on the volumetric wear rate k of PTFE material of disc roughness coefficient Ra (a) 2.349 μm , (b) 0.611 μm

4.2. ANFIS essential and exchange effect curves

The base curves and 3D surface complex were predicted by examining the influence of two parameters simultaneously while keeping the third parameter constant to a mean level to determine the interaction of input parameters on output parameters.

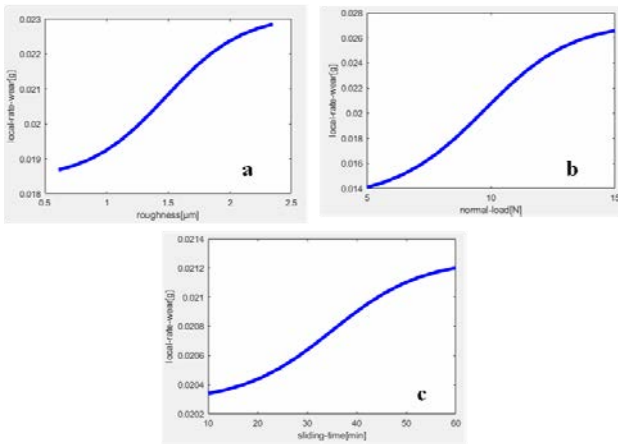


Figure 12. Prediction of the basic curves of wear rate change with: a) roughness coefficient, b) vertical load, and c) sliding time of PTFE specimens.

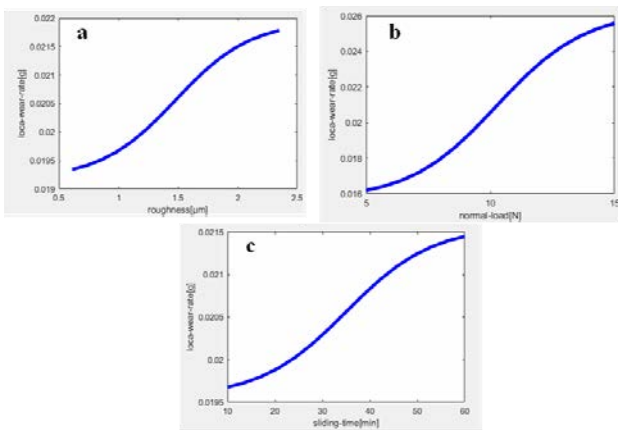


Figure 13. Prediction of the basic curves of wear rate change with: a) roughness coefficient, b) vertical load, and c) sliding time of PVC specimens.

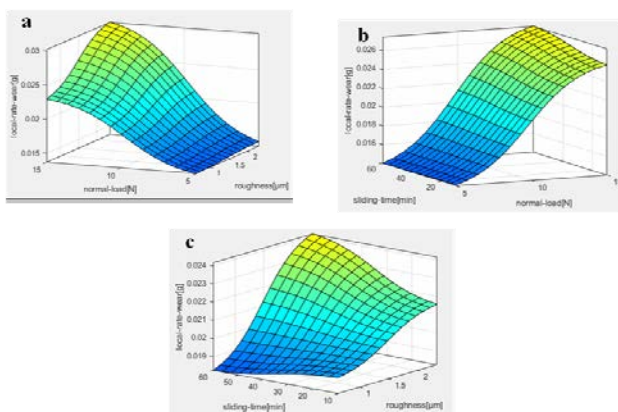


Figure 14. Prediction of the mutual effect of local wear rate for PTFE specimens with a) roughness modulus and vertical load, b) vertical load and slip time, and c)

roughness modulus and slip time.

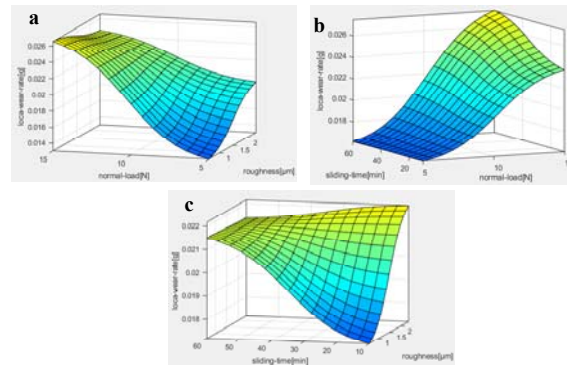


Figure 15. Prediction of the mutual effect of local wear rate for PVC specimens with a) roughness modulus and vertical load, b) vertical load and slip time, and c) roughness modulus and slip time.

Figure 12a shows the predicted increase in the local wear rate with the gradual increase in the roughness coefficient for PTFE specimens. It is evident from the curve that the change and the relationship are non-linear, which is a logical result. Figure.12 b shows the same for the change in the local wear rate with the change in the vertical load and sliding time. Predictive results showed a similar trend for PVC specimens, except that as the roughness coefficient R was raised, the local wear rate was lower for PVC than for PTFE (Figure 13a). Figures (12 b and c) and (11 b and c) respectively, demonstrate that as the vertical load and sliding time changed, the local wear rate of the PVC specimens increased but that of the PTFE specimens did not, confirming the anticipated results.

To explore and assess the influence of test disc roughness coefficient, vertical load, and sliding duration on local wear rate by doubling two parameters while retaining one parameter, as illustrated in Figure 14 for PTFE specimens and Figure 15 for PVC specimens.

4.3. ANFIS model test for local wear rate predictions.

Checking predictive models and estimating error rates were required. Six new tests were conducted from different experiments using the proposed ANFIS model for PTFE and PVC local wear rate. The roughness coefficient of the two test discs was fixed with vertical force and sliding time. As demonstrated in Tables 3 and 4 for PTFE and PVC specimens, the individual error % was validated by the recorded vertical load and sliding time using the statistical standard square error (RMSE).

Tables 2 and 3 show that experimentally determined wear rates and ANFIS predictions accord well. The ANFIS model can forecast local polymer wear well.

Table 2. Testing the Prediction Model for Local wear rate PTFE specimens

roughness Ra[μm]	sliding time [min]	normal load FN[N]	Δmex [g]	manfis Δ	error%
0.611	7.3	12	0.016	0.0152	5
0.611	12.8	8	0.023505	0.0228	3
0.611	6.5	36	0.014796	0.0145	2
2.349	8.5	5	0.019787	0.0186	6
2.349	13.1	18	0.028404	0.0267	6

Table 3. Testing the Prediction Model for Local wear rate PVC specimens

roughness Ra[μm]	sliding time [min]	normal load FN[N]	Δmex [g]	manfis Δ	error%
0.611	6	13	0.013617021	0.0128	6
0.611	9	25	0.017157895	0.0163	5
0.611	12	33	0.023958333	0.023	4
2.349	8.5	37	0.021020408	0.0206	2
2.349	13.1	43	0.025698925	0.0239	7
2.349	7.5	57	0.021304348	0.0196	8

Figure 16a predicts an increase in total wear rate with a rising roughness coefficient for PTFE specimens, as the curve indicates a non-linear change and relationship, which is logical. Figure 16b predicts an increase in total wear rate with changing vertical load and sliding time. Same behaviour for PVC specimens, but with the roughness coefficient, where the prediction findings revealed that the overall wear rate is lower for PVC specimens than PTFE specimens when the roughness coefficient is increased (Figure 17a). As for the vertical load and sliding time, the prediction results were validated by the rise in the overall wear rate of the PVC specimens from the PTFE specimens (Figures 16b and c and 17 b and c).

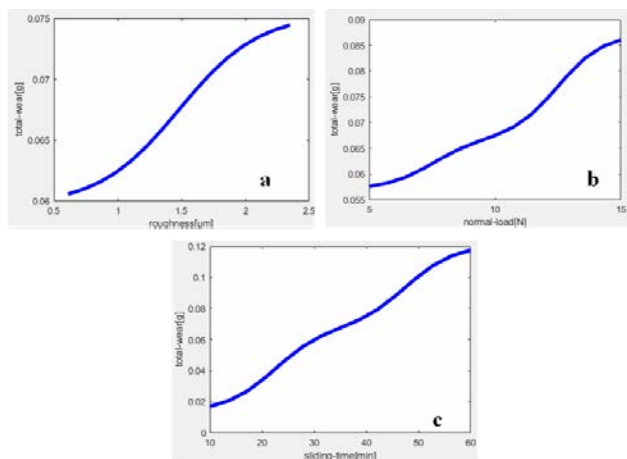


Figure 16. Prediction of the basic curves of total wear rate change with: a) roughness coefficient, b) vertical load, and c) sliding time of PTFE specimens.

To examine and assess the prediction of the total wear rate from the effect of the test disc roughness coefficient, vertical load, and sliding time by doubling two factors with the diaper for PTFE specimens and PVC specimens.

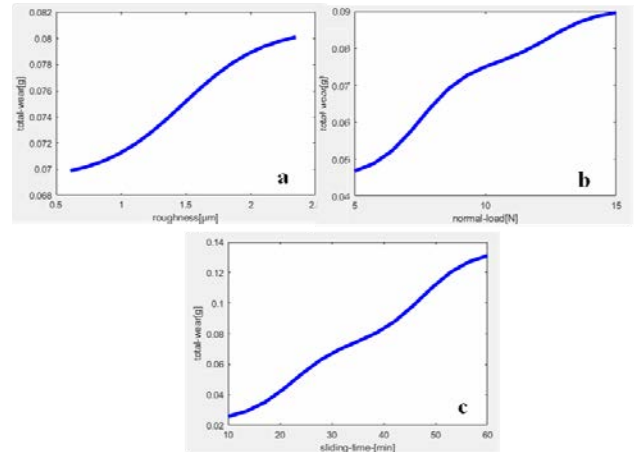


Figure 17. Prediction of the basic curves of total wear rate change with: a) roughness coefficient, b) vertical load, and c) sliding time of PVC specimens.

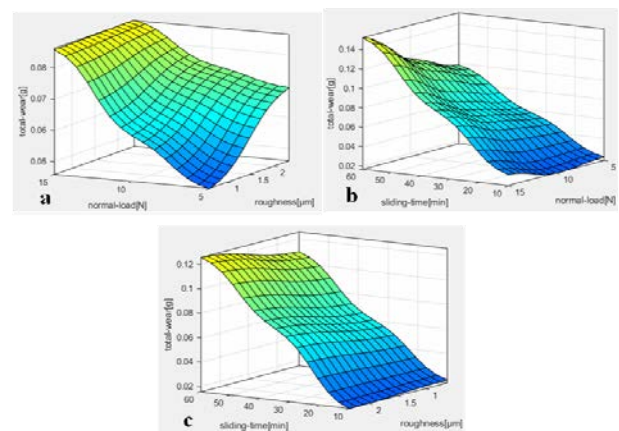


Figure 18. Predicting the interaction of the total wear rate of PTFE samples with a) roughness modulus-vertical load, b) vertical load-slipping time, and c) roughness modulus-slipping time.

The total wear rate increases (Fig. 18a and 19a) with rising roughness coefficient and vertical load for both polymers (PTFE and PVC), but more for PTFE. As the

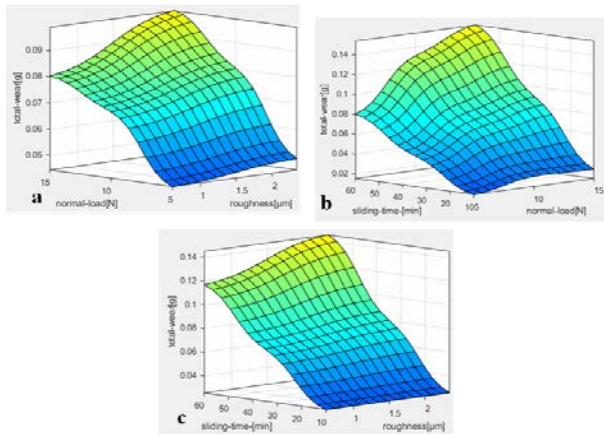


Figure 19. Predicting the interaction of the total wear rate of PTFE samples with a) roughness modulus-vertical load), b) vertical load-slipping time, and c) roughness modulus-slipping time.

vertical load and sliding duration double, the total wear rate increases slightly, as seen in Figures 16b and 17b. Figures 16c and 17c show that the total wear rate increases gradually with a rise in sliding time and a decrease in the roughness coefficient of the contact surfaces, and it is larger for PTFE.

4.4. ANFIS total Wear Rate Model Test:

Total wear rate prediction models and error ratio estimates were tested. By employing the suggested ANFIS model for the total wear rate of PTFE and PVC in six new tests, the roughness modulus of the test discs was set with vertical load and sliding time. As indicated in Tables 4 and 5 for PTFE and PVC materials, the individual error % was validated by the recorded vertical load and sliding time using statistical standard square error (RMSE).

Tables 4 and 5 show that experimentally determined wear rates and ANFIS predictions accord well. The ANFIS model predicts polymer wear well generally.

Table 4. Testing the Prediction Model for Total wear rate PTFE specimens

roughness Ra[μm]	sliding time [min]	normal load FN[N]	Δmex [g]	manfis Δ	error%
0.611	7	15	0.0198	0.0187	6
0.611	12	22	0.043	0.0422	2
0.611	6.5	43	0.060	0.059	2
2.349	8.2	17	0.030	0.0288	5
2.349	11.7	28	0.067	0.0646	4

Table 5 Testing the Prediction Model for Total wear rate PVC specimens

roughness Ra[μm]	sliding time [min]	normal load FN[N]	Δmex [g]	manfis Δ	error%
0.611	8	18	0.032	0.0309	4
0.611	11.5	27	0.061	0.0598	2
0.611	13.2	33	0.076	0.0748	2
2.349	7.3	14	0.024	0.0237	5
2.349	12	26	0.069	0.0671	4
2.349	14	56	0.169	0.1657	2

4.5. Volumetric wear rate

To research and assess the prediction of the influence of the test disc roughness coefficient, vertical load, and sliding time of test specimens on the volumetric wear rate by changing one parameter at a time, as illustrated in Fig. 20 for PTFE specimens and Fig. 21 for PVC specimens.

Figure 20 a predicts a rise in volumetric wear rate with increasing roughness coefficient for PTFE specimens, as the change and connection are non-linear. Same behavior for PVC specimens with predictive results, but with roughness modulus, where predictive results showed that volume wear rate of PVC and PTFE when roughness modulus was raised (Fig. 21a). As vertical load and sliding period changed, the predictive results indicated a decrease in the total wear rate of PTFE specimens vs to PVC specimens (Figures 20 b and c), (21 b, and c) respectively.

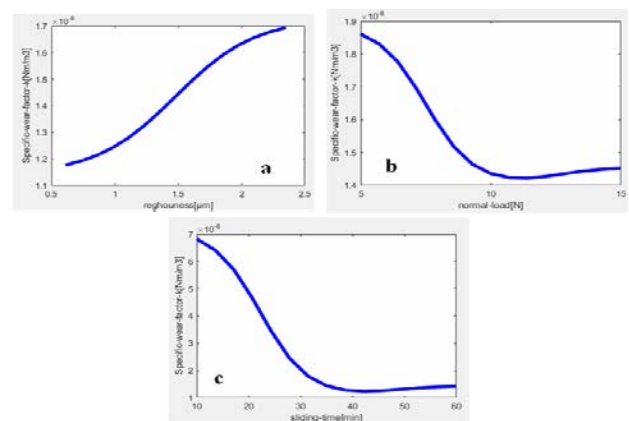


Figure 20. Prediction of the basic curves of volumetric wear rate change with: a) roughness coefficient, b) vertical load, and c) sliding time of PTFE specimens.

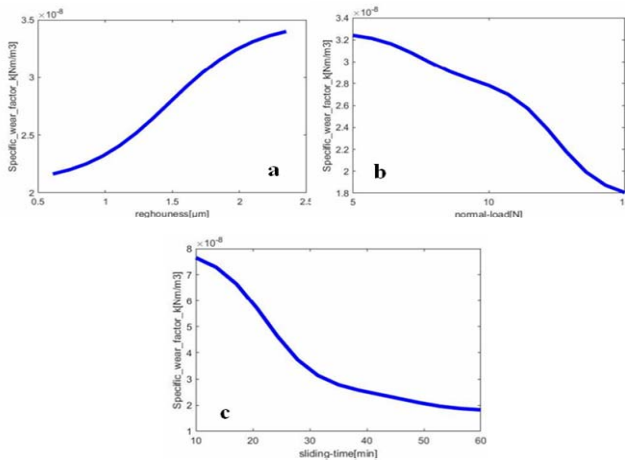


Figure 21. Prediction of the basic curves of volumetric wear rate change with: a) roughness coefficient, b) vertical load, and c) sliding time of PVC specimens.

To determine the influence of test disc roughness coefficient, vertical load, and sliding time on volumetric wear rate by changing two parameters while retaining one parameter, as illustrated in Figure 22 for PTFE specimens and Figure 23 for PVC specimens.

Figures 22a 23a show that the volumetric wear rate goes up when the roughness coefficient and vertical load go up. This is true for both PTFE and PVC copolymers, but the PVC rate is lower. As the vertical load and sliding time both go up twice, the volumetric wear rate goes up gradually. This increase is close to what is shown in figures 22b and 23b.

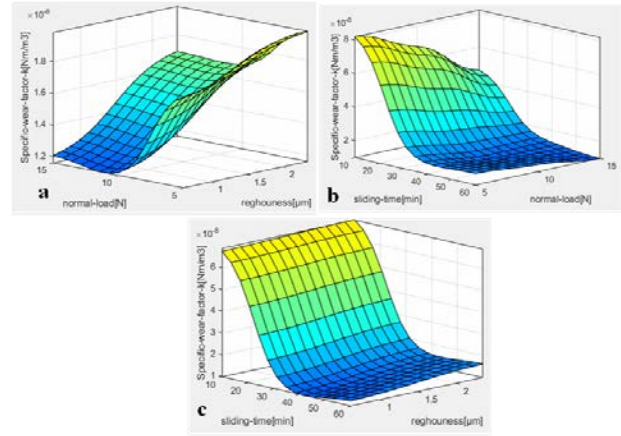


Figure 22. Predicting the mutual effect of volume wear rate K for PTFE specimens with a) Roughness modulus-vertical load), b) Vertical load-sliding time, and c) Roughness modulus-sliding time.

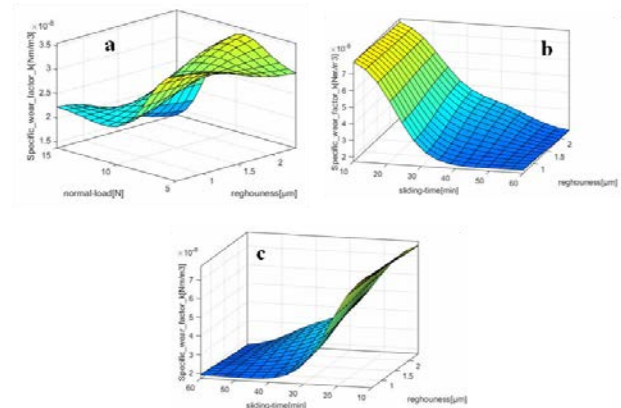


Figure 23. Predicting the mutual effect of volume wear rate K for PVC specimens with a) Roughness modulus-vertical load), b) Vertical load-sliding time, and c) Roughness modulus-sliding time.

Table 6. Testing the Prediction Model for Volumetric wear Rate of PTFE specimens

Ra [μm]	Load [N]	sliding time [min]	K_{ex} [Nm/m ³]*1.0e-07	K_{anfis} [Nm/m ³]*1.0e-07	error%
0.611	6.4	13	0.775789	0.737	5
0.611	12	22	0.367755	0.3604	2
0.611	14.5	44	0.101031	0.098	3
2.349	8	18	0.654086	0.6083	7
2.349	6	38	0.185789	0.1765	5

Table 7. Testing the Prediction Model for Volumetric wear Rate of PVC specimens

Ra [μm]	Load [N]	sliding time [min]	K_{ex} [Nm/m ³]*1.0e-07	K_{anfis} [Nm/m ³]*1.0e-07	error%
0.611	6	12	1.09E-01	1.06E-01	3
0.611	11	27	3.61E-02	3.36E-02	7
0.611	14	55	1.96E-02	1.90E-02	3
2.349	6	14	2.02E-01	1.96E-01	3
2.349	11	29	3.89E-02	3.81E-02	2
2.349	14	54	1.70E-02	1.67E-02	2

Regarding the changes in the volumetric wear rate with the double change of the roughness coefficient and the sliding time, it is clear from Figures 22c and 23c that the volumetric wear rate goes up gradually with increasing sliding time and, to some extent, the roughness coefficient. Six new experiments were performed. While the suggested ANFIS volumetric wear rate model was used for PTFE and PVC test specimens, the roughness coefficient of the test discs was fixed. As indicated in Tables 5 to 7 for PTFE and 5 to 8 for PVC, the individual error percentage was validated by measuring the vertical load and sliding time. The standard is RMSE.

5. CONCLUSIONS

ANFIS was used to predict the wear behavior of PTFE and PVC polymeric materials. The results showed that applying an ANFIS-based model to predict the amount of local and total wear and the volumetric wear coefficient is possible for the independent variables to test disk roughness coefficient, sliding time variance and vertical load variance, producing the best match between the predicted data and the experimental data. The predicted values were compared with the experimental values and their closeness was determined. The ANFIS model can predict the values of local, total, and volumetric wear coefficients with an error rate of less than 10%. The results presented in this paper are expected to be very useful to bearing designers as well as the academic community.

Reference

- [1] Shibo, W., C. Niu, and B.J.J.o.T. Teng, Tribological behavior of polytetrafluoroethylene: effect of sliding motion. 2017. 139(1): p. 011301.
- [2] Hüseyin, Ü., K.J.J.o.M. ERMİŞ, and M. A, Rulmanlı Yatak Uygulamaları için Çok Yüksek Molekül Ağırlıklı Polietilen ve Döküm Poliamit Termoplastik Esaslı Polimerlerinin Tribolojik Performanslarının karşılaştırılması. 1(2): p. 85-96.
- [3] Xu, Q., et al., Tribological Behavior of Poly (tetrafluoroethylene) and Its Composites Reinforced by Carbon Nanotubes and Graphene Sheets: Molecular Dynamics Simulation. 2022. 16(3): p. 2100298.
- [4] Guo, Y., et al., Friction heating and effect on tribological properties of soft polyvinyl chloride sliding against steel. 2018. 106: p. 85-91.
- [5] Jemii, H., et al., Tribological behavior of virgin and aged polymeric pipes under dry sliding conditions against steel. 2021. 154: p. 106727.
- [6] Luo, N., et al., Controlling the tribological behavior at the friction interface by regulating the triboelectrification. 2021. 87: p. 106183.
- [7] Umar Nirmal, Prediction of friction coefficient of treated betelnut fibre reinforced polyester(T-BFRP) composite using artificial neural networks, Tribology International 43, 1417–1429, 2010.
- [8] K. Roushangar, et al, Effect of Channel Boundary Conditions in Predicting
- [9] Hydraulic Jump Characteristics using an ANFIS-Based Approach, Journal of Applied Fluid Mechanics, Vol. 11, No. 3, pp. 555-565, 2018.



ANFIS PREDICTION IN PLASMA ARC CUTTING

MADINA ISAMETOVA

Institute of Energy and Mechanical Engineering, Satbayev University, Almaty, Kazakhstan
isametova69@mail.ru

MILOŠ MLOVANČEVIĆ

Faculty of Mechanical Engineering, University of Nis, Niš, Serbia
milovancevic@masfak.ni.ac.rs

DALIBOR PETKOVIĆ

Pedagogical Faculty in Vranje, University of Niš, Serbia
dalibortc@gmail.com

Abstract: Plasma arc cutting process is very sensitive process which has to be optimized before application. There are different input factors which need adjustment in order to find the optimal combinations for the best final product. Therefore the main aim of the study was to establish predictive models for the plasma arc cutting in order to determine the cutting quality before real application of the plasma arc cutting. As cutting material Quard-400 was used. Input factors cutting speed and gas pressure were used during experimental procedure and for the predictive models crating. As the output quality parameters, mean surface roughness – Ra and material removal rate – MRR were used. Higher material rate means more profit for industry and vice versa. In the same time higher removal rate could increase surface roughness which is not desirable. Surface roughness needs to be minimized as much as possible which depends on the product application purpose. Predictive models were created based on adaptive neuro fuzzy inference system – ANFIS, which is suitable for nonlinear and redundant dataset. Results shown high predictive accuracy for the both output parameters.

Keywords: plasma arc cutting; prediction; surface roughness; ANFIS

1. INTRODUCTION

Plasma state is the fourth state of material after solid, liquid and gaseous states. Plasma state occurs after very high heating of the material. In other words the first state is solid state which converts in the liquid state after heating. The liquid state converts further in gaseous state after more heating. And finally the gaseous state converts into plasma state after more heating. Plasma represent in ionized gas which is electro conductive and operated on temperatures between 10000°C and 14000°C. Plasma arc cutting is based on the ionized gas and it represents one type of thermal cutting process which uses a jet of the plasma gas in order to melt and cut material. The plasma arc cutting is very attractive process for material removal or cutting because of high quality of the final product. However the plasma arc cutting process is very expensive process in comparison to laser cutting or cutting by oxygen fuel.

Plasma arc cutting (PAC) is well recognized non-conventional machining processes widely used to fabricate intricate part profiles for diverse electrically conductive materials including superalloys and composites [1]. Plasma arc cutting process is frequently used to cut stainless steel, alloy steel, aluminum and other materials [2]. The application of teaching learning based optimization (TLBO) algorithm in order to analyze the

effect of process parameters on surface roughness in plasma arc cutting of AISI D2 steel has been performed in article [3]. The optimum selection of process parameters is essential for smoother and faster cutting and in research work [4], experimental investigation of plasma arc cutting has been carried out where Taguchi based desirability analysis (TDA) was observed to find the optimal cutting conditions for improving the quality characteristics of the plasma arc cutting process. The quality of the cut of the plasma arc cutting proces has been monitored by measuring the kerf taper angle (conicity), the edge roughness and the size of the heat-affected zone (HAZ) [5]. Results in paper [6] have been shown that this fuzzy control and PID neural network improves the precision, ripples, finish and other comprehensive indexes of the workpiece compared with conventional PI control, and the plasma arc cutting power supply based on the fuzzy-neural network has excellent control performance. Plasma arc cutting (PAC) is a thermal cutting process that makes use of a constricted jet of high-temperature plasma gas to melt and separate (cut) metal [7]. In work [8], the microstructural modifications of the Hf insert in plasma arc cutting (PAC) electrodes operating at 250 A were experimentally investigated during first cycles, in order to understand those phenomena occurring on and under the Hf emissive surface and involved in the electrode erosion process where macrocracking was observed in the oxide

layer, while microcracking and grain growth were detected in the remelted Hf. The paper [9] pointed out that high quality parts of the plasma arc cutting can be obtained as a result of an experimental investigation aimed at selecting the proper values of process parameters. There is need to develop and optimize novel plasma arc heat source such as cross arc and coupling arc [10]. In study [11] has been studied the influences of plasma arc remelting on the microstructure and properties of thermal sprayed $\text{Cr}_3\text{C}_2\text{-NiCr/NiCrAl}$ composite coating. To reduce the kerf width and to improve the kerf quality, the hydro-magnetically confined plasma arc was used to cut engineering ceramic plates [12]. The quality of cuts performed on titanium sheets using high tolerance plasma arc cutting (HTPAC) process was investigated under different process conditions and a comparison between predicted thermal cycles, experimental measurements and microstructural observations confirmed the reliability of the estimation in terms of extension of microstructural modifications [13].

In order to decrease price of the plasma arc cutting process there is need to establish predictive models of the process. In other words the models could suggest future quality of the plasma arc process for the given combination of the input parameters. In order to do the predictive models there is need for an advanced computational models like soft computing or computational intelligence. Therefore in this article is used adaptive neuro fuzzy inference system or ANFIS [14-18] in order to predict laser arc cutting output parameters based on the input processing factors like cutting speed and plasma gas pressure. The output factors are mean surface roughness and material removal rate.

2. METHODOLOGY

2.1. Experimental procedure

Figure 1 shows the total experimental procedure of the plasma arc cutting. As can be seen there are nine main steps of the procedure. The torch body contains cathode which is non-melting. Working material represent anode or positive electrode where high temperature plasma gas or primary gas will be impinged. Kerf represent width of material removal during cutting process where molten metal is removed. For the cooling purpose secondary gas is used.

As working material Quard-400 is used which is abrasion resistant steel. This material has optimal combination of hardness, ductility and strength and it is very suitable for cutting process. Chemical composition of the material has following elements: C, Mn, P, Si, Al, Cu, Nb, Ni, Cr, V, Ti, N_2 , B and Fe.

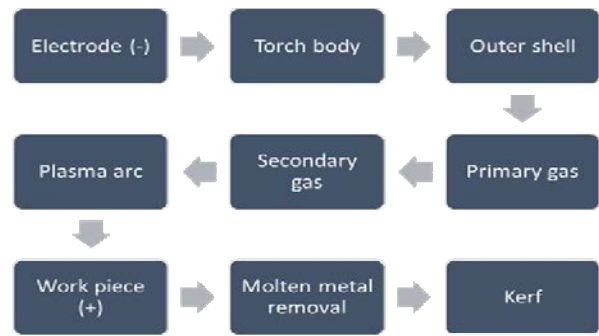


Figure 1. Experimental procedure of the plasma arc cutting process.

For the experimental procedure CNCN plasma arc cutting machine is used. Cutting specimens are dimension of $20 \times 20 \times 10 \text{mm}$. As cutting gas oxygen is used. Table 1 shows the numerical values (minimum and maximum) of the input and output factors which are used and obtained during cutting process.

Material removal rate or MRR is calculated based on the weight of the final product after cutting process. Surface roughness is measured by surface roughness tester and Ra value is measured based on three positions of the work piece. Based on the three measurements mean surface roughness is calculated.

Table 1: Input and output factors of the plasma arc cutting process

Input factors		Output factors	
Cutting speed (mm/min)	Pressure (psi)	Mean surface roughness, Ra (μm)	Material removal rate (gm/sec)

2.1. ANFIS methodology

ANFIS network has five layers as it shown in Figure 2. The main core of the ANFIS network is fuzzy inference system. Layer 1 receives the inputs and convert them in the fuzzy value by membership functions. In this study bell shaped membership function is used since the function has the highest capability for the regression of the nonlinear data.



Figure 2. ANFIS layers.

Bell-shaped membership functions is defined as follows:

$$\mu(x) = \text{bell}(x; a_i, b_i, c_i) = \frac{1}{1 + \left[\frac{x - c_i}{a_i} \right]^{2b_i}} \quad (1)$$

where $\{a_i, b_i, c_i\}$ is the parameters set and x is input.

Second layer multiplies the fuzzy signals from the first layer and provides the firing strength of as rule. The third layer is the rule layers where all signals from the second layer are normalized. The fourth layer provides the inference of rules and all signals are converted in crisp values. The final layers summarized the all signals and provided the output crisp value.

3. RESULTS

3.1. Accuracy indicies

Performances of the proposed models are presented as root means square error (RMSE), Coefficient of determination (R^2) and Pearson coefficient (r) as follows:

1) RMSE

$$RMSE = \sqrt{\frac{\sum_{i=1}^n (P_i - O_i)^2}{n}} \tag{2}$$

Pearson correlation coefficient (r)

$$r = \frac{n \left(\sum_{i=1}^n O_i \cdot P_i \right) - \left(\sum_{i=1}^n O_i \right) \cdot \left(\sum_{i=1}^n P_i \right)}{\sqrt{\left(n \sum_{i=1}^n O_i^2 - \left(\sum_{i=1}^n O_i \right)^2 \right) \cdot \left(n \sum_{i=1}^n P_i^2 - \left(\sum_{i=1}^n P_i \right)^2 \right)}} \tag{3}$$

2) Coefficient of determination (R^2)

$$R^2 = \frac{\left[\sum_{i=1}^n (O_i - \bar{O}_i) \cdot (P_i - \bar{P}_i) \right]^2}{\sum_{i=1}^n (O_i - \bar{O}_i)^2 \cdot \sum_{i=1}^n (P_i - \bar{P}_i)^2} \tag{4}$$

where P_i and O_i are known as the experimental and forecast values, respectively, and n is the total number of dataset.

3.2. ANFIS prediction

Figure 3 shows ANFIS prediction of mean surface roughness (Ra) based on cutting speed and for three different values of pressure, 65, 80 and 90 (psi). Figure 4 shows ANFIS prediction of Ra based on pressure and for six different values of cutting speed, 1000, 1500, 2500, 3000, 3500 and 4000 (mm/min). Figure 5 shows ANFIS-Ra prediction based on the both inputs simultaneously.

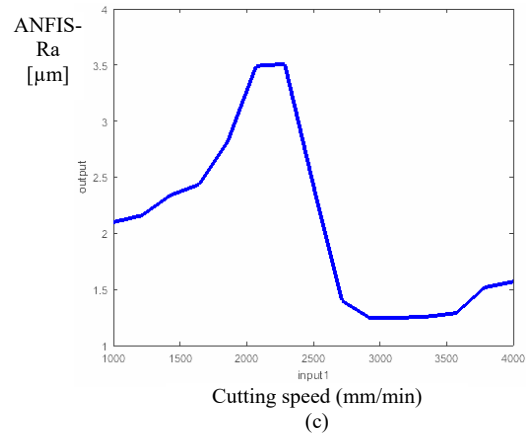
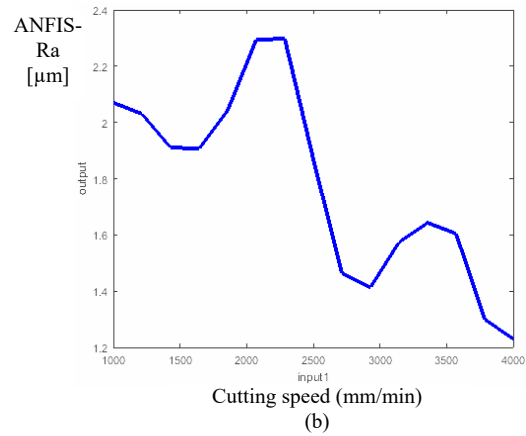
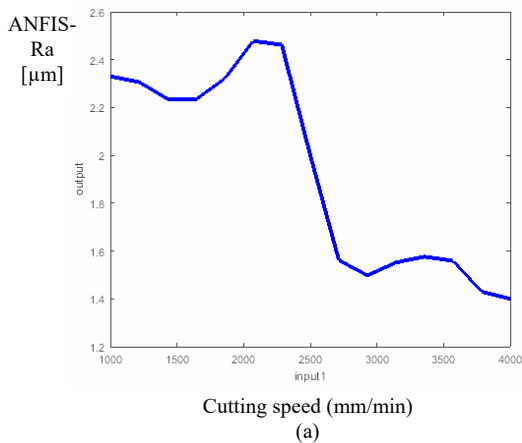
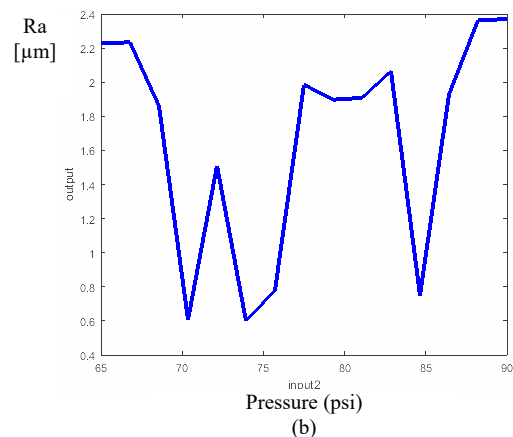
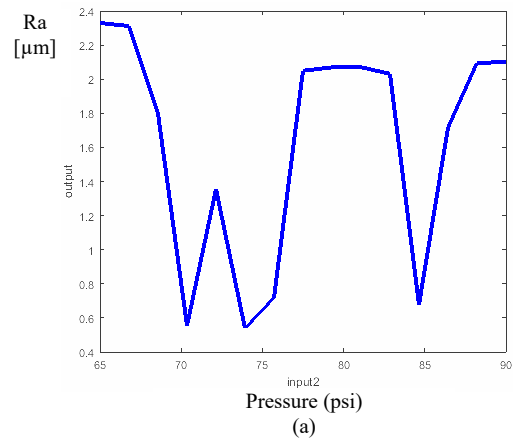


Figure 3. ANFIS-Ra prediction based on cutting speed and for pressure of: (a) 65, (b) 80 and (c) 90 (psi).



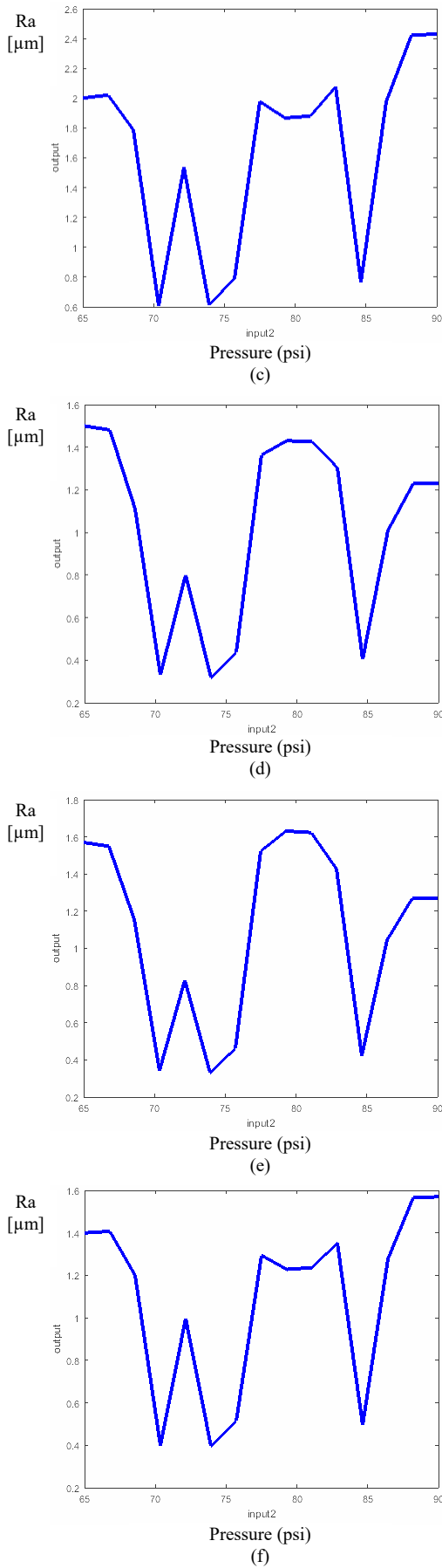


Figure 4. ANFIS-Ra prediction based on pressure and for cutting speed of: (a) 1000, (b) 1500, (c) 2500, (d) 3000, (e) 3500 and (f) 4000.

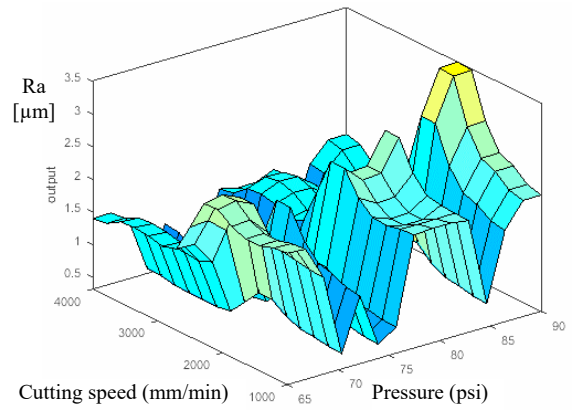
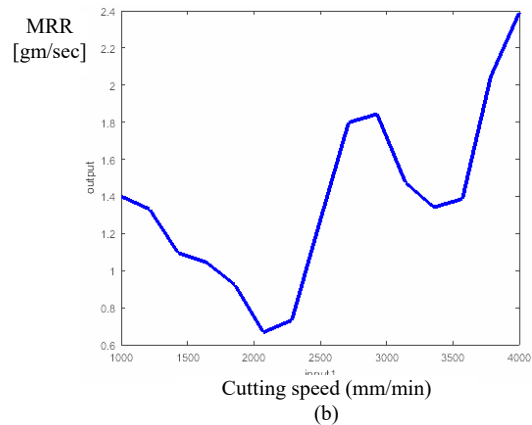
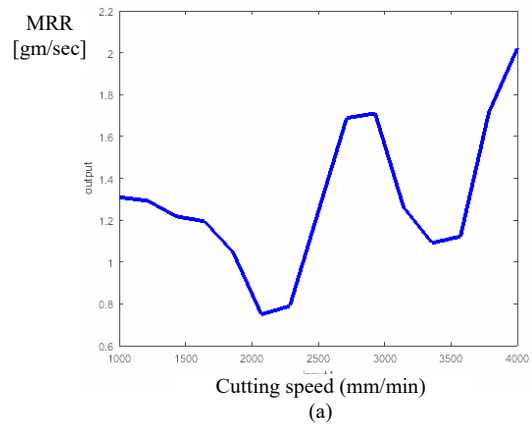


Figure 5. ANFIS-Ra prediction based on pressure and for cutting speed.

Figure 6 shows ANFIS prediction of material removal rate (MRR) based on cutting speed and for three different values of pressure, 65, 80 and 90 (psi). Figure 7 shows ANFIS prediction of MRR based on pressure and for six different values of cutting speed, 1000, 1500, 2500, 3000, 3500 and 4000 (mm/min). Figure 8 shows ANFIS-MRR prediction based on the both inputs simultaneously.



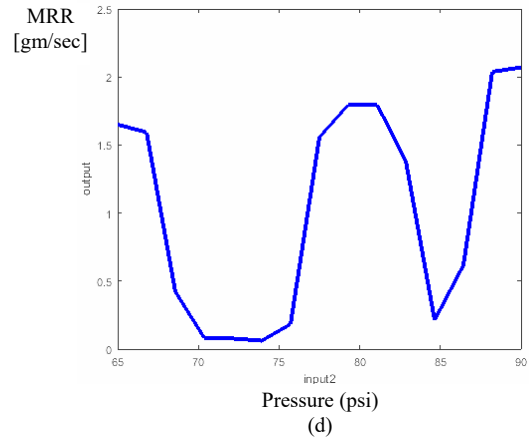
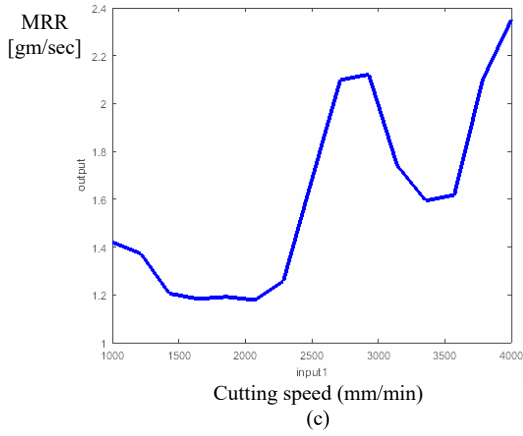


Figure 6. ANFIS-MRR prediction based on cutting speed and for pressure of: (a) 65, (b) 80 and (c) 90 (psi).

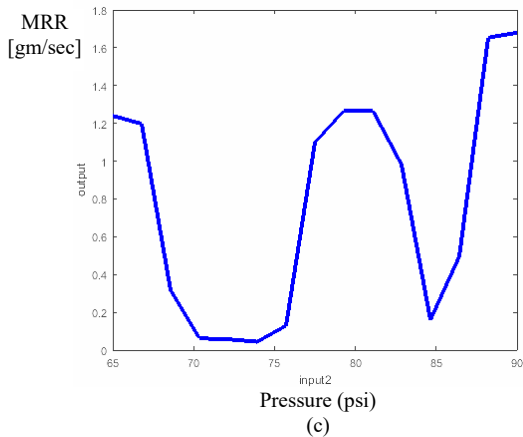
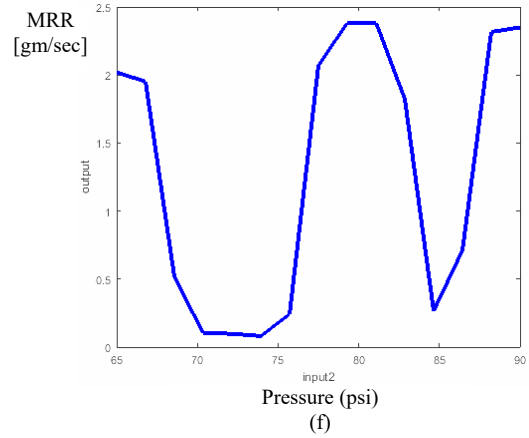
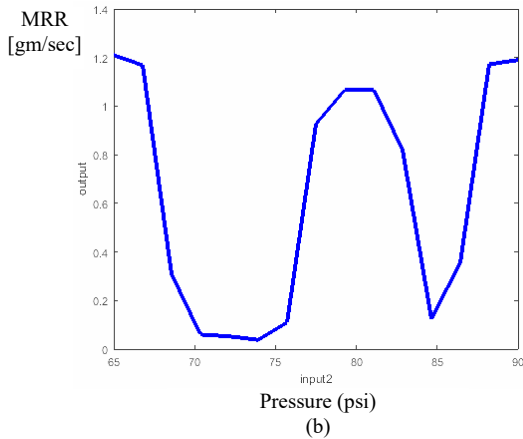
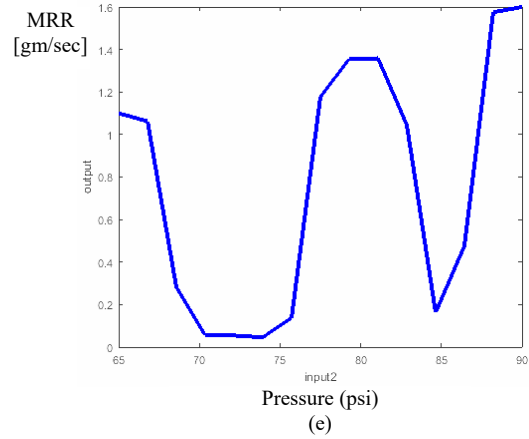
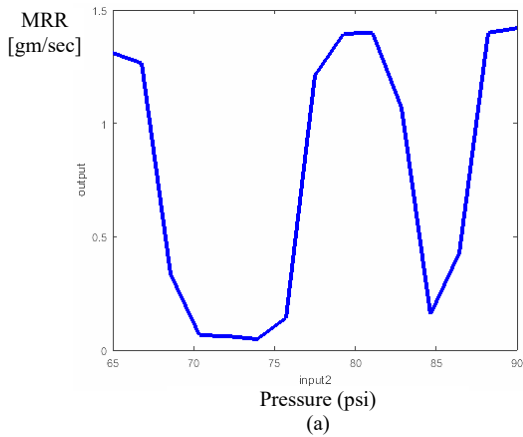


Figure 7. ANFIS-Ra prediction based on pressure and for cutting speed of: (a) 1000, (b) 1500, (c) 2500, (d) 3000, (e) 3500 and (f) 4000.

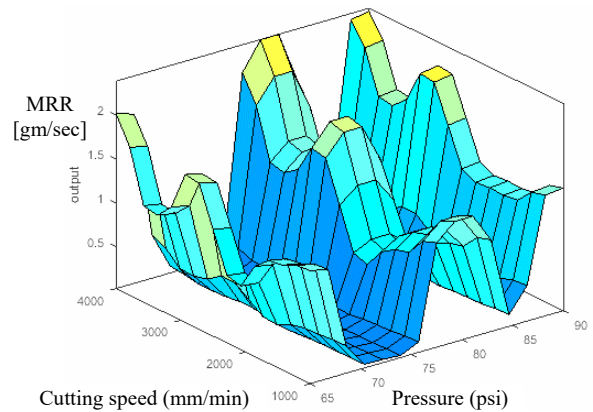


Figure 8. ANFIS-MRR prediction based on pressure and for cutting speed.

Figure 9 shows scatter plots of the ANFIS prediction of Ra based on the experimental measured data. It can be noted high predictive accuracy based on R^2 coefficient. Also, Pearson coefficient (r) is 0.873243 and root mean square error (RMSE) is 0.873243 for the Ra prediction.

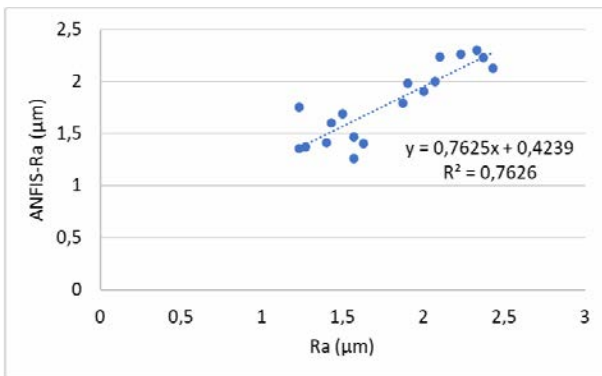


Figure 9. Scatter plot of ANFIS-Ra prediction.

Figure 10 shows scatter plots of the ANFIS prediction of MRR based on the experimental measured data. It can be noted high predictive accuracy based on R^2 coefficient. Also, Pearson coefficient (r) is 0.804839 and root mean square error (RMSE) is 0.173676 for the Ra prediction.

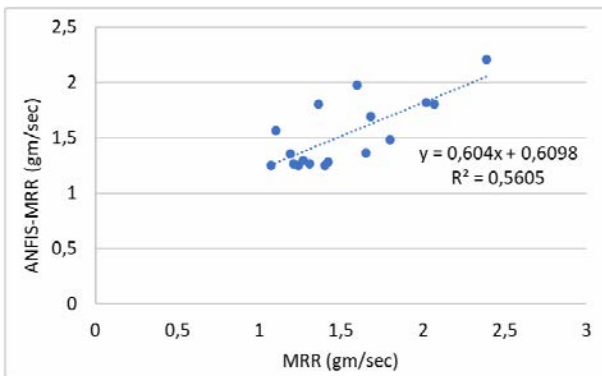


Figure 10. Scatter plot of ANFIS-MRR prediction.

4. CONCLUSION

In this paper was investigated predictive performance of adaptive neuro fuzzy inference system or ANFIS for prediction of output factors of plasma art cutting process. The output factors are mean surface roughness and material removal rate. The main purpose of the ANFIS predictive models was to determine which cutting quality will be obtained for different set of input parameters. ANFIS can eliminate the vagueness in the process in order to produce the best prediction conditions. In other words ANFIS network was used to convert the multiple performance characteristics into the single performance index.

References

- [1] Ananthakumar, K., Rajamani, D., Balasubramanian, E., & Davim, J. P. (2019). Measurement and optimization of multi-response characteristics in plasma arc cutting of Monel 400™ using RSM and TOPSIS. *Measurement*, 135, 725-737.
- [2] Bhowmick, S., Basu, J., Majumdar, G., & Bandyopadhyay, A. (2018). Experimental study of plasma arc cutting of AISI 304 stainless steel. *Materials Today: Proceedings*, 5(2), 4541-4550.
- [3] Patel, P., Nakum, B., Abhishek, K., Kumar, V. R., & Kumar, A. (2018). Optimization of Surface Roughness in Plasma Arc Cutting of AISID2 Steel Using TLBO. *Materials Today: Proceedings*, 5(9), 18927-18932.
- [4] Kumar Naik, D., & Maity, K. P. (2017). An optimization and experimental analysis of plasma arc cutting of Hardox-400 using Taguchi based desirability analysis.
- [5] Salonitis, K., & Vatousianos, S. (2012). Experimental investigation of the plasma arc cutting process. *Procedia CIRP*, 3, 287-292.
- [6] Deli, J., & Bo, Y. (2011). An intelligent control strategy for plasma arc cutting technology. *Journal of Manufacturing Processes*, 13(1), 1-7.
- [7] Chamarthi, S., Reddy, N. S., Elipey, M. K., & Reddy, D. R. (2013). Investigation Analysis of Plasma arc cutting Parameters on the Unevenness surface of Hardox-400 material. *Procedia Engineering*, 64, 854-861.
- [8] Rotundo, F., Martini, C., Chiavari, C., Ceschini, L., Concetti, A., Ghedini, E., ... & Dallavalle, S. (2012). Plasma arc cutting: Microstructural modifications of hafnium cathodes during first cycles. *Materials Chemistry and Physics*, 134(2-3), 858-866.
- [9] Bini, R., Colosimo, B. M., Kutlu, A. E., & Monno, M. (2008). Experimental study of the features of the kerf generated by a 200 A high tolerance plasma arc cutting system. *Journal of materials processing technology*, 196(1-3), 345-355.
- [10] Chen, S., Zhang, R., Jiang, F., & Dong, S. (2018). Experimental study on electrical property of arc column in plasma arc welding. *Journal of Manufacturing Processes*, 31, 823-832.
- [11] Ji-yu, D., Fang-yi, L., Yan-le, L., Li-ming, W., Hai-yang, L., Xue-ju, R., & Xing-yi, Z. (2019). Influences of plasma arc remelting on microstructure and service performance of Cr3C2-NiCr/NiCrAl composite coating. *Surface and Coatings Technology*.
- [12] Xu, W. J., Fang, J. C., & Lu, Y. S. (2002). Study on ceramic cutting by plasma arc. *Journal of Materials Processing Technology*, 129(1-3), 152-156.
- [13] Gariboldi, E., & Previtali, B. (2005). High tolerance plasma arc cutting of commercially pure titanium. *Journal of Materials Processing Technology*, 160(1), 77-89.
- [14] Jang, J.-S.R, ANFIS: Adaptive-Network-based Fuzzy Inference Systems, *IEEE Trans. On Systems, Man, and Cybernetics* (1993), Vol.23, 665-685.
- [15] Petković, D., Issa, M., Pavlović, N.D., Pavlović, N.T., Zentner, L., Adaptive neuro-fuzzy estimation of conductive silicone rubber mechanical properties, *Expert Systems with Applications*, ISSN 0957-4174,

- 39 (2012), 9477-9482.
- [16] Petković D, Čojbašić Ž (2012) Adaptive neuro-fuzzy estimation of automatic nervous system parameters effect on heart rate variability, *Neural Computing & Application*, 21(8):2065-2070 (2012)
- [17] Kurnaz S, Cetin O, Kaynak O, Adaptive neuro-fuzzy inference system based autonomous flight control of unmanned air vehicles, *Expert Systems with Applications* (2010), 37, 1229-1234.
- [18] Petković, D., Issa, M., Pavlović, N.D., Zentner, L., Čojbašić, Ž., Adaptive neuro fuzzy controller for adaptive compliant robotic gripper, *Expert Systems with Applications*, ISSN 0957-4174, 39, (2012), 13295-13304.



10th INTERNATIONAL SCIENTIFIC CONFERENCE
ON DEFENSIVE TECHNOLOGIES
OTEH 2022

Belgrade, Serbia, 13 – 14 October 2022



SECTION VIII

**Quality, standardization, metrology,
maintenance and exploitation - QSMME**

CHAIRMAN
Srđan Živković, PhD

SECURITY SYSTEM DESIGN USING A SOFTWARE SOLUTION

PREDRAG RANITOVIĆ

School of Business, Novi Sad, predrag.ranitovic@gmail.com

SANJA LONČAR

School of Business, Novi Sad, sanja.lonchar@gmail.com

Abstract: The development and design of a security system is a complex process, made up of a number of specific elements. Defining and taking into account that, there are two basic elements in the design of security systems: the basic functional model of security systems and the model of management and protection of information as a key resource of security systems. There is a need to analyse the basic architecture of the security system and define its framework and to analyse the management system and information protection and to define its framework. By observing and analysing these systems in the context of the application of information technology solutions in the process of development and design of security systems, we get a key basis for the application of software solutions in the process of designing security systems. This application of software solutions is reflected in the development of conceptual software under the test name "projectdrive" the expediency of which would be characterised through a more efficient and effective manner in the approach to the design and development of security systems. This would give us a unique functional approach-concept-model of the security system, but also an information technology tool "software" (beta phase) for the purpose of designing and developing security systems.

Keywords: Software - Security system - ISO standards - IT system

1. INTRODUCTION

Modern security systems are prone to global security pressures which produce unsafe activities, by creating new phenomena, models and conditions in which and under which the functioning of a security system takes place.

Therefore, security systems require reengineering and adaptation to these new tendencies, through designing a new security system based on software solutions.

Also, the generally growing dependence on information puts in focus information as a dominant resource of the security system, stating the need to ensure appropriate steps in order to form adequate information protection.

The feature of the importance of information as a resource of the security system, as well as the function of its flow speed, places them among the key elements of the security system, Figure 1 [1].

Availability, integrity and confidentiality of information are the main carriers of the function of information flow speed.

Observing current events in the world regarding information protection as well as other security aspects, it is concluded that it is impossible to predict the "dynamics" of threats to the security system.

The speed at which they arise, the forms of the attacks and their actions are on increase thus it is completely pointless to take effective measures against specific and established threats.

Modern security threats, more precisely their advanced sophistication, have imposed the need to deal with general

and systemic security issues. Classical security systems such as the army, police, intelligence and security services and civil protection must adapt to the new security reality and, through adequate design of the security system, seek solutions for new "security challenges" [2].

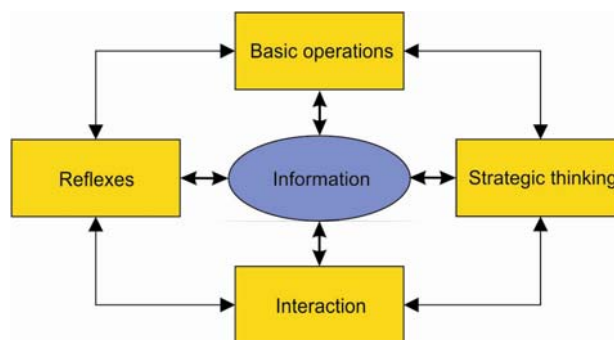


Figure 1. System function of information

Only a comprehensive, systematic approach to the design of an adequate security system on the basis of software solutions and supported by them, will contribute to establishing a satisfactory level of security.

2. MODEL OF A SECURITY SYSTEM

A security model is defined by the application of certain activities to the area of security, characterizing security as a concept of protection-security against danger, damage, loss and crime.

Taking into account the aspiration towards designing an "adequate" security system, determining the concept directly affects the design context and the approach to

designing a security system through software solutions.

By analysing the macro/micro model of the security system, we define the basic model of the security system, Figure 2 [3,4].

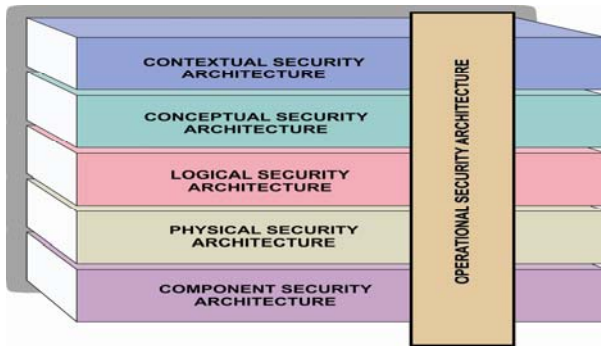


Figure 2. Basic model of the security system

The basic model of the security system includes elements defined according to the levels of their activity:

- Contextual elements represent the first level of the security system and they are conceptually defined by the formulation of the basic “framework” of the system, its flaws and approaches to solving those issues. They were designed in compliance with the following elements:

- Field of activity,
- Risk model
- Process model,
- Organisation
- System positioning and
- Time positioning.

- Conceptual elements represent the second level of the security system and they are conceptually defined by the formulation of the comprehensive system strategy. They were designed in compliance with the following elements:

- Features,
- Objective,
- Strategy,
- Entity model,
- Domain model and
- Deadline.

- Logical elements represent the third level of the security system and they are conceptually defined by the formulation of the form of the system and its effects. They were designed in compliance with the following elements:

- Information model,
- Policy
- Services,
- Entity scheme
- Domain scheme and
- Process cycle.

- Physical elements represent the fourth level of the security system and they are conceptually defined by the formulation of the forms of applied resources and system

carriers. They were designed in compliance with the following elements:

- Information system,
- Procedures,
- Mechanisms,
- Entity interface,
- Domain platform and
- Time structuring.

- Component elements represent the fifth level of the security system and they are conceptually defined by the formulation of the consistency of the original form of a resource and the system carriers. They were designed in compliance with the following elements:

- Information structure,
- Standards,
- Tools,
- Identity,
- Location and
- Time.

- Operational elements represent the sixth level of the security system and they are conceptually defined by the formulation of the effects of the management. They were designed in compliance with the following elements:

- Management,
- Risk management,
- Strategic management,
- Management of Human Resources,
- Operational management and
- Time management.

- Architecture of the implementation of the system represents the seventh level of the security system. It is conceptually defined by the formulation of the security system implementation course. They were designed in compliance with the following elements:

1. Implementation plan
2. Implementation management
3. Testing

- Architecture of the analysis of the system represents the eighth level of the security system. It is conceptually defined by the formulation of the security system analysis course. They were designed in compliance with the following elements:

- Set of reports and
- Improvement plan.

According to the characteristics of the elements they project, the "factors" of real application and the basic conceptual solution, the presented levels are formulated in the basic model of a security system. Looking at the basic model of a security system, the levels are clearly visible as the carriers of the system architecture. In order for them to be formulated more precisely through the characteristics of the elements that make them up, they are systematized into a constructive model of a security system, Table 1.

Table 1. A constructive model of a security system

Matrix	Property (What?)	Motivation (Why?)	Processes (How?)	People (Who?)	Location (Where?)	Time (When?)
Contextual elements	activity	risk model	process model	organization	system positioning	time positioning
Conceptual elements	characteristics	aim	strategy	model of an entity	domain model	deadline
Logic elements	information model	policy	services	entity scheme	domain scheme	process cycle
Physical elements	information system	procedures	mechanisms	entity interface	domain platform	time structuredness
Component elements	information structure	standards	tools	identity	position	time
Operational elements	management	risk management	strategic management	human resources management	operational management	time management

3. INFORMATION SECURITY MODEL

An information security management system (ISMS) represents one of the most dominant forms of the information protection method according to the generally accepted context and an integral part of the security system [5, 6].

The basic principle that defines an information security management system (ISMS) is based on the PDCA Plan-Do-Check-Act model, Figure 3. It formulates the elements of establishment, implementation, enforcement, monitoring, analysis, maintenance and improvement of information security.

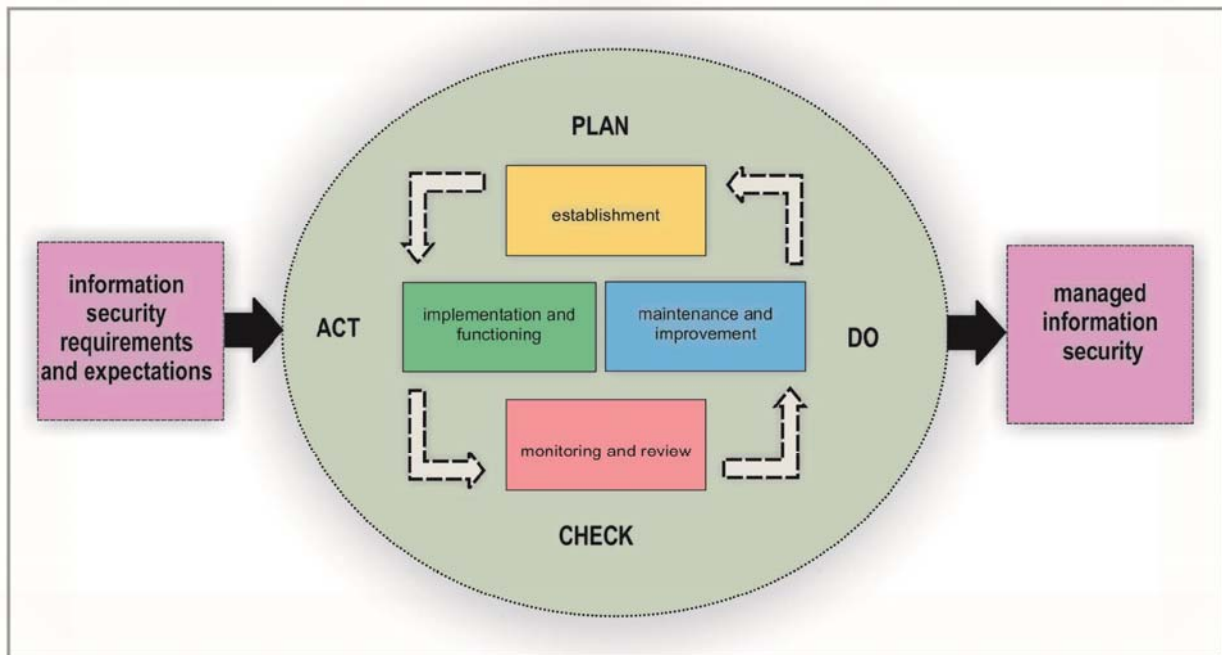


Figure 3. Information security management system (ISMS) model

PHASE (PLAN)

The Plan phase establishes the preparation of the implementation of the information security management system (ISMS). The preparation includes defining the scope and policy of the mentioned, thereby ensuring a focus on appropriate assets, human resources, system

processes and risk assessment, on the basis of which risks to information are identified and analyzed. By formulating a risk assessment, the direction of the implementation of the information protection system (ISMS) is designed.

The phase (Plan) is conceptually defined by a model, Figure 4.

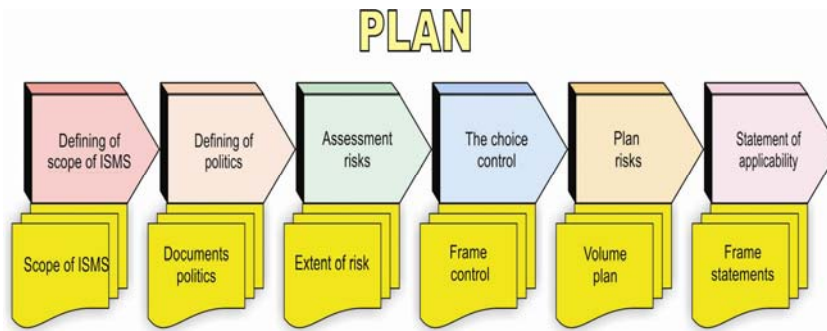


Figure 4. Model of (Plan) phase concept

PHASE (DO)

Phase Do implements the defined elements of the Plan phase. As the basis of the mentioned, the risk remediation project plan and its implementers are identified, thus

guiding the information protection system (ISMS).

The phase (Do) is conceptually defined by a model, Figure 5.

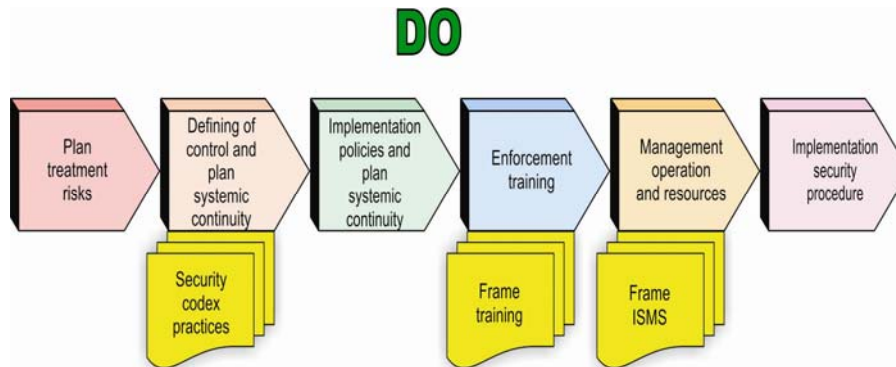


Figure 5. Model of (Do) phase concept

PHASE (CHECK)

The Check phase reviews policy, procedures and records with the aim of checking their effectiveness and efficiency in terms of risk management, while also

defining the internal audit of the ISMS.

The phase (Check) is conceptually defined by a model, Figure 6.

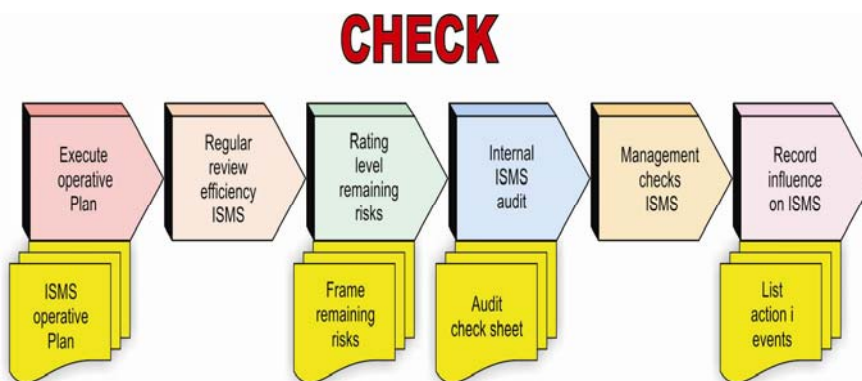


Figure 6. Model of (Check) phase concept

PHASE (ACT)

The Phase Act defines the improvement of an information security system (ISMS) by incorporating changes, additions, preventive measures or the overall improvement of the system and viewing security as a

process of continuous review and improvement rather than a specific "destination".

The phase (Act) is conceptually defined by a model, Figure 7.

ACT

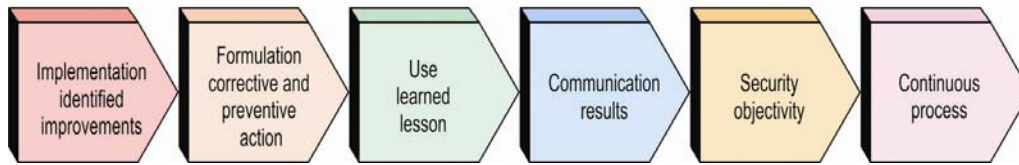


Figure 7. Model of (Act) phase concept

4. SOFTWARE

Model testing was performed on a pilot project - the PROJECTDRIVE software tool, Figure 8, constructed in line with a new approach-concept-model of the security system based on the intersection of the constructive model of the basic security system and the model of information protection and the basics of software design [7-11].

The PROJECTDRIVE source code is based on functionally dependent integration of security system elements and information protection methods, defined according to schemes.

PROJECTDRIVE was designed for the purpose of conducting testing of a new approach-concept-model of a security system and was constructed through a team collaboration with a software developer, making a new and completely unique software of its kind

PROJECTDRIVE

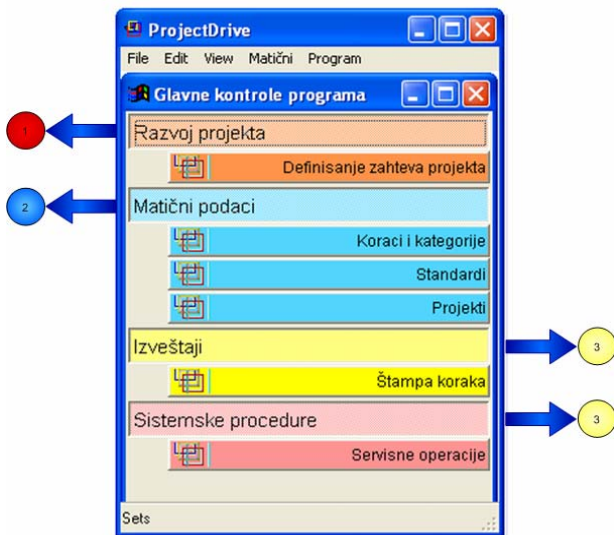


Figure 8. Software's main Interface

The concept of PROJECTDRIVE is to provide an easier approach to defining security system design requirements. The basis for this are three sub-modules marked with symbols, Table 2.

Table 2. Basic modules

1	Project development
2	Master data
3	Reports - system procedures

4.1. Project development

The development of a project defines the basic requirements of designing a security system of the civil-military management system. It is represented by a software interface for defining project requirements, Figure 9.

The concept of MODULE 1 includes 36 steps within which certain values are formulated. By characterizing the ones with the same name, a list of security system design requirements is formulated, which is a practical instruction for the formation of the security system of the civil-military management system.

The topography of the software interface (defining project requirements) is marked according to symbols, Table 3.

Table 3. Basic elements of software interface (defining the project requirements)

1	Basic steps
2	Values
3	Tools
4	Integration values

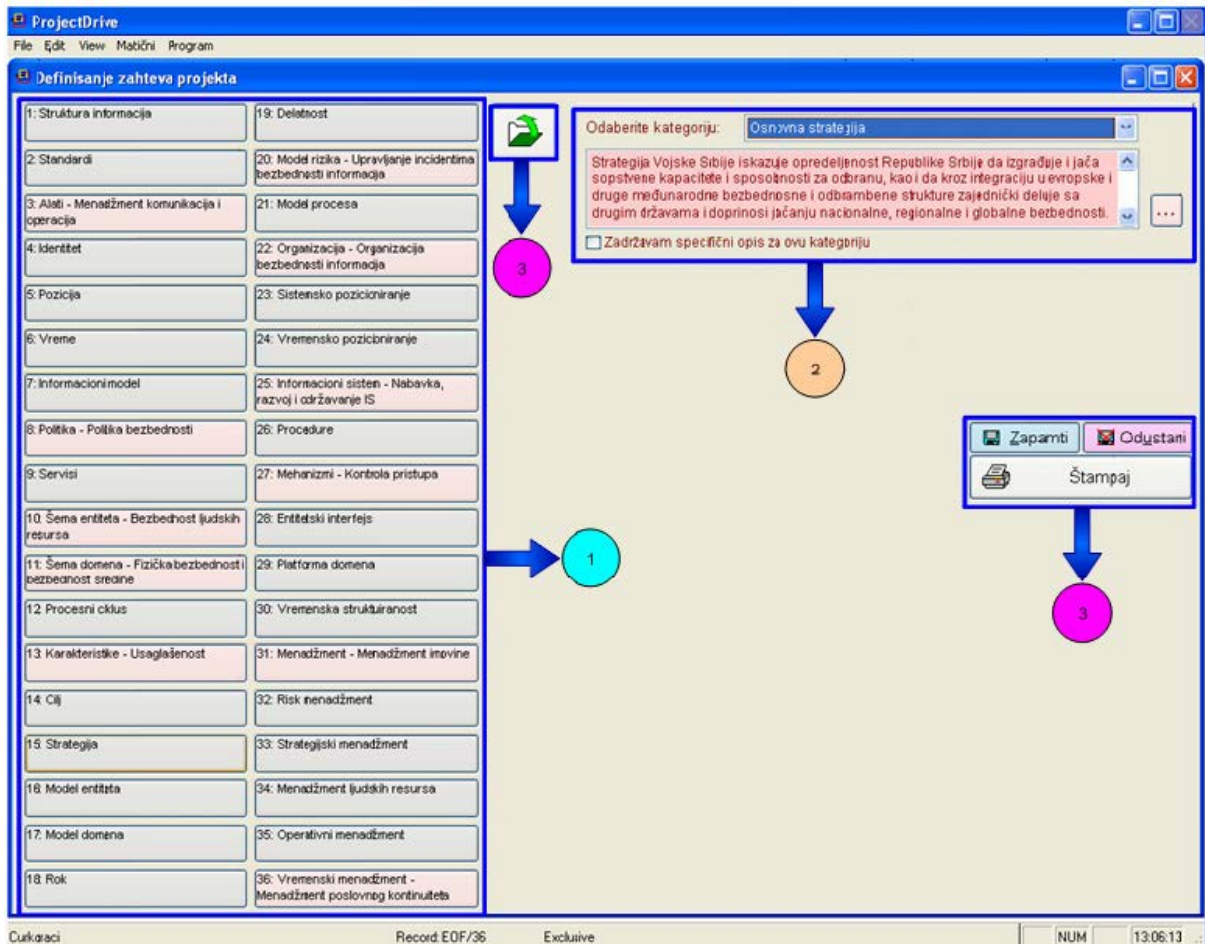


Figure 9-1. Defining project requirements Interface

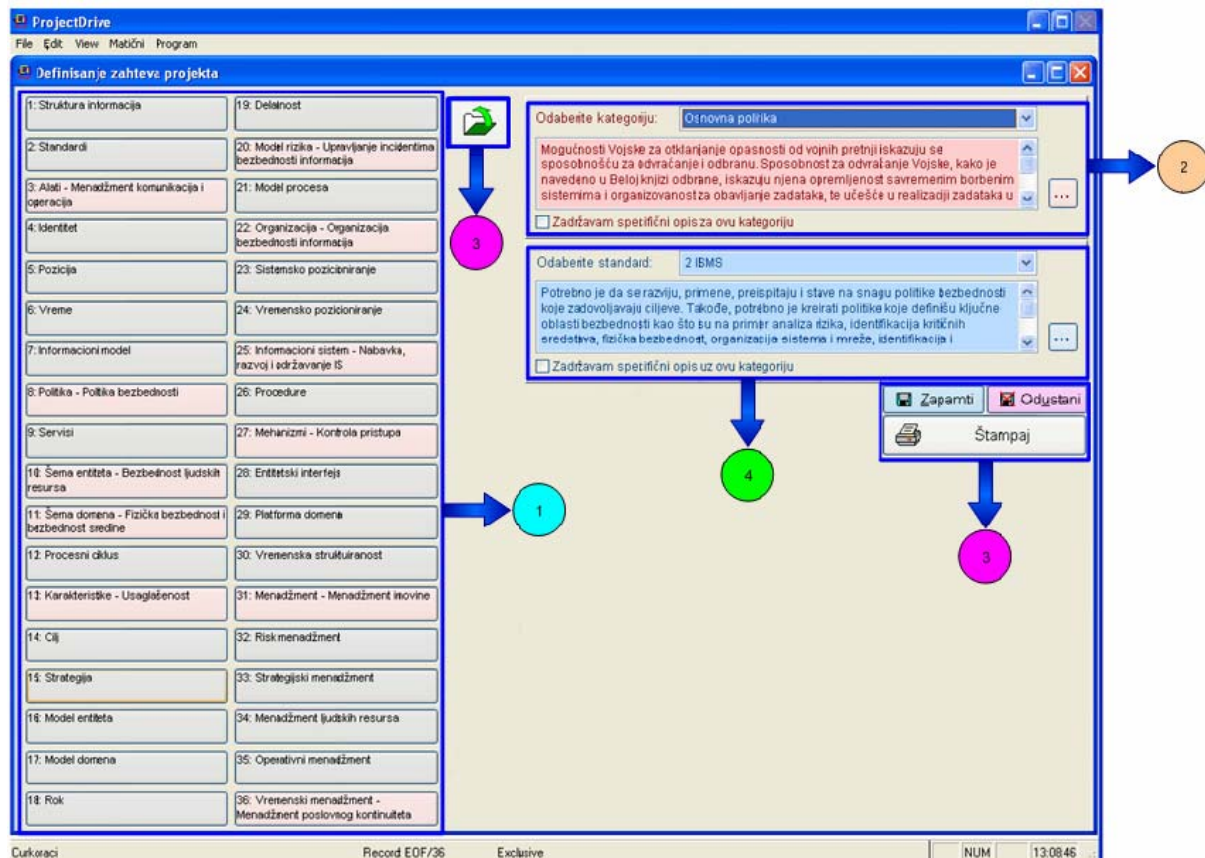


Figure 9-2. Defining project requirements Interface

4.2. Master data

The master data define the values of the security system design requirements of security system representing MODULE 2. They are logically classified according to the software interface:

1. Steps and categories,
2. Standards and
3. Projects.

1. Steps and categories

The steps and categories define the values of the basic requirements of designing the security system. They are shown by the software interface, in steps in defining a project, Figure 10.

The concept of steps and categories of MODULE 2 includes the formulation of the values related to the 36 steps of MODULE 1. The form and the meaning of each

step is determined according to the character of the steps in the process of forming the security system. The topography of the software interface (steps in defining a project) is marked according to symbols, Table 4.

Table 4. Basic elements of software interface (steps in defining a project)

1	Basic steps
2	Description of the steps
3	Step categories
4	Category values
5	Integration
6	Tools

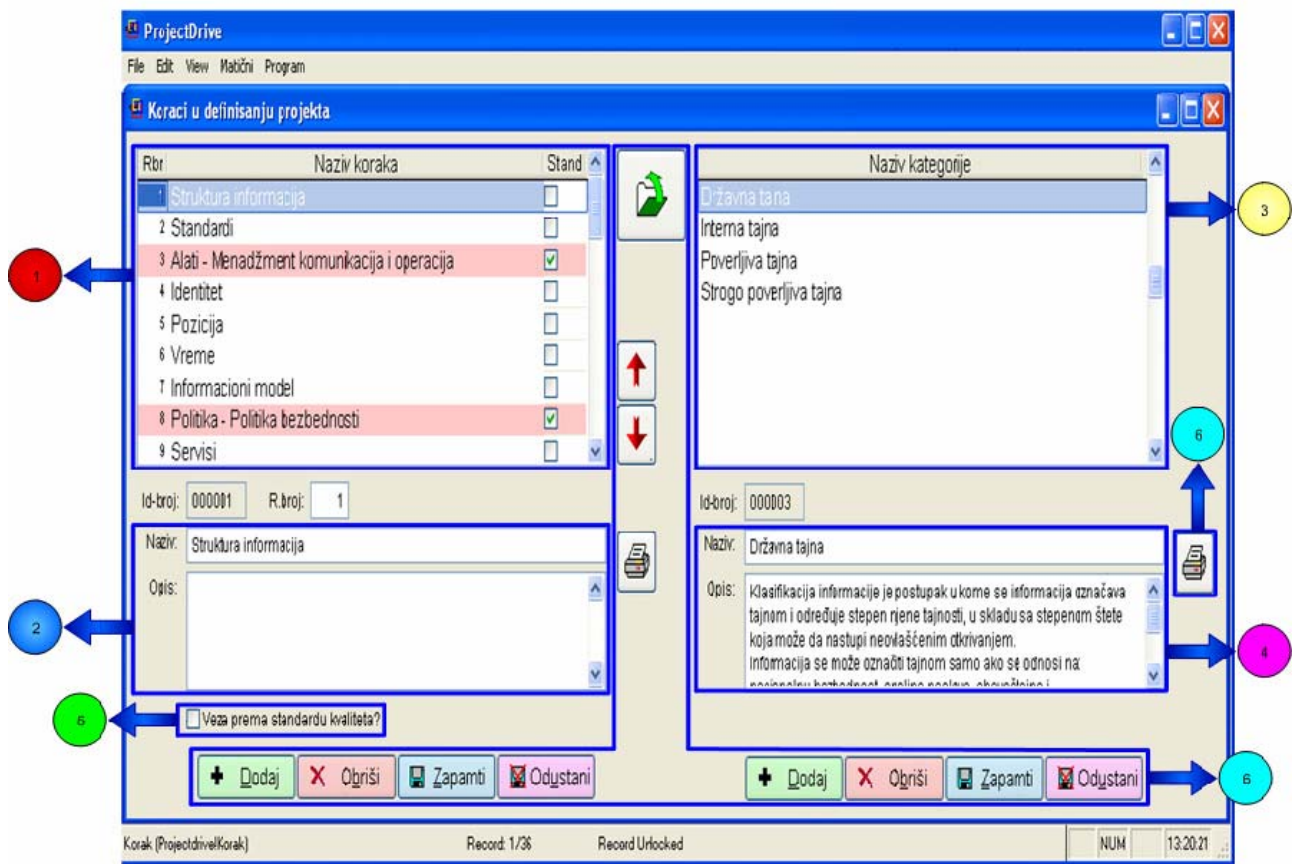


Figure 10. Interface steps in defining a project

2. Standards

Standards define the values of the integration of the basic requirements of designing a security system. They are represented by a software interface (list of reference standards), Figure 11.

The concept of the MODULE 2 standard includes formulating the values of 11 steps of integration with 36

steps of MODULE 1. The steps of integration are formulated according to the requirements of the information protection system ISMS. The topography of the software interface (the list of reference standards) is marked according to the symbols, Table 5.

Table 5. Basic elements of software interface (a list of reference standards)

1	Основни кораци
2	Вредности
3	Алати

3. Projects

The projects define the framework of the basic requirements for designing a security system.. Projects are represented by the software interface, Figure 12.

The concept of the MODULE 2 project includes a unique marking of separate projects of the design process of a security system, indicating the possibility of limiting the

scope of the project by canceling certain steps of the security system. The topography of the software interface (projects) is marked according to symbols, Table 6.

Table 6. Basic elements of software interface (projects)

1	Basic projects
2	Project description
3	Step frame
4	Step base
5	Tools

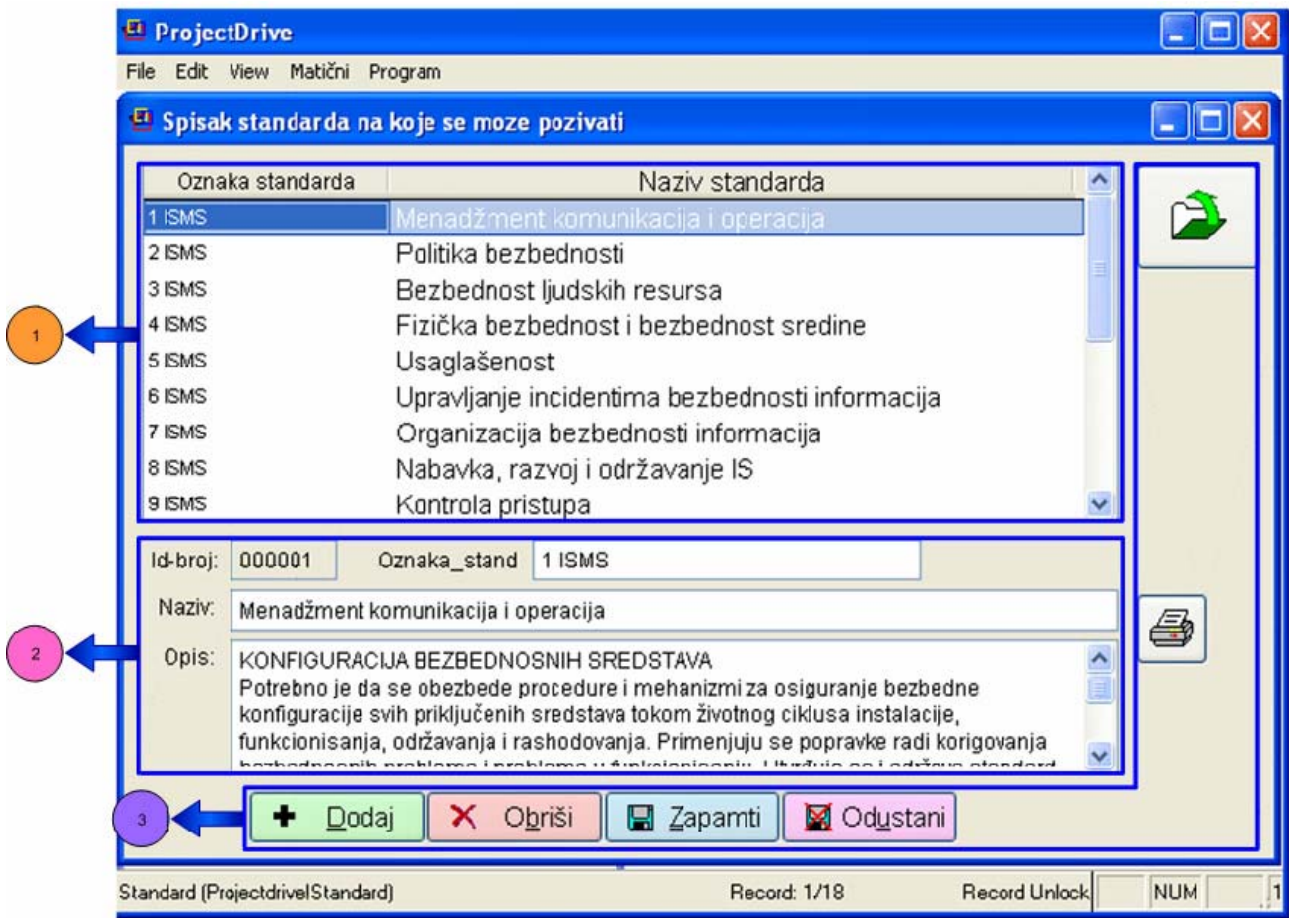


Figure 11. Interface list of reference standards

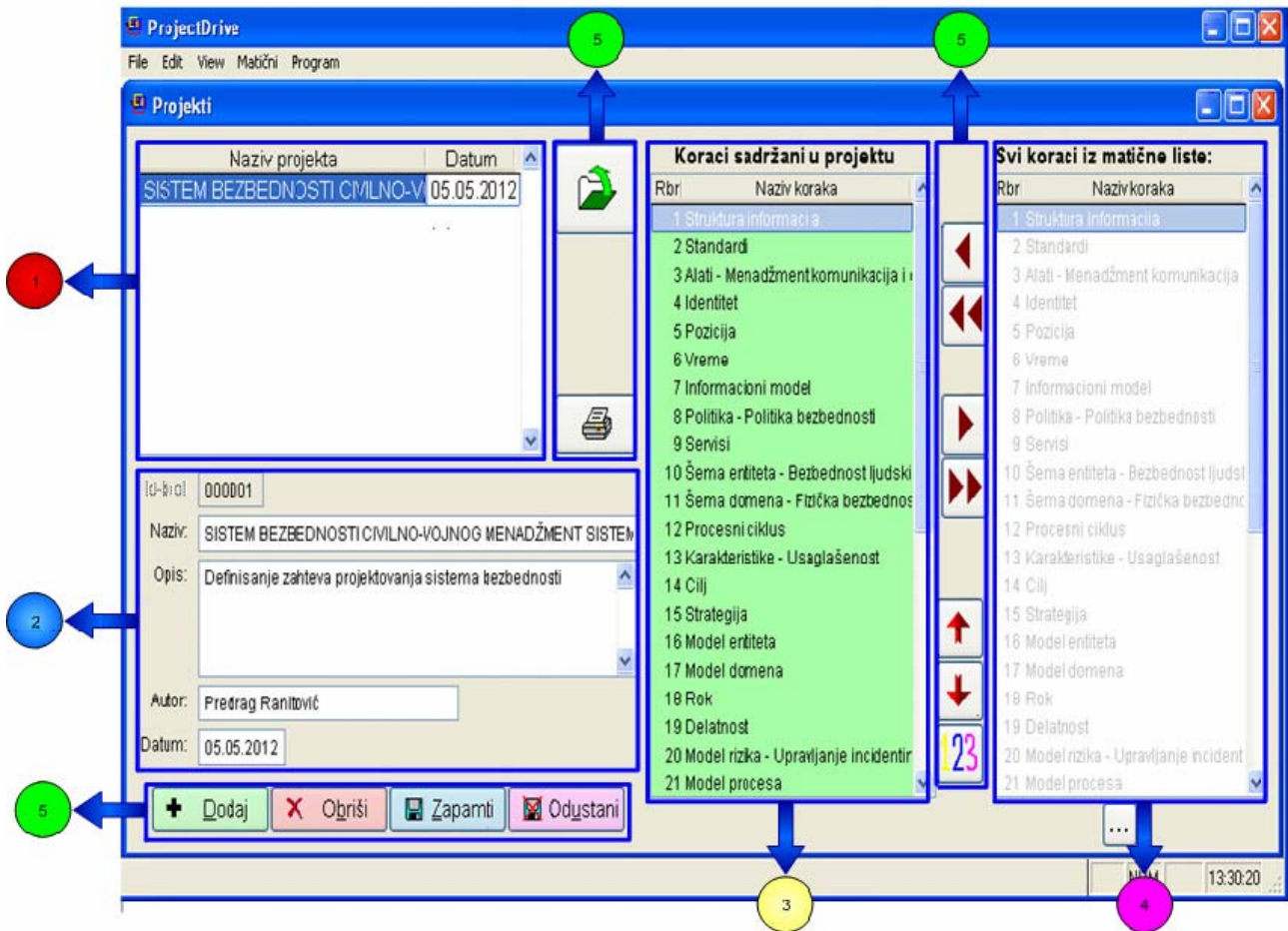


Figure 12. Interface projects

4.3. Reports-system procedures

Reports-system procedures define logistic support options for the tools for designing security systems of the civil-military management system representing MODULE 3, classified according to the hypothetical software interface:

- 1. Print steps and
- 2. Service information.

1. Print steps

Print steps should hypothetically define the archive of MODULE 1 and MODULE 2 as the conditions for designing a security system of the civil-military management system. The concept of print steps of MODULE 3 includes organizational support for the design of a security system of the civil-military management system.

2. Service information

Service information should hypothetically define the logistic basis of HELP of all the MODULES. The concept of service information of MODULE 3 includes the logistics support to the tools for designing a security system of the civil-military management system.

5. CONCLUSION

The main aim was to create a new approach-concept-model of the security system based on the research of the

concept of functional dependence of information protection methods and the security system through a software solution.

Analyzing and observing the elements of the security architecture through the prism of the new approach-concept-model of the security system, contributed to the improvement of the existing ones and the acquisition of new practical-theoretical knowledge in the field of designing modern security systems.

The prominent key result of the paper is the formulation of unique system security schemes integrated through a security platform (software) which represents a new functional model of a modern security system.

The concept of the entire operation of functional dependence of information protection methods and security systems based on software development is defined in accordance with the conceptual flow of the basic phases of the security system.

By combining all aspects of this process, a clear picture of the scientific idea based on practical-theoretical elements is produced, Figure 13.

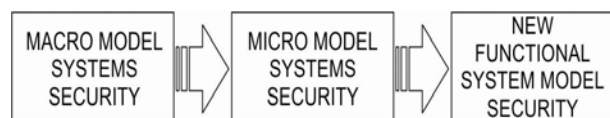


Figure 13. Model-concept

References

- [1] Tipont, H., Krause, M.: "Information Security Management - Sixth Edition", Auerbach Publications, 2007.
- [2] Andress, J.: "The Basic of Information Security", Elsevier, 2011.
- [3] Andy, J., Ashenden, D.: "Risk Management for Computer Security", Elsevier, 2005.
- [4] Hangos, K., Cameron, I.: "Process Modelling and Model Analysis", Academic Press, 2001.
- [5] Arnason, S., Willett, K.: "How to Achieve 27001 Certification", Auerbach Publications, 2008.
- [6] Calder, A., Watkins, S.: "IT Governance A Managers Guide to Data Security and ISO 27001/ ISO 27001", Kogan Page Science, 2008,
- [7] Stewart, M. J.: "Certified Information Systems Security Professional", John Wiley&Sons, 2001.
- [8] Alberts, C.; Dorofee, A.: "Managing Information Security Risk", Addison Wesley, 2002.
- [9] Pour, K. M.: "Cases on Information Technology" Idea Group. 2006.
- [10] Rocheleau, B.: "Case Studies on Digital Government", Idea Group, 2007.
- [11] Media Garrido, J. A., Martinez Fierro, S., Ruiz Navarro, J.: "Cases on Information Technology Entrepreneurship", Igi Publishing, 2008.



RISK MANAGEMENT AT PUBLIC COMPANY „NUCLEAR FACILITIES OF SERBIA“

BOJAN RADOŠ

PC „Nuclear Facilities of Serbia“, Mike Petrovića Alasa 12-14, Vinča, Belgrade
+381628869090, bojan.rados@nuklearniobjekti.rs

NATAŠA LAZAREVIĆ

PC „Nuclear Facilities of Serbia“, Mike Petrovića Alasa 12-14, Vinča, Belgrade
+381628869118, natasa.lazarevic@nuklearniobjekti.rs

JOVANA KNEŽEVIĆ

PC „Nuclear Facilities of Serbia“, Mike Petrovića Alasa 12-14, Vinča, Belgrade
+381628869113, jovana.knezevic@nuklearniobjekti.rs

DALIBOR ARBUTINA

PC „Nuclear Facilities of Serbia“, Mike Petrovića Alasa 12-14, Vinča, Belgrade
+381628869007, dalibor.arbutina@nuklearniobjekti.rs

Abstract: Public Company "Nuclear Facilities of Serbia" has an established risk management system. This system is designed to reflect the regulatory requirements related to the financial management and control system, as well as the requirements related to the standards SRPS ISO 9001:2015 and SRPS ISO/IEC 17025:2017 regarding the actions to address risks and opportunities. The adequacy of the established system corresponds to the complexity and activities of the company as the only nuclear operator in the country, taking into account the concept of risk-based thinking, risk analysis and preventive actions which are components of planning and implementation of nuclear facilities management activities. The efficiency of the risk management system ensures that the company's risk profile is in accordance with the established level of risk acceptance, which is confirmed by appropriate certification and accreditation. This paper presents the methodology of risk management in PC "Nuclear Facilities of Serbia" with challenges to improve and support business strategy and development.

Keywords: risk, control, management, information, organization.

1. INTRODUCTION

The main and highest risk in the work of the Public Company of "Nuclear Facilities of Serbia" is the occurrence of a radiological or nuclear emergency during the management of nuclear facilities. A radiological or nuclear emergency may be the result of regular activities, but also of diversion, sabotage and terrorist attack.

All activities are performed at a high quality level of radiation and nuclear safety and security, with a constant emphasis on their improvement, and in accordance with the licenses and authorizations issued by the regulatory body and the established quality management system according to the standards SRPS ISO/IEC 17025:2017 and SRPS ISO 9001:2015, trained staff and available resources[1].

An integral part of the quality management system is the risk management process. This process is designed to identify potential risk events that can affect the business, then to respond to the identified risks through the system of internal controls, as well as to communicate and supervise the risks.

All activities are planned, taking into account the risk and the obligation to reduce it to the lowest possible level, which is made possible by the implementation of measures in each business process [2].

The entire process of risk management is supported by the established system of financial management and control, which is a regulatory requirement and consists of a set of adopted strategies, policies, procedures and activities that provide reasonable assurance that the goals of the long-term and medium-term plan of the business strategy and development of the company can be to achieve in a proper, economical, efficient and effective way [3].

2. RISK MANAGEMENT PROCESS

According to its characteristics, system of risk management is designed to be continuous in its application and to refer to the entire internal organization, work resources and human resources in the company. The system includes two key and strategic documents that define the entire risk management process: Risk Management Strategy and Methodology for identifying, measuring, communicating and monitoring risks.

The risk management strategy defines the structure of the risk management process, which consists of four sub-processes that maintain their interdependence of functioning: risk assessment, risk treatment, risk communication and risk supervision. In addition, content of appendix of this document shows risks to which business processes are exposed and which represent the context of understanding the environment and internal organization of work processes [4].

The methodology for identifying, measuring, communicating and monitoring risks defines the procedures for managing the aforementioned structure of the risk management process [5].

These documents are reviewed periodically in terms of effectiveness, as well as in situations where there are significant changes related to the component of the control environment of the COSO (Committee of Sponsoring Organizations of the Treadway Commission) system of internal controls, which the company applies as a regulatory requirement of the system of the financial management and control.

2.1. Risk assessment

Risk assessment includes three sub-processes: identification, analysis and classification of risks.

The risk identification proceeding is carried out in relation to the created Map of Business Processes, which provides an overview of all processes and sub-processes that are defined by the Rulebook on the Organization and systematization of work in the company. Risk identification is focused on data collection in order to determine the types of risks to which the processes and sub-processes from the Business Process Map are exposed. In addition to the type of risk, the sources of risk are also defined, which can be: intentional or accidental error, mechanical execution of activities, inexperience or insufficient number of executors, and force majeure. The process of identifying the type of risk as well as the source of risk is carried out by managers of organizational units in the form of self-assessment, since managers know best the business processes they manage and can most objectively comment on which risk the business process is exposed to [6].

As part of the risk analysis, each risk is considered in relation to its components: the impact of the risk, the likelihood of the realization of the risk event, the vulnerability to the risk event and the speed of the realization of the risk. The basis of the risk analysis proceeding is the assignment of a weight value that expresses the significance of that risk in relation to its components. The weighting values assigned represent the significance of the risk component to which business processes are exposed in the execution of their activities. Each weight in relation to its given description corresponding to the significance of the risk, which can be of no significance, low, medium, high or extreme risk is expressed in relation to its assigned numerical value on the weight value scale.

The values on the weighting scale are in the range from 1-

5. By selecting weights per component and multiplying them, the measured risk value per process is obtained. Each assigned weighting value is presented in its descriptive form. The descriptive description is designed to specify the situation that corresponds to the assigned weighting level. Based on the assigned values, the significance of the risk components on the realization of the risky event is determined. The risk calculation procedure itself primarily boils down to the multiplication of the risk impact component and the likelihood of the realization of the risky event. In this way, the inherent value of the risk is expressed without the application of control activities that serve to mitigate its value.

The risk impact component has a dominant importance, because it is the one that shows what can happen with the realization of a risky event and what its consequences are. On the other hand, the likelihood of realization is a key component, because whether a risky event can happen and how often, it determines the character of the risk as well as the internal controls that are applied to mitigate the impact of such a risky event.

An example of the description of the value for the likelihood of the realization of a risk event of high risk significance is given in table 1. An example of the description of the significance of a high risk in relation to its weighting value according to the risk impact component is given in table 2.

Table 1. Risk component - The likelihood of occurrence of a risk event of a high level of significance

Weight value	Description of Likelihood	Time Frame
4	It is likely that the event will come occur	Event will happened once per 6 months

Table 2. Risk component – Impact of risk

Weight value	Description of criteria
High level of significance	Absence of control mechanisms and activities that can have a material impact on the execution of business process activities.
	There is an outflow of professional personnel, which causes a decrease in the effectiveness of control activities.
	Risk event prevention and detection mechanisms have shortcomings that may miss signaling events that have a material impact on human and material resources.
	The resulting failures in business have a materially significant impact and cannot be covered from the Financial result/Capital.
	Absence of reputational risk management mechanisms due to which attention-grabbing information can flow unchecked.

By calculating the inherent risk value, the need to introduce internal controls is determined, especially if the exposure is materially significant. The amount of the costs of introducing controls can be in the maximum amount of consequences that a risky event can bring if it

is realized. The introduced control and verification of its effectiveness should result in a residual risk that corresponds to the defined level of acceptable risk.

Beside to this, another model is used that takes into consideration the impact and vulnerability on the risk event, if this determinant determines the value of the risk more precisely. This risk calculation proceeding is applied at the level of each sub-process and organizational unit process within the Business Process Map. Since each process can be exposed to more risks, the one that has the greatest material impact on the realization of the risky event and its consequences for the business is taken into consideration. The measured risk values can range from 1-25 weighting points. Depending on the obtained values of the measured risks, their importance is determined, i.e. risk classification. Based on the measured significance of the risk, it is determined which risks have priority in their monitoring and action according to prevention measures.

The calculated risk value per business process is considered in relation to the Risk Measurement Matrix according to Table 3, as well as in relation to the defined clusters of obtained weighting points that determine the importance of risks and their consideration priority in relation to supervision and action according to prevention measures according to Table 4.

Depending on the selected weight per risk component, its measured value depends, as well as the classification of the significance of such measured risks. The value of the measured risk is a function of the assigned weighting values for the risk components.

Table 3. Risk Measurement Matrix

		Likelihood				
		1	2	3	4	5
Impact	1	2	3	4	5	
	2	4	6	8	10	
	3	6	9	12	15	
	4	8	12	16	20	
	5	10	15	20	25	

Table 4. Risk significance of business processes

1-5	6-10	11-15	16-20	21-25
No significance	Low risk	Medium risk	High risk	Extreme risk

Those business processes whose significance has been determined at the level of high or extreme level of risk significance have priority in consideration. These processes form the basis for consideration of the risk treatment procedure and creation of the Risk Register.

Since the process of risk management is by its nature continuous, analyzes of the measured significance of risks are performed periodically. These considerations for business processes are constantly applied, because the measured values are not constant over the time and can change according to their significance and priorities for action. These changes can occur due to changes in the business environment as well as changes in the work process itself. For this reason, the data collection procedure is carried out through a quarterly questionnaire

on realized risk events at the level of organizational units.

This questionnaire is made up of assumed risk events that can have an impact on business processes. In the questionnaire, it is stated whether any of the risky events took place, along with a description of the risky event, what specifically happened and what consequences resulted from the realization of the risky event. For each listed risk event, data is entered as to whether its realization resulted in material or monetary damage, as well as the type of risk associated with such a risk event.

The questionnaire is also an instrument of communication about risks, as it takes into account the corrective measures taken in order to mitigate its effects, as well as reporting on the state of the risk management system. In this way reported risk events it can be seen the scenarios of the realization of the events, their frequency of realization, the source of the risky events as well as the location of its realization concerning the specific organizational unit and the business process that is subject to its realization.

Based on the questionnaire in which the data on realized risk events and the Risk Register are entered, it is determined through self-assessment whether the significance of the risk has remained at the same reference values during the period or whether there have been changes. All resulting changes are recorded in the Map of business processes. In this way, the updating of the Map of business processes and current values of the significance of risks is ensured.

2.2. Risk treatment

The risk treatment proceeding aims to show in which way will be resolved the question of materially most important risks. In this regards there is four available options to take into consideration: risk acceptance, risk avoidance, risk mitigation and risk transfer. Which option will be chosen depends on each individually identified materially significant risk.

Within the proceeding of risk treatment, the following activities are carried out: designing a map of the interaction of risks and risk events, creating a risk register and determining which risks are prioritized for consideration and taking corrective actions.

The interaction map consists of all risk events reported through quarterly questionnaires.

Relating each reported risk event to another reported risk event determines whether the event is related separately to the business process of a specific organizational unit that reported the risk, or whether such a risk event has an impact on the realization of another risk event that is related to another business process other organizational units in the company. Likewise, whether a risky event by its nature leads to an interruption in the work of business processes of all organizational units and on which the company has no influence, as may be the case when there is an interruption in the supply of electricity or an internet network failure. An example of an interaction map is given in Table 5.

Table 5. The interaction map

Interaction map	Risk event 1
Risk event 1	-
Risk event 2	X
Risk event 3	X
Risk event 4	X
Risk event 5	X

In this way, it is determined whether there is a risk event that is primary by its character and on which it depends, whether other risk events are only a consequence of its realization, and in this regards the real source is determined that needs to be treated.

The second segment of the risk treatment procedure refers to the preparation of the Risk Register. This document represents a regulatory requirement and contains data related to business processes for which risk analysis has determined which risks have the highest material significance. The essence of the Risk Register consists of the description of the risk, the measured significance, the chosen procedure for treating the risk, the response to the risk in the form of activities and measures taken to mitigate the risk and/or reduce it to an acceptable level, responsible person for execution of the response to the risk, the deadline for the implementation of corrective measures, the date when the verification of the execution of the measure was done, as well as the status of the implementation of the measures, which can be that the measures were executed, in the process of execution, partially executed, or the implementation has not started. In accordance with the regulatory requirements, this control activity is carried out periodically every six months or less if there is a specific need for it [7].

2.3. Risk Communication

Risk communication is the most important feature of the risk management process and it takes place permanently. The exchange of information about risks is transparent and takes place in two directions: from top management to employees and vice versa.

For the understanding the importance of risk management in the company, the Working group for financial management and control periodically submits materials in written or electronic format on topics related to the risk management process. At the sessions of this working group, risk management issues are periodically considered through quarterly questionnaires on realized risk events, risk register, evaluations of internal controls, annual questionnaires on the state of the COSO internal control system, as well as annual reporting on the state of the risk management system [8].

Likewise, an important role in assessing the effectiveness and communicating about risks is played by the internal audit activity established in the company. Internal audit, on its part, and in accordance with its strategies and work plans, conducts engagements of organizational units according to business processes where the materially most

significant risks have been identified through risk analysis. These engagements check the effectiveness of the risk management process, internal controls and governing of business process. Through its reports internal audit communicates with the management of the company about the identified risks and ways to manage them in such a way that they are managed within the scale of risk profile and an acceptable risk level. This procedure includes actions related to the creation of a database of recommendations on an annual level, in which the realization of the implementation of given internal audit recommendations is monitored. Implementation of recommendations and removal of identified deficiencies that imply the effectiveness of the system of risk management processes is the scope of work and supervision carried out in this matter by the Audit Supervision Committee as a body established in accordance with the regulatory requirements described under the law governing the work of public companies in the country.

In addition to the above, the documentation of the risk management system is an integral part of communication on this issue with regulatory authorities and external controls during their periodic checks. The topic of risk management is an indispensable item in every external control that is carried out, which indicates the importance of the topic for the needs of looking at the way of management and achieving the goals of the company's operations [9].

2.4. Risk Supervision

Supervision of the risk management system is set up to support the application of The Three Lines of Defense Model. This mechanism clearly defines the role and responsibility of management, organizational units, as well as internal audit.

The mechanism itself is designed to ensure the exchange of information on key risks with all interested parties participating in the business risk management process [10].

The first line consists of organizational units of the sectors and they are the holders of the risk management process. This is about organizational units and business processes that are key for performing business activities.

Managers of organizational units and their employees are a resource that manages the business process and who applying procedure activities carries out actions related to the identification and response to risks. In this way, the potential cost and damage that a risk event can produce is directly affected.

Here, the key emphasis is placed on risk awareness as a business principle that indicates the presence of thinking and reacting to the appearance of factors that can lead to the realization of a materially significant risk event.

The second line of defense consists of organizational units that basically support the first line. These organizational units include the departments of commercial and foreign trade affairs, legal, HR, general affairs, financial and accounting affairs, occupational safety and health, and information technology.

Their task is to provide support in the activities carried out by the first line of defense, which relate to the execution of those activities in which the second line also participates, in control activities that ensure the regularity of the execution of process activities of organizational units belonging to the first line of defense.

If this line detects a factor that implies the stated influence of the realization of a risk event, it signals the first line of defense in order to prevent the possibility of the realization of a risk event.

The third line of defense consists of an internal audit activity that considers the effectiveness of risk management from the first two lines of defense and, if they have not identified a risk, it signals how to react to it.

Further transfer of risk supervision is aimed at the work of the Audit Committee as a body that provides support in the work of the Supervisory Board as the highest management body in the company. At its meetings, the Audit Committee considers issues related to the risk management, primarily financial, as well as others that may arise from the performance of the company's activities [11]. In accordance with the informations which are provided by the Internal audit and the Head of the Working group for financial management and control, proposals are made in the form of actions to be taken in order to manage risks effectively.

The ultimate instance consists of the company director and the company's supervisory board. All questions that direct their attention to the topic of risk management are directed at these positions that are at the top of management and business decision-making process in the company. As the holders of the risk management process, by directing them, they provide actions that should be taken in order to manage the company in accordance with the entrusted resources and goals that should be achieved from the company's operations.

3. RISK MANAGEMENT IN PRACTICE - FRAUDULENT ACTIONS

Fraud risk management is an integral part of the Risk Management Strategy and the Financial Management and Control System. For these needs, the Policy of Combating Fraud was defined, based on examples of good risk control practices and fraud response plans. The main objective of the policy is the protection of property and reputation through the adequacy of risk management and the application of controls. The fraud risk management process includes assessing its overall vulnerability to fraud as well as the scope and magnitude of fraud risk from inaccurate financial reporting and misappropriation of assets. The risk is considered periodically or more often if there are negative impacts. A special segment of fraud risk management is the development of fraud awareness, ethical values and employee training.

For the purpose of performing a risk analysis of fraudulent activities, a questionnaire is used that is divided into two key areas in which the potential risk of committing a fraudulent activity is assessed. Those areas are dishonest financial reporting and misappropriation of

assets. On the basis of the completed questionnaire, the likelihood of the occurrence of fraudulent actions are considered. When the questionnaire is processed, the analysis of the risk of fraudulent actions is carried out. Risk analysis of dishonest financial reporting and misappropriation of assets is considered in relation to risk factors related to possible incentives/pressures, opportunities and attitudes, i.e. rationalization of fraudulent actions. Each of the mentioned factors is considered in relation to a predefined set of indicators which is considered in relation to risk components, namely impact, likelihood, vulnerability and speed of realization. Each component is assigned one of the offered weights.

Depending on the selected weighting value, a calculated risk value is obtained (impact*likelihood or impact*vulnerability). The value that corresponds to the actual situation is the one that is taken. The evaluation proceeding is carried out according to the principle of self-assessment. Indicators for which it is determined that their measured risk value is at the level of significance that requires risk treatment are taken into consideration with the aim of defining the control measures that should be taken in order to manage the risk of fraudulent actions. The proposed measures are being considered by the Working Group for Financial Management and Control. The established measures are integral part of the Risk Register and as such are binding upon their application at the level of each organizational unit.

On a periodic basis, the execution of measures by organizational units as well as the possibilities for further improvement are considered. A confidential line for reporting fraudulent actions was also created, to which employees can make reports if they have information that may indicate suspicion of fraudulent actions.

According to the Action Plan of the Working Group for Financial Management and Control, employees are trained on topics about the system of ethical values, corruption and fraud.

The Policy of Combating Fraud prescribes the conduct of disciplinary proceedings against employees in order to determine the validity of the suspicion of committing a fraudulent action, as well as to make appropriate conclusions in accordance with the presented argumentation and material evidence.

In connection with the performed procedures, regular reports are carried out, which are an integral part of reporting on the risk management system as well on financial management and control.

3. CONCLUSION

The public company "Nuclear Facilities of Serbia" has successfully implemented the requirements of standards and financial management and control related to the design and implementation of the risk management system. The risk management system is documented, adequate mechanisms have been created for the identification and evaluation of risks, their ranking by importance and the determination of monitoring priorities.

A Risk Register was created, which is periodically reviewed for the effectiveness of the controls applied in order to manage business risks. A system of reporting on the state of the risk management system was implemented. An internal audit activity has been established, which provides assurance services on the effectiveness of the risk management system, internal controls and governing business processes. Likewise, a Working group for financial management and control was formed, which primarily deals with monitoring the risk management system according to the adopted Action Plan for the establishment and further improvement of the financial management and control system.

An Audit Committee was formed to monitor the risk management process and make recommendations for its effective managing. External controls by Certification bodies, External audits and the State Audit Institution gave a positive opinion on the established risk management system in the company.

The risk management process is an integral part of daily activities and as such is integrated into every business process. Further improvement of this system will maintain requirements regarding the introduction of new technologies, business processes and information technologies as support in performing regular business activities.

References

- [1] SRPS ISO/IEC 17025:2017, General requirements for the competence of testing laboratories and calibration laboratories;
- [2] SRPS ISO 9001:2015, Quality management systems - Requirements;
- [3] Law on the Budget System ("Official Gazette of RS", No. 54/2009, 73/2010, 101/2010, 93/2012, 62/2013, 63/2013 - amended, 108/2013, 142/2014, 68/2015 - Dr. Law, 103/2015, 99/2016, 113/2017, 95/2018, 31/2019, 72/2019, 149/2020 and 118/2021);
- [4] PUBLIC COMPANY "NUCLEAR FACILITIES OF SERBIA": Risk Management Strategy, Belgrade, Vinča 2018.
- [5] PUBLIC COMPANY "NUCLEAR FACILITIES OF SERBIA": Methodology for identifying, measuring, communicating and monitoring risks, Belgrade, Vinča 2018;
- [6] SRPS ISO 31000:2019, Risk management - Guidelines;
- [7] MINISTRY OF FINANCE, Central Unit for Harmonization: Guidelines for Risk Management, Belgrade, 2020;
- [8] Rulebook on common criteria and standards for the establishment, functioning and reporting of the financial management and control system in the public sector ("Official Gazette of RS", No. 89/2019);
- [9] PROCEEDINGS OF THE SINGIDUNUM UNIVERSITY INTERNATIONAL SCIENTIFIC CONFERENCE: Risks in modern business conditions, Singidunum University, Belgrade, 2016;
- [10] INSTITUTE OF INTERNAL AUDITORS (IIA): Three lines of defense for an effective risk management process and internal control system, Association of Internal Auditors of Serbia, Belgrade, 2013;
- [11] Law on Public Companies ("Official Gazette of RS", No. 15/2016 and 88/2019);



DATA-DRIVEN RELIABILITY OF ELECTRONIC EQUIPMENT

SLAVKO POKORNI

Information Technology School, Belgrade, slavko.pokorni@its.edu.rs

Abstract: Reliability is important especially for military, medical and other professional equipment. Reliability management and/or prognostic reliability calculation have always been data-driven. The definition of data-driven concept, then definition of reliability is briefly discussed, and after that the impact of uncertain data on prognostic reliability calculation and also reliability and availability of data is discussed in this paper.

Keywords: data-driven, reliability, availability, data, equation.

1. INTRODUCTION

Reliability as theory and practice appeared at fifties of the last century. First it was applied to hardware, then software and human. Reliability is still actual and very important in nowadays [1].

Reliability has always been data-driven [2]. Without good data prognostic reliability is useless, in spite of good reliability model. So, input data in reliability model and in decision making system in reliability management are of crucial importance.

How to obtain good data is big problem. We can rarely get such data from producers of components or devices (electronic, mechanical) and/or software. Up to nineties of last century we were able to use data about failure rate of electronic elements from well known military handbook MIL-HDBH-217 [3]. But these are data from the past, and the last version of that handbook is from 1995, so that data are obsolete [1]. And that data is statistical, and reliability (in other word probability) which we calculate based on this data is valid only with a certain probability. We can use some data from other sources but they also usually are not up to date.

So, we can put the question: calculate reliability or not to calculate? From this author experience (of almost 30 years of teaching (talking to students that input data is the biggest problem in reliability calculation) and 40 years of practice in reliability calculation of electronic equipment) it is better do the calculation even based on an obsolete data, specially at the beginning of designing device or system, because it can help to chose better solution (alternative) from the point of view of reliability.

Of course, when we need to decide if such devices, software or system satisfies certain required reliability requirements, then we can not rely on obsolete or uncertain data.

In [4] is concluded that the problem is how to cope with large amounts of data on the one hand, and with very small amounts of data on the other hand. Both of these can be the case in reliability and maintenance, and more often we have problem with not enough or no any data.

First the definition of data-driven concept, then definition of reliability is briefly discussed, and after that the impact of uncertain data on prognostic reliability calculation and reliability and availability of data is discussed.

2. DEFINITION OF DATA-DRIVEN

Being data-driven means that all decisions and processes are based on the data. This is most evident in the field of big data [2, 5]. It is in connection with data science, data mining, etc. The term data-driven is used in many fields, also in reliability.

Being based on data means using data, and using data means at least collecting and analysing data. And this implies using some kind of communication. To achieve this, we as a person or organisation use technology (different devices, networks, software, Internet of Things, etc.), and anything of these can fail. Of course, we want to avoid failures and resolve them if they happen, and this is the task of reliability.

Data-driven as a term describes a decision-making process which involves collecting data, extracting patterns and facts from that data, and utilizing those facts to make inferences that influence decision-making [6].

Making decisions, is a fundamental component of business and personal management. Good decisions lead to success while poor decisions lead to loss or failure. And this depends of data.

Every organisation today aims to be data-driven. Data-driven decision making is the process of making organizational decisions based on actual data rather than intuition or observation alone. This is the case in reliability also.

Before analysing impact of data on reliability, we will, in short, explain the definition of reliability.

3. DEFINITION OF RELIABILITY

Reliability is very important not only in military and professional products. Reliability in nowadays also plays a crucial role for safety and adoption of driverless cars.

Reliability is the probability that a device will meet intended standards of performance and deliver the desired results within a specified period of time under specified (environmental) conditions [2].

4. IMPACT OF DATA ON RELIABILITY

As we stated before, reliability has always been data-driven (if being data-driven means that all decisions and processes are based on the data), and valid and relevant data always has been main problem. It only depends if that data is historical (from past experience on failures) or data gathered from new device for which we calculate reliability. Of course, data gathered from new device for which we calculate reliability are more valuable than data from the past experience, because data from past are from different devices and older components, if we are using data from handbooks, for example MIL-HDBK 217. Data about failure rate of new components are rare available from producers.

In MIL-HDBK-217E (1986) is stated that „Considerable effort is required to generate sufficient data on a part class to report a statistically valid reliability figure for that class. Casual data gathering on a part class occasionally accumulates data more slowly than the advance of technology in that class; consequently, a valid level of data is never attained.“ [3].

In MIL-HDBK-217F (1991) is stated “The first limitation is that the failure rate models are point estimates which are based on available data.”

Obviously, there are problems to gather sufficient and good data, in spite of our effort. The problem is not only insufficient data, but also accuracy of that data.

We will discuss impact of data on reliability from several aspects: accuracy, availability, and up to date of data, experience, culture in organisation, and etc. Data also are the base for reliability test developing.

Reliability calculation (or better to say estimation) is always predictive (prognostic) because we want to know what will happen in the future, for example what is probability that that device will not fail after a certain time of using. First let us see how error or accuracy in input data in simple reliability model (reliability block diagram, RBD) can affect results for prognostic reliability calculation. In so called Parts Count reliability calculation which is implemented in MIL-HDBK-217, serial configuration RBD model is used (Fig. 1.) [7].

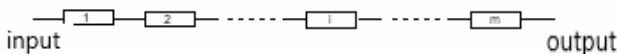


Figure 1. Serial RBD model

Fig. 2. shows reliability of serial RBD model R_s as function of reliability of element (all elements are with the same reliability R) and number of these elements m . From Fig. 2. we can see that error in input data (if we consider difference in R as an error in input data) for reliability of one element has bigger impact on reliability when system has more components, and this is usually the case. For example if we have serial RBD with 5 elements, and reliability of each element is $R=0,8$, than error of

$\pm 10\%$ will produce error in reliability of system R_s of + 61% and - 41%.

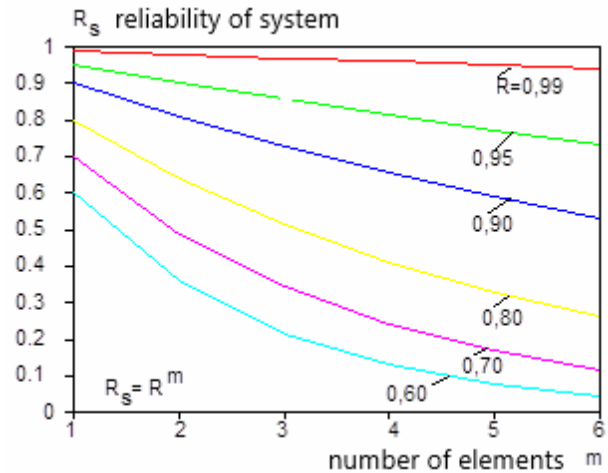


Figure 2. Reliability of serial RBD model

In Fig 3. is shown parallel RBD model of a system. Fig. 4. shows reliability of parallel RBD model as function of reliability of element (all elements are with the same reliability) and number of these elements n . From Fig. 4. we can see that error in input data for one element has smaller impact on reliability when system has more components, but in this case system is more costly. Adding second element with mean time to failure (MTTF) will increase mean time to failure of system (MTTF_s) for 50%, adding third element for 33%, adding fourth element for 25%, and this is obvious from equation [7]

$$MTTF_s = MTTF \left(1 + \frac{1}{2} + \dots + \frac{1}{n} \right) \quad (1)$$

So, adding more elements in parallel to increase reliability will more increase cost then reliability. Reliability and cost are mutually dependent. Higher reliability means higher cost, but cost for maintenance will be lower.

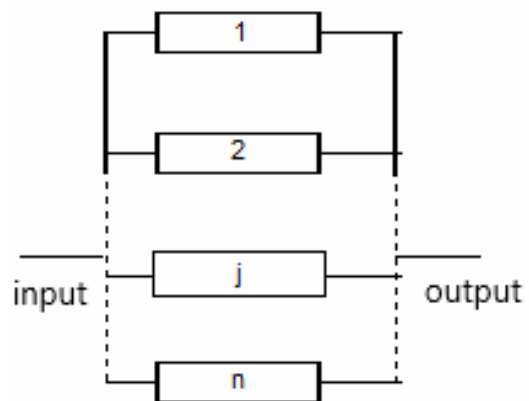


Figure 3. Parallel RBD model

Experience of this author has shown that the calculated prognostic MTBF of electronic equipment, using MIL-HDBK-217, should be at least or about twice of the required MTBF in order to have operational (actual, correct) MTBF equal to required (original) MTBF and that was applied as a rule when Parts Count reliability calculation has been made [7].

This is not only experience of this author that the problem is also in inadequate input data of electronic elements and inadequate estimation of this input data in the calculation of reliability [7].

And another problem with data is when we have small number of produced devices, so we have not enough data.

Another problem is with devices with very high required reliability: In this case we will get real data after a long time after entering this devices in usage.

Availability of good data is very big problem, specially today, when technology is changing very fast, and some components are very reliable (but we don't know how much) and do not have timely and accurate data about its failure rate, in other words reliability.

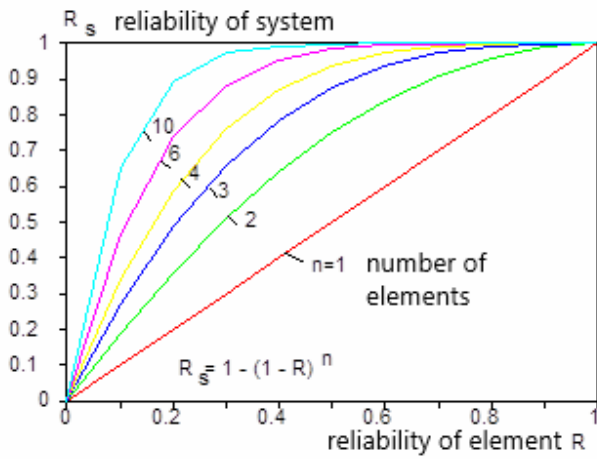


Figure 4. Reliability of parallel RBD model

One solution for problem when there is not enough relevant data is seen in so called Physics of failure, but it is applicable in wear area of failure rate. But in Physics of failure we again have problem not only with relevant data but also of knowledge of different processes in component material [1].

Besides of input data in models for reliability calculation, data from reliability analysis of a system or device can tell us more. For example, in [8] The Boeing 787 Dreamliner reliability is analysed using data-driven approach. From the various documents and trends they concluded that Boeing did not adopt an effective Reliability Program Plan, where best practice tasks are implemented to produce reliable products. Boeing opted to widen its supplier base and reduce costs by including manufacturers who were new to the aircraft development industry. The events that led to delays during manufacturing and failures during operation are a testament to Boeing's flawed practices.

Just as an example let us see what they concluded (learned) from that data. Lessons learned:

- Short development cycle and highly complex supply chains,
- Lack of accurate and timely information sharing,
- Lack of relevant data,
- Lack of valid testing on innovative technologies,
- Difficulty in fault detection,
- Lack of balance between autonomy and oversight.

Furthermore, these deficiencies are seldom independent of each other and can have a compounding effect on product reliability.

Data quality is of course only one problem in reliability. In [9] it is stated that there is no standard method for creating hardware reliability prediction, so predictions vary widely in terms of methodological rigor, data quality, extent of analysis, and uncertainty, and documentation of the prediction process employed is often not presented. Because of that IEEE has created a standard IEEE Std.1413 (Standard Framework for the Reliability Prediction of Hardware) in 2009.

Gathering good data is in connection with people and organization culture. The most important part of the development of a reliability program in the organization is to have a culture of reliability. It is extremely important that everyone who is involved in the creation of products, from top to down, realize that a good reliability program is necessary for the success of the organization [7, 10].

The reliability effort produces and uses a different amount of information and data.

One possible solution when there is not enough relevant data and we can not derive analytical reliability model, is simulation [11]. As an example of not so complex problem is illustrated in [12].

Reliability is connected with maintainability. Reliability and maintainability are important factors in the total cost of equipment. An increase in maintainability can lead to reduction in operation and support costs. For example, a more maintainable product lowers maintenance time and operating costs. Furthermore, more efficient maintenance means a faster return to operation or service, decreasing downtime [13]. Again, we need good and timely data.

5. RELIABILITY AND AVAILABILITY OF DATA

We can discuss also reliability of data, and availability of data. In order to build trust in data, it's critical that it's reliable, which means that it's complete and accurate.

Data reliability means that data is complete and accurate, and it is a crucial foundation for building data trust across the any organization. Ensuring data reliability is one of the main objectives of data integrity initiatives, which are also used to maintain data security, data quality, and regulatory compliance [14, 2].

Reliability leaders need reliable data to make reliable decisions. So, in data-driven reliability, data reliability is of crucial importance. Data reliability is not the same as data validity. The reliability of the data is based on the validity, completeness, and uniqueness of the data [2].

In reliability, nowadays we are facing not only with lack of good data, but with lack of any data. People dealing with reliability calculation can see that obviously.

If we using internet of things (IoT) to gathered data, because of unreliable IoT, data can be missing, incomplete and/or corrupted [2].

Data for maintainability are usually gathered from sensors or IoT, if these are not reliable, data can also be unreliable. Unreliable IoT can produce unreliable data as input in decision-making system, so decision can be wrong.

Similar situation can be with artificial intelligence incorporated in decision-making system. Can artificial intelligence recognize bad data, or we will believe in decision get in such way.

6. RELIABILITY EQUATION

Because data-driven reliability system includes hardware, software, sometimes humans, and data, we suggest assessing the reliability of the data-driven reliability system by changing the equation from the [2, 15, 16] to next:

$$R_S(t) = R_{HW}(t)R_{SF}(t)R_H(t)R_D(t) \quad (2)$$

where R_{HW} , R_{SF} , R_H and R_D are reliability of hardware, software, human and data subsystem, respectively.

7. CONCLUSION

Reliability is still very important. Reliability has always been data-driven and valid and relevant data always has been main problem. Without good data prognostic reliability is useless, inspite of good reliability model. It can be the case with maintainability also.

In reliability calculation we usually have bigger problem with not enough relevant data than with large amounts of data. The problem is not only insufficient data, but also accuracy of that data.

In reliability calculation usually data from MIL-HDBK-217 are used, and these are data form the past, usually obsolete. Up to date data of failure rate of elements are rarely available.

References

- [1] POKORNI S.: *Problems of reliability prediction of electronic equipment*. 6th International Scientific Conference on Defensive Technologies OTEH 2014, 9-10 October 2014, pp 835-838
- [2] POKORNI, S.: *The Reliability of Data-driven Internet of Things Systems*, Annals of Spiru Haret University. Economic Series, 2021, 21(4) 43-52, doi: <https://doi.org/10.26458/2141>, <https://drive.google.com/file/d/18medRDVNqEJzqbeORQUkobRgItBnu2Xu/view>
- [3] MILITARY HANDBOOK, Reliability Prediction of Electronic Equipment, Department of Defense, Washington DC, MIL-HDBK-217E, 1986.
- [4] POKORNI S.: *Current State of the Artificial Intelligence in Reliability and Maintainability*, Vojnotehnički glasnik/Military Technical Courier, 2021, Vol. 69, Issue 3, pp. 578-593, DOI: <https://doi.org/10.5937/vojtehg69-30434>, ISSN 0042-8469, UDC 623 + 355/359
- [5] Techopedia. Available at <https://www.techopedia.com/definition/18687/data-driven>
- [6] Northeastern University. <https://www.northeastern.edu/graduate/blog/data-driven-decision-making/>
- [7] POKORNI S.: *Reliability and maintenance of technical systems*. Military academy, Belgrade, 2004. (In Serbian)
- [8] PANDIAN G., PECHT M., ZIO E., HODKIEWICZ M. Data-driven reliability analysis of Boeing 787 Dreamliner. Chinese Journal of Aeronautics (on line) Available at: <https://www.sciencedirect.com/science/article/pii/S100936120300546>
- [9] ELEARTH G. J., PECHT M., "IEEE 1413: A Standard for Reliability Predictions", *IEEE Transactions on Reliability*, Vol. 61, No. 1, March 2012, pp. 125-129
- [10] POKORNI S.: *Reliability prediction of electronic equipment: Problems and experience*. 7th International Scientific Conference on Defensive Technologies OTEH 2016, Belgrade, 6-7 October 2016
- [11] POKORNI S.: *Reliability estimation of a complex communication network by simulation*. 19th Telecommunications Forum (TELFOR) 2011. Proceedings of Papers, pp 226-229
- [12] POKORNI S., RAMOVIĆ R.: *Reliability and availability of telecommunication system of four ring connected stations*. Communications in Dependability and Quality Management, An International Journal
- [13] Data-Driven Aerospace Engineering: Reframing the Industry with Machine Learning <https://arc.aiaa.org/doi/10.2514/1.J060131> (on line): 20 Jul 2021 <https://doi.org/10.2514/1.J060131>
- [14] Talend. Available at <https://www.talend.com/resources/what-is-data-reliability/>
- [15] POKORNI S.: *Artificial Intelligence in Reliability and Maintainability*, 9th International Scientific Conference on Defensive Technologies OTEH 2020, Belgrade, 8-9 October 2020 (on line)
- [16] POKORNI S.: *Reliability and Availability of the Internet of Things*, Vojnotehnički glasnik / Military Technical Courier, 2019, pp. 588-600, 67(3), <https://doi.org/10.5937/vojtehg67-21363>



IMPLEMENTATION OF Y-FACTOR METHOD FOR NOISE FIGURE MEASUREMENT USING EMI MEASURING RECEIVER

NENAD MUNIĆ

Technical Test Center, Belgrade, nenadmunic@yahoo.com

ALEKSANDAR M. KOVAČEVIĆ

Faculty of technical sciences, University of Kragujevac, Čačak, aleksandarkovacevic1962@yahoo.com

NENKO BRKLJAČ

Technical Test Center, Belgrade, brkljacnenko@gmail.com

LJUBIŠA TOMIĆ

Technical Test Center, Belgrade, ljubisa.tomic@gmail.com

MIROSLAV JOVANOVIĆ

Technical Test Center, Belgrade, jovanovic.miroslav.77@gmail.com

Abstract: This paper presents the implementation of the Y-factor method for noise figure measurement using the EMI measuring receiver. The measurement results of the new method were compared with the results obtained using noise figure meters. Measurement results were compared using z-score criteria. The comparison of results was performed in order to confirm the accuracy of the new method.

Keywords: Noise figure, Y-factor method, Noise figure meters, z-score, Intercomparison.

1. INTRODUCTION

Different measuring equipment can be used during the tests. Their accuracy can significantly affect the reliability of the measurements. Therefore, “Ensuring the validity of results,” is a wonderful tool for laboratories confirming their end data is accurate and reliable [1]. In doing so, each laboratory must establish a program and procedure for validate its measuring procedures. Due to all the above, the Technical Test Center (TTC) [2], a specialized military scientific research institution, in accordance with the requirements of the quality management system [3], can develop and use a new measuring method procedure [4].

One of the ways to determine and review measuring accuracy for new development method is interlaboratory comparisons. Participation in intercomparison is one of the requirements for laboratories that are entering the accreditation process or have already been accredited [5]. Positive results of intercomparison are confirmation of the accuracy of measurements performed in the laboratory and the competence of that laboratory.

Intercomparison is performed at the request of the user. In doing so, the intercomparison is performed by the laboratory user of the measuring equipment, and if necessary, other laboratories and the competent metrological laboratory can also participate [4]. Measurement intercomparison means the comparison of metrological characteristics of meters of the same type and approximately the same measurement uncertainty under established conditions.

Due to the need to validate the accuracy of the implemented Y-factor method of measuring the noise figure using an EMI measuring receiver (in general, a spectrum analyzer), the Department for Electromagnetic Compatibility and Environmental Impacts in the TTC initiated and organized an intercomparison of the noise figure and gain measurement for the amplifier devices. A total of four meters from two laboratories, were used in this intercomparison. Three meters (one EMI receiver and two spectrum analyzers) were provided by TTC, while the noise figure meter was provided by the Military academy [6].

The intercomparison was made in two measurement variants: the first variant using a noise figure meter, while in the second variant software written in Matlab [7] was developed, which enables automated measurement of the noise figure by implementing the Y-factor method [8, 9]. It should certainly be noted that the noise figure meter itself uses the Y-factor method for measurement [10]. Measurement results were compared using the z-score criterion.

The goal of the intercomparison is to validate implementation of Y-factor method for noise figure measurement using EMI measuring receiver. Namely, the aim of processing the results of intercomparison of these measures is to analyze the results according to the criteria for measures of the same type and approximately the same measurement uncertainty, under established conditions, then to determine the acceptability of results, and thus confirm their applicability to measure noise figure and gain of RF amplifier.

2. INTERCOMPARISON CONDITIONS

The intercomparison was performed in the Laboratory for electromagnetic compatibility of Technical Test Center. The subject of the intercomparison is the implemented Y-factor method of measuring the noise figure and the gain level of the RF amplifier on the EMI measuring receiver with the corresponding values obtained using the noise figure meter and the spectrum analyzers.

A total of four laboratory values of noise figure and gain level were obtained using the following measuring instruments:

- HP 8970B, Noise Figure Meter (Lab 1);
- Agilent E4447A, PSA Spectrum Analyzer (Lab 2);
- Rohde&Schwarz, ESR26, EMI test receiver (Lab 3);
- HP 8568B Spectrum Analyzer with RF Preselector (Lab 4);

When using the noise figure meter (Lab 1), the Y-factor measurement method was implemented in the software of the instrument [10], while in the other three cases (Lab 2-4) a same method for automation of measurement and processing of measured values is implemented.

Intercomparison was performed by comparing the measured noise figure and gain values using Noise Figure Meter and spectrum analyzer/EMI receiver. The device

under test (DUT) was a pulse RF amplifier, MINI-CIRCUITS, model: ZPUL-30P, s/n: 15542.

Noise Figure measurements with consist of two main tasks:

- Calibration of the setup,
- Measurement of the DUT.

In both tasks, the noise level values are measured by the instrument and calculate the Y-factor values. Finally, the Noise Figure and Gain of the DUT are calculated.

2.1. Calculation (Y-factor method)

The Y-factor method is a widely used technique for measuring the gain and noise figure of the amplifiers [9]. It is based on the Johnson–Nyquist noise of a resistor at two different, known temperatures [11] (Fig 1).

The Y-factor method uses the measured noise power of the DUT output with a room temperature noise source (noise source off) at the input, and with a high temperature noise source (noise source biased with 28 V) at the input. Noise sources are commonly specified by their excess noise ratio or ENR value, which is expressed in dB. The relationship between noise temperature and ENR is shown in equation (1). The calibrated ENR values supplied by the noise source manufacturer are generally referenced to $T_0=290$ K.

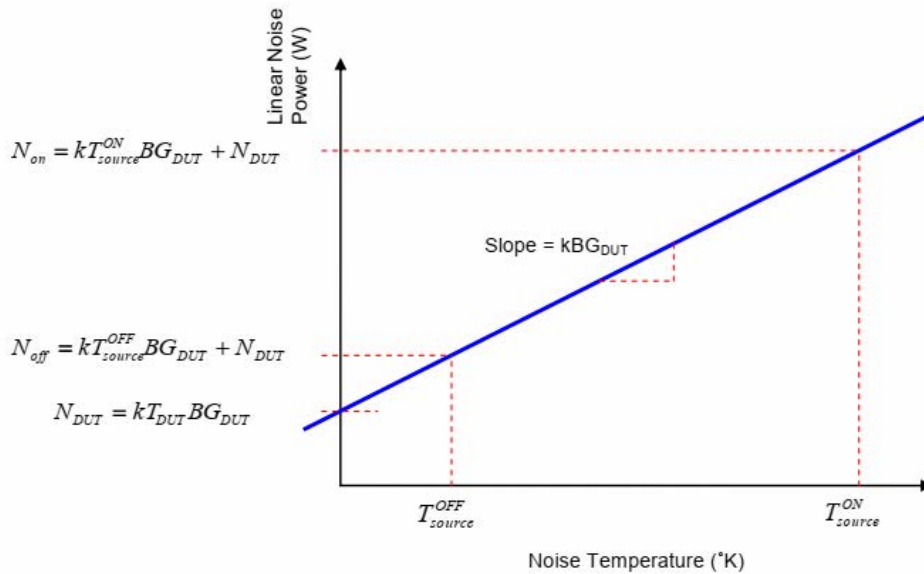


Figure 1. Diagram showing the Y factor variables.

$$ENR_{dB} = 10 \log\left(\frac{T_{source}^{ON} - T_{source}^{OFF}}{T_0}\right) \quad (1)$$

The Y-factor (2) is the ratio of the measured (linear) noise power at the DUT output when the noise source is “on” and “off” (fig 2).

$$Y_{dB} = \frac{N_{on}}{N_{off}} \quad (2)$$

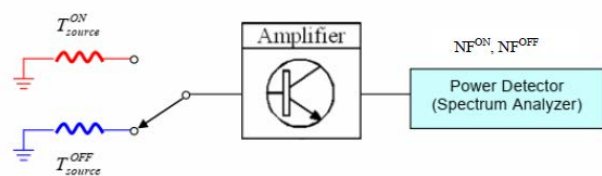


Figure 2. Diagram showing the Y factor noise figure variables.

The noise figure is given in simplified form in equation 3, using equations 1 and 2. The noise figure (NF) is defined as the noise factor (F) in units of decibels (4).

$$NF_{dB} = ENR_{dB} - 10\log(Y - 1) \quad (3)$$

$$NF_{dB} = 10\log(F) \quad (4)$$

2.2. Calibration

Connect the equipment as shown in Figure 3. (No DUT)

- Connect the output of the noise source to the RF input of the spectrum analyzer/receiver.
- Connect the noise source control of the spectrum analyzer/EMI receiver to the noise source (for HP 8568B Spectrum Analyzer noise source was driven manually by using external power supply).
- Set the spectrum analyzer to the desired test frequency.
- Set the RBW to be less than the BW of the DUT (For EMI receiver: 1 MHz).
- Enable the preamplifier.
- Set the minimum RF attenuator (For EMI receiver: 0 dB).
- Set the Reference level to a fairly low value (For example: -80 dBm.).
- Set the Log range to a fairly low value (For EMI receiver: 30 dB.).
- Select the RMS detector.
- Select a slower sweep time to RMS average the results (For example: 1 second.).
- Turn the noise source on or off and measure the noise power of the trace.
- Calculate the linear Y factor using equation (2).
- Finally, calculate a noise figure by using equation (3).

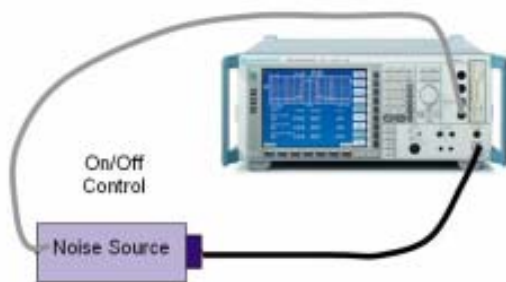


Figure 3. Connection diagram for the calibration step.

HP 346B noise source was used for these measurements. ENR value of the noise source is printed directly on the source in a table.

2.3. Measurement of the DUT

In this step the cascaded noise figure of the device under test and the spectrum analyzer are measured. The DUT is connected between the noise source and the spectrum analyzer/EMI receiver as shown in Figure 4. All settings and measuring are the same as during calibration. Finally, in this step we got noise figure for measuring step.

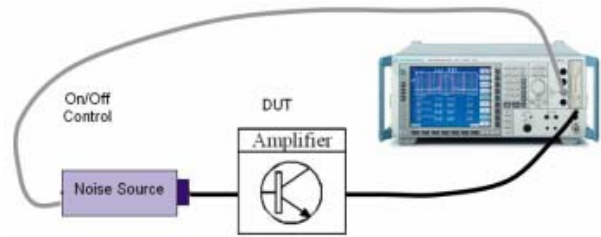


Figure 4. Connection diagram for the measurement of the DUT's noise figure.

In the final step calculate the gain and the noise figure of the DUT by applying the cascaded noise figure equations. Use equation (5) to calculate the linear gain of the DUT and equation (3) for noise figure.

$$G_{DUT} = \frac{N_{on}^{meas} - N_{off}^{meas}}{N_{on}^{cal} - N_{off}^{cal}} \quad (5)$$

At the same time, the characteristics of the measuring equipment meet the prescribed standards [12, 13].

Environmental conditions:

- temperature: 24 °C ± 2 °C,
- relative humidity: 50 % ± 15 %.

3. INTERCOMPARISON CRITERIA

As a criterion for evaluating the results of intercomparison, taking into account all the specifics of the measurement, the z-score was adopted, in accordance with the standard ISO 13528: 2005 [12, 13]. As four test samples participated in the comparison, the mean value of the test results for all samples was taken as the assigned (reference) value X_{ref} . The z-score should indicate whether the measured value deviates significantly from the assigned value, in our case from the mean value of the test results, taking into account the standard deviation σ .

The z-score is calculated as follows [12]:

$$z_i = \frac{x_{lab_i} - X_{ref}}{\sigma}, i = 1, 2, \dots, 4, \quad (6)$$

where:

x_{lab_i} test results for each sample ($i = 1, 2, 3, 4$),

X_{ref} the assigned (reference) value is the mean value of the test results of all samples,

$$x_{ref} = \frac{\sum_{i=1}^n x_{lab_i}}{n}, n=4, \quad (7)$$

σ standard deviation for non-repeat testing,

$$\sigma = \sqrt{\frac{\sum_{i=1}^n (x_{lab_i} - x_{ref})^2}{n}}, n=4. \tag{8}$$

The z-score coefficient can be positive or negative and determines the number of standard deviations of the data set from the arithmetic mean. A negative result indicates a value less than the mean, and a positive result indicates a value greater than the mean, with the average of each z-score weighing to zero.

The value of z-score is interpreted as follows:

- A result that gives $|z| \leq 2,0$ is considered to be acceptable;
- A result that gives $2,0 < |z| < 3,0$ is considered to give a warning signal;

A result that gives $|z| \geq 3, 0$ is considered to be unacceptable (or action signal) and the participants should be advised to check their measurement procedures following warning signals in case they indicate an emerging or recurrent problem [13].

4. RESULTS OF INTERCOMPARISON

The results of intercomparison the parameters gain (G) and noise figure (NF) of the pulse amplifier, for different frequencies are shown in Table I and represented in figures 5 and 6. Based on the results obtained from Table I and the calculation of mean and standard deviation, and using formula (6) obtained values of z-score coefficient, shown in Table II and Table III.

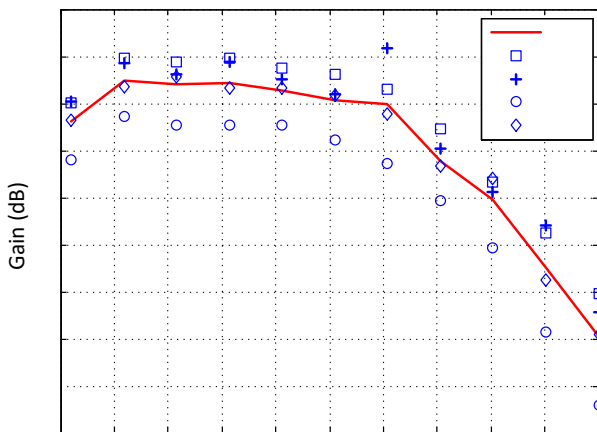


Figure 5. Results of gain (G) measurement of the pulse amplifier, for different frequencies.

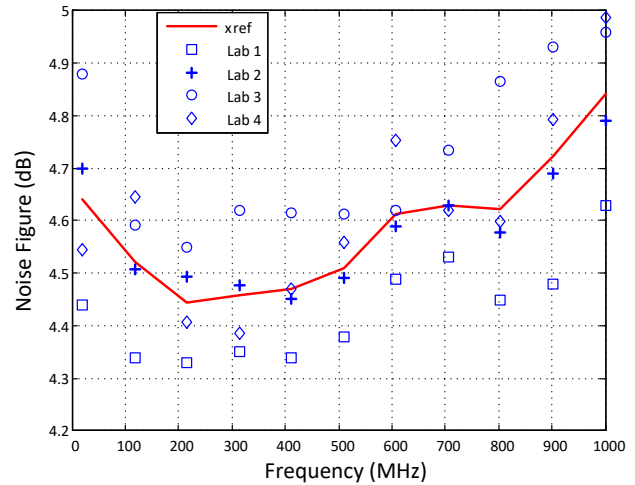


Figure 6. Results of noise figure (NF) measurement of the pulse amplifier, for different frequencies.

Table 1. Results of measurement the parameters gain (G) and noise figure (NF) of the pulse amplifier, for different frequencies.

f (MHz)	G_{lab1} (dB)	NF_{lab1} (dB)	G_{lab2} (dB)	NF_{lab2} (dB)	G_{lab3} (dB)	NF_{lab3} (dB)	G_{lab4} (dB)	NF_{lab4} (dB)
20	36.0	4.4	36.0	4.7	34.8	4.9	35.7	4.5
118	37.0	4.3	36.9	4.5	35.7	4.6	36.4	4.6
216	36.9	4.3	36.6	4.5	35.5	4.6	36.6	4.4
314	37.0	4.4	36.9	4.5	35.5	4.6	36.3	4.4
412	36.8	4.3	36.5	4.5	35.5	4.6	36.3	4.5
510	36.6	4.4	36.2	4.5	35.2	4.6	36.2	4.6
608	36.3	4.5	37.2	4.6	34.7	4.6	35.8	4.8
706	35.5	4.5	35.0	4.6	33.9	4.7	34.7	4.6
804	34.3	4.5	34.1	4.6	32.9	4.9	34.4	4.6
902	33.2	4.5	33.4	4.7	31.2	4.9	32.2	4.8
1000	32.0	4.6	31.6	4.8	29.6	5.0	31.1	5.0

Table 2. Results of z-score for gain (G) of the pulse amplifier, for different frequencies.

f (MHz)	z_{Glab1}	z_{Glab2}	z_{Glab3}	z_{Glab4}
20	0.77	0.83	-1.65	0.05
118	0.99	0.78	-1.53	-0.24
216	0.93	0.43	-1.69	0.33
314	0.92	0.82	-1.56	-0.19
412	1.03	0.49	-1.64	0.11
510	1.12	0.29	-1.62	0.21
608	0.34	1.34	-1.43	-0.25
706	1.21	0.47	-1.51	-0.18
804	0.64	0.29	-1.70	0.77
902	0.81	1.00	-1.50	-0.30
1000	1.02	0.57	-1.62	0.04

Table 3. Results of z-score for noise figure (NF) of the pulse amplifier, for different frequencies.

f (MHz)	$z_{NF1lab1}$	$z_{NF1lab2}$	$z_{NF1lab3}$	$z_{NF1lab4}$
20	-1.21	0.36	1.44	-0.58
118	-1.57	-0.12	0.61	1.07
216	-1.37	0.57	1.26	-0.46
314	-1.04	0.19	1.55	-0.70
412	-1.32	-0.18	1.49	0.01
510	-1.50	-0.22	1.18	0.55
608	-1.31	-0.25	0.07	1.49
706	-1.36	0.00	1.47	-0.10
804	-1.15	-0.30	1.60	-0.16
902	-1.48	-0.21	1.26	0.42
1000	-1.47	-0.36	0.82	1.01

5. CONCLUSION

Due to the need to validate the accuracy of the implemented Y-factor method of measuring the noise figure using an EMI measuring receiver (in general, a spectrum analyzer), the Department for Electromagnetic Compatibility and Environmental Impacts in the TTC initiated and organized an intercomparison of the noise figure and gain measurement for the amplifier. A total of four meters from two laboratories, were used in this intercomparison. Three meters (one EMI receiver and two spectrum analyzers) were provided by TTC, while the noise figure meter was provided by the Military academy.

The result of intercomparison (gain and noise figure) according to frequencies is represented by the numerical value of the z-score model in Tables 2 and Table 3. Based on the presented results, we conclude that the values of z-score, $|z| \leq 2$ and that the results are satisfactory (acceptable), and no corrective measures are needed. This shows that the deviations in the measurements, the values of the gain or noise figure between the four meters are acceptable in the entire frequency range of the meters.

The goal of the intercomparison is to validate implementation of Y-factor method for noise figure

measurement using EMI measuring receiver is fulfilled. EMI measurement receiver can be used to measure noise figure and gain of amplifier.

For the further work was planned to calculate the budget of measurement uncertainly.

References

- [1] Opšti zahtevi za kompetentnost laboratorija za ispitivanje i laboratorija za etaloniranje, SRPS ISO/IEC 17025:2017/Ispr.1:2018.
- [2] <http://www.toc.vs.rs>.
- [3] Sistemi menadžmenta kvalitetom — Zahtevi, SRPS ISO 9001:2015.
- [4] Poslovnik o kvalitetu tehničkog opitnog centra, Interni dokument A.00.001, TOC, 2010.
- [5] Pravila o učešću u programima za ispitivanje osposobljenosti i međulaboratorijskim poređenjima, ATS-PA02, Akreditaciono telo Srbije, Beograd, jul 2021.
- [6] <http://www.va.mod.gov.rs>.
- [7] <http://www.mathworks.com>.
- [8] NENAD M.: Upporedna analiza merenja faktora šuma, 14. Telekomunikacioni forum TELFOR 2006, Belgrade, 2006.
- [9] W. J. ANSON: The Measurement of Noise Performance Factor: a Metrology Guide, U. S. government printing office, WA, 1972
- [10] Service Manual for Noise Figure Meter HP 8970B, HP, CA, USA.
- [11] Noise Figure Measurement Accuracy – The Y-Factor Method (PDF), Application Note 57-2, Keysight Technologies, 2010, retrieved 2 September 2011
- [12] Conformity assessment – General requirements for proficiency testing, ISO/IEC 17043:2010,
- [13] Statistical methods for use in proficiency testing by interlaboratory comparisons, ISO 13528:2005.



CONTROLLING AND INTERNAL AUDITING AT THE MINISTRY OF DEFENCE

IGOR ĐORIĆ

Military Technical Institute, Belgrade, allslovenac@yahoo.com

MIHAJLO RANISAVLJEVIĆ

Military Technical Institute, Belgrade, mranisan@gmail.com

MARKO MILOJEVIĆ

Singidunum University, Belgrade, mmilojevic@singidunum.ac.rs

Abstract: *This paper discusses the theoretical foundations and definitions of controlling and internal auditing as tools that help the organisation's management in managing business compliance and business continuity, with the purpose of meeting the organisation's objectives, by assessing the effectiveness of risk management inside the organisation, as well as of control and management. Considering the contemporary trends in organisational management, where the management is faced with frequent crises that require rapid and comprehensive action and response to risks, where internal auditing information is focused on the past, there is a need to implement controlling in organisations to provide help to the management for the future. The aim of this paper is to highlight the need to introduce controlling at the Ministry of Defence in order to improve the work of this organisation and to provide strong support in preventing the existing problems and to develop innovative systems of solutions that go beyond mere financial reporting.*

Keywords: *controlling; audit; management; Ministry of Defence.*

1. INTRODUCTION

System of internal controls, being one of the segments of controlling public spending in the Republic of Serbia, is defined by regulations governing financial business risk management. Ministries and public sector companies have an obligation to establish such organisational and managerial structure so as to provide for the legitimacy of the business, including adherence to guidelines and applicable standards, with continued monitoring of adequacy and effectiveness of this structure in practice. Monitoring and control over public spending should also ensure the achievement of strategic objectives and an organisation's objectives, which are to be used to inform the public on a regular and transparent basis of the results and activities of all actors in the public sector (1).

The Ministry of Defence is one of the key beneficiaries of public funds that has introduced the principle of internal controls by way of legal regulations. The system of internal controls includes a series of controlling activities of individual sections and individuals in the defence system, but this paper will focus on the financial management and control system and internal auditing. The person responsible for establishing the said systems by applying and developing them is the Minister of Defence. The implementation of the systems of internal control is the responsibility of all categories of beneficiaries.

The purpose of this paper is to highlight the need of introducing and permanently applying controlling at the Ministry of Defence. The first part of the paper defines

the concepts of controlling and internal auditing in general. The second part of the paper presents an analysis of the existing legal norms governing internal controls in the Republic of Serbia by introducing the system of financial management and control (FMC) and internal audit. The third part of the paper examines the efficiency and content of the system of internal controls, financial management and control and internal audit at the Ministry of Defence, the regulations that govern it, thus demonstrating to the scientific community that the system of internal controls is an effective way to ensure that an organisation conducts its business based on public spending in a legal and cost-saving way.

The primary hypothesis of the paper is: Controlling, as a partner to management, is a necessary tool for effective risk management and response.

The paper includes an analysis of the Consolidated Annual Report on the Status of Internal Financial Control in the Public Sector in 2020 and an analysis of the measures provided in the Reports on Overview of the Work Quality of Internal Auditing in the Republic of Serbia in 2016, 2017 and 2019, as well as in the reports of the State Audit Institution for 2018, 2019 and 2020, which imply the direction in which the very system of internal controls should evolve.

2. THE CONCEPT OF CONTROLLING AND INTERNAL AUDIT

The need for establishing internal controls in the public sector emerged in the second half of the 20th century as a

democratic legacy in countries with developed economies. As education and eloquence of their citizens continued to grow, a need to make the public sector's business more transparent also emerged, thus boosting the interest among the public. Systems of internal controls are to provide support and help the management of businesses of public fund beneficiaries. The purpose of internal controls is to ensure a legitimate course of action in achieving the set objectives, to enhance and monitor efficiency and effectiveness of doing business, to protect against non-earmarked expenditure of funds and to assist in discovering frauds. By way of reporting, it should also present results of the organisation as "public value" (2).

Internal control in general can be observed from a timeline perspective, it being:

1. preventive – before or at the very beginning of an activity;
2. ongoing or detective – during the activity;
3. subsequent or corrective – at the very end or after the activity has been conducted, with the purpose of reviewing mistakes, omissions and frauds (3).

Controlling originally appeared as a form of assistance to company management, prior to and during the process of planning and conducting the activities. It emerged as a key factor of management focused on profit, whereas in the non-profit organisations it served as assistance to public fund beneficiaries in managing and achieving the set objectives. Therefore, controlling is a process and way of thinking that is formed inside a team of managers and controllers as a cross-section of two sets of responsibilities and duties (Figure 1) (4).

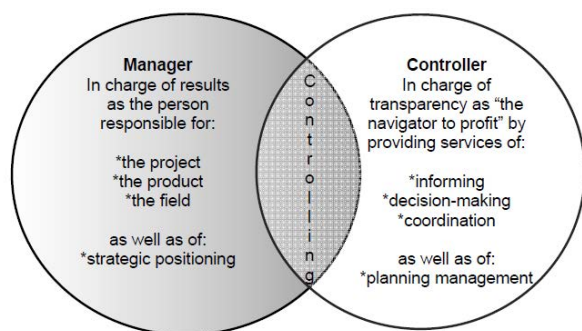


Figure 1. Controlling as a cross-section of activities of managers and controllers.

Source: (Marjanović V. 2013).

Control is often identified with controlling. These two concepts, however, are not identical in their primary function. Controlling refers to the function within an entity dedicated to enhancing efficiency and effectiveness in the implementation of plans for the purpose of achieving objectives and adapting the processes threatened by internal and external risks. As a tool for coordination of business processes, controlling is focused on the future (5).

Internal audit is, on the other hand, a control of public spending conducted after the activity has been completed and it ranges from verifying the accuracy of financial documents to making a critical assessment of the activity completed.

In contemporary practice, audit is a process of independent and objective verification of an organisation's financial accounts. The importance of audit depends on the context in which it appears. Nowadays there have been quite a few talks about the audit of privatisation, which essentially means to revise the transformation of property structure of social enterprises and public companies. This term is sometimes observed also in the judiciary sector – in the form of auditing questionable processes or laws. This refers to the renewal of certain judicial procedures, based on evidence, that might radically alter the court's final decision, or to the revision of laws that need to be adapted to new trends. The most important forms of auditing, however, take place in the economy sector. Throughout the history of evolution of economic thought, many authors and institutions have tackled the scientific definition of the concept of audit.

International standards on auditing define auditing as follows: the objective of auditing of financial statements is to enable the auditor to express an opinion on whether the financial statements are prepared, in all material respects, in accordance with an applicable financial reporting framework (6).

G. Vinten points out that internal auditing is a continued and detailed inspection of seemingly sound organisations with the aim of obtaining insight into the actual status or position of the organisation and its environment, so as to attain better control over its future business (7). Unlike other definitions of internal auditing, this definition emphasises the need to place focus of internal auditing on improvement of future business and not only on reviewing past events.

Essentially, internal auditing is an inspection of accounts relying on financial indicators and statements, whereas controlling is a permanent inspection of the achievement of the set objectives of the entire organisation.

3. LEGAL GOVERNANCE OF INTERNAL CONTROLS IN PUBLIC FUND BENEFICIARIES

A series of legal documents has been adopted in the Republic of Serbia that monitors and controls public expenditure through budget and special types of controls. Budget execution implies control of budget funds expenditure, whereby the Law on Budget System envisages several levels of control, organised as internal and external control. The Law on Budget System defines that public fund beneficiaries are to establish two forms of internal controls in their respective organisations, those being financial management and control and internal auditing (8).

The legislator has defined financial management and control in the form of a rulebook as a system of policies, procedures and activities aimed at achieving objectives. The primary objectives that public fund beneficiaries are to set through risk management are the following:

1. doing business in compliance with regulations, internal acts and contracts;

2. completeness, veracity and integrity of financial and business statements; and
3. sound financial management and protection of assets and data (9).

System of financial management and control is in the jurisdiction of the manager of a public fund beneficiary and the managers of their lower-level organisational units. Monitoring and evaluation of this system is carried out by the employees by way of self-assessment based on the 2013 COSO framework and by way activities of internal auditing. Therefore, this system does not exclude subjectivity, whereas the responsibility for establishing and developing the system is delegated on a beneficiary level.



Figure 2. Establishing a system of financial management and control in the key public fund beneficiaries in the Republic of Serbia.

Source: Consolidated Annual Report on the Status of Internal Financial Control in the Public Sector in the Republic of Serbia in 2020.

Based on the Consolidated Annual Report on the Status of Internal Financial Control in the Public Sector in the Republic of Serbia in 2020, it is evident that this status is

not at the required level in ministries, which are expected to adopt a higher standard of implementing financial management and control. Insufficient attention is being paid to introducing systems of internal controls, risk management strategy and description of the business processes (Figure 2).

On the other hand, independent internal audit in an organisation is a prerequisite for objective overview of the status and for making an evaluation of the results that corresponds to the requirements of the legislator and the public. This is also supported by the fact that when internal audit operates independently, it provides objective assessments and recommendations and it is efficient in providing an added, higher level of monitoring of the internal controls and has a vital role in the risk management process.

According to the Rulebook on Common Criteria for Organisation and Standards and Methodological Instructions for Internal Audit Operations and Reporting in the Public Sector, public fund beneficiaries have an obligation to establish internal audit. They are required to do so by forming a functionally independent organisational internal auditing unit within their organisation (if they have more than 250 employees) or to hire an internal auditor (if the public fund beneficiary is under the threshold for forming a separate organisational unit) (10).

Establishing internal audit units in the public sector

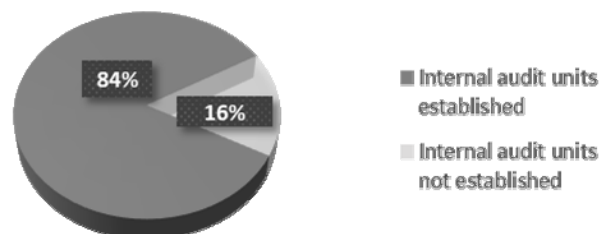


Figure 3. Establishing internal audit units in ministries and organisations of public fund beneficiaries in the Republic of Serbia.

Source: Reports on Overview of the Work Quality of Internal Auditing in the Republic of Serbia for 2016, 2017 and 2019. Central Harmonization Unit, Internal Audit Department, Ministry of Finance.

Reports on Overview of the Work Quality of Internal Auditing in the Republic of Serbia for 2016, 2017 and 2019, covering the period from January 1st, 2015 to September 30th, 2019 and including 31 entities with obligation to introduce internal auditing, state that 83.9% of the ministries and organisations of public fund beneficiaries have established internal auditing units (Figure 3).

Out of the total number of inspections of the work quality of internal auditing, 18 entities, i.e., 58.1%, did not provide even the minimum prescribed number of internal auditors, which raises doubts concerning absolute adherence to the internal auditing standards (11).

4. FINANCIAL MANAGEMENT AND CONTROL AND INTERNAL AUDIT AT THE MINISTRY OF DEFENCE AND THE SERBIAN ARMED FORCES

System of internal controls of public spending in the Ministry of Defence and the Serbian Armed Forces is defined pursuant to bylaws in jurisdiction of the Minister of Defence, whereas the authorising officers are responsible for establishing efficient internal control when it comes to the defence system.

Internal control of costs for military purposes, expressed in the budget of the Republic of Serbia, is carried out by the financial service authorities of units and departments of the Ministry of Defence and the Serbian Armed Forces, the Accounting Centre of the Budget and Finance Sector with the Ministry of Defence, the Defence Inspectorate, the Military Intelligence Agency and Criminal-Investigation Team and internal audit of the Ministry of Defence (12).

In 2011, the Rulebook on Financial Operations in the Ministry of Defence and the Serbian Armed Forces introduced the principle of financial management and control. Organisational unit of the Ministry of Defence in charge of the budget and finance manages the operations of the finance department within its jurisdiction and, in addition to other tasks, it is in charge of introducing the system of financial management and control in the Ministry of Defence. Authorising officers on all levels of command up to level-four material and financial authorities (MFO) are responsible for establishing the system of financial management and control, and it is the duty of both authorising officers and all the employees to implement this system (13).

The Rulebook specifies that the system of financial management and control is a component of public internal financial control and that it is observed as an entire system of financial and nonfinancial controls, including all elements of the organisation. It also stipulates that risk management will, to a reasonable extent, provide guarantees that the organisation's objectives will be achieved.

The Consolidated Annual Report on the Status of Public Internal Financial Control in the Republic of Serbia in 2020 does not say that the Ministry of Defence has had any omissions whatsoever in carrying out its implementation and reporting duties. The system of financial management and control at the Ministry of Defence works, but not to the extent that is necessary. The key reasons that justify this relate, primarily, to the fact that while introducing the system, the managing officers in charge did not pay sufficient attention to it nor did they have interest in doing so (14).

The fact that the risk management strategy is updated every three years and that the controls that are to reduce risks to an acceptable level are carried out once a year leads to a conclusion that in times of frequent global crises, especially in light of the recent events including the COVID-19 pandemic and the Ukraine war, the

dynamics of risk management is not appropriate and that the response to the challenges is untimely.

In the same year when the system of financial management and control was established at the Ministry of Defence, the internal auditing department was established, as well, and internal acts were adopted, as well as the Internal Auditing Charter and internal auditing ethical code, all of which has made it possible to establish internal auditing in the defence system. On the other hand, the internal auditing department is an independent authority in the organisation of the public fund beneficiary that reports directly to the incumbent Minister of Defence.

The tasks of the internal auditing department at the Ministry of Defence are governed by the Rulebook on Internal Organisation and Job Systematisation. Those are the following: reviewing compliance with the existing financial regulations, instructions and procedures; evaluating effectiveness of internal controls; evaluating effectiveness of exploitation of funds; inspecting reliability and integrity of record-keeping and reporting; payments and contracts; reviewing accounting statements; inspecting irregularities; regularity of revenue collection and record-keeping thereof; security of property and lists thereof, i.e., cataloguing property; inspection of the budget distribution, so as to ensure legal compliance and secure sufficient funds; and other tasks included in the scope of the department's operations (15).

The scope of operations of the internal auditing department is not limited. It includes all programmes, procedures and activities. It has free access to all managing officers and their employees, all the records, property and data that are the subject of auditing. Internal audit at the Ministry of Defence operates independently and plans its work programme based on an overall risk assessment. It regularly adopts a three-year internal auditing strategic plan, as well as annual plans of internal auditing. From 2018 to 2020, it audited 13 entities and issued 93 recommendations (Figure 4).

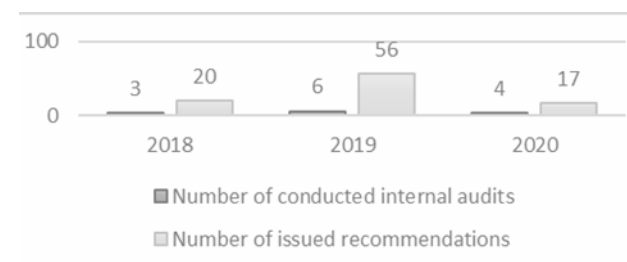


Figure 4. Overview of conducted internal audits at the Ministry of Defence and the number of issued recommendations.

Source: Report on Auditing Financial Reports of the Ministry of Defence for 2018, 2019 and 2020. State Audit Institution.

All incompliances and irregularities identified while auditing the presented documentation of the inspected activities relate to the financial indicators and data. Recommendations have been made regarding thereof so as to eliminate the said irregularities. There were no

recommendations classified as high or low priority. In the statements, the auditors only identified medium-priority reporting errors, irregularities and mistakes that affect the financial reports when there is no immediate risk of loss (Figure 5). No immediate response upon identifying the problems was necessary. They were rather to be rectified before preparing the following report.

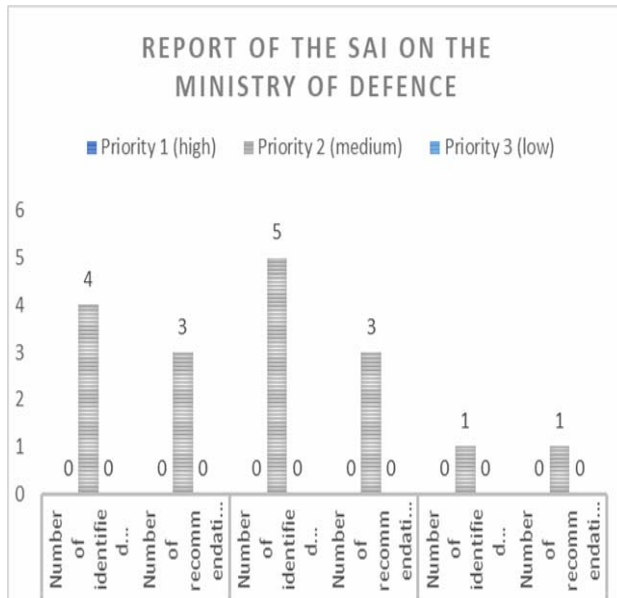


Figure 5. Overview of the issued recommendations per priority for the Ministry of Defence.

Source: *Report on Auditing Financial Reports of the Ministry of Defence for 2018, 2019 and 2020.* State Audit Institution.

The system of internal controls at the Ministry of Defence is legally governed by a series of regulations, instructions, procedures and activities, including the organisational structure, and it is formally introduced on all levels of command and management and implemented in practice. Internal controls, financial management and control and internal audit are defined as components of internal financial controls, but due to insufficient attention paid to the nonfinancial indicators, there is a need to introduce controlling. Among other things, the role of controlling is to plan and report, continually, by combining nonfinancial and financial reports, with the purpose of achieving the organisation's set objectives.

5. CONCLUSION

Modern way of managing business entities is not just the focus of managing budget execution and controlling the earmarked funds expenditure, but also nowadays, in this growingly turbulent business environment, successful risk management, as well as compliance with the legal norms, are becoming the objectives of success. Such defined objectives focus on financial management, and insufficient attention is being paid to the results.

Internal auditing as a function of subsequent control provides entry parameters for establishing an efficient system of financial management and control, but in the very delivery of material and financial management. The

overall objectives of an organisation require constant monitoring of procedures, activities, management operations and risks. Therefore, introducing controlling as a separate function and employing expert personnel, a certified controller, would provide the management with full control over achievement of objectives for the benefit of the entire organisation. The proposed thesis is confirmed by the fact that subjectivity is not excluded from the system of financial management and control. An independent and well-trained controller with full integrity would serve as a partner to the management, working together on identifying incompliances with the objectives, on having complete monitoring of risks and would also testify to the success of the organisation's business.

Controlling affects the quality of making business decisions and management, and it contributes to enhancing business quality. Based on above, a conclusion can be made that the level of development of controlling in the Republic of Serbia is not fully aligned with contemporary notions of its role in business, i.e., that the level of its development does not correspond to the attained level of development of this profession in countries with developed marked economies, but also that its implementation at the Ministry of Defence would offer a new dimension for a more efficient management of the entire organisation.

References:

- [1] Prirucnik za finansijsko upravljanje i kontrolu (2011). Ministarstvo finansija https://www.mfin.gov.rs/upload/media/s2Uug9_6010215bf36a9.pdf
- [2] Čupić, M. (2019). "Finansijsko upravljanje javnom upravom i vrednost za javnost" Zbornik radova sa 23. Međunarodnog kongresa „Jačanje kredibiliteta računovodstvene profesije kao imperativ zaštite javnog interesa“ (pp. 317-331). Savez računovođa i revizora Republike Srpske. Available at SSRN: <https://ssrn.com/abstract=3710687>
- [3] Stanišić M., Radović N. (2013). "Interna kontrola kao element kvaliteta u hotelskom poslovanju", Zbornik radova Sinergija 2013, Bijeljina, p. 633
- [4] Marjanovic V. (2013). "KONTROLING-skripta, Univerzitet Singidunum, ISBN: 978-86-7912-500-2
- [5] Osmanagić Bedenik, N. (2007). "Kontroling – Abeceda poslovnog uspjeha" (p. 80.) 3. dop. izd. Zagreb: Školska knjiga d.d.
- [6] Međunarodni okvir profesionalne prakse (MOPP), Udruženje internih revizora Srbije, edicija 2011. (6)
- [7] Pickett, S. (1997). "Profesionalna praksa interne revizije", Savez računovođa i revizora Srbije, Beograd. (7)
- [8] Zakon o budžetskom sistemu, Sl. glasnik RS, 54/09, 73/10, 101/10, 101/11, 93/12, 62/13, 63/13 - ispr., 108/13, 142/14, 68/15 - dr. zakon, 103/15, 99/16 i 113/17 (8)
- [9] Strategija razvoja interne finansijske kontrole u javnom sektoru u Republici Srbiji za period 2017–2020. godine, Sl. glasnik RS, 51/17 (9)

- [10] Ministarstvo finansija, Pravilnik o zajedničkim kriterijumima za organizovanje i standardima i metodološkim uputstvima za postupanje i izveštavanje interne revizije u javnom sektoru („Sl. glasnik RS“, br. 99/2011 i 106/2013). (10)
- [11] sajt Ministarstva finansija (11)
- [12] Knežević, M., Nikolić, S., & Neševski, A. (2021). Kontrola budžeta u funkciji civilne demokratske kontrole vojske u Republici Srbiji. *Vojno delo*, 73(3), 103-120. <https://doi.org/10.5937/vojdela2103103K> (12)
- [13] Ministarstvo odbrane i VS, Pravilnik o finansijskom poslovanju u MO i VS, Službeni vojni list, broj 17/11. (13)
- [14] Kostić, R. O., Žugić, R., & Radojković, M. (2014). Interna finansijska kontrola i finansijsko upravljanje u javnom sektoru i njihova uloga u sistemu odbrane. *Vojno delo*, 66(3), 238-254. <https://doi.org/10.5937/vojdela1403238k> (14)
- [15] Radojković, M. N., Žugić, R., & Trandafilović, S. K. (2016). Značaj interne revizije za Ministarstvo odbrane i Vojsku Srbije. *Vojno delo*, 68(2), 212-220. <https://doi.org/10.5937/vojdela1602212R> (15)



PROPOSAL OF SOLUTION FOR HYDRAULIC CONTROL OF OUTBOARD ENGINE ON "RIB-720 CANDO"

DRAGAN TRIFKOVIĆ

University of Defense in Belgrade, Military Academy, address: Pavla Jurisica Sturma 33, Belgrade, , dragantrif@ptt.rs

DARKO STRIČIĆ

Serbian Army, River Flotilla Command, address: 1300 Corporal 11, Novi Sad, strelens@gmail.com

ENIS DAUTI

Serbian Army, River Flotilla Command, address: 1300 kaplara 11, Novi Sad, dautienis1907@gmail.com

PREDRAG DOBRATIĆ

University of Defense in Belgrade, Military Academy, address: Pavla Jurisica Sturma 33, Belgrade, dobratipc@yahoo.com

SERIF BAJRAMI

University of Defense in Belgrade, Military Academy, address: Pavla Jurisica Sturma 33, Belgrade, bajramiserif@gmail.com

JELENA PAUNOVIĆ

Serbian Army, River Flotilla, address: 1300 Corporal 11, Novi Sad, jelenapaunovic95@gmail.com

Abstract: *The subject of this paper is analysis of the existing mechanical control system of outboard four-cylinder gasoline engine, model Yamaha F150FET 6 BMX, from the aspect of reliability and sustainability of the existing system. Followed with a detailed description of failure, the impact on maneuverability and problems faced by crew with reference to the material and the existing solution for making the sides of the boat (tube), resulted in finding a proposal for a solution to this problem. The following problems were observed in the work: inaccuracy and failure of the control system, poor response and poor sensitivity of the control system, frequent cracking of the existing PVC tube due to minimal mechanical damage. Therefore, in order to eliminate the identified deficiencies and engineering solutions for outboard management engine followed with replacement of the sides of the boat with a more durable material will result in fully meeting the requirements for the operation of the boat. Looking at the advantages and disadvantages of hydraulic and mechanical control systems, it was decided to approach the installation of a hydraulic control system, which characteristics (response, precision, ergonomics, reliability in operation) completely surpassed the existing mechanical control system. Also, considering the conditions of exploitation, which derive primarily from the specifics of the user (military unit), and following the poor characteristics of the PVC material along with the frequent bursting of the boat's tubes, market research was undertaken with the aim of rebuilding the old tubes and replacing them with a new tube made of the most modern, very durable material (Hypalon-Neopren).*

Keywords: *control system, worm gears, hydraulic gears, outboard engine, tube.*

1. INTRODUCTION

Rubber boat with a solid hull - RIB is a multi-purpose vessel with exceptional maneuverability, characterized by high speed, ease of handling, comfort, excellent navigational characteristics and stability.

The RIB-720 CANDO type boat (picture 1) definitely belongs to the group of vessels that can have all the features of a modern rubber boat with a solid hull, whose basic technical and nautical characteristics ensure efficient and effective execution of tasks on the water.



Figure 1. RIB 720 rigid hull inflatable boat – CANDO

It is primarily intended for the execution of a wide range of combat and non-combat activities, such as: search and rescue of victims, longitudinal and transverse transportation, patrolling in the area of ports and anchorages, reconnaissance of rivers, canals and lakes, support for diving activities, evacuation of the population by waterways and distribution of vital foodstuffs in case of natural disasters.

The basic parts of the boat are: flexible rubber tube, underwater part-hull, control panel and drive part.

The flexible rubber tube is made of five independent sections. It represents a part of the boat whose main purpose is to provide additional buoyancy, unsinkability and stability. Considering the purpose and important meaning, the tube is most often made of several sections, which increases the toughness of the boat in the event of a possible puncture or burst. In this case, the other, undamaged sections retain their function and ensure the boat's buoyancy, and all sections separately have valves for injecting or expelling air from the tube. The tube of the boat RIB-720 is made of PVC material, and it can be made of different types of materials: hypalon combined with neoprene, polyurethane or polyamide and the like.

The underwater part of the boat-hull is made of fiberglass in the so-called "V" profile in order to provide the necessary hydrodynamic form necessary for achieving high speeds and overcoming large waves while driving.

In case of water penetration, the boat is equipped with a drainage pump, which is located in the stern part.

The control panel is intended for remote control of the boat, monitoring driving parameters such as speed, distance traveled, boat position, fuel level and other information required for nautical driving. Commands are transmitted to the boat's drive through the control panel and in this way the desired action is realized (driving on the course, speed control, various maneuvers, etc.).



Figure 2. Outboard engine Yamaha type F150FET 6 BMX

The boat is powered by an installed outboard four-stroke engine manufactured by Yamaha type F150FET 6 BMX. The engine has a supporting electro-hydraulic system that, in addition to changing the trim while driving, also ensures bringing the engine into the transport position during transport by trailer.

In order to protect against corrosion, it has zinc protectors installed (on the outside of the engine and in the cooling system). The engine has a so-called "Trim & Tilt" system intended for adjusting the angle of the engine or propeller while driving, which results in better performance of the boat as a whole (start, acceleration, speed, economy).

Table 1. Basic technical data of the outboard engine

BASIC TECHNICAL DATA			
Basic information about the boat CANDO		Basic information about the engine Yamaha type F150FET 6 BMX	
type	RIB	outboard type	four-stroke gasoline
length over all	7.20 m	volume	2670 cm ³
width over all	2.85 m	number of cylinders	16
internal length	5.35 m	diameter of cylinder	94 mm
max. internal width	1.75 m	power on the propeller	110.3 kW (150HP)
tube diameter	0.54 m	maximum number of revolutions	4500–5500 min
number of chambers	5	dry engine weight	223 kg
weight, without engine	815 kg	transmission ratio	2.0 (28/14)
the maximum number of persons allowed	15	/	/
maximum load capacity	3600 kg	/	/

The advantages that RIBs have over vessels of similar size are primarily the result of excellent nautical characteristics. For example, one of the positive nautical features of this boat is its excellent stability. Through testing, it was established that thanks to the given constructive solutions, the boat can successfully resist the force that causes tilting, due to the unevenly distributed load, and thus prevent unwanted overturning.

The turn maneuver with full deflection of the engine to one side and the other is performed with about 85% of the maximum power of the engine, whereby the boat successfully performs the turn without feeling a loss of stability or an excessive heeling angle. Also, at small deflections of the rudder and at maximum speed, the vessel has excellent maneuverability and stability. Finally, at low speeds it is possible to successfully maintain the set course, and the stopping manoeuver after reducing the maximum engine throttle to zero is realized in a short time and over a short distance (the stopping distance is 3-4 boat lengths).

2. ENGINE MANAGEMENT SYSTEM ON RIB-720 CANDO BEFORE REPLACEMENT

Control of the Yamaha F150FET 6 BMX outboard engine, changing the direction of the vessel, was done through the steering head (a mechanical steering system consisting of a worm gear system and a toothed cable).

The mechanical control system in the previous examples proved to be very unreliable in operation. Given that the RIB-720 "CANDO" as a vessel is used in dynamic conditions that require sudden changes in the direction and direction of navigation, the mechanical steering system was not able to keep up with the required work dynamics, precision in management and system response. During sudden changes in the sailing direction, due to the small pitch of the thread on the toothed cable of the mechanical system, as well as the poor characteristics of the material of the worm gears, the cable "skipped" and the control system failed.



Figure 3. Previous mechanical control system

The failure of the mechanical control system was manifested by inaccuracy and the impossibility of controlling the RIB-720 CANDO, poor (late) response of the control system, the impossibility of positioning the RIB in the desired direction as well as the turn and greatly affected the ergonomic working conditions of the crew.

Given that the current mechanical control system has proven to be very unreliable in operation, considering the advantages and disadvantages of hydraulic systems, experts from the flotilla proposed replacing the existing mechanical control system with a new hydraulic control system.

3. NEW HYDRAULIC STEERING SYSTEM ON RIB 720 CANDO

3.1. Advantages and disadvantages of hydraulic systems

Hydraulic system is a technical system, which in general, represents set of devices capable of transferring energy and information using hydraulic fluid.

The hydraulic system converts the mechanical energy into hydraulic one and vice versa.

A medium for converting and transferring energy to hydraulic systems is fluid in which the volume must not significantly change by the action of an external force (incompressible fluids).

The main advantages of hydraulic drives are:

- very low weight, dimensions and moments of inertia,
- simple overload protection,
- the possibility of obtaining large transmission ratios without use of reducers,
- possibility of continuous change of speed and direction,
- very simple conversion of rotary to translational getting around,
- high speed of response, due to practical incompressibility hydraulic oil.

Basic disadvantages of hydraulic systems:

- sensitivity to dirt,
- loss of energy, which turns into heat, especially in throttle control,
- occurrence of internal and external losses,
- the possibility of air penetration into the system,
- the influence of temperature changes on the operation of the system.

3.2. Description of the newly installed hydraulic control system

Due to the previously mentioned malfunctions, the existing mechanical control system was replaced by a new ULTRAFLEX hydraulic system.

Newly installed hydraulic steering system (ULTRAFLEX) consists of a hydraulic steering pump located on instrument panel, cylinder which is connected to the outboard engine and connecting hoses. In normal working conditions and initiated by turning the steering wheel, the pump will pump the oil flowing through the engine and hose to the cylinder, in the desired direction of deflection. As a result, there is the movement of a cylinder which instantly moves the engine connected to the cylinder. The pump is equipped non-return valve, which prevents the return of outgoing liquid along the same hose, and therefore system operation and engine management with two or more control stations is enabled.

The system consists of:

1. Hydraulic pump UP28 T (It can only be used with the tilt X52 mechanism). Working volume per revolution - 28 cc. Number of clips - 5 pieces. Pressure 70 bar. Weight - 5 kg. Maximum supported steering wheel diameter - 710mm.
2. Steering wheel tilt mechanism X52. It allows a maximum tilt of 48°.
3. Hydraulic hoses Length - 6.5 m (Number - 2 pieces).
4. Hydraulic cylinder UC-128-OBF/1. Cylinder volume - cc 120. Thrust - 450 kg. Diameter Extensions - 3/8".

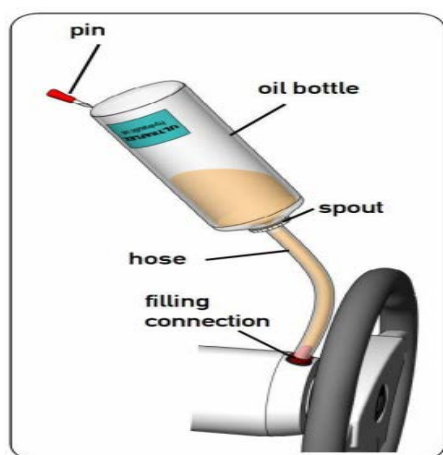


Figure 4. New hydraulic steering system (ULTRAFLEX)

The new hydraulic control system is designed in accordance with UNI-EN-ISO 10592 and A.B.I.C. P21 regulations, and can operate at temperatures between -18°C (0°F) and $+77^{\circ}\text{C}$ ($+170^{\circ}\text{F}$). All components are made using materials and work processes that offer system safety and reliability in the most extreme conditions.

4. REPLACING THE TUBE ON THE RIB-720 CANDO

4.1. Description and characteristics of the tube before replacement

The flexible rubber tube of the boat RIB-720 was made of PVC material, where it was transversely divided into five independent sections.

As a part of the boat whose basic purpose is to provide additional buoyancy, unsinkability and stability, the characteristics of the material from which it was made (PVC), did not fully meet the strict requirements of the user (military unit), and above all in the domain of reliability and durability of the tube.

In the conditions of dynamic driving, during the realization of regular and training tasks, violent landings on untidy shores of water surfaces, there were bursts of existing tubes and due to small mechanical damages, which greatly affected the navigation of the boat, the performance of tasks as well as demotivating the boat's crew.



Figure 5. Damaged tube on the bow part

Due to the poor characteristics of the PVC material and the frequent bursting of the boat's tubes, market research was undertaken with the aim of rebuilding the old tubes and replacing them with a new tube made of the most modern, very durable material (Hypalon-Neopren).

4.2. Description and characteristics of the newly installed tube

After market research, the replacement of the existing (PVC) tubes with new tubes was carried out at the plant of ADVANCE, which also replaced the control system with a new hydraulic control system. The newly installed tubes are made of the most modern Hypalon-Neoprene (CSM) material.

The French company Pannel & Flipo is the world's most famous company specializing in production Hypalon-Neoprene material for special purposes, under the brand name "Orca". Tradition in this company has been producing materials for over 50 years. Premium Hypalon-Neoprene canvas is the highest quality material for making tubes in the world.

This is supported by the fact that all military and special purpose boats are made from of this material. Durability, elasticity, resistance to wear, damage and UV rays, the simplicity of maintenance, and the tightness of the chambers on the seams of the boats, are fundamental characteristics that set this material apart from all others. It is safe to say that the tubes produced from this material are in the category the best in the world.

5. CONCLUSION

The newly installed hydraulic control system has completely surpassed the existing mechanical control system in terms of its characteristics (responsiveness, control precision, ergonomics, operational reliability).

The first replacement of this control system was carried out in 2020, after which no malfunctions were observed in the operation of the new control system during a regular operation. The new outboard motor management system ensured the reliability of the RIB-720 CANDO, providing reliable maneuverability and precision. The improvement of these characteristics was especially noticed by the boat's crew during practice tasks in more extreme conditions and dynamic driving with sudden changes in manoeuvres. By replacing the mechanical control system with a new hydraulic system, as well as replacing the tube from PVC with a new tube made of durable Hypalon-Neoprene material, it fully met the expectations of the user. Lastly, based on empirical conclusions after two years of exploitation, RIB 720 CANDO can safely conclude that the new solution in fully responded to the strict demands of the user, and made the RIB 720 Cando more reliable and tougher.

References

- [1] Bajrami. S., *Modern means of river units - a rubber boat with a solid hull type RIB 720*, Military edition, Belgrade, 2017.

- [2] Advertout Advance-report, *Instructions for using and maintaining the tube*, Belgrade 2020.
- [3] Advertout Advance-report, *ULTRAFLEX hydraulic control system*, Belgrade 2020.
- [4] Askovic R., *Basics of hydraulics and pneumatics*, Faculty of Mechanical Engineering, Belgrade 1978.
- [5] Jovanovic, Z., *Hydraulics and pneumatics*, University of Belgrade in 2015.